EXPERIMENTALLY DETERMINED FULL-FIELD STRESS, STRAIN AND DISPLACEMENT ANALYSES OF PERFORATED FINITE MEMBERS

submitted to the Graduate School of the
University of Wisconsin-Madison
in partial fulfillment of the requirements for the
degree of Doctor of Philosophy

By

Abdul Aziz Khaja

Date of final oral examination: 05/03/2012

Month and year degree to be awarded: May 2012

The dissertation is approved by the following members of the Final Oral Committee:

Robert E. Rowlands, Professor, Mechanical Engineering
Roxann L. Engelstad, Professor, Mechanical Engineering
Dan Negrut, Associate Professor, Mechanical Engineering
Robert J. Witt, Associate Professor, Engineering Physics
Matt S. Allen, Assistant Professor, Engineering Physics

Experimentally Determined Full-Field Stress, Strain and Displacement Analyses of Perforated Finite Members

Abdul Aziz Khaja
Under the supervision of Professor Robert E. Rowlands
At the University of Wisconsin-Madison

Abstract

The integrity assessment of an engineering structure or member often requires knowledge of the full-field individual components of stress, strain and/or displacement. Evaluating these can be difficult for finite structures, contact problems, or if the material properties, loading or boundary conditions are unknown. Theoretical stress analyses of finite perforated geometries are virtually impossible. Both analytical and numerical techniques necessitate knowing the boundary conditions, the latter often being unavailable in practice. Results show errors can occur as one approaches a purely boundary collocation approach. Combining experimental information with analytical and numerical tools enables one to solve aforementioned situations. For example, values of a single component of displacement are used here to determine full-field individual components of stress, strain and displacements in isotropic or orthotropic structures and without explicitly differentiating the measured displacements. Discretely located single-element strain gages are used to determine full-field individual components of stress, strain and displacement in a perforated finite tensile plate and a diametrally-loaded ring. Thermoelastic stress analysis is combined with an Airy's stress function (in real polar coordinates) to stress analyze a mechanical

joint, a concentrated-loaded plate, and members containing an elliptical or multiple circular hole(s). The displacements and strains at the interface of a loaded bimetallic disk are determined.

Acknowledgements

All praise goes to Allah Subhanahu wa Ta'Ala (God Almighty) without whose help this dissertation would not have come about. To say that is also to acknowledge the support and guidance of all those that He placed around me all along, from beginning to the end.

I count myself fortunate in having been blessed with a mentor and advisor as knowledgeable and as fatherly as Professor Robert E. Rowlands. I want to thank him for his constant encouragement, his technical guidance and his editorial meticulousness. It is rare to find a supervisor who would pore through the advisee's thesis drafts as carefully as if it were his own work. I thank him for keeping me sane and stable.

I am no less grateful to my committee members, Professors Roxann L. Engelstad, Dan Negrut, Matthew S. Allen and Robert J. Witt.

Kudos to Carl J. Martin at UW-Madison for helping me in addressing numerical analysis; and to William G. Lang of Structures Lab for ensuring my teaching went about effortlessly in ME/EMA 307 – Mechanics of Materials Lab.

I would also like to make special mention of Dr. Don Matthys S.J. at Marquette University for his extensive technical help; similarly, John W. Dreger deserves all the gratitude I can show for skillfully mounting strain gages. Special thanks to Hidayath Ansari for helping me in computational programming, Luke Rucks for checking complex mathematical equations and

Nathan Matthew Cholewa for mounting strain gages and Dave Arawinko for his machining skills.

Of course I cannot thank enough my immediate family, my parents, Khaja Abdul Bari and Aysha Azeeza, my brothers, Khaja Abdul Baqui, Khaja Abdul Basith, and Khaja Abdul Muqtadar, and last but not the least my wife, Mohib Fatima for motivating and supporting me. Needless to say that I take full responsibility for all the blemishes and mistakes herein.

Table of Contents

Abstract ..... **i**

Acknowledgements ..... **iv**

List of Figures ..... **xiv**

List of Tables ..... **xlviii**

List of Symbols ..... **xlix**

Chapter 1 : Introduction **1**

1.1 Background 1

1.2 Novelty 2

1.3 Experimental Techniques 5

1.4 Analytical Background 7

Chapter 2 : Determining Individual Components of Stress, Strain and Displacement at and in the Neighborhood of a Cutout from Measuring a Single Component of Displacement **8**

2.1 Introduction 8

2.2 Relevant Equations 12

2.3 Simulated Experimental Input Data (FEA) 25

2.3.1 Introduction 25

2.3.2 Determining Individual Components of Stresses, Strains and Displacements from Measuring either u or v Displacements using FEA–Evaluated Airy Coefficients 36

2.4 Digital Image Correlation (DIC) 43

2.4.1 Introduction..... 43

2.4.2 Specimen Details 46

2.4.3 Data Processing and Number of Coefficients..... 51

2.4.4 Finite Element Analysis..... 54

2.4.5 Determining Individual Components of Displacement, Strain, and Stress from Measured *v* Displacements using Experimentally-DIC Evaluated Airy Coefficients..... 56

2.4.6 Experimental Validation..... 61

2.4.7 General Comments..... 64

2.5 Summary, Discussion and Conclusions.....65

Chapter 3 : Full-Field Determining Stress and Strain Components in the Vicinity of a Cutout from Discretely Measured Strains Only in One Direction 67

3.1 Introduction.....67

3.2 Relevant Stress Function (Airy's Stress Function) 70

3.3 Specimen Details and Loading 73

3.4 Data Processing and Number of Coefficients 83

3.5 Finite Element Analysis.....89

3.6 Results.....90

3.7 Validation of Results 100

3.8 Summary, Discussion and Conclusions.....101

Chapter 4 : Full-Field Stress Analysis of a Diametrically Loaded Ring using Five Stain Gages 103

4.1 Introduction.....103

4.2 Physical Set-up 105

4.3 Relevant Stress Function (Airy's Stress Function) 108

4.4 Experimental Details 112

4.5 Data Processing.....115

4.6 Finite Element Analysis.....119

4.7 Results.....120

4.8 Validation.....128

4.9 Summary, Discussion and Conclusions.....131

Chapter 5 : Thermoelastic Stress Analysis of a Finite-Plate containing an Elliptical Hole.....135

5.1 Introduction.....135

5.2 General Comments 138

5.3 Airy Function and Stresses 145

5.4 Experimental Details 155

5.4.1 Specimen Details and Preparation 155

5.4.2 Specimen Loading 157

5.4.3 TSA Recording 160
5.4.4 TSA Calibration 164
5.5 Data Processing 168
5.6 Analysis 170
5.6.1 Measured TSA Input Data and the Number of Airy Coefficients 170
5.6.2 Finite Element Analysis 181
5.6.3 Results 183
5.7 Strain Gage Analysis: 192
5.8 Checking Equilibrium 201
5.9 Effect of Varying Pixel Distance from the Edge of the Hole 202
5.10 Summary, Discussion and Conclusions 203
Chapter 6 : Investigation of Inverse Problem Using Thermoelastic Stress Analysis 207
6.1 Introduction 207
6.2 Relevant Stress Function and Stress Components 211
6.3 Test Configurations 217
6.3.1 Considering two different Test Configurations 217
6.3.2 Test Specimen Details 222
6.3.3 Circular Pin/Bolt 224
6.3.4 Non-circular Pin/Bolt 226
6.3.5 Back loading Fixture 228
6.3.6 Assembly 231

6.4 Experimental Details 233
6.4.1 Specimen Preparation and Loading 233
6.4.2 Circular Pin 239
6.4.3 Non-circular Pin 242
6.4.4 Calibration 244
6.5 Data Processing 250
6.5.1 Imposing Traction-free conditions 254
6.5.2 Number of Coefficients and Input Values 268
6.6 Strain Gage Readings 273
6.7 Numerical Analysis 277
6.7.1 Finite Element Modeling 277
6.7.2 Geometry 279
6.7.3 Mesh Generation 282
6.7.4 Boundary Conditions and Loading 285
6.7.5 General Details 288
6.8 Results 300
6.8.1 Contour Plots 311
6.9 Load Equilibrium 319
6.10 Summary, Discussion and Conclusions 324
6.11 Acknowledgement 331
Chapter 7 : Simplified Stress Functions for Complicated Geometries and Loading 332
7.1 Introduction 332

7.2 Stress Functions and Stresses 338
7.3 Thermoelastic Stress Analysis 357
7.4 Finite Element Analysis 365
7.5 Results 368
7.6 Summary and Conclusions 373

Chapter 8 : Thermoelastically Determined Stresses of Multiple Holes in a Finite Plate 375

8.1 Introduction 375
8.2 Experimental Details 382
8.2.1 Specimen Details, Preparation and Loading 382
8.2.2 TSA Recording and Calibration 387
8.3 Data Processing 397
8.4 Finite Element Analysis 400
8.5 Number of Coefficients and Input Values 404
8.5.1 General Comments 404
8.5.2 Analyses of Symmetrically-Loaded Plate 406
8.5.3 Analyses of Unsymmetrically-Loaded Plate 413
8.6 Results 421
8.6.1 General Comments 421
8.6.2 Results for the Symmetrically-Loaded Plate 422
8.6.3 Results for the Unsymmetrically-Loaded Plate 429
8.7 Strain Gage Analysis 436

8.8 Imposing Stress Compatibility between the Holes in the Symmetrically-Loaded Plate.....448

8.9 Checking Load Equilibrium 455

8.10 Summary, Discussion and Conclusions.....456

Chapter 9 : Determining the Full Field Displacement, Strain and Stress Components in a Perforated Finite Orthotropic Plate from a Single Component of Displacement 458

9.1 Introduction.....458

9.2 Relevant Equations 460

9.3 Literature Review 471

9.4 Analysis and Results.....476

9.5 Conclusion 483

Chapter 10 : Summary and Conclusions 485

Considerations for Future Research 487

Bibliography 491

Appendices.....502

A2 Evaluating Strain and Displacement Equations for a Finite Plate with Circular Hole.....502

A3.1 Additional Results for Number of Coefficients, *k = 13*. 537

A3.2 Determining the Cartesian Components of Stress and Strain. 547

A4 Approaching the Boundary Collocation Method 566

A5 Stress Equations Corresponding to a Finite plate containing an Elliptical Hole. [25, 29 - 35] 584

A6 Thermoelastic Stress Analysis of a Finite Plate Loaded by a Circular Pin. 625

A7 Stress Equations for a Plate Symmetric about x-axis. 646

A8 Check against the Assumption of Plane Stress using 3-D FEA ...689

A* Non-Destructive Evaluation of Diametrically-Loaded Bimetallic Disk 694

List of Figures

Fig. 1.1: Thermoelastic effect on the specimen [3] 6
Fig. 2.1: Uniaxially-loaded plate 13
Fig. 2.2: Displacement components, *u* and *v*, with respect to rectangular Cartesian coordinates (x,y) and u_r and u_θ with respect to polar coordinates (r, θ) when point P moves to P* [7] 22
Fig. 2.3: Plate Geometry (actual plate loaded horizontally but shown here vertically so to locate its length in the long direction of the page) 26
Fig. 2.4: Finite Element Model for the perforated plate of *figure 2.3* 28
Fig. 2.5: (a) Selected data locations for displacement components determination. (b) Source locations of 651 individually used inputs for determining Airy coefficients when satisfying traction-free conditions *analytically* at the hole 29
Fig. 2.6: Plot of condition number, *C*, vs. number of coefficients, *k*, for *m = 651* input values .. 33
Fig. 2.7: Plot of $\mathrm{Log}_{10}(C)$ vs. number of coefficients, *k*, for *m = 651* input values 33
Fig. 2.8: Plot of *RMS* vs. number of coefficients (for displacement *v*), *k*, for *m* = 651 input values 33
Fig. 2.9: Contour plots of *u/d* from FEA (left side) and reconstructed displacement *u/d* (right side) using *m = 651* input numerically simulated measured *u* displacements, *k = 5* coefficients throughout $0.5 \leq r/d \leq 0.9$ region adjacent to hole 34
Fig. 2.10: Contour plot of *v/d* from FEA (left side) and reconstructed displacement *v/d* (right side) using *m = 651* input numerically simulated measured *v* displacements, *k = 5* coefficients throughout $0.5 \leq r/d \leq 0.9$ region adjacent to hole 34
Fig. 2.11: Contour plot of *v/d* throughout $0.5 \leq r/d \leq 0.9$ region adjacent to hole predicted by FEA (left side) and based on evaluated Airy coefficients (right side) for *m = 651* input numerically simulated measured *u* displacements and *k = 5* coefficients 38

Fig. 2.12: Contour plot of u/d throughout $0.5 \leq r/d \leq 0.9$ region adjacent to hole predicted by FEA (left side) and based on evaluated Airy coefficients (right side) for $m = 651$ input numerically simulated measured v displacements and $k = 5$ coefficients..... 38

Fig. 2.13: Contour plot of u_r/d throughout $0.5 \leq r/d \leq 0.9$ region adjacent to hole predicted by FEA (left side) and from evaluated Airy coefficients (right side) for $m = 651$ input numerically simulated measured v displacements and $k = 5$ coefficients..... 39

Fig. 2.14: Contour plot of u_θ/d throughout $0.5 \leq r/d \leq 0.9$ region adjacent to hole predicted by FEA (left side) and from evaluated Airy coefficients (right side) for $m = 651$ input numerically simulated measured v displacements and $k = 4$ coefficients..... 39

Fig. 2.15: Contour plot of $\varepsilon_{rr}/\varepsilon_0$ throughout $0.5 \leq r/d \leq 0.9$ region adjacent to hole predicted by FEA (left side) and from evaluated Airy coefficients (right side) for $m = 651$ input numerically simulated measured v displacements and $k = 5$ coefficients..... 40

Fig. 2.16: Contour plot of $\varepsilon_{\theta\theta}/\varepsilon_0$ throughout $0.5 \leq r/d \leq 0.9$ region adjacent to hole predicted by FEA (left side) and from evaluated Airy coefficients (right side) for $m = 651$ input numerically simulated measured v displacements and $k = 5$ coefficients..... 40

Fig. 2.17: Contour plot of σ_{rr}/σ_0 throughout $0.5 \leq r/d \leq 0.9$ region adjacent to hole predicted by FEA (left side) and from evaluated Airy coefficients (right side) for $m = 651$ input numerically simulated measured v displacements and $k = 5$ coefficients..... 41

Fig. 2.18: Contour plot of $\sigma_{\theta\theta}/\sigma_0$ throughout $0.5 \leq r/d \leq 0.9$ region adjacent to hole predicted by FEA (left side) and from evaluated Airy coefficients (right side) for $m = 651$ input numerically simulated measured v displacements and $k = 5$ coefficients..... 41

Fig. 2.19: Contour plot of $\sigma_{r\theta}/\sigma_0$ throughout $0.5 \leq r/d \leq 0.9$ region adjacent to hole predicted by FEA (left side) and from evaluated Airy coefficients (right side) for $m = 651$ input numerically simulated measured v displacements and $k = 4$ coefficients..... 42

Fig. 2.20: Image of the tested specimen with the speckle pattern 44

Fig. 2.21: Specimen with the strain gages 46

Fig. 2.22: DIC Plate Geometry and Loading – Unclamped specimen length = 93.98 mm (3.7”) 47

Fig. 2.23: Specimen loaded in hydraulic grips 49

Fig. 2.24: Specimen loading and DIC recording 50

Fig. 2.25: Actual recorded v-displacement data from Vic-2D..... 50

Fig. 2.26: DIC source locations for $m = 861$ input values 51
Fig. 2.27: Plot of 'RMS' values of (d'- d) vs. number of coefficients, k, for $m = 861$ input values 52
Fig. 2.28: Plot of condition number, C, vs. number of coefficients, k, for $m = 861$ input values 52
Fig. 2.29: Plot of $\log_{10}(C)$ vs. number of coefficients, k, for $m = 861$ input values 52
Fig. 2.30: MATLAB processed experimentally determined v/d (right) and reconstructed v/d displacements based on the DIC evaluated Airy coefficients for $k = 5$ coefficients and $m = 861$ input values (left) 53
Fig. 2.31: Finite element model for the plate with circular hole 55
Fig. 2.32: ANSYS predicted vertical stress σ_{yy} (psi) between loading grips of DIC analyzed plate of *figure 2.22* 55
Fig. 2.33: Contour plot of v/d throughout $0.5 \leq r/d \leq 0.9$ region adjacent to hole predicted by FEA (left side) and based on Airy coefficients evaluated from DIC-measured v displacements (right side) for $m = 861$ input and $k = 5$ coefficients 57
Fig. 2.34: Contour plot of u/d throughout $0.5 \leq r/d \leq 0.9$ region adjacent to hole predicted by FEA (left side) and based on Airy coefficients evaluated from DIC-measured v displacements (right side) for $m = 861$ input and $k = 5$ coefficients 57
Fig. 2.35: Contour plot of u_r/d throughout $0.5 \leq r/d \leq 0.9$ region adjacent to hole predicted by FEA (left side) and based on Airy coefficients evaluated from DIC-measured v displacements (right side) for $m = 861$ input and $k = 5$ coefficients 58
Fig. 2.36: Contour plot of u_θ/d throughout $0.5 \leq r/d \leq 0.9$ region adjacent to hole predicted by FEA (left side) and based on Airy coefficients evaluated from DIC-measured v displacements (right side) for $m = 861$ input and $k = 4$ coefficients 58
Fig. 2.37: Contour plot of ε_{rr} (micro strain) throughout $0.5 \leq r/d \leq 0.9$ region adjacent to hole predicted by FEA (left side) and based on Airy coefficients evaluated from DIC-measured v displacements (right side) for $m = 861$ input and $k = 5$ coefficients 59
Fig. 2.38: Contour plot of $\varepsilon_{\theta\theta}$ (micro strain) throughout $0.5 \leq r/d \leq 0.9$ region adjacent to hole predicted by FEA (left side) and based on Airy coefficients evaluated from DIC-measured v displacements (right side) for $m = 861$ input and $k = 5$ coefficients 59

Fig. 2.39: Contour plot of σ_{rr}/σ_{net} throughout $0.5 \leq r/d \leq 0.9$ region adjacent to hole predicted by FEA (left side) and based on Airy coefficients evaluated from DIC-measured *v* displacements (right side) for *m = 861* input and *k = 5* coefficients 60
Fig. 2.40: Contour plot of $\sigma_{\theta\theta}/\sigma_{net}$ throughout $0.5 \leq r/d \leq 0.9$ region adjacent to hole predicted by FEA (left side) and based on Airy coefficients evaluated from DIC-measured *v* displacements (right side) for *m = 861* input and *k = 5* coefficients 60
Fig. 2.41: Contour plot of $\sigma_{r\theta}/\sigma_{net}$ throughout $0.5 \leq r/d \leq 0.9$ region adjacent to hole predicted by FEA (left side) and based on Airy coefficients evaluated from DIC-measured *v* displacements (right side) for *m = 861* input and *k = 5* coefficients 60
Fig. 2.42: Plot of $\sigma_{\theta\theta}/\sigma_{net}$ vs. Angle ϕ^o (= 90 - θ^o) along boundary of the hole from ANSYS and evaluated Airy coefficients (*k = 5* coefficients) from *m = 861* input DIC measured *v* displacements 62
Fig. 2.43: Plot of $\sigma_{\theta\theta}/\sigma_{net}$ around the boundary of the hole from TSA-determined and ANSYS [4, 5]..... 62
Fig. 2.44: Plot of ε_{yy} along AB of *figure 2.22* form ANSYS, evaluated Airy coefficients (*k = 5* coefficients) from *m = 861* input DIC measured *v* displacements and Strain gage..... 63
Fig. 3.1: Schematic geometry of a finite plate with a hole 69
Fig. 3.2: Strain gage numbers corresponding to Table 3.1 (front face)..... 78
Fig. 3.3: Strain gage numbers corresponding to Table 3.1 (back face) 79
Fig. 3.4: Front view of the Specimen with the gages..... 80
Fig. 3.5: Rear view of the Specimen with the gages..... 80
Fig. 3.6: Strain-gage locations on the Specimen..... 81
Fig.3.7: Specimen Loaded in the Instron Machine 82
Fig. 3.8: Strain-gages connected to the Strain-gage Conditioner 82
Fig. 3.9-A: Source locations of 45 strain-gages (in inches) relative to the x- and y-coordinate of *figure 3.1* 85
Fig. 3.9-B: Normalized strain-gage coordinate locations, *m = 45* input values. 86
Fig. 3.10: Plot of *RMS* vs. number of coefficients, *k*, for *m* = 45 input values..... 87
Fig. 3.11: Plot of condition number, *C*, vs. number of coefficients, *k*, for *m* = 45 input values... 87
Fig. 3.12: Plot of $\text{Log}_{10}(C)$ vs. number of coefficients, *k*, for *m* = 45 input values 88

Fig. 3.13: Finite element model for the plate with central circular hole, *figure 3.1*. 89
Fig. 3.14: Plot of $\varepsilon_{rr}/\varepsilon_0$ along boundary of the hole from strain-gage evaluated Airy coefficients for $k = 7$ coefficients ($m = 45$ strain-gage input values) and ANSYS 91
Fig. 3.15: Plot of $\varepsilon_{rr}/\varepsilon_0$ along r/R = 1.5 from strain-gage evaluated Airy coefficients for $k = 7$ coefficients ($m = 45$ strain-gage input values) and ANSYS 91
Fig. 3.16: Plot of $\varepsilon_{rr}/\varepsilon_0$ along r/R = 2 from strain-gage evaluated Airy coefficients for $k = 7$ coefficients ($m = 45$ strain-gage input values) and ANSYS 92
Fig. 3.17: Plot of $\varepsilon_{\theta\theta}/\varepsilon_0$ along boundary of the hole from strain-gage evaluated Airy coefficients for $k = 7$ coefficients ($m = 45$ strain-gage input values) and ANSYS 92
Fig. 3.18: Plot of $\varepsilon_{\theta\theta}/\varepsilon_0$ along r/R = 1.5 from strain-gage evaluated Airy coefficients for $k = 7$ coefficients ($m = 45$ strain-gage input values) and ANSYS 92
Fig. 3.19: Plot of $\varepsilon_{\theta\theta}/\varepsilon_0$ along r/R = 2 from strain-gage evaluated Airy coefficients for $k = 7$ coefficients ($m = 45$ strain-gage input values) and ANSYS 93
Fig. 3.20: Plot of $\varepsilon_{xx}/\varepsilon_0$ along boundary of the hole from strain-gage evaluated Airy coefficients for $k = 7$ coefficients ($m = 45$ strain-gage input values) and ANSYS 93
Fig. 3.21: Plot of $\varepsilon_{xx}/\varepsilon_0$ along r/R = 1.5 from strain-gage evaluated Airy coefficients for $k = 7$ coefficients ($m = 45$ strain-gage input values) and ANSYS 93
Fig. 3.22: Plot of $\varepsilon_{xx}/\varepsilon_0$ along r/R = 2 from strain-gage evaluated Airy coefficients for $k = 7$ coefficients ($m = 45$ strain-gage input values) and ANSYS 94
Fig. 3.23: Plot of $\varepsilon_{xx}/\varepsilon_0$ along AB of *figure 3.1* from strain-gage evaluated Airy coefficients for $k = 7$ coefficients ($m = 45$ strain-gage input values) and ANSYS 94
Fig. 3.24: Plot of $\varepsilon_{yy}/\varepsilon_0$ along boundary of the hole from strain-gage evaluated Airy coefficients for $k = 7$ coefficients ($m = 45$ strain-gage input values) and ANSYS 94
Fig. 3.25: Plot of $\varepsilon_{yy}/\varepsilon_0$ along r/R = 1.5 from strain-gage evaluated Airy coefficients for $k = 7$ coefficients ($m = 45$ strain-gage input values) and ANSYS 95
Fig. 3.26: Plot of $\varepsilon_{yy}/\varepsilon_0$ along r/R = 2 from strain-gage evaluated Airy coefficients for $k = 7$ coefficients ($m = 45$ strain-gage input values) and ANSYS 95
Fig. 3.27: Plot of $\varepsilon_{yy}/\varepsilon_0$ along AB of *figure 3.1* from strain-gages (reconstructed using the evaluated Airy coefficients and discrete gages) for $k = 7$ coefficients ($m = 45$ strain-gage input values) and ANSYS 95

Fig. 3.28: Plot of σ_{rr}/σ_0 along boundary of the hole from strain-gage evaluated Airy coefficients for $k = 7$ coefficients ($m = 45$ strain-gage input values) and ANSYS 96
Fig. 3.29: Plot of σ_{rr}/σ_0 along r/R = 1.5 from strain-gage evaluated Airy coefficients for $k = 7$ coefficients ($m = 45$ strain-gage input values) and ANSYS 96
Fig. 3.30: Plot of σ_{rr}/σ_0 along r/R = 2 from strain-gage evaluated Airy coefficients for $k = 7$ coefficients ($m = 45$ strain-gage input values) and ANSYS 96
Fig. 3.31: Plot of σ_{xx}/σ_0 (= σ_{rr}/σ_0) along AB of *figure 3.1* from strain-gage evaluated Airy coefficients for $k = 7$ coefficients ($m = 45$ strain-gage input values) and ANSYS 97
Fig. 3.32: Plot of $\sigma_{r\theta}/\sigma_0$ along boundary of the hole from strain-gage evaluated Airy coefficients for $k = 7$ coefficients ($m = 45$ strain-gage input values) and ANSYS 97
Fig. 3.33: Plot of $\sigma_{r\theta}/\sigma_0$ along r/R = 1.5 from strain-gage evaluated Airy coefficients for $k = 7$ coefficients ($m = 45$ strain-gage input values) and ANSYS 97
Fig. 3.34: Plot of $\sigma_{r\theta}/\sigma_0$ along r/R = 2 from strain-gage evaluated Airy coefficients for $k = 7$ coefficients ($m = 45$ strain-gage input values) and ANSYS 98
Fig. 3.35: Plot of $\sigma_{r\theta}/\sigma_0$ along AB of *figure 3.1* from strain-gage evaluated Airy coefficients for $k = 7$ coefficients ($m = 45$ strain-gage input values) and ANSYS 98
Fig. 3.36: Plot of $\sigma_{\theta\theta}/\sigma_0$ along boundary of the hole from strain-gage evaluated Airy coefficients for $k = 7$ coefficients ($m = 45$ strain-gage input values) and ANSYS 98
Fig. 3.37: Plot of $\sigma_{\theta\theta}/\sigma_0$ along r/R = 1.5 from strain-gage evaluated Airy coefficients for $k = 7$ coefficients ($m = 45$ strain-gage input values) and ANSYS 99
Fig. 3.38: Plot of $\sigma_{\theta\theta}/\sigma_0$ along r/R = 2 from strain-gage evaluated Airy coefficients for $k = 7$ coefficients ($m = 45$ strain-gage input values) and ANSYS 99
Fig. 3.39: Plot of σ_{yy}/σ_0 (= $\sigma_{\theta\theta}/\sigma_0$) along AB of *figure 3.1* from strain-gage evaluated Airy coefficients for $k = 7$ coefficients ($m = 45$ strain-gage input values) and ANSYS 99
Fig. 4.1: Schematic of diametrically-loaded annular disk 105
Fig. 4.2: Diametrically-loaded annular disk 106
Fig. 4.3: Front face of the strain-gaged ring in the screw-driven testing machine 113
Fig. 4.4: Back face of the strain-gaged ring in the testing machine..... 113
Fig. 4.5: Test setup..... 114
Fig. 4.6: Data points generated upon rotating the five strain gages by 10 degree intervals 116

Fig. 4.7: Plot of condition number, C vs. number of coefficients, k for $m = 48$ measured strains 117
Fig. 4.8: Plot of $\log_{10}(C)$ vs. number of coefficients, k for $m = 48$ measured strains..... 117
Fig. 4.9: Plot of RMS vs. number of coefficients, k for $m = 48$ measured strains 118
Fig. 4.10: Finite element model for diametrically-loaded annular disk..... 119
Fig. 4.11: Plot of $\varepsilon_{yy}/\varepsilon_{net}$ along vertical axis of *figure 4.1* from hybrid method (strain-gage evaluated Airy coefficients) and ANSYS 121
Fig. 4.12: Plot of $\varepsilon_{xx}/\varepsilon_{net}$ along vertical axis of *figure 4.1* from hybrid method (strain-gage evaluated Airy coefficients) and ANSYS 121
Fig. 4.13: Plot of $\varepsilon_{yy}/\varepsilon_{net}$ along horizontal axis of *figure 4.1* from hybrid method (strain-gage evaluated Airy coefficients) and ANSYS 122
Fig. 4.14: Plot of $\sigma_{\theta\theta}/\sigma_0$ along boundary of the hole from hybrid method (strain-gage evaluated Airy coefficients) and ANSYS..... 122
Fig. 4.15: Contours of u/R from FEA (left side) and hybrid method (strain-gage evaluated Airy coefficients) (right side) 123
Fig. 4.16: Contours of v/R from FEA (left side) and hybrid method (strain-gage evaluated Airy coefficients) (right side) 123
Fig. 4.17: Contours of u_r/R from FEA (left side) and hybrid method (strain-gage evaluated Airy coefficients) (right side) 124
Fig. 4.18: Contours of u_θ/R from FEA (left side) and hybrid method (strain-gage evaluated Airy coefficients) (right side) 124
Fig. 4.19: Contours of $\varepsilon_{rr}/\varepsilon_{net}$ from FEA (left side) and hybrid method (strain-gage evaluated Airy coefficients) (right side) 125
Fig. 4.20: Contours of $\varepsilon_{\theta\theta}/\varepsilon_{net}$ from FEA (left side) and hybrid method (strain-gage evaluated Airy coefficients) (right side)..... 125
Fig. 4.21: Contours of σ_{rr}/σ_{net} from FEA (left side) and hybrid method (strain-gage evaluated Airy coefficients) (right side)..... 126
Fig. 4.22: Contours of $\sigma_{\theta\theta}/\sigma_{net}$ from FEA (left side) and hybrid method (strain-gage evaluated Airy coefficients) (right side)..... 126

Fig. 4.23: Contours of $\sigma_{r\theta}/\sigma_{net}$ from FEA (left side) and hybrid method (strain-gage evaluated Airy coefficients) (right side) 127
Fig. 4.24: Plot of $\varepsilon_{rr}/\varepsilon_{net}$ along r/R = 1.75 from hybrid method (strain-gage evaluated Airy coefficients) and ANSYS 128
Fig. 4.25: Plot of $\sigma_{\theta\theta}/(2P/\pi b)$ along vertical axis of *figure 4.1* from hybrid method (strain-gage evaluated Airy coefficients) and Timoshenko [25] 129
Fig. 4.26: Plot of $\sigma_{\theta\theta}/(2P/\pi b)$ along horizontal axis of *figure 4.1* from hybrid method (strain-gage evaluated Airy coefficients) and Timoshenko [25] 130
Fig. 5.1: Coordinate Representations 140
Fig. 5.2: Schematic of symmetrically-loaded aluminum plate containing an elliptical hole plate 141
Fig. 5.3: Aluminum plate coated with Krylon Ultra-Flat black paint 156
Fig. 5.4: Aluminum plate surface preparation (front side of the plate before spraying) 156
Fig. 5.5: Oscilloscope for accurate measurement of cyclic loads 158
Fig. 5.6: Specimen in loading frame with Delta Therm DT1410 infrared camera 159
Fig. 5.7: Specimen loaded in hydraulic grips 159
Fig. 5.8: Test Setup 162
Fig. 5.9: TSA image, S*, for a load range of 4448.22 N (1000lb) 162
Fig. 5.10: Oscilloscope image while performing TSA 163
Fig. 5.11: Calibration specimen 166
Fig. 5.12: Experimental setup for the calibration specimen 167
Fig. 5.13: TSA source locations ($m = 1,703$) for 1,849 input values ($m+h = 1,849$). 170
Fig. 5.14: Plot of condition number, C, vs number of coefficients, k, for $m+h = 1,849$ input values ($m = 1,703$ TSA values) 173
Fig. 5.15: Plot of $\text{Log}_{10}(C)$ vs number of coefficients, k, for $m+h = 1,849$ input values ($m = 1,703$ TSA values) 173
Fig. 5.16: Plot of 'RMS' values of (d'-d) vs number of coefficients, k, for $m+h = 1,849$ input values ($m = 1,703$ TSA values) 175
Fig. 5.17: MATLAB processed Experimental TSA input data S/σ_0 177
Fig. 5.18: MATLAB processed Experimental TSA input data S/σ_0 177

Fig. 5.19: Reconstructed S/σ_0 for $m+h = 1,849$, $m = 1,703$ and $k = 26$ 177
Fig. 5.20: Reconstructed S/σ_0 for $m+h = 1,849$, $m = 1,703$ and $k = 18, 22$ and 30 for (a), (b) and (c), respectively 178
Fig. 5.21: Finite element model for analyzing the finite plate having an elliptical hole 182
Fig. 5.22: Contour plot of σ_{xx}/σ_0 from TSA (a) and ANSYS (b) 184
Fig. 5.23: Contour plot of σ_{yy}/σ_0 from TSA (a) and ANSYS (b) 184
Fig. 5.24: Contour plot of σ_{xy}/σ_0 from TSA (a) and ANSYS (b) 184
Fig. 5.25: Plot of hoop stress $\sigma\eta\eta/\sigma_0$ on the boundary of the hole (2a= 38.10 mm (1.5"), 2b = 19.05 mm (0.75")) from ANSYS and TSA ($m+h = 1,849$ input values, $k = 26$ coefficients and $m = 1,703$ TSA values) 186
Fig. 5.26: Plot of $\sigma_{\theta\theta}/\sigma_0$ on the boundary of the hole (2a= 38.10 mm (1.5"), 2b = 19.05 mm (0.75")) from ANSYS and TSA ($m+h = 1,849$ input values $k = 26$ coefficients and $m = 1,703$ TSA values) 186
Fig. 5.27: Plot of $\sigma_{\theta\theta}/\sigma_0$ along elliptical curve defined by 2a= 40.64 mm (1.6") and 2b = 20.32 mm (0.8") from ANSYS and TSA ($m+h = 1,849$ input values, $k = 26$ coefficients and $m = 1,703$ TSA values) 187
Fig. 5.28: Plot of σ_{rr}/σ_0 along elliptical curve defined by 2a= 40.64 mm (1.6") and 2b = 20.32 mm (0.8") from ANSYS and TSA ($m+h = 1,849$ input values, $k = 26$ coefficients and $m = 1,703$ TSA values) 187
Fig. 5.29: Plot of $\sigma_{r\theta}/\sigma_0$ along elliptical curve defined by 2a= 40.64 mm (1.6") and 2b = 20.32 mm (0.8") from ANSYS and TSA ($m+h = 1,849$ input values, $k = 26$ coefficients and $m = 1,703$ TSA values) 188
Fig. 5.30: Plot of $\sigma_{\theta\theta}/\sigma_0$ along elliptical curve defined by 2a= 45.72 mm (1.8") and 2b = 22.86 mm (0.9") from ANSYS and TSA ($m+h = 1,849$ input values, $k = 26$ coefficients and $m = 1,703$ TSA values) 188
Fig. 5.31: Plot of $\sigma_{\theta\theta}/\sigma_0$ along elliptical curve defined by 2a= 50.8 mm (2") and 2b = 25.4 mm (1") from ANSYS and TSA ($m+h = 1,849$ input values, $k = 26$ coefficients and $m = 1,703$ TSA values) 189

Fig. 5.32: Plot of $\sigma_{\theta\theta}/\sigma_0$ along elliptical curve defined by 2a= 60.96 mm (2.4") and 2b = 30.48 mm (1.2") from ANSYS and TSA (*m+h = 1,849* input values, *k = 26* coefficients and *m = 1,703* TSA values) 189

Fig. 5.33: Plot of normal stress $\sigma\xi\xi/\sigma_0$ on the boundary of the hole (2a= 38.10 mm (1.5") and 2b = 19.05 mm (0.75")) from ANSYS and TSA (*m+h = 1,849* input values, *k = 26* coefficients and *m = 1,703* TSA values) 190

Fig. 5.34: Plot of shear stress $\sigma\xi\eta/\sigma_0$ on the boundary of the hole (2a= 38.10 mm (1.5") and 2b = 19.05 mm (0.75")) from ANSYS and TSA (*m+h = 1,849* input values, *k = 26* coefficients and *m = 1,703* TSA values) 190

Fig. 5.35: Plot of σ_{xx}/σ_0 along AB (*figure 5.2*) from ANSYS and TSA (*m+h = 1,849* input values, *k = 26* coefficients and *m = 1,703* TSA values) 191

Fig. 5.36: Plot of σ_{yy}/σ_0 along AB (*figure 5.2*) from ANSYS and TSA (*m+h = 1,849* input values, *k = 26* coefficients and *m = 1,703* TSA values) 191

Fig. 5.37: Specimen FRONT with mounted strain gages (coated with M-coat) and then sprayed with Krylon Ultra-Flat black paint 194

Fig. 5.38: Specimen FRONT with mounted strain gages 194

Fig. 5.39: Specimen BACK with mounted strain gages 194

Fig. 5.40: Strip gage adjacent to elliptical hole along line AB of *figure 5.2 (*also seen in *figure 5.38)* 195

Fig. 5.41: Strip gage mounted along line AB of *figure 5.2 (*also seen in *figures 5.38 and 5.40)* 195

Fig. 5.42: Strip gage and strain gage on the front 196

Fig. 5.43: Distant longitudinal strain gage on the front used to check for any out-of-plane bending (also seen in *figure 5.42*) 196

Fig. 5.44: Distant longitudinal strain gage on the back used to check for any out-of-plane bending (also seen in *figure 5.42*) 197

Fig. 5.45: Calibration specimen BACK, having mounted horizontal and vertical strain gages . 197

Fig. 5.46: Overview of the testing setup, including the strain gage switching, oscilloscope and balancing equipment 198

Fig. 5.47: 16 Channel, variable excitation strain gage conditioner 198

Fig. 5.48: Strain ε_{yy} along AB of *figure 5.2* from TSA, ANSYS and strain gages for *m+h = 1,849* input values, *m = 1,703* TSA values, *k = 26* and F = 4448.2 N (1000 lbs) 199
Fig. 5.49: Strain ε_{yy} obtained from strain gages along AB for different loads 200
Fig. 5.50: Comparison plot of hoop stress $\sigma\eta\eta/\sigma_0$ on the boundary of the hole (2a= 38.10 mm (1.5"), 2b = 19.05 mm (0.75")) from ANSYS and TSA varying from 1 pixel to 4 pixels 202
Fig. 6.1: Bolted joint utilized in the support structure of a bridge [64] 207
Fig. 6.2: Plate loaded with a circular bolt 212
Fig. 6.3: Initial setup 3D CAD model 217
Fig. 6.4: Initial setup experiment 219
Fig. 6.5: Raw TSA data from initial setup experiment 220
Fig. 6.6: 3D CAD model of the final setup 221
Fig. 6.7: 2D sketch of test specimen (left) and 3D CAD model of test specimen (right) 223
Fig. 6.8: 3D CAD model of circular pin 224
Fig. 6.9: 2D side view of the circular pin 225
Fig. 6.10: 3D CAD model of the non-circular pin 226
Fig. 6.11: 2D side view of the non-circular pin 227
Fig. 6.12: 3D CAD model of fixture (left) and CAD side view of fixture (right) 229
Fig. 6.13(a): Front view of back loading fixture showing pin and set screw which bears against the pin 229
Fig. 6.13(b): Back view of back loading fixture showing pin and set screw which bears against the pin 230
Fig. 6.14: Separate assembly components 232
Fig. 6.15: 3D CAD model of the setup with the non-circular pin (left) and circular pin (right) 233
Fig. 6.16: Oscilloscope 235
Fig. 6.17: MTS hydraulic grips 235
Fig. 6.18: TSA Delta Therm camera 237
Fig. 6.19: Experimental setup 238
Fig. 6.20: Raw TSA S* Image for the plate with circular pin 240
Fig. 6.21: Raw TSA S* data for the plate with circular pin reconstructed in MATLAB 241

Fig. 6.22: Raw TSA S* data for the plate with non-circular pin 242
Fig. 6.23: Raw TSA S* data for the plate with non-circular pin reconstructed in MATLAB.... 243
Fig. 6.24: Calibration Specimen 245
Fig. 6.25: Calibration sample experimental setup 247
Fig. 6.26: Calibration TSA S* image (data) for the plate with circular hole..... 248
Fig. 6.27: Calibration TSA S* image (data) for the plate with circular hole..... 249
Fig. 6.28: TSA input locations for circular pin with $m_1 = 3413$ (left side) and non-circular pin with $m_2 = 3458$ (right side) 251
Fig. 6.29: Raw TSA S* data (not averaged about the x-axis) for the circular pin..... 251
Fig. 6.30: Raw TSA S* data (not averaged about the x-axis) for the non-circular pin 252
Fig. 6.31: Raw TSA S* data (averaged about the x-axis) for the circular pin..... 252
Fig. 6.32: Raw TSA S* data (averaged about the x-axis) for the non-circular pin 253
Fig. 6.33: Marks on right boundary of the hole after loading with the round pin 257
Fig. 6.34: Marks on left boundary of the hole after loading with the round pin..... 258
Fig. 6.35: Residual marks on the right boundary of the circular pin (contact surface of the hole shown in *figure 6.33*)..... 258
Fig. 6.36: Residual marks on the left boundary of the circular pin (contact surface of the hole shown in *figure 6.34*)..... 259
Fig. 6.37-A: TSA-determined σ_{rr}/σ_0 around the boundary of the hole (r/R = 1) for $m_1+h_1+t_1 = 5,479$ input values, $k = 9$ coefficients and $m_1 = 3,413$ TSA values, $h_1 = 2*831$, $t_1 = 2*101+2*301$ 259
Fig. 6.37-B: Plot of $cos(\phi)$ and TSA-determined σ_* (= $\sigma_{rr}/\sigma_{rr(max)}$) vs. angle ϕ (=180^o - θ) around the boundary of the hole (r/R = 1) for $m_1+h_1+t_1 = 5,479$ input values, $k = 9$ coefficients and $m_1 = 3,413$ TSA values, $h_1 = 2*831$, $t_1 = 2*101+2*301$ 260
Fig. 6.38: TSA-determined $\sigma_{r\theta}/\sigma_0$ around the boundary of the hole (r/R = 1) for $m_1+h_1+t_1 = 5,479$ input values, $k = 9$ coefficients and $m_1 = 3,413$ TSA values, $h_1 = 2*831$, $t_1 = 2*101+2*301$ 260
Fig. 6.39-A: Right boundary of the non-circular pin when facing the plate/pin from TSA side 262
Fig. 6.39-B: Left boundary of the non-circular pin when facing the plate/pin from TSA side .. 263
Fig. 6.40-A: Top view of non-circular pin..... 263

Fig. 6.40-B: Side view of non-circular pin 264

Fig. 6.41-A: TSA-determined σ_{rr}/σ_0 around the boundary of the hole (r/R = 1) for $m_2+h_2+t_2 = 6{,}592$ input values, $k = 9$ coefficients and $m_2 = 3{,}458$ TSA values, $h_2 = 2*871$, $t_2 = 2*101+2*301$ 264

Fig. 6.41-B: Plot of $cos(\phi)$ and σ_* (= $\sigma_{rr}/\sigma_{rr(max)}$) vs. angle ϕ (=180^o - θ) around the boundary of the hole (r/R = 1) for $m_2+h_2+t_2 = 6{,}592$ input values, $k = 9$ coefficients and $m_2 = 3{,}458$ TSA values, $h_2 = 2*871$, $t_2 = 2*101+2*301$ 265

Fig. 6.42: TSA-determined $\sigma_{r\theta}/\sigma_0$ around the boundary of the hole (r/R = 1) for $m_2+h_2+t_2 = 6{,}592$ input values, $k = 9$ coefficients and $m_2 = 3458$ TSA values, $h_2 = 2*871$, $t_2 = 2*101+2*301$ 265

Fig. 6.43: Plot of condition number, C, vs. number of coefficients, k, for $m_1+h_1+t_1 = 5{,}479$ input values, ($m_1 = 3{,}413$ TSA values, $h_1 = 2*831$, $t_1 = 2*101+2*301$); circular pin 268

Fig. 6.44: Plot of $\log_{10}$(C) vs. number of coefficients, k, for $m_1+h_1+t_1 = 5{,}479$ input values, ($m_1 = 3{,}413$ TSA values, $h_1 = 2*831$, $t_1 = 2*101+2*301$); circular pin 269

Fig. 6.45: Plot of RMS vs. number of coefficients, k, for $m_1+h_1+t_1 = 5{,}479$ input values, ($m_1 = 3{,}413$ TSA values, $h_1 = 2*831$, $t_1 = 2*101+2*301$); circular pin 269

Fig. 6.46: Plot of condition number, C, vs. number of coefficients, k, for $m_2+h_2+t_2 = 6{,}592$ input values, ($m_2 = 3458$ TSA values, $h_2 = 2*871$, $t_2 = 2*101+2*301$); non-circular pin 270

Fig. 6.47: Plot of $\log_{10}$(C) vs. number of coefficients, k, for $m_2+h_2+t_2 = 6{,}592$ input values, ($m_2 = 3458$ TSA values, $h_2 = 2*871$, $t_2 = 2*101+2*301$); non-circular pin 270

Fig. 6.48: Plot of RMS vs. number of coefficients, k, for $m_2+h_2+t_2 = 6{,}592$ input values, ($m_2 = 3458$ TSA values, $h_2 = 2*871$, $t_2 = 2*101+2*301$); non-circular pin 271

Fig. 6.49: MATLAB processed experimentally-based TSA input data S* (left) and reconstructed S* (right) for plate loaded by circular pin [$m_1+h_1+t_1 = 5{,}479$ input values and $k = 9$ ($m_1 = 3{,}413$ TSA values, $h_1 = 2*831$, $t_1 = 2*101+2*301$)] 272

Fig. 6.50: MATLAB processed experimentally-based TSA input data S* (left) and reconstructed S* (right) for plate loaded by non-circular pin [$m_2+h_2+t_2 = 6{,}592$ input values and $k = 9$ ($m_2 = 3458$ TSA values, $h_2 = 2*871$, $t_2 = 2*101+2*301$)] 272

Fig. 6.51: Strain gage on front side of test specimen 273

Fig. 6.52: Strain gage on back side of test specimen 273

Fig. 6.53: Strain gage conditioner monitoring the output from mounted gages 274
Fig. 6.54: Front (TSA side) and back strain gage readings (circular pin experiment) 275
Fig. 6.55: Front (TSA side) and back strain gage readings (non-circular pin experiment) 276
Fig. 6.56-a: Geomtery of the circular pin (Symmetric model) 280
Fig. 6.56-b: Geomtery of the non-circular pin (Symmetric model) 280
Fig. 6.57-a: Geomtery of the plate for circular and non-circular pins (Symmetric model) with dimensions 280
Fig. 6.57-b: Geomtery of the plate for circular and non-circular pins (Symmetric model) 281
Fig. 6.58-a: Finite Element model of the round pin configuration 283
Fig. 6.58-b: Finite Element model of the non-circular pin configuration 283
Fig. 6.59: Finite Element model of the plate 284
Fig. 6.60-a: Boundary Conditions applied to the circular pin 285
Fig. 6.60-b: Boundary Conditions applied to the non-circular pin 286
Fig. 6.61: Boundary Conditions and the loads applied to the plate 286
Fig. 6.62: Boundary Conditions and the loads associated with the entire assembly for the circular pin specimen 287
Fig. 6.63: Boundary Conditions and the loads associated with the entire assembly for the non-circular pin specimen 287
Fig. 6.64: Contact surfaces defined on the plate and circular pin 289
Fig. 6.65: Contact surfaces defined on the plate and non-circular pin 289
Fig. 6.66: Contour plot of stress in the x-direction (σ_{xx}) for the plate with circular pin 291
Fig. 6.67: Contour plot of stress in the y-direction (σ_{yy}) for the plate with circular pin 291
Fig. 6.68: Contour plot of shear stress (σ_{xy}) for the plate with circular pin 292
Fig. 6.69: Contour plot of radial stress (σ_{rr}) for the plate with circular pin 292
Fig. 6.70: Contour plot of tangential stress ($\sigma_{\theta\theta}$) for the plate with circular pin 293
Fig. 6.71: Contour plot of polar shear stress ($\sigma_{r\theta}$) for the plate with circular pin 293
Fig. 6.72: Contour plot of stress in the x-direction (σ_{xx}) for the plate with non-circular pin 294
Fig. 6.73: Contour plot of stress in the y-direction (σ_{yy}) for the plate with non-circular pin 294
Fig. 6.74: Contour plot of shear stress (σ_{xy}) for the plate with non-circular pin 295
Fig. 6.75: Contour plot of radial stress (σ_{rr}) for the plate with non-circular pin 295

Fig. 6.76: Contour plot of tangential stress ($\sigma_{\theta\theta}$) for the plate with non-circular pin 296
Fig. 6.77: Contour plot of polar shear stress ($\sigma_{r\theta}$) for the plate with non-circular pin..... 296
Fig. 6.78: Predicted vertical (i.e. y direction) displacements (inches)..... 298
Fig. 6.79: Predicted vertical (i.e. y direction) displacements in the region of the round pin..... 299
Fig. 6.80: Plot of $\sigma_{\theta\theta}/\sigma_0$ around the boundary of the hole (r/R = 1) from ABAQUS and TSA for $m_1+h_1+t_1 = 5{,}479$ input values and $k = 9$ ($m_1 = 3{,}413$ TSA values, $h_1 = 2*831$, $t_1 = 2*101+2*301$) 301
Fig. 6.81: Plot of $\sigma_{\theta\theta}/\sigma_0$ along r/R = 1.5 from ABAQUS and TSA for $m_1+h_1+t_1 = 5{,}479$ input values and $k = 9$ ($m_1 = 3{,}413$ TSA values, $h_1 = 2*831$, $t_1 = 2*101+2*301$) 302
Fig. 6.82: Plot of σ_{rr}/σ_0 around the boundary of the hole (r/R = 1) from ABAQUS and TSA for $m_1+h_1+t_1 = 5{,}479$ input values and $k = 9$ ($m_1 = 3{,}413$ TSA values, $h_1 = 2*831$, $t_1 = 2*101+2*301$) 302
Fig. 6.83: Plot of σ_{rr}/σ_0 along r/R = 1.5 from ABAQUS and TSA for $m_1+h_1+t_1 = 5{,}479$ input values and $k = 9$ ($m_1 = 3{,}413$ TSA values, $h_1 = 2*831$, $t_1 = 2*101+2*301$) 303
Fig. 6.84: Plot of $\sigma_{r\theta}/\sigma_0$ around the boundary of the hole (r/R = 1) from ABAQUS and TSA for $m_1+h_1+t_1 = 5{,}479$ input values and $k = 9$ ($m_1 = 3{,}413$ TSA values, $h_1 = 2*831$, $t_1 = 2*101+2*301$) 303
Fig. 6.85: Plot of $\sigma_{r\theta}/\sigma_0$ along r/R = 1.5 from ABAQUS and TSA for $m_1+h_1+t_1 = 5{,}479$ input values and $k = 9$ ($m_1 = 3{,}413$ TSA values, $h_1 = 2*831$, $t_1 = 2*101+2*301$) 304
Fig. 6.86: Plot of σ_{xx}/σ_0 along the line extending from the edge of the hole (x = 0 or $\theta = 90^o$) from ABAQUS and TSA for $m_1+h_1+t_1 = 5{,}479$ input values and $k = 9$ ($m_1 = 3{,}413$ TSA values, $h_1 = 2*831$, $t_1 = 2*101+2*301$)..... 304
Fig. 6.87: Plot of σ_{xx}/σ_0 around the boundary of the hole (r/R = 1) from ABAQUS and TSA for $m_1+h_1+t_1 = 5{,}479$ input values and $k = 9$ ($m_1 = 3{,}413$ TSA values, $h_1 = 2*831$, $t_1 = 2*101+2*301$) 305
Fig. 6.88: Plot of $\sigma_{\theta\theta}/\sigma_0$ around the boundary of the hole (r/R = 1) from ABAQUS and TSA for $m_2+h_2+t_2 = 6{,}592$ input values and $k = 9$ ($m_2 = 3458$ TSA values, $h_2 = 2*871$, $t_2 = 2*101+2*301$) 306
Fig. 6.89: Plot of $\sigma_{\theta\theta}/\sigma_0$ along r/R = 1.5 from ABAQUS and TSA for $m_2+h_2+t_2 = 6{,}592$ input values and $k = 9$ ($m_2 = 3458$ TSA values, $h_2 = 2*871$, $t_2 = 2*101+2*301$) 307

Fig. 6.90: Plot of σ_{rr}/σ_0 around the boundary of the hole (r/R = 1) from ABAQUS and TSA for $m_2+h_2+t_2 = 6{,}592$ input values and $k = 9$ ($m_2 = 3458$ TSA values, $h_2 = 2*871$, $t_2 = 2*101+2*301$) 307

Fig. 6.91: Plot of σ_{rr}/σ_0 along r/R = 1.5 from ABAQUS and TSA for $m_2+h_2+t_2 = 6{,}592$ input values and $k = 9$ ($m_2 = 3458$ TSA values, $h_2 = 2*871$, $t_2 = 2*101+2*301$) 308

Fig. 6.92: Plot of $\sigma_{r\theta}/\sigma_0$ around the boundary of the hole (r/R = 1) from ABAQUS and TSA for $m_2+h_2+t_2 = 6{,}592$ input values and $k = 9$ ($m_2 = 3458$ TSA values, $h_2 = 2*871$, $t_2 = 2*101+2*301$) 308

Fig. 6.93: Plot of $\sigma_{r\theta}/\sigma_0$ along r/R = 1.5 from ABAQUS and TSA for $m_2+h_2+t_2 = 6{,}592$ input values and $k = 9$ ($m_2 = 3458$ TSA values, $h_2 = 2*871$, $t_2 = 2*101+2*301$) 309

Fig. 6.94: Plot of σ_{xx}/σ_0 along the line extending from the edge of the hole (x = 0 or θ = 90o) from ABAQUS and TSA for $m_2+h_2+t_2 = 6{,}592$ input values and $k = 9$ ($m_2 = 3458$ TSA values, $h_2 = 2*871$, $t_2 = 2*101+2*301$) 309

Fig. 6.95: Plot of σ_{xx}/σ_0 around the boundary of the hole (r/R = 1) from ABAQUS and TSA for $m_2+h_2+t_2 = 6{,}592$ input values and $k = 9$ ($m_2 = 3458$ TSA values, $h_2 = 2*871$, $t_2 = 2*101+2*301$) 310

Fig. 6.96: Contour plot of σ_{xx}/σ_0 (loading direction) from TSA (left) for $m_1+h_1+t_1 = 5{,}479$ input values and $k = 9$ ($m_1 = 3{,}413$ TSA values, $h_1 = 2*831$, $t_1 = 2*101+2*301$) and ABAQUS (right) 312

Fig. 6.97: Contour plot of σ_{yy}/σ_0 (lateral direction) from TSA (left) for $m_1+h_1+t_1 = 5{,}479$ input values and $k = 9$ ($m_1 = 3{,}413$ TSA values, $h_1 = 2*831$, $t_1 = 2*101+2*301$) and ABAQUS (right) 312

Fig. 6.98: Contour plot of σ_{xy}/σ_0 (shear stress) from TSA (left) for $m_1+h_1+t_1 = 5{,}479$ input values and $k = 9$ ($m_1 = 3{,}413$ TSA values, $h_1 = 2*831$, $t_1 = 2*101+2*301$) and ABAQUS (right) 313

Fig. 6.99: Contour plot of σ_{rr}/σ_0 (radial stress) from TSA (left) for $m_1+h_1+t_1 = 5{,}479$ input values and $k = 9$ ($m_1 = 3{,}413$ TSA values, $h_1 = 2*831$, $t_1 = 2*101+2*301$) and ABAQUS (right) 313

Fig. 6.100: Contour plot of $\sigma_{\theta\theta}/\sigma_0$ (tangential stress) from TSA (left) for $m_1+h_1+t_1 = 5,479$ input values and $k = 9$ ($m_1 = 3,413$ TSA values, $h_1 = 2*831$, $t_1 = 2*101+2*301$) and ABAQUS (right) 314

Fig. 6.101: Contour plot of $\sigma_{r\theta}/\sigma_0$ (shear stress) from TSA (left) for $m_1+h_1+t_1 = 5,479$ input values and $k = 9$ ($m_1 = 3,413$ TSA values, $h_1 = 2*831$, $t_1 = 2*101+2*301$) and ABAQUS (right) 314

Fig. 6.102: Contour plot of σ_{xx}/σ_0 (loading direction) from TSA (left) for $m_2+h_2+t_2 = 6,592$ input values and $k = 9$ ($m_2 = 3458$ TSA values, $h_2 = 2*871$, $t_2 = 2*101+2*301$) and ABAQUS (right) 315

Fig. 6.103: Contour plot of σ_{yy}/σ_0 (lateral direction) from TSA (left) for $m_2+h_2+t_2 = 6,592$ input values and $k = 9$ ($m_2 = 3458$ TSA values, $h_2 = 2*871$, $t_2 = 2*101+2*301$) and ABAQUS (right) 316

Fig. 6.104: Contour plot of σ_{xy}/σ_0 (shear stress) from TSA (left) for $m_2+h_2+t_2 = 6,592$ input values and $k = 9$ ($m_2 = 3458$ TSA values, $h_2 = 2*871$, $t_2 = 2*101+2*301$) and ABAQUS (right) 316

Fig. 6.105: Contour plot of σ_{rr}/σ_0 (radial stress) from TSA (left) for $m_2+h_2+t_2 = 6,592$ input values and $k = 9$ ($m_2 = 3458$ TSA values, $h_2 = 2*871$, $t_2 = 2*101+2*301$) and ABAQUS (right) 317

Fig. 6.106: Contour plot of $\sigma_{\theta\theta}/\sigma_0$ (tangential stress) from TSA (left) for $m_2+h_2+t_2 = 6,592$ input values and $k = 9$ ($m_2 = 3458$ TSA values, $h_2 = 2*871$, $t_2 = 2*101+2*301$) and ABAQUS (right) 317

Fig. 6.107: Contour plot of $\sigma_{r\theta}/\sigma_0$ (shear stress) from TSA (left) for $m_2+h_2+t_2 = 6,592$ input values and $k = 9$ ($m_2 = 3458$ TSA values, $h_2 = 2*871$, $t_2 = 2*101+2*301$) and ABAQUS (right) 318

Fig. 6.108: Load equilibrium from scanning TSA-based vertical stress along the boundary of the hole and at different horizontal levels of x of the plate with circular pin 320

Fig. 6.109: Load ratio from scanning TSA-based vertical stress along the boundary of the hole to that applied physically at different horizontal levels of x of the plate with circular pin 321

Fig. 6.110: Load equilibrium from scanning TSA-based vertical stress along the boundary of the hole to that applied physically at different horizontal levels of x of the plate with non-circular pin 322
Fig. 6.111: Load ratio from scanning TSA-based vertical stress along the boundary of the hole and at different horizontal levels of x of the plate with non-circular pin 323
Fig. 7.1: Plate containing a near-edge hole beneath a concentrated load 336
Fig. 7.2: Schematic geometry of a large plate containing a near edge hole subjected to an offset concentrated load 337
Fig. 7.3: Thermoelastic stress analysis experimental set up for the centrally loaded plate (left) and the offset loaded plate (right) with a near edge hole 358
Fig. 7.4: Thermoelastic images of loaded specimen, centrally loaded plate (left), *figure 7.1* and the offset loaded plate (right), *figure 7.2* 358
Fig. 7.5: Plot of condition number, *C*, vs. number of coefficients, *k*, for the presently analyzed centrally loaded plate with *m* = 300 input values 361
Fig. 7.6: Plot of $\log_{10}$(C) vs. number of coefficients, *k*, for the presently analyzed centrally loaded plate with *m* = 300 input values 361
Fig. 7.7: Plot of condition number, *C*, vs. number of coefficients, *k*, for the presently analyzed offset loaded plate with *m* = 849 input values 361
Fig. 7.8: Plot of $\log_{10}$(C) vs. number of coefficients, *k*, for the presently analyzed offset loaded plate with *m* = 849 input values 362
Fig. 7.9: Plot of 'RMS' values of (d'-d) vs. number of coefficients, *k*, for the presently analyzed centrally loaded plate with *m* = 300 input values 364
Fig. 7.10: Plot of 'RMS' values of (d'-d) vs. number of coefficients, *k*, for the presently analyzed offset loaded plate with *m* = 849 input values 364
Fig. 7.11: Finite element model for the analysis of the centrally loaded plate of *figure 7.1* 366
Fig. 7.12: Finite element model for the analysis of the offset loaded plate of *figure 7.2* 367
Fig. 7.13.A: Plot of $\sigma_{\theta\theta}/\sigma_0$ around the boundary of the hole (r/R = 1) from ANSYS and presently analyzed TSA for centrally loaded plate of *figure 7.1* with *m = 300* input values, and *k = 9* coefficients 369
Fig. 7.13.B: Plot of $\sigma_{\theta\theta}/\sigma_0$ at the boundary of the hole (r/R = 1) from references [4 and 111] ... 369

Fig. 7.14.A: Plot of $\sigma_{\theta\theta}/\sigma_0$ along r/R = 1.18 from ANSYS and for presently analyzed TSA for centrally loaded plate of *figure 7.1* with *m = 300* input values, and *k = 9* coefficients 369

Fig. 7.14.B: Plot of $\sigma_{\theta\theta}/\sigma_0$ for selected locations shown in *figure 7.15* from references [4 and 111] 369

Fig. 7.15: Selected data locations for stress component determination 370

Fig. 7.16: Plot of σ_{yy}/σ_0 along AB of *figure 7.15* from ANSYS and for presently analyzed TSA for centrally loaded plate of *figure 7.1* with *m = 300* input values and *k = 9* coefficients 370

Fig. 7.17: Plot of σ_{xx}/σ_0 along AB of *figure 7.15* from ANSYS and for presently analyzed TSA for centrally loaded plate of *figure 7.1* with *m = 300* input values and *k = 9* coefficients 370

Fig. 7.18.A: Plot of $\sigma_{\theta\theta}/\sigma_0$ around the boundary of the hole (r/R = 1) from ANSYS and for presently analyzed TSA for offset loaded plate of *figure 7.2* with *m = 849* input values, and *k = 17* coefficients 371

Fig. 7.18.B: Plot of plate of *figure 7.2* $\sigma_{\theta\theta}/\sigma_0$ at the boundary of the hole (r/R = 1) from references [4 and 116] 371

Fig. 7.19.A: Plot of $\sigma_{\theta\theta}/\sigma_0$ for the hole along r/R = 1.24 from ANSYS and for presently analyzed TSA for offset loaded plate of *figure 7.2* with *m = 849* input values, and *k = 17* coefficients 371

Fig. 7.19.B: Plot of $\sigma_{\theta\theta}/\sigma_0$ for selected locations shown in *figure 7.21* of plate of *figure 7.2* from references [4 and 116] 372

Fig. 7.20.A: Plot of σ_{rr}/σ_0 along r/R = 1.24 from ANSYS and for presently analyzed TSA for offset loaded plate of *figure 7.2* with *m = 849* input values, and *k = 17* coefficients 372

Fig. 7.20.B: Plot of σ_{rr}/σ_0 for selected locations of plate of *figure 7.2* shown in *figure 7.21* from reference [4 and 116] 372

Fig. 7.21: Selected data locations for stress component determination 372

Fig. 8.1: Schematic geometry of a uniaxial tensile finite plate containing two side holes 377

Fig. 8.2: Schematic geometry of an end-loaded finite incline plate (~15^o with respect to loading) containing two side holes 378

Fig. 8.3: Aluminum plate coated with Krylon Ultra-Flat black paint 383
Fig. 8.4: Symmetrically-loaded specimen in hydraulic grips 385
Fig. 8.5: Unsymmetrically-loaded specimen in hydraulic grips 386
Fig. 8.6: Specimen loading and recording for the symmetrically-loaded plate 389
Fig. 8.7: Specimen loading and recording for the unsymmetrically-loaded plate 389
Fig. 8.8: Oscilloscope for accurate measurement of cyclic loads 390
Fig. 8.9: Actual recorded TSA image, S* for the symmetrically-loaded plate, for a load range of 4448.22 N (1000lb) 390
Fig. 8.10: Actual recorded TSA image, S* for the unsymmetrically-loaded plate, for a load range of 4448.22 N (1000lb) 391
Fig. 8.11: Original recorded TSA pixel data, S* of *figure 8.9* re-plotted using MATLAB 391
Fig. 8.12: Original recorded TSA pixel data, S* of *figure 8.10* re-plotted using MATLAB 392
Fig. 8.13: Schematic of the TSA calibration specimen 394
Fig. 8.14: Calibration specimen loaded in hydraulic grips 395
Fig. 8.15: Actual recorded TSA image for the calibration specimen, S*, for a load range of 4448.22 N (1000lb) 396
Fig. 8.16: Finite element model for the analysis of the large hole in the symmetrically-loaded plate 402
Fig. 8.17: Finite element model for the analysis of the small hole in the symmetrically-loaded plate 402
Fig. 8.18: Finite element model for the analysis of the large hole in the unsymmetrically-loaded plate 403
Fig. 8.19: Finite element model for the analysis of the small hole in the unsymmetrically-loaded plate 403
Fig. 8.20: Displacement plot for the unsymmetrically-loaded specimen from finite element analysis 404
Fig. 8.21: TSA source locations for large hole, m_1 = 4,378 input values 407
Fig. 8.22: TSA source locations for small hole, $m_2 = 2{,}031$ input values 407
Fig. 8.23: Plot of condition number, C, vs. number of coefficients, k, for $m_1 = 4{,}378$ input values 408

Fig. 8.24: Plot of $Log_{10}(C)$ vs. number of coefficients, k, for $m_1 = 4,378$ input values 409
Fig. 8.25: Plot of condition number, C, vs. number of coefficients, k, for $m_2 = 2,031$ input values for the small hole 409
Fig. 8.26: Plot of $Log_{10}(C)$ vs. number of coefficients, k, for $m_2 = 2,031$ input values for the small hole 409
Fig. 8.27: Plot of 'RMS' values of (d'-d) vs. number of coefficients, k, for $m_1 = 4,378$ input values 409
Fig. 8.28: Plot of 'RMS' values of (d'-d) vs. number of coefficients, k, for $m_2 = 2,031$ input values 410
Fig. 8.29: MATLAB processed Experimental TSA input data S* for large hole 411
Fig. 8.30: MATLAB processed Experimental TSA input data S* for small hole 411
Fig. 8.31: Reconstructed S* for the large hole with $m_1 = 4,378$ and $k = 9$ 412
Fig. 8.32: Reconstructed S* for the large hole with $m_2 = 2,031$ and $k = 9$ 413
Fig. 8.33: TSA source locations for large hole, $m_3 = 9,372$ input values 414
Fig. 8.34: TSA source locations for small hole, $m_4 = 4,094$ input values 415
Fig. 8.35: Plot of condition number, C, vs. number of coefficients, k, for $m_3 = 9,372$ input values 416
Fig. 8.36: Plot of $Log_{10}(C)$ vs. number of coefficients, k, for $m_3 = 9,372$ input values 416
Fig. 8.37: Plot of condition number, C, vs. number of coefficients, k, for $m_4 = 4,094$ input values for the small hole 416
Fig. 8.38: Plot of $Log_{10}(C)$ vs. number of coefficients, k, for $m_4 = 4,094$ input values for the small hole 417
Fig. 8.39: Plot of 'RMS' values of (d'-d) vs. number of coefficients, k, for $m_3 = 9,372$ input values 417
Fig. 8.40: Plot of 'RMS' values of (d'-d) vs. number of coefficients, k, for $m_4 = 4,094$ input values 417
Fig. 8.41: MATLAB processed Experimental TSA input data S* for large hole 418
Fig. 8.42: MATLAB processed Experimental TSA input data S* for small hole 419
Fig. 8.43: Reconstructed S* for the large hole with $m_3 = 9,372$ and $k = 17$ 419
Fig. 8.44: Reconstructed S* for the small hole with $m_4 = 4,094$ and $k = 17$ 420

Fig. 8.45: Plot of σ_{rr}/σ_0 on the boundary of the large hole from ANSYS and TSA for $k = 9$ coefficients and $m_1 = 4{,}378$ TSA values 422
Fig. 8.46: Plot of σ_{rr}/σ_0 for large hole along $r/r_2 = 1.5$ from ANSYS and TSA for $k = 9$ coefficients and $m_1 = 4{,}378$ TSA values. 423
Fig. 8.47: Plot of σ_{rr}/σ_0 for large hole along $r/r_2 = 2$ from ANSYS and TSA for $k = 9$ coefficients and $m_1 = 4{,}378$ TSA values. 423
Fig. 8.48: Plot of $\sigma_{r\theta}/\sigma_0$ on the boundary of the large hole from ANSYS and TSA for $k = 9$ coefficients and $m_1 = 4{,}378$ TSA values. 423
Fig. 8.49: Plot of $\sigma_{r\theta}/\sigma_0$ for large hole along $r/r_2 = 1.5$ from ANSYS and TSA for $k = 9$ coefficients and $m_1 = 4{,}378$ TSA values. 423
Fig. 8.50: Plot of $\sigma_{r\theta}/\sigma_0$ for large hole along $r/r_2 = 2$ from ANSYS and TSA for $k = 9$ coefficients and $m_1 = 4{,}378$ TSA values. 424
Fig. 8.51: Plot of $\sigma_{\theta\theta}/\sigma_0$ on the boundary of the large hole from ANSYS and TSA for $k = 9$ coefficients and $m_1 = 4{,}378$ TSA values 424
Fig. 8.52: Plot of $\sigma_{\theta\theta}/\sigma_0$ for large hole along $r/r_2 = 1.5$ from ANSYS and TSA for $k = 9$ coefficients and $m_1 = 4{,}378$ TSA values 424
Fig. 8.53: Plot of $\sigma_{\theta\theta}/\sigma_0$ for large hole along $r/r_2 = 2$ from ANSYS and TSA for $k = 9$ coefficients and $m_1 = 4{,}378$ TSA values. 424
Fig. 8.54: Plot of σ_{xx}/σ_0 along CD of *figure 8.1* obtained from ANSYS and TSA for $k = 9$ coefficients and $m_1 = 4{,}378$ TSA values 425
Fig. 8.55: Plot of σ_{yy}/σ_0 along CD of *figure 8.1* obtained from ANSYS and TSA for $k = 9$ coefficients and $m_1 = 4{,}378$ TSA values 425
Fig. 8.56: Plot of σ_{rr}/σ_0 on the boundary of the small hole from ANSYS and TSA for $k = 9$ coefficients and $m_2 = 2{,}031$ TSA values 425
Fig. 8.57: Plot of σ_{rr}/σ_0 for small hole along $r/R_1 = 1.5$ from ANSYS and TSA for $k = 9$ coefficients and $m_2 = 2{,}031$ TSA values 425
Fig. 8.58: Plot of σ_{rr}/σ_0 for small hole along $r/R_1 = 2$ from TSA and ANSYS for $k = 9$ coefficients and $m_2 = 2{,}031$ TSA values 426
Fig. 8.59: Plot of $\sigma_{r\theta}/\sigma_0$ on the boundary of the small hole from ANSYS and TSA for $k = 9$ coefficients and $m_2 = 2{,}031$ TSA values 426

Fig. 8.60: Plot of $\sigma_{r\theta}/\sigma_0$ for small hole along $r/R_1 = 1.5$ from ANSYS and TSA for $k = 9$ coefficients and $m_2 = 2{,}031$ TSA values 426

Fig. 8.61: Plot of $\sigma_{r\theta}/\sigma_0$ for small hole along $r/R_1 = 2$ from ANSYS and TSA for $k = 9$ coefficients and $m_2 = 2{,}031$ TSA values 426

Fig. 8.62: Plot of $\sigma_{\theta\theta}/\sigma_0$ on the boundary of the small hole from ANSYS and TSA for $k = 9$ coefficients and $m_2 = 2{,}031$ TSA values 427

Fig. 8.63: Plot of $\sigma_{\theta\theta}/\sigma_0$ for small hole along $r/R_1 = 1.5$ from ANSYS and TSA for $k = 9$ coefficients and $m_2 = 2{,}031$ TSA values 427

Fig. 8.64: Plot of $\sigma_{\theta\theta}/\sigma_0$ for small hole along $r/R_1 = 2$ from ANSYS and TSA for $k = 9$ coefficients and $m_2 = 2{,}031$ TSA values 427

Fig. 8.65: Plot of σ_{xx}/σ_0 along AB of *figure 8.1* obtained from ANSYS and TSA for $k = 9$ coefficients and $m_1 = 4{,}378$ TSA values 427

Fig. 8.66: Plot of σ_{yy}/σ_0 along AB of *figure 8.1* obtained from ANSYS and TSA for $k = 9$ coefficients and $m_1 = 4{,}378$ TSA values 428

Fig. 8.67: Plot of σ_{rr}/σ_0 on the boundary of the large hole from ANSYS and TSA for $k = 17$ coefficients and $m_3 = 9{,}372$ TSA values 429

Fig. 8.68: Plot of σ_{rr}/σ_0 for large hole along $r/R_1 = 1.5$ from ANSYS and TSA for $k = 17$ coefficients and $m_3 = 9{,}372$ TSA values 430

Fig. 8.69: Plot of σ_{rr}/σ_0 for large hole along $r/R_1 = 2$ from ANSYS and TSA for $k = 17$ coefficients and $m_3 = 9{,}372$ TSA values 430

Fig. 8.70: Plot of $\sigma_{r\theta}/\sigma_0$ on the boundary of the large hole from ANSYS and TSA for $k = 17$ coefficients and $m_3 = 9{,}372$ TSA values 430

Fig. 8.71: Plot of $\sigma_{r\theta}/\sigma_0$ for large hole along $r/R_1 = 1.5$ from ANSYS and TSA for $k = 17$ coefficients and $m_3 = 9{,}372$ TSA values 430

Fig. 8.72: Plot of $\sigma_{r\theta}/\sigma_0$ for large hole along $r/R_1 = 2$ from ANSYS and TSA for $k = 17$ coefficients and $m_3 = 9{,}372$ TSA values 431

Fig. 8.73: Plot of $\sigma_{\theta\theta}/\sigma_0$ on the boundary of the large hole from ANSYS and TSA for $k = 17$ coefficients and $m_3 = 9{,}372$ TSA values 431

Fig. 8.74: Plot of $\sigma_{\theta\theta}/\sigma_0$ for large hole along $r/R_1 = 1.5$ from ANSYS and TSA for $k = 17$ coefficients and $m_3 = 9{,}372$ TSA values 431

Fig. 8.75: Plot of $\sigma_{\theta\theta}/\sigma_0$ for large hole along $r/R_1 = 2$ from ANSYS and TSA for $k = 17$ coefficients and $m_3 = 9{,}372$ TSA values 431
Fig. 8.76: Plot of σ_{rr}/σ_0 along C'D' of *figure 8.2* obtained from ANSYS and TSA for $k = 17$ coefficients and $m_3 = 9{,}372$ TSA values 432
Fig. 8.77: Plot of $\sigma_{\theta\theta}/\sigma_0$ along C'D' of *figure 8.2* obtained from ANSYS and TSA for $k = 17$ coefficients and $m_3 = 9{,}372$ TSA values 432
Fig. 8.78: Plot of σ_{rr}/σ_0 on the boundary of the small hole from ANSYS and TSA for $k = 17$ coefficients and $m_4 = 4{,}094$ TSA values 432
Fig. 8.79: Plot of σ_{rr}/σ_0 for small hole along $r/R_2 = 1.5$ from ANSYS and TSA for $k = 17$ coefficients and $m_4 = 4{,}094$ TSA values 432
Fig. 8.80: Plot of σ_{rr}/σ_0 for small hole along $r/R_2 = 2$ from ANSYS and TSA for $k = 17$ coefficients and $m_4 = 4{,}094$ TSA values 433
Fig. 8.81: Plot of $\sigma_{r\theta}/\sigma_0$ on the boundary of the small hole from ANSYS and TSA for $k = 17$ coefficients and $m_4 = 4{,}094$ TSA values 433
Fig. 8.82: Plot of $\sigma_{r\theta}/\sigma_0$ for small hole along $r/R_2 = 1.5$ from ANSYS and TSA for $k = 17$ coefficients and $m_4 = 4{,}094$ TSA values 433
Fig. 8.83: Plot of $\sigma_{r\theta}/\sigma_0$ for small hole along $r/R_2 = 2$ from ANSYS and TSA for $k = 17$ coefficients and $m_4 = 4{,}094$ TSA values 433
Fig. 8.84: Plot of $\sigma_{\theta\theta}/\sigma_0$ on the boundary of the small hole from ANSYS and TSA for $k = 17$ coefficients and $m_4 = 4{,}094$ TSA values 434
Fig. 8.85: Plot of $\sigma_{\theta\theta}/\sigma_0$ for small hole along $r/R_2 = 1.5$ from ANSYS and TSA for $k = 17$ coefficients and $m_4 = 4{,}094$ TSA values 434
Fig. 8.86: Plot of $\sigma_{\theta\theta}/\sigma_0$ for small hole along $r/R_2 = 2$ from ANSYS and TSA for $k = 17$ coefficients and $m_4 = 4{,}094$ TSA values 434
Fig. 8.87: Plot of σ_{rr}/σ_0 along A'B' of *figure 8.2* obtained from ANSYS and TSA for $k = 17$ coefficients and $m_4 = 4{,}094$ TSA values 434
Fig. 8.88: Plot of $\sigma_{\theta\theta}/\sigma_0$ along A'B' of *figure 8.2* obtained from ANSYS and TSA for $k = 17$ coefficients and $m_4 = 4{,}094$ TSA values 435
Fig. 8.89: Strain gage mounted at point C of *figure 8.1* and C' of *figure 8.2* on the curved edge of the hole 438

Fig. 8.90: Strip gage mounted along line CD of *figure 8.1 and* C'D' of *figure 8.2* 438
Fig. 8.91: Strip gage mounted along line CD and C'D' of *figures 8.1 and 8.2* respectively, strain gage along the curved edge of the hole and the distant transverse strain gage 439
Fig. 8.92: Distant longitudinal strain gage used to check for any out-of-plane bending (gage length = 3.175mm = 0.125") 439
Fig. 8.93: Calibration specimen with mounted horizontal and vertical strain gages on both sides of the plate 440
Fig. 8.94: 16 Channel, variable excitation strain gage conditioner 440
Fig. 8.95: Strain gage on back side of the symmetrically-loaded specimen 441
Fig. 8.96: Strain gage on the back side of unsymmetrically-loaded specimen 441
Fig. 8.97: Overview of the testing setup, including the MTS loading frame, hydraulic grips, TSA camera, strain gage switching, oscilloscope and balancing equipment 442
Fig. 8.98: Load (lbs) vs. Strain ε_{yy} for different strain gages along line CD of plate of specimen *figure 8.1* 443
Fig. 8.99: Load (N) vs. Strain ε_{yy} for different strain gages along line CD of plate of *figure 8.1* 444
Fig. 8.100: Strain ε_{yy} from strain gages along CD of *figure 8.1* for different loads 444
Fig. 8.101: Strain ε_{yy} along CD of *figure 8.1* obtained from ANSYS, strain gages and TSA for $k = 9$ coefficients and $m_1 = 4{,}378$ TSA values 445
Fig. 8.102: Load (lbs) vs. Strain $\varepsilon_{\theta\theta}$ for different strain gages along the line C'D' of plate of *figure 8.2* 446
Fig. 8.103: Load (N) vs. Strain $\varepsilon_{\theta\theta}$ for different strain gages along the line CD of plate of *figure 8.1* 446
Fig. 8.104: Strain $\varepsilon_{\theta\theta}$ obtained from strain gages along C'D' of *figure 8.2* for different loads .. 447
Fig. 8.105: Strain $\varepsilon_{\theta\theta}$ along C'D' of *figure 8.2* obtained from ANSYS, strain gages and TSA for $k = 17$ coefficients and $m_4 = 9{,}372$ TSA values 447
Fig. 8.106: Values of the Airy coefficients obtained from the TSA measured data (S*) for the large hole after imposing traction-free conditions only at the edge of the large hole 450
Fig. 8.107: Values of the Airy coefficients obtained from the TSA measured data (S*) for the small hole after imposing traction-free conditions only at the edge of the small hole451

Fig. 8.108: Relative changes in the Airy coefficients for the small hole by satisfying stress compatibility between the holes 452

Fig. 8.109: Relative change in the Airy coefficients for the large hole by satisfying stress compatibility between the holes 453

Fig. 8.110: Plot of $\sigma_{\theta\theta}/\sigma_0$ around the boundary of the large hole ($r/R_2 = 1$) from ANSYS and TSA using coefficients (b_o, c_o, d_1', b_2', d_2', c_3', d_3', b_4' *and* d_4') of case 3 of *figure 8.106*.. 454

Fig. 8.111: Strain ε_{yy} along CD of *figure 8.1* obtained from ANSYS, strain gages and TSA using coefficients (b_o, c_o, d_1', b_2', d_2', c_3', d_3', b_4' *and* d_4') of case 3 of *figure 8.106* 454

Fig. 8.112: Plot of $\sigma_{\theta\theta}/\sigma_0$ around the boundary of the small hole ($r/R_1 = 1$) from ANSYS and TSA using coefficients (b_o, c_o, d_1', b_2', d_2', c_3', d_3', b_4' *and* d_4') of case 3 of *figure 8.107*.. 454

Fig. 9.1: Schematic of symmetrically-loaded glass-epoxy orthotropic composite plate with a central circular hole 459

Fig. 9.2: Finite element model for the analysis of *figure 9.1* 476

Fig. 9.3: Source locations of $m = 3,449$ simulated experimental data 477

Fig. 9.4: Plot of σ_{xx}/σ_0 around the boundary of the hole ($r/R = 1$) from FEA and hybrid method for $m = 3,449$ input u-displacements and $k = 2$ coefficients..... 478

Fig. 9.5: Plot of σ_{yy}/σ_0 around the boundary of the hole ($r/R = 1$) from FEA and hybrid method for $m = 3,449$ input u-displacements and $k = 2$ coefficients..... 479

Fig. 9.6: Contour plot of u/r throughout $6.35\text{mm} \le r \le 12.7\text{mm}$ region adjacent to hole predicted by FEA (left side) and based on evaluated coefficients (right side) for $m = 3,449$ input numerically simulated measured u-displacements and $k = 2$ coefficients (right side) 479

Fig. 9.7: Contour plot of v/r throughout $6.35\text{mm} \le r \le 12.7\text{mm}$ region adjacent to hole predicted by FEA (left side) and based on evaluated coefficients (right side) for $m = 3,449$ input numerically simulated measured u-displacements and $k = 2$ coefficients 480

Fig. 9.8: Contour plot of σ_{xx}/σ_0 throughout $6.35\text{mm} \le r \le 12.7\text{mm}$ region adjacent to hole predicted by FEA (left side) and based on evaluated coefficients (right side) for $m = 3,449$ input numerically simulated measured u-displacements and $k = 2$ coefficients 480

Fig. 9.9: Contour plot of σ_{yy}/σ_0 throughout 6.35mm ≤ r ≤ 12.7mm region adjacent to hole predicted by FEA (left side) and based on evaluated coefficients (right side) for $m = 3,449$ input numerically simulated measured u-displacements and $k = 2$ coefficients 481

Fig. 9.10: Contour plot of σ_{xy}/σ_0 throughout 6.35mm ≤ r ≤ 12.7mm region adjacent to hole predicted by FEA (left side) and based on evaluated coefficients (right side) for $m = 3,449$ input numerically simulated measured u-displacements and $k = 2$ coefficients 481

Fig. 9.11: Contour plot of u/r throughout 6.35mm ≤ r ≤ 12.7mm region adjacent to hole predicted by FEA (left side) and based on evaluated coefficients (right side) for $m = 3,449$ input numerically simulated measured v-displacements and $k = 2$ coefficients 482

Fig. 9.12: Contour plot of v/r throughout 6.35mm ≤ r ≤ 12.7mm region adjacent to hole predicted by FEA (left side) and based on evaluated coefficients (right side) for $m = 3,449$ input numerically simulated measured v-displacements and $k = 2$ coefficients 482

Fig. A3.1: Plot of $\varepsilon_{rr}/\varepsilon_0$ along boundary of the hole from strain-gage evaluated Airy coefficients for $k = 13$ coefficients ($m = 45$ strain-gage input values) and ANSYS 538

Fig. A3.2: Plot of $\varepsilon_{rr}/\varepsilon_0$ along r/R = 1.5 from strain-gage evaluated Airy coefficients for $k = 13$ coefficients ($m = 45$ strain-gage input values) and ANSYS 538

Fig. A3.3: Plot of $\varepsilon_{rr}/\varepsilon_0$ along r/R = 2 from strain-gage evaluated Airy coefficients for $k = 13$ coefficients ($m = 45$ strain-gage input values) and ANSYS 538

Fig. A3.4: Plot of $\varepsilon_{\theta\theta}/\varepsilon_0$ along boundary of the hole from strain-gage evaluated Airy coefficients for $k = 13$ coefficients ($m = 45$ strain-gage input values) and ANSYS 539

Fig. A3.5: Plot of $\varepsilon_{\theta\theta}/\varepsilon_0$ along r/R = 1.5 from strain-gage evaluated Airy coefficients for $k = 13$ coefficients ($m = 45$ strain-gage input values) and ANSYS 539

Fig. A3.6: Plot of $\varepsilon_{\theta\theta}/\varepsilon_0$ along r/R = 2 from strain-gage evaluated Airy coefficients for $k = 13$ coefficients ($m = 45$ strain-gage input values) and ANSYS 539

Fig. A3.7: Plot of $\varepsilon_{xx}/\varepsilon_0$ along boundary of the hole from strain-gage evaluated Airy coefficients for $k = 13$ coefficients ($m = 45$ strain-gage input values) and ANSYS 540

Fig. A3.8: Plot of $\varepsilon_{xx}/\varepsilon_0$ along r/R = 1.5 from strain-gage evaluated Airy coefficients for $k = 13$ coefficients ($m = 45$ strain-gage input values) and ANSYS 540

Fig. A3.9: Plot of $\varepsilon_{xx}/\varepsilon_0$ along r/R = 2 from strain-gage evaluated Airy coefficients for *k = 13* coefficients (*m = 45* strain-gage input values) and ANSYS 540

Fig. A3.10: Plot of $\varepsilon_{xx}/\varepsilon_0$ along AB of *figure 3.1* from strain-gage evaluated Airy coefficients for *k = 13* coefficients (*m = 45* strain-gage input values) and ANSYS..... 541

Fig. A3.11: Plot of $\varepsilon_{yy}/\varepsilon_0$ along boundary of the hole from strain-gage evaluated Airy coefficients for *k = 13* coefficients (*m = 45* strain-gage input values) and ANSYS 541

Fig. A3.12: Plot of $\varepsilon_{yy}/\varepsilon_0$ along r/R = 1.5 from strain-gage evaluated Airy coefficients for *k = 13* coefficients (*m = 45* strain-gage input values) and ANSYS 541

Fig. A3.13: Plot of $\varepsilon_{yy}/\varepsilon_0$ along r/R = 2 from strain-gage evaluated Airy coefficients for *k = 13* coefficients (*m = 45* strain-gage input values) and ANSYS 542

Fig. A3.14: Plot of $\varepsilon_{yy}/\varepsilon_0$ along AB of *figure 3.1* from strain-gage (experimental result and reconstructed using the known Airy coefficients) for *k = 13* coefficients (*m = 45* strain-gage input values) and ANSYS..... 542

Fig. A3.15: Plot of σ_{rr}/σ_0 along boundary of the hole from strain-gage evaluated Airy coefficients for *k = 13* coefficients (*m = 45* strain-gage input values) and ANSYS 542

Fig. A3.16: Plot of σ_{rr}/σ_0 along r/R = 1.5 from strain-gage evaluated Airy coefficients for *k = 13* coefficients (*m = 45* strain-gage input values) and ANSYS 543

Fig. A3.17: Plot of σ_{rr}/σ_0 along r/R = 2 from strain-gage evaluated Airy coefficients for *k = 13* coefficients (*m = 45* strain-gage input values) and ANSYS 543

Fig. A3.18: Plot of σ_{xx}/σ_0 (= σ_{rr}/σ_0) along AB of *figure 3.1* from strain-gage evaluated Airy coefficients for *k = 13* coefficients (*m = 45* strain-gage input values) and ANSYS . 543

Fig. A3.19: Plot of $\sigma_{r\theta}/\sigma_0$ along boundary of the hole from strain-gage evaluated Airy coefficients for *k = 13* coefficients (*m = 45* strain-gage input values) and ANSYS 544

Fig. A3.20: Plot of $\sigma_{r\theta}/\sigma_0$ along r/R = 1.5 from strain-gage evaluated Airy coefficients for *k = 13* coefficients (*m = 45* strain-gage input values) and ANSYS 544

Fig. A3.21: Plot of $\sigma_{r\theta}/\sigma_0$ along r/R = 2 from strain-gage evaluated Airy coefficients for *k = 13* coefficients (*m = 45* strain-gage input values) and ANSYS 544

Fig. A3.22: Plot of $\sigma_{r\theta}/\sigma_0$ along AB of *figure 3.1* from strain-gage evaluated Airy coefficients for *k = 13* coefficients (*m = 45* strain-gage input values) and ANSYS..... 545

Fig. A3.23: Plot of $\sigma_{\theta\theta}/\sigma_0$ along boundary of the hole from strain-gage evaluated Airy coefficients for $k = 13$ coefficients ($m = 45$ strain-gage input values) and ANSYS . 545

Fig. A3.24: Plot of $\sigma_{\theta\theta}/\sigma_0$ along r/R = 1.5 from strain-gage evaluated Airy coefficients for $k = 13$ coefficients ($m = 45$ strain-gage input values) and ANSYS 545

Fig. A3.25: Plot of $\sigma_{\theta\theta}/\sigma_0$ along r/R = 2 from strain-gage evaluated Airy coefficients for $k = 13$ coefficients ($m = 45$ strain-gage input values) and ANSYS 546

Fig. A3.26: Plot of σ_{yy}/σ_0 (= $\sigma_{\theta\theta}/\sigma_0$) along AB of *figure 3.1* from strain-gage evaluated Airy coefficients for $k = 13$ coefficients ($m = 45$ strain-gage input values) and ANSYS . 546

Fig. A4.1: Plot of $\varepsilon_{yy}/\varepsilon_{net}$ along vertical line CD ($\theta = 90^o$) of *figure 4.1* from hybrid method (strain-gage evaluated Airy coefficients, 5 input strains) and ANSYS..... 567

Fig. A4.2: Plot of $\varepsilon_{xx}/\varepsilon_{net}$ along vertical line CD ($\theta = 90^o$) of *figure 4.1* from hybrid method (strain-gage evaluated Airy coefficients, 5 input strains), discrete strain gages and ANSYS 567

Fig. A4.3: Plot of $\varepsilon_{yy}/\varepsilon_{net}$ along horizontal line AB ($\theta = 0^o$) of *figure 4.1* from hybrid method (strain-gage evaluated Airy coefficients, 5 input strains), discrete strain gages and ANSYS 568

Fig. A4.4: Plot of $\sigma_{\theta\theta}/\sigma_0$ along boundary of the hole from hybrid method (strain-gage evaluated Airy coefficients, 5 input strains) and ANSYS 568

Fig. A4.5: Plot of $\varepsilon_{rr}/\varepsilon_{net}$ at r/R = 1.75 from hybrid method (strain-gage evaluated Airy coefficients, 5 input strains) and ANSYS 569

Fig. A4.6: Plot of $\sigma_{\theta\theta}/(2P/\pi b)$ along vertical line CD ($\theta = 90^o$) of *figure 4.1* from hybrid method (strain-gage evaluated Airy coefficients, 5 input strains) and Timoshenko [26] 569

Fig. A4.7: Plot of $\sigma_{\theta\theta}/(2P/\pi b)$ along horizontal line AB ($\theta = 0^o$) of *figure 4.1* from hybrid method (strain-gage evaluated Airy coefficients, 5 input strains) and Timoshenko [26] 570

Fig. A4.8: Contours of u/R from FEA (left side) and hybrid method (strain-gage evaluated Airy coefficients, 5 input strains) (right side)..... 570

Fig. A4.9: Contours of v/R from FEA (left side) and hybrid method (strain-gage evaluated Airy coefficients, 5 input strains) (right side)..... 571

Fig. A4.10: Contours of u_r/R from FEA (left side) and hybrid method (strain-gage evaluated Airy coefficients, 5 input strains) (right side)..... 571

Fig. A4.11: Contours of u_θ/R from FEA (left side) and hybrid method (strain-gage evaluated Airy coefficients, 5 input strains) (right side) 572
Fig. A4.12: Contours of $\varepsilon_{rr}/\varepsilon_{net}$ from FEA (left side) and hybrid method (strain-gage evaluated Airy coefficients, 5 input strains) (right side) 572
Fig. A4.13: Contours of $\varepsilon_{\theta\theta}/\varepsilon_{net}$ from FEA (left side) and hybrid method (strain-gage evaluated Airy coefficients, 5 input strains) (right side) 573
Fig. A4.14: Contours of σ_{rr}/σ_{net} from FEA (left side) and hybrid method (strain-gage evaluated Airy coefficients, 5 input strains) (right side) 573
Fig. A4.15: Contours of $\sigma_{\theta\theta}/\sigma_{net}$ from FEA (left side) and hybrid method (strain-gage evaluated Airy coefficients, 5 input strains) (right side) 574
Fig. A4.16: Contours of $\sigma_{r\theta}/\sigma_{net}$ from FEA (left side) and hybrid method (strain-gage evaluated Airy coefficients, 5 input strains) (right side) 574
Fig. A4.17: 25 strain gages locations 575
Fig. A4.18: Plot of $\varepsilon_{yy}/\varepsilon_{net}$ along vertical line CD ($\theta = 90^o$) of *figure 4.1* from hybrid method (strain-gage evaluated Airy coefficients, 25 input strains) and ANSYS 576
Fig. A4.19: Plot of $\varepsilon_{xx}/\varepsilon_{net}$ along vertical line CD ($\theta = 90^o$) of *figure 4.1* from hybrid method (strain-gage evaluated Airy coefficients, 25 input strains), discrete strain gages and ANSYS 576
Fig. A4.20: Plot of $\varepsilon_{yy}/\varepsilon_{net}$ along horizontal line AB ($\theta = 0^o$) of *figure 4.1* from hybrid method (strain-gage evaluated Airy coefficients, 25 input strains), discrete strain gages and ANSYS 577
Fig. A4.21: Plot of $\sigma_{\theta\theta}/\sigma_0$ along boundary of the hole from hybrid method (strain-gage evaluated Airy coefficients, 25 input strains) and ANSYS 577
Fig. A4.22: Plot of $\varepsilon_{rr}/\varepsilon_{net}$ at r/R = 1.75 from hybrid method (strain-gage evaluated Airy coefficients, 25 input strains) and ANSYS 578
Fig. A4.23: Plot of $\sigma_{\theta\theta}/(2P/\pi b)$ along vertical line CD ($\theta = 90^o$) of *figure 4.1* from hybrid method (strain-gage evaluated Airy coefficients, 25 input strains) and Timoshenko [26] 578
Fig. A4.24: Plot of $\sigma_{\theta\theta}/(2P/\pi b)$ along horizontal line AB ($\theta = 0^o$) of *figure 4.1* from hybrid method (strain-gage evaluated Airy coefficients, 25 input strains) and Timoshenko [26] 579

Fig. A4.25: 13 strain gages locations 579
Fig. A4.26: Plot of $\varepsilon_{yy}/\varepsilon_{net}$ along vertical line CD ($\theta = 90^o$) of *figure 4.1* from hybrid method (strain-gage evaluated Airy coefficients, 13 input strains) and ANSYS 580
Fig. A4.27: Plot of $\varepsilon_{xx}/\varepsilon_{net}$ along vertical line CD ($\theta = 90^o$) of *figure 4.1* from hybrid method (strain-gage evaluated Airy coefficients, 13 input strains), discrete strain gages and ANSYS 580
Fig. A4.28: Plot of $\varepsilon_{yy}/\varepsilon_{net}$ along horizontal line AB ($\theta = 0^o$) of *figure 4.1* from hybrid method (strain-gage evaluated Airy coefficients, 13 input strains), discrete strain gages and ANSYS 581
Fig. A4.29: Plot of $\sigma_{\theta\theta}/\sigma_0$ along boundary of the hole from hybrid method (strain-gage evaluated Airy coefficients, 13 input strains) and ANSYS 581
Fig. A4.30: Plot of $\varepsilon_{rr}/\varepsilon_{net}$ at r/R = 1.75 from hybrid method (strain-gage evaluated Airy coefficients, 13 input strains) and ANSYS 582
Fig. A4.31: Plot of $\sigma_{\theta\theta}/(2P/\pi b)$ along vertical line CD ($\theta = 90^o$) of *figure 4.1* from hybrid method (strain-gage evaluated Airy coefficients, 13 input strains) and Timoshenko [26] 582
Fig. A4.32: Plot of $\sigma_{\theta\theta}/(2P/\pi b)$ along horizontal line AB ($\theta = 0^o$) of *figure 4.1* from hybrid method (strain-gage evaluated Airy coefficients, 13 input strains) and Timoshenko [26] 583
Fig. A5.1: Ellipse showing the major axis (2a) and minor axis (2b) 584
Fig. A5.2: Coordinates Representation 586
Fig. A5.3 Family of conical ellipses [30] 587
Fig. A5.4: Coordinate system 588
Fig. A6.1: TSA-determined σ_{rr}/σ_0 around the boundary of the hole (r/R = 1) for $m_1+h_1+t_1 = 11,279$ input values, $k = 9$ coefficients and $m_1 = 3,413$ TSA values, $h_1 = 2*831$, $t_1 = 2*101+2*3001$ 626
Fig. A6.2: Plot of $cos(\phi)$ and TSA-determined σ_* ($= \sigma_{rr}/\sigma_{rr(max)}$) vs. angle ϕ ($=180^o - \theta$) around the boundary of the hole (r/R = 1) for $m_1+h_1+t_1 = 11,279$ input values, $k = 9$ coefficients and $m_1 = 3,413$ TSA values, $h_1 = 2*831$, $t_1 = 2*101+2*3001$ 626

Fig. A6.3: TSA-determined $\sigma_{r\theta}/\sigma_0$ around the boundary of the hole (r/R = 1) for $m_1+h_1+t_1 = 11,279$ input values, $k = 9$ coefficients and $m_1 = 3,413$ TSA values, $h_1 = 2*831$, $t_1 = 2*101+2*3001$ 627
Fig. A6.4: Finite Element model of the plate with circular pin in ANSYS 628
Fig. A6.5: Contour plot of stress in the x-direction (σ_{xx}) for the plate with circular pin 629
Fig. A6.6: Contour plot of stress in the y-direction (σ_{yy}) for the plate with circular pin 630
Fig. A6.7: Contour plot of shear stress (σ_{xy}) for the plate with circular pin 631
Fig. A6.8: Contour plot of radial stress (σ_{rr}) for the plate with circular pin 632
Fig. A6.9: Contour plot of tangential stress ($\sigma_{\theta\theta}$) for the plate with circular pin 633
Fig. A6.10: Contour plot of polar shear stress ($\sigma_{r\theta}$) for the plate with circular pin 634
Fig. A6.11: Plot of σ_{rr}/σ_0 around the boundary of the hole (r/R = 1) from ANSYS and TSA for $m_1+h_1+t_1 = 11,279$ input values and $k = 9$ ($m_1 = 3,413$ TSA values, $h_1 = 2*831$, $t_1 = 2*101+2*3001$) 635
Fig. A6.12: Plot of $\sigma_{\theta\theta}/\sigma_0$ around the boundary of the hole (r/R = 1) from ANSYS and TSA for $m_1+h_1+t_1 = 11,279$ input values and $k = 9$ ($m_1 = 3,413$ TSA values, $h_1 = 2*831$, $t_1 = 2*101+2*3001$) 636
Fig. A6.13: Plot of $\sigma_{r\theta}/\sigma_0$ around the boundary of the hole (r/R = 1) from ANSYS and TSA for $m_1+h_1+t_1 = 11,279$ input values and $k = 9$ ($m_1 = 3,413$ TSA values, $h_1 = 2*831$, $t_1 = 2*101+2*3001$) 636
Fig. A6.14: Plot of σ_{xx}/σ_0 around the boundary of the hole (r/R = 1) from ANSYS and TSA for $m_1+h_1+t_1 = 11,279$ input values and $k = 9$ ($m_1 = 3,413$ TSA values, $h_1 = 2*831$, $t_1 = 2*101+2*3001$) 637
Fig. A6.15: Plot of σ_{rr}/σ_0 along r/R = 1.05 from ANSYS and TSA for $m_1+h_1+t_1 = 11,279$ input values and $k = 9$ ($m_1 = 3,413$ TSA values, $h_1 = 2*831$, $t_1 = 2*101+2*3001$) 637
Fig. A6.16: Plot of $\sigma_{\theta\theta}/\sigma_0$ along r/R = 1.05 from ANSYS and TSA for $m_1+h_1+t_1 = 11,279$ input values and $k = 9$ ($m_1 = 3,413$ TSA values, $h_1 = 2*831$, $t_1 = 2*101+2*3001$) 638
Fig. A6.17: Plot of $\sigma_{r\theta}/\sigma_0$ along r/R = 1.05 from ANSYS and TSA for $m_1+h_1+t_1 = 11,279$ input values and $k = 9$ ($m_1 = 3,413$ TSA values, $h_1 = 2*831$, $t_1 = 2*101+2*3001$) 638
Fig. A6.18: Plot of σ_{rr}/σ_0 along r/R = 1.1 from ANSYS and TSA for $m_1+h_1+t_1 = 11,279$ input values and $k = 9$ ($m_1 = 3,413$ TSA values, $h_1 = 2*831$, $t_1 = 2*101+2*3001$) 639

Fig. A6.19: Plot of $\sigma_{\theta\theta}/\sigma_0$ along r/R = 1.1 from ANSYS and TSA for $m_1+h_1+t_1 = 11,279$ input values and $k = 9$ ($m_1 = 3,413$ TSA values, $h_1 = 2*831$, $t_1 = 2*101+2*3001$) 639

Fig. A6.20: Plot of $\sigma_{r\theta}/\sigma_0$ along r/R = 1.1 from ANSYS and TSA for $m_1+h_1+t_1 = 11,279$ input values and $k = 9$ ($m_1 = 3,413$ TSA values, $h_1 = 2*831$, $t_1 = 2*101+2*3001$) 640

Fig. A6.21: Plot of σ_{rr}/σ_0 along r/R = 1.5 from ANSYS and TSA for $m_1+h_1+t_1 = 11,279$ input values and $k = 9$ ($m_1 = 3,413$ TSA values, $h_1 = 2*831$, $t_1 = 2*101+2*3001$) 640

Fig. A6.22: Plot of $\sigma_{\theta\theta}/\sigma_0$ along r/R = 1.5 from ANSYS and TSA for $m_1+h_1+t_1 = 11,279$ input values and $k = 9$ ($m_1 = 3,413$ TSA values, $h_1 = 2*831$, $t_1 = 2*101+2*3001$) 641

Fig. A6.23: Plot of $\sigma_{r\theta}/\sigma_0$ along r/R = 1.5 from ANSYS and TSA for $m_1+h_1+t_1 = 11,279$ input values and $k = 9$ ($m_1 = 3,413$ TSA values, $h_1 = 2*831$, $t_1 = 2*101+2*3001$) 641

Fig. A6.24: Plot of σ_{xx}/σ_0 along the line extending from the edge of the hole (x = 0 or $\theta = 90^o$) from ANSYS and TSA for $m_1+h_1+t_1 = 11,279$ input values and $k = 9$ ($m_1 = 3,413$ TSA values, $h_1 = 2*831$, $t_1 = 2*101+2*3001$) 642

Fig. A6.25: Contour plot of σ_{xx}/σ_0 from TSA (left) for $m_1+h_1+t_1 = 11,279$ input values and $k = 9$ ($m_1 = 3,413$ TSA values, $h_1 = 2*831$, $t_1 = 2*101+2*3001$) and ANSYS (right)..... 642

Fig. A6.26: Contour plot of σ_{yy}/σ_0 from TSA (left) for $m_1+h_1+t_1 = 11,279$ input values and $k = 9$ ($m_1 = 3,413$ TSA values, $h_1 = 2*831$, $t_1 = 2*101+2*3001$) and ANSYS (right)..... 643

Fig. A6.27: Contour plot of σ_{xy}/σ_0 from TSA (left) for $m_1+h_1+t_1 = 11,279$ input values and $k = 9$ ($m_1 = 3,413$ TSA values, $h_1 = 2*831$, $t_1 = 2*101+2*3001$) and ANSYS (right)..... 643

Fig. A6.28: Contour plot of σ_{rr}/σ_0 from TSA (left) for $m_1+h_1+t_1 = 11,279$ input values and $k = 9$ ($m_1 = 3,413$ TSA values, $h_1 = 2*831$, $t_1 = 2*101+2*3001$) and ANSYS (right)..... 644

Fig. A6.29: Contour plot of $\sigma_{\theta\theta}/\sigma_0$ from TSA (left) for $m_1+h_1+t_1 = 11,279$ input values and $k = 9$ ($m_1 = 3,413$ TSA values, $h_1 = 2*831$, $t_1 = 2*101+2*3001$) and ANSYS (right)..... 644

Fig. A6.30: Contour plot of $\sigma_{r\theta}/\sigma_0$ from TSA (left) for $m_1+h_1+t_1 = 11,279$ input values and $k = 9$ ($m_1 = 3,413$ TSA values, $h_1 = 2*831$, $t_1 = 2*101+2*3001$) and ANSYS (right)..... 645

Fig. A8.1: 3-D Finite element model for the symmetrically-loaded plate, *figure 8.1* 689

Fig. A8.2: 3-D contour plots of σ_{xx} (psi) through the plate thickness 690

Fig. A8.3: 3-D contour plots of σ_{yy} (psi) through the plate thickness 690

Fig. A8.4: 3-D contour plots of σ_{zz}/σ_0 through the plate thickness 691

Fig. A8.5: 3-D contour plots of σ_{rr} (psi) through the plate thickness 691

Fig. A8.6: 3-D contour plots of $\sigma_{\theta\theta}$ (psi) through the plate thickness 692
Fig. A8.7: 3-D contour plots of $\sigma_{r\theta}$ (psi) through the plate thickness 692
Fig. A8.8: 3-D contour plots of σ_{rz} (psi) through the plate thickness 693
Fig. A8.9: 3-D contour plots of $\sigma_{\theta z}$ (psi) through the plate thickness 693
Fig. A1: Specimen loaded in Fixture 696
Fig. A2: Specimen in loading frame with DIC cameras 697
Fig. A3: Test Setup 698
Fig. A4: Additional photograph of test setup 699
Fig. A5: Actual recorded *u*-displacement data from Vic-2D 700
Fig. A6: Actual recorded *v*-displacement data from Vic-2D 701
Fig. A7: Actual recorded first principal Lagrange strain (ε_1) from Vic-2D 702
Fig. A8: Actual recorded second principal Lagrange strain (ε_2) from Vic-2D 703
Fig. A9: Actual recorded strain in x-direction (ε_{xx}) from Vic-2D 704
Fig. A10: Actual recorded strain in y-direction (ε_{yy}) from Vic-2D 705
Fig. A11: Actual recorded shear strain (ε_{xy}) from Vic-2D 706
Fig. A12: *u*-displacement (in inches) from ANSYS 707
Fig. A12-A: *u*-displacement (in inches) from ANSYS 708
Fig. A13: *v*-displacement (in inches) from ANSYS 709
Fig. A13-A: *v*-displacement (in inches) from ANSYS 710
Fig. A14: Strain (ε_{xx}) from ANSYS 711
Fig. A14-A: Strain (ε_{xx}) from ANSYS 712
Fig. A15: Strain (ε_{yy}) from ANSYS 713
Fig. A15-A: Strain (ε_{yy}) from ANSYS 714
Fig. A16: Shear strain (ε_{xy}) from ANSYS 715
Fig. A16-A: Shear strain (ε_{xy}) from ANSYS 716

List of Tables

Table 3.1: Gage numbers and descriptions 76

Table 3.2: Normalized strains, $\varepsilon_{yy}/\varepsilon_0$ at discretely measured positions along line AB and those evaluated using the known Airy coefficients ($m = 41$). 100

Table 6.1: Total load from TSA-based vertical stress scanned at different horizontal levels of x for the plate with circular pin. 320

Table 6.2: Total load from TSA-based vertical stress scanned at different horizontal levels of x for the plate with non-circular pin. 322

List of Symbols

∇^4	Biharmonic operator
Δ	Change
$a_o, b_o, c_o, a_n , b_n , c_n , d_n$	Airy coefficients
N	Terminating value of the summation series
S_1, S_2	Rigid body translations
R*	Rigid body rotation
ϕ	Potential function
r	Radial coordinate measured from the center of the hole
θ	Angle
υ	Poisson's ratio
E	Elastic Modulus
d	Diameter of the hole
R	Radius of the hole
t	Thickness of the plate
L	Length of the plate
W	Width of the plate
F	Applied Load
σ_o	Far-Field Stress
ε_o	Far-Field Strain
\	Matrix division operator in MATLAB
pinv	pseudo inverse operator in MATLAB
[A]	Airy matrix
{c}	Airy coefficient vector
{d}	Input data vector

{d*}	Predicted vector
S	Isopachic stress
S^*	Recorded system signal
K	Thermomechanical coefficient
C	Condition number
RMS	Root Mean Square
m	Number of input data values
k	Number of unknown Airy Coefficients
u, v	Cartesian displacement components
u_r, u_θ	Polar displacement components
$\epsilon_{rr}, \varepsilon_{\theta\theta}$	Polar strain components
$\epsilon_{xx}, \varepsilon_{yy}$	Cartesian strain components
σ_{rr},$\sigma_{\theta\theta}$, $\sigma_{r\theta}$	Polar stress components
σ_{xx},σ_{yy}, σ_{xy}	Cartesian stress components
ξ, η	Elliptical coordinates

Chapter 1 : Introduction

1.1 Background

This research employs several experimental techniques to determine full-field individual stress, strain or displacement components in engineering members. The variations in the stress experienced by the structural components due to the effects of the shape of one or more holes, pin-loaded holes and unknown loading/boundary conditions in isotropic or composite structure are investigated. The thesis provides quantitative experimental methodologies using optical techniques (digital image correlation, thermoelastic stress analysis) and strain gages to investigate structural integrity.

The objective of this research was to use contemporary experimental methods, and analytical and numerical tools to analyze finite structural members. Quantitative experimental methods are enhanced and applied, and Finite Element Analysis (FEA) was used for validation. Determining the full-field individual stress, strain and displacement components employing DIC, strain gages or TSA is emphasized. A hybrid experimental-numerical-analytical approach is utilized whereby discretely measured information is processed with a stress function to evaluate the stresses, strains and displacements. Different approaches are developed to solve engineering problems such as a finite plate with a single (circular or non-circular) or multiple hole(s) whose stress fields interact, contact problems, simplifying the stress function for the finite members with complicated loading and strain interaction between dissimilar metals.

1.2 Novelty

Traditional displacement–based methods (moiré, holography, speckle, digital image correlation) involve differentiating the measured information to obtain strains and stresses. However, differentiating measured data has its perils. The author is unaware of any previously reported research on evaluating the full-field individual stress, strain and displacement components from recording only a single component of displacement at discrete locations. This is demonstrated for isotropic materials in Chapter 2 using DIC measured displacement and for orthotropic materials in Chapter 9 using simulated displacement data. It is also notable that measuring a single component of displacement is advantageous particularly in composite structures. This ability is significant since obtaining both displacement components can be non-trivial with moiré or speckle. Moreover, it is not uncommon in practice to find regions where one of the displacement components is very small or is unreliable.

Conventional strain gages are used as point-wise measuring devices. They are the most widely used strain sensor in industry. Reference [1] utilizes three-elements to measure the full-field stress in a bolted aluminum joint. Baek and Rowlands [9] used two-element rosettes to evaluate the strains throughout a perforated orthotropic tensile plate. On the other hand, Chapter 3 employs only forty-five single-element strain gages for the full-field stress/strain analysis of a finite plate containing a circular hole. This experimental method is further simplified in Chapter 4 where five strain gages are used for full-field strain, strain and displacement analysis of a diametrically-loaded ring. The successful ability to use only single-element gages greatly reduces the foot-print covered as well as minimizes the data acquisition equipment needed. Two- or three-element rosettes also pose the challenge in that the various individual gage elements of a

rosette occur at different geometric locations. This can be particularly concerning in regions of high strain gradients.

Chapter 5 demonstrates the ability to determine the individual stress components experimentally in a finite tensile plate containing an elliptical hole using a series representation of an Airy stress function in terms of polar coordinates. Most theoretical stress analyses of multiple- or non-circular-perforated components involve a complex-variable stress function or are restricted to an infinite geometry. Employing real, rather than the commonly used complex, variables is easier for such problems, avoids inconveniences associated with conformal mapping and extends thermoelastic capability to stress analyze components containing non-circular discontinuities or multiple holes. This is the first known application of (real) polar coordinates to non-round cutouts. This is significant in that there is a simple general solution to the governing biharmonic equation in (real) polar coordinates but that seemingly is not so in elliptical or generalized orthogonal coordinates.

One might question the significance of evaluating the stresses, strains or displacements in finite perforated plane stressed members or pinned connections experimentally in light of available theoretical and numerical approaches. Theoretical, analytical or numerical (FEM, FD) solutions can be challenging and they necessitate knowing reliably the boundary (loading) conditions, which are often unavailable in practice. Also, few purely analytical (theoretical) solutions are available, and those that are available typically assume an infinite geometry. The present method circumvents this difficulty as is demonstrated in Chapter 2 for unknown far-field load/displacement, Chapter 6 for bolted joints, Chapter 7 for a concentrated load at a near- edge hole, and Chapter 8 for an arbitrarily loaded incline plate with multiple holes. In this research,

the analysis considers any typical symmetry in the component and imposes (often *analytically*) the traction-free boundary conditions on the boundary of a cut-out.

Finally, an experimental study is conducted in Appendix A* to determine the effect of interface strains between dissimilar materials, i.e., full-field strain and displacement fields are determined using DIC in a diametrically-loaded structure consisting of a ring of one material within which is a disk of a different material.

1.3 Experimental Techniques

Digital Image Correlation (DIC) is a contemporary optical technique to measure full-field 2D or 3D individual components of displacement. It employs tracking and image registration techniques for displacement measurements when the material deforms. Advantages of DIC include full-field, non-contacting, non-destructive, static/dynamic measurements. The DIC system employed here is that by Correlation Solutions, Columbia, SC

A strain gage is a discrete device used to measure the strain of an object when deformed. When an object is loaded/deformed, the foil of a bonded strain gage is deformed, causing a change in electrical resistance. This change in resistance, usually measured using a Wheatstone bridge, is related to the strain by the manufacturer's supplied gage factor. Most applications of strain gages are point-wise measurements.

Thermoelastic Stress Analysis (TSA) is a contemporary full-field, non-contacting technique for determining stresses in engineering structures under their operating conditionings. Thermoelastic coupling is the temperature change caused by mechanical loading when compressed or expanded (i.e., experience a change in volume). These small temperature variations range from a few milli Kelvin (mK) to a tenth of a Kelvin in solids [2]. Under adiabatic and reversible conditions these temperature variations are proportional to the first stress invariant. For materials having a positive coefficient of thermal expansion, thermoelastic temperature variations are positive during compression and negative during expansion [2]. The adiabatic conditions are achieved by cyclically loading the structure such that heat diffusion effects are negligible. If the load causing the volumetric change is removed and the material

returns to its original temperature and shape, the process is reversible. *Figure 1.1* represents the thermoelastic effect and identifies the governing relationship between the change in the spectral radiant photon emittance derived from Planck's law and the temperature change under isotropic plane stress. At room temperature the peak photon emittance occurs at a wavelength of 12µm and photodetector is restricted to two discrete window of operations 3-5µm and 8-13µm [10]. The TSA system used is that by Stress Photonics, Madison, WI. The sampling rate of the camera exceeds 1000 frames/sec and the loading frequency range is 0.6 – 1000Hz.

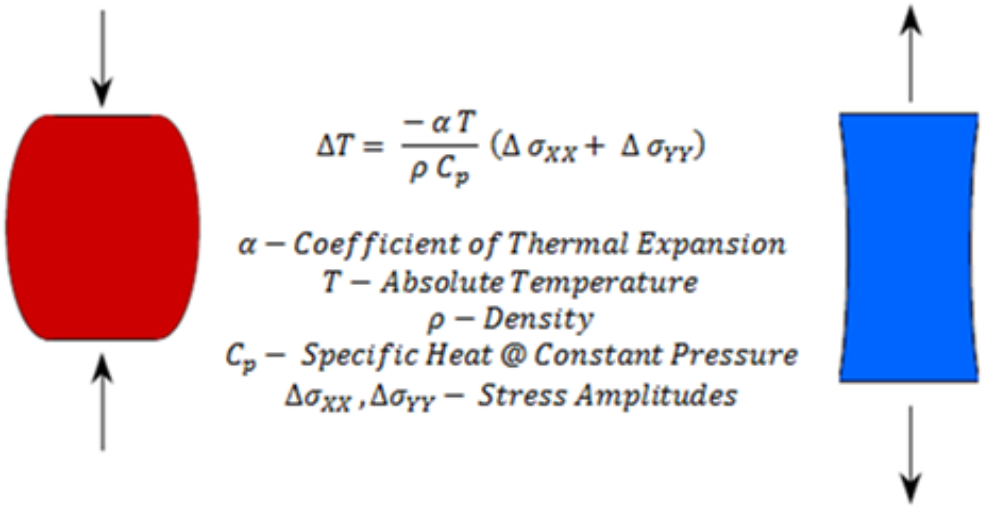

Fig. 1.1: Thermoelastic effect on the specimen [3]

1.4 Analytical Background

Experimental information is combined with a series representation of Maxwell's form of an Airy's stress function to evaluate the individual stress, strain or displacement components. For isotropy, Airy's stress formulation (based on equilibrium and compatibility equations) is the solution of $\nabla^4\phi=0$, where ϕ is the Airy stress function [1, 3 - 6]. The assumptions associated with this stress function are that there are no body forces and is applicable to plane-stress or plane-strain situations. Derivatives of Airy's stress function provide the individual stress components, and associated strain and displacement expressions are available based on elasticity. With orthotropic materials, the stress functions are usually in terms of complex variables.

The specific form of the Airy's stress function for a particular case can depend on conditions of symmetry, whether or not the coordinate origin is within the component, and single-valued stresses, strains and displacements. Previously, stress functions were derived based on the geometry and the loading conditions which made the stress function complicated, i.e., the individual components of stress involve many unknown coefficients and require knowing the geometry and applied loading. The stress function used here is simplified based on the geometry of the specimen and the experimental data accounts for the loading conditions.

Numerical techniques are utilized to evaluate the coefficients of the Airy stress function from measured data, thereby providing the individual stress, strain or displacement components.

Chapter 2 : Determining Individual Components of Stress, Strain and Displacement at and in the Neighborhood of a Cutout from Measuring a Single Component of Displacement

2.1 Introduction

This chapter demonstrates the ability to determine the individual components of displacement, strain and stress by processing a single measured component of displacement with a series representation of the Airy stress function. The present case of a loaded plate containing a central circular hole uses simulated experimental input from FEM, and measured displacements from Digital Image Correlation (DIC). It is usually more convenient to measure a single component of displacement rather than measuring all components of displacement, stress or strain. Being able to evaluate both displacement components (and hence the three independent components of strain and/or stress) from one component of displacement field is particularly advantageous with methods such as moiré, holography and speckle. Even with DIC (Digital Image Correlation), one can encounter situations where one of the measured in-plane displacements is of inferior quality. A case is demonstrated here using the DIC, in which one component of displacement was reliable and the other component of displacement (much less reliable) was evaluated using the herein developed technique. The stresses and strains were then evaluated using this measured displacement data.

Unlike purely analytical or numerical (FEM or FD) methods, the present technique does not require knowing the far-field boundary conditions. Although the specimen (between the loading grips) of the present DIC analyzed case is too short to know the far-field boundary conditions accurately, one is able to numerically model the situation approximately. This specimen was chosen because the individual components of stress were available from a previous TSA analysis.

A particular advantage of the present approach is its ability to evaluate all of the Airy coefficients from measuring only one component of displacement, and to reduce the number of these experimentally-determined coefficients by incorporating the traction-free conditions on the edge of the hole *analytically*. Fewer coefficients can reduce the amount of measured input data required and simplify the data processing (particularly the least square analysis). Using the stress, strain and displacement equations, the individual components of stress, strain and displacement are evaluated from recorded information of the single displacement component. Moreover, this is accomplished without explicitly differentiating the displacements spatially, which is typically necessary with traditional displacement measured techniques. Differentiating measured data can have its perils. It is also particularly challenging to obtain accurate experimental displacements or strains on the edge of geometric cutouts (often the locations of the greatest interest). This challenge is overcome here in that the stresses, strains and displacements at, and in the neighborhood of the hole, are obtained from measured displacement data away from the edge of the hole.

As mentioned above, traditional displacement–based methods (moiré, holography, speckle, digital image correlation) typically involve differentiating the measured information to

obtain strains and stresses, and differentiating measured data can be unreliable. However this is not the issue here that it is in the traditional sense since the present approach uses measured displacement data to evaluate the Airy coefficients, and the later appear in the expressions for the stresses and strains. The expressions for the strains are analytical derivatives of the displacements. Moreover, the displacements are represented by a series, and the form of the series (based on the Airy stress function) has a mechanics foundation i.e., equilibrium and compatibility.

It is usually easier to measure displacements with respect to a rectangular Cartesian rather than a polar coordinate system, and employing stresses, strains and displacements in terms of an Airy stress function can be advantageous. However, there are conveniences to utilizing an Airy stress function in terms of polar, rather than rectangular, coordinates, i.e., there is a general convenient expression for the Airy stress function in polar coordinates. Fortunately, one can relatively easily transform the components of stress, strain and displacement at a point in terms of polar coordinates to those with respect to rectangular Cartesian coordinates, and vice-versa.

This chapter utilizes rectangular components of an experimentally measured displacement, but employs an Airy stress function in polar coordinates. All of the Airy coefficients, and hence the complete state (all components) of stress, strain and displacement on and in the neighborhood of the edge of a hole can be obtained from measuring only one component of displacement. The present ability is significant in that it is typically difficult to record reliable stress, strain or displacement data on the edge of a hole or notch, and yet such geometric cut–outs produce stress concentrations which can control a component's mechanical

integrity. This motivates having an ability to evaluate such mechanical information on the edge of a hole or notch from recorded data away from the hole or notch.

Although the coefficients of a relevant Airy stress function have been evaluated previously from measure temperature (Thermoelastic Stress Analysis, TSA), strain gage or photoelastic information [1, 3 - 5], this chapter emphasizes doing so from DIC–measured displacements in a single direction. Once the Airy coefficients have been evaluated, the in-plane individual components of displacement, strain and stress are available.

The present displacement–based approach involving the Airy stress function is demonstrated here by application to a tensile component containing a single circular hole. This problem will be analyzed initially by employing FE-simulated displacement data in order to substantiate the viability, robustness, and numerical stability of the described numerical method. DIC measured displacement data will then be utilized to investigate the displacement, strain and stress distributions in the actual plate. The described concept of using an Airy stress function in polar coordinates and the measured displacement data can be extended to stress analyze more involved situations such as structures containing multiple holes, loaded holes (bolted joints) and/or more complicated shapes or loadings.

2.2 Relevant Equations

A general Airy's stress function in polar co-ordinates satisfying the biharmonic equation $\nabla^4\phi = 0$, equilibrium and compatibility can be written as [1]:

$$\begin{aligned}
&\phi = a_0 + b_0 \ln r + c_0 r^2 + d_0 r^2 \ln r + \left(A_0 + B_0 \ln r + C_0 r^2 + D_0 r^2 \ln r\right)\theta \\
&+ \left(a_1' r + b_1' r \ln r + \frac{c_1'}{r} + d_1' r^3 \right) \sin\theta + \left(a_1 r + b_1 r \ln r + \frac{c_1}{r} + d_1 r^3 \right) \cos\theta \\
&+ \left(A_1' r + B_1' r \ln r\right)\theta \sin\theta + \left(A_1 r + B_1 r \ln r\right)\theta \cos\theta \\
&+ \sum_{n=2}^{\infty} \left(a_n' r^n + b_n' r^{n+2} + c_n' r^{-n} + d_n' r^{2-n}\right) \sin(n\theta) \\
&+ \sum_{n=2}^{\infty} \left(a_n r^n + b_n r^{n+2} + c_n r^{-n} + d_n r^{2-n}\right) \cos(n\theta)
\end{aligned} \tag{2.1}$$

As seen from *equation 2.1*, the stress function,ϕ, contains numerous unknown Airy coefficients, a_o , b_o , c_o , d_o and so forth. This chapter involves evaluating these Airy coefficients experimentally using DIC or ESPI–measured displacements and some local boundary conditions. Previous literature demonstrates the ability to evaluate the Airy coefficients of *equation 2.1* from recorded photoelastic, strain or temperature data [1, 3 - 5, 8, 12]. Although the displacements are measured here using DIC, one could also employ techniques such as moiré, ESPI or holography.

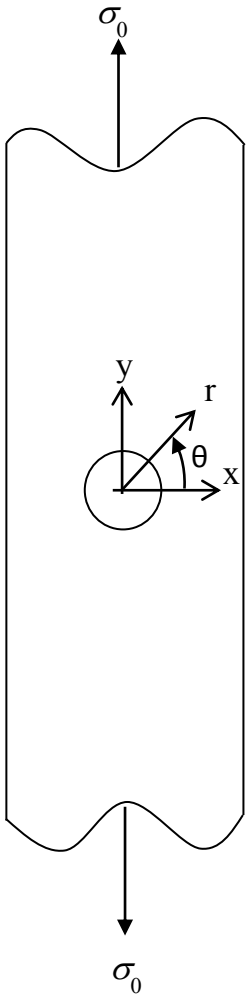

Fig. 2.1: Uniaxially-loaded plate

Knowing ϕ, the individual components of stresses can be obtained by differentiating the stress function as shown in *equations 2.2 through 2.4* [1, 3 - 8]

$$\sigma_{rr} = \frac{1}{r}\frac{\partial \phi}{\partial r} + \frac{1}{r^2}\frac{\partial^2 \phi}{\partial \theta^2} \tag{2.2}$$

$$\sigma_{\theta\theta} = \frac{\partial^2 \phi}{\partial r^2} \tag{2.3}$$

$$\sigma_{r\theta} = -\frac{\partial}{\partial r}\left(\frac{1}{r}\frac{\partial \phi}{\partial \theta}\right) \tag{2.4}$$

For isotropic materials, the displacements are then obtained by integrating *equations 2.5 and 2.6, i.e.,*

$$\frac{\partial u_r}{\partial r} = \epsilon_{rr} = \frac{1}{E}\left(\sigma_{rr} - \upsilon\, \sigma_{\theta\theta}\right) \tag{2.5}$$

$$\frac{\partial u_\theta}{\partial \theta} = r.\varepsilon_{\theta\theta} - u_r \tag{2.6}$$

Based on the previous equations, unknown Airy coefficients of *equation 2.1* will appear in the equations for individual components of displacement (as well as the strain and stress). Hence, in order to determine the individual components of displacement, it is necessary to first evaluate these unknown Airy coefficients. The number of these (initially) unknown coefficients can often be reduced by considering factors such as any geometric and loading symmetry, and eliminating any terms that lead to multivalued displacements, strains or stresses. For a case such as that in *figure 2.1*, since the displacements, strains and stresses must be single-valued functions of θ and that there is no resultant force at the origin, coefficients d_0, B_0, C_0, D_0, B_1, B_1' and A_0, A_1, A_1', b_1, b_1' are all zero [6]. Again, referring to *figure 2.1*, the plate is symmetrical about both vertical x-axis and horizontal y-axis. Symmetry about the x-axis means that stresses occurring at any angle, say when θ = +β would be the same as those at θ = -β. Thus, $\phi(r, \theta) = \phi(r, -\theta)$. This indicates that ϕ must be an even function of θ. Also there is symmetry about the x-axis, so all sine terms go to zero. For a_n, b_n, c_n, d_n (for $n \geq 1$) the value of n is then a positive even integer.

Based on comments of the previous paragraph, a relevant Airy stress function satisfying the biharmonic equation $\nabla^4\phi = 0$, equilibrium and compatibility for the finite geometry associated with *figure 2.1* can therefore be written as [1, 5, 6]

$$\phi = a_0 + b_0 \ln r + c_0 r^2 + \sum_{n=2,4,6,..}^{N} \left\{ \left(a_n r^n + b_n \mathrm{r}^{\mathrm{n}+2} + c_n r^{-n} + d_n \mathrm{r}^{-(\mathrm{n}-2)} \right) \cos n\theta \right\} \quad (2.7)$$

The individual components of displacement are obtained by evaluating the stresses from *equations 2.2 and 2.3*, then integrating *equations 2.5 and 2.6 (equation 2A.11* of Appendix A2*):*

$$u_r = \frac{1}{\mathrm{E}} \cdot \left[- \sum_{n=2,4,\ldots}^{\mathrm{N}} \begin{pmatrix} \frac{-b_0(1+\upsilon)}{r} + 2c_0(1-\upsilon)r \\ a_n\, n\, (1+\upsilon)\; r^{n-1} \\ + b_n\, [(n-2) + \upsilon(n+2)]\, r^{n+1} \\ - \; c_n\, n\, (1+\upsilon)\, r^{-(n+1)} \\ - d_n\, [(n+2) + \upsilon(n-2)]\, r^{-(n-1)} \end{pmatrix} cos(n\theta) + g(\theta) \right] \quad (2.8)$$

where, $g(\theta) = \mathrm{S}_1 \cos\theta - \mathrm{S}_2 \sin\theta$. Also, (*equations 2A.11 and 2A.20* of Appendix A2)

$$u_\theta = \frac{1}{\mathrm{E}} \cdot \left[\sum_{n=2,4,\ldots}^{\infty} \begin{pmatrix} a_n\, n\, (1+\upsilon)\, r^{n-1} \\ + b_n\, [n(1+\upsilon) + 4]\, r^{n+1} \\ + \; c_n\, n(1+\upsilon)\, r^{-(n+1)} \\ + d_n [n(1+\upsilon) - 4]\, r^{-(n-1)} \end{pmatrix} sin(n\theta) - \mathrm{S}_1 \sin\theta - \mathrm{S}_2 \cos\theta + \mathrm{R}^* \mathrm{r} \right] \quad (2.9)$$

Radial coordinate *r* is measured from the center of the hole, angle θ is measured counter-clockwise from the horizontal x-axis *(figure 2.1)* and *N* is the terminating value of the summation series (*N* can be any positive even integer). S_1 and S_2 represent rigid body translations and R* represents a rigid body rotation [7, p.472]. Hence for a physical plate loaded in a testing

machine, S_1, S_2 and R* can be equated to zero. While coefficient a_0 appears in the relevant Airy potential function, ϕ, of *equation 2.7*, it is absent in the expressions for the individual displacement components *(equations 2.8 and 2.9)*. Coefficient a_0 disappears in the differentiation of *equations 2.2 and 2.3* and hence does not appear in the expression for the stresses, strains or displacements.

The Airy coefficients present in the expressions of *equations 2.8 and 2.9* can be evaluated from measured polar displacement data. However, experimentally it is often more convenient to measure rectangular component of displacement, u and v, rather than u_r and u_θ. Moreover, it is subsequently demonstrated that the expression for both u and v contains all of the relevant Airy coefficients. Hence one can evaluate both u and v (and all components of stress and strain) from measured data of either one of these two displacements (i.e., u or v). This can be advantageous in practice since it means one has to record only one of the displacement components experimentally. It can also happen that one can have the ample measurable and reliable displacement information in one coordinate direction but not in the orthogonal direction. The displacement data are from simulated displacements from Finite Element Analysis, Digital Image Correlation (DIC) and Electronic Speckle Pattern Interferometry (ESPI) experiment. Note that *equations 2.8 and 2.9* do not have the same coefficients. Referring to *equations 2.8 and 2.9,*

$$u_r = f(b_o, c_o, a_n, b_n, c_n, d_n \text{ for } n = 2,4,6\ldots) \tag{2.10}$$

$$u_\theta = f(a_n, b_n, c_n, d_n \text{ for } n = 2,4,6\ldots) \tag{2.11}$$

Comparing *equations 2.10 and 2.11* shows that coefficients present in the expression for radial displacement (u_r) are also present in the expression for the hoop component of

displacement (u_θ). On the other hand, the radial component of displacement also contains coefficients b_o, and c_o which are not present in the expression for the hoop displacement. It will be shown that if one transforms the polar components of displacement to rectangular displacement components, both of the latter will contain all of the Airy coefficients. Moreover, imposing the traction-free boundary conditions *analytically* on the boundary of the hole will result in reducing the number of coefficients in the present equations for the displacements.

Imposing the traction–free boundary conditions *analytically* on the boundary of the hole in the plate of *figure 2.1* ($\sigma_{r\theta} = 0$ and $\sigma_{rr} = 0$ at r = R and for all values of θ) results in some independent Airy coefficients becoming dependent functions of other Airy independent coefficients, i.e.

$$b_o \equiv f(c_o)$$

$$a_n \equiv f(b_n, d_n) \qquad (2.12)$$

$$c_n \equiv f(b_n, d_n)$$

A detailed derivation of the expressions of *equations 2.12* is contained in Appendix A2. By replacing these dependent coefficients (b_o, a_n, c_n), of *equation 2.12* by their corresponding independent coefficients (c_o, b_n, d_n), the displacement components of *equations 2.8 and 2.9* can be rewritten as in *equations 2.13* (from *equation 2A.32*) *and 2.14* (from *equation 2A.33*). Similarly *equations 2.15 through 2.19* correspond to the polar components of strain and stress after imposing traction-free conditions on the boundary of the hole.

$$u_r = \frac{1}{E}\left[-\sum_{n=2,4,\ldots}^{N} \begin{Bmatrix} \left\{\frac{2R^2}{r}(1+v) + 2(1-v)r\right\} c_0 \\ \begin{pmatrix} -(1+v)(n+1)R^2 r^{n-1} \\ -(1+v)R^{2(n+1)} r^{-(n+1)} \\ +[(n-2)+v(n+2)]\, r^{n+1} \end{pmatrix} b_n \\ + \begin{pmatrix} -(1+v)R^{-2(n-1)} r^{n-1} \\ +(1+v)(n-1)R^2 r^{-(n+1)} \\ -[(n+2)+v(n-2)]\, r^{-n+1} \end{pmatrix} d_n \end{Bmatrix} cos(n\theta) + g(\theta) \right] \quad (2.13)$$

where, $g(\theta) = S_1 \cos\theta - S_2 \sin\theta$, and

u_θ

$$= \frac{1}{E}.\left[\sum_{n=2,4,\ldots}^{N} \left(\begin{pmatrix} -(1+v)(n+1)R^2 r^{n-1} \\ +[n(1+v)+4]\, r^{n+1} \\ +(1+v)R^{2(n+1)} r^{-(n+1)} \end{pmatrix} b_n + \begin{pmatrix} -(1+v)R^{-2(n-1)} r^{n-1} \\ -(1+v)(n-1)R^2 r^{-(n+1)} \\ +[n(1+v)-4]\, r^{-(n-1)} \end{pmatrix} d_n \right) sin(n\theta) - S_1 \sin\theta - S_2 \cos\theta + R^* r \right]$$

(2.14)

Moreover from *equations 2A.27a and 2A.29*

$$\epsilon_{rr} = \frac{1}{E}\left[-\sum_{n=2,4,\ldots}^{N} \begin{Bmatrix} \left\{\frac{-2R^2}{r^2}(1+v) + 2(1-v)\right\} c_0 \\ \begin{pmatrix} -(1+v)(n-1)(n+1)R^2 r^{n-2} \\ +(1+v)(n+1)R^{2(n+1)} r^{-(n+2)} \\ +(n+1)[(n-2)+v(n+2)]\, r^{n} \end{pmatrix} b_n \\ + \begin{pmatrix} -(1+v)(n-1)R^{-2(n-1)} r^{n-2} \\ -(1+v)(n-1)(n+1)R^2 r^{-(n+2)} \\ +(n-1)[(n+2)+v(n-2)]\, r^{-n} \end{pmatrix} d_n \end{Bmatrix} cos(n\theta) \right] \quad (2.15)$$

$$\varepsilon_{\theta\theta} = \frac{1}{E}\left[\begin{array}{c}\left\{\frac{2R^2}{r^2}(1+\upsilon) + 2(1-\upsilon)\right\}c_0 \\ + \sum_{n=2,4,\ldots}^{N} \left\{\begin{array}{c}\left(\begin{array}{c}-(1+\upsilon)(n+1)(n-1)R^2 r^{n-2} \\ +(1+\upsilon)(n+1)R^{2(n+1)} r^{-(n+2)}\\ +(n+1)[(n+2)+\upsilon(n-2)]r^n\end{array}\right) b_n \\ +\left(\begin{array}{c}-(1+\upsilon)(n-1)R^{-2(n-1)} r^{n-2} \\ -(1+\upsilon)(n-1)(n+1)R^2 r^{-(n+2)}\\ +(n-1)[(n-2)+\upsilon(n+2)]r^{-n}\end{array}\right) d_n\end{array}\right\} cos(n\theta)\end{array}\right] \quad (2.16)$$

and from *equations 2A.25 through 2A.27*

$$\sigma_{rr} = \left(\frac{-2R^2}{r^2} + 2\right)c_0 - \sum_{n=2,4,\ldots}^{N}\left[\begin{array}{c}\left\{\begin{array}{c}-(n-1)(n+1)R^2 r^{n-2} \\ +(n+1)R^{2(n+1)} r^{-(n+2)} \\ +(n+1)(n-2)r^n\end{array}\right\} b_n \\ +\left\{\begin{array}{c}-(n-1)R^{-2(n-1)} r^{n-2} \\ -(n-1)(n+1)R^2 r^{-(n+2)} \\ +(n-1)(n+2)r^{-n}\end{array}\right\} d_n\end{array}\right] cos(n\theta) \quad (2.17)$$

$$\sigma_{\theta\theta} = \left(\frac{2R^2}{r^2} + 2\right)c_0 + \sum_{n=2,4,\ldots}^{N}\left[\begin{array}{c}\left\{\begin{array}{c}-(n+1)(n-1)R^2 r^{n-2} \\ +(n+1)R^{2(n+1)} r^{-(n+2)} \\ +(n+1)(n+2)r^n\end{array}\right\} b_n \\ +\left\{\begin{array}{c}-(n-1)R^{-2(n-1)} r^{n-2} \\ -(n-1)(n+1)R^2 r^{-(n+2)} \\ +(n-1)(n-2)r^{-n}\end{array}\right\} d_n\end{array}\right] cos(n\theta) \quad (2.18)$$

$$\sigma_{r\theta} = \sum_{n=2,4,\ldots}^{N}\left[\begin{array}{c}\left\{\begin{array}{c}-(n+1)(n-1)R^2 r^{n-2} \\ -(n+1)R^{2(n+1)} r^{-(n+2)} \\ +n(n+1)r^n\end{array}\right\} b_n \\ +\left\{\begin{array}{c}-(n-1)R^{-2(n-1)} r^{n-2} \\ +(n-1)(n+1)R^2 r^{-(n+2)} \\ -n(n-1)r^{-n}\end{array}\right\} d_n\end{array}\right] sin(n\theta) \quad (2.19)$$

where R is the radius of the hole. When the physical plate is loaded in a testing machine, the rigid body motions S_1, S_2 and R* in *equations 2.13 and 2.14* can be equated to zero [7, P.472]. The stresses, strains and displacements (*equations 2.13 through 2.19)* now involve only the coefficients c_o, b_n and d_n. This reduces the number of Airy coefficients that must be evaluated

experimentally by essentially 50% compared to imposing the traction-free conditions on the edge of the hole point–wise. This can be advantageous since it can reduce the amount of measured data needed, and simplifies the associated least–square computation.

With respect to *figure 2.2*, *equations 2.20 through 2.23* [7] relate the displacement components *u* and *v* with respect to the x and y direction in terms of u_r and u_θ with respect to the polar coordinates (*r, θ*), and vice-versa.[1]

$$u = u_r \cos\theta - u_\theta \sin\theta \tag{2.20}$$

$$v = u_r \sin\theta + u_\theta \cos\theta \tag{2.21}$$

$$u_r = u \cos\theta + v \sin\theta \tag{2.22}$$

$$u_\theta = -u \sin\theta + v \cos\theta \tag{2.23}$$

Although *equations 2.20 through 2.23* are emphasized here relative to the displacements near a circular hole, they are general in nature. As such if one represents u_r and u_θ in terms of the series (such as here from a stress function), *u* and *v* involve all of the unknown coefficients even if u_r and u_θ do not do so separately. The displacement expressions for each of the *u* and *v* Cartesian components will now have the same coefficients. Therefore, the displacement in any

[1] *Equations 2.22 and 2.23* obtained by solving *equations 2.20 and 2.21* simultaneously

one or all directions can be evaluated from measuring any one displacement in the Cartesian coordinates, i.e.,

$$u = f(b_o, c_o, a_n, b_n, c_n, d_n \text{ for } n = 2,4,6\ldots) \tag{2.24}$$

$$v = f(b_o, c_o, a_n, b_n, c_n, d_n \text{ for } n = 2,4,6\ldots) \tag{2.25}$$

A detailed derivation of the expressions of *equations 2.13 through 2.19* is contained in Appendix A2. By replacing u_r and u_θ of *equations 2.20 and 2.21* by their corresponding equations, the displacement components in the Cartesian directions, u and v, are given in *equations 2.26* (from *equation 2A.36*) *and 2.27* (from *equation 2A.38*).

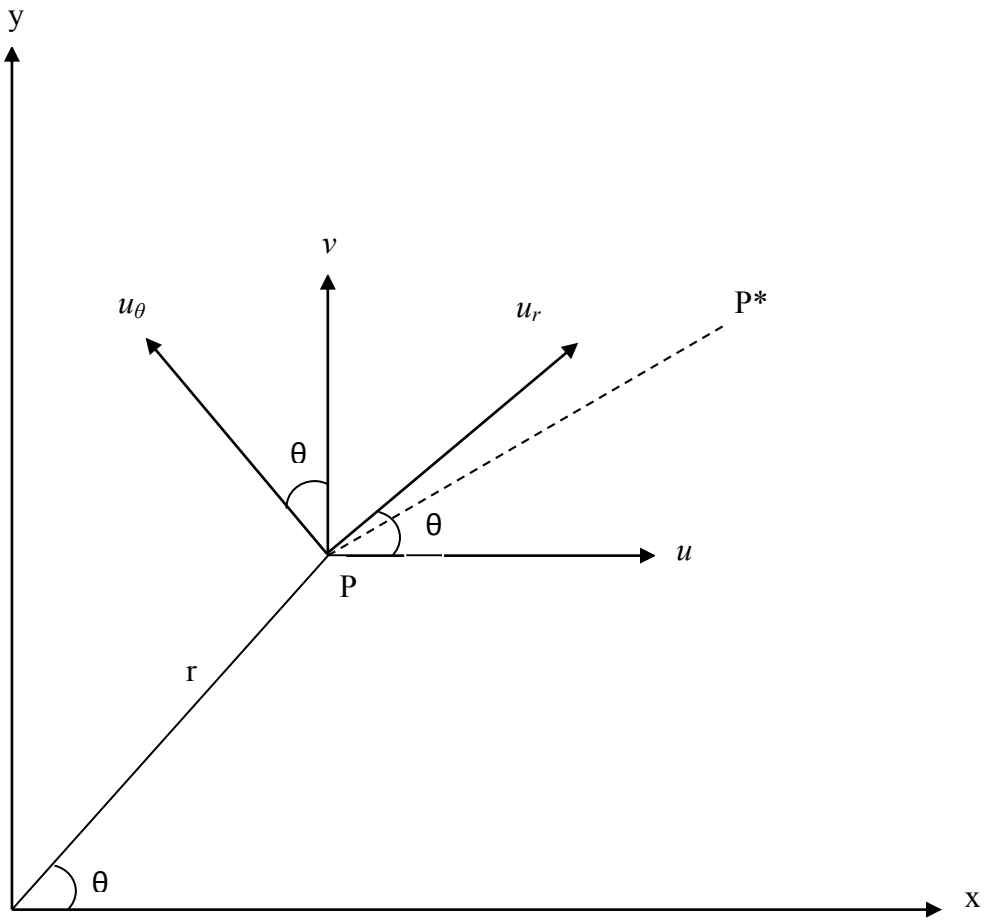

Fig. 2.2: Displacement components, u and v, with respect to rectangular Cartesian coordinates (x,y) and u_r and u_θ with respect to polar coordinates (r, θ) when point P moves to P* [7]

$$u = \frac{1}{E}\left[\begin{array}{c} \left\{\frac{2R^2}{r}(1+v) + 2(1-v)r\right\} \cos\theta \;\; c_0 \\ -\sum_{n=2,4,\ldots}^{N} \left\{ \begin{array}{c} -(1+v)(n+1)R^2\, r^{n-1} \;\; (\, cos(n-1)\,\theta) \\ -(1+\;v)R^{2(n+1)}\, r^{-(n+1)} \;(\, cos(n+1)\,\theta) \\ +\begin{pmatrix} n(1+v)\;(\, cos(n-1)\,\theta) - 2(\, cos(n+1)\,\theta) \\ +2v\cos\theta \;\; cos(n\theta) + 2\sin\theta \;\; sin(n\theta) \end{pmatrix} r^{n+1} \end{array} \right\} b_n \\ +\left\{ \begin{array}{c} -(1+\;v)\; R^{-2(n-1)}\, r^{n-1}(\, cos(n-1)\,\theta) \\ +(1+\;v)(n-1)\; R^2 r^{-(n+1)}(\, cos(n+1)\,\theta) \\ -\begin{pmatrix} n(1+v)(\, cos(n+1)\,\theta) + 2(\, cos(n-1)\,\theta) \\ -2v\cos\theta \;\; cos(n\theta) + 2\sin\theta \;\; sin(n\theta) \end{pmatrix} r^{-n+1} \end{array} \right\} d_n \end{array} \right] \qquad (2.26)$$

and

$$v = \frac{1}{E}\left[\begin{array}{c} \left\{\frac{2\,R^2}{r}(1+\upsilon) + 2(1-\upsilon)r\right\} sin\,\theta\ \ c_0 \\ - \sum_{n=2,4,\ldots}^{N} \left\{ \begin{array}{c} (1+\upsilon)(n+1)R^2\, r^{n-1}\ \big(\, sin(n-1)\theta\big) \\ -(1+\ \upsilon)R^{2(n+1)}\, r^{-(n+1)}\ \big(\, sin(n+1)\theta\big) \\ -\Big(n(1+\upsilon)\ \big(\, sin(n-1)\theta\big) + 2\big(\, sin(n+1)\theta\big)\Big)\, r^{n+1} \end{array} \right\} b_n \\ + \left\{ \begin{array}{c} (1+\ \upsilon)\, R^{-2(n-1)}\, r^{n-1}\big(\, sin(n-1)\theta\big) \\ +(1+\ \upsilon)(n-1)\, R^2 r^{-(n+1)}\big(\, sin(n+1)\theta\big) \\ +\Big(-n(1+\upsilon)\ \big(\, sin(n+1)\theta\big) + 2\big(\, sin(n-1)\theta\big)\Big) r^{-n+1} \end{array} \right\} d_n \end{array} \right] \quad (2.27)$$

From *equations 2.13 through 2.19, 2.26 and 2.27* one sees, in the absence of rigid body motion,

$u_r = f(\, c_o,\ b_n\,,\ d_n\ for\ n = 2,4,6\ldots)$ (2.28)

$u_\theta = f(\, b_n\,,\, d_n\ for\ n = 2,4,6\ldots)$ (2.29)

$\epsilon_{rr} = f(\, c_o,\ b_n\,,\ d_n\ for\ n = 2,4,6\ldots)$ (2.30)

$\varepsilon_{\theta\theta} = f(c_o,\ b_n\,,\ d_n\ for\ n = 2,4,6\ldots)$ (2.31)

$\sigma_{rr} = f(\, c_o,\ b_n\,,\ d_n\ for\ n = 2,4,6\ldots)$ (2.32)

$\sigma_{\theta\theta} = f(c_o,\ b_n\,,\ d_n\ for\ n = 2,4,6\ldots)$ (2.33)

$\sigma_{r\theta} = f(b_n\,,\ d_n\ for\ n = 2,4,6\ldots)$ (2.34)

$u = f(\, c_o,\, b_n\,,\, d_n\ for\ n = 2,4,6\ldots)$ (2.35)

$v = f(\, c_o,\, b_n\,,\, d_n\ for\ n = 2,4,6\ldots)$ (2.36)

Note that *f( )* represent different functions which appear in the *equations 2.12 through 2.36*.

Once all of the Airy coefficients *(c_o, b_n, d_n for n = 2,4,6…)* are known (say from measured values of *u* or *v*), the individual components of displacement, stress and strain can be evaluated using *equations 2.13 through 2.19, 2.26 and 2.27. Equation 2.35 or 2.36* suggests that one could record many values of the same component of displacement (displacement component with respect to any rectangular Cartesian direction) at many different locations throughout some region and from which evaluate all of the relevant Airy coefficients. Moreover, *equations 2.35 and 2.36* indicate that, assuming one uses the same number of coefficients of b_n and d_n in *u* and *v* then all the Airy coefficients are available from measured data of either *u* or *v*.

2.3 Simulated Experimental Input Data (FEA)

2.3.1 Introduction

The problem of *figure 2.3* will be analyzed initially by employing FE-simulated displacement data in order to substantiate the viability, robustness, and numerical stability of the technique. This section will apply FE ANSYS simulated displacements, *u or v*, to evaluate the unknown Airy coefficients of *equations 2.26 or 2.27* and then employ these determined coefficients to evaluate individual components of stress, strain and displacement using *equations 2.13 through 2.19, 2.26 and 2.27*. The displacement evaluated stresses, strains and displacements will be compared subsequently with those predicted discretely by ANSYS to assess the validity of the described approach. Such numerical experiments employing simulated displacement test data from ANSYS help verify that there are no algebraic errors and substantiate that the system is numerically robust.

Following are the details of the plate for the associated analyses and results:

- Material of the plate: Aluminum 6061-T6 (Wiedenbeck, Inc., Madison, WI); Ultimate strength = 275 to 311 MPa (40 to 45 ksi) and Yield strength = 241 to 275 MPa (35 to 40 ksi).
- Far-Field stress (σ_o) = 1000 psi.
- Diameter of the hole (d) = 25.4 mm (1”).
- Thickness of the plate (t) = 6.35mm (0.25”).
- Plate is symmetrical about the horizontal (x-axis) and vertical axis (y-axis).
- Length of the plate (L) ≈ 406.4 mm (16”), *figure 2.3*.
- Width of the plate (W) = 50.8 mm (2”), *figure 2.3*.

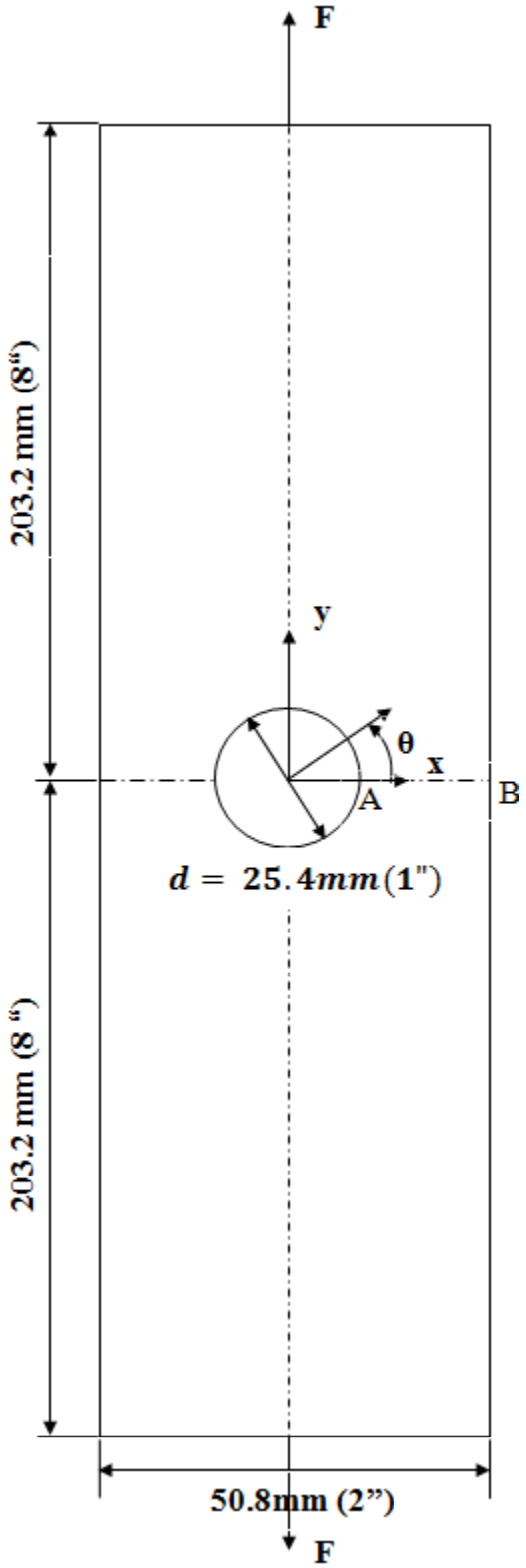

Fig. 2.3: Plate Geometry (actual plate loaded horizontally but shown here vertically so to locate its length in the long direction of the page)

The following considerations helped to motivate using this particular specimen *(figure 2.3)* to illustrate the objective of this chapter: (i) The geometry contains a hole. Engineering components often contain holes or notches and these give rise to stress concentrations. (ii) It has two axis of symmetry. In addition to simplifying the stress function and reducing the number of Airy coefficients, this acknowledges that engineering components often possess mechanical and geometric symmetry. (iii) A feature of this present approach is its ability to evaluate all the Airy coefficients and to reduce the number of these experimentally-determined coefficients by incorporating the traction–free conditions on the edge of the hole *analytically*.

The loaded aluminum plate of *figure 2.3* was accurately modeled in ANSYS having geometric and loading symmetry about both the x and y-axes so as to obtain the displacement distributions in the plate. *Figure 2.4* shows the finite element ANSYS model of the plate of *figure 2.3*. This FEA uses isoparametric elements (ANSYS element type: Plane-82), which have 8 nodes per element. This element gives better results than does the Plane-42 element which has 4 nodes per element. A very fine mesh was used near the hole to enhance accuracy. Symmetry about x-axis and y-axis were employed. Using the symmetry boundary condition enables one to increase the number of nodes i.e., a fine mesh in the region of the hole. It also simplifies the finite element calculation. The quarter model of *figure 2.4* involves 727 elements and 2304 nodes.

Figures 2.3 and 2.4 show that the plate is symmetrical about both the x- and y-axes and there is an applied far-field stress of 6.90 MPa (1000 psi) in the y-direction. The origin of the coordinate system is located at the center of the hole, *figure 2.3*.

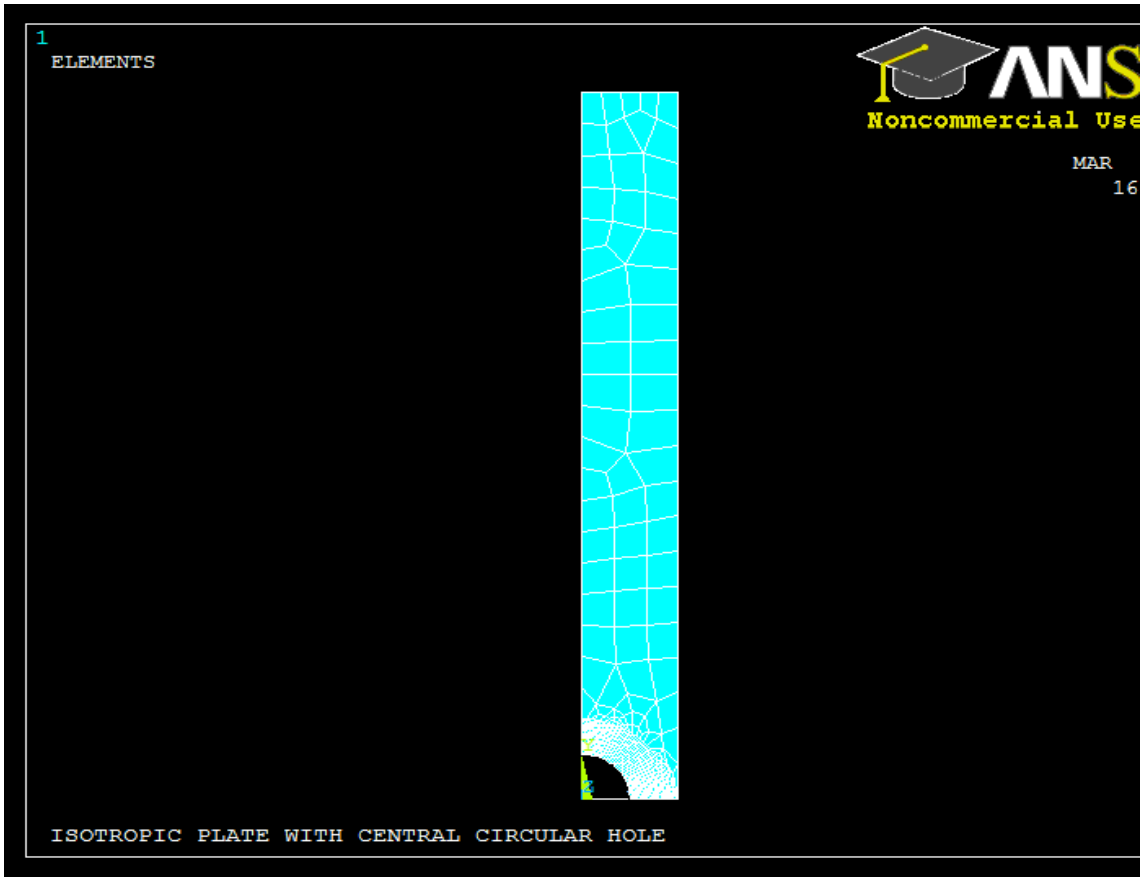

Fig. 2.4: Finite Element Model for the perforated plate of *figure 2.3*

The ANSYS–simulated test data originate in the region near the hole, i.e., $0 \leq r/d \leq 0.9$ (where d = 25.4 mm (1")), *figures 2.5*. The 651 source locations of the input values of the ANSYS displacements are indicated in *figure 2.5-b*.

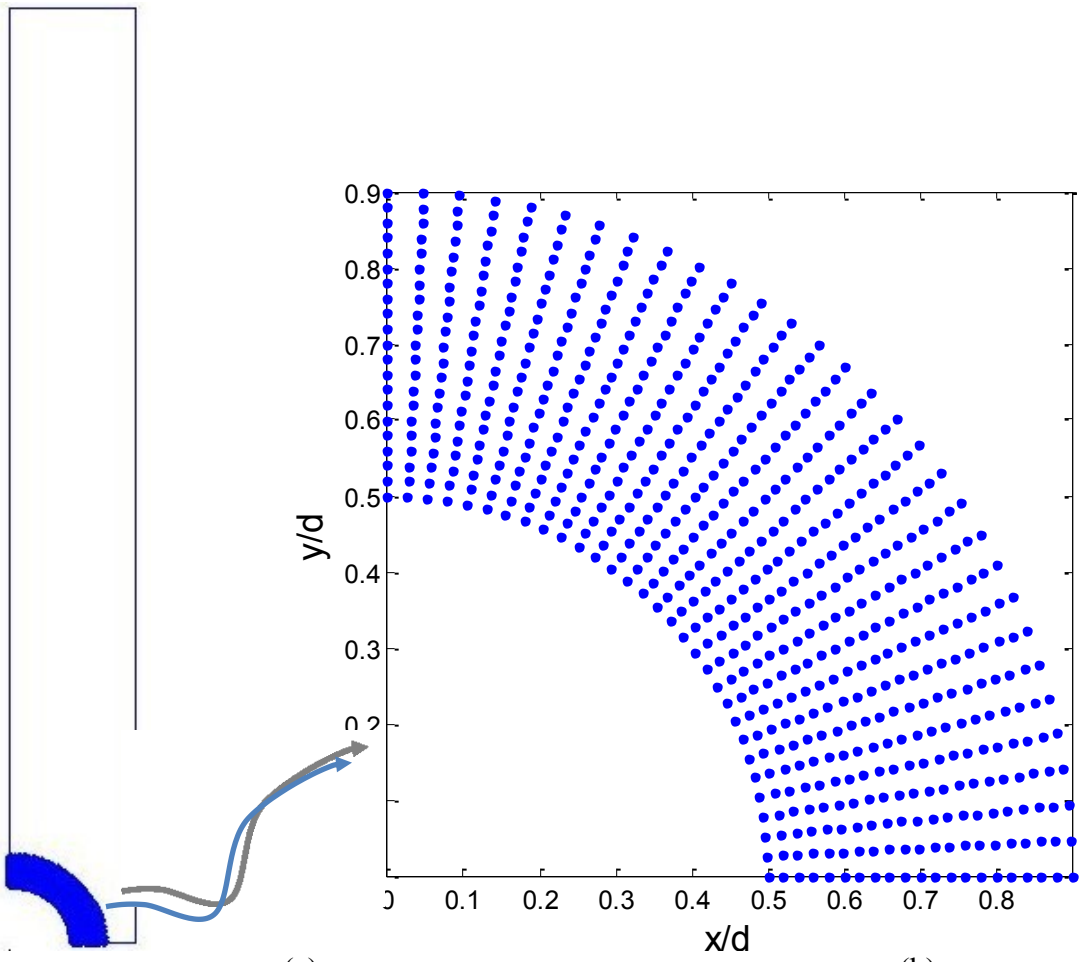

(a) (b)

Fig. 2.5: (a) Selected data locations for displacement components determination. (b) Source locations of 651 individually used inputs for determining Airy coefficients when satisfying traction-free conditions *analytically* at the hole

Figures 2.5 show the 651 source locations for the ANSYS-evaluated values of displacements. The selected ANSYS nodes for input values are located in a region adjacent to the hole as shown in *figures 2.5*. Using FE-generated vertical displacements at the 651 locations of *figures 2.5*, one can form the following linear matrix equation $Ac = d$ of *equations 2.37 and 2.38.*

$$\begin{bmatrix} v.(c_0,bn,dn) \\ v.(c_0,bn,dn) \\ . \\ . \\ . \\ . \\ v.(c_0,bn,dn) \end{bmatrix} \begin{bmatrix} c_0 \\ b_n \\ d_n \end{bmatrix} = \begin{bmatrix} v_1 \\ v_2 \\ . \\ . \\ . \\ v_N \end{bmatrix} \quad \text{(a)}; \quad \begin{bmatrix} u.(c_0,bn,dn) \\ u.(c_0,bn,dn) \\ . \\ . \\ . \\ u.(c_0,bn,dn) \end{bmatrix} \begin{bmatrix} c_0 \\ b_n \\ d_n \end{bmatrix} = \begin{bmatrix} u_1 \\ u_2 \\ . \\ . \\ . \\ u_N \end{bmatrix} \quad \text{(b)}; \quad \begin{bmatrix} u_r(c_0,bn,dn) \\ u_r(c_0,bn,dn) \\ . \\ . \\ . \\ u_r(c_0,bn,dn) \end{bmatrix} \begin{bmatrix} c_0 \\ b_n \\ d_n \end{bmatrix} = \begin{bmatrix} u_{r_1} \\ u_{r_2} \\ . \\ . \\ . \\ u_{r_N} \end{bmatrix}$$

$$\begin{bmatrix} u_\theta(bn,dn) \\ u_\theta(bn,dn) \\ . \\ . \\ . \\ u_\theta(bn,dn) \end{bmatrix} \begin{bmatrix} b_n \\ d_n \end{bmatrix} = \begin{bmatrix} u_{\theta_1} \\ u_{\theta_2} \\ . \\ . \\ . \\ u_{\theta_N} \end{bmatrix} \; ; \quad \begin{bmatrix} \varepsilon_{rr}(c_0,bn,dn) \\ \varepsilon_{rr}(c_0,bn,dn) \\ . \\ . \\ . \\ \varepsilon_{rr}(c_0,bn,dn) \end{bmatrix} \begin{bmatrix} c_0 \\ b_n \\ d_n \end{bmatrix} = \begin{bmatrix} \varepsilon_{rr1} \\ \varepsilon_{rr2} \\ . \\ . \\ . \\ \varepsilon_{rrN} \end{bmatrix} \; ; \quad \begin{bmatrix} \varepsilon_{\theta\theta}(c_0,bn,dn) \\ \varepsilon_{\theta\theta}(c_0,bn,dn) \\ . \\ . \\ . \\ \varepsilon_{\theta\theta}(c_0,bn,dn) \end{bmatrix} \begin{bmatrix} c_0 \\ b_n \\ d_n \end{bmatrix} = \begin{bmatrix} \varepsilon_{\theta\theta1} \\ \varepsilon_{\theta\theta2} \\ . \\ . \\ . \\ \varepsilon_{\theta\theta N} \end{bmatrix}$$

$$\begin{bmatrix} \sigma_{rr}(c_0,bn,dn) \\ \sigma_{rr}(c_0,bn,dn) \\ . \\ . \\ . \\ \sigma_{rr}(c_0,bn,dn) \end{bmatrix} \begin{bmatrix} c_0 \\ b_n \\ d_n \end{bmatrix} = \begin{bmatrix} \sigma_{rr1} \\ \sigma_{rr2} \\ . \\ . \\ . \\ \sigma_{rrN} \end{bmatrix} \; ; \quad \begin{bmatrix} \sigma_{\theta\theta}(c_0,bn,dn) \\ \sigma_{\theta\theta}(c_0,bn,dn) \\ . \\ . \\ . \\ \sigma_{\theta\theta}(c_0,bn,dn) \end{bmatrix} \begin{bmatrix} c_0 \\ b_n \\ d_n \end{bmatrix} = \begin{bmatrix} \sigma_{\theta\theta1} \\ \sigma_{\theta\theta2} \\ . \\ . \\ . \\ \sigma_{\theta\theta N} \end{bmatrix} \; ; \quad \begin{bmatrix} \sigma_{r\theta}(bn,dn) \\ \sigma_{r\theta}(bn,dn) \\ . \\ . \\ . \\ \sigma_{r\theta}(bn,dn) \end{bmatrix} \begin{bmatrix} b_n \\ d_n \end{bmatrix} = \begin{bmatrix} \sigma_{r\theta1} \\ \sigma_{r\theta2} \\ . \\ . \\ . \\ \sigma_{r\theta N} \end{bmatrix}$$

(2.37)

Airy coefficients of *equation 2.37(a) or 2.37(b)* can be evaluated using the *u or v* displacements, respectively, from FEA or measured experimental data. Using the now known Airy coefficients, the individual components of stress, strain and displacement are evaluated from the other expressions of *equations 2.37*.

Equation 2.37(a) or (b) can be written in simplified form,

$$[A]_{m\times k}\{c\}_{k\times 1} = \{d\}_{m\times 1} \tag{2.38}$$

where A is an m (number of input data values, i.e., m source locations = 651) by k (number of unknown Airy coefficients to be evaluated) matrix containing a set of 651 linear displacement equations, with k independent variables of *figures 2.5*, vector c contains k unknown Airy coefficients, and the d vector is composed of the 651 ANSYS-generated displacement values corresponding to the displacement equations in matrix A. There are more equations than the number of unknown, i.e., $m > k$. The least-squares process is therefore used to solve the over-determined matrix expression $Ac = d$ of *equations 2.37*.

Either of two methods is commonly employed to solve such a matrix equation: the traditional linear least-squares method which involves taking matrix inverses, and the method of Singular Value Decomposition (SVD) which decomposes the original matrix into a set of matrices with special properties. The SVD approach, which was utilized here, has the advantage that it allows the condition number C of the matrix to be easily determined. With the value of C known, accuracy of the calculations can then be approximately determined by removing as many decimal places from the answer as are found in C. That is, if C = 1 x 10^9, then nine digits of accuracy are lost in the calculation. Since the calculations in this thesis are all done in double precision format which generally gives an accuracy of about 12 digits, the above condition number would limit the accuracy of results to approximately three digits (12 – 9), which is a rough gauge of the accuracy. *Figures 2.6 and 2.7* plot the condition number, c, and log(condition number) vs. the number of Airy coefficients, k from MATLAB. The condition number and log (condition number) plots are the same for both u and v displacements i.e., the condition number is based on the matrix A of *equation 2.38*. Either of these methods, traditional linear least-

squares or SVD gives equivalent values for the coefficients {c}, and once these Airy coefficient (c_o, b_n, d_n) values are known, the individual components of stress, strain and displacement are available at any point from *equations 2.13 through 2.19, 2.26 and 2.27*. *Equation 2.38* was solved using the '\' matrix division operator and pseudo inverse 'pinv' operator in MATLAB (theoretically both computes the same least squares solution c). This operators uses the algorithm for least squares and calculates vector {c} by *c = A\d or c = pinv*d.*

When, as is the case here, the analysis involves a series representation, the question arises as to how many coefficients, *k*, to retain in the series. Previous analysis have utilized information on the condition number, *C*, of the Airy matrix, [A] (discussed in previous paragraph), the root mean square (*RMS*) between the calculated, d′, and input, d, vectors of *equation 2.31* or compared the reconstructed information to the experimental data [4, 5, 8]. The present *RMS* plot (*figure 2.8,* based on the displacement *v*) is sufficiently flat when $k > 5$ as to provide little guidance as to how many coefficients, *k,* to use. Since the displacements are small numbers, the scale of the *RMS* plot is small. Comparing the reconstructed displacement-images (*figures 2.9 and 2.10*) after substituting the various number of ANSYS-evaluated Airy coefficients with those predicted directly by FEM (ANSYS), together with the information of *figures 2.6 through 2.8,* further supports using $k = 5$ as the number of coefficients. Such information indicate 5 coefficients (i.e., $k = 5$) for *u and v* as the best choices for the current study and the matrix equation $Ac = d$. Thus, the terminating index value $N = k - 1 = 4$ is used here for the ANSYS numerical–experimental analysis. The matrix *equation 2.38* becomes over-determined with $m = 651 > N = 4$. Solving the over-determined linear matrix equation $Ac = d$ of *equation 2.38* by least-squares, evaluates all of the Airy coefficients existing in the stress, strain and displacement

expressions, *equations 2.13 through 2.19, 2.26 and 2.27*. Using the now known coefficients, one can obtain the strain, strain and displacement at any point in the region.

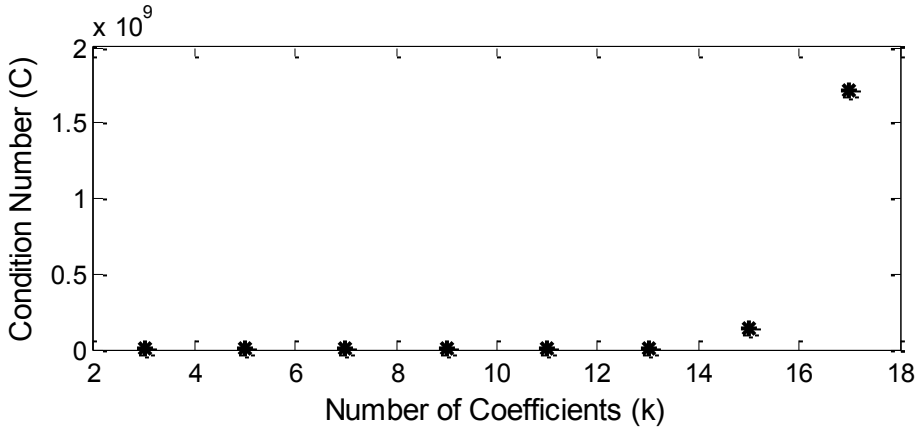

Fig. 2.6: Plot of condition number, C, vs. number of coefficients, k, for $m = 651$ input values

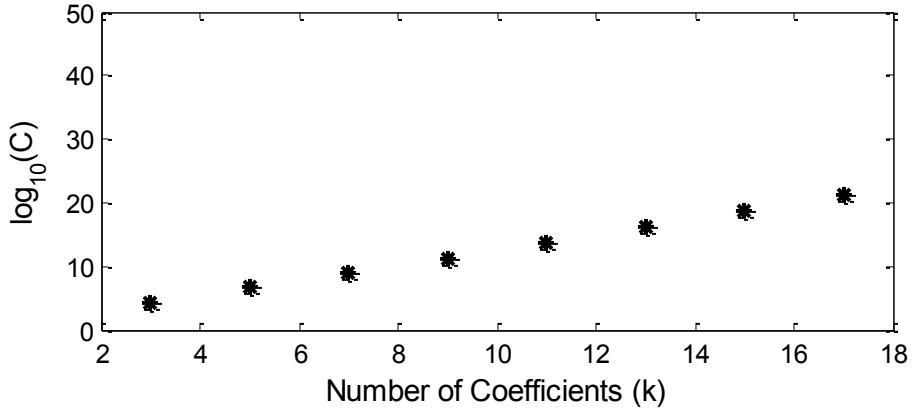

Fig. 2.7: Plot of $\mathrm{Log}_{10}(C)$ vs. number of coefficients, k, for $m = 651$ input values

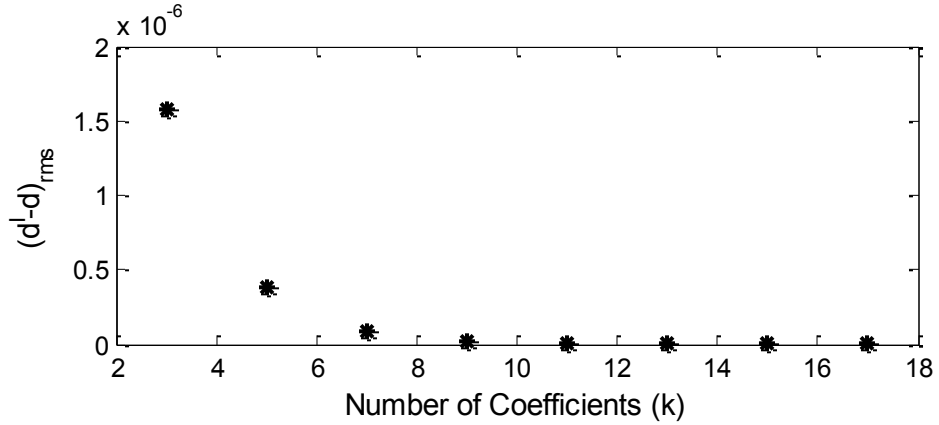

Fig. 2.8: Plot of *RMS* vs. number of coefficients (for displacement v), k, for $m = 651$ input values

Contour plots such as those of *figures 2.9 through 2.19* are often generated using the 'contourf ( )' function in MATLAB. However, I found it preferable to write and use my own contour-plotting algorithm in MATLAB for preparing images such as *figures 2.9 through 2.19*. These contour plots are normalized with respect to the diameter of the hole (d = 25.4 mm = 1").

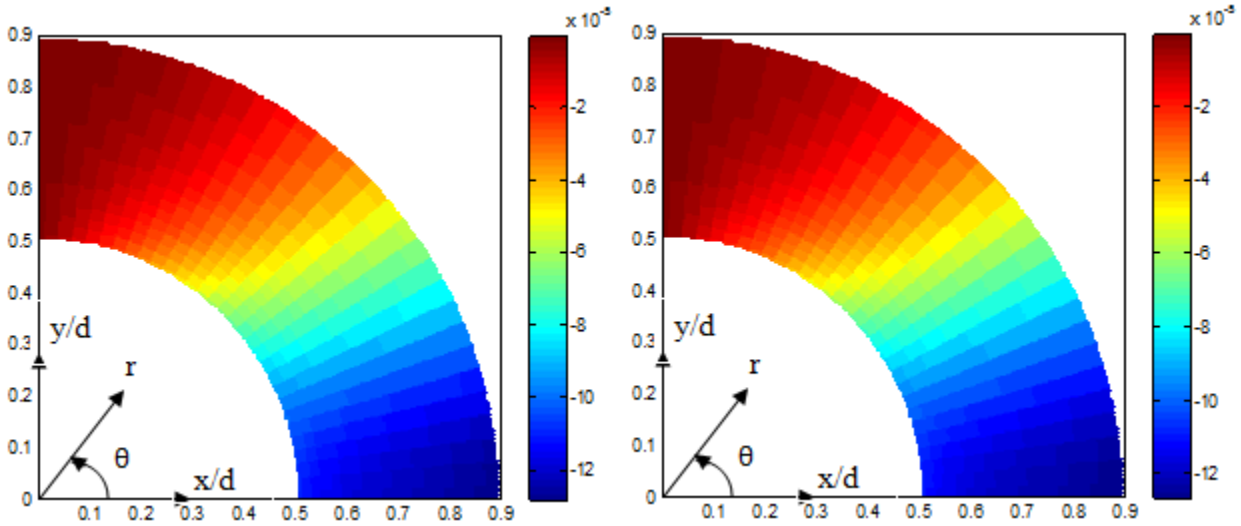

Fig. 2.9: Contour plots of *u/d* from FEA (left side) and reconstructed displacement *u/d* (right side) using *m = 651* input numerically simulated measured *u* displacements, *k = 5* coefficients throughout $0.5 \leq r/d \leq 0.9$ region adjacent to hole

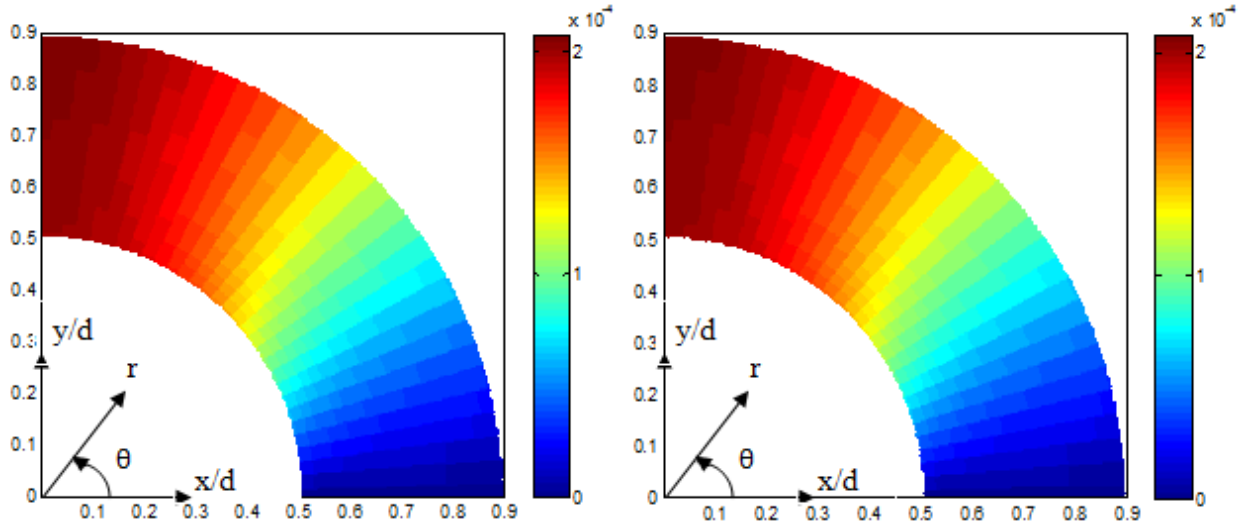

Fig. 2.10: Contour plot of *v/d* from FEA (left side) and reconstructed displacement *v/d* (right side) using *m = 651* input numerically simulated measured *v* displacements, *k = 5* coefficients throughout $0.5 \leq r/d \leq 0.9$ region adjacent to hole

Figures 2.9 and 2.10 show excellent agreement between the reconstructed displacements from images (for $k = 5$) generated by substituting the Airy Coefficients evaluated from ANSYS simulated displacements into *equations 2.26 and 2.27* with those predicted directly by FEM (ANSYS), i.e., the simulated measured values.

By expressing displacements in terms of the Airy coefficients of an Airy Stress function, and satisfying local traction–free conditions *analytically*, this chapter develops and demonstrates the ability to evaluate the individual components of stress, strain or displacement on, and in the neighborhood of, the edge of a single hole from displacement information away from the hole. Notwithstanding such positions near the edge of the hole are often locations of high stress which can control structural integrity, it has been challenging by more traditional methods to obtain reliable displacement (strain, stress) information right on the edge of a hole or notch.

2.3.2 Determining Individual Components of Stresses, Strains and Displacements from Measuring either u or v Displacements using FEA–Evaluated Airy Coefficients

As illustrated here, it is particularly interesting that individual components of displacement, strain and stress can be determined from discretely measured displacements in just either *x(u) or y(v)* direction. This can simplify measurement techniques. In some respects the present ability to obtain rectangular/polar components of displacement, strain and stress from one measured displacement is not unlike the ability to obtain the three components of stress TSA–wise from one measured quantity, temperatures [1, 3 - 5, 8].

Figures 2.12 through 2.19 illustrate the ability to evaluate the displacements, strains and stresses (using *equations 2.13 through 2.19, 2.26 and 2.27*) from measured Cartesian displacement *v* (in this case from the FEA), when evaluating all of the relevant Airy coefficients *(c_o, b_n, d_n for n = 4)* in *equation 2.27 or 2.37a*. It is important to maintain the same number of coefficients of b_n and d_n in the equations for the stresses, strains and displacements. Once all of the Airy coefficients are known, the stress, strain and displacement components with respect to any rectangular Cartesian, or the polar coordinate system can be evaluated using *equations 2.13 through 2.19, 2.26 and 2.27.*

The $k = 5$ coefficients, *i.e.,* c_o, b_n, *and* d_n of *equation 2.27* were evaluated using ANSYS-predicted $m = 651$ input values of *v* displacements throughout $0.5 \leq r/d \leq 0.9$ region adjacent to hole of *figure 2.5* and using least-square, *equation 2.38.* Then substitute these coefficients into *equations 2.37* for evaluating the individual components of displacement, strain and stress. Contours plots of *figures 2.11 through 2.19* were predicted directly by ANSYS (left side) and

using the now known Airy coefficients evaluated from the discretely measured *v* displacement (right side). This could be repeated using the measured input displacements *u* rather than *v*. *Figures 2.12 through 2.19* show excellent agreement between the evaluated displacements, strains and stresses after substituting the Airy Coefficients evaluated from displacements *v,* respectively, with those predicted directly by FEM (ANSYS). These results demonstrate the ability to evaluate Cartesian/polar components of stress/strain/displacement from input (e.g., measured) information of only one component of displacement. The images of *figures 2.11 through 2.19* are for plate loading in the vertical y-direction. In the previous section, two sets of unknown Airy coefficients were evaluated using the FEM simulated *u* and *v* displacements. *Figure 2.11* compares *v* displacement predicted directly by FEM and using the Airy coefficients evaluated from the *u* displacement. Similarly, *figure 2.12* compares the *u* displacement predicted directly by FEM and using the Airy coefficients evaluated from the *v* displacement.

The stress contour plots are normalized with respect to the far-field stress (σ_0 = 6.90 MPa). Strain contour plots are normalized with respect to far-field strain ($\varepsilon_0 = 100\mu\varepsilon$) and the displacement contour plots are normalized with respect to the diameter (d = 25.4 mm = 1") of the hole. The normalizing strain, $\varepsilon_0 = 1*10^{-4}$ in/in is evaluated based on the stress-strain relationship i.e., $\varepsilon_0 = \sigma_0/E$.

$$\varepsilon_o = \frac{\sigma_o}{E} = \frac{1000}{10*10^6} = 100\mu\varepsilon$$

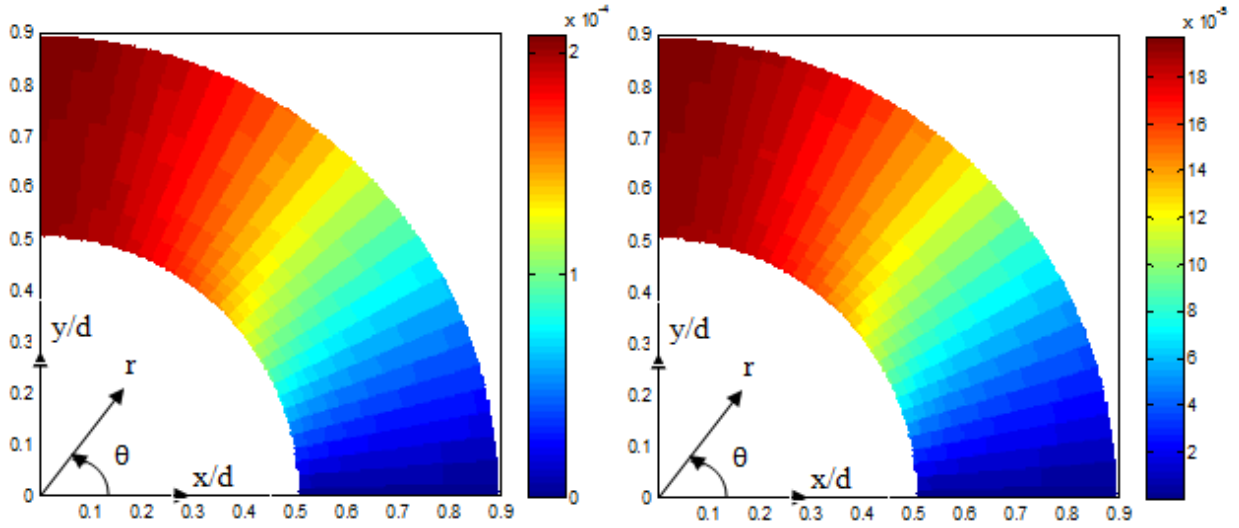

Fig. 2.11: Contour plot of *v/d* throughout 0.5 ≤ r/d ≤ 0.9 region adjacent to hole predicted by FEA (left side) and based on evaluated Airy coefficients (right side) for *m = 651* input numerically simulated measured *u* displacements and *k = 5* coefficients

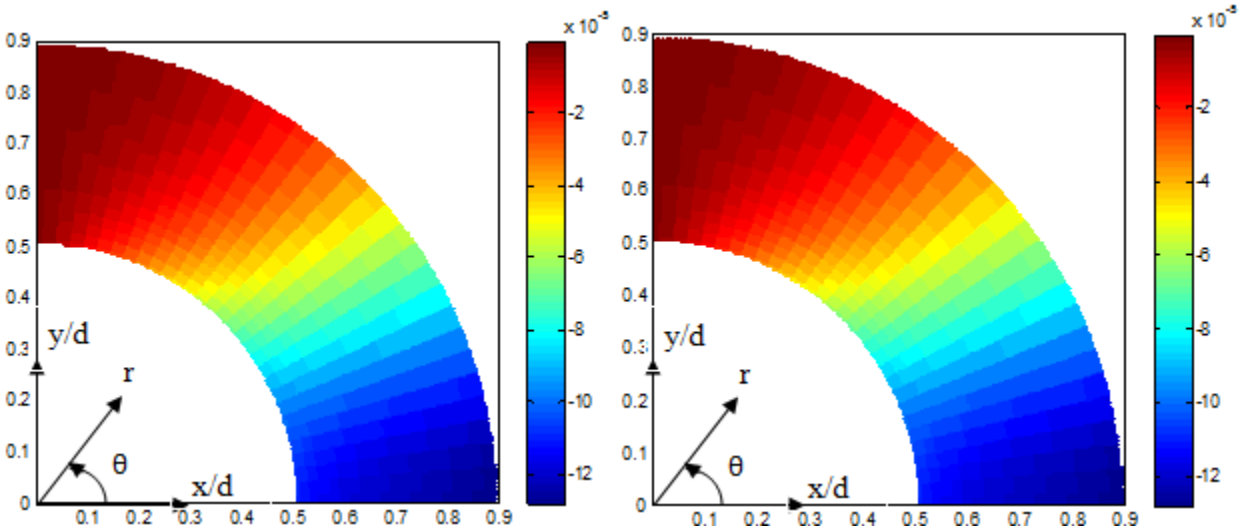

Fig. 2.12: Contour plot of *u/d* throughout 0.5 ≤ r/d ≤ 0.9 region adjacent to hole predicted by FEA (left side) and based on evaluated Airy coefficients (right side) for *m = 651* input numerically simulated measured *v* displacements and *k = 5* coefficients

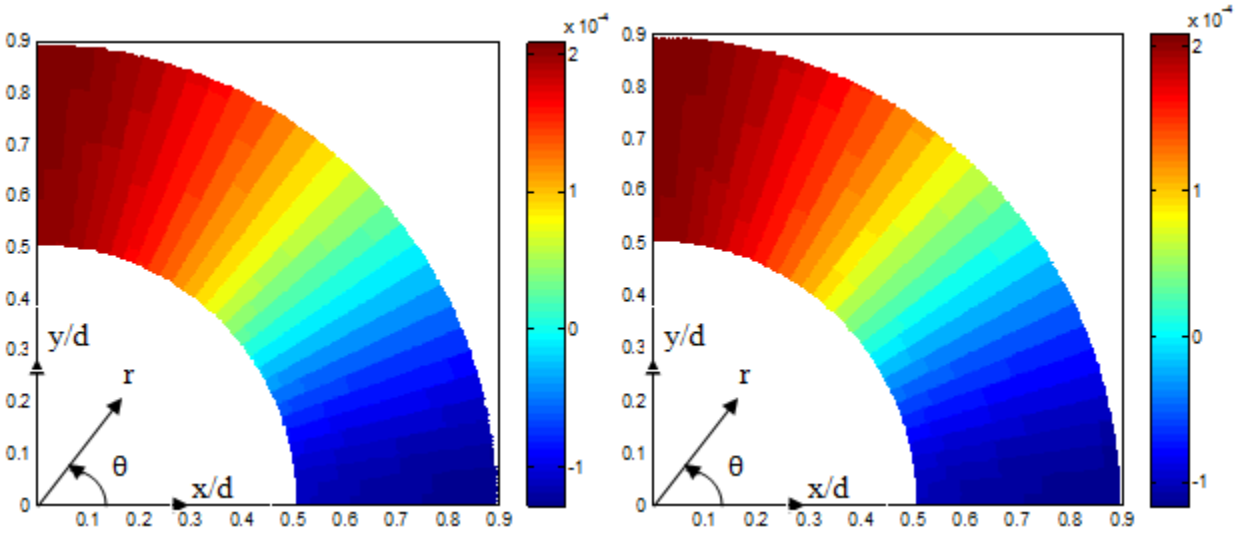

Fig. 2.13: Contour plot of u_r/d throughout $0.5 \leq r/d \leq 0.9$ region adjacent to hole predicted by FEA (left side) and from evaluated Airy coefficients (right side) for $m = 651$ input numerically simulated measured v displacements and $k = 5$ coefficients

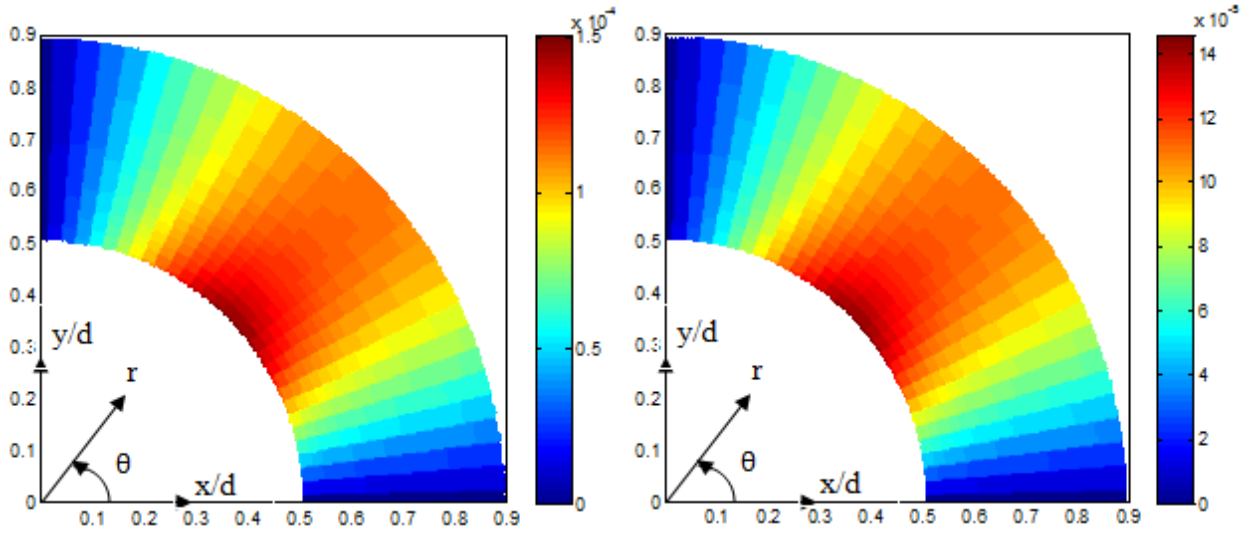

Fig. 2.14: Contour plot of u_θ/d throughout $0.5 \leq r/d \leq 0.9$ region adjacent to hole predicted by FEA (left side) and from evaluated Airy coefficients (right side) for $m = 651$ input numerically simulated measured v displacements and $k = 4$ coefficients

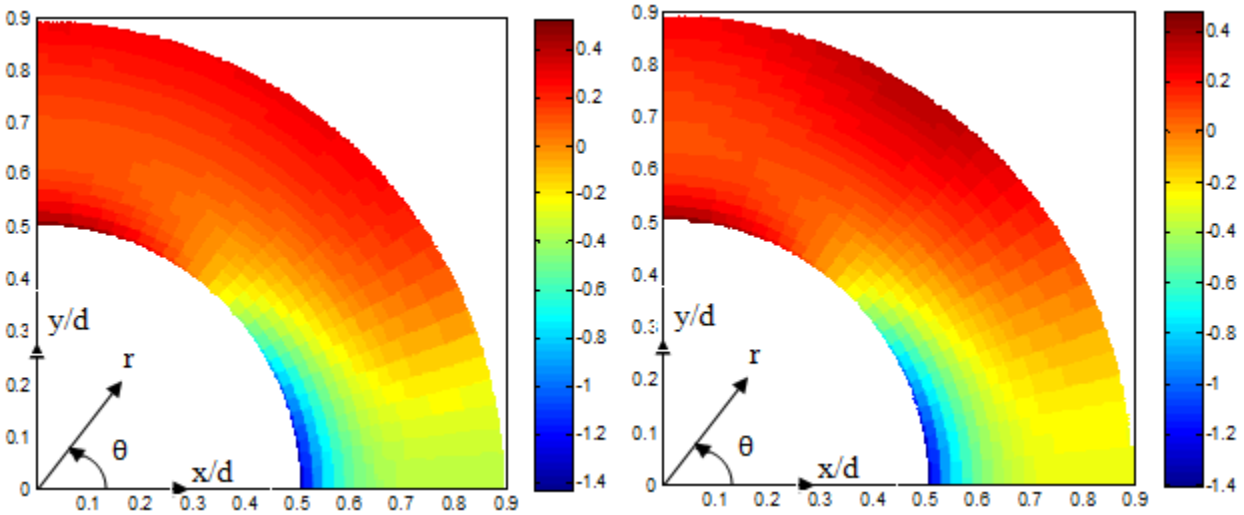

Fig. 2.15: Contour plot of $\varepsilon_{rr}/\varepsilon_0$ throughout $0.5 \leq r/d \leq 0.9$ region adjacent to hole predicted by FEA (left side) and from evaluated Airy coefficients (right side) for $m = 651$ input numerically simulated measured v displacements and $k = 5$ coefficients

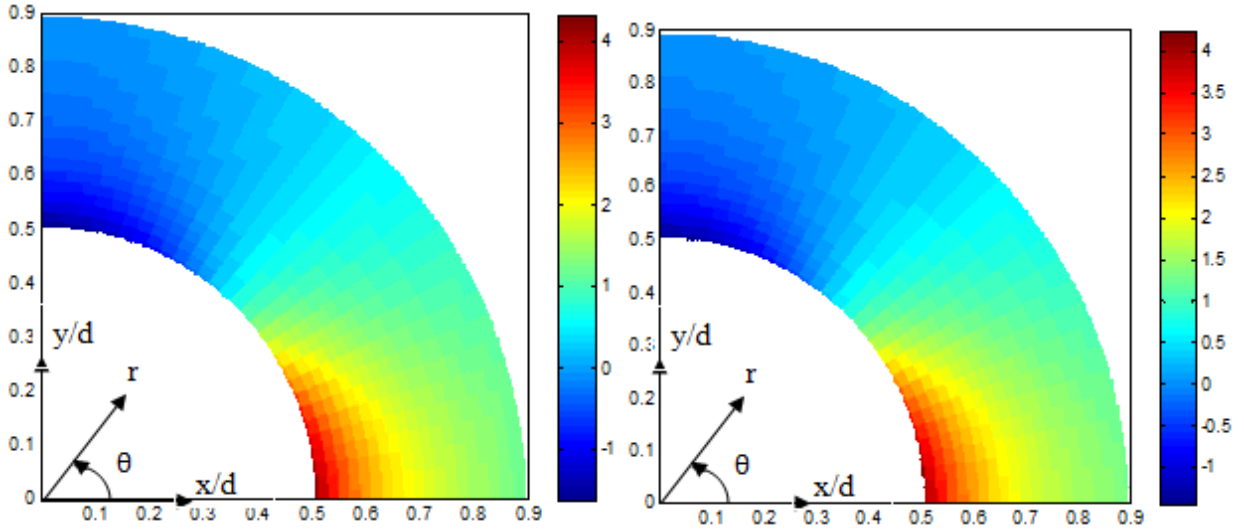

Fig. 2.16: Contour plot of $\varepsilon_{\theta\theta}/\varepsilon_0$ throughout $0.5 \leq r/d \leq 0.9$ region adjacent to hole predicted by FEA (left side) and from evaluated Airy coefficients (right side) for $m = 651$ input numerically simulated measured v displacements and $k = 5$ coefficients

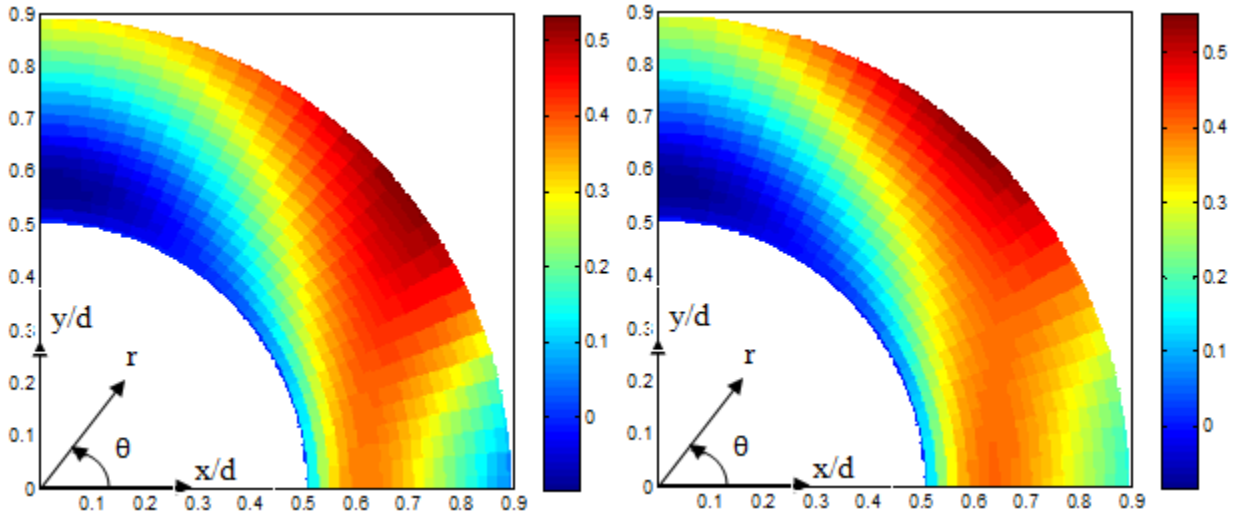

Fig. 2.17: Contour plot of σ_{rr}/σ_0 throughout $0.5 \leq r/d \leq 0.9$ region adjacent to hole predicted by FEA (left side) and from evaluated Airy coefficients (right side) for $m = 651$ input numerically simulated measured v displacements and $k = 5$ coefficients

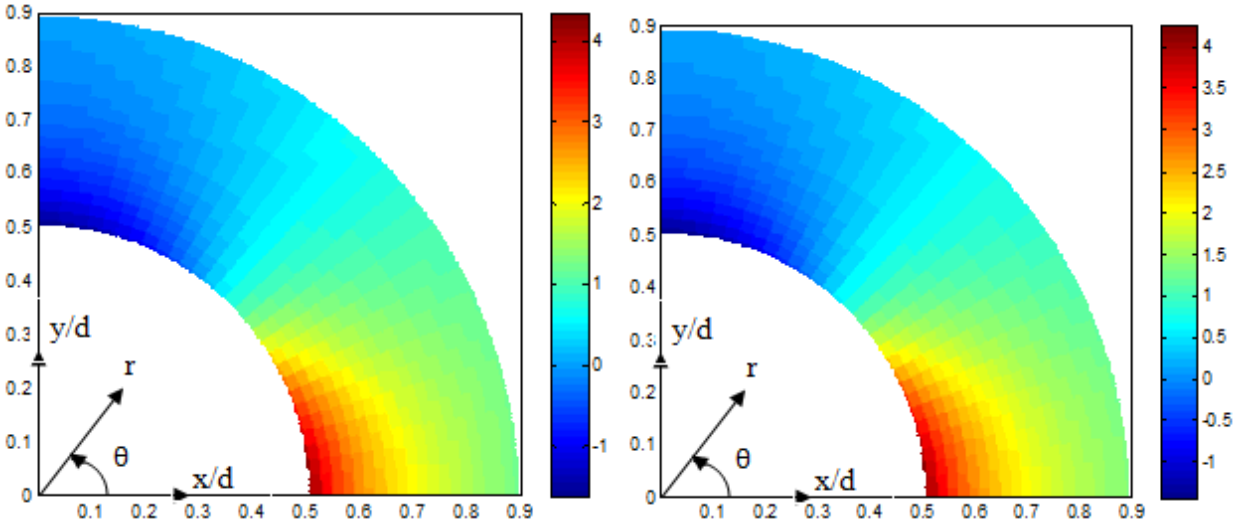

Fig. 2.18: Contour plot of $\sigma_{\theta\theta}/\sigma_0$ throughout $0.5 \leq r/d \leq 0.9$ region adjacent to hole predicted by FEA (left side) and from evaluated Airy coefficients (right side) for $m = 651$ input numerically simulated measured v displacements and $k = 5$ coefficients

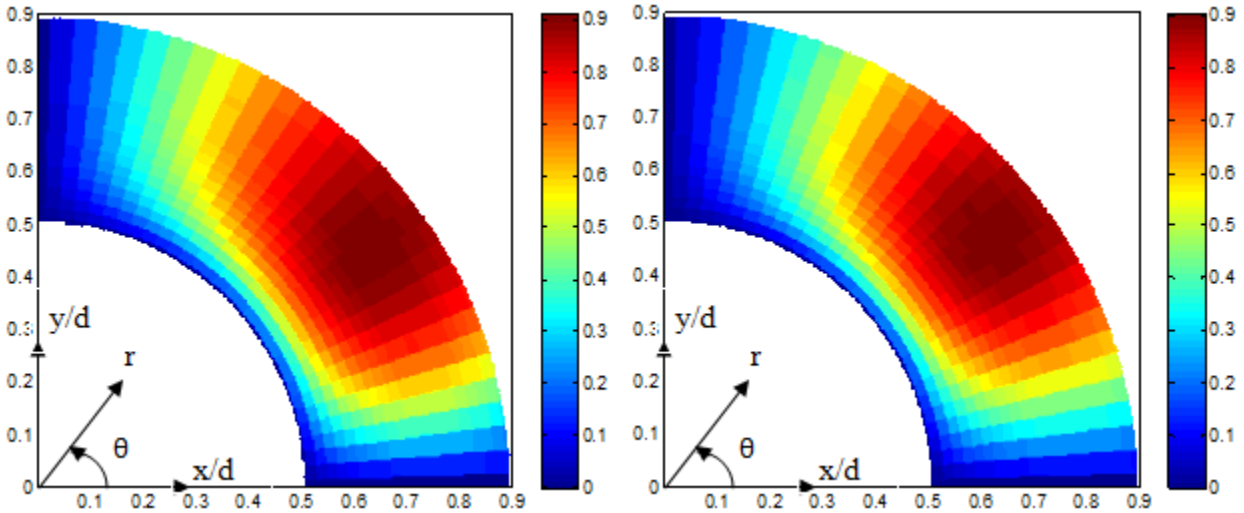

Fig. 2.19: Contour plot of $\sigma_{r\theta}/\sigma_0$ throughout $0.5 \leq r/d \leq 0.9$ region adjacent to hole predicted by FEA (left side) and from evaluated Airy coefficients (right side) for $m = 651$ input numerically simulated measured v displacements and $k = 4$ coefficients

2.4 Digital Image Correlation (DIC)

2.4.1 Introduction

Digital image correlation (DIC) is a computer-based image analysis technique that enables the non-contact measurement of displacements or strains of a surface having a speckle pattern [13]. The method tracks (records) the motion of the speckle pattern by comparing the gray scale value at a point (subset) in the deformed and un-deformed configuration. Therefore two sets of images are recorded: the first image normally being the case of zero applied load and the second image in the loaded condition. With a standard single camera setup, 2D (u and v) in-plane full-field deformations can be monitored. Out-of-plane motions can also be recorded if one employs two cameras. The resolution achievable using DIC depends on a number of factors, including but not limited to camera resolution, lens optical quality, and marker (speckle) size and quality.

The roughness of the surface of the aluminum specimen surface was initially prepared using 320 grid sand paper. Then the specimen was coated with RUST OLEUM (ULTRA COVER 2x coverage) Ultra-Flat white paint to reduce the surface's reflectiveness. The speckle coating should be applied after the base coat has dried. If the undercoat is wet when applying the speckles, the paints will blend and blur. A speckle pattern was provided on the aluminum specimen using RUST OLEUM (ULTRA COVER 2x coverage) Ultra-Flat black paint. This was accomplished by simply using the spray feature of the commercial container containing the paint. *Figure 2.20* is the image of the specimen with the speckle pattern.

While conducting the 2D DIC experiment, a single camera was pointed straight onto the specimen. The room had enough light and therefore no extra lights were used to illuminate the specimen. The longest available lens were selected that allowed the camera to view the specimen normal to its line of sight and still image the entire area of interest of the specimen plate. Once the camera (appropriate lens, etc.) were set-up, Vic-Snap software (Correlation Solutions, Inc.) was employed to preview the image.

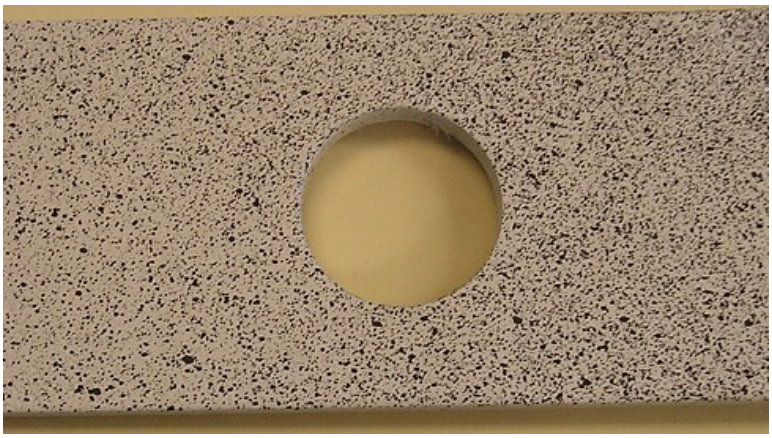

Fig. 2.20: Image of the tested specimen with the speckle pattern

A few operational details are included here for information purposes. Once the camera had been positioned, the next step was to set focus. This was done by opening the aperture of the lens all the way to the lowest F-number which greatly reduces the depth of field. This will exaggerates any out-of-focus areas. The aperture was then returned to the appropriate setting. Use the focus control on the lens to achieve a sharp focus on the entire specimen. It will usually be necessary to zoom in on the image to check fine focus; slight defocus will not be visible with the image zoomed out to fit on screen.

Vic-Snap software was used to record the images of the specimen (*figure 2.20*) in its loaded and unloaded conditions. Vic-2D (Correlation Solutions, Inc.) was employed for

evaluating the displacements or strains using the images from Vic-Snap and to post-process the results.

Before recording the displacements, a calibration was done to obtain the results in physical units rather than in pixels. In this case there was no need to use the separate calibration specimen to get the displacement data. Rather the calibration was done by selecting the known distance on the image and entering it into the system. The recorded data were analyzed and exported to an Excel® spreadsheet which was subsequently imported into MATLAB for further analysis.

2.4.2 Specimen Details

Figure 2.21 is the image of the tested specimen and *figure 2.22* is the geometric representation of *figure 2.21*. The problem of *figure 2.22* is analyzed here using the DIC experimental data. *Figure 2.22* shows the plate geometry, dimension, loading and orientation and location of the co-ordinate axes.

Following are the details of the plate for the associated analyses and results:

- Material of the plate: Aluminum 6061-T6 (Wiedenbeck, Inc., Madison, WI); Ultimate strength = 275 to 311 MPa (40 to 45 ksi) and Yield strength = 241 to 275 MPa (35 to 40 ksi).
- Diameter of the hole (d) = 25.4 mm (1”).
- Thickness of the plate (t) = 6.35mm (0.25”).
- Plate is symmetrical about the horizontal (x-axis) and vertical axis (y-axis).
- Length of the plate (L) ≈ 203.2 mm (8”), *figure 2.22*.
- Width of the plate (W) = 50.8 mm (2”), *figure 2.22*.
- Two strains gages was mounted on the curved edge of the hole (y = 0 i.e., location A and A′ of *figure 2.22*).
- Two strain gages was mounted at a distance x = ±1.11 R along the line y = 0, *figure 2.21*.

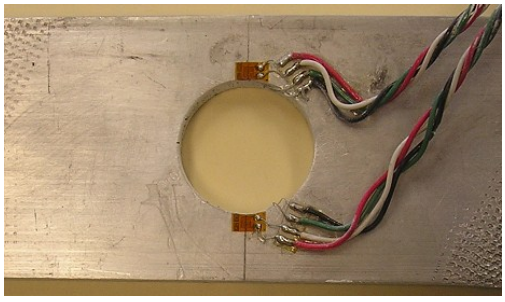

Fig. 2.21: Specimen with the strain gages

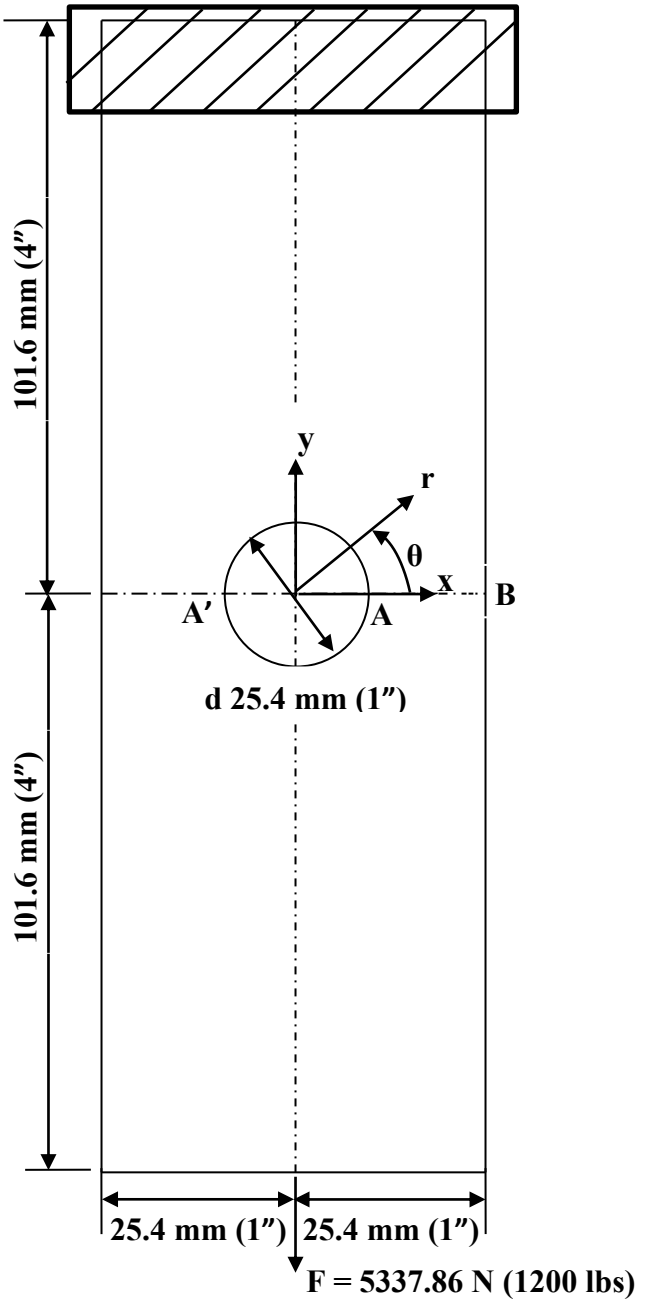

Fig. 2.22: DIC Plate Geometry and Loading – Unclamped specimen length = 93.98 mm (3.7”)

The following considerations helped to motivate using this particular specimen *(figure 2.22)* to illustrate the objective of this chapter: (i) Prior TSA results were available for this geometry and loading conditions [4]. (ii) The geometry contains a hole. Engineering components

often contain holes or notches and these give rise to stress concentrations. (iii) A confident FEA cannot be executed. (iv) The component has two axis of symmetry. (v) The present approach does not require knowledge of the loading details, distant geometry or boundary conditions. (vi) A feature of this present approach is its ability to evaluate all the Airy coefficients and to reduce the number of these experimentally-determined coefficients by incorporating the traction–free conditions on the edge of the hole *analytically*.

The plate was clamped between the cross heads of the MTS hydraulic testing machine (20 Kips capacity having hydraulic grips capable up to 18.5 Kips, Rm. B321, EH) with the help of hydraulic grips, *figures 2.23 and 2.24*. *Figure 2.24* shows the physical set up and DIC recording. Of the two camera's shown in *figure 2.24*, only one was used to record (normal to the flat front surface of the specimen) 2D images. The top cross head of the loading machine was fixed and the bottom cross head moved vertically according to the applied hydraulic pressure. A static load of 5337.86 N (1200 lbs) was applied to the specimen. *Figure 2.25* shows an actual *v*-displacement image as recorded and displayed by the Vic-2D software. The unsymmetrical type (from top to bottom) data of *figure 2.25* was converted to the symmetrical data using MATLAB i.e., equivalent to both top and bottom ends moving. This is done by scaling the data such that the y-displacement is zero along the line y = 0 (*figure 2.22*), i.e., horizontal through the center of the hole of *figure 2.25*. Since the geometry and loading were symmetrical about both x- and y-axes, the data were averaged about x- and y-axes.

The *u*-displacements are relatively small and their DIC-evaluated values are not as reliable as the *v*-displacements. Although not appreciated a priori, this turned out to be an example where one of the two displacement fields was not highly reliable but by using the

technique based on the Airy's stress function, one could obtain the displacement in the other directions. Moreover without differentiating the displacements, one can evaluate the full-field individual stress and strain components.

Fig. 2.23: Specimen loaded in hydraulic grips

Fig. 2.24: Specimen loading and DIC recording

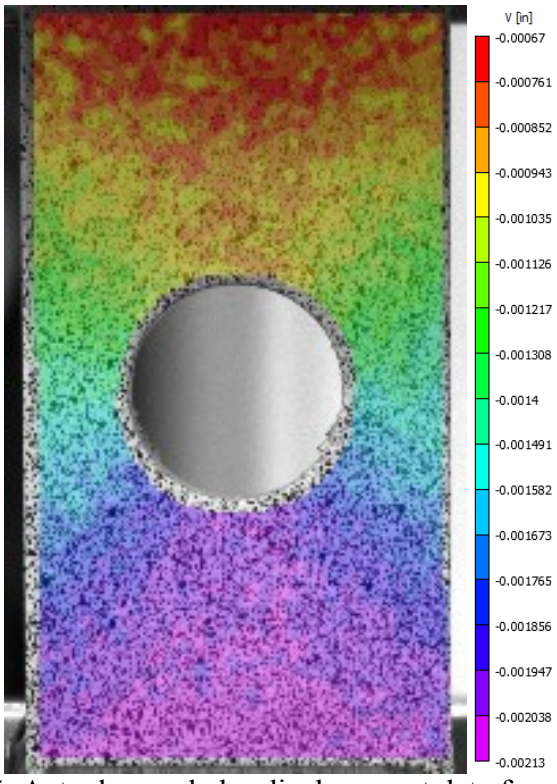

Fig. 2.25: Actual recorded v-displacement data from Vic-2D

2.4.3 Data Processing and Number of Coefficients

Figure 2.26 shows the source locations of the 861 DIC recorded input *v*-displacements which were used to evaluate the unknown Airy coefficients. To assist in determining an appropriate number of Airy coefficients, *k*, *RMS* and condition number plots were prepared. The RMS value represents the discrepancy between the experimental and calculated displacements evaluated from the known Airy coefficients. The condition number, *C*, or $\log_{10}C$ of the Airy matrix indicate the accuracy associated with solving the linear equation Ax = b.

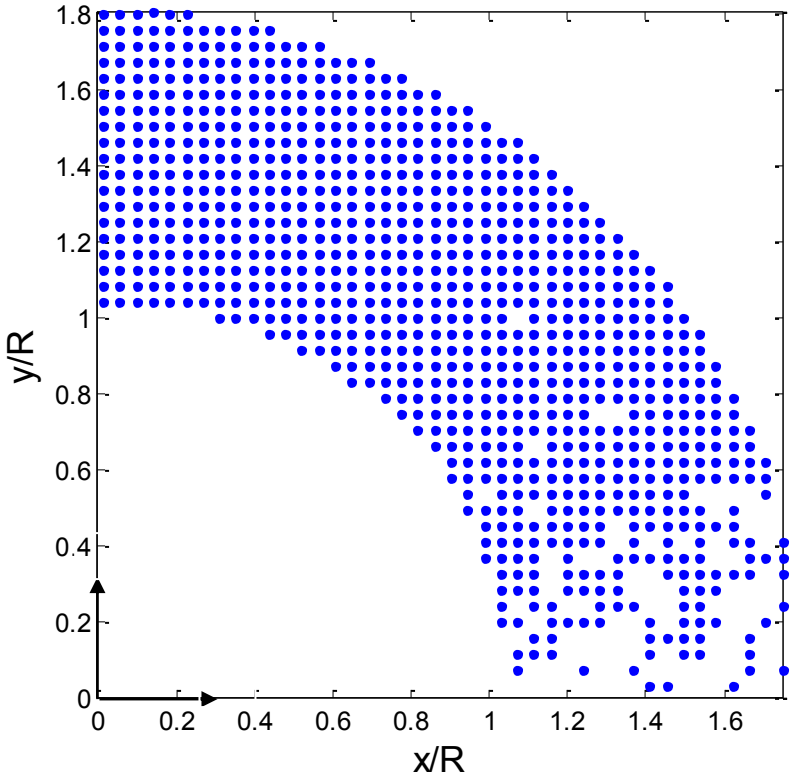

Fig. 2.26: DIC source locations for *m = 861* input values

Figure 2.27 is the plot of RMS against the number of coefficients, *k*. *Figures 2.28 and 2.29* are the plot of condition number and $\log_{10}C$ of Airy matrix against the number of coefficients, *k*. From *figures 2.27 through 2.29, k = 5* is a reasonable choice.

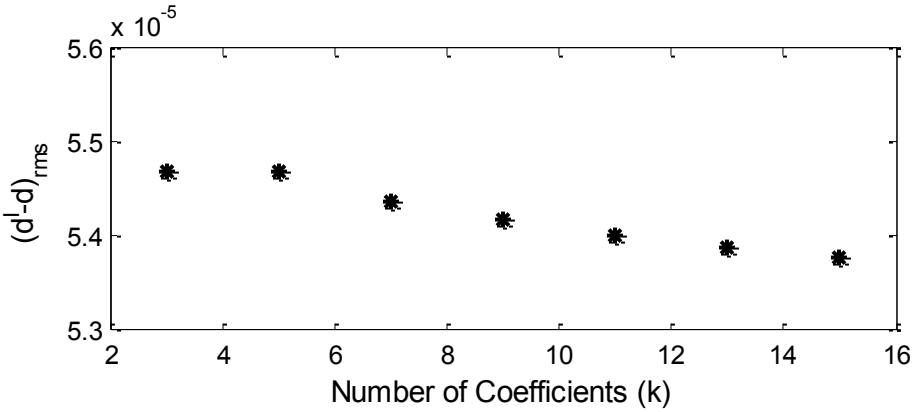

Fig. 2.27: Plot of 'RMS' values of (d′- d) vs. number of coefficients, *k*, for *m = 861* input values

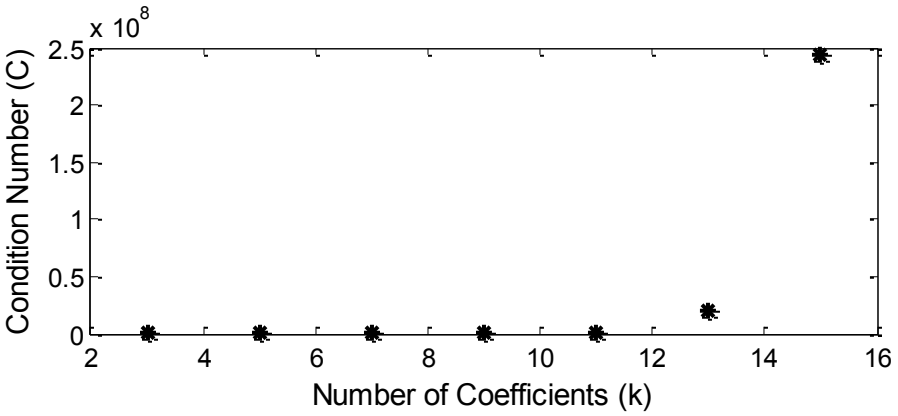

Fig. 2.28: Plot of condition number, *C*, vs. number of coefficients, *k*, for *m = 861* input values

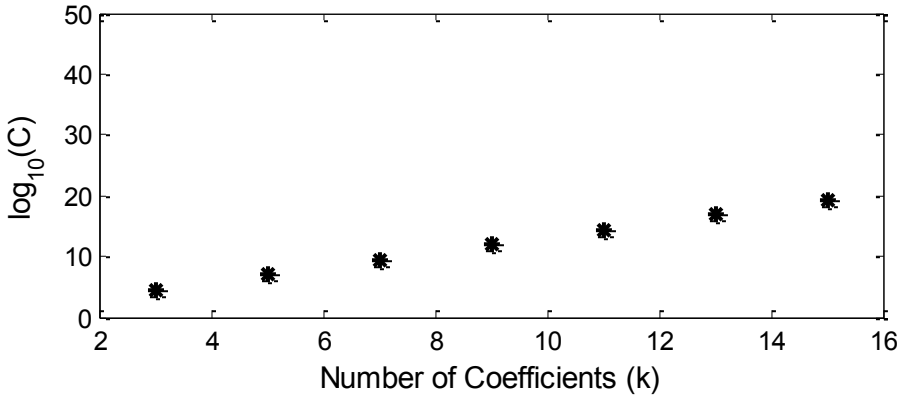

Fig. 2.29: Plot of $\log_{10}(C)$ vs. number of coefficients, *k*, for *m = 861* input values

Figures 2.30 are the normalized (displacements normalized in terms of hole diameter, d = 25.4 mm = 1") contour plots of the DIC measured *v/d* (right) and reconstructed *v/d* (left) displacements based on the DIC evaluated Airy coefficients. These contour plots are plotted on

the same scale which is indicated on the far right of the figure. The good agreement between the experimental and reconstructed *v/d* displacement further validates the previously suggested the use of $k = 5$ coefficients.

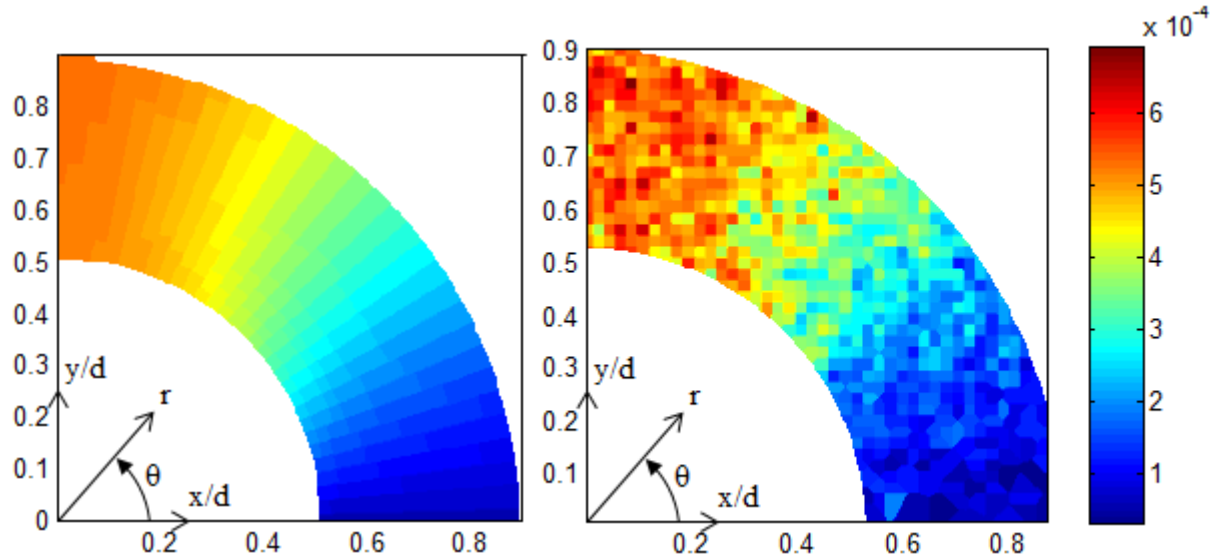

Fig. 2.30: MATLAB processed experimentally determined *v/d* (right) and reconstructed *v/d* displacements based on the DIC evaluated Airy coefficients for $k = 5$ coefficients and $m = 861$ input values (left)

2.4.4 Finite Element Analysis

The DIC results are compared with those from an approximated finite element analysis (FEA). Since the plate is short (unclamped specimen length = 93.98 mm = 3.7" for a free aspect ratio (length to width) of only 1.85), the far-field stress in not a known uniform P/A i.e., the far-field boundary/loading conditions are not well known. An exact FE modal therefore cannot be made. An approximate finite element modal was prepared based on the TSA results for the same sample from reference [4, 5]. Since the vertical end loads applied by the MTS hydraulic-grips, and recognizing the loading system did not have any universal provisions, the top and bottom ends of the 9.4 cm length of the specimen between loading grips were subjected numerically to a constant deformation across the 50.8 mm width of the specimen, *figures 2.22 and 2.23*. Based on this assumption (approximation) the top and bottom ends of the specimen were deformed numerically iteratively until the ANSYS predicted measure stress on the edge of the hole became essentially equal to that from TSA [4, 5].

Isoparametric elements (ANSYS element type: Plane-82) having 8 nodes per element were employed. Since the plate is symmetric about both x- and y-axes, a quarter modal was prepared, *figure 2.31*. After iteration a far-field y-displacement of 0.655e-3" (0.01664 mm) was applied. The corner node at the loaded end of the plate was also constrained to be zero in x-direction. The mesh covering the quarter plate utilizes a total of 849 elements and 2672 nodes. *Figure 2.32* is the plot of stress σ_{yy} from ANSYS and it is noted that the far-field stress is not constant.

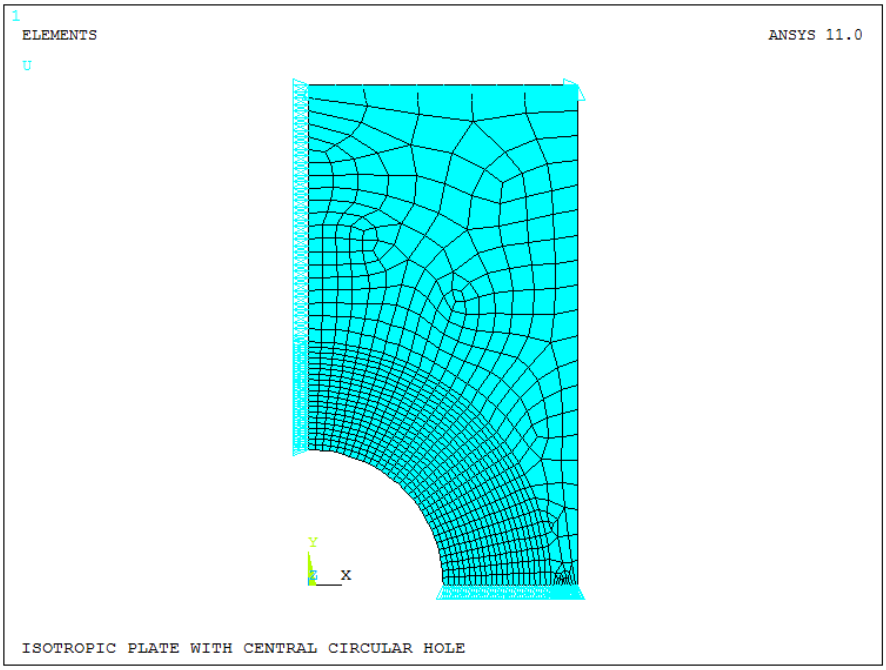

Fig. 2.31: Finite element model for the plate with circular hole

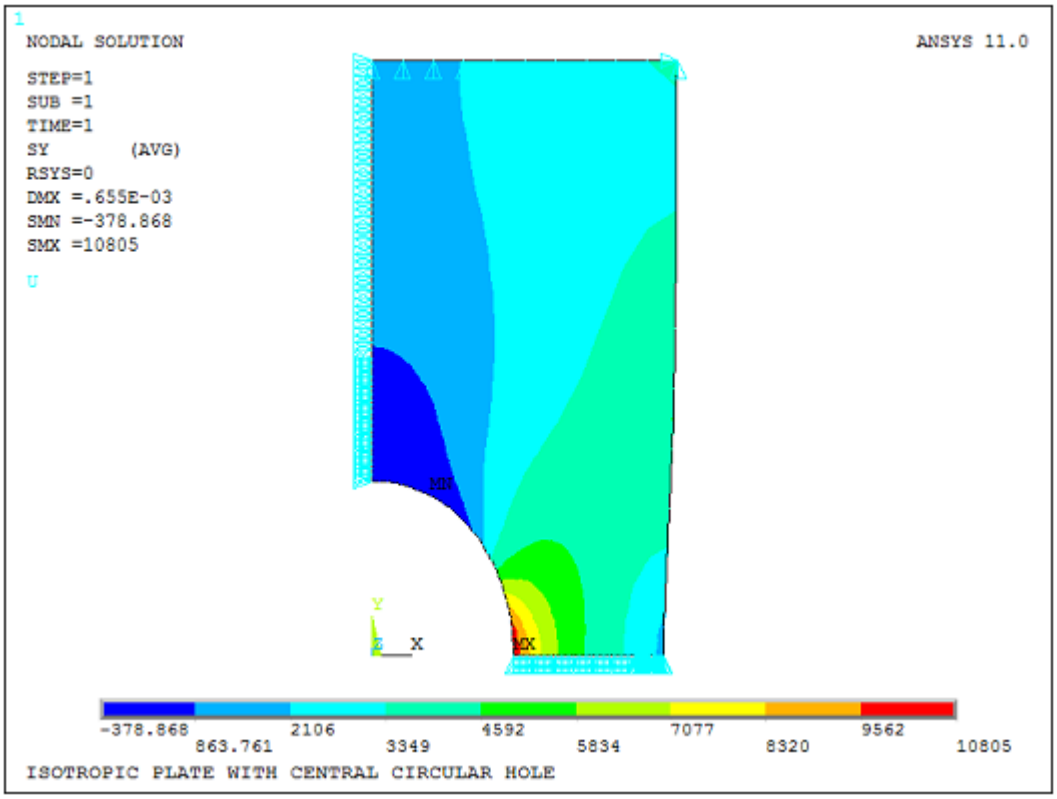

Fig. 2.32: ANSYS predicted vertical stress σ_{yy} (psi) between loading grips of DIC analyzed plate of *figure 2.22*

2.4.5 Determining Individual Components of Displacement, Strain, and Stress from Measured *v* Displacements using Experimentally-DIC Evaluated Airy Coefficients

After determining all the unknown Airy coefficients from the DIC measured *v* – displacements, one can evaluate the individual components of displacement, strain and stress. *Figure 2.33* shows contour plots of the normalized *v/d* displacement predicted by FEA and from the now known Airy coefficients. Substituting these known Airy coefficients into *equations 2.13 through 2.19, 2.26 and 2.27* provides the full-field individual components of stress, strain and displacement. *Figure 2.34* plots the normalized *u/d* displacements from FEA and using evaluated Airy coefficients from DIC measured *v* displacements. This is an example of where the measured *u* displacements is not highly reliable but is derived from measured *v* displacements i.e., it simplifies that only one component of the displacement is measured and processed.

Figures 2.35 through 2.41 are the normalized polar components of displacements, polar components of strain and normalized polar components of stress from FEA and known Airy coefficients from measured *v* displacements. *Figures 2.33 through 2.41* shows excellent agreement between FEA predicted and DIC evaluated displacements, strains and stresses.

The normalizing stress, σ_{net} = 16.54 MPa (2400 psi) is based on the applied tensile load, F = 5337.86 N (1200 lbs), divided by the net area (i.e. away from the region of the hole), *figure 2.22*. The displacement contour plots are normalized with respect to the diameter (d = 25.4 mm = 1") of the hole.

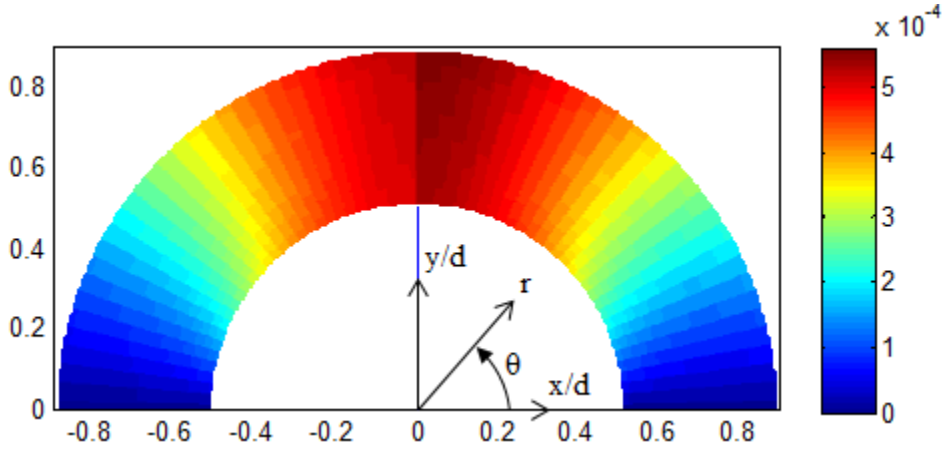

Fig. 2.33: Contour plot of *v/d* throughout 0.5 ≤ r/d ≤ 0.9 region adjacent to hole predicted by FEA (left side) and based on Airy coefficients evaluated from DIC-measured *v* displacements (right side) for *m = 861* input and *k = 5* coefficients

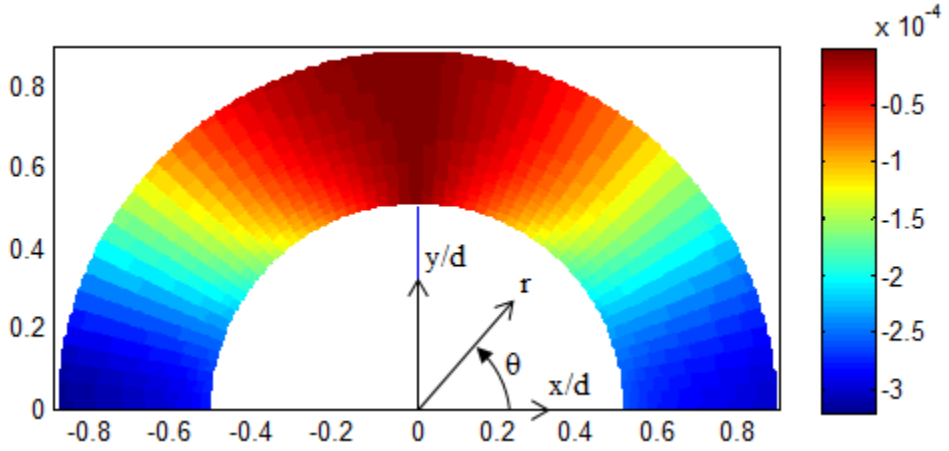

Fig. 2.34: Contour plot of *u/d* throughout 0.5 ≤ r/d ≤ 0.9 region adjacent to hole predicted by FEA (left side) and based on Airy coefficients evaluated from DIC-measured *v* displacements (right side) for *m = 861* input and *k = 5* coefficients

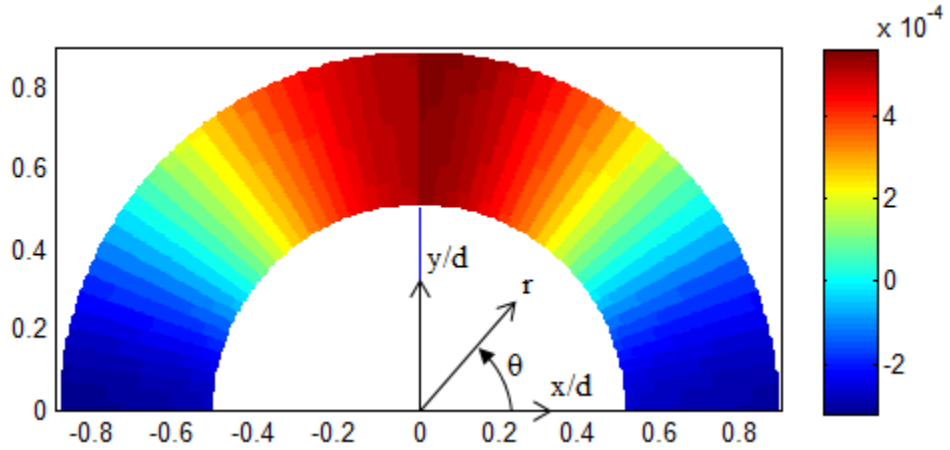

Fig. 2.35: Contour plot of u_r/d throughout $0.5 \leq r/d \leq 0.9$ region adjacent to hole predicted by FEA (left side) and based on Airy coefficients evaluated from DIC-measured *v* displacements (right side) for $m = 861$ input and $k = 5$ coefficients

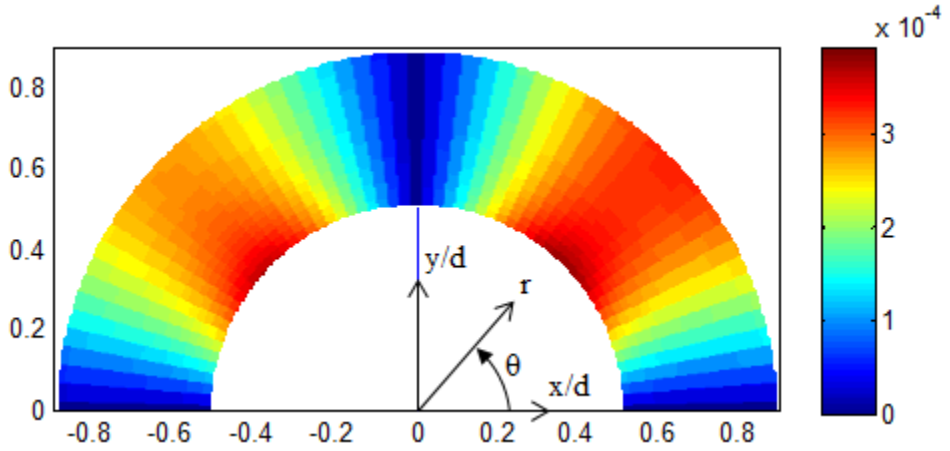

Fig. 2.36: Contour plot of u_θ/d throughout $0.5 \leq r/d \leq 0.9$ region adjacent to hole predicted by FEA (left side) and based on Airy coefficients evaluated from DIC-measured *v* displacements (right side) for $m = 861$ input and $k = 4$ coefficients

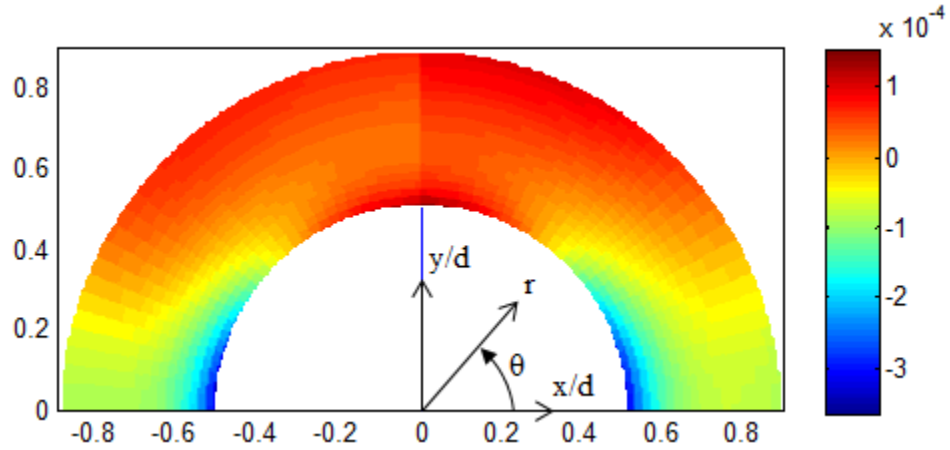

Fig. 2.37: Contour plot of ε_{rr} (micro strain) throughout $0.5 \leq r/d \leq 0.9$ region adjacent to hole predicted by FEA (left side) and based on Airy coefficients evaluated from DIC-measured *v* displacements (right side) for $m = 861$ input and $k = 5$ coefficients

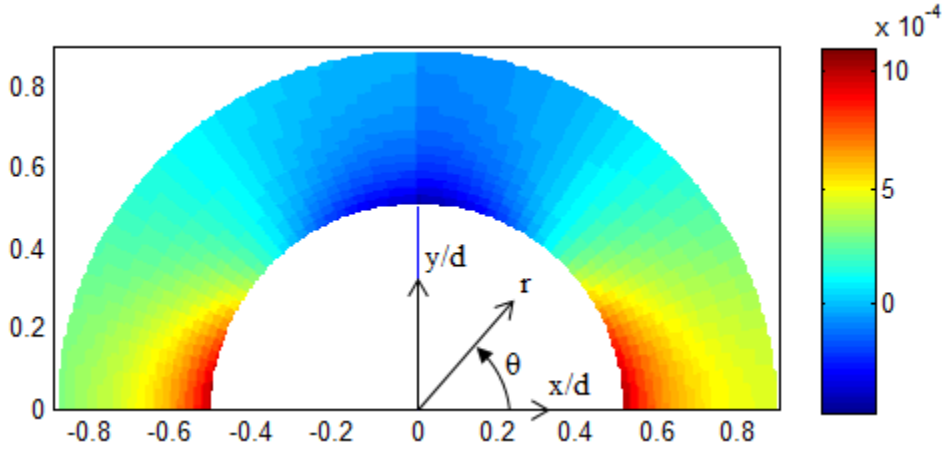

Fig. 2.38: Contour plot of $\varepsilon_{\theta\theta}$ (micro strain) throughout $0.5 \leq r/d \leq 0.9$ region adjacent to hole predicted by FEA (left side) and based on Airy coefficients evaluated from DIC-measured *v* displacements (right side) for $m = 861$ input and $k = 5$ coefficients

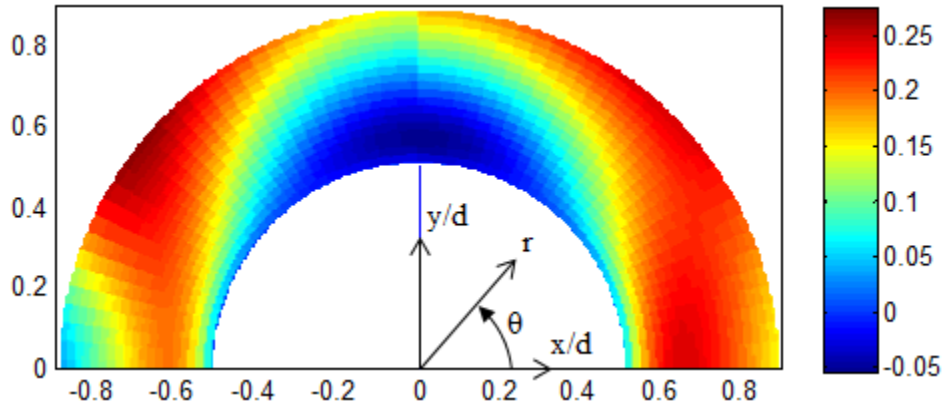

Fig. 2.39: Contour plot of σ_{rr}/σ_{net} throughout $0.5 \leq r/d \leq 0.9$ region adjacent to hole predicted by FEA (left side) and based on Airy coefficients evaluated from DIC-measured *v* displacements (right side) for $m = 861$ input and $k = 5$ coefficients

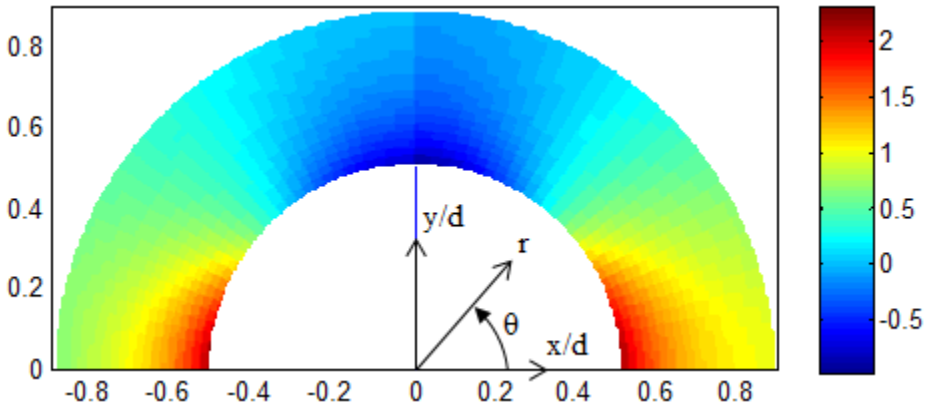

Fig. 2.40: Contour plot of $\sigma_{\theta\theta}/\sigma_{net}$ throughout $0.5 \leq r/d \leq 0.9$ region adjacent to hole predicted by FEA (left side) and based on Airy coefficients evaluated from DIC-measured *v* displacements (right side) for $m = 861$ input and $k = 5$ coefficients

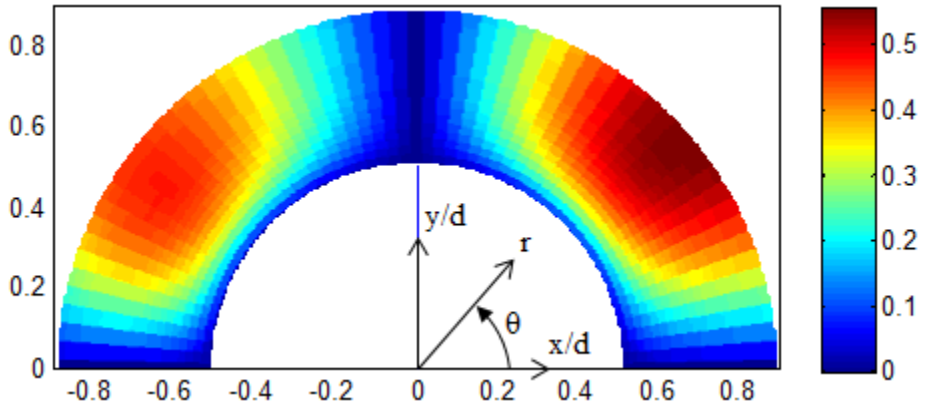

Fig. 2.41: Contour plot of $\sigma_{r\theta}/\sigma_{net}$ throughout $0.5 \leq r/d \leq 0.9$ region adjacent to hole predicted by FEA (left side) and based on Airy coefficients evaluated from DIC-measured *v* displacements (right side) for $m = 861$ input and $k = 5$ coefficients

2.4.6 Experimental Validation

The DIC-based results are compared with those from TSA and strain gages. *Figure 2.42* plots the tangential stress on the boundary of the hole from DIC and FEA against angle ϕ^o (= 90 – angle θ of *figures 2.1 and 2.22*). *Figure 2.43* plots the tangential stress on the boundary of the hole from ANSYS and TSA [4, 5]. The angle ϕ^o of *figure 2.42* corresponds to angle θ of *figure 2.43*. There is an excellent agreement between the TSA determined and present DIC evaluated tangential stress on the boundary of the hole.

Four single-element Micro-Measurements strain gages (EA-13-060LZ-120) were mounted along the line AB, each having gage resistance of 120Ω and a gage factor of 2.055 ± 0.5%. Two gages were mounted on the curved boundary of the hole and the other two gages next to the boundary at a distance x = 0.555" along the line AB, *figure 2.21*.

Figure 2.44 plots ε_{yy} along line AB of *figure 2.22* from ANSYS, strain gages and evaluated Airy coefficients ($k = 5$ coefficients) from $m = 861$ input DIC measured v displacements. Particularly the good agreement between the current DIC results and those from TSA and the strain gages provided strong confidence in the presently developed ability to obtain reliable stresses from only a single measured component of displacement.

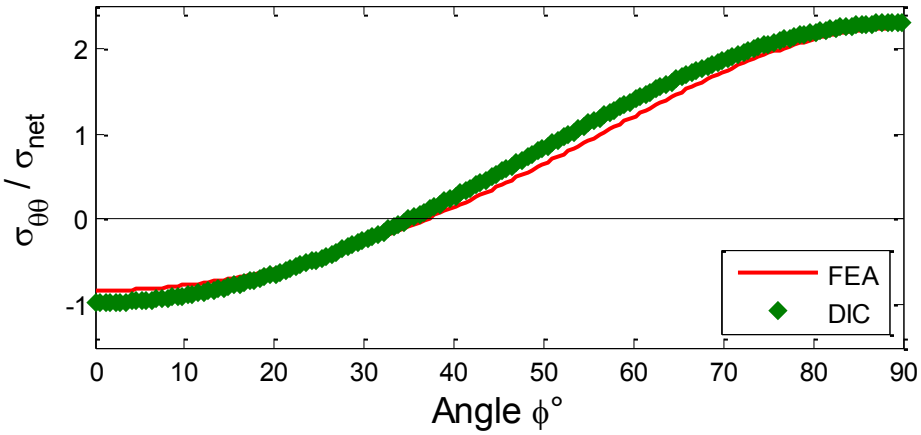

Fig. 2.42: Plot of $\sigma_{\theta\theta}/\sigma_{net}$ vs. Angle ϕ^o (= 90 - θ^o) along boundary of the hole from ANSYS and evaluated Airy coefficients ($k = 5$ coefficients) from $m = 861$ input DIC measured v displacements

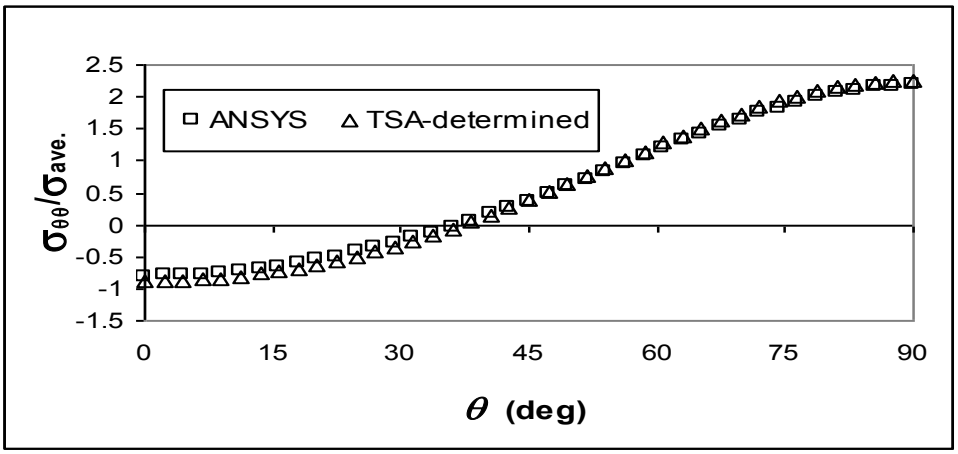

Fig. 2.43: Plot of $\sigma_{\theta\theta}/\sigma_{net}$ around the boundary of the hole from TSA-determined and ANSYS [4, 5]

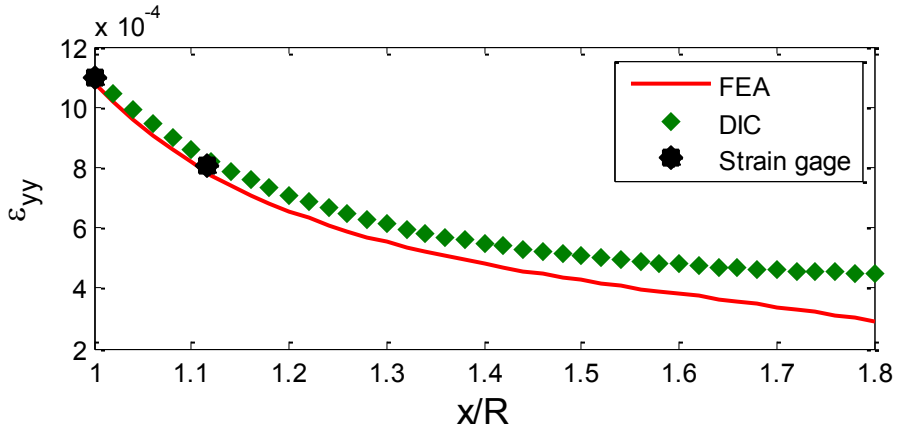

Fig. 2.44: Plot of ε_{yy} along AB of *figure 2.22* form ANSYS, evaluated Airy coefficients ($k = 5$ coefficients) from $m = 861$ input DIC measured v displacements and Strain gage

2.4.7 General Comments

The present 2-D DIC analysis was conducted using commercial hardware and software from Correlation Solutions, Inc. The system's software VicSnap and Vic-2D records, processes and displays the captured displacement data as displacements and strains. Rather than employ the VicSnap provided strains, I utilized MATLAB to import only the DIC- recorded v (vertical) displacements and processed these data accordingly to the Airy stress function scheme developed in section 2.1 of this chapter. The excellent agreement between the results from DIC, strain gages and TSA demonstrates the reliability with which one can evaluate the individual components of displacement, strain and stress from a single measured component of displacement.

2.5 Summary, Discussion and Conclusions

Unidirectionally measured displacements is combined with an Airy stress function to determine the individual components of stress on and in the neighborhood of a centrally-circular geometric discontinuity in a tensile strip without knowing the loading, far-field geometry or boundary conditions. This technique is demonstrated using the simulated experimental data from FEM and experimental data from DIC i.e., full-field individual components of displacement, strain and stress were evaluated using the unidirectionally measured displacements. This technique is further validated using the known results from TSA and strain gages.

The most advantageous feature of the present approach is to evaluate all the unknown Airy coefficients from single component of measured displacements, full-field strain/stress determination without physically differentiating the measured displacement data i.e., having rigorous mechanics basis and to reduce these experimentally-determined coefficients by approximately half by *analytically* imposing the traction-free conditions on the boundary of the hole. The present approach provides accurate displacements/strains/stresses on the boundary of the hole without the knowledge of any measured data on and near the boundary of the hole. This is important because instances such as failure criteria and fatigue-life predictions are based on individual components of stress or the maximum stress which lies on the boundary of the hole. Irrespective of number of simulated or experimental measured input data, $k = 5$ was found to be an appropriate number of Airy coefficient to be used.

Future consideration should consider application of the present concept to more generally-shaped geometric discontinuities, more complicated members, and the feasibility of

employing the displacement component u and v as represented directly in rectangular coordinates [14] rather than those from any Airy stress function. Although demonstrated here for a symmetrical uniaxially-loaded central circular finite perforated plate, the present approach could be extended to more irregular-shaped discontinuities, as well as fairly arbitrary external geometry and loading.

Chapter 3 : Full-Field Determining Stress and Strain Components in the Vicinity of a Cutout from Discretely Measured Strains Only in One Direction

3.1 Introduction

Chapter 2 illustrates how to determine the individual components of strain and stress from one component of displacement. This chapter develops the ability to evaluate full-field the three independent components of stress in an engineering member from only one component of discretly measured strains. The classical problem of stress analysis of a finite tensile plate containing a central circular hole is employed as an illustrative example, *figure 3.1*. A hybrid experimental-numerical-analytical approach is utilized, i.e., combine the experimental data (strain gage results) with least-squares and an Airy stress function to evaluate the individual components of strain and stress. An advantage of this technique is that by evaluating the unidirectional strain at a common direction at few discrete locations, all of the individual components of strain and stress are available (full-field). Moreover, the measured data need not be differentiated (as is usually necessary with other full-field techniques like moiré, holography, digital image analysis, speckle), it is not necessary to cycle the specimen (as required with TSA) or somehow calibrate the system (such as with TSA and photoelasticity), and single element strain gages are less expensive, involve less wiring and have a smaller foot-print than do 2- or 3-element rosettes. The present ability to obtain all three components of strain from single-element gages rather than multiple-element gages reduces the number of electronic channels needed and

hence simplifies the data acquisition requirements. Two- and three-element rosettes also pose the challenges that not all elements of the rosette are at the same location. The question therefore arises at what common position does one assume the three strain occurs. The current concept is invented and developed by the author. The results obtained here are compared with those from FEA and other strain gages.

Figure 3.1 shows the plate geometry, dimension, and orientation and location of the co-ordinate axes. The plate is symmetrical about x- and y-axes with respect to geometry and loading.

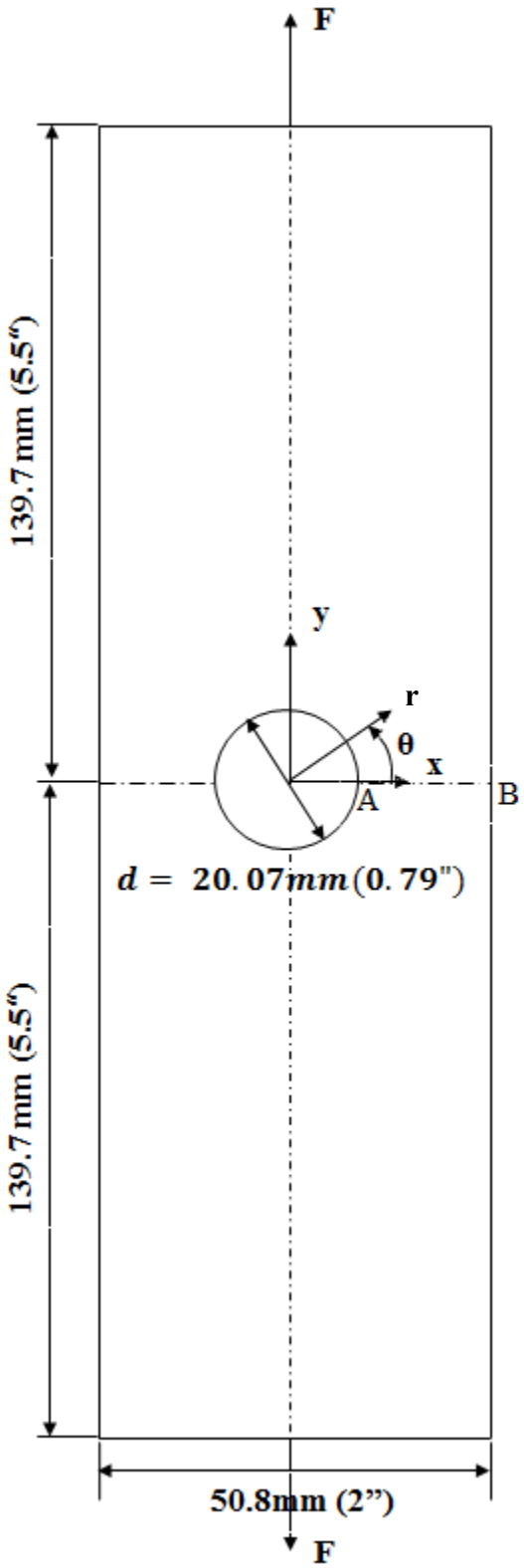

Fig. 3.1: Schematic geometry of a finite plate with a hole

3.2 Relevant Stress Function (Airy's Stress Function)

A relevant Airy stress function, ϕ, satisfying the biharmonic equation $\nabla^4\phi = 0$, equilibrium and compatibility for the finite geometry associated with *figure 3.1* can be written as (*equation 2.7*) [4, 6]

$$\phi = a_0 + b_0 \ln r + c_0 r^2 + \sum_{n=2,4,6,..}^{N} \left\{ \left(a_n r^n + b_n r^{n+2} + c_n r^{-n} + d_n r^{-(n-2)} \right) \cos n\theta \right\} \quad (3.1)$$

Imposing the traction-free condition on the boundary of circular hole ($\sigma_{r\theta} = 0$ and $\sigma_{rr} = 0$ at r = R (= 10.03 mm = 0.395″), and for all values of θ) and evaluating the individual components of stress and strain (detailed derivations are presented in Appendices A2 and A3.2)

$$\sigma_{rr} = \left(\frac{-2R^2}{r^2} + 2 \right) c_0 - \sum_{n=2,4,...}^{N} \left[\begin{Bmatrix} -(n-1)(n+1)R^2 r^{n-2} \\ +(n+1)R^{2(n+1)} r^{-(n+2)} \\ +(n+1)(n-2) r^n \end{Bmatrix} b_n + \begin{Bmatrix} -(n-1) R^{-2(n-1)} r^{n-2} \\ -(n-1)(n+1) R^2 r^{-(n+2)} \\ +(n-1)(n+2) r^{-n} \end{Bmatrix} d_n \right] cos(n\theta) \quad (3.2)$$

$$\sigma_{\theta\theta} = \left(\frac{2R^2}{r^2} + 2 \right) c_0 + \sum_{n=2,4,...}^{N} \left[\begin{Bmatrix} -(n+1)(n-1)R^2 r^{n-2} \\ +(n+1)R^{2(n+1)} r^{-(n+2)} \\ +(n+1)(n+2) r^n \end{Bmatrix} b_n + \begin{Bmatrix} -(n-1) R^{-2(n-1)} r^{n-2} \\ -(n-1)(n+1)R^2 r^{-(n+2)} \\ +(n-1)(n-2) r^{-n} \end{Bmatrix} d_n \right] cos(n\theta) \quad (3.3)$$

$$\sigma_{r\theta} = \sum_{n=2,4,...}^{N} \left[\begin{Bmatrix} -(n+1)(n-1)R^2 r^{n-2} \\ -(n+1)R^{2(n+1)} r^{-(n+2)} \\ +n(n+1) r^n \end{Bmatrix} b_n + \begin{Bmatrix} -(n-1)R^{-2(n-1)} r^{n-2} \\ +(n-1)(n+1)R^2 r^{-(n+2)} \\ -n(n-1) r^{-n} \end{Bmatrix} d_n \right] sin(n\theta) \quad (3.4)$$

$$\sigma_{xx} = \left[\begin{array}{c} \left\{ -\cos 2\theta \frac{2R^2}{r^2} + 2 \right\} c_0 \\ + \sum_{n=2,4,\ldots}^{N} \left\{ \begin{array}{c} \left\{ \begin{array}{c} (n+1)(n-1)R^2 r^{n-2}(\cos(n\theta - 2\theta)) \\ -(n+1)R^{2(n+1)} r^{-(n+2)} \left(cos(n\theta + 2\theta)\right) \\ -(n+1)r^n (n\cos(n\theta - 2\theta) - 2cosn\theta) \end{array} \right\} b_n \\ + \left\{ \begin{array}{c} (n-1)R^{-2(n-1)}\, r^{n-2}(\cos(n\theta - 2\theta)) \\ +(n-1)(n+1)R^2 r^{-(n+2)} \left(cos(n\theta + 2\theta)\right) \\ -(n-1)r^{-n}(ncos(n\theta + 2\theta) + 2cosn\theta) \end{array} \right\} d_n \end{array} \right\} \end{array} \right] \tag{3.5}$$

$$\sigma_{yy} = \left[\begin{array}{c} \left\{ \cos 2\theta \frac{2R^2}{r^2} + 2 \right\} c_0 \\ + \sum_{n=2,4,\ldots}^{N} \left\{ \begin{array}{c} \left\{ \begin{array}{c} -(n+1)(n-1)R^2 r^{n-2}\cos(n\theta - 2\theta) \\ +(n+1)R^{2(n+1)} r^{-(n+2)} cos(n\theta + 2\theta) \\ +(n+1)r^n (n\cos(n\theta - 2\theta) + 2cosn\theta) \end{array} \right\} b_n \\ + \left\{ \begin{array}{c} -(n-1)R^{-2(n-1)}\, r^{n-2}\cos(n\theta - 2\theta) \\ -(n-1)(n+1)R^2 r^{-(n+2)} cos(n\theta + 2\theta) \\ +(n-1)r^{-n}(ncos(n\theta + 2\theta) - 2cosn\theta) \end{array} \right\} d_n \end{array} \right\} \end{array} \right] \tag{3.6}$$

$$\epsilon_{rr} = \frac{1}{E} \left[\begin{array}{c} \left\{ \frac{-2R^2}{r^2}(1+\upsilon) + 2(1-\upsilon) \right\} c_0 \\ - \sum_{n=2,4,\ldots}^{\mathrm{N}} \left\{ \begin{array}{c} \left(\begin{array}{c} -(1+\upsilon)(n-1)(n+1)R^2\, r^{n-2} \\ +(1+\upsilon)(n+1)R^{2(n+1)}\, r^{-(n+2)} \\ +(n+1)[(n-2) + \upsilon(n+2)]\, r^n \end{array} \right) b_n \\ + \left(\begin{array}{c} -(1+\upsilon)(n-1)\, R^{-2(n-1)}\, r^{n-2} \\ -(1+\upsilon)(n-1)(n+1)\, R^2 r^{-(n+2)} \\ +(n-1)[(n+2) + \upsilon(n-2)]\, r^{-n} \end{array} \right) d_n \end{array} \right\} cos(n\theta) \end{array} \right] \tag{3.7}$$

$$\varepsilon_{\theta\theta} = \frac{1}{E} \left[\begin{array}{c} \left\{ \frac{2R^2}{r^2}(1+\upsilon) + 2(1-\upsilon) \right\} c_0 \\ + \sum_{n=2,4,\ldots}^{N} \left\{ \begin{array}{c} \left(\begin{array}{c} -(1+\upsilon)(n+1)(n-1)R^2\, r^{n-2} \\ +(1+\upsilon)(n+1)R^{2(n+1)}\, r^{-(n+2)} \\ +(n+1)[(n+2) + \upsilon(n-2)]r^n \end{array} \right) b_n \\ + \left(\begin{array}{c} -(1+\upsilon)(n-1)\, R^{-2(n-1)} r^{n-2} \\ -(1+\upsilon)(n-1)(n+1)R^2\, r^{-(n+2)} \\ +(n-1)[(n-2) + \upsilon(n+2)]\, r^{-n} \end{array} \right) d_n \end{array} \right\} cos(n\theta) \end{array} \right] \tag{3.8}$$

$$\epsilon_{xx}= \frac{1}{\mathrm{E}}\left[\begin{array}{c}\left\{-\cos 2\theta \frac{2R^2}{r^2}(1+\upsilon)\ +2(1-\upsilon)\right\}c_0 \\ +\sum_{n=2,4,\ldots}^{N}\left[\begin{array}{c}\left\{\begin{array}{c}(n+1)(n-1)R^2r^{n-2}(\cos(n\theta-2\theta))(1+\upsilon) \\ -(n+1)R^{2(n+1)}r^{-(n+2)}\big(cos(n\theta+2\theta)\big)(1+\upsilon) \\ -(n+1)r^n(n\cos(n\theta-2\theta)(1+\upsilon)-2cosn\theta(1-\upsilon))\end{array}\right\}b_n \\ +\left\{\begin{array}{c}(n-1)R^{-2(n-1)}\ r^{n-2}(\cos(n\theta-2\theta))(1+\upsilon) \\ +(n-1)(n+1)R^2r^{-(n+2)}\big(cos(n\theta+2\theta)\big)(1+\upsilon) \\ -(n-1)r^{-n}(n\,cos(n\theta+2\theta)(1+\upsilon)+2\,cosn\theta\,(1-\upsilon))\end{array}\right\}d_n\end{array}\right]\end{array}\right] \quad (3.9)$$

$$\epsilon_{yy}= \frac{1}{\mathrm{E}}\left[\begin{array}{c}\left\{\cos 2\theta \frac{2R^2}{r^2}(1+\upsilon)+2(1-\upsilon)\right\}c_0 \\ +\sum_{n=2,4,\ldots}^{N}\left\{\begin{array}{c}\left\{\begin{array}{c}-(n+1)(n-1)R^2r^{n-2}\cos(n\theta-2\theta)\,(1+\upsilon) \\ +(n+1)R^{2(n+1)}r^{-(n+2)}cos(n\theta+2\theta)(1+\upsilon) \\ +(n+1)r^n(n\cos(n\theta-2\theta)\,(1+\upsilon)+2cosn\theta(1-\upsilon))\end{array}\right\}b_n \\ +\left\{\begin{array}{c}-(n-1)R^{-2(n-1)}\ r^{n-2}\cos(n\theta-2\theta)\,(1+\upsilon) \\ -(n-1)(n+1)R^2r^{-(n+2)}cos(n\theta+2\theta)(1+\upsilon) \\ +(n-1)r^{-n}(ncos(n\theta+2\theta)(1+\upsilon)-2cosn\theta(1-\upsilon))\end{array}\right\}d_n\end{array}\right\}\end{array}\right] \quad (3.10)$$

where r is the radius measured from the center of a hole, angle θ is measured counter-clockwise from the horizontal x-axis (*figure 3.1*), c_0, b_n, and d_n are Airy coefficients, E is the elastic modulus, υ is the Poisson's ratio, and N is the terminating index value of the summation series (N is an even positive integer greater than 1).

Comparing *equations 3.2 through 3.10* shows that coefficients present in all the expressions are the same except coefficient c_0 does not occur in the expression of polar shear stress (*equation 3.4*). Therefore, while evaluating the polar shear stress ($\sigma_{r\theta}$) the magnitude of coefficient c_0 is not needed.

3.3 Specimen Details and Loading

The specimen has unidirectional strain gages mounted as shown in *figures 3.2 through 3.8*. With reference to section 3.2, only single-element strain gages in the y-direction are used such that ϵ_{yy} is measured at numerous discrete locations and the Airy coefficients are determined from *equation 3.10* and these measured values of ϵ_{yy}. These strain gages are connected to the strain gage conditioner (*figure 3.8*) for evaluating the unidirectional strains. Strain gages were mounted throughout the four quadrants (coordinate origin being at the center of the hole) and on the front and back of the plate. Since the plate is symmetrical about both the x- and y-axes, care was taken while locating the gages such that every strain gage has different coordinate when shifted to the first quadrant. Most of the individual gages are too large to actually mount them all in a single quadrant (one common face) of the plate.

Following are the details of the plate tested for the succeeding analyses and results:

Material of the plate: Aluminum 6061-T6 (Wiedenbeck, Inc., Madison, WI); Elastic Modulus E = 68.95 GPa (10 x 10^6 psi), Poisson's ratio υ = 0.33, Ultimate strength = 275 to 311 MPa (40 to 45 ksi) and Yield strength = 241 to 275 MPa (35 to 40 ksi).

- Applied Range (F) = 4448.22 N (1000lb).
- Diameter of the hole (d) = 20.07 mm (0.79").
- Thickness of the plate (t) = 6.35 mm (0.25").
- Total length of the plate (L) ≈ 279.4 mm (11").
- Total width of the plate (W) = 50.8 mm (2").
- Plate of *figure 3.1* is symmetrical about both x- and y-axes.

- Far-field stress (at F = 1000lb), σ_0 = 2000 psi (13.79 MPa).

Strain gage details:

The strain gages were mounted near the region of circular hole, *table 3.1* and *figures 3.2 through 3.5*. Fifty seven (*table 3.1*) strain gages were applied so that no two gages are mirrored about either the horizontal or vertical axis centered at the hole, ensuring that unique strains can be recorded. Twelve out of the fifty seven gages malfunctioned leaving 45 strain inputs.

Gage application necessitates considerable care to ensure that accurate data are obtained. The first step in this process is to sand the surface of the aluminum to remove any scratches or voids. This is done by first sanding the area of interest with 120 grid sandpaper and then progressively moving to a finer grid with 400 being the last used in the process. After final sanding, the area is inspected once again to ensure no scratches or voids remain.

Any contaminants such as fine particles from the sanding process or fingerprints must be removed using an acid/base solution. First an acid solution M-Prep Conditioner A (by Vishay) is dropped on the area and wet sanded with 400 grid sandpaper is done. Then a few drops of the base solution M-Prep Neutralizer A (by Vishay) are applied to the same area and wet sanded with a new piece of 400 grid sandpaper. After this the area is wiped clean using Surpass tissue paper and to ensure no new contaminants are brought to the area, the motion of wiping begins from the area of interest outward. After the area has been wiped dry, a Cotton-Tipped Applicator is rubbed on the area and the area is inspected for any residue. If no visible residue can be seen, the area is ready for application of the strain gage.

Relative to gage application, a gage is first removed from the supplier's (Vishay, Micromeasurements) transparent envelope in which it is contained and a piece of PCT - 2M gage installation scotch tape is applied over the gage. The tape is then peeled back at a shallow angle so not to damage the gage. The gage is then positioned over the previously provided layout lines on the specimen with the triangle alignment marks of the gage aligned with the desired direction of strain to be measured. The tape is again peeled back at an acute angle to the specimen surface until the gage is free of the specimen surface. Next M-Bond Catalyst-C (by Vishay) is applied to the bonding side of the gage surface and allowed to dry fully. When fully dried, one to two drops of M-Bond 200 adhesive (by Vishay) is applied to the specimen surface and the bonding side of the gage is then pressed on to the specimen area with slight pressure from the thumb maintain the pressure for a minimum of one minute. At this point the gage is fully bonded to the surface so the tape can be removed. The tape should be peeled back slowly and directly over itself. Finally check the edges of the gage carefully with a tooth pick to ensure that the entire gage is bonded to the surface.

Table 3.1 lists all gages applied to the specimen along with their resistance, gage factor, designation (Vishay, Micromeasurements) and locations. All locations were measured to the center position on the gage using a 32 divisions per inch triangular engineer's scale. The x- and y-coordinates in the table 3.1 is based on the origin which is chosen to be the bottom right corner of the aluminum bar on the front face*, figure 3.2* and bottom left corner of the aluminum bar on the back face, *figure 3.3*. The highlighted gages of table 3.1 malfunctioned and are not used. Gage identification numbers of table 3.1 are indicated on the respective terminal tabs in *figures 3.2 and 3.3*. Gage 57 of *figure 3.3* is on the boundary of the hole.

Table 3.1: Gage numbers and descriptions

Gage Number	Gage Factor	Resistance (Ω)	Gage Designation	x (in)	y (in)
1	2.070 ± 0.5%	120.1	EA-13-125-AD-120	0.094	5.406
2	2.070 ± 0.5%	120.0	EA-13-125-AD-120	0.266	5.406
3	2.070 ± 0.5%	120.0	EA-13-125-AD-120	0.438	5.406
4	2.070 ± 0.5%	120.1	EA-13-125-AD-120	1.422	5.125
5	2.070 ± 0.5%	119.8	EA-13-125-AD-120	1.594	5.125
6	2.070 ± 0.5%	119.9	EA-13-125-AD-120	1.781	5.125
7	2.060 ± 0.5%	119.8		0.063	5.813
8	2.060 ± 0.5%	119.9		0.219	5.813
9	2.060 ± 0.5%	119.8		0.406	5.813
10	2.060 ± 0.5%	119.9		1.469	5.5
11	2.060 ± 0.5%	120.0		1.625	5.5
12	2.060 ± 0.5%	119.9		1.781	5.5
13	2.130 ± 0.5%	119.7	EA-13-125-AD-120	1.844	5.328
14	2.130 ± 0.5%	119.9	EA-13-125-AD-120	1.672	5.328
15	2.130 ± 0.5%	119.8	EA-13-125-AD-120	1.469	5.328
16	2.130 ± 0.5%	119.7	EA-13-125-AD-120	0.5	5.719
17	2.130 ± 0.5%	120.0	EA-13-125-AD-120	0.313	5.719
18	2.130 ± 0.5%	119.8	EA-13-125-AD-120	0.125	5.719
19	2.04 ± 1.0%	119.0	EA-06-031MF-120	0.969	6.234
20	2.04 ± 1.0%	120.1	EA-06-031MF-120	1.047	6.234
21	2.04 ± 1.0%	119.5	EA-06-031MF-120	1.125	6.234
22	2.04 ± 1.0%	119.6	EA-06-031MF-120	1.219	6.234
23	2.04 ± 1.0%	119.5	EA-06-031MF-120	1.297	6.234
24	2.04 ± 1.0%	104.2	EA-06-031MF-120	1.375	6.234
25	2.04 ± 1.0%	119.5	EA-06-031MF-120	1.469	6.234
26	2.04 ± 1.0%	NA	EA-06-031MF-120	1.547	6.234
27	2.04 ± 1.0%	119.3	EA-06-031MF-120	1.625	6.234
28	2.04 ± 1.0%	119.5	EA-06-031MF-120	1.703	6.234
29	2.04 ± 1.0%	118.2	EA-06-031MF-120	0.391	4.938
30	2.04 ± 1.0%	NA	EA-06-031MF-120	0.469	4.938
31	2.04 ± 1.0%	119.6	EA-06-031MF-120	0.547	4.938
32	2.04 ± 1.0%	NA	EA-06-031MF-120	0.641	4.938
33	2.04 ± 1.0%	120.3	EA-06-031MF-120	0.719	4.938
34	2.04 ± 1.0%	120.1	EA-06-031MF-120	0.813	4.938
35	2.04 ± 1.0%	120.0	EA-06-031MF-120	0.891	4.938
36	2.04 ± 1.0%	92.6	EA-06-031MF-120	0.953	4.938
Gage Number	**Gage Factor (%)**	**Resistance (Ω)**	**Gage Designation**	**x (in)**	**y (in)**
37	2.04 ± 1.0%	119.3	EA-06-031MF-120	1.031	4.938
38	2.04 ± 1.0%	119.8	EA-06-031MF-120	1.125	4.938
39	2.06 ± 0.5%	119.9	EA-13-125AD-120	0.828	6.125

40	2.06 ± 0.5%	119.8	EA-13-125AD-120	1	6.125
41	2.06 ± 0.5%	119.8	EA-13-125AD-120	1.188	6.125
42	2.130 ± 0.5%	120.1	EA-13-125AD-120	1.531	6.156
43	2.130 ± 0.5%	120.1	EA-13-125AD-120	1.688	6.156
44	2.130 ± 0.5%	119.9	EA-13-125AD-120	1.844	6.156
45	2.130 ± 0.5%	120.0	EA-13-125AD-120	1.516	5.031
46	2.130 ± 0.5%	120.1	EA-13-125AD-120	1.688	5.031
47	2.130 ± 0.5%	120.1	EA-13-125AD-120	0.781	4.656
48	2.130 ± 0.5%	120.1	EA-13-125AD-120	0.938	4.656
49	2.130 ± 0.5%	120.2	EA-13-125AD-120	1.125	4.656
50	2.060 ± 0.5%	120.0		0.063	6.438
51	2.060 ± 0.5%	119.8		0.25	6.438
52	2.060 ± 0.5%	119.9		0.422	6.438
53	2.060 ± 0.5%	119.7		0.578	6.438
54	2.060 ± 0.5%	120.0		0.094	4.328
55	2.060 ± 0.5%	120.2		0.266	4.328
56	2.060 ± 0.5%	120.1		0.438	4.328
57	2.130 ± 0.5%	120.3	EA-13-032VW-120	0.605	5.5

*Red highlighting for gages that measured a significant resistance difference from the expected.
**Yellow highlighting represents slight deviations from the actual gage resistance.

The plate of *figure 3.1* was clamped in the loading frame between the cross heads of the Instron screw driven testing machine (Rm. B325 Engineering Hall) to employing the screws as seen in *figure 3.6*. The plate was aligned between the top and the bottom grips to ensure symmetric loading. *Figures 3.6 through 3.8* show the experimental test setup which includes the 16-channel strain gage conditioner, the Instron Model 1000 universal testing machine, and the loaded specimen. The Instron testing machine has a load transducer with a maximum capacity of 1000 lbs (4448.22 N) and the grips used are a screw-action 2" (50.8 mm) with serrated faces (*figure 3.6*). A 16-channel, strain-gage conditioner box (*figure 3.8*) was used to process the 45 separate channels of strain gage data. There are 45 active strain gages but the strain gage conditioner box has only 16 channels. This necessitated monitoring the 45 gage-recorded strains

in three separate steps under the same loading condition. Gages were scanned and recorded at several discrete increasing and decreasing load levels.

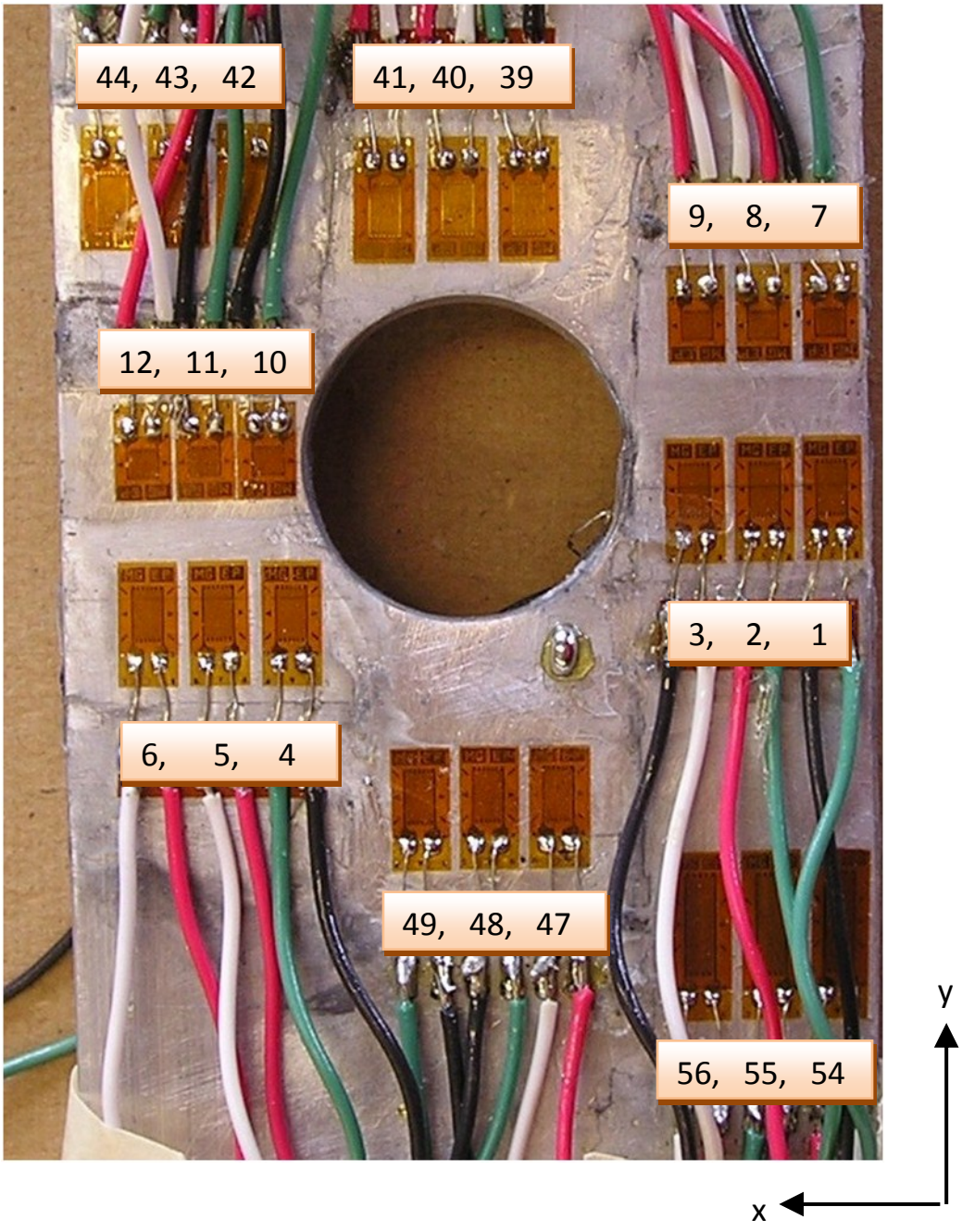

Fig. 3.2: Strain gage numbers corresponding to Table 3.1 (front face)

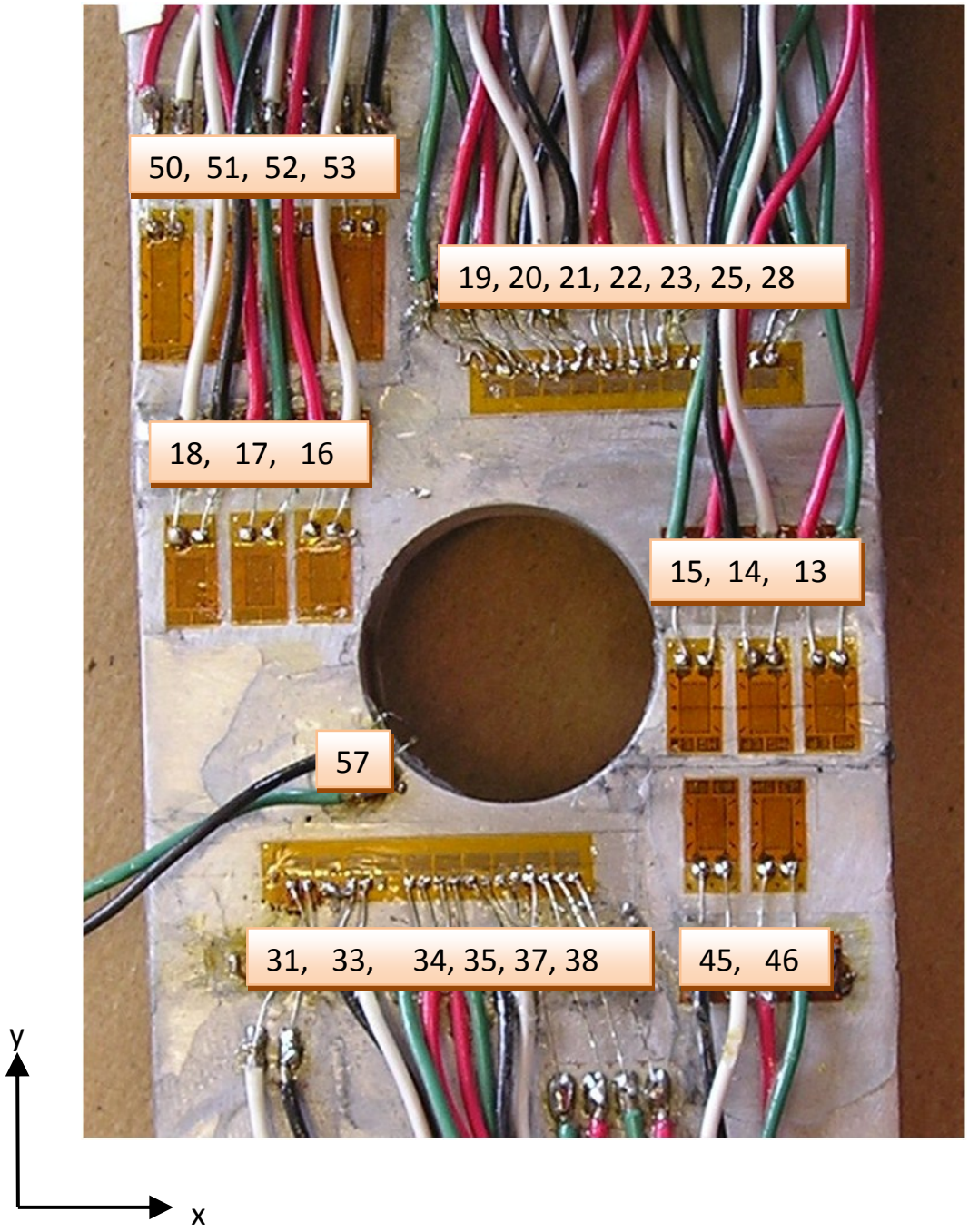

Fig. 3.3: Strain gage numbers corresponding to Table 3.1 (back face)

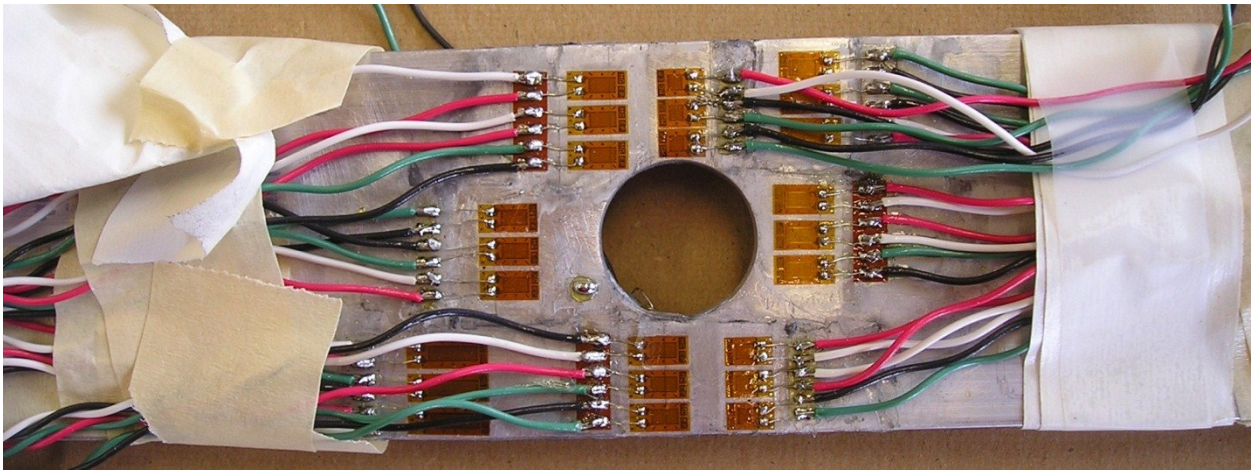

Fig. 3.4: Front view of the Specimen with the gages

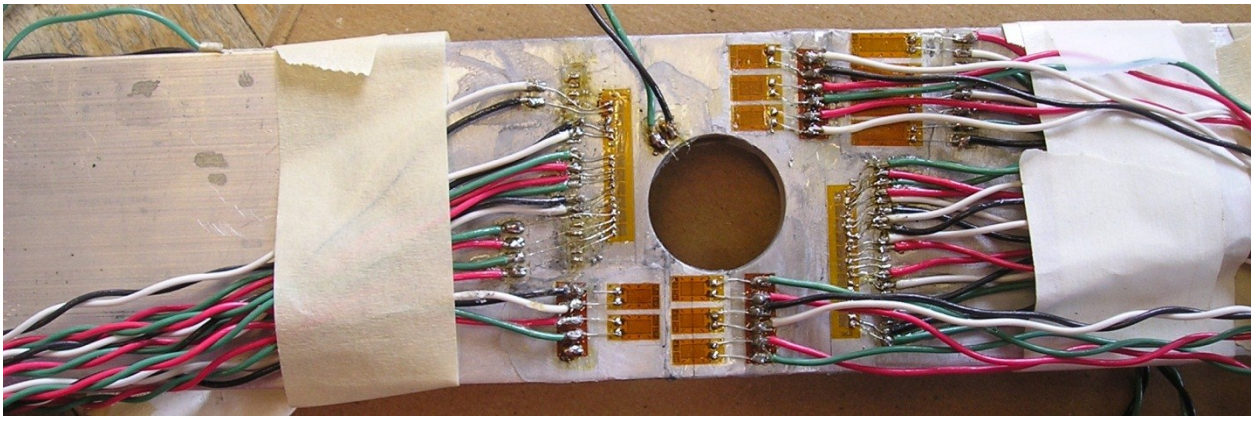

Fig. 3.5: Rear view of the Specimen with the gages

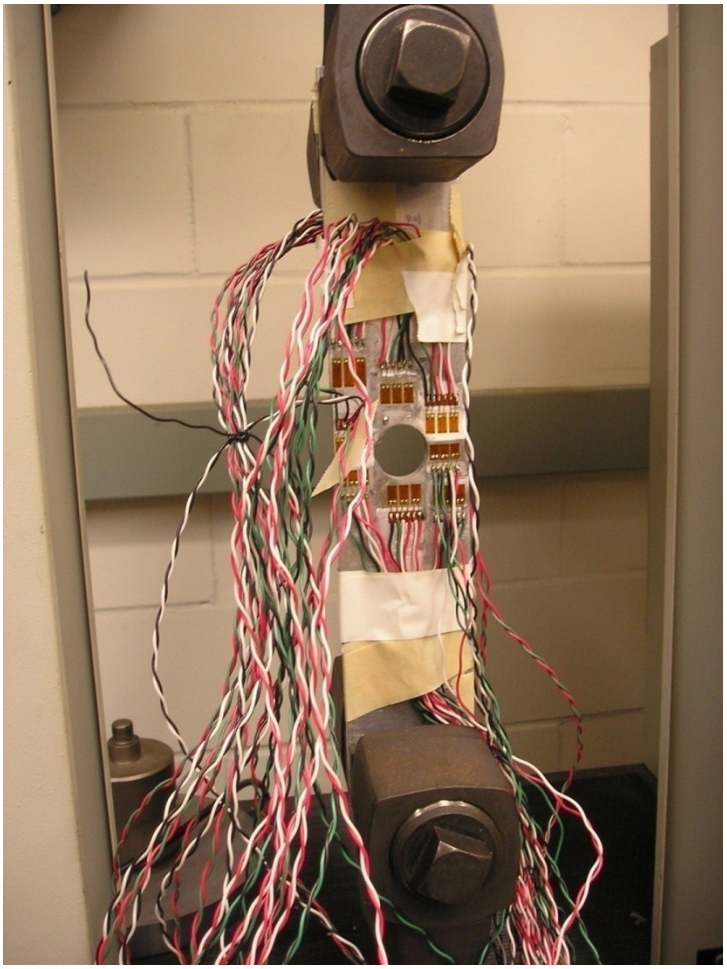

Fig. 3.6: Strain-gage locations on the Specimen

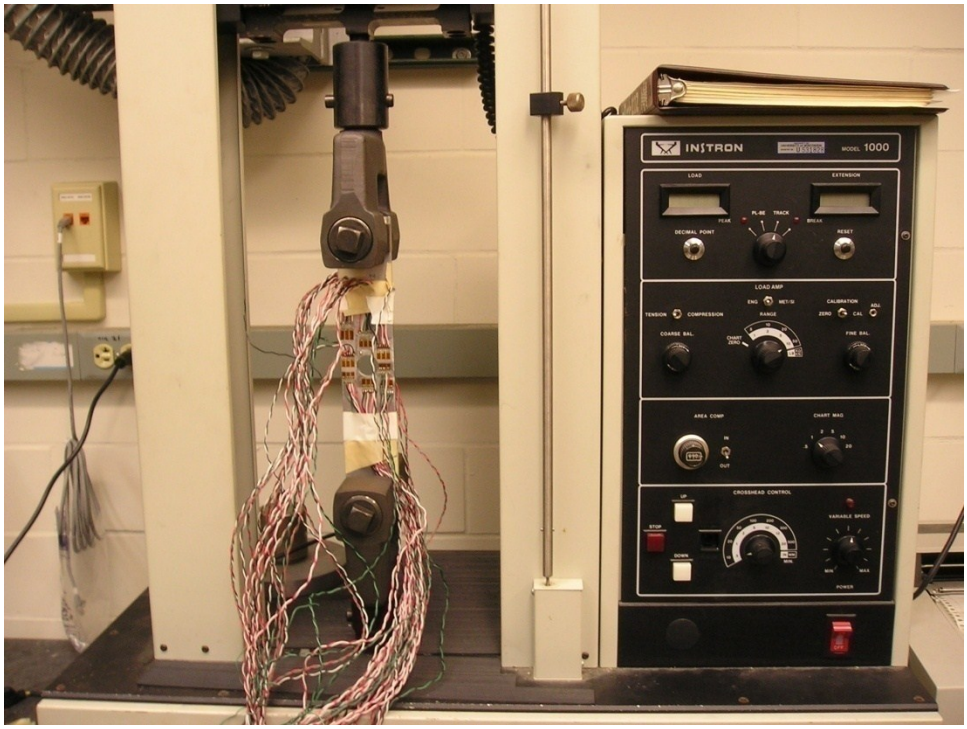

Fig.3.7: Specimen Loaded in the Instron Machine

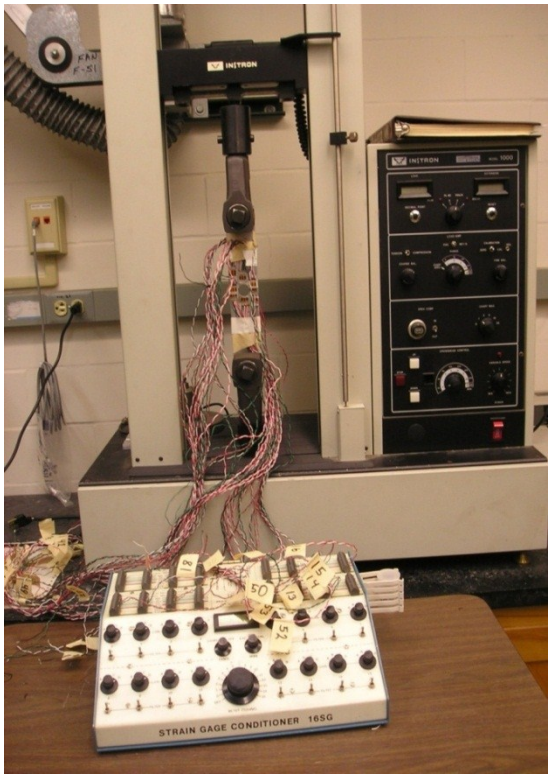

Fig. 3.8: Strain-gages connected to the Strain-gage Conditioner

3.4 Data Processing and Number of Coefficients

The objective of this research was to evaluate the individual components of stress and strain on the edge and in the vicinity of hole from the measure unidirectional strains (ε_{yy}) of table 3.1 and *figures 3.2 through 3.8*. As mentioned previously, in that the plate is symmetrical about both x- and y-axes, all the strain gage locations are shifted to the first quadrant as shown in *figures 3.9* (also see actual gage coordinates in Table 3.1). In *figure 3.9-A* the dimensions are in inches and in *figure 3.9-B* the dimensions are normalized with respect to the radius of the hole. The various individual unidirectional strain gages are mounted in the y-direction with respect to the coordinate orientation of *figure 3.1*. Therefore *equation 3.10* is written in matrix form (*equation 3.11*) and the unknown Airy coefficients of *equations 3.10 and 3.11* are evaluated from the measured ε_{yy} strains by solving this matrix equation using linear least squares. Employing the now known Airy coefficients (c_0, b_n, and d_n), the individual components of strain and stress are available from *equations 3.2 through 3.9* throughout at least the region containing the gages.

Re-writing *equation 3.10,*

$$\begin{bmatrix} \varepsilon_y(c_0, bn, dn) \\ \varepsilon_y(c_0, bn, dn) \\ . \\ . \\ . \\ . \\ \varepsilon_y(c_0, bn, dn) \end{bmatrix} \begin{bmatrix} c_0 \\ b_n \\ d_n \end{bmatrix} = \begin{bmatrix} \varepsilon_{y1} \\ \varepsilon_{y2} \\ . \\ . \\ . \\ \varepsilon_{yN} \end{bmatrix} \tag{3.11}$$

or, in simplified form,

$$[A]_{m\times k}\{c\}_{k\times 1} = \{d\}_{m\times 1} \tag{3.12}$$

where matrix A is an m (number of input data values, i.e., m source locations, *figures 3.9* = 45) by k (number of unknown Airy Coefficients) matrix containing a set of 45 linear strain equations, with k independent variables. Vector c contains the k unknown Airy coefficients, and the vector d is composed of the 45 measured strain gage readings corresponding to the strain equations in matrix A. Since there are more equations than the number of unknown, i.e., $m > k$, the linear least-squares process is utilized to solve the over-determined matrix expression $Ac = d$ of *equations (3.11) and (3.12)*. *Equation 3.12* can be solved using the MATLAB backslash operator ('\') or pseudo inverse 'pinv' operator. Either of these operators uses the algorithm for least squares and calculates vector by *c = A\d or c = pinv*d.*

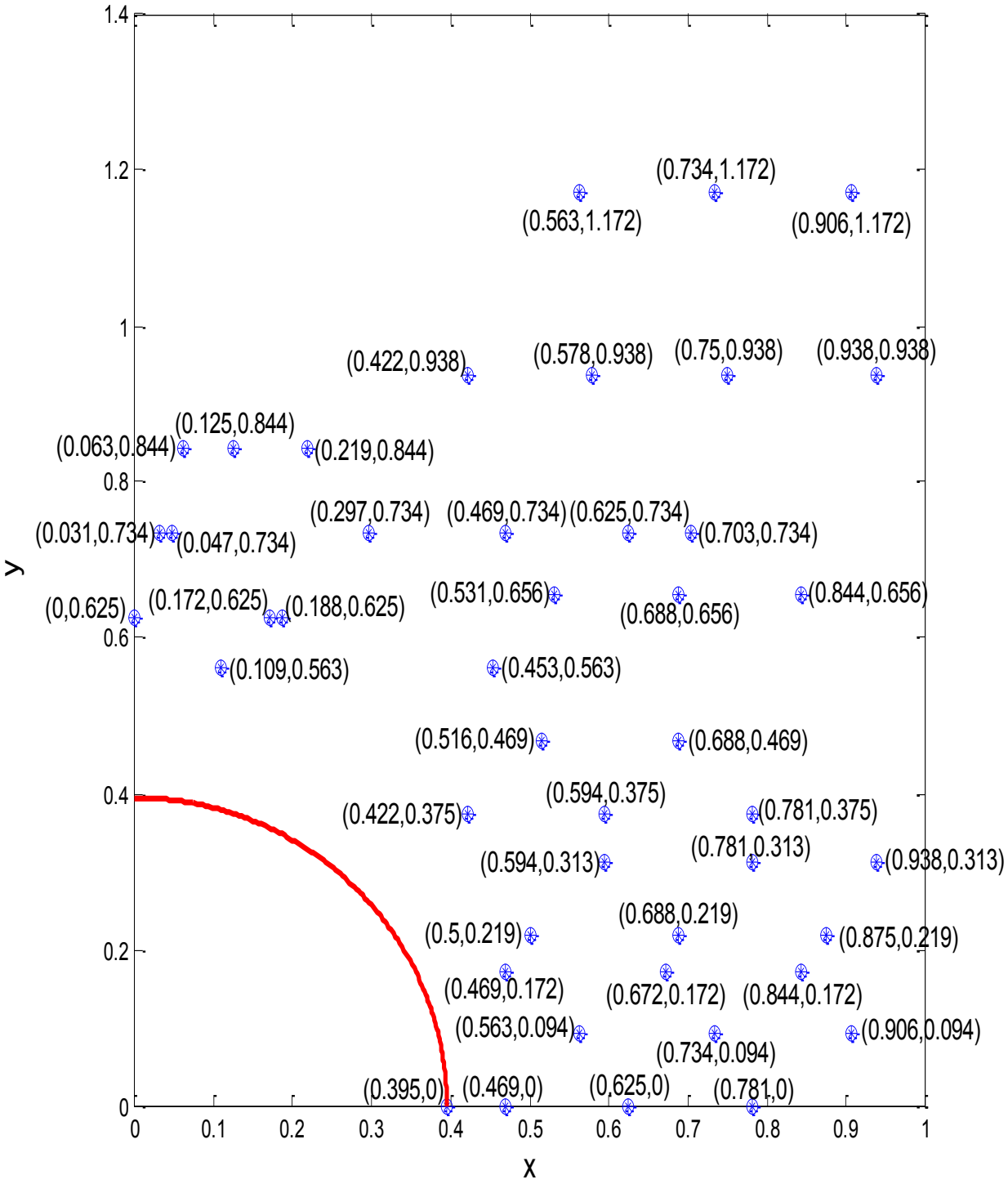

Fig. 3.9-A: Source locations of 45 strain-gages (in inches) relative to the x- and y-coordinate of *figure 3.1*

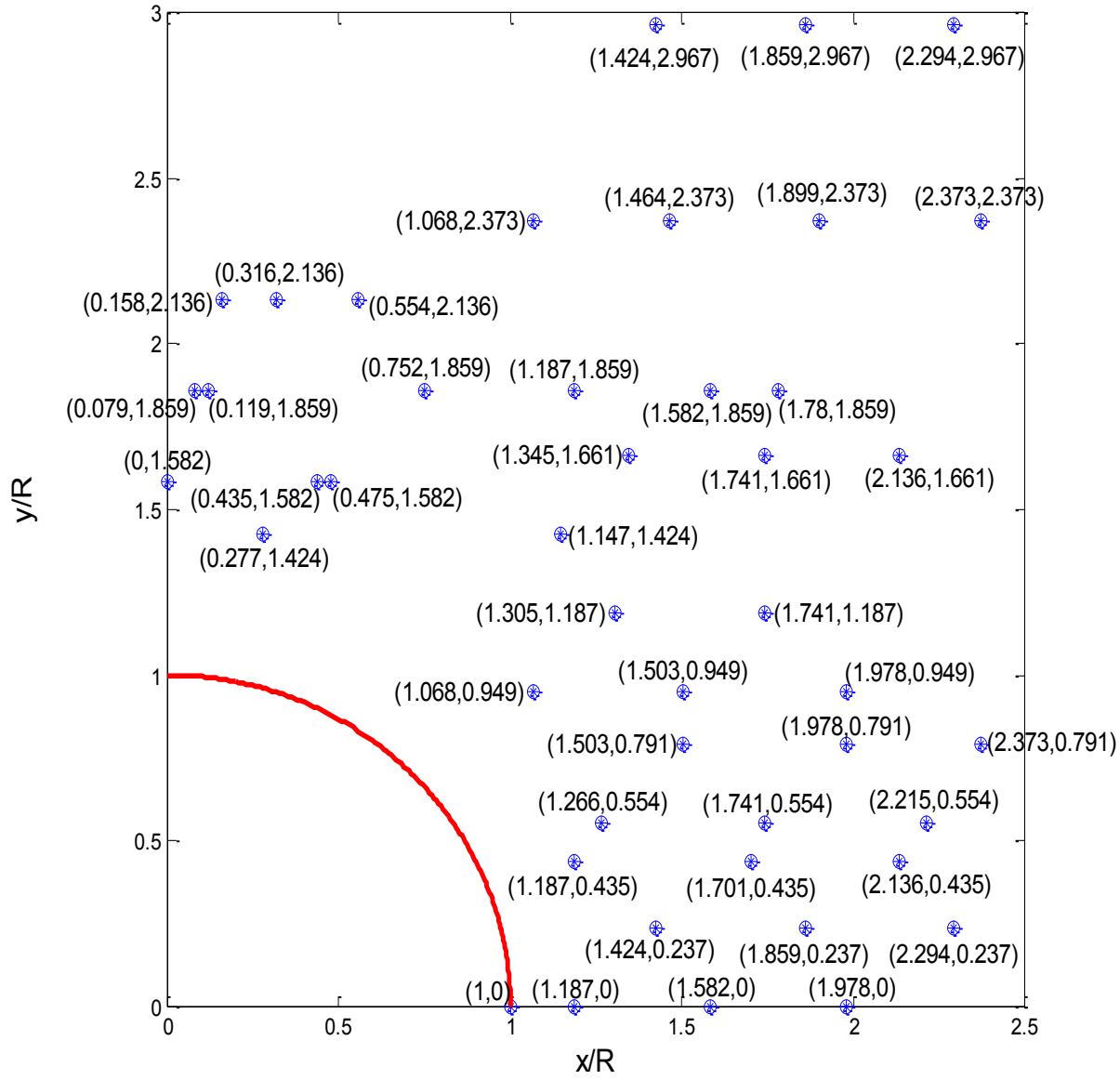

Fig. 3.9-B: Normalized strain-gage coordinate locations, $m = 45$ input values.

Equations 3.2 through 3.10 involve a summation over *n,* where *n* goes through positive even integers from 2 to *N*, and the total number of coefficients is given by $k = N+1$. To evaluate an appropriate number of coefficients to retain, the *RMS* and condition number, c, of matrix A are used. Since the strains ϵ_{yy} are evaluated at 45 locations, virtually no change is seen when comparing with the measured strains with those processed by the Airy stress functions. Therefore *RMS* values (the difference between the processed/predicted and recorded strains) are close to

zero, *figure 3.10*. The condition number, *C*, of matrix A measures the sensitivity of the solution of the system of linear expressions of *equation 3.12*. It also indicates the accuracy of the results from the matrix inversion and the linear equation solution. The condition number can be evaluated in MATLAB using cond(A). *Figure 3.11* is a plot of the condition number, C, against the number of coefficients, *k*, whereas *figure 3.12* is a plot of log (condition number) versus the number of coefficients. These condition number results indicate $k > 7$ number of coefficients is sufficient for generating the solutions with adequate reliability. Moreover, information of *figures 3.10 and 3.11* show little change for $7 \leq k \leq 13$. The results plotted in section 3.6 utilize $k = 7$ coefficients, the terminating index N = 6 and Appendix 3.1 utilizes $k = 13$ coefficients, the terminating index N = 6.

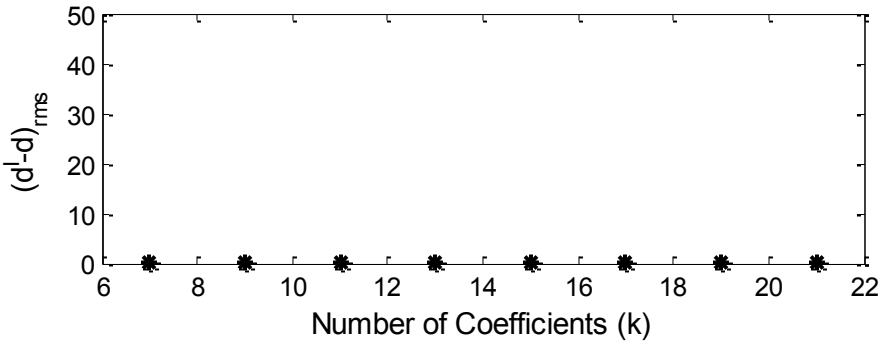

Fig. 3.10: Plot of *RMS* vs. number of coefficients, *k*, for *m* = 45 input values

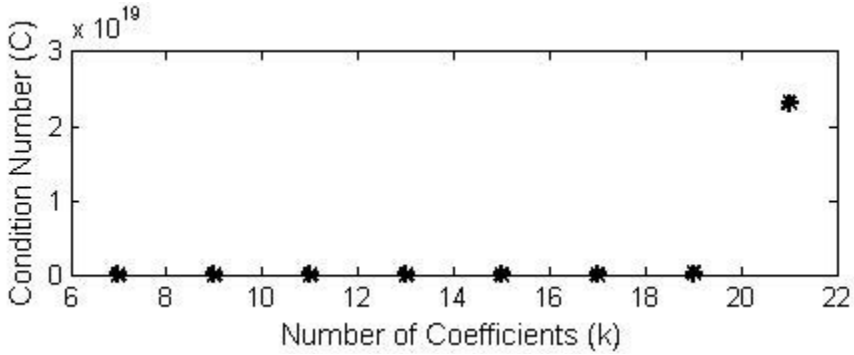

Fig. 3.11: Plot of condition number, *C*, vs. number of coefficients, *k*, for *m* = 45 input values

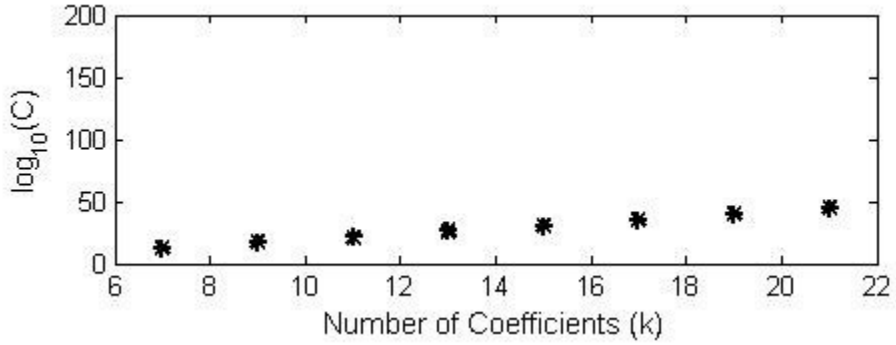

Fig. 3.12: Plot of $\text{Log}_{10}(C)$ vs. number of coefficients, k, for $m = 45$ input values

3.5 Finite Element Analysis

The results based on the recorded ϵ_{yy} strains are compared with those predicted by Finite Element Analysis (FEA). The aluminum plate described in sections 3.1 and 3.3 was modeled using ANSYS. Since the plate is symmetric about both x- and y-axes, a quarter model is analyzed. Isoparametric elements (ANSYS element type: Plane-82) having 8 nodes per element were employed. A very fine mesh was used in the neighborhood of the holes to enhance accuracy as shown in *figure 3.13*. The mesh covering the one quarter of the plate utilizes a total of 6,700 elements and 20,473 nodes. The mesh was refined until the ANSYS results did not vary more than 0.1% on the periphery of hole. A far field stress of 13.79 MPa =2000 psi (corresponding to the 1000 pound applied physically to the plate) was applied at the ends of the numerical model.

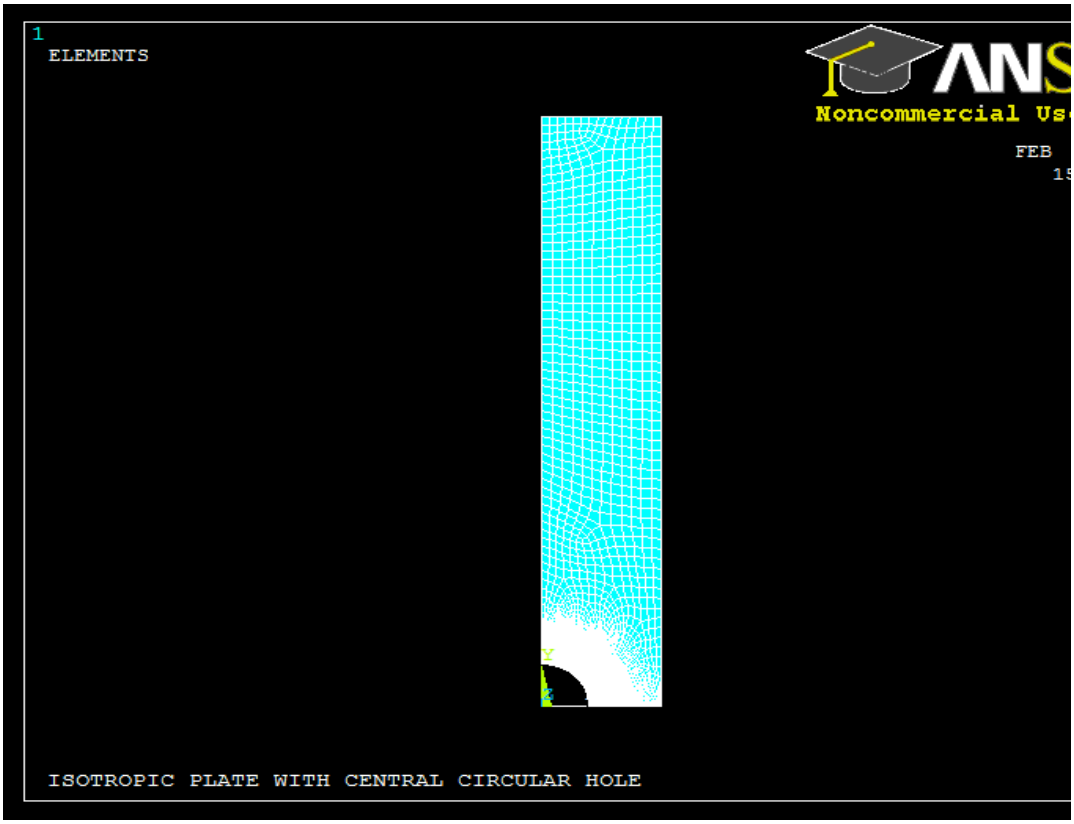

Fig. 3.13: Finite element model for the plate with central circular hole, *figure 3.1*.

3.6 Results

After evaluating all the unknown Airy coefficients (c_0, b_n and d_n, for n = 6) from *equation 3.11* and the measured strain gage readings, the individual components of stress and strain were obtained from *equations 3.2 through 3.10*. These strain gage results are compared with those from finite element analysis (ANSYS) and some discrete strain gages. Tangential strain, $\varepsilon_{\theta\theta}$, radial strain, ε_{rr}, longitudinal strain, ε_{yy}, and lateral strain, ε_{xx}, are normalized with respect to the far field strain, ε_0 = 200 $\mu\varepsilon$ (based on the applied load and gross area as detailed in next paragraph), and are plotted for $k = 7$ (N = 6) at various radii around and away from the boundary of the hole and along the line AB of *figure 3.1* in *figures 3.14 through 3.27*. Tangential stress, $\sigma_{\theta\theta}$, radial stress, σ_{rr}, shear stress, $\sigma_{r\theta}$, vertical stress, σ_{yy}, and horizontal stress, σ_{xx}, are normalized with respect to the far field stress, σ_0, and are plotted at various radii around and away from the boundary of the hole and along the line AB of *figure 3.1* in *figures 3.28 through 3.39*. The strain gage results agree very well with the finite element prediction. The discrepancies in *figure 3.35* near the edge of the plate might be due to the computational error in FEM but are small by comparison to the other stress values.

The normalizing stress, σ_0 = 13.79 MPa (2000 psi) is based on the applied tensile load, F, divided by the gross area (i.e. away from the region of the hole), *figure 3.1*. The normalizing strain, $\varepsilon_0 = 2*10^{-4}$ in/in is evaluated based on the stress-strain relationship i.e., $\varepsilon_0 = \sigma_0/E$.

Applied load range (F) = 4448.2 N (1000lb)

Gross-Sectional Area (A) = Width (W) x Thickness (t)

= 50.8 x 6.35 = 322.58 mm^2 (0.5 in^2)

$$\sigma_o = \frac{4448.2}{322.58} = 13.79\ MPa = (2000\ psi)$$

and $\varepsilon_o = \frac{\sigma_o}{E} = \frac{2000}{10*10^6} = 200\mu\varepsilon$

Angle θ of *figures 3.14 through 3.22, 3.24 through 3.26, 3.28 through 3.30, 3.32 through 3.34, and 3.36 through 3.38,* is measured counter-clockwise from the positive horizontal x-axis and r is measured here from the center of the hole of *figure 3.1*. The actual in-plane dimensions associated with *figures 3.23, 3.27, 3.31, 3.35, and 3.39* are plotted normalized with respect to the radius, R = 10.08 mm = 0.395" of the hole. The ratios of values of $\varepsilon_{rr}/\varepsilon_0$ and $\varepsilon_{\theta\theta}/\varepsilon_0$ from *figures 3.14 and 3.17* agree with the value of υ = 0.33 for Aluminum, as it should. As expected, *figures 3.17 and 3.36* are identical.

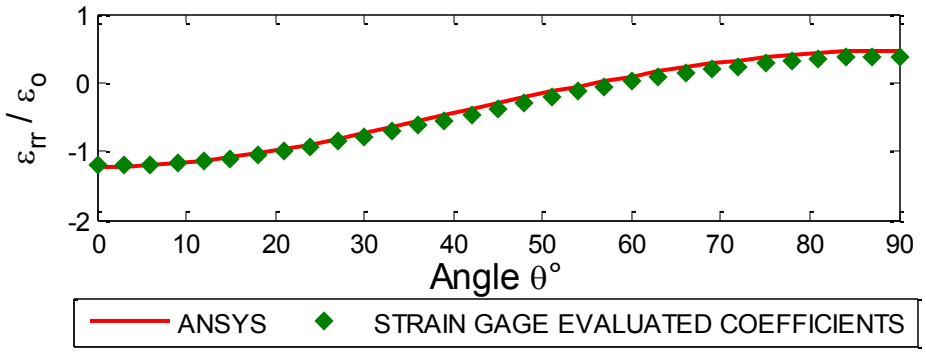

Fig. 3.14: Plot of $\varepsilon_{rr}/\varepsilon_0$ along boundary of the hole from strain-gage evaluated Airy coefficients for $k = 7$ coefficients ($m = 45$ strain-gage input values) and ANSYS

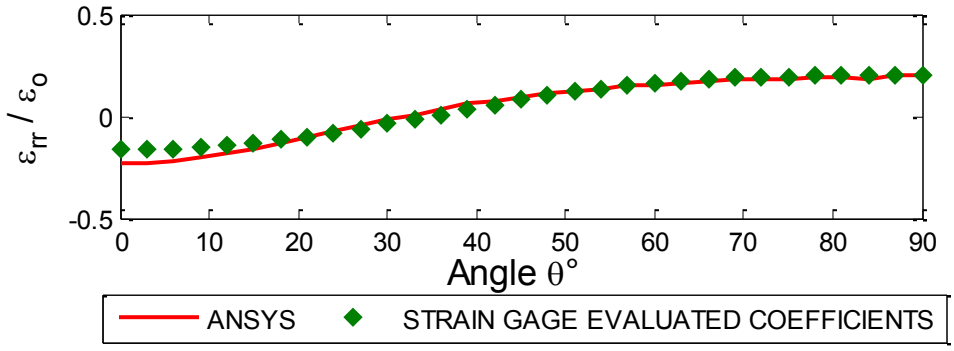

Fig. 3.15: Plot of $\varepsilon_{rr}/\varepsilon_0$ along r/R = 1.5 from strain-gage evaluated Airy coefficients for $k = 7$ coefficients ($m = 45$ strain-gage input values) and ANSYS

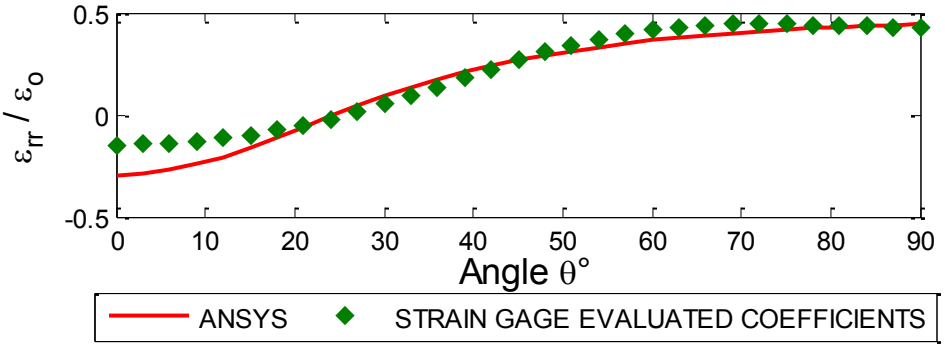

Fig. 3.16: Plot of $\varepsilon_{rr}/\varepsilon_0$ along r/R = 2 from strain-gage evaluated Airy coefficients for $k = 7$ coefficients ($m = 45$ strain-gage input values) and ANSYS

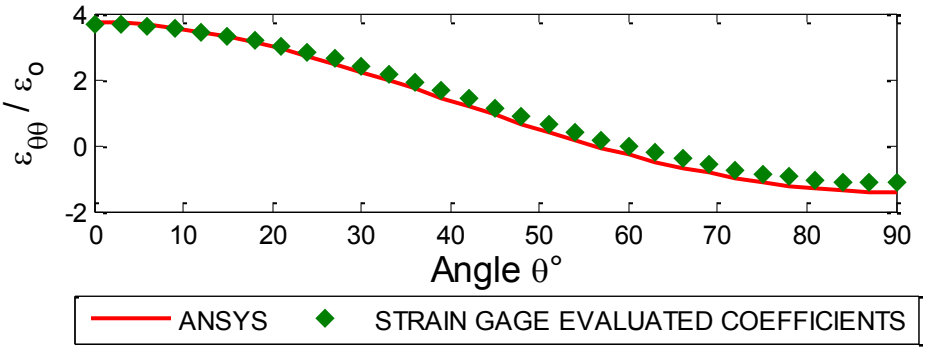

Fig. 3.17: Plot of $\varepsilon_{\theta\theta}/\varepsilon_0$ along boundary of the hole from strain-gage evaluated Airy coefficients for $k = 7$ coefficients ($m = 45$ strain-gage input values) and ANSYS

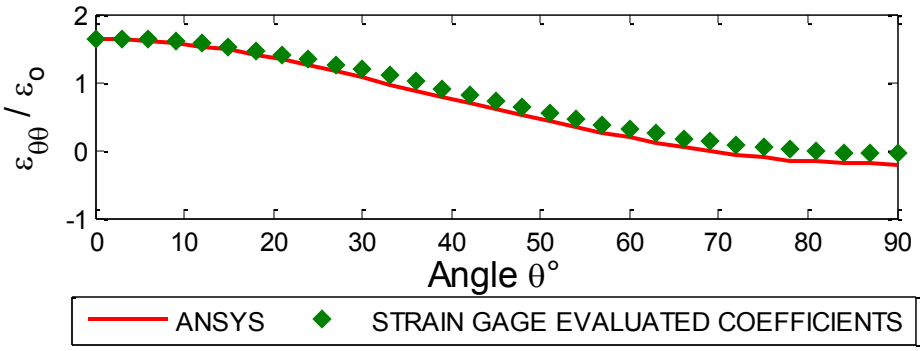

Fig. 3.18: Plot of $\varepsilon_{\theta\theta}/\varepsilon_0$ along r/R = 1.5 from strain-gage evaluated Airy coefficients for $k = 7$ coefficients ($m = 45$ strain-gage input values) and ANSYS

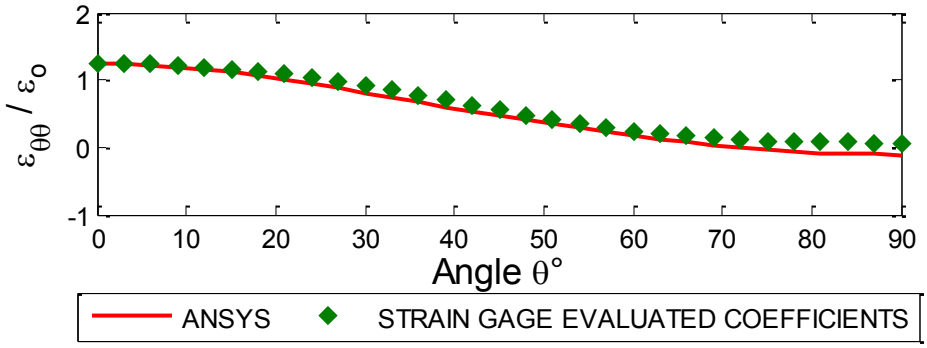

Fig. 3.19: Plot of $\varepsilon_{\theta\theta}/\varepsilon_0$ along r/R = 2 from strain-gage evaluated Airy coefficients for $k = 7$ coefficients ($m = 45$ strain-gage input values) and ANSYS

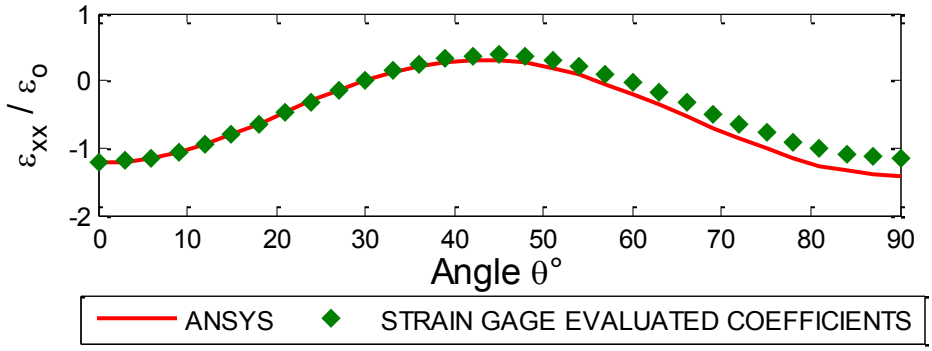

Fig. 3.20: Plot of $\varepsilon_{xx}/\varepsilon_0$ along boundary of the hole from strain-gage evaluated Airy coefficients for $k = 7$ coefficients ($m = 45$ strain-gage input values) and ANSYS

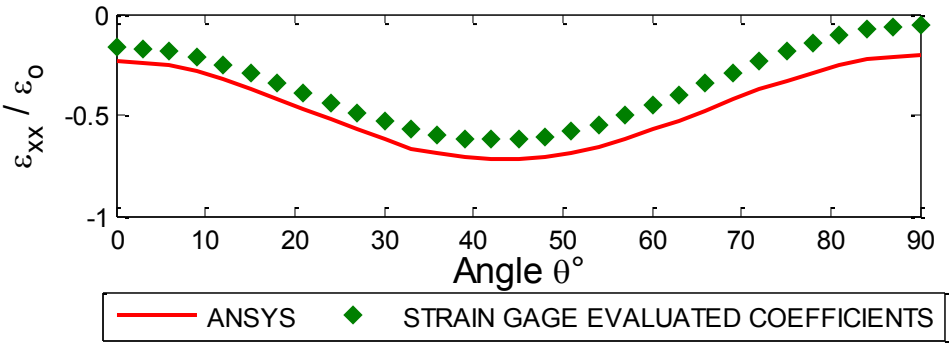

Fig. 3.21: Plot of $\varepsilon_{xx}/\varepsilon_0$ along r/R = 1.5 from strain-gage evaluated Airy coefficients for $k = 7$ coefficients ($m = 45$ strain-gage input values) and ANSYS

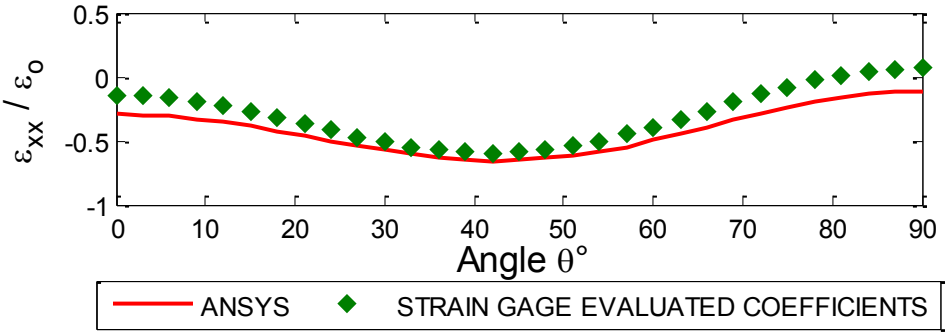

Fig. 3.22: Plot of $\varepsilon_{xx}/\varepsilon_0$ along r/R = 2 from strain-gage evaluated Airy coefficients for $k = 7$ coefficients ($m = 45$ strain-gage input values) and ANSYS

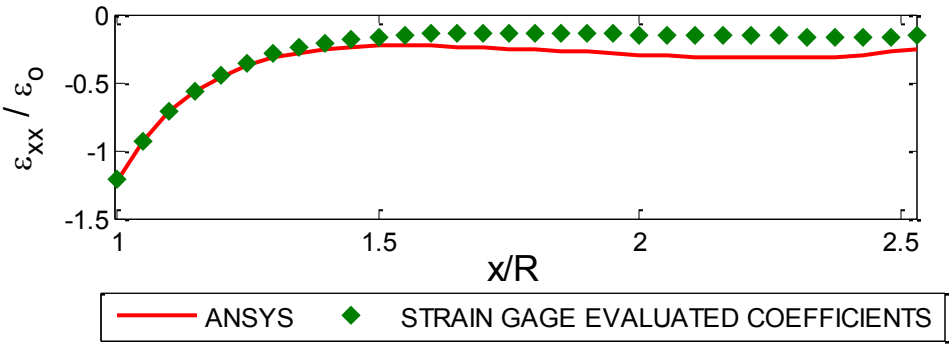

Fig. 3.23: Plot of $\varepsilon_{xx}/\varepsilon_0$ along AB of *figure 3.1* from strain-gage evaluated Airy coefficients for $k = 7$ coefficients ($m = 45$ strain-gage input values) and ANSYS

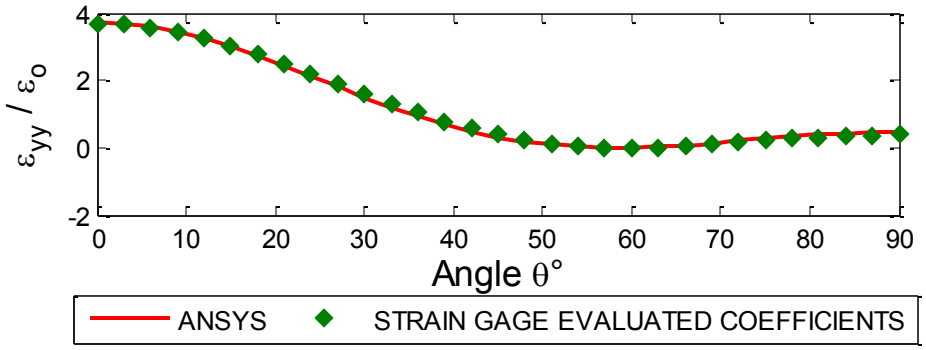

Fig. 3.24: Plot of $\varepsilon_{yy}/\varepsilon_0$ along boundary of the hole from strain-gage evaluated Airy coefficients for $k = 7$ coefficients ($m = 45$ strain-gage input values) and ANSYS

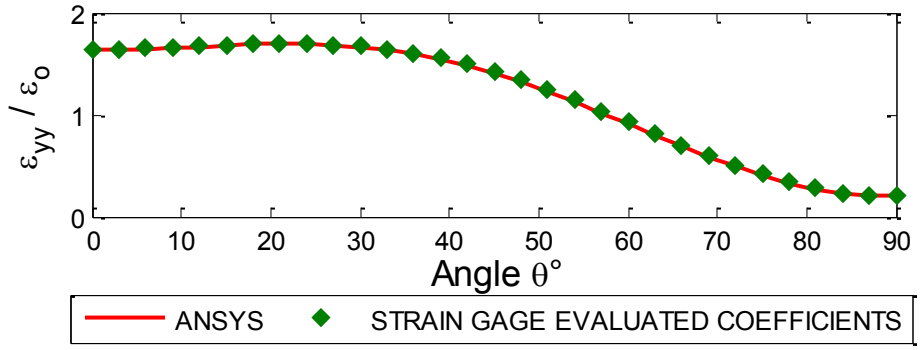

Fig. 3.25: Plot of $\varepsilon_{yy}/\varepsilon_0$ along r/R = 1.5 from strain-gage evaluated Airy coefficients for $k = 7$ coefficients ($m = 45$ strain-gage input values) and ANSYS

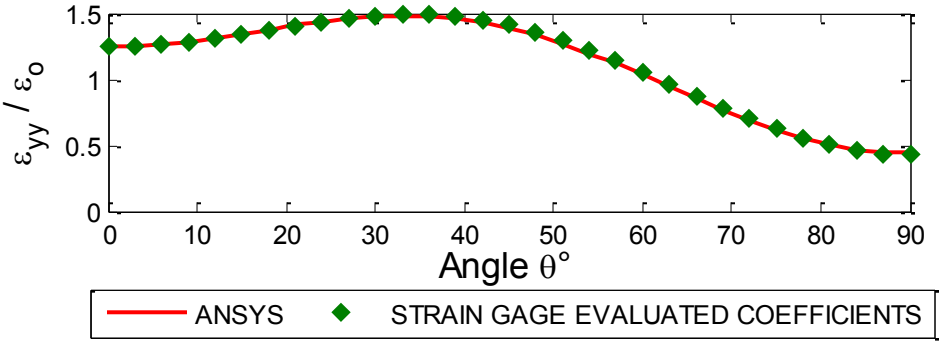

Fig. 3.26: Plot of $\varepsilon_{yy}/\varepsilon_0$ along r/R = 2 from strain-gage evaluated Airy coefficients for $k = 7$ coefficients ($m = 45$ strain-gage input values) and ANSYS

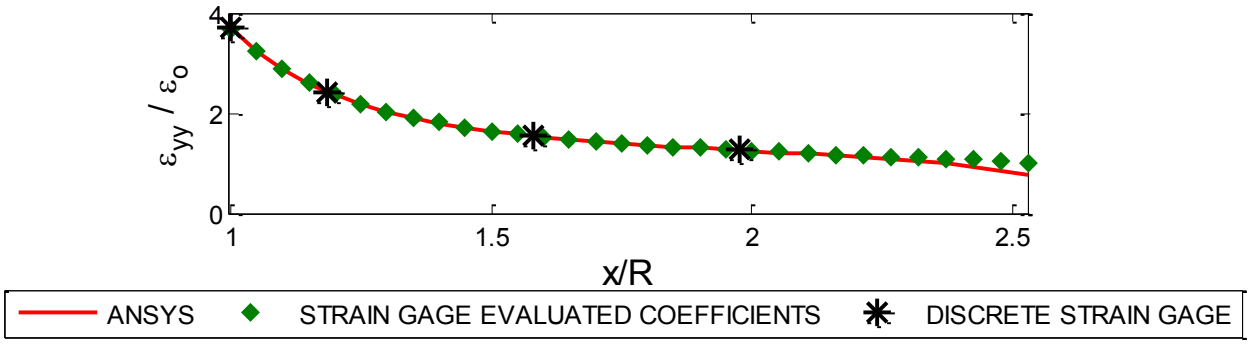

Fig. 3.27: Plot of $\varepsilon_{yy}/\varepsilon_0$ along AB of *figure 3.1* from strain-gages (reconstructed using the evaluated Airy coefficients and discrete gages) for $k = 7$ coefficients ($m = 45$ strain-gage input values) and ANSYS

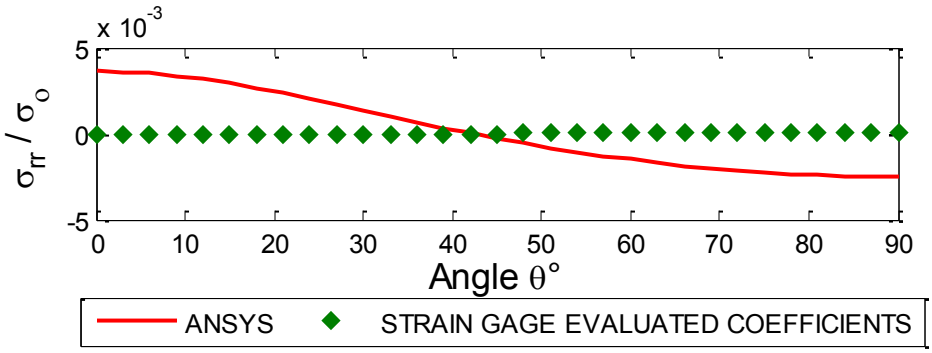

Fig. 3.28: Plot of σ_{rr}/σ_0 along boundary of the hole from strain-gage evaluated Airy coefficients for $k = 7$ coefficients ($m = 45$ strain-gage input values) and ANSYS

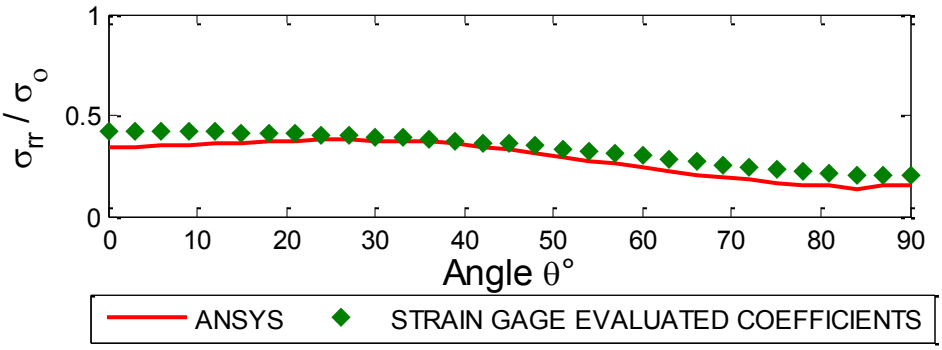

Fig. 3.29: Plot of σ_{rr}/σ_0 along r/R = 1.5 from strain-gage evaluated Airy coefficients for $k = 7$ coefficients ($m = 45$ strain-gage input values) and ANSYS

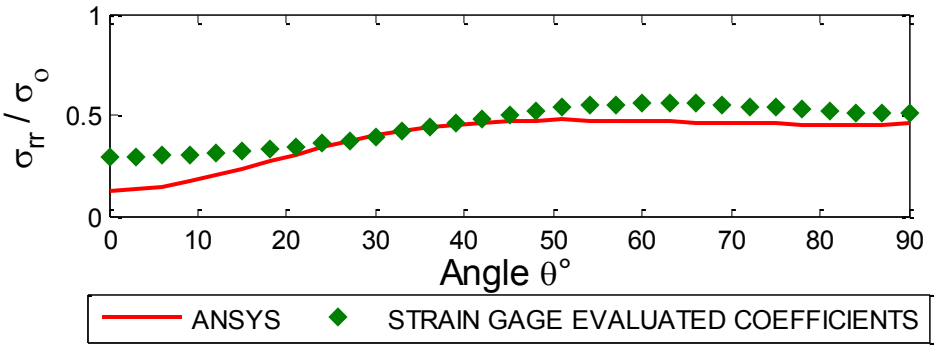

Fig. 3.30: Plot of σ_{rr}/σ_0 along r/R = 2 from strain-gage evaluated Airy coefficients for $k = 7$ coefficients ($m = 45$ strain-gage input values) and ANSYS

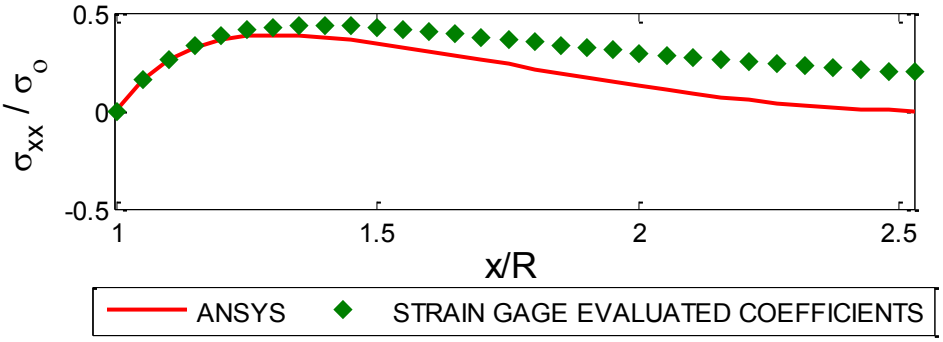

Fig. 3.31: Plot of σ_{xx}/σ_0 (= σ_{rr}/σ_0) along AB of *figure 3.1* from strain-gage evaluated Airy coefficients for $k = 7$ coefficients ($m = 45$ strain-gage input values) and ANSYS

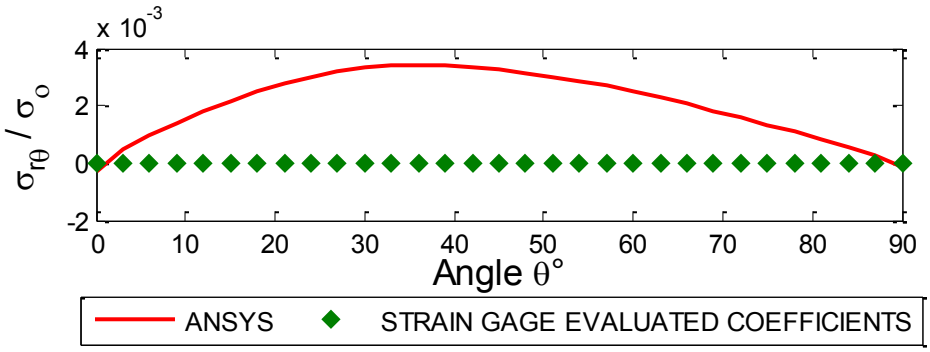

Fig. 3.32: Plot of $\sigma_{r\theta}/\sigma_0$ along boundary of the hole from strain-gage evaluated Airy coefficients for $k = 7$ coefficients ($m = 45$ strain-gage input values) and ANSYS

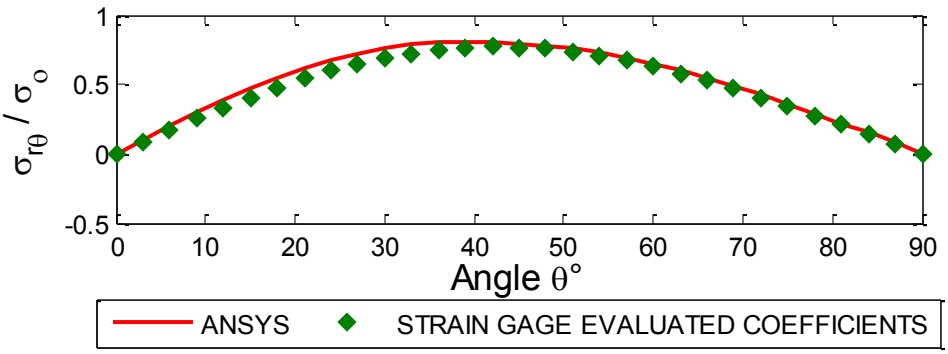

Fig. 3.33: Plot of $\sigma_{r\theta}/\sigma_0$ along r/R = 1.5 from strain-gage evaluated Airy coefficients for $k = 7$ coefficients ($m = 45$ strain-gage input values) and ANSYS

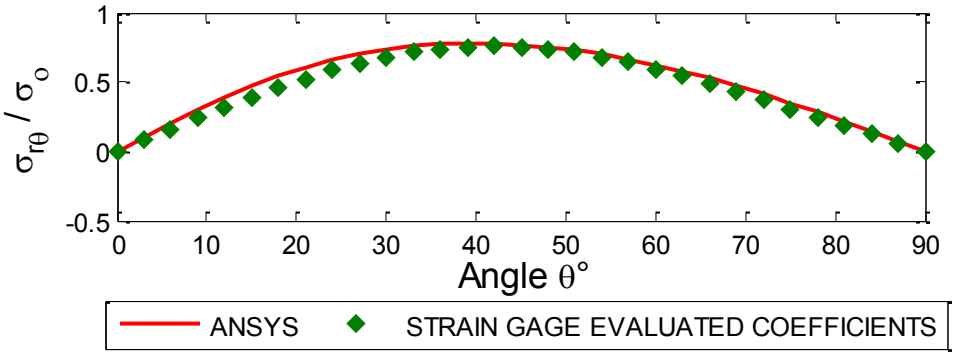

Fig. 3.34: Plot of $\sigma_{r\theta}/\sigma_0$ along r/R = 2 from strain-gage evaluated Airy coefficients for $k = 7$ coefficients ($m = 45$ strain-gage input values) and ANSYS

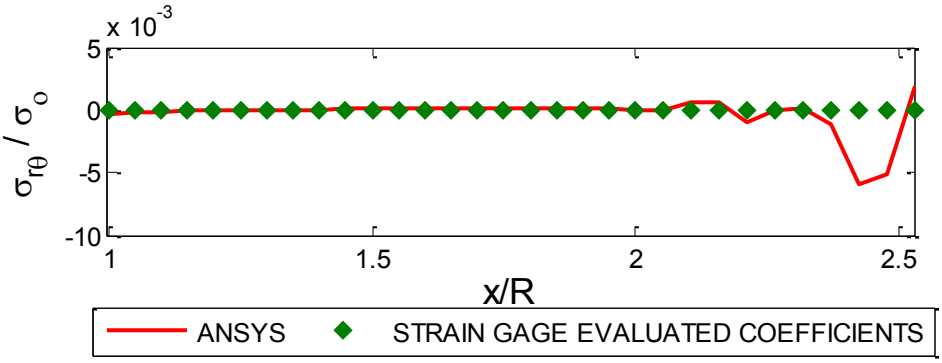

Fig. 3.35: Plot of $\sigma_{r\theta}/\sigma_0$ along AB of *figure 3.1* from strain-gage evaluated Airy coefficients for $k = 7$ coefficients ($m = 45$ strain-gage input values) and ANSYS

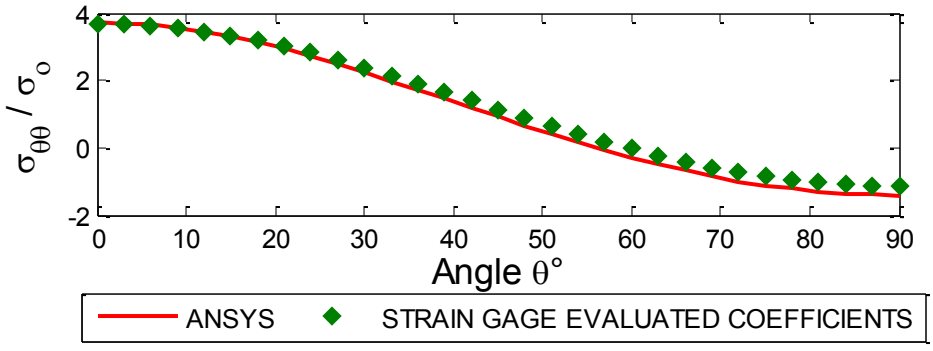

Fig. 3.36: Plot of $\sigma_{\theta\theta}/\sigma_0$ along boundary of the hole from strain-gage evaluated Airy coefficients for $k = 7$ coefficients ($m = 45$ strain-gage input values) and ANSYS

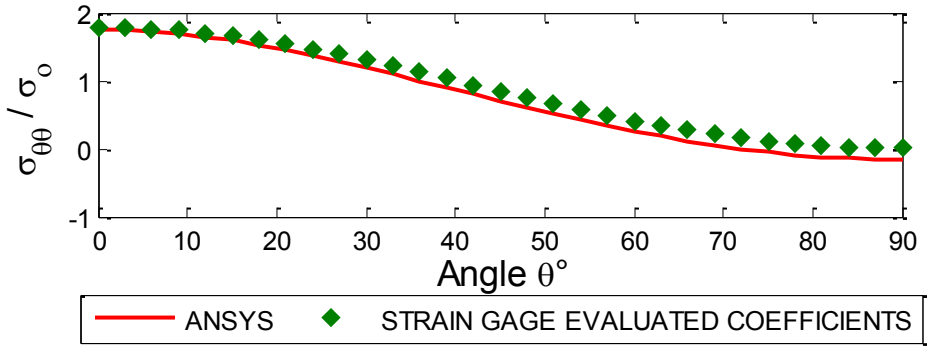

Fig. 3.37: Plot of $\sigma_{\theta\theta}/\sigma_0$ along r/R = 1.5 from strain-gage evaluated Airy coefficients for $k = 7$ coefficients ($m = 45$ strain-gage input values) and ANSYS

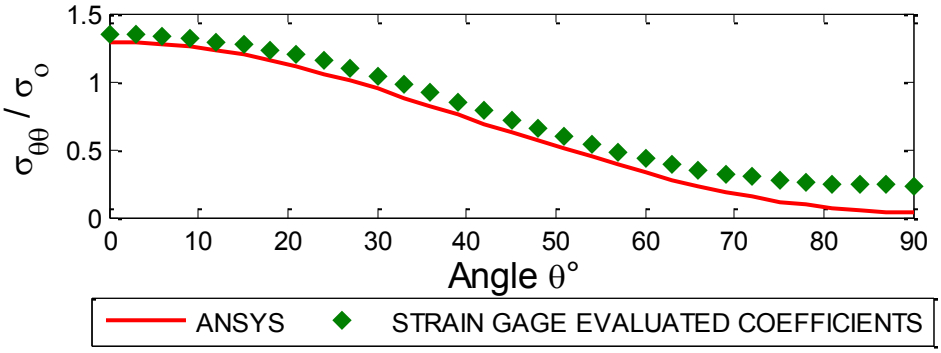

Fig. 3.38: Plot of $\sigma_{\theta\theta}/\sigma_0$ along r/R = 2 from strain-gage evaluated Airy coefficients for $k = 7$ coefficients ($m = 45$ strain-gage input values) and ANSYS

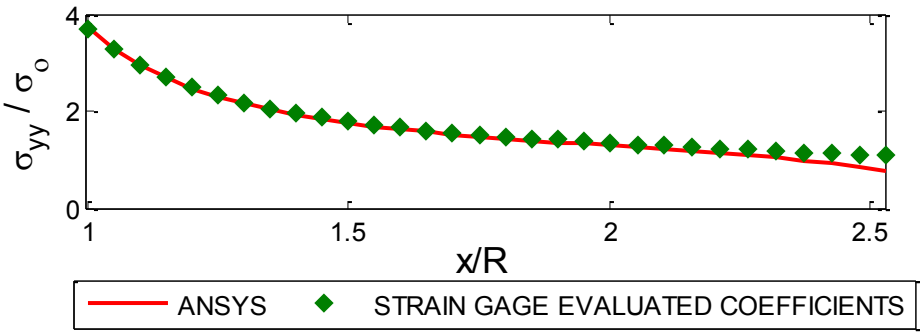

Fig. 3.39: Plot of σ_{yy}/σ_0 (= $\sigma_{\theta\theta}/\sigma_0$) along AB of *figure 3.1* from strain-gage evaluated Airy coefficients for $k = 7$ coefficients ($m = 45$ strain-gage input values) and ANSYS

3.7 Validation of Results

The results of *figures 3.14 through 3.39* are based on 45 measured strains associated with the 45 gage locations of *figure 3.9*. In this section, the number of input values is reduced from 45 to 41, i.e., the four recorded strains along line AB were not used as an input for evaluating the unknown Airy coefficients. Using these 41 input values and $k = 7$ *or* 13 (Appendix A3.1), the normalized strains ($\varepsilon_{yy}/\varepsilon_0$) are evaluated along line AB. Table 3.2 shows the excellent agreement between the discretely measured strains at the four gages and those strains from the evaluated Airy coefficients (based on 41 input strains). These results further validate the reliability of this technique. Strains/stresses i.e., σ_{xx} and ε_{xx} evaluated in other direction do not agree that well for $k = 7$ and $m = 41$, but they are small by comparison. I did not check the strains/stresses in other directions for $k = 13$.

Table 3.2: Normalized strains, $\varepsilon_{yy}/\varepsilon_0$ at discretely measured positions along line AB and those evaluated using the known Airy coefficients ($m = 41$).

		Normalized Strains evaluated using Airy's stress function	
x/R	**Individual strain gages**	**# of coefficients, *k* = 7**	**# of coefficients, *k* = 13**
1.0	3.70	3.61	3.69
1.19	2.42	2.42	2.41
1.58	1.55	1.55	1.54
1.98	1.26	1.26	1.25

3.8 Summary, Discussion and Conclusions

This chapter demonstrates the ability to determine the independent components of strain and stress at and throughout the neighborhood of a cutout in a plane-stress engineering member from discretely measured uniaxial strains having a common direction. The strains were recorded with commercial single-element foil strain gages and an Airy stress function was employed to process these measured strains. All strain gages were aligned in the direction of loading (i.e., recorded ε_{yy} strains), but one could conceivably utilize discretely measured values of ε_{xx}, ε_{yy}, ε_{rr} or $\varepsilon_{\theta\theta}$. However at least for uniaxially-loaded members, it might be advantageous to use measured strain in the direction of specimen loading as they will tend to be relatively large. Reference [9] involves 2- and 3-element strain gages rosettes, but the present approach necessitates only single-element gages.

Advantages of the present approach include the use of single-element commercial strain gages (they are less expensive, consume a smaller footprint, involve less wiring and fewer channels of strain conditioning equipment than do 2- or 3-element rosettes, and they circumvent the challenge that strains from the different elements of a rosette do not occur at a common point); strain and stress contours are available from the discretely measured data; and unlike photomechanical approaches (e.g., moiré, holography, speckle or digital image correlation), no differentiating of the measured values is involved. Available information suggests relatively large gages (compared with the size of the discontinuity) can be used throughout much of the structure. Reliable results (at least compared with those from discrete strain gages and FEM) are obtained from 41 to 45 measured uniaxial strains and seven Airy coefficients, although results are included for up to 13 coefficients in Appendix A3.1. Interestingly, the present ratio of the

amount of input data, m, to the number of Airy coefficients, k, i.e., 3.5 (45/13) $\leq m/k \leq$ 6.5 (45/7), is less than that $m/k \geq 10$ which has been recommended for Thermoelastic Stress Analysis (TSA) [8]. Notwithstanding the aforementioned comments, strains and stresses by the present hybrid concept differ little whether one uses 7 or 13 Airy coefficients.

Future consideration might be given to assessing the consequences of the further reducing the number of measured input strain, the influence of the relative source locations of the measured input strain and to extending the present concept to orthotropic materials and more complicated components such as bolted joints.

Chapter 4 : Full-Field Stress Analysis of a Diametrically Loaded Ring using Five Stain Gages

4.1 Introduction

In this chapter an experimental-numerical hybrid technique is used to stress analyze a diametrically-loaded annular ring. This is achieved by combining the measured strains in the tangential direction with an Airy's stress function. Five tangential strain gages are mounted along the line AB of *figures 4.1 and 4.2* (the inner most gage being on the transverse curved surface of the inside radius). An additional strain gages is mounted in the radial direction at the common radius (r/R = 1.75) each of lines CD and EF. Lines AB, CD and EF are fixed to and rotate with the ring. Strains from the gages along AB are used as input data and those along CD and EF are for validation. Since the ring geometry is axisymmetric, the amount of input data is increased by rotating the annular disk at ten degree intervals; i.e., recording the strains at every interval from each of the seven strain gages for the same applied load.

The annular disk is a common structural component, often commercially used in applications such as load cells, and in rock/concrete cutting and earth excavation cutters. The theoretical solution for a diametrically-loaded ring is available only for the case where the ratio of outer to inner diameter is two [25] although stress concentration factors have been determined photoelastically for other ratios of the radii [26]. Seratia, Alehosseina and Williams recently extended the theoretical analyses of loaded ring and disk to a wide range of loading conditions

[27]. Advantages of the present technique include: (i) able to evaluate all of the unknown Airy coefficients (i.e., determine the full-field individual stress/strain/displacement components) using only five strain gages while reducing the number of these experimentally-determined coefficients by incorporating the traction–free conditions *analytically* on the inner edge of the hole; (ii) easier to wire seven strain gages rather than forty-five strain gages as in Chapter 3; (iii) single element strain gages were used here which are less expensive and involve a smaller foot print compared to 2- or 3-element rosettes; (iv) while a theoretical solution is available only for ratio of outer to inner diameter of two, the current approach benefits from the possible increase/decrease in the ratio of outer to inner diameters; (v) numerical solutions like finite elements are not trivial due to the point loads at the top and bottom edges; (vi) not have to physically differentiate the measure data; (vii) no additional calibrating specimen is needed (such as would be with TSA); and (viii) do not require knowing the loading or external boundary conditions, i.e., one could perhaps use a more general stress function and then extend this technique to a non-circular outside edge.

This chapter emphasizes determining the stresses, strains and displacements throughout the diametrally-loaded ring by processing measured strains from just five strain gages with a stress function, and the relevance to load cells. However, a significant ‘by-product’ is the demonstrated difficulties which can occur if trying to fully stress analyze structures using essentially only boundary conditions, i.e., a purely boundary collocation technique.

4.2 Physical Set-up

Figure 4.1 is the geometric representation of the actual instrumented ring of *figure 4.2*. The x-y coordinate system of *figure 4.1* is fixed in space and the ring is rotated. Lines AB, CD and EF rotate with the ring. The coordinate origin is at the center of the hole and the angle θ is measured counter-clock wise from the fixed positive horizontal x-axis. The results of the experimental-numerical hybrid (based on five measured strains) method obtained here are compared with those from an approximate finite element analysis, strain gages and a theoretical solution from Timoshenko and Goodier [25].

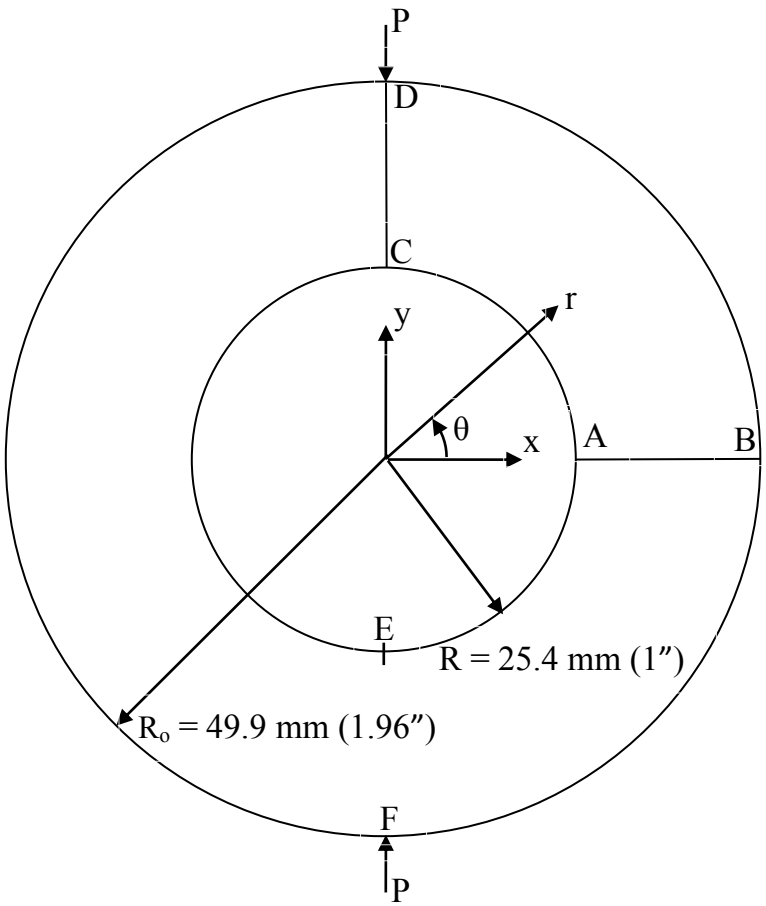

Fig. 4.1: Schematic of diametrically-loaded annular disk

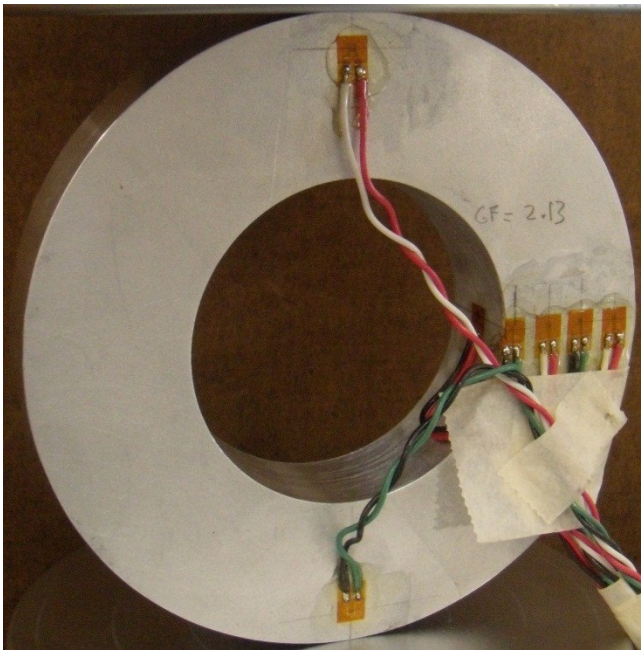

Fig. 4.2: Diametrically-loaded annular disk

All the strain gages that were mounted on the specimen of *figure 4.2* are Micro-Measurements strain gages (CEA-13-032UW-120) having a gage resistance of 120Ω and a gage factor of 2.13 ± 1%. When measuring from the center of the hole, the gages along the line AB are at a distance of r/R = 1, 1.075, 1.32, 1.54 and 1.8. The top and the bottom gages along the lines CD and EF of *figure 4.2* are at r/R = 1.75.

Following are the details of the ring tested for the associated analyses and results:

- Material of the plate: Aluminum 6061-T6 (Wiedenbeck, Inc., Madison, WI); Ultimate strength = 275 to 311 MPa (40 to 45 ksi) and Yield strength = 241 to 275 MPa (35 to 40 ksi).
- Static load (F) = 6672.33 N (1500 lbs.).
- Inner diameter of the disk (d_1) = 50.97 mm = 2.003″, *figures 4.1 and 4.2.*

- Outer diameter of the disk (d_2) = 99.87 mm = 3.932″ (i.e., d_2/d_1 = 1.96), *figures 4.1 and 4.2*.
- Thickness of the disk (t) = 19.05 mm = 0.75″.
- A tangential strain gage was mounted on the inner curved edge at point A in *figure 4.1*.
- Four additional tangential strain gages were mounted along line AB, *figures 4.1 and 4.2*.
- One radial strain gage was along each of lines CD and EF at r/R = 1.75, *figures 4.1 and 4.2*.

4.3 Relevant Stress Function (Airy's Stress Function)

The relevant stress function and associated individual components of stress, strain and displacement equations are the same as those of Chapter 2 and 3. The ring geometry and loading is symmetrical about both the stationary x- and y-axes and traction-free boundary conditions are *analytically* imposed on the inner radius of the ring; i.e., at r = R = 25.43 mm = 1.0015″, and for all values of θ. The stress function and individual stress, strain and displacement components are from Chapters 2 and 3, i.e.,

$$\phi = a_0 + b_0 \ln r + c_0 r^2 + \sum_{n=2,4,6,..}^{N} \left\{ \left(a_n r^n + b_n \mathrm{r}^{\mathrm{n+2}} + c_n r^{-n} + d_n \mathrm{r}^{-(\mathrm{n-2})} \right) \cos n\theta \right\} \quad (4.1)$$

$$\sigma_{rr} = \left(\frac{-2\,R^2}{r^2} + 2 \right) c_0 - \sum_{n=2,4,\ldots}^{\mathrm{N}} \left[\begin{Bmatrix} -(n-1)(n+1)R^2\, r^{n-2} \\ +\,(n+1)R^{2(n+1)}\, r^{-(n+2)} \\ +(n+1)\,(n-2)\, r^n \end{Bmatrix} b_n + \begin{Bmatrix} -(n-1)\,R^{-2(n-1)}\, r^{n-2} \\ -(n-1)(n+1)\,R^2 r^{-(n+2)} \\ +\,(n-1)(n+2)\, r^{-n} \end{Bmatrix} d_n \right] cos(n\theta) \quad (4.2)$$

$$\sigma_{\theta\theta} = \left(\frac{2\,R^2}{r^2} + 2 \right) c_0 + \sum_{n=2,4,\ldots}^{N} \left[\begin{Bmatrix} -\,(n+1)(n-1)R^2\, r^{n-2} \\ +\,(n+1)R^{2(n+1)}\, r^{-(n+2)} \\ +\,(n+1)\,(n+2)\, r^n \end{Bmatrix} b_n + \begin{Bmatrix} -\,(n-1)\,R^{-2(n-1)} r^{n-2} \\ -(n-1)(n+1)R^2\, r^{-(n+2)} \\ +\,(n-1)(n-2)\, r^{-n} \end{Bmatrix} d_n \right] cos(n\theta) \quad (4.3)$$

$$\sigma_{r\theta} = \sum_{n=2,4,\ldots}^{N} \left[\begin{Bmatrix} -(n+1)(n-1)R^2\, r^{n-2} \\ -\,(n+1)R^{2(n+1)}\, r^{-(n+2)} \\ +\,n\,(n+1)\, r^n \end{Bmatrix} b_n + \begin{Bmatrix} -\,(n-1)R^{-2(n-1)}\, r^{n-2} \\ +\,(n-1)(n+1)R^2\, r^{-(n+2)} \\ -\,n\,(n-1)\, r^{-n} \end{Bmatrix} d_n \right] sin(n\theta) \quad (4.4)$$

$$\sigma_{xx} = \left[\begin{array}{c} \left\{ -\cos 2\theta \frac{2R^2}{r^2} + 2 \right\} c_0 \\ + \sum_{n=2,4,\ldots}^{N} \left\{ \begin{array}{c} \left\{ \begin{array}{c} (n+1)(n-1)R^2 r^{n-2}(\cos(n\theta - 2\theta)) \\ -(n+1)R^{2(n+1)} r^{-(n+2)} \left(cos(n\theta + 2\theta)\right) \\ -(n+1)r^n (n\cos(n\theta - 2\theta) - 2cosn\theta) \end{array} \right\} b_n \\ + \left\{ \begin{array}{c} (n-1)R^{-2(n-1)}\, r^{n-2}(\cos(n\theta - 2\theta)) \\ +(n-1)(n+1)R^2 r^{-(n+2)} \left(cos(n\theta + 2\theta)\right) \\ -(n-1)r^{-n}(ncos(n\theta + 2\theta) + 2cosn\theta) \end{array} \right\} d_n \end{array} \right\} \end{array} \right] \tag{4.5}$$

$$\sigma_{yy} = \left[\begin{array}{c} \left\{ \cos 2\theta \frac{2R^2}{r^2} + 2 \right\} c_0 \\ + \sum_{n=2,4,\ldots}^{N} \left\{ \begin{array}{c} \left\{ \begin{array}{c} -(n+1)(n-1)R^2 r^{n-2}\cos(n\theta - 2\theta) \\ +(n+1)R^{2(n+1)} r^{-(n+2)} cos(n\theta + 2\theta) \\ +(n+1)r^n (n\cos(n\theta - 2\theta) + 2cosn\theta) \end{array} \right\} b_n \\ + \left\{ \begin{array}{c} -(n-1)R^{-2(n-1)}\, r^{n-2}\cos(n\theta - 2\theta) \\ -(n-1)(n+1)R^2 r^{-(n+2)} cos(n\theta + 2\theta) \\ +(n-1)r^{-n}(ncos(n\theta + 2\theta) - 2cosn\theta) \end{array} \right\} d_n \end{array} \right\} \end{array} \right] \tag{4.6}$$

$$\epsilon_{rr} = \frac{1}{E} \left[\begin{array}{c} \left\{ \frac{-2R^2}{r^2}(1+\upsilon) + 2(1-\upsilon) \right\} c_0 \\ - \sum_{n=2,4,\ldots}^{\mathrm{N}} \left\{ \begin{array}{c} \left(\begin{array}{c} -(1+\upsilon)(n-1)(n+1)R^2\, r^{n-2} \\ +(1+\upsilon)(n+1)R^{2(n+1)}\, r^{-(n+2)} \\ +(n+1)[(n-2) + \upsilon(n+2)]\, r^n \end{array} \right) b_n \\ + \left(\begin{array}{c} -(1+\upsilon)(n-1)\, R^{-2(n-1)}\, r^{n-2} \\ -(1+\upsilon)(n-1)(n+1)\, R^2 r^{-(n+2)} \\ +(n-1)[(n+2) + \upsilon(n-2)]\, r^{-n} \end{array} \right) d_n \end{array} \right\} cos(n\theta) \end{array} \right] \tag{4.7}$$

$$\varepsilon_{\theta\theta} = \frac{1}{E} \left[\begin{array}{c} \left\{ \frac{2R^2}{r^2}(1+\upsilon) + 2(1-\upsilon) \right\} c_0 \\ + \sum_{n=2,4,\ldots}^{N} \left\{ \begin{array}{c} \left(\begin{array}{c} -(1+\upsilon)(n+1)(n-1)R^2\, r^{n-2} \\ +(1+\upsilon)(n+1)R^{2(n+1)}\, r^{-(n+2)} \\ +(n+1)[(n+2) + \upsilon(n-2)]r^n \end{array} \right) b_n \\ + \left(\begin{array}{c} -(1+\upsilon)(n-1)\, R^{-2(n-1)} r^{n-2} \\ -(1+\upsilon)(n-1)(n+1)R^2\, r^{-(n+2)} \\ +(n-1)[(n-2) + \upsilon(n+2)]\, r^{-n} \end{array} \right) d_n \end{array} \right\} cos(n\theta) \end{array} \right] \tag{4.8}$$

$$\epsilon_{xx}= \frac{1}{\mathrm{E}}\left[\begin{array}{c}\left\{-\cos 2\theta\frac{2\,R^2}{r^2}(1+\upsilon)\ +2(1-\upsilon)\right\}c_0 \\ +\sum_{n=2,4,\ldots}^{N}\left[\begin{array}{c}\left\{\begin{array}{c}(n+1)(n-1)R^2r^{n-2}(\cos(n\theta-2\theta))(1+\upsilon)\\ -(n+1)R^{2(n+1)}r^{-(n+2)}\big(cos(n\theta+2\theta)\big)(1+\upsilon)\\ -(n+1)r^n(n\cos(n\theta-2\theta)(1+\upsilon)-2cosn\theta(1-\upsilon))\end{array}\right\}b_n \\ +\left\{\begin{array}{c}(n-1)R^{-2(n-1)}\,r^{n-2}(\cos(n\theta-2\theta))(1+\upsilon)\\ +(n-1)(n+1)R^2r^{-(n+2)}\big(cos(n\theta+2\theta)\big)(1+\upsilon)\\ -(n-1)r^{-n}(n\,cos(n\theta+2\theta)(1+\upsilon)+2\,cosn\theta\,(1-\upsilon))\end{array}\right\}d_n\end{array}\right]\end{array}\right] \quad (4.9)$$

$$\epsilon_{yy}= \frac{1}{\mathrm{E}}\left[\begin{array}{c}\left\{\cos 2\theta\frac{2\,R^2}{r^2}(1+\upsilon)+2(1-\upsilon)\right\}c_0 \\ +\sum_{n=2,4,\ldots}^{N}\left\{\begin{array}{c}\left\{\begin{array}{c}-(n+1)(n-1)R^2r^{n-2}\cos(n\theta-2\theta)\,(1+\upsilon)\\ +(n+1)R^{2(n+1)}r^{-(n+2)}cos(n\theta+2\theta)(1+\upsilon)\\ +(n+1)r^n(n\cos(n\theta-2\theta)\,(1+\upsilon)+2cosn\theta(1-\upsilon))\end{array}\right\}b_n \\ +\left\{\begin{array}{c}-(n-1)R^{-2(n-1)}\,r^{n-2}\cos(n\theta-2\theta)\,(1+\upsilon)\\ -(n-1)(n+1)R^2r^{-(n+2)}cos(n\theta+2\theta)(1+\upsilon)\\ +(n-1)r^{-n}(ncos(n\theta+2\theta)(1+\upsilon)-2cosn\theta(1-\upsilon))\end{array}\right\}d_n\end{array}\right\}\end{array}\right] \quad (4.10)$$

$$u_r = \frac{1}{E}\left[\begin{array}{c}\left\{\frac{2\,R^2}{r}(1+\upsilon)\ +2(1-\upsilon)r\right\}c_0 \\ -\sum_{n=2,4,\ldots}^{\mathrm{N}}\left\{\begin{array}{c}\left(\begin{array}{c}-(1+\upsilon)(n+1)R^2\,r^{n-1}\\ -(1+\ \upsilon)R^{2(n+1)}\,r^{-(n+1)}\end{array}\right)b_n \\ +\left(\begin{array}{c}+[(n-2)+\ \upsilon\,(n+2)]\,r^{n+1}\\ -(1+\ \upsilon)\,R^{-2(n-1)}\,r^{n-1}\\ +(1+\ \upsilon)(n-1)\,R^2r^{-(n+1)}\\ -[(n+2)+\ \upsilon\,(n-2)]\,r^{-n+1}\end{array}\right)d_n\end{array}\right\}cos(n\theta)\end{array}\right] \quad (4.11)$$

$$u_\theta = \frac{1}{\mathrm{E}}\left[\sum_{n=2,4,\ldots}^{N}\left(\begin{array}{c}\left(\begin{array}{c}-(1+\upsilon)(n+1)R^2r^{n-1}\\ +[n(1+\upsilon)+4]\,r^{n+1}\\ +(1+\upsilon)R^{2(n+1)}r^{-(n+1)}\end{array}\right)b_n \\ +\left(\begin{array}{c}-(1+\upsilon)R^{-2(n-1)}\,r^{n-1}\\ -(1+\upsilon)(n-1)R^2r^{-(n+1)}\\ +[n(1+\upsilon)-4]\,r^{-(n-1)}\end{array}\right)d_n\end{array}\right)sin(n\theta)\right] \quad (4.12)$$

$$u = \frac{1}{E}\left[\begin{array}{c} \left\{\frac{2R^2}{r}(1+\upsilon)+2(1-\upsilon)r\right\}\cos\theta\ c_0 \\ -\sum_{n=2,4,\ldots}^{N} \left\{ \begin{array}{c} -(1+\upsilon)(n+1)R^2\, r^{n-1}\ (\cos(n-1)\,\theta) \\ -(1+\upsilon)R^{2(n+1)}\, r^{-(n+1)}\ (\cos(n+1)\,\theta) \\ +\left(\begin{array}{c} n(1+\upsilon)\,(\cos(n-1)\,\theta) - 2(\cos(n+1)\,\theta) \\ +2\upsilon\cos\theta\ \cos(n\theta) + 2\sin\theta\ \sin(n\theta) \end{array} \right) r^{n+1} \end{array} \right\} b_n \\ +\left\{ \begin{array}{c} -(1+\upsilon)\,R^{-2(n-1)}\, r^{n-1}(\cos(n-1)\,\theta) \\ +(1+\upsilon)(n-1)\,R^2 r^{-(n+1)}(\cos(n+1)\,\theta) \\ -\left(\begin{array}{c} n(1+\upsilon)(\cos(n+1)\,\theta) + 2(\cos(n-1)\,\theta) \\ -2\upsilon\cos\theta\ \cos(n\theta) + 2\sin\theta\ \sin(n\theta) \end{array} \right) r^{-n+1} \end{array} \right\} d_n \end{array} \right] \quad (4.13)$$

$$v = \frac{1}{E}\left[\begin{array}{c} \left\{\frac{2R^2}{r}(1+\upsilon)+2(1-\upsilon)r\right\}\sin\theta\ c_0 \\ -\sum_{n=2,4,\ldots}^{N} \left\{ \begin{array}{c} (1+\upsilon)(n+1)R^2\, r^{n-1}\ \big(\sin(n-1)\theta\big) \\ -(1+\upsilon)R^{2(n+1)}\, r^{-(n+1)}\ \big(\sin(n+1)\theta\big) \\ -\left(\begin{array}{c} n(1+\upsilon)\,\big(\sin(n-1)\theta\big) + 2\big(\sin(n+1)\theta\big) \\ -2\upsilon\sin\theta\ \cos(n\theta) + 2\cos\theta\ \sin(n\theta) \end{array} \right) r^{n+1} \end{array} \right\} b_n \\ +\left\{ \begin{array}{c} (1+\upsilon)\,R^{-2(n-1)}\, r^{n-1}\big(\sin(n-1)\theta\big) \\ +(1+\upsilon)(n-1)\,R^2 r^{-(n+1)}\big(\sin(n+1)\theta\big) \\ +\left(\begin{array}{c} -n(1+\upsilon)\,\big(\sin(n+1)\theta\big) + 2\big(\sin(n-1)\theta\big) \\ +2\upsilon\sin\theta\ \cos(n\theta) + 2\cos\theta\ \sin(n\theta) \end{array} \right) r^{-n+1} \end{array} \right\} d_n \end{array} \right] \quad (4.14)$$

where r is the radius measured from the center of a hole, angle θ is measured counter-clockwise from the horizontal fixed x-axis (*figure 4.1*), c_0, b_n, and d_n are Airy coefficients, E is the elastic modulus, υ is the Poisson's ratio, and N is the terminating index value of the summation series (N is an even positive integer greater than 1). The x- and y-axes are fixed in space and the disk (with its lines AB, CD and EF) is rotated at equal intervals of ten degrees.

4.4 Experimental Details

The specimen instrumented with unidirectional strain gages was diametrically-loaded in the Sintech screw-driven testing machine (Rm. 1313 Engineering Hall), *figure 4.3*. A total of seven single-element strain gages are mounted on the specimen. Only the five strain gages in the tangential direction ($\varepsilon_{\theta\theta}$) along line AB are used to provide input for evaluating the unknown Airy coefficients. The output of the other two gages (along lines CD and EF) in the radial direction (ε_{rr}) was used to validate the results of the hybrid (stress function) technique. These strain gages along lines CD and EF are at the common radius (r/R = 1.75), *figure 4.3*. The output of the seven strain gages was processed using a 16-channel strain gage conditioner. The present use of only seven strain gages significantly simplifies the measurement compared to mounting, wiring and measuring the forty-five strain gage readings by the approach of Chapter 3. The number of input values is increased here from five to forty-eight by rotating the disk by ten degree angle intervals each time and applying the same load. Strains from the two outermost gages were not used when line AB (hence these hoop gages) are underneath the applied load (i.e., any strain gage where $\theta = \pm 90^{o}$ and r/R > 1.4) due to the high load effect of the concentrated load. To help in correctly rotating the ring by ten degrees increment, radii lines are marked at every ten degrees, *figure 4.4*. *Figure 4.5* is the test setup.

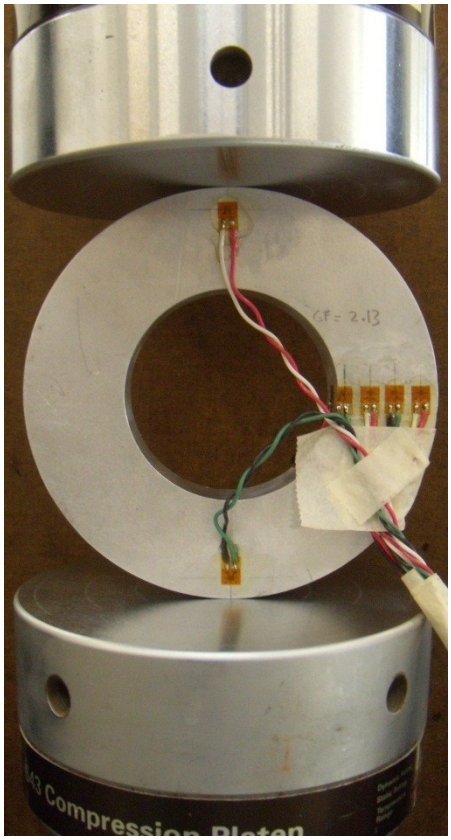

Fig. 4.3: Front face of the strain-gaged ring in the screw-driven testing machine

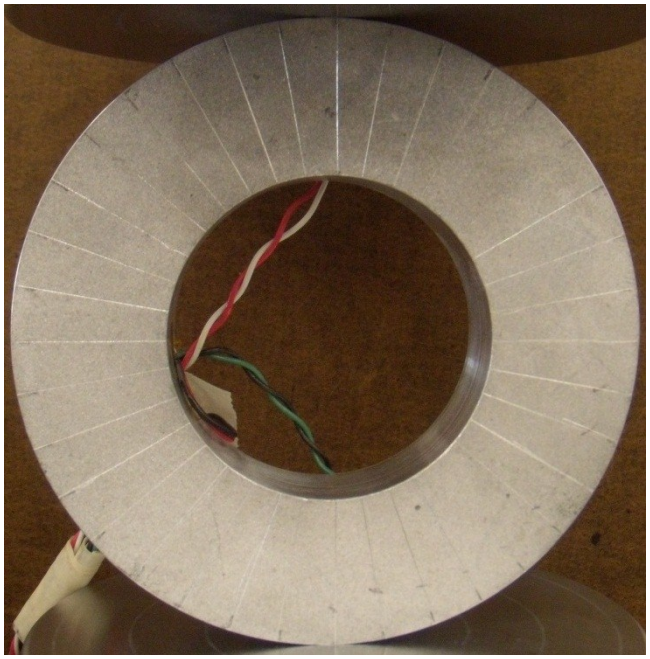

Fig. 4.4: Back face of the strain-gaged ring in the testing machine

Fig. 4.5: Test setup

4.5 Data Processing

An objective here is to evaluate full-field individual stress, strain and displacement components in the ring. Since the diametrically-loaded ring is symmetrical about both x- and y-axes, only the first quadrant is analyzed. Moreover the ring (with its lines AB, CD and EF) was rotated by ten degree intervals and the strains were recorded at every rotation. As mentioned previously, the output of the two outermost hoop gages along line AB (r/R > 1.4) was not considered when the gages were underneath the applied load ($\theta = \pm 90^{o}$). Using the measured forty-eight tangential strains from the five transverse strain gages and *analytically* imposed traction-free boundary conditions on the inner edge of the ring, the unknown Airy coefficients were evaluated using linear least-squares. *Figure 4.6* shows the source locations of the input data values generated when the line AB and its five strain gages have been rotated through the 10 degree intervals.

The expression for tangential strain, $\varepsilon_{\theta\theta}$, (*equation 3.8*) is written in matrix form as

$$\begin{bmatrix} \varepsilon_{\theta\theta}(c_0, bn, dn) \\ \varepsilon_{\theta\theta}(c_0, bn, dn) \\ \vdots \\ \varepsilon_{\theta\theta}(c_0, bn, dn) \end{bmatrix} \begin{bmatrix} c_0 \\ b_n \\ d_n \end{bmatrix} = \begin{bmatrix} \varepsilon_{\theta\theta 1} \\ \varepsilon_{\theta\theta 2} \\ \vdots \\ \varepsilon_{\theta\theta N} \end{bmatrix} \tag{4.15}$$

or, in simplified form,

$$[A]_{m\times k}\{c\}_{k\times 1} = \{d\}_{m\times 1} \tag{4.16}$$

where matrix A is an m (number of input tangential strains = 48) by k (number of unknown Airy coefficients), vector c contains the k unknown Airy coefficients, and the vector d is composed of the 48 measured tangential strains corresponding to the strain equations in matrix A. Since *equation 4.8* involves n (= N+1) unknown coefficients starting from N = 2, there are more equations than the number of unknowns, i.e., $m > k$. Therefore linear least-squares is utilized in MATLAB to solve the over-determined matrix expression $Ac = d$. Either '\' or 'pinv' operator in MATLAB can be used for least squares and therefore the vector c is calculated by $c = A\backslash d$ *or* $c =$ *pinv*d.*

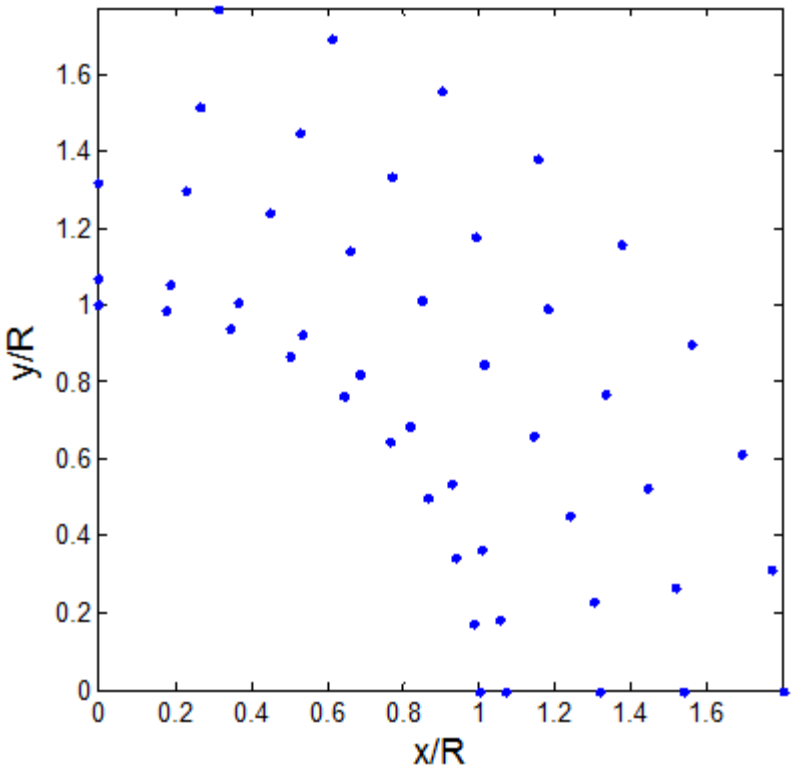

Fig. 4.6: Data points generated upon rotating the five strain gages by 10 degree intervals

The number of unknown Airy coefficients to use was evaluated using the condition number of matrix [A] and the RMS. The RMS measures the error between the measured and

evaluated strains. *Figures 4.7 and 4.8* are plots of the condition number, C, and $\log_{10}$(condition number) of the Airy matrix [A] vs. the number of coefficients, *k*, for the *m = 48* inputs. The condition number measures the sensitivity of matrix [A] in *equation 4.2*. *Figure 4.9* is the plot of the RMS vs. the number of coefficients, *k* for *m = 48* inputs. From these plots of the condition number, RMS and ignoring coefficients a_0, a_n and c_n since they do not appear in the expressions for the stresses, strains and displacements of *equations 4.2 through 4.14*, *k = 5* was selected as an appropriate number of coefficients to use here.

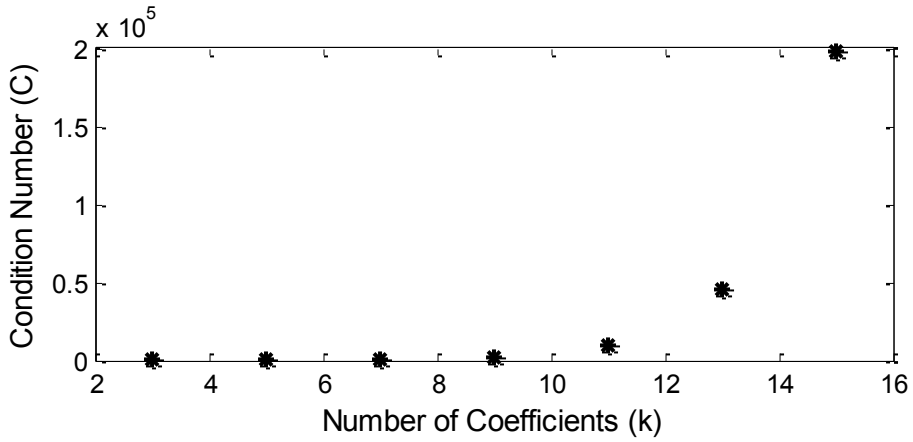

Fig. 4.7: Plot of condition number, C vs. number of coefficients, *k* for *m = 48* measured strains

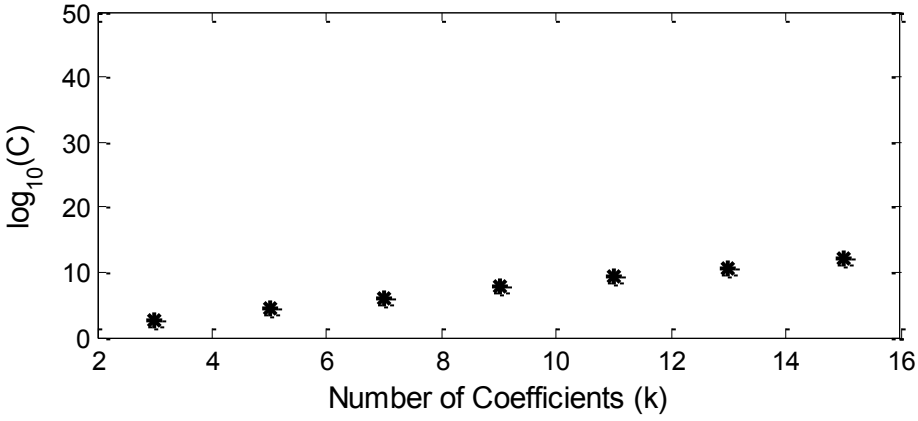

Fig. 4.8: Plot of $\log_{10}$(C) vs. number of coefficients, *k* for *m = 48* measured strains

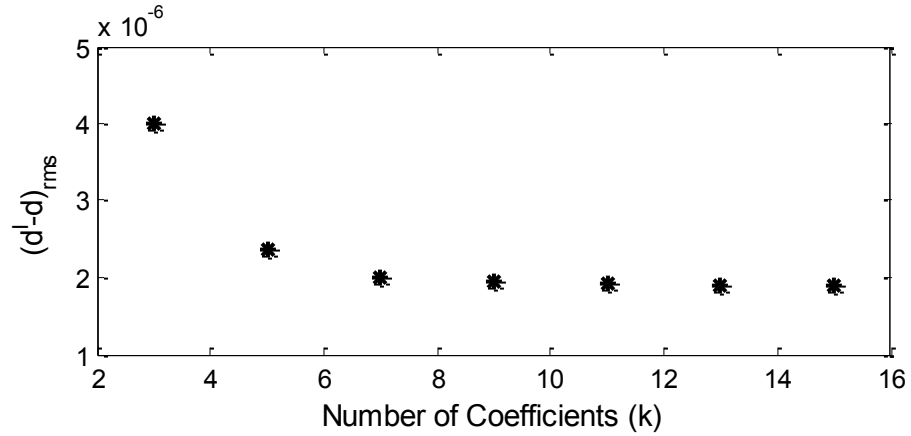

Fig. 4.9: Plot of RMS vs. number of coefficients, *k* for *m = 48* measured strains

4.6 Finite Element Analysis

Individual hybrid (strain gages output processed by the Airy stress function) determined components of stress, strain and displacement are to be compared full-field against the FEM predictions. Isoparametric elements (Plane-82) having 8 nodes per element were employed. A very fine mesh (mapped mesh) was used throughout the entire quarter ring as shown in *figure 4.10*. The mapped mesh used here involves only quadrilateral elements. A total of 10,000 elements and 30,401 nodes are used to mesh one quarter of the disk. Since the diametrically-loaded annular disk is symmetrical about the x-and y-axes, a quarter model with symmetrical boundary conditions (along x-and y-axes) is analyzed. Because only a quarter model of the entire geometry is modeled, a point load of 750 lb. was applied at the outer vertical edge of the FEM model.

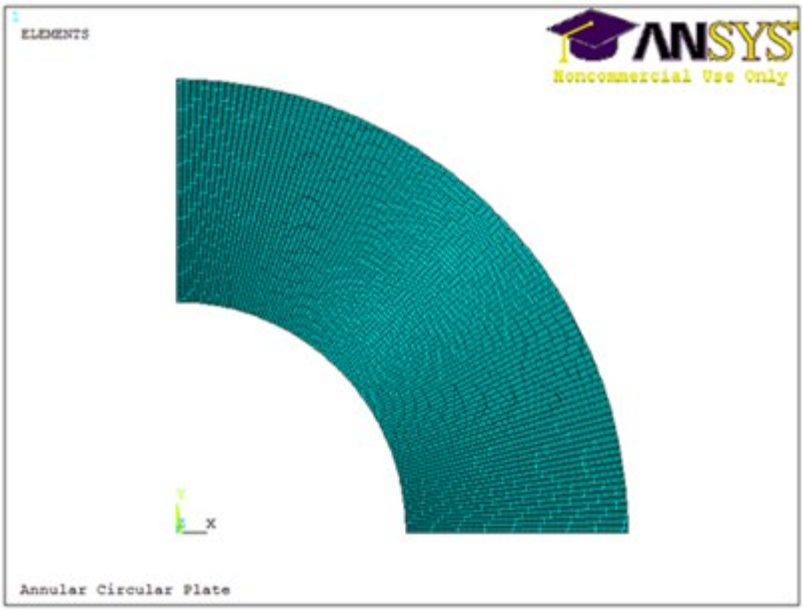

Fig. 4.10: Finite element model for diametrically-loaded annular disk

4.7 Results

After evaluating the unknown Airy coefficients from the five measured tangential strains along line AB, the hybrid (based on processing the output of the five strain gages with an Airy's stress function) individual stress, strain and displacement components were determined. Normalized vertical strain, ε_{yy}, and horizontal strain, ε_{xx}, are evaluated using the present hybrid technique, ANSYS and the two discrete strain gages located along lines CD and EF in *figures 4.2 and 4.3*; and are plotted along the horizontal x-axis and vertical y-axis of *figure 4.1* in *figures 4.11 through 4.13*. Tangential stress, $\sigma_{\theta\theta}$, is normalized by the net stress σ_{net} and is plotted on the boundary of the hole from strain gage evaluated Airy coefficients (i.e., hybrid quantities) and ANSYS in *figure 4.14*. These individual components of stress and strain (and the subsequent displacement) are evaluated using $k = 5$ coefficients and $m = 48$ measured tangential strains. There is excellent agreement between the hybrid evaluated stresses or strains, ANSYS and discrete strain gage results. However, at the outer edge of the ring underneath the concentrated load, the ANSYS results in *figures 4.11 and 4.12* are excessively high due to the singularity caused by point load.

The normalizing stress, σ_{net} = 1500/((3.932-2.003)*0.75) = 1036.8 psi (= 7.15 MPa) is based on the applied load, F = 6672.33 N (1500 lbs), divided by the net cross-sectional area (i.e., at the region of the hole), *figure 4.1*. The normalizing strain, $\varepsilon_{net} = 1036.8*10^{-6}$ is evaluated on the stress-strain relationship i.e., $\varepsilon_{net} = \sigma_{net}/E$ (E = 68.95 GPa = 10 x 10^6 psi). The displacement contour plots of *figures 4.15 through 4.18* are normalized with respect to the inner radius of the ring (R = 25.4 mm = 1.0015").

There is considerable discrepancy between the current hybrid and FEM predicted strains for y/R ≥ 1.45 in *figures 4.11 and 4.12*. Recognizing that neither of these analyzes accounts for the theoretical singularity which occurs under the applied load, P, probably neither of the results is valid for y/R ≥ 1.45.

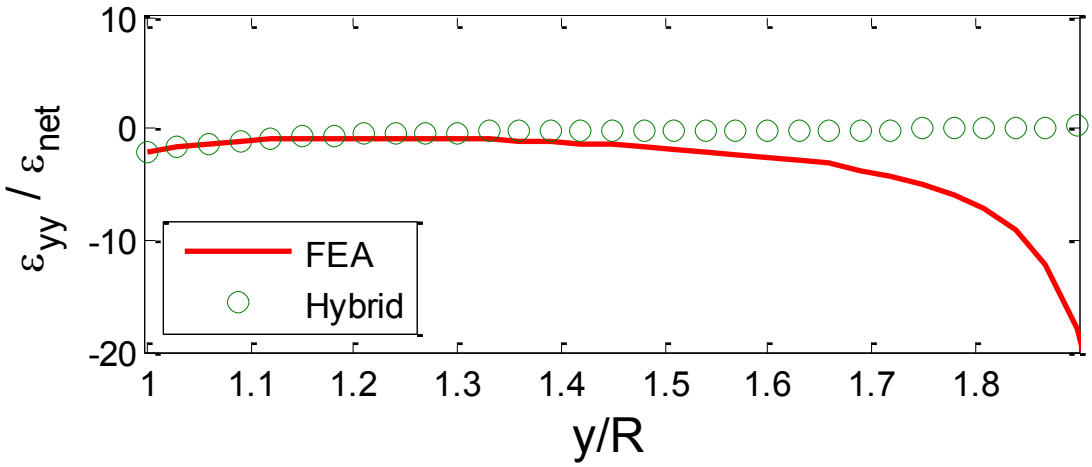

Fig. 4.11: Plot of $\varepsilon_{yy}/\varepsilon_{net}$ along vertical axis of *figure 4.1* from hybrid method (strain-gage evaluated Airy coefficients) and ANSYS

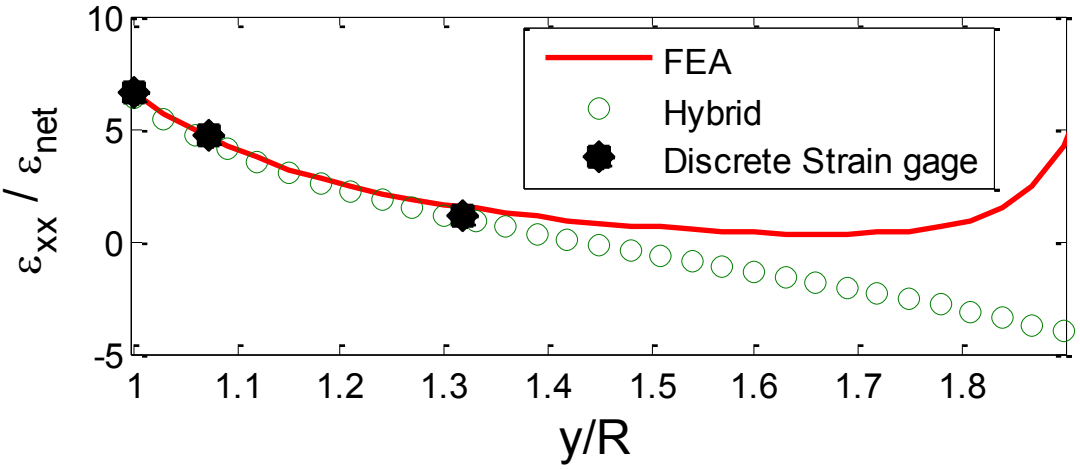

Fig. 4.12: Plot of $\varepsilon_{xx}/\varepsilon_{net}$ along vertical axis of *figure 4.1* from hybrid method (strain-gage evaluated Airy coefficients) and ANSYS

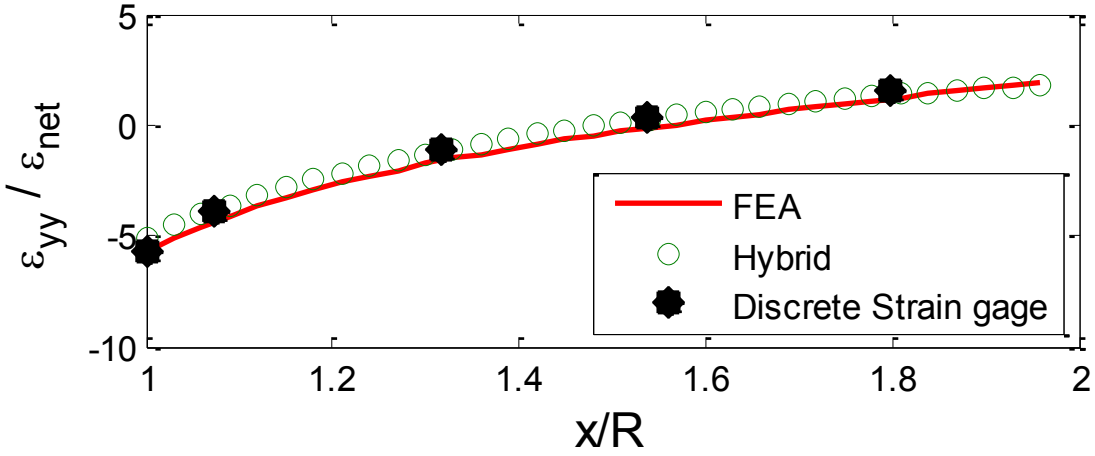

Fig. 4.13: Plot of $\varepsilon_{yy}/\varepsilon_{net}$ along horizontal axis of *figure 4.1* from hybrid method (strain-gage evaluated Airy coefficients) and ANSYS

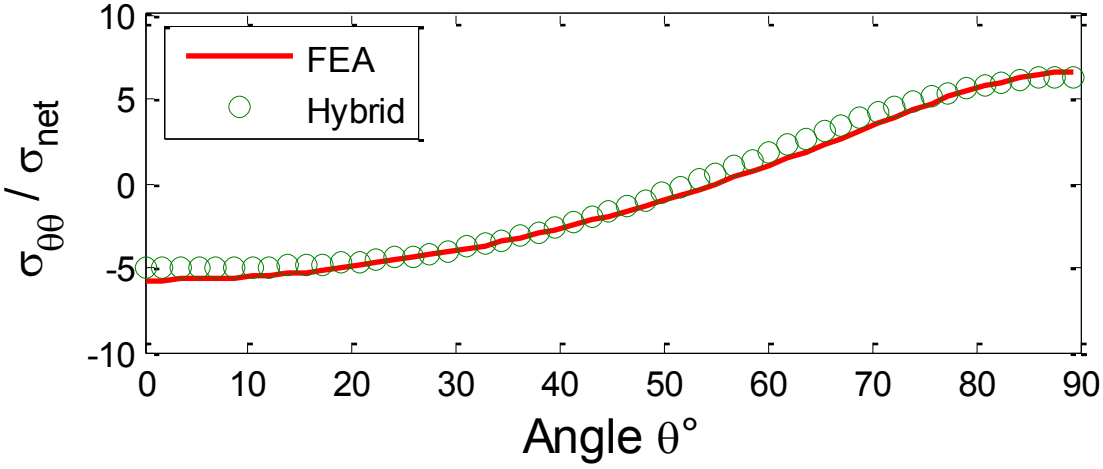

Fig. 4.14: Plot of $\sigma_{\theta\theta}/\sigma_0$ along boundary of the hole from hybrid method (strain-gage evaluated Airy coefficients) and ANSYS

Figures 4.15 through 4.23 are the normalized full-field contour plots of individual stress, strain and displacement components from the hybrid method (strain-gage evaluated Airy coefficients) and ANSYS. There is excellent agreement between the hybrid (strain gage and Airy stress function) evaluated stresses, strains and displacements and FEM predictions except under the applied load, P. The invalid FEA predictions and strain gage-hybrid analyses in the region at the top concentrated load are again apparent in *figures 4.19, 4.21 and 4.23*.

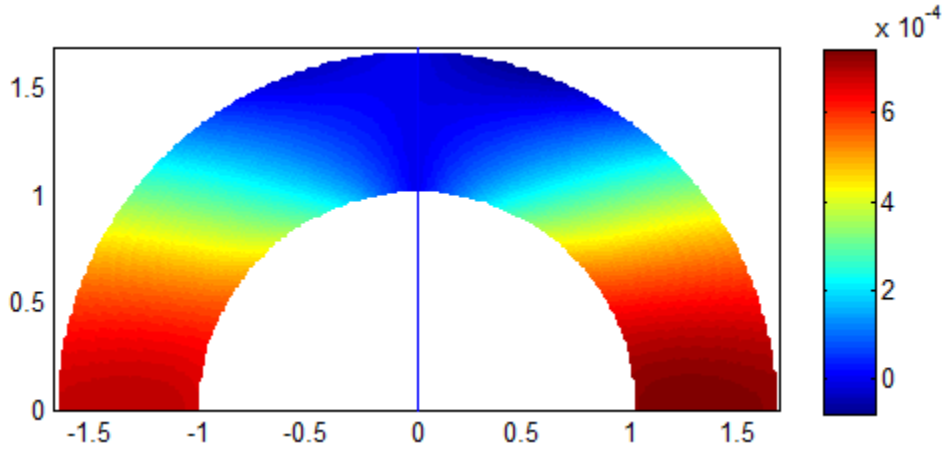

Fig. 4.15: Contours of *u/R* from FEA (left side) and hybrid method (strain-gage evaluated Airy coefficients) (right side)

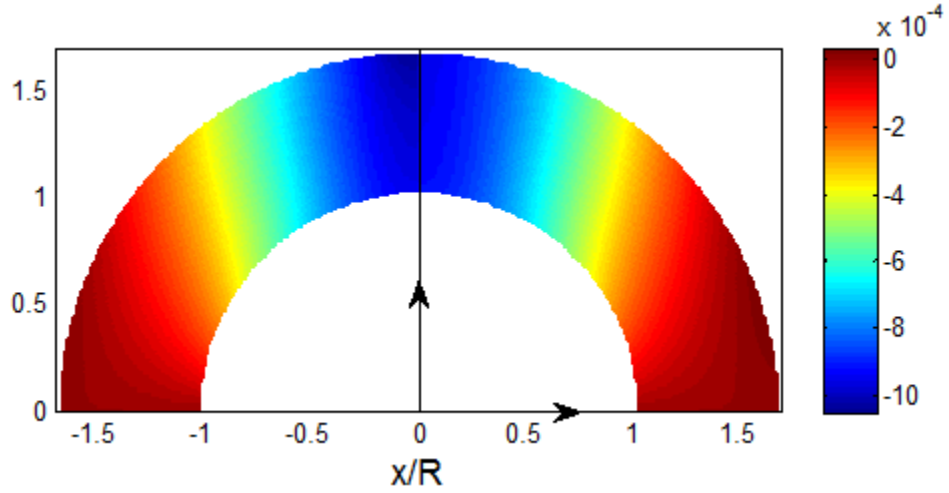

Fig. 4.16: Contours of *v/R* from FEA (left side) and hybrid method (strain-gage evaluated Airy coefficients) (right side)

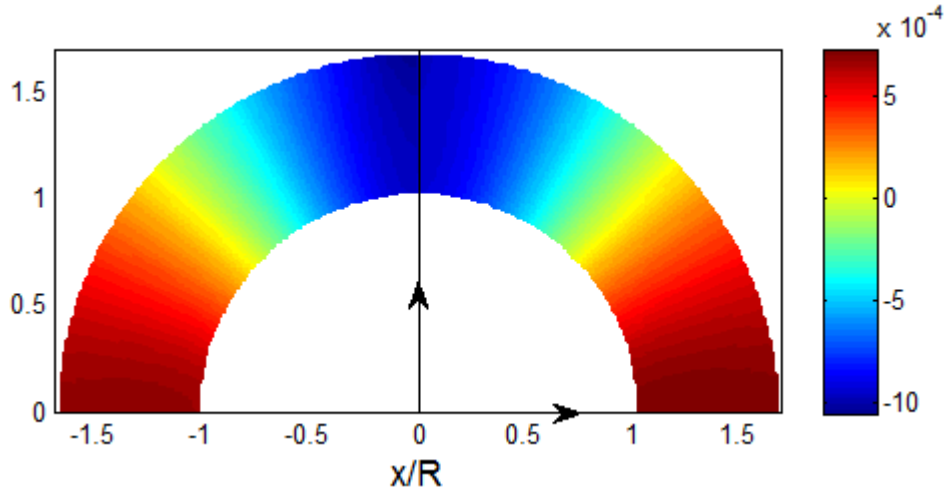

Fig. 4.17: Contours of u_r/R from FEA (left side) and hybrid method (strain-gage evaluated Airy coefficients) (right side)

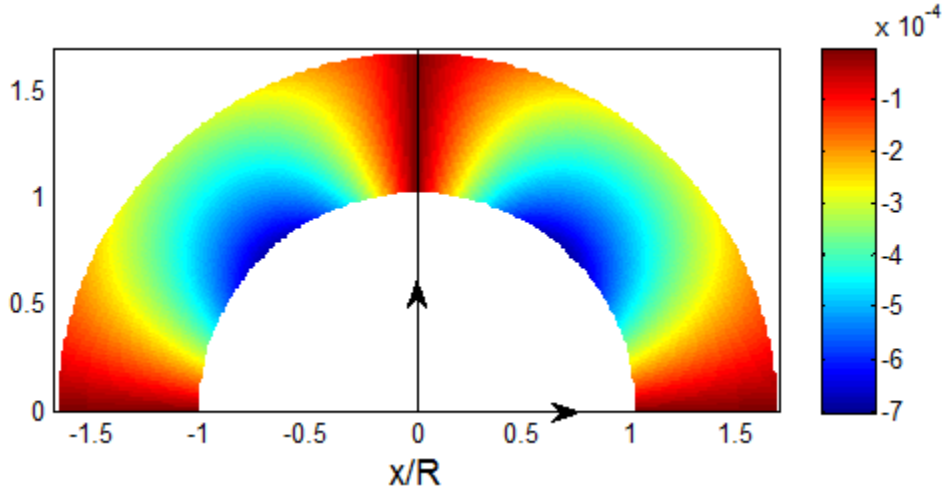

Fig. 4.18: Contours of u_θ/R from FEA (left side) and hybrid method (strain-gage evaluated Airy coefficients) (right side)

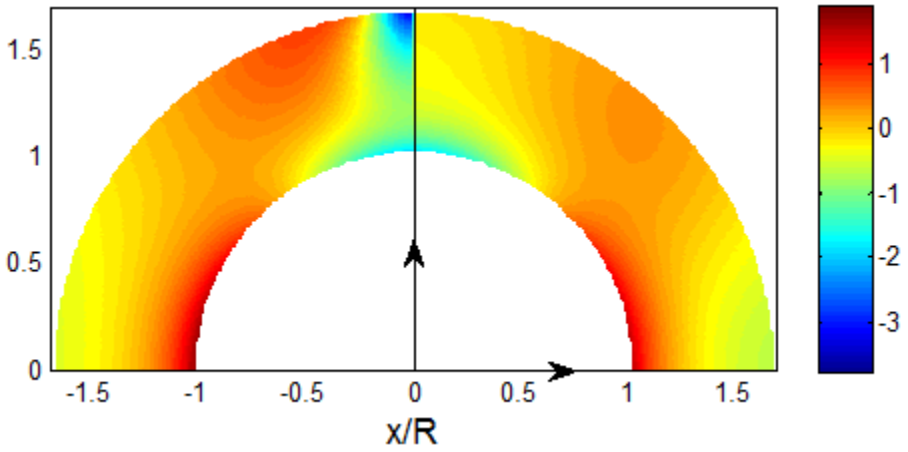

Fig. 4.19: Contours of $\varepsilon_{rr}/\varepsilon_{net}$ from FEA (left side) and hybrid method (strain-gage evaluated Airy coefficients) (right side)

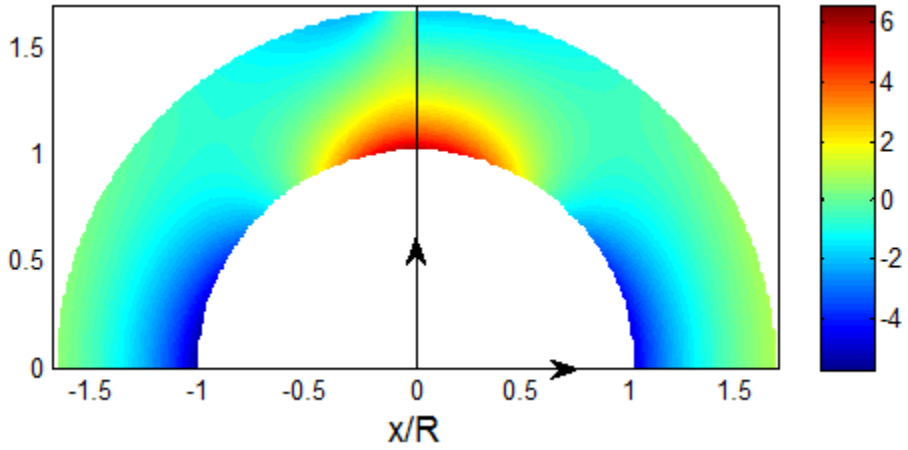

Fig. 4.20: Contours of $\varepsilon_{\theta\theta}/\varepsilon_{net}$ from FEA (left side) and hybrid method (strain-gage evaluated Airy coefficients) (right side)

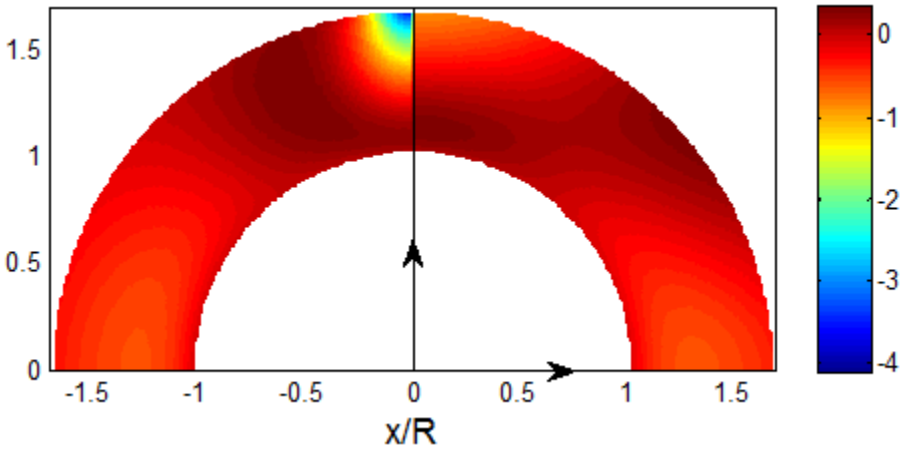

Fig. 4.21: Contours of σ_{rr}/σ_{net} from FEA (left side) and hybrid method (strain-gage evaluated Airy coefficients) (right side)

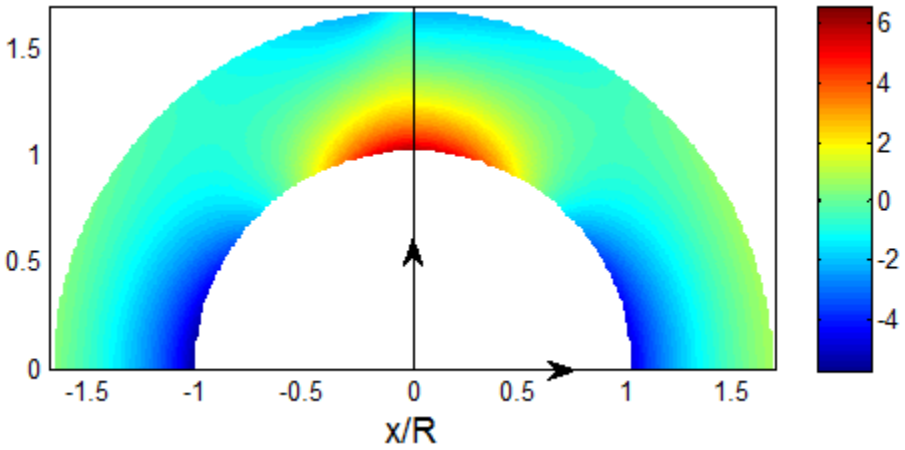

Fig. 4.22: Contours of $\sigma_{\theta\theta}/\sigma_{net}$ from FEA (left side) and hybrid method (strain-gage evaluated Airy coefficients) (right side)

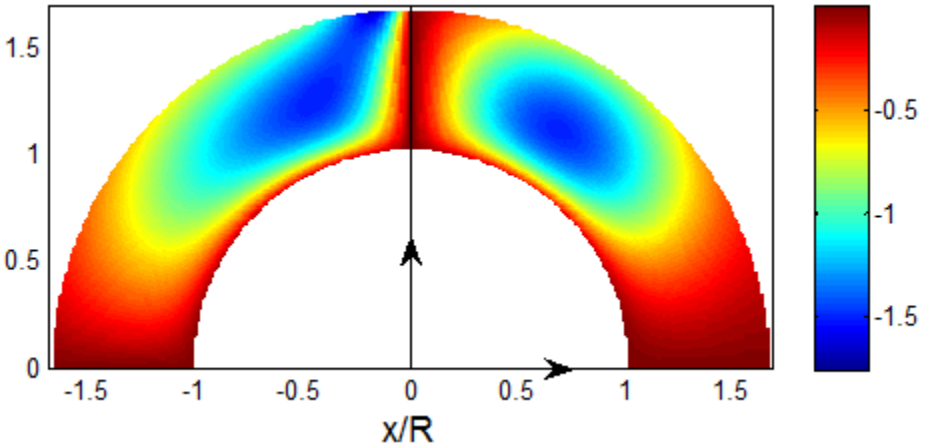

Fig. 4.23: Contours of $\sigma_{r\theta}/\sigma_{net}$ from FEA (left side) and hybrid method (strain-gage evaluated Airy coefficients) (right side)

4.8 Validation

The present hybrid results are further validated using the two additional strain gages which are mounted in the radial direction along lines CD and EF of the ring at r/R = 1.75, *figures 4.1 through 4.3*. As the ring was rotated at ten degree intervals, the strains of these two gages are recorded and averaged at each interval of θ. However, the strains from those two gages are neglected when CD and EF are aligned with the loading because of the high local load influence. *Figure 4.24* is the plot of radial strain at r/R = 1.75 from the hybrid method (strain-gage evaluated Airy coefficients), ANSYS and the two discrete strain gages along lines CD and EF in *figures 4.1 through 4.3*. The output of these two radial strain gages was not used as input for evaluating the unknown Airy coefficients, only for validating the hybrid results. The invalid FEA prediction in *figure 4.24* as one approaches θ = 90° due to the nearby singularity associated with concentrated load is again apparent.

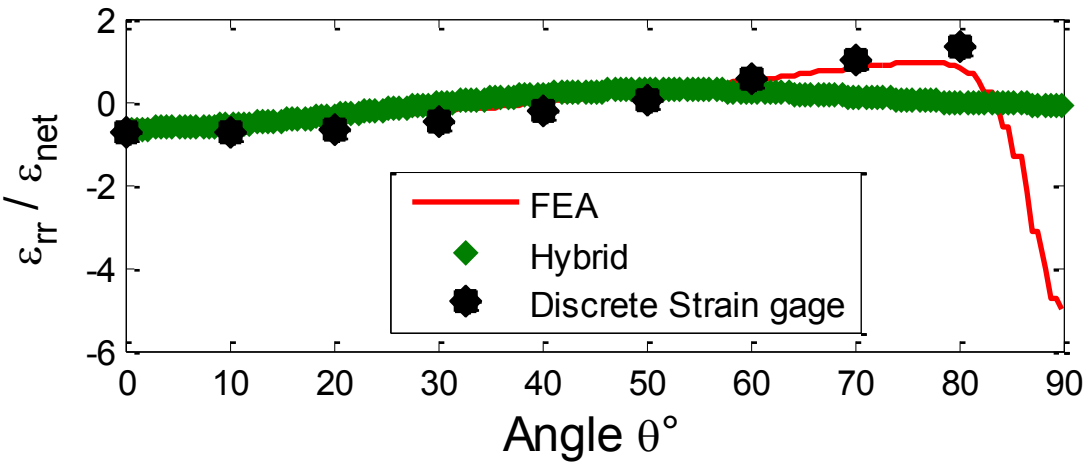

Fig. 4.24: Plot of $\varepsilon_{rr}/\varepsilon_{net}$ along r/R = 1.75 from hybrid method (strain-gage evaluated Airy coefficients) and ANSYS

The results of the hybrid method (Airy stress functions processed strain gage data) are further compared against theory which is available for the ratio of outer-to-inner radius equal to

two [25]. In this chapter the ratio of outer radius to inner radius equals 1.96 which is approximately two. *Figures 4.25 and 4.26* are plots of the normalized tangential stress based on the present hybrid method of strain-gaged evaluated Airy coefficients and Timoshenko [25] along the vertical y and horizontal x axes. In *figures 4.25 and 4.26,* P equals load per unit thickness and $b = R_0$ is the outer radius. Except as one approaches the concentrated load there is good agreement between the strain gage evaluated coefficients, FEA, discrete strain gage and theory (*figures 4.24 through 4.26*).

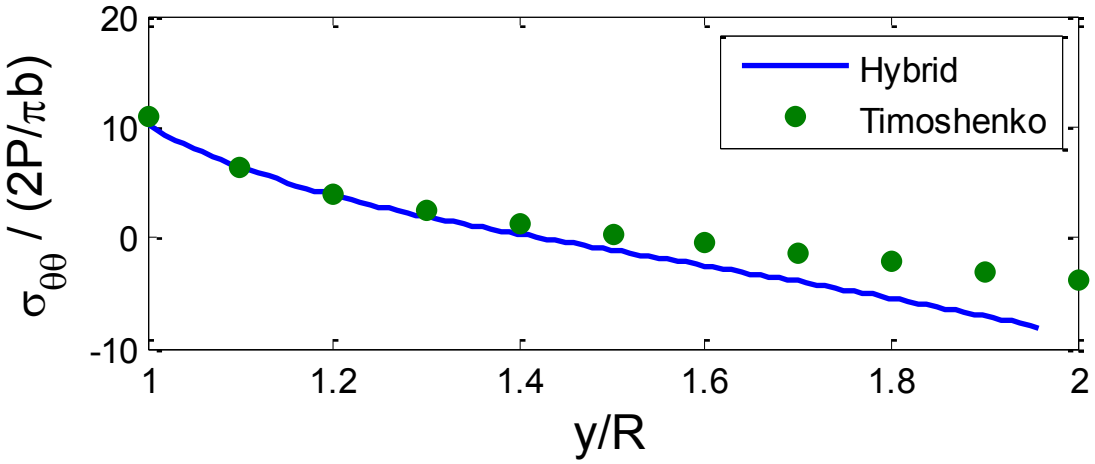

Fig. 4.25: Plot of $\sigma_{\theta\theta}/(2P/\pi b)$ along vertical axis of *figure 4.1* from hybrid method (strain-gage evaluated Airy coefficients) and Timoshenko [25]

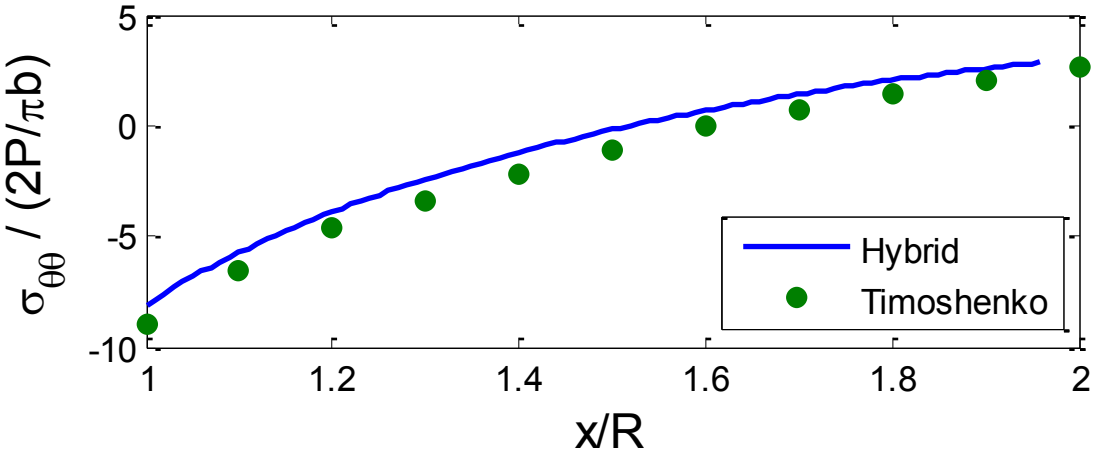

Fig. 4.26: Plot of $\sigma_{\theta\theta}/(2P/\pi b)$ along horizontal axis of *figure 4.1* from hybrid method (strain-gage evaluated Airy coefficients) and Timoshenko [25]

4.9 Summary, Discussion and Conclusions

In this chapter the experimental hybrid technique was sufficiently simplified so that the full-field individual stress, strain and displacement components can be determined throughout a diametrically-loaded ring from the output of only five single-element strain gages. Airy's stress function is employed to process the measured strains. By rotating the annular disk at ten degree intervals, the input strain data were increased from five to forty eight and for these input measured strains, $k = 5$ was found to be an appropriate number of Airy coefficients to use. The measured strains are evaluated in the tangential direction, but one could conceivably mount the strain gages in the radial or longitudinal direction.

The present approach overcomes the experimental challenges such as having to mount, wire and calibrate/measure the strains at as many locations as in Chapter 3, thereby reducing the number of channels of strain-gage conditioner needed while providing full-field stress, strain or displacement contours from a single component of strain recorded at few discrete locations. The approach also circumvents the need of a photoelastic model or birefringent coating or spray painting, or applying a speckle pattern or grids/rulings as required with photoelastic stress analysis (PSA), thermoelastic stress analysis (TSA), digital image correlation (DIC) or moiré.

Reliable results are available throughout the ring by processing the hoop component of strain with an Airy's stress function. The hybrid (strain gages plus Airy stress function) results agree with those from discrete strain gages, FEM and theory. The present analysis was conducted for a ratio of outer- to -inner diameter of very close to two. This enabled checking the present

hybrid results with theory. However, an advantage of the present approach is it is applicable for any ratio of outer-to-inner diameter.

This problem could conceptually be solved numerically by only boundary correlation. Having satisfied the traction-free boundary conditions *analytically* everywhere on the inside of the diametrically-loaded ring (r = R), one could evaluate all of the Airy coefficients of *equations 4.2 through 4.14* by imposing $\sigma_{rr} = \sigma_{r\theta} = 0$ at numerous discrete locations on the outer boundary of the ring ($r = R_o$) but away from the applied load without involving any of the presently recorded strains. However, doing so would not account for variations in the loads applied along the diameter (e.g., whether any transverse shear/friction accompanies normal loads). Moreover, if one employs too little measured strain data compared with the number of locations at which one impose $\sigma_{rr} = \sigma_{r\theta} = 0$ on the outside boundary, the results can be unreliable, Appendix A4. On the other hand, results of Appendix A4 show that for $\sigma_{rr} = \sigma_{r\theta} = 0$ *analytically* on the edge of the hole but only 13 measured input strains provide reliable results throughout the ring except again under the concentrated load.

This research has potential application to load cells (for example weighing trucks on highways). *Figure 4.26* is a possible design of a load cell in which a strain-gaged annular disk is loaded using rollers. The rollers would rotate on shafts connected to the rectangular sections, *figure 4.26*. These rollers would rotate the ring while the strains are recorded. The gage at location A (*figure 4.1*) could form (via telemetry or slip rings) one leg of a Wheatstone bridge.

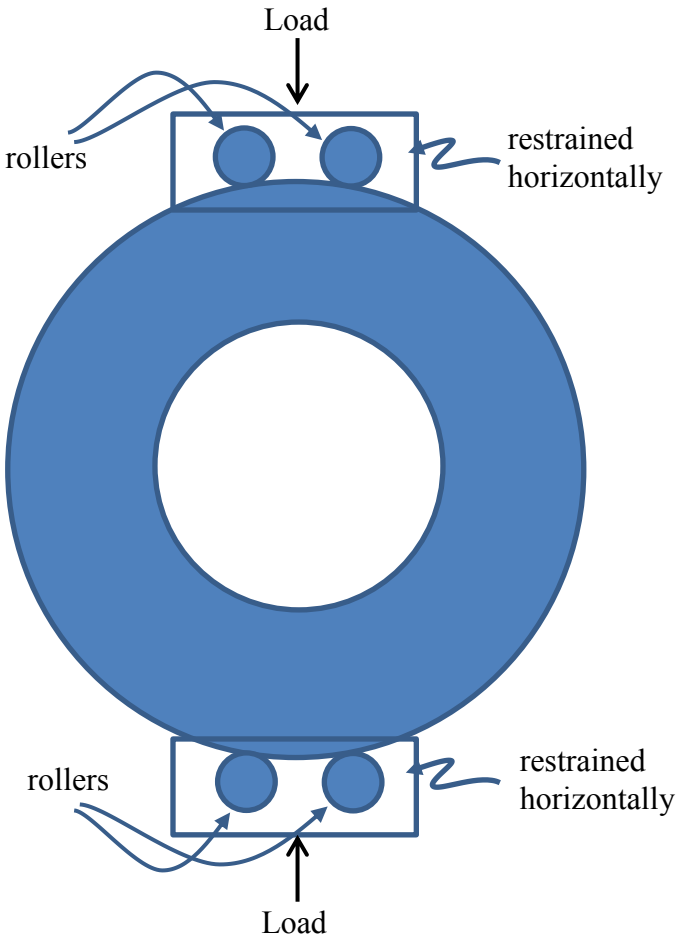

Fig. 4.26: Schematic of possible design for a load cell in compression

Relative to using this concept as a load cell, by monitoring the strains of the gage at points A on the ring, *figure 4.1*, and locating this gage in a Wheatstone bridge, the strain at position A, ϵ_A, associated with this gage would correlate with the output voltage of the bridge, E_o, according to [35 and 104]

$$E_o = \frac{V}{4} S_g \epsilon_A \tag{4.17}$$

where V is the excitation voltage and S_g is the gage factor. Strain gages from a common package could be used to complete the bridge such that $R_2/R_1 = 1$. The bridge might include a shunt

circuit containing a variable resistor to aid in initially balancing the bridge. The magnitude of strain ϵ_A could be calibrated in terms of applied load, P, as a function of ring rotation, angle θ, so as to correlate E_o in terms of the load (perhaps as a graph) for any angle θ.

Another potential load-cell design but which can be used either in compression or tension could use rollers at both the inner and outer edges of the ring. For compressive loading the rollers at the outer radius would contact the ring and one could impose the traction-free boundary condition *analytically* on the inner boundary. For tensile loading, the rollers at the inner radius would contact the ring and one would impose the traction-free boundary condition *analytically* on the outer boundary. Rather than using a strain gage at location A of *figure 4.1*, one could now employ a gage which is bonded slightly beyond the inner ring radius (perhaps that at r/R = 1.075 in *figure 4.2*) to avoid its being contacted by the inside roller. Load-cell concepts such as proposed here would enjoy the advantage that the ring is not always loaded at the same position, therefore providing increased (fatigue performance) life.

Under axisymmetric condition, apart from the specific design of load cell, this technique can be applied to multiple point loads or pressure loading at inner or outer boundaries.

Chapter 5 : Thermoelastic Stress Analysis of a Finite-Plate containing an Elliptical Hole

5.1 Introduction

Holes of various shapes are frequently employed in engineering structures. Such geometric discontinuities produce stress concentrations that are often the source of mechanical or structural failures. As such, this chapter demonstrates the ability to determine thermoelastically (TSA) the individual components of stress in a finite-width tensile plate containing an elliptical hole. This study of elliptical-shaped holes extends the ability of TSA to evaluate stress distributions in components containing other than circular-shaped cutouts. An earlier TSA approach to stress analyzing a member containing an elliptical-shape hole used complex variables and mapping techniques [15, 19]. However, the current use of a series representation of an Airy stress function in terms of polar coordinates offers the advantages and convenience of real variables. In addition to being simpler mathematically the present real-variable approach enables determining the stresses around the total hole boundary at once. This is unlike the mapping technique which necessitates applying the technique incrementally around the hole.

The author is unaware of prior utilization of polar coordinates to experimentally evaluate the stresses associated holes or notches which are other than round. This is significant since while a general solution is available to the biharmonic equation, the relevant differential equation, in polar coordinates, such is not so in rectangular or elliptical coordinates [6]. However

as detailed in Appendix A5, the stresses in polar coordinates can be readily converted to those in elliptical or rectangular coordinates are needed. Indeed, elliptical coordinates are employed to satisfy the traction-free conditions on the edge of the hole. The coefficients of the Airy's stress function are evaluated here from the thermoelastically measured isopachic stress supplemented with known boundary conditions at and away from the hole so as to determine the individual components of stresses in the elliptically-perforated plate. Having the stress components available in polar coordinates away from the edge of the hole would be convenient for example of there were neighboring holes or notches such that the stresses associated with the individual geometric discontinuities interacted with each other (see Chapter 8). For an isotropic material, and adiabatic reversible conditions exhibited by cyclic loading, the stress-induced temperature change in a structure is proportional to the sum of changes in the normal stresses. These TSA-determined stresses are available on and in the neighborhood of the edge of the hole without knowing the distant geometry or boundary conditions. Unlike displacement-based experimental techniques (e.g., moiré, speckle, digital image correlation), the method does not necessitate differentiating the measured information. The present analysis involves a central traction-free elliptical hole and symmetry about the horizontal and vertical axes. The concept is applicable to more general shaped holes or notches in unsymmetrical situations or under more loading conditions. The current approach is applicable to cases of multiple elliptical holes, notches or combination thereof. Also, and unlike stress analyses based on isochromatic data which necessitates non-linear least squares, TSA involves only linear least-squares. As demonstrated here, the technique is very effective for finite components. This is important because very few theoretical solutions are available for finite geometries and strictly numerical (finite element or finite difference) methods necessitate knowing the external loading and geometry. The reliability

of the present TSA-evaluated results is substantiated by comparison with those from finite element analysis and commercial strain gages. The integrated TSA-evaluated stresses also satisfy force equilibrium. While applied here to thermoelasticity, many of the present concepts could be useful with other areas of experimental mechanics.

The major contribution of this chapter is the development and demonstration of the ability to thermoelastically stress analyze finite components containing a non-circular geometric discontinuity using a stress function in real (polar) coordinates.

5.2 General Comments

Thermoelastic stress analysis (TSA) is a modern experimental technique for determining the stress distribution in engineering components. TSA is usually performed under adiabatic and reversible conditions and which is achieved by cyclically loading the structure. The cyclic loading produces an in-phase temperature variation which, for isotropic materials, is proportional to the change in the sum of the principal stresses (i.e., isopachic stress). Thermoelastic stress analysis uses a scanning infra-red (IR) radiometer system to record the local temperature fluctuations and relates these changes to the associated isopachic stress. TSA is a full-field, non-contacting, nondestructive, technique which enables the stress analysis of actual structures in their operating environment with sensitivity equal to that of strain gages. Moreover, the measured TSA data is digitalized in matrix form which vastly reduces the time needed for analyzing the experimental information. The present hybrid concept of combining an Airy stress function (which is derived from stress equilibrium and strain compatibility), local boundary conditions, and measured TSA data in the neighborhood of the geometric-discontinuity of interest is advantageous. The present TSA approach is particularly suitable for stress analyzing finite structures, whose distant geometry or loading is not well known, something which is difficult to do theoretically or numerically. An over-determined least-squares routine was implemented to evaluate the unknown Airy coefficients and hence determine the complete state of stress. Although measured TSA information on and near and edge is typically unreliable, the current method also provides stresses at the boundary of the elliptical hole. Challenges of TSA have been that measured data can be noisy, the recorded isopachic stress S* must be separated into individual stresses, calibration is required, recorded temperatures at and near the edge are

usually not reliable and the component typically must be cyclically loaded. Past and present advances developed at University of Wisconsin-Madison can overcome many of these features[1].

Under proportional plane-stress isotropy, the measured TSA temperature signal, S*, is related to the stresses by

$$S^* = K\Delta S$$

$$S^* = K\Delta\left[(\sigma_1 + \sigma_2) = (\sigma_{rr} + \sigma_{\theta\theta}) = \left(\sigma_{xx} + \sigma_{yy}\right) = \sigma_{\xi\xi} + \sigma_{\eta\eta}\right] \quad (5.1)$$

where S is sometimes called the first stress invariant, the trace of the stress tensor or the isopachic stress value, K is the isotropic thermoelastic coefficient, and $(\sigma_1 + \sigma_2), (\sigma_{rr} + \sigma_{\theta\theta}), \left(\sigma_{xx} + \sigma_{yy}\right)$ and $\left(\sigma_{\xi\xi} + \sigma_{\eta\eta}\right)$ are the sum of the stresses in the principal directions, in polar coordinates, in Cartesian coordinates or in elliptical coordinates, respectively, *figure 5.1*. The presented technique does not need any prior filtering of the recorded data.

Elliptical holes often occur in finite engineering components but such situations are difficult to stress analyze, particularly for finite components whose far-field boundary conditions are not well known. The recorded Thermoelastic Stress Analysis data (isopachic stress or 'sum' of the principal stresses) are separated in this chapter into individual components of stress in a uniaxially loaded, elliptically-perforated, finite aluminum plate which is symmetrical about both

---

[1]This includes TSA under random loading, non-adiabatic behavior and stress separation [4, 6, 8, 10, 15 through 19].

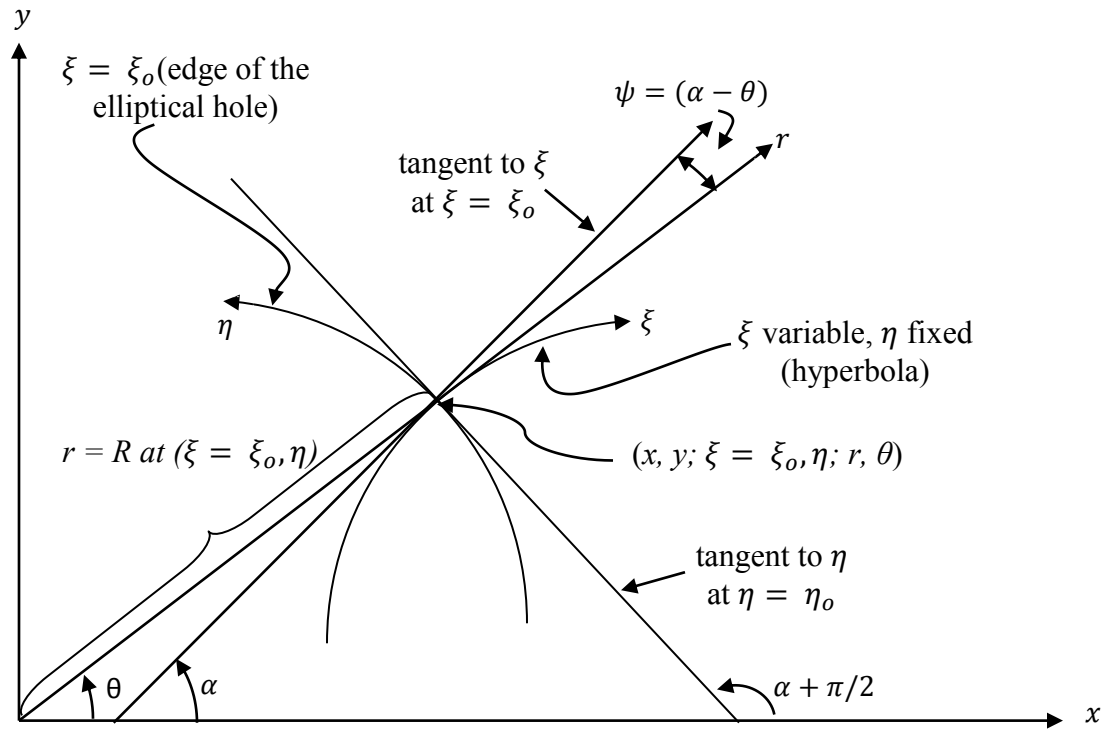

Fig. 5.1: Coordinate Representations

the axes *(figure 5.2).* Measured TSA data are combined with the Airy`s stress function (in real variables, polar coordinates r and θ) to evaluate individual components of stress. A particularly advantageous feature of the present approach is its ability to evaluate all of the Airy (real, not complex) coefficients (and hence the independent components of stress on and beyond the edge of the hole) from measured temperatures and the local traction-free conditions. In this particular case, the coordinate origin is at the center of the hole which makes the plate symmetric about both x- and y-axes, thereby simplifying the stress function and hence the number of Airy coefficients. The traction-free conditions on the boundary of the elliptical hole are imposed here *discretely*. The measured TSA data are unreliable at and very near the boundary of the hole. However, accurate edge information is needed when determining boundary stresses or stress

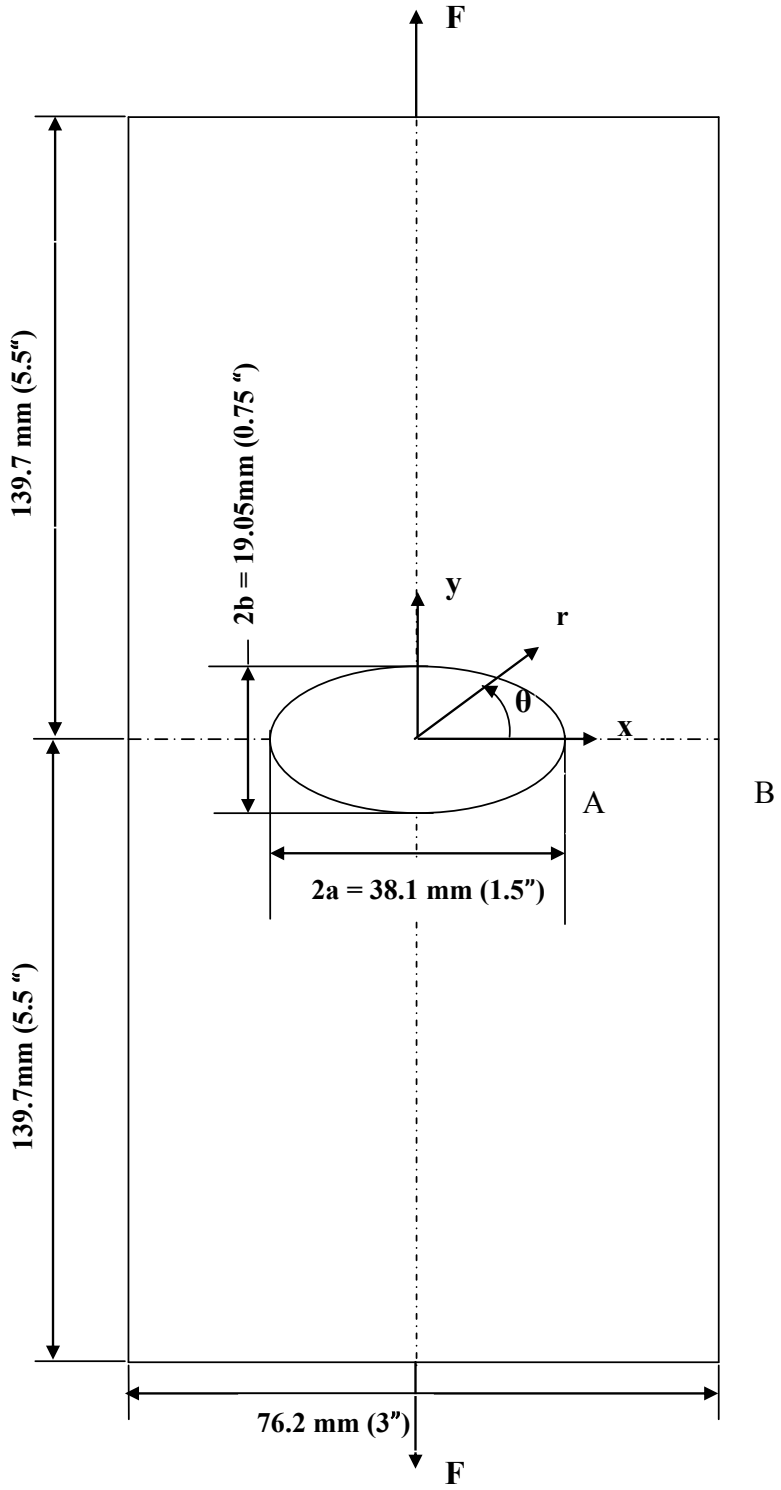

Fig. 5.2: Schematic of symmetrically-loaded aluminum plate containing an elliptical hole plate

concentration factors. The concept of synergizing the Airy's stress function with the measured temperature information provides the individual components of stress 'full-field', including on the edge of the hole. This ability to stress analyze members containing non-circular (including elliptical) holes is significant. Relatively little information associated with elliptical holes in finite plates is available. However, the ability to do is convenient in that a general series solution of $\nabla^4\phi = 0$, the governing equation, is available in polar coordinates.

The appropriate number of Airy coefficients to retain in the stress function is determined here in at least two ways. The source locations of the measured input temperature data can be important. Since the plate of *figure 5.2*, is symmetrical about both horizontal and vertical axes, the raw recorded TSA data are averaged throughout the four quadrants so as to eliminate any possible non-symmetry.

The three independent components of stress can then be determined by combining a series representation of the Airy stress function with measured TSA data. Moreover, unlike evaluating stress from isochromatic data, TSA analysis requires only linear (rather than non-linear) least-squares. This circumvents the time consuming and challenging iterative process of non-linear least-squares. Unlike displacement-based methods such as moiré, holography, speckle and digital image correlation, TSA requires neither differentiating the measured information nor knowledge of the constitutive material properties. No surface preparation is required other than applying a Krylon Ultra-Flat black paint which provides an enhanced and uniform emissivity. Many photomechanical techniques tend to be highly labor-intensive and time-consuming. On the other hand, recent commercial hardware and software developments enable TSA results to be available within minutes.

In addition to demonstrating the practical ability of TSA to handle non-circular geometric discontinuities using polar coordinates, the following considerations helped to motivate this particular geometry *(figure 5.2)*: (i) It has two axes of symmetry which simplifies the stress function and thereby reduces the number of Airy coefficients [1, 4, 6, 8]. (ii) Ability to work with real variables since earlier approaches used a stress functions in terms of complex variables and mapping techniques [15, 19]. (iii) In the present case of the MTS hydraulic grip loading, the far-field loading conditions are well known. It is therefore possible to conduct a confident finite element analysis of this loaded plate against which to compare experimental results.

Relatively little information is available on finite members containing elliptical holes and even less on elliptical notches, [20 – 26, 28, 29]. Most of what is available treats infinite geometries, involves numerical analyses for specific cases, or employs a complex stress function and perhaps mapping techniques. Unlike the present approach, strictly numerical or theoretical methods necessitate knowing reliably the far-field geometry and loading conditions. The present availability of the independent stress components away from the edge of the hole in polar coordinates is convenient if there were neighboring geometric discontinuities whose separate stresses interact with each other (Chapter 7). Reference [15] is the only known thermoelastic stress analysis to an elliptical hole, and that solution uses a complex variable stress function and mapping.

The following includes details of the plate tested:

- Material of the plate: Aluminum 6061-T6 (Wiedenbeck, Inc., Madison, WI); Ultimate strength = 275 to 311 MPa (40 to 45 ksi) and yield strength = 241 to 275 MPa (35 to 40 ksi).
- Cyclic Load = 3558.57 N (800lb) ± 2224.11 N (500lb) at 10Hz, unless indicated otherwise.
- Loading Range (F) = 4448.2 N (1000lb), unless indicated otherwise.
- Major Diameter of the elliptical hole (2a) = 38.10 mm (1.5″), *figure 5.2*.
- Minor Diameter of the elliptical hole (2b) = 19.05 mm (0.75″), *figure 5.2*.
- Thickness of the plate (t) = 6.35mm (0.25″).
- Plate is symmetrical about the both the horizontal and vertical axes (x- and y-axes).
- Length of the plate (L) ≈ 279.4 mm (11″), *figure 5.2*.
- Width of the plate (W) = 76.2 mm (3″), *figure 5.2*.
- A strip gage consisting of eight strain gages was mounted along line AB extending horizontally from the edge from the major diameter of *figure 5.2*.
- Two individual strain gages were mounted, one on the front and one on the back, to ensure proper specimen alignment by minimizing any out-of-plane bending.

5.3 Airy Function and Stresses

For thermoelastically stress analyzing the elliptically-perforated vertically-loaded finite plate of *figure 5.2*, one can utilize the Airy's stress function in polar coordinates, including assuming symmetry about both x- and y-axes. In addition to the measured temperature data some traction-free conditions are imposed *discretely* on the boundary of the elliptical hole. The Airy stress function satisfies stress equilibrium and the associated strains of the compatibility condition give the biharmonic equation $\nabla^4\phi = 0$ (where ∇^2 is the Laplacian operator and $\nabla^2 = \frac{\partial^2}{\partial r^2} + \frac{1}{r}\frac{\partial}{\partial r} + \frac{1}{r^2}\frac{\partial^2}{\partial \theta^2}$) of *equation 5.2* [1, 4, 6, 8]. However, while a general solution to $\nabla^4\phi = 0$ is not readily available in either rectangular or elliptical coordinates, it is (*equation 5.2*) in polar coordinates. Appendix A5 contains the necessary equations to relate the geometry and stresses in terms of radial, rectangular or elliptical coordinates.

$$
\begin{aligned}
\phi = {} & a_0 + b_0 \ln r + c_0 r^2 + d_0 r^2 \ln r + \left(A_0 + B_0 \ln r + C_0 r^2 + D_0 r^2 \ln r\right)\theta \\
& + \left(a_1 r + b_1 r \ln r + \frac{c_1}{r} + d_1 r^3\right)\sin\theta + \left(a_1' r + b_1' r \ln r + \frac{c_1'}{r} + d_1' r^3\right)\cos\theta \\
& + \left(A_1 r + B_1 r \ln r\right)\theta \sin\theta + \left(A_1' r + B_1' r \ln r\right)\theta \cos\theta \\
& + \sum_{n=2,3,4\ldots}^{\infty} \left(a_n r^n + b_n r^{(n+2)} + c_n r^{-n} + d_n r^{-(n-2)}\right)\sin(n\theta) \\
& + \sum_{n=2,3,4\ldots}^{\infty} \left(a_n' r^n + b_n' r^{(n+2)} + c_n' r^{-n} + d_n' r^{-(n-2)}\right)\cos(n\theta)
\end{aligned}
\tag{5.2}
$$

In the absence of body forces, a classical plane-stress elasto-static stress analysis involves solving the biharmonic equation, $\nabla^4\phi = 0$, (to obtain *equation 5.2*) and differentiating the obtained stress function, ϕ, to evaluate the stresses subjected to boundary conditions. Therefore (provided one knows the values of the Airy coefficients of *equation 5.2*), individual components

of stresses can be evaluated by differentiating the stress function of *equation 5.2* as shown in *equations 5.3 through 5.5*:

$$\sigma_{rr} = \frac{1}{r}\frac{\partial \phi}{\partial r} + \frac{1}{r^2}\frac{\partial^2 \phi}{\partial \theta^2} \tag{5.3}$$

$$\sigma_{\theta\theta} = \frac{\partial^2 \phi}{\partial r^2} \tag{5.4}$$

$$\sigma_{r\theta} = -\frac{\partial}{\partial r}\left(\frac{1}{r}\frac{\partial \phi}{\partial \theta}\right) \tag{5.5}$$

The above differentiations of *equation 5.2* involve the same unknown coefficients as in the Airy's stress function. Determination of individual stresses therefore necessitates somehow evaluating these unknown coefficients. As indicated shortly, the number of these unknown coefficients (typically referred to as Airy coefficients) in *equation 5.2* can often be reduced significantly by considering factors such as any geometric and loading symmetry conditions.

Since the displacements, strains and stresses for *figure 5.2* cannot be multi-valued functions of θ, the coordinate origin is not in the component (but within the cavity) and there is no resultant force at the origin, coefficients d_0, B_0, C_0, D_0, B_1, B_1' and A_1, A_1', b_1, b_1' are all zero [6, 10, 17, 18]. The plate of *figure 5.2* is symmetrical about both the vertical *y*-axis and horizontal *x*-axes. In addition to $A_0 = 0$, symmetry about *x*-axis means that stresses occurring at any angle, say when θ = +β would be the same as those at θ = -β. Thus, $\phi(r, \theta) = \phi(r, -\theta)$. This indicates that ϕ must be an even function of θ. Symmetry about the y-axis, means that all sine terms of *equation 5.2* go to zero. For, a_n, b_n, c_n, d_n (for $n \geq 1$) the value of n is a positive even

integer. Therefore, for the present case of *figure 5.2*, the Airy stress function of *equation 5.2*, reduces to:

$$\phi = a_0 + b_0 \ln r + c_0 r^2 + \sum_{n=2,4,6,..}^{N} \left\{ \left(a_n r^n + b_n \mathrm{r}^{\mathrm{n+2}} + c_n r^{-n} + d_n \mathrm{r}^{-(\mathrm{n-2})} \right) \cos n\theta \right\} \tag{5.6}$$

Upon differentiating *equation 5.6* according to *equations 5.3 through 5.5*, the individual polar components of stress can be written as follows:

$$\sigma_{rr} = \frac{b_0}{r^2} + 2c_0 - \sum_{n=2,4,\ldots}^{\mathrm{N}} \begin{bmatrix} a_n\, n\,(n-1)\, r^{n-2} + b_n\,(n+1)\,(n-2)\, r^n \\ + c_n\, n\,(n+1)\, r^{-(n+2)} + d_n\,(n-1)(n+2)\, r^{-n} \end{bmatrix} cos(n\theta) \tag{5.7}$$

$$\sigma_{\theta\theta} = \frac{-b_0}{r^2} + 2c_0 + \sum_{n=2,4,\ldots}^{N} \begin{bmatrix} a_n\, n\,(n-1)\, r^{n-2} + b_n\,(n+1)\,(n+2)\, r^n \\ + c_n\, n\,(n+1)\, r^{-(n+2)} + d_n\,(n-1)(n-2)\, r^{-n} \end{bmatrix} cos(n\theta) \tag{5.8}$$

$$\sigma_{r\theta} = \sum_{n=2,4,\ldots}^{N} \begin{bmatrix} a_n\, n\,(n-1)\, r^{n-2} + b_n\, n\,(n+1)\, r^n \\ - c_n\, n\,(n+1)\, r^{-(n+2)} - d_n\, n\,(n-1)\, r^{-n} \end{bmatrix} sin(n\theta) \tag{5.9}$$

Quantity r is the radial coordinate measured from the center of the cavity and angle θ is measured counterclockwise from the horizontal x-axis, *figure 5.2*. N is the terminating index value of the series (since in practice one can only handle a finite number of terms) and it can be any positive even integer.

Rectangular component of stresses are also needed for the analyzing the stresses in Cartesian coordinates. The stresses of *equations 5.7 through 5.9* are therefore converted from

polar to rectangular coordinates by means of the standard transformation expression of *equation 5.10,* [8].

$$\begin{bmatrix}\sigma_{xx}\\ \sigma_{yy}\\ \sigma_{xy}\end{bmatrix}=\begin{bmatrix}\cos^2\theta & \sin^2\theta & -2\sin\theta.\cos\theta\\ \sin^2\theta & \cos^2\theta & 2\sin\theta.\cos\theta\\ \sin\theta.\cos\theta & -\sin\theta.\cos\theta & \cos^2\theta-\sin^2\theta\end{bmatrix}\begin{bmatrix}\sigma_{rr}\\ \sigma_{\theta\theta}\\ \sigma_{r\theta}\end{bmatrix} \tag{5.10}$$

From *equations 5.7 through 5.10*, the rectangular component of stresses become as shown in *equations 5A.100, 5A.110 and 5A.120,* and identified here as *equations 5.11 through 5.13*.

$$\sigma_{xx}=\left[\begin{matrix}\frac{b_0}{r^2}cos2\theta+2c_0\\ -\sum_{n=2,4,\ldots}^{N}\end{matrix}\left\{\begin{matrix}a_n\,n\,(n-1)\,r^{n-2}\,[cos(n\theta-2\theta)]\\ +b_n\,(n+1)r^n[n(cos(n\theta-2\theta))-2\,cos(n\theta)]\\ +\,c_n\,n\,(n+1)\,r^{-(n+2)}[cos(n\theta+2\theta)]\\ +d_n\,(n-1)r^{-n}\,[n(cos(n\theta+2\theta))+2\,cos(n\theta)]\end{matrix}\right\}\right] \tag{5.11}$$

$$\sigma_{yy}=\left[\begin{matrix}-\frac{b_0}{r^2}cos2\theta+2c_0\\ +\sum_{n=2,4,\ldots}^{N}\end{matrix}\left\{\begin{matrix}a_n\,n\,(n-1)\,r^{n-2}\,[cos(n\theta-2\theta)]\\ +b_n\,(n+1)r^n[n(cos(n\theta-2\theta))+2\,cos(n\theta)]\\ +\,c_n\,n\,(n+1)\,r^{-(n+2)}[cos(n\theta+2\theta)]\\ +d_n\,(n-1)r^{-n}\,[n(cos(n\theta+2\theta))-2\,cos(n\theta)]\end{matrix}\right\}\right] \tag{5.12}$$

$$\sigma_{xy}=\left[\begin{matrix}\frac{b_0}{r^2}sin2\theta\\ -\sum_{n=2,4,\ldots}^{N}\end{matrix}\left\{\begin{matrix}a_n\,n\,(n-1)\,r^{n-2}\sin(2\theta-n\theta)\\ +b_n n\,(n+1)r^n\sin(2\theta-n\theta)\\ +\,c_n\,n\,(n+1)\,r^{-(n+2)}\sin(n\theta+2\theta)\\ +\,d_n n\,(n-1)r^{-n}\sin(n\theta+2\theta)\end{matrix}\right\}\right] \tag{5.13}$$

Stresses acting in the polar co-ordinate system can be transformed to those in the elliptical co-ordinates using the following transformation matrix equation:

$$\begin{Bmatrix}\sigma_{\xi\xi}\\ \sigma_{\eta\eta}\\ \sigma_{\xi\eta}\end{Bmatrix} = \begin{bmatrix} cos^2\psi & sin^2\psi & 2\,cos\psi\,sin\psi \\ sin^2\psi & cos^2\psi & -2\,sin\psi\,cos\psi \\ -sin\psi\,cos\psi & sin\psi\,cos\psi & (cos^2\psi - sin^2\psi)\end{bmatrix}\begin{Bmatrix}\sigma_{rr}\\ \sigma_{\theta\theta}\\ \sigma_{r\theta}\end{Bmatrix} \tag{5.14}$$

where $\psi = \alpha - \theta$, *figure 5.1*.

From *equations 5.7 through 5.9* in terms of polar coordinates, the elliptical components of stress of *equations 5A.51, 5A.61 and 5A.71* of Appendix A5 are identified here as *equations 5.15 through 5.17*.

$$\sigma_{\xi\xi} = \left[\begin{matrix} \frac{b_0}{r^2} cos2\psi + 2c_0 \\ -\sum_{n=2,4,\ldots}^{N} \end{matrix} \begin{Bmatrix} a_n\, n\,(n-1)\, r^{n-2}\ cos(n\theta + 2\psi) \\ +b_n\,(n+1) r^n [\, n\, cos(n\theta + 2\psi) - 2\, cos(n\theta)] \\ +\, c_n\, n\,(n+1)\, r^{-(n+2)}\, cos(n\theta - 2\psi) \\ +d_n\,(n-1) r^{-n}\,[n\, cos(n\theta - 2\psi) + 2\, cos(n\theta)] \end{Bmatrix} \right] \tag{5.15}$$

$$\sigma_{\eta\eta} = \left[\begin{matrix} -\frac{b_0}{r^2} cos2\psi + 2c_0 \\ +\sum_{n=2,4,\ldots}^{N} \end{matrix} \begin{Bmatrix} a_n\, n\,(n-1)\, r^{n-2}\,[cos(n\theta + 2\psi)] \\ +b_n\,(n+1) r^n [n(cos(n\theta + 2\psi)) + 2\, cos(n\theta)] \\ +\, c_n\, n\,(n+1)\, r^{-(n+2)} [cos(n\theta - 2\psi)] \\ +d_n\,(n-1) r^{-n}\,[n(cos(n\theta - 2\psi)) - 2\, cos(n\theta)] \end{Bmatrix} \right] \tag{5.16}$$

$$\sigma_{\xi\eta} = \left[\begin{matrix} -\frac{b_0}{r^2} sin2\psi \\ +\sum_{n=2,4,\ldots}^{N} \end{matrix} \begin{Bmatrix} a_n\, n\,(n-1)\, r^{n-2}\, \sin(n\theta + 2\psi) \\ +b_n n\,(n+1) r^n\, \sin(n\theta + 2\psi) \\ -\, c_n\, n\,(n+1)\, r^{-(n+2)} \sin(n\theta - 2\psi) \\ -\, d_n n\,(n-1) r^{-n}\, \sin(n\theta - 2\psi) \end{Bmatrix} \right] \tag{5.17}$$

Adding stresses in polar coordinates (*equations 5.7 and 5.8*) or in Cartesian coordinates (*equations 5.11 and 5.12*) or in elliptical coordinates (*equations 5.15 and 5.16*) gives the following equation for isopachic stress.

$$S = \sigma_{xx} + \sigma_{yy} = \sigma_{rr} + \sigma_{\theta\theta} = \sigma_{\xi\xi} + \sigma_{\eta\eta} \tag{5.18}$$

$$S = \left[4\,c_0 + \sum_{n=2,4,\ldots}^{N} \begin{Bmatrix} +b_n\, 4\,(n+1) r^{n} \cos(n\theta) \\ -d_n\, 4\,(n-1) r^{-n} \cos(n\theta) \end{Bmatrix} \right] \tag{5.19}$$

A detailed derivation of the expressions of *equations 5.7 through 5.19* is contained in *equations 5A.36 through 5A.123* of Appendix A5. While coefficient a_0 appears in the Airy potential function ϕ of *equation 5.6*, it is absent in the expressions for the individual stress components *(equations 5.7 through 5.19)* as a result of differentiation. All of the coefficients present in this expression of *equation 5.19* for isopachic stress can be evaluated experimentally from measured temperatures, that is by recording the TSA signal, *S**, which is proportional to the sum of the radial and tangential stresses *(equation 5.1)*. However, referring to *equation 5.19,*

$$S = f(c_o, b_n, d_n \text{ for } n = 2, 4, 6\ldots N) \tag{5.20}$$

and from *equations 5.7 through 5.17,*

$$\sigma_{rr} = f(b_o, c_o, a_n, b_n, c_n, d_n \text{ for } n = 2, 4, 6\ldots N) \tag{5.21}$$

$$\sigma_{\theta\theta} = f(b_o, c_o, a_n, b_n, c_n, d_n \text{ for } n = 2, 4, 6\ldots N) \tag{5.22}$$

$$\sigma_{r\theta} = f(a_n, b_n, c_n, d_n \text{ for } n = 2, 4, 6\ldots N) \tag{5.23}$$

$$\sigma_{xx} = f(b_o, c_o, a_n, b_n, c_n, d_n \text{ for } n = 2, 4, 6\ldots N) \tag{5.24}$$

$$\sigma_{yy} = f(b_o, c_o, a_n, b_n, c_n, d_n \text{ for } n = 2, 4, 6....N) \quad (5.25)$$

$$\sigma_{xy} = f(b_o, a_n, b_n, c_n, d_n \text{ for } n = 2, 4, 6....N) \quad (5.26)$$

$$\sigma_{\xi\xi} = f(b_o, c_o, a_n, b_n, c_n, d_n \text{ for } n = 2, 4, 6....N) \quad (5.27)$$

$$\sigma_{\eta\eta} = f(b_o, c_o, a_n, b_n, c_n, d_n \text{ for } n = 2, 4, 6....N) \quad (5.28)$$

$$\sigma_{\xi\eta} = f(b_o, a_n, b_n, c_n, d_n \text{ for } n = 2, 4, 6....N) \quad (5.29)$$

If all coefficients which appear in the individual components of stress (*equations 5.21 through 5.29*) also exist in the equation for isopachic stress (*equation 5.20*), then the individual components of in-plane stress in the plate of *figure 5.2* could be evaluated from only measured TSA data. Comparing *equations 5.20 through 5.31* shows that coefficients present in the expression for isopachic stress are also present in the expressions for individual stresses. However, the individual components of stress also contain the Airy coefficients b_o, a_n and c_n *(equations 5.21 through 5.29)* which are absent in the isopachic stress, *equation 5.19*. Therefore the separate stress components cannot be determined from only thermoelastic data through the expression for the isopachic stress *(equation 5.19)*. But imposing the traction-free conditions i.e., zero normal and shear stress around the boundary of the elliptical hole, together with measured temperature information (and *equation 5.1*) does enable all of the Airy coefficients of *equations 5.21 through 5.29* to be evaluated.

Imposing the traction-free boundary conditions *discretely* on the boundary of the elliptical hole ($\sigma_{\xi\xi} = \sigma_{\xi\eta} = 0$ at r = R (where R of *equation 5.30* maps the boundary of the elliptical hole for a = 19.05mm (0.75″) and b = 9.525mm (0.357″))) and for all values of θ), together with measured TSA data, evaluates all the unknown Airy coefficients.

Referring to *figures 5.1 and 5.2 and* Appendix A5*,*

$$R^2 = \frac{a^2 b^2}{a^2 sin^2\theta + b^2 cos^2\theta} \tag{5.30}$$

where a = 38.1 mm, b = 19.05 mm and θ is the polar angle in first quadrant.

From *equations 5.15 and 5.17 and figure 5.1*, one obtains on the edge of the hole,

$$\sigma_{\xi\xi}(@\ r = R) = \left[\begin{array}{c} \frac{b_0}{R^2} cos2\psi + 2c_0 \\ -\sum_{n=2,4,\ldots}^{N} \left\{ \begin{array}{c} a_n\, n\,(n-1)\, R^{n-2}\ cos(n\theta + 2\psi) \\ +b_n\,(n+1) R^n [\, n\, cos(n\theta + 2\psi) - 2\, cos(n\theta)] \\ +\, c_n\, n\,(n+1)\, R^{-(n+2)}\, cos(n\theta - 2\psi) \\ +d_n\,(n-1) R^{-n}\,[n\, cos(n\theta - 2\psi) + 2\, cos(n\theta)] \end{array} \right\} \end{array} \right] = 0 \tag{5.31}$$

$$\sigma_{\xi\eta}(@\ r = R) = \left[\begin{array}{c} -\frac{b_0}{R^2} sin2\psi \\ +\sum_{n=2,4,\ldots}^{N} \left\{ \begin{array}{c} a_n\, n\,(n-1)\, R^{n-2} \sin(n\theta + 2\psi) \\ +b_n n\,(n+1) R^n \sin(n\theta + 2\psi) \\ -\, c_n\, n\,(n+1)\, R^{-(n+2)} \sin(n\theta - 2\psi) \\ -\, d_n n\,(n-1) R^{-n} \sin(n\theta - 2\psi) \end{array} \right\} \end{array} \right] = 0 \tag{5.32}$$

Gathering *equations 5.19, 5.31 and 5.32* together gives:

$$[A]\ \{c\}\ = \{d\} \tag{5.33}$$

$$\begin{bmatrix} \sigma_{\xi\xi}(r=R) \\ \vdots \\ S \\ \vdots \\ \sigma_{\xi\eta}(r=R) \end{bmatrix} = \begin{bmatrix} cos2\psi/R^2 & \cdots & \cdots & (n-1)R^{-n}\left[n\,cos(n\theta-2\psi)+2\,cos(n\theta)\right] \\ \vdots & \vdots & & \vdots \\ 0 & \cdots & \cdots & -4\,(n-1)r^{-n}\,cos(n\theta) \\ \vdots & \vdots & & \vdots \\ -sin2\psi/R^2 & \cdots & \cdots & -n\,(n-1)R^{-n}\sin(n\theta-2\psi) \end{bmatrix} \begin{bmatrix} b_o \\ \vdots \\ \vdots \\ \vdots \\ d_n \end{bmatrix}$$

$$= \begin{bmatrix} 0 \\ \vdots \\ S \\ \vdots \\ 0 \end{bmatrix} \tag{5.34}$$

Thus, by incorporating the boundary conditions around the central hole *discretely*, all the unknown Airy coefficients b_o , c_o , a_n , b_n , c_n , d_n *for n = 2, 4, 6.…N* can be evaluated from the measured TSA data. Recognizing it is advantageous to employ more side conditions (temperature data plus discrete local traction-free boundary conditions) than unknown, an effective way to evaluate the large number of unknowns from the over-determined system of equations is to utilize least-squares method. An over-determined system has more equations (i.e., collect more values of S) than unknowns. Doing so enables one to obtain the individual components of stress from the thermoelastically measured S (= S^*/K). Moreover, equilibrium and compatibility are automatically satisfied within experimental error and the consequences of truncating the series expressions of *equation 5.2* at some finite number of terms.

The traction-free conditions on the edge of the elliptical hole are imposed *discretely* rather than *analytically* because the terms inside and outside the summation in the equations for the normal and shear stresses at the boundary of the elliptical hole are dependent, i.e., *equations 5.15 and 5.17,* and cannot be separated when equating the expressions for these stresses to zero. Not being able (as can sometimes be done, [4, 8]) to reduce the number of coefficients here by imposing the traction-free conditions on the edge of the hole *analytically* means one cannot

match the coefficients in the expressions for the individual stresses are as in the isopachic stress, *equation 5.19*. However, imposing $\sigma_{\xi\xi} = \sigma_{\xi\eta} = 0$ at r = R (where R maps the boundary of the elliptical hole having a = 19.05 mm (0.75″) and b = 9.525 mm (0.357″)) on the boundary of the elliptical hole *point-wise/discretely* enables the Airy matrix expression *Ac = d* of *equations 5.33 and 5.34* to also include the additional normal and shear stress expressions of *equations 5.31 and 5.32*, thereby containing the coefficients that are absent in the isopachic stress of *equation 5.19*. Reducing the number of coefficients by incorporating the local traction-free conditions *analytically/continuously*, as opposed to *piece-wise/discretely*, can be advantageous. However, reference [8] shows that although imposing the traction-free conditions on the edge of a hole discretely rather than *analytically* means more coefficients must now be evaluated which causes the least-squares process to involve more equations, imposing traction-free condition *discretely* or *analytically* gives the some results. This concept to reduce the number of thermoelastic coefficients by imposing local conditions *analytically* in believed to be new with reference [10]. Fewer independent Airy coefficients can simplify the least-square calculation and means less measured input information might be needed for their determination.

Measured TSA data can be noisy so it is advantageous to use more measured input values of S plus known boundary conditions than unknowns and to determine the Airy coefficients by least squares using the commercial MATLAB software as discussed in section 5.4.

Detailed derivations of all of the previous the equations are contained in Appendix A5.

5.4 Experimental Details

5.4.1 Specimen Details and Preparation

Figure 5.2 shows the aluminum specimen (alloy 6061-T6), its geometry, dimensions, and orientation and location of the co-ordinate axes. Explanations for studying this geometry and loading are discussed previously in section 5.2, General Comments. Following are the details of the plate tested for the succeeding analyses and results:

- Material of the plate: Aluminum 6061-T6 (Wiedenbeck, Inc., Madison, WI); Ultimate strength = 275 to 311 MPa (40 to 45 ksi) and Yield strength = 241 to 275 MPa (35 to 40 ksi).
- Unless stated otherwise, the plate was subjected to a cyclically varying sinusoidal load with a mean value of 3558.57 N (800lb), maximum value of 5782.68 N (1300lb) and a minimum value of 1334.46 N (300lb) at a frequency of 10Hz.
- 3558.57 N (800lb) ± 2224.11 N (500lb) at 10Hz, unless state otherwise.
- Loading Range (F) = 4448.22 N (1000lb), unless state otherwise.
- Major Diameter of the Elliptical hole (2a) = 38.10 mm (1.5″), *figure 5.2*.
- Minor Diameter of the Elliptical hole (2b) = 19.05 mm (0.75″), *figure 5.2*.
- Thickness of the plate (t) = 6.35mm (0.25″).
- Length of the plate (L) ≈ 279.4 mm (11″), *figure 5.2*.
- Width of the plate (W) = 76.2 mm (3″), *figure 5.2*.
- Plate of *figure 5.2* is symmetrical about both axes (x- and y-axes).

The aluminum plate was sprayed with Krylon Ultra-Flat black paint to provide an enhanced and uniform emissivity *(figure 5.3)*. However, before applying the black paint, the plate was polished with a 400 grit sand paper so as to have an ideal surface finish for the black paint to adhere to *(figure 5.4)*. This slightly-roughened surface also provided a desirable surface finish on which to bond the strain gages. Since one wishes to be able to record reliable temperatures as close as possible to the edge of the holes, care was taken when sanding the faces of the specimen not to round-off the edge of the hole.

Fig. 5.3: Aluminum plate coated with Krylon Ultra-Flat black paint

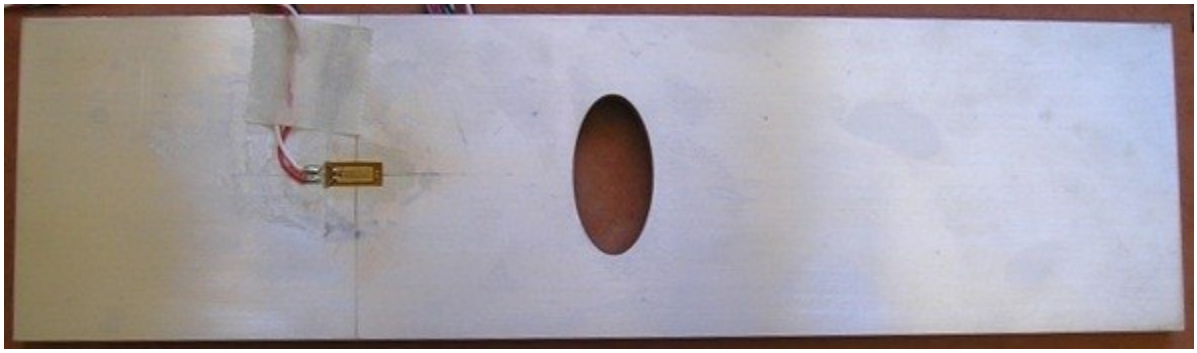

Fig. 5.4: Aluminum plate surface preparation (front side of the plate before spraying)

5.4.2 Specimen Loading

TSA is based on the fact that materials experience a temperature change when compressed or expanded. *Figures 5.5 through 5.8* show the specimen loading and TSA recording equipment employed. The aluminum plate was mounted in the loading frame of the hydraulic testing machine *figures 5.6 through 5.8,* and subjected to a cyclic loading varying sinusoidally from 3558.57 N (800lb) to 5782.68 N (1300lb) at a rate of 10Hz. The oscilloscope of *figure 5.5* was employed to accurately monitor the applied load and frequency. The loading was applied using an MTS machine (20Kips capacity having hydraulic grips capable up to 18.5 Kips, Rm. B321, EH) that can operate in either load or displacement control with any of four ranges (10%, 20%, 50% and 100% measure of capacity), *figure 5.8.* For the current analysis, the 50% range was utilized in load control which allows for a maximum load of 44482.2 N (50% of 20,000lb = 10,000lb). The hydraulic grips apply a uniform clamping pressure (which can be adjusted as per the material) over both ends of the specimen, *figures 5.6 and 5.7.* The corresponding load-induced temperature effect was recorded by a TSA Delta Therm model DT1410 camera (sensor array of 256 horizontal x 256 vertical pixels), *figures 5.6 and 5.8*.

The test plate was aligned between the top and the bottom grips as illustrated in *figure 5.7.* When clamping the specimen between the hydraulically operated grips, particular care was taken that the plate is symmetrically loaded about vertical *y*-axis. This was done by measuring the distance from the end of the grips to the plate edge (on either side, *figure 5.7*). Any possible out-of-plane plate bending was minimized by monitoring the strains obtained from the strain gages mounted on the front and the back faces of the plate. Details about strain gage mounting, location and type of gages used are included in section 5.8.

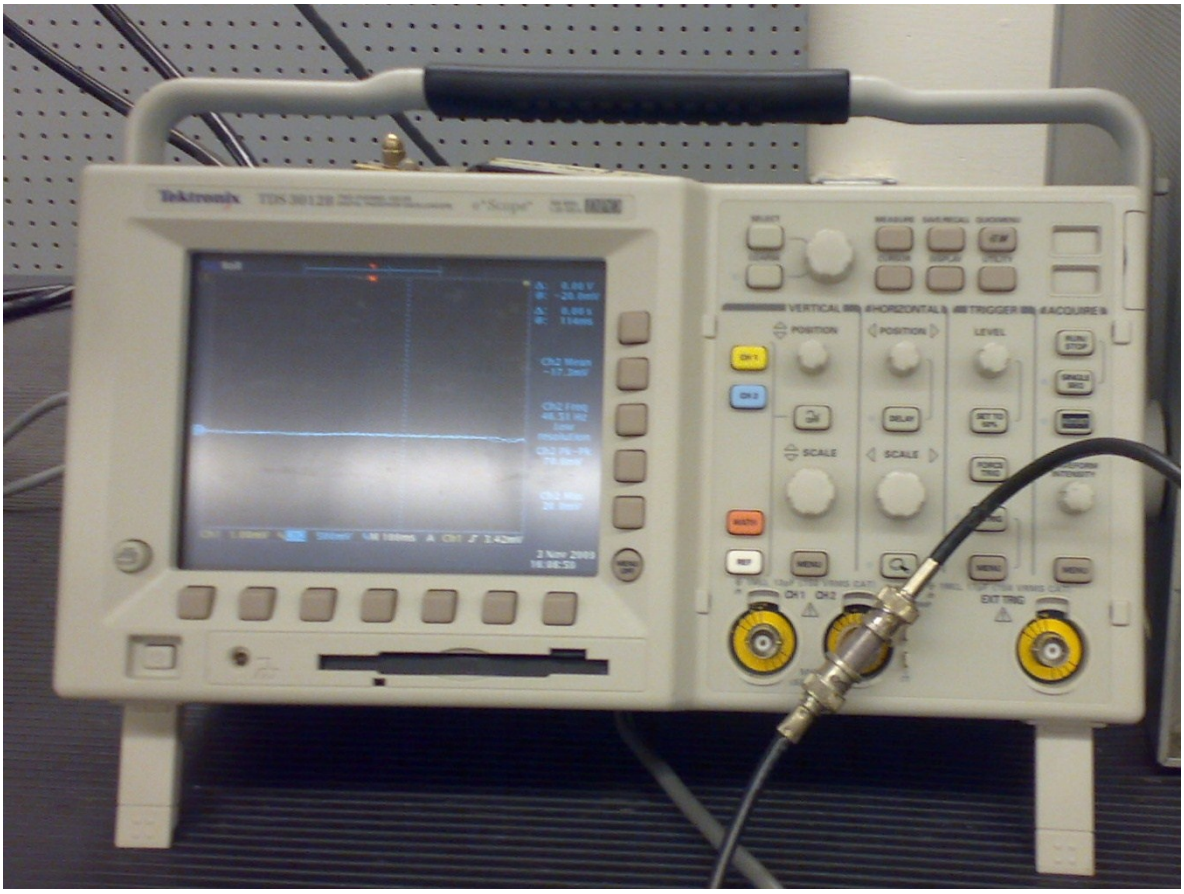

Fig. 5.5: Oscilloscope for accurate measurement of cyclic loads

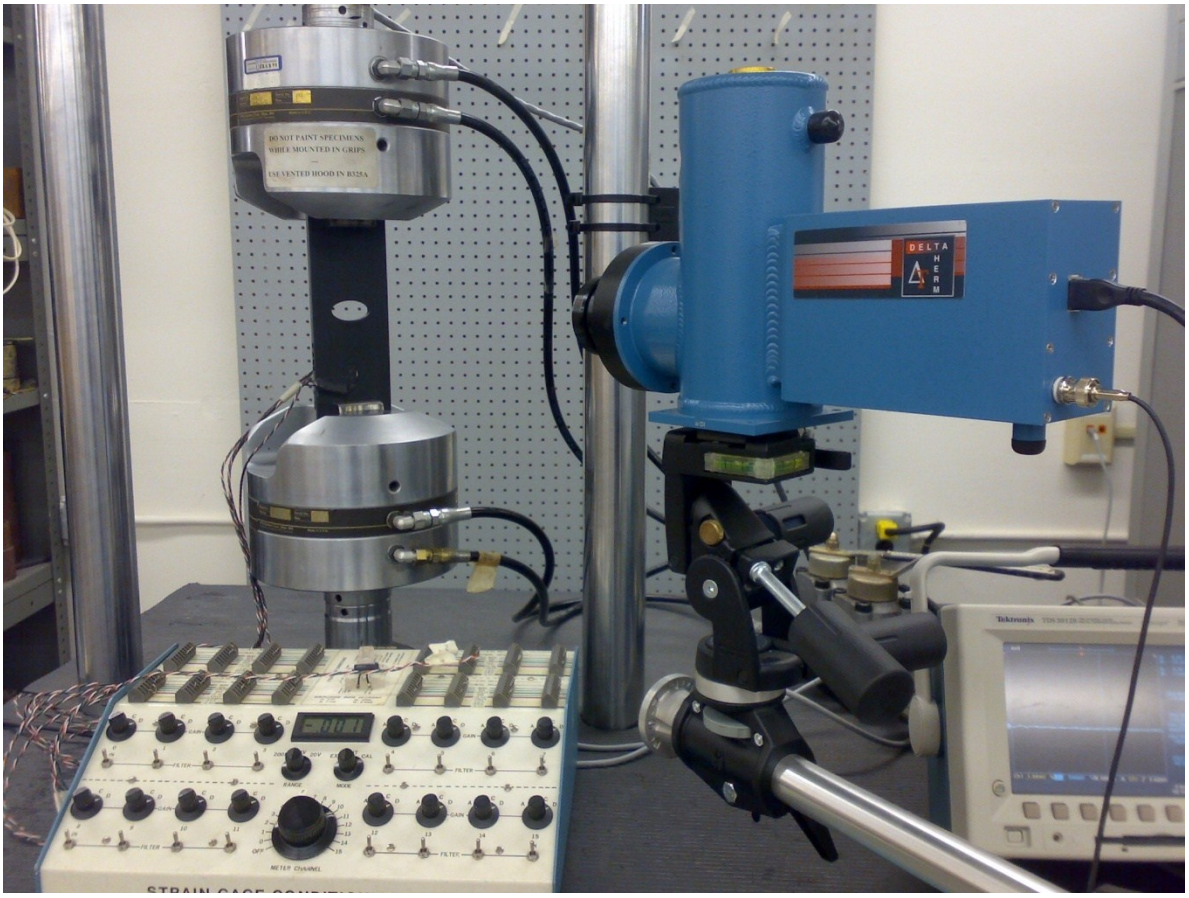

Fig. 5.6: Specimen in loading frame with Delta Therm DT1410 infrared camera

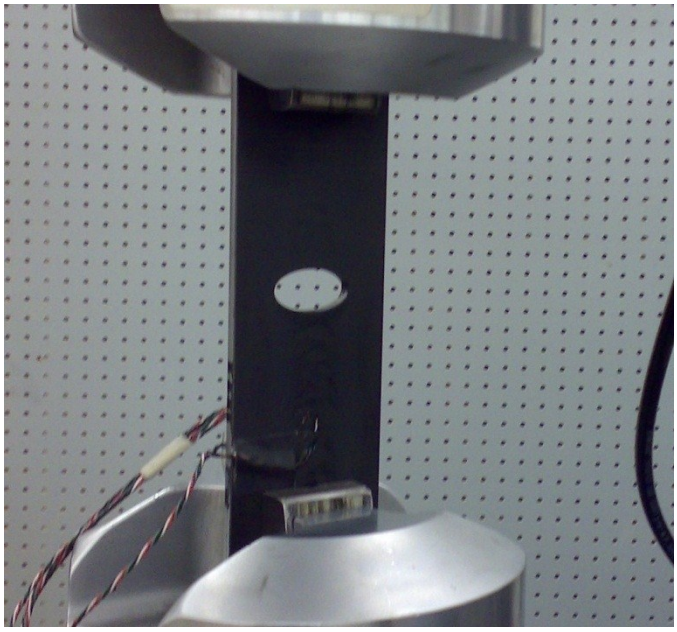

Fig. 5.7: Specimen loaded in hydraulic grips

5.4.3 TSA Recording

TSA temperature data were recorded by a DeltaTherm model DT1410 staring-array infrared system (Stress Photonics Inc., Madison, WI, USA) which is cooled with liquid-nitrogen, *figure 5.6*. The DeltaTherm model DT1410 has a sensor array with a spatial resolution of 256 horizontal x 256 vertical pixels. The prepared specimen was loaded in the MTS machine, the TSA camera focused on the specimen and the thermoelastically-recorded signal, S*, was recorded by the data acquisition system which is equipped with the Delta Vision software as seen in *figure 5.8*. TSA images were captured and averaged over two-minute durations. The TSA images (such as that of *figure 5.9*) were then exported to Excel®, converting each pixel into a data point i.e., giving a 256 x 256 matrix which provides the ability to carry out further analysis. The Delta Vision software gives a pixel size of approximately 0.272mm (0.01″) covering the specimen. This Delta Vision pixel size differs from the actual size a pixel covers on the specimen. The actual pixel size on the specimen was evaluated from the dimensions of the plate i.e., the major and minor diameters of the elliptical hole, and the width of the plate. The actual pixel size here at the plate was found to be 0.48 mm (0.0189″). *Figure 5.9* shows an actual TSA image from the Delta Vision software which contains (256x256 = 65,536) data values, of which approximately 40,000 pixels cover the plate. Since TSA data are typically unreliable on and near an edge, no recorded temperatures were used within at least two data (pixel) positions (~ 0.96 mm or 0.038″) of the boundary of the elliptical hole.

The specimen of *figures 5.2 through 5.4, 5.6, 5.7 and 5.8* was loaded in a MTS machine (RM B321 Engineering Hall, UW Madison) which has cyclic capability. The applied sinusoidal load was accurately monitored with the oscilloscope seen in *figure 5.5*. Load control was

employed with the maximum load capacity of 44482.2 N (10,000 lbs). This means 10 volts = 10,000 lbs (or 1 volt = 1,000 lbs). *Figure 5.10* is the image from the oscilloscope which can be obtained using a floppy drive (usually done) or by connecting the oscilloscope to a Local Area Network (LAN) connection and receiving the oscilloscope image through the following link: http://scope2.ep.wisc.edu/ while performing the TSA experiment. The oscilloscope of *figure 5.5,* contains grid markings which permit one to measure both voltage on the vertical axis (associated with load) and time on the horizontal axis of the waveform. The frequency at which the specimen is being cycled can also be determined by measuring the waveform period and taking it's reciprocal. In the case of *figure 5.10* the mean load signal is 803 mV which corresponds to 803 lbs (since 1V = 1,000lb), peak to peak load applied to the specimen is 1.04 volts (~1040 lbs) at a frequency of ~10Hz, and the maximum load on the specimen is the 1.30 V (1,300 lbs).

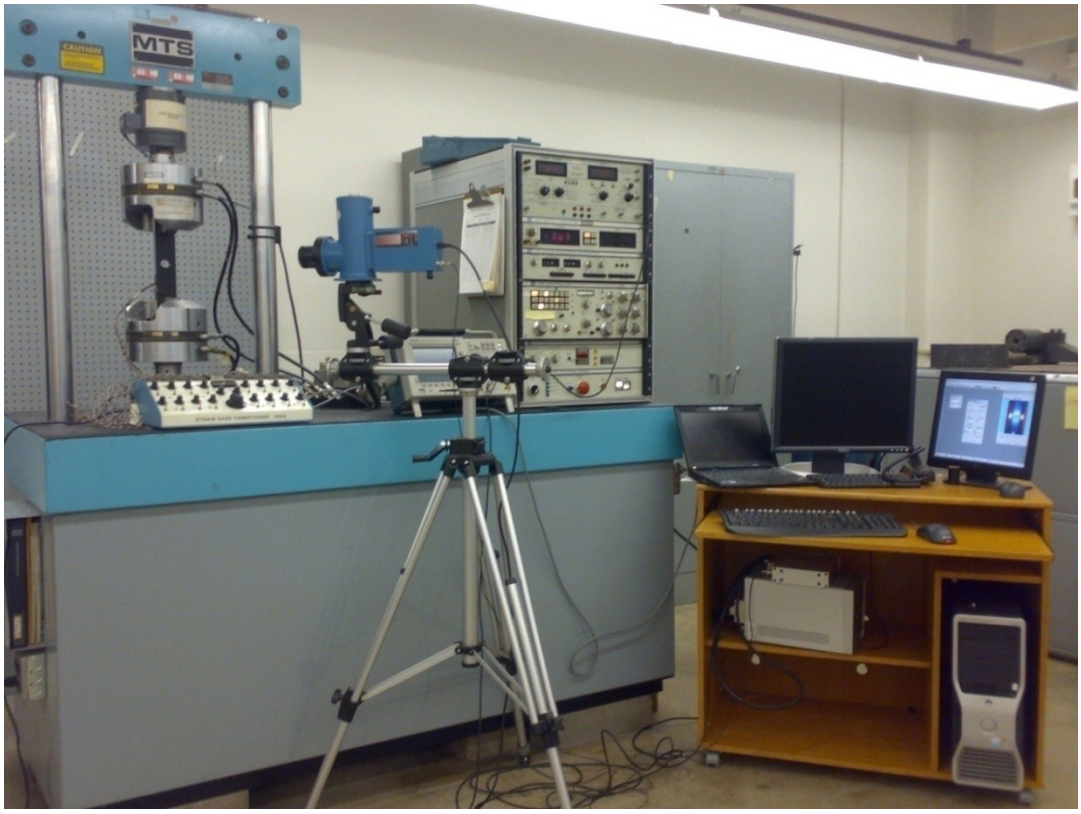

Fig. 5.8: Test Setup

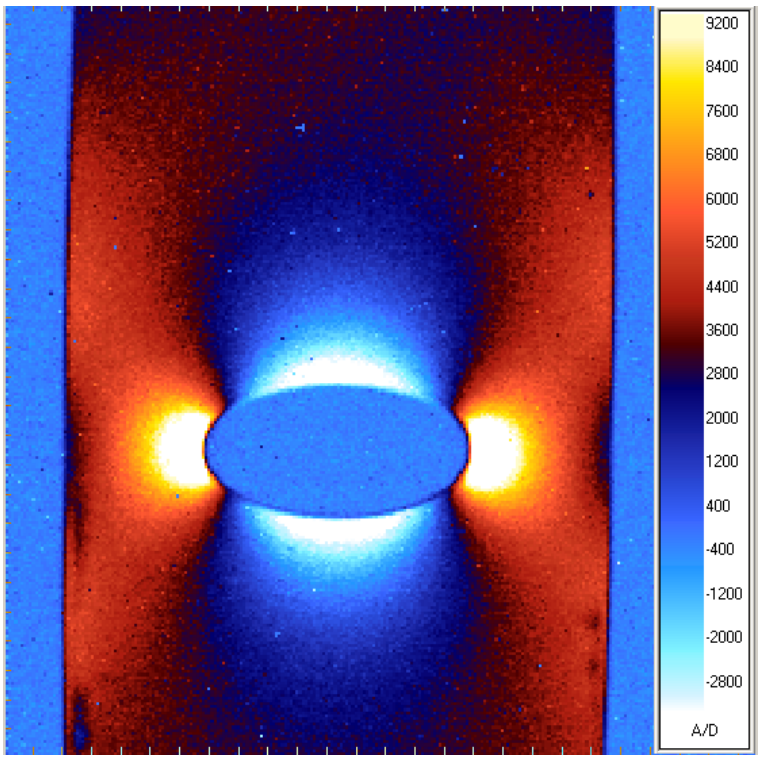

Fig. 5.9: TSA image, S*, for a load range of 4448.22 N (1000lb)

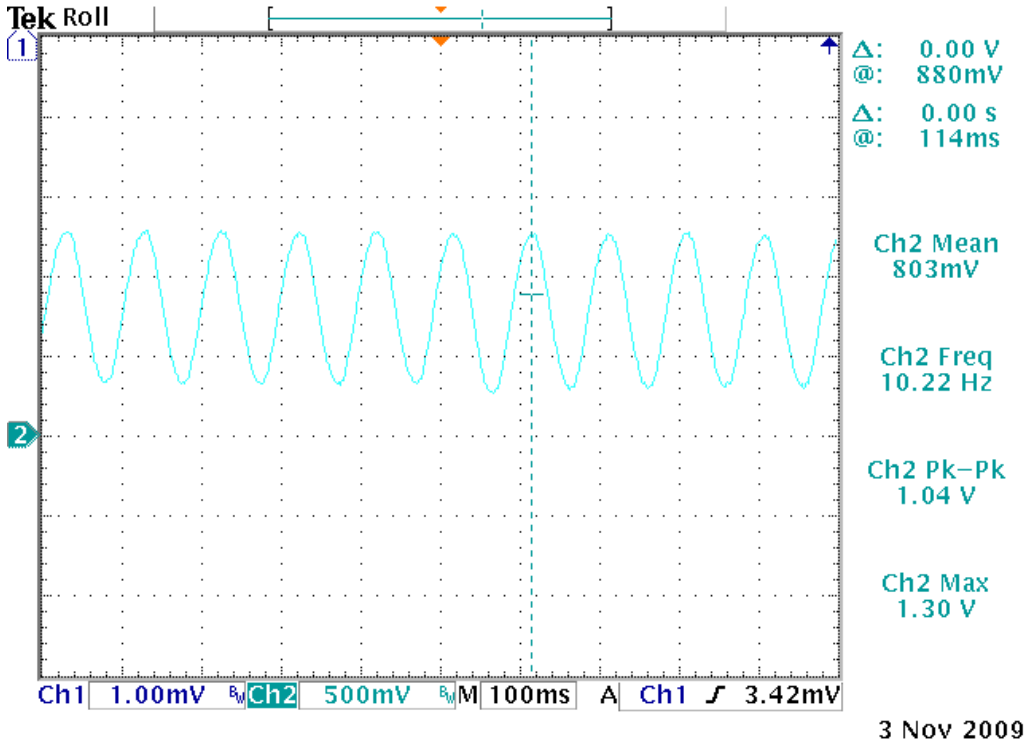

Fig. 5.10: Oscilloscope image while performing TSA

The oscilloscope used to monitor accurately the specimen cyclic loading rate and specified load range is visible between the TSA camera and the MTS control box in *figure 5.8*. The Delta Therm camera (Stress Photonics Inc., Madison, WI, USA), which records the temperature variations in the perforated plate, is aligned to be exactly perpendicular to the surface of the plate. This was done with the aid of two spirit levelers which are mounted at the base of the TSA camera *(figures 5.6 and 5.8)*.

Figure 5.9 shows an actual TSA image as recorded and displayed by the Delta Vision software which provides data acquisition and interpretation tools. Note that the TSA image (*figure 5.9*) captures only about 120.6 mm (4.75″) of the total specimen length, *figure 5.2*. This image of *figure 5.9* was averaged and recorded over a period of two minutes.

5.4.4 TSA Calibration

TSA Calibration simply means to determine the thermoelastic constant, K, as defined by *equation 5.1*. The coefficient, K is often evaluated in a component whose complete state of stress is known, usually at a location far from any stress concentration and/or where there is a uniform 1-D state of stress. Since the plate geometry of *figure 5.2* does not contain any region possessing a known or uniform 1-D state of stress, *figure 5.9*, an indirect approach was utilized to calibrate the experimental data. The thermoelastic calibration was achieved here from a tensile specimen of the same material and "identical" (thickness, etc.) coating of flat black paint and tested using the same TSA recording characteristics. This can be accomplished by spraying both the test and calibration specimens simultaneous, or by subsequently machining a tensile specimen from the actual component. A separate uniaxial tensile calibration specimen was used here, *figure 5.11*. It is best to calibrate the TSA data on the same day as the component environmental effects (temperature and humidity). Other calibration approaches could utilize strain gages to determine the isopachic stress at a location. If strain gages are used, one should employ symmetrical positions (gages at one and record S* at the other), or record S* on one face of the component and the gages on the back face. This is to ensure the strain gages do not influence the local stress field and hence the TSA signal. As discussed in section 5.2, under plane stress, the temperature effects relating the stresses for an isotropic material are governed by the following equation:

$$S^* = K\Delta S$$

$$S^* = K\Delta\left[(\sigma_1 + \sigma_2) = (\sigma_{rr} + \sigma_{\theta\theta}) = \left(\sigma_{xx} + \sigma_{yy}\right) = \left(\sigma_{\xi\xi} + \sigma_{\eta\eta}\right)\right] \quad (5.1)$$

where S^* is the recorded TSA signal, K is the thermo-mechanical coefficient (determined experimentally), and ΔS is the change in isopachic stress or the sum of the normal stresses.

The only difference between this calibration specimen and the perforated test component is the former does not have any holes or any such irregularity and is symmetrical about both of its x and y axes *(figure 5.11)*. The stress distribution is consequently uniform and known (only uniaxial tension). The calibration specimen used is of the same material as the actual test specimen (Aluminum 6061-T6), 279.4 mm (11″) long, 25.4 mm (1″) wide and 6.35 mm (0.25″) thick. Thus, knowing the recorded thermoelastic signal, S^* (which was scanned along horizontal lines at different levels/height of the strip and then averaged), applied load and the cross sectional area of the specimen, the thermomechanical coefficient K was determined from S^*/uniform stress, giving K = 265.42 U/MPa (1.83 U/psi). The holes at the ends (within the grips) of the calibration specimen of *figure 5.11* are irrelevant to the present situation.

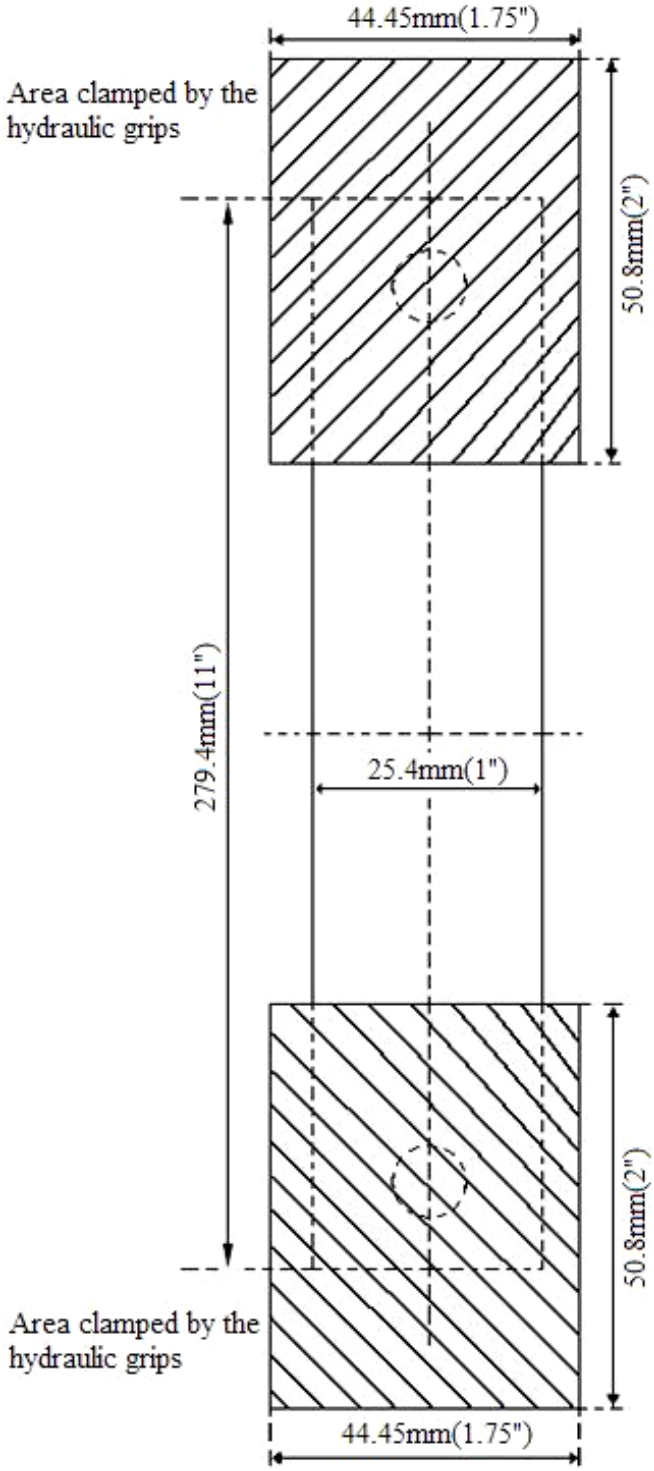

Fig. 5.11: Calibration specimen

Figure 5.12 shows the experimental setup while calibrating the specimen. The calibration specimen contained a total of four strain gages, two on the front and two on the back (one longitudinal and one transverse on each side), to monitor the strains. Particular care was taken to ensure proper specimen alignment during testing by monitoring the strains on the front and back surfaces of the calibration specimen.

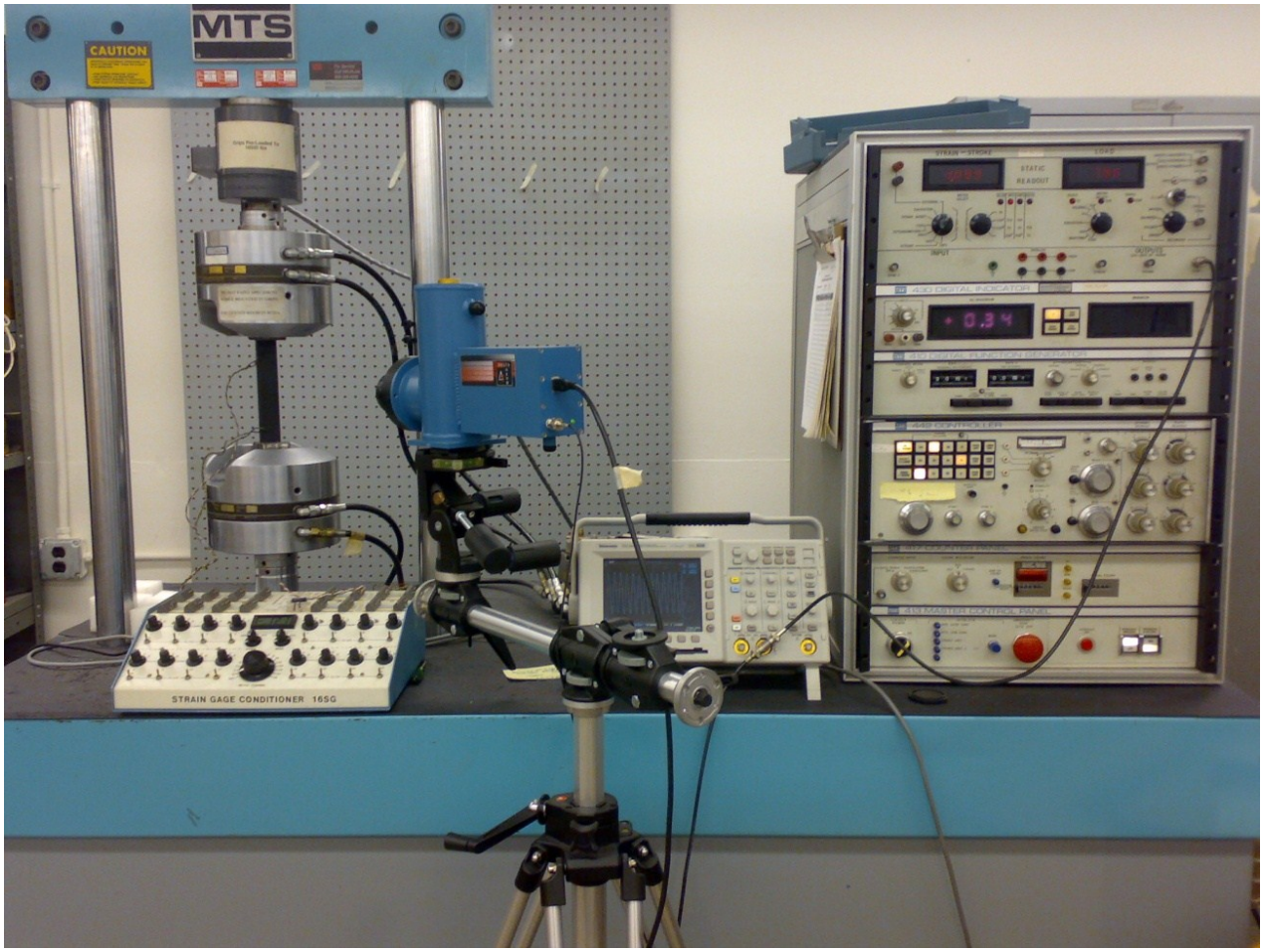

Fig. 5.12: Experimental setup for the calibration specimen

5.5 Data Processing

Thermoelastic stress analysis assumes adiabatic and reversible conditions to obtain isopachic stress information from measure temperatures. The measured TSA data, along with satisfying the traction-free conditions ($\sigma_\xi = \sigma_{\xi\eta} = 0$) on the edge of the hole, enables evaluating all of the unknown Airy coefficients. Commercial TSA systems are able to provide vast amounts of measured temperature information expeditiously, something which can be tedious for alternative experimental approaches such as strain gages. The actual recorded TSA image *(figure 5.9)* contains approximately 40,000 data values of S^* associated with the stresses in the plate (i.e., 40,000 data values cover the plate). Since an objective of this research is to evaluate individual components of stress in the vicinity of the hole, the analysis emphasizes utilizing measured thermal data S^* which originate in the neighborhood of the hole *(figure 5.9)*. That the test plate is symmetrical about the both the *x* and *y* axes *(figure 5.2)* permits averaging the TSA data throughout the four quadrants[2]. However, recognizing the typical unreliability of TSA data near an edge *(figure 5.9)*, it is convenient to omit using measured data at least two data positions (~ 0.96 mm or 0.0378″) away from the boundary of the elliptical hole.

---

[2]The Delta Therm system displays the recorded experimental data, S^*, in the form of a matrix containing 256 horizontal rows and 256 vertical columns such that each entry/cell represents the respective measured TSA value, S^*. Corresponding entries/cells are symmetrical about the both the x and y-axes when the origin is at the center of the elliptical hole. The recorded temperature information was therefore added from all the four quadrants and divided by four to provide average TSA data throughout a quadrant.

The $m = 1703$ measured TSA values of S^* utilized and the $h = 146$ traction-free conditions on the boundary of the hole (i.e. for a total of $m+h = 1849$ input values or side conditions) were combined to evaluate the k unknown Airy coefficients. The matrix *equations 5.33 and 5.34* can be written as

$$[A]_{(m+h)xk}\{c\}_{kx1} = \{d\}_{(m+h)x1} \tag{5.35}$$

where matrix [A] includes the m Airy isopachic equations in polar coordinates, r and θ, such that one horizontal expression of the [A] matrix of *equation 5.34* exists for each measured input data value of S (= S^*/K) associated with *figure 5.9* (but temperature data averaged about both the axes). Matrix [A] also contains $h/2 = 73$ expressions for each of $\sigma_{\xi\xi} = \sigma_{\xi\eta} = 0$ imposed at the boundary of the elliptical hole. Vector {c} of *equation 5.35* contains the k unknown Airy coefficients (i.e., b_o , c_o , a_n , b_n , c_n , d_n *for n = 2, 4,...N*). The stress vector {d} of *equation 5.35* therefore contains the traction-free normal and shear stresses at the boundary of the elliptical hole as well as measured values of S within the plate near the hole.

Not unlike most test information, recognizing that the actual measured data often incorporates some noise/scatter, it is beneficial to employ significantly more equations (i.e., more side conditions) than the number of unknown coefficients, k, i.e., $(m+h) > k$. The linear least-squares method is a convenient way to solve the over-determined matrix equation $Ac = d$ of *equations 5.34 and 5.35*. *Equation 5.35* was solved using the '\' matrix division operator and pseudo inverse 'pinv' operator in MATLAB. This operators employs the algorithm for least squares and calculates vector {c} by $c = A\backslash d$ *or* $c = pinv*d$ *or* $c = \{[A]^T[A]\}^{-1}[a]^T\{d\}$.

5.6 Analysis

5.6.1 Measured TSA Input Data and the Number of Airy Coefficients

As discussed in the previous section, a total of 1,849 input values were used to evaluate the unknown Airy coefficients for analyzing the elliptically perforated finite-plate of *figure 5.2.* Of these, 1,703 are measured TSA values originating at source locations which are averaged in all the four quadrants as shown in *figure 5.13,* and 146 are the traction-free conditions $\sigma_{\xi\xi} = \sigma_{\xi\eta} = 0$ imposed *discretely* at 73 locations along the quarter boundary of the elliptical hole, *figure 5.2*.

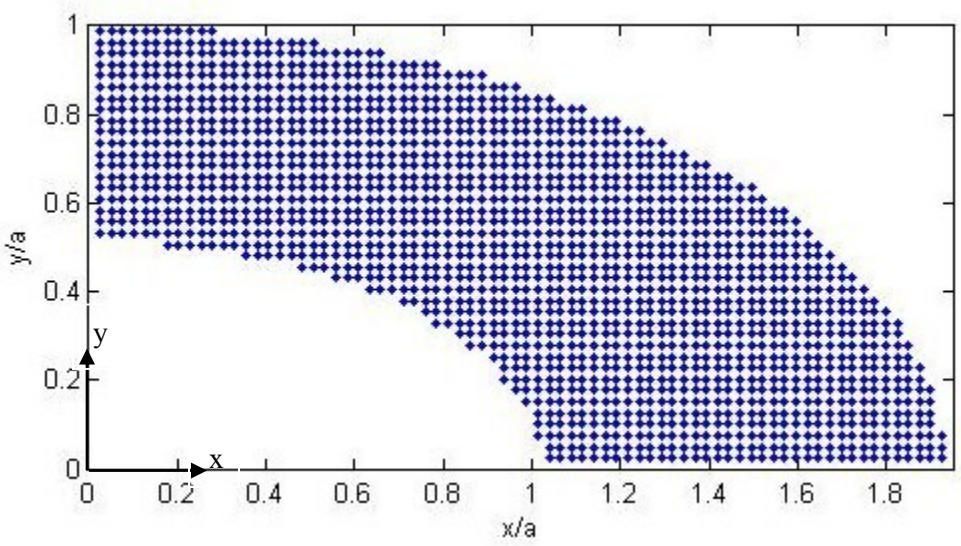

Fig. 5.13: TSA source locations (*m = 1,703*) for 1,849 input values (*m+h = 1,849*).

Referring to *figures 5.9 and 5.13*, the distance between the adjacent TSA centers is written in the form of pixels i.e., the number of pixels lying between the centers of the adjacent source locations. However, when operating with the Delta Vision software for data interpretation, each pixel position of *figures 5.9 and 5.13* is represented in the form of a

cell/entry of a huge matrix consisting of rows and columns. Each cell/entry of the matrix stores the respective value of the recorded TSA data S^*, as described in sections 5.4.3 and 5.5.

TSA-recorded information within at least two pixel locations (~ 0.96 mm or 0.038″) of an edge is usually unreliable. The utilized TSA measured data of *figure 5.13* are all at least two pixels away from the elliptical boundary. The subsequent analysis will demonstrate that the described approach is able to evaluate stresses reliably at the edge of the elliptical hole without using any input measured temperatures on, or very near, the edge. Having the 1,703 measured isopachic stresses S (= S^*/K) plus the *discretely* imposed traction-free condition on the boundary of the hole, one is able to set up the matrix equation $Ac = d$ of *equation 5.35*. Matrix [A] contains $m+h = 1{,}849$ side conditions (isopachic expressions along with traction-free conditions) having k unknown Airy coefficients for the m = 1,703 TSA recorded values at the locations of *figure 5.13* and h = 146 imposed traction-free condition. Vector $\{c\}$ contains k Airy coefficients and vector $\{d\}$ is composed of the m = 1,703 TSA values of S at locations in *figure 5.13* and the 146 *discretely* imposed traction-free condition (at h/2 = 73 locations) associated with the $m+h = 1{,}849$ equations forming the matrix [A].

It is important to determine an appropriate number of Airy coefficients, k, to be used for $m+h = 1{,}849$ input side values. *Equations 5.6 through 5.19* involve a summation over n where n goes through positive even integers from 2 to N. Evaluating the appropriate number of Airy coefficient is important because too few Airy coefficients can produce inaccurate results, while too many Airy coefficients can cause the Airy matrix, [A] of *equation 5.35* to become unstable or even singular due to computer round-off errors. The amount of measured input data needed could depend on the number of coefficients, k, i.e., an increase in the number of coefficients can

necessitate more experimental values of S^*. A prevalent method of assessing an appropriate number of coefficients to use employs the condition number, C, of the matrix $[A]$, as an indicator of potential matrix singularity. Since matrix $[A]$ (*equation 5.35*) in this analysis contains many zero terms due to absence of coefficients b_o, a_n, *and* c_n in the equation for the isopachic stress S (i.e., *equations 5.19 and 5.20*), it will be shown that this is not a viable way in this situation to evaluate the number of coefficients to retains[3]. The alternative techniques employed here to evaluate an appropriate number of coefficients in the analyses are based on the *RMS* (Root Mean Square) method and reconstructed images of S.

Figures 5.14 and 5.15 demonstrate that for a fixed number of input values, the matrix instability grows exponentially with increasing number of Airy coefficients. That is because the number of zero-terms in the matrix [A] (*equation 5.34*) is increasing i.e., as the value of summation N in *equation 5.19* increases, the number of zeros in matrix *equation 5.34* increases. This tends to increase the instability of the [A] matrix exponentially. This precludes using the condition number from providing a value for the number of Airy coefficients to retain. However, the *RMS* (Root Mean Square) method is effective for determining an appropriate number of Airy coefficients. It is desired that *RMS* value be small. After evaluating (experimentally for a selected

[3]The many zeros in matrix [A] are associated with imposing $\sigma_{\xi\xi} = \sigma_{\xi\eta} = 0$ *discretely* on the edge of the hole. This satiation does not occur when imposing the traction-free condition on the edge of the hole *analytically*.

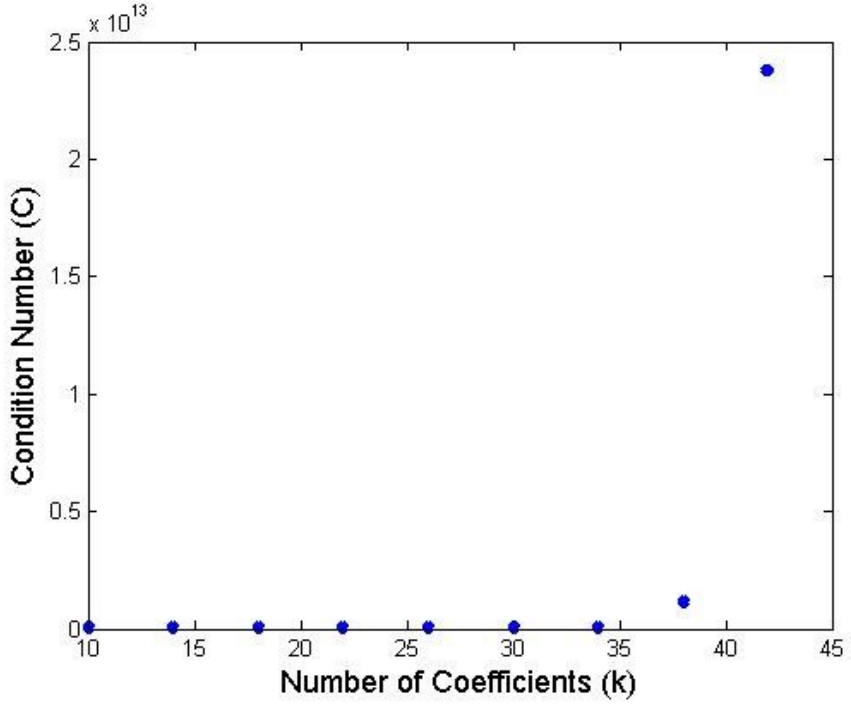

Fig. 5.14: Plot of condition number, *C*, vs number of coefficients, *k*, for *m+h = 1,849* input values (*m = 1,703* TSA values)

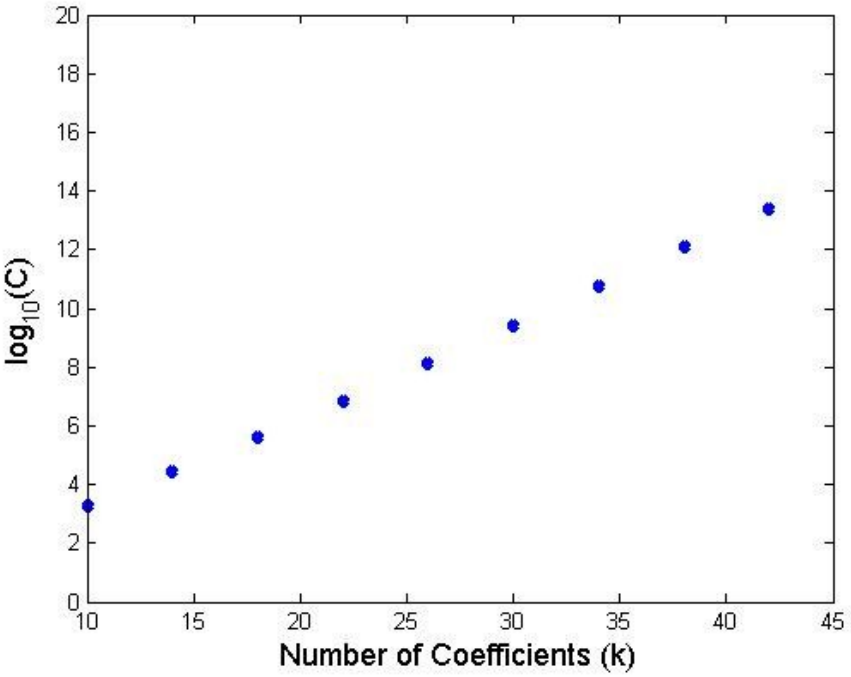

Fig. 5.15: Plot of $Log_{10}(C)$ vs number of coefficients, *k*, for *m+h = 1,849* input values (*m = 1,703* TSA values)

number of coefficients) all the unknown Airy coefficients vector $c = A\backslash d$ or c = pinv*d (MATLAB notation), these coefficients are now substituted into the original matrix equation give $Ac = d'$, where in general the vector $\{d'\}$ is typically not exactly the same as the input data, $\{d\}$. The *RMS* value represents the discrepancy between the calculated isopachic data $\{d'\}$ and thermoelastically measured (plus imposing traction-free conditions at the edge of the hole) $\{d\}$, and which will vary for each matrix having a different number of coefficients. The *RMS* (*root mean square*) method involves minimizing the difference of the vector elements of $(d' - d)$, where *RMS* values are defined by

$$(d' - d)_{RMS} = \sqrt{\sum_{i=1}^{m+h} (d_i' - d)^2 / (m+h)}$$

$$= \sqrt{\sum_{i=1}^{1849} (d_i' - d)^2 / 1849} \qquad (5.36)$$

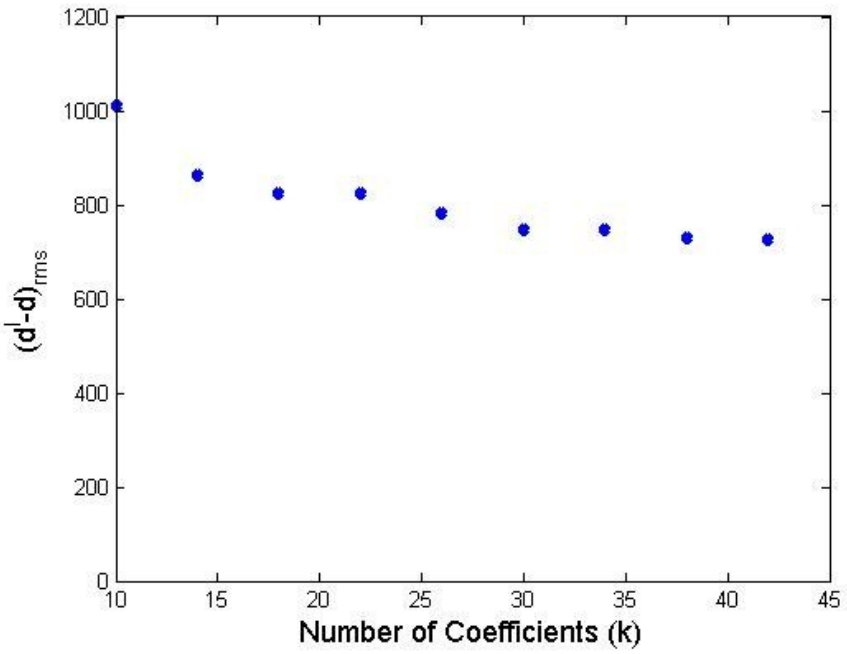

Fig. 5.16: Plot of 'RMS' values of (d'-d) vs number of coefficients, *k*, for *m+h = 1,849* input values (*m = 1,703* TSA values)

Figure 5.16 illustrates that the *RMS* values are reasonably consistent for $26 \leq k \leq 42$. It is desirable to use the smallest number of coefficients that gives sufficient accuracy. Since adding more coefficients than necessary could necessitate more measured input data, the *RMS* values decrease little beyond $k = 26$, and $k > 26$ would involve more extend the least-squares calculation and increase computation time, the RMS results indicate $k = 26$ would be realistic. Subsequent reconstructed S images support using $k = 26$.

Normalized contour plots of the reconstructed S/σ_o (= $(S^*/K)/\sigma_o$) (determined using the now evaluated Airy coefficients and *equation 5.19*) were also prepared for various number of coefficients and compared with the measured experimental information, *figures 5.17 through 5.20*. The normalized images of *figure 5.17* of the response in the neighborhood of the elliptical hole were obtained using MATLAB by importing the matrix of recorded temperature data into

MATLAB. *Figures 5.16 through 5.19* (also prepared utilizing MATLAB) support the selection of $k = 26$ as an appropriate number of coefficients to use. The normalized contour plot of *figure 5.19* was obtained based on the TSA-determined values of the 26 Airy coefficients and *equation 5.19*. All the values of such plots of S and S/σ_0 (height matrices in the Contourf function with corresponding x- and y-coordinates) have been normalized with respect to the far field stress of σ_o = 9.19 MPa (1333.33 psi), where σ_o is based on the load of 4448.2 N (1000 lbs) over the gross area 0.00635 m (0.25″) times 0.0762 m (3″). *Figures 5.17, 5.19 and 5.20* utilize the same color scale (color bar) and *figures 5.18, 5.19 and 5.20* utilize the same colors scheme (i.e., have different color bar but utilize the same colors) but different color scale. While comparing the images of *figures 5.17 through 5.19* further supports the present use of $k = 26$, the unreliability of the recorded TSA information on and near the edge of the hole (particularly as θ and α of *figure 5.1* approach zero) is apparent in images of *figures 5.17 and 5.18*. *Equations 5.6 through 5.18* involve a summation over n, where n goes through positive even integers from 2 to N, and the total number of coefficients is given by $k = 2N + 2$. Thus, for $k = 26$ coefficients, the terminating index N = 12.

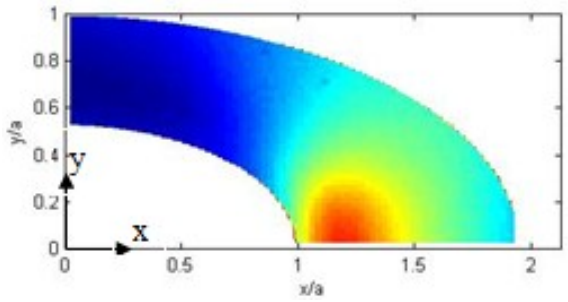

Fig. 5.17: MATLAB processed Experimental TSA input data S/σ_0

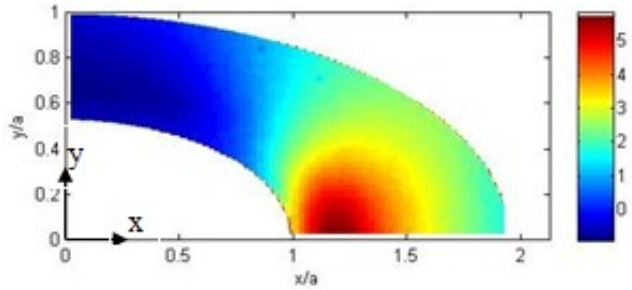

Fig. 5.18: MATLAB processed Experimental TSA input data S/σ_0

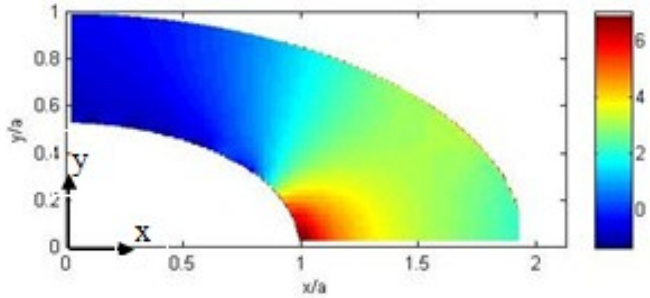

Fig. 5.19: Reconstructed S/σ_0 for $m+h = 1{,}849$, $m = 1{,}703$ and $k = 26$

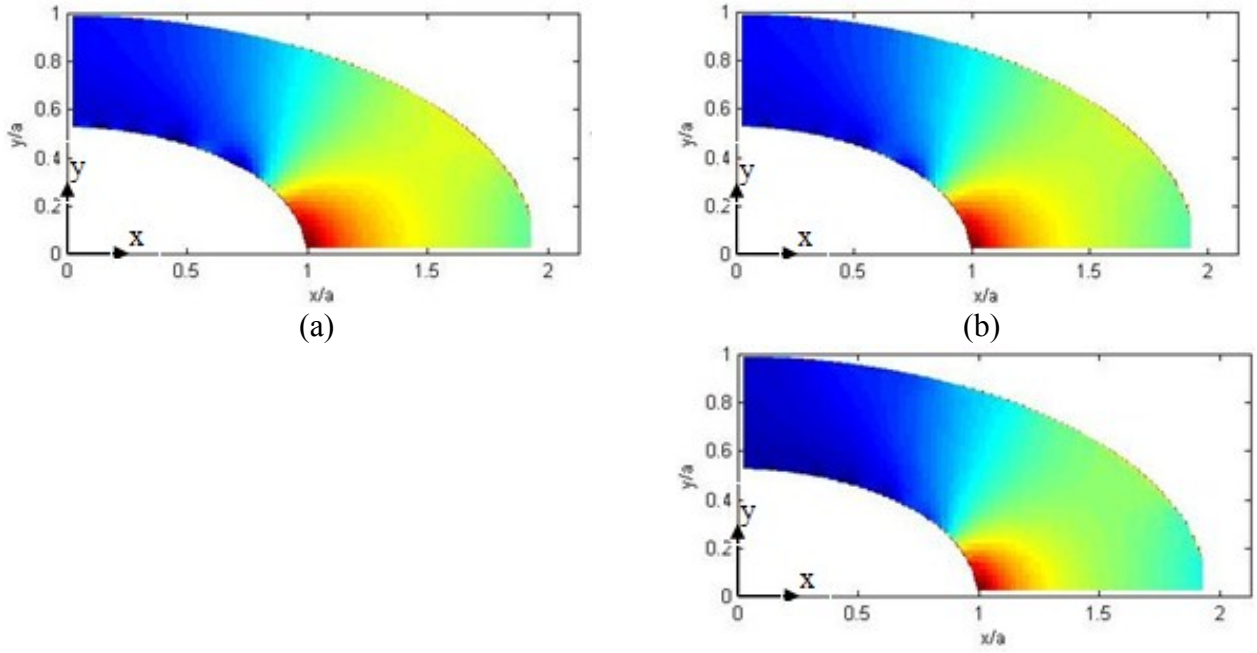

Fig. 5.20: Reconstructed S/σ_0 for $m+h = 1,849$, $m = 1,703$ and $k = 18, 22$ *and* 30 for (a), (b) and (c), respectively

Using least-squares with $m+h = 1,849$ equations to evaluate the 26 Airy coefficients enables reliable results to be obtained even if some scatter is present in the measured input TSA data (isopachic stress, S values) after having been averaged throughout the four quadrants of the plate. Least-squares minimizes the cumulative error of the system according to the matrix algebra and provides some smoothing, such that no additional filtering of TSA-measured data S* is needed prior to evaluating the coefficients and hence the stresses. The thesis previously mentioned the unreliability of recorded TSA data on and near edges. Comparing *figures 5.17 and 5.19* demonstrates such lack of reliability, particularly at the high tensile stressed regions at the right end of the hole of these images. It is worth nothing from *figures 5.17 through 5.20*, that while TSA input on and very near the edge of the hole was not used because of stated unreliability, the present hybrid technique provides reliable edge stresses when reconstructed using the now known Airy coefficients. This current approach of combining measured

temperatures with an Airy stress function (in real variables), and also imposing traction-free conditions $\sigma_{\xi\xi} = \sigma_{\xi\eta} = 0$ on the edge of a hole in forming the reconstructed images of *figures 5.19 and 5.20*, demonstrates the ability to overcome this inherent challenge of unreliable edge data while avoiding having to use stress function in complex form [15, 16].

Figures 5.17 through 5.20 are plotted in MATLAB using 'contourf ( )' function. This MATLAB function requires four input arguments in the form of matrices, i.e. a 2-D form of the matrix to be plotted (also called the *height* in MATLAB), two vectors which contain the limits of the *x* and *y* co-ordinates to be plotted (i.e. the region of the plate to be mapped for contours) and a vector which contains the intervals at which contours are to be generated. This fourth argument can be optional and depends upon the user. If using the original contour function, the color scheme selected in MATLAB for a contour plot is done automatically by MATLAB. In the case of *figures 5.17 through 5.20*, S/σ_o is the height matrix, {x} and {y} are two vectors which contain the corresponding 'x' and 'y' co-ordinates associated with each value of the isopachic stress, S*. However, I modified the default scheme and wrote my own code in MATLAB for preparing contour plots. This scheme maps all the contour data points and has a user-controlled color scheme. The motivation behind writing my own code includes the following: (i) One has three column matrices corresponding to *x*, *y* and S/σ_o but the 'contourf ( )' function routine requires the S/σ_o to be a two-dimensional matrix, and the respective x and y matrices information to be of the same dimensions (two-dimensional matrix corresponding to each value of S/σ_o), which eliminates the mapping of S/σ_o with corresponding x and y, (ii) The user can employ a fine mesh (grid) along the *x* and *y* axes to obtain fine continuous contours, (iii) It gives me the ability to

adjust the color scheme such that (unlike MATLAB's default program) the range covered by individual contours is now operator controlled.

5.6.2 Finite Element Analysis

The TSA results are compared with those predicted from finite element analysis (FEA). The aluminum (E = 68.95 GPa = 10 x 10^6 psi and Poisson's ratio ν = 0.33) plate described in section 5.2 was modeled using ANSYS. Isoparametric elements (ANSYS element type: Plane-82) which have 8 nodes per element i.e., four corner nodes and four mid nodes per element, were employed. A very fine mesh was used in the neighborhood of the elliptical hole to ensure enhance accuracy as shown in *figure 5.21*. The coordinate values are given at all the eight nodes per element but the stresses are obtained only at the corner nodes i.e., four nodes per element. Therefore after refining the mesh near the elliptical hole, only the corner nodes for every element are selected manually. The mesh covering the entire one quarter of the plate of *figure 5.2* utilizes 5175 elements and 15,750 nodes. The mesh had been refined until the ANSYS results did not vary more than 0.2% on the periphery of the hole. A far field stress of 9.19 MPa (1333.33 psi) was applied at the ends as shown in *figure 5.21*.

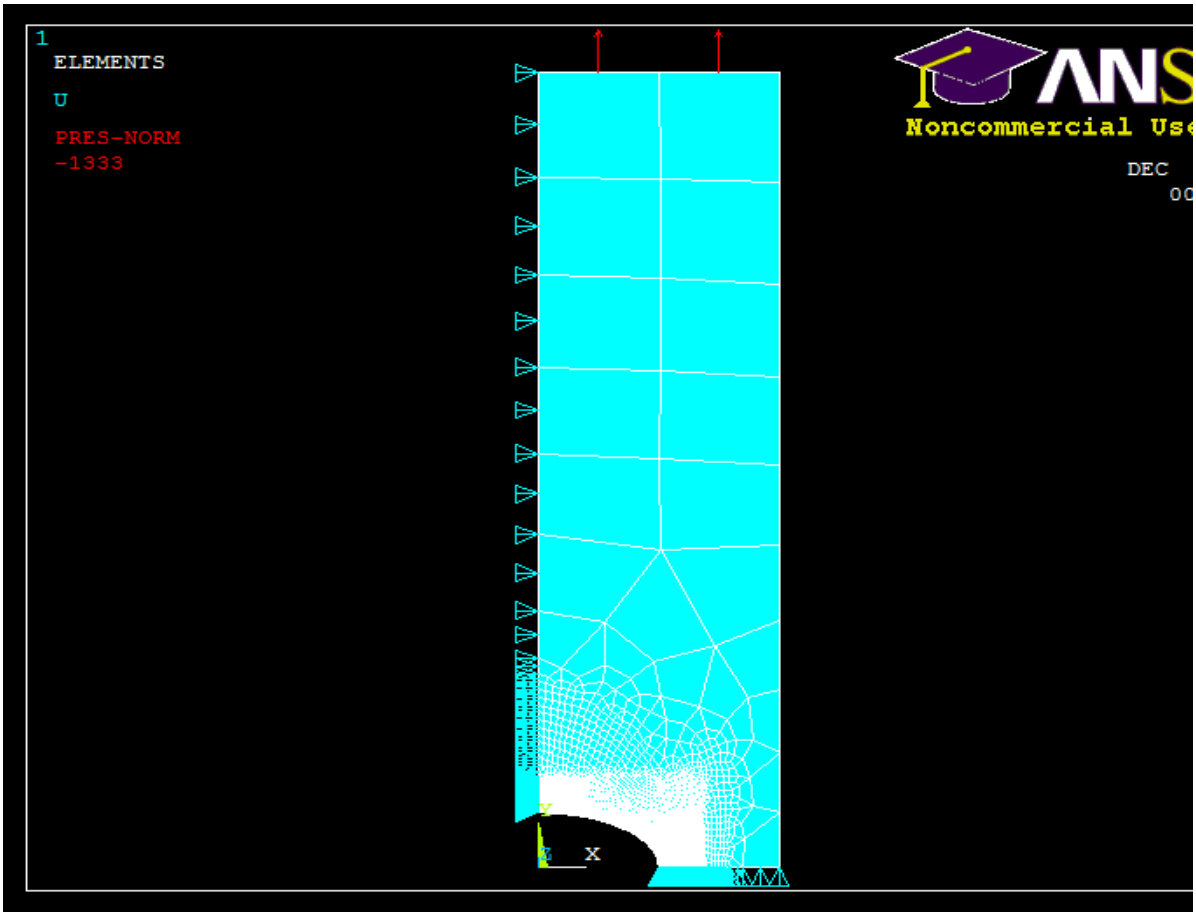

Fig. 5.21: Finite element model for analyzing the finite plate having an elliptical hole

Figure 5.21 shows the finite element model of the elliptically-perforated plate having the coordinate origin at the center of the hole. Plate geometry and loading are symmetrical about both the x- and y-axes. As shown in *figure 5.21*, the plate is subjected to an applied far-field stress of 9.19 MPa (1333.33 psi), based on a load of 1000 pound and plate width and thickness of 3″ and 0.25″, respectively.

5.6.3 Results

After evaluating all the unknown Airy coefficients *(b_o , c_o , a_n , b_n , c_n , d_n for n = 2, 4, 6….N = 12)* from the measured data, S*, at the source locations shown in *figure 5.13* along with the h = 146 traction-free conditions on the boundary of the elliptical hole of *figure 5.2*, the individual components of stress were obtained from *equations 5.7 through 5.32*. Finite element results from the commercial ANSYS software are compared with those from TSA. Normalized contour plots are illustrated, stresses in elliptical coordinates ($\sigma_{\xi\xi}$, $\sigma_{\eta\eta}$, $and\ \sigma_{\xi\eta}$) are plotted around the boundary of the elliptical hole, those in polar coordinates ($\sigma_{\theta\theta}$, σ_{rr} and $\sigma_{r\theta}$) were evaluated and normalized with respect to the far field stress, σ_o, and are plotted on the edge of the hole and along ellipses (based on various major and minor axes combinations) away from the hole, and the normalized Cartesian components of stress $\sigma_{\theta\theta} = \sigma_{yy}$ and $\sigma_{rr} = \sigma_{xx}$, are plotted along line AB of *figure 5.2.* The normalizing stress, σ_0 = 9.19 MPa (1333.33 psi) is based on the applied tensile load, F, divided by the gross area (i.e. away from the region of the hole), *figure 5.2*.

Applied load range (F) = 4448.2 N (1000lb)

Cross-Sectional Area (A) = Width (W) x Thickness (t)

= 76.2 x 6.35 = 483.87 mm^2 (0.75 in^2)

$$\sigma_o = \frac{4448.2}{483.87} = 9.19\ MPa = (1333.33\ psi)$$

Figures 5.22 through 5.24 contain contour plots of the normalized Cartesian components of stress using the TSA (and imposed traction-free stresses on the edge of the hole) evaluated coefficients and from ANSYS. In each of these individual cases the experimental and ANSYS

results utilizes the same color scheme. The x and y axes of *figures 5.22 through 5.24* are normalized by a = 19.05 mm = 0.75″ (half of the major axis of the elliptical hole), *figure 5.2*.

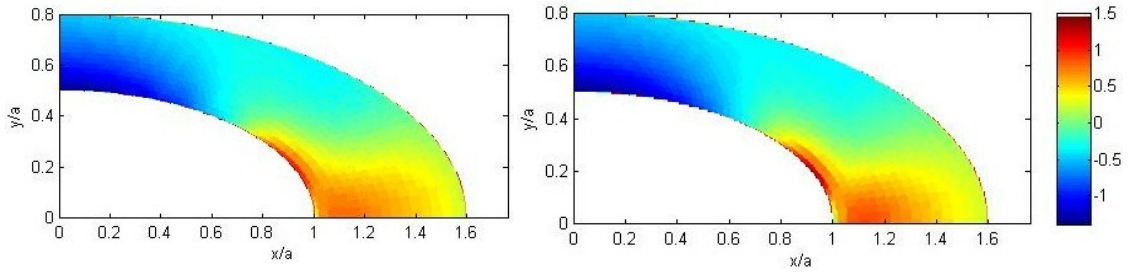

(a) (b)

Fig. 5.22: Contour plot of σ_{xx}/σ_0 from TSA (a) and ANSYS (b)

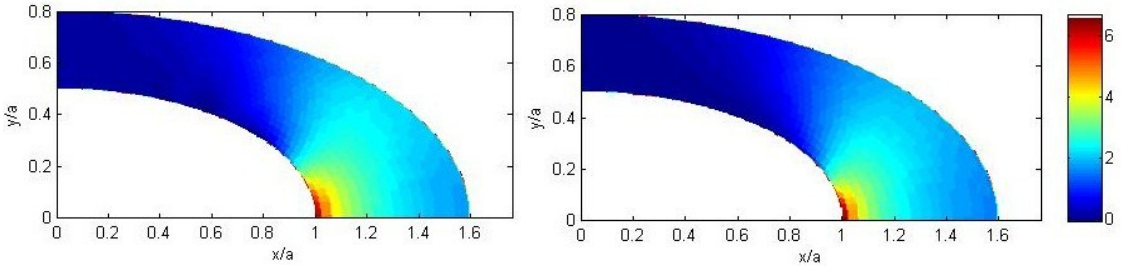

(a) (b)

Fig. 5.23: Contour plot of σ_{yy}/σ_0 from TSA (a) and ANSYS (b)

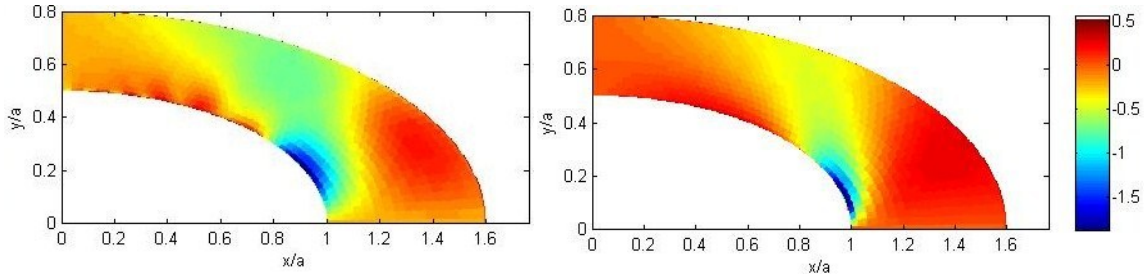

(a) (b)

Fig. 5.24: Contour plot of σ_{xy}/σ_0 from TSA (a) and ANSYS (b)

Angle θ of *figures 5.25 through 5.34* is measured counter-clockwise from the positive *x*-axis, and the radial coordinate, r, is measured here from the center of the elliptical hole ($x = y = 0$) of *figure 5.2* (also see *figure 5.1 and 5A.3* of Appendix A5). The actual in-plane dimensions associated with *figures 5.35 and 5.36* are plotted normalized with respect to the radius a = 19.05 mm = 0.75″. Note that for $0 \leq \theta < 90^{o}$, $\sigma_{\theta\theta}$ and $\sigma_{\eta\eta}$ differ slightly from each other on the edge of the hole, *figures 5.25 and 5.26*. Stress $\sigma_{\theta\theta} = \sigma_{\eta\eta}$ at θ = 0 since θ = α at θ = 0. However, θ and α are measured from different origins and hence their magnitudes are not identical when $\theta = 90^{o}$, *figure 5.1*. The agreement between the TSA-based and ANSYS predicted results of *figures 5.22 through 5.32, 5.35 and 5.36* is very good. Although $\sigma_{\xi\xi} = \sigma_{\xi\eta} = 0$ were imposed only *discretely* on the edge of the hole, *figures 5.33 and 5.34* illustrate this prevails for all $0 \leq \theta \leq 90^{o}$.

The TSA-evaluated tensile stress concentration factor of 6.14 from image *figure 5.25* compares with 6.24 from reference [26].

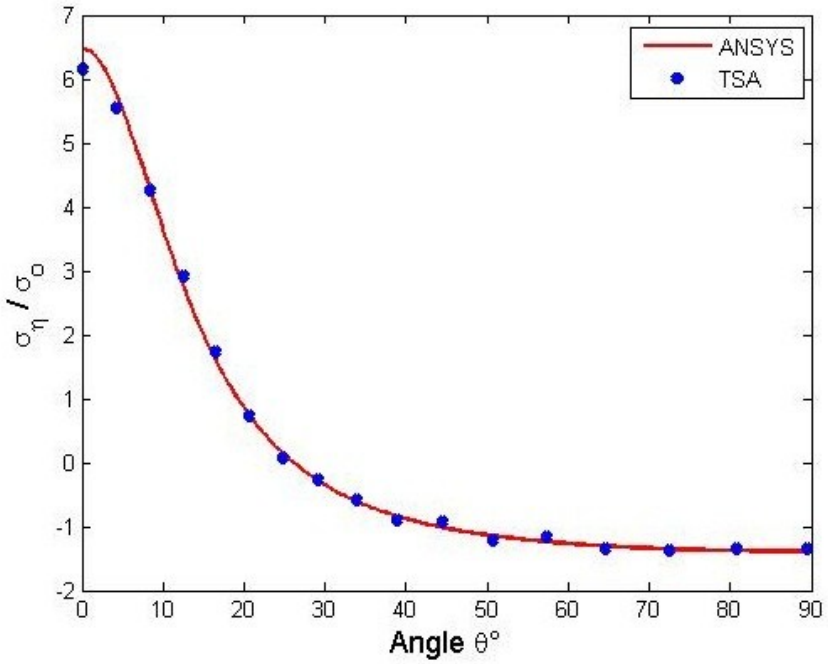

Fig. 5.25: Plot of hoop stress $\sigma_{\eta\eta}/\sigma_0$ on the boundary of the hole (2a= 38.10 mm (1.5″), 2b = 19.05 mm (0.75″)) from ANSYS and TSA (*m+h = 1,849* input values, *k = 26* coefficients and *m = 1,703* TSA values)

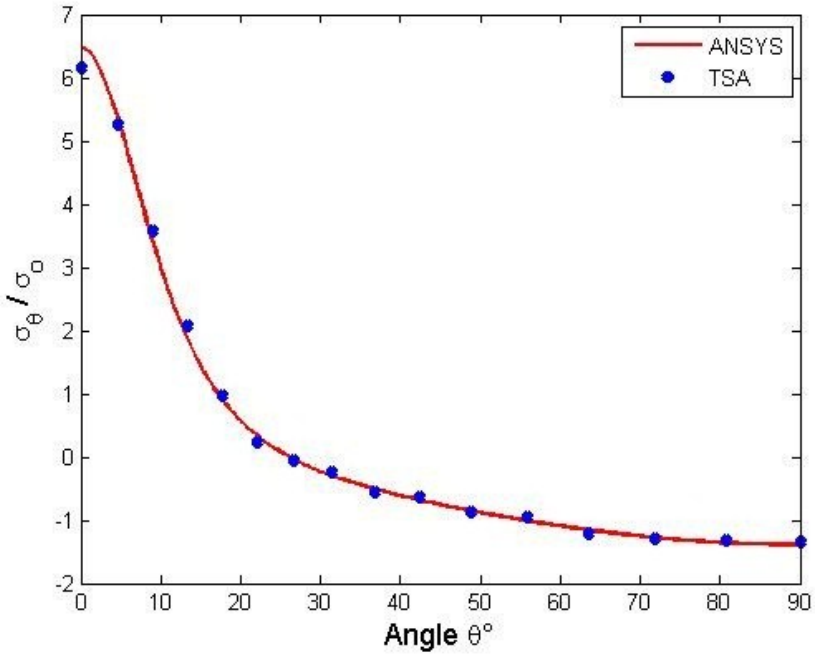

Fig. 5.26: Plot of $\sigma_{\theta\theta}/\sigma_0$ on the boundary of the hole (2a= 38.10 mm (1.5″), 2b = 19.05 mm (0.75″)) from ANSYS and TSA (*m+h = 1,849* input values *k = 26* coefficients and *m = 1,703* TSA values)

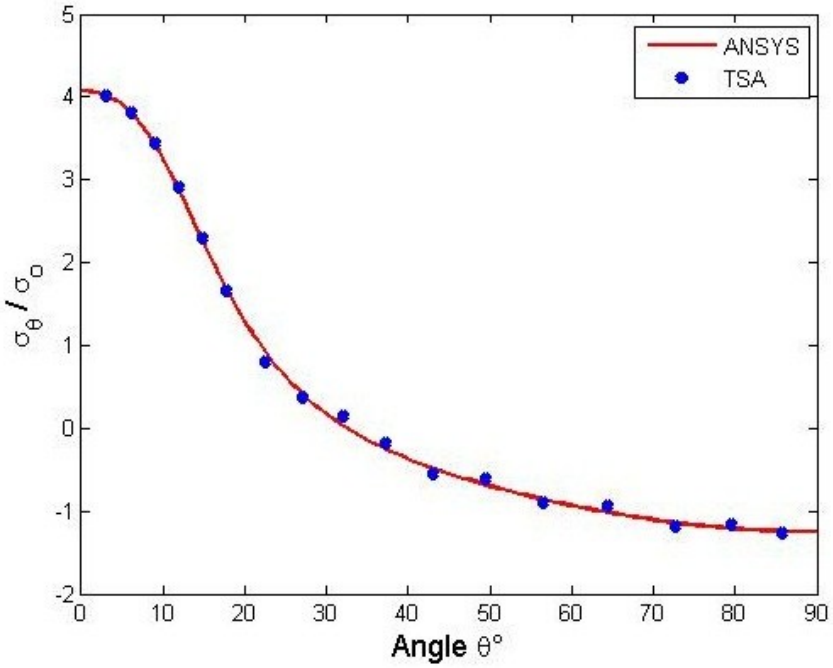

Fig. 5.27: Plot of $\sigma_{\theta\theta}/\sigma_0$ along elliptical curve defined by 2a= 40.64 mm (1.6″) and 2b = 20.32 mm (0.8″) from ANSYS and TSA (*m+h = 1,849* input values, *k = 26* coefficients and *m = 1,703* TSA values)

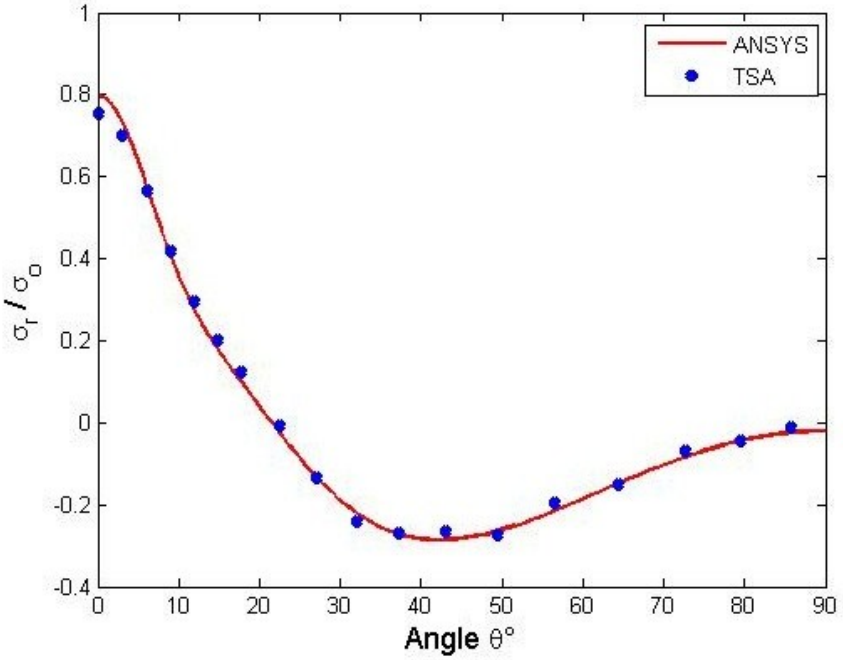

Fig. 5.28: Plot of σ_{rr}/σ_0 along elliptical curve defined by 2a= 40.64 mm (1.6″) and 2b = 20.32 mm (0.8″) from ANSYS and TSA (*m+h = 1,849* input values, *k = 26* coefficients and *m = 1,703* TSA values)

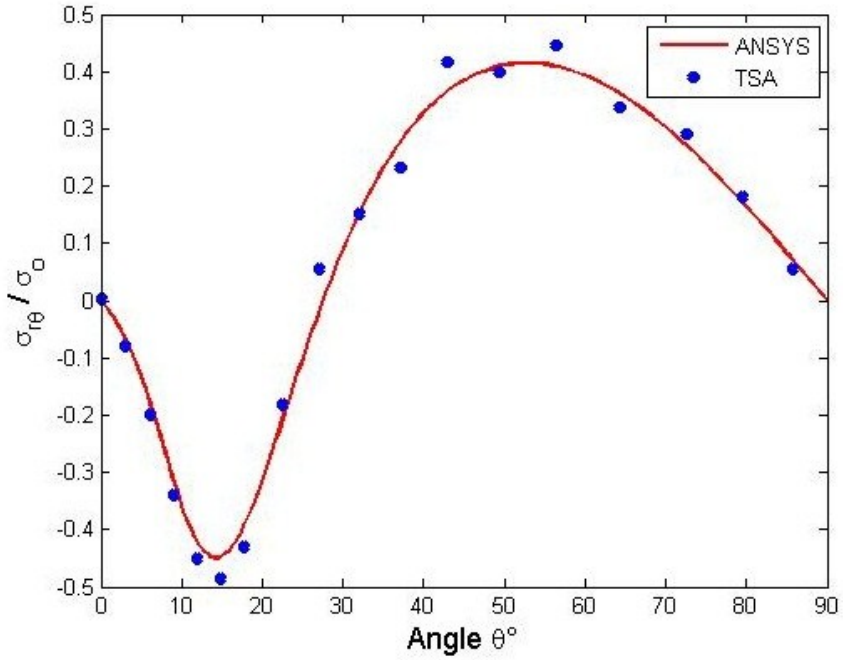

Fig. 5.29: Plot of $\sigma_{r\theta}/\sigma_0$ along elliptical curve defined by 2a= 40.64 mm (1.6″) and 2b = 20.32 mm (0.8″) from ANSYS and TSA (*m+h = 1,849* input values, *k = 26* coefficients and *m = 1,703* TSA values)

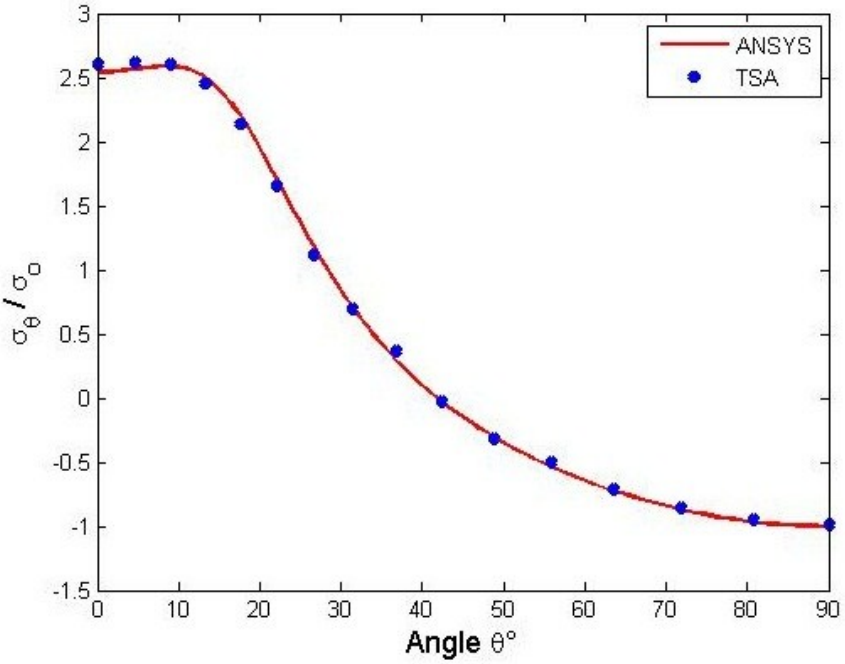

Fig. 5.30: Plot of $\sigma_{\theta\theta}/\sigma_0$ along elliptical curve defined by 2a= 45.72 mm (1.8″) and 2b = 22.86 mm (0.9″) from ANSYS and TSA (*m+h = 1,849* input values, *k = 26* coefficients and *m = 1,703* TSA values)

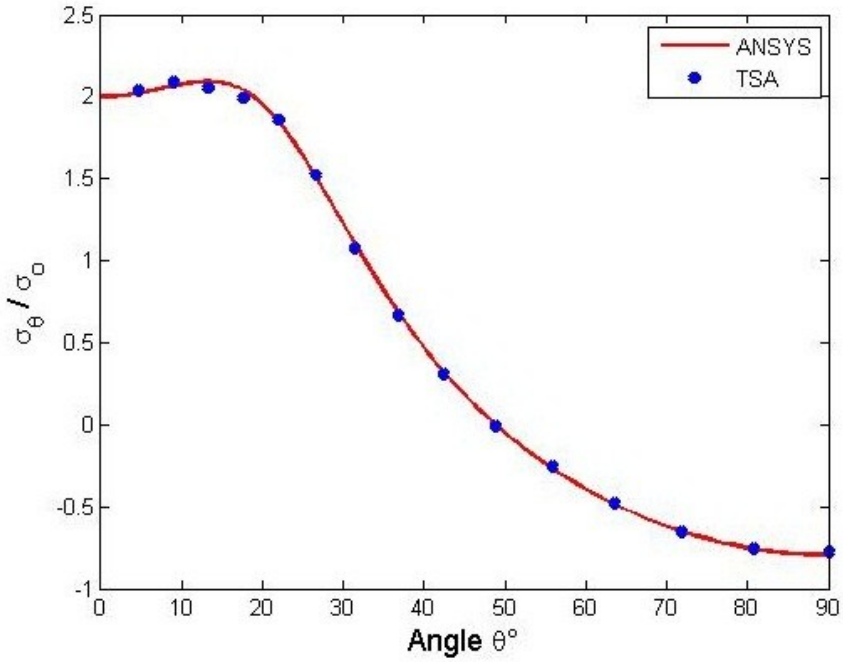

Fig. 5.31: Plot of $\sigma_{\theta\theta}/\sigma_0$ along elliptical curve defined by 2a= 50.8 mm (2″) and 2b = 25.4 mm (1″) from ANSYS and TSA (*m+h = 1,849* input values, *k = 26* coefficients and *m = 1,703* TSA values)

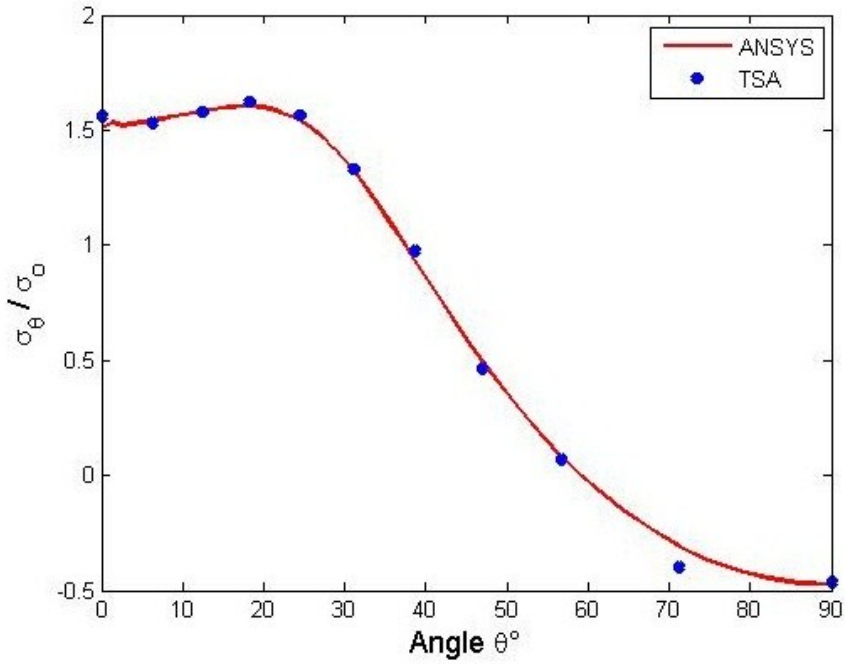

Fig. 5.32: Plot of $\sigma_{\theta\theta}/\sigma_0$ along elliptical curve defined by 2a= 60.96 mm (2.4″) and 2b = 30.48 mm (1.2″) from ANSYS and TSA (*m+h = 1,849* input values, *k = 26* coefficients and *m = 1,703* TSA values)

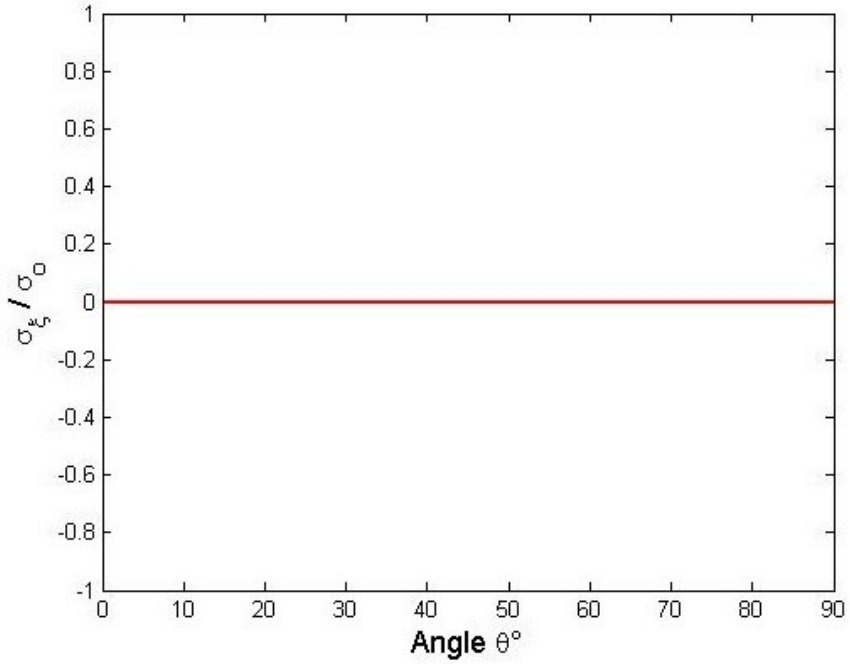

Fig. 5.33: Plot of normal stress $\sigma_{\xi\xi}/\sigma_0$ on the boundary of the hole (2a= 38.10 mm (1.5″) and 2b = 19.05 mm (0.75″)) from ANSYS and TSA (*m+h = 1,849* input values, *k = 26* coefficients and *m = 1,703* TSA values)

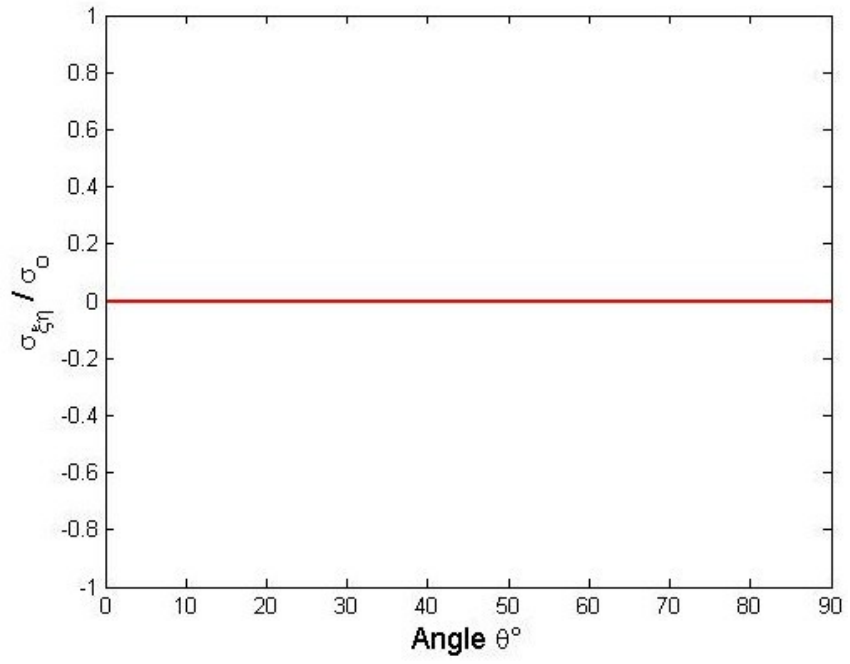

Fig. 5.34: Plot of shear stress $\sigma_{\xi\eta}/\sigma_0$ on the boundary of the hole (2a= 38.10 mm (1.5″) and 2b = 19.05 mm (0.75″)) from ANSYS and TSA (*m+h = 1,849* input values, *k = 26* coefficients and *m = 1,703* TSA values)

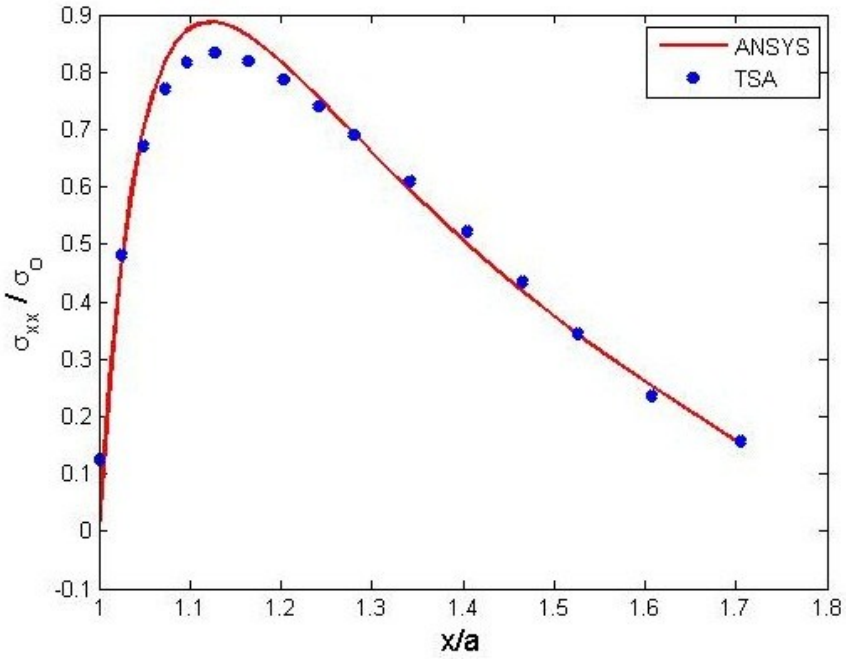

Fig. 5.35: Plot of σ_{xx}/σ_0 along AB (*figure 5.2*) from ANSYS and TSA (*m+h = 1,849* input values, *k = 26* coefficients and *m = 1,703* TSA values)

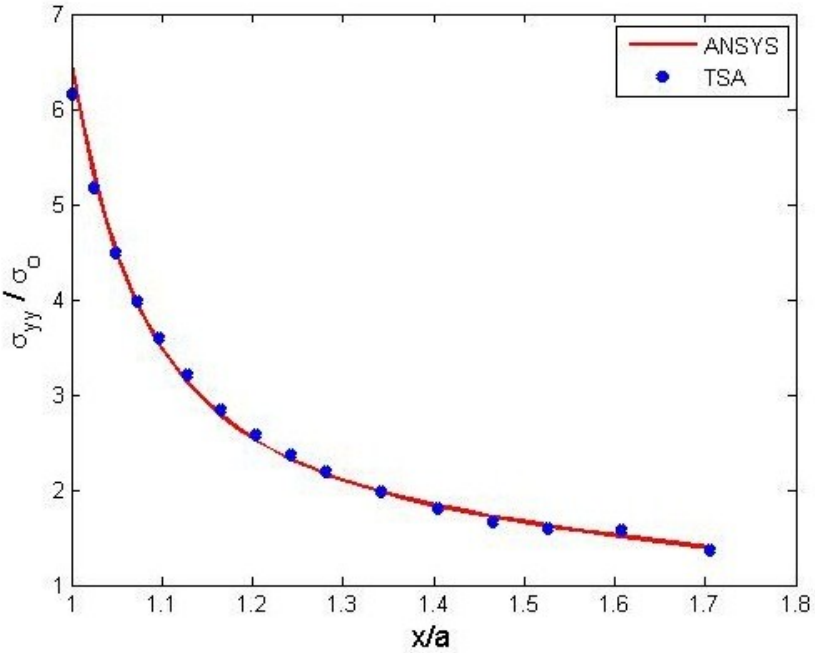

Fig. 5.36: Plot of σ_{yy}/σ_0 along AB (*figure 5.2*) from ANSYS and TSA (*m+h = 1,849* input values, *k = 26* coefficients and *m = 1,703* TSA values)

5.7 Strain Gage Analysis:

Commercial strain gages were implemented with which to also check TSA results. Electrical resistance strain gages are probably the most widely used experimental technique available. Strain gages are fairly inexpensive, have good sensitivity, a wide range of associated instrumentation is available, they can be utilized to monitor steady or transient phenomena, determine residual stresses, measure non-linear strain/stress response and are applicable for impact situations. However, the method requires some surface preparation and gage mounting, it can be arduous for a large number of gage locations, does not (by itself) provide full-field data and gage locations can be critical. Strain gages measure the average strain over the gage length and might not capture the largest value. This can be of concern in highly localized stress concentration regions having sharp strain gradients, implying the need to use small gages in such locations.

The present gages were mounted using standard strain gage procedures suggested by Vishay Micro-Measurements. The recommended conditioners and neutralizers were used on the aluminum before mounting the gages. M-Bond 200 adhesive (marketed by Vishay Micro-Measurements) was utilized in conjunction with a catalyst (200 Catalyst-C, recommended for use with M-Bond adhesive) for better adhesion, quicker drying rate and superior long-time stability. A protective air drying polyurethane coating, M-Coat, was applied over the gages (and their wiring) after the adhesive had dried. This was done to prevent any electrical shorting due to the subsequently applied Krylon Ultra-Flat black paint. Since most of the strain gages are self-temperature compensating, and gages were mounted and the testing conducted at room temperature, no dummy temperature compensating gages were employed.

To monitor and minimize any possible out-of-plane bending during loading, two single-element Micro-Measurements strain gages (EA-13-250BG-120), each having gage resistance of 120Ω each and gage factor of 2.09 ± 0.5%, were mounted on the specimen (one gage on each face), *figures 5.37 through 5.39*. A portion of a Micro-Measurements strain strip gage (EA-06-031PJ-120) consisting of eight strain gages (measure longitudinal ε_{yy}) on a common backing, with a gage factor of 2.04 ± 1% and a gage resistance of 120.0 ± 0.5% Ω, was mounted along line AB of *figure 5.2,* see *figures 5.38, 5.40, 5.41 and 5.42*[4]. These eight gages came from an original 10-gage strip gage. Individual elements of the strip-gage have a common space between centers of 2.03 mm (0.08 inch). The strip-gage was placed symmetrically along lone AB (of *figure 5.2*) of the *x*-axis with the respective gage elements in the orthogonal (specimen loading) direction. *Figures 5.43 and 5.44* are photographs of the more distant individual gages mounted on the front and back of the perforated plate. The calibration specimen described in section 5.4.4 also contained four Micro-Measurements strain gages (EA-13-125-AD-120), two on the front and two on the back, to monitor any possible misalignment and minimize out-of-plane bending when loaded *(figure 5.45). Figure 5.46* is an overview of the test set-up including the strain gages, associated wiring and instrumentation. *Figures 5.46 and 5.47* show the employed 16-channel variable but controllable excitation, strain gage conditioner.

[4]Such commercial strip gages typically include 10 individual gage elements. However, the distance along line AB of *figure 5.2* was sufficient for only eight gages (*figure 5.38*) so two individual gages were removed (cut) from the original strip.

Fig. 5.37: Specimen FRONT with mounted strain gages (coated with M-coat) and then sprayed with Krylon Ultra-Flat black paint

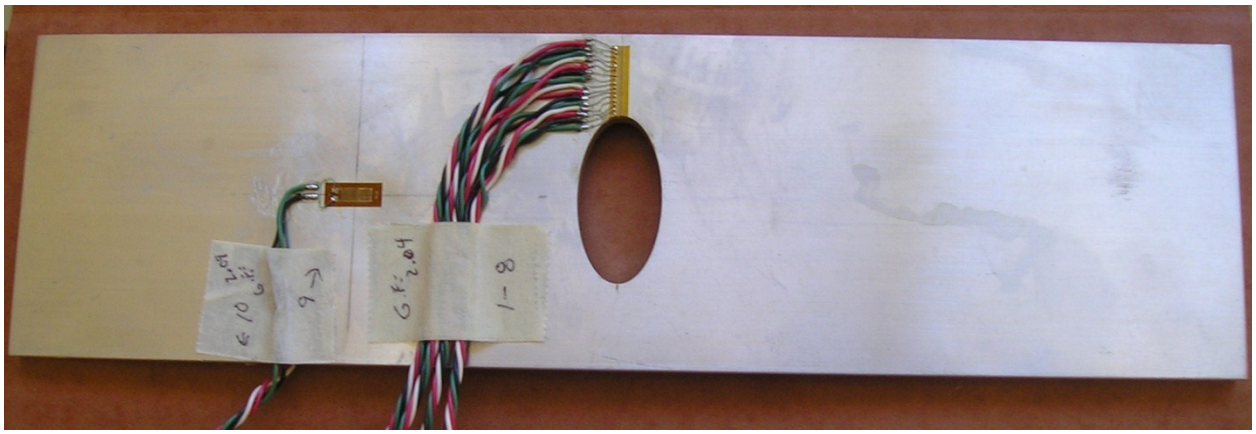

Fig. 5.38: Specimen FRONT with mounted strain gages

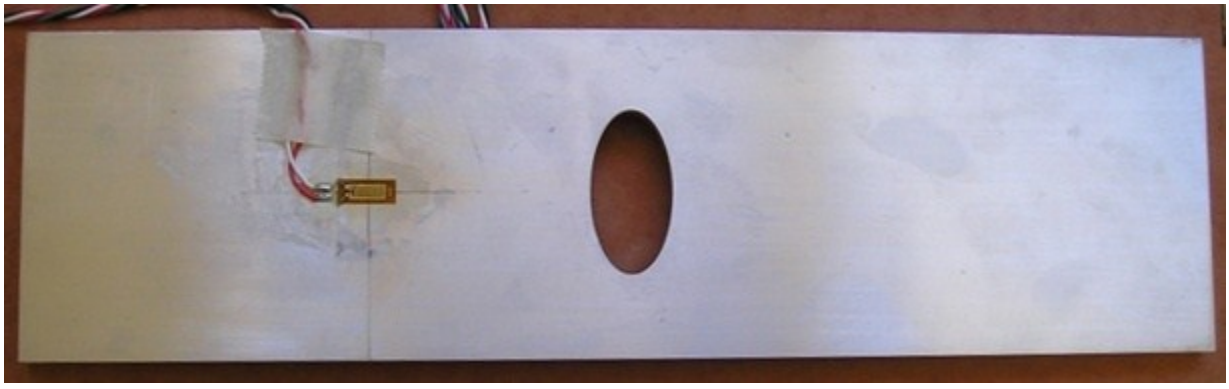

Fig. 5.39: Specimen BACK with mounted strain gages

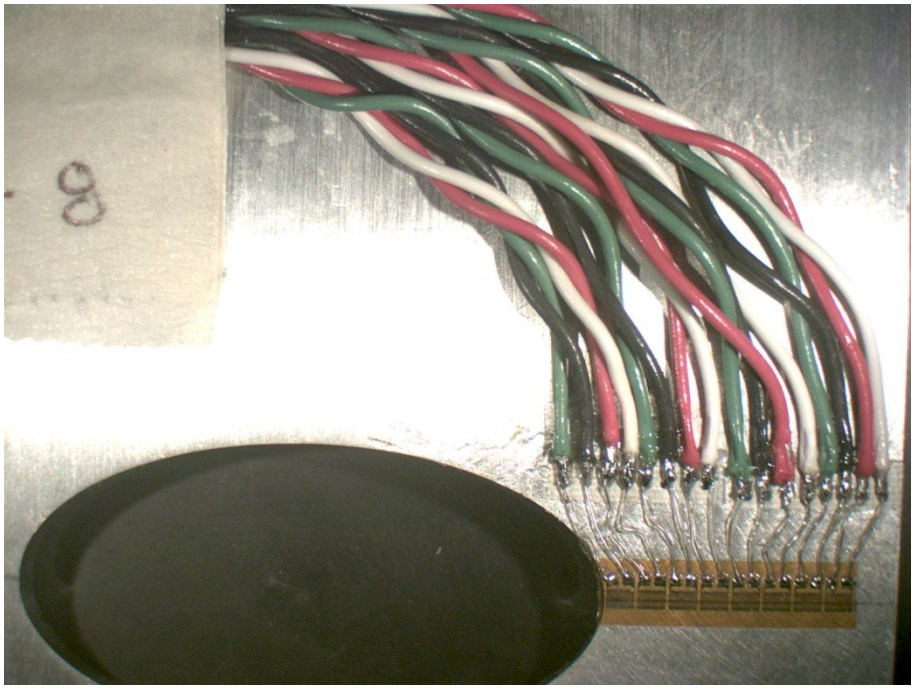

Fig. 5.40: Strip gage adjacent to elliptical hole along line AB of *figure 5.2 (*also seen in *figure 5.38)*

Fig. 5.41: Strip gage mounted along line AB of *figure 5.2 (*also seen in *figures 5.38 and 5.40)*

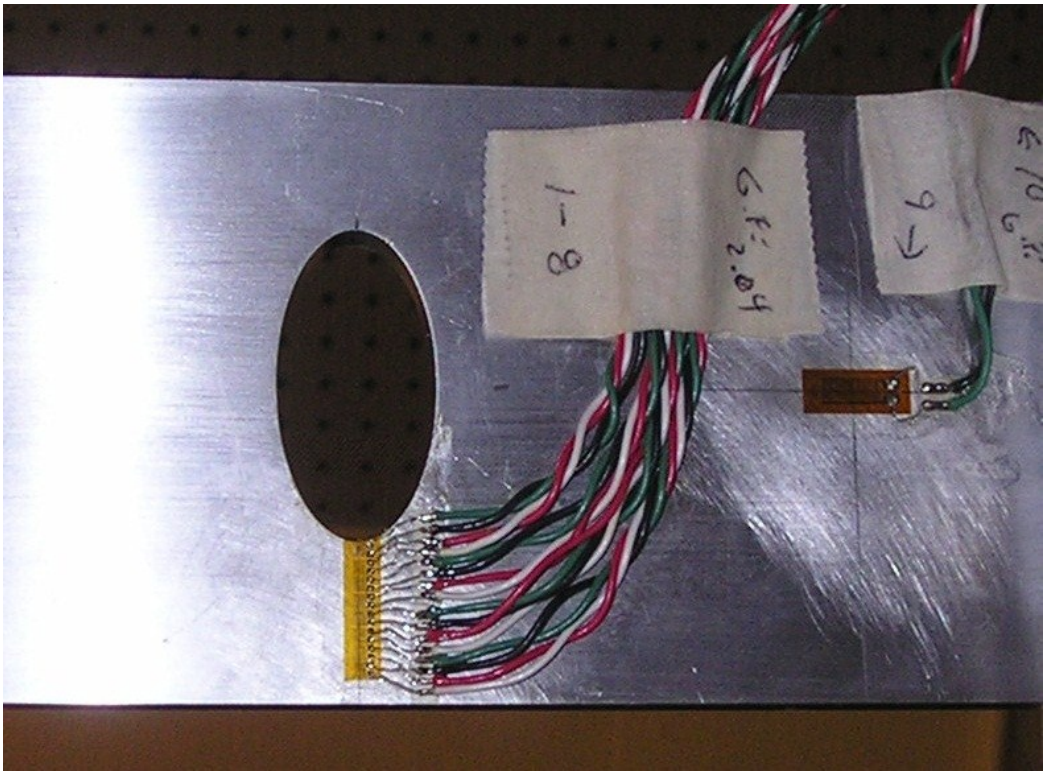

Fig. 5.42: Strip gage and strain gage on the front

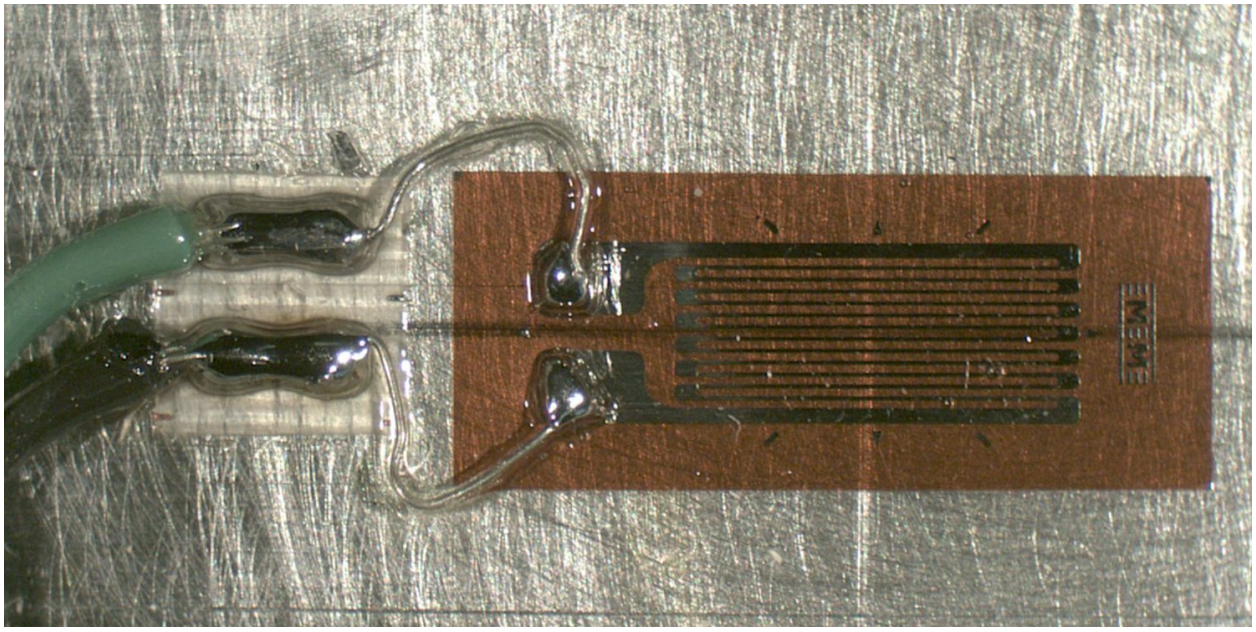

Fig. 5.43: Distant longitudinal strain gage on the front used to check for any out-of-plane bending (also seen in *figure 5.42*)

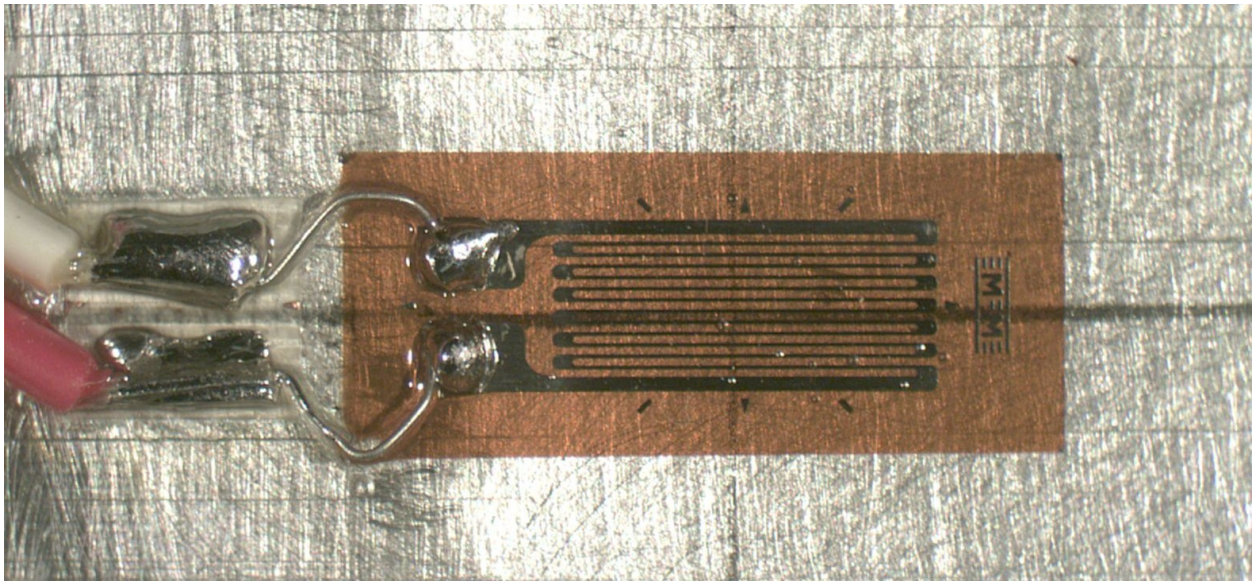

Fig. 5.44: Distant longitudinal strain gage on the back used to check for any out-of-plane bending (also seen in *figure 5.42*)

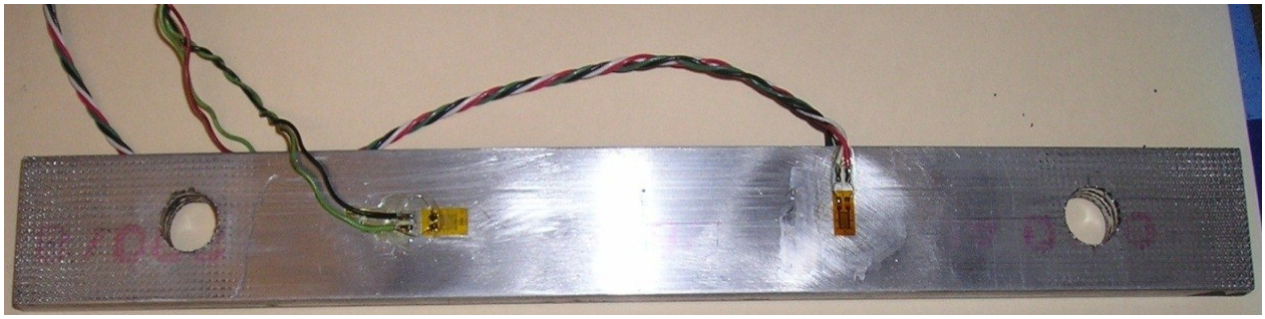

Fig. 5.45: Calibration specimen BACK, having mounted horizontal and vertical strain gages

TSA-based strains were evaluated from the TSA measured stresses and Hooke's law (E = 68.95 GPa = 10 x 10^6 psi and Poisson's ratio ν = 0.33). *Figure 5.46* shows the test arrangement for recording the strain gage data. This photograph includes the overall testing of the hydraulically-loaded perforated plate, and associated strain gage cables and instrumentation. A close-up of the strain gage conditioning unit is seen in *figure 5.47*.

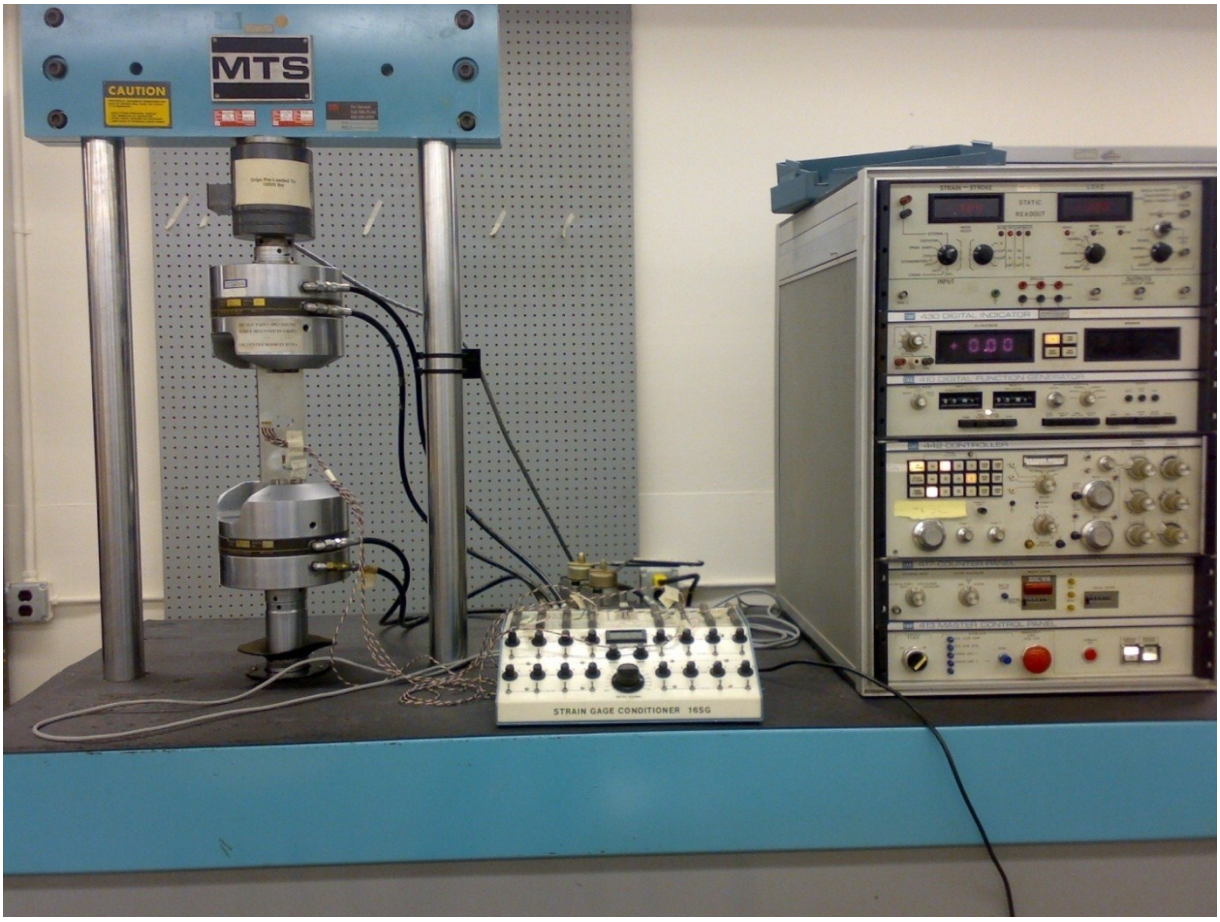

Fig. 5.46: Overview of the testing setup, including the strain gage switching, oscilloscope and balancing equipment

Fig. 5.47: 16 Channel, variable excitation strain gage conditioner

Figure 5.48 compares the strains (static equivalent specimen load of F = 4,448.22 N = 1,000lb) along the line AB extending from the end of the elliptical hole (*figure 5.2)* obtained from Thermoelastic Stress Analysis with those from finite element analysis (ANSYS) and strain gages. *Figure 5.49* contains strain-gage recorded strains along AB for various levels of plate loading. These later results demonstrate the response remains linear with load. All strain-gage results were recorded under static loading. Note that the element of the strip gage furthest from the hole is beyond x/a = 1.7 in *figure 5.48*.

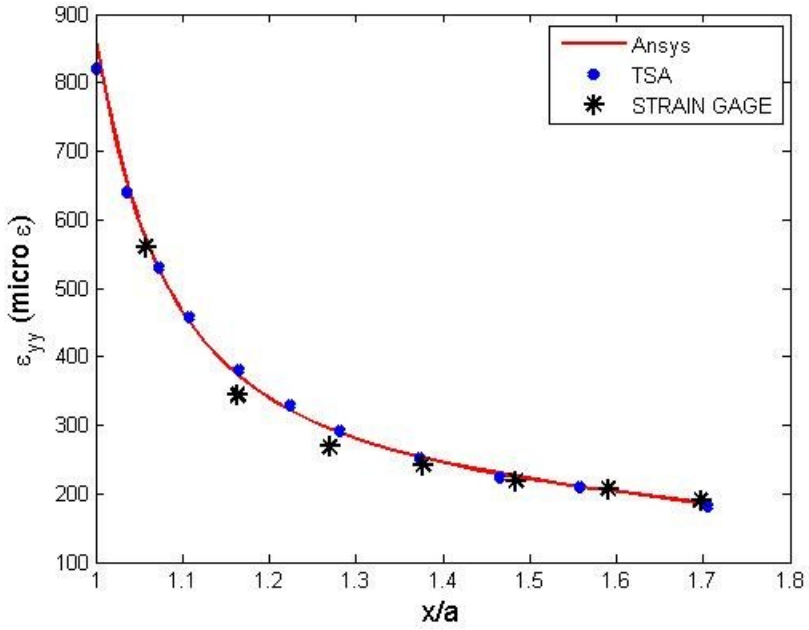

Fig. 5.48: Strain ε_{yy} along AB of *figure 5.2* from TSA, ANSYS and strain gages for *m+h = 1,849* input values, *m = 1,703* TSA values, *k = 26* and F = 4448.2 N (1000 lbs)

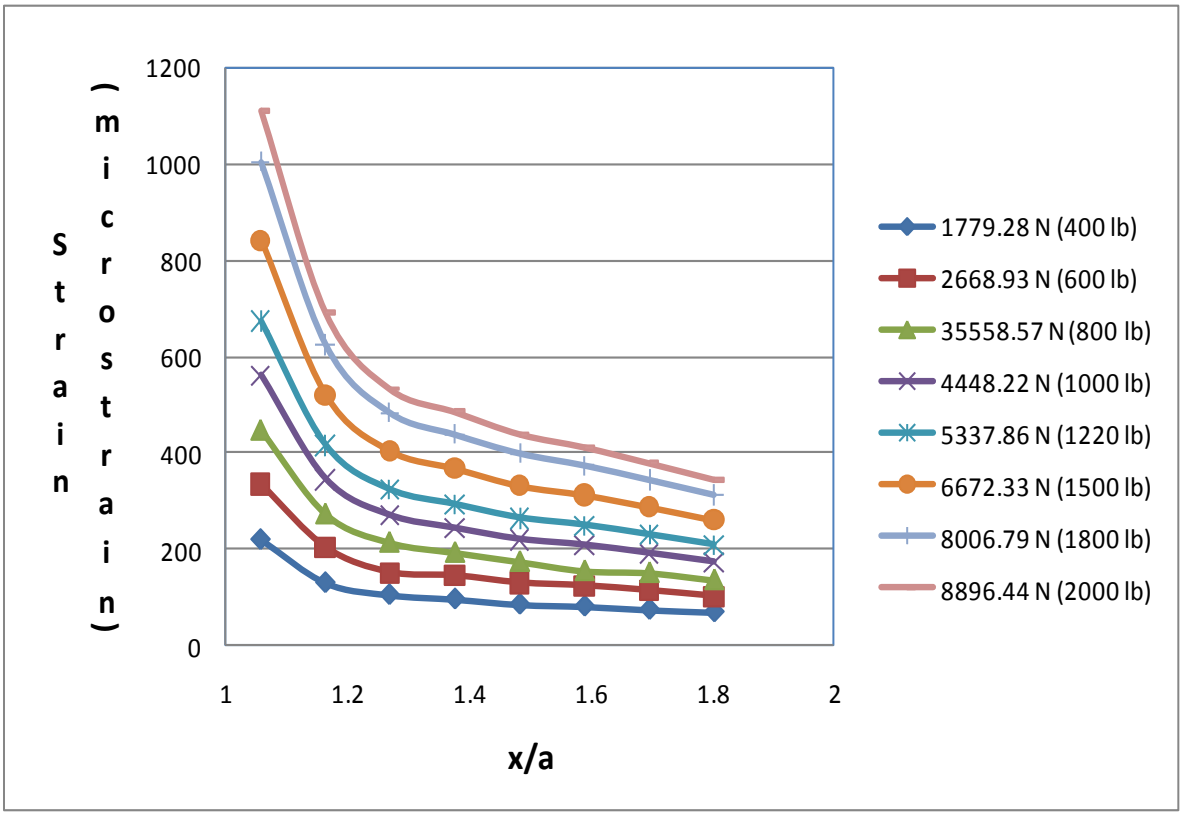

Fig. 5.49: Strain ε_{yy} obtained from strain gages along AB for different loads

5.8 Checking Equilibrium

It is information to integrate the TSA-determined stress in the direction of loading, σ_{yy}, across the horizontal section of the vertically loaded plate of *figure 5.2* to see how well load equilibrium is satisfied. Summing σ_{yy} across twice the area associated with line AB of *figure 5.2,* i.e., $2\int_A^B \sigma_{yy} t\, dy$ (where t is the thickness), gives a load of 4409.1 N (991.2 lbs). This agrees with the applied load of 4448 N (1000 lbs) within one percent. The TSA-based equilibrium check along line AB at the elliptical hole is based on the 26 Airy coefficients and the $m+h$ = *1,849* side conditions associated with the hole.

The equilibrium analysis along line AB is relatively simple in that $\sigma_{yy} = \sigma_{\theta\theta}$ at $\theta = 0^o$ readily provides σ_{yy} as an analytic function along the line (series involving the 26 Airy coefficients) and which could be easily integrate analytically. However, for the transverse line AB extending from the hole of *figure 5.2*, stress σ_{yy} was evaluated instead at 31 discrete locations along the line from TSA determined values of $\sigma_{yy} = \sigma_{\theta\theta}$ at these discrete locations and the area under the σ_{yy} curve integrated using a MATLAB code.

The TSA analysis does not involve knowing the value of the applied load, F. Rather than integrating the longitudinal stress across the plate as an equilibrium check, one could use such an action to make this into an inverse problem, i.e., compute the external loads from the experimentally-determined longitudinal stresses. Furthermore, using the known magnitude of the applied load, F, one could conceivably consider the thermomechanical coefficient, K, as an unknown (initially) and evaluate it (perhaps iteratively) by summing the longitudinal stress distribution across some transverse plane and equating that value to F/t.

5.9 Effect of Varying Pixel Distance from the Edge of the Hole

To provide further assessment of the results, the input data was selected by moving from one pixel to four pixels away from the boundary. The pixel size was found to be 0.48 mm (0.0189″). *Figure 5.50* shows the comparison of hoop stress $\sigma_{\eta\eta}/\sigma_0$ on the boundary of the hole by moving 1 pixel to 4 pixels away from the boundary of the hole. For convenience, in this analysis the number of coefficients and the input data were kept the same. From *figure 5.50*, it can be seen that the pixel action has less of an effect on the results.

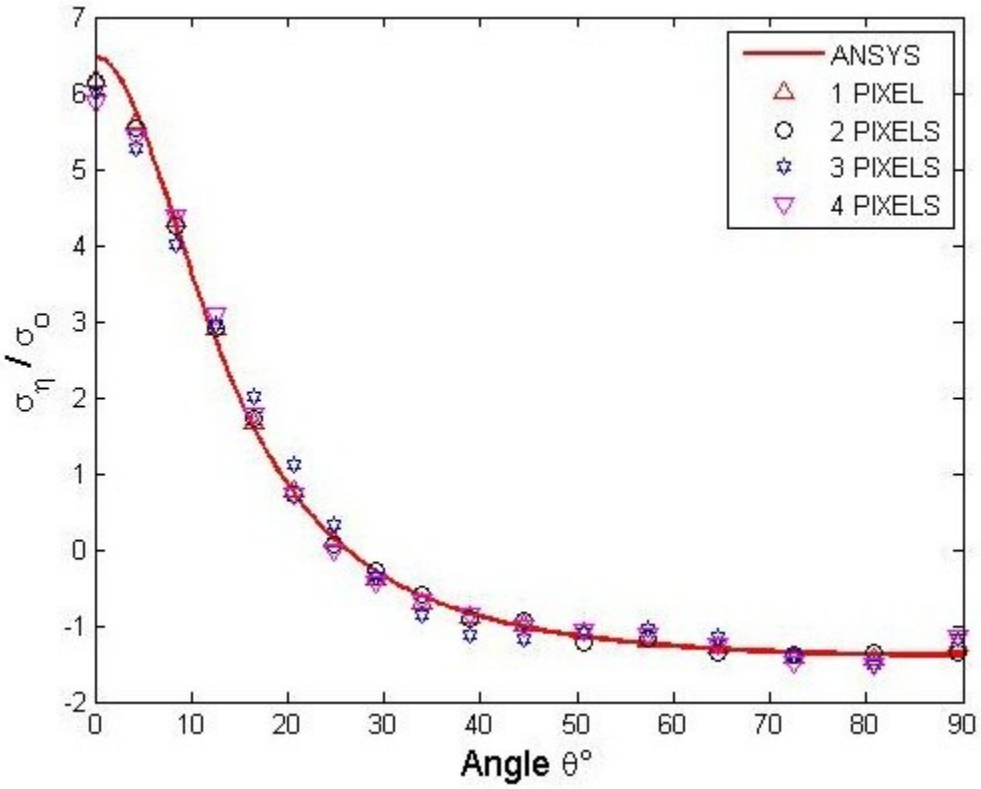

Fig. 5.50: Comparison plot of hoop stress $\sigma_{\eta\eta}/\sigma_0$ on the boundary of the hole (2a= 38.10 mm (1.5″), 2b = 19.05 mm (0.75″)) from ANSYS and TSA varying from 1 pixel to 4 pixels

5.10 Summary, Discussion and Conclusions

Thermoelasticity is a full-field, non-contacting technique capable of determining isopachic stress information of actual structures in their operating environments with a resolution comparable to that of strain gages. Contemporary commercial hardware and software enable TSA results to be available within minutes. This contrasts with more labor-intensive and time-consuming techniques such as moiré, holography, digital image correlation, speckle or strain gages. Since TSA directly gives the stresses, unlike displacement-based methods, it does not involve differentiating measured information. Combining a stress function with the recorded temperature information, plus perhaps some local boundary conditions, makes this general TSA approach amenable to a variety of engineering problems, thereby enhancing TSA's practical applicability. The demonstrated use of real variables (in polar coordinates) to evaluate the stresses in a finite plate containing an elliptical hole is particularly noteworthy. The TSA-based results agree with those from FEM and commercial strain gages. The integrated longitudinal TSA-based stress, σ_{yy}, satisfies load equilibrium.

Stress-induced temperature information is combined with a series representation of the Airy stress function and the local traction-free conditions at the boundary of the elliptical hole to determine the individual components of stress on and in the neighborhood of the hole in a finite tensile plate without knowing the constitutive properties, or far-field geometry or loading. Measured TSA data were averaged throughout all four quadrants of the plate and the coordinate origin is at the center of the hole. Employing more input/side conditions (including measured TSA input values) unknown coefficients removing any experimental noise/scatter and thereby smoothes the results. Since recorded TSA data are unreliable at edges, the described scheme

employs temperature information only beyond at least two pixel locations from the boundary of the hole. Nevertheless, and in addition to giving individual components of stress, the current technique provides accurate stress values at the boundary of the elliptical hole. Force equilibrium is also satisfied along the line AB of *figure 5.2*. Perhaps the most advantageous feature of the present approach is its ability to use a stress function in real (rather than complex) variables for other than a circular cut-out. Stress functions formulated in terms of complex variables are mathematically more cumbersome. While the traction-free conditions at the hole are applied here *discretely* rather the *analytically*, the present approach also enjoys the advantage over the complex-variable technique of references [15, 19] in that the latter necessitates an iterative application for implementation around an entire hole.

Although demonstrated here successfully for a symmetrical uniaxially-loaded central elliptical hole in a finite plate, the present general approach offers the potential for application to more irregular-shaped discontinuities, as well as fairly arbitrary external geometry and loading. The relatively simple geometry of an elliptical cutout conveniently enables one to *discretely* impose the normal and shear stress-free conditions on the boundary of the hole. More complicated-shaped geometric discontinuities might require a more general form of the stress function, or benefit from a different (e. g., curvilinear, bipolar) coordinate system. As illustrated in Appendix A5, once the stress components have been obtained (all coefficients evaluated) in polar coordinates, they can be transformed to most other coordinate systems.

To my knowledge, this represents the first time measured temperature information has been combined with real variables to determine the stresses on and in the neighborhood of the edge of the geometric discontinuity other than circular in shape. The author was unaware of any

previous application of experimental methods employing polar coordinates to evaluate the stresses associated with holes or notches which are not round (circular). The present application of polar coordinates to handle an elliptical cut-out in a finite component is also noteworthy since a general form of the Airy stress function is available in polar coordinates. In fact, relatively little stress information is available for elliptical cut-outs in members [15, 20 – 26, 28, 29]. Most existing solutions are restricted to finite geometries, FEM or BEM techniques to specific cases or use complex variables and mapping techniques. Unlike the present TSA approach purely numerical and/or strictly analytical methods require accurately knowing the far-field boundary conditions. The present availability of the stresses in terms of polar coordinates is convenient if there were neighboring geometric discontinuities so that stresses associated with the separate discontinuities interacted with each other.

The stress/strain gradients are quite steep at location A (small radius of curvature, *figure 5.2*) on the edge of the hole, *figures 5.19, 5.20, 5.25, 5.26 and 5.48*. The magnitude of the TSA results tends to be slightly less than the ANSYS prediction at such location. Although not done so in that TSA results are already very acceptable, future TSA analyses might consider incrementally increasing the number of location at which one imposes $\sigma_{\xi} = \sigma_{\xi\eta} = 0$ on the edge of the cut-out to see if this affects the results. The small effective radius of the hole at point A essentially precluded locating a strain gage on the curved surface at this location. The present general TSA approach is expected to be applicable to elliptical holes in more complicated components, under more complicated loading, as well as more complicated shaped cut-outs (holes, notches). The technique is not restricted to cases having the current symmetry.

The major contribution of this chapter is the demonstrated ability to thermoelastically determine the independent components of stress, including on the edge of the hole, in components other than circular cut-outs using real (polar) coordinates.

Chapter 6 : Investigation of Inverse Problem Using Thermoelastic Stress Analysis

6.1 Introduction

Mechanical fasteners such as bolted, nailed, doweled or riveted connections are a prevalent means of transferring load among individual members of engineering structures or machinery. Applications of mechanical joints include those to pressure vessels, buildings, towers, bridges, automobiles, motor cycles, bicycles, motor scooters, airplanes, space vehicles, machine tools and home appliances, *figure 6.1*. However, mechanical fasteners are often the

Fig. 6.1: Bolted joint utilized in the support structure of a bridge [64]

source of structural failures and have received considerable prior attention. References [1, 20, 23, 39 - 63, 65 - 99] are representative of such studies, including the effects of fastener clearance. Determination of the contact stresses between the bolts and a connecting plate is among the challenges of this type of problem. Cases where the contact boundary conditions are not known are a type of inverse problem in that the unknown boundary conditions, and hence the stresses throughout the component, are sometimes evaluated from interior measured information. Not knowing the complete boundary conditions can render the ability to obtain reliable purely analytical or numerical solutions of such problems essentially impossible, thereby motivating experimental approaches.

Field-assembled mechanical fasteners often possess a reasonable amount of clearance between the bolts and the holes. Bolted wood or steel structures typically (but not always [95]) utilize holes which are 1/16 inch (1.6 mm) oversize [99 and 100]. This can contrast with the clearances in the micron range for the thousands of mechanical fasteners employed in a commercial aircraft or other aerospace vehicles, although the fastener diameters of the latter are often considerably smaller than with earth-bound structures [61, 89, 90, 93 and 94]. Reference [98] demonstrates the serious stress consequences due to clearance in pin-loaded photoelastic and aluminum plates, particularly as the plate end-distance decreases. The significant influence of fastener clearance is attributed to the sharp load-induced local changes in curvature of an originally round hole. Compared to snugly (neat) fitting connections, bolt-hole clearance tends to reduce the interface contact area and the fastener stiffness, increase the maximum normal/radial bolt-hole contact stress and hence increase early damage, and can influence ultimate strength. Inadequate clearance tolerances among separate fasteners of a multi-bolted connection can cause

individual holes to load up non-uniformly and/or other than desired/anticipated, as well as be problematic fatigue-wise under cyclic loading.

Influenced by Bickley's 1928 paper [65], it is not uncommon to assume that the normal stress at a bolt/pin-hole interface obeys a cosine distribution, this stress being a maximum at the point of initial pin-hole contact and decreasing to zero at ~90^o from the position of initial pin-hole contact. The cosine distribution of the contact interface normal stress in a pin-loaded plate is of the same form as the radial stress beneath a concentrated load applied to the edge of a semi-infinite plate (Flamant solution), page 36 of [98]. Bickley's analysis, which is for a rigid pin in an infinite tensile plate, also has zero shear/frictional stress throughout the pin-hole interface.

Using photoelasticity, Hyer [77] showed that the radial interface stress approximated a cosine distribution for a snugly-fitting pin in a finite-width quasi-isotropic composite plate, but that stress did not become zero until at least 100^o from the point of initial pin-hole contact. The only known previous applications of TSA associated with contact situations appear to be those of [53, 54, 62, 101 and 102]. While individual component of stress were not determined on the boundary of the hole, Dulieu-Smith and Fulton [54] utilized TSA to evaluate the distribution of the isopachic stress $S = (\sigma_{rr} + \sigma_{\theta\theta})$ around the hole of a snugly-fitting pin-loaded connector.

Recognizing that mechanical connectors often have little bolt-hole clearance, and the superior performance thereof, this chapter applies TSA to determine the stresses in snugly fitting fasteners. Under such conditions one often assumes a cosine distribution of the normal stress at the bolt-hole interface and, irrespective of whether or not there is any bolt-hole clearance, it is not uncommon to simplify the problem by considering the pin to be rigid and ignoring any

contact shear/friction stress between the bolt and hole, e.g., [70, 71, 73-76]. If there is pin-hole clearance there are high radial stresses (due to the fact that there is less contact between the pin and plate) in the contact region when compared to no clearance. A pinned, finite aluminum joint is stress analyzed here by synergizing measured temperature data with an Airy stress function and available boundary conditions. An over-determined least-squares routine is implemented to evaluate the unknown Airy coefficients of the stress function and thereby evaluate the individual components of stress at and in the neighborhood of the edge of the loaded hole. The TSA results are supported by those from force equilibrium and FEM. The author is unaware of any previously published situations where individual stresses have been evaluated on and away from the pin-hole contact surface in a pinned connection using TSA.

Two cases will be discussed in this chapter, the first involves a pin which has a circular cross section, and the second where the pin is non-circular. The hole is round in both cases. Geometric details will be discussed in section 6.3. The first case will be referred to as plate with circular pin and the second as plate with non-circular pin.

All associated 2D and 3D CAD drawings were modeled using SOLIDWORKS design software. Unless mentioned otherwise, all dimensions and units shown on the CAD drawings are in inches, which are compatible with the initial design of the specimen, pins, fixture, and applied cyclic loads. English units are given in SI units based on one inch = 25.4 mm and one pound = 4.448 Newtons.

6.2 Relevant Stress Function and Stress Components

The general method employed here uses an Airy stress function along with recorded TSA data near the contact area in the pinned connections and *discretely* imposes the traction-free boundary conditions to determine the complete state of stress within a loaded body. Traction-free conditions were imposed on the unloaded portion of the pin-loaded hole and on the external edges of the aluminum plate. For a two-dimensional continuous medium, a classical plane-stress elasto-static stress analysis involves solving the biharmonic equation, $\nabla^4\phi = 0$, for the stress function ϕ and deriving the individual stresses from derivative of ϕ. The solution to the biharmonic equation is given by Michell solution [6] as follows:

$$\begin{aligned}\phi &= a_0 + b_0 \ln r + c_0 r^2 + d_0 r^2 \ln r + \left(A_0 + B_0 \ln r + C_0 r^2 + D_0 r^2 \ln r\right)\theta \\ &+ \left(a_1 r + b_1 r \ln r + \frac{c_1}{r} + d_1 r^3\right)\sin\theta + \left(a_1' r + b_1' r \ln r + \frac{c_1'}{r} + d_1' r^3\right)\cos\theta \\ &+ \left(A_1 r + B_1 r \ln r\right)\theta \sin\theta + \left(A_1' r + B_1' r \ln r\right)\theta \cos\theta \\ &+ \sum_{n=2,3,4\ldots}^{\infty}\left(a_n r^n + b_n r^{(n+2)} + c_n r^{-n} + d_n r^{-(n-2)}\right)\sin(n\theta) \\ &+ \sum_{n=2,3,4\ldots}^{\infty}\left(a_n' r^n + b_n' r^{(n+2)} + c_n' r^{-n} + d_n' r^{-(n-2)}\right)\cos(n\theta)\end{aligned} \tag{6.1}$$

The relevant Airy stress function is evaluated based on the given geometry and loading. For the pin loaded connection having no conditions of regularity either at the origin or at infinity, the generalized Airy stress function of *equation 6.1* is simplified here which satisfies the boundary conditions, equilibrium and compatibility [1, 6]:

$$
\begin{aligned}
\phi &= a_0 + b_0 \cdot \ln r + c_0 \cdot r^2 + A_0 \cdot \theta \\
&+ \left(a_1 \cdot r + b_1 \cdot r \cdot \ln r + \frac{c_1}{r} + d_1 \cdot r^3 \right) \cdot Sin\theta + \left(a_1^{'} \cdot r + b_1^{'} \cdot r \cdot \ln r + \frac{c_1^{'}}{r} + d_1^{'} \cdot r^3 \right) \cdot Cos\theta \\
&+ A_1 \cdot r \cdot \theta \cdot Sin\theta + A_1^{'} \cdot r \cdot \theta \cdot Cos\theta \\
&+ \sum_{n=2}^{\infty} \left(a_n \cdot r^n + b_n \cdot r^{n+2} + c_n \cdot r^{-n} + d_n \cdot r^{2-n} \right) \cdot Sin(n \cdot \theta) \\
&+ \sum_{n=2}^{\infty} \left(a_n^{'} \cdot r^n + b_n^{'} \cdot r^{n+2} + c_n^{'} \cdot r^{-n} + d_n^{'} \cdot r^{2-n} \right) \cdot Cos(n \cdot \theta)
\end{aligned}
\tag{6.2}
$$

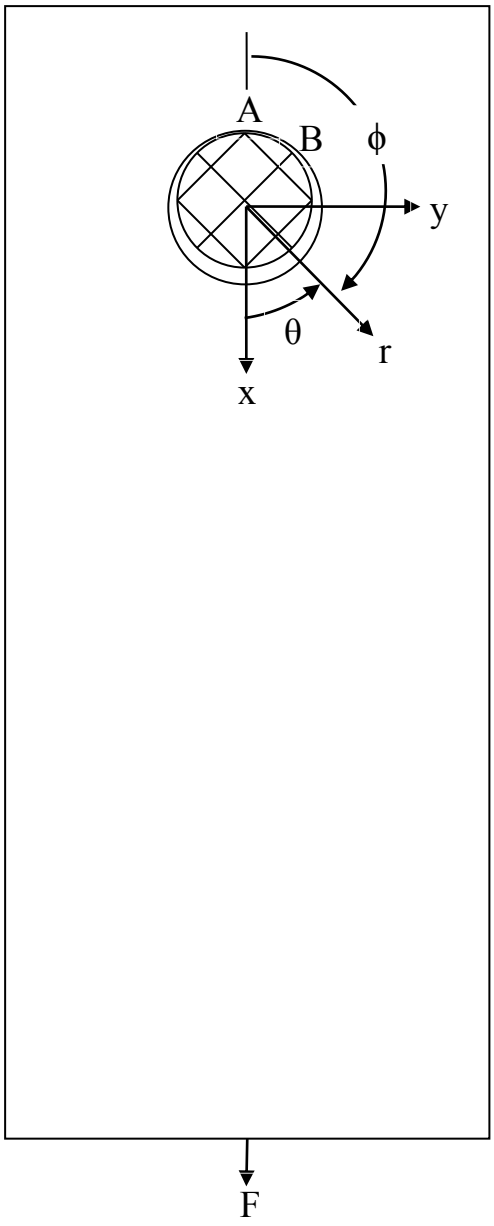

Fig. 6.2: Plate loaded with a circular bolt

The loaded connection plate can only be in equilibrium if the resultant force which acts on its external boundary is balanced by force on the inner boundary of the plate, *figure 6.2*. Coefficients A_1 and A_1' of *equation 6.2* are related to the resultant forces acting on the inner closed contour. Also b_1 and b_1' must be included for single valued displacements if the A_1 and A_1' terms are present. Since the pinned connections are symmetric about the vertical x-axis, the sine terms and A_o of *equation 6.2* will be omitted. However, the problem is not symmetric about the y-axis so both even and odd powers of *n* must be retained. Imposing these restrictions, the polar components of individual stresses are given throughout the plate by *equations 6.2 through 6.5*.

$$\sigma_{rr} = \frac{1}{r}\frac{\partial \phi}{\partial r} + \frac{1}{r^2}\frac{\partial^2 \phi}{\partial \theta^2} \tag{6.3}$$

$$\sigma_{\theta\theta} = \frac{\partial^2 \phi}{\partial r^2} \tag{6.4}$$

$$\sigma_{r\theta} = -\frac{\partial}{\partial r}\left(\frac{1}{r}\frac{\partial \phi}{\partial \theta}\right) \tag{6.5}$$

Differentiating the stress function as *equations 6.3 through 6.5*, the polar components of individual stresses throughout the plate of the pinned connection become [1]:

$$\sigma_{rr} = \frac{b_0}{r^2} + 2\cdot c_0 + \left(-\frac{2\cdot c_1'}{r^3} + 2\cdot d_1'\cdot r\right)\cdot \mathrm{Cos}\theta - \frac{R_x}{2\cdot\pi}\cdot\frac{(3+\nu)}{2}\cdot\frac{\mathrm{Cos}\theta}{r}$$
$$-\sum_{n=2,3,4\ldots}^{\infty}\left[\begin{matrix} a_n'\cdot n\cdot(n-1)\cdot r^{(n-2)} + b_n'\cdot(n+1)\cdot(n-2)\cdot r^n \\ + c_n'\cdot n\cdot(n+1)\cdot r^{-(n+2)} + d_n'\cdot(n-1)\cdot(n+2)\cdot r^{-n}\end{matrix}\right]\cdot \mathrm{Cos}(n\cdot\theta) \tag{6.6}$$

$$\sigma_{\theta\theta} = -\frac{b_0}{r^2} + 2\cdot c_0 + \left(\frac{2\cdot c_1'}{r^3} + 6\cdot d_1'\cdot r\right)\cdot \mathrm{Cos}\theta + \frac{R_x}{2\cdot\pi}\cdot\frac{(1-\nu)}{2}\cdot\frac{\mathrm{Cos}\theta}{r} + \sum_{n=2,3,4\ldots}^{\infty}\left[\begin{array}{l} a_n'\cdot n\cdot(n-1)\cdot r^{(n-2)} + b_n'\cdot(n+1)\cdot(n+2)\cdot r^n \\ + c_n'\cdot n\cdot(n+1)\cdot r^{-(n+2)} + d_n'\cdot(n-1)\cdot(n-2)\cdot r^{-n}\end{array}\right]\cdot \mathrm{Cos}(n\cdot\theta) \tag{6.7}$$

$$\sigma_{r\theta} = \frac{A_0}{r^2} + \left(-\frac{2\cdot c_1'}{r^3} + 2\cdot d_1'\cdot r\right)\cdot \mathrm{Sin}\theta + \frac{R_x}{2\cdot\pi}\cdot\frac{(1-\nu)}{2}\cdot\frac{\mathrm{Sin}\theta}{r} + \sum_{n=2,3,4\ldots}^{\infty}\left[\begin{array}{l} a_n'\cdot n\cdot(n-1)\cdot r^{(n-2)} + b_n'\cdot n\cdot(n+1)\cdot r^n \\ - c_n'\cdot n\cdot(n+1)\cdot r^{-(n+2)} - d_n'\cdot n\cdot(n-1)\cdot r^{-n}\end{array}\right]\cdot \mathrm{Sin}(n\cdot\theta) \tag{6.8}$$

Along the vertical line of symmetry the shear stress is zero. In *equation 6.8*, all the terms are a function of θ except A_o, therefore A_o is equal to zero. Therefore *equation 6.8* becomes:

$$\sigma_{r\theta} = \left(-\frac{2\cdot c_1'}{r^3} + 2\cdot d_1'\cdot r\right)\cdot \mathrm{Sin}\theta + \frac{R_x}{2\cdot\pi}\cdot\frac{(1-\nu)}{2}\cdot\frac{\mathrm{Sin}\theta}{r} + \sum_{n=2,3,4\ldots}^{\infty}\left[\begin{array}{l} a_n'\cdot n\cdot(n-1)\cdot r^{(n-2)} + b_n'\cdot n\cdot(n+1)\cdot r^n \\ - c_n'\cdot n\cdot(n+1)\cdot r^{-(n+2)} - d_n'\cdot n\cdot(n-1)\cdot r^{-n}\end{array}\right]\cdot \mathrm{Sin}(n\cdot\theta) \tag{6.9}$$

Values of the stresses of *equations 6.6 through 6.8* require their Airy coefficients be evaluated. Moreover, in practiced one can only retain a finite number of coefficients. *Equations 6.6 through 6.8* involve the material's Poisson's ratio, *v*, and R_x. These are present due to the fact that the mechanical connection of *figure 6.1* has non self-equilibrating internal (edge of the hole) and external boundaries. Quantity R_x (= P/t) is the resultant force per unit thickness in the vertical *x*-direction of the stress distribution around an interior boundary about the origin. From *equations 6.6 and 6.7*, the isopachic stress becomes:

$$\begin{aligned} S &= (\sigma_{rr} + \sigma_{\theta\theta}) = (\sigma_{xx} + \sigma_{yy}) = (\sigma_1 + \sigma_2) \\ S &= 4\cdot c_0 + 8\cdot d_1'\cdot r\cdot \mathrm{Cos}\theta - \frac{R_x}{2\cdot\pi}\cdot\frac{\mathrm{Cos}\theta}{r}\cdot(1+\nu) \\ &+ \sum_{n=2,3,4\ldots}^{\infty}\left[4\cdot b_n'\cdot(n+1)\cdot r^n - 4\cdot d_n'\cdot(n-1)\cdot r^{-n}\right]\cdot \mathrm{Cos}(n\cdot\theta) \end{aligned} \tag{6.10}$$

Based on the coordinates of *figure 6.2, equations 6.11 through 6.13* are the Cartesian components of stress which are derived from the polar components of stress and transformation matrix.

$$\sigma_{xx} = \frac{b_0}{r^2}\cdot\mathrm{Cos}(2\cdot\theta) + 2\cdot c_0 - \frac{2\cdot c_1'}{r^3}\cdot\mathrm{Cos}(3\cdot\theta)$$
$$+ d_1'\cdot r\cdot\left(2\cdot\mathrm{Cos}^3\theta + 6\cdot\mathrm{Cos}\theta\cdot\mathrm{Sin}^2\theta - 2\cdot\mathrm{Sin}\theta\cdot\mathrm{Sin}(2\cdot\theta)\right)$$
$$+ \frac{R_x}{4\cdot\pi\cdot r}\cdot\left[(-3-\nu)\cdot\mathrm{Cos}^2\theta - (1-\nu)\cdot\mathrm{Sin}^2\theta\right]\cdot\mathrm{Cos}\theta +$$
$$\sum_{n=2,3,4\ldots}^{\infty}\begin{bmatrix} -a_n'\cdot n\cdot(n-1)\cdot r^{(n-2)}\cdot\mathrm{Cos}((n-2)\cdot\theta) \\ +b_n'\cdot(n+1)\cdot r^n\cdot\left[\mathrm{Cos}(n\cdot\theta)\cdot\left[(2-n)\cdot\mathrm{Cos}^2\theta + (n+2)\cdot\mathrm{Sin}^2\theta\right] - n\cdot\mathrm{Sin}(2\cdot\theta)\cdot\mathrm{Sin}(n\cdot\theta)\right] \\ -c_n'\cdot n\cdot(n+1)\cdot r^{-(n+2)}\cdot\mathrm{Cos}((n+2)\cdot\theta) \\ +d_n'\cdot(n-1)\cdot r^{-n}\cdot\left[\mathrm{Cos}(n\cdot\theta)\cdot\left[(-n-2)\cdot\mathrm{Cos}^2\theta + (n-2)\cdot\mathrm{Sin}^2\theta\right] + n\cdot\mathrm{Sin}(2\cdot\theta)\cdot\mathrm{Sin}(n\cdot\theta)\right]\end{bmatrix}$$

(6.11)

$$\sigma_{yy} = -\frac{b_0}{r^2}\cdot\mathrm{Cos}(2\cdot\theta) + 2\cdot c_0 + \frac{2\cdot c_1'}{r^3}\cdot\mathrm{Cos}(3\cdot\theta) + 6\cdot d_1'\cdot r\cdot\mathrm{Cos}\theta$$
$$+ \frac{R_x}{4\cdot\pi\cdot r}\cdot\left[(1-\nu)\cdot\mathrm{Cos}^2\theta + (-1-3\cdot\nu)\cdot\mathrm{Sin}^2\theta\right]\cdot\mathrm{Cos}\theta +$$
$$\sum_{n=2,3,4\ldots}^{\infty}\begin{bmatrix} a_n'\cdot n\cdot(n-1)\cdot r^{(n-2)}\cdot\mathrm{Cos}((n-2)\cdot\theta) \\ +b_n'\cdot(n+1)\cdot r^n\cdot\left[\mathrm{Cos}(n\cdot\theta)\cdot\left[(n+2)\cdot\mathrm{Cos}^2\theta + (-n+2)\cdot\mathrm{Sin}^2\theta\right] + n\cdot\mathrm{Sin}(2\cdot\theta)\cdot\mathrm{Sin}(n\cdot\theta)\right] \\ +c_n'\cdot n\cdot(n+1)\cdot r^{-(n+2)}\cdot\mathrm{Cos}((n+2)\cdot\theta) \\ +d_n'\cdot(n-1)\cdot r^{-n}\cdot\left[\mathrm{Cos}(n\cdot\theta)\cdot\left[(n-2)\cdot\mathrm{Cos}^2\theta - (n+2)\cdot\mathrm{Sin}^2\theta\right] - n\cdot\mathrm{Sin}(2\cdot\theta)\cdot\mathrm{Sin}(n\cdot\theta)\right]\end{bmatrix}$$

(6.12)

$$\sigma_{xy} = \frac{b_0}{r^2}\cdot\mathrm{Sin}(2\cdot\theta) - \frac{2\cdot c_1'}{r^3}\cdot\mathrm{Sin}(3\cdot\theta) - 2\cdot d_1'\cdot r\cdot\mathrm{Sin}\theta$$
$$+ \frac{R_x}{4\cdot\pi\cdot r}\cdot\left[-4\cdot\mathrm{Cos}^2\theta + (1-\nu)\cdot\mathrm{Cos}(2\cdot\theta)\right]\cdot\mathrm{Sin}\theta +$$
$$\sum_{n=2,3,4\ldots}^{\infty}\begin{bmatrix} a_n'\cdot n\cdot(n-1)\cdot r^{(n-2)}\cdot\mathrm{Sin}((n-2)\cdot\theta) + b_n'\cdot n\cdot(n+1)\cdot r^n\cdot\mathrm{Sin}((n-2)\cdot\theta) \\ -c_n'\cdot n\cdot(n+1)\cdot r^{-(n+2)}\cdot\mathrm{Sin}((n+2)\cdot\theta) - d_n'\cdot n\cdot(n-1)\cdot r^{-n}\cdot\mathrm{Sin}((n+2)\cdot\theta)\end{bmatrix}$$

(6.13)

The individual components of stresses (be they in polar or Cartesian coordinates) involve the same unknown coefficients as in the final relevant Airy's stress function, *equation 6.2*. The coefficient a_0 of *equation 6.2* disappears in the stress expressions of *equations 6.6 through 6.13* due to differentiation of *equation 6.2*. Moreover, the equations for Cartesian and polar components of stress involve coefficients b_o, c_1', a_n' or c_n' which are unfortunately not contained in the equation of S of *equation 6.10*. Therefore the individual stress components cannot be derived from thermoelastic data alone. However, if one could find any non-contact area between the pin and the hole, the traction-free conditions of $\sigma_{rr} = 0$ and $\sigma_{r\theta} = 0$ can be imposed *discretely* on that region of the edge of the hole. Therefore to determine the individual stresses from an Airy stress function, these coefficients are evaluated experimentally, in this case from measured TSA data along with *discretely* imposing the boundary condition along the un-contact region between the pin and the hole. Although not necessary for evaluating stresses on and near the edge of the hole, far-field traction-free conditions were also imposed.

6.3 Test Configurations

6.3.1 Considering two different Test Configurations

Figure 6.3 represents the first approach which involved a setup symmetric about the vertical x-axis.

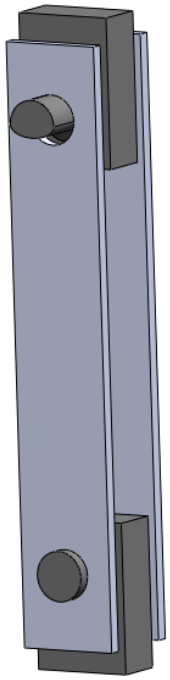

Fig. 6.3: Initial setup 3D CAD model

This arrangement involved two 6061-T6 aluminum specimens (elastic modulus, E = 68.95 GPa (10 x 10^6 psi), Poisson's ratio, ν = 0.33, ultimate strength = 275 to 311 MPa (40 to 45 ksi) and yield strength = 241 to 275 MPa = 35 to 40 ksi) each containing two equal size circular holes. The idea behind this setup was to perform two experiments at the same time and avoid any bending stresses. The two experiments differ in that the top and bottom holes would be loaded through different size pins so as to have different clearance between the top and bottom holes of each specimen and its pin. Each pin contacted both samples.

This arrangement proved difficult in that it was challenging to assemble the various separate components together. Due to the tight fit between the two pins and the two specimens (essentially no pin/plate clearance), it was hard to assemble the separate components together, not to mention the difficulty in correctly aligning the two samples on opposite sides of the end loading fixtures. As the diameter of the tight pin was virtually identical to that of its hole in the plate, the pin was shrunk using liquid nitrogen and was then inserted into the plate. The liquid nitrogen destroyed the black paint (used for TSA) on the specimen. The essentially total lack of pin/hole clearance also did not provide any clearance (necessary for imposing traction-free boundary conditions when doing the stress analysis later). Moreover, it was necessary to operate the MTS machine (Rm. 1341E EH) used for this experiment in displacement-control, not load-control, which compounded the difficulties. *Figure 6.4* is a photograph of the experiment for this initial specimen configuration and test setup. Interestingly, loading the clearance-less end of the specimen arrangement of *figures 6.3 and 6.4* introduced us to the topic of 'friction welding'.

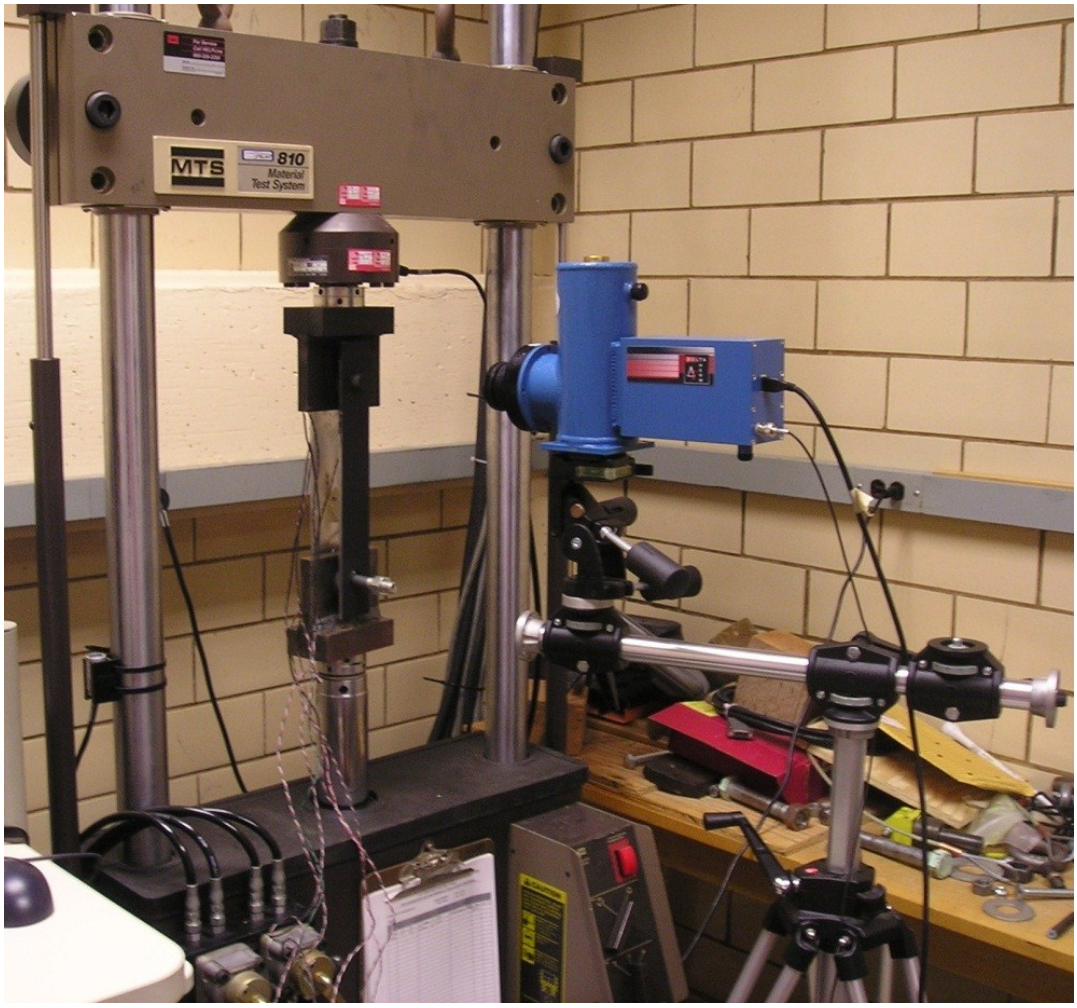

Fig. 6.4: Initial setup experiment

Figure 6.5 is shows the raw TSA data recorded from this setup of *figures 6.3 and 6.4*. The image is not overly sharp, but the TSA image is fairly symmetrical about the vertical x-axis. However, as previously mentioned there was insufficient clearance between the pin and hole for the traction-free boundary conditions to be imposed, by which to determine the unknown Airy coefficients.

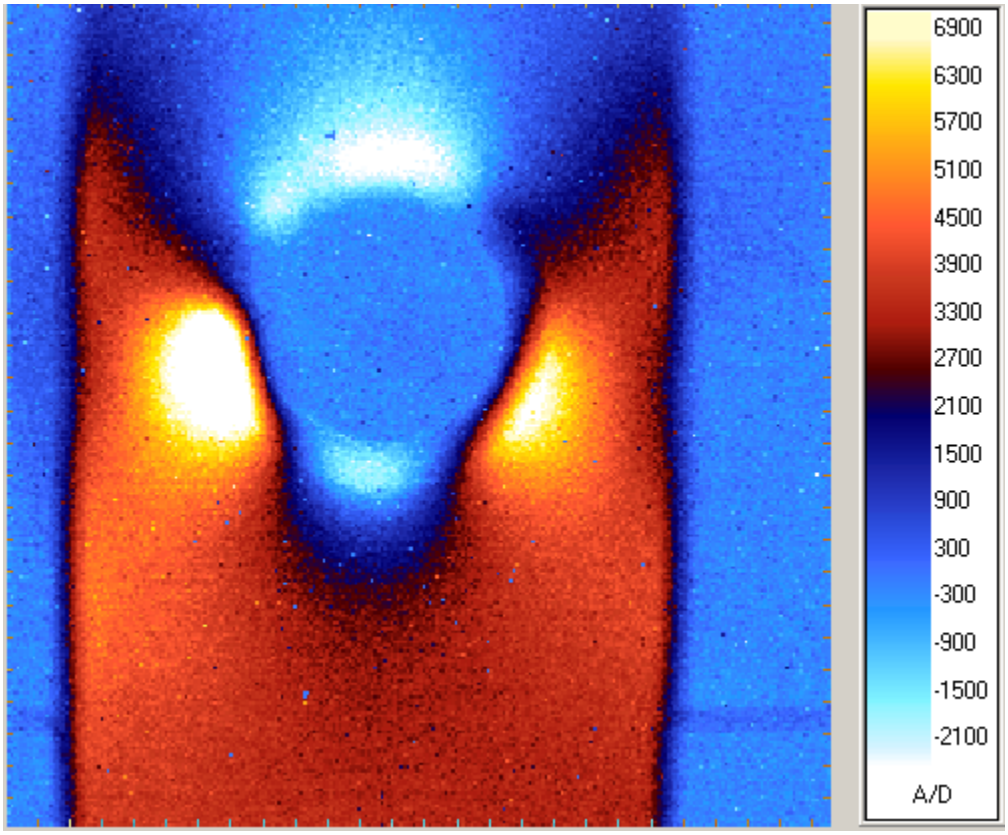

Fig. 6.5: Raw TSA data from initial setup experiment

After encountering the above experimental difficulties, multiple test setups were analyzed using FEA/CAD modals and Mr. Dave Arawinko, an instrument maker specialist at the machine shop (Rm. B1060 ECB), provided meaningful information on appropriate clearances, etc. As a result, a different setup was decided (*figure 6.6*) that involves only one specimen with one circular hole to be tested twice with two different types of pins as to achieve different pin-hole clearances i.e., by using a circular and non-circular pin.

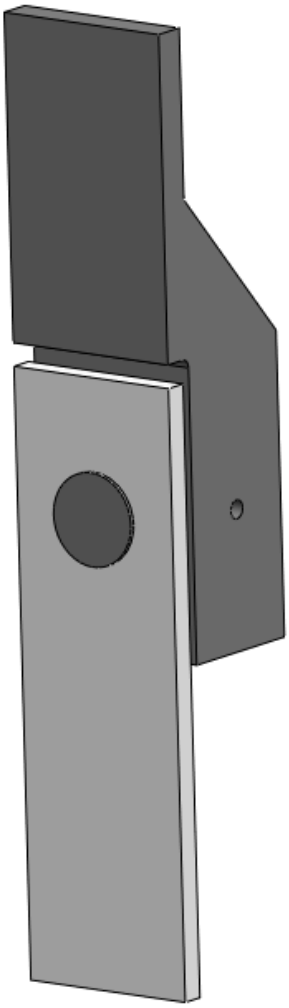

Fig. 6.6: 3D CAD model of the final setup

The same new fixture and test specimen were used for both experiments, the only difference being the pin. The following subsections will discuss and show the details of the specimen, fixture, and the two pins used.

6.3.2 Test Specimen Details

Figures 6.7 show a 2D sketch and isometric 3D CAD model of the specimen. Care was taken in evaluating the dimensions that the specimen can be clamped between the hydraulic grips of the MTS machine (B321 EH – Fatigue lab). The following include details of the specimen tested here:

- Material of the plate: Aluminum 6061-T6; Elastic Modulus, E = 68.95 GPa (10 x 10^6 psi), Poisson's ratio, ν = 0.33, Ultimate strength = 275 to 311 MPa (40 to 45 ksi) and Yield strength = 241 to 275 MPa (35 to 40 ksi), purchased from Wiedenbeck Inc., Madison WI.
- Length of the specimen = 165 mm (6.5″).
- Width of the specimen = 50.8 mm (2″).
- Diameter of the circular hole = 25.4 mm (1.000″).
- Thickness of the specimen = 6.37 mm (0.25″).
- Specimen is symmetric about the vertical axis (x-axis).
- Two strain gages were mounted, one on the front and one on the back, to ensure proper specimen alignment by monitoring and minimizing any potential bending. (A detailed description of the strain gages used and the strain gage analyses is contained in section 6.6).
- As mentioned previously, unless indicated otherwise, all dimensions were originally in inches. The English units have been converted to mm based on one inch = 25.40 mm.

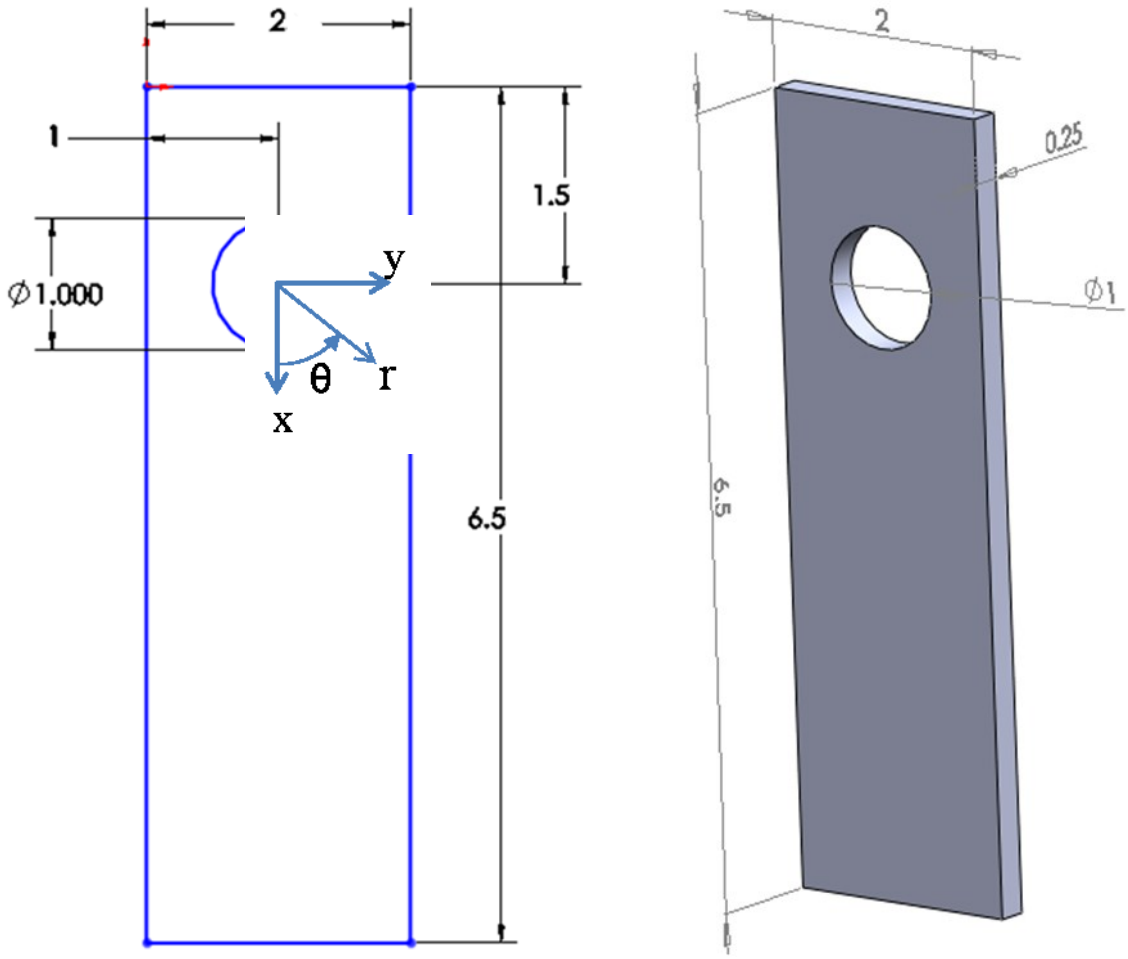

(a) (b)

Fig. 6.7: 2D sketch of test specimen (left) and 3D CAD model of test specimen (right)

6.3.3 Circular Pin/Bolt

The circular pin/bolt geometry (*figures 6.8* and *6.9*) is that of a step cylinder with the addition of a flat surface (left side in *figure 6.8* and top in *figure 6.9*) such that a screw can be tightened against the surface of the pin to hold the pin in place, i.e., the pin is constrained so that it cannot rotate during the test. The diameter of the back portion of the small cross-section of the pin in *figure 6.8* and bottom section of that portion in *figure 6.9* is not of prime interest since it does not contact the specimen. The diameter of the second portion (front section, larger cross-section in *figures 6.8 and 6.9*) of the cylinder is 0.9991 inches (25.3771 mm) in diameter providing a 0.0009 inch (0.0229 mm) diameter clearance between the plate hole (1.0000 inches = 2.540 mm diameter) and the pin. Again, and compatible with the actual machining and dimensional measurements, the dimensions in *figures 6.8 and 6.9* are in inches. Both the circular and non-circular pins were machined from 4140 steel (chromium-molybdenum steel) having an ultimate tensile strength = 655 MPa = 95 ksi, yield strength = 417.1 MPa = 60.5 ksi.

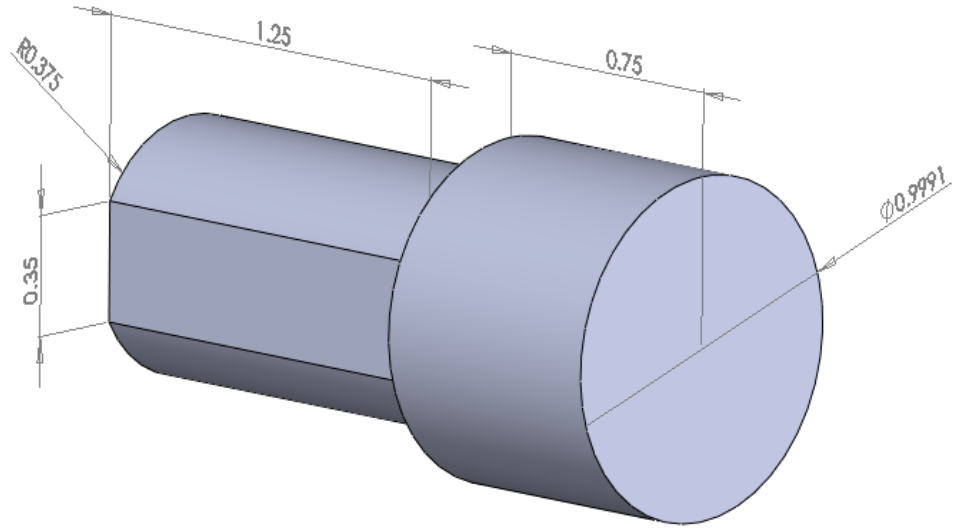

Fig. 6.8: 3D CAD model of circular pin

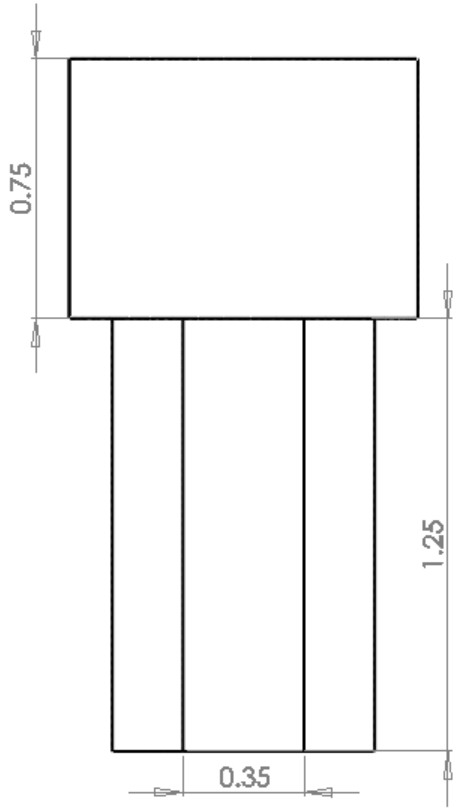

Fig. 6.9: 2D side view of the circular pin

6.3.4 Non-circular Pin/Bolt

The non-circular pin geometry (*figures 6.10* and *6.11*) is similar to that of the circular bolt with two main differences. The first is that the right portion of the cylinder in *figure 6.10* is half circular and half non-circular. Although there is some uncertainty that the semicircular portion is exactly half, the subsequent TSA analysis demonstrates that the pin/plate contact region with this pin exceeds 180^{o}. The second difference between this pin of *figures 6.10* and *6.11* and the previously described round pin is that the diameter (of the semicircle in this case) is 0.9993 inch (25.3822 mm) resulting in a pin-hole diametral clearance of 0.0007" = 0.0178 mm. As with *figures 6.8 and 6.9*, the dimensions in *figures 6.10 and 6.11* are in inches.

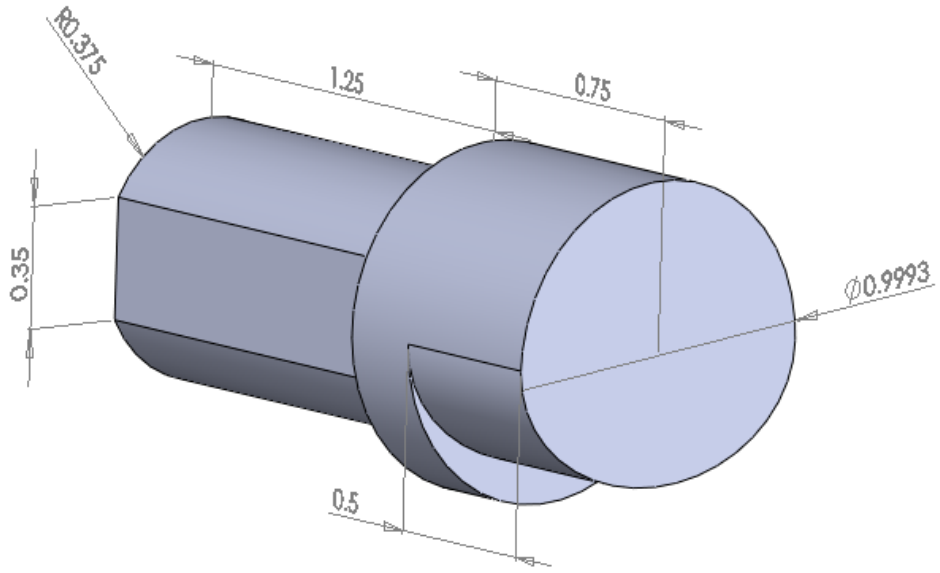

Fig. 6.10: 3D CAD model of the non-circular pin

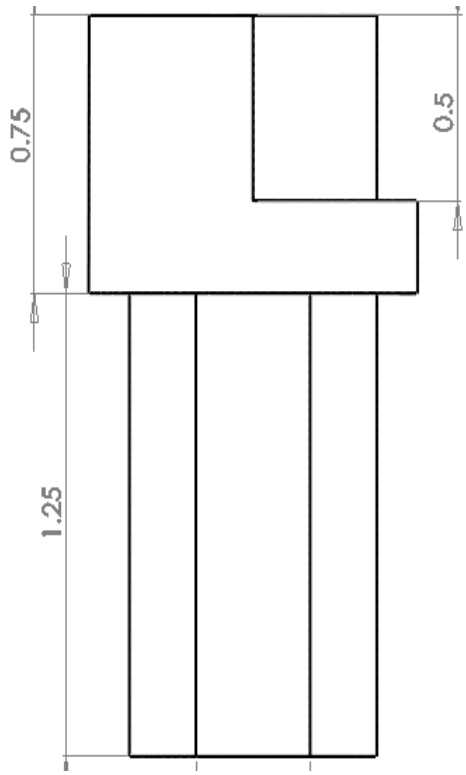

Fig. 6.11: 2D side view of the non-circular pin

6.3.5 Back loading Fixture

The purpose of the top-back fixture in *figure 6.6* is to hold the assembly together and transmit the load from the MTS loading machine to the aluminum plate specimen through the steel pin. This is done by gripping the top flat part of the fixture of *figure 6.6* into the MTS hydraulic grips and by holding the pin-plate interface. The back fixture (*figures 6.12 and 6.13*) has a 0.75 inch (19.05 mm) diameter round hole through it to accommodate the pin, *figure 6.12 (a)*. A small, threaded round hole is provided (right face in *figure 6.12 (a)* and top in *figure 6.12 (b)* to accommodate a set screw to tighten against the flat side of the pin (*figures 6.8 through 6.13*). *Figures 6.12 (a) and 6.12 (b)* are a 3D CAD model of the back loading fixture in isometric and side views with all dimensions in inches. *Figures 6.13* are photographs of the back loading fixture with a pin in place. The set screw, which prevents the pin from rotating, and its threaded hole, are visible on the side of the loading fixture in *figures 6.12 and 6.13*. The loading fixture was machined from cold rolled 1020 steel having an ultimate tensile strength = 420 MPa = 60.91 ksi, yield strength = 350 MPa = 50.76 ksi.

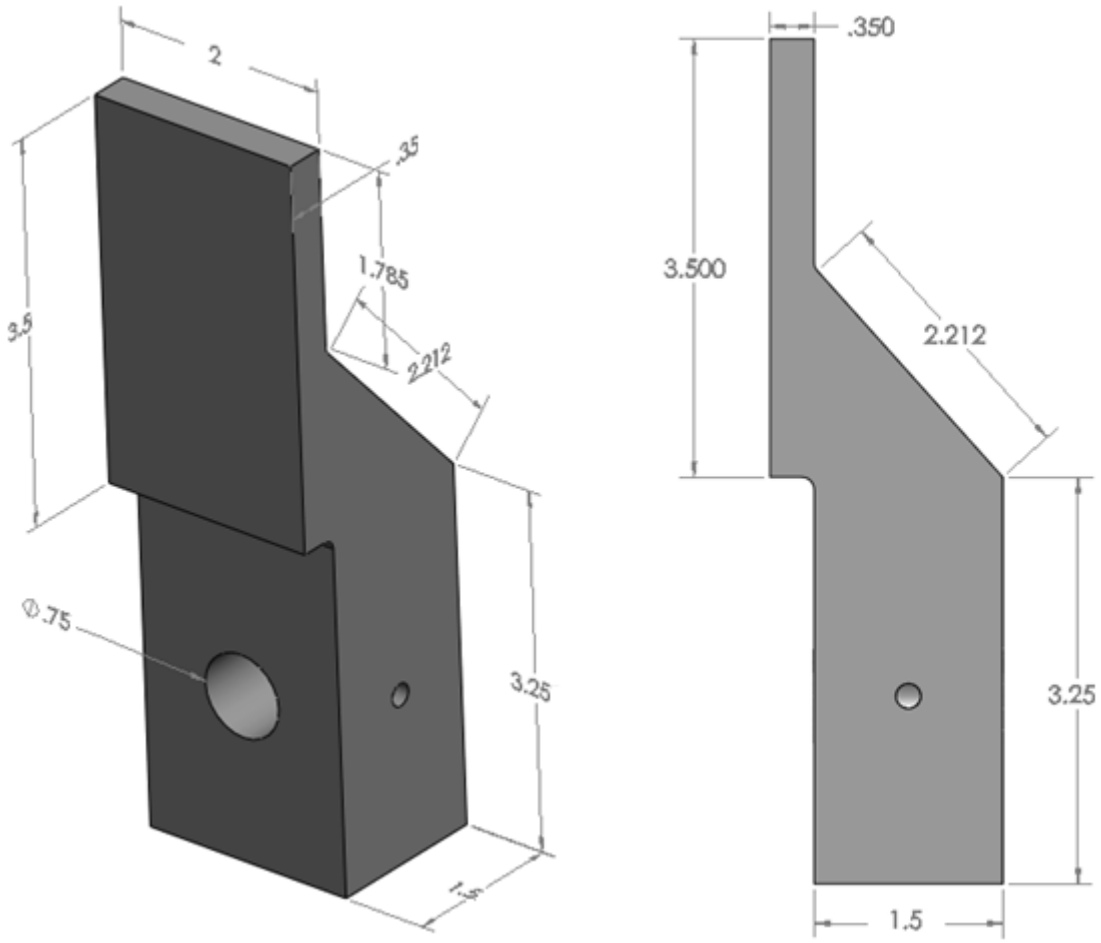

(a) (b)

Fig. 6.12: 3D CAD model of fixture (left) and CAD side view of fixture (right)

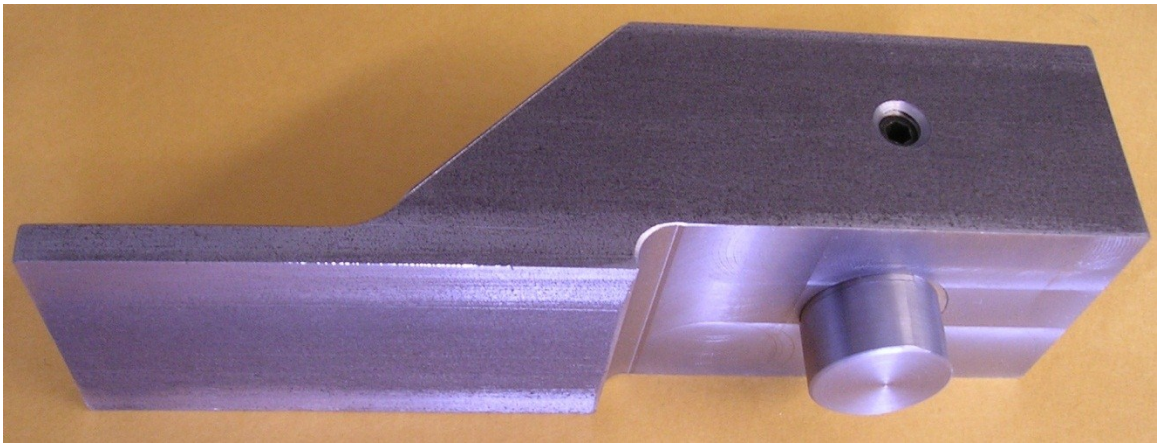

Fig. 6.13(a): Front view of back loading fixture showing pin and set screw which bears against the pin

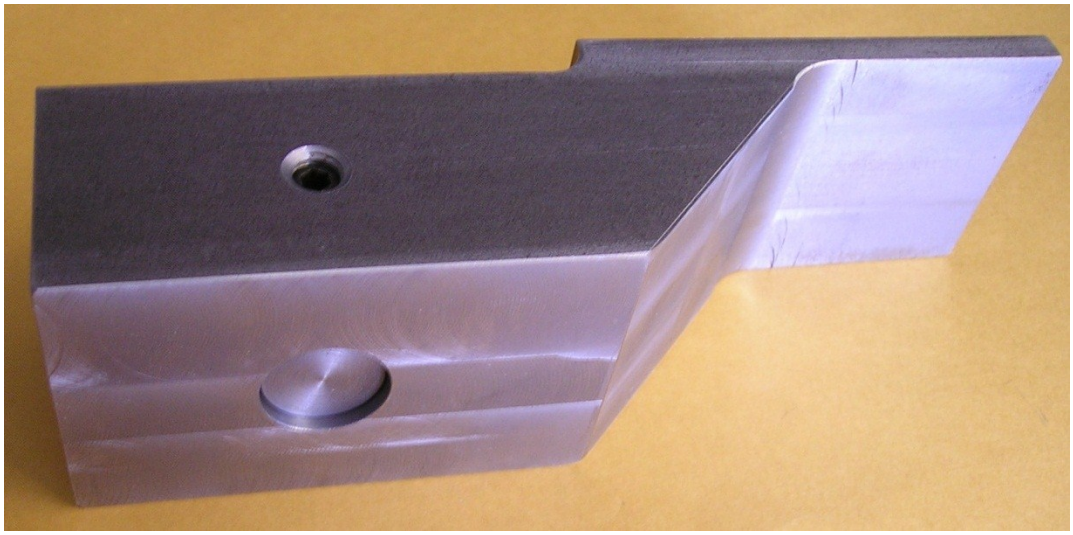

Fig. 6.13(b): Back view of back loading fixture showing pin and set screw which bears against the pin

6.3.6 Assembly

Assembling the separate components with either the circular or non-circular pin was considerable easier using the arrangements of *figures 6.6 through 6.13* than the earlier scheme of *figures 6.3 and 6.4*. This was largely because of the fewer parts to assemble, better dimensions, and more appropriate pin/hole clearances. Recall that the following clearance dimensions were used here:

- Plate hole diameter (drilled and reamed) = 1.0000 inch
- Circular pin diameter = 0.9991 inch (0.0009" pin/hole diametrical clearance)
- Non-circular pin diameter = 0.9993 inch (0.0007" pin/hole diametrical clearance)

The pins were machined on a lathe and then polished with emery clothe. Part of a round pin was milled off to provide a non-circular contact area.

Figure 6.14 shows the separate components (strain-gage test specimen and the loading fixture with its pin) before assembly, whereas *figures 6.15* are the 3D CAD drawings of the complete assembly for both the non-circular and circular pins. The top vertical flat portion of the back loading fixture of *figures 6.12 and 6.15* was inserted into the top hydraulic grip and the bottom of the aluminum connector plate into the bottom hydraulic grip of the MTS machine.

A sheet of insulating material (G10 phenolic, top black perforated item in *figure 6.14*) was initially placed between the specimen and the loading fixture in order to reduce the friction and any possible heat transfer from the loaded plate specimen. The thickness of this sheet introduced some specimen misalignment, causing the specimen to bend out-of-its plane.

Therefore this insulating sheet was subsequently removed and the perforated aluminum plate was allowed to self-align between the hydraulic grips.

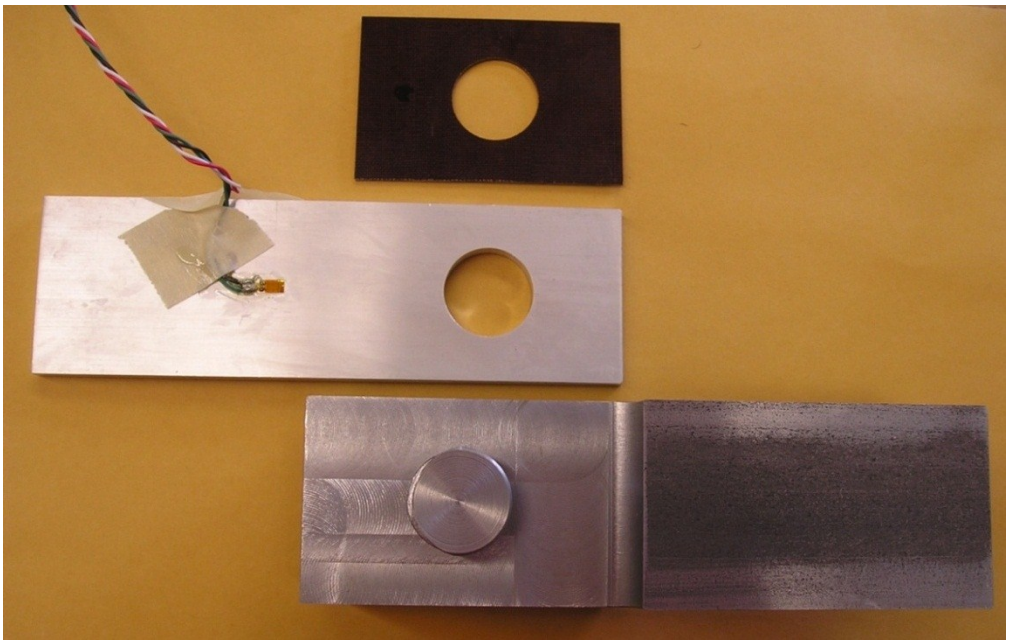

Fig. 6.14: Separate assembly components

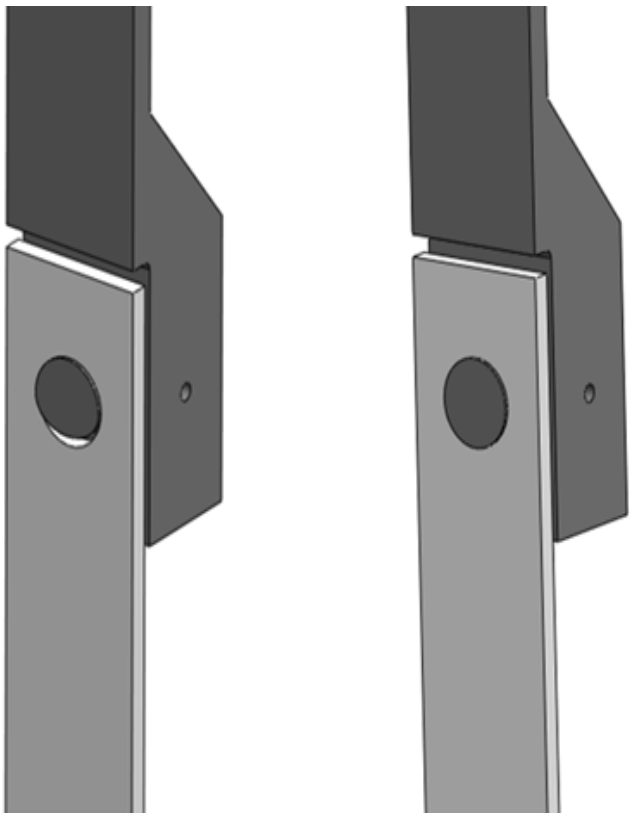

(a) (b)

Fig. 6.15: 3D CAD model of the setup with the non-circular pin (left) and circular pin (right)

6.4 Experimental Details

6.4.1 Specimen Preparation and Loading

The first step involved in preparing the specimen was to polish it with 400 grit sandpaper in order to have a clean surface finish for the black paint to adhere to. While polishing the plate with 400 grit sand paper, care was taken to ensure the edges of the holes were not rounded-off. Then two longitudinal strain gages were mounted on the specimen's surface (one on the front side and one on the back). Those are to be used to insure the proper specimen alignment by checking for any potential out-of-plane bending during plate loading. Finally, the aluminum specimen was sprayed with Krylon Ultra-Flat black paint to provide an enhanced and uniform

emissivity. The strain gages and their leads were covered with gage-coat before applying the paint to prevent the paint from causing any electrical shorts. The specimen was then ready for the TSA experiment.

The specimen was mounted and properly gripped (in the hydraulic grips) in the loading frame of the MTS hydraulic testing machine (B321 EH) and subjected to a cyclic sinusoidal loading varying from 3,558.6 N (800 lbs) ± 2,669 N (600 lbs) at a rate of 20 Hz for both circular and non-circular pins. An oscilloscope, *figure 6.16,* was used to accurately monitor the applied cyclic load and frequency. The loading was applied using an MTS machine (20Kips capacity having hydraulic grips capable up to 18.5 Kips) that can operate in either load or displacement control with any of four ranges (10%, 20%, 50% and 100% measure of capacity). For the current experiment, 20% range was utilized in load control which allows for a maximum load of 17,793N (20% of 20,000lb = 4,000lb). The hydraulic grips apply a uniform clamping pressure (which can be adjusted as per the material) over the bottom end of the aluminum specimen and the top section of the back steel loading fixture (*figure 6.17*).

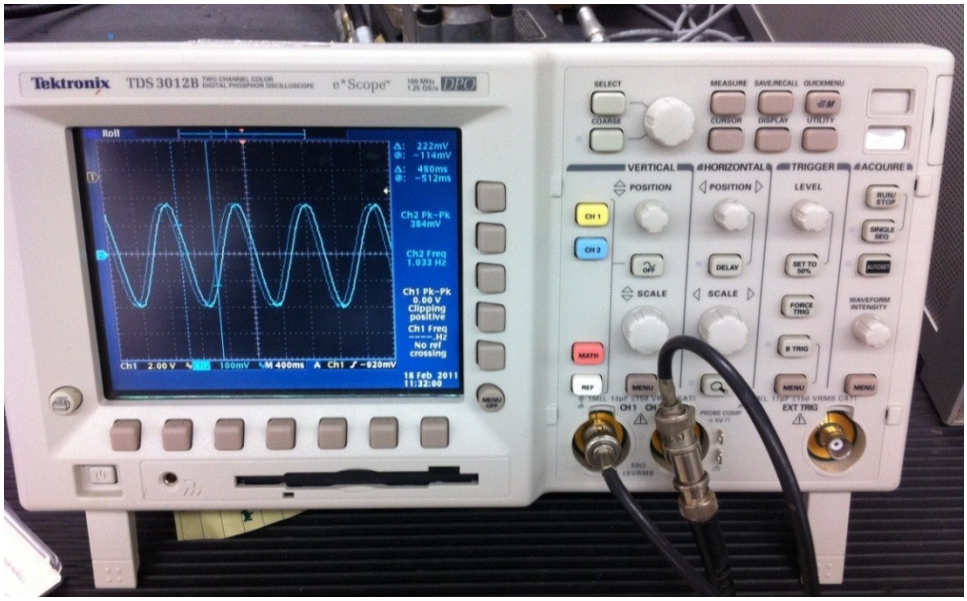

Fig. 6.16: Oscilloscope

Fig. 6.17: MTS hydraulic grips

The test plate was aligned between the top and the bottom grips as illustrated in *figure 6.17* such that the top front plate-like section of the loading fixture of *figure 6.6* and the test specimen were co-linearly loaded in the MTS grips. When clamping the specimen between the hydraulically operated grips, particular care was taken to ensure that the plate is symmetrically loaded about vertical x-axis. This was done by measuring the distance from the end of the grips to the plate edge (on either side, *figure 6.17*). Of course TSA images provided the final assessment of symmetry about the vertical axis. Any possible out-of-plane bending of aluminum plate was minimized by monitoring the strains obtained from the strain gages mounted on the front and the back faces of the aluminum plate i.e., the experimental arrangement (loading, plate geometry) is symmetrical, so there will be uniform stress across the plate thickness. Details about strain gage readings are included in section 6.6.

The corresponding load-induced temperature data on the surface of the specimen were recorded by a TSA Delta Therm model DT1410 camera (Stress Photonics, Madison, WI) as shown in *figure 6.18*. The TSA camera has a sensor array of 256 horizontal x 256 vertical pixels. TSA experimental setup (including labels) can be seen in *figure 6.19*.

Note that the plate with a non-circular pin was the first experiment. Then that pin was replaced with the circular pin and same plate was used for second experiment. The order shown in this chapter tends to be reversed i.e., the analysis and results for the circular pin are presented first.

Fig. 6.18: TSA Delta Therm camera

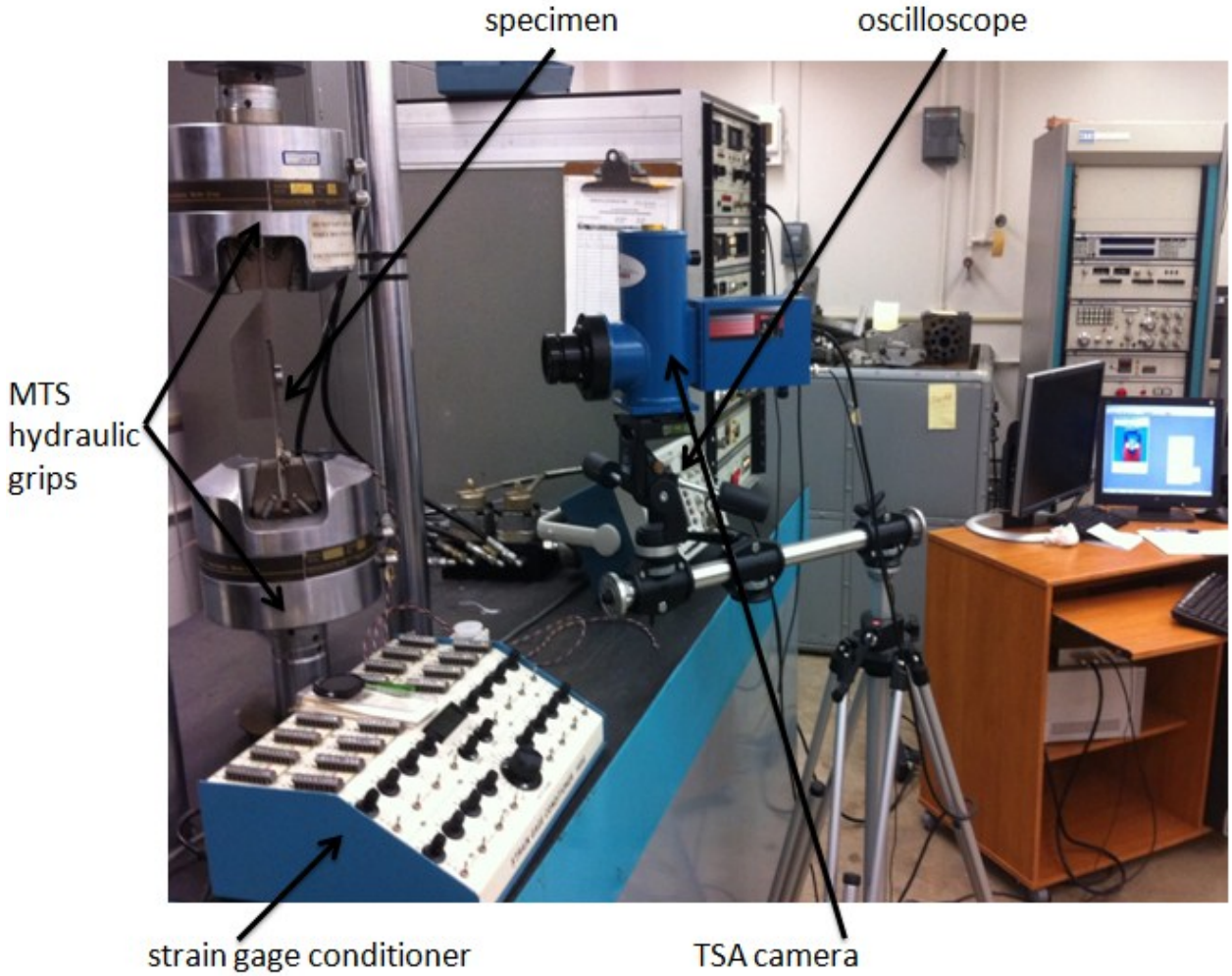

Fig. 6.19: Experimental setup

Sections 6.4.2 through 6.4.4 contain some photographs and raw TSA data images for the two experiments performed (i.e., the plate with the circular and non-circular pin/bolt) and corresponding TSA calibrations.

6.4.2 Circular Pin

Figure 6.20 shows a raw TSA image provided by the Delta Vision software for the experiment using the circular pin. The TSA sensor array has a spatial resolution of 256 horizontal x 256 vertical pixels and approximately 27,000 pixels cover the aluminum test plate. Using the Delta Vision software, the TSA data was exported to Excel®. The raw TSA data were then imported into MATLAB and *figure 6.21* is the MATLAB reconstructed image of the raw TSA data of *figure 6.20*. Knowing the diameter of the hole or the width of the plate, one can obtain the pixel size for the specimen. The pixel size at the plate in the analyses was found to be 0.4 mm (0.016″). Since the plate is symmetrical about vertical x-axis, the measured TSA data were averaged about this vertical axis. Recognizing recorded TSA data tend to be unreliable at and near an edge, no TSA input values were used within two pixels of edges of the hole, i.e., approximately 0.79 mm (0.03″) from the boundary of a hole. A FEA (discussed later in section 6.7) indicates that the pin (top of the pin), where it contacts the top of the hole, moves vertically less than 0.01 mm during the cyclic applied load range of 1,200 pounds (5,337.86 N), which is much smaller than this two-pixel distance of 0.8 mm.

The “contourf( )” function in MATLAB can be used for making contour plots but I preferred writing my own algorithm for making the contour plots like that of *figure 6.21*.

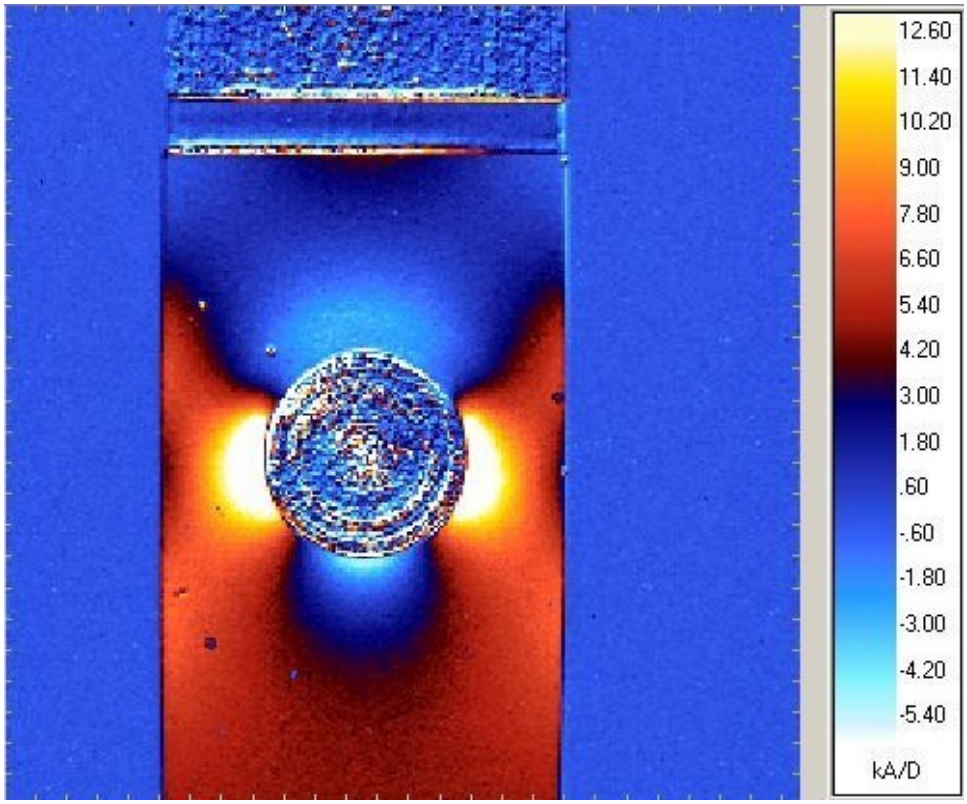

Fig. 6.20: Raw TSA S* Image for the plate with circular pin

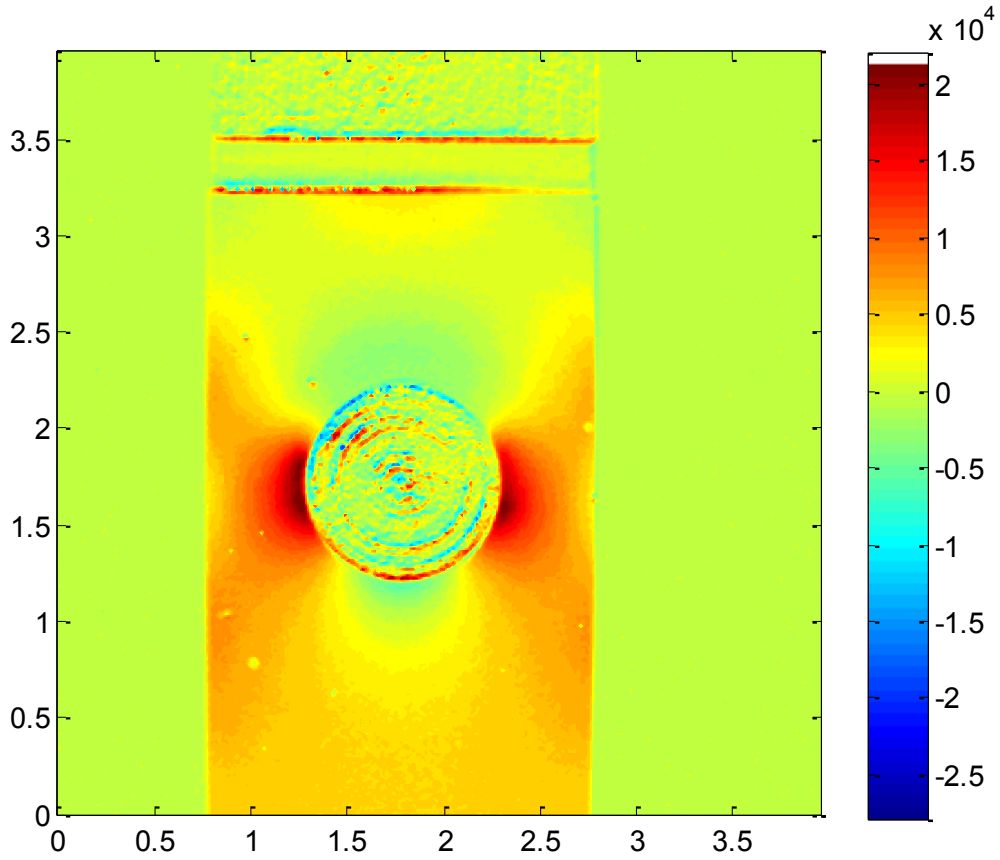

Fig. 6.21: Raw TSA S* data for the plate with circular pin reconstructed in MATLAB

6.4.3 Non-circular Pin

Figure 6.22 shows the raw TSA image (from the Delta Vision software) for the aluminum plate loaded by the non-circular pin. Approximately 29,000 pixels cover the plate. The raw TSA data was again imported into MATLAB and *figure 6.23* is the MATLAB reconstructed image of the raw TSA data of *figure 6.22* for the plate with non-circular pin. Pixel size was again found to be 0.4 mm (0.016″), which is same as plate with circular pin. As done earlier for the circular-pin case, the measured TSA data were averaged about the vertical x-axis. Recognizing the unreliable edge data, no recorded TSA values are used within two pixels of the boundary of a hole, i.e., approximately 0.79 mm (0.03″). The clearance between the bottom of the hole in the plate hole and the non-circular pin is noticeable in *figures 6.22 and 6.23*.

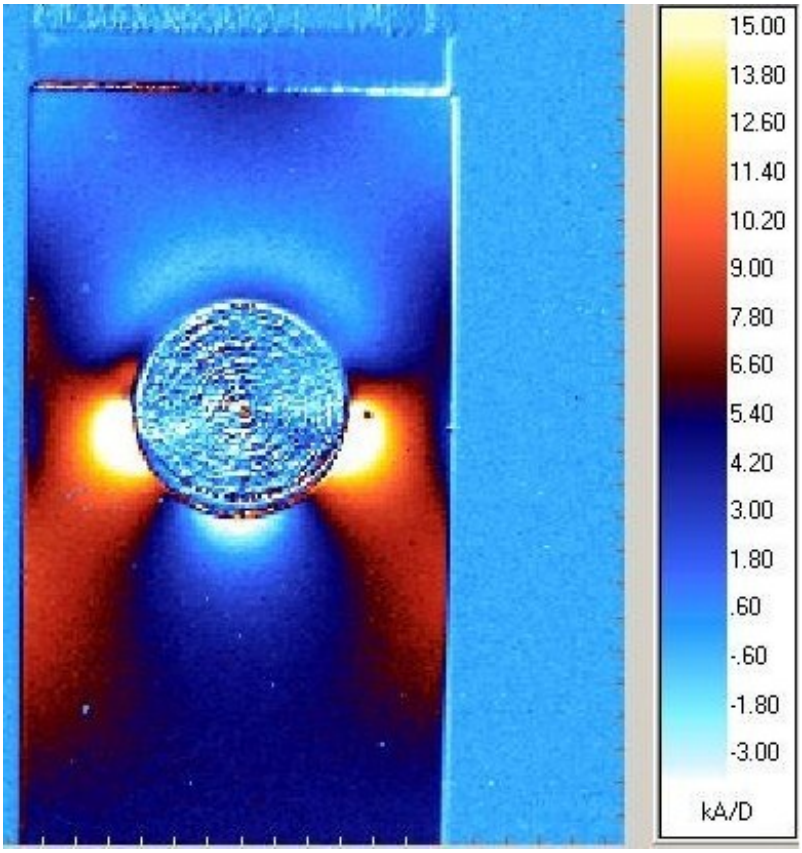

Fig. 6.22: Raw TSA S* data for the plate with non-circular pin

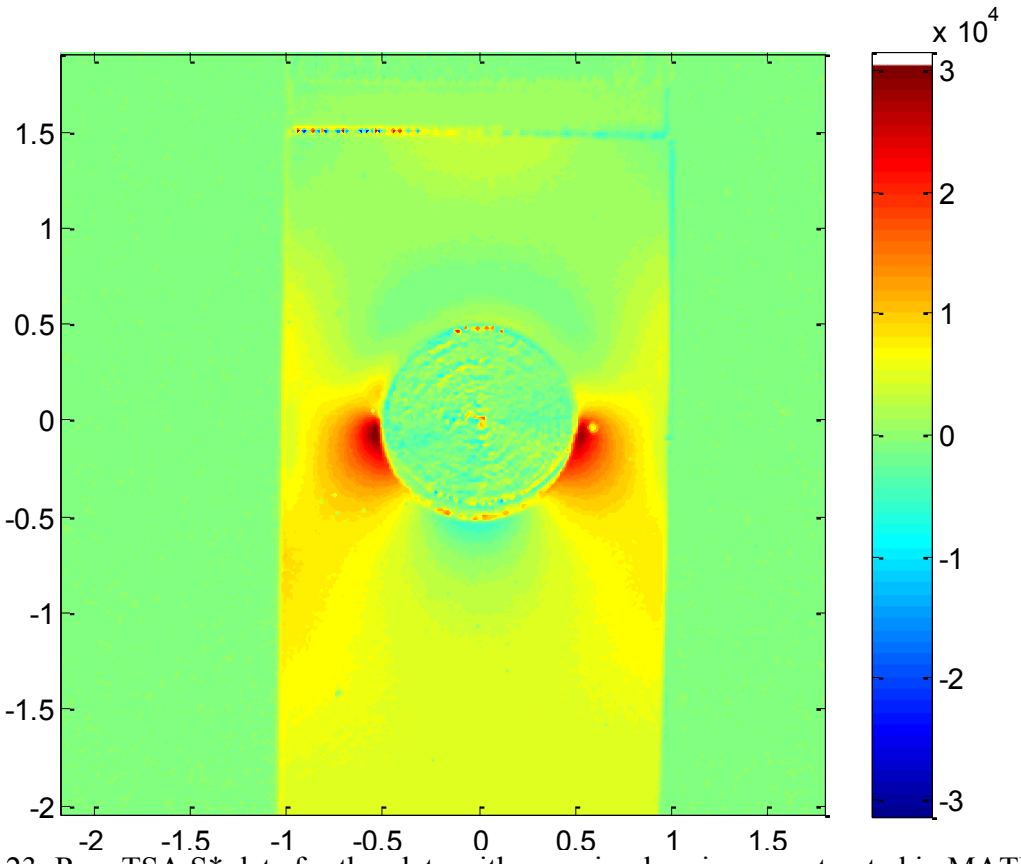

Fig. 6.23: Raw TSA S* data for the plate with non-circular pin reconstructed in MATLAB

6.4.4 Calibration

The reason behind performing a TSA calibration experiment is to simply determine the thermoelastic constant K as defined by the equation below:

$$S^* = K\Delta\left[(\sigma_1 + \sigma_2) = (\sigma_{rr} + \sigma_{\theta\theta}) = \left(\sigma_{xx} + \sigma_{yy}\right)\right] \tag{6.14}$$

where S^* is the recorded TSA signal/data and ΔS is the change in isopachic stress or the sum of the orthogonal stresses. The coefficient K can be evaluated from a region whose state of stress is known, preferably at a location far from any geometric discontinuity where the state of state of stress is uniaxial. Since the aluminum test specimen contains a circular hole and the MTS hydraulic grips consume a significant portion for the rest of the specimen's area, a separate uniaxial tensile specimen was used for calibration. The calibration specimen has the exact same material properties (as it was machined from the same aluminum plate) as the test specimen, as well as an identical coating of flat black paint and cyclically-loaded at the same frequency. Moreover, the calibration sample was tested on the same day as was the test specimen, thereby avoiding any potential effects of changes in temperature and humidity conditions. The same specimen was used for calibrating both the experiments.

Figure 6.24 shows the geometry of the calibration specimen. The only difference between this calibration specimen and the test specimen is the former does not have any pin-loading hole or any such irregularity and is symmetrical about both of its x- and y-axes.

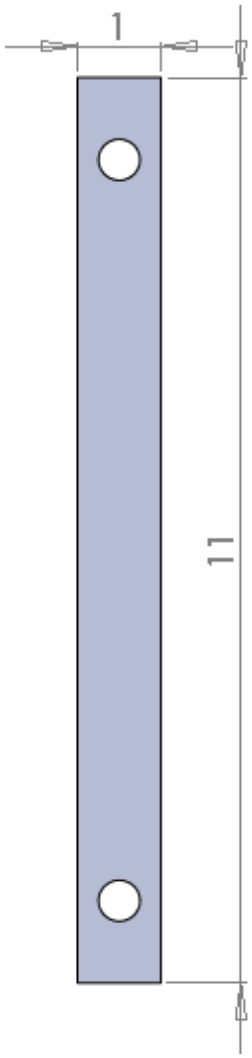

Fig. 6.24: Calibration Specimen

The following include details of the calibration specimen tested here:

- Material: Aluminum 6061-T6 (Wiedenbeck, Inc., Madison, WI); Ultimate strength = 275 to 311 MPa (40 to 45 ksi) and yield strength = 241 to 275 MPa (35 to 40 ksi)
- Length of the specimen = 279.4 mm (11″)
- Width of the specimen = 25.4 mm (1″)

- Thickness of the specimen = 6.37 mm (0.25″)

- Specimen is symmetric about the both the horizontal and vertical axes

The stress distribution is uniform and known (only uniaxial tension). Thus, knowing the recorded thermoelastic signal, S* (which was scanned along horizontal lines at different levels/heights of the strip and then averaged), applied load and the cross sectional area of the specimen, the coefficient K was determined from S*/uniform stress. The calibration values for the circular-pin case and non-circular-pin case were found to be K = 261 U/MPa (1.8 U/psi) and K = 246.58 U/MPa (1.7 U/psi), respectively. There are two different calibration values because the plate loaded was first loaded with a non-circular pin on a different day than the plate with a circular pin. The original black paint was removed from the calibration specimen using CSM-2 Degreaser and then this calibration specimen was repainted at the same time as repainting the plate for circular pin test.

Note that the holes at the ends of the calibration specimen are irrelevant to the present situation and were covered by the hydraulic grips, *figure 6.24*. *Figure 6.25* shows the experimental setup for the calibration specimen.

Figures 6.26 and 6.27 are the raw TSA data obtained from performing the TSA experiment on the calibration sample for the circular and non-circular pin cases.

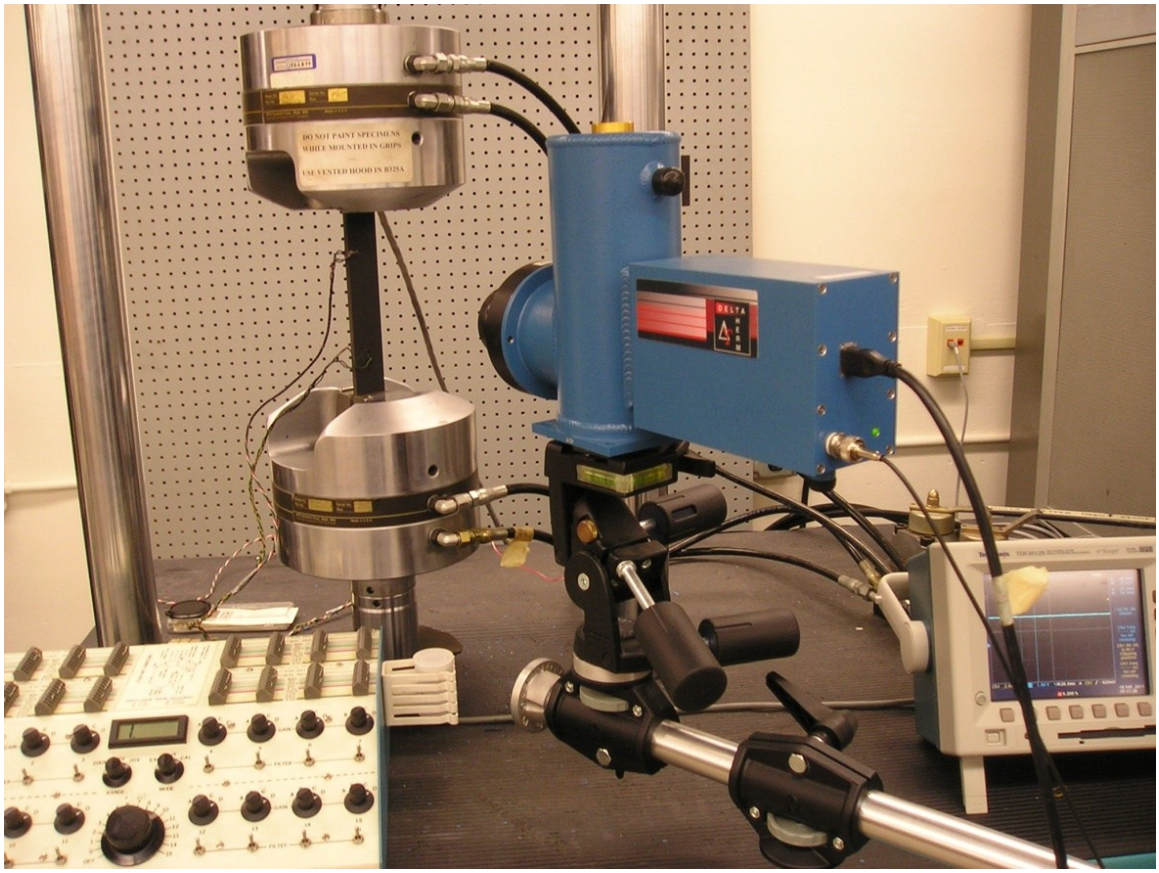

Fig. 6.25: Calibration sample experimental setup

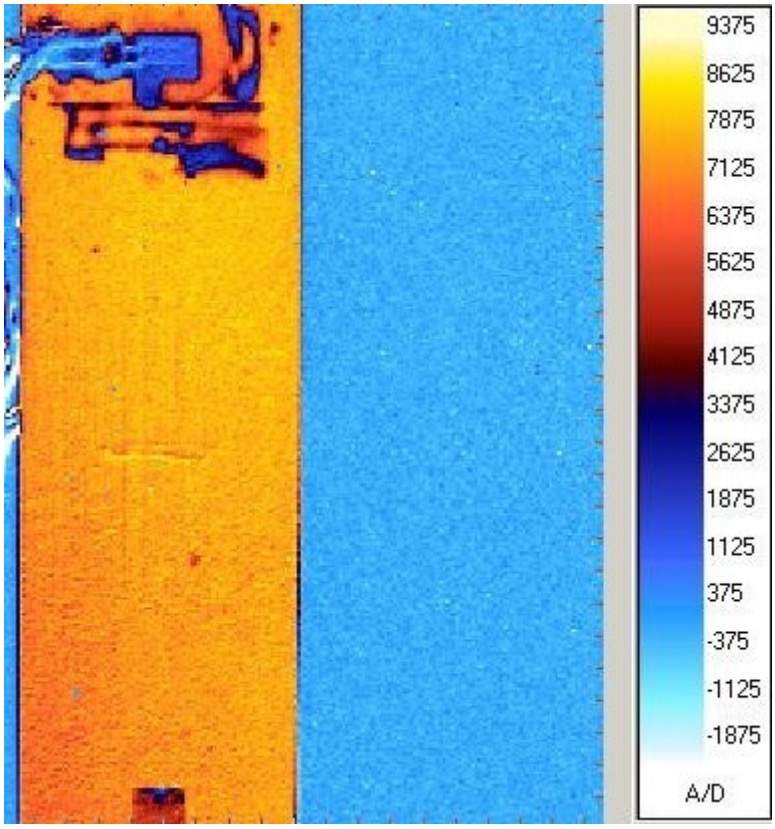

Fig. 6.26: Calibration TSA S* image (data) for the plate with circular hole

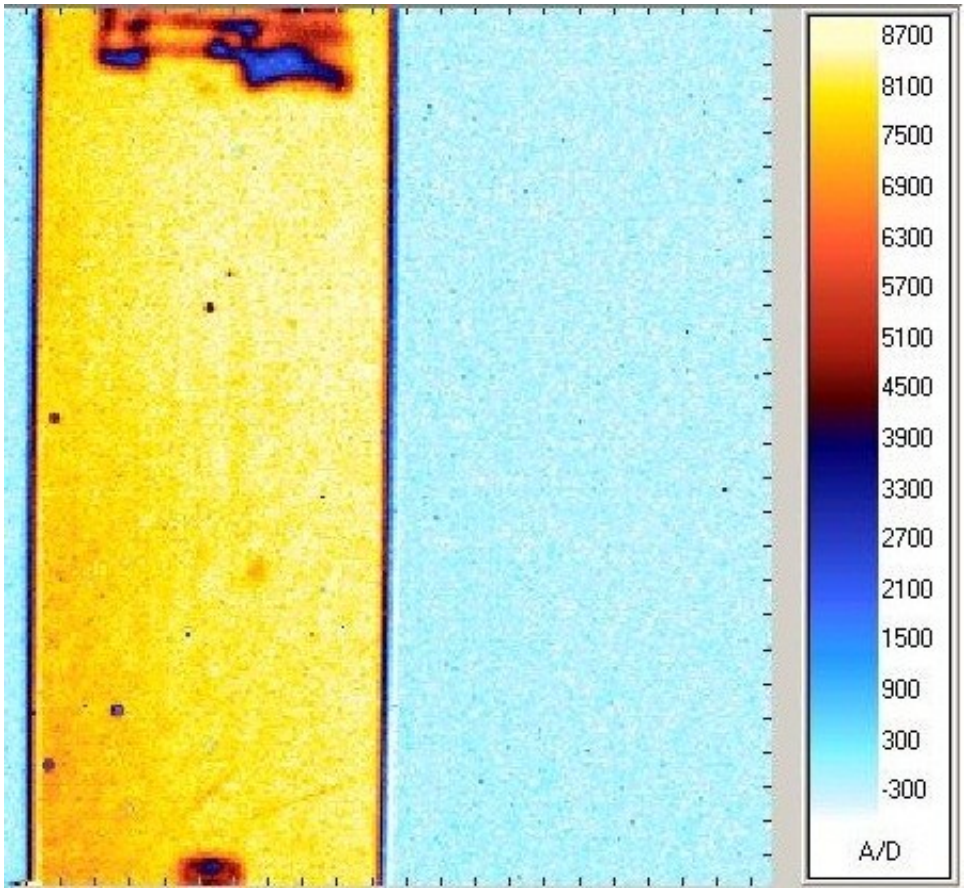

Fig. 6.27: Calibration TSA S* image (data) for the plate with circular hole

The calibration specimen contained a total of four strain gages, two on the front and two on the back (one longitudinal and one transverse on each side), to monitor the strains and thereby ensure proper specimen alignment during testing. The local temperature perturbations due to the strain gages are apparent towards the ends of the thermograms of *figures 6.26 and 6.27*.

6.5 Data Processing

The objective of this research is to evaluate the individual components of stresses at and in the vicinity of the hole in a pinned/bolted joint problem from the measured isopachic stresses. As the plate is symmetrical about the longitudinal x-axis, the TSA data were averaged about the x-axis i.e., one half of the plate is used for the analysis. The pixel size was found to be 0.4 mm (0.016″) for both the plate with circular pin and non-circular pin experiment, respectively. However, the TSA data is unreliable near an edge, and therefore no TSA input values are employed within at least two data positions i.e., source locations of TSA input data selected extend from near the inner radius for the hole [radius of hole + (2 x pixel size)] to an outer radius of 22.86 mm (0.9″). *Figure 6.28* indicates the area covered by the source locations of the TSA input data used in the analyses of the plate when loaded by the circular pin (the number of TSA input values is $m_1 = 3{,}413$ inputs) and $m_2 = 3{,}458$ inputs for non-circular pin, respectively. *Figures 6.29 and 6.30* are the contour plots of the raw TSA data near the edge of the hole i.e., these data are before averaging about the vertical x-axis, for the circular pin and non-circular shaped pin, respectively. *Figures 6.31 and 6.32* are the contour plots after averaging the TSA data about the vertical x-axis for the circular pin and non-circular shaped pin, respectively. One could use the ‘contourf ( )’ function in MATLAB to make such contour plots but I wrote my own algorithm for making the contour plots in this thesis.

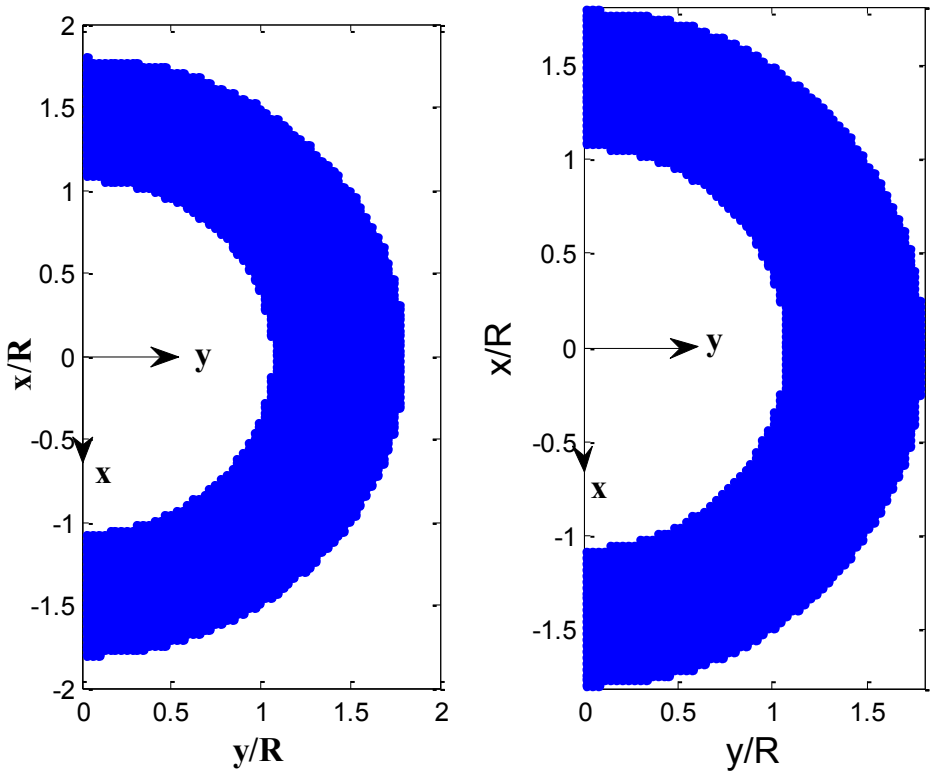

Fig. 6.28: TSA input locations for circular pin with $m_1 = 3413$ (left side) and non-circular pin with $m_2 = 3458$ (right side)

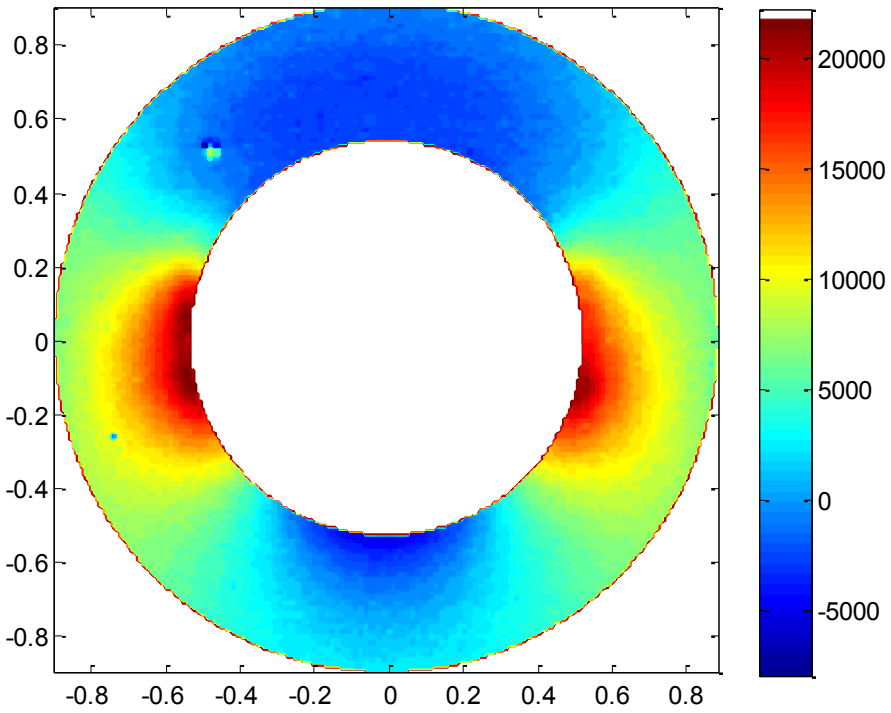

Fig. 6.29: Raw TSA S* data (not averaged about the x-axis) for the circular pin

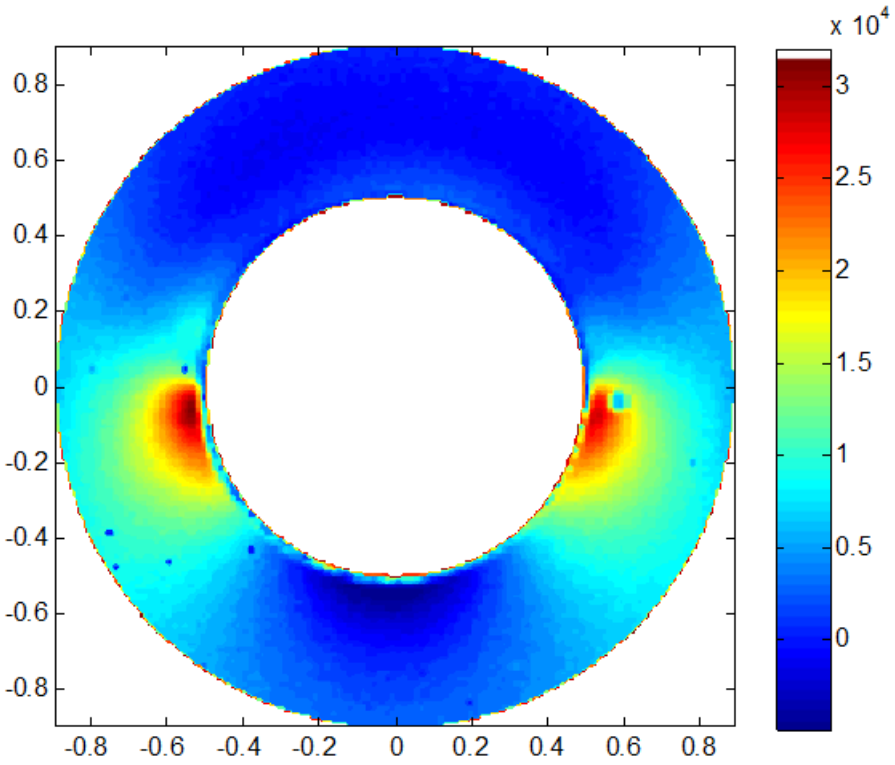

Fig. 6.30: Raw TSA S* data (not averaged about the x-axis) for the non-circular pin

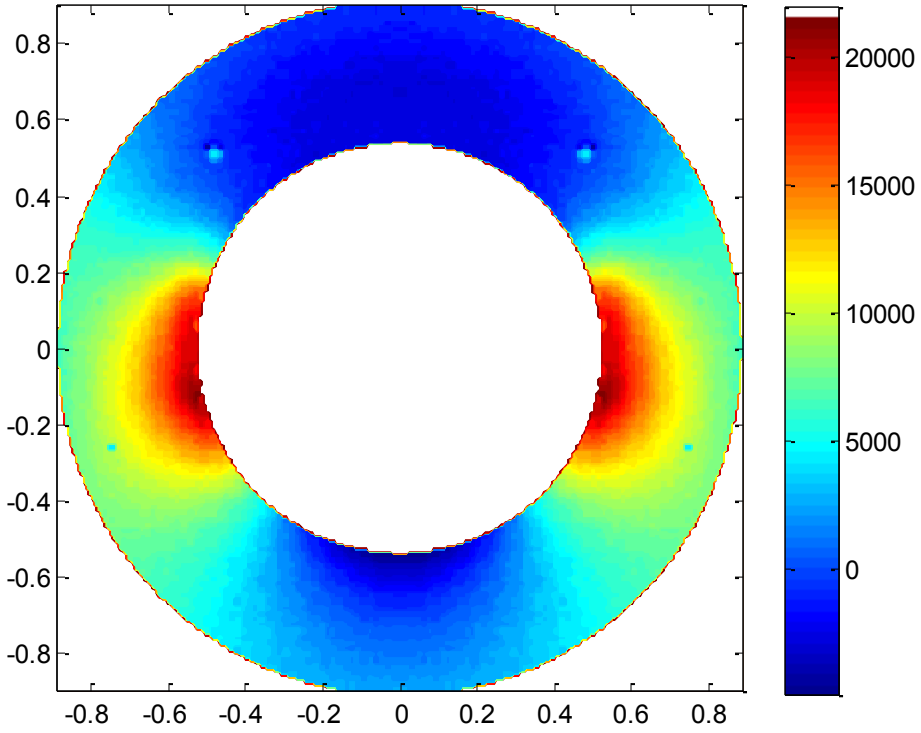

Fig. 6.31: Raw TSA S* data (averaged about the x-axis) for the circular pin

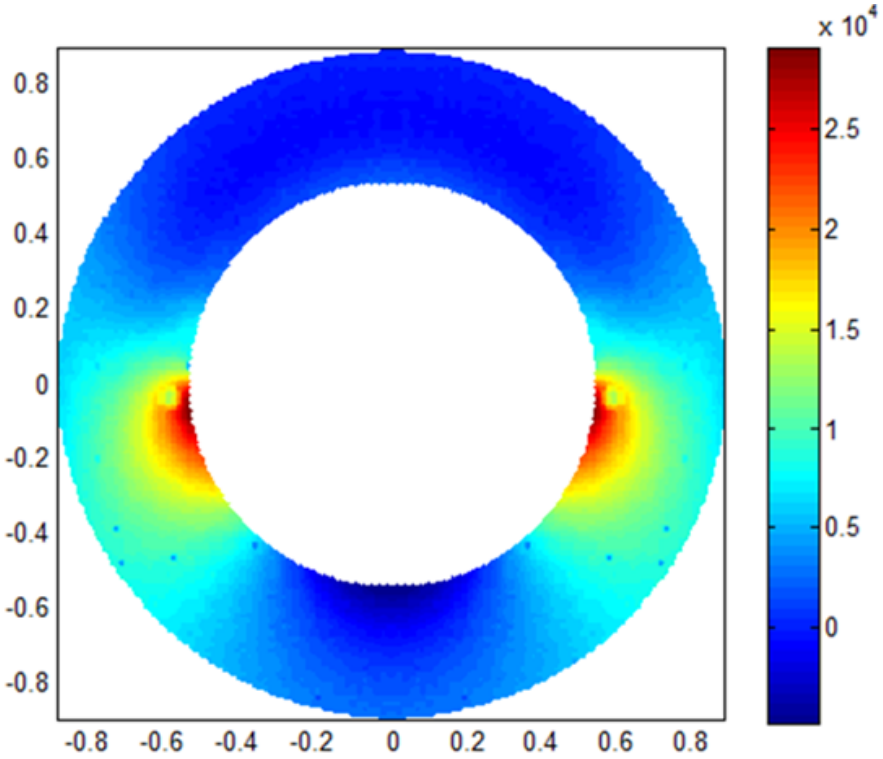

Fig. 6.32: Raw TSA S* data (averaged about the x-axis) for the non-circular pin

6.5.1 Imposing Traction-free conditions

Note that the expressions for the individual components of stress of *equations 6.6, 6.7, 6.9, and 6.11 through 6.13* contain coefficients b_o, c_1', a_n' and c_n' which do not appear in the expression for the isopachic stress, S, of *equation 6.10*. This precludes being able to evaluate the coefficients, and hence the stresses, from recorded TSA data (i.e., values of S) alone. However, needed additional side conditions with which to help evaluate all of the Airy coefficients in the expressions for the stresses are available by the imposing $\sigma_{rr} = \sigma_{r\theta} = 0$ on the non-contacting region of the hole between pin and the plate. Although not necessary, traction-free boundary conditions are also imposed on the right vertical ($\sigma_{yy} = \sigma_{xy} = 0$) and top ($\sigma_{xx} = \sigma_{xy} = 0$) edges of the plate. Condition number and RMS plots were made at every iteration in determining the traction-free boundary which is further discussed in section 6.5.2.

Plate loaded with circular pin:

For the plate loaded by the circular pin, traction-free boundary conditions $\sigma_{rr} = \sigma_{r\theta} = 0$ are imposed *discretely* on boundary of the hole from $\theta = 0^o$ to 83^o measured countered-clockwise from vertically downward positive x-axis, *figure 6.2*. In this case the traction-free conditions were found to exist over less than $\theta = 90^o$ i.e., the contact region ($83^o \leq \theta \leq 180^o$) exceeds 90^o for the half plate. Hyer observed a similar phenomenon [77]. Why the contact angle between the pin and the edge of the hole exceeds $\theta = 90^o$ could be due to the small initial diametral pin/hole clearance of only 0.0009 inches such that the originally round hole deforms under connector loading to become somewhat elliptical in shape and wraps around the pin so as to contact the latter beyond 90^o. This is supported by marks found after the experiment (and the joint dis-

assembled) on the boundary of the hole in the aluminum plate, *figures 6.33 and 6.34*. These marks, were measured to start on the surface of the hole from $\theta = +80^{o}$ (*figure 6.33*) on the right edge of the hole and $\theta = -87^{o}$ (*figure 6.34*) on the left edge of the hole when facing the plate such as in *figure 6.15 (b)*, with θ again measured counter-clockwise from the vertically downward positive x-axis. Some marks were also present on the round pin after its test. They are less noticeable than those on the aluminum, perhaps due to the steel pins having a higher yield stress (417 MPa vs. ~ 250 MPa) than the aluminum, *figures 6.35 and 6.36*. Based on this information, and since the TSA data are averaged about the vertical longitudinal x-axis, an average non-contacting angle for applying the traction-free conditions on the hole here is taken to be $\theta = 83^{o}$. This non-contacting angle of $\theta = 83^{o}$ is further supported by TSA-determined radial stress, $\sigma_{rr} = 0$ (*figure 6.37-A*) on the boundary of the hole. The comparatively small value of the TSA-determined shear stress, $\sigma_{r\theta}$ (*figure 6.38*) renders this it to be of little assistance in this matter.

Application of the zero radial and shear stresses of *equations 6.6 and 6.9* along the traction-free edge of the hole necessitated numerically determining where on the hole the pin loses contact with the plate. This was accomplished iteratively. For the 1200-pound load applied to the connector, the point of pin-hole departure was located initially at $\theta = \pi/2$ and the radial stress distribution determined on the edge of the hole from the TSA-evaluated Airy coefficients. Where this radial stress σ_{rr} passed through, or approached, zero became a new, updated, location of pin-plate departure. With the radial and shear stresses set to zero along this new/expanded arc length along the edge of the hole, the analysis was rerun and new Airy coefficients were determined making it possible to yet again update the location where the pin and plate lose contact based on where the correspondingly updated radial stress passed through zero. After very

few such iterations of relocating where the pin and plate depart at this load level, the evaluated stresses (σ_{rr}, $\sigma_{\theta\theta}$ and $\sigma_{r\theta}$) remained essentially unchanged on loaded arc length *AB* (location A being where θ = 180, *figure 6.2*) with subsequent iterations and this dictated the final position of *B* for this connector load level.

Figures 6.37 and 6.38 are the plots by imposing the traction-free boundary condition from θ = 0^o to 83^o (measured from the vertically downward positive x-axis) on the boundary of the hole (*figure 6.2*), and on the top and the right edges of the plate, $m_1 = 3413$ TSA values and using $k = 9$ Airy coefficients. For *discretely* imposing the traction-free boundary conditions, 831 points are used on the edge of the hole i.e., $h_1 = 2*831$, 101 points are used on the top half edge of the plate and another set of 301 points on the right edge of the plate i.e., the total number of traction-free conditions on the side and top edge are $t_1 = 2*101+2*301$. Details on determining how many Airy coefficients to retain, and how to evaluate them, will be discussed in this chapter subsequently. Note that, this experiment was done on the same plate after doing the plate with non-circular pin experiment.

For tightly-fitting bolted connections, the shear stress between the bolt and plate is often taken to be zero. Moreover, for such conditions the radial contact stress is assumed to be of the form $\sigma = \sigma^* \times \cos\phi$, where angle ϕ is measured from the initial point of bolt-hole contact (θ = 180^o here) and σ^* is the radial stress at $\phi = 0$. The present connection has extremely little pin-hole clearance and indeed *figures 6.37-B and 6.38* demonstrate that the TSA-determined radial contact stress obeys the cosine ϕ assumption and the shear stress is very small at the pin-hole contact surface. In *figures 6.37-B,* stress σ^* is determined by dividing the radial stress by the absolute value of maximum radial stress so that cos(ϕ) and σ^* is 1 at ϕ = 0. The slight departure

between the TSA result and the cosϕ assumption for the radial contact stress at $\phi \geq 75^{o}$ is perhaps associated with the fact that physically the pin-hole clearance is not exactly zero or that the pin actually contacts the hole beyond $\phi = 90^{o}$. Moreover, Bickley assumed an infinite plate and a rigid pin.

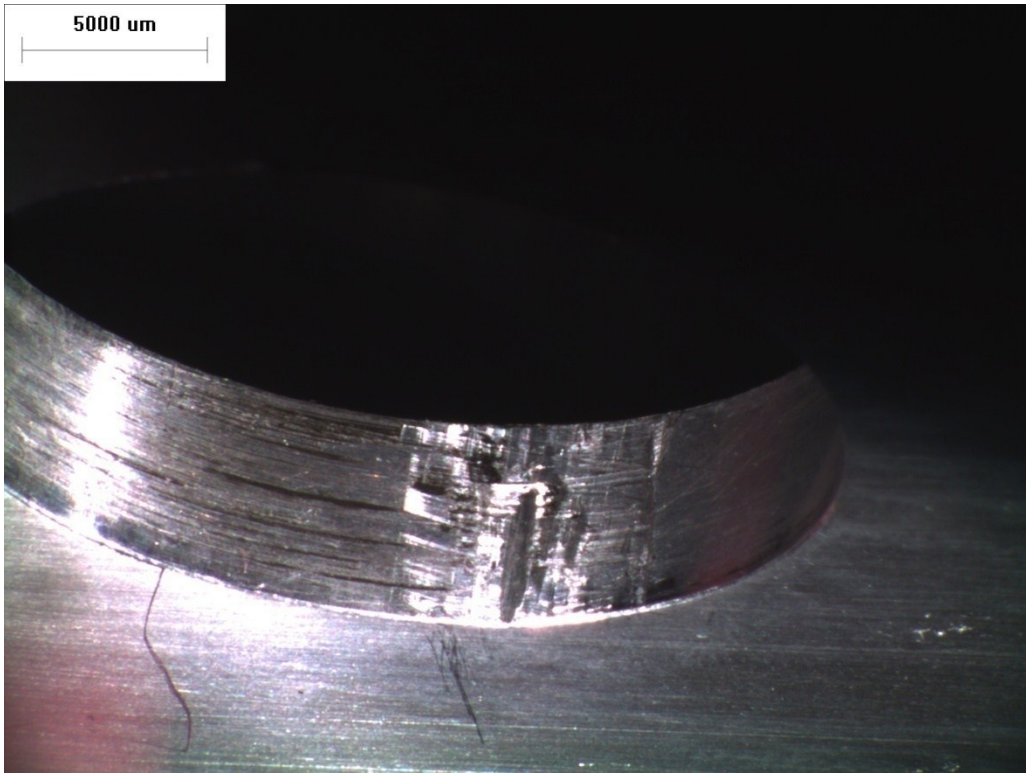

Fig. 6.33: Marks on right boundary of the hole after loading with the round pin

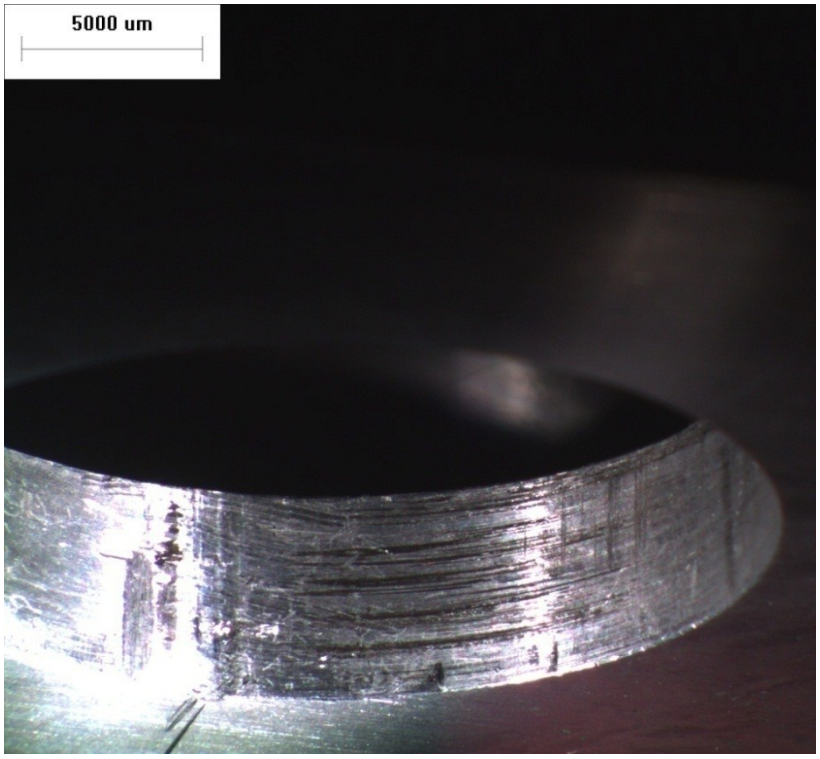

Fig. 6.34: Marks on left boundary of the hole after loading with the round pin

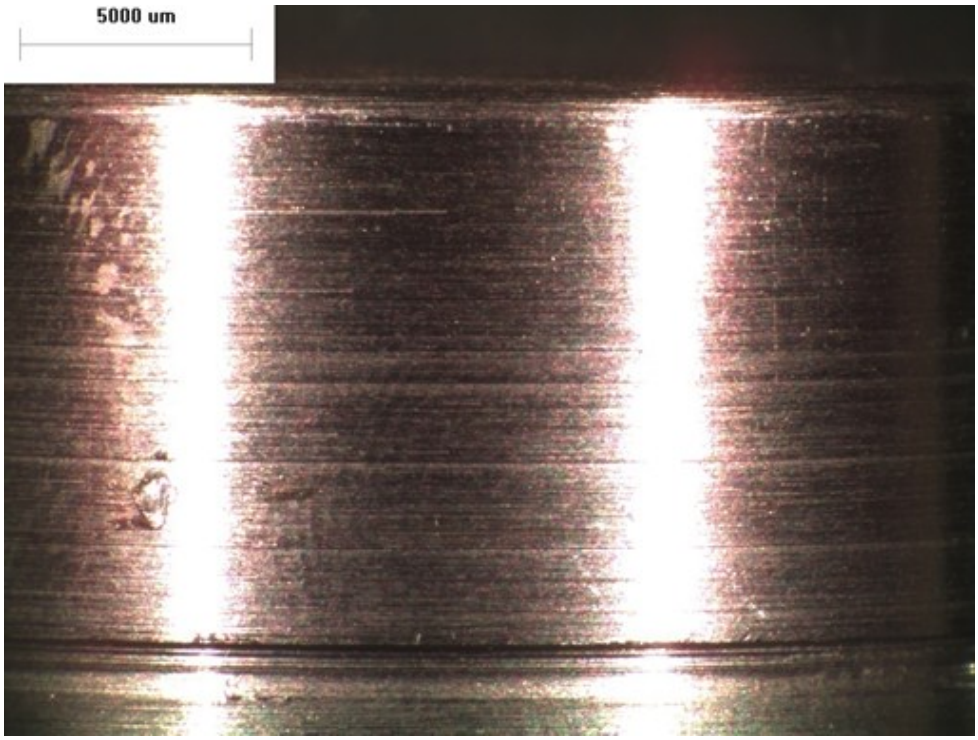

Fig. 6.35: Residual marks on the right boundary of the circular pin (contact surface of the hole shown in *figure 6.33*)

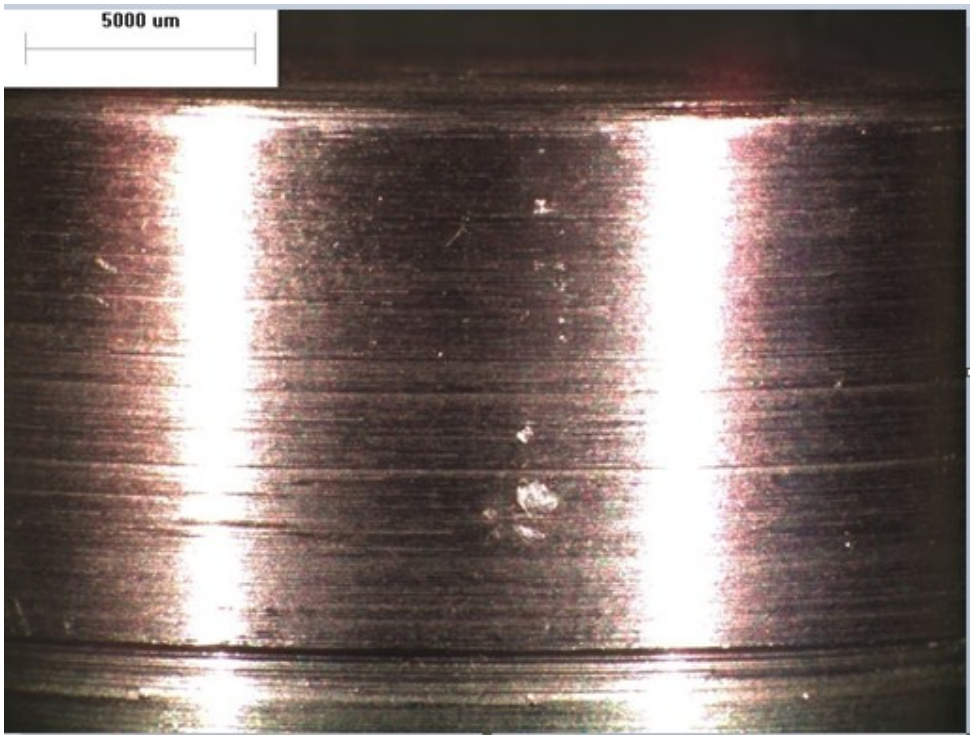

Fig. 6.36: Residual marks on the left boundary of the circular pin (contact surface of the hole shown in *figure 6.34*)

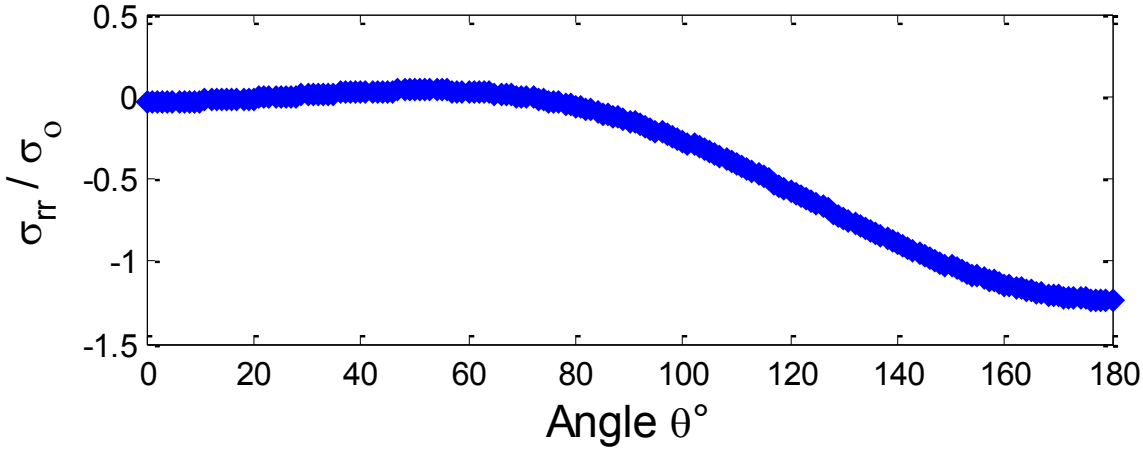

Fig. 6.37-A: TSA-determined σ_{rr}/σ_0 around the boundary of the hole (r/R = 1) for $m_1+h_1+t_1 = 5{,}479$ input values, $k = 9$ coefficients and $m_1 = 3{,}413$ TSA values, $h_1 = 2*831$, $t_1 = 2*101+2*301$

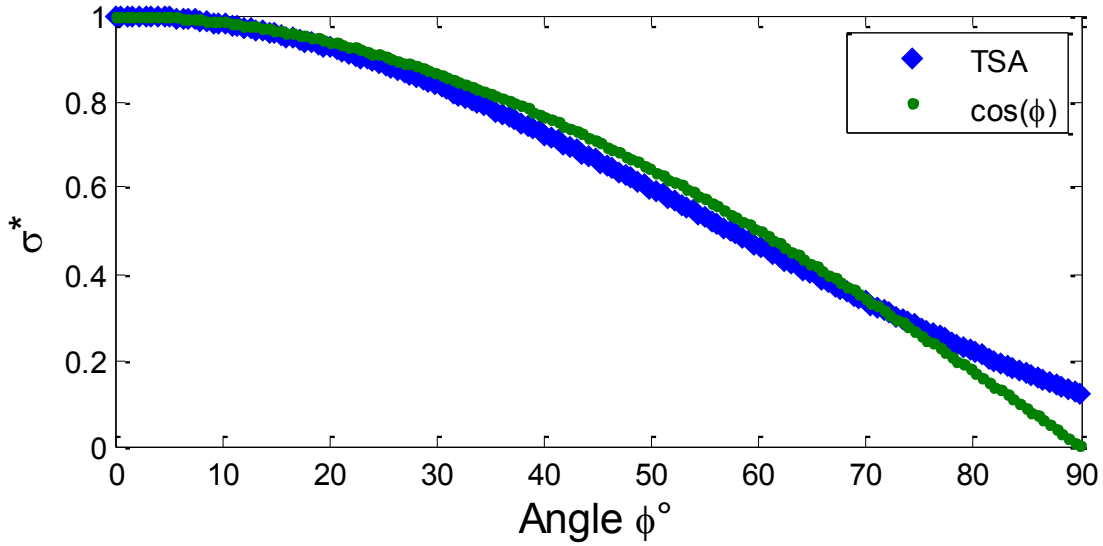

Fig. 6.37-B: Plot of *cos(ϕ)* and TSA-determined σ_* (= $\sigma_{rr}/\sigma_{rr(max)}$) vs. angle ϕ (=180^o - θ) around the boundary of the hole (r/R = 1) for $m_1+h_1+t_1 = 5,479$ input values, $k = 9$ coefficients and $m_1 = 3,413$ TSA values, $h_1 = 2*831$, $t_1 = 2*101+2*301$

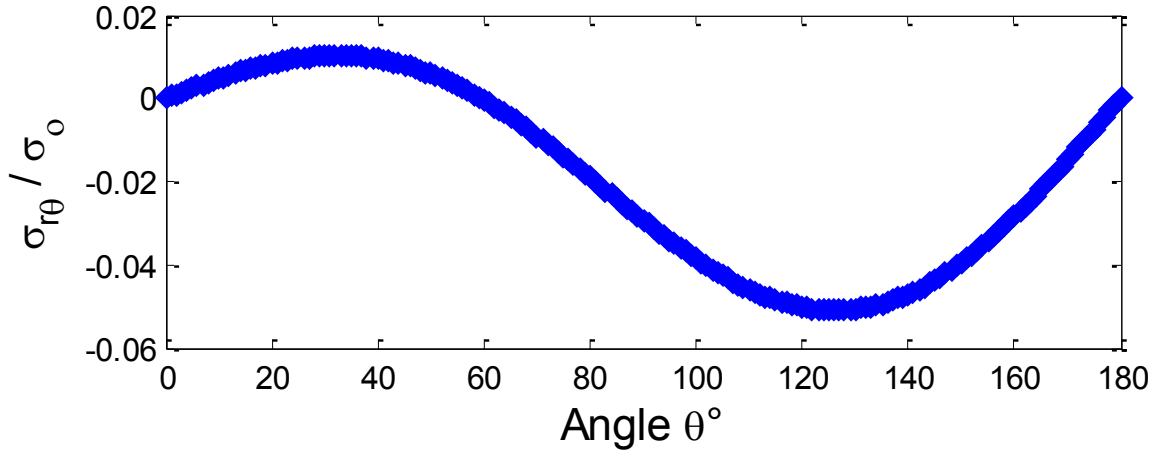

Fig. 6.38: TSA-determined $\sigma_{r\theta}/\sigma_0$ around the boundary of the hole (r/R = 1) for $m_1+h_1+t_1 = 5,479$ input values, $k = 9$ coefficients and $m_1 = 3,413$ TSA values, $h_1 = 2*831$, $t_1 = 2*101+2*301$

.

Plate loaded with non-circular pin:

For the plate loaded by the non-circular pin, traction-free boundary conditions on the boundary of the hole are imposed from $\theta = 0^o$ to 87^o measured from the vertically downward positive x-axis. Here the pin is not entirely circular i.e., the pin is semicircular for essentially its top half which contacts with the round surface of the hole in the plate. Upon careful examination of the pin, it is found that the upper portion of the pin which is expected to be exactly semicircle is exceeded by $+2^o$ and -3^o i.e., the semicircle portion of the non-circular pin is not exactly 180^o (exceeds $\sim 3^o$ when considering symmetry). In this experiment, the non-contacting traction-free condition between the pin and the hole was found to be less than 90^o (or the contact region is greater than 90^o). The reason for this could again be associated with the relatively small diameter (0.0007") clearance between the pin and the plate hole. The marks on the sides of the pin (*figures 6.39*) illustrate the extent of pin-hole contact. The plate used in this experiment is the same as that used subsequently (this test with the non-round pin was done before that with the round pin) for the circular pin. Note that the pin/hole clearance in this case is less than that with the circular pin. Evidence subsequently will show that the marks on the plate are made by the circular pin. This phenomenon is further validated by the plot of TSA-determined radial stress, σ_{rr} (*figure 6.41-A*), on the boundary of the hole. The magnitude of the contact shear stress, $\sigma_{r\theta}$ (*figure 6.42*), is again sufficiently small as to offer little evidence on the extent of the pin/plate contact. *Figures 6.41 and 6.42* are the plots by imposing the traction-free boundary condition from $\theta = 0^o$ to 87^o (θ measured from the vertically downward positive x-axis) (again used iteration to assess where the pin and hole depart) on the boundary of the hole and traction-free boundary conditions on the top half edge and the side edge of the plate, $m_2 = 3458$ TSA values and $k = 9$ Airy coefficients.

For imposing the traction-free boundary conditions, 871 points are used on the contact-free edge of the hole i.e., $h_2 = 2*871$, 101 points are used on the top edge and another set of 301 points on the right edge of the plate i.e., $t_2 = 2*101+2*301$.

Figures 6.41 are the photograph of the non-circular pin. *Figures 6.41-B and 6.42* again support the prevalent assumptions for zero pin hole clearance that any shear stress between the pin and hole can be ignored and contact radial stress can be approximated by a cosine distribution.

Plots of *figures 6.41-A and 6.42* were obtained iteratively similarly as described above relative to *figures 6.37 and 6.38*.

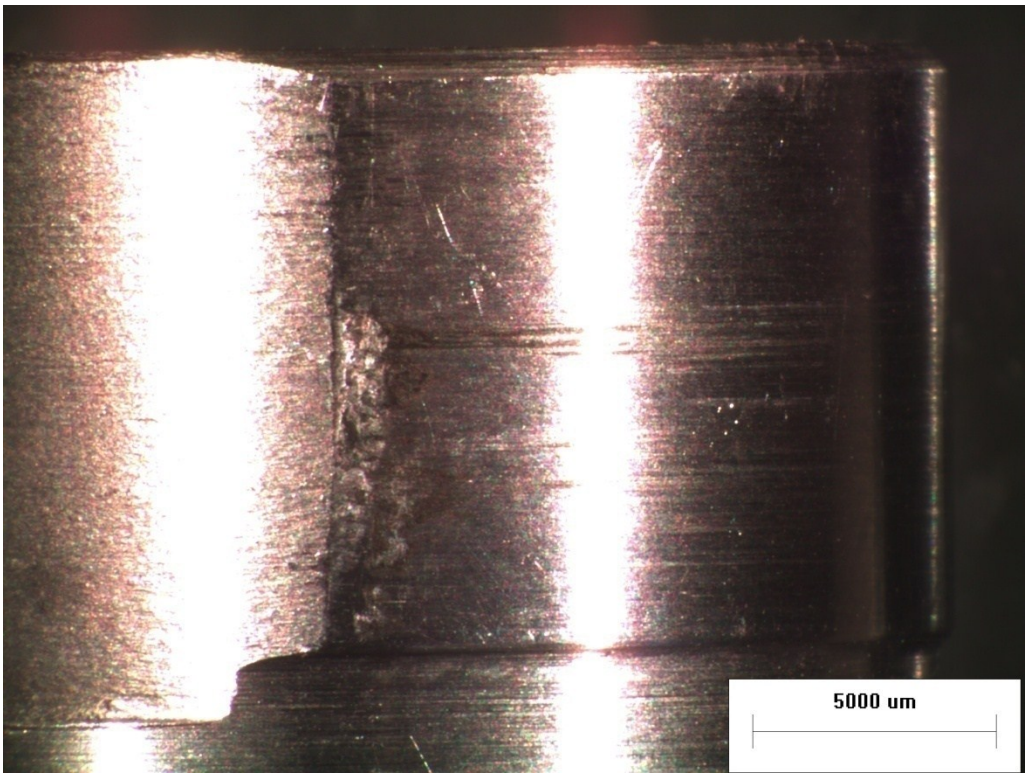

Fig. 6.39-A: Right boundary of the non-circular pin when facing the plate/pin from TSA side

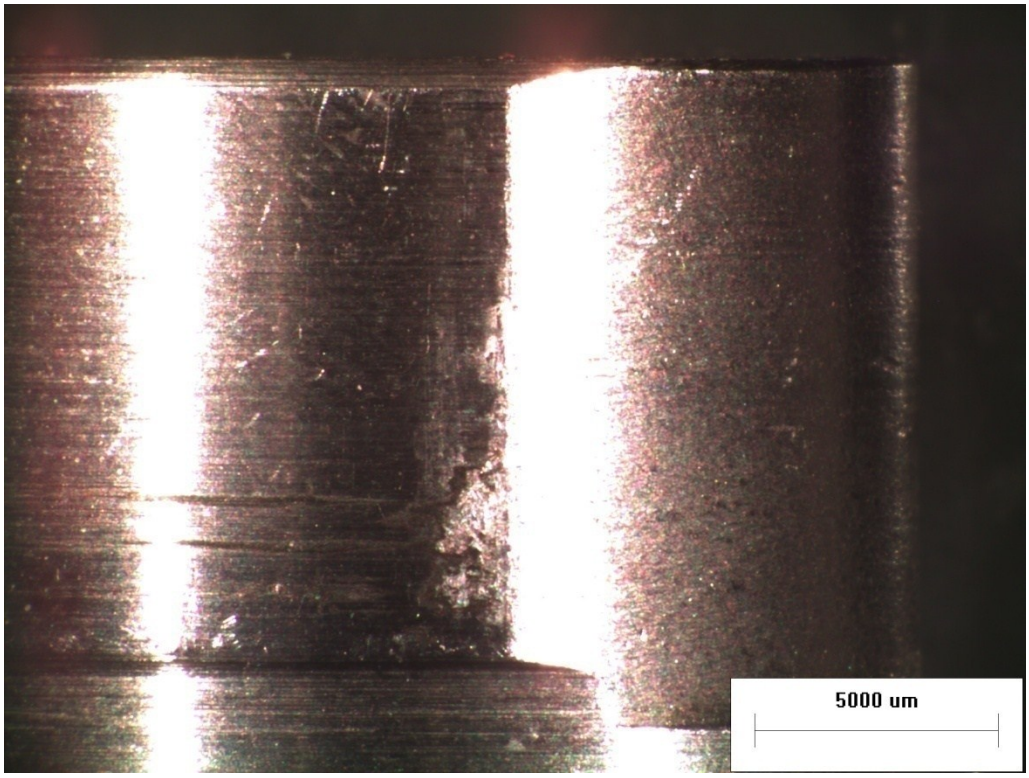

Fig. 6.39-B: Left boundary of the non-circular pin when facing the plate/pin from TSA side

Fig. 6.40-A: Top view of non-circular pin

Fig. 6.40-B: Side view of non-circular pin

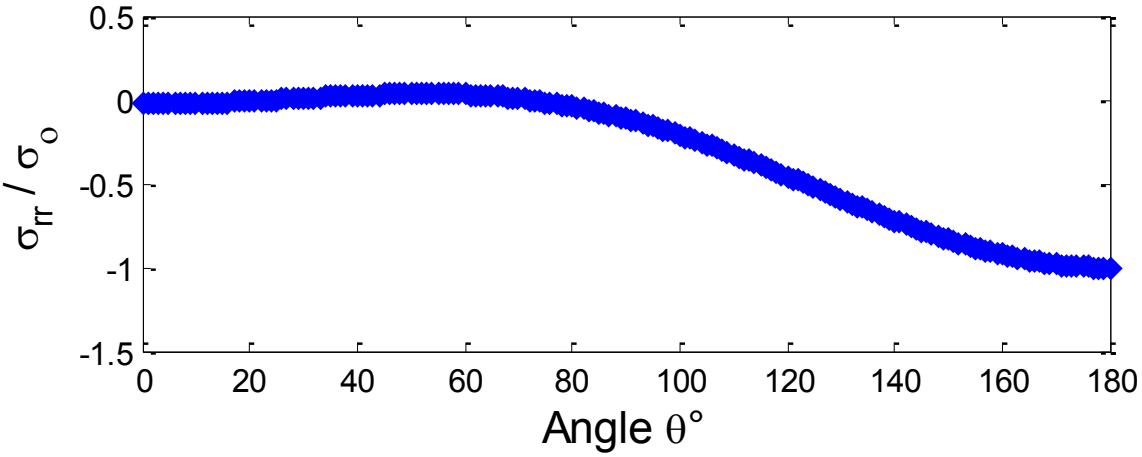

Fig. 6.41-A: TSA-determined σ_{rr}/σ_0 around the boundary of the hole (r/R = 1) for $m_2+h_2+t_2$ = *6,592* input values, k = *9* coefficients and m_2 = *3,458* TSA values, h_2 = *2*871*, t_2 = *2*101+2*301*

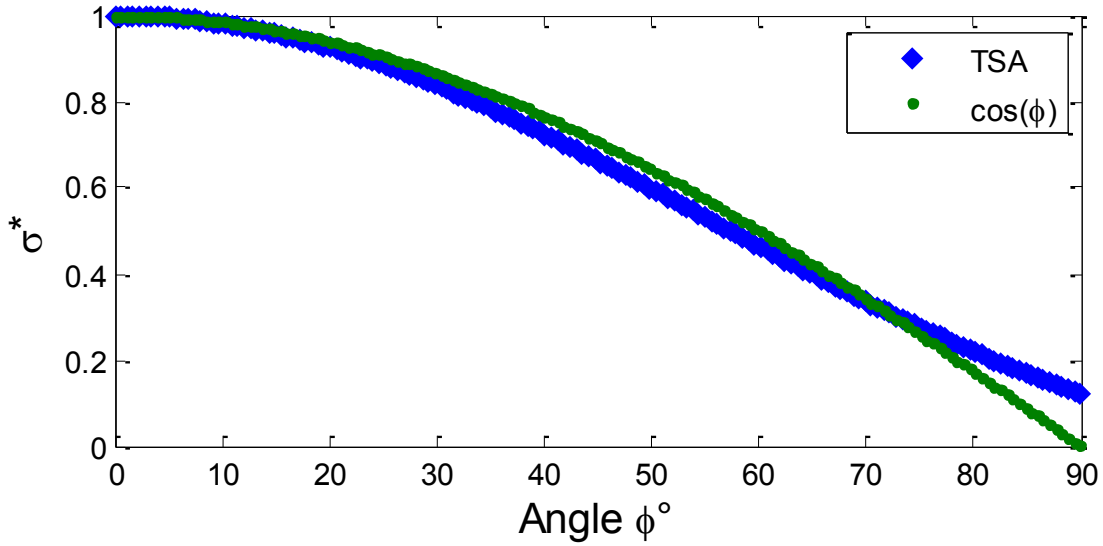

Fig. 6.41-B: Plot of *cos(ϕ)* and σ_* (= $\sigma_{rr}/\sigma_{rr(max)}$) vs. angle ϕ (=180^o - θ) around the boundary of the hole (r/R = 1) for $m_2+h_2+t_2 = 6{,}592$ input values, $k = 9$ coefficients and $m_2 = 3{,}458$ TSA values, $h_2 = 2*871$, $t_2 = 2*101+2*301$

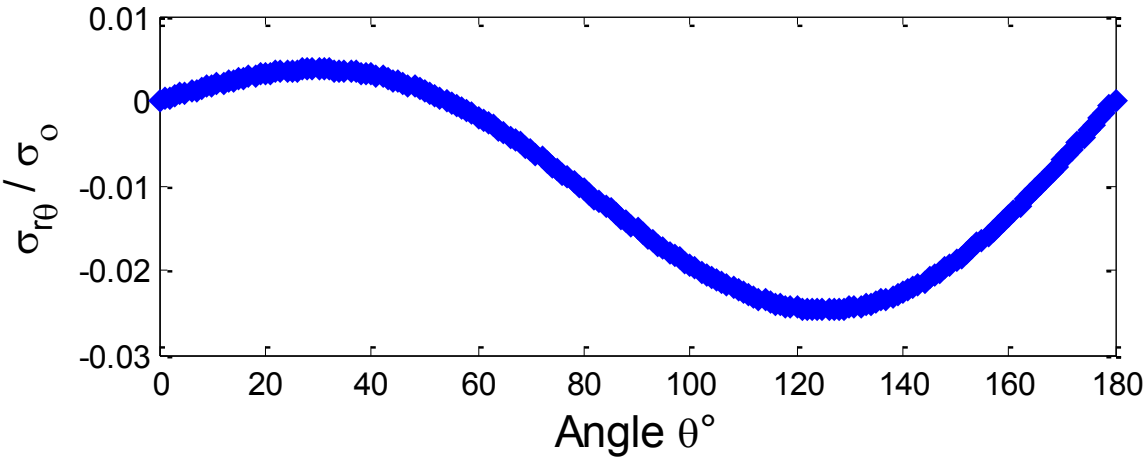

Fig. 6.42: TSA-determined $\sigma_{r\theta}/\sigma_0$ around the boundary of the hole (r/R = 1) for $m_2+h_2+t_2 = 6{,}592$ input values, $k = 9$ coefficients and $m_2 = 3458$ TSA values, $h_2 = 2*871$, $t_2 = 2*101+2*301$

Having quantified the extent of the non-contacting region on the hole, and therefore the number and locations where to impose $\sigma_{rr} = \sigma_{r\theta} = 0$ on the edge of the hole, one turns attention to assessing how many Airy coefficients to retain in each case (circular and non-circular hole) and how to evaluate these coefficients. Recognizing that the actual measured TSA data often

incorporates some noise/scatter, it is typically advantageous to employ significantly more equations (i.e., more TSA measured input values of S plus number of traction-free boundary conditions on the boundary of hole, and on the right vertical edge ($\sigma_{yy} = \sigma_{xy} = 0$) and top edge ($\sigma_{xx} = \sigma_{xy} = 0$) of the plate) than the number of unknown coefficients, k, i.e., $(m_1+h_1+t_1) > k$ *or* $(m_2+h_2+t_2) > k$. Based on the measured TSA data for the plate with circular shaped or non-circular shaped pin, traction-free boundary conditions at discrete locations, expression for the isopachic stress and individual components of stresses, one can develop the following matrix equation:

$$[A]_{(m+h+t)xk}\{c\}_{kx1} = \{d\}_{(m+h+t)x1} \tag{6.15}$$

where matrix [A] involves the m (m_1 for the plate with circular pin and m_2 for the plate with non-circular pin) Airy isopachic equations in polar coordinates, r and θ, for the corresponding input locations (i.e., the measured input data value of S (= S^*/K)). Matrix [A] also contains h ($h_1$for the plate with circular pin and h_2 for the plate with non-circular pin) expressions for traction-free boundary conditions on the boundary of the hole ($\sigma_{rr} = \sigma_{r\theta} = 0$), t ($t_1$for the plate with circular pin and t_2 for the plate with non-circular pin) expressions for traction-free boundary conditions on the right edge ($\sigma_{yy} = \sigma_{xy} = 0$) and the top edge ($\sigma_{xx} = \sigma_{xy} = 0$) of the plate. Vector {c} of *equation 6.15* involves the k unknown Airy coefficients. Note that the same number of coefficients is used for the analysis of the plate with the circular pin and the non-circular shaped pin. This is based on analysis in the following section. Vector {d} contains m measured TSA data values of $S = S^*/K$ corresponding to the data points used in the S to form matrix [A] as well as the zeros corresponding to every expression of h and t traction-free boundary conditions. The

least-squares method is used to solve the over-determined matrix equation $Ac = d$ of *equation 6.15*.

6.5.2 Number of Coefficients and Input Values

It is important to determine a suitable number of Airy coefficients, k, to use here for a given set of input values, $m_1+h_1+t_1$ or $m_2+h_2+t_2$. To evaluate an appropriate value for k, the condition number, C, of the Airy matrix and the *RMS* are plotted against the number of Airy coefficients, k, for $m_1+h_1+t_1 = 5,479$ (plate with circular pin) and $m_2+h_2+t_2 = 6,592$ (plate with non-circular pin) input values. Moreover, the raw TSA data S* are compared with the reconstructed plot of S* evaluated using the now known Airy coefficients. *Figures 6.43 through 6.45* are the plots of condition number, $\log_{10}$(C) and *RMS* against the number of Airy coefficients (k) for the analysis of plate with circular pin. Similarly *figures 6.46 through 6.48* are the plots of condition number, $\log_{10}$(C) and *RMS* against the number of Airy coefficients (k) for the analysis of plate with non-circular pin.

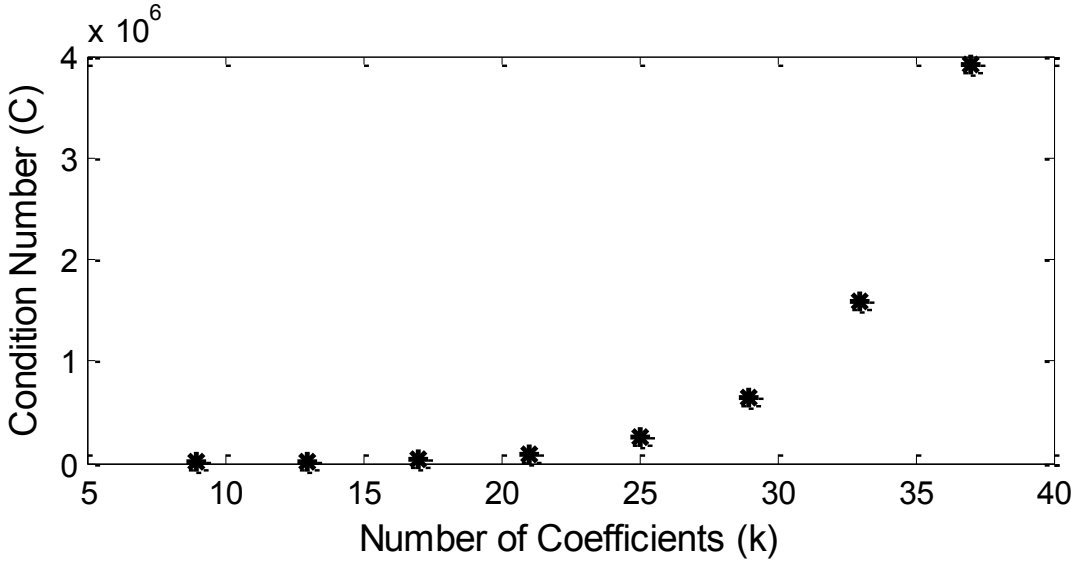

Fig. 6.43: Plot of condition number, C, vs. number of coefficients, k, for $m_1+h_1+t_1 = 5,479$ input values, ($m_1 = 3,413$ TSA values, $h_1 = 2*831$, $t_1 = 2*101+2*301$); circular pin

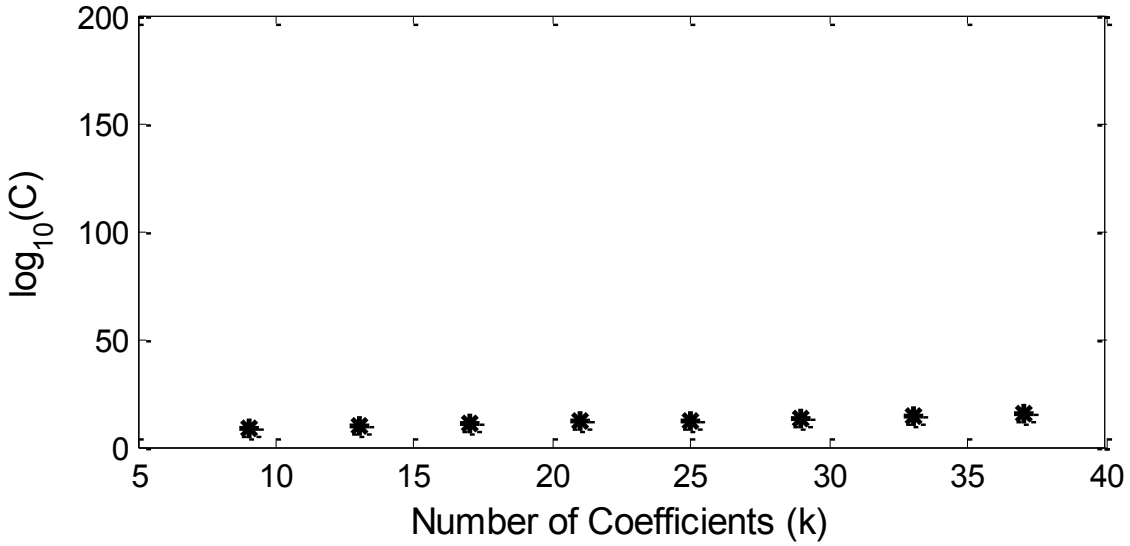

Fig. 6.44: Plot of $\log_{10}(C)$ vs. number of coefficients, k, for $m_1+h_1+t_1 = 5,479$ input values, ($m_1 = 3,413$ TSA values, $h_1 = 2*831$, $t_1 = 2*101+2*301$); circular pin

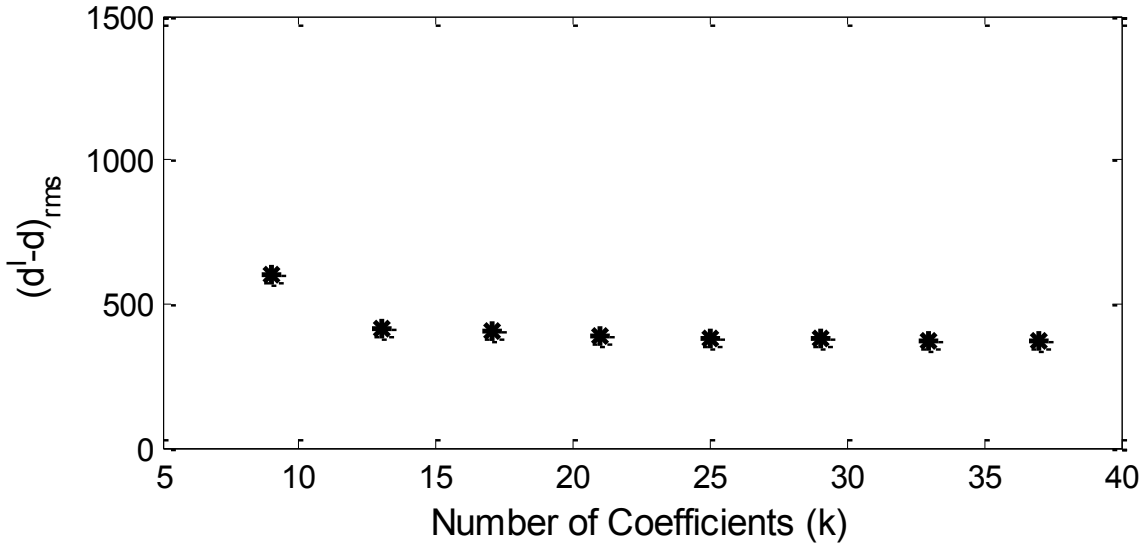

Fig. 6.45: Plot of RMS vs. number of coefficients, k, for $m_1+h_1+t_1 = 5,479$ input values, ($m_1 = 3,413$ TSA values, $h_1 = 2*831$, $t_1 = 2*101+2*301$); circular pin

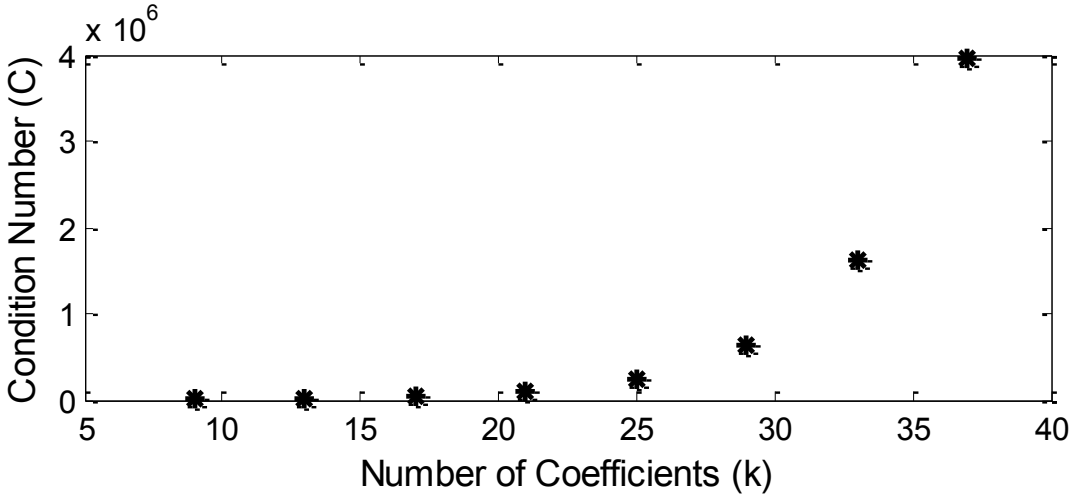

Fig. 6.46: Plot of condition number, *C*, vs. number of coefficients, *k*, for $m_2+h_2+t_2 = 6{,}592$ input values, ($m_2 = 3458$ TSA values, $h_2 = 2*871$, $t_2 = 2*101+2*301$); non-circular pin

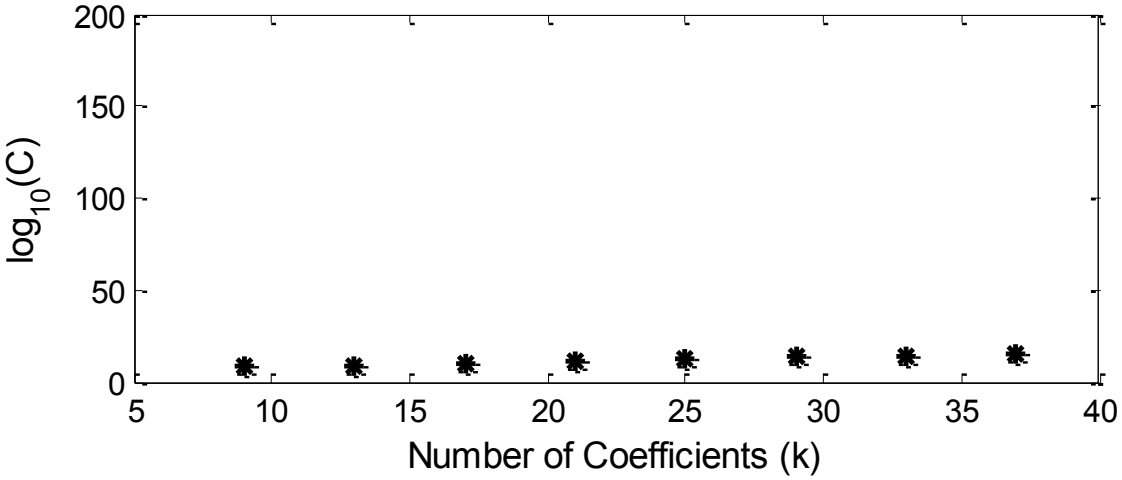

Fig. 6.47: Plot of $\log_{10}$(C) vs. number of coefficients, *k*, for $m_2+h_2+t_2 = 6{,}592$ input values, ($m_2 = 3458$ TSA values, $h_2 = 2*871$, $t_2 = 2*101+2*301$); non-circular pin

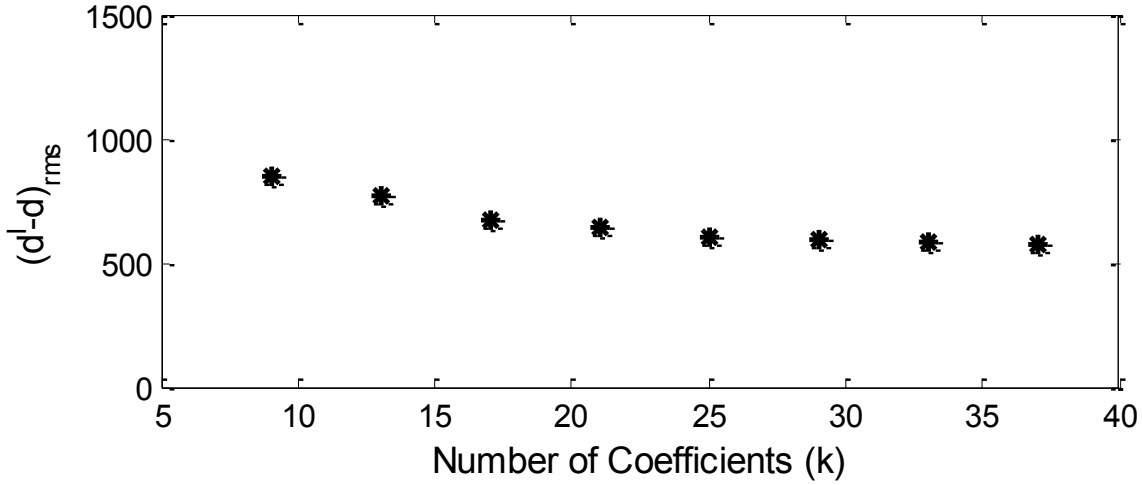

Fig. 6.48: Plot of RMS vs. number of coefficients, *k*, for $m_2+h_2+t_2 = 6{,}592$ input values, ($m_2 = 3458$ TSA values, $h_2 = 2*871$, $t_2 = 2*101+2*301$); non-circular pin

Note that from *figures 6.43 through 6.48*, the value of C or $\log_{10}$C or *RMS* are reasonably consistent for $9 \leq k \leq 25$. Having large number of Airy coefficients can cause the Airy matrix, [A], of *equation 6.15* to become unstable or near-singular due to computer round-off errors. Moreover adding more coefficients than necessary could require more measured input data. Information of *figures 6.43 through 6.48* suggests $k = 9$ (terminating index N = 2) would be a reasonable choice with either the round or non-circular pin.

Figure 6.49 compares contour plots of the experimental TSA data (S*) with the reconstructed S* using $m_1+h_1+t_1 = 5{,}479$ input values and $k = 9$ ($m_1 = 3{,}413$ TSA values, $h_1 = 2*831$, $t_1 = 2*101+2*301$) for the analysis of the plate loaded by the circular pin. Similarly *figure 6.50* makes a similar comparison (using $m_2+h_2+t_2 = 6{,}592$ input values and $k = 9$; $m_2 = 3458$ TSA values, $h_2 = 2*871$, $t_2 = 2*101+2*301$) for the analysis of the plate loaded with the non-circular pin. Information of *figures 6.49 and 6.50* supports the selection of $k = 9$ in both cases.

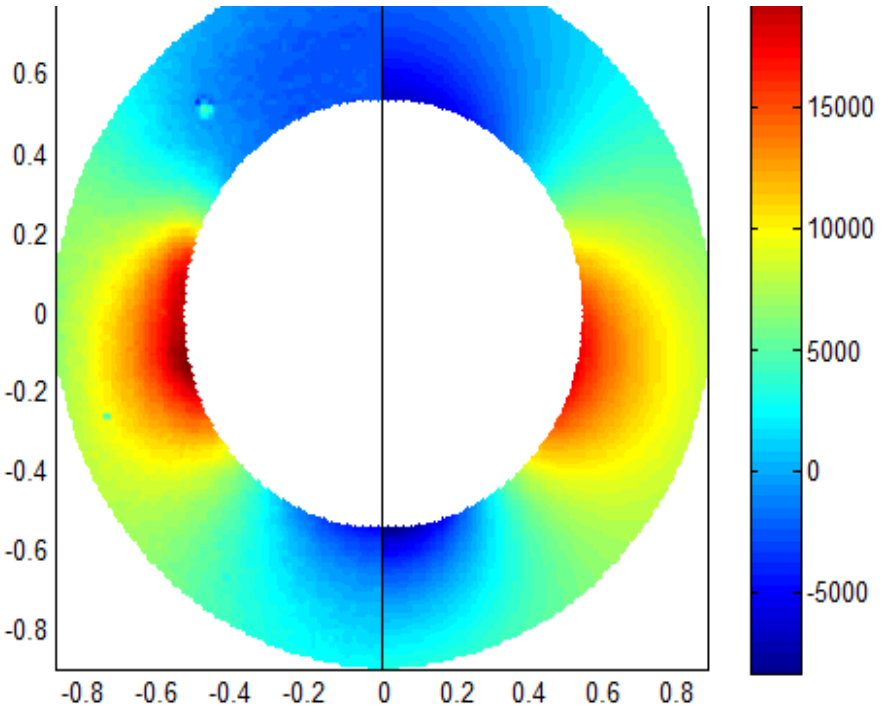

Fig. 6.49: MATLAB processed experimentally-based TSA input data S* (left) and reconstructed S* (right) for plate loaded by circular pin [$m_1+h_1+t_1 = 5,479$ input values and $k = 9$ ($m_1 = 3,413$ TSA values, $h_1 = 2*831$, $t_1 = 2*101+2*301$)]

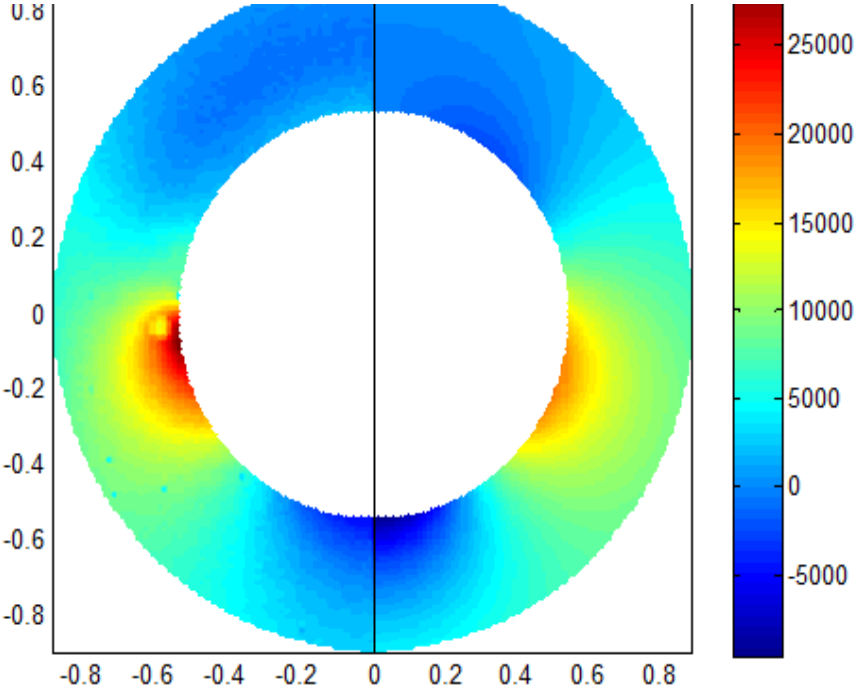

Fig. 6.50: MATLAB processed experimentally-based TSA input data S* (left) and reconstructed S* (right) for plate loaded by non-circular pin [$m_2+h_2+t_2 = 6,592$ input values and $k = 9$ ($m_2 = 3458$ TSA values, $h_2 = 2*871$, $t_2 = 2*101+2*301$)]

6.6 Strain Gage Readings

As mentioned earlier, a longitudinal strain gage was mounted on each of the back and front sides of the test specimen to check for any possible out-of-plane bending while loading the sample. These single-element Micro-Measurements strain gages (EA-06-050AH-120) have gage resistance of 120.0 ± 0.15%, Ω and a gage factor of 2.02 ± 1.0%, and were mounted on the opposite sides of the specimen. *Figures 6.51* and *6.52* show the strain gages mounted on the specimen. A 16-channel variable, but controllable, excitation-voltage strain gage conditioner (*figure 6.53)* was used to record the strain readings.

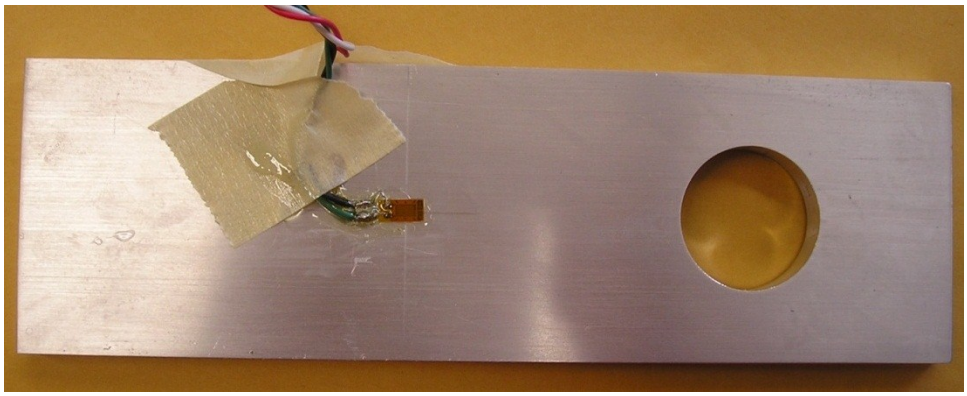

Fig. 6.51: Strain gage on front side of test specimen

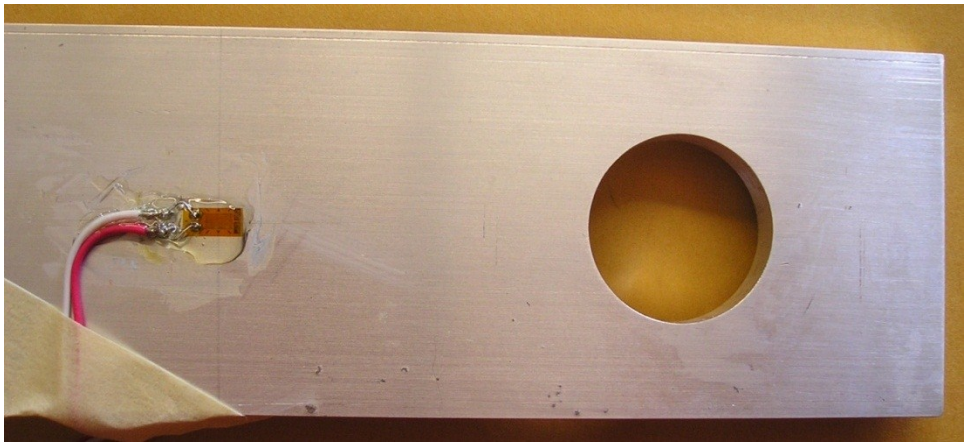

Fig. 6.52: Strain gage on back side of test specimen

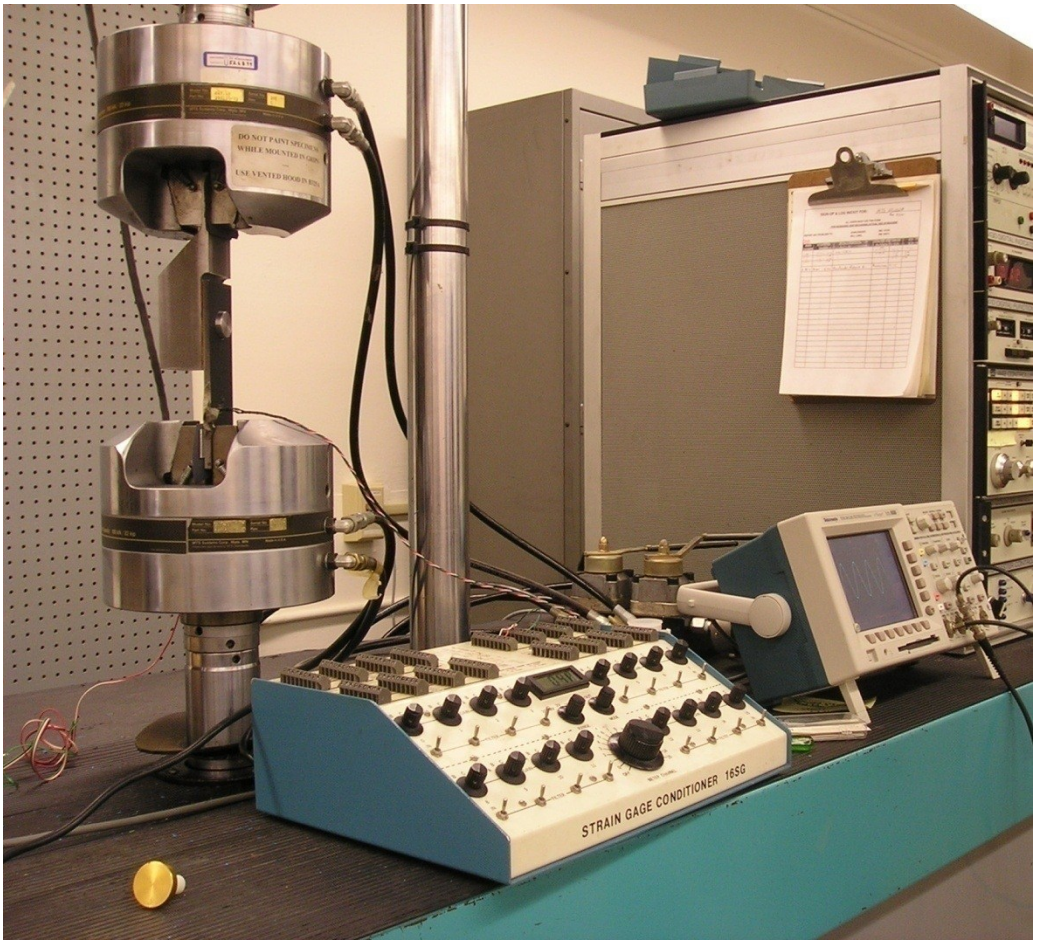

Fig. 6.53: Strain gage conditioner monitoring the output from mounted gages

The output of the gages was recorded during incremental increasing and decreasing static loading of the specimen. *Figures 6.54* and *6.55* show the strains from both gages for plate loading by each of the circular and non-circular pin/bolt. Based on a maximum stress concentration factor at the edge of the hole not exceeding 5 (*figures 6.80 and 6.88*), the maximum stress in the aluminum plate at the largest applied static load (<17 ksi) remains within the elastic limit of the aluminum (35 – 40 ksi). In each case these static strains were recorded immediately after the completing the cyclic loading for the respective TSA analysis and without totally unloading the plate so as to ensure the same degree of symmetry in loading prevailed with

the static and cyclic loading. The strains are fairly consistent, although in both cases the front of the plate was strained slightly more than the back. While any such bending from front to back is what one might contemplate based on the loading arrangement, *figures 6.15, 6.17 and 6.19*, 3-D FEM results (section 6.7, *figure 6.79*) suggests the vertical motion of the pin under system loading is essentially uniform along the length of the pin which contacts the edge of the hole. Residual markings on the surfaces of either the pins or the hole do not appear greater associated with one or other faces of the aluminum plate, further suggesting any plate bending was very minor.

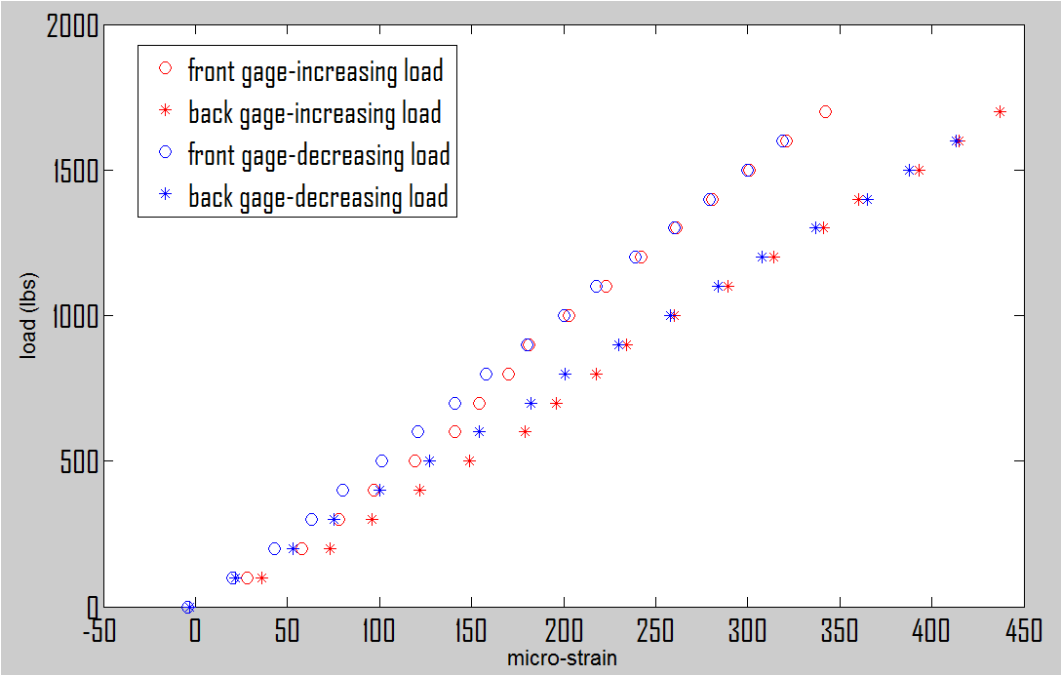

Fig. 6.54: Front (TSA side) and back strain gage readings (circular pin experiment)

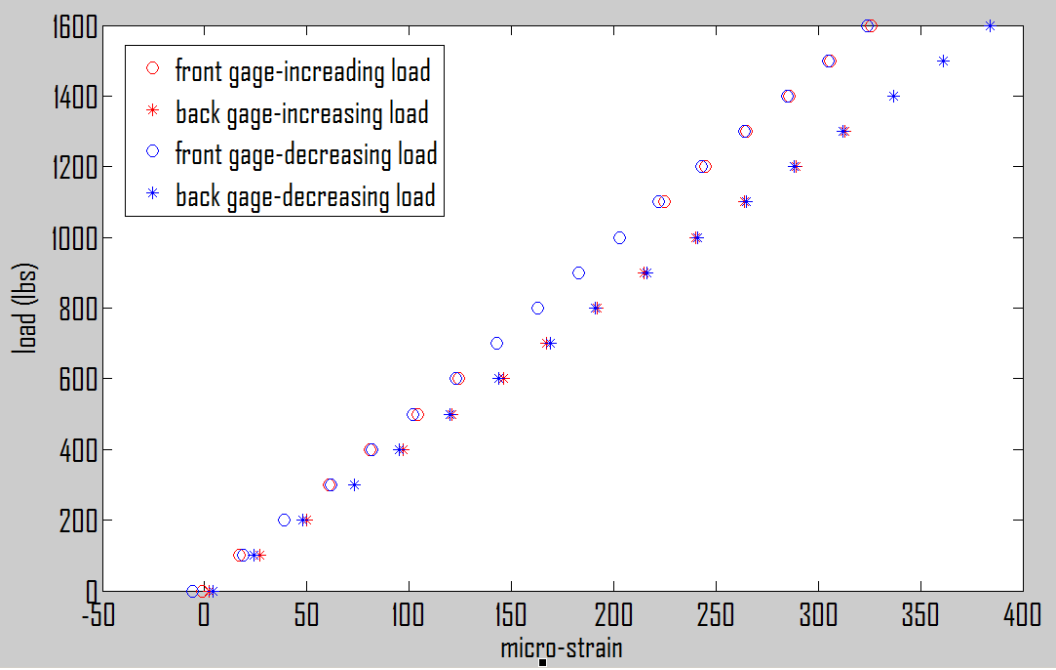

Fig. 6.55: Front (TSA side) and back strain gage readings (non-circular pin experiment)

6.7 Numerical Analysis

6.7.1 Finite Element Modeling

The finite element method is one of the most popular numerical stress analysis methods used in structural engineering. The solution approach is based either on eliminating the differential equation completely (steady state problems), or rendering the PDE into an approximating system of ordinary differential equations, which are then numerically integrated using standard techniques such as Euler's method, Runge-Kutta, etc. Commercially available finite element software ABAQUS 6.83 / CAE and Intel Visual Fortran 10.01 were used here for all the finite element analysis. ABAQUS 6.83/CAE is versatile software and is widely used in the industry and academia to solve complex problems. The motivation behind choosing this particular finite element software (ABAQUS) over others (like ANSYS, NASTRAN) is its reputed ability to handle contact problems well with robust contact algorithms. Another advantage of using ABAQUS is its well documented resources for user defined sub-routines if one decides to code his/her own material or sub-routines to solve a particular problem.

The purpose was to conduct a 2-D and a 3-D FEM stress/displacement analysis of a two-dimensional pin-loaded member for comparison with experimental results. ABAQUS/Standard was used instead of ABAQUS/Explicit as the problem was modeled as a static problem. The main disadvantages of this method are the significant computing time that can be needed due to the requirement to recalculate the tangent stiffness matrix in each iteration using the Newton-Raphson method and the difficulty of defining this matrix in some cases. However, the Newton-Raphson method is the only procedure which can provide quadratic convergence. The solution

obtained is reliable as ABAQUS/Standard uses a stiffness-based solution technique that is unconditionally stable.

6.7.2 Geometry

The single-pin, single-lap specimen geometry considered is shown in *figures 6.56 and 6.57*. The geometry of the aluminum plate and the steel pin were modeled using the graphical user interface in ABAQUS/Standard.

The CAD models for the geometry of the configuration are detailed below. Since the entire configuration was symmetric only half of the geometry was modeled for the purpose of finite element analysis. The following components were modeled -

Pin – The circular pin is modeled as 2-D geometry with a radius of 12.5857 mm. The half symmetric model is as shown in *figure 6.56-a*.

The non-circular pin is modeled as 2-D geometry. One half is cylindrical with a radius of 12.5857 mm and the other half is non-circular. The circular half ensures that contact is established for ~180^{o}. The half symmetric model is as shown in *figure 6.56-b*. Note: Hole and pin diameters were measured by the machinist in inches. The numbers in mm are based on 25.40 mm = 1.00 inches.

Aluminum Plate - The aluminum plate is also modeled as 2-D geometry with a length of 152.4 mm and width of 25.4 mm. A hole of diameter 1.0000 inches (25.4 mm) is located at a distance of 38.1 mm from the end. The half symmetric model is as shown in *figure 6.57*. Same plate was used for the circular and non-circular pin specimen.

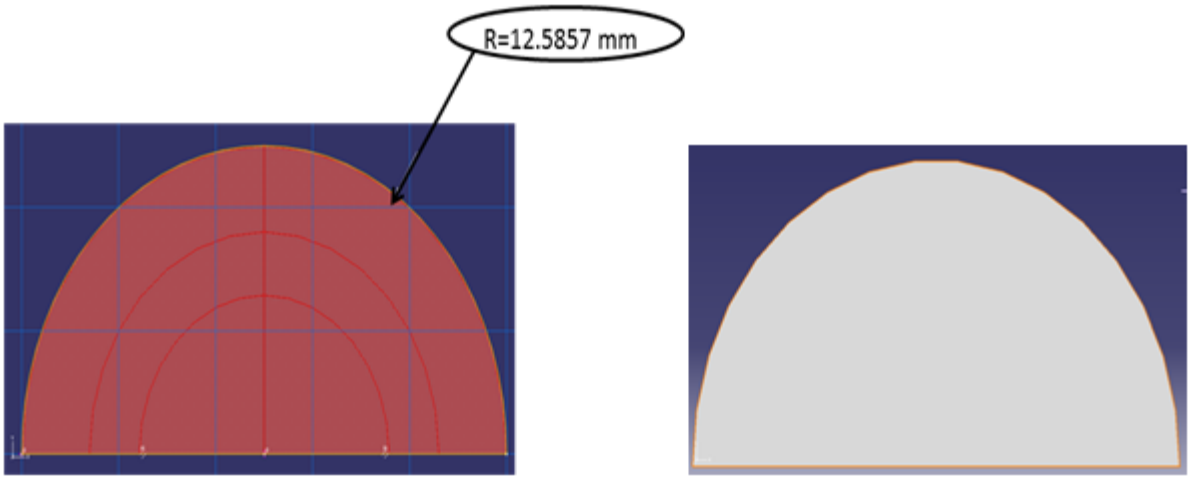

Fig. 6.56-a: Geomtery of the circular pin (Symmetric model)

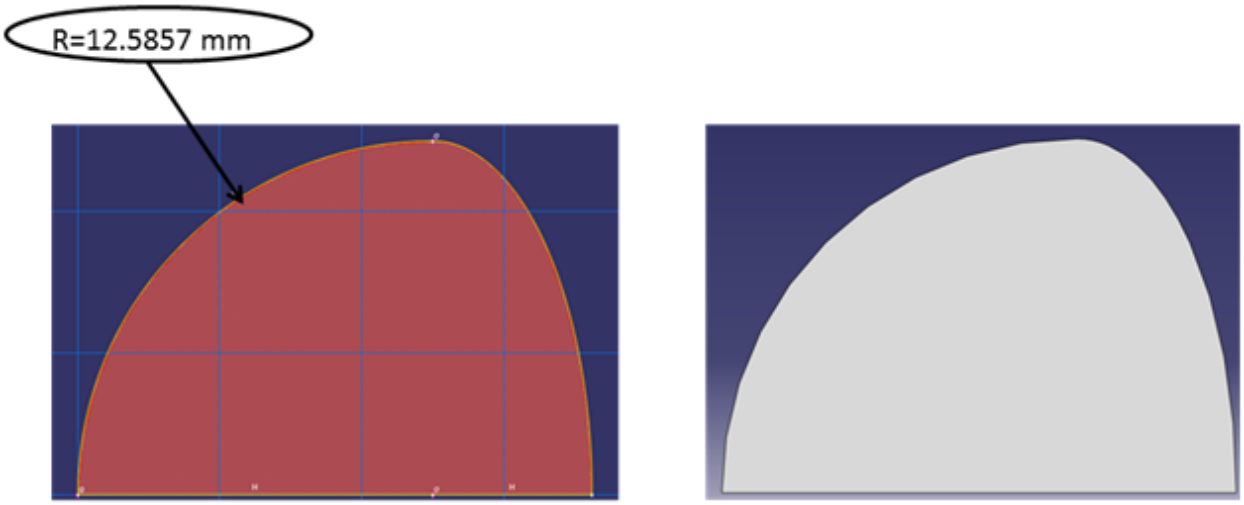

Fig. 6.56-b: Geomtery of the non-circular pin (Symmetric model)

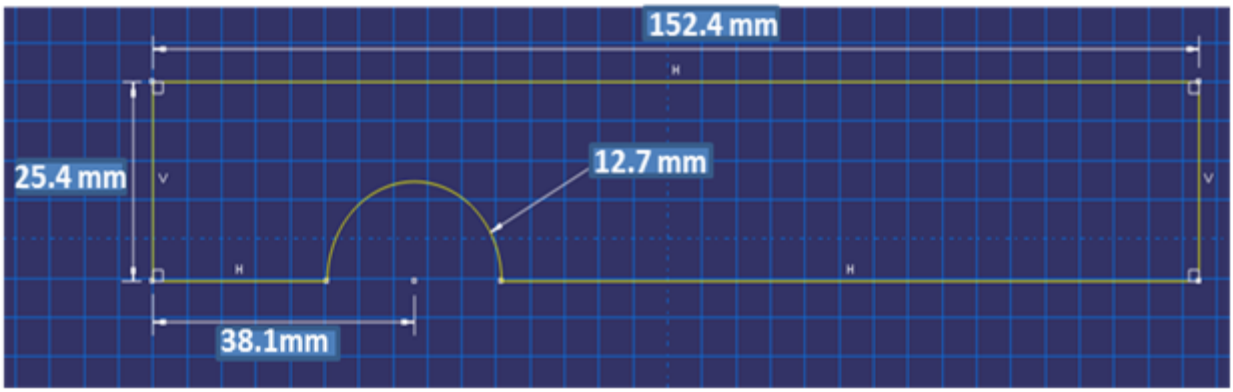

Fig. 6.57-a: Geomtery of the plate for circular and non-circular pins (Symmetric model) with dimensions

Fig. 6.57-b: Geomtery of the plate for circular and non-circular pins (Symmetric model)

6.7.3 Mesh Generation

The automatic mesh generator built into the ABAQUS 6.83 graphical user-interface was used to create the finite element mesh. The 2-D analysis utilized a plane stress formulation with a plate thickness of 6.37 mm. The element type used is CPS4R, which is a 4-node bilinear plane stress quadrilateral element with reduced integration and hourglass control. The exact element size and the procedure followed to generate the mesh is described as follows.

Pin – For the circular and non-circular pins, the constant element size of 0.2032 mm was used for the entire surface of the pin as shown in *figures 6.58*. This resulted in a fine mesh being generated on the geometry of the pin i.e., 8,384 elements were used to model the half pin. Increasing the mesh density (number of elements) did not change the results but increased the computational time.

Aluminum Plate – Element size around the hole is constant and is equal to 0.254 mm. At a distance of 40 mm away from the center of the hole, the mesh size is increased to 0.354 mm and remains constant as shown in the *figures 6.59* i.e., 42,593 elements were used to model the (half) aluminum plate. The same geometry and mesh were used to analyze both the circular and non-circular pin configurations.

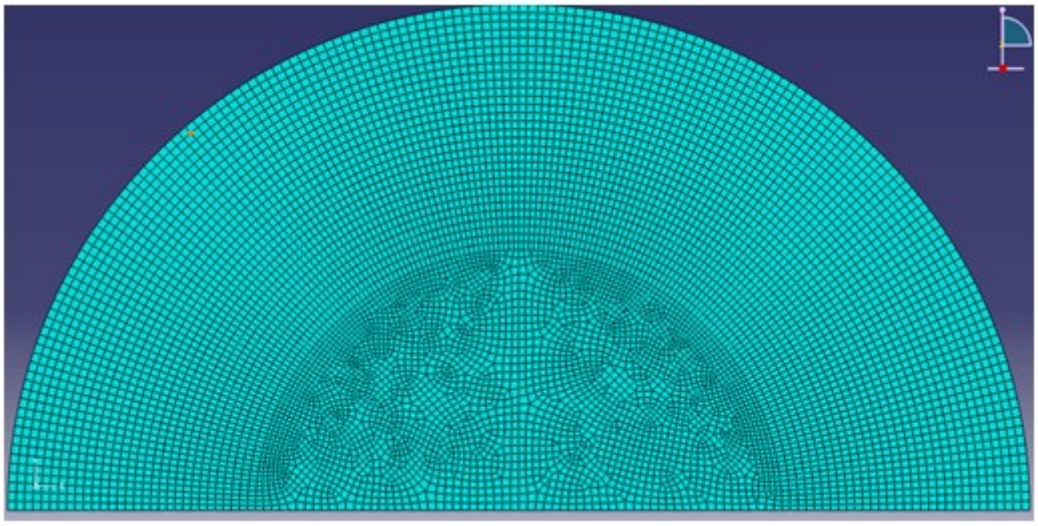

Fig. 6.58-a: Finite Element model of the round pin configuration

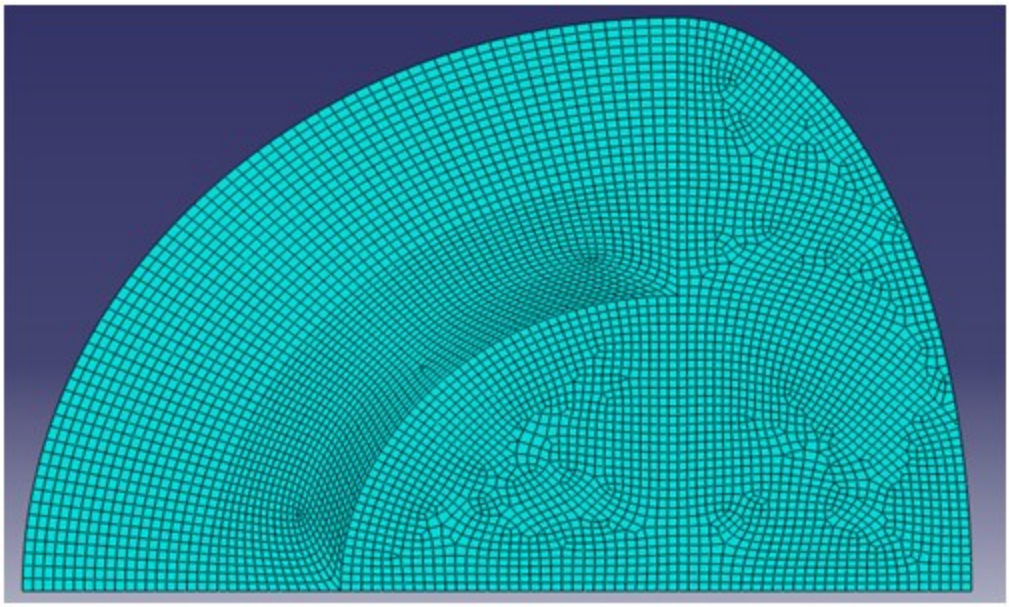

Fig. 6.58-b: Finite Element model of the non-circular pin configuration

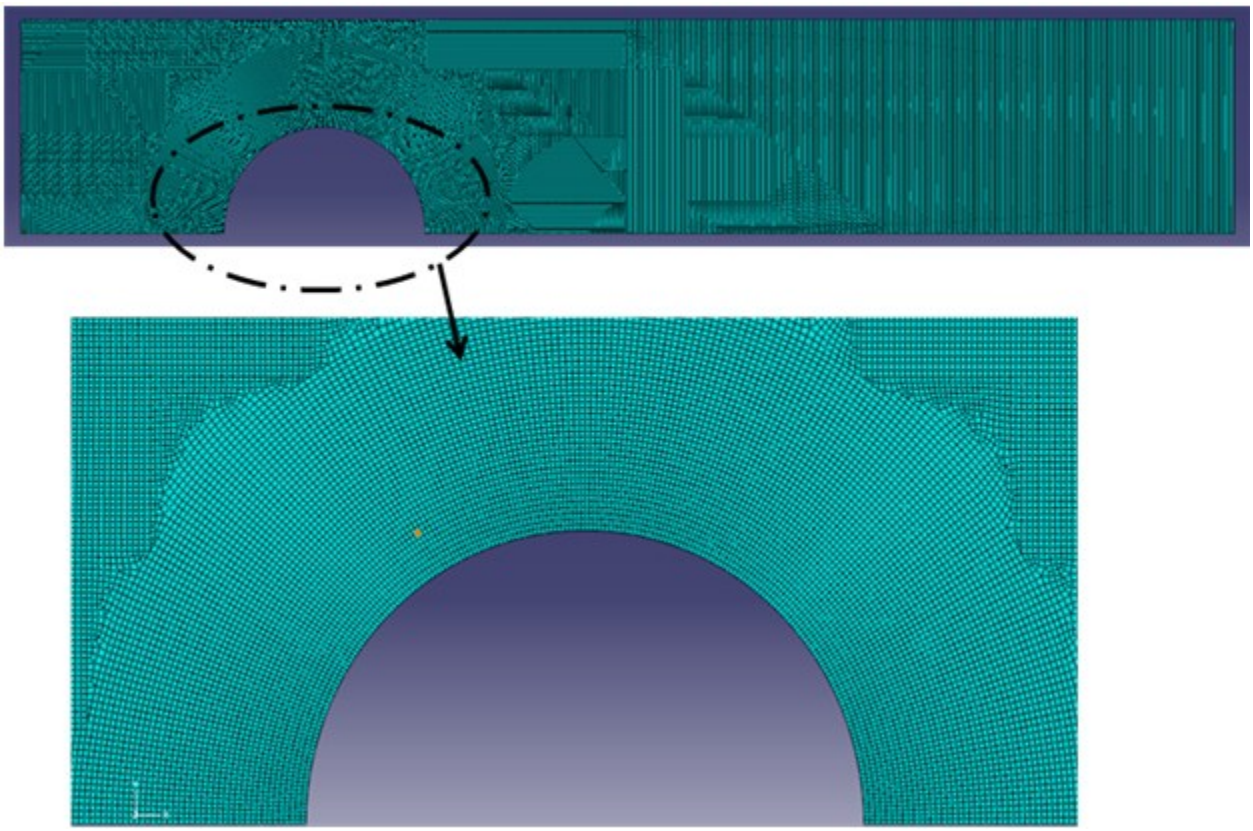

Fig. 6.59: Finite Element model of the plate

6.7.4 Boundary Conditions and Loading

Due to symmetry, only one-half of the assembly was modeled and symmetric boundary conditions were applied. The circular and non-circular pin was completely constrained at a small region near the center as shown in *figures 6.60* (i.e. x = y = z = 0 and Rotx = Roty = Rotz = 0 where x, y, z are the translational displacements in the x, y, z directions and Rotx, Roty, Rotz are the rotational displacements in the x, y, z directions). Moreover, y-symmetry (y = 0 and Rotx = Rotz = 0) was also applied along the diameter of the pin as shown in *figures 6.60*.

The aluminum plate was constrained along its length with the constraints y = 0, Rotx = Rotz = 0 (i.e. y-Symmetry) and a force of 1200 pounds (5337.8 N) was applied to the right end as shown in the *figure 6.61*. The complete assembly of all the parts involved with the associated boundary conditions is shown in *figure 6.62* (circular pin case) and *figure 6.63* (non-circular pin configuration).

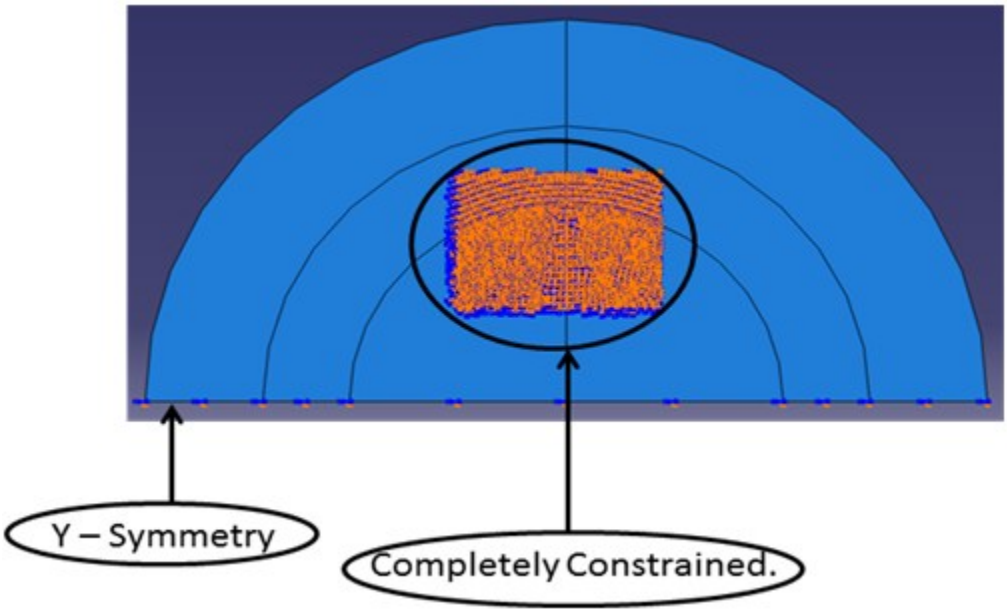

Fig. 6.60-a: Boundary Conditions applied to the circular pin

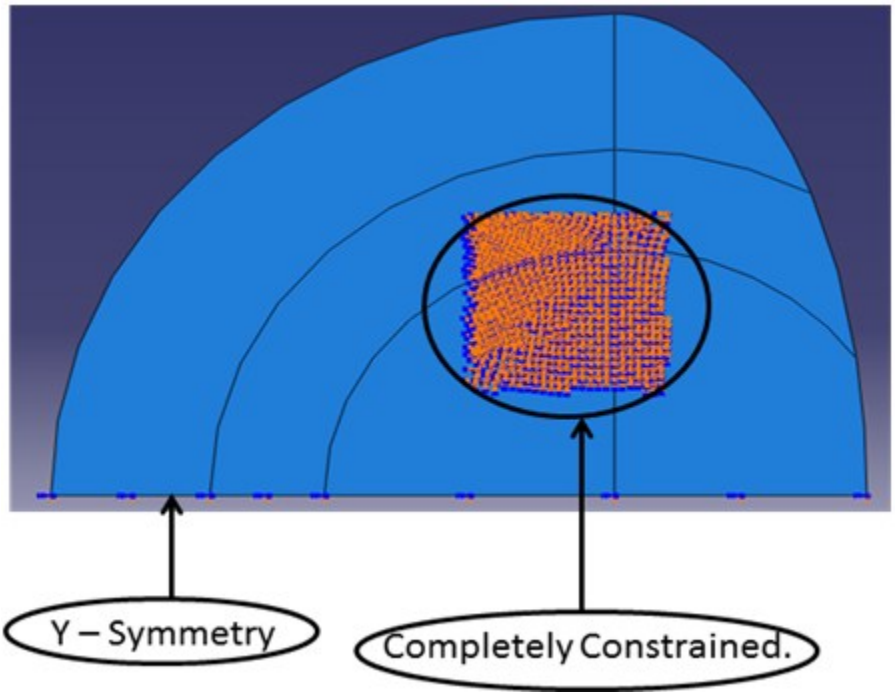

Fig. 6.60-b: Boundary Conditions applied to the non-circular pin

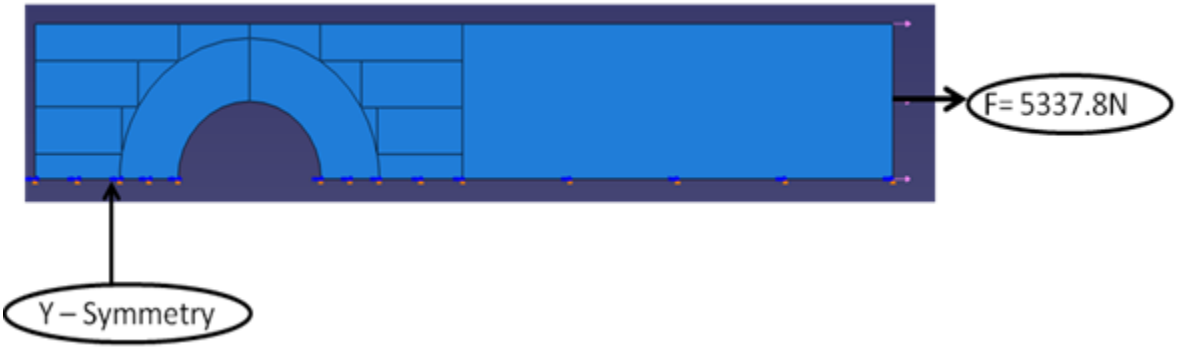

Fig. 6.61: Boundary Conditions and the loads applied to the plate

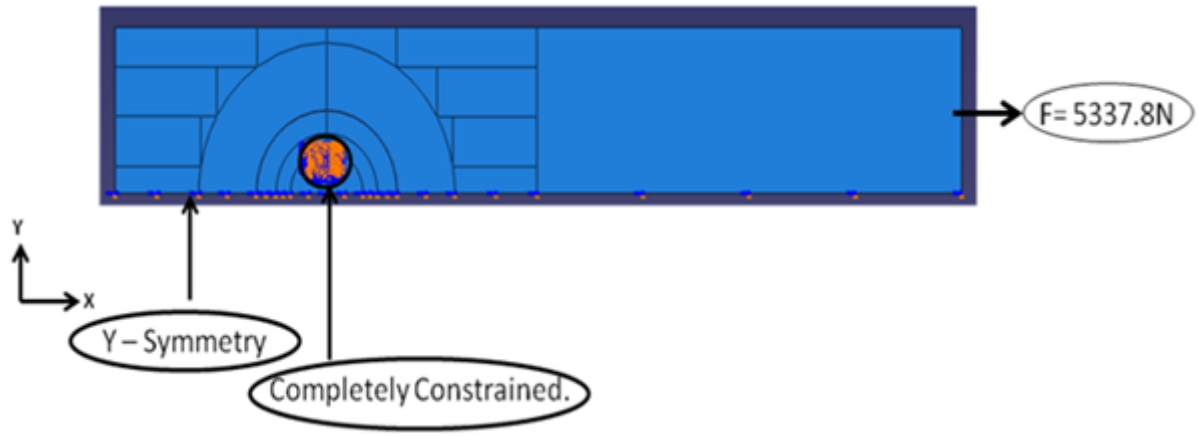

Fig. 6.62: Boundary Conditions and the loads associated with the entire assembly for the circular pin specimen

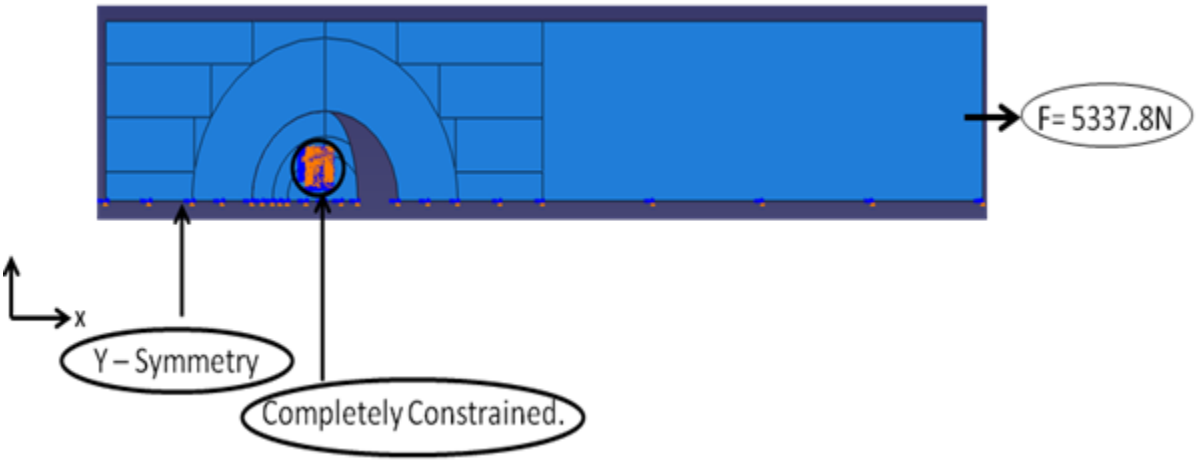

Fig. 6.63: Boundary Conditions and the loads associated with the entire assembly for the non-circular pin specimen

6.7.5 General Details

Material Modeling

The material library in ABAQUS allows most engineering materials to be modeled, including metals, plastics, rubbers, foams, composites, granular soils, rocks, and plain and reinforced concrete. The two materials that were considered here are steel and aluminum. The pinned joint is subjected to a cyclic loading while performing the thermoelastic stress analysis which keeps everything in the linear realm. Hence only linear material properties were incorporated into the model. The default material properties used are:

Steel (pin): Young's Modulus = 200.003 GPa and Poisons ratio = 0.25

Aluminum (plate): Young's Modulus = 69.002 GPa and Poisons ratio = 0.33

Contact Definitions

Selection of surfaces for the contact pair must be done before proceeding with the contact definition. Numerical conditional constraints were applied by ABAQUS at various locations on each surface to replicate contact conditions. The contact discretization used in the overall contact formulation dictates the locations and conditions of these constraints. The contact formulation in ABAQUS works using the master-slave approach wherein surfaces were initially defined as a master/slave and the slave surface slides on the master when they come in contact. The relative motion of the surfaces involved in the contact formulations were accounted for by two tracking approaches built into ABAQUS/Standard: the finite-sliding tracking approach and the small sliding tracking approach. *Figures 6.64 and 6.65* represent the contact situations for the plate with circular and non-circular pin, respectively.

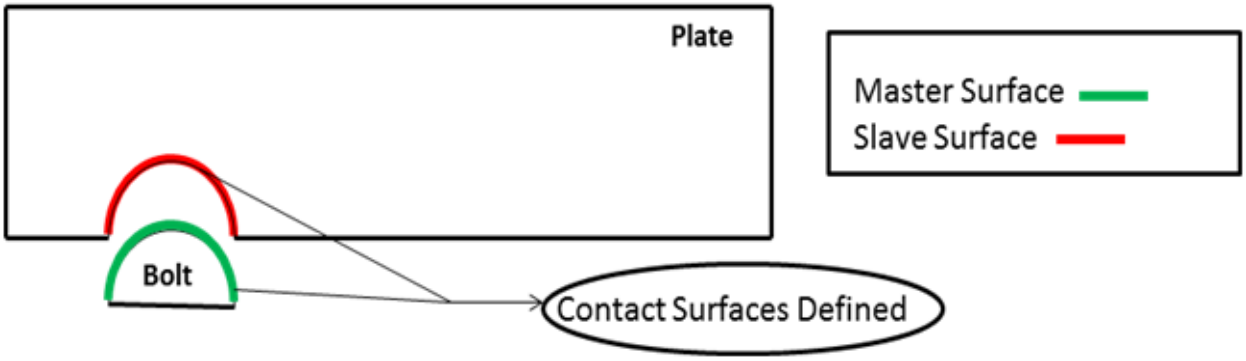

Fig. 6.64: Contact surfaces defined on the plate and circular pin

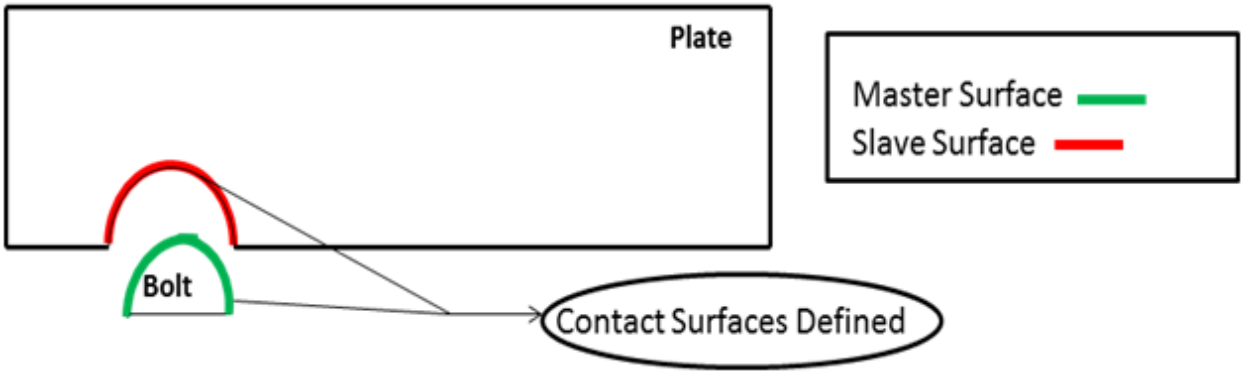

Fig. 6.65: Contact surfaces defined on the plate and non-circular pin

The finite-sliding tracking approach

This is a general approach used for tracking where ABAQUS allows for arbitrary relative separation, sliding, and rotation of the contacting surfaces. A bucket sorting technique was used to check for penetration of the slave surface and penetration is checked for every iteration.

The small-sliding tracking approach

This approach assumes that there will be relatively little sliding of the master and slave surfaces involved. Small-sliding contact formulations are useful as they are computationally less expensive and are more stable. The small sliding approach was used in the current study.

Master and slave surface selection in small-sliding problems

When using the small-sliding formulation, the slave surface should have a refined mesh or the surface on the more deformable body. In the current study the pin was chosen as the slave surface and the plate was chosen as the master surface as shown in *figures 6.64 and 6.65*.

Friction

A coulomb friction model was used to define the frictional coefficients. The coulomb friction model works by relating the maximum allowable shear stress across an interface to the contact pressure between the contacting bodies. Two contacting surfaces can carry shear stresses up to a certain magnitude across their interface before they start sliding relative to one another. The state when they are not sliding is known as sticking. ABAQUS also provides a model to specify a static and a kinetic friction coefficient directly. A static friction coefficient of 0.2 between the steel-aluminum interfaces was used here.

Results

The finite element model used ABAQUS/Standard 6.83. *Figures 6.66 through 6.68* show the contour plots for the Cartesian components of stress (σ_{xx}, σ_{yy} and σ_{xy}) and *figures 6.69 through 6.71* show the contour plots for polar components of stress (σ_{rr}, $\sigma_{\theta\theta}$ and $\sigma_{r\theta}$) for the plate with circular pin. *Figures 6.72 through 6.74* show the contour plots for the Cartesian components of stress (σ_{xx}, σ_{yy} and σ_{xy}) and *figures 6.75 through 6.77* show the contour plots for polar components of stress (σ_{rr}, $\sigma_{\theta\theta}$ and $\sigma_{r\theta}$) for the plate with non-circular pin. Since the finite model was modeled in inches, the stresses are in lbs/in^2.

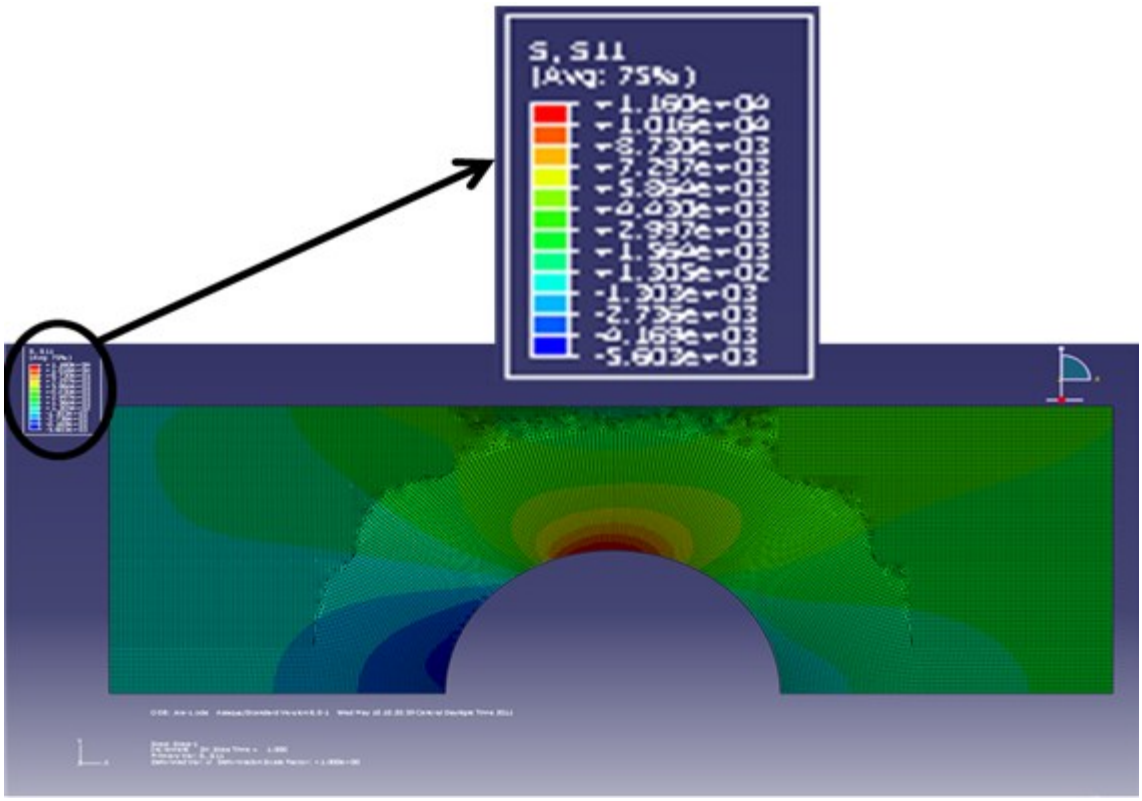

Fig. 6.66: Contour plot of stress in the x-direction (σ_{xx}) for the plate with circular pin

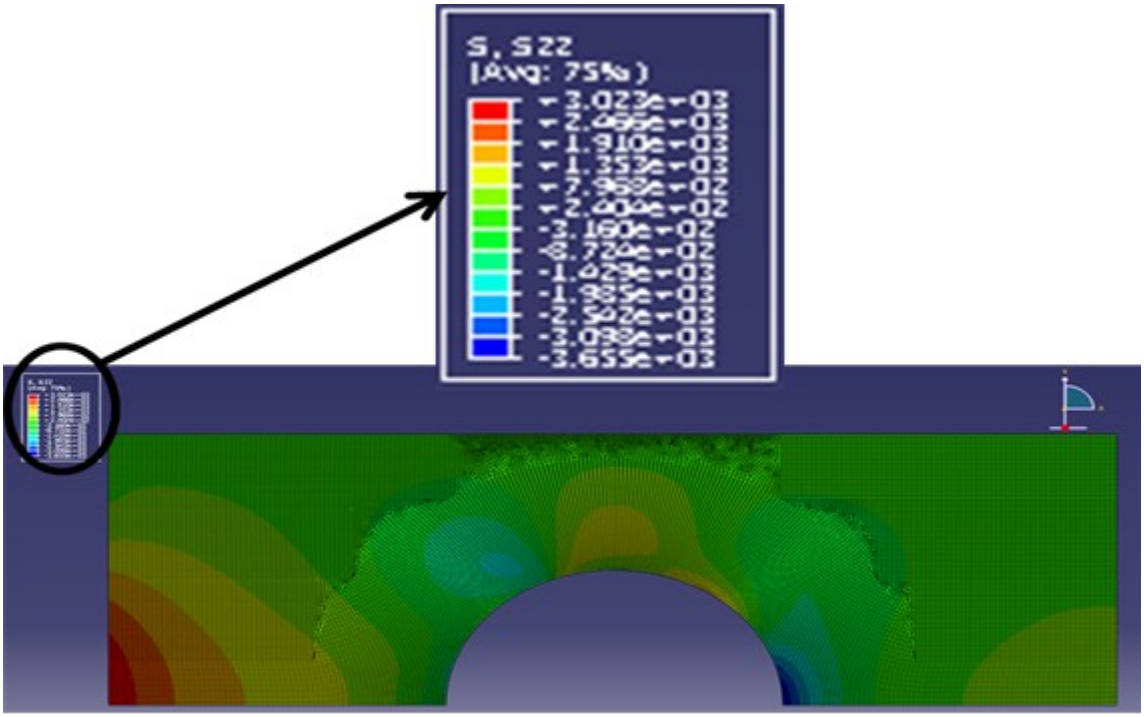

Fig. 6.67: Contour plot of stress in the y-direction (σ_{yy}) for the plate with circular pin

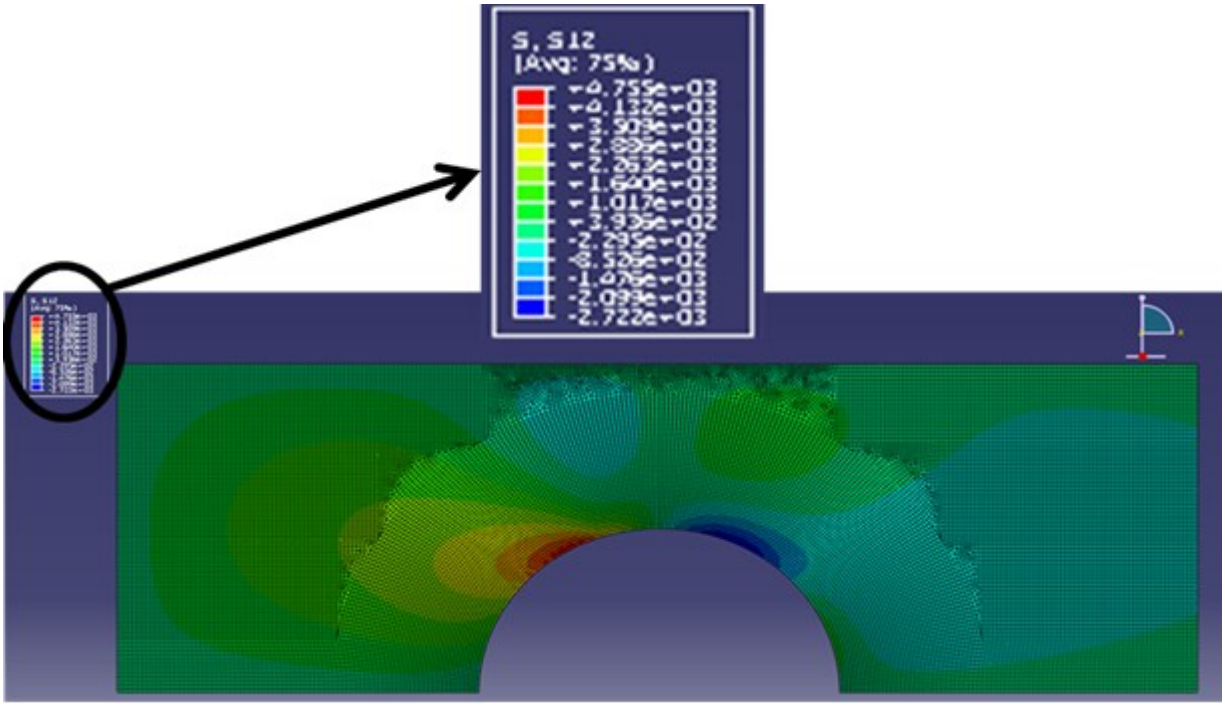

Fig. 6.68: Contour plot of shear stress (σ_{xy}) for the plate with circular pin

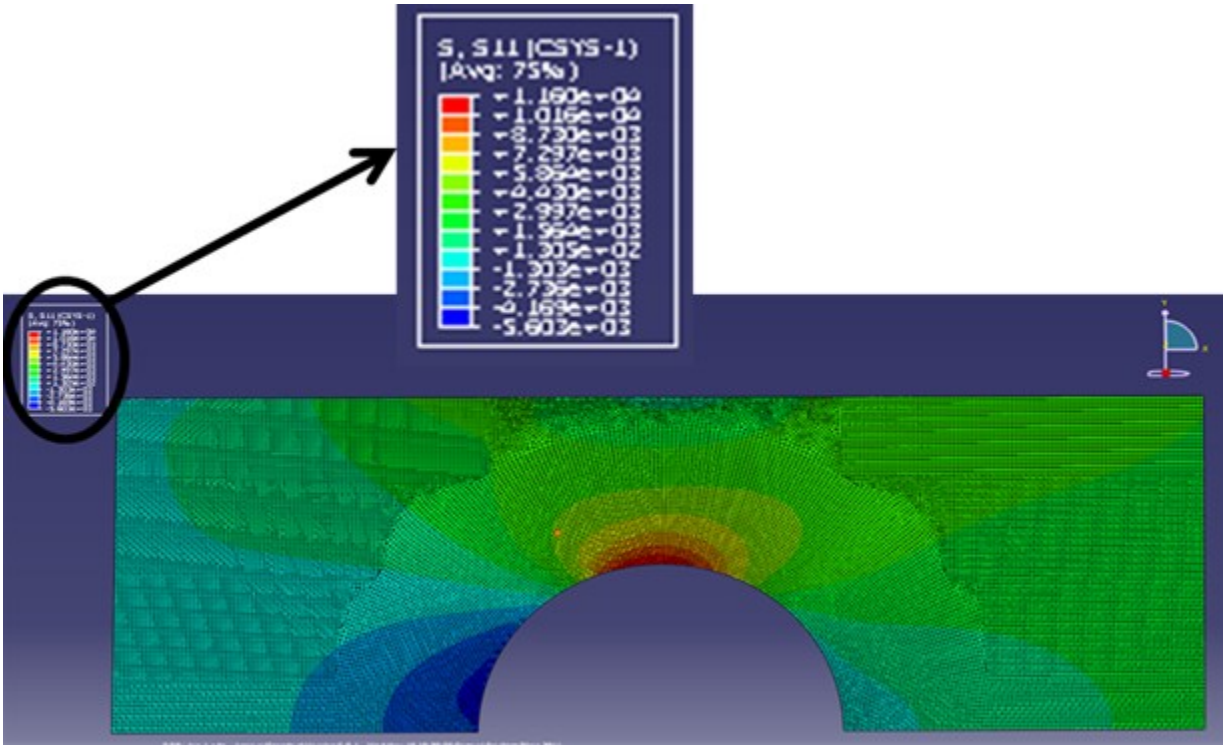

Fig. 6.69: Contour plot of radial stress (σ_{rr}) for the plate with circular pin

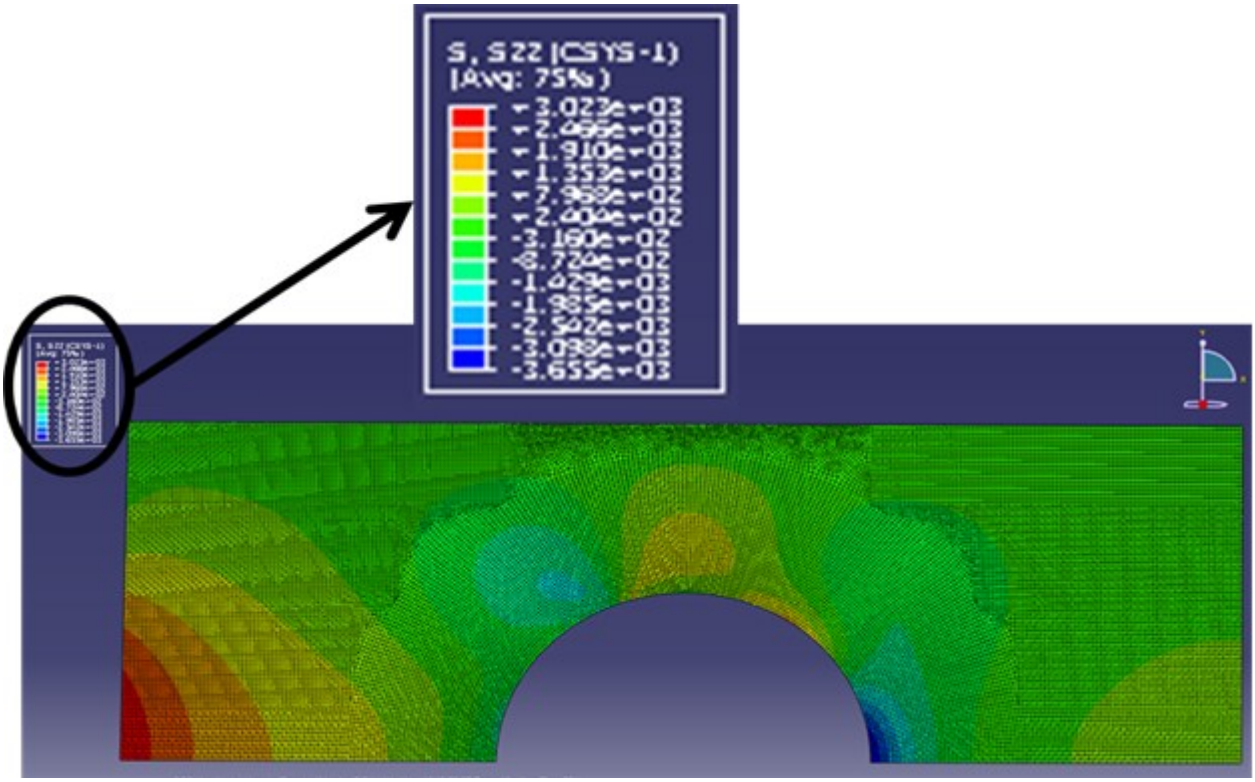

Fig. 6.70: Contour plot of tangential stress ($\sigma_{\theta\theta}$) for the plate with circular pin

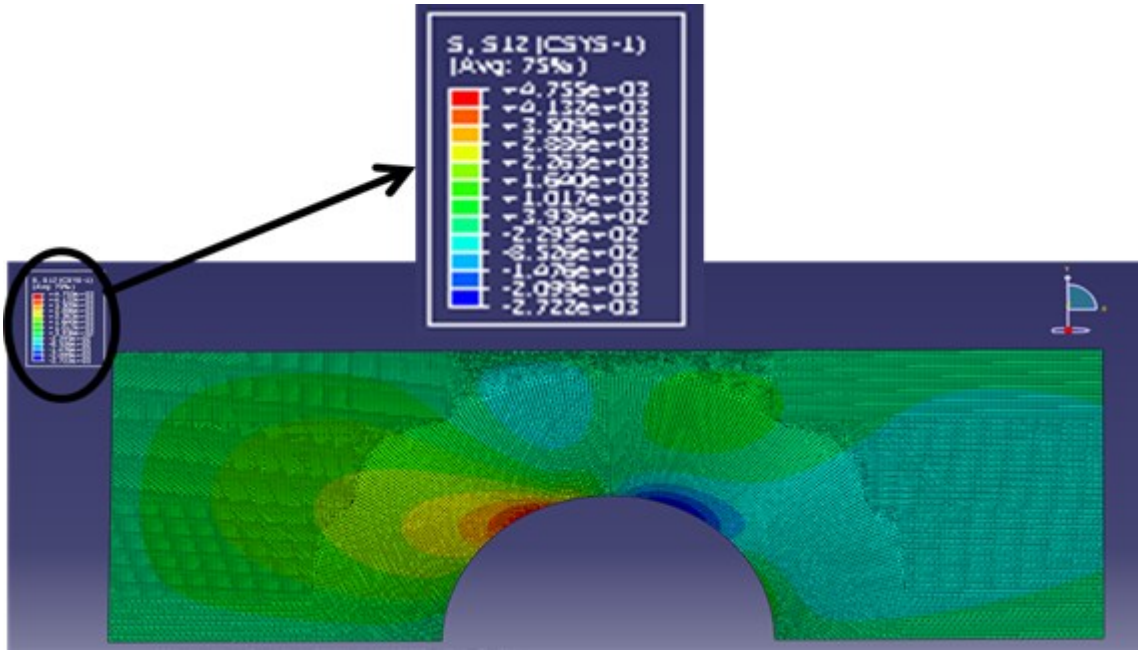

Fig. 6.71: Contour plot of polar shear stress ($\sigma_{r\theta}$) for the plate with circular pin

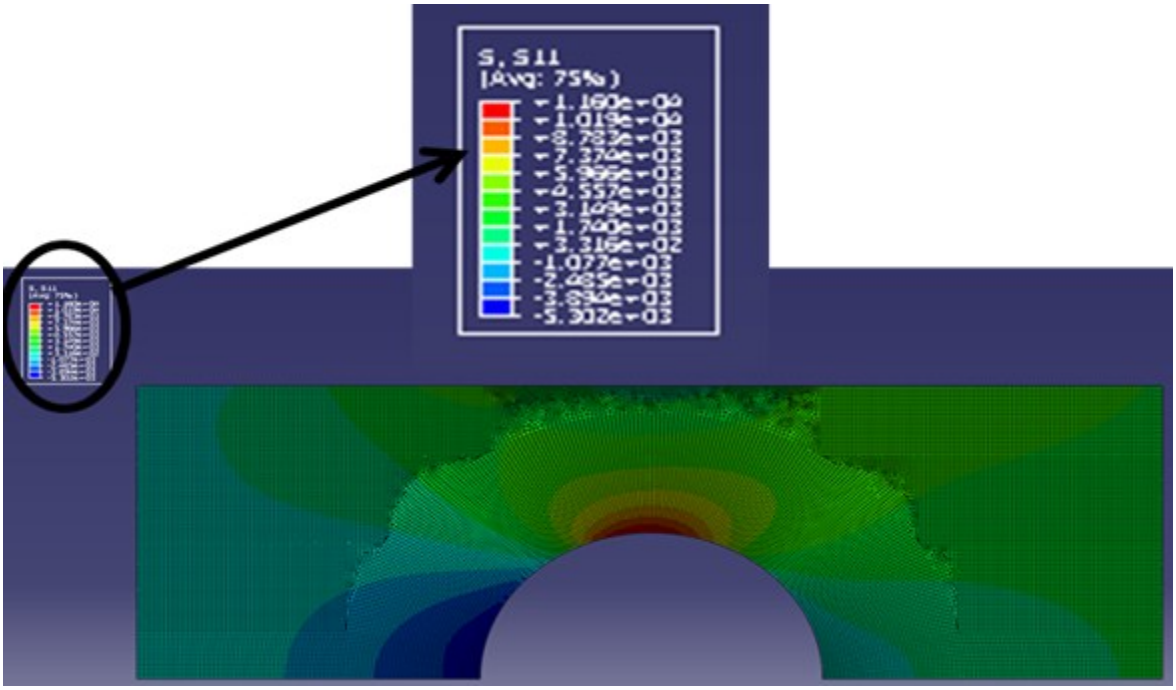

Fig. 6.72: Contour plot of stress in the x-direction (σ_{xx}) for the plate with non-circular pin

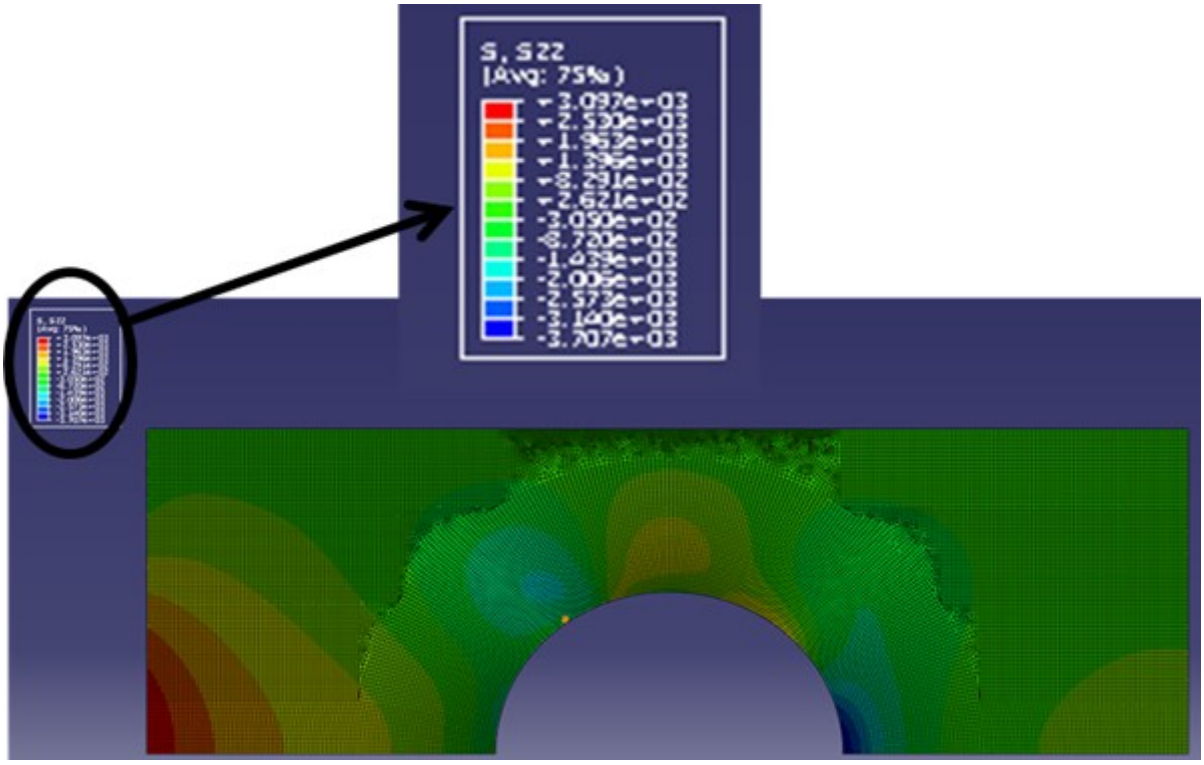

Fig. 6.73: Contour plot of stress in the y-direction (σ_{yy}) for the plate with non-circular pin

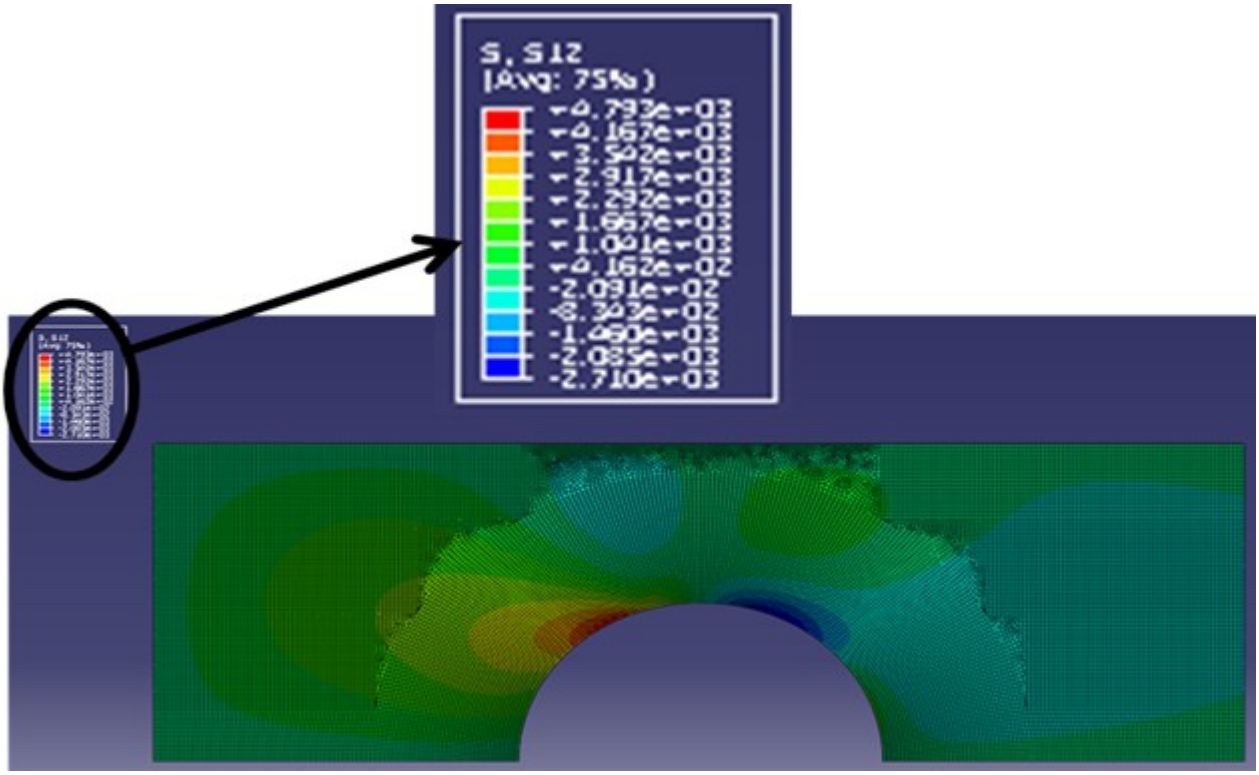

Fig. 6.74: Contour plot of shear stress (σ_{xy}) for the plate with non-circular pin

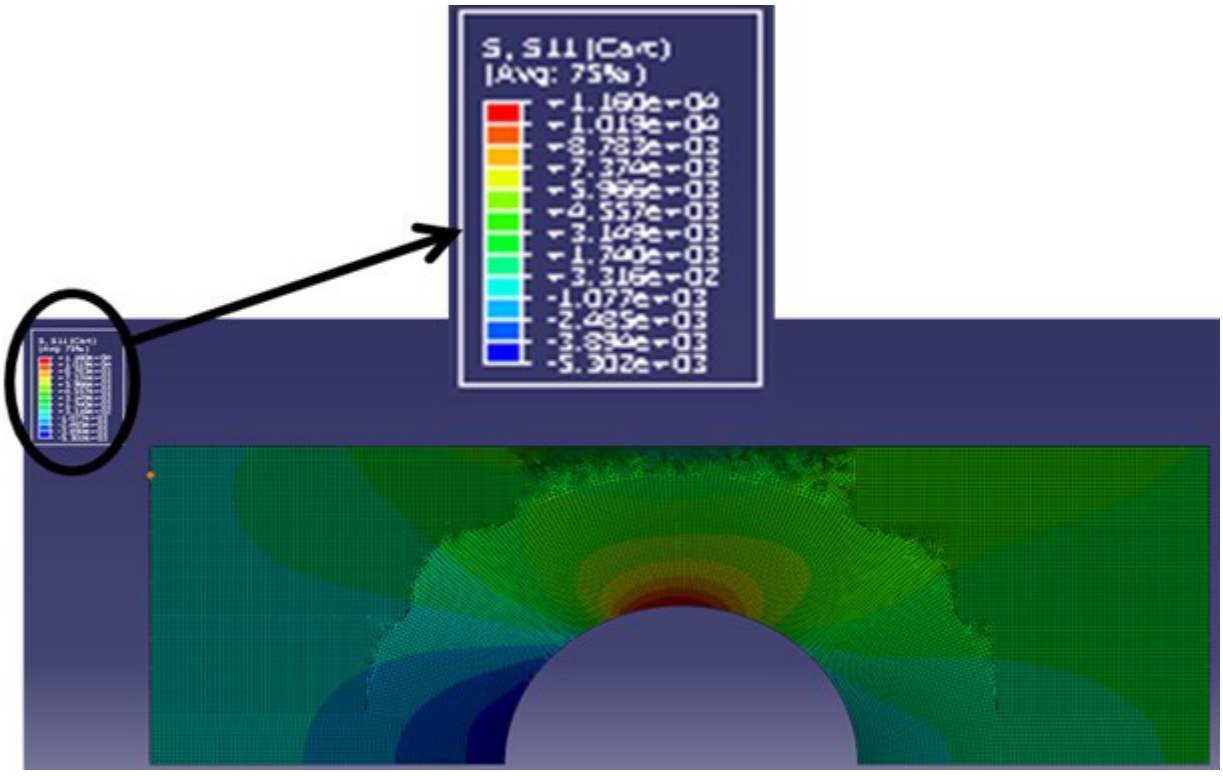

Fig. 6.75: Contour plot of radial stress (σ_{rr}) for the plate with non-circular pin

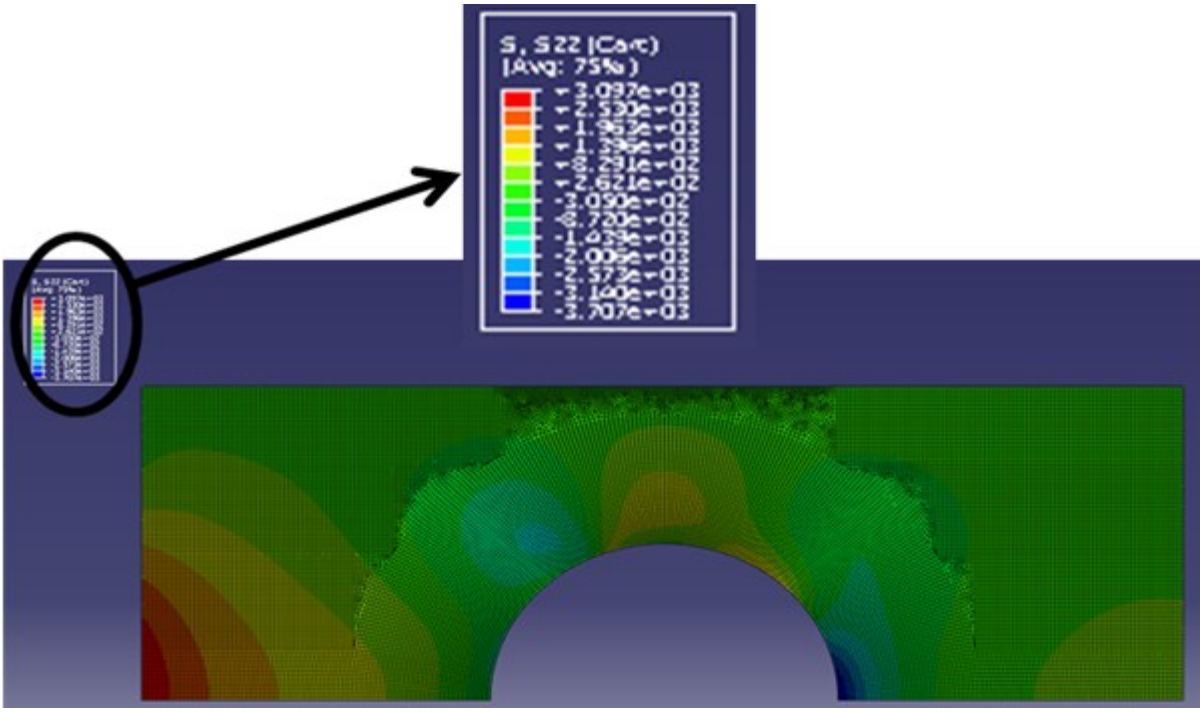

Fig. 6.76: Contour plot of tangential stress ($\sigma_{\theta\theta}$) for the plate with non-circular pin

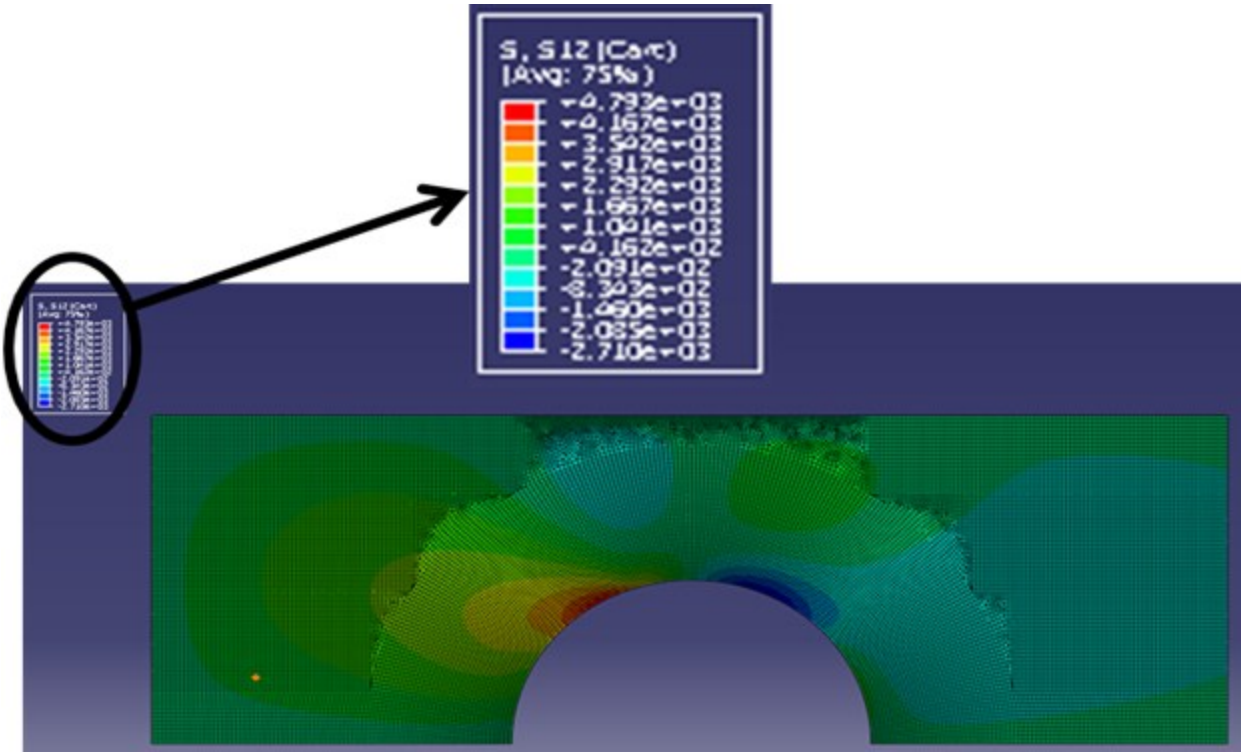

Fig. 6.77: Contour plot of polar shear stress ($\sigma_{r\theta}$) for the plate with non-circular pin

Possible Pin Bending.

For an applied load of 5,553 N (1,200 pounds), *figure 6.78* shows the FEM-predicted vertical displacements (inches) throughout the complete assembly while *figure 6.79* emphasizes those in the region near the round pin. The top grip of a closed-loop hydraulic MTS testing machine remains stationary and the bottom grip moves downward when loading the aluminum specimen in tension, *figures 6.4*, *6.17* and *6.19*. Compatible with this, the upper vertical section of the loading fixture of *figure 6.78,* which would be engaged physically in the top MTS grip, does not move. *Figures 6.78* and *6.79* suggest extremely little bending occurs in the loading fixture or the aluminum test plate. The numerically-predicted vertical motion of the pin from its very back (back right surface of the back steel loading plate of *figures 6.6*, *6.12*, *6.13* through *6.15* and *6.17*) to the front (TSA side) is 4.834×10^{-6} inches (~0.0001 mm) upward (back) to 2.881×10^{-4} inches (0.007 mm) downward (front). While the top of the hole on front face (TSA side) of the aluminum specimen is therefore predicted to move downward 0.007 mm, the pin at the backside of the aluminum plate (hence the top of the hole on the backside of the specimen) is predicted to move downward only 0.004 mm. Since the top of the steel loading fixture and the bottom of the aluminum specimen plate are loaded vertically, the FEM would therefore suggest a slight bending of the plate, producing a slightly smaller longitudinal strain/stress on the front (TSA side) compared to on the back side of the specimen. This prediction agrees with the measured strains on the back of the plate exceeding those on the front of the plate, *figure 6.54*. The top of the hole in the aluminum specimen is predicted to move vertically < 0.1 mm under the 5.6 N (1,200 pound) load and the TSA pixel spacing is approximately 0.4 mm. Not using TSA (Thermoelastic Stress Analysis) data within two pixels of an edge, including the top of the hole,

therefore means the motion of the edge of the hole during the cycling action is not a technical concern.

The present 3-D CAD models were meshed (ABAQUS C3D8R, continuum elements with reduced integration element type) with an element size of 0.2 in (5.08 mm) for a total of 2604 elements. The numerical solutions were conducted on a Dell Studio 1555 laptop computer having an Intel (R) Core (TM) 2 Duo CPU T6600 @ 2.20 GHz processor and 4.0 GB of RAM. A 64-bit Operating system with a 500 GB internal hard disk was used for storage. The analyses took approximately four to five minutes for each run due to the simplified geometry that was used to model the problem.

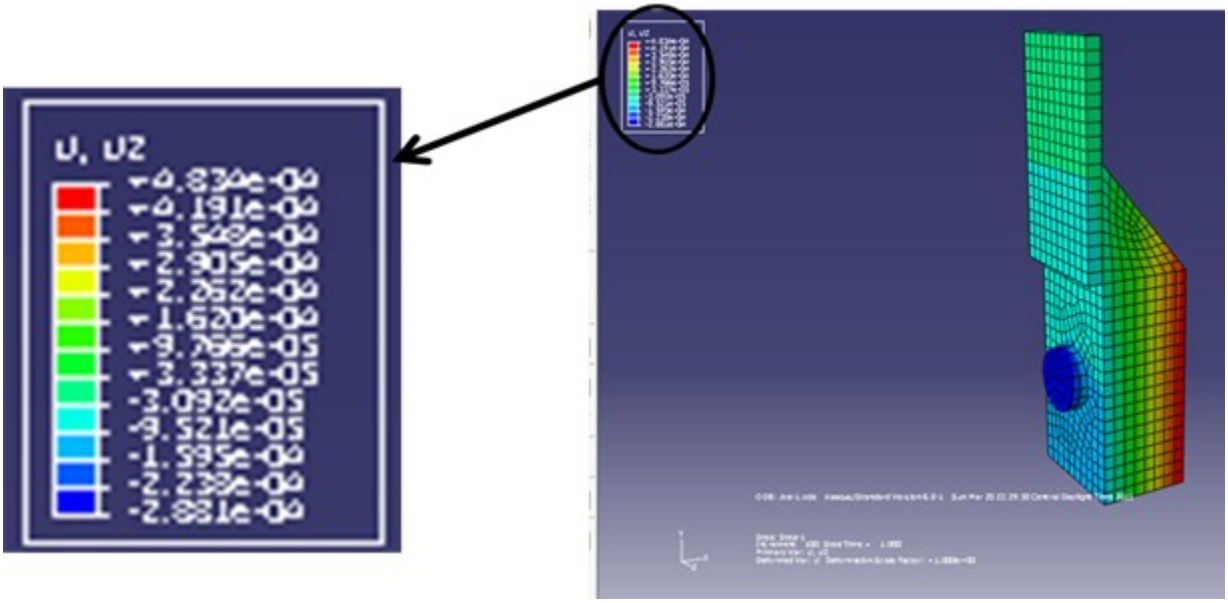

Fig. 6.78: Predicted vertical (i.e. y direction) displacements (inches)

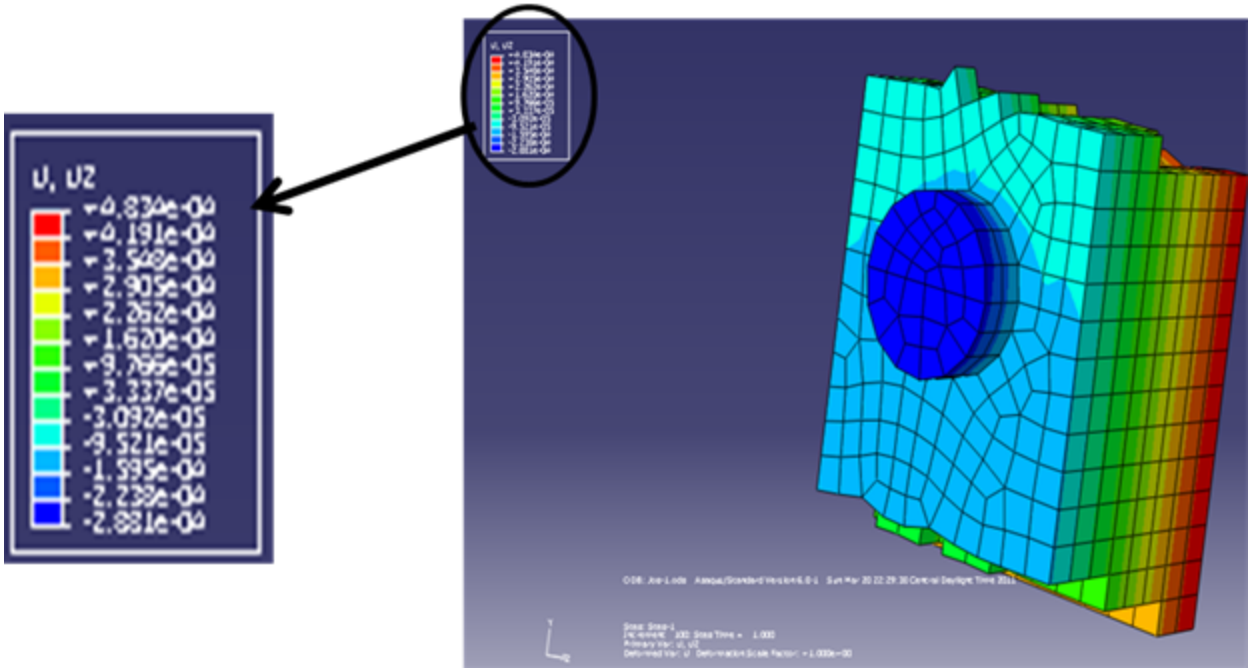

Fig. 6.79: Predicted vertical (i.e. y direction) displacements in the region of the round pin

6.8 Results

After determining all of the unknown Airy coefficients, the individual components of stress are evaluated and the results are compared with those from finite element analysis (ABAQUS). Cartesian and polar components of stress are normalized with respect to the far field stress, σ_0 (= 16.56 MPa or 2400 psi). Normalized tangential stress, $\sigma_{\theta\theta}$, radial stress, σ_{rr} and shear stress, $\sigma_{r\theta,}$ are plotted at various radii on and away from the boundary of the hole, as are normalized $\sigma_{\theta\theta} = \sigma_{xx}$ along line $\theta = 90^o$ and σ_{xx} on the boundary of hole.

Applied load range (F) = 5337.8 N (1200lb)

Cross-Sectional Area (A) = Width (W) x Thickness (t)

= 50.8 x 6.37 = 322.58 mm^2 (0.5 in^2)

$$\sigma_o = \frac{5337.8}{322.58} = 16.56\ MPa = (2400\ psi)$$

Plate loaded by circular pin:

Using $k = 9$ now known Airy coefficients evaluated from $m_1+h_1+t_1 = 5{,}479$ input values ($m_1 = 3{,}413$ TSA values, $h_1 = 2*831$, $t_1 = 2*101+2*301$) for the plate with circular pin, normalized individual components of stress are plotted on and away from the boundary of the hole, *figures 6.80 through 6.87*. The results are compared here with those evaluated from an approximate finite element analysis. Note that the FEM (ABAQUS) predicts the contact-free region between the pin and hole commences at $\theta > 90^o$ whereas TSA indicates this occurs at $\theta \sim 83^o$, *figure 6.82*. As noted previously, residual markings on the pin and hole support the TSA observation that the pin loses contact with the hole at $\theta \sim 83^o$. This difference in the contact region leads to some discrepancy between the results, *figure 6.82*. The extremely small shear

stress on the contact surface of the hole is not incompatible with the frequent approach of ignoring any such shearing stress in an absence of any pin/bolt-hole clearance [Bickley], *figure 6.84*. The radial clearance here is only 0.00045 inches (0.01 mm) which is less than 0.1 % of the pin radius. There is some discrepancy between the TSA and FEM results in *figure 6.86,* near the edge of the plate. This is probably due to the fact that although traction-free conditions were imposed on the vertical edge of the plate, no TSA data were collected in the region r/R > 1.8 with which to evaluate the Airy coefficients.

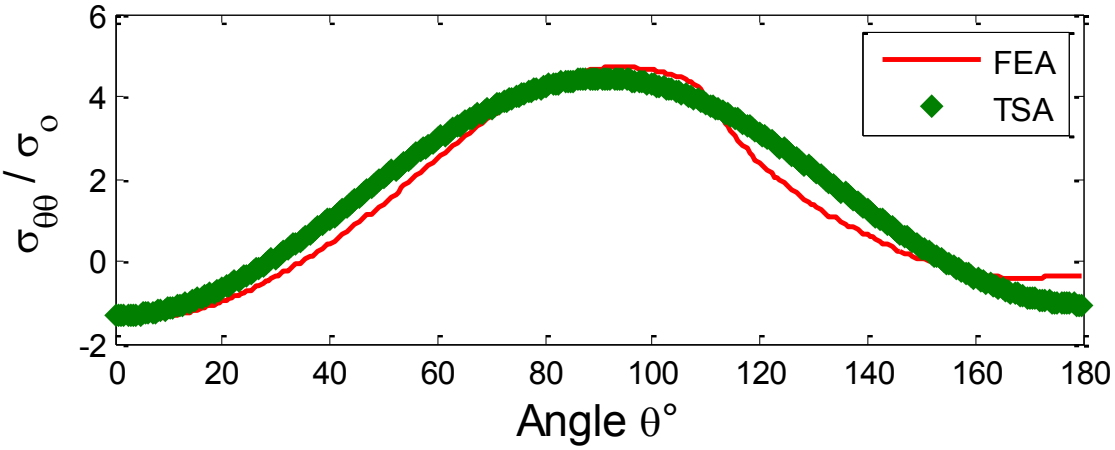

Fig. 6.80: Plot of $\sigma_{\theta\theta}/\sigma_0$ around the boundary of the hole (r/R = 1) from ABAQUS and TSA for $m_1+h_1+t_1 = 5{,}479$ input values and $k = 9$ ($m_1 = 3{,}413$ TSA values, $h_1 = 2*831$, $t_1 = 2*101+2*301$)

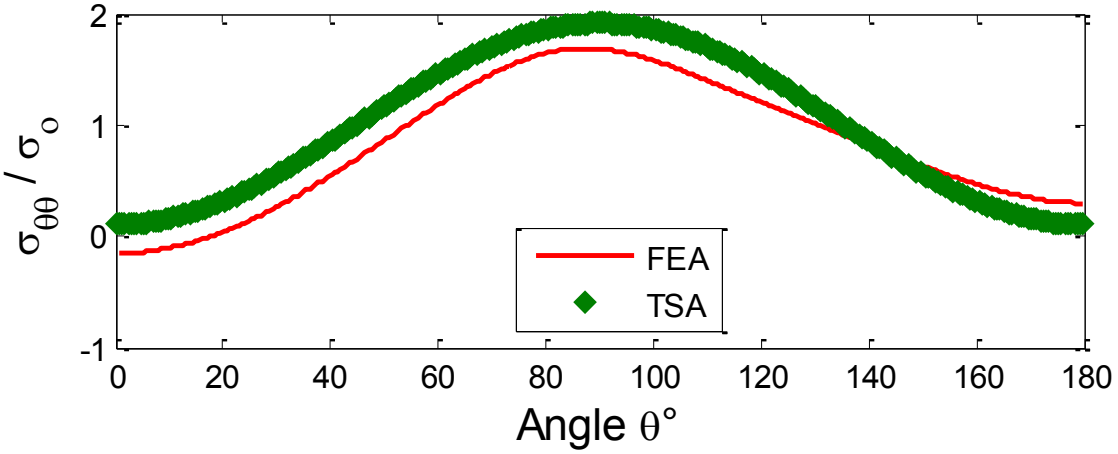

Fig. 6.81: Plot of $\sigma_{\theta\theta}/\sigma_0$ along r/R = 1.5 from ABAQUS and TSA for $m_1+h_1+t_1 = 5,479$ input values and $k = 9$ ($m_1 = 3,413$ TSA values, $h_1 = 2*831$, $t_1 = 2*101+2*301$)

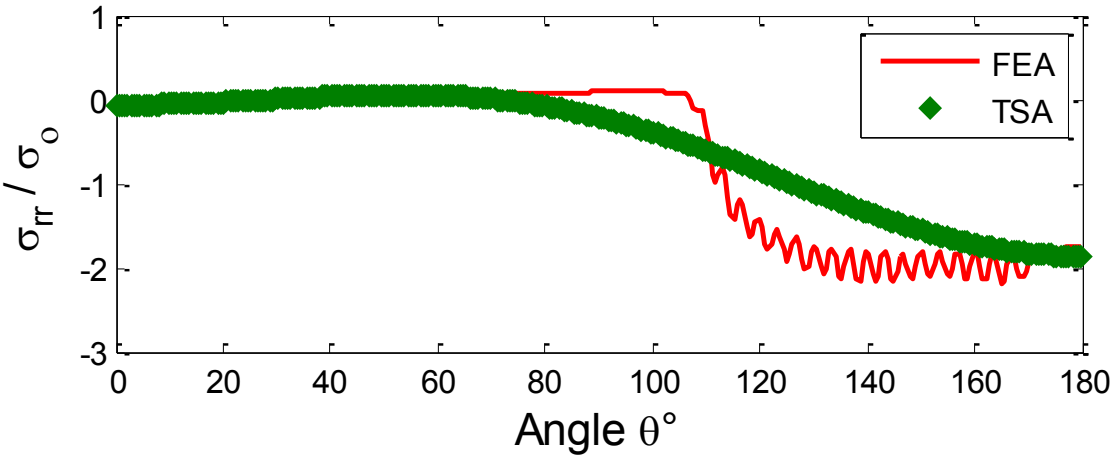

Fig. 6.82: Plot of σ_{rr}/σ_0 around the boundary of the hole (r/R = 1) from ABAQUS and TSA for $m_1+h_1+t_1 = 5,479$ input values and $k = 9$ ($m_1 = 3,413$ TSA values, $h_1 = 2*831$, $t_1 = 2*101+2*301$)

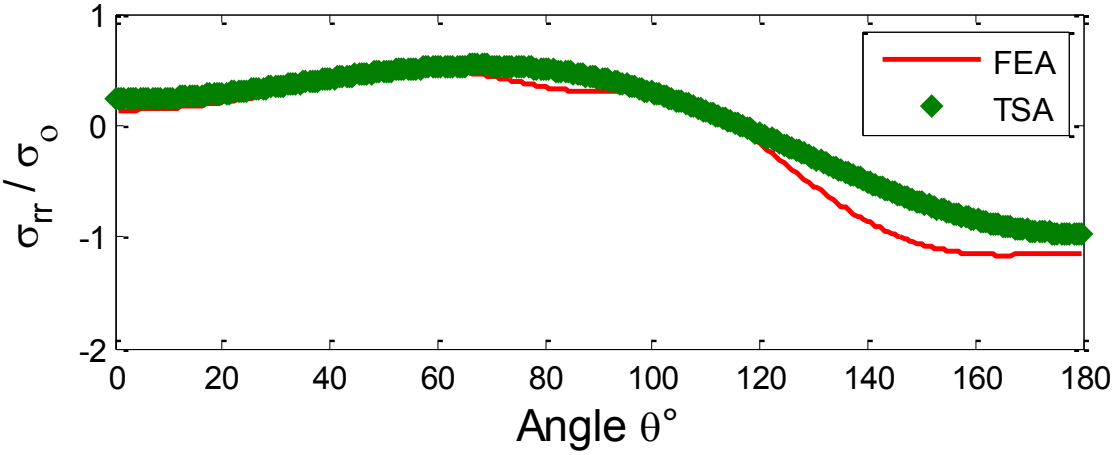

Fig. 6.83: Plot of σ_{rr}/σ_0 along r/R = 1.5 from ABAQUS and TSA for $m_1+h_1+t_1 = 5,479$ input values and $k = 9$ ($m_1 = 3,413$ TSA values, $h_1 = 2*831$, $t_1 = 2*101+2*301$)

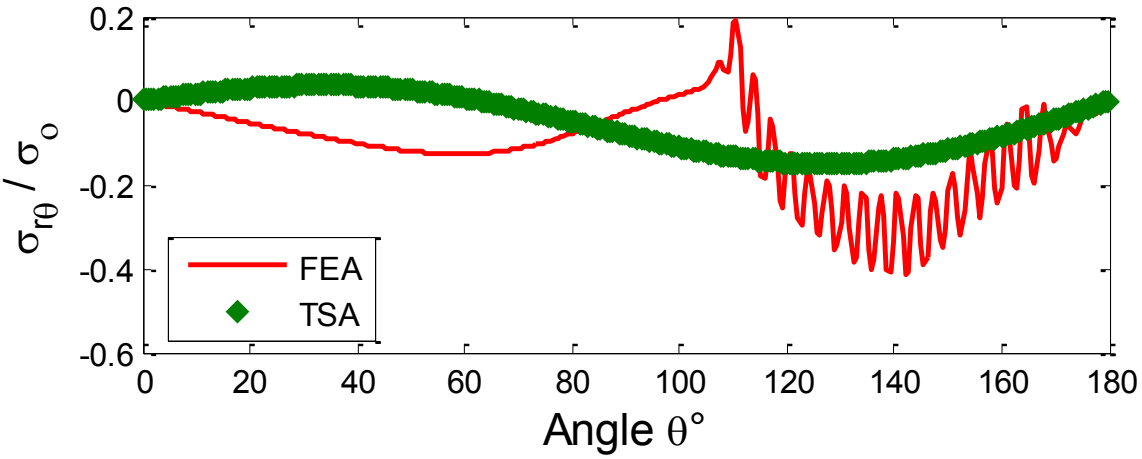

Fig. 6.84: Plot of $\sigma_{r\theta}/\sigma_0$ around the boundary of the hole (r/R = 1) from ABAQUS and TSA for $m_1+h_1+t_1 = 5,479$ input values and $k = 9$ ($m_1 = 3,413$ TSA values, $h_1 = 2*831$, $t_1 = 2*101+2*301$)

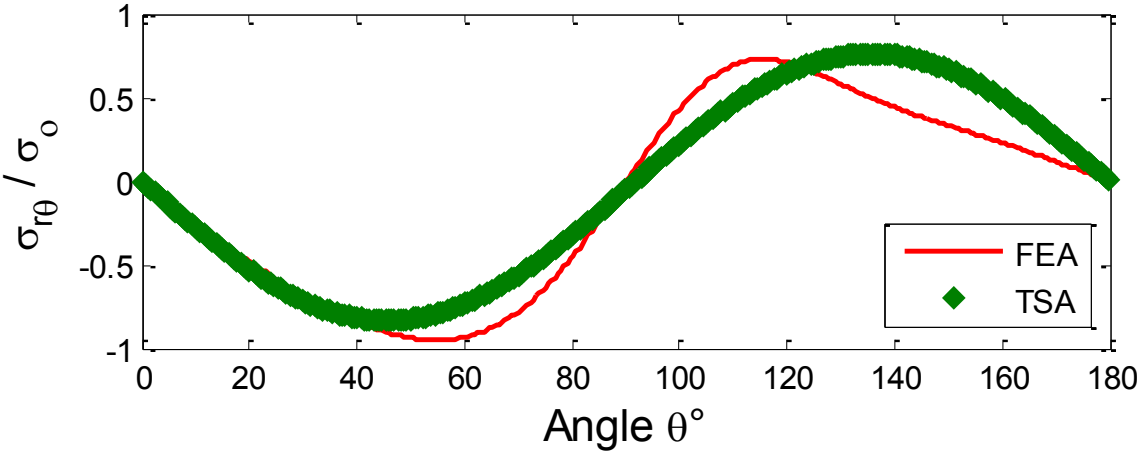

Fig. 6.85: Plot of $\sigma_{r\theta}/\sigma_0$ along r/R = 1.5 from ABAQUS and TSA for $m_1+h_1+t_1 = 5{,}479$ input values and $k = 9$ ($m_1 = 3{,}413$ TSA values, $h_1 = 2*831$, $t_1 = 2*101+2*301$)

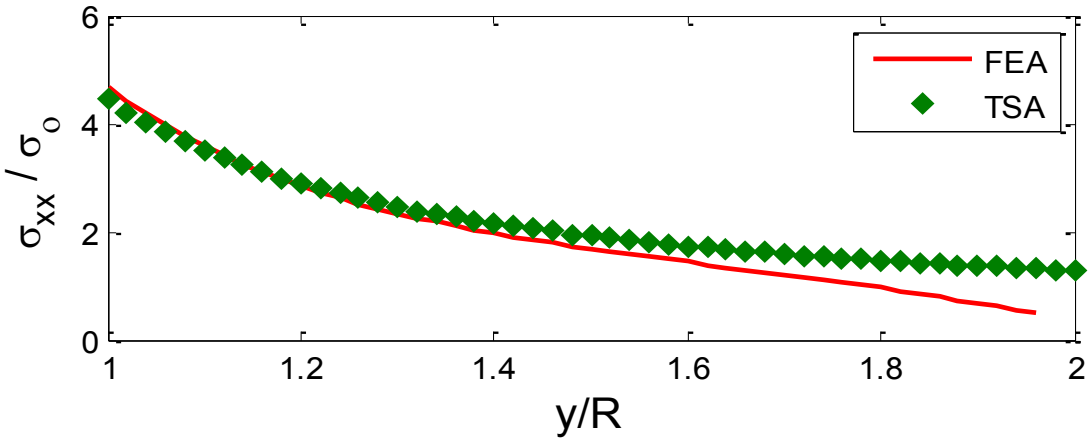

Fig. 6.86: Plot of σ_{xx}/σ_0 along the line extending from the edge of the hole (x = 0 or $\theta = 90^o$) from ABAQUS and TSA for $m_1+h_1+t_1 = 5{,}479$ input values and $k = 9$ ($m_1 = 3{,}413$ TSA values, $h_1 = 2*831$, $t_1 = 2*101+2*301$)

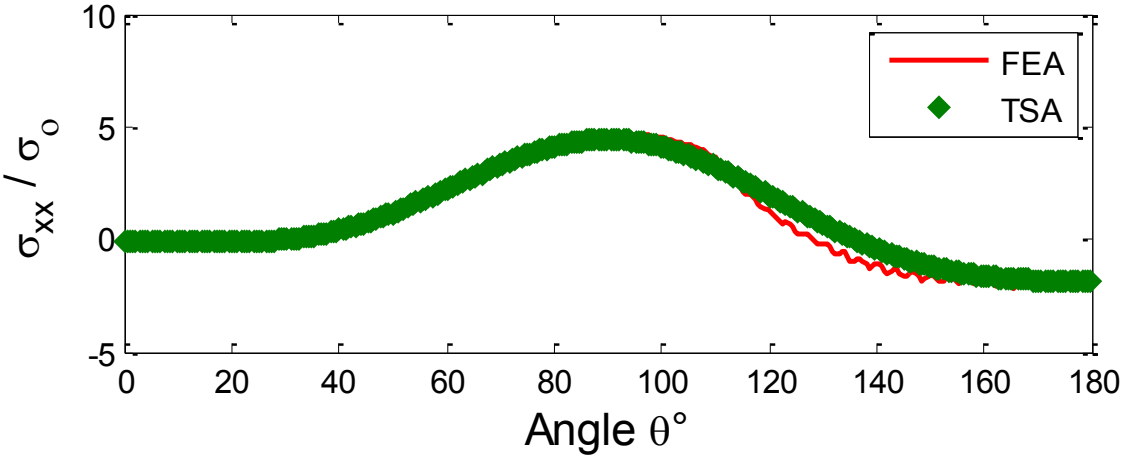

Fig. 6.87: Plot of σ_{xx}/σ_0 around the boundary of the hole (r/R = 1) from ABAQUS and TSA for $m_1+h_1+t_1 = 5,479$ input values and $k = 9$ ($m_1 = 3,413$ TSA values, $h_1 = 2*831$, $t_1 = 2*101+2*301$)

Plate loaded by non-circular pin:

Using $k = 9$ and the now evaluated Airy coefficients from $m_2+h_2+t_2 = 6{,}592$ input values ($m_2 = 3458$ TSA values, $h_2 = 2*871$, $t_2 = 2*101+2*301$) for the plate loaded by the non-circular pin, normalized individual components of stress on and away from the boundary of the hole are plotted in *figures 6.88 through 6.95*. The results are compared here with those from ABAQUS. Not unlike when the plate was loaded by the round pin, FEA (ABAQUS) predicts the pin-plate contact-free region exceeds 90^o whereas TSA indicates this occurs at $\theta \sim 87^o$. This difference in the contact region leads to some discrepancy between the results, *figure 6.90*. The shear stress on the contact surface of the hole is again extremely small, again supporting the frequent assumption of zero pin/bolt-hole shearing stress for connector having a closely fitting bolt/pin [Bickley], *figure 6.92*. The radial clearance here is again less than 0.1 % of the pin radius.

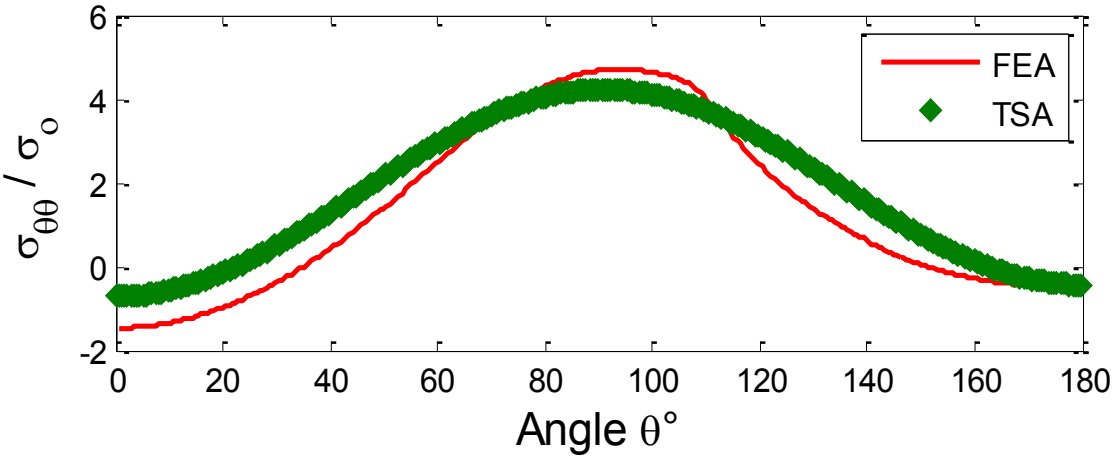

Fig. 6.88: Plot of $\sigma_{\theta\theta}/\sigma_0$ around the boundary of the hole (r/R = 1) from ABAQUS and TSA for $m_2+h_2+t_2 = 6{,}592$ input values and $k = 9$ ($m_2 = 3458$ TSA values, $h_2 = 2*871$, $t_2 = 2*101+2*301$)

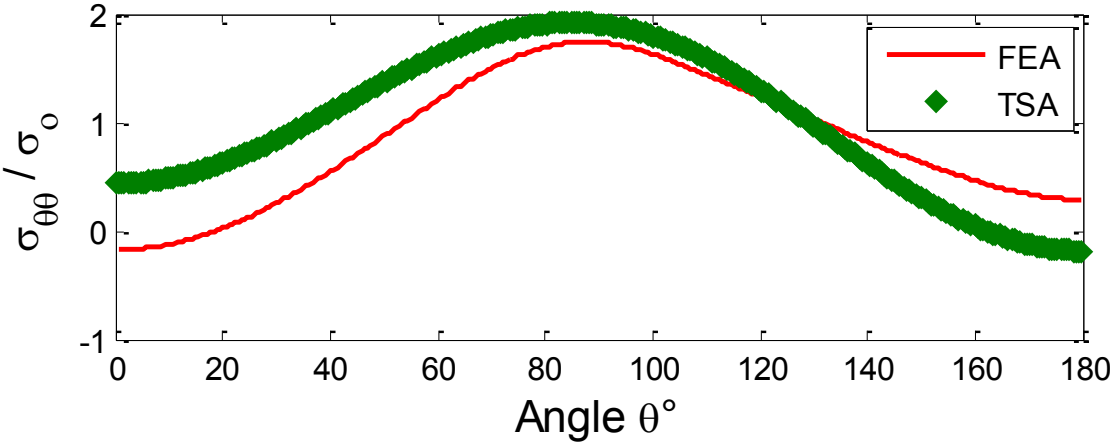

Fig. 6.89: Plot of $\sigma_{\theta\theta}/\sigma_0$ along r/R = 1.5 from ABAQUS and TSA for $m_2+h_2+t_2 = 6{,}592$ input values and $k = 9$ ($m_2 = 3458$ TSA values, $h_2 = 2*871$, $t_2 = 2*101+2*301$)

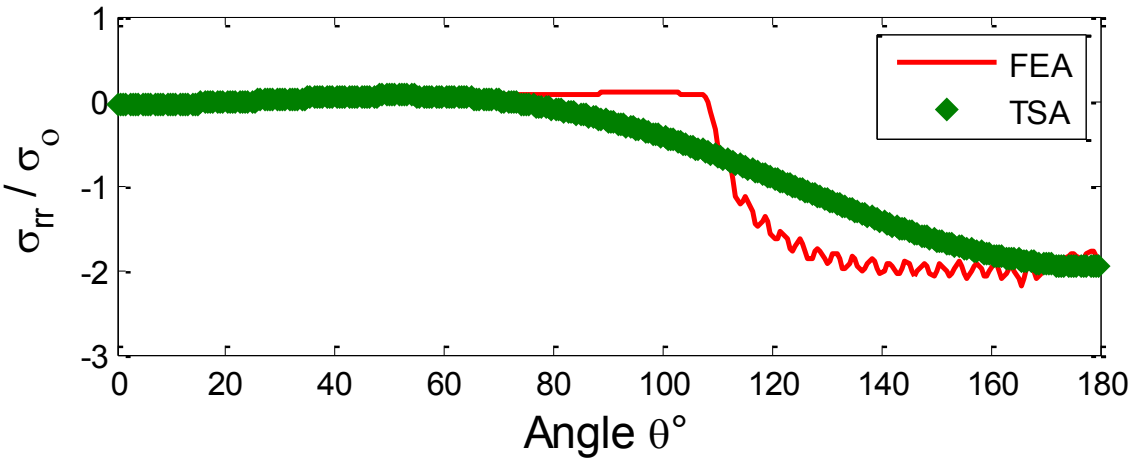

Fig. 6.90: Plot of σ_{rr}/σ_0 around the boundary of the hole (r/R = 1) from ABAQUS and TSA for $m_2+h_2+t_2 = 6{,}592$ input values and $k = 9$ ($m_2 = 3458$ TSA values, $h_2 = 2*871$, $t_2 = 2*101+2*301$)

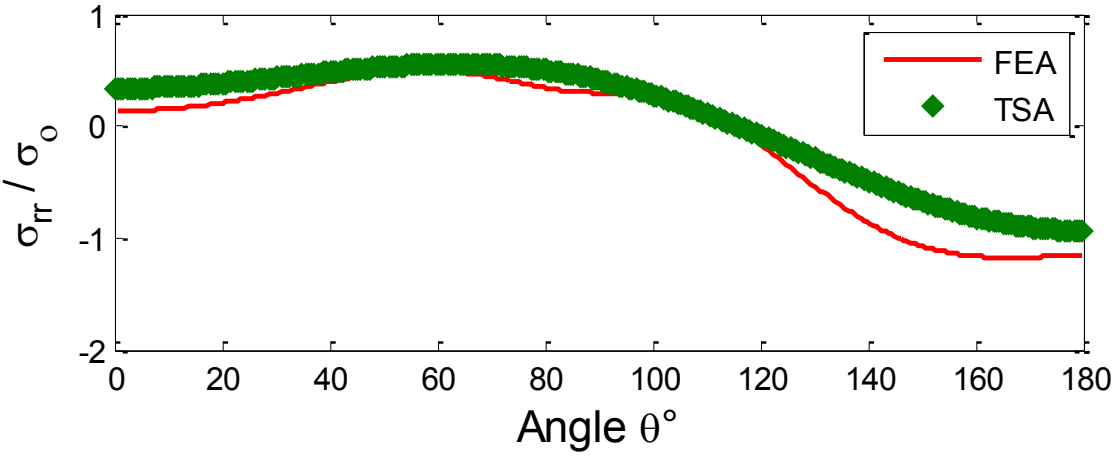

Fig. 6.91: Plot of σ_{rr}/σ_0 along r/R = 1.5 from ABAQUS and TSA for $m_2+h_2+t_2 = 6{,}592$ input values and $k = 9$ ($m_2 = 3458$ TSA values, $h_2 = 2*871$, $t_2 = 2*101+2*301$)

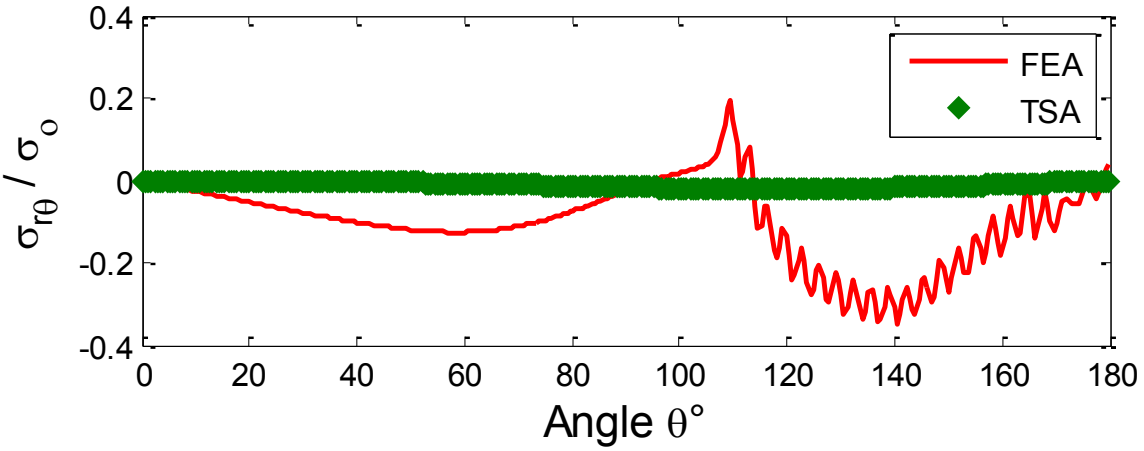

Fig. 6.92: Plot of $\sigma_{r\theta}/\sigma_0$ around the boundary of the hole (r/R = 1) from ABAQUS and TSA for $m_2+h_2+t_2 = 6{,}592$ input values and $k = 9$ ($m_2 = 3458$ TSA values, $h_2 = 2*871$, $t_2 = 2*101+2*301$)

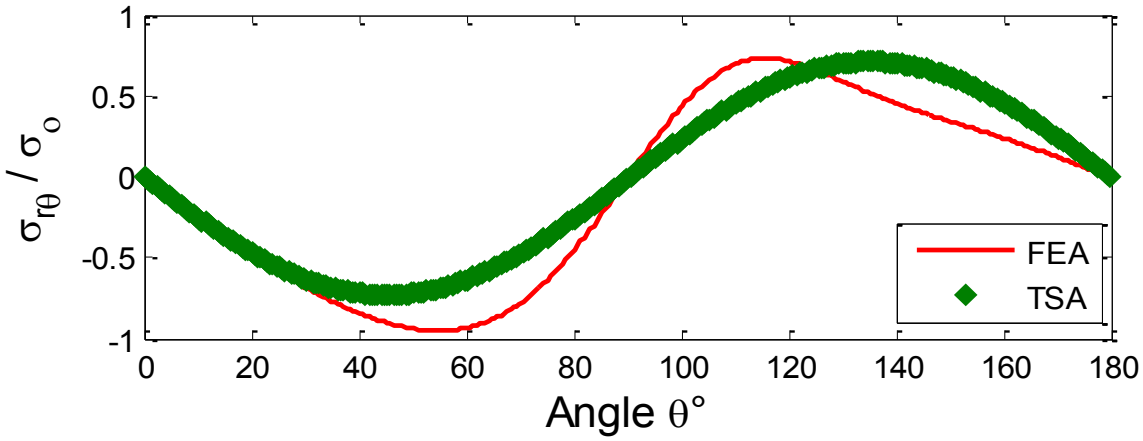

Fig. 6.93: Plot of $\sigma_{r\theta}/\sigma_0$ along r/R = 1.5 from ABAQUS and TSA for $m_2+h_2+t_2 = 6{,}592$ input values and $k = 9$ ($m_2 = 3458$ TSA values, $h_2 = 2*871$, $t_2 = 2*101+2*301$)

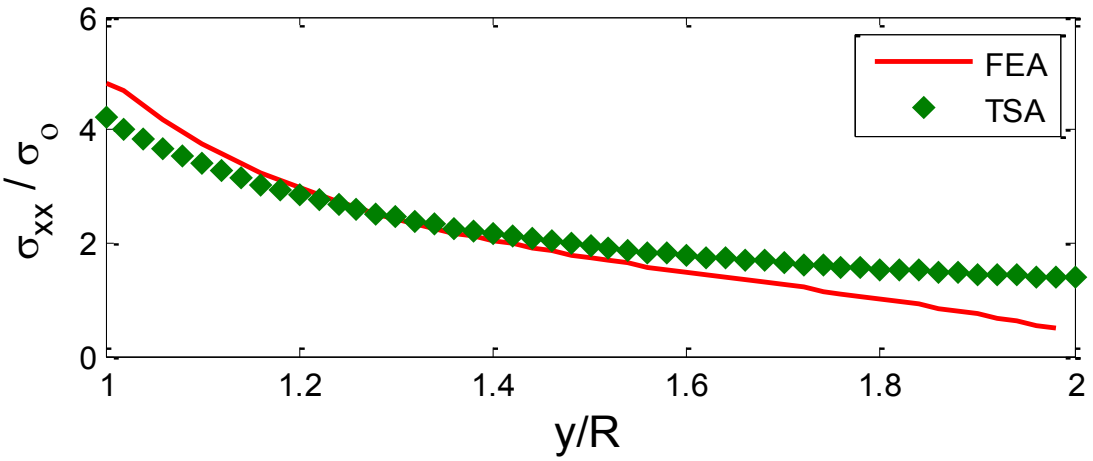

Fig. 6.94: Plot of σ_{xx}/σ_0 along the line extending from the edge of the hole (x = 0 or θ = 90o) from ABAQUS and TSA for $m_2+h_2+t_2 = 6{,}592$ input values and $k = 9$ ($m_2 = 3458$ TSA values, $h_2 = 2*871$, $t_2 = 2*101+2*301$)

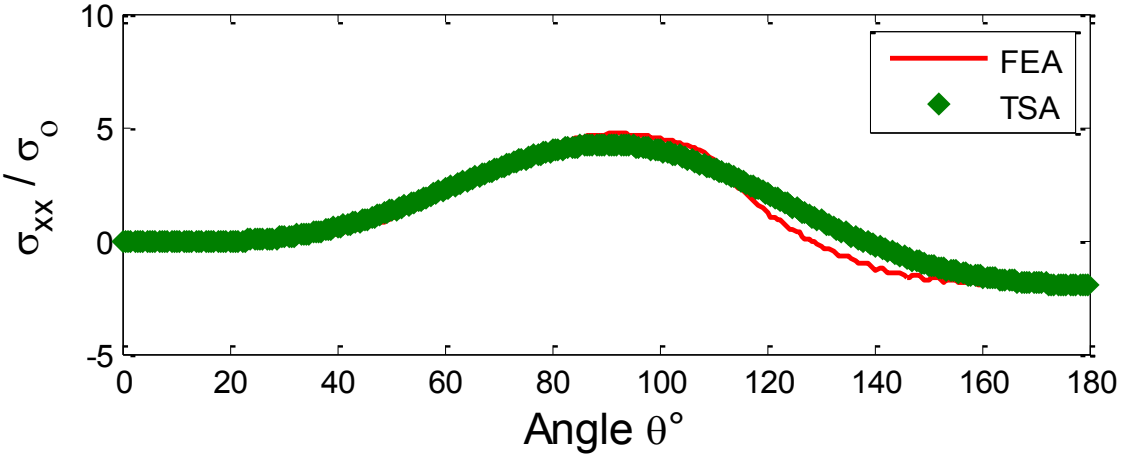

Fig. 6.95: Plot of σ_{xx}/σ_0 around the boundary of the hole (r/R = 1) from ABAQUS and TSA for $m_2+h_2+t_2 = 6{,}592$ input values and $k = 9$ ($m_2 = 3458$ TSA values, $h_2 = 2*871$, $t_2 = 2*101+2*301$)

Compared to the FEA (ABAQUS) results, the deteriorating TSA evaluated stress of *figure 6.94* is probably again influence by the lack of any measure TSA input data beyond r/R = 1.8.

6.8.1 Contour Plots

Using the now known Airy coefficients, the complete state of stress can be determined throughout the plate of the loaded connector, i.e., the full-field individual Cartesian and polar components of stress can be evaluated. Contour plots showing the stress distributions near the pinned end of the specimen are plotted using MATLAB. Again the individual stress components are normalized with respect to the far field stress, σ_0 (= 16.56 MPa or 2400 psi). The results are compared with those from FEM. MATLAB was also used to plot the contours of the raw FEM (ABAQUS) data.

Plate loaded by circular pin:

Using the $k = 9$ now known Airy coefficients evaluated from $m_1+h_1+t_1 = 5,479$ input values ($m_1 = 3,413$ TSA values, $h_1 = 2*831$, $t_1 = 2*101+2*301$) for the plate with circular pin, the full-field individual Cartesian and polar components of stress can be evaluated. *Figures 6.96 through 6.98* are the contour plots of normalized Cartesian components of stress for the plate with the circular pin. Similarly *figures 6.99 through 6.101* are the contour plots of normalized polar components of stress for the plate loaded by the circular pin. There is a good agreement between the TSA and ABAQUS results. The slightly high radial stress (*figure 6.99*) may be due to the stress discontinuities from ABAQUS at the interface of pin and plate hole.

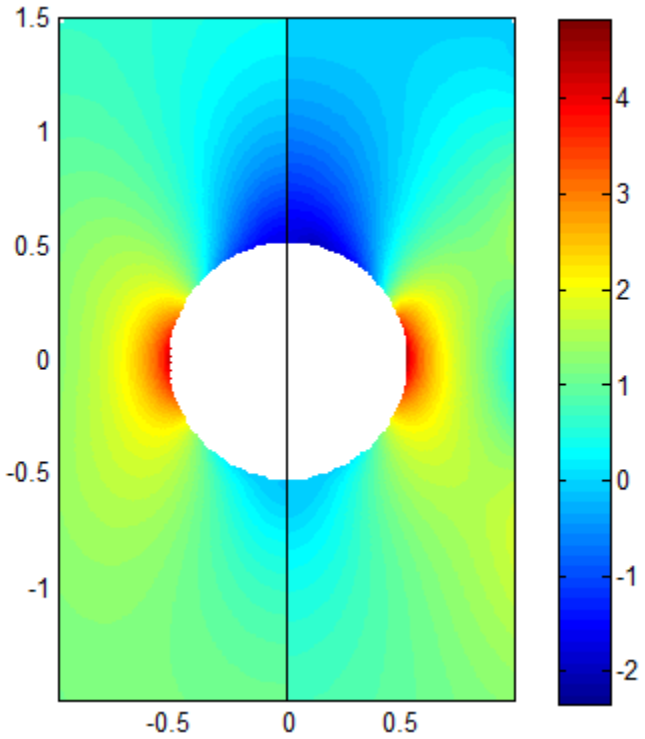

Fig. 6.96: Contour plot of σ_{xx}/σ_0 (loading direction) from TSA (left) for $m_1+h_1+t_1 = 5{,}479$ input values and $k = 9$ ($m_1 = 3{,}413$ TSA values, $h_1 = 2*831$, $t_1 = 2*101+2*301$) and ABAQUS (right)

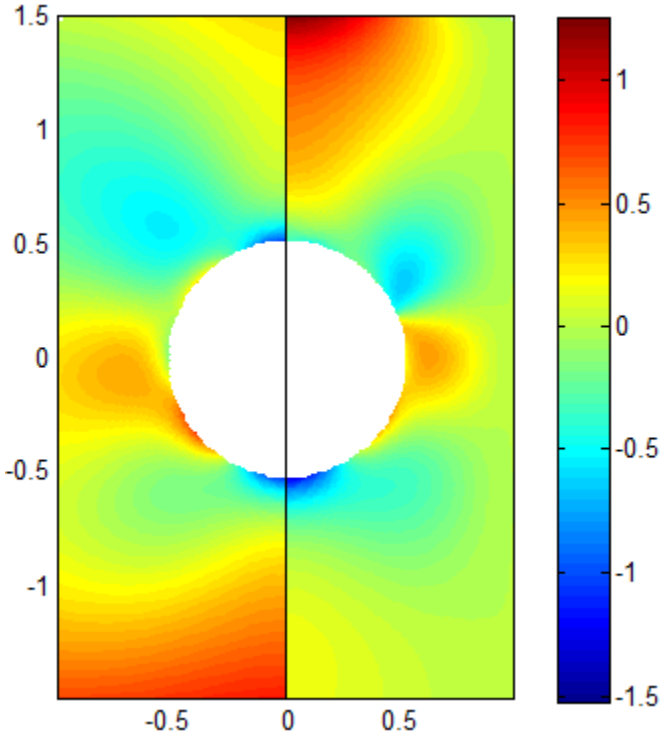

Fig. 6.97: Contour plot of σ_{yy}/σ_0 (lateral direction) from TSA (left) for $m_1+h_1+t_1 = 5{,}479$ input values and $k = 9$ ($m_1 = 3{,}413$ TSA values, $h_1 = 2*831$, $t_1 = 2*101+2*301$) and ABAQUS (right)

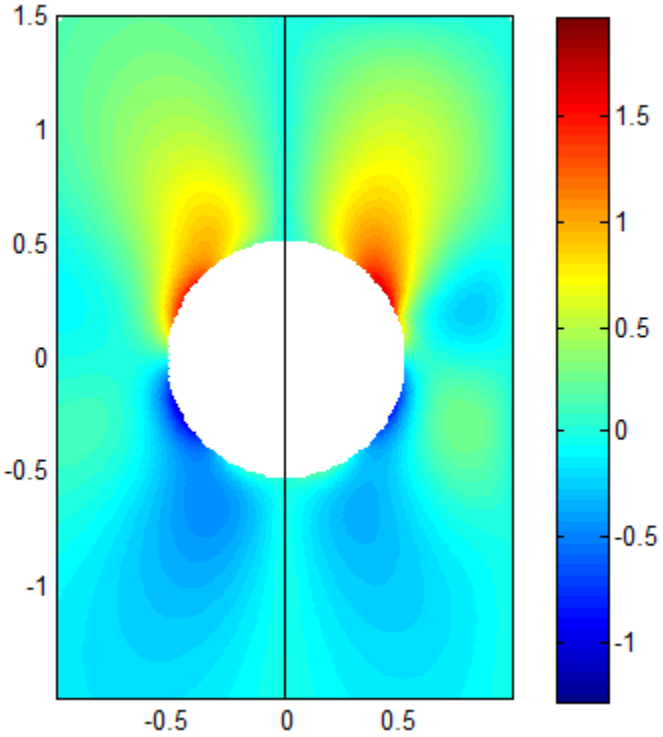

Fig. 6.98: Contour plot of σ_{xy}/σ_0 (shear stress) from TSA (left) for $m_1+h_1+t_1 = 5{,}479$ input values and $k = 9$ ($m_1 = 3{,}413$ TSA values, $h_1 = 2*831$, $t_1 = 2*101+2*301$) and ABAQUS (right)

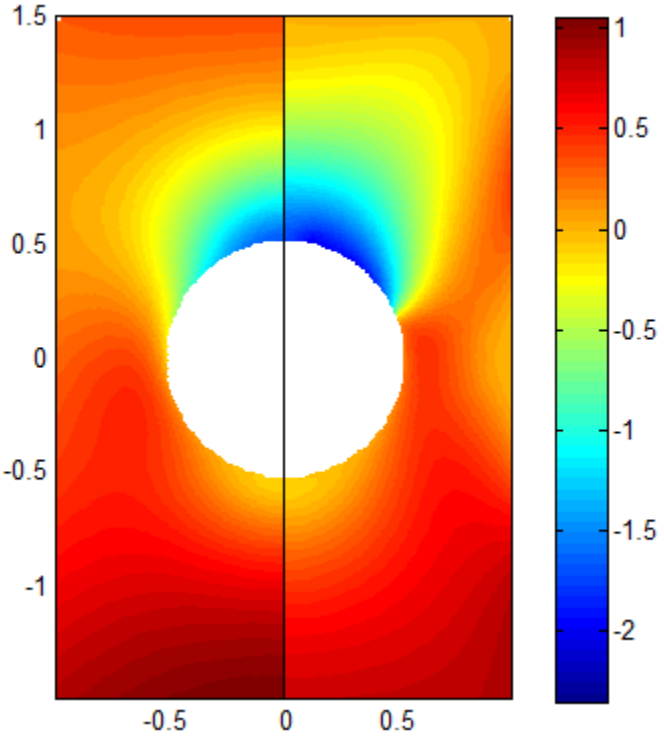

Fig. 6.99: Contour plot of σ_{rr}/σ_0 (radial stress) from TSA (left) for $m_1+h_1+t_1 = 5{,}479$ input values and $k = 9$ ($m_1 = 3{,}413$ TSA values, $h_1 = 2*831$, $t_1 = 2*101+2*301$) and ABAQUS (right)

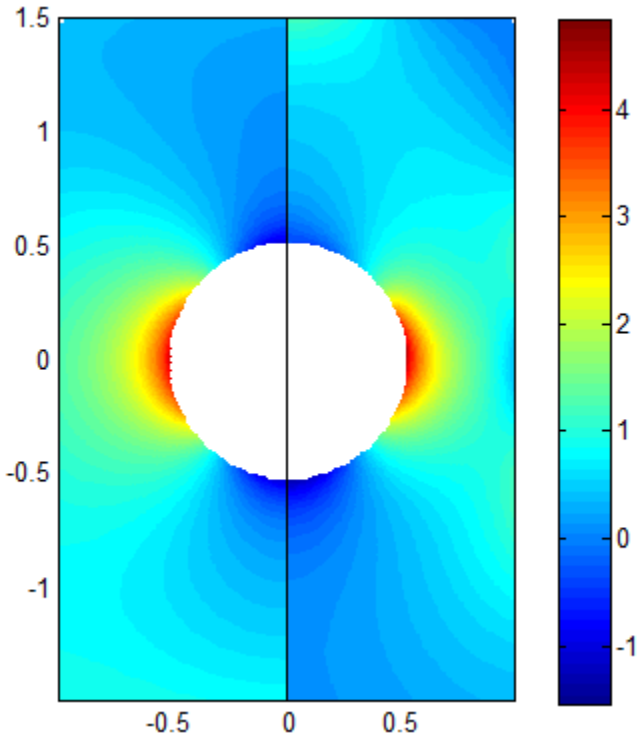

Fig. 6.100: Contour plot of $\sigma_{\theta\theta}/\sigma_0$ (tangential stress) from TSA (left) for $m_1+h_1+t_1 = 5{,}479$ input values and $k = 9$ ($m_1 = 3{,}413$ TSA values, $h_1 = 2*831$, $t_1 = 2*101+2*301$) and ABAQUS (right)

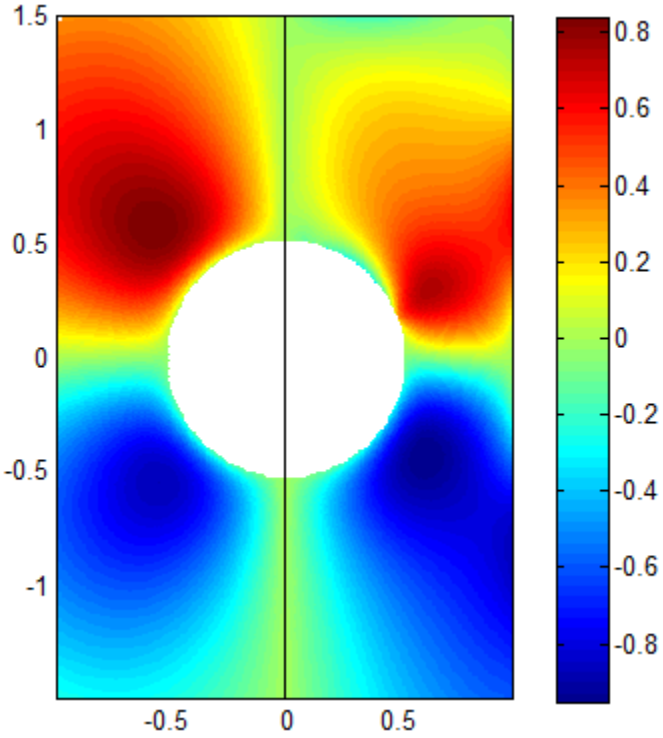

Fig. 6.101: Contour plot of $\sigma_{r\theta}/\sigma_0$ (shear stress) from TSA (left) for $m_1+h_1+t_1 = 5{,}479$ input values and $k = 9$ ($m_1 = 3{,}413$ TSA values, $h_1 = 2*831$, $t_1 = 2*101+2*301$) and ABAQUS (right)

Plate with non-circular pin:

Using the $k = 9$ now known Airy coefficients evaluated from $m_2+h_2+t_2 = 6{,}592$ input values ($m_2 = 3458$ *TSA values,* $h_2 = 2*871$, $t_2 = 2*101+2*301$) for the plate with non-circular pin, the full-field individual Cartesian and polar components of stress can be evaluated. *Figures 6.102 through 6.104* are the contour plots of normalized Cartesian components of stress for the plate with non-circular pin. Similarly *figures 6.105 through 6.107* are the contour plots of normalized polar components of stress for the plate with non-circular pin. There is good agreement between the TSA and ABAQUS results. The slightly high radial stress (*figure 6.105*) may be due to the stress discontinuities (*figure 6.90*) from ABAQUS at the interface of pin and plate hole.

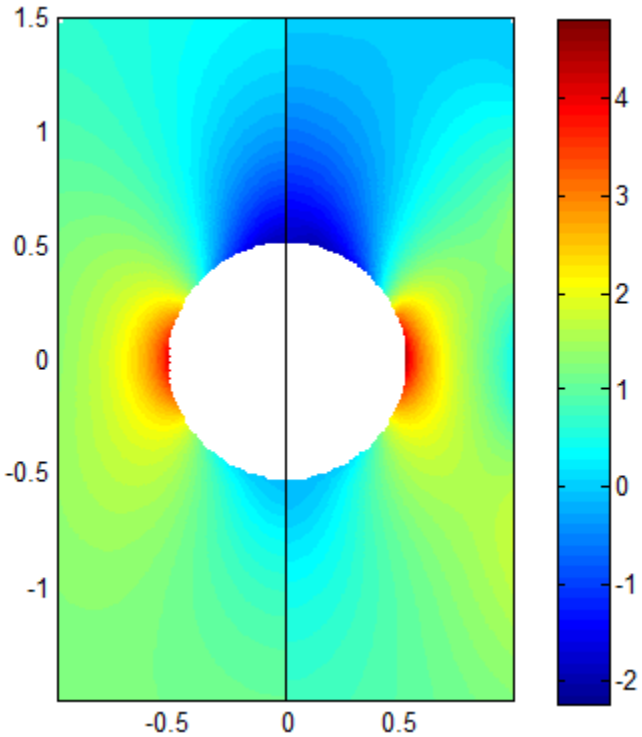

Fig. 6.102: Contour plot of σ_{xx}/σ_0 (loading direction) from TSA (left) for $m_2+h_2+t_2 = 6{,}592$ input values and $k = 9$ ($m_2 = 3458$ TSA values, $h_2 = 2*871$, $t_2 = 2*101+2*301$) and ABAQUS (right)

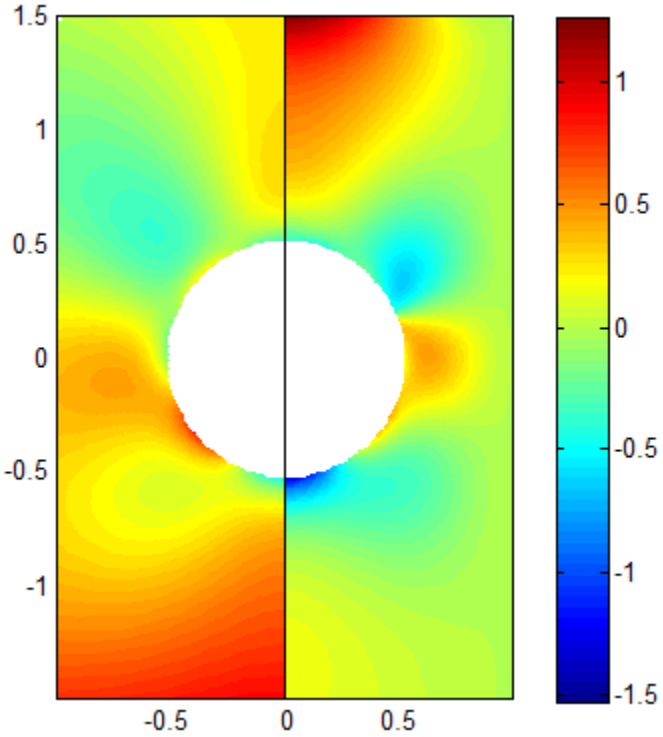

Fig. 6.103: Contour plot of σ_{yy}/σ_0 (lateral direction) from TSA (left) for $m_2+h_2+t_2 = 6{,}592$ input values and $k = 9$ ($m_2 = 3458$ TSA values, $h_2 = 2*871$, $t_2 = 2*101+2*301$) and ABAQUS (right)

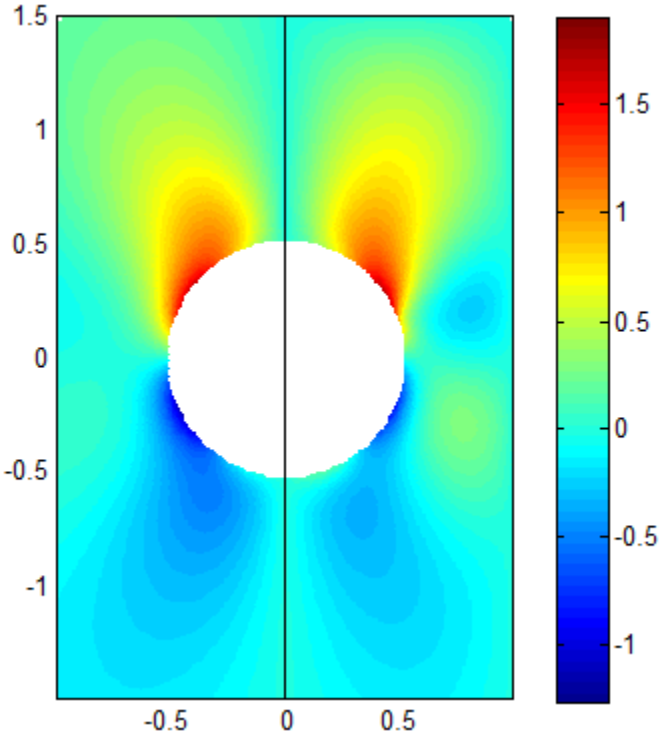

Fig. 6.104: Contour plot of σ_{xy}/σ_0 (shear stress) from TSA (left) for $m_2+h_2+t_2 = 6{,}592$ input values and $k = 9$ ($m_2 = 3458$ TSA values, $h_2 = 2*871$, $t_2 = 2*101+2*301$) and ABAQUS (right)

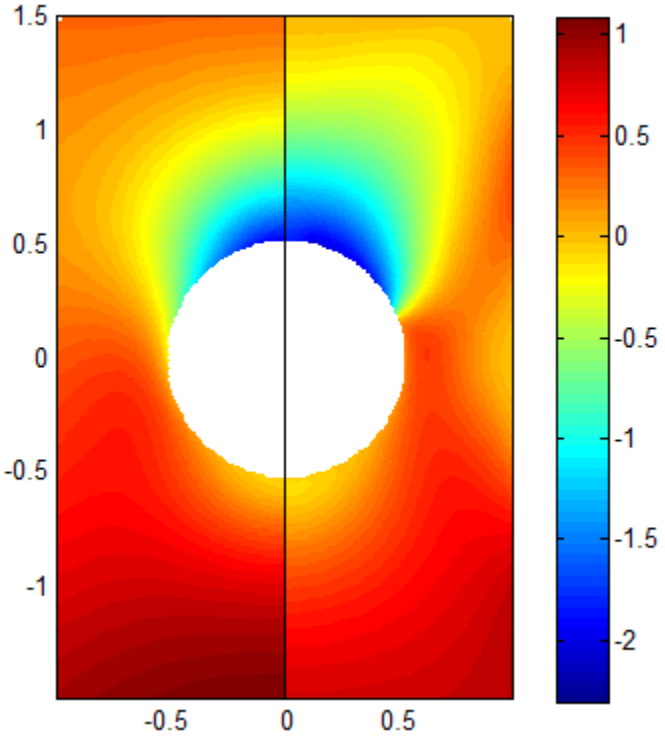

Fig. 6.105: Contour plot of σ_{rr}/σ_0 (radial stress) from TSA (left) for $m_2+h_2+t_2 = 6{,}592$ input values and $k = 9$ ($m_2 = 3458$ TSA values, $h_2 = 2*871$, $t_2 = 2*101+2*301$) and ABAQUS (right)

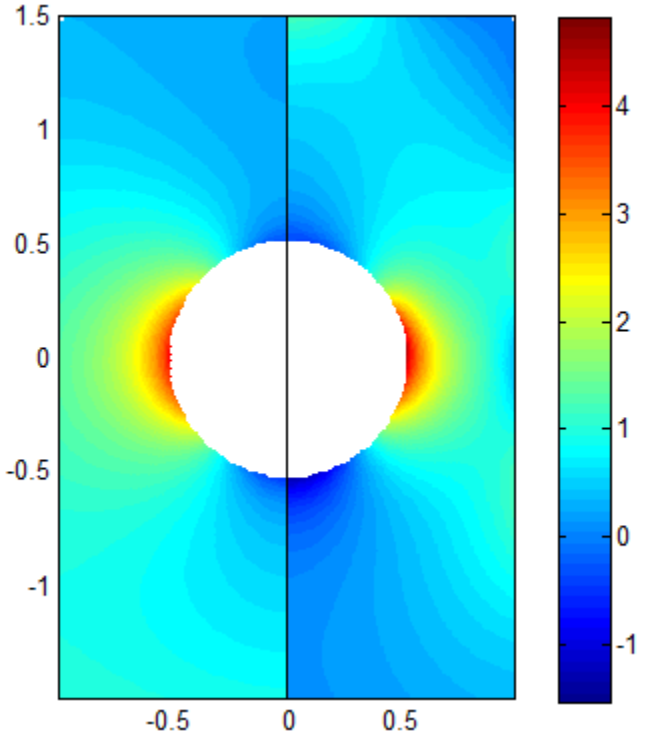

Fig. 6.106: Contour plot of $\sigma_{\theta\theta}/\sigma_0$ (tangential stress) from TSA (left) for $m_2+h_2+t_2 = 6{,}592$ input values and $k = 9$ ($m_2 = 3458$ TSA values, $h_2 = 2*871$, $t_2 = 2*101+2*301$) and ABAQUS (right)

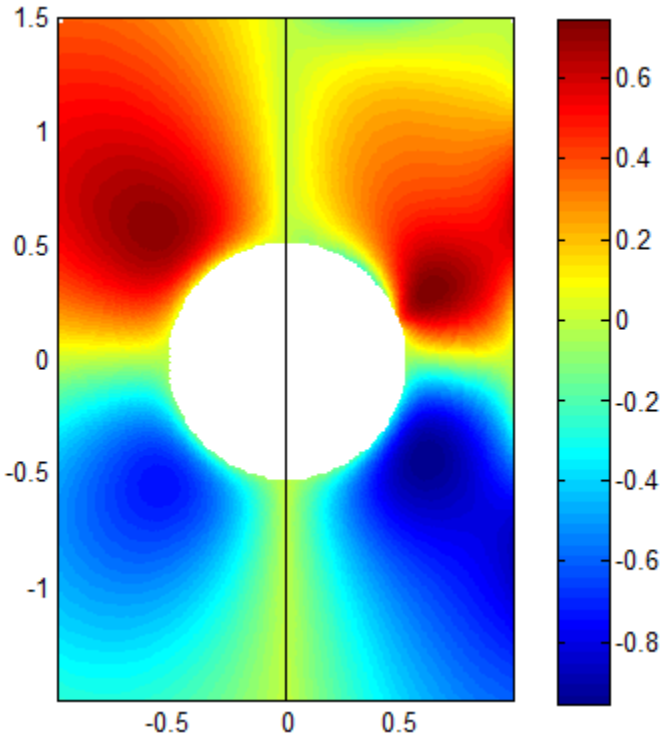

Fig. 6.107: Contour plot of $\sigma_{r\theta}/\sigma_0$ (shear stress) from TSA (left) for $m_2+h_2+t_2 = 6{,}592$ input values and $k = 9$ ($m_2 = 3458$ TSA values, $h_2 = 2*871$, $t_2 = 2*101+2*301$) and ABAQUS (right)

6.9 Load Equilibrium

The reliability of the TSA results is evaluated by integrating the vertical (longitudinal) stress σ_{xx} over the contact region of the hole (*figures 6.2 and 6.6*) and across horizontal sections of the loaded connectors (included sections where the pin does or does not contact the hole) to see if equilibrium is satisfied, i.e., to see how well these computations agree with the applied load of 5.33 kN (1200 lbs). Load equilibrium is determined by summing/integrating the TSA-determined σ_{xx} across twice (due to symmetry) the area associated with the horizontal lines i.e., $2\int \sigma_{xx} t\, dy$, and on the contact boundary of the hole i.e., $2\int \sigma_{xx} t\, R\, d\theta$ (where t is the plate thickness and R is the radius of the hole). For the circular pin the contact region between the plate and pin is from $\theta = 83^{o}$ to 180^{o} and the corresponding value of load based on summing the TSA-determined vertical stress on the contact edge of the hole is 1106 lbs (4.91 kN) i.e., 8% error (based on the applied load of 5.33 kN). *Figures 6.108 and 6.109* are the load equilibrium and load ratio plots for the plate loaded by the circular pin. The fact that these load equilibrium calculations are quite well satisfied provides confidence in the TSA results. Load equilibrium at different horizontal levels (different values of x) based on the TSA-determined vertical stress also agree well with the physically applied load (the error is less than 10%, of the applied load table 6.1). The angles θ associated with plate of *figures 6.108 and 6.109* are the same as those in table 6.1. The x-levels in *figures 6.108 through 6.111* are in inches (table 6.1).

Table 6.1: Total load from TSA-based vertical stress scanned at different horizontal levels of x for the plate with circular pin.

R	θ	ϕ (180° - θ)	ψ (θ + ψ = 90°)	Sin(ψ)	x = R*Sin(ψ)	Load Equilibrium (lbs)	Load Equilibrium (kN)	% error
0.5"	80°	100°	10°	0.1736	0.0868"	1319	5.86	+ 9.9
0.5"	83°	97°	7°	0.1219	0.0609"	1319	5.86	+ 9.9
0.5"	90°	90°	0°	0	0	1316	5.85	+ 9.7
0.5"	97°	83°	- 7°	- 0.1219	- 0.0609"	1312	5.83	+ 9.3
0.5"	100°	80°	- 10°	- 0.1736	- 0.0868"	1308	5.82	+ 9

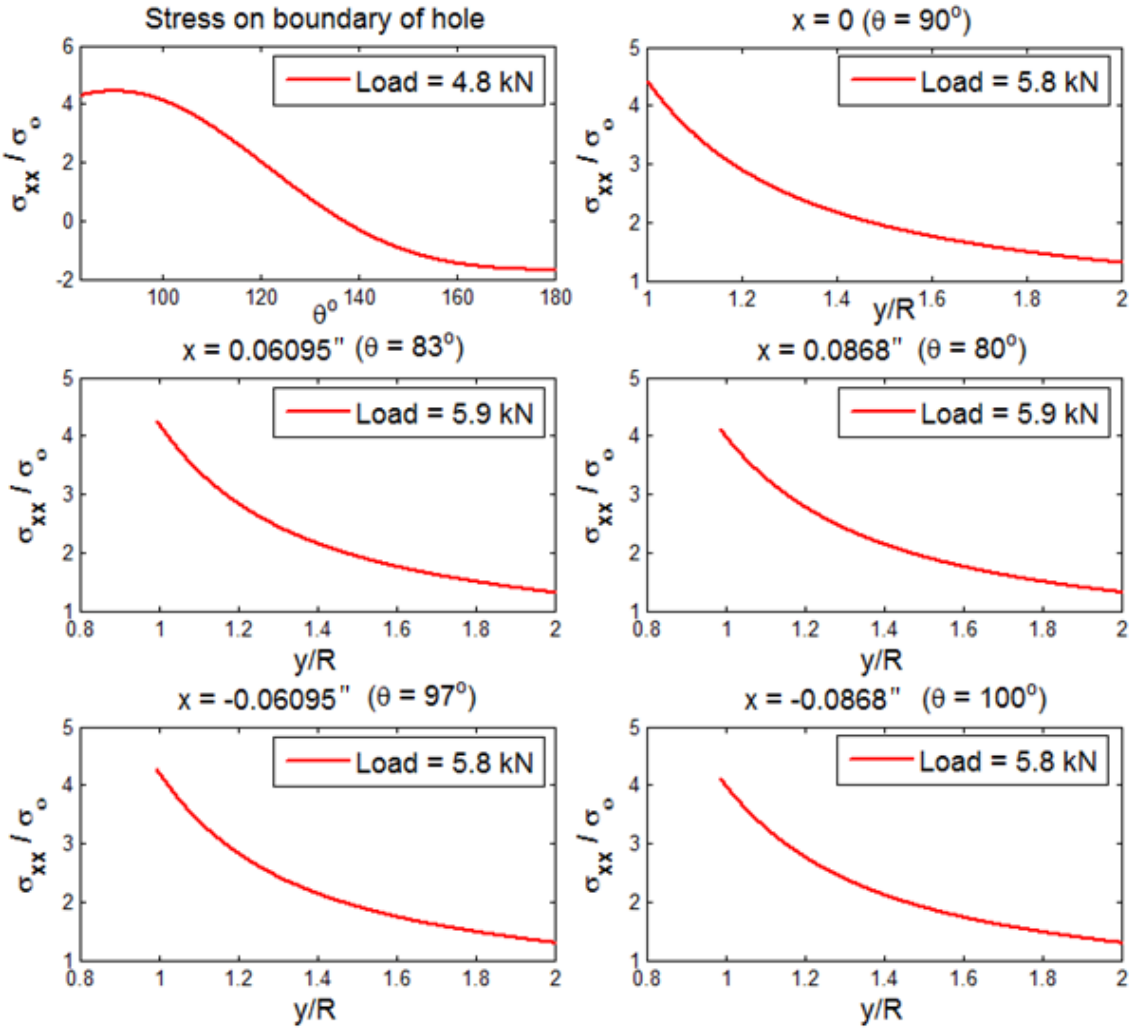

Fig. 6.108: Load equilibrium from scanning TSA-based vertical stress along the boundary of the hole and at different horizontal levels of x of the plate with circular pin

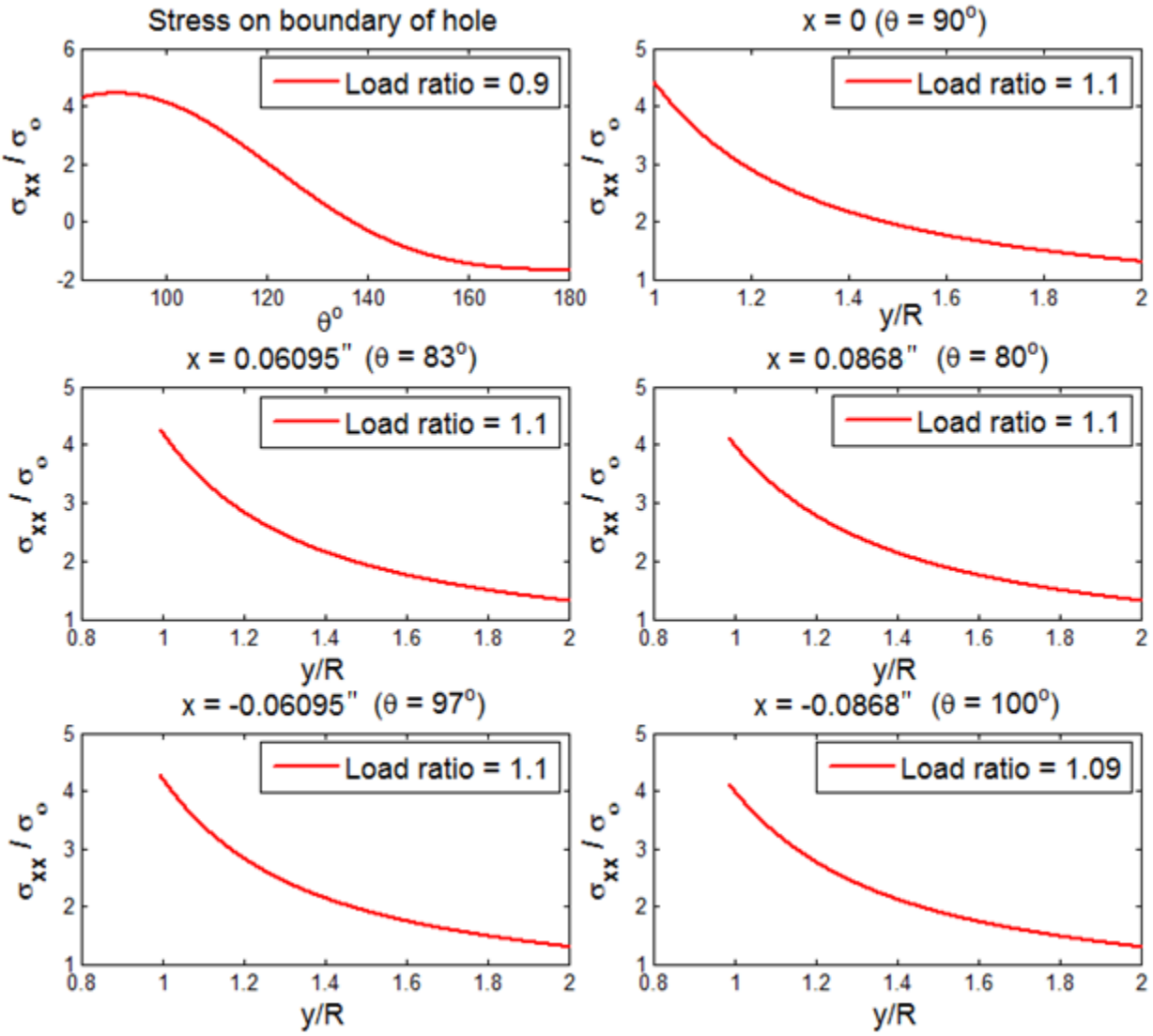

Fig. 6.109: Load ratio from scanning TSA-based vertical stress along the boundary of the hole to that applied physically at different horizontal levels of x of the plate with circular pin

For the plate loaded by the non-circular pin, the contact-free region between the plate and pin was found to be from $\theta = 87^o$ to 180^o. *Figures 6.110 and 6.111* are the load equilibrium and load ratio plots for the plate for the non-circular pin loading. Load equilibrium check at different horizontal levels of x are again satisfactory (the error is less than 10%, of the applied load table 6.2) and in the contact region of plate and the pin the error is less than 14%, *figures 6.110 and 6.111*. The angles θ of *figures 6.110 and 6.111* are the same as those in table 6.2.

Table 6.2: Total load from TSA-based vertical stress scanned at different horizontal levels of x for the plate with non-circular pin.

R	θ	ϕ (180° - θ)	ψ (θ + ψ = 90°)	Sin(ψ)	x = R*Sin(ψ)	Load Equilibrium (lbs)	Load Equilibrium (kN)	% error
0.5"	80°	100°	10°	0.1736	0.0868"	1312	5.83	+ 9.3
0.5"	83°	97°	7°	0.1219	0.0609"	1312	5.83	+ 9.3
0.5"	90°	90°	0°	0	0	1309	5.82	+ 9.1
0.5"	97°	83°	- 7°	- 0.1219	- 0.0609"	1306	5.81	+ 8.8
0.5"	100°	80°	- 10°	- 0.1736	- 0.0868"	1303	5.79	+ 8.6

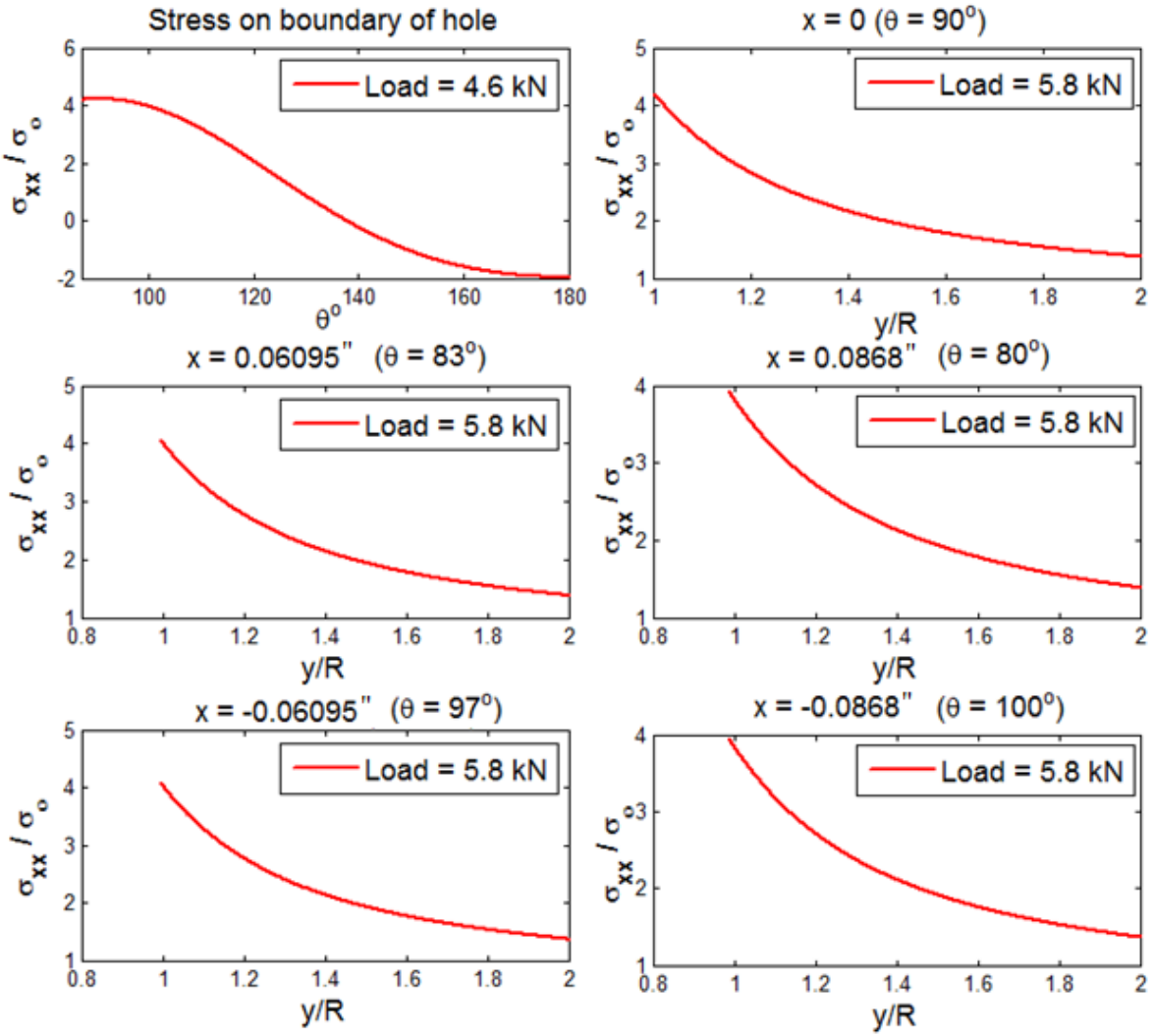

Fig. 6.110: Load equilibrium from scanning TSA-based vertical stress along the boundary of the hole to that applied physically at different horizontal levels of x of the plate with non-circular pin

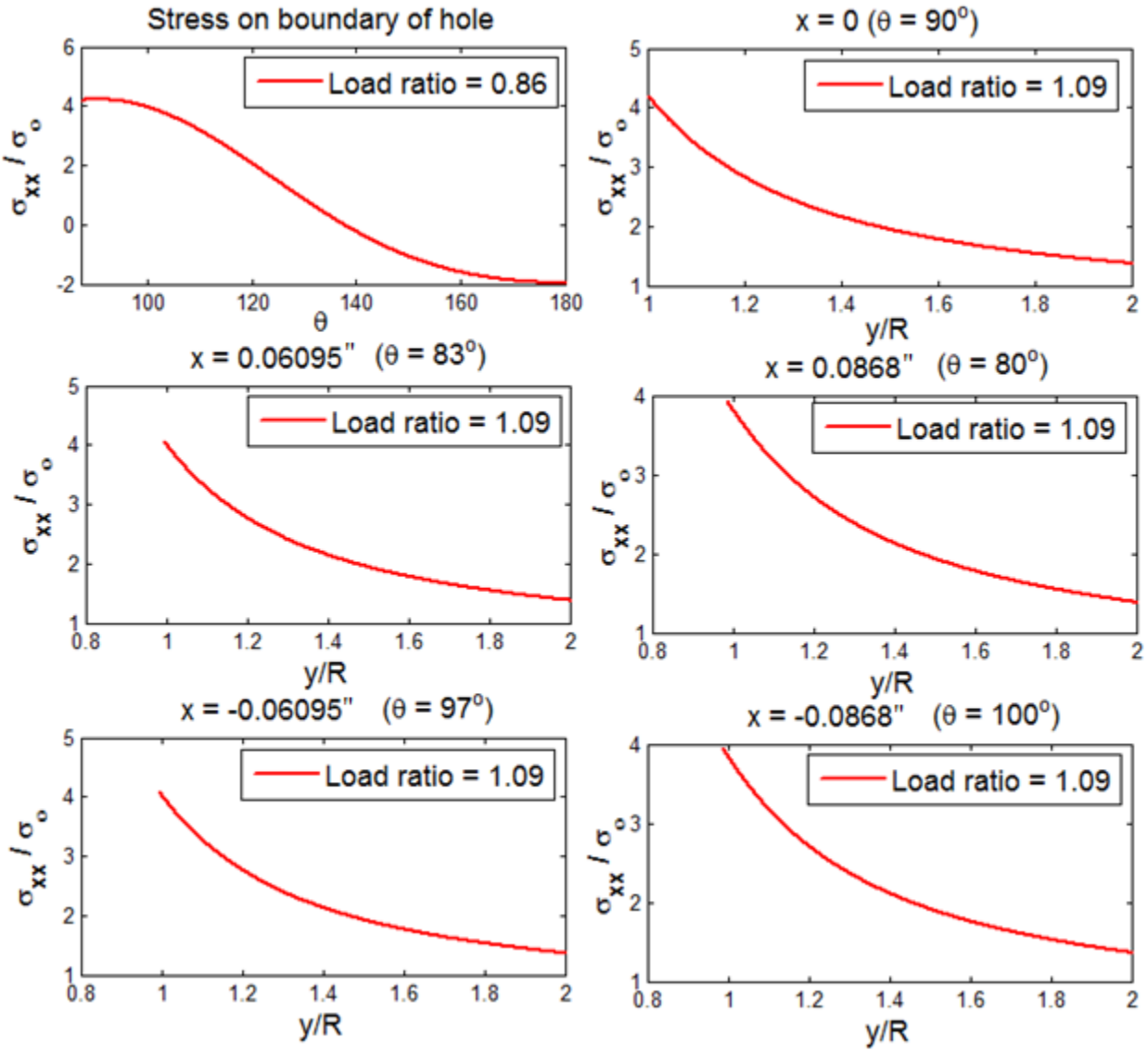

Fig. 6.111: Load ratio from scanning TSA-based vertical stress along the boundary of the hole and at different horizontal levels of x of the plate with non-circular pin

6.10 Summary, Discussion and Conclusions

Bolted connections are prevalently used to fasten separate mechanical or structural members together. Since such joints are frequently the 'Achilles heel' relative to physical integrity, it is important that their stresses be known. Attempting to fully stress analyze a bolted joint is challenging if some of the stresses at the bolt-hole interface are unknown. As with any situation when some of the loads are unknown, inadequate information on the contact stresses at the edge of the hole makes it difficult to stress analyze bolted connections theoretically or numerically. Whereas studies such as that of reference [63] treat 3-D fasteners, including inelastically deformed bolts and clamping forces between the plates, the present analyses do not admit any transverse clamping loads and assume plane-stress elasticity. Acknowledging the aforementioned situations, thermoelastic stress analysis (TSA) is utilized here to stress analyze a 2-D pin-loaded plate. Synergizing the measured temperature information with an Airy stress function is advantageous for such situations in that the technique provides the individual components of stress full-field (including on the loaded edge of the hole) in the actual members. This is accomplished without necessitating (other than perhaps a black paint) a photoelastic model or birefringent coating [45, 51, 60, 77 and 98], any surface pattern or ruling [50] or *discretely* bonded strain gages [59, 98]. Contrasted with moiré, holography, speckle or digital image correlation, the present approach requires neither knowing the elastic modulus nor differentiating the recorded information. *Equations 6.6* through *6.13* involve Poisson's ratio, ν. However, changes in ν tend to be small for different structural materials and Chapter 6 of reference [98] demonstrates the relative insignificant effects variations in ν have on the stresses in bolted connectors. Unlike other experimental approaches, the present method of processing of

the recorded data with an Airy stress function plays a major role in providing reliable individual components of stress on the contact edge of the hole. To simplify the analysis, many fastener studies assume that the pin/bolt is rigid. Since the modulus of the current steel pin is only three times that of the aluminum plate, the pin is not rigid by comparison and the present technique account for the latter's elasticity.

Recognizing that aerospace mechanical connections, in particular, frequently have little bolt-hole clearance, and the importance thereof, this chapter emphasizes snugly fitting fasteners [60, 87 – 89, 91 – 93]. Under such conditions the normal stress at the bolt-hole interface is often assumed to vary as a cosine function of the angle measured from the point of initial contact [64]. Irrespective of whether or not there is any bolt-hole clearance, persons have frequently simplified an analysis by ignoring any contact shear/friction stress between the bolt and hole. There will always be some normal and hoop stresses at the edge of the bolt-loaded hole. Since equilibrium must be satisfied, a solution approach which ignores the contacting shear stress, or assumes an incorrect normal stress, might result in an incorrect stress analysis, e.g., consider a boundary-value stress analysis based on wrong boundary conditions. Incorrectly assuming $\sigma_{r\theta} = 0$ on the edge of the loaded hole could well have adverse consequences on the other calculated stress components on that boundary. This might be serious as failure initiation can be influenced by the polyaxiality of the stresses, e.g., von Mises-type criteria. The situation could be of even greater concern with orthotropic materials where strength is directionally dependent [43, 44, 58 and 63]. However, the shear stress at the present pin-hole interface is determined to be small and so it is of relatively little concern.

References [41, 54, 68, 72, 77 and 95] consider snugly fitting pins, [41] also ignored friction and analyses such as those of [72 and 73] assumed the cosine contact radial stress distribution which was suggested originally by Bickley [65]. As observed here, Hyer and Lui [77] also report that the compressive normal stress at the pin-hole interface in a quasi-isotropic plate occurs over a total angle exceeding 180^{o}. No information is given on their contact shear stress. On-the-other-hand, and unlike here, the TSA study analysis of [54] did not evaluate the individual components of stress on the edge of the pin-loaded hole.

A double shear-plane mechanical joint arrangement was initially tested in which there was no pin-hole clearance. This scheme was subsequently replaced by a single-shear plane arrangement consisting of a steel pin and an aluminum plate. The latter loading configuration was also analyzed using 2-D ABAQUS. A 3-D analysis was conducted initially to assess for any potential bending of the loading fixture. During loading, any out-of-plane bending was minimized physically by monitoring strains from gages mounted on the front and back faces of the plate. However, the recorded longitudinal tensile strain (stress) on the front (TSA) face of the aluminum test plate was slightly less than that on the back face (*figures 6.54 and 6.55*) which may be due to little pin bending as predicted by 3-D FEA. This might suggest that the TSA-determines stresses would be on the low side and hence under-predict the applied load. Tables 6.1 and 6.2, and *figures 6.108 through 6.111*, which show that summing the TSA-determined stresses results in a connector load slightly higher than that applied physically, indicate just the opposite to be the case. These differences are small and for which I do not have an explanation. As discussed subsequently the FEA did not ‘pick-up’ some of the details which actually occur physically at the pin-hole interface.

Two slightly different single-shear, plane-stressed pinned connections were analyzed. Both cases involved virtually no pin-hole clearance. One fastener employed a 0.9991" = 25.377mm diameter round steel pin in a 1.0000" = 25.400 diameter hole for a diametral clearance of 0.0009" = 22.9μ or 0.09% in the aluminum plate, the other connector used a slightly non-round pin with major diameter 0.9993" = 25.382mm in the 1.0000" = 25.400mm diameter hole in the same aluminum plate, for a diametral clearance of 0.0007" = 17.8μ or 0.07%[1]. These are the smallest clearance which permitted the pin to be inserted into the hole without force [114]. Machining-wise, the hole in the aluminum plate was bored while the longitudinal surface of the pins was ground.

The plate was first tested with the non-circular pin and subsequently with the circular pin but the results shown in this chapter are for circular pin first and then the non-circular pin. The larger non-circular pin resulted in a smaller diametral clearance (17.8μ) compared with 22.9μ for the smaller round pin. Neither the scratches on the loading pins or the curved surface of the hole were noticed until both cases had been tested and the TSA results showed that in each situation the total pin/hole contact angle exceeded 180^o. TSA information at the edge of the hole indicates that the residual scratches on the surface of the hole are due to loading by the round pin. When iterating the TSA analysis to find the traction-free boundary condition on the edge of the hole, interestingly it was found that the non-circular pin and plate were in contact from $\theta = 87^o$ to 180^o and circular pin and plate remained in contact from $\theta = 83^o$ to 180^o. This information supports

[1]These bolt diameters and diametral clearances compare with 8" (20.32 cm) and 0.0005" (12.7μ) or 0.006%, respectively, for the pin-loaded aluminum plates described in Reference [98].

the position that although the non-circular pin experiment was done prior to the circular pin experiment the non-circular pin cannot make any marks on the plate for $\theta < 87^o$. Therefore at least the marks found on the curved surface of the hole in the plate from $\theta = 83^o$ to 87^o were from the circular pin experiment.

The present TSA approach consisted of processing the measured temperatures in the aluminum plate with an Airy stress function, plus imposing the traction-fee conditions *discretely* on the non-contact portion part of the edge of the hole. There was originally almost no pin-hole clearance but a portion of the boundary of the hole became unloaded (traction-free) once the connection was loaded. The combination of measured temperatures and traction-free conditions on the edge of the hole enabled the Airy coefficients to be evaluated. Although unnecessary for the purposes of evaluating the Airy coefficients, the traction-free conditions were also imposed *discretely* on the external boundaries of the plate. Knowing the Airy coefficients, the individual components of stress were determination on and in the neighborhood of the edge of the hole. While not particularly effective, the intent behind using the non-round pin was hopefully to provide an increased non-contacting pin-hole boundary over which to impose the traction-free conditions.

In addition to agreeing (approximately, in that the current normal stress on the edge of the hole extended to beyond $\varphi = 90^o$) with the frequently assumed interface contact stresses in mechanical connections which have zero bolt-hole clearance, the present TSA-determined stresses satisfy force equilibrium. TSA results also correlate with those from FEM, although the latter exhibit some variations at the pin-hole interface. While perhaps contrary to intuition, *figures 6.81 and 6.88*, like [43, 47 and 60], show that the hoop stress on the edge of the hole is

compressive at $\theta = 180^o$ ($\varphi = 0^o$, $\psi = -90^o$) and subsequently changes to tension upon progressing around the hole. Not unlike the photoelastic analysis by Hyer and Lui [77], the present TSA results indicate the pin and edge of the hole in the aluminum plate remained in contact beyond an angle of $\varphi = \pm 90^o$. The fact that the total pin-hole contact region exceeded 180^o is further supported by residual markings on the pins and on the transverse curved surface of the hole[2]. It is speculated that the tendency for the originally round hole to become somewhat elliptical so its minor diameter (transverse to the vertical direction of plate loading) decreased under load could contribute to the total pin-hole contact angle exceeding 180^o. The horizontal diameter of the pin probably also increased slightly under connector loading. Although extremely small local dimensional variations in the diameters of the hole and pin might have contributed, the load-induced desire for the hole to contract, and the pin to expand, in the direction normal to the vertically applied connector load was probably a key factor in the total contact angle exceeding 180^o. The FEA was not sufficiently sophisticated to provide any meaningful information relative to the total pin-hole contact angle $> 180^o$. Neither increasing the FEM element density nor changes in the coefficient of friction between the steel and aluminum had any appreciable influence on the results. The fact that the FEA fails to predict the pin-hole contact exceeding 180^o illustrates the challenges that can occur in trying to numerically predict the actual response of mechanical fasteners; hence the need for experimental analyses.

It is uncertain whether possible increases in the local temperatures accompanying the physical actions associated with producing the observed residual marks on the surfaces of the

---

[2]That the contact angle $\varphi \geq \pm 90^o$ results in the normal pin/hole interface stress deviating from the often assumed cosine distribution at $\varphi \geq 75^o$.

hole and pin influenced the TSA results. Temperature increases can be a symptom of a compressive stress, *figures 6.37 and 6.41* indicate a compressive contact normal stress on the edge of the hole greater than the often assumed for $\varphi \geq 75^{o}$ and extending beyond $\varphi = 90^{o}$, and equilibrium calculations based on the TSA-determined stresses tend to exceed the actual applied load. Since the specimen is cycled at a higher frequency (20Hz, usually use 10Hz with Aluminum), the effect of this local temperature changes are probably negligible. Also, doing the analysis, the temperature data were collected only two pixels beyond the boundary of the hole. As such the cyclically induced adiabaticity would reduce any potential contamination of the employed experimental input data.

I am unaware of any previous use of TSA to fully stress analyze a mechanical fastener, including providing the individual stresses at the pin-hole interface. The only other thermoelastic stress analyses involving contact situations appear to be those of [53, 54, 62, 101 and 102].

A novel aspect of this chapter is the demonstrated ability to determine the individual components of stress on and in the vicinity of the edge of a pin-loaded hole in a finite plate from recorded temperature information. In addition to agreeing basically with Bickley's concept that for a tightly-fitting pin, the normal bolt-hole contact stress is reasonably predicted by a cosine distribution and the interface shear/friction stress is small [65], the current results support the observation by Hyer and Lui that a pin can contact the edge of the hole of a loaded fastener beyond a total angle of 180^{o}. The inability of the FEM to predict better the presently observed pin-hole behavior illustrates some of the difficulties when trying to predict numerically the physical response of bolted joints.

The present joint analyses emphasize those having virtually no bolt-hole clearance. In addition to agreeing approximately with the frequently assumed zero shear stress and cosine dependency of the normal stress at the bolt-plate interface under such conditions, stresses are proportional to the applied load. The latter simplifies the analysis since TSA involves cycling the load to satisfy adiabatically. Contemplated future TSA studies of mechanical fasteners include multiple pins/bolts [3], elliptically-shaped bolts/holes [23], a square or rectangular bolt in a square or rectangular hole [103], bolt-hole clearance, and pin-loaded orthotropic/composite plates [15, 43, 44, 46, 62 and 63]. The current formulation is for a plate of finite geometry. The approach could be extended to infinite (physically very large) plates by modifying the stress function so as to remove any terms which would cause the stresses to become infinite as r (radius) goes to infinity.

Appendix A6 contains some corresponding ANSYS predictions as well as imposing the traction-free condition at more locations along the vertical edge of the plate.

6.11 Acknowledgement

This topic forms a chapter in my thesis. However, Wa'el Samad and Aneesh Kaliyanda participated in the testing, Mr. Samad contributed significant CAD contributions and Mr. Kaliyanda did the ABAQUS FEM analyses. They will be co-authors on submitted papers based on this chapter. Mr. Dave Arawinko of the CoE machine shop, offered many practical suggestions and machined the parts.

Chapter 7 : Simplified Stress Functions for Complicated Geometries and Loading

7.1 Introduction

The cases of *figures 7.1 and 7.2* were previously stress analyzed by processing the recorded load-induced temperature data with an Airy stress function [4, 111 and 116]. Those analyses utilized very complicated stress functions which explicitly include the consequence of the applied concentrated load, P. While giving correct stresses throughout essentially the entire plate, the stress functions were very involved. Contrasted with the earlier analyzes, the presently simpler stress function of the present technique does not presuppose the knowledge of the external geometry, loading or boundary conditions. The Airy's stress function is a useful means of condensing the stress formulation of a plane stress problem and by just imposing the local boundary conditions one can obtain a simplified and much easier to formulate stress function. The measured temperature data analyzed here are from reference [4], and are the same as those used with the more complicated stress functions of references [4, 111 and 116]. A similar finite element modal was constructed and the present TSA results are compared with those obtained using finite element methods, the results obtained from reference [4] and strain gages. The stress distribution is similar to that obtained from reference [4].

While applied here to a particular engineering problem and provided one is primarily interested in the stresses only at and in the vicinity of a hole or notch, the current concepts can be

extended to more complicated situations and/or other techniques of experimental mechanics, i.e., there is no need to develop a more complicated stress function which explicitly involves the external shape or boundary conditions. The present approach is expected to provide many worthwhile solutions based only on the local geometry, i.e., as done here by satisfying the traction-free conditions *analytically* on the edge of the hole. The concept also overcomes the traditional difficulties of unreliable measured edge data, and reduces the number of Airy coefficients needed. For the same temperature input data, many fewer Airy coefficients were needed here compared to the number of coefficients used to stress analyze (TSA) the same two cases in references [4, 111 and 116]. As before, the present technique utilizes measured temperature data and an Airy stress function in which the traction-free conditions are imposed *analytically* at the boundary of the hole and the individual stresses evaluated by linear least-squares. This general method is widely applicable for plane stress problems of elasticity.

The main objective of this study is to demonstrate the accuracy and simplicity of the presented solution for stress analysis of edge-loaded plates having a near surface circular cutout. As in references [111] and [116], the cases when the edge load is immediately above the hole [111] and when it is off-set from [116] the hole are considered separately. The results herein demonstrate the effectiveness of the presented method to determine accurately the stresses, stress gradients and stress concentrations for such situations. Numerical methods such as FEA typically require accurately knowing the far-field geometry and distant boundary conditions. The latter are often unreliable or unavailable in industrial situations. While providing reliable results at and in the neighborhood of a geometric discontinuity such as a hole, the current TSA approach

involving the relatively simple stress functions does not necessitate knowing the external loading or geometry.

Thermoelastic stress analysis (TSA) is a contemporary full-field, non-contacting method of experimental stress analysis that relates the local change in temperature to the change in first stress invariant and ($\sigma_{xx} + \sigma_{yy} = \sigma_{rr} + \sigma_{\theta\theta} = \sigma_1 + \sigma_2$). On the other hand, engineering applications often require knowing the individual components of stress. The individual components of stresses are evaluated here by *analytically* imposing the traction-free conditions on the edge of the hole in combination with the measured TSA (isopachic) data for the plane problem of an edge-loaded finite elastic plate having a near surface circular hole. It is convenient to acquire all the necessary measured data from a single experimental method in that no supplementary measured data are required. That the technique also does not involve differentiating the measured temperature data is advantageous. The individual stress components are consequently obtained here reliably at least in the region of interest, *i.e.*, at, and adjacent to, the edge of the hole. The edge load is either immediately over the hole (*figure 7.1*) or offset from the hole (*figure 7.2*). Knowing the effects of cutouts relative to the locations of the loads, stress concentrations of such plates are important for circuit boards and buried structures.

For the cases of *figures 7.1 and 7.2*, the region of interest is in the vicinity of the hole. The analysis of *figure 7.1* enjoys the advantage of symmetry about the vertical x-axis. The offset loading of *figure 7.2* lacks symmetry about both of these axes. This will necessitate many more Airy coefficients than with the central loading of *figure 7.1*. Particularly the offset load of *figure 7.2* complicated formulating a relevant stress function in terms of polar coordinates whose origin is at the center of the hole by the original approach of reference [116]. Having the origin of the

polar coordinates at the center of the hole is virtually necessary in order to satisfy the traction-free conditions at the hole *analytically*. On the other hand, a fairly simple relevant stress function(s) in terms of polar coordinates can be developed by restricting one's interest to the neighborhood of the hole and imposing the traction-free conditions *analytically* at the boundary of the hole. By focusing on the region at and near the hole, this method ignores the explicit contributions of the external geometry or loading. The obtained stresses are consequently not applicable far away from the hole, including very close to the applied concentrated load. However, in return for giving up reliable stress information far from the hole, one can a use much simpler stress function and fewer Airy coefficients. This general approach is thus applicable irrespective of the form or magnitude of the loading and stresses are provided without the use of measured data on, or immediately near, the edge of the hole. The latter is very important because it is the difficult to record reliable temperature information at the edge of a discontinuity. In addition to not explicitly incorporating the distant geometry or external boundary conditions, including the concentrated load, P (per unit thickness), knowledge of the material constitutive properties is not required. As such the method is capable of solving inverse problems.

Dimensions of the perforated plate of *figures 7.1 and 7.2* are 88.9 mm (3.5″) by 88.9 mm (3.5″) and 9.53 mm (3/8″) thick. The hole has a diameter of 19.05 mm (3/4″) and the distance from the center of the hole to the top edge of the plate is D = 19.05 mm (3/4″). The same physical plate was utilized for the two respective cases of *figures 7.1 and 7.2*. Although the radius of the hole is equal to the plate thickness, information of reference [111] substantiated the validity of assuming plane stress.

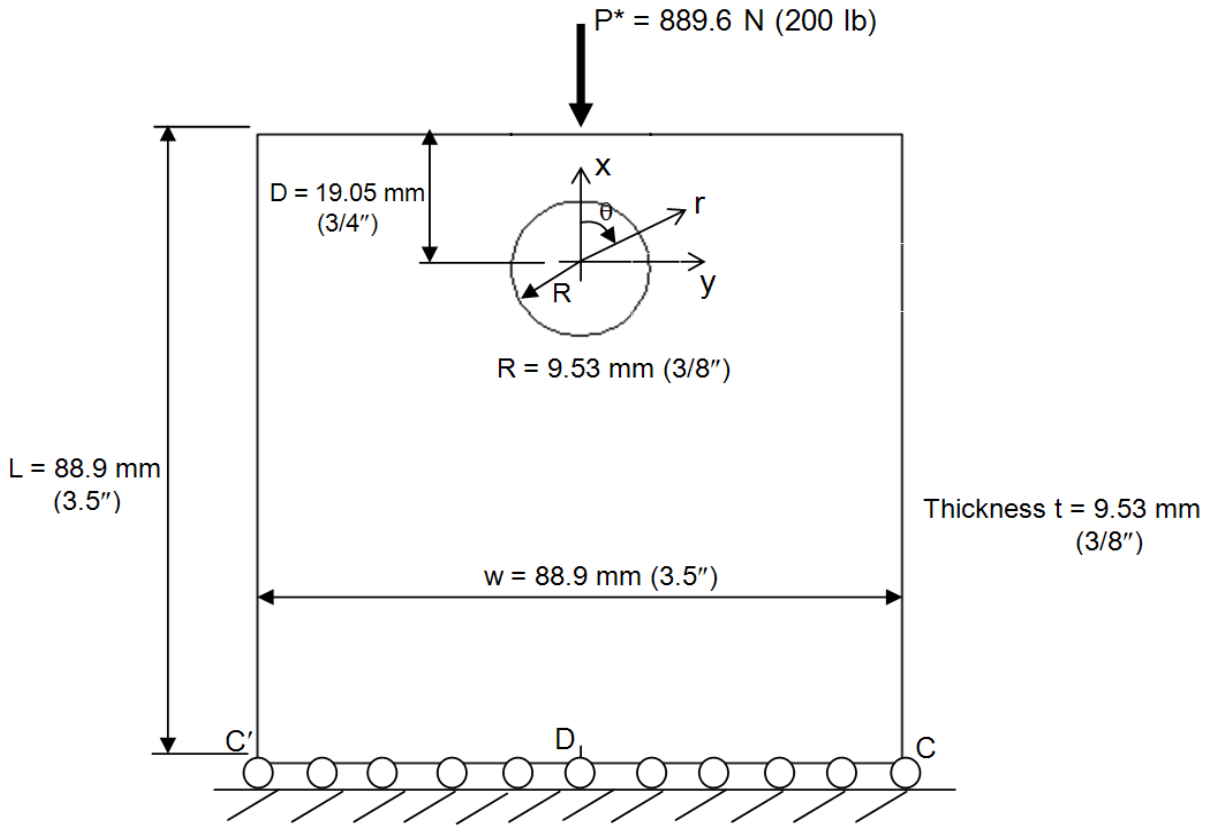

Fig. 7.1: Plate containing a near-edge hole beneath a concentrated load

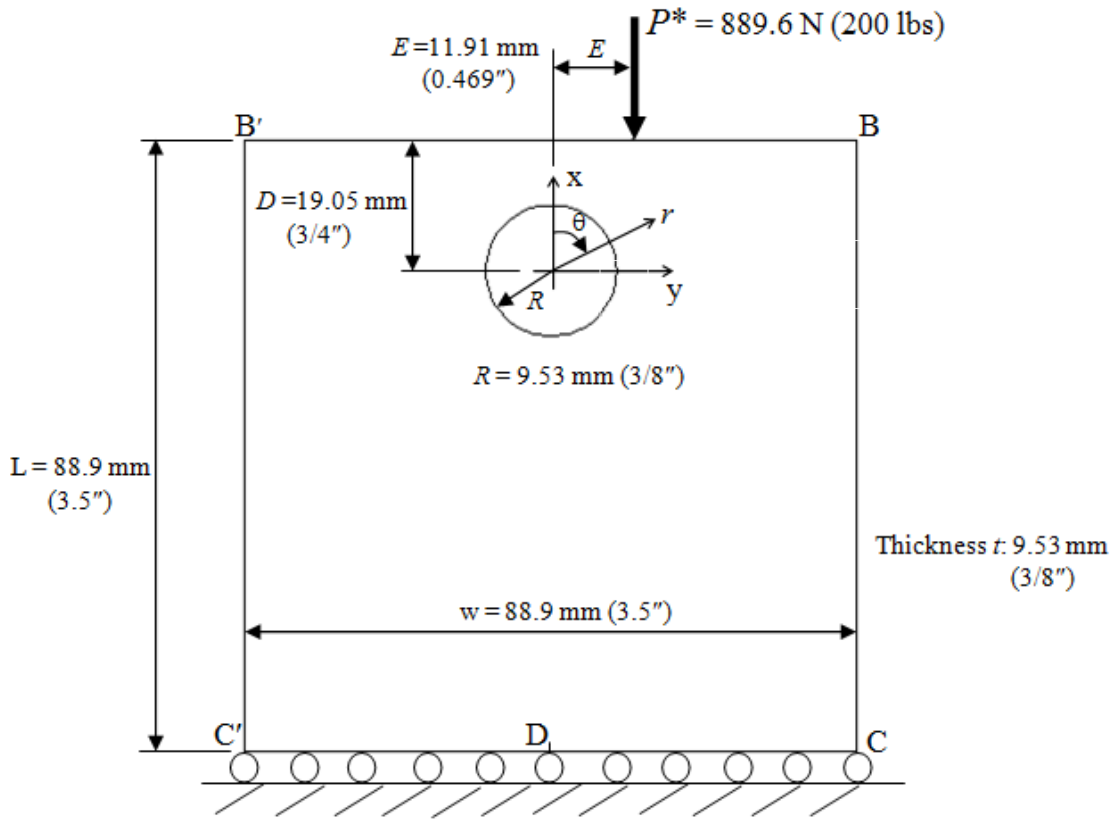

Fig. 7.2: Schematic geometry of a large plate containing a near edge hole subjected to an offset concentrated load

The general approach is applicable irrespective of the form or magnitude of the loading and stresses are provided without the use of measured data on, or immediately near, the boundary of the hole. In *figures 7.1 and 7.2*, the present region of interest is in the vicinity of the hole. Therefore, a relevant stress function(s) in terms of polar coordinates can be developed by imposing the traction-free conditions *analytically* at the boundary of the hole so as to further reduce the number of needed Airy coefficients.

7.2 Stress Functions and Stresses

This section introduces relevant specific Airy stress functions and their derived stress equations for the (i) central and (ii) offset loading conditions for the cases of interest of *figures 7.1 and 7.2,* respectively. For two-dimensional isotopic elasticity, the Airy's stress function, ϕ, of *equation 7.1*, is the solution of the governing differential equation, $\nabla^4\phi = 0$, which consists of

$$\begin{aligned}\phi &= a_0 + b_0 \ln r + c_0 r^2 + d_0 r^2 \ln r + \left(A_0 + B_0 \ln r + C_0 r^2 + D_0 r^2 \ln r\right)\theta \\ &+ \left(a_1 r + b_1 r \ln r + \frac{c_1}{r} + d_1 r^3\right)\sin\theta + \left(a_1' r + b_1' r \ln r + \frac{c_1'}{r} + d_1' r^3\right)\cos\theta \\ &+ \left(A_1 r + B_1 r \ln r\right)\theta \sin\theta + \left(A_1' r + B_1' r \ln r\right)\theta \cos\theta \\ &+ \sum_{n=2,3,4\ldots}^{\infty}\left(a_n r^n + b_n r^{(n+2)} + c_n r^{-n} + d_n r^{-(n-2)}\right)\sin(n\theta) \\ &+ \sum_{n=2,3,4\ldots}^{\infty}\left(a_n' r^n + b_n' r^{(n+2)} + c_n' r^{-n} + d_n' r^{-(n-2)}\right)\cos(n\theta)\end{aligned} \tag{7.1}$$

numerous terms, a_o, b_o, c_o, d_o and so forth. Many of these Airy coefficients can often be eliminated for a particular situation by various conditions and/or arguments, *e.g.*, any symmetry, single-value stresses, strains and displacements, whether or not the origin is within the body, self-equilibrated at individual boundaries and whether the component is finite or infinite in size. For the analyses associated with *figures 7.1 and 7.2*, the origin is at the center of the cut-out so it does not occur within the plate, and the shape of the cut-out is defined by *analytically* imposing the traction-free conditions on the edge of the hole. The situation is symmetrical about the vertical x-axis for the problem of *figure 7.1* but unsymmetrical about both the x- and y-axes in *figure 7.2*.

For the unsymmetrically-loaded offset plate in *figure 7.2*, since the displacements, strains and stresses must be single-valued functions of θ, and there is no resultant force at the origin, coefficients d_0, B_0, C_0, D_0, B_1, B_1' and A_1, A_1', b_1, b_1' of the complete general expression for the stress function, ϕ, are all zero [1, 4 and 6]. Restricting the response at and in the area of the hole, the stress function of *equation 7.1* for the finite plate which is unsymmetrical about both the x- and y-axes is given by ϕ_{unsym} of *equation 7.2*. Since the consequence of the external geometry and loading is not directly accounted for here, the stress function of *equation 7.2* does not contain P. The expressions for ϕ of *equation 7.2* contrasts with that of *equation 7.2-A* as used in reference [116]. The latter explicitly accounts for the external loading and geometry through P, D and E.

$$\begin{aligned}\phi_{unsym} &= a_0 + b_0 \cdot ln\, r + c_0 \cdot r^2 + A_0 \cdot \theta \\ &+ \left(a_1 \cdot r + \frac{c_1}{r} + d_1 \cdot r^3 \right) \cdot sin\,\theta + \left(a_1' \cdot r + \frac{c_1'}{r} + d_1' \cdot r^3 \right) \cdot cos\,\theta \\ &+ \sum_{n=2,3,4\ldots}^{N} \left[a_n \cdot r^n + b_n \cdot r^{(n+2)} + c_n \cdot r^{-n} + d_n \cdot r^{-(n-2)} \right] \cdot sin\left(n \cdot \theta\right) \\ &+ \sum_{n=2,3,4\ldots}^{N} \left[a_n' \cdot r^n + b_n' \cdot r^{(n+2)} + c_n' \cdot r^{-n} + d_n' \cdot r^{-(n-2)} \right] \cdot cos\left(n \cdot \theta\right)\end{aligned} \tag{7.2}$$

The derivation of the stress function ϕ_{offset} of *equation 7.2-A,* which was developed in reference [4 and 116] for the offset loaded plate of *figure 7.2*, involved extensive amount of algebra and many Airy coefficients. Upon *analytically* imposing the traction-free boundary condition on the edge of the hole, the individual components of stress from *equation 7.2-A* involve the coefficients $F_1, \ldots, F_9$ (corresponding to *ORPTERM, OSPTERM, etc.,* in reference [4]) as will be seen in the ultimate expression of the isopachic stress for the offset loaded

specimen, *equation 7.22-A*. These coefficients of *equation 7.22-A* are functions of geometric quantities *R*, *D and E of figure 7.2* [4 and 111]. The stress function of *equation 7.2-A* includes the applied load, *P* and will ultimately involve more coefficients than *equation 7.2*. That the stresses of the present analysis (based on *equation 7.2-A*) do not directly involve the applied load *P,* plate dimensions or the location of the hole in the plate is advantageous. Evaluating individual components of stress using the technique of references [4 and 116] involves complicated programming, increased computation time, and the stress function of *equation 7.2-A* differs explicitly as the loading condition changes. However, it is important to be reminded that simplifications associated with ϕ_{unsym} of *equation 7.2* (compared to that of *equation 7.2-A*) for the situation of *figure 7.2* imply the deduced stresses are only reliable at and in a reasonable neighborhood extending away from the hole.

$$\begin{aligned}\phi_{offset} = & -\frac{P}{\pi}\cdot tan^{-1}\left(\frac{r\cdot sin\theta - E}{D - r\cdot cos\theta}\right)\cdot\left(r\cdot sin\theta - E\right) \\ & + a_0 + b_0\cdot ln\, r + c_0\cdot r^2 + A_0\cdot\theta \\ & + \left(a_1\cdot r + \frac{c_1}{r} + d_1\cdot r^3\right)\cdot sin\theta + \left(a_1'\cdot r + \frac{c_1'}{r} + d_1'\cdot r^3\right)\cdot cos\,\theta \\ & + \sum_{n=2,3,4\ldots}^{N}\left[a_n\cdot r^n + b_n\cdot r^{(n+2)} + c_n\cdot r^{-n} + d_n\cdot r^{-(n-2)}\right]\cdot sin\left(n\cdot\theta\right) \\ & + \sum_{n=2,3,4\ldots}^{N}\left[a_n'\cdot r^n + b_n'\cdot r^{(n+2)} + c_n'\cdot r^{-n} + d_n'\cdot r^{-(n-2)}\right]\cdot cos\left(n\cdot\theta\right)\end{aligned} \tag{7.2-A}$$

For the symmetrically loaded plate of *figure 7.1*, since the displacements, strains and stresses must again be single-valued functions of θ and there is no resultant force at the origin, coefficients d_0, B_0, C_0, D_0, B_1, B_1' and A_1, A_1', b_1, b_1' are again all zero [4 and 111]. The symmetry about the vertical x-axis of *figure 7.1* means that stresses occurring at any angle, θ =

+β would be the same as those at θ = -β i.e., $\phi_{sym}(r, \theta) = \phi_{sym}(r, -\theta)$. Thus ϕ_{sym} for the plate of *figure 7.1* must be an even function of θ. As a result, A_0, a_n, b_n, c_n, d_n (for n ≥ 1) can all be equated here to zero such that only, and cosine terms of *equation 7.2* are retained in the present stress function (*i.e.*, omit sine and theta terms) for the plate of *figure 7.1*.

The stress function of *equation 7.2* associated with *figure 7.1* can therefore be simplified here as ϕ_{sym} of *equation 7.3*:

$$\phi_{sym} = a_0 + b_0 \ln r + c_0 r^2 + \left(a_1' r + \frac{c_1'}{r} + d_1' r^3 \right) \cos\theta + \sum_{n=2,3\ldots}^{N} \left[\; a_n' r^n + b_n' r^{(n+2)} + c_n' r^{-n} + d_n' r^{-(n-2)} \; \right] \cos(n\theta) \tag{7.3}$$

where r is the radius from the center of the hole and θ is the angle measured clockwise from vertical x-axis, *figure 7.1*. N is the terminating index value of the summation series and it could (theoretically) approach infinity (N is a positive integer greater than 1). Taking the x-axis to be positive vertical is compatible with the common practice of measuring angle θ in the stress function from the x-axis which is the direction of loading. Other than that the coordinate origin not being within the structural component, the shape of the cut-out is not yet defined. The counterpart of *equation 7.2-A* for the plate of *figure 7.1* is

$$\phi_{cen} = \frac{-P}{\pi} \cdot tan^{-1}\left(\frac{r \cdot sin\theta}{D - r \cdot cos\theta} \right) \cdot r \cdot sin\theta + a_0 + b_0 \cdot ln\, r + c_0 \cdot r^2 + \left(a_1 \cdot r + \frac{c_1}{r} + d_1 \cdot r^3 \right) \cdot cos\theta + \sum_{n=2,3,4\ldots}^{N} \left(a_n \cdot r^n + b_n \cdot r^{n+2} + c_n \cdot r^{-n} + d_n \cdot r^{2-n} \right) \cdot cos\,(n \cdot \theta) \tag{7.3-A}$$

Equation 7.3-A is similar to *equation 7.2-A* except now E = 0 (loading is vertically above the coordinate origin) and $A_o = a_1 = c_1 = d_1 = a_n = b_n = c_n = d_n = 0$ (due to symmetry about the x-axis).

The derivation of stress function, ϕ_{cen} of *equation 7.3-A* for the centrally loaded specimen of *figure 7.1* also involved appreciable algebra and many coefficients other than polar coordinates *r* and θ [4 and 111]. Upon *analytically* imposing the traction-free boundary condition on the edge of the round hole of radius R, the individual components of stresses (based on *equation 7.3-A*) involve the coefficients, $C_1, \ldots, C_9$ [111] (corresponding to *RPTERM, SPTERM, etc.,* in reference [4]) as seen in the expression of isopachic stress for the centrally loaded specimen, *equation 7.14-A*. The coefficients C_i of *equation 7.14-A* are based on the geometric dimensions *R* and *D of figure 7.1* [4 and 112]. Moreover, the expressions for the individual components of stress also involve Airy coefficients c_0, d_1, c_2, d_2, b_3, c_3, d_3, and c_n and d_n for $n > 3$ (which depend indirectly on *P*), which are determined experimentally. On the other hand, the present (based on *equation 7.3*) analysis advantageously determines the stresses without explicitly involving the applied load *P,* plate dimensions or the location of the hole in the plate. Of course changes in P or extreme shape could be accounted in the experimentally determined values of the Airy coefficients. It is also worth noting that the number of unknown coefficients ultimately involved in the stress function of *equations 7.2-A and 7.3-A* are more when compared to the present approach of the simplified stress function (*equations 7.2 and 7.3*).

The current plate is finite in size. If the geometry were infinite (mathematically), at least a_n and b_n, and a_n' and b_n' of *equations 7.1 and 7.2* must be zero to ensure stresses do not grow to infinity as $r \rightarrow \infty$.

Individual components of stress can be obtained by differentiating the stress function(s) of *equations 7.2 and 7.3* according to *equations 7.4 through 7.6*:

$$\sigma_{rr} = \frac{1}{r}\cdot\frac{\partial\phi}{\partial r} + \frac{1}{r^2}\frac{\partial^2\phi}{\partial\theta^2} \tag{7.4}$$

$$\sigma_{\theta\theta} = \frac{\partial^2\phi}{\partial r^2} \tag{7.5}$$

$$\sigma_{r\theta} = -\frac{\partial}{\partial r}\cdot\left(\frac{1}{r}\cdot\frac{\partial\phi}{\partial\theta}\right) \tag{7.6}$$

Symmetry about vertical x-axis related to *figure 7.1*

Using *equations 7.4 through 7.6,* the following expressions for individual polar components of stress are obtained by differentiating the reduced stress function ϕ_{sym} of *equation 7.3,* (without regard to most of the specific boundary conditions of *figure 7.1*), [8] *i.e.*,

$$\begin{aligned}(\sigma_{rr})_{sym} &= \frac{b_0}{r^2} + 2c_0 - \frac{2c_1'}{r^3}\cos\theta + 2rd_1'\cos\theta \\ &- \sum_{n=2,3\ldots}^{N}\Big[\, a_n' n(n-1)r^{(n-2)} + b_n'(n-2)(n+1)r^n \\ &\qquad + c_n' n(n+1)r^{-(n+2)} + d_n'(n+2)(n-1)r^{-n} \,\Big]\cos(n\theta)\end{aligned} \tag{7.7}$$

$$\begin{aligned}(\sigma_{\theta\theta})_{sym} &= -\frac{b_0}{r^2} + 2c_0 + \frac{2c_1'}{r^3}\cos\theta + 6rd_1'\cos\theta \\ &+ \sum_{n=2,3\ldots}^{N}\Big[\, a_n' n(n-1)r^{(n-2)} + b_n'(n+2)(n+1)r^n \\ &\qquad + c_n' n(n+1)r^{-(n+2)} + d_n'(n-2)(n-1)r^{-n} \,\Big]\cos(n\theta)\end{aligned} \tag{7.8}$$

$$(\sigma_{r\theta})_{sym} = -\frac{2c_1'}{r^3}\sin\theta + 2rd_1'\sin\theta + \sum_{n=2,3\ldots}^{N}\left[\, a_n' n(n-1)r^{(n-2)} + b_n' n(n+1)r^n - c_n' n(n+1)r^{-(n+2)} - d_n' n(n-1)r^{-n} \,\right]\sin(n\theta) \tag{7.9}$$

As a result of differentiation, the coefficients a_0 and a_1' which appear in the Airy stress function ϕ_{sym}, *equation 7.2*, are absent in the expressions for the individual stress components, *equations 7.7 through 7.9*. For isotropy under cyclic loading condition, the Thermoelastic Stress Analysis (TSA) recorded temperature variation at a point in a loaded member is linearly proportional to the change in the isopachic stress or the first stress invariant. The isopachic stress is obtained by adding the radial and tangential components of stress *equations 7.7 and 7.8*, i.e:

$$S_{sym} = (\sigma_{rr})_{sys} + (\sigma_{\theta\theta})_{sys}$$

$$S_{sym} = 4c_0 + 8rd_1'\cos\theta + \sum_{n=2,3\ldots}^{N}\left[\, b_n' 4(n+1)r^n - d_n' 4(n-1)r^{-n} \,\right]\cos(n\theta) \tag{7.10}$$

Comparing *equations 7.7 through 7.10* shows that the Airy coefficients present in the expression for isopachic stress of *equation 7.10* are also present in the expressions for individual stresses. However, the expressions for the individual components of stress, *equations 7.7 through 7.9,* also contain the Airy coefficients b_0, a_n', c_n' *(for* $n \geq 2$*)* and c_1' which are absent in the equation for isopachic stress, *equation 7.10*. Therefore, using only Thermoelastic Stress Analysis data and the expression for the isopachic stress will not suffice to evaluate the individual components of stress. However, imposing the traction-free boundary conditions *analytically* on the boundary of the hole will result in all of the coefficients that are present in the equations for

individual stresses to also appear in the expression for the isopachic stress. One can then evaluate all the three individual components of stress from only measured temperature information. Incorporating zero radial and shear stresses on the edge of the hole *analytically/continuously* is advantageous in that it also significantly reduces the number of independent coefficients in the stress components. Fewer coefficients typically decrease the number of equations (involved in the least squares process) and potentially the amount of measured input data needed to evaluate these unknown coefficients. Contemporary commercial TSA systems can provide extensive amounts of measured S^* expeditiously. However, obtaining sufficient amounts of measured input data can be challenging using other experimental techniques, for instance strain gages.

In addition to defining the shape of the cut-out, imposing the traction-free boundary conditions *analytically* on the boundary of the hole ($\sigma_{r\theta} = 0$ and $\sigma_{rr} = 0$ at r = R = 12.7 mm = 1/2″ is the radius of the hole), and for all values of θ, results in some of the originally independent coefficients of *equation 7.3* becoming dependent functions of other independent coefficients. By replacing these dependent coefficients (c_1', a_n', c_n', a_2', c_2', a_3', b_3') by their corresponding independent coefficients (d_1', b_n', d_n', b_2', d_2', b_0, c_0, c_3' and d_3'), the stress components of *equations 7.7 through 7.9* can be rewritten as *equations 7.11 through 7.13*[*].

---

[*] Corresponding equations were originally derived in reference [8]. *Equations 7.7 through 7.10* come from reference [8] and are the equations before imposing the traction-free conditions on the edge of the hole. However, after imposing these local traction-free boundary conditions, the expressions of reference [8] corresponding to *equations 7.11 through 7.14* contained some typographical errors. These equations are re-derived and simplified in Appendix 7. *Equations 7.11 through 7.14* are the correct form of the equations but they have not been simplified. The form of the present *equations 7.11 through 7.14* is simplified as *equations 7A.23, 7A.29, 7A.35 and 7A.42* in Appendix A7.

$$(\sigma_{rr})_{sym\_analy} = \left(\frac{1}{r^2} - \frac{3r}{2R^3} + \frac{r^3}{2R^5}\right)b_0 + \left[2 - \frac{3r}{R} + \left(\frac{r}{R}\right)^3\right]c_0 + \left(\frac{-2R^4}{r^3} + 2r\right)\cos\theta d_1^{'}$$

$$+ 3R^2\left(1 - r^{-4}R^4\right)\cos(2\theta)b_2^{'} + \left(R^{-2} + 3r^{-4}R^2 - 4r^{-2}\right)\cos(2\theta)d_2^{'}$$

$$+ \left(\frac{24r}{R^6} - \frac{12r^3}{R^8} - \frac{12}{r^5}\right)\cos(3\theta)c_3^{'} + \left(\frac{18r}{R^4} - \frac{8r^3}{R^6} - \frac{10}{r^3}\right)\cos(3\theta)d_3^{'}$$

$$+ \sum_{n=4,5,\ldots}^{N} \left\{ \begin{array}{l} \left[(n^2-1)r^{(n-2)}R^2 - (n+1)(n-2)r^n - (n+1)r^{-(n+2)}R^{(2n+2)}\right]\cos(n\theta)b_n^{'} \\ + \left[(n-1)r^{(n-2)}R^{-(2n-2)} - (1-n^2)r^{-(n+2)}R^2 - (n-1)(n+2)r^{-n}\right]\cos(n\theta)d_n^{'} \end{array} \right\} \tag{7.11}$$

$$(\sigma_{\theta\theta})_{sym\_analy} = \left(-\frac{1}{r^2} + \frac{3r}{2R^3} - \frac{5r^3}{2R^5}\right)b_0 + \left(2 + \frac{3r}{R} - \frac{5r^3}{R^3}\right)c_0 + \left(\frac{2R^4}{r^3} + 6r\right)\cos\theta d_1^{'}$$

$$+ \left[\left((-3)R^2 + 12r^2 + 3r^{-4}R^6\right)\right]\cos(2\theta)b_2^{'} - \left(R^{-2} + 3r^{-4}R^2\right)\cos(2\theta)d_2^{'}$$

$$+ \left(\frac{-24r}{R^6} + \frac{60r^3}{R^8} + \frac{12}{r^5}\right)\cos(3\theta)c_3^{'} + \left(\frac{-18r}{R^4} + \frac{40r^3}{R^6} + \frac{2}{r^3}\right)\cos(3\theta)d_3^{'}$$

$$+ \sum_{n=4,5\ldots}^{N} \left\{ \begin{array}{l} \left[-(n^2-1)r^{(n-2)}R^2 + (n+1)(n+2)r^n + (n+1)r^{-(n+2)}R^{(2n+2)}\right]\cos(n\theta)b_n^{'} \\ + \left[-(n-1)r^{(n-2)}R^{-(2n-2)} + (1-n^2)r^{-(n+2)}R^2 + (n-2)(n-1)r^{-n}\right]\cos(n\theta)d_n^{'} \end{array} \right\} \tag{7.12}$$

$$(\sigma_{r\theta})_{sym\_analy} = \left[\frac{3r\tan(3\theta)}{2R^3} - \frac{3r^3\tan(3\theta)}{2R^5}\right]b_0 + \left[\frac{3r\tan(3\theta)}{R} - \frac{3r^3\tan(3\theta)}{R^3}\right]c_0$$

$$-\left(\frac{2R^4}{r^3} - 2r\right)\sin\theta d_1' - \left(3R^2 - 6r^2 + 3r^{-4}R^6\right)\sin(2\theta)b_2'$$

$$-\left(R^{-2} - 3r^{-4}R^2 + 2r^{-2}\right)\sin(2\theta)d_2' - \left(\frac{24r}{R^6} - \frac{36r^3}{R^8} + \frac{12}{r^5}\right)\sin(3\theta)c_3'$$

$$-\left(\frac{18r}{R^4} - \frac{24r^3}{R^6} + \frac{6}{r^3}\right)\sin(3\theta)d_3'$$

$$+\sum_{n=4,5\ldots}^{N}\left\{\begin{array}{l}\left[-(n^2-1)r^{(n-2)}R^2 + n(n+1)r^n - (n+1)r^{-(n+2)}R^{(2n+2)}\right]\sin(n\theta)b_n' \\ +\left[-(n-1)r^{(n-2)}R^{-(2n-2)} - (1-n^2)r^{-(n+2)}R^2 - n(n-1)r^{-n}\right]\sin(n\theta)d_n'\end{array}\right\} \quad (7.13)$$

Again adding *equations 7.11 and 7.12* for the radial and tangential components of stress to determine the equation for the isopachic stress (*equation 7.14*) gives

$$S_{sym\_analy} = (\sigma_{rr})_{sym\_analy} + (\sigma_{\theta\theta})_{sym\_analy}$$

$$S_{sym\_analy} = -\frac{2r^3}{R^5}b_0 + \left(4 - \frac{4r^3}{R^3}\right)c_0 + 8r\cos\theta d_1' + 12r^2\cos(2\theta)b_2' - 4r^{-2}\cos(2\theta)d_2'$$

$$+\frac{48r^3}{R^8}\cos(3\theta)c_3' + \left(\frac{32r^3}{R^6} - \frac{8}{r^3}\right)\cos(3\theta)d_3'$$

$$+\sum_{n=4,5\ldots}^{N}\left[4(n+1)r^n\cos(n\theta)b_n' - 4(n-1)r^{-n}\cos(n\theta)d_n'\right] \quad (7.14)$$

Note the *equations 7.11 through 7.14* for the symmetrical case of *figure 7.1* can be reduced to *equations 7A.23, 7A.29, 7A.35 and 7A.42* in Appendix A7 by substituting *equation 7A.14* in *equations 7.11 through 7.14*. The reason *equations 7.11 through 7.14* were not replaced with those from the Appendix A7 is because these equations were used in the analysis of this chapter. Moreover, when imposing the stress compatibility between the two holes in Chapter 8, the Airy coefficients of *figures 8.106 through 8.109* are also based on *equations 7.11 through 7.14* assuming symmetry with respect to x-axis.

All of the coefficients present in this expression for isopachic stress of *equation 7.14* can be evaluated experimentally from thermoelastic stress analysis (i.e., measured TSA data, S^*, which is proportional to the sum of the radial and tangential stresses) and by imposing the traction free condition *analytically* on the boundary of the hole. Since all the coefficients which appear in the individual stress components (*equations 7.11 through 7.13*) for the plate of *figure 7.1* also exist in the equation for isopachic stress (*equation 7.11*), the complete state of in-plane stress for that case is evaluated from the load-induced temperature information (i.e. TSA).

Equation 7.14-A is the corresponding expression for S associated with the plate of *figure 7.1* but based on the much more complex stress function of *equation 7.3-A*.

$$
\begin{aligned}
S_{cen\_analy} &= 4\cdot c_0 + 8\cdot r\cdot \cos\theta\cdot d_1 \\
&+ 24\cdot r^2\cdot R^{-6}\cdot \cos(2\cdot\theta)\cdot c_2 + \left(12\cdot r^2\cdot R^{-4} - 4\cdot r^{-2}\right)\cdot \cos(2\cdot\theta)\cdot d_2 \\
&+ \left\{ \frac{C_9\cdot(-4)\cdot R^3\cdot \sin(6\cdot\theta)}{\left[C_4\cdot \sin(3\cdot\theta) + C_5\cdot\cos(3\cdot\theta)\right]} + 16\cdot r^3\cdot\cos(3\cdot\theta) \right\}\cdot b_3 \\
&+ \frac{C_9\cdot 12\cdot R^{-5}\cdot \sin(6\cdot\theta)}{\left[C_4\cdot \sin(3\cdot\theta) + C_5\cdot\cos(3\cdot\theta)\right]}\cdot c_3 \\
&+ \left\{ \frac{C_9\cdot 8\cdot R^{-3}\cdot \sin(6\cdot\theta)}{\left[C_4\cdot \sin(3\cdot\theta) + C_5\cdot\cos(3\cdot\theta)\right]} - 8\cdot r^{-3}\cdot\cos(3\cdot\theta) \right\}\cdot d_3 \\
&+ \sum_{n=4,5,6\ldots}^{N} \left\{ \begin{array}{l} 4\cdot n\cdot(n+1)\cdot r^n\cdot R^{-(2n+2)}\cdot\cos(n\cdot\theta)\cdot c_n \\ +\left[4\cdot(n^2-1)\cdot r^n\cdot R^{-2n} - 4\cdot(n-1)\cdot r^{-n}\right]\cdot\cos(n\cdot\theta)\cdot d_n \end{array} \right\}
\end{aligned}
\tag{7.14-A}
$$

Non-symmetry related to *figure 7.2*

Using *equations 7.4 through 7.6,* the following expressions for individual polar components of stress are obtained by differentiating the reduced stress function ϕ_{unsym} of *equation 7.2,* (without regard to most of the specific boundary conditions of *figure 7.2*) [4], *i.e.*,

$$
\begin{aligned}
\left(\sigma_{rr}\right)_{unsym} &= \frac{1}{r^2}\cdot b_0 + 2\cdot c_0 + \left(-\frac{2\cdot c_1}{r^3} + 2\cdot r\cdot d_1\right)\cdot \sin\theta + \left(-\frac{2\cdot c_1'}{r^3} + 2\cdot r\cdot d_1'\right)\cdot\cos\theta \\
&- \sum_{n=2,3,4\ldots}^{N} \left[\begin{array}{l} a_n\cdot n\cdot(n-1)\cdot r^{(n-2)} + b_n\cdot(n+1)\cdot(n-2)\cdot r^n \\ +c_n\cdot n\cdot(n+1)\cdot r^{-(n+2)} + d_n\cdot(n-1)\cdot(n+2)\cdot r^{-n} \end{array} \right]\cdot \sin(n\cdot\theta) \\
&- \sum_{n=2,3,4\ldots}^{N} \left[\begin{array}{l} a_n'\cdot n\cdot(n-1)\cdot r^{(n-2)} + b_n'\cdot(n+1)\cdot(n-2)\cdot r^n \\ +c_n'\cdot n\cdot(n+1)\cdot r^{-(n+2)} + d_n'\cdot(n-1)\cdot(n+2)\cdot r^{-n} \end{array} \right]\cdot \cos(n\cdot\theta)
\end{aligned}
\tag{7.15}
$$

$$\left(\sigma_{\theta\theta}\right)_{unsym} = -\frac{1}{r^2}\cdot b_0 + 2\cdot c_0 + \left(\frac{2\cdot c_1}{r^3} + 6\cdot r\cdot d_1\right)\cdot \sin\theta + \left(\frac{2\cdot c_1^{'}}{r^3} + 6\cdot r\cdot d_1^{'}\right)\cdot \cos\theta$$
$$+ \sum_{n=2,3,4...}^{N}\begin{bmatrix} a_n\cdot n\cdot(n-1)\cdot r^{(n-2)} + b_n\cdot(n+1)\cdot(n+2)\cdot r^n \\ +c_n\cdot n\cdot(n+1)\cdot r^{-(n+2)} + d_n\cdot(n-2)\cdot(n-1)\cdot r^{-n}\end{bmatrix}\cdot \sin(n\cdot\theta)$$
$$+ \sum_{n=2,3,4...}^{N}\begin{bmatrix} a_n^{'}\cdot n\cdot(n-1)\cdot r^{(n-2)} + b_n^{'}\cdot(n+1)\cdot(n+2)\cdot r^n \\ +c_n^{'}\cdot n\cdot(n+1)\cdot r^{-(n+2)} + d_n^{'}\cdot(n-2)\cdot(n-1)\cdot r^{-n}\end{bmatrix}\cdot \cos(n\cdot\theta) \tag{7.16}$$

$$\left(\sigma_{r\theta}\right)_{unsym} = \frac{1}{r^2}\cdot A_0 + \left(\frac{2\cdot c_1}{r^3} - 2\cdot r\cdot d_1\right)\cdot \cos\theta - \left(\frac{2\cdot c_1^{'}}{r^3} - 2\cdot r\cdot d_1^{'}\right)\cdot \sin\theta$$
$$- \sum_{n=2,3,4...}^{N}\begin{bmatrix} a_n\cdot n\cdot(n-1)\cdot r^{(n-2)} + b_n\cdot n\cdot(n+1)\cdot r^n \\ -c_n\cdot n\cdot(n+1)\cdot r^{-(n+2)} - d_n\cdot n\cdot(n-1)\cdot r^{-n}\end{bmatrix}\cdot \cos(n\cdot\theta)$$
$$+ \sum_{n=2,3,4...}^{N}\begin{bmatrix} a_n^{'}\cdot n\cdot(n-1)\cdot r^{(n-2)} + b_n^{'}\cdot n\cdot(n+1)\cdot r^n \\ -c_n^{'}\cdot n\cdot(n+1)\cdot r^{-(n+2)} - d_n^{'}\cdot n\cdot(n-1)\cdot r^{-n}\end{bmatrix}\cdot \sin(n\cdot\theta) \tag{7.17}$$

As a result of differentiation, the coefficients a_0 and a_1' which appear in the Airy stress function ϕ_{unsym}, *equation 7.2*, are absent in the expressions for the individual stress components, *equations 7.15 through 7.17*. For isotropy under cyclic loading condition, the Thermoelastic Stress Analysis (TSA) measures the temperature variation in a loaded member which is linearly proportional to the change in the isopachic or the first stress invariant. Therefore the isopachic stress S_{unsym} of *equation 7.18* is obtained by adding the radial and tangential components of stress *equations 7.15 and 7.16*, which is as follows:

$$
\begin{aligned}
S_{unsym} &= \left(\sigma_{rr}\right)_{unsym} + \left(\sigma_{\theta\theta}\right)_{unsym} \\
&= 4\cdot c_0 + 8\cdot r\cdot \sin\theta\cdot d_1 + 8\cdot r\cdot \cos\theta\cdot d_1^{'} \\
&+ \sum_{n=2,3,4\ldots}^{N}\left[4\cdot(n+1)\cdot r^{n}\cdot b_n - 4\cdot(n-1)\cdot r^{-n}\cdot d_n\right]\cdot \sin(n\cdot\theta) \\
&+ \sum_{n=2,3,4\ldots}^{N}\left[4\cdot(n+1)\cdot r^{n}\cdot b_n^{'} - 4\cdot(n-1)\cdot r^{-n}\cdot d_n^{'}\right]\cdot \cos(n\cdot\theta)
\end{aligned}
\tag{7.18}
$$

Comparing *equations 7.15 through 7.18* shows that coefficients present in the expression for isopachic stress are also present in the expressions for individual stresses. However, the expression of isopachic stress S_{unsym}, of *equation 7.18* excludes coefficients b_0, c_1, c_1', A_0, and a_n, c_n, a_n', c_n' for n >1 which appear in the individual stress components, *equations 7.15 through 7.17*. Therefore, the individual stresses are not available from the isopachic stress expression of *equation 7.18* and TSA data alone. However, by again imposing the traction-free boundary conditions *analytically* on the boundary of the hole will result in all of the coefficients that are present in the equations for individual stresses to also appear in the expression for the isopachic stress. This will enable one to evaluate all the three individual components of stress from only measured temperature information.

If the traction-free conditions on the edge of the hole ($\sigma_{r\theta} = 0$ and $\sigma_{rr} = 0$ at r = R (= 12.7 mm = 1/2″ is the radius of the hole) and for all values of θ) of *figure 7.2* are *analytically* incorporated, coefficients c_1, c_1', a_2, c_2, a_3, b_3, a_n and c_n (n > 3), and a_n' and c_n' (n > 1) in the individual components of stress become dependent variables and the stress components of *equations 7.15 through 7.17* can be rewritten as *equations 7.19 through 7.21*. (detailed derivations are in Chapter 4 of reference [4].)

$$
\begin{aligned}
\left(\sigma_{rr}\right)_{unsym\_analy} &= \left(\frac{1}{r^2}-\frac{3\cdot r}{2\cdot R^3}+\frac{r^3}{2\cdot R^5}\right)\cdot b_0+\left[2-\frac{3\cdot r}{R}+\left(\frac{r}{R}\right)^3\right]\cdot c_0 \\
&+\left[\frac{r\cdot tan\left(3\cdot\theta\right)}{2\cdot R^3}-\frac{r^3\cdot tan\left(3\cdot\theta\right)}{2\cdot R^5}\right]\cdot A_0 \\
&+\left(\frac{-2\cdot R^4}{r^3}+2\cdot r\right)\cdot sin\,\theta\cdot d_1+\left(\frac{-2\cdot R^4}{r^3}+2\cdot r\right)\cdot cos\,\theta\cdot d_1^{'} \\
&+3\cdot R^2\cdot\left(1-r^{-4}\cdot R^4\right)\cdot sin\left(2\cdot\theta\right)\cdot b_2+\left(R^{-2}+3\cdot r^{-4}\cdot R^2-4\cdot r^{-2}\right)\cdot sin\left(2\cdot\theta\right)\cdot d_2 \\
&+\left(\frac{24\cdot r}{R^6}-\frac{12\cdot r^3}{R^8}-\frac{12}{r^5}\right)\cdot sin\left(3\cdot\theta\right)\cdot c_3+\left(\frac{18\cdot r}{R^4}-\frac{8\cdot r^3}{R^6}-\frac{10}{r^3}\right)\cdot sin\left(3\cdot\theta\right)\cdot d_3 \\
&+\sum_{n=4,5,6\ldots}^{N}\left\{\begin{array}{l}\left[\begin{array}{l}\left(n^2-1\right)\cdot r^{(n-2)}\cdot R^2-\left(n+1\right)\cdot\left(n-2\right)\cdot r^n \\ -\left(n+1\right)\cdot r^{-(n+2)}\cdot R^{(2\cdot n+2)}\end{array}\right]\cdot sin\left(n\cdot\theta\right)\cdot b_n \\ +\left[\begin{array}{l}\left(n-1\right)\cdot r^{(n-2)}\cdot R^{-(2\cdot n-2)}-\left(1-n^2\right)\cdot r^{-(n+2)}\cdot R^2 \\ -\left(n-1\right)\cdot\left(n+2\right)\cdot r^{-n}\end{array}\right]\cdot sin\left(n\cdot\theta\right)\cdot d_n\end{array}\right. \\
&+\sum_{n=2,3,4\ldots}^{N}\left\{\begin{array}{l}\left[\begin{array}{l}\left(n^2-1\right)\cdot r^{(n-2)}\cdot R^2-\left(n+1\right)\cdot\left(n-2\right)\cdot r^n \\ -\left(n+1\right)\cdot r^{-(n+2)}\cdot R^{(2\cdot n+2)}\end{array}\right]\cdot cos\left(n\cdot\theta\right)\cdot b_n^{'} \\ +\left[\begin{array}{l}\left(n-1\right)\cdot r^{(n-2)}\cdot R^{-(2\cdot n-2)}-\left(1-n^2\right)\cdot r^{-(n+2)}\cdot R^2 \\ -\left(n-1\right)\cdot\left(n+2\right)\cdot r^{-n}\end{array}\right]\cdot cos\left(n\cdot\theta\right)\cdot d_n^{'}\end{array}\right.
\end{aligned}
\tag{7.19}
$$

$$
\begin{aligned}
\left(\sigma_{\theta\theta}\right)_{unsym\_analy} = & \left(-\frac{1}{r^2}+\frac{3\cdot r}{2\cdot R^3}-\frac{5\cdot r^3}{2\cdot R^5}\right)\cdot b_0+\left(2+\frac{3\cdot r}{R}-\frac{5\cdot r^3}{R^3}\right)\cdot c_0 \\
& +\left[-\frac{r\cdot tan\left(3\cdot\theta\right)}{2\cdot R^3}+\frac{5\cdot r^3\cdot tan\left(3\cdot\theta\right)}{2\cdot R^5}\right]\cdot A_0+\left(\frac{2\cdot R^4}{r^3}+6\cdot r\right)\cdot sin\,\theta\cdot d_1 \\
& +\left(\frac{2\cdot R^4}{r^3}+6\cdot r\right)\cdot cos\,\theta\cdot d_1^{'}+\left[\left(-3\right)\cdot R^2+12\cdot r^2+3\cdot r^{-4}\cdot R^6\right]\cdot sin\left(2\cdot\theta\right)\cdot b_2 \\
& -\left(R^{-2}+3\cdot r^{-4}\cdot R^2\right)\cdot sin\left(2\cdot\theta\right)\cdot d_2+\left(-\frac{24\cdot r}{R^6}+\frac{60\cdot r^3}{R^8}+\frac{12}{r^5}\right)\cdot sin\left(3\cdot\theta\right)\cdot c_3 \\
& +\left(-\frac{18\cdot r}{R^4}+\frac{40\cdot r^3}{R^6}+\frac{2}{r^3}\right)\cdot sin\left(3\cdot\theta\right)\cdot d_3 \\
& +\sum_{n=4,5,6\ldots}^{N}\left\{\begin{array}{l}\left[\begin{array}{l}-\left(n^2-1\right)\cdot r^{(n-2)}\cdot R^2+\left(n+1\right)\cdot\left(n+2\right)\cdot r^n \\ +\left(n+1\right)\cdot r^{-(n+2)}\cdot R^{(2\cdot n+2)}\end{array}\right]\cdot sin\left(n\cdot\theta\right)\cdot b_n \\ +\left[\begin{array}{l}-\left(n-1\right)\cdot r^{(n-2)}\cdot R^{-(2\cdot n-2)}+\left(1-n^2\right)\cdot r^{-(n+2)}\cdot R^2 \\ +\left(n-2\right)\cdot\left(n-1\right)\cdot r^{-n}\end{array}\right]\cdot sin\left(n\cdot\theta\right)\cdot d_n\end{array}\right\} \\
& +\sum_{n=2,3,4\ldots}^{N}\left\{\begin{array}{l}\left[\begin{array}{l}-\left(n^2-1\right)\cdot r^{(n-2)}\cdot R^2+\left(n+1\right)\cdot\left(n+2\right)\cdot r^n \\ +\left(n+1\right)\cdot r^{-(n+2)}\cdot R^{(2\cdot n+2)}\end{array}\right]\cdot cos\left(n\cdot\theta\right)\cdot b_n^{'} \\ +\left[\begin{array}{l}-\left(n-1\right)\cdot r^{(n-2)}\cdot R^{-(2\cdot n-2)}+\left(1-n^2\right)\cdot r^{-(n+2)}\cdot R^2 \\ +\left(n-2\right)\cdot\left(n-1\right)\cdot r^{-n}\end{array}\right]\cdot cos\left(n\cdot\theta\right)\cdot d_n^{'}\end{array}\right\}
\end{aligned}
\tag{7.20}
$$

$$
\begin{aligned}
\left(\sigma_{r\theta}\right)_{unsym\_analy} = & \left[-\frac{3\cdot r\cdot cot\left(3\cdot\theta\right)}{2\cdot R^3}+\frac{3\cdot r^3\cdot cot\left(3\cdot\theta\right)}{2\cdot R^5}\right]\cdot b_0 \\
& +\left[-\frac{3\cdot r\cdot cot\left(3\cdot\theta\right)}{R}+\frac{3\cdot r^3\cdot cot\left(3\cdot\theta\right)}{R^3}\right]\cdot c_0 \\
& +\left(\frac{r}{2\cdot R^3}-\frac{3\cdot r^3}{2\cdot R^5}+\frac{1}{r^2}\right)\cdot A_0+\left(\frac{2\cdot R^4}{r^3}-2\cdot r\right)\cdot cos\,\theta\cdot d_1 \\
& -\left(\frac{2\cdot R^4}{r^3}-2\cdot r\right)\cdot sin\,\theta\cdot d_1^{'}+\left(3\cdot R^2-6\cdot r^2+3\cdot r^{-4}\cdot R^6\right)\cdot cos\left(2\cdot\theta\right)\cdot b_2 \\
& +\left(R^{-2}-3\cdot r^{-4}\cdot R^2+2\cdot r^{-2}\right)\cdot cos\left(2\cdot\theta\right)\cdot d_2 \\
& +\left(\frac{24\cdot r}{R^6}-\frac{36\cdot r^3}{R^8}+\frac{12}{r^5}\right)\cdot cos\left(3\cdot\theta\right)\cdot c_3+\left(\frac{18\cdot r}{R^4}-\frac{24\cdot r^3}{R^6}+\frac{6}{r^3}\right)\cdot cos\left(3\cdot\theta\right)\cdot d_3 \\
& +\sum_{n=4,5,6\ldots}^{N}\left\{\begin{array}{l}\left[\begin{array}{l}\left(n^2-1\right)\cdot r^{(n-2)}\cdot R^2-n\cdot\left(n+1\right)\cdot r^n \\ +\left(n+1\right)\cdot r^{-(n+2)}\cdot R^{(2\cdot n+2)}\end{array}\right]\cdot cos\left(n\cdot\theta\right)\cdot b_n \\ +\left[\begin{array}{l}\left(n-1\right)\cdot r^{(n-2)}\cdot R^{-(2\cdot n-2)}+\left(1-n^2\right)\cdot r^{-(n+2)}\cdot R^2 \\ +n\cdot\left(n-1\right)\cdot r^{-n}\end{array}\right]\cdot cos\left(n\cdot\theta\right)\cdot d_n\end{array}\right\} \\
& +\sum_{n=2,3,4\ldots}^{N}\left\{\begin{array}{l}\left[\begin{array}{l}-\left(n^2-1\right)\cdot r^{(n-2)}\cdot R^2+n\cdot\left(n+1\right)\cdot r^n \\ -\left(n+1\right)\cdot r^{-(n+2)}\cdot R^{(2\cdot n+2)}\end{array}\right]\cdot sin\left(n\cdot\theta\right)\cdot b_n^{'} \\ +\left[\begin{array}{l}-\left(n-1\right)\cdot r^{(n-2)}\cdot R^{-(2\cdot n-2)}-\left(1-n^2\right)\cdot r^{-(n+2)}\cdot R^2 \\ -n\cdot\left(n-1\right)\cdot r^{-n}\end{array}\right]\cdot sin\left(n\cdot\theta\right)\cdot d_n^{'}\end{array}\right\}
\end{aligned}
\tag{7.21}
$$

Based on imposing $\sigma_{rr} = \sigma_{r\theta} = 0$ *analytically* on the edge of the hole, the isopachic equation S_{unsym_analy} in terms of independent coefficients is available from adding the radial and hoop stresses of *equations 7.19 and 7.20* together to give *equation 7.22*.

$$
\begin{aligned}
S_{unsym\_analy} &= \left(\sigma_{rr}\right)_{unsym\_analy} + \left(\sigma_{\theta\theta}\right)_{unsym\_analy} \\
&= -\frac{2\cdot r^3}{R^5}\cdot b_0 + \left(4 - \frac{4\cdot r^3}{R^3}\right)\cdot c_0 + \frac{2\cdot r^3\cdot tan\left(3\cdot\theta\right)}{R^5}\cdot A_0 \\
&+ 8\cdot r\cdot sin\,\theta\cdot d_1 + 8\cdot r\cdot cos\,\theta\cdot d_1^{'} \\
&+ 12\cdot r^2\cdot sin\left(2\cdot\theta\right)\cdot b_2 - 4\cdot r^{-2}\cdot sin\left(2\cdot\theta\right)\cdot d_2 \\
&+ \frac{48\cdot r^3}{R^8}\cdot sin\left(3\cdot\theta\right)\cdot c_3 + \left(\frac{32\cdot r^3}{R^6} - \frac{8}{r^3}\right)\cdot sin\left(3\cdot\theta\right)\cdot d_3 \\
&+ \sum_{n=4,5,6\ldots}^{N}\left[4\cdot\left(n+1\right)\cdot r^n\cdot sin\left(n\cdot\theta\right)\cdot b_n - 4\cdot\left(n-1\right)\cdot r^{-n}\cdot sin\left(n\cdot\theta\right)\cdot d_n\right] \\
&+ \sum_{n=2,3,4\ldots}^{N}\left[4\cdot\left(n+1\right)\cdot r^n\cdot cos\left(n\cdot\theta\right)\cdot b_n^{'} - 4\cdot\left(n-1\right)\cdot r^{-n}\cdot cos\left(n\cdot\theta\right)\cdot d_n^{'}\right]
\end{aligned}
\tag{7.22}
$$

Equation 7.22-A is the isopachic stress for the plate of *figure 7.2* based on the stress function of *equation 7.2-A* but having satisfied the traction-free condition on the edge of the hole [116]. This equation associated with the case of *figure 7.2* is the counterpart of *equation 7.14-A* for the plate of *figure 7.1*.

$$
\begin{aligned}
S_{offset\_analy} &= \sigma_{rr} + \sigma_{\theta\theta} \\
&= 4\cdot c_0 + 8\cdot r\cdot \sin\theta\cdot\cos\theta\cdot d_1 + 8\cdot r\cdot\cos\theta\cdot d_1^{'} \\
&+ 24\cdot r^2\cdot R^{-6}\cdot\cos(2\cdot\theta)\cdot c_2^{'} + (12\cdot r^2\cdot R^{-4} - 4\cdot r^{-2}).\cos(2\cdot\theta)\cdot d_2^{'} \\
&+ \left\{\frac{F_9\cdot(-4)\cdot R^3\cdot\sin(6\cdot\theta)}{\left[F_4\cdot\sin(3\cdot\theta)+F_5\cdot\cos(3\cdot\theta)\right]} + 16\cdot r^3\cdot\cos(3\cdot\theta)\right\}\cdot b_3^{'} \\
&+ \frac{F_9\cdot 12\cdot R^{-5}\cdot\sin(6\cdot\theta)}{\left[F_4\cdot\sin(3\cdot\theta)+F_5\cdot\cos(3\cdot\theta)\right]}\cdot c_3^{'} \\
&+ \left\{\frac{F_9\cdot 8\cdot R^{-3}\cdot\sin(6\cdot\theta)}{\left[F_4\cdot\sin(3\cdot\theta)+F_5\cdot\cos(3\cdot\theta)\right]} - 8\cdot r^{-3}\cdot\cos(3\cdot\theta)\right\}\cdot d_3^{'} \\
&+ \left\{\frac{F_9\cdot(-1)\cdot R^{-2}\cdot\cos(3\cdot\theta)}{\left[F_4\cdot\sin(3\cdot\theta)+F_5\cdot\cos(3\cdot\theta)\right]}\right\}\cdot A_0 \\
&+ \sum_{n=4,5,6,\ldots}^{N}\left\{\begin{aligned}&4\cdot n\cdot(n+1)\cdot r^n\cdot R^{-(2n+2)}\cdot\cos(n\cdot\theta)\cdot c_n^{'} \\ &+\left[4\cdot(n^2-1)\cdot r^n\cdot R^{-2n} - 4\cdot(n-1)\cdot r^{-n}\right]\cdot\cos(n\cdot\theta)\cdot d_n^{'}\end{aligned}\right\} \\
&+ \sum_{n=2,3,4,\ldots}^{N}\left[4\cdot(n+1)\cdot r^n\cdot b_n - 4\cdot(n-1)\cdot r^{-n}\cdot d_n\right]\cdot\sin(n\cdot\theta)
\end{aligned}
\qquad \text{(7.22-A)}
$$

The isopachic stress S_{unsym_analy} of *equation 7.22* associated with the plate of *figure 7.2* contains all of the Airy coefficients which appear in the relevant expressions for the individual components of stress, *equations 7.19 through 7.21*, i.e., b_0, c_0, A_0, d_1, d_1', b_2, d_2, c_3, d_3, and b_n and d_n (for all n>3), and b_n' and d_n' (for all n>1). Thus, once all of the unknown Airy coefficients of the isopachic stress expression of *equation 7.22* are thermoelastically evaluated ($S^* = KS = K(\sigma_{rr} + \sigma_{\theta\theta} = \sigma_{xx} + \sigma_{yy} = \sigma_1 + \sigma_2)$), individual stresses which satisfy equilibrium and compatibility, at least on and near the edge of the hole, can consequently be investigated from *equations 7.19 through 7.21* even without knowledge of the material constitutive information, or external geometry or distant boundary conditions.

7.3 Thermoelastic Stress Analysis

Thermoelastic stress analysis provides full-field stress information over the surface. Processing the recorded temperature data with a relevant Airy stress function enables one to obtain the individual stresses at and in the vicinity of the geometric discontinuity without any complicated mathematical algebra or additional experimental and/or numerical techniques. The TSA data analyzed here, which are from reference [4, 111 and 116], are for the aluminum (6061 T6511, ultimate strength of 275 to 311 MPa (= 40 to 45 ksi) and yield point of 241 to 275 MPa (= 35 to 40 ksi) plate of *figures 7.1 and 7.2*. *Figure 7.3* are photographs of the experimental set-up for each of the centrally loaded plate (left) and an offset loaded plate (right). These photographs include the DeltaTherm DT1410 infrared camera (sensor array of 256 x 256 pixels) used to record the load-induced temperature variations, the loaded plate and the MTS loading system. The plate was sprayed with Krylon flat black paint prior to testing to provide an enhanced surface emissivity and then was mounted in the 88.96 kN (20,000 lbs) capacity MTS testing frame (*figure 7.3*) and loaded sinusoidally between 222.4 N (50 lbs) and 1112 N (250 lbs) at 20 Hz. In each case the load was applied through a short piece of drill rod between the top flat platen of the MTS machine and the top of the plate.

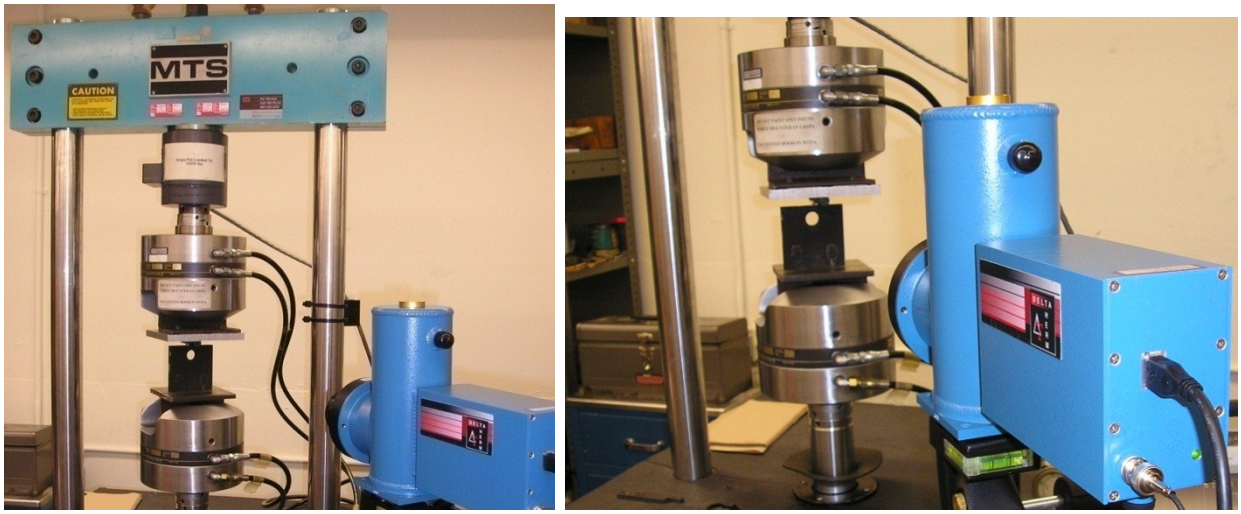

Fig. 7.3: Thermoelastic stress analysis experimental set up for the centrally loaded plate (left) and the offset loaded plate (right) with a near edge hole

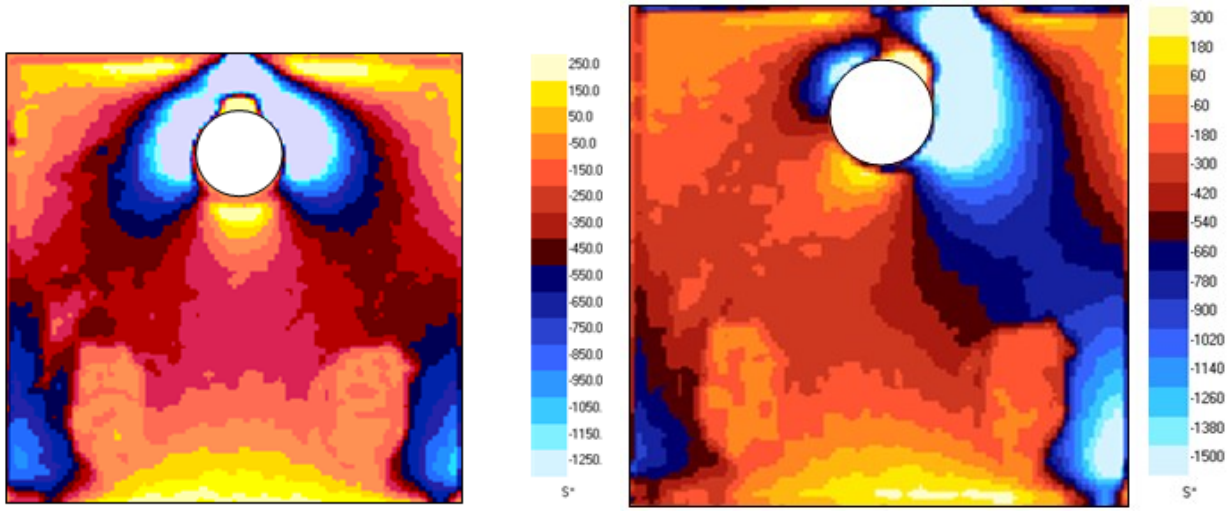

Fig. 7.4: Thermoelastic images of loaded specimen, centrally loaded plate (left), *figure 7.1* and the offset loaded plate (right), *figure 7.2*

The thermoelastic images of *figure 7.4* were recorded over duration of two minutes. For the centrally loaded plate (left image in *figure 7.4*), the pixel size is 0.73 mm (0.029″) and approximately 14,500 TSA discrete values cover the entire plate. For offset loaded plate (right image in *figure 7.4*), the pixel size is 0.72 mm (0.028″) and approximately 15,000 TSA discrete values cover the entire plate. The utilized TSA measured data from the thermograms of *figures 7.4* originated at least 4 pixels away from the hole boundary and the top edge of *figures 7.1 and*

7.2. The number of measured isopachics S (= S^*/K) employed here for the analyses of the centrally loaded plate is 300 and for offset loaded plate is 849. The thermo-mechanical coefficient, K, for both the central and offset loadings is 319 U/MPa (2.21 U/psi). The unit U is used to signify the raw TSA output, in un-calibrated signal units. These amounts and source locations of the input temperature data, S, and the present value of K are those of references [4, 111 and 116].

Based on the TSA-measured stress information ($S = S^*/K = \sigma_{rr} + \sigma_{\theta\theta}$), and when the traction-free boundary conditions, $\sigma_{rr} = \sigma_{r\theta} = 0$, are *analytically* imposed on the edge of the hole for the central loaded or the offset loaded plate, one can form the linear matrix equation $Ac = d$ of *equations 7.23* (central loading, *figure 7.1*) *and 7.24* (offset loading, *figure 7.2*), where matrix A contains isopachic expressions of the form of *equations 7.14 or 7.22,* respectively, with k unknown Airy coefficients for the TSA recorded values from *figure 7.4*. Vector c contains k Airy coefficients and vector d contains the thermoelastically measured $S = \sigma_{rr} + \sigma_{\theta\theta} = S^*/K$ information which is based on the analysis of the centrally loaded or offset loaded plate corresponding to the set of equations in the isopachic matrix A. Since the expressions for $S = \sigma_{rr} + \sigma_{\theta\theta}$ for *figures 7.1 (equation 7.23) and 7.2 (equation 7.24)* contain all of the unknown Airy coefficients involved in σ_{rr}, $\sigma_{\theta\theta}$, and $\sigma_{r\theta}$, the individual stresses can be acquired from the measured thermoelastic data without engaging any other information beyond the previously imposed traction-free conditions at the hole boundary.

Experience indicates that too few coefficients can produce inaccurate results, while too many coefficients, k, can cause the Airy matrix, A of *equations 7.23 and 7.24* to become unstable

or even singular due to computer round-off errors and can also increases the computation time. The number of coefficients was efficiently determined here by monitoring the condition number of the Airy matrix relative to it becoming singular and the *RMS* values of TSA measured $S = S^*/K$, as well as calculated isopachics, *equations 7.23 and 7.24* (*figures 7.5 through 7.10*)

$$\begin{bmatrix} S_{r_1,\theta_1}(b_0,c_0,d_1',b_2',d_2',b_3',d_3',b_4',d_4',b_5',d_5'.....b_N',d_N') \\ S_{r_2,\theta_2}(b_0,c_0,d_1',b_2',d_2',b_3',d_3',b_4',d_4',b_5',d_5'.....b_N',d_N') \\ S_{r_3,\theta_3}(b_0,c_0,d_1',b_2',d_2',b_3',d_3',b_4',d_4',b_5',d_5'.....b_N',d_N') \\ . \\ . \\ . \\ . \\ S_{r_m,\theta_m}(b_0,c_0,d_1',b_2',d_2',b_3',d_3',b_4',d_4',b_5',d_5'.....b_N',d_N') \end{bmatrix}_{mxk} \begin{bmatrix} b_0 \\ c_0 \\ d_1' \\ b_2' \\ d_2' \\ . \\ b_N' \\ d_N' \end{bmatrix}_{kx1} = \begin{bmatrix} S_1 \\ S_2 \\ S_3 \\ S_4 \\ . \\ . \\ . \\ S_m \end{bmatrix}_{mx1} \tag{7.23}$$

$$\begin{bmatrix} S_{r_1,\theta_1}(b_0,c_0,A_0,d_1,d_1',b_2,d_2,c_3,d_3,b_4,d_4,...,b_N,d_N,b_2',d_2',...,b_N',d_N') \\ S_{r_2,\theta_2}(b_0,c_0,A_0,d_1,d_1',b_2,d_2,c_3,d_3,b_4,d_4,...,b_N,d_N,b_2',d_2',...,b_N',d_N') \\ S_{r_3,\theta_3}(b_0,c_0,A_0,d_1,d_1',b_2,d_2,c_3,d_3,b_4,d_4,...,b_N,d_N,b_2',d_2',...,b_N',d_N') \\ . \\ . \\ . \\ . \\ S_{r_m,\theta_m}(b_0,c_0,A_0,d_1,d_1',b_2,d_2,c_3,d_3,b_4,d_4,...,b_N,d_N,b_2',d_2',...,b_N',d_N') \end{bmatrix}_{mxk} \begin{bmatrix} b_0 \\ c_0 \\ A_0 \\ d_1 \\ d_1' \\ b_2 \\ d_2 \\ . \\ b_N \\ d_N \\ . \\ b_N' \\ d_N' \end{bmatrix}_{kx1} = \begin{bmatrix} S_1 \\ S_2 \\ S_3 \\ S_4 \\ . \\ . \\ . \\ S_m \end{bmatrix}_{mx1}$$

(7.24)

or, the simplified form for *equations 7.23 and 7.24*,

$$[A]_{m\times k}\{c\}_{k\times 1} = \{d\}_{m\times 1} \tag{7.25}$$

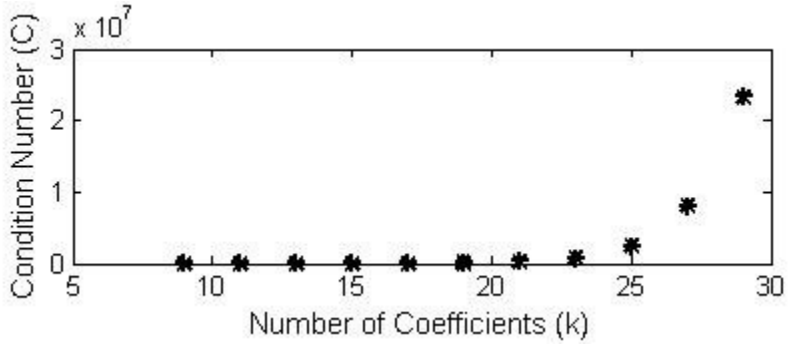

Fig. 7.5: Plot of condition number, *C*, vs. number of coefficients, *k*, for the presently analyzed centrally loaded plate with *m* = 300 input values

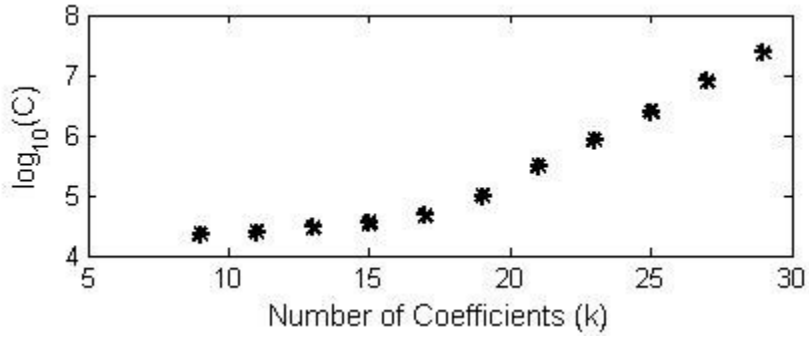

Fig. 7.6: Plot of $\log_{10}$(C) vs. number of coefficients, *k*, for the presently analyzed centrally loaded plate with *m* = 300 input values

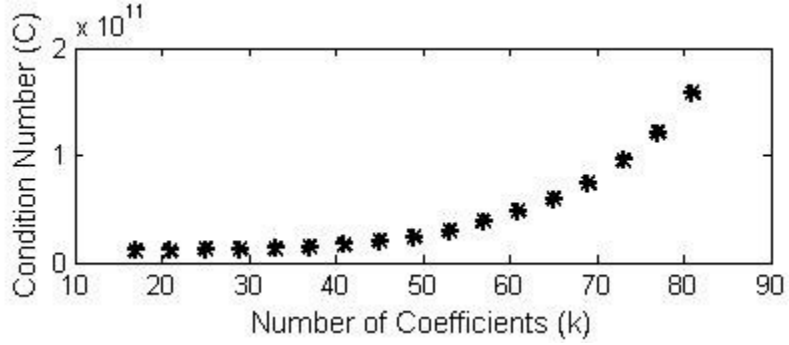

Fig. 7.7: Plot of condition number, *C*, vs. number of coefficients, *k*, for the presently analyzed offset loaded plate with *m* = 849 input values

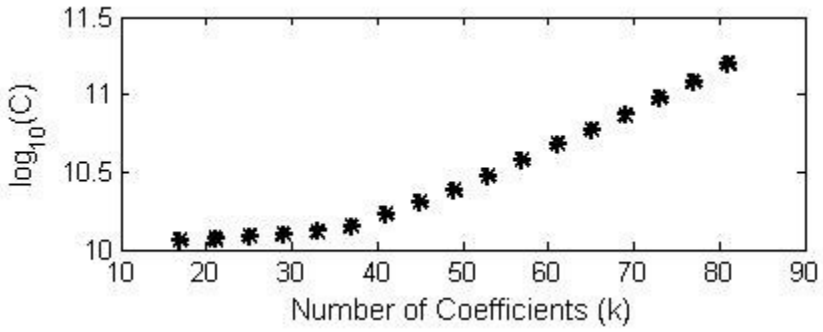

Fig. 7.8: Plot of $\log_{10}$(C) vs. number of coefficients, *k*, for the presently analyzed offset loaded plate with *m* = 849 input values

One of the considerations for evaluating an appropriate number of coefficients to use here is based on the condition number, *C*, of the matrix *A*, that is an indicator to express matrix singularity. *Figures 7.5 and 7.7* are the plots for condition number *C* versus the different number of coefficients for the Airy matrix *A,* for central loaded based on the 300 measured input data and the offset loaded plate based on the 849 measured input data respectively. *Figures 7.6 and 7.8* are the $\log_{10}$ values of the condition numbers for the central loaded and offset loaded plate, respectively, for different number of coefficients. It is worth noting from *figures 7.5 through 7.8* that for a fixed number of equations, the condition number of the matrix *A* grows exponentially with increased number of coefficients. It is therefore preferable to employ the fewest number of coefficients that produces sufficient precisions and advantageously reduces the computation time.

To further assess a realistic number of Airy coefficients to utilize, the *RMS* (*R*oot *M*ean *S*quare) value of *equation 7.26* is used. *RMS* evaluates the discrepancy between the calculated isopachics $\{d'\}$ and the measured values of *S* in vector $\{d\}$ of each of *equations 7.23 and 7.24*. If the Airy matrix equation $Ac = d$ of *equations 7.23 and 7.24* is over-determined, i.e., $m > k$, where *m* is the number of equations and *k* is the number of coefficients, the linear matrix equation will

be solved in the least-squares process. Therefore, for an over-determined matrix equation, $Ac = d$, the now-known coefficient vector, $\{c\}$, as calculated from $c = A\backslash d$ or c = pinv(A)*d (MATLAB notation) (where [A] and {d} consist of known or measured values) and substituting the now-known coefficient vector, $\{c\}$, into the original matrix equation will give $Ac = d'$, where vector $\{d'\}$ is typically not exactly the same as the input data $\{d\}$ (actually consists of m values of S = S*/K). A small *RMS* value is desired between the evaluated isopachic data, $\{d'\}$, and thermoelastically measured, $\{d\}$.

$$(d^{'} - d)_{RMS} \equiv \sqrt{\sum_{i=1}^{m} \left(d_i^{'} - d_i\right)^2 / m} \tag{7.26}$$

Figures 7.9 and 7.10 plot the *RMS* values versus the different number of coefficients, k, for central loaded based on the 300 measured input data and offset loaded plate based on the 849 measured input data, respectively. Inspection for centrally loaded and offset loaded plate illustrates that the condition number increases exponentially and *RMS* values remains almost constant with the number of coefficients, k. Therefore $k = 9$ for the central loaded plate and $k = 17$ for the offset loaded plate are satisfactory choices (where is *RMS* become reasonably constant (C indicative of a stable matrix A). More coefficients do not reduce the *RMS* value very much, and would entail more calculations and a bigger condition number for the analytical matrix. This can increase the chances of the matrix becoming singular and increases the computation time. Moreover more coefficients may possibly imply a need for more measured input data. *Equations 7.14 and 7.22* involve a summation over n, where n goes through positive integers, and the total number of coefficients is given by $k = 7 + 2(N-3) = 2N+1$ for central loaded plate and $k = 7+$

*(2*N) + 2(N-3) = 4N+1* for the offset loaded plate. These imply the terminating index N = 4 in both the cases.

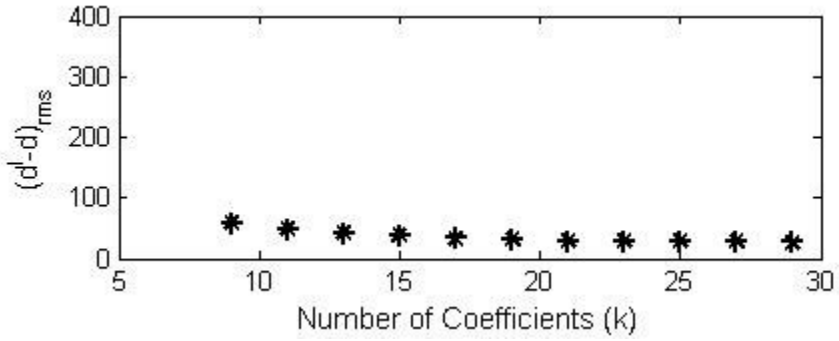

Fig. 7.9: Plot of 'RMS' values of (d'-d) vs. number of coefficients, *k*, for the presently analyzed centrally loaded plate with *m* = 300 input values

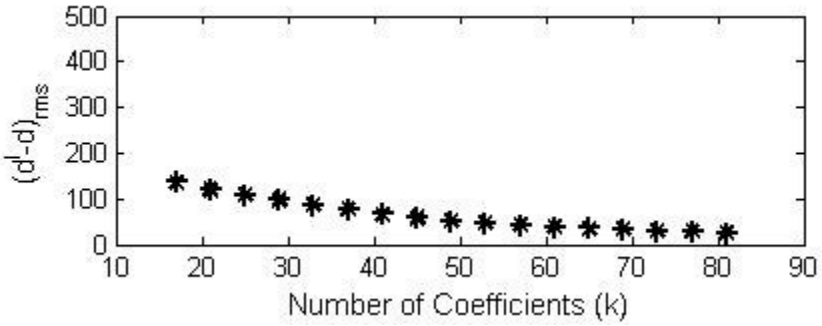

Fig. 7.10: Plot of 'RMS' values of (d'-d) vs. number of coefficients, *k*, for the presently analyzed offset loaded plate with *m* = 849 input values

7.4 Finite Element Analysis

For comparing TSA results on the boundary of the hole with those predicted by FEA (ANSYS), the aluminum (elastic modulus, E = 68.95 GPa = (10 x 10^6 psi) and Poisson's ratio ν = 0.33) plate described in section 7.1 was modeled in ANSYS. *Figures 7.11 and 7.12* are the finite element ANSYS models of the case of *figures 7.1 and 7.2,* respectively. Unlike the described experimental approach which does not require knowledge of the external boundary conditions, finite element analysis requires accurately knowing the material properties, loading and external boundary conditions. For this analyses, isoparametric elements (ANSYS element type: Plane-82) having 8 nodes per element were employed.

For the centrally loaded plate where one has, the geometric and loading symmetry about the x-axis, the FE model is simplified to one half of the entire plate of *figure 7.1* and thus subjected to one half of the full edge load (i.e., ½ *P**, *P** = 200 lbs), *figure 7.11*. The half–plate was modeled with a total of 5,956 elements and 18,305 nodes. The mesh was refined until the ANSYS results did not change by more than 0.2% on the boundary of the hole. Symmetrical boundary conditions are applied along the vertical line of symmetry to simulate the perforated plate of *figure 7.1* and a roller constraint is applied along its bottom edge, DC, *figure 7.11*, therefore satisfying the geometric and loading symmetry about the x-axis, *figure 7.1*.

For the offset loaded plate, the lack of geometric and loading symmetry necessitated a full FE model of *figure 7.2*. A load of *P** = 200 lbs was applied at a top of the plate and at distance E = 11.91 mm (= 0.469") from the x-axis as shown in *figures 7.2 and 7.12*. The full–

plate was modeled with a total of 10,341 elements and 31,487 nodes. Roller constraint (assuming no vertical motion) was applied along the lower edge of the plate, CDC′ of *figures 7.2 and 7.11*.

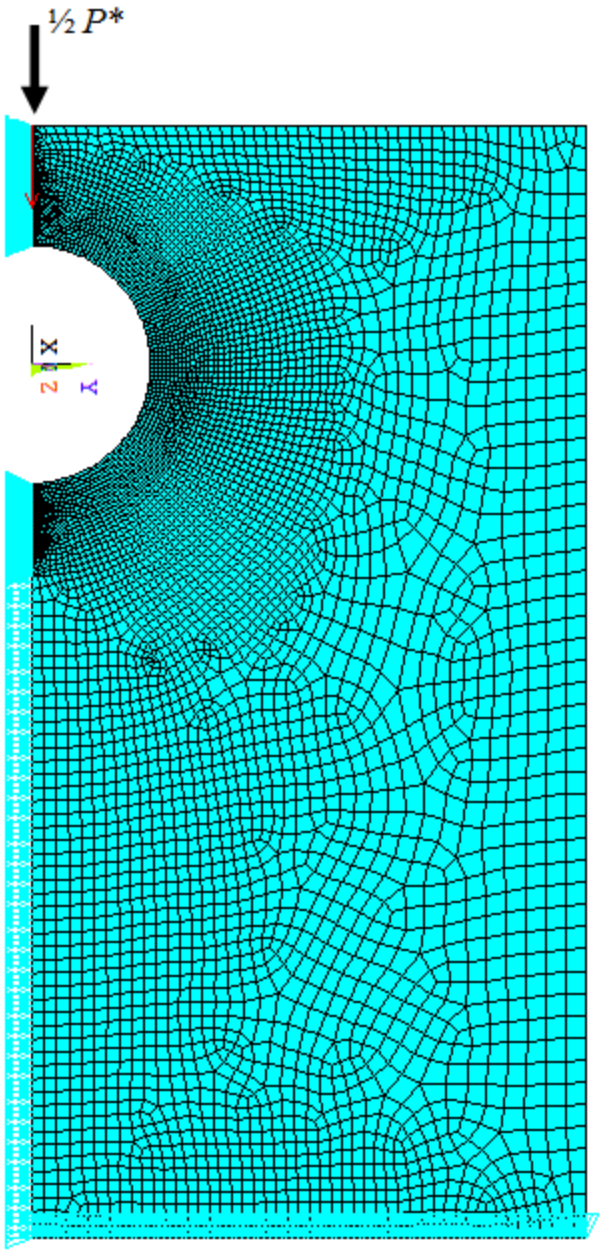

Fig. 7.11: Finite element model for the analysis of the centrally loaded plate of *figure 7.1*

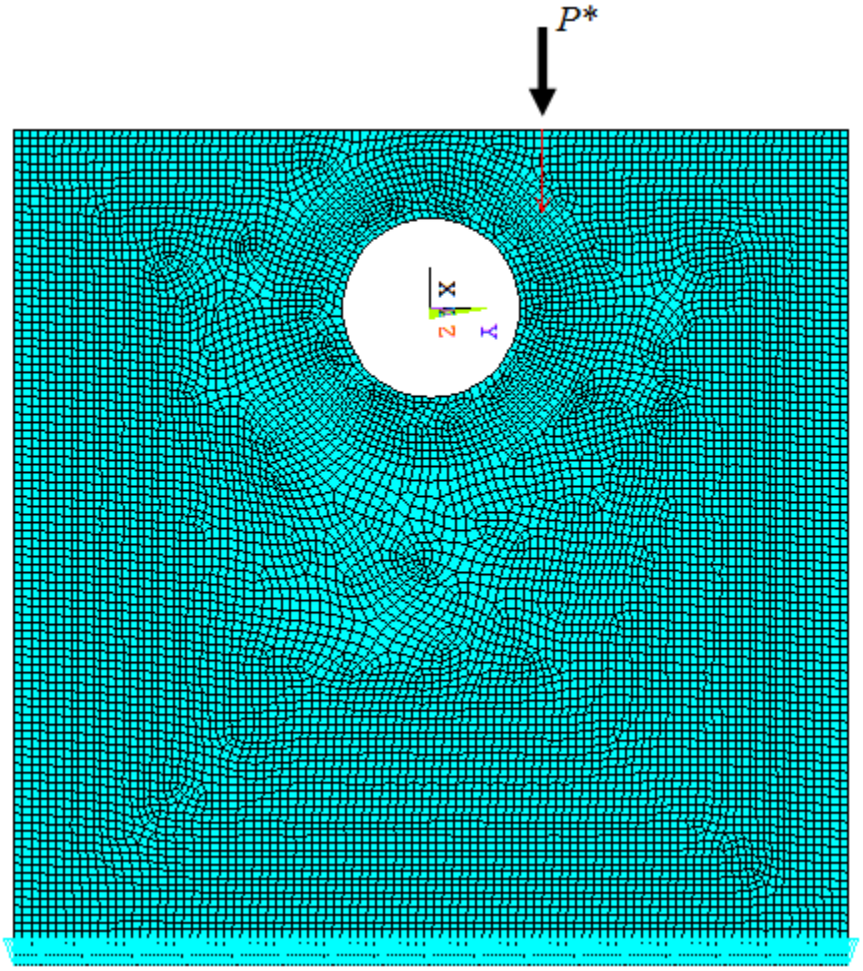

Fig. 7.12: Finite element model for the analysis of the offset loaded plate of *figure 7.2*

7.5 Results

After evaluating all the unknown Airy coefficients for each of the centrally loaded and offset loaded plate from the measured S*, the individual components of stress were obtained from *equations 7.11 through 7.13 and 7.19 through 7.21* respectively. These TSA results are compared with finite element analysis (ANSYS) predictions and those of references [4, 111 and 116]. Stresses are normalized with respect to σ_0 (= concentrated edge load P*/gross cross-sectional area = 200 lbs/(3.5″*3/8″) = 1.05 MPa (152.38 psi)). Stresses for the centrally loaded plate are plotted around and away from the boundary of the hole in *figures 7.13 and 7.14*, whereas normalized $\sigma_{rr} = \sigma_{yy}$ and $\sigma_{\theta\theta} = \sigma_{xx}$ are plotted along line AB of *figure 7.15* in *figures 7.16 and 7.17*. Stress results for the offset loaded plate are plotted around and away from the boundary of the hole in *figures 7.18 through 7.20*.

Angle θ of *figures 7.13, 7.14 and 7.18 through 7.20* is measured clockwise from the vertical x-axis, *figures 7.1 and 7.2*, and r is measured from the center of the hole, *figures 7.1 and 7.2*. The actual in-plane dimensions associated with *figures 7.16 and 7.17* are plotted normalized with respect to the radius R = 9.525 mm = 0.375″ of the hole.

The TSA results based on the presently simpler stress function agree with those from FEM and from the references [4, 111 and 116], although the transverse stress (*figure 7.17*) tends to differ from those by FEM along line AB as one move away from the hole. The reliability (or lack thereof) of the present TSA-determined σ_{xx} along line AB away from the hole might be influenced by the fact that the current stress function does not explicitly involve the contribution of the concentrated load, P as does that of reference [116].

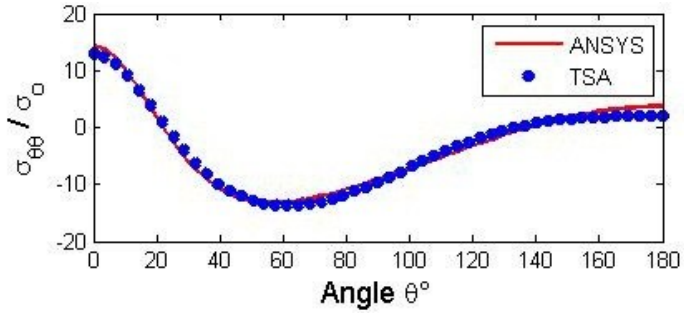

Fig. 7.13.A: Plot of $\sigma_{\theta\theta}/\sigma_0$ around the boundary of the hole (r/R = 1) from ANSYS and presently analyzed TSA for centrally loaded plate of *figure 7.1* with $m = 300$ input values, and $k = 9$ coefficients

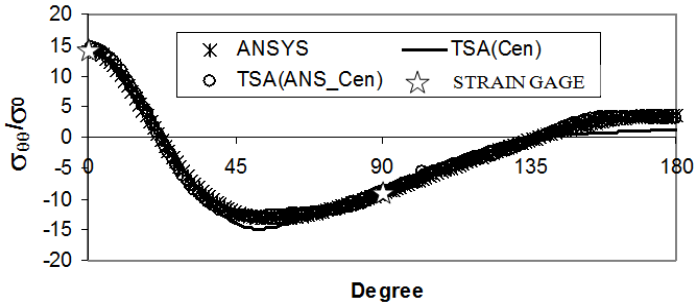

Fig. 7.13.B: Plot of $\sigma_{\theta\theta}/\sigma_0$ at the boundary of the hole (r/R = 1) from references [4 and 111]

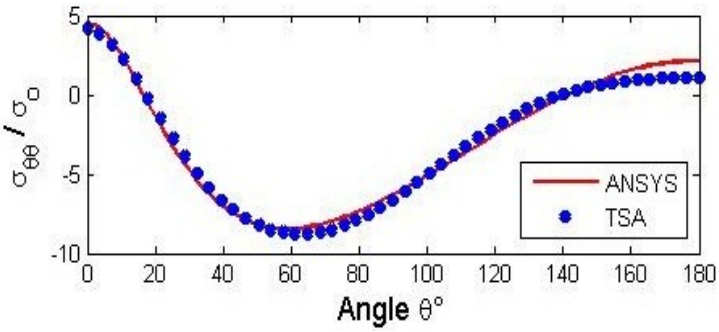

Fig. 7.14.A: Plot of $\sigma_{\theta\theta}/\sigma_0$ along r/R = 1.18 from ANSYS and for presently analyzed TSA for centrally loaded plate of *figure 7.1* with $m = 300$ input values, and $k = 9$ coefficients

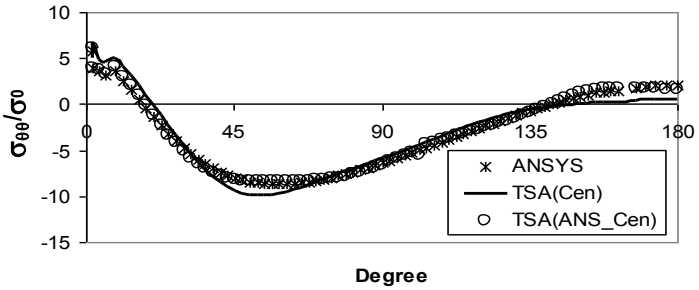

Fig. 7.14.B: Plot of $\sigma_{\theta\theta}/\sigma_0$ for selected locations shown in *figure 7.15* from references [4 and 111]

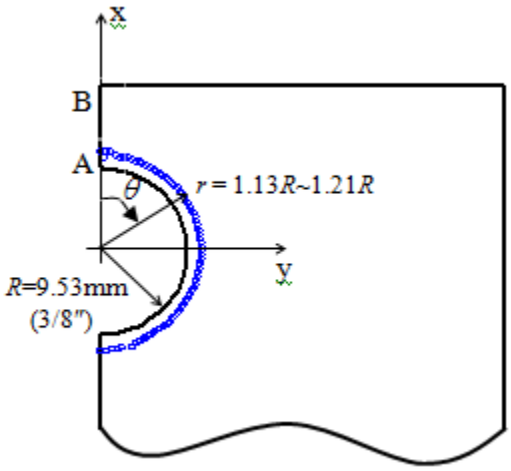

Fig. 7.15: Selected data locations for stress component determination

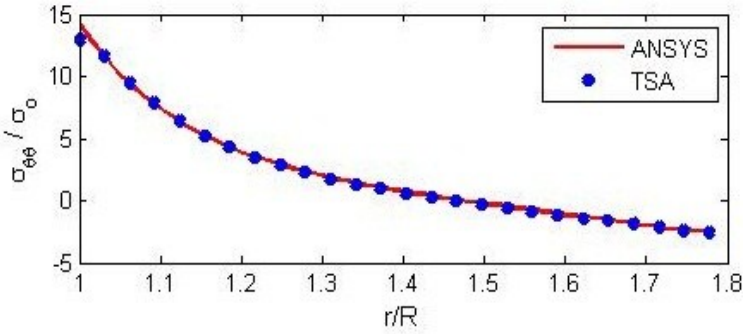

Fig. 7.16: Plot of σ_{yy}/σ_0 along AB of *figure 7.15* from ANSYS and for presently analyzed TSA for centrally loaded plate of *figure 7.1* with $m = 300$ input values and $k = 9$ coefficients

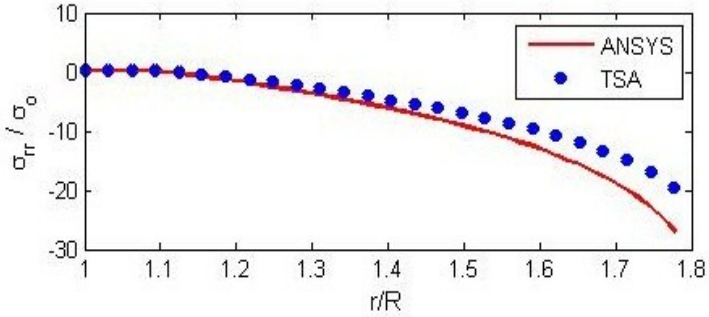

Fig. 7.17: Plot of σ_{xx}/σ_0 along AB of *figure 7.15* from ANSYS and for presently analyzed TSA for centrally loaded plate of *figure 7.1* with $m = 300$ input values and $k = 9$ coefficients

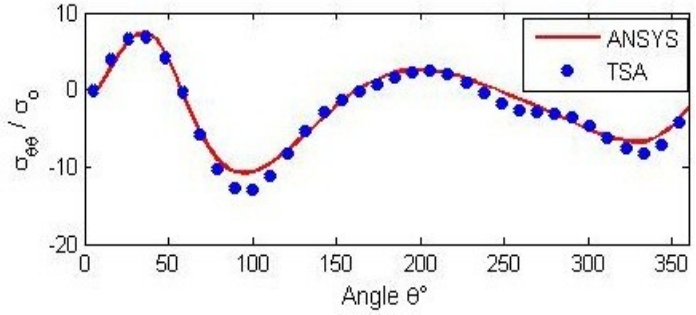

Fig. 7.18.A: Plot of $\sigma_{\theta\theta}/\sigma_0$ around the boundary of the hole (r/R = 1) from ANSYS and for presently analyzed TSA for offset loaded plate of *figure 7.2* with $m = 849$ input values, and $k = 17$ coefficients

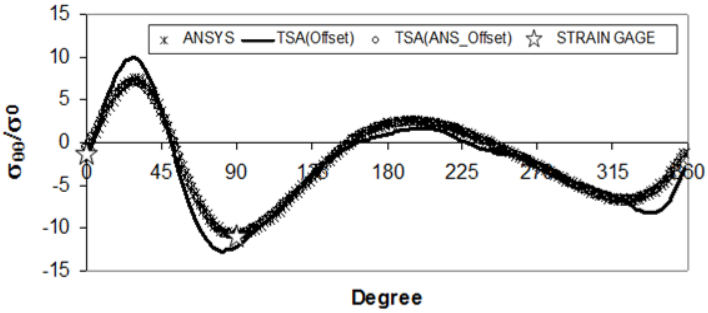

Fig. 7.18.B: Plot of plate of *figure 7.2* $\sigma_{\theta\theta}/\sigma_0$ at the boundary of the hole (r/R = 1) from references [4 and 116]

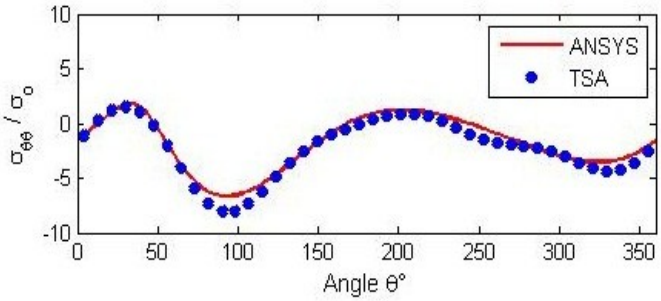

Fig. 7.19.A: Plot of $\sigma_{\theta\theta}/\sigma_0$ for the hole along r/R = 1.24 from ANSYS and for presently analyzed TSA for offset loaded plate of *figure 7.2* with $m = 849$ input values, and $k = 17$ coefficients

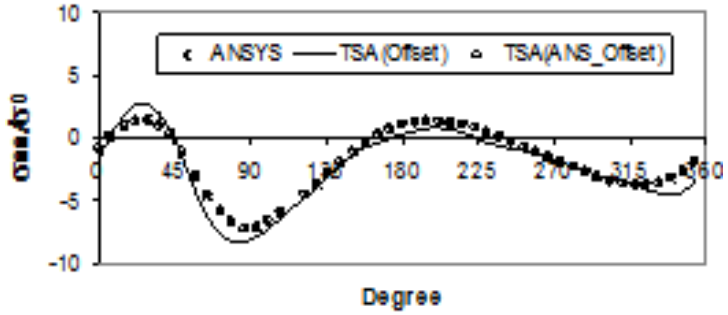

Fig. 7.19.B: Plot of $\sigma_{\theta\theta}/\sigma_0$ for selected locations shown in *figure 7.21* of plate of *figure 7.2* from references [4 and 116]

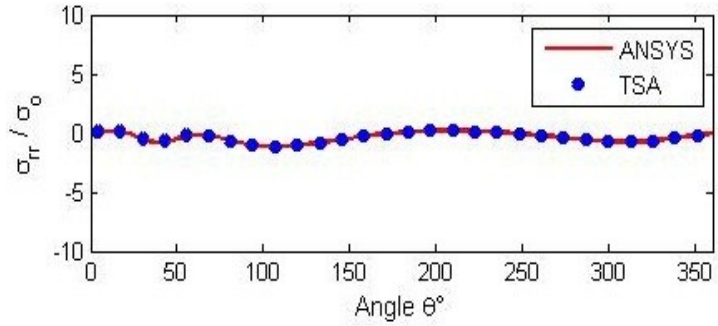

Fig. 7.20.A: Plot of σ_{rr}/σ_0 along r/R = 1.24 from ANSYS and for presently analyzed TSA for offset loaded plate of *figure 7.2* with $m = 849$ input values, and $k = 17$ coefficients

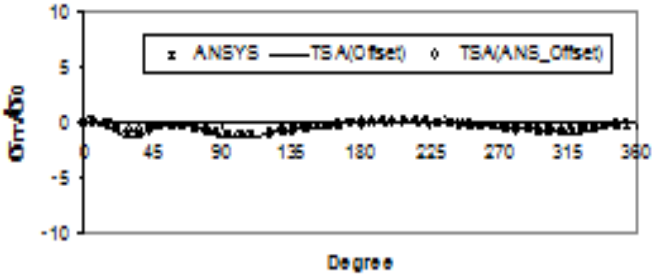

Fig. 7.20.B: Plot of σ_{rr}/σ_0 for selected locations of plate of *figure 7.2* shown in *figure 7.21* from reference [4 and 116]

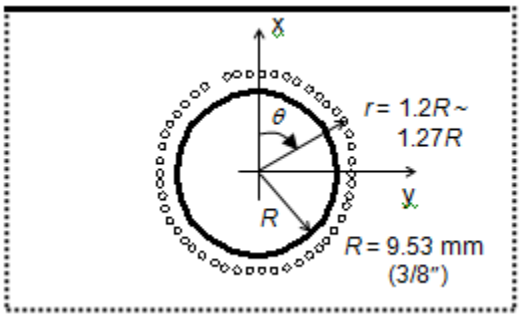

Fig. 7.21: Selected data locations for stress component determination

7.6 Summary and Conclusions

The stress analyses of the loaded perforated plate of *figures 7.1 and 7.2* are conducted by combining measured TSA temperatures with the relevant Airy's stress function based only on the extent of symmetry and *analytically* imposing traction-free conditions on the boundary of the hole. Unlike the original approach which explicitly included the contribution of the contact edge load, P, and thereby employed extensive amounts of algebra to form the more complicated stress functions [4, 111 and 116], the present method demonstrates excellent results are obtainable on and in the neighborhood of the hole for either case but by using the much simpler stress functions. The number of Airy coefficients employed here is also less than used in references [4, 111 and 116]. The number of Airy coefficients used for the centrally loaded plate by the present technique is $k = 9$ compared to $k = 15$ in reference [111]. Similarly, the number of Airy coefficients used for the present offset loaded plate used is $k = 17$ compared to $k = 25$ in reference [116]. The same number and source locations of the measured TSA input values are used here as in references [4, 111 and 116]. The presently evaluated individual components of the stresses compare well here with those from finite element analysis and reference [4, 111 and 116], *figures 7.13, 7.14 and 7.17 through 7.20*. Current results therefore demonstrate the ability to separate measured TSA data reliably into the individual stress components for these relative complicated situations without knowledge of the material constitutive properties, or distant geometry or loading conditions. The general method is suitable for finite (can be difficult theoretically) or infinite geometries. TSA enjoys the advantage of not having to differentiate the measured data. Imposing the traction-free conditions ($\sigma_{rr} = \sigma_{r\theta} = 0$) on the edge of the hole

analytically enables all of the Airy coefficients to be evaluated from measured TSA data. No supplemental experimental data (such as moiré or DIC or speckle, etc.) are needed.

The major contribution of this chapter is to demonstrate the ability to evaluate the stresses at and in the neighborhood of geometric discontinuities by TSA without the knowledge of the far-field loading conditions and to do so using simple stress functions. This technique gives the ability to obtain stresses on the edge of the geometric discontinuities despite unreliable measured data at such locations. While the presently relatively simple stress functions provide excellent stresses at and in the neighborhood of the hole, the current stresses are not reliable far away from the hole, particularly as one approaches the applied edge load. Although this research emphasizes the circular geometric discontinuity and a point load, the concept can be extended to more complicated geometries and loading conditions.

Chapter 8 : Thermoelastically Determined Stresses of Multiple Holes in a Finite Plate

8.1 Introduction

In the present chapter, Thermoelastic stress analysis (TSA) is used to determine the stresses in the vicinity of multiple holes in a finite geometry. The presence of smaller auxiliary hole near a central circular hole in a uniaxially loaded plate makes the stress analysis complicated. A major objective of the present work was to evaluate the stresses associated with two neighboring holes which are perpendicular and oblique to the direction of the loading and whose respective stresses interact and so as to influence the stress concentration factor at the boundary of the original hole, *figures 8.1 and 8.2*. Reference [3] used a similar technique to analyze the multiple perforated plate having the holes in the direction of loading. In that case the action of the smaller auxiliary hole reduced the tensile stress concentration factor at the larger (original) hole. Many engineering structures involve multiple perforated finite plate and it is important to be able to evaluate the stresses reliably for cases where theoretical or numerical approaches are not available. Some theoretical solutions and finite element analyses (FEA) can predict stresses provided the material constitutive properties and boundary/loading conditions are sufficiently well known. However, it is extremely difficult to obtain theoretical solutions for finite plates and for the finite element analysis boundary conditions are not always sufficiently well-known which is illustrated in this chapter for the oblique plate. Recognizing this difficulty

in obtaining theoretical solutions and finite element analysis for finite geometries, the present TSA results are compared with those from strain gages and approximated finite element analysis.

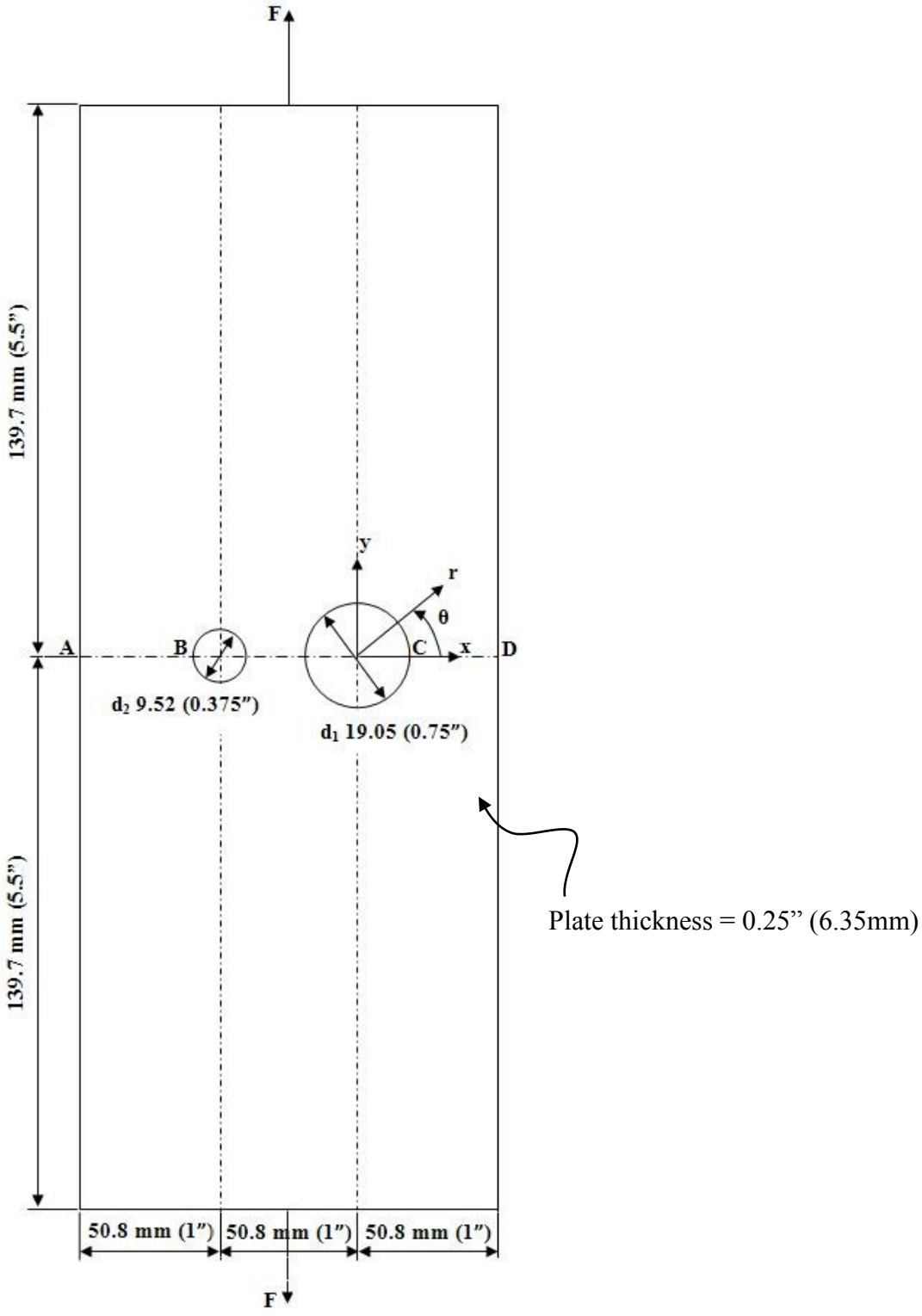

Fig. 8.1: Schematic geometry of a uniaxial tensile finite plate containing two side holes

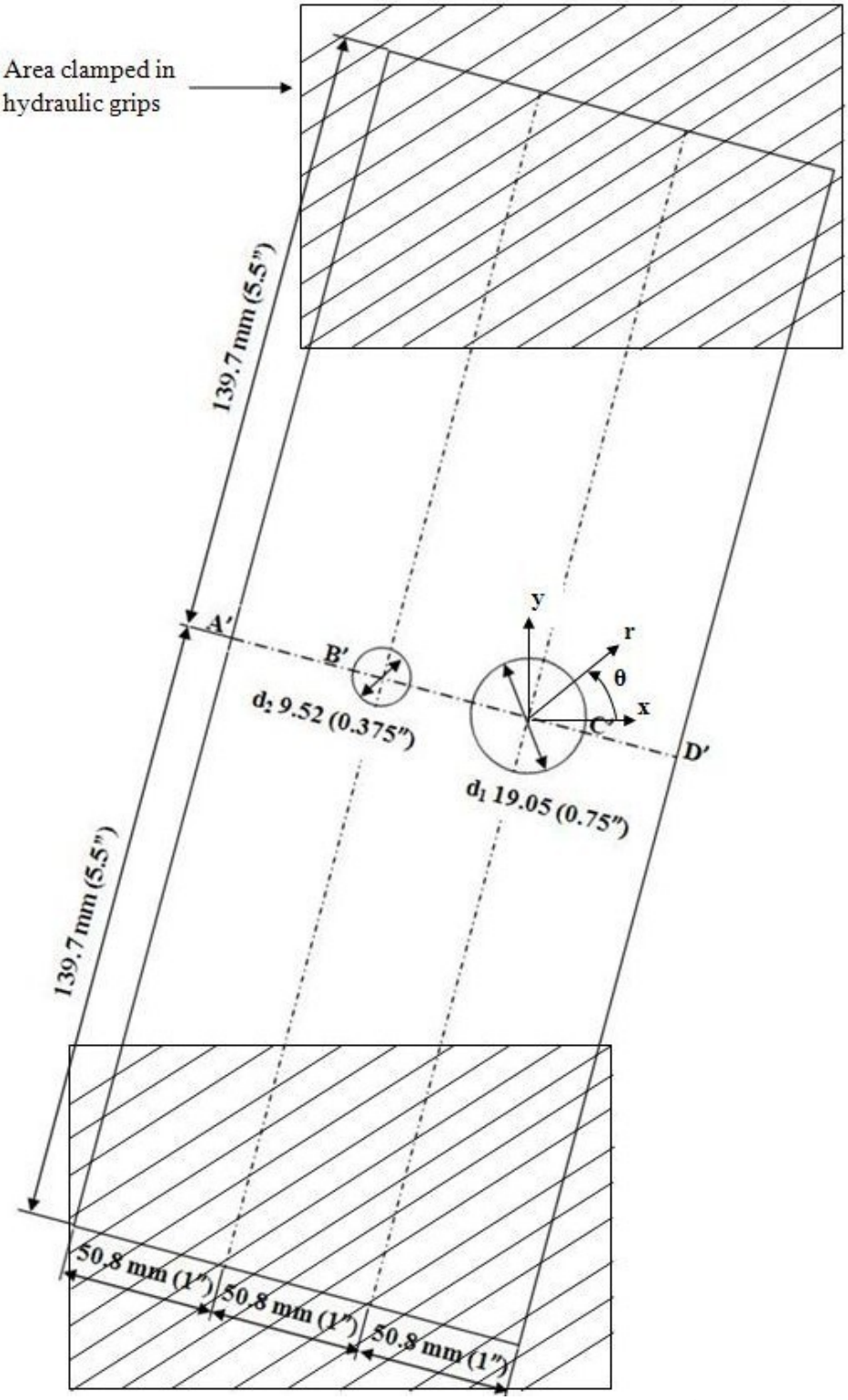

Fig. 8.2: Schematic geometry of an end-loaded finite incline plate (~15^{o} with respect to loading) containing two side holes

Following are the details of the plate tested for the associated analyses and results:

- Material of the plate: Aluminum 6061-T6 (Wiedenbeck, Inc., Madison, WI); Ultimate strength = 275 to 311 MPa (40 to 45 ksi) and Yield strength = 241 to 275 MPa (35 to 40 ksi).
- Cyclic Load = 3558.57 N (800lb) ± 2224.11 N (500lb) at 20Hz, unless indicated otherwise.
- Loading Range (F) = 4448.2 N (1000lb), unless indicated otherwise.
- Diameter of the large hole (d_1) = 19.05 mm (0.75″), drilled, *figures 8.1 and 8.2*.
- Diameter of the small hole (d_2) = 9.52 mm (0.375″), drilled, *figures 8.1 and 8.2*.
- Thickness of the plate (t) = 6.35mm (0.25”).
- Plate is symmetrical about the horizontal x-axis, *figure 8.1* and plate is inclined at an angle 15 deg with respect to the loading, *figure 8.2*.
- Length of the plate (L) ≈ 279.4 mm (11”), *figure 8.1*.
- Width of the plate (W) = 76.2 mm (3”), *figures 8.1 and 8.2*.
- Center distance between holes (c) = 25.4 mm (1”), *figures 8.1 and 8.2*.
- A strip gage consisting of 4 strain gages was mounted along CD in *figure 8.1;* C’D’ in *figure 8.2*.
- A strain gage was mounted on the curved edge of the hole to determine the strains accurately at the hole boundary.
- Four strain gages were mounted, two on the front and two on the back, to ensure proper specimen alignment by minimizing any out-of-plane bending.

The holes in the plate of *figure 8.1* are circular and horizontal with respect to the vertical direction of loading. The holes in that of *figure 8.2* are circular and inclined at angles of 15 deg with respect to the vertical direction of loading. The same plate was actually used in both cases. TSA is a non-contacting, non-destructive and non-invasive experimental technique that provides full-field stress on the surface of a mechanical component based on the temperature changes that occur with cyclic loading as result of the thermoelastic effect. If one records TSA measured data $S^* = K(\sigma_{xx} + \sigma_{yy}) = K(\sigma_{rr} + \sigma_{\theta\theta})$ and employs a relevant Airy stress function, it is possible to obtain the individual stress distributions in the multiply perforated plates, at least at and in the vicinity of the geometric discontinuities, without any complex mathematical algebra or additional experimental (like morié, holography, speckle, digital image correlation) and/or numerical techniques (nonlinear least squares). A two dimensional thermoelastic stress analysis was therefore conducted in a uniaxially loaded finite plate to determine the magnitude and distribution of stresses around two neighboring horizontal holes (*figure 8.1*) and inclined holes (*figure 8.2*) which are sufficiently close together that their respective stress fields interact. In addition to the present TSA results showed good agreement with the strain gages and finite element analyses, integrating the TSA evaluated stresses across the plate also satisfies equilibrium.

The stress functions utilized here are the same utilized in the Chapter 7 i.e., ϕ_{sym} of Chapter 7 is used to analyze the symmetrically-loaded plate and ϕ_{offset} of Chapter 7 is used to analyzed the unsymmetrically-loaded plate. Relative to evaluating the individual components of stresses, $R = r_1$, radius of the large hole or $R = r_2$, radius of the small hole and for all values of θ. Individual coordinate system is used in the analyses of each hole of *figures 8.1 and 8.2*. TSA-

wise, the doubly perforated plate of *figure 8.1 or 8.2* are analyzed by employing separate stress functions associated with individual coordinate systems, these individual coordinate systems having their origins at the center of the respective holes. Also, for the analysis associated with the large hole the recorded TSA data near that large hole was used along with respective stress function (based on the geometry) and similarly for the analyses of the small hole the data near the small hole was used along with the respective stress function (based on the geometry). *Figures 8.1 and 8.2* explicitly indicate the coordinates for the large hole. Coordinates with the origin now at the center of the small hole were similarly used relative to the small hole. The plate in *figure 8.1* has an axis of symmetry (x-axis) which simplifies the stress function by having a number of Airy coefficients going to zero and further reducing the number of Airy coefficients by *analytically* imposing the traction-free conditions on the edge of the respective holes. For the analysis of *figure 8.1,* the plate is loaded vertically with the MTS hydraulic grips, and the far-field loading conditions are well known. It is therefore possible to conduct a confident finite element analysis of this loaded plate against which to compare TSA results. That the plate in *figure 8.2* is unsymmetrical about both the x- and y-axes implies a more complicated stress function necessitating more Airy coefficients. Reducing the number of these coefficients by imposing the traction-free conditions on the edge of the respective holes *analytically* now becomes increasingly important. Furthermore, the boundary conditions in the unsymmetrical plate of *figure 8.2* are not well known, so it is very complicating the ability to confident finite element analysis. This makes the strain gage results more important for comparison with TSA results.

8.2 Experimental Details

8.2.1 Specimen Details, Preparation and Loading

Figures 8.1 and 8.2 show the plate geometry, dimensions, and orientation and location of the coordinate axes. It is worth mentioning that the same experimental setup was used to analyze both the symmetrical and unsymmetrical plate. Following are the details of the horizontal plate of *figure 8.1* and incline plate of *figure 8.2*, tested for the succeeding analyses and results:

Material of the plate: Aluminum 6061-T6 (Wiedenbeck, Inc., Madison, WI); Ultimate strength = 275 to 311 MPa (40 to 45 ksi), Yield strength = 241 to 275 MPa (35 to 40 ksi), Elastic Modulus E = 68.95 GPa (10 x 10^6 psi) and Poisson's ratio $\nu = 0.33$).

- Unless stated otherwise, the plate was subjected to a cyclically varying sinusoidal load with a mean value of 3558.57 N (800lb), maximum value of 5782.68 N (1300lb) and a minimum value of 1334.46 N (300lb) at a frequency of 20Hz.

- 3558.57 N (800lb) ± 2224.11 N (500lb) at 20Hz, unless state otherwise.
- Loading Range (F) = 4448.22 N (1000lb), unless state otherwise.
- Diameter of the large hole (d_1) = 19.05 mm (0.75″).
- Diameter of the small hole (d_2) = 9.52 mm (0.375″).
- Thickness of the plate (t) = 6.35 mm (0.25″).
- Length of the plate (L) ≈ 279.4 mm (11”).
- Width of the plate (W) = 76.2 mm (3”).
- Center distance between holes (c) = 25.4 mm (1”).

- Plate is symmetrical about the horizontal x-axis, *figure 8.1* and plate is inclined at an angle 15 deg with respect to the loading, *figure 8.2.*

The aluminum plate was sprayed with Krylon Ultra-Flat black paint to enhance the thermoelastic pattern *(figure 8.3)*. However, before applying the black paint, the plate was polished with 400 grit sand paper so as to have an ideal surface finish. Care was taken when machining to ensure that the holes in the specimen do not have round edges. The enhanced emissivity and sharp edges of the holes provides reliable temperature data up to near the edge of the holes. Plane stress is assumed and the stresses through the thickness remain unchanged.

Fig. 8.3: Aluminum plate coated with Krylon Ultra-Flat black paint

The symmetrical plate of *figure 8.1*, was clamped vertically between the cross heads of the MTS closed-loop hydraulic testing machine with the help of hydraulic grips making the plate symmetrical about x-axes as seen in *figure 8.4* The unsymmetrical plate of *figure 8.2* was made incline at an angle of 15 deg with respect to the loading vertical and clamped between the hydraulic grips. The hydraulic grips apply a uniform clamping pressure over both ends of the specimen of *figures 8.1 and 8.2.* The loads were applied using a load cell 20 Kips capacity and hydraulic grips are capable of applying up to 18.5 Kips (Room B321, Engineering Hall). This MTS machine can operate in any of the following four ranges 10%, 20%, 50% and 100%

measure of capacity (i.e., 2 Kips, 4 Kips, 10 Kips and 20 Kips). For the ongoing analyses, the 10% range was utilized which allows for a maximum load of 8896.45 N (10% of 20,000 lbs = 2000 lbs). For the TSA analyses, the specimen was tested at a loading range (minimum to maximum) of 4448.2 N (1000 lbs) at a sinusoidal frequency of 20Hz.

The test plate of *figures 8.1 and 8.4* was aligned between the top and the bottom grips which provides symmetrical loading about the horizontal axis (x-axis) and the plate that of *figures 8.2 and 8.5* was inclined at an angle of 15^{o} (with respect to the vertical loading) which makes the plate unsymmetrical about both the x- and y-axes. In clamping the specimen between the hydraulically operated grips, particular care was taken to minimize any out-of-plane bending of the plate by ensuring agreement of the strains obtained from the strain gages mounted on the front and the back faces of the plate.

Fig. 8.4: Symmetrically-loaded specimen in hydraulic grips

Fig. 8.5: Unsymmetrically-loaded specimen in hydraulic grips

8.2.2 TSA Recording and Calibration

TSA is based on the fact that materials experience small temperature changes when compressed or expanded. A sensitive infrared camera records the small temperature changes due to applied mechanical loads. This experimental technique makes it possible to infer the in-plane stresses in the multiply perforated plate by computing the small temperature changes induced as a result of a cyclic load. It is worth mentioning that the amplitude of a TSA signal is linearly dependent on the cyclic stress amplitude. A DeltaTherm DT1410 camera produced by Stress Photonics Inc., was employed to acquire the full-field thermal measurements in this study. This DT1410 camera uses 256 horizontal × 256 vertical staring photon detector arrays to detect the thermal emissivity. The photon detectors require cooling by liquid nitrogen in order to achieve high resolution. The DeltaTherm's photon array detectors synchronize with the applied cyclic loading with a sufficient frequency to maintain the adiabatic state in the tested material. Therefore, sine function cyclic loading was applied to the specimens at a frequency of 20 Hz. Since the input signal to the DeltaTherm camera comes from the MTS machine, only the thermal emissivity that responds to the applied frequency will be integrated. The applied cyclic loading not only avoids any transient thermoelastic effect but also rejects any non-relevant background thermal emissivity. When adiabatic conditions are achieved and maintained during the test, the relation between the induced temperature changes and the change in the sum of principal stresses is linear, and thus the variation in the sum of principal stresses can be experimentally inferred by processing the recorded thermoelastic signal, S.

The loading and recording for the symmetrically-loaded and unsymmetrically-loaded plate is illustrated in *figures 8.6 and 8.7* respectively. The Delta Therm camera (Stress Photonics

Inc., Madison, WI, USA), which is utilized to record the temperature variations in the perforated plates, is aligned to be exactly perpendicular to the surface of the plate. This was done with the aid of two spirit levelers which are mounted at the base of the TSA camera *(figures 8.6 and 8.7)*. The experimental setup includes the DeltaTherm DT1410 camera, and aluminum plate loaded, *figure 8.5* in-plane bending as was in tension through the hydraulic grips. *Figure 8.8* is photograph of an oscilloscope used to monitor the applied load and the sinusoidal frequency. The actual pixel size at the plate in the analyses was found to be 0.323 mm (0.0127"). *Figures 8.9 and 8.10* show an actual TSA image for each of the symmetrical and unsymmetrical loading. They contain (256x256 = 65,536) data values, of which approximately 60,000 pixels cover the plate. The DT1410 camera records the full-field IR images integrated over a two minutes duration. Recognizing the typical inability to provide reliable edge data, no TSA input values are used within at least two data positions (pixels), i.e. approximately 0.65 mm (0.025") of the boundary of a hole.

Figures 8.9 and 8.10 shows an actual TSA image for symmetrical and unsymmetrical plate as recorded and displayed by the Delta Vision software which provides data acquisition and interpretation. Delta Vision Software records the 256 horizontal x 256 vertical pixels and this information was exported to EXCEL® in the form of 256 x 256 matrix. The pixel S* data associated with *figures 8.9 and 8.10* were subsequently processed using MATLAB and the corresponding MATLAB images are shown in *figures 8.11 and 8.12.* The 'contourf ( )' function in MATLAB is one of the more practical ways of making contour plots. The scales in *figures 8.9 through 8.12* are in terms of S* temperature data and this temperature data can easily be converted to S by dividing by *K*, calibration coefficient.

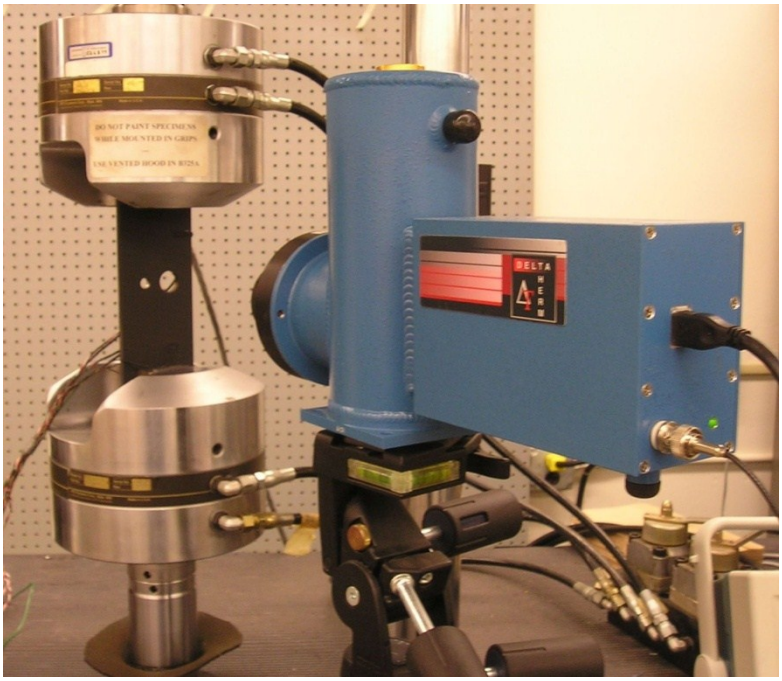

Fig. 8.6: Specimen loading and recording for the symmetrically-loaded plate

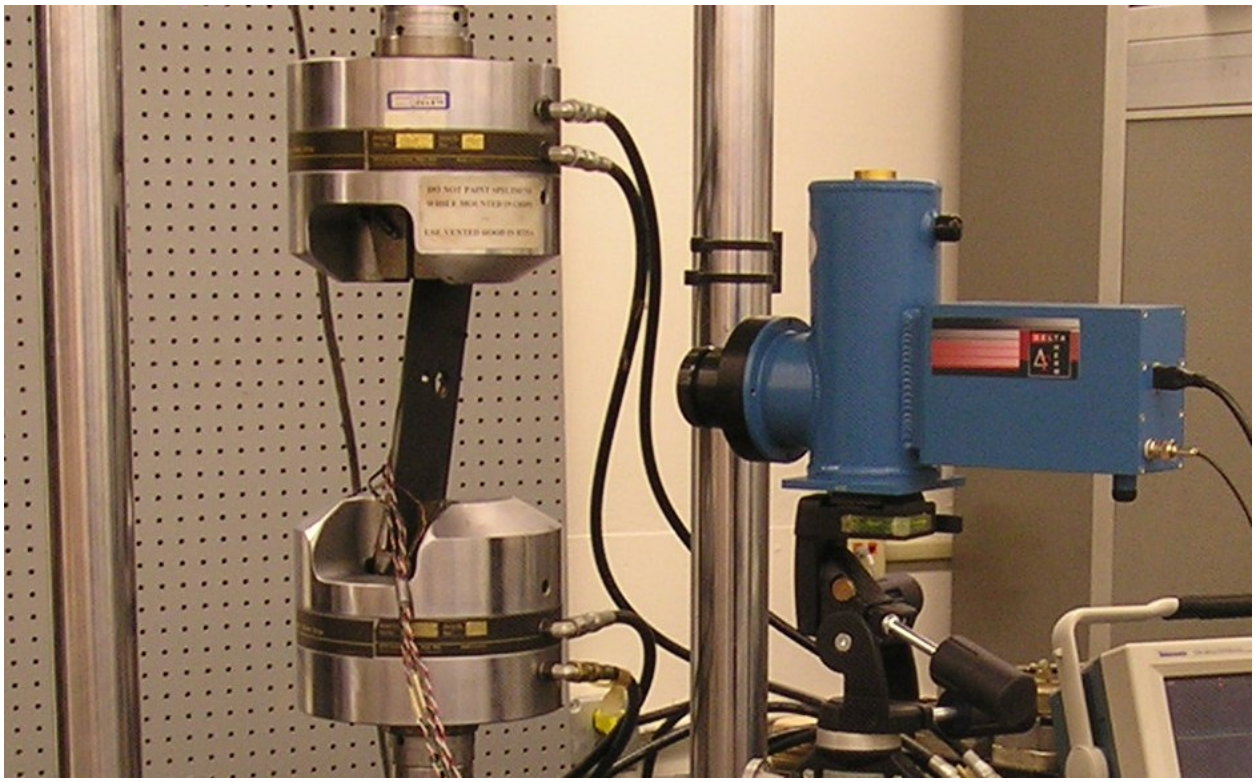

Fig. 8.7: Specimen loading and recording for the unsymmetrically-loaded plate

Fig. 8.8: Oscilloscope for accurate measurement of cyclic loads

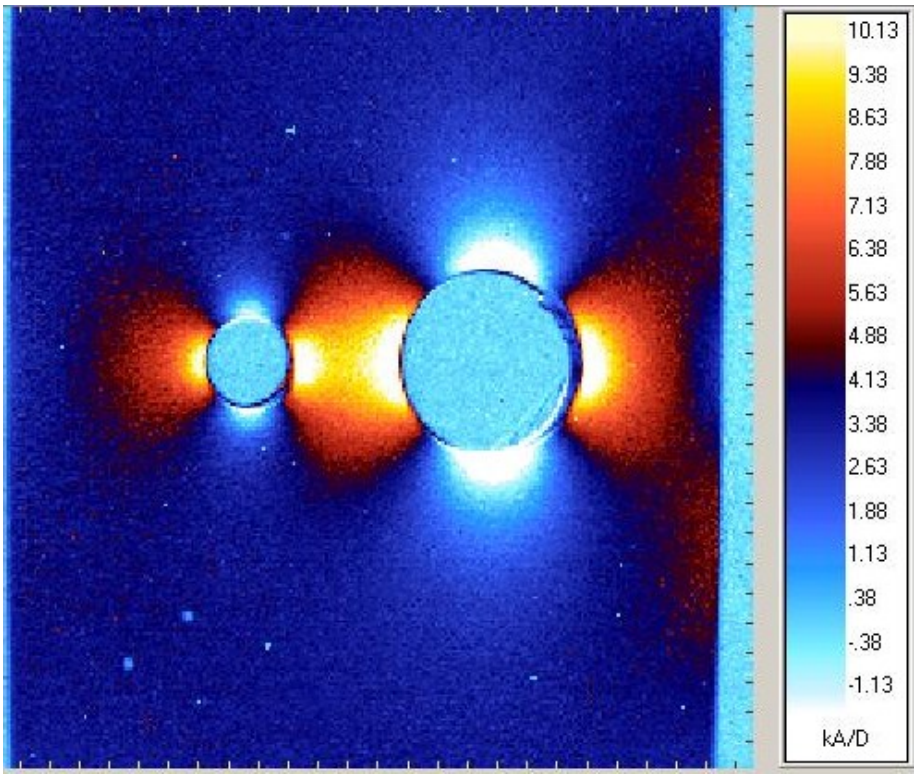

Fig. 8.9: Actual recorded TSA image, S* for the symmetrically-loaded plate, for a load range of 4448.22 N (1000lb)

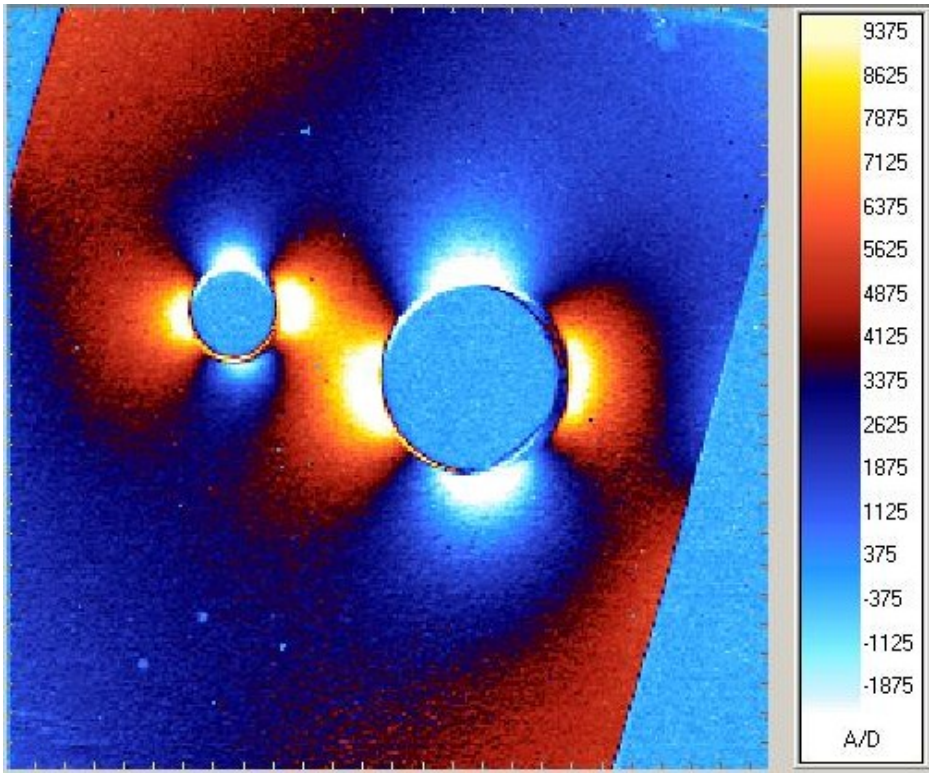

Fig. 8.10: Actual recorded TSA image, S* for the unsymmetrically-loaded plate, for a load range of 4448.22 N (1000lb)

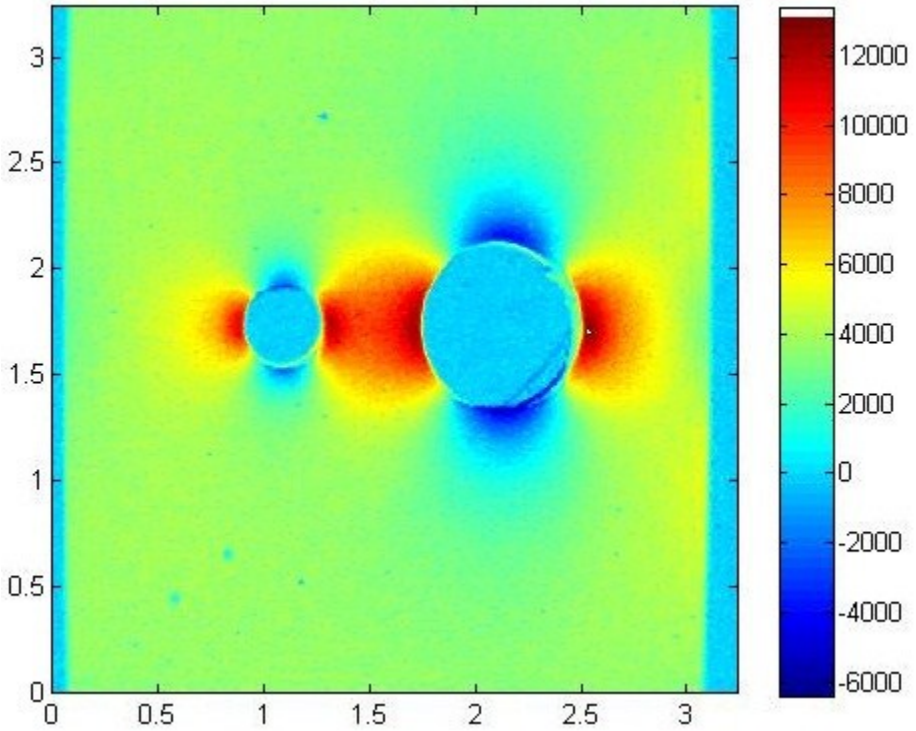

Fig. 8.11: Original recorded TSA pixel data, S* of *figure 8.9* re-plotted using MATLAB

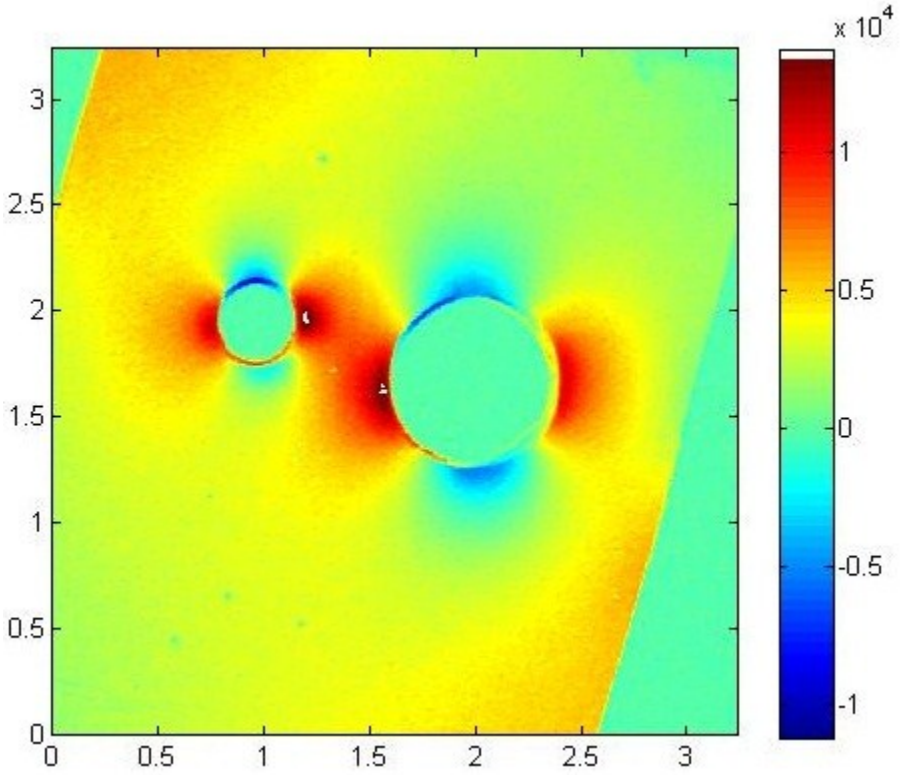

Fig. 8.12: Original recorded TSA pixel data, S* of *figure 8.10* re-plotted using MATLAB

The strain gages which were bonded on the right curved surface of the large hole and associated electrical leads are visible in *figures 8.9 through 8.12*

Thermoelastic images are normally presented referred to a scale expressed in thermal units. These thermal units can be converted to the units of the using *equation 8.1*. As discussed in this section, under plane stress, the temperature effects relating the stresses for isotropic materials are governed by the following equation:

$$S^* = K\Delta S = K[\Delta(\sigma_1 + \sigma_2)] = K[\Delta(\sigma_{rr} + \sigma_{\theta\theta})] = K[\Delta(\sigma_{XX} + \sigma_{YY})] \quad (8.1)$$

where S^* is the recorded TSA signal, K is the thermo-mechanical coefficient (determined experimentally), and ΔS is the change of the sum of the normal stresses. S is also called the isopachic stress or the first stress invariant.

The Thermo-mechanical coefficient can after be determined in a region of uniform known stress field. The holes in the present specimen did not provide a uniform stress field. Therefore uniaxial uniform tensile calibration specimen was consequently needed which is exactly similar to the actual test specimen in terms of the material, painted surface and loading rate *(figure 8.13)*. The calibration specimen was coated at the same time by the same person, with the same Krylon black paint, using an identical technique as used for the actual test specimens of *figures 8.1 and 8.2*. The calibration specimen used is of the same material as the actual test specimen (Aluminum 6061-T6), 279.4 mm (11″) in length, 25.4 mm (1″) wide and 6.35 mm (0.25″) thick. Thus, knowing the recorded thermoelastic signal, S^*, applied load and the cross sectional area of the specimen, the value of the thermomechanical coefficient, K = 406 U/MPa (2.8 U/psi), was obtained. Since both these experiments (*figures 8.1 and 8.2*) were performed on the same day, the same calibration value can be used for both the experiments.

Figure 8.14 shows the calibration specimen in the hydraulic grips. While *figure 8.15* is the TSA recorded image for the same load range of 4448.22 N (1000lb). The calibration specimen contained a total of four strain gages(away from the TSA scanned region), two on the front and two on the back (one longitudinal and one transverse on each side), to monitor any out of plane bending in the specimen. The holes at the ends of the tensile specimen of *figure 8.12* were associated with the specimen and play no present role in the present analysis.

The local perturbations to the uniform stress in TSA image at top and bottom in *figure 8.15* are due to strain gages.

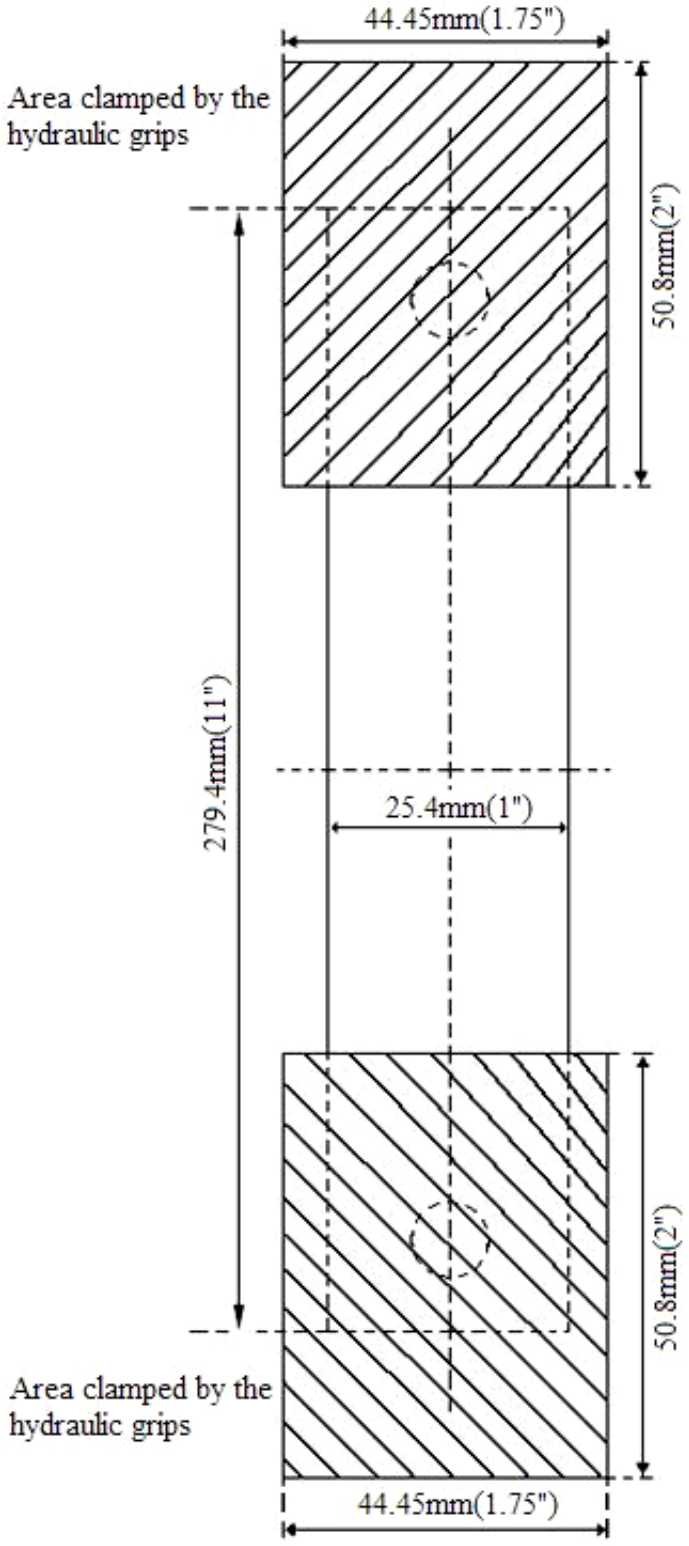

Fig. 8.13: Schematic of the TSA calibration specimen

Fig. 8.14: Calibration specimen loaded in hydraulic grips

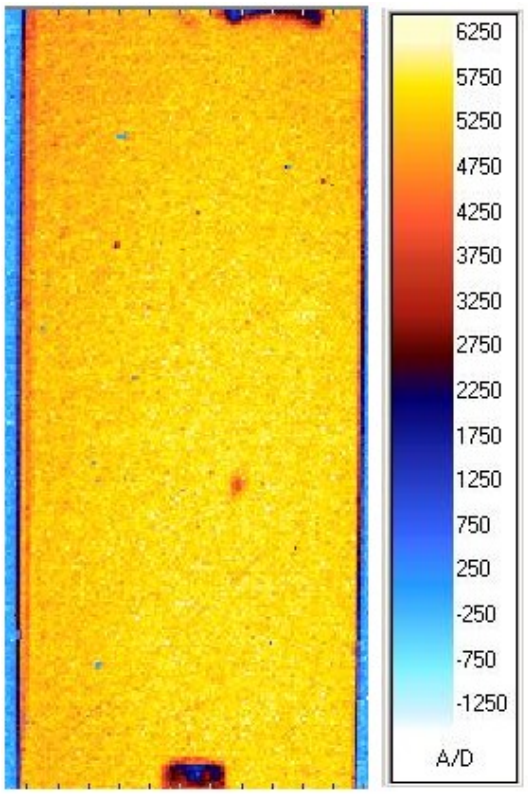

Fig. 8.15: Actual recorded TSA image for the calibration specimen, S*, for a load range of 4448.22 N (1000lb)

8.3 Data Processing

The thermal images of *figures 8.9 and 8.10* each contains approximately 60 thousands TSA measured values throughout the specimens of *figures 8.1 and 8.2*. Since the objective of this research was to evaluate individual components of stress in the region of both the holes, the analyses emphasize utilizing measured thermal data *S** which originate in the neighborhood of the respective holes. However, recognizing the typical unreliability of TSA data near an edge, no TSA input values are employed within at least two (pixels) data positions approximately 0.6451 mm (0.0254″) from the boundary of the each hole. Therefore, the source locations of TSA input data selected for the small and the large hole extend from near the inner radius for each hole [corresponding radius of hole + (2 x actual pixel size)] and the outer radius is [2 x radius of small hole] and [2 x radius of large hole] respectively. The symmetrically-loaded plate is symmetrical about the x-axis *(figure 8.1)*. Therefore the recorded TSA data obtained were averaged about the x-axis so that only one half of the plate is considered during thermoelastic stress analyses. For the analysis of the unsymmetrically-loaded plate, the recorded S data were selected without considering any symmetry.

With reference to the symmetrically-loaded the measured TSA values of *S** is averaged about the symmetrical x-axis and for unsymmetrically-loaded plate the measured TSA values of *S** in complete region in the vicinity of the hole is taken as input, and the isopachic stress expressions in Chapter 6 (which are based on imposing $\sigma_{rr} = \sigma_{r\theta} = 0$ *analytically* at r = R (where $R = R_1$, radius of the large hole or $R = R_2$, radius of the small hole) and for all values of θ), one can develop the following matrix equation:

$$[A]_{mxk}\{c\}_{kx1} = \{d\}_{mx1} \tag{8.2}$$

Re-writing *equation 8.2* for the symmetrically-loaded plate gives *equation 8.3 as follows,*

$$\begin{bmatrix} S_{r_1,\theta_1}(b_0,c_0,d_1',b_2',d_2',b_3',d_3',b_4',d_4',b_5',d_5'.....b_N',d_N') \\ S_{r_2,\theta_2}(b_0,c_0,d_1',b_2',d_2',b_3',d_3',b_4',d_4',b_5',d_5'.....b_N',d_N') \\ S_{r_3,\theta_3}(b_0,c_0,d_1',b_2',d_2',b_3',d_3',b_4',d_4',b_5',d_5'.....b_N',d_N') \\ . \\ . \\ . \\ . \\ S_{r_m,\theta_m}(b_0,c_0,d_1',b_2',d_2',b_3',d_3',b_4',d_4',b_5',d_5'.....b_N',d_N') \end{bmatrix}_{mxk} \begin{bmatrix} b_0 \\ c_0 \\ d_1' \\ b_2' \\ d_2' \\ . \\ b_N' \\ d_N' \end{bmatrix}_{kx1} = \begin{bmatrix} S_1 \\ S_2 \\ S_3 \\ S_4 \\ . \\ . \\ . \\ S_m \end{bmatrix}_{mx1} \tag{8.3}$$

Re-writing *equation 8.2* for the unsymmetrically-loaded plate gives *equation 8.4 as follows,*

$$\begin{bmatrix} S_{r_1,\theta_1}(b_0,c_0,A_0,d_1,d_1',b_2,d_2,c_3,d_3,b_4,d_4,...,b_N,d_N,b_2',d_2',...,b_N',d_N') \\ S_{r_2,\theta_2}(b_0,c_0,A_0,d_1,d_1',b_2,d_2,c_3,d_3,b_4,d_4,...,b_N,d_N,b_2',d_2',...,b_N',d_N') \\ S_{r_3,\theta_3}(b_0,c_0,A_0,d_1,d_1',b_2,d_2,c_3,d_3,b_4,d_4,...,b_N,d_N,b_2',d_2',...,b_N',d_N') \\ . \\ . \\ . \\ . \\ S_{r_m,\theta_m}(b_0,c_0,A_0,d_1,d_1',b_2,d_2,c_3,d_3,b_4,d_4,...,b_N,d_N,b_2',d_2',...,b_N',d_N') \end{bmatrix}_{mxk} \begin{bmatrix} b_0 \\ c_0 \\ A_0 \\ d_1 \\ d_1' \\ b_2 \\ d_2 \\ . \\ b_N \\ d_N \\ . \\ b_N' \\ d_N' \end{bmatrix}_{kx1} = \begin{bmatrix} S_1 \\ S_2 \\ S_3 \\ S_4 \\ . \\ . \\ . \\ S_m \end{bmatrix}_{mx1} \tag{8.4}$$

where matrix [A] involves the *m (*m_1 for the small hole, m_2 for the large hole for symmetrically-loaded plate and m_3 for the small hole, m_4 for the large hole for unsymmetrically-loaded plate*)* Airy isopachic equations in polar coordinates, *r* and θ. One horizontal expression of the upper

portion of the [A] matrix of *equations 8.3 and 8.4* exists for each measured input data value of S (= S^*/K) associated with symmetrically and unsymmetrically-loaded plate. Vector {c} of *equation 8.3* contains the k unknown Airy coefficients (i.e., b_0, c_0, d_1', b_2', d_2', …, b_N', d_N') and vector {c} of *equation 8.4* containing k unknown Airy coefficient (i.e., b_0, c_0, A_0, d_1, d_1', b_2, d_2, c_3, d_3, b_4, d_4,…, b_N, d_N, b_2', d_2', …, b_N', d_N'). Vector {d} of *equations 8.3* and 8.4 are composed of the m measured TSA data values of $S=S^*/K$ corresponding to the recorded data for the respective loaded plate used in the S to form matrix [A]. The least-squares method was employed to solve the over-determined matrix equation $Ac = d$ of *equations 8.3 and 8.4*. *Equations 8.3 and 8.4* are solved for unknown Airy coefficients using the '\' matrix division operator or pseudo inverse 'pinv' operator in MATLAB. Both of these operators use the algorithm for least squares and calculates vector {c} by *c = A\d or c = pinv(A)*d.*

For analyzing the rectangular component of stresses, one uses the following transformation matrix:

$$\begin{bmatrix} \sigma_{XX} \\ \sigma_{YY} \\ \sigma_{XY} \end{bmatrix} = \begin{bmatrix} \cos^2\theta & \sin^2\theta & -2\sin\theta.\cos\theta \\ \sin^2\theta & \cos^2\theta & 2\sin\theta.\cos\theta \\ \sin\theta.\cos\theta & -\sin\theta.\cos\theta & \cos^2\theta-\sin^2\theta \end{bmatrix} \begin{bmatrix} \sigma_{rr} \\ \sigma_{\theta\theta} \\ \sigma_{r\theta} \end{bmatrix} \tag{8.5}$$

8.4 Finite Element Analysis

As means of assessing the quality of the TSA results, the latter are compared with those predicted from finite element analysis (FEA). The aluminum (E = 68.95 GPa (10 x 10^6 psi) and Poisson's ratio ν = 0.33) plate described in section 8.1 was modeled using ANSYS. A finite element analysis requires accurately knowing the loading and external boundary conditions. For the symmetrically-loaded plate of *figures 8.1 and 8.4*, one can apply symmetry boundary condition along the line of symmetry and a uniform tensile stress of 9.19 MPa (1333.33 psi) at the other end as shown in *figures 8.16 and 8.17*. This assumes that the specimen is sufficiently long that the lack of symmetry about vertical central line is insignificant at the loading ends. The boundary conditions of the unsymmetrically-loaded plate are not well known, which challenges the modeling of finite element analysis. The vertical movement of the hydraulic grips of *figure 8.5* will include both tension and in-plane bending to the ends of the plate. Nevertheless an approximate finite element model was made for the unsymmetrically-loaded plate having x-constraint at both the ends of the plate which is the case in the experimental setup that the ends of the plate do not move in x-direction (horizontally) when loaded. The far-field stress of 9.19 MPa (1333.33 psi) is also applied at both the ends. The FE model used 8-node Isoparametric elements (ANSYS element type: Plane-82). A very fine mesh was used in the neighborhood of the holes to enhance accuracy as shown in *figures 8.16 through 8.19*. For the analysis of the large hole in the symmetrically-loaded plate, the mesh covering the entire one half of the plate utilizes a total of 3,500 elements and 10,829 nodes. For the analysis of small hole in the symmetrically-loaded plate, the mesh covering the entire one half of the plate utilizes a total of 3,323 elements and 10,302 nodes. The mesh covering the entire plate for the analysis of large hole in the

unsymmetrically-loaded plate utilizes a total of 9,495 elements and 28,990 nodes. For the analysis of small hole in the unsymmetrically-loaded plate, the mesh covering the entire plate utilizes a total of 8,236 elements and 25,195 nodes. These FEM meshes had been refined until the ANSYS results did not vary more than 0.2% on the periphery of either the small or large hole.

Figure 8.20 is the displacement plot (USUM) of unsymmetrically-loaded plate. It is worth nothing that the plate is tilted by small amount along the loading direction which does not occur physically in the experiment i.e., experimentally the entire far-field will experience the same displacement. Although challenging, that there are no theoretical solutions for these perforated cases motivating one to try to predict the situation.

The results of a 3-D FEM analysis in the Appendix A8 validate the plane-stress assumptions.

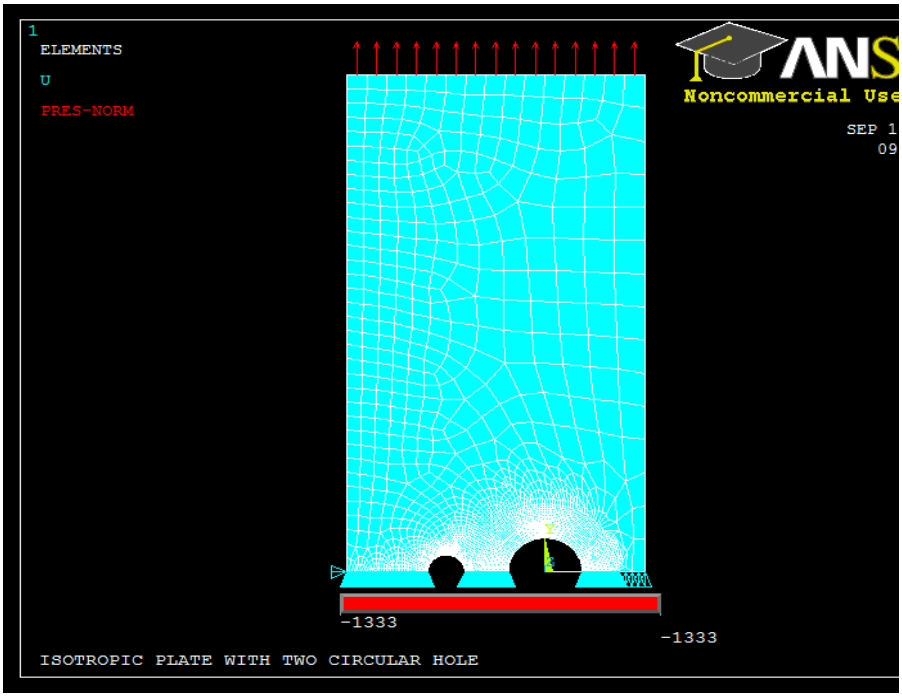

Fig. 8.16: Finite element model for the analysis of the large hole in the symmetrically-loaded plate

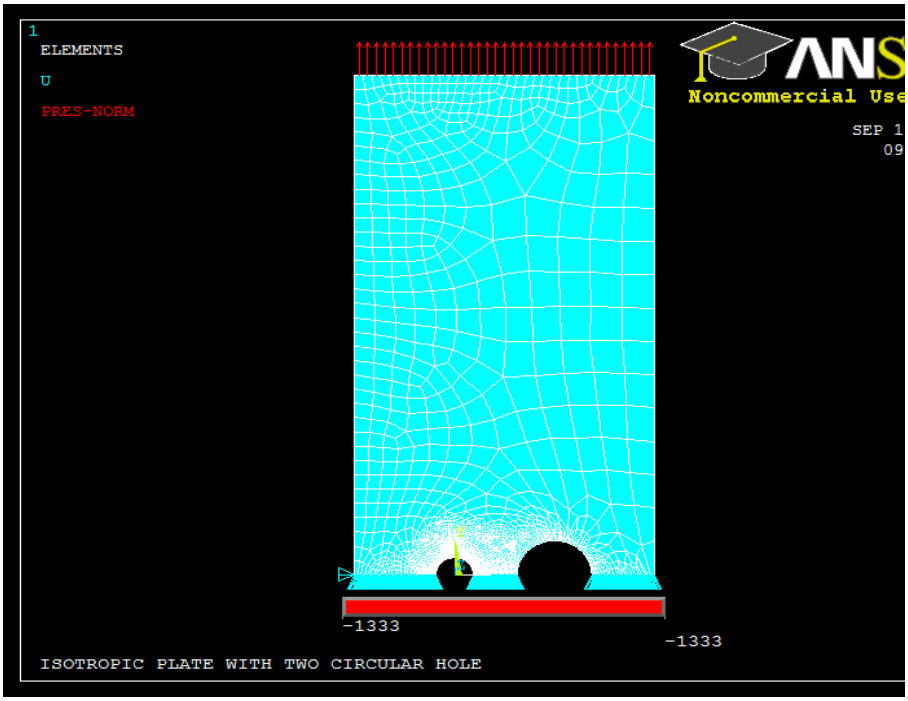

Fig. 8.17: Finite element model for the analysis of the small hole in the symmetrically-loaded plate

Fig. 8.18: Finite element model for the analysis of the large hole in the unsymmetrically-loaded plate

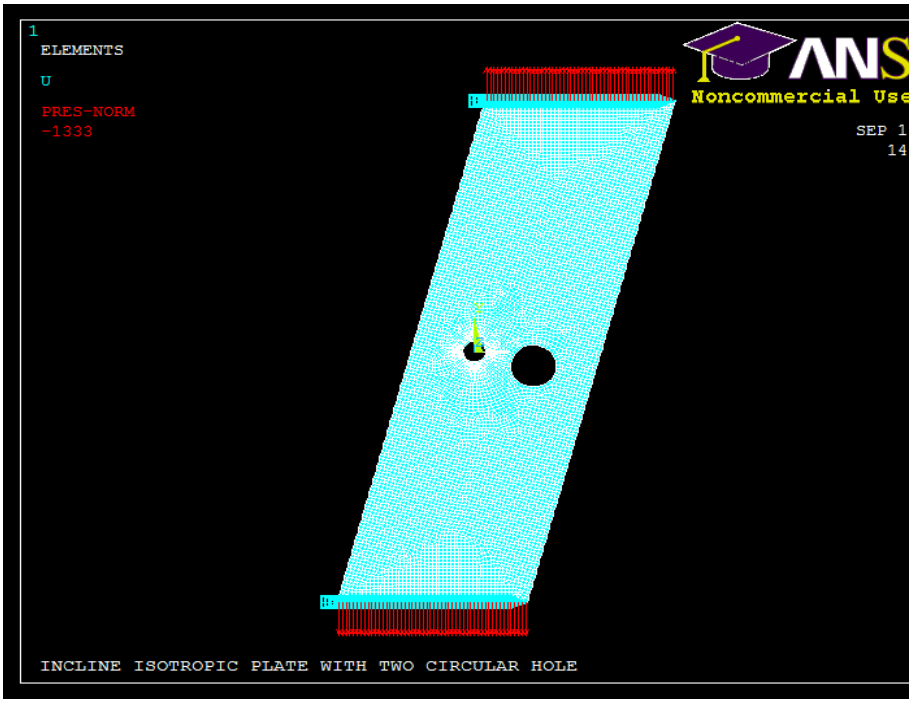

Fig. 8.19: Finite element model for the analysis of the small hole in the unsymmetrically-loaded plate

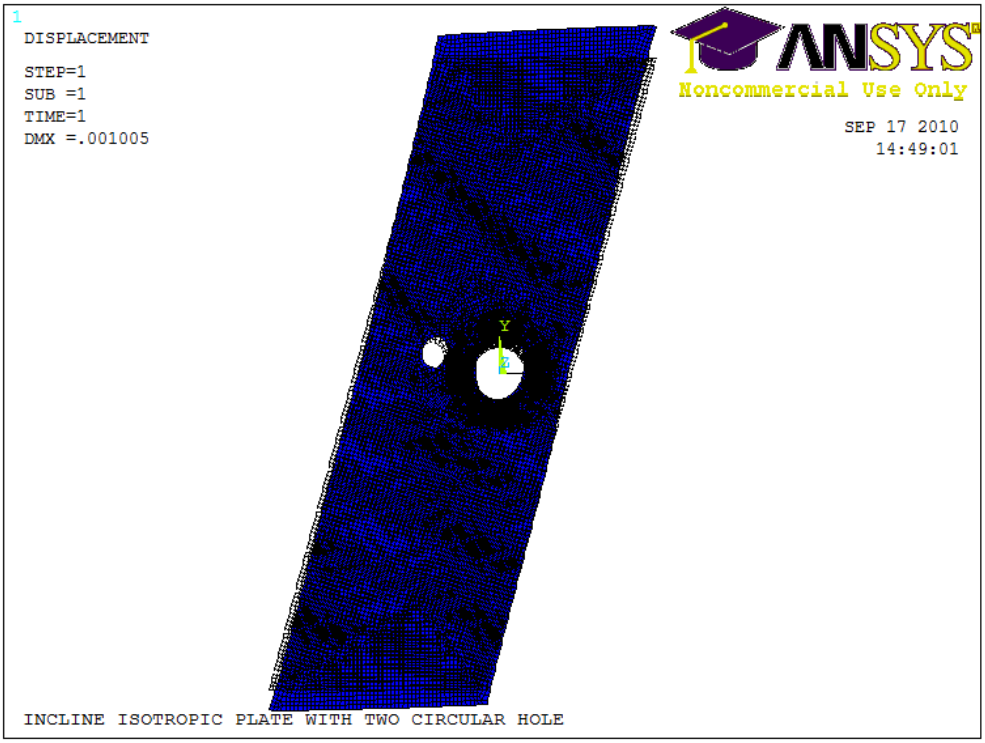

Fig. 8.20: Displacement plot for the unsymmetrically-loaded specimen from finite element analysis

8.5 Number of Coefficients and Input Values

8.5.1 General Comments

Equations 8.2 through 8.4 were solved by *least squares.* Since the number of equations (i.e. amount of measured input TSA data) is greater than the number of unknown Airy coefficients, it is important to determine an appropriate number of Airy coefficients *k*. Too small a number of coefficients, *k,* can give unreliable results, while too many coefficients can cause the Airy matrix of *m* equations by *k* coefficients of *equations 8.2 through 8.4* to become unstable or near-singular due to computer round-off errors. It also requires more computation time. The amount of measured input data needed can also depend on the choice of *k*, in that, more coefficients can necessitate more experimental values of S^*. To assist in determining an

appropriate value for k, the condition number, C, and $\log_{10}C$ of the Airy matrix was plotted against the number of coefficients, k. Based on the concept of SVD, MATLAB now provides a function (i.e., cond(A)) which gives the condition number of the matrix A.

To further assess in determining the appropriate number of Airy coefficients, self-consistency of the Airy coefficients was also used to evaluate a minimum value of k for reliable results. For this, the over-determined matrix equation, $Ac = d$, is solved using $c = A\backslash d$ (MATLAB notation) and utilizing the now-known coefficient vector, c, in the original matrix equation will give $Ac = d'$, where d' is typically not exactly the same as the input data d. The discrepancy between the calculated isopachic data d' and thermoelastically measured d can be represented by the *RMS* (*Root Mean Square*) value of *equation 8.5,* which is desired to be small, to obtain reliable results.

$$(d' - d)_{RMS} = \sqrt{\sum_{i=1}^{m} (d_i' - d)^2 / m} \tag{8.5}$$

8.5.2 Analyses of Symmetrically-Loaded Plate

For analyzing the symmetrically-loaded plate of *figures 8.1,* the large and small hole are analyzed individually i.e., when analyzing the large hole, the data near that large hole is taken along with the corresponding stress function (similarly for the small hole). Since the plate is symmetrical about the x-axis, the data was averaged about the axis. A total of m_1 = 4,378 and m_2 = 2,031 input values were used to evaluate the corresponding unknown Airy coefficients for the large and the small hole, respectively, and their source locations as shown in the *figures 8.21 and 8.22*. The source location data will be a cell/entry in the matrix of *equation 8.3* that stores the respective value of the recorded TSA data *S (= S*/K)*.

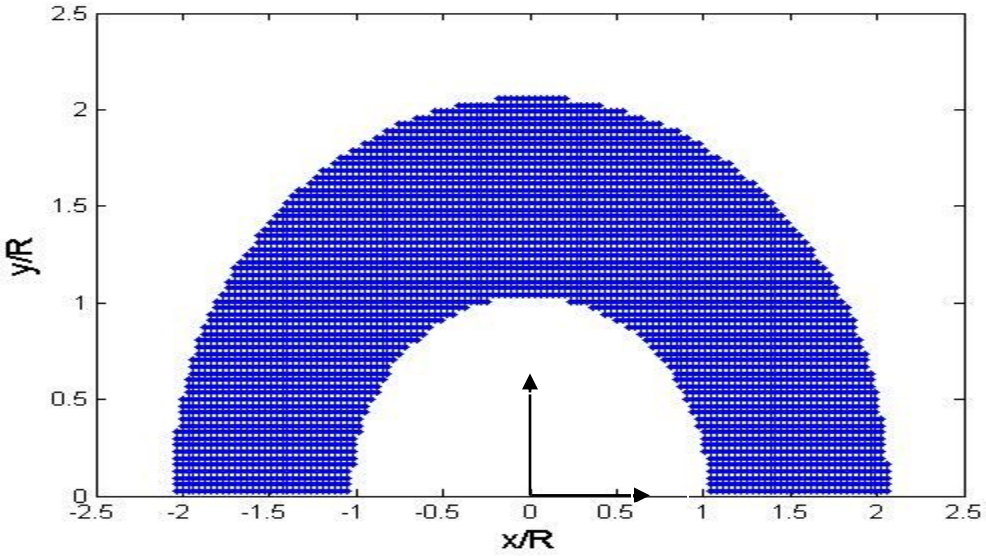

Fig. 8.21: TSA source locations for large hole, m_1 = 4,378 input values

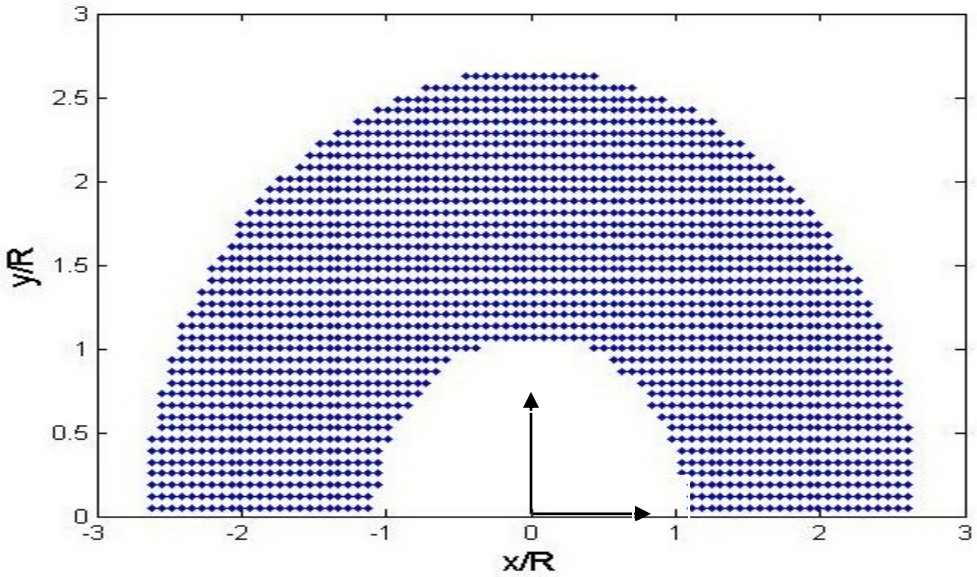

Fig. 8.22: TSA source locations for small hole, m_2 = *2,031* input values

Using these source locations data for the large and the small hole, appropriate number of unknown Airy coefficients to use is evaluated as discussed in section 8.4. *Figures 8.23 and 8.24* are the plots of condition number, C and $\log_{10}$C, vs. the number of Airy coefficients, *k,* for the large hole. Similarly *figures 8.25 and 8.26* are the plots of condition number, C and $\log_{10}$C, vs.

the number of Airy coefficients, *k,* for the small hole. The values of C or $\log_{10}$C, are reasonably consistent for $9 \leq k \leq 13$ for the large hole in *figures 8.23 and 8.24,* and $k = 9$ is minimum for the small hole. Based on the condition number results, this number of coefficients $k = 9$ is considered sufficient for generating the solutions with adequate reliability. Adding more coefficients than necessary could necessitate the more measured input data and adversely increases the computation time. These data therefore suggest $k = 9$ as a reasonable choice for both the large and small hole of the plate of *figures 8.1, 8.4 and 8.6*. The isopachic and individual components of stress involve summation over *n,* where *n* goes through positive integers from 4 to *N*, and the total number of coefficients is given by $k = 2(N-3) + 7 = 2N+1$. Thus, for $k = 9$ coefficients, the terminating index N = 4. *Figures 8.27 and 8.28* are the plots of Root Mean Square, *RMS* vs. the number of Airy coefficients, *k,* for this large and small hole, respectively. These *RMS* plots further suggest $k = 9$ as an appropriate choice for number of Airy coefficients for both small and the large hole of the plate of *figures 8.1, 8.4 and 8.6*.

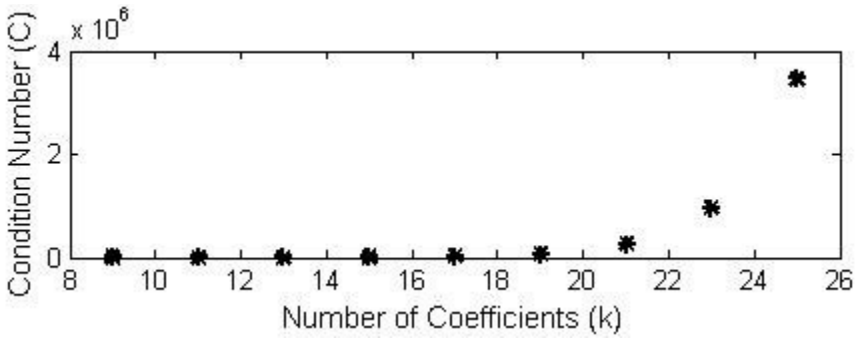

Fig. 8.23: Plot of condition number, *C*, vs. number of coefficients, *k*, for $m_1 = 4{,}378$ input values

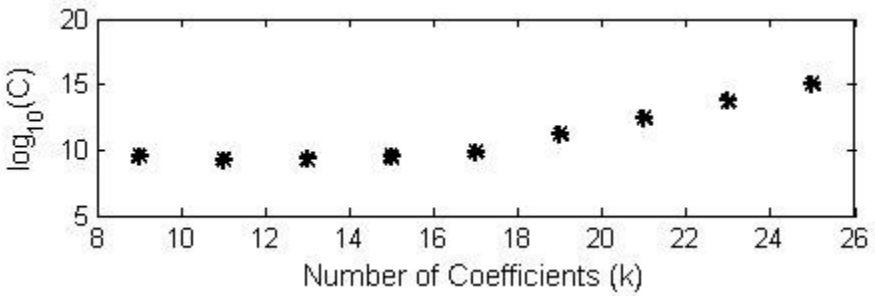

Fig. 8.24: Plot of $Log_{10}(C)$ vs. number of coefficients, k, for $m_1 = 4,378$ input values

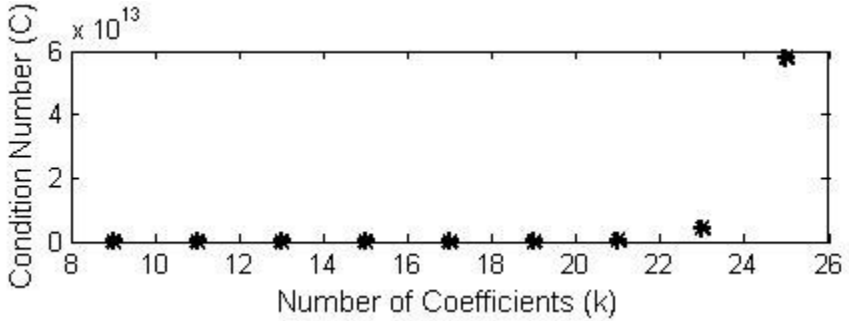

Fig. 8.25: Plot of condition number, C, vs. number of coefficients, k, for $m_2 = 2,031$ input values for the small hole

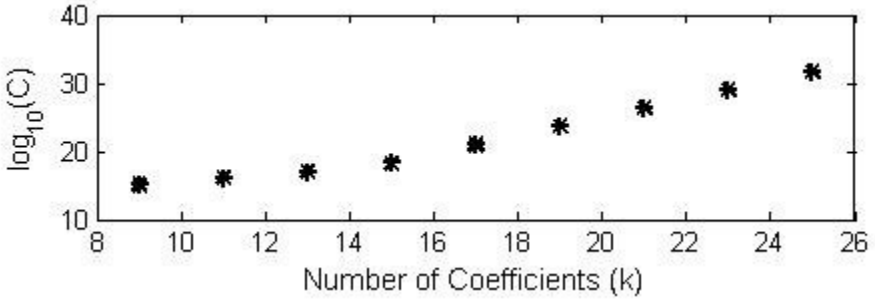

Fig. 8.26: Plot of $Log_{10}(C)$ vs. number of coefficients, k, for $m_2 = 2,031$ input values for the small hole

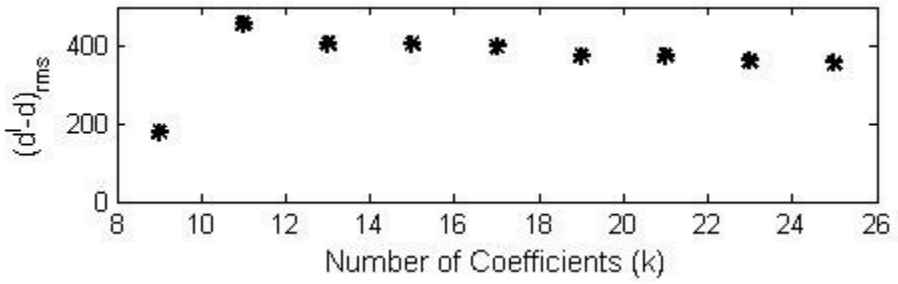

Fig. 8.27: Plot of 'RMS' values of (d'-d) vs. number of coefficients, k, for $m_1 = 4,378$ input values

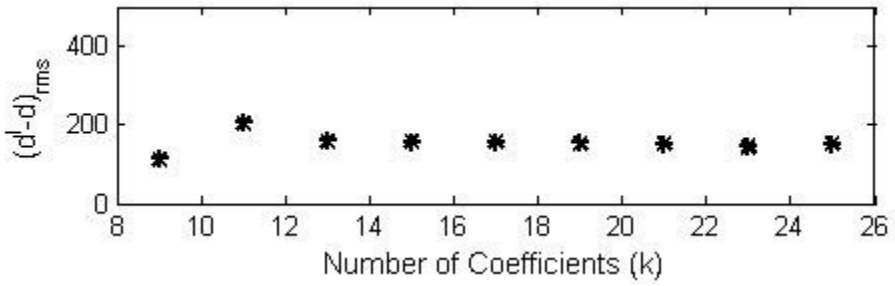

Fig. 8.28: Plot of 'RMS' values of (d'-d) vs. number of coefficients, *k*, for $m_2 = 2{,}031$ input values

Figures 8.29 and 8.30 are the contour plots for the large and the small hole from the experimental data (S*) after averaging about the x-axis and as processed by MATLAB.

Figures 8.31 and 8.32 are the reconstructed contour plots (S*) based on the measured information and using the now-known Airy coefficients for the large and small hole respectively. Results of *figures 8.29 through 8.32* further support using $k = 9$ for both the holes of the plate of *figures 8.1, 8.4 and 8.6*. The reconstructed images of *figures 8.31 and 8.32* are obtained by taking the data individually in the neighborhood of the large hole and the small hole, and combining those data with the Airy's stress function to form the matrix of *equation 8.3*. This matrix was solved using the least squares technique to evaluate the unknown Airy coefficients. Using the now-known Airy coefficients for the large and the small hole, a MATLAB plots (*figures 8.31 and 8.32*) were created. Therefore reconstructed contour plot of *figures 8.31 and 8.32* was obtained based on the TSA-determined values of the nine Airy coefficients, which the latter values being different for the large and the small hole. The x- and y-axes of *figures 8.29 through 8.32* are normalized with respect to the center distance (c) between the holes.

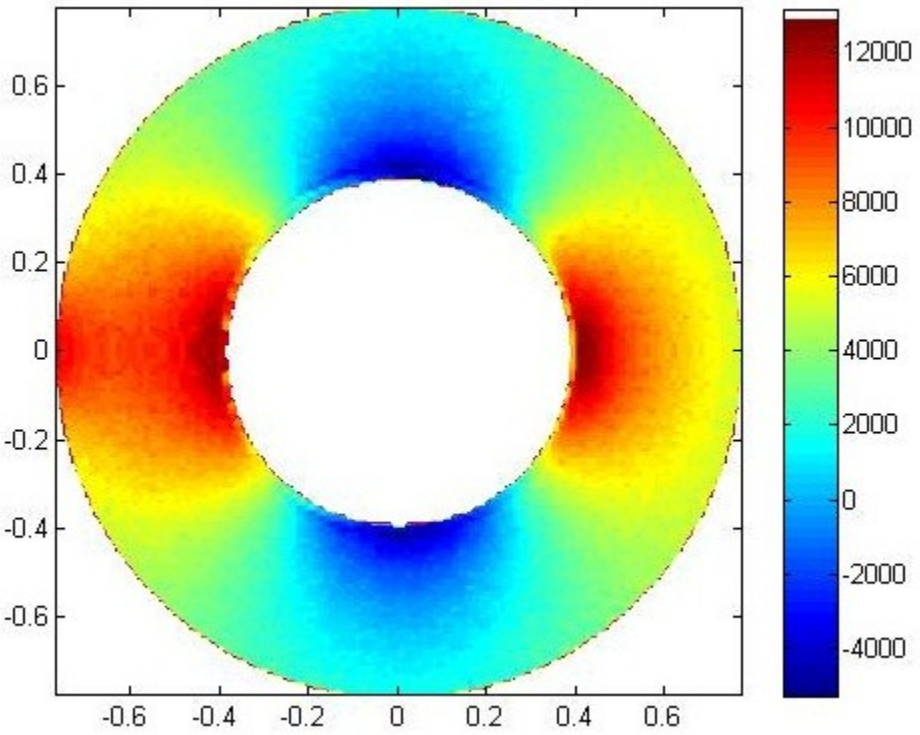

Fig. 8.29: MATLAB processed Experimental TSA input data S* for large hole

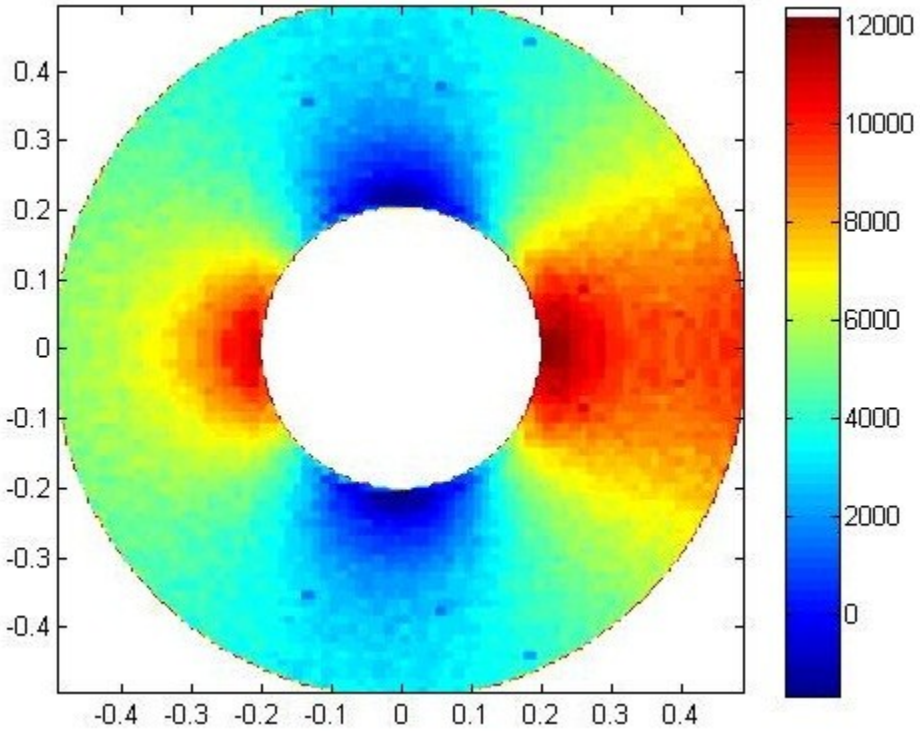

Fig. 8.30: MATLAB processed Experimental TSA input data S* for small hole

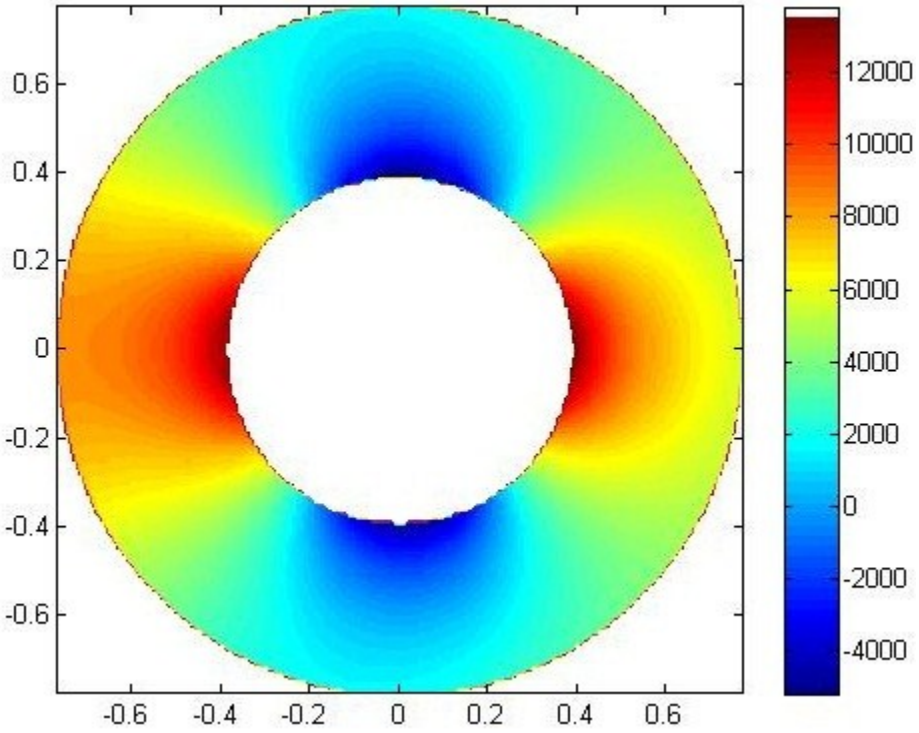

Fig. 8.31: Reconstructed S* for the large hole with $m_1 = 4{,}378$ and $k = 9$

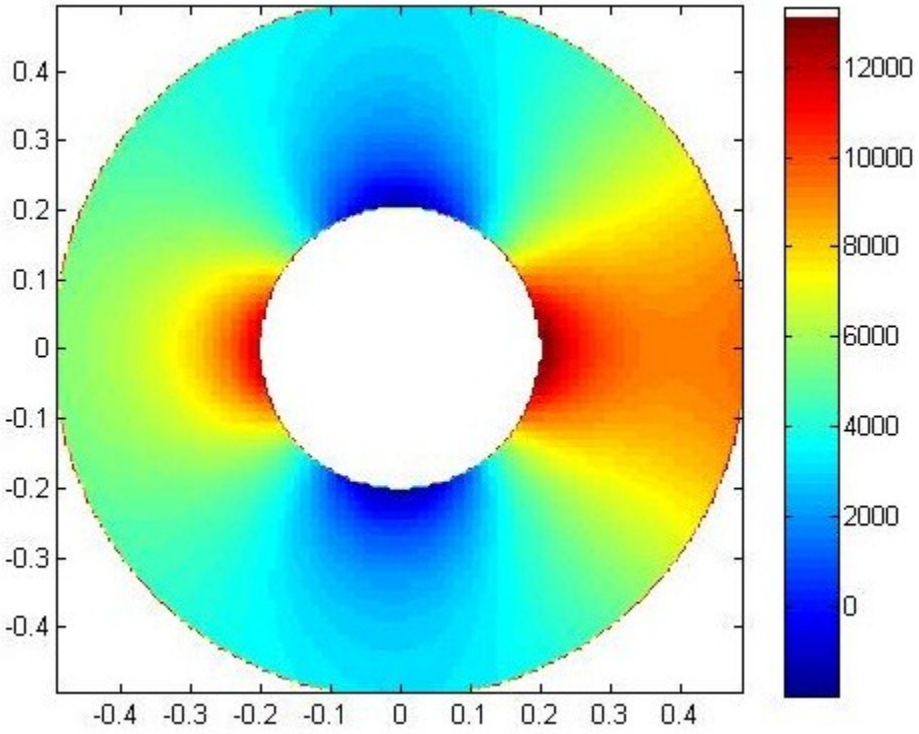

Fig. 8.32: Reconstructed S* for the large hole with $m_2 = 2,031$ and $k = 9$

8.5.3 Analyses of Unsymmetrically-Loaded Plate

For the analysis of the unsymmetrically-loaded plate of *figures 8.2, 8.5 and 8.7,* the large and the small hole are analyzed individually i.e., when analyzing the large hole the data near that large hole are taken along with the corresponding stress function (similarly for the small hole). A total of m_3 = 9,372 and m_4 = 4,094 input values were used to evaluate the corresponding unknown Airy coefficients for the large and the small hole, respectively, and their respective source locations is shown in the *figures 8.33 and 8.34*. The source location data will be a cells/entries in the matrix of *equation 8.4* which stores the respective values of the recorded TSA data *S (=S*/K)*.

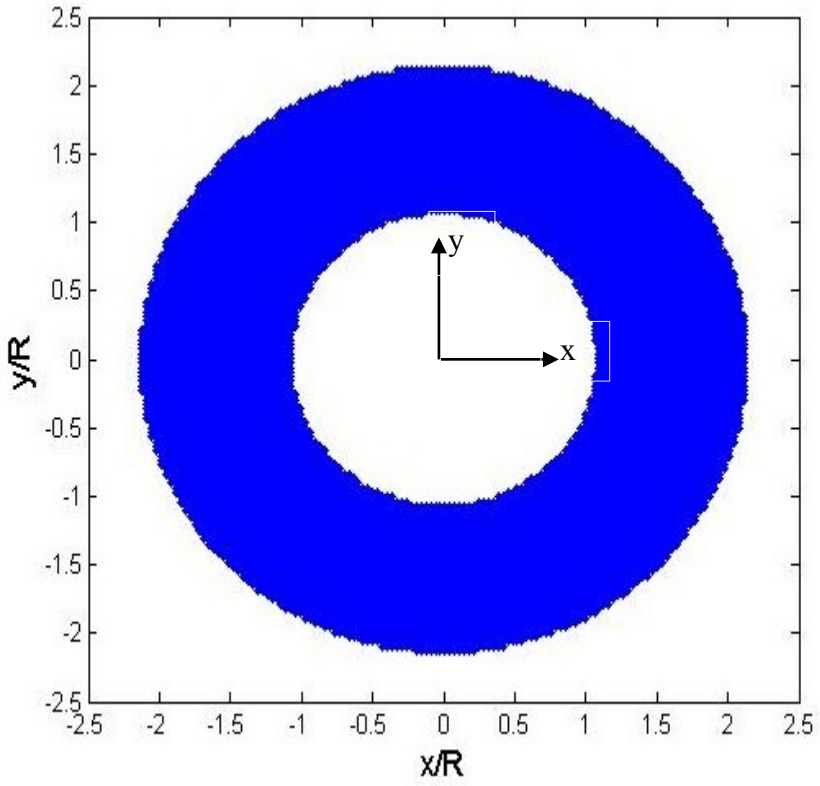

Fig. 8.33: TSA source locations for large hole, $m_3 = 9{,}372$ input values

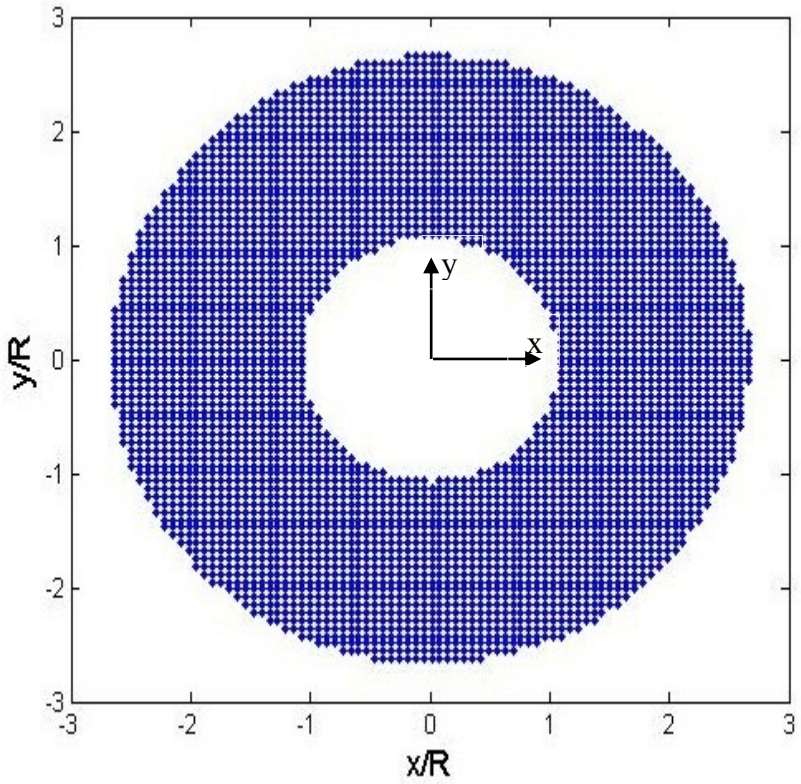

Fig. 8.34: TSA source locations for small hole, $m_4 = 4{,}094$ input values

These source location data for the large and the small hole are used to evaluate the appropriate number of unknown Airy coefficients to use as discussed in section 8.4. *Figures 8.35 and 8.36* are plots of the condition number, C and $\log_{10}$C vs. the number of Airy coefficients, *k,* for the large hole. *Figures 8.37 and 8.38* are corresponding plots for the small hole. The values of C and $\log_{10}$C increase rapidly for $k \geq 17$, for both the large and the small hole. These condition number results suggest $k = 17$ is adequate. Using too many coefficients there is a risk of making the matrix A of *equation 8.2* ill-conditional matrix, as well as possibly necessitating the more measured input data and adversely increasing the computation time. Since the isopachic and individual components of stress involve two summation series over *n,* where one summation series *n* goes through positive integers from 4 to *N* and the other goes from 2 to *N*, the total number of coefficients is given by $k = 2(N\text{-}3) + 2(N\text{-}1) + 9 = 4N+1$. The terminating index for *k*

= 17 coefficients is N = 4. *Figures 8.39 and 8.40* are the plots of Root Mean Square, *RMS* vs. the number of Airy coefficients, *k,* for the large and small hole, respectively. Results of these *RMS* plots further supports *k = 17* as an appropriate choice for number of Airy coefficients for both small and the large hole.

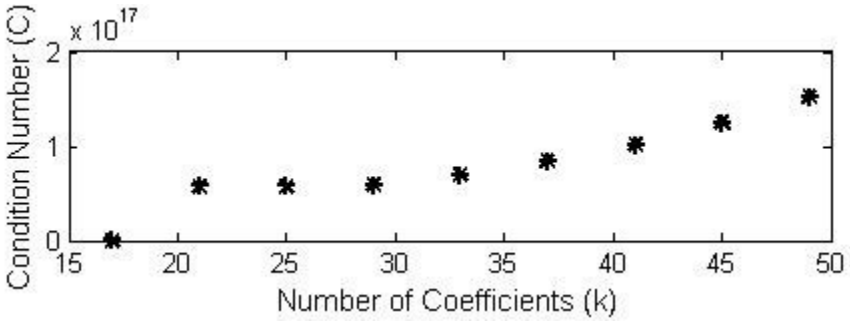

Fig. 8.35: Plot of condition number, *C*, vs. number of coefficients, *k*, for $m_3 = 9{,}372$ input values

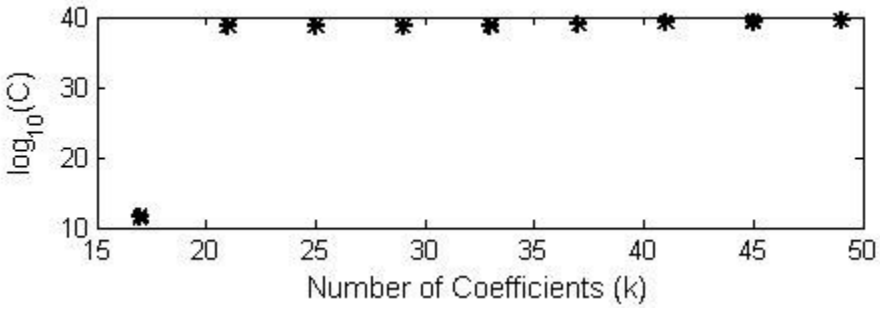

Fig. 8.36: Plot of $Log_{10}(C)$ vs. number of coefficients, *k*, for $m_3 = 9{,}372$ input values

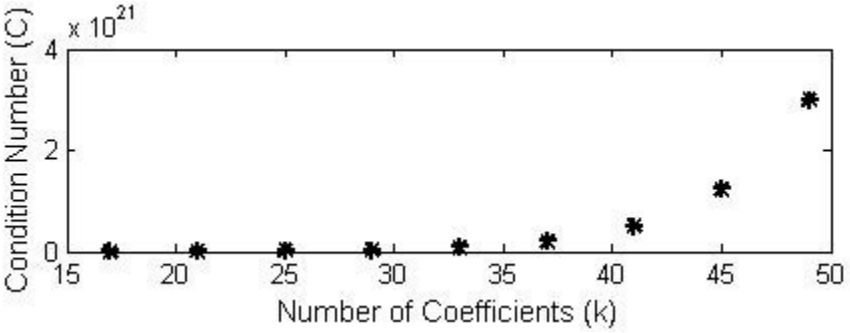

Fig. 8.37: Plot of condition number, *C*, vs. number of coefficients, *k*, for $m_4 = 4{,}094$ input values for the small hole

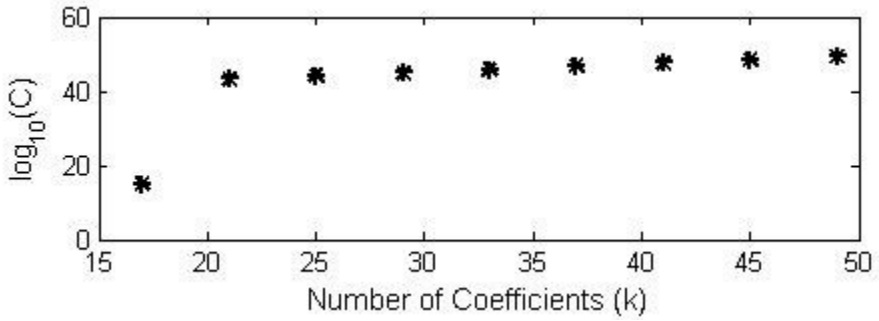

Fig. 8.38: Plot of $Log_{10}(C)$ vs. number of coefficients, *k*, for $m_4 = 4{,}094$ input values for the small hole

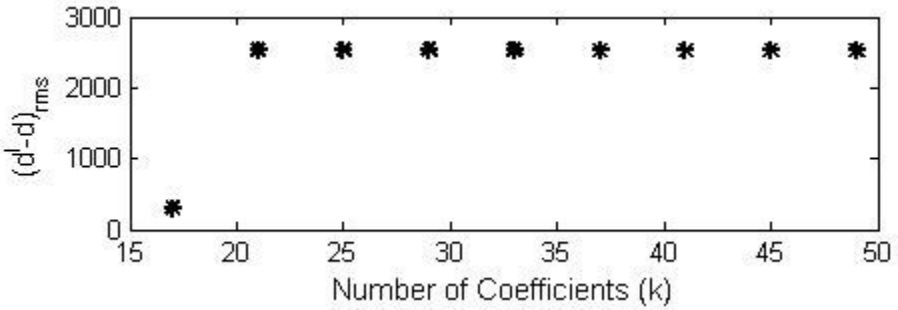

Fig. 8.39: Plot of 'RMS' values of (d'-d) vs. number of coefficients, *k*, for $m_3 = 9{,}372$ input values

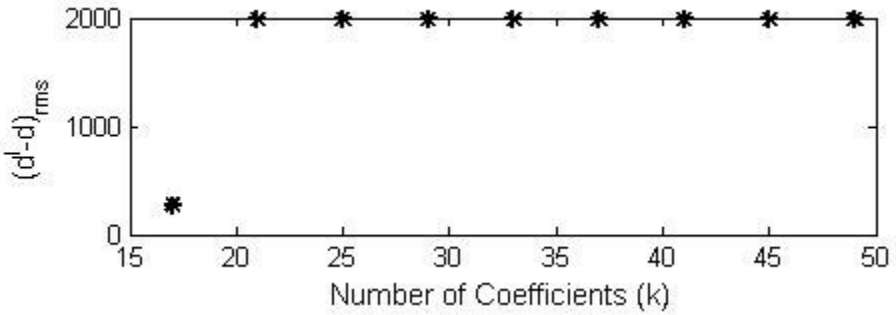

Fig. 8.40: Plot of 'RMS' values of (d'-d) vs. number of coefficients, *k*, for $m_4 = 4{,}094$ input values

Figures 8.41 and 8.42 are the contour plots for the large and the small hole from the experimental data (S*). *Figures 8.43 and 8.44* are the reconstructed contour plots (S*) based on the measured TSA information and using the now-known Airy coefficients for the large and small holes respectively. Information of *figures 8.41 through 8.43* support the present use of *k* =

17. As for the plate of *figures 8.1, 8.4, and 8.6,* reconstructed images of *figures 8.43 and 8.44* were obtained by taking the data separately in the neighborhood of the large hole and the small hole and combining then with the Airy's stress function to form the matrix of *equation 8.4*. This matrix was solved using least squares to evaluate the unknown Airy coefficients. The MATLAB plots of *figures 8.43 and 8.44* were then created using the now-known Airy coefficients for the large and the small hole. The reconstructed contour plots of *figures 8.43 and 8.44* are based on the TSA-determined values of the seventeen Airy coefficients, the value of the seventeen coefficients being different for the large and the small hole. The x- and y-axes of *figures 8.41 through 8.44* are normalized with respect to the inclined center distance (c) between the holes of *figure 8.2*.

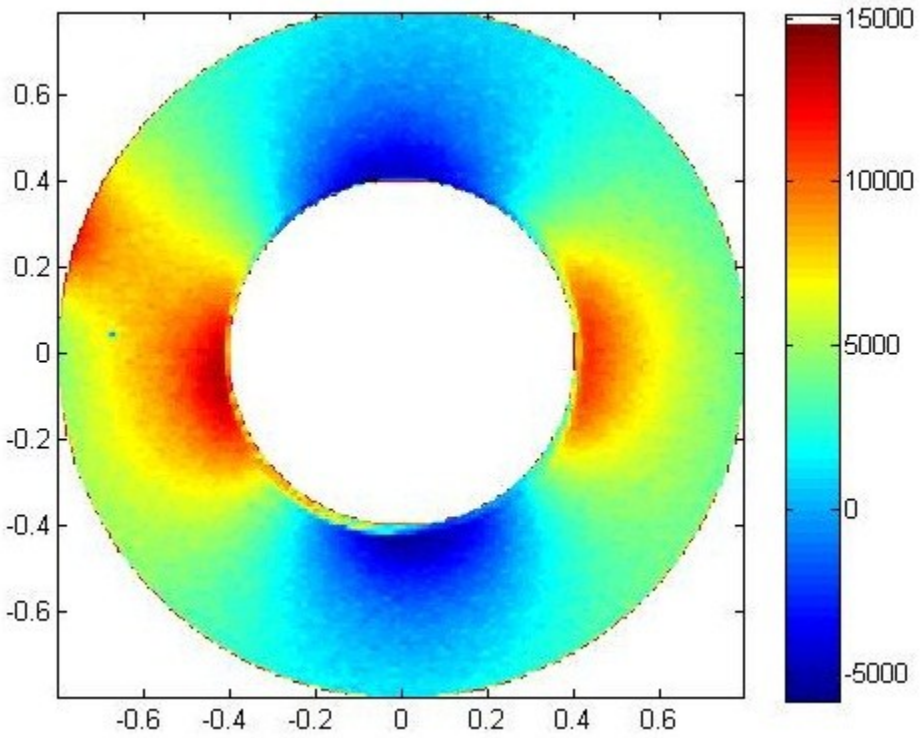

Fig. 8.41: MATLAB processed Experimental TSA input data S* for large hole

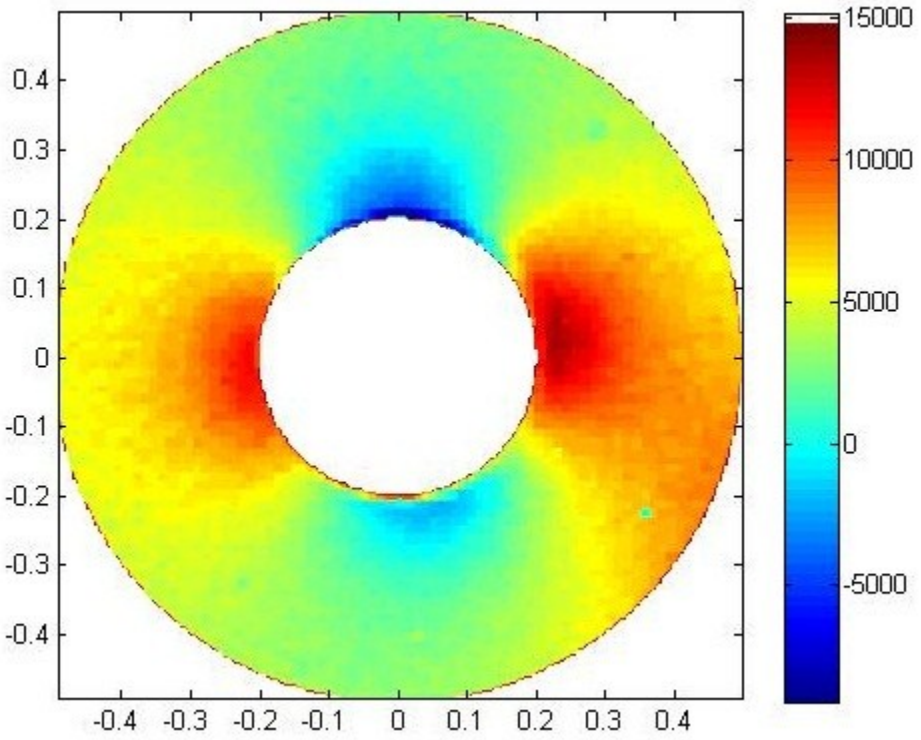

Fig. 8.42: MATLAB processed Experimental TSA input data S* for small hole

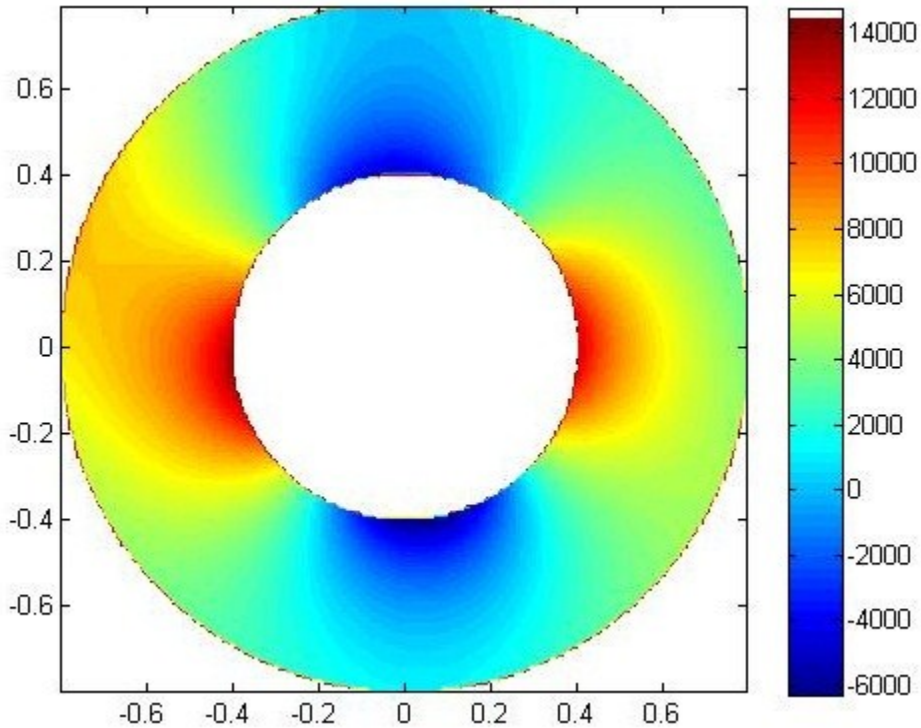

Fig. 8.43: Reconstructed S* for the large hole with $m_3 = 9{,}372$ and $k = 17$

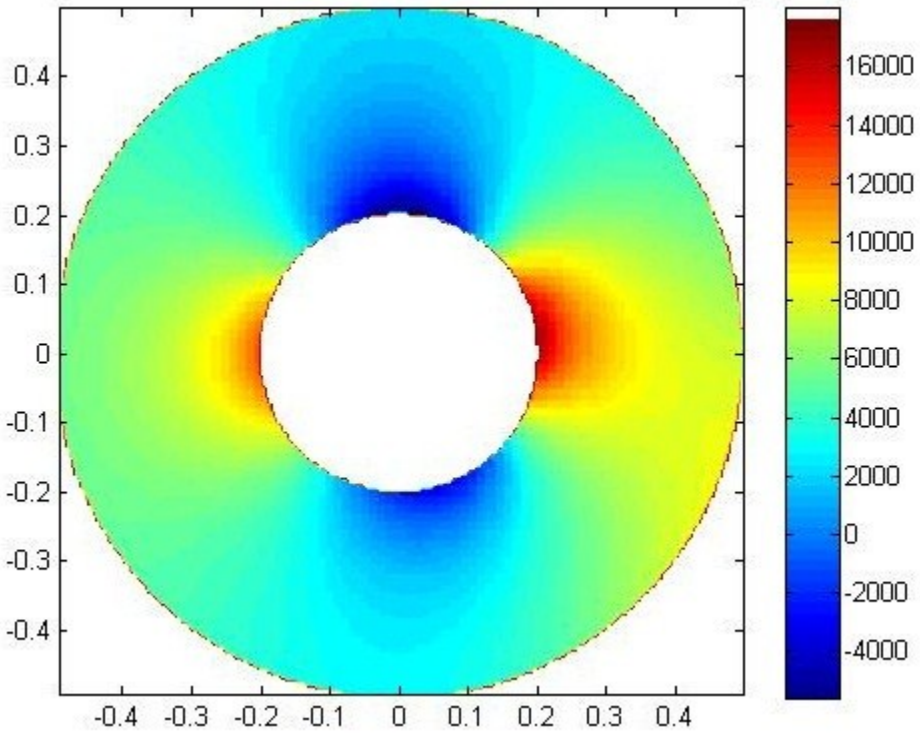

Fig. 8.44: Reconstructed S* for the small hole with $m_4 = 4{,}094$ and $k = 17$.

8.6 Results

8.6.1 General Comments

The TSA results obtained are compared with those from finite element analysis (ANSYS). Tangential stress, $\sigma_{\theta\theta}$, radial stress, σ_{rr} and shear stress, $\sigma_{r\theta}$, are normalized with respect to the far field stress, σ_0, and are plotted at various radii around and away from the boundary of respective holes, whereas normalized $\sigma_{rr} = \sigma_{xx}$ and $\sigma_{\theta\theta} = \sigma_{yy}$ are plotted along line AB of *figures 8.1 and 8.2*. TSA-computed normalized radial stress, σ_{rr}, and shear stress, $\sigma_{r\theta}$, are plotted around the boundary of the each hole. The normalizing stress, $\sigma_0 = 9.2$ MPa (1333.33 psi) is based on the applied tensile load, F, divided by the gross area (i.e. away from the regions of the holes), *figures 8.1 and 8.2*.

Applied load range (F) = 4448.2 N (1000lb)

Cross-Sectional Area (A) = Width (W) x Thickness (t)

= 76.2 x 6.35 = 483.87 mm^2 (0.75 in^2)

$$\sigma_o = \frac{4448.2}{483.87} = 9.2\ MPa = (1333.33\ psi)$$

The TSA results agree with those from FEM. Although the transverse stress (*figure 3.28*) tends to differ from those by FEM along line AB as one move away from the hole, these latter stresses are very small.

8.6.2 Results for the Symmetrically-Loaded Plate

After evaluating all the unknown Airy coefficients (b_0, c_0, d_1', b_2', d_2', c_3', d_3', b_n' and d_n', for n = 4) for the symmetrically-loaded plate from the measured S* based separately on the input data for the large and the small hole, the individual components of stress were obtained for each hole of the plate of *figure 8.1*. *Figures 8.45 through 8.55* are the results for the large hole of the symmetrically-loaded plate based on the Airy coefficients for that large hole, while *figures 8.56 through 8.64* are the results for the small hole of the symmetrically-loaded plate based on the Airy coefficients for the small hole. Angle θ of *figures 8.45 through 8.53 and 8.56 through 8.64,* is measured counter-clockwise from the positive x-axis and r is measured here from the center of the large and small hole, respectively, of *figure 8.1*. The actual in-plane dimensions associated with *figures 8.54 and 8.55* are plotted normalized with respect to the radius r_1 = 9.525 mm = 0.375″ of the large hole. The actual in-plane dimensions associated with *figures 8.65 and 8.66* are plotted normalized with respect to the radius r_2 = 4.76 mm = 0.1875″ of the small hole.

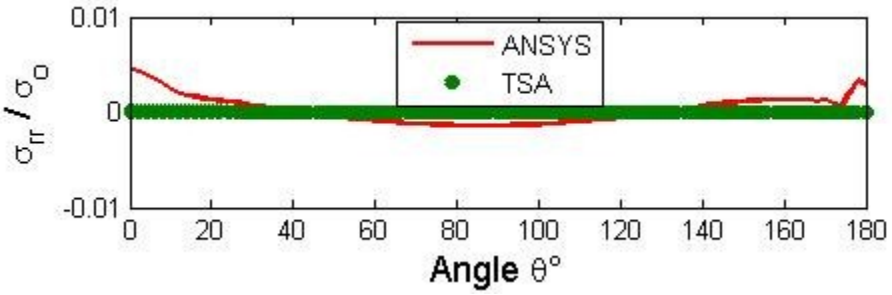

Fig. 8.45: Plot of σ_{rr}/σ_0 on the boundary of the large hole from ANSYS and TSA for $k = 9$ coefficients and $m_1 = 4{,}378$ TSA values

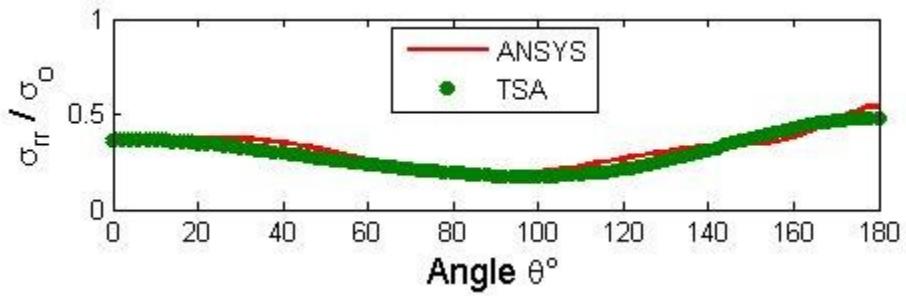

Fig. 8.46: Plot of σ_{rr}/σ_0 for large hole along $r/r_2 = 1.5$ from ANSYS and TSA for $k = 9$ coefficients and $m_1 = 4{,}378$ TSA values.

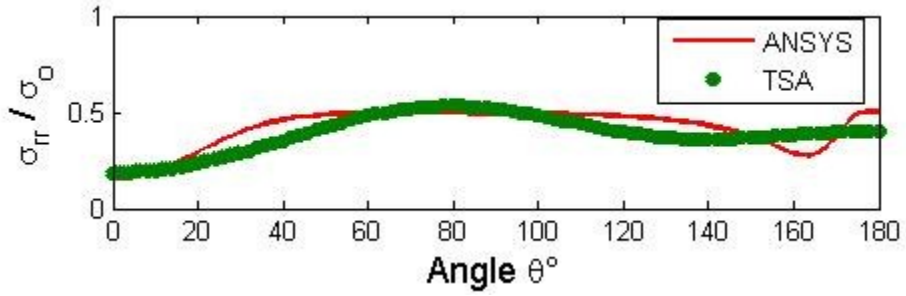

Fig. 8.47: Plot of σ_{rr}/σ_0 for large hole along $r/r_2 = 2$ from ANSYS and TSA for $k = 9$ coefficients and $m_1 = 4{,}378$ TSA values.

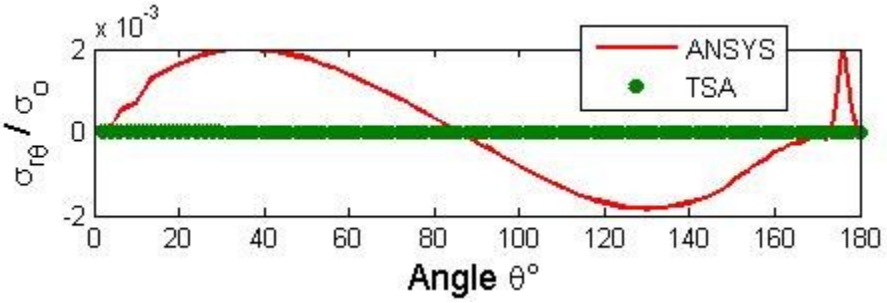

Fig. 8.48: Plot of $\sigma_{r\theta}/\sigma_0$ on the boundary of the large hole from ANSYS and TSA for $k = 9$ coefficients and $m_1 = 4{,}378$ TSA values.

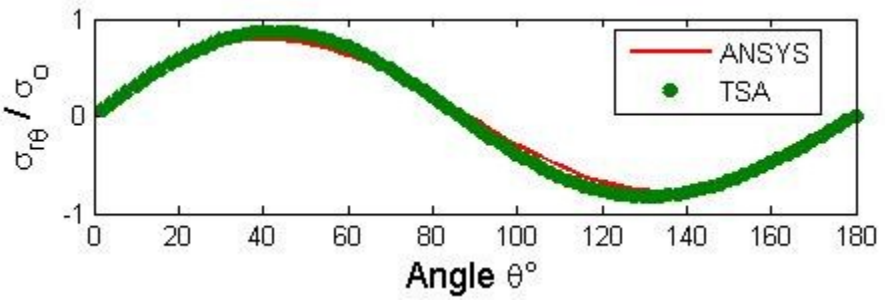

Fig. 8.49: Plot of $\sigma_{r\theta}/\sigma_0$ for large hole along $r/r_2 = 1.5$ from ANSYS and TSA for $k = 9$ coefficients and $m_1 = 4{,}378$ TSA values.

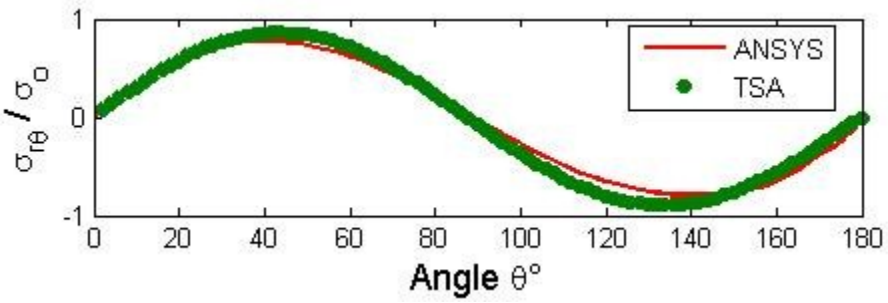

Fig. 8.50: Plot of $\sigma_{r\theta}/\sigma_0$ for large hole along $r/r_2 = 2$ from ANSYS and TSA for $k = 9$ coefficients and $m_1 = 4{,}378$ TSA values

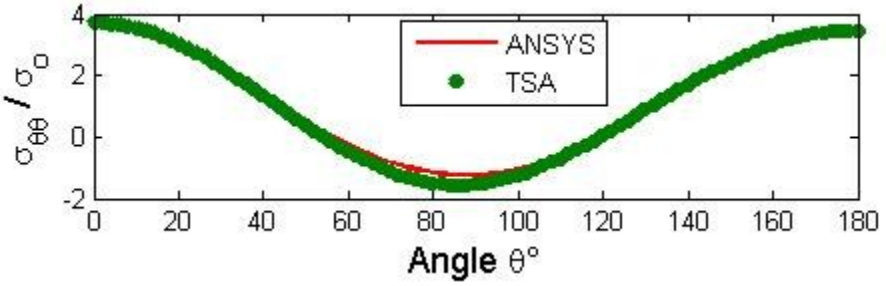

Fig. 8.51: Plot of $\sigma_{\theta\theta}/\sigma_0$ on the boundary of the large hole from ANSYS and TSA for $k = 9$ coefficients and $m_1 = 4{,}378$ TSA values

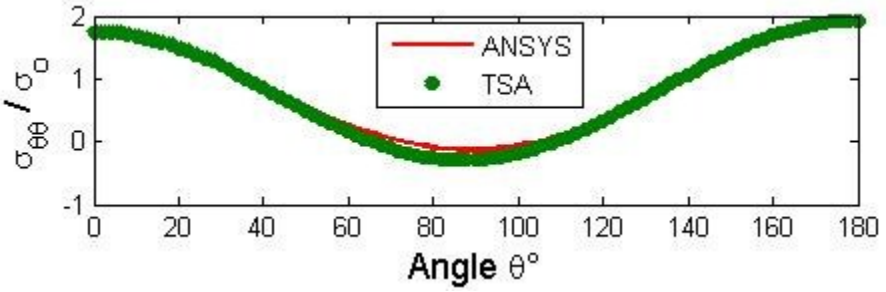

Fig. 8.52: Plot of $\sigma_{\theta\theta}/\sigma_0$ for large hole along $r/r_2 = 1.5$ from ANSYS and TSA for $k = 9$ coefficients and $m_1 = 4{,}378$ TSA values

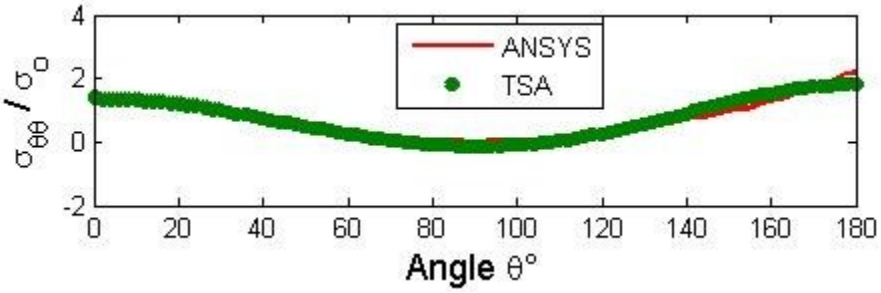

Fig. 8.53: Plot of $\sigma_{\theta\theta}/\sigma_0$ for large hole along $r/r_2 = 2$ from ANSYS and TSA for $k = 9$ coefficients and $m_1 = 4{,}378$ TSA values

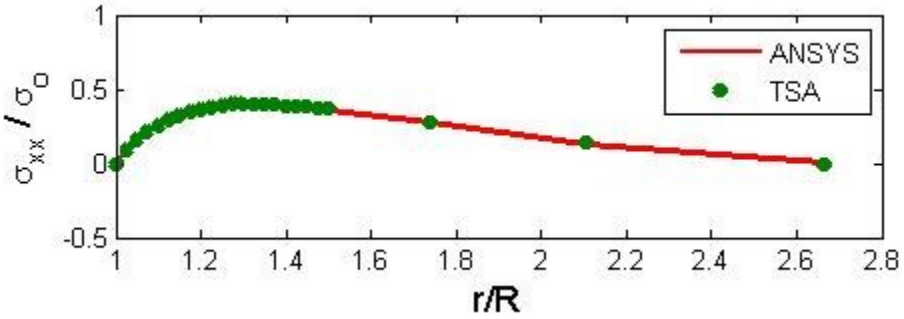

Fig. 8.54: Plot of σ_{xx}/σ_0 along CD of *figure 8.1* obtained from ANSYS and TSA for $k = 9$ coefficients and $m_1 = 4{,}378$ TSA values

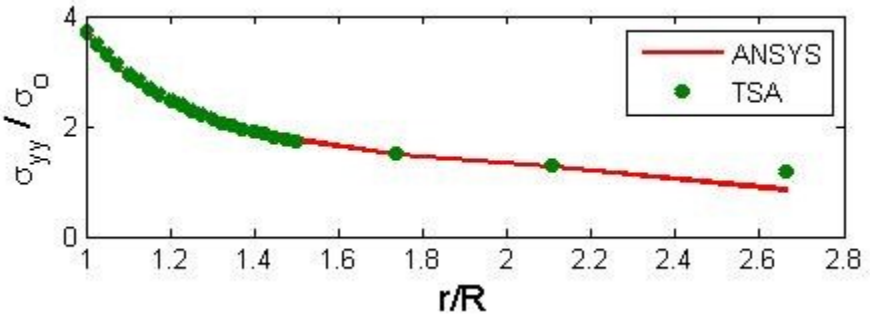

Fig. 8.55: Plot of σ_{yy}/σ_0 along CD of *figure 8.1* obtained from ANSYS and TSA for $k = 9$ coefficients and $m_1 = 4{,}378$ TSA values

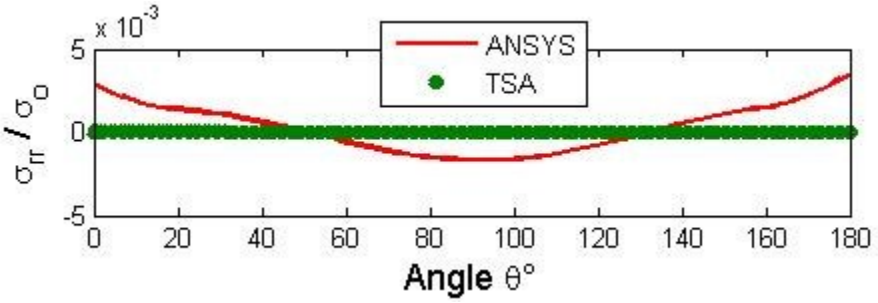

Fig. 8.56: Plot of σ_{rr}/σ_0 on the boundary of the small hole from ANSYS and TSA for $k = 9$ coefficients and $m_2 = 2{,}031$ TSA values

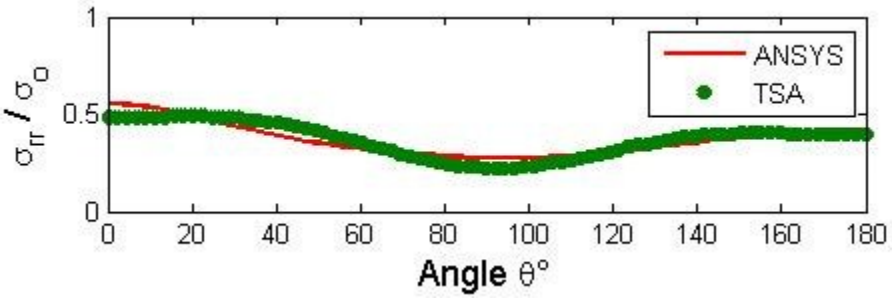

Fig. 8.57: Plot of σ_{rr}/σ_0 for small hole along $r/R_1 = 1.5$ from ANSYS and TSA for $k = 9$ coefficients and $m_2 = 2{,}031$ TSA values

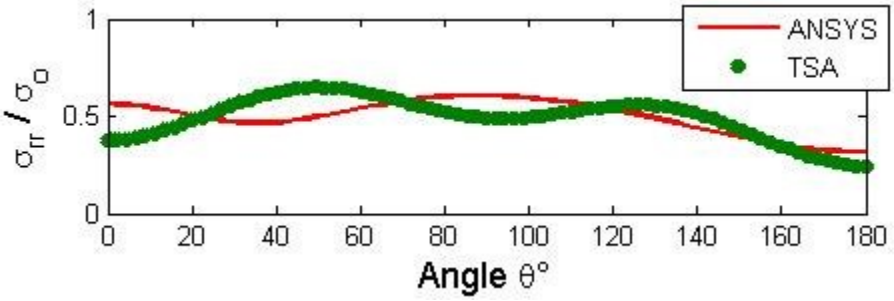

Fig. 8.58: Plot of σ_{rr}/σ_0 for small hole along $r/R_1 = 2$ from TSA and ANSYS for $k = 9$ coefficients and $m_2 = 2{,}031$ TSA values

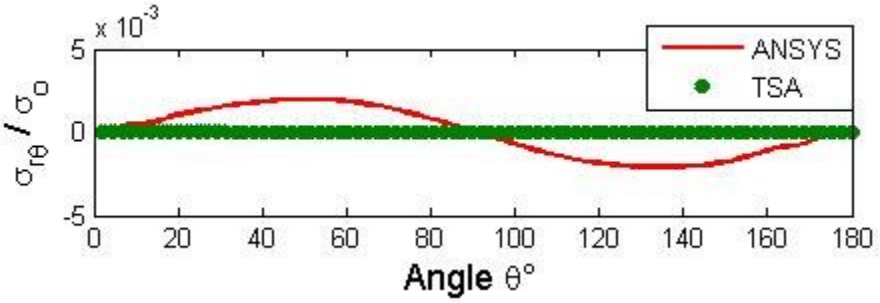

Fig. 8.59: Plot of $\sigma_{r\theta}/\sigma_0$ on the boundary of the small hole from ANSYS and TSA for $k = 9$ coefficients and $m_2 = 2{,}031$ TSA values

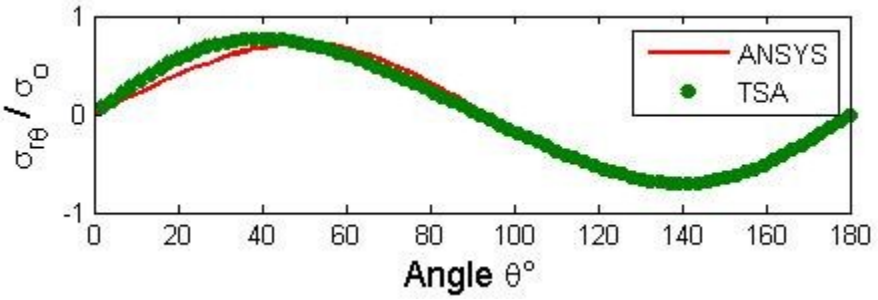

Fig. 8.60: Plot of $\sigma_{r\theta}/\sigma_0$ for small hole along $r/R_1 = 1.5$ from ANSYS and TSA for $k = 9$ coefficients and $m_2 = 2{,}031$ TSA values

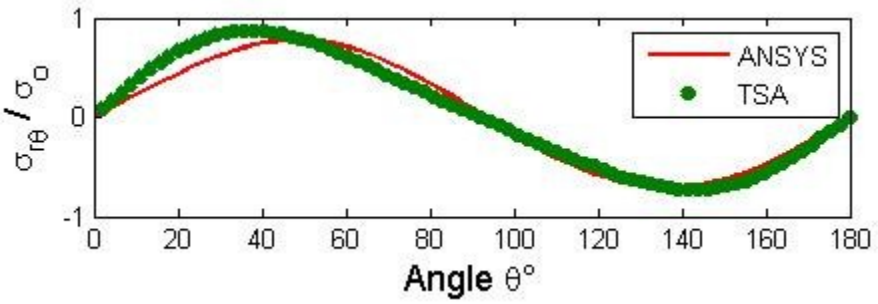

Fig. 8.61: Plot of $\sigma_{r\theta}/\sigma_0$ for small hole along $r/R_1 = 2$ from ANSYS and TSA for $k = 9$ coefficients and $m_2 = 2{,}031$ TSA values

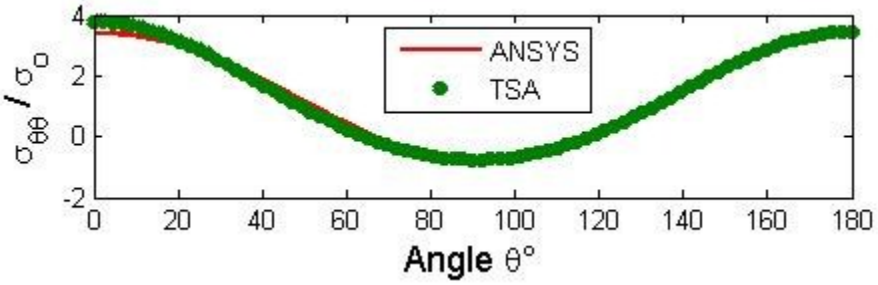

Fig. 8.62: Plot of $\sigma_{\theta\theta}/\sigma_0$ on the boundary of the small hole from ANSYS and TSA for $k = 9$ coefficients and $m_2 = 2{,}031$ TSA values

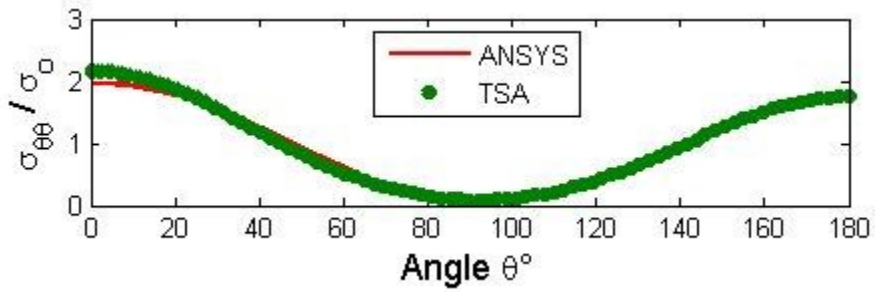

Fig. 8.63: Plot of $\sigma_{\theta\theta}/\sigma_0$ for small hole along $r/R_1 = 1.5$ from ANSYS and TSA for $k = 9$ coefficients and $m_2 = 2{,}031$ TSA values

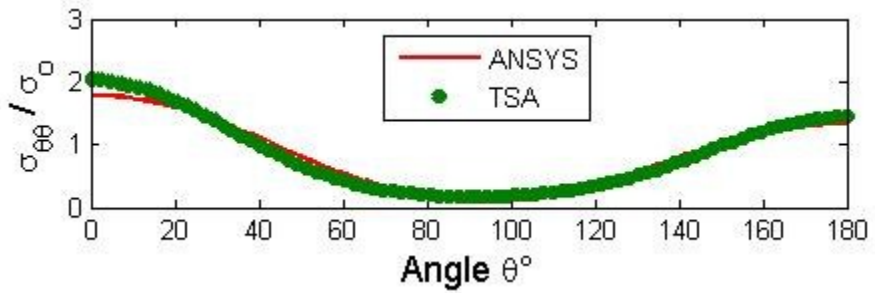

Fig. 8.64: Plot of $\sigma_{\theta\theta}/\sigma_0$ for small hole along $r/R_1 = 2$ from ANSYS and TSA for $k = 9$ coefficients and $m_2 = 2{,}031$ TSA values

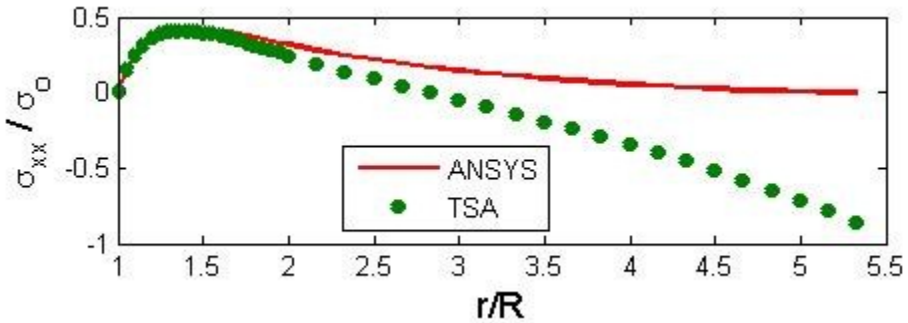

Fig. 8.65: Plot of σ_{xx}/σ_0 along AB of *figure 8.1* obtained from ANSYS and TSA for $k = 9$ coefficients and $m_1 = 4{,}378$ TSA values

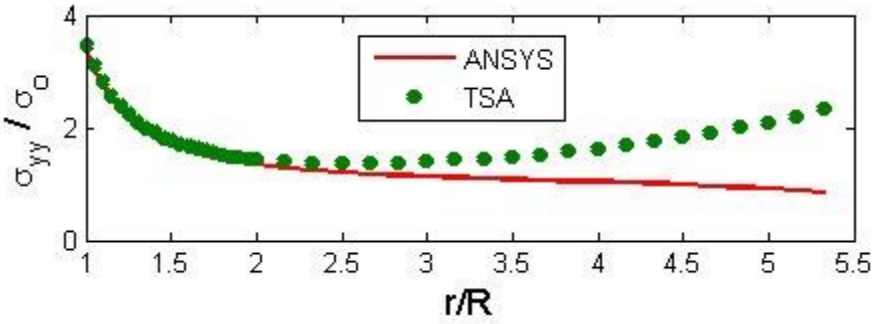

Fig. 8.66: Plot of σ_{yy}/σ_0 along AB of *figure 8.1* obtained from ANSYS and TSA for $k = 9$ coefficients and $m_1 = 4{,}378$ TSA values

The experimental TSA and ANSYS-predicted results of *figure 8.45 through 8.66* associated with the large and small holes tend to agree very well. Only far from the large hole along line AB are there significant difference between measured (TSA) and predicted (ANSYS) results. These discrepancy are probably due to the fact that no TSA input data are used beyond r/R = x/R = 2 (*figure 8.21*). Interestingly, the values of $\sigma_{\theta\theta}/\sigma_0$ on the edges of the large (*figure 8.51*) and small (*figure 8.62*) are very similar. The slight non-symmetry with respect to θ of both these plots reflects the lack of vertical axis of symmetry. Not surprisingly, the values of $\sigma_{\theta\theta}/\sigma_0$ on the edge of the small hole at $\theta = 90^o$ exceeds that at $\theta = 180^o$ on the edge of the large hole.

8.6.3 Results for the Unsymmetrically-Loaded Plate

After evaluating all the unknown Airy coefficients(b_0, c_0, A_0, d_1, d_1', b_2, d_2, c_3, d_3, b_4, d_4,…, b_N, d_N, b_2', d_2', …, b_N', d_N') for the unsymmetrically-loaded plate from the measured S* based on the input data for the large and the small hole, the individual components of stress were obtained for the large and small holes respectively. *Figures 8.67 through 8.77* contain the results for the large hole of the unsymmetrically-loaded plate based on the Airy coefficients for the large hole while *figures 8.78 through 8.88* are those for the small hole of the unsymmetrically-loaded plate based on the Airy coefficients for the small hole. Angle θ of *figures 8.67 through 8.75 and 8.76 through 8.86,* is measured counter-clockwise from the positive x-axis and r is measured here from the center of the large and the small hole of *figure 8.2* respectively. The actual in-plane dimensions associated with *figures 8.76 and 8.77* are plotted normalized with respect to the radius r_1 = 9.525mm = 0.375″ of the large hole. The actual in-plane dimensions associated with *figures 8.87 and 8.88* are plotted normalized with respect to the radius r_2 = 4.76 mm = 0.1875″ of the small hole.

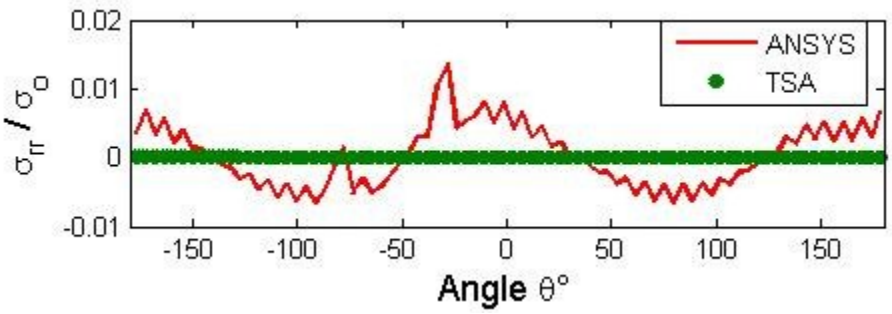

Fig. 8.67: Plot of σ_{rr}/σ_0 on the boundary of the large hole from ANSYS and TSA for $k = 17$ coefficients and m_3 = 9,372 TSA values

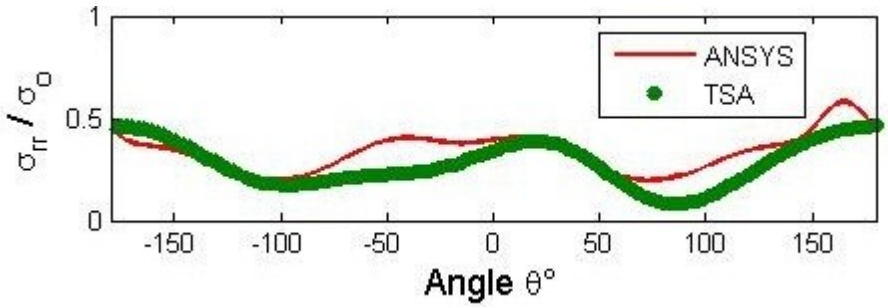

Fig. 8.68: Plot of σ_{rr}/σ_0 for large hole along $r/R_1 = 1.5$ from ANSYS and TSA for $k = 17$ coefficients and $m_3 = 9{,}372$ TSA values

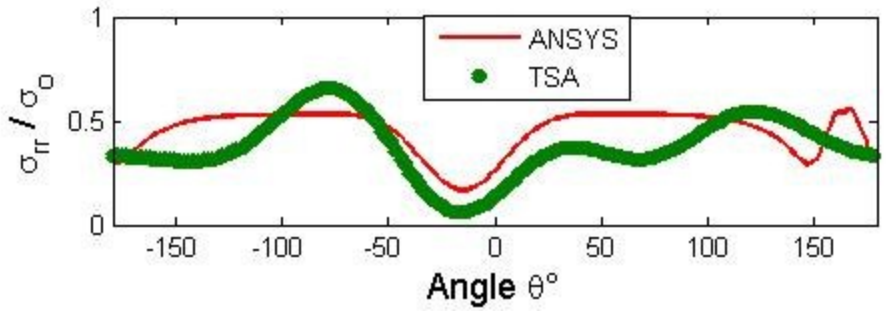

Fig. 8.69: Plot of σ_{rr}/σ_0 for large hole along $r/R_1 = 2$ from ANSYS and TSA for $k = 17$ coefficients and $m_3 = 9{,}372$ TSA values

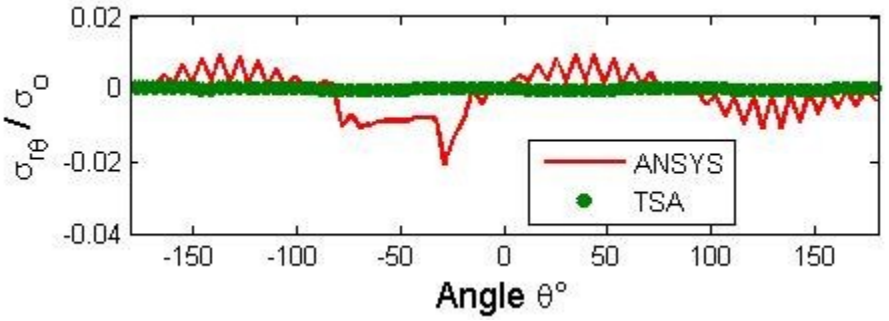

Fig. 8.70: Plot of $\sigma_{r\theta}/\sigma_0$ on the boundary of the large hole from ANSYS and TSA for $k = 17$ coefficients and $m_3 = 9{,}372$ TSA values

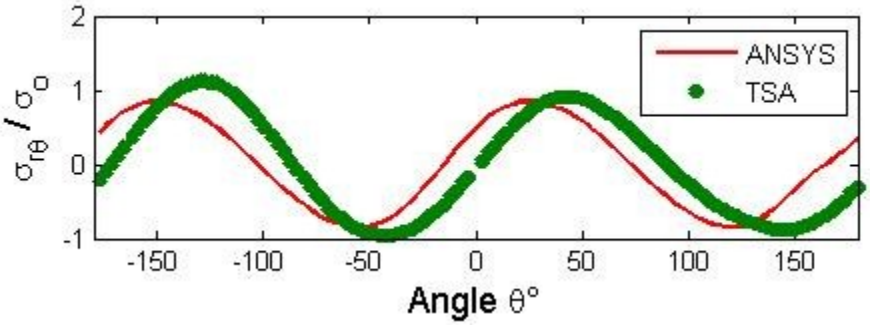

Fig. 8.71: Plot of $\sigma_{r\theta}/\sigma_0$ for large hole along $r/R_1 = 1.5$ from ANSYS and TSA for $k = 17$ coefficients and $m_3 = 9{,}372$ TSA values

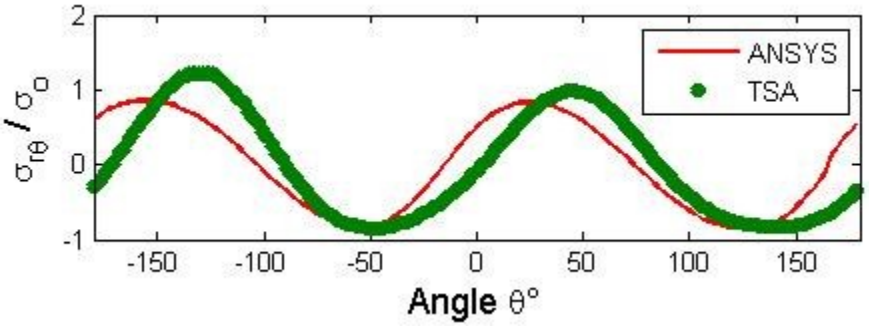

Fig. 8.72: Plot of $\sigma_{r\theta}/\sigma_0$ for large hole along $r/R_1 = 2$ from ANSYS and TSA for $k = 17$ coefficients and $m_3 = 9{,}372$ TSA values

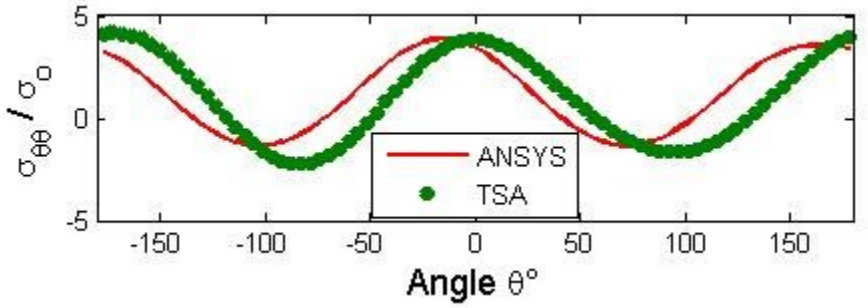

Fig. 8.73: Plot of $\sigma_{\theta\theta}/\sigma_0$ on the boundary of the large hole from ANSYS and TSA for $k = 17$ coefficients and $m_3 = 9{,}372$ TSA values

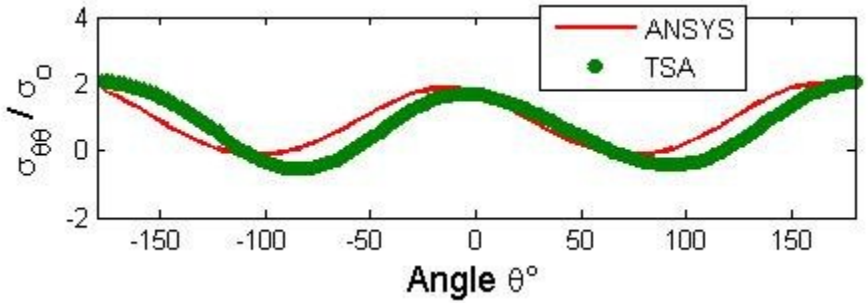

Fig. 8.74: Plot of $\sigma_{\theta\theta}/\sigma_0$ for large hole along $r/R_1 = 1.5$ from ANSYS and TSA for $k = 17$ coefficients and $m_3 = 9{,}372$ TSA values

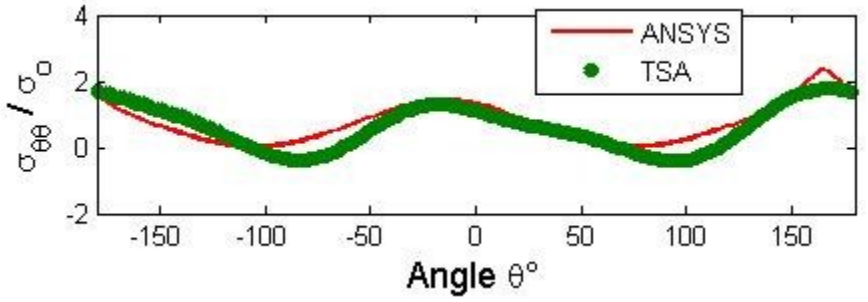

Fig. 8.75: Plot of $\sigma_{\theta\theta}/\sigma_0$ for large hole along $r/R_1 = 2$ from ANSYS and TSA for $k = 17$ coefficients and $m_3 = 9{,}372$ TSA values

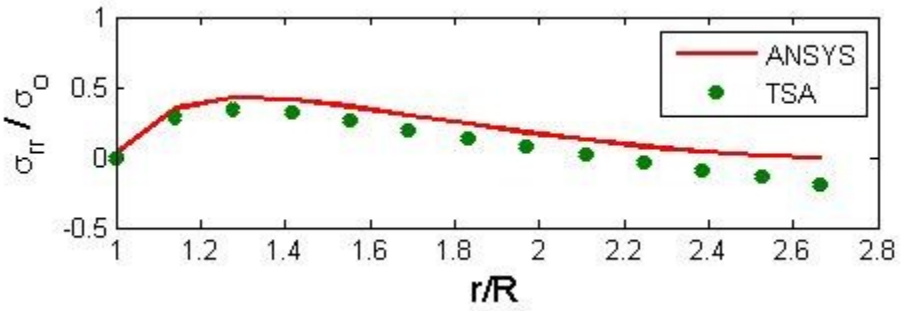

Fig. 8.76: Plot of σ_{rr}/σ_0 along C'D' of *figure 8.2* obtained from ANSYS and TSA for $k = 17$ coefficients and $m_3 = 9{,}372$ TSA values

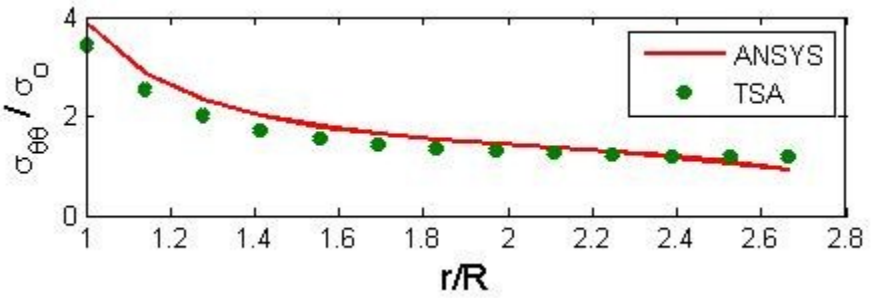

Fig. 8.77: Plot of $\sigma_{\theta\theta}/\sigma_0$ along C'D' of *figure 8.2* obtained from ANSYS and TSA for $k = 17$ coefficients and $m_3 = 9{,}372$ TSA values

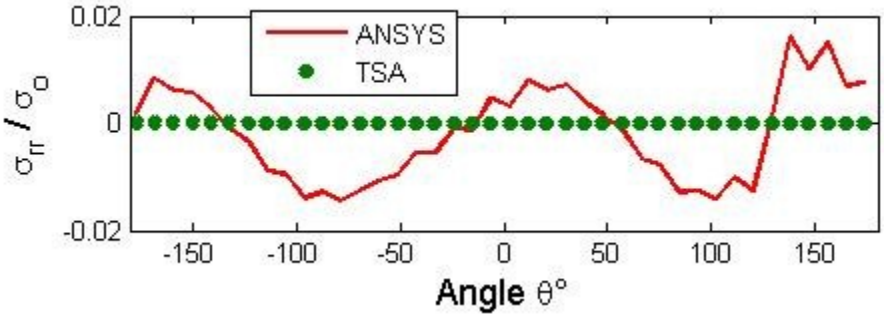

Fig. 8.78: Plot of σ_{rr}/σ_0 on the boundary of the small hole from ANSYS and TSA for $k = 17$ coefficients and $m_4 = 4{,}094$ TSA values

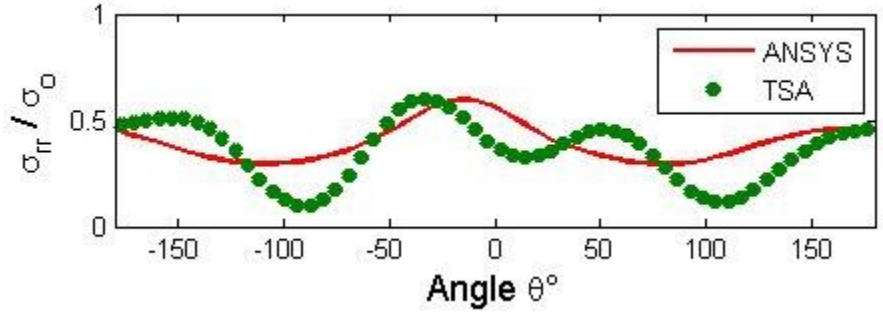

Fig. 8.79: Plot of σ_{rr}/σ_0 for small hole along $r/R_2 = 1.5$ from ANSYS and TSA for $k = 17$ coefficients and $m_4 = 4{,}094$ TSA values

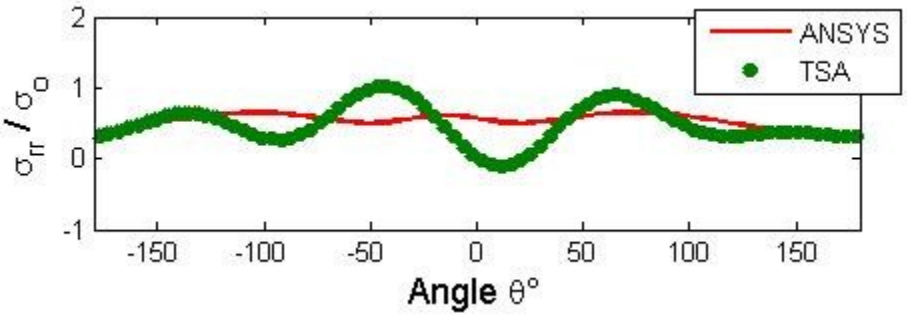

Fig. 8.80: Plot of σ_{rr}/σ_0 for small hole along $r/R_2 = 2$ from ANSYS and TSA for $k = 17$ coefficients and $m_4 = 4{,}094$ TSA values

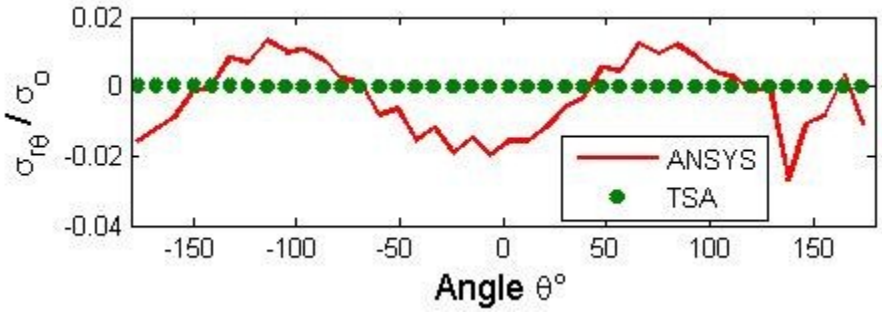

Fig. 8.81: Plot of $\sigma_{r\theta}/\sigma_0$ on the boundary of the small hole from ANSYS and TSA for $k = 17$ coefficients and $m_4 = 4{,}094$ TSA values

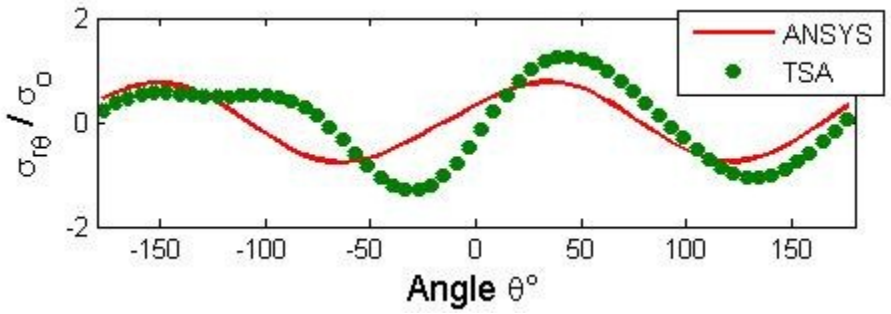

Fig. 8.82: Plot of $\sigma_{r\theta}/\sigma_0$ for small hole along $r/R_2 = 1.5$ from ANSYS and TSA for $k = 17$ coefficients and $m_4 = 4{,}094$ TSA values

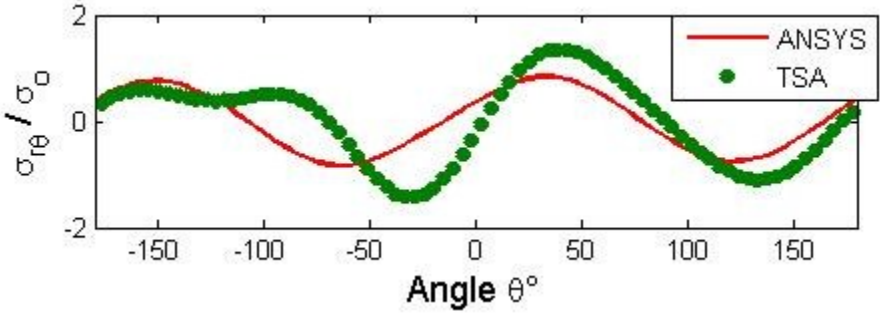

Fig. 8.83: Plot of $\sigma_{r\theta}/\sigma_0$ for small hole along $r/R_2 = 2$ from ANSYS and TSA for $k = 17$ coefficients and $m_4 = 4{,}094$ TSA values

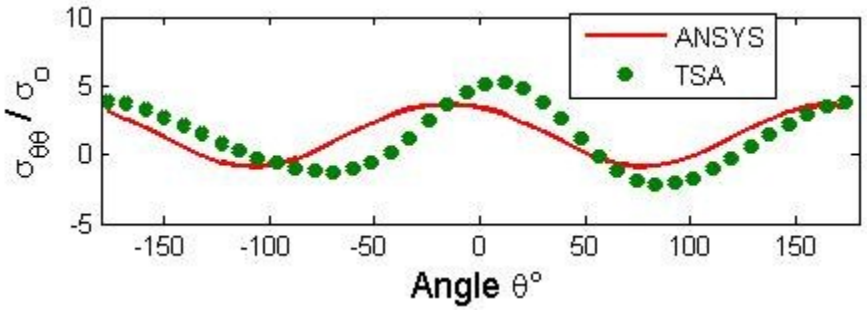

Fig. 8.84: Plot of $\sigma_{\theta\theta}/\sigma_0$ on the boundary of the small hole from ANSYS and TSA for *k = 17* coefficients and m_4 = *4,094* TSA values

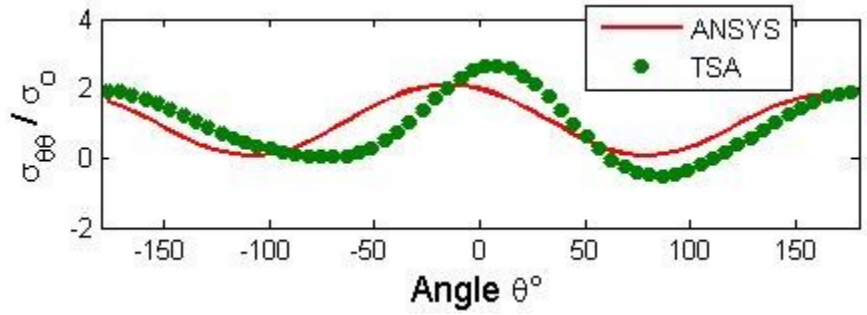

Fig. 8.85: Plot of $\sigma_{\theta\theta}/\sigma_0$ for small hole along $r/R_2 = 1.5$ from ANSYS and TSA for *k = 17* coefficients and m_4 = *4,094* TSA values

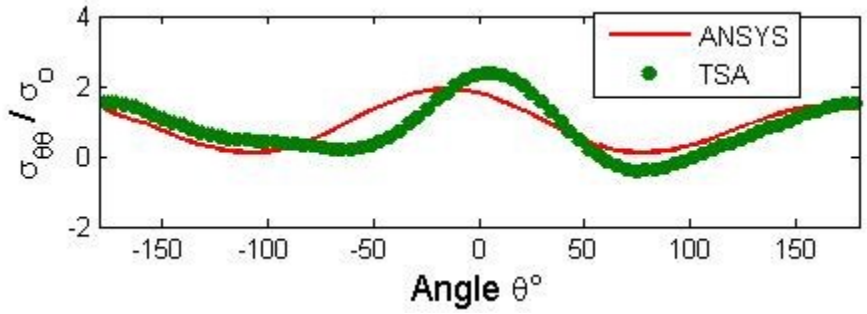

Fig. 8.86: Plot of $\sigma_{\theta\theta}/\sigma_0$ for small hole along $r/R_2 = 2$ from ANSYS and TSA for *k = 17* coefficients and m_4 = *4,094* TSA values

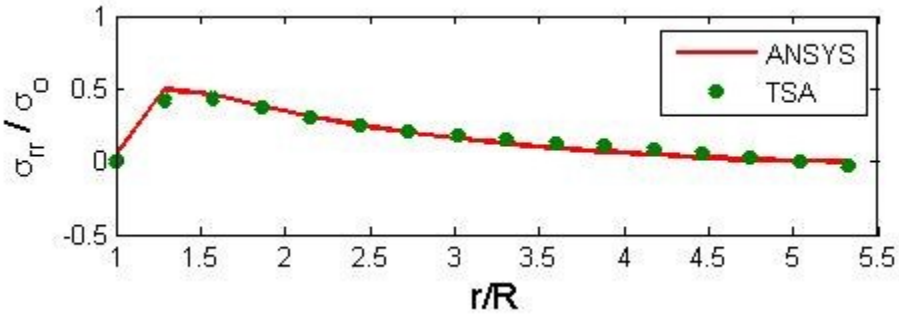

Fig. 8.87: Plot of σ_{rr}/σ_0 along A'B' of *figure 8.2* obtained from ANSYS and TSA for *k = 17* coefficients and m_4 = *4,094* TSA values

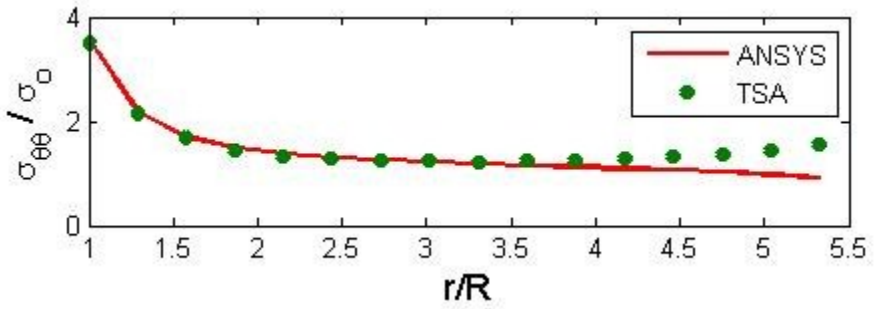

Fig. 8.88: Plot of $\sigma_{\theta\theta}/\sigma_0$ along A'B' of *figure 8.2* obtained from ANSYS and TSA for $k = 17$ coefficients and $m_4 = 4{,}094$ TSA values

Many of the *figures 8.67 through 8.88* illustrate the consequence of the uncertain ANSYS model of the top and bottom end loadings on the plate of *figures 8.2, 8.5 and 8.7*. The maximum values of $\sigma_{\theta\theta}/\sigma_0$ on the large and small holes (*figures 8.73 and 8.84*) are approximately 5. In retrospect although somewhat related the large stress at and near the edge of the holes in the incline-loaded plate are not greatly different from those of the vertically-loaded plate.

8.7 Strain Gage Analysis

TSA-based strains were evaluated from the TSA measured stresses and Hooke's law (E = 68.95 GPa (10 x 10^6 psi) and Poisson's ratio $\nu = 0.33$). These strains which were obtained from Thermoelastic Stress Analysis are compared with those obtained using commercial strain gages, *figures 8.89 through 8.93*. In the case of vertical (*figure 8.1*) and incline (*figure 8.2*) plate specimen there are no analytical solutions and only an approximated finite element model. Strain gage results are therefore very important particularly for assessing the reliability of the TSA result for the plate associated with *figures 8.2, 8.5 and 8.7*. Strain gages were mounted before spray painting the specimen. M-Bond 200 adhesive (marketed by Vishay Micro-Measurements) was used in conjunction with a catalyst (200 Catalyst-C, recommended for use with M-Bond adhesive) for long time stability. M-Coat, was applied over the gages to prevent the gages from shorting due to the Krylon Ultra-Flat black paint. Since most of the strain gages utilized are self-temperature compensating, and gages were mounted and testing conducted at room temperature, no dummy temperature compensating gages were employed. These Strains were recorded using a 16-channel, variable excitation strain gage conditioner *(figure 8.94).*

Four single element Micro-Measurements strain gages (EA-13-125-AD-120; gage length = 0.125", overall length = 0.250", grid width = 0.125", overall width = 0.125", matrix length = 0.40" and matrix width = 0.22"), with a gage resistance of 120Ω each and gage factor of 2.095 ± 0.5% were mounted two on the front and two on the back of the specimen to monitor and minimize any possible out-of-plane bending during loading. Four strain gages (measure $\varepsilon_{\theta\theta}$) of a Micro-Measurements strip gage (EA-06-031MF-120) on a common backing, with each gage

having a gage length of 0. 31", a gage factor of 2.1± 1% and a gage resistance of 120Ω, were mounted along line CD of *figure 8.1,* which is same as C'D' of *figure 8.2,* see *figures 8.90 and 8.91* (four gage elements were cut from the regular commercial 10-element strip gage). A Micro-Measurements strain gage (CEA-13-032UW-120) having a gage resistance of 120Ω and a gage factor of 2.13± 1% (gage length = 0.032", overall length = 0.180", grid width = 0.06", overall width = 0.12", matrix length = 0.27" and matrix width = 0.19") was also mounted on the curved edge of the hole as shown in *figure 8.89*. The calibration specimen described in section 8.2.2 also contained four Micro-Measurements strain gages (EA-13-125-AD-120), two on the front and two on the back, to monitor alignment and minimize out-of-plane bending *(figure 8.93).*

Figures 8.95 and 8.96 are the photographs of the symmetrically- and unsymmetrically-loaded specimen while doing the strain gage testing. *Figure 8.97* is a photograph of the overall testing of the hydraulically-loaded perforated plate, associated strain gage cables, strain gage conditioner, TSA camera, oscilloscope, and MTS machine. The oscilloscope connected to the MTS control box used to monitor accurately the specified load range is visible in *figure 8.97*.

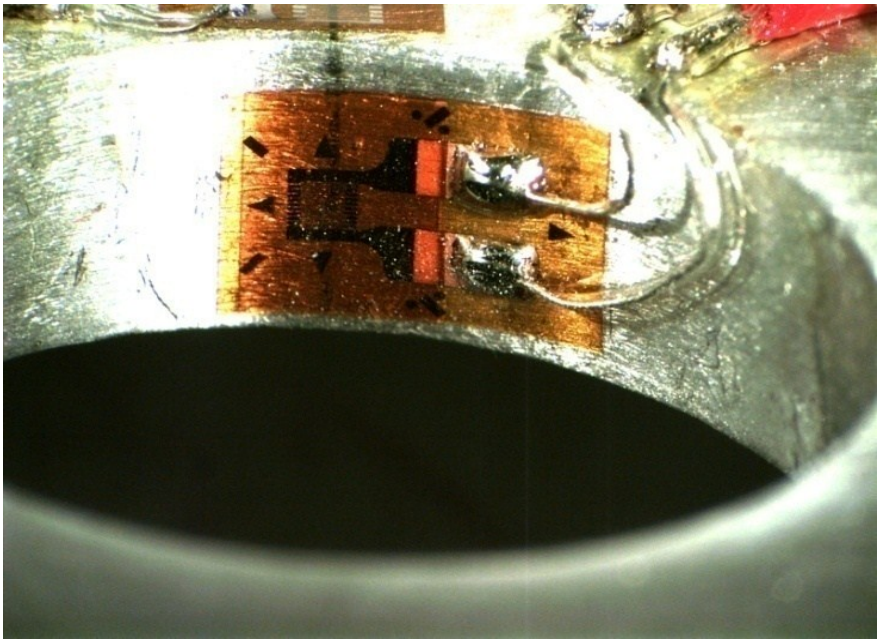

Fig. 8.89: Strain gage mounted at point C of *figure 8.1* and C' of *figure 8.2* on the curved edge of the hole

Fig. 8.90: Strip gage mounted along line CD of *figure 8.1 and* C'D' of *figure 8.2*

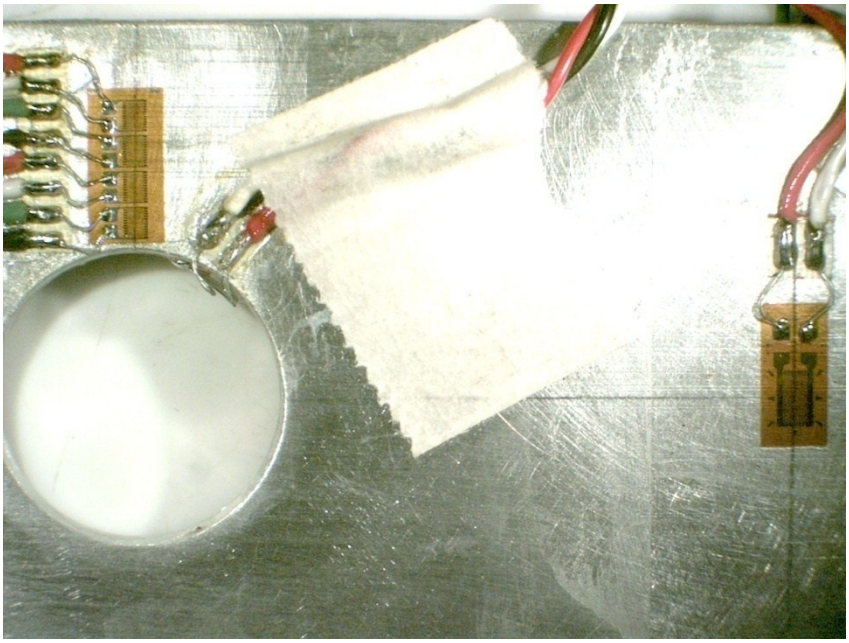

Fig. 8.91: Strip gage mounted along line CD and C'D' of *figures 8.1 and 8.2* respectively, strain gage along the curved edge of the hole and the distant transverse strain gage

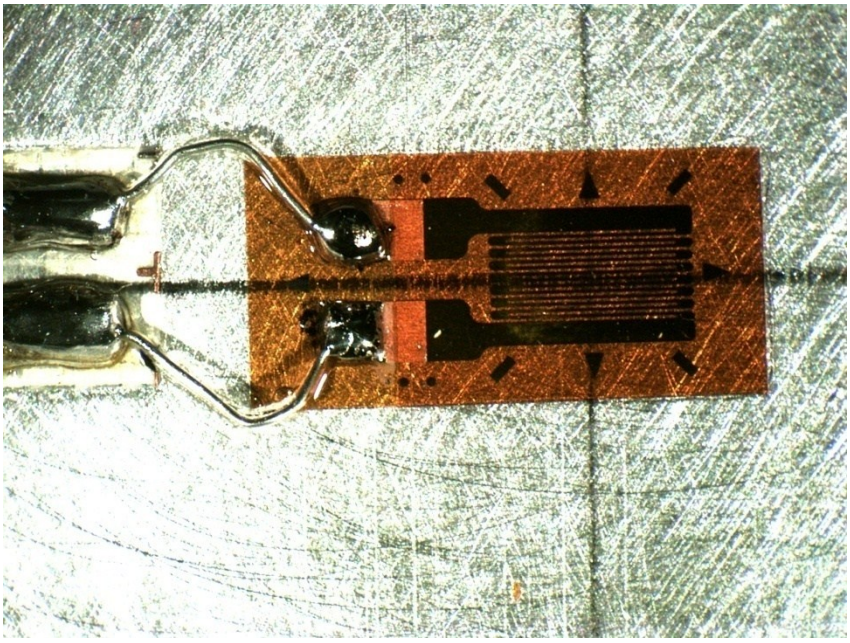

Fig. 8.92: Distant longitudinal strain gage used to check for any out-of-plane bending (gage length = 3.175mm = 0.125")

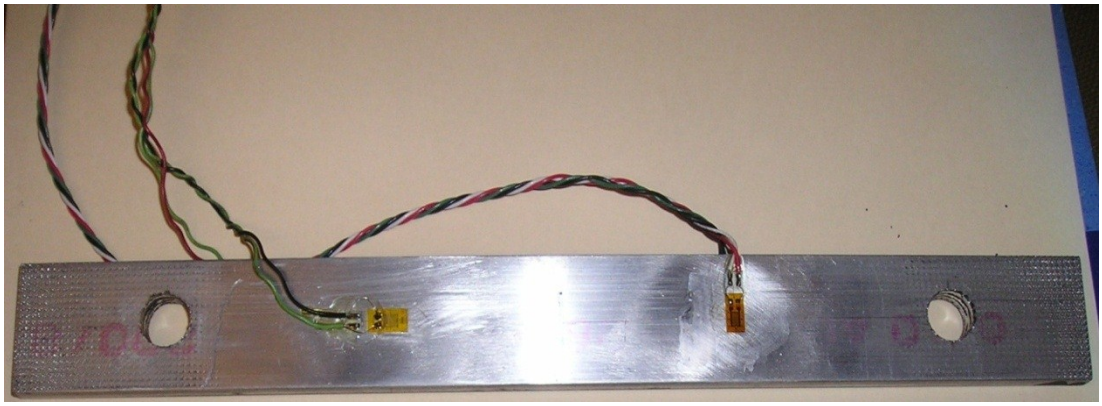

Fig. 8.93: Calibration specimen with mounted horizontal and vertical strain gages on both sides of the plate

Fig. 8.94: 16 Channel, variable excitation strain gage conditioner

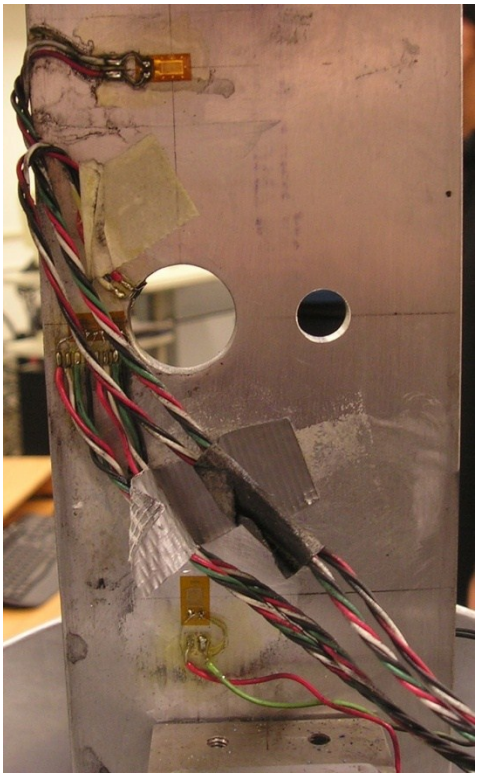

Fig. 8.95: Strain gage on back side of the symmetrically-loaded specimen

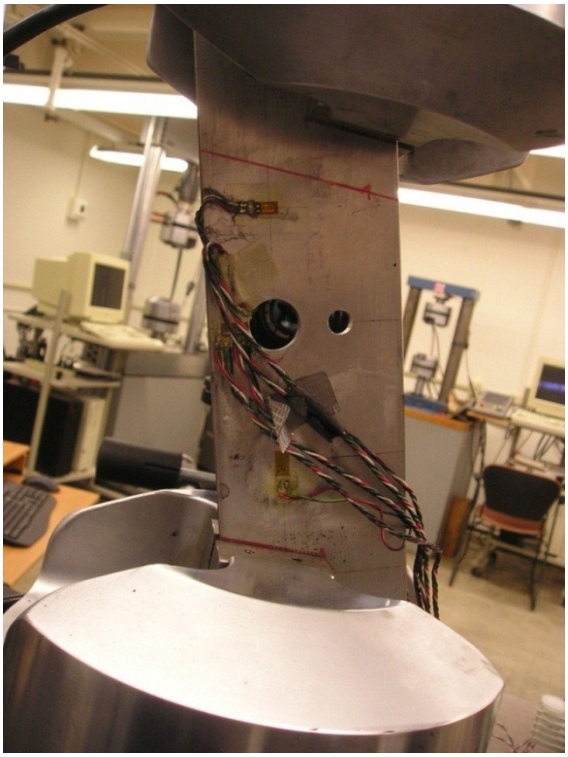

Fig. 8.96: Strain gage on the back side of unsymmetrically-loaded specimen

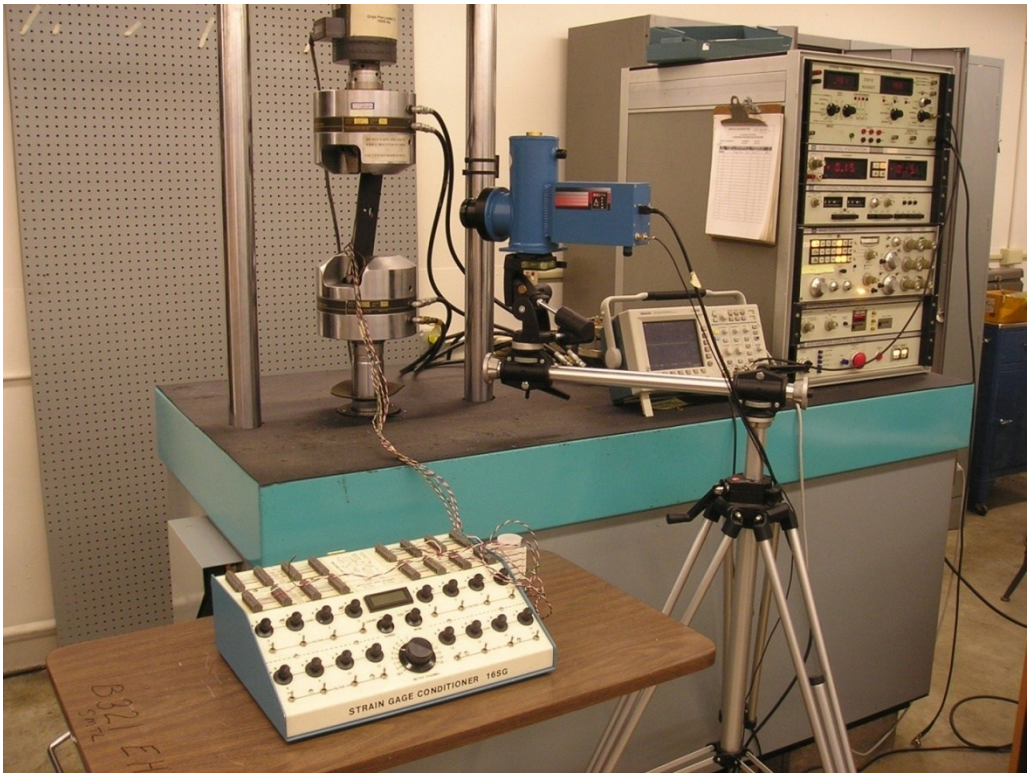

Fig. 8.97: Overview of the testing setup, including the MTS loading frame, hydraulic grips, TSA camera, strain gage switching, oscilloscope and balancing equipment

For the symmetrically-loaded plate, *figures 8.98 and 8.99* illustrate the load in pounds and Newton vs. strain (ε_{yy}) plots for the different strain gages which are bonded along line CD (*figure 8.1*), gage no.1 on the curved edge of the hole. These results demonstrate the response remains linear with load. *Figure 8.100* contains strain-gage recorded strains along CD for various levels of plate loading. *Figure 8.101* compares the strains (static equivalent specimen load of F = 4,448.22 N = 1,000lb) along the line CD extending from the large hole (*figure 8.1*) obtained from Thermoelastic Stress Analysis with those from finite element analysis (ANSYS) and strain gages. All strain-gage results were recorded under static loading. Of course ε_{yy} at x/r_1 = 1 of *figure 8.101* is point C (i.e., $\theta = 0^o$) of *figure 8.1*. This is the location of the maximum stress on the edge of the large hole, *figure 8.101*. It is worth noting that the TSA results agree well with those from strain gages.

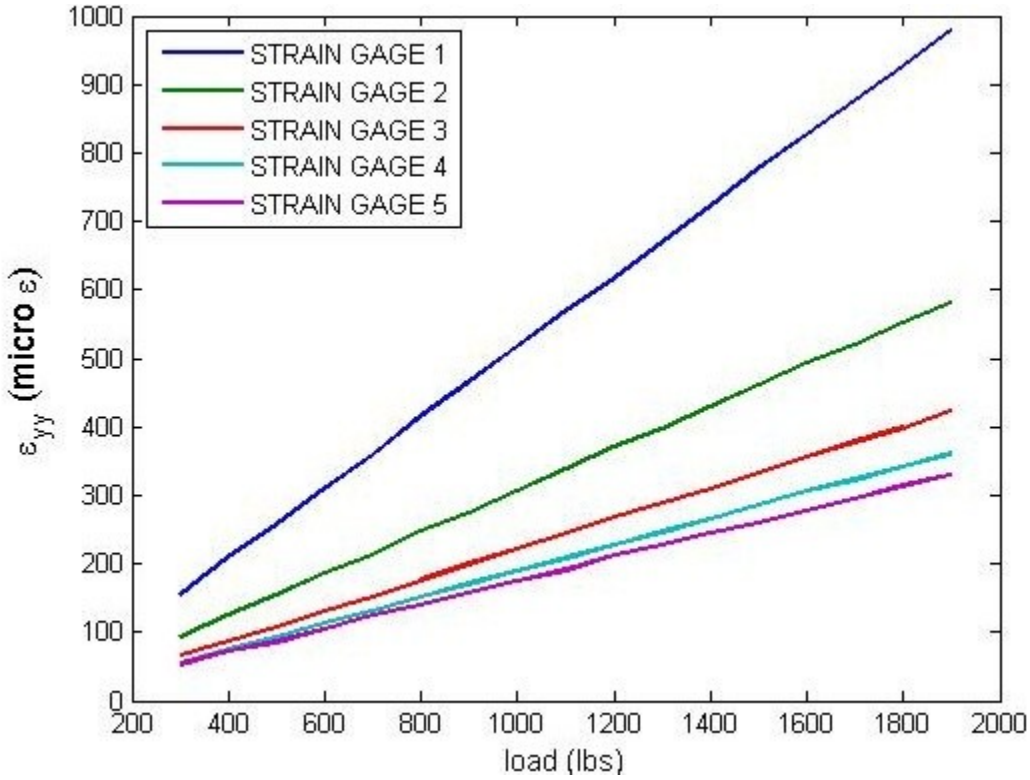

Fig. 8.98: Load (lbs) vs. Strain ε_{yy} for different strain gages along line CD of plate of specimen *figure 8.1*

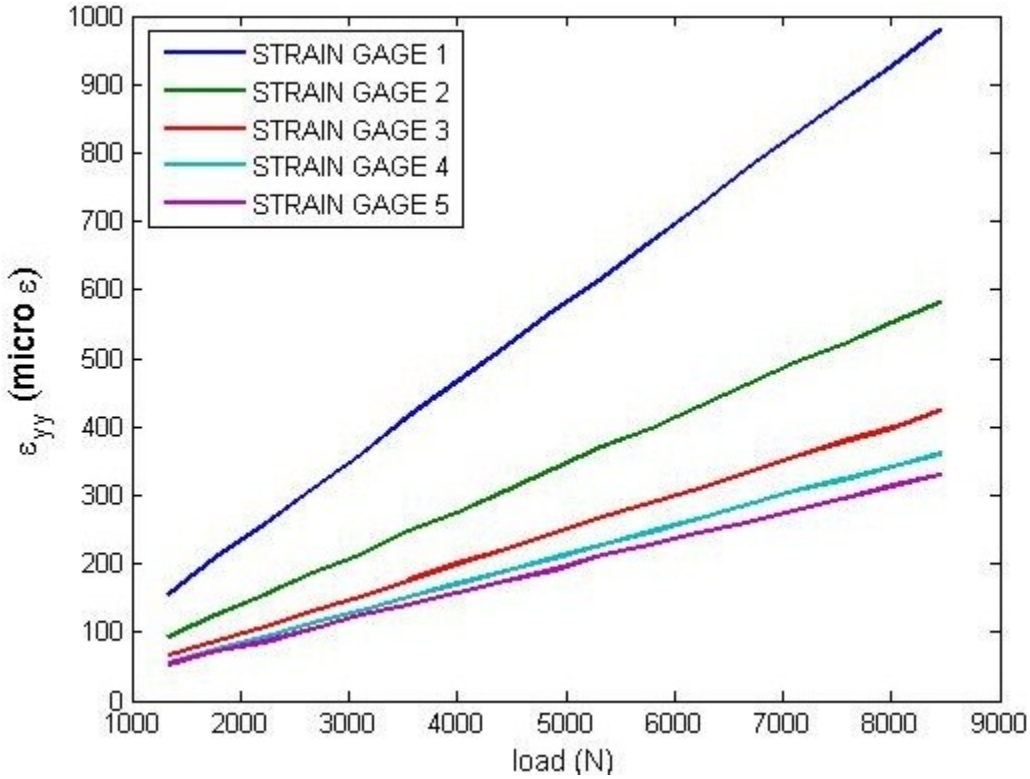

Fig. 8.99: Load (N) vs. Strain ε_{yy} for different strain gages along line CD of plate of *figure 8.1*

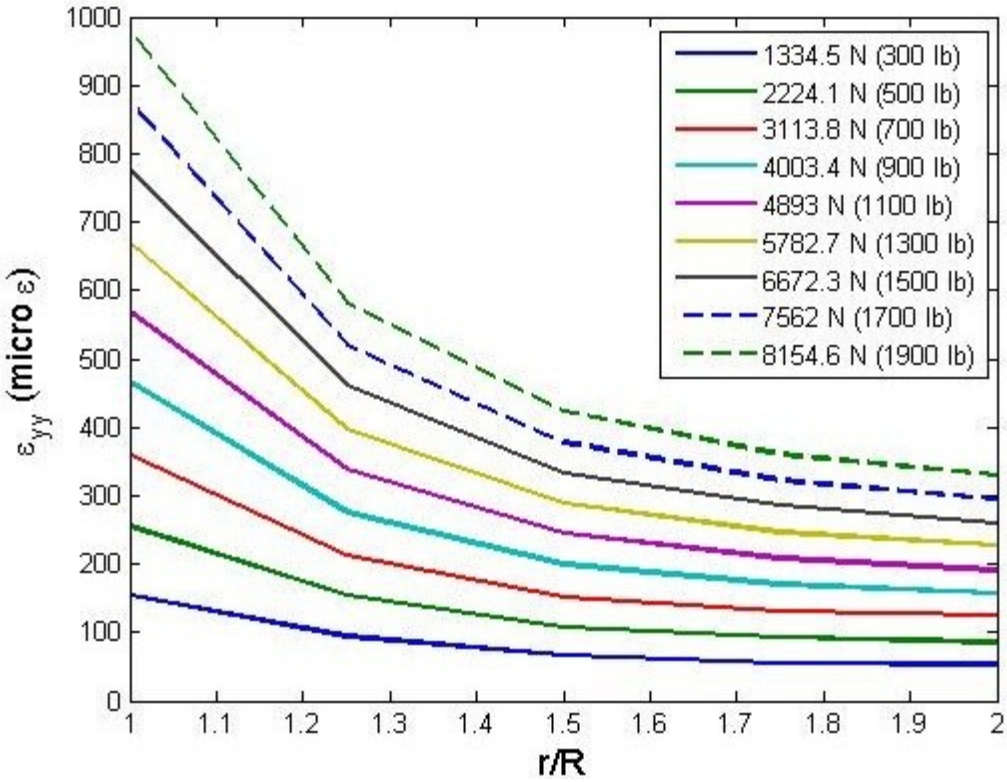

Fig. 8.100: Strain ε_{yy} from strain gages along CD of *figure 8.1* for different loads

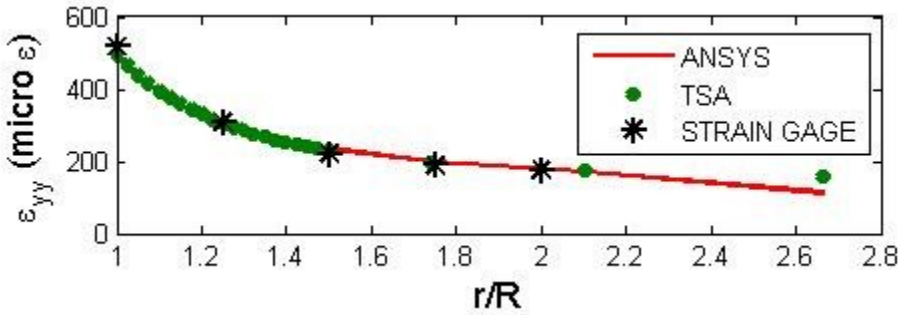

Fig. 8.101: Strain ε_{yy} along CD of *figure 8.1* obtained from ANSYS, strain gages and TSA for $k = 9$ coefficients and $m_1 = 4{,}378$ TSA values

For the unsymmetrically-loaded plate, *figures 8.102 and 8.103* show the load in pounds and Newton vs. strain ($\varepsilon_{\theta\theta}$) plots for different strain gages which are along line C'D' (*figure 8.2*), gage #1 on the curved edge of the plate. These results demonstrate the response remains linear with load. *Figure 8.104* contains strain-gage recorded strains along C'D' for various levels of plate loading. *Figure 8.105* compares the strains (static equivalent specimen load of F = 4,448.22 N = 1,000lb) along the line C'D' extending from the large hole (*figure 8.2*) obtained from Thermoelastic Stress Analysis with those from finite element analysis (ANSYS) and strain gages. All strain-gage results were recorded under static loading. Of course $\varepsilon_{\theta\theta}$ at $x/r_1 = 1$ of *figure 8.101* is point C' (i.e., $\theta = -15^o$) of *figure 8.1*. This is not the exact location of the maximum stress on the edge of the large hole, *figure 8.73*. It is worth noting that the strain gage results had a good agreement with the results obtained from TSA.

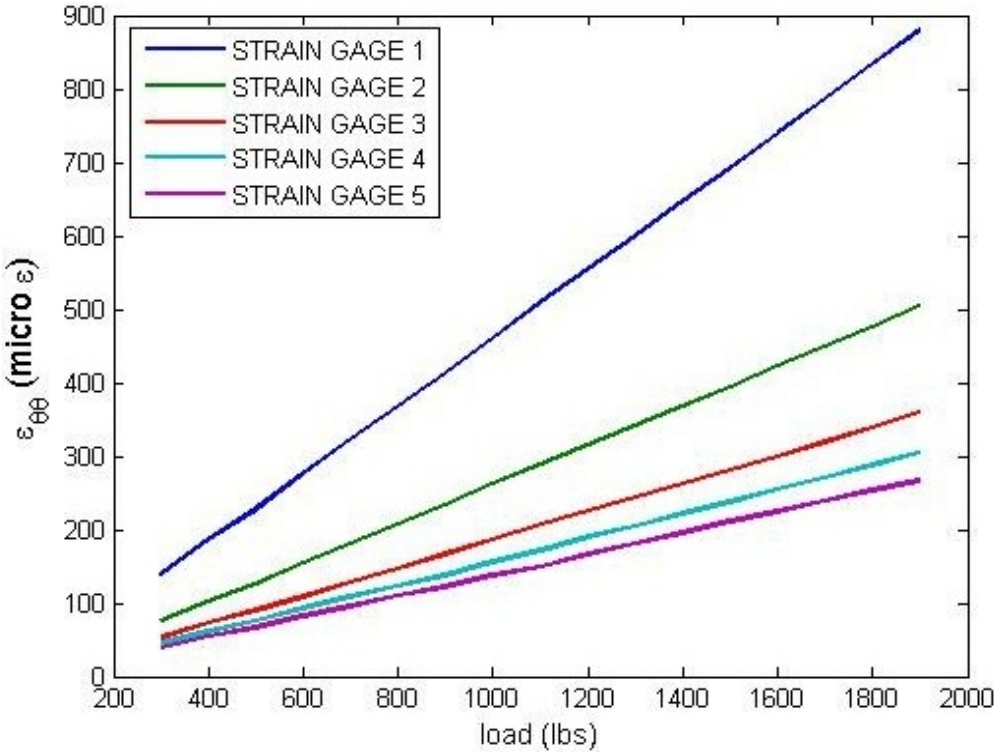

Fig. 8.102: Load (lbs) vs. Strain $\varepsilon_{\theta\theta}$ for different strain gages along the line C'D' of plate of *figure 8.2*

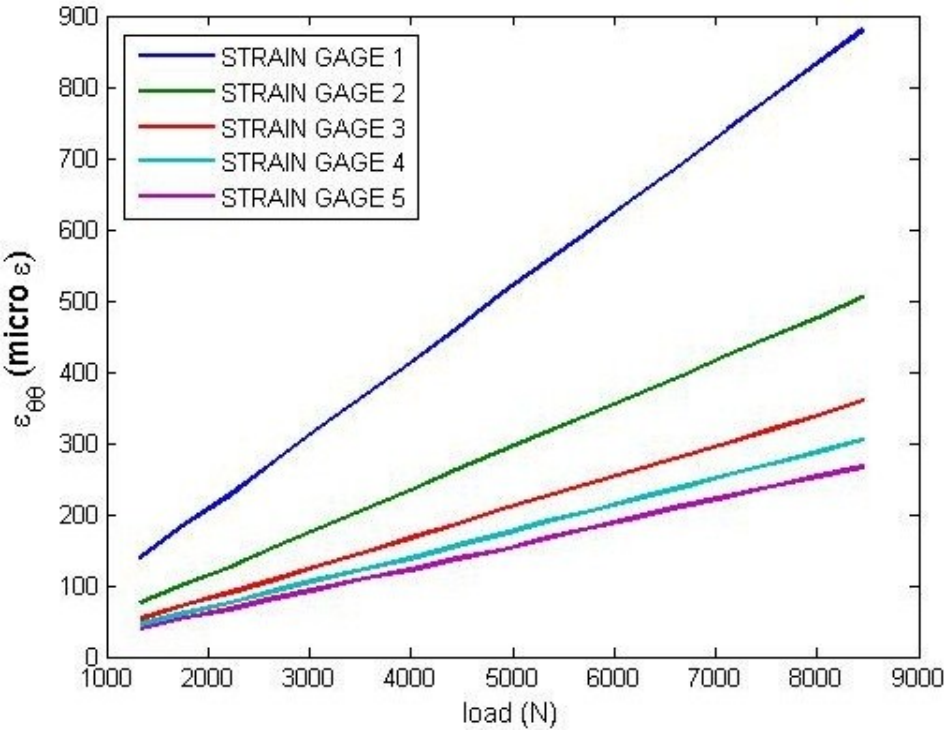

Fig. 8.103: Load (N) vs. Strain $\varepsilon_{\theta\theta}$ for different strain gages along the line CD of plate of *figure 8.1*

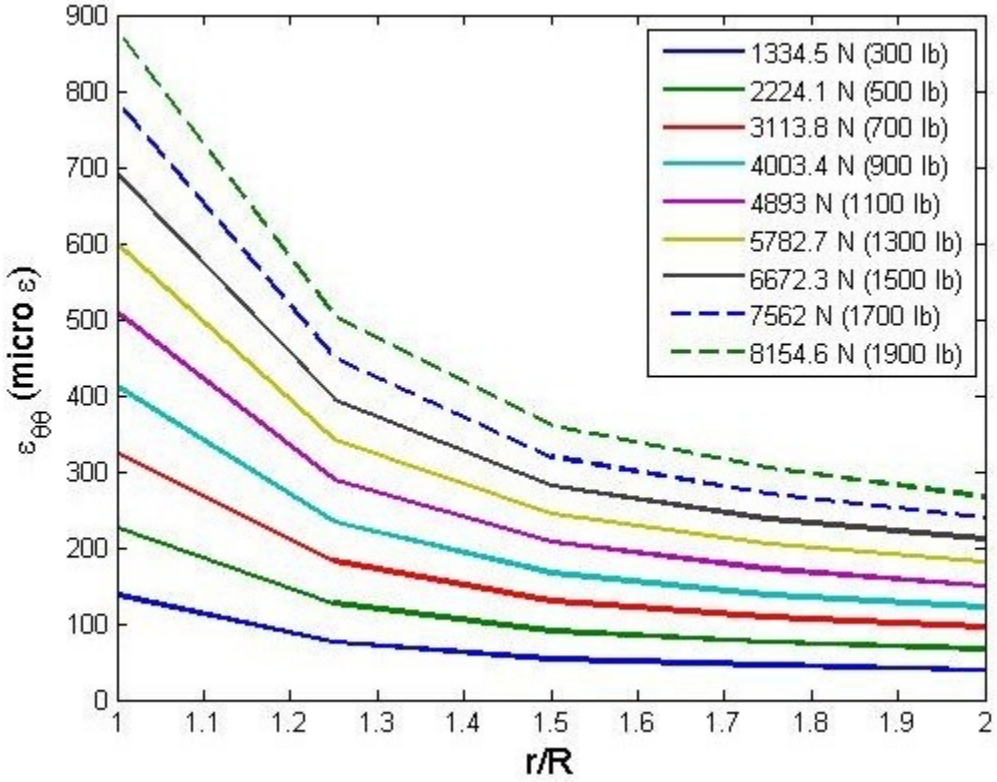

Fig. 8.104: Strain $\varepsilon_{\theta\theta}$ obtained from strain gages along C'D' of *figure 8.2* for different loads

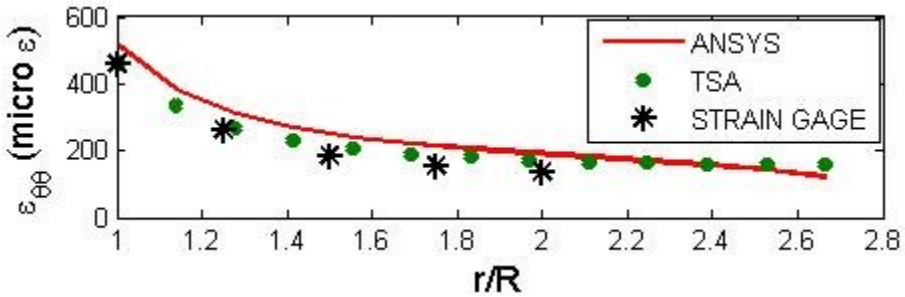

Fig. 8.105: Strain $\varepsilon_{\theta\theta}$ along C'D' of *figure 8.2* obtained from ANSYS, strain gages and TSA for $k = 17$ coefficients and $m_4 = 9{,}372$ TSA values

8.8 Imposing Stress Compatibility between the Holes in the Symmetrically-Loaded Plate

The measure temperature information around that individual hole was used to analyze the stresses associated with each of the small and large hole. Until now there was no attempt here to incorporate explicitly the consequence of the stresses associated with one hole with those of the other hole. It is worth noting that the measured input TSA data around either one of the holes automatically includes the consequences of the other hole, *figures 8.29 through 8.32 and 8.41 through 8.44*. As in Reference [3], the effect of the stress associated with one of the holes on the those of the other hole is now done by imposing compatibility conditions for the analyses of the stresses associated with the large and the small holes, i.e., ensuring the stresses σ_{xx}, σ_{yy} and σ_{xy} given by the individual analysis for each of the large and the small hole are approximately equal in the common region between the holes. Based on Airy coefficients of the respective holes, the rectangular stress components, σ_{xx}, σ_{yy} and σ_{xy}, in the common overlapping area associated with each hole were evaluated at 63 discrete locations in this overlapping region. The common value for each of σ_{xx}, σ_{yy} and σ_{xy} at each of the 63 locations (using the stress function and Airy coefficients for the individual holes) in the overlapping region between the holes is the average value of the respective rectangular components of stress based on the analysis associated with each of the small and large hole. The inner radius for each of these regions is the [radius of the particular hole + (4 x actual pixel size)] and the outer radius associated with the large and small holes are (2 x radius of the large hole) and (2 x radius of the small hole), respectively i.e., the common region is the intersection of these two regions. Each stress component, σ_{xx}, σ_{yy} and σ_{xy} therefore provides 63 additional conditions so 3*63 = 189 more conditions which are then

employed to solve the matrix expression of *equation 8.6* and which is solved using least squares to evaluate the unknown Airy coefficients. The total number of input values used now becomes $m_1 + 189 = 4{,}567$ for the large hole and $m_2 + 189 = 2{,}220$ for the small hole, quantities $m_1 = 4{,}378$, and $m_2 = 2{,}031$ are the measured TSA values with $k = 9$ coefficients for the analysis of either hole. Having solved *equation 8.6* for the newly-evaluated Airy coefficients, the analysis for each of the small and the large holes was again carried out individually at these 63 locations

$$\begin{bmatrix} S_{r_1,\theta_1}(b_0,c_0,d_1',b_2',d_2',b_3',d_3',b_4',d_4',b_5',d_5'.....b_N',d_N') \\ S_{r_2,\theta_2}(b_0,c_0,d_1',b_2',d_2',b_3',d_3',b_4',d_4',b_5',d_5'.....b_N',d_N') \\ S_{r_3,\theta_3}(b_0,c_0,d_1',b_2',d_2',b_3',d_3',b_4',d_4',b_5',d_5'.....b_N',d_N') \\ \vdots \\ S_{r_m,\theta_m}(b_0,c_0,d_1',b_2',d_2',b_3',d_3',b_4',d_4',b_5',d_5'.....b_N',d_N') \\ \sigma_{X_1X_1}(b_0,c_0,d_1',b_2',d_2',b_3',d_3',b_4',d_4',b_5',d_5'.....b_N',d_N') \\ \sigma_{Y_1Y_1}(b_0,c_0,d_1',b_2',d_2',b_3',d_3',b_4',d_4',b_5',d_5'.....b_N',d_N') \\ \sigma_{X_1Y_1}(b_0,c_0,d_1',b_2',d_2',b_3',d_3',b_4',d_4',b_5',d_5'.....b_N',d_N') \\ \vdots \\ \sigma_{X_{P/3}X_{P/3}}(b_0,c_0,d_1',b_2',d_2',b_3',d_3',b_4',d_4',b_5',d_5'.....b_N',d_N') \\ \sigma_{Y_{P/3}Y_{P/3}}(b_0,c_0,d_1',b_2',d_2',b_3',d_3',b_4',d_4',b_5',d_5'.....b_N',d_N') \\ \sigma_{X_{P/3}Y_{P/3}}(b_0,c_0,d_1',b_2',d_2',b_3',d_3',b_4',d_4',b_5',d_5'.....b_N',d_N') \end{bmatrix}_{(m+p)xk} \begin{bmatrix} b_0 \\ c_0 \\ d_1' \\ b_2' \\ d_2' \\ \vdots \\ b_N' \\ d_N' \end{bmatrix}_{kx1} = \begin{bmatrix} S_1 \\ S_2 \\ S_3 \\ S_4 \\ \vdots \\ S_m \\ \sigma_{X_1X_1} \\ \sigma_{Y_1Y_1} \\ \sigma_{X_1Y_1} \\ \vdots \\ \sigma_{X_{P/3}X_{P/3}} \\ \sigma_{Y_{P/3}Y_{P/3}} \\ \sigma_{X_{P/3}Y_{P/3}} \end{bmatrix}_{(m+p)x1} \tag{8.6}$$

Figures 8.106 and 8.107 show the values of Airy coefficients *(b_o, c_o, d_1', b_2', d_2', c_3', d_3', b_4' and d_4')* evaluated from the individual analysis of the large and small hole using the measured

TSA data. *Figures 8.106 and 8.107* illustrate the first few Airy coefficients i.e., b_o, c_o, d_1', b_2', d_2' here tend to be large compared to the last few *(c_3', d_3', b_4' and d_4'),* the latter being comparatively close to zero. Therefore a small change in the later coefficients would be significant, when plotting apparent changes in each Airy coefficient for the small and the large holes, *figures 8.108 and 8.109*. All of the coefficients in *figures 8.108 and 8.109* are normalized by the corresponding respective values in *figures 8.106 and 8.107*, e.g., all the values of b_o in *figures 8.108 and 8.109* are normalized by the corresponding respective value of b_o in *figures 8.106 and 8.107* and so on (similarly for c_o, d_1', b_2', d_2', c_3', d_3', b_4' and d_4'). *Figures 8.45 and 8.55* are plotted using the coefficients of *figure 8.106* and *figures 8.56 through 8.66* are plotted using the coefficients of *figure 8.107*.

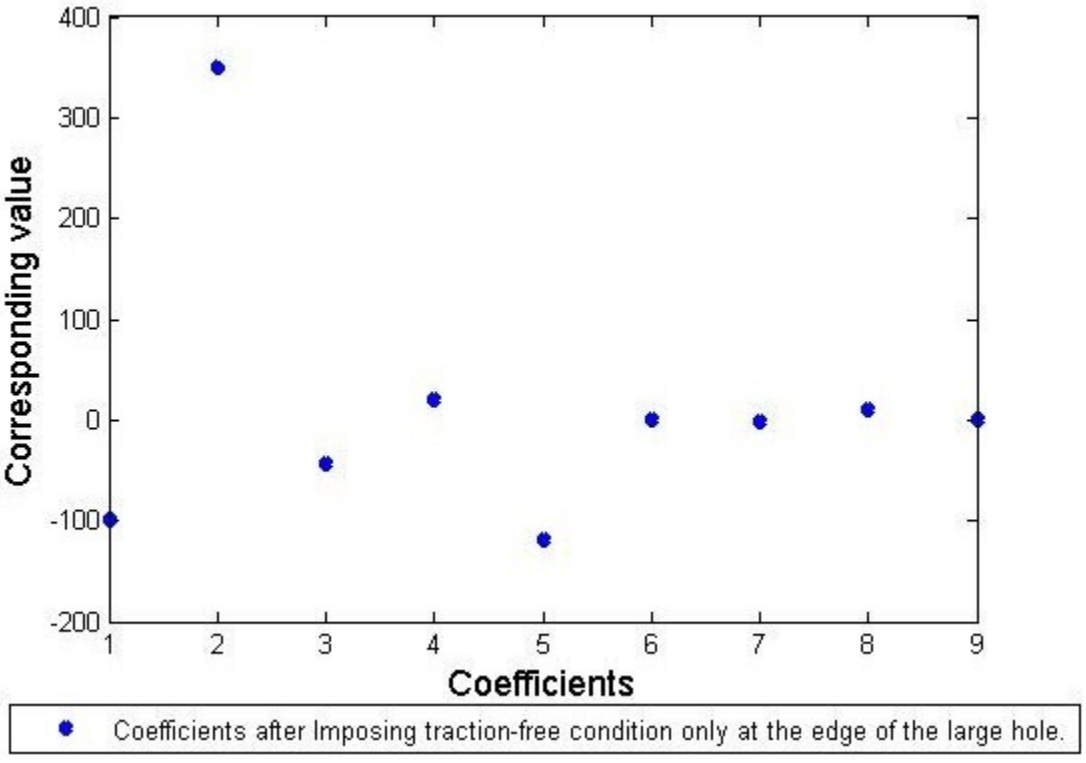

Fig. 8.106: Values of the Airy coefficients obtained from the TSA measured data (S*) for the large hole after imposing traction-free conditions only at the edge of the large hole

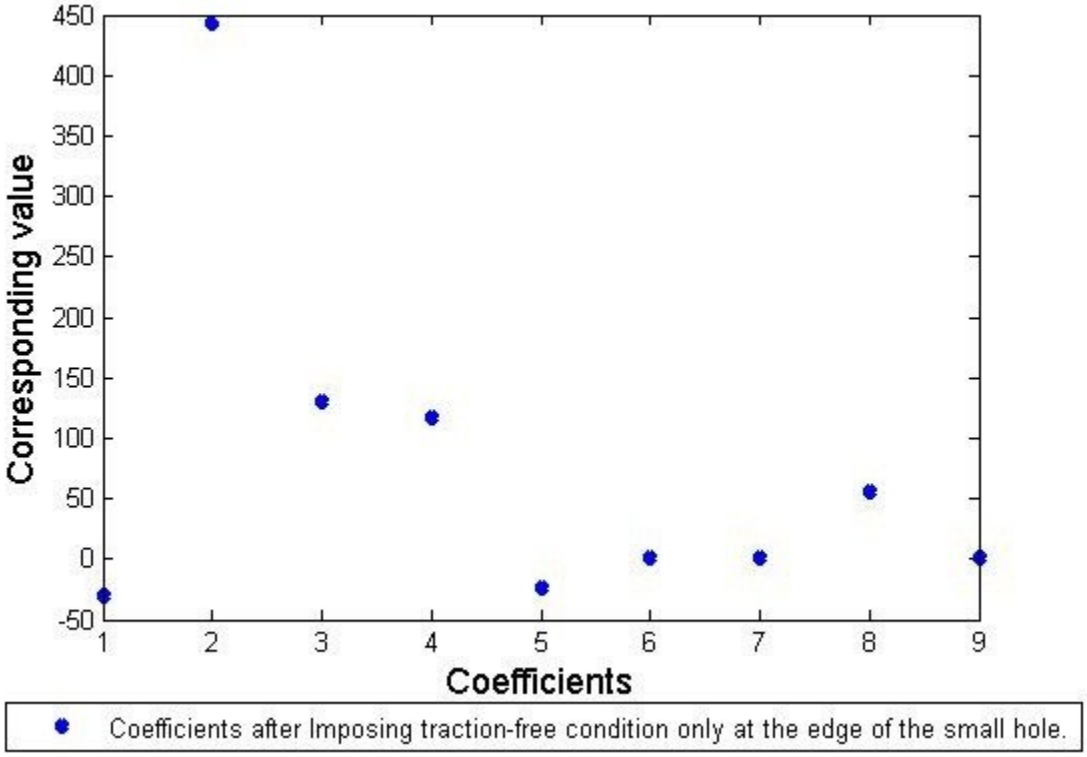

Fig. 8.107: Values of the Airy coefficients obtained from the TSA measured data (S*) for the small hole after imposing traction-free conditions only at the edge of the small hole

Case 1 - in *figures 8.108 and 8.109*, corresponds to the normalized values of the Airy coefficients evaluated from TSA measured data and imposing only the traction-free conditions *analytically* at the boundary of the large and the small hole (i.e., situation of *figures 8.106 and 8.107*; case 2 - once all the Airy coefficients for each of the small and the large holes have been calculated based on the coefficients of case 1, then the individual rectangular stress components in the common region are evaluated separately i.e., at 63 points. New Airy coefficients associated with each of the large and small hole are now obtained by imposing these 3*63 = 189 averaged stresses in this common region as additional conditions, along with the recorded temperature data, *equation 8.6*; case 3 - once all the Airy coefficients are known from case 2, then the stresses in the common region associated with each of the large and small hole are evaluated (using the Airy coefficients obtained from case 2) and their respective components

again averaged at each of the 63 locations. It is worth nothing that averaging twice did not made much difference i.e., the coefficients of case 2 and case 3 of *figures 8.108 and 8.109* are mostly identical.

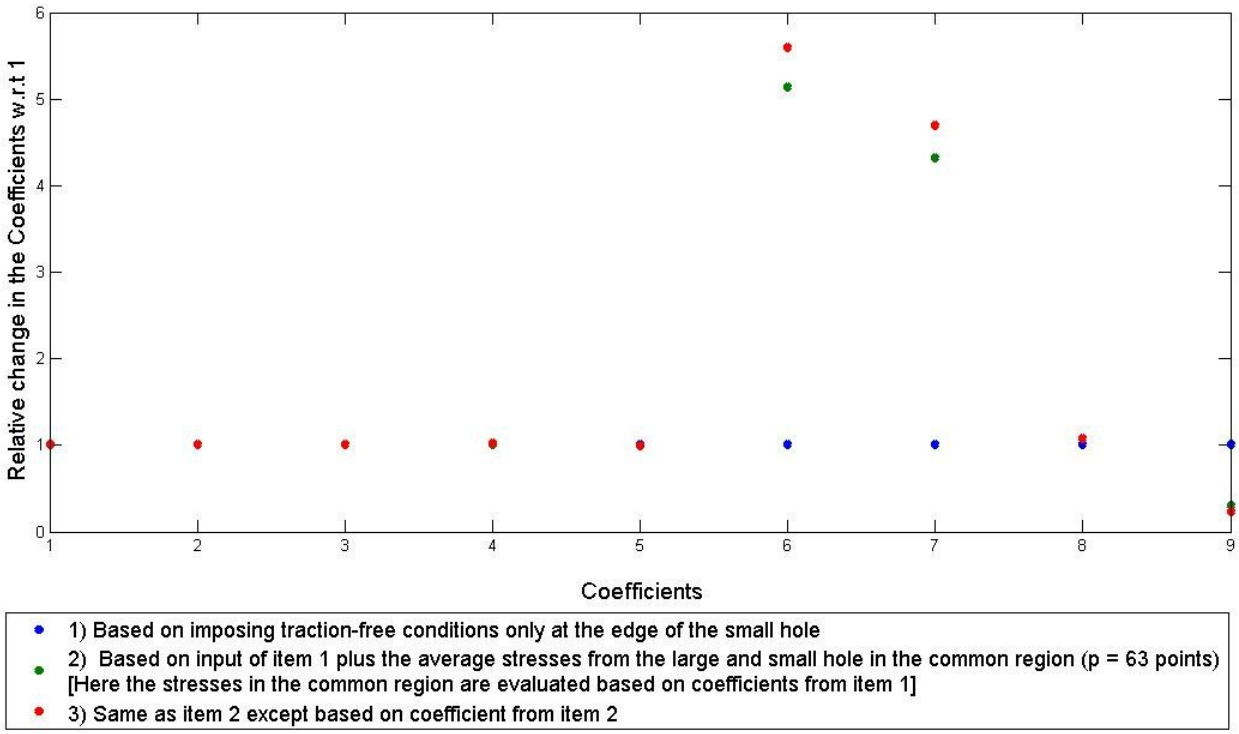

Fig. 8.108: Relative changes in the Airy coefficients for the small hole by satisfying stress compatibility between the holes

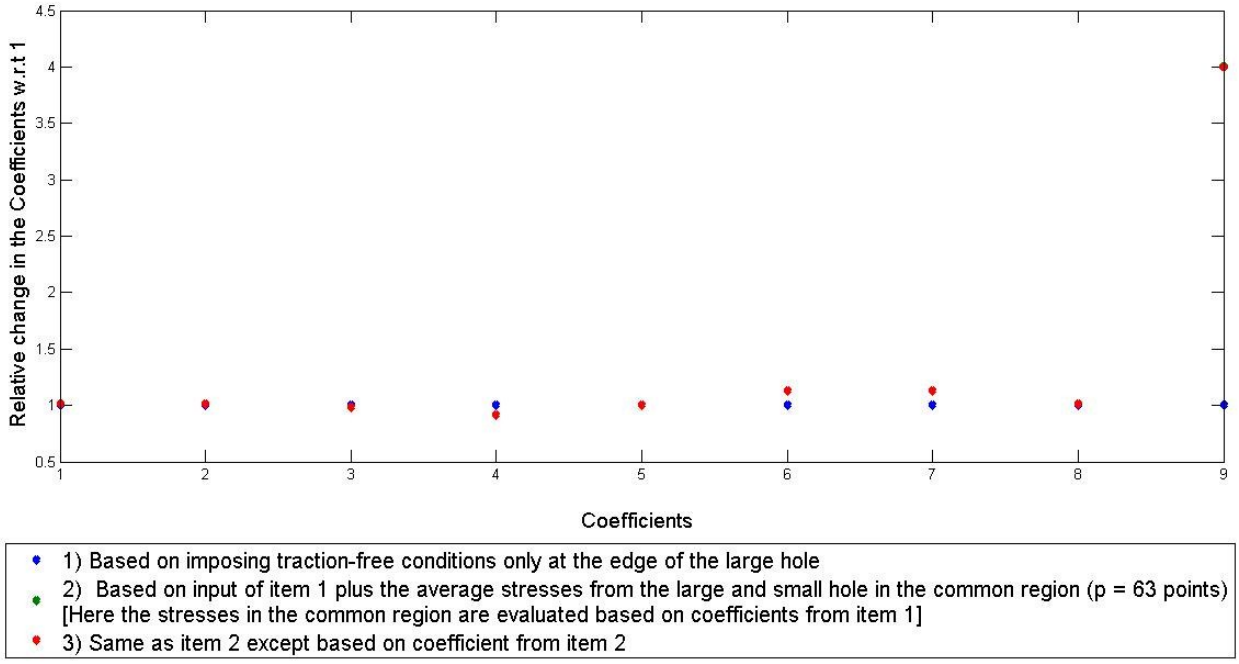

Fig. 8.109: Relative change in the Airy coefficients for the large hole by satisfying stress compatibility between the holes

Figure 8.110 is the plot of TSA and ANSYS determined $\sigma_{\theta\theta}/\sigma_o$ around the edge of the large hole while *figure 8.111* plots the ε_{yy} along CD of *figure 8.1* based on the nine Airy coefficients of the respective case 3 of *figure 8.106*. *Figure 8.112* is the plot of TSA and ANSYS determined $\sigma_{\theta\theta}/\sigma_o$ around the edge of the small hole based on the nine Airy coefficients of the case 3 of *figure 8.107*. Imposing the stress compatibility between the holes has little effect i.e., results of *figures 8.110, 8.111 and 8.112* are very similar to those of *figures 8.51, 8.101 and 8.66* respectively. These results indicate that whether or not one mathematically imposes stress compatibility between the holes produces relatively little change, i.e., sufficiently reliable results are available here on the edge of an individual hole based exclusively on measured temperature data associated with that hole. Since the results did not changed much in the case of symmetrically-loaded plate, there is no point in doing for unsymmetrically-loaded plate.

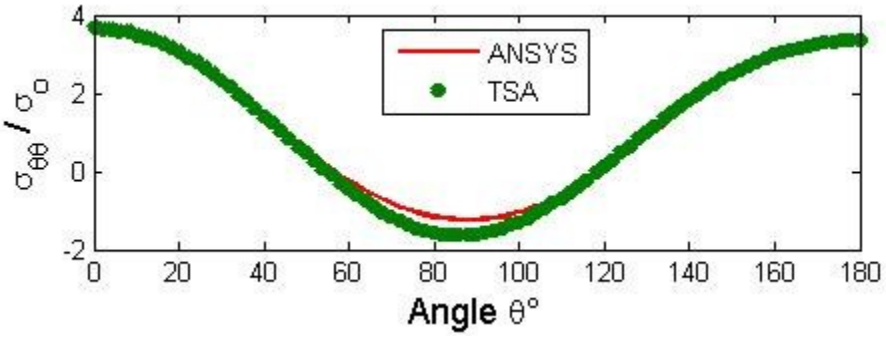

Fig. 8.110: Plot of $\sigma_{\theta\theta}/\sigma_0$ around the boundary of the large hole ($r/R_2 = 1$) from ANSYS and TSA using coefficients (b_o, c_o, d_1', b_2', d_2', c_3', d_3', b_4' *and* d_4') of case 3 of *figure 8.106*

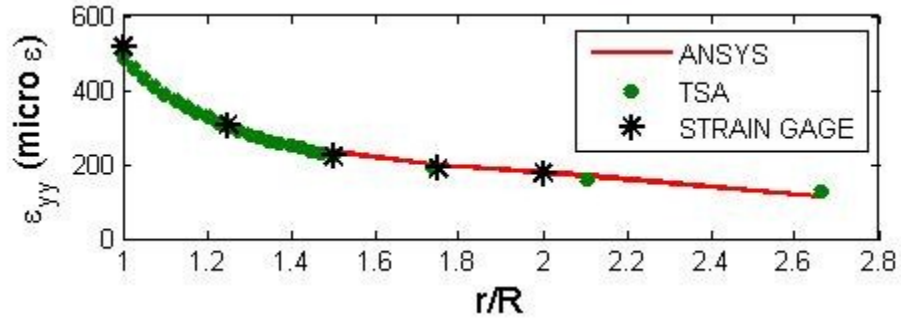

Fig. 8.111: Strain ε_{yy} along CD of *figure 8.1* obtained from ANSYS, strain gages and TSA using coefficients (b_o, c_o, d_1', b_2', d_2', c_3', d_3', b_4' *and* d_4') of case 3 of *figure 8.106*

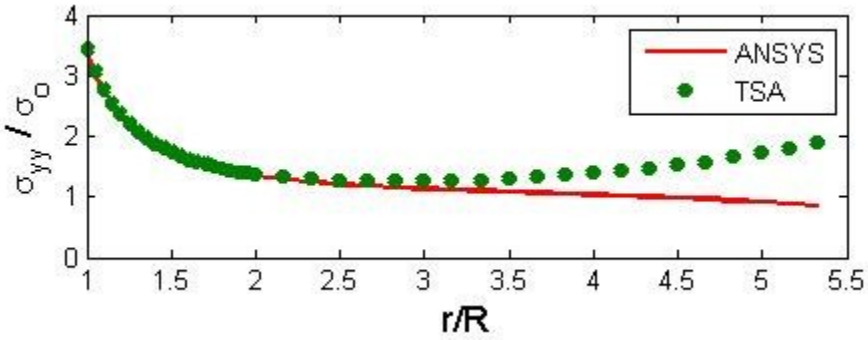

Fig. 8.112: Plot of $\sigma_{\theta\theta}/\sigma_0$ around the boundary of the small hole ($r/R_1 = 1$) from ANSYS and TSA using coefficients (b_o, c_o, d_1', b_2', d_2', c_3', d_3', b_4' *and* d_4') of case 3 of *figure 8.107*

8.9 Checking Load Equilibrium

Load equilibrium was verified for the symmetrically and unsymmetrically-loaded plate along the horizontal line of *figures 8.1 and 8.2*. Since the TSA analyses requires calibration, one can use the TSA data (which linearly dependent on the applied load, F) along with load equilibrium to evaluate the applied load i.e., considering the thermomechanical coefficient, K, as an unknown (initially) and evaluate it (perhaps iteratively) by summing the longitudinal stress distribution across some transverse plane and equating that value to applied load, F. This approach eliminates having to conduct a separate experiment for the TSA calibration. For the symmetrically-loaded plate of *figure 8.1*, the TSA-determined stress σ_{yy} was integrated across a horizontal section (AD) of the plate of *figure 8.1*. For the unsymmetrically-loaded plate the TSA determined stress σ_{yy} was integrated along a horizontal line 3.3 mm (0.13") above the origin of the large hole of *figure 8.2*. Before imposing the stress compatibility between the holes, summing σ_{yy} across line AD (using the coefficients of *figure 8.106*) of *figure 8.1,* i.e., $\int_A^D \sigma_{yy} t \, dy$ (where t is the thickness) gives a load 4537 N (1060 lbs) and after imposing the compatibility conditions between the holes (i.e., using the case 3 of *figure 8.108*), the load equilibrium was found to be 4684 N (1053 lbs). Integrating the stress σ_{yy} (using the coefficient of *figure 8.107*) across a section slightly above the large hole of *figure 8.2* gives load equilibrium of 4657 (1047 lbs). This differs from the applied load of 4715 N (1000 lbs) by only 4 to 6%. These checks on load equilibrium by integrating the TSA determined stresses further substantiate the reliability of the present TSA analysis.

8.10 Summary, Discussion and Conclusions

This chapter demonstrates the ability to determine the stress component in a multiple perforated plate using a hybrid experimental-numerical method which is highly effective for stress analysis finite plane-problems. This combines measured temperature information with a series representation of an Airy stress function along with *analytically* imposing the traction-free boundary condition on the edge of the hole. The determination of individual components of stress is very important in the engineering structures. The present technique is not restricted to a specific arrangement of multiple holes and loading conditions. Two different cases were conducted: out in which a plate is symmetrical about horizontal x-axis, the other does not enjoy such symmetry. The associated stress functions are based on the geometry and traction-free conditions, and irrespective of far field loading conditions. For the symmetrically-loaded plate, the stress functions assume symmetry only about the horizontal axis, while no symmetry was accounted in the stress function for unsymmetrically-loaded plate. The number of Airy coefficients utilized is substantiated experimentally. Individual stress components in the multiple holes in the finite domain subjected the arbitrary loading is determined. Advantages of the presented method includes no limitation for the number of holes, hole spacing, finite/infinite geometries, and arbitrary loading conditions. TSA results agree with those predicted by FEM, measured strains and load equilibrium is satisfied for both symmetrically-and unsymmetrically cases. The uncertain external loading conditions of the symmetrically-loaded plate necessitate an assumed FEM model. Whether or not stress compatibility is enforced between the holes, it has little effect on the results. The present TSA approach assumes plane-stress. The radius of the small hole considered is less than the thickness of the plate. Notwithstanding this situation, a 3-D

FEM analysis verifies the stresses are sufficiently uniform through the plate thickness to justify this plane stress assumption (Appendix 8).

The uncertainty of the ANSYS model (results) for the unsymmetrically-loaded plate of *figure 8.2* raises the validity of the question of the usefulness of comparing TSA and ANSYS results for that case. However, the excellent agreement between TSA and measured strains for the unsymmetrical situation further substantiates the reliability of TSA for stress analyzing practical engineering members. The uncertainty of ANSYS prediction for the plate of *figure 8.2* demonstrates challenges which can occur in numerical modeling engineering problems when the external loading (boundary conditions) are not adequately known, therefore necessitating an experimental analysis.

The present analysis considers the stress interactions among two circular holes in a two-dimensional finite domain. Since stresses at a geometric discontinuity can be influenced by the neighboring structural compliance, this chapter emphasizes determining the individual stress components in a region containing two different-size neighboring holes whose stress fields interact. Interaction effects among holes can be accurately evaluated through stress compatibility between the holes for the symmetrically-loaded plate. Little information is available for such cases, purely analytical solutions are extremely difficult for finite geometries, and reliable numerical approaches are challenging if the external loading is not well known. Although illustrated here for neighboring circular holes, the present approach is applicable to non-circular holes or notches, or combinations thereof.

Chapter 9 : Determining the Full Field Displacement, Strain and Stress Components in a Perforated Finite Orthotropic Plate from a Single Component of Displacement

9.1 Introduction

Composite components having holes or cut-outs are frequently used as load bearing structural members. Advantages of composites over conventional isotropic materials include their superior stiffness-and strength-to-weight ratios. However, composite materials are often non-isotropic and the anisotropy can significantly complicate the stresses in the vicinity of any geometric discontinuities. This chapter utilizes a hybrid method to evaluate from a single component of displacement the full-field stresses (strains, displacements) around a circular hole in a finite tensile plate. The method is applicable for both isotropic and orthotropic materials.

Stress determination by conventional displacement measurement techniques (digital image correlation, moiré, and speckle) require physically differentiating the measured displacements. Differentiation of such measured data has its own perils. Determining both Cartesian components of displacement is often non-trivial using techniques such as moiré, holography or speckle. It can also be difficult to measure quality displacements at and very close to the edge of the holes or notches (frequently the locations of interest) to say nothing about differentiating them reliably.

The glass-epoxy orthotropic composite laminate $[0/90/0_{10}/90/0]$ of *figure 9.1* is analyzed here. The geometry and material properties are taken from [118]. Recognizing the previously discussed challenges of sometimes having both components of displacement available, this chapter demonstrates the ability to determine the individual stress components from a single component of displacement. The technique utilizes complex variables and mapping, and satisfies the traction-free condition *analytically* at the hole. Simulated measured displacement information from ANSYS is used as input data.

This chapter also compares the various expressions from the literature used for conformal mapping, and individual stress and displacement components. The equations used here are from references [9, 117 and 118] publications and Baek's FORTRAN code. However, a few the typographical errors in Baek's equations have been corrected in this chapter. An objective of this chapter was to assemble a consistent set of equations free of errors or incompatibilities to evaluate the displacements, strains or stresses from one input component of displacement. Results of this chapter also somewhat extend those of reference [118].

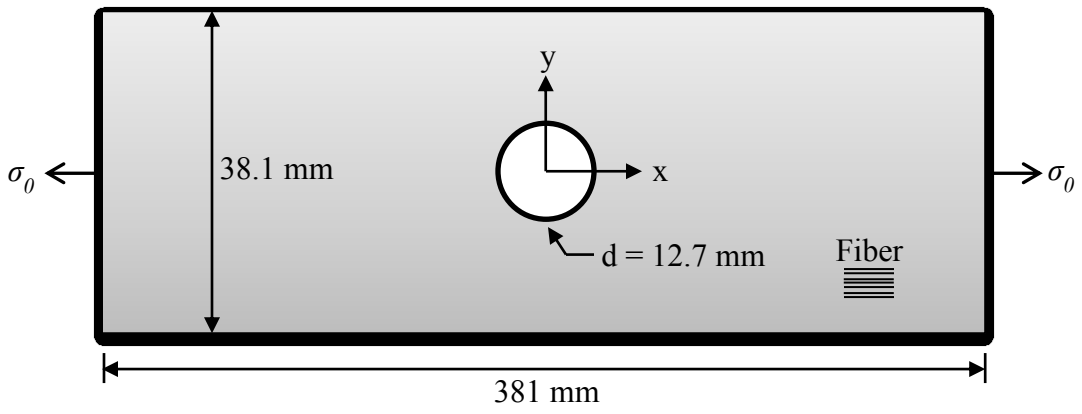

Fig. 9.1: Schematic of symmetrically-loaded glass-epoxy orthotropic composite plate with a central circular hole

9.2 Relevant Equations

For orthography, the equations of stress equilibrium and strain compatibility can be represented in terms of Airy's stress function, F [119]:

$$\frac{\partial^4 F}{\partial x^4} - \frac{2S_{26}}{S_{22}}\frac{\partial^4 F}{\partial x^3 \partial y} + \frac{(2S_{12}+S_{66})}{S_{22}}\frac{\partial^4 F}{\partial x^2 \partial y^2} - \frac{2S_{16}}{S_{22}}\frac{\partial^4 F}{\partial x \partial y^3} + \frac{S_{11}}{S_{22}}\frac{\partial^4 F}{\partial y^4} = 0 \qquad (9.1)$$

This equation can also be written as $D_1 D_2 D_3 D_4 F = 0$

where $D_k(k = 1,2,3,4) = \frac{\partial}{\partial y} - \mu_k \frac{\partial}{\partial x}$

The terms μ_k are the roots of the characteristic equation which are associated with the compatibility equation given below [119]

$$S_{11}\mu^4 - 2S_{16}\mu^3 + (2S_{12} + S_{66})\mu^2 - 2S_{26}\mu + S_{22} = 0 \qquad (9.2)$$

where, S_{11}, S_{12}, S_{16}, S_{22}, S_{26}, $and\ S_{66}$ are elastic compliances. When aligned in the direction of material symmetry, the elastic compliances (S_{ij}) are related to the engineering elastic quantities as follows.

$$S_{11} = \frac{1}{E_{11}}; \qquad S_{22} = \frac{1}{E_{22}}; \qquad S_{12} = -\frac{\upsilon_{12}}{E_{11}}; \qquad S_{66} = \frac{1}{G_{12}} \qquad (9.3)$$

By expressing the response of an orthotropic material in its directions of material symmetry, and using *equations 9.3*, *equation 9.1* reduces to *equation 9.4* [119] and *equation 9.2* to *equation 9.5*.

$$\frac{1}{E_{22}}\frac{\partial^4 F}{\partial x^4} + \left(\frac{1}{G_{12}} - 2\frac{\upsilon_{12}}{E_{11}}\right)\frac{\partial^4 F}{\partial x^2 \partial y^2} + \frac{1}{E_{11}}\frac{\partial^4 F}{\partial y^4} = 0 \qquad (9.4)$$

$$S_{11}\mu^4 + (2S_{12} + S_{66})\mu^2 + S_{22} = 0 \tag{9.5}$$

Combining *equations 9.5 and 9.3* yields *equation 9.6*

$$\mu^4 + \left(\frac{E_{11}}{G_{12}} - 2\upsilon_{12}\right)\mu^2 + \frac{E_{11}}{E_{22}} = 0 \tag{9.6}$$

The roots of the characteristic equation of *equation 9.6* can be seen in *equation 9.7*

$$\mu_1 = \alpha + i\beta, \qquad \mu_2 = \gamma + i\delta, \qquad \bar{\mu}_1 = \alpha - i\beta, \qquad \bar{\mu}_2 = \gamma - i\delta \tag{9.7}$$

Quantities $\alpha, \beta, \gamma, \delta$ of *equation 9.7* are real numbers, both β and δ are positive ($\beta > 0$, $\delta > 0$) and $i = \sqrt{-1}$. *Equation 9.6* indicates that these values depend only on material properties. If the roots are pair-wise equal, $\mu_1 = \mu_2 = \alpha + i\beta$ and $\bar{\mu}_1 = \bar{\mu}_2 = \alpha - i\beta$.

For an isotropic material, the elastic moduli are equal and the shear modulus can be written in terms of the elastic modulus and Poisson's ratio, as seen in *equation 9.8*

$$E_{11} = E_{22} = E; \qquad G = \frac{E}{2(1+\upsilon)} \tag{9.8}$$

Equations 9.9a and 9.9b then follow [119].

$$\frac{\partial^4 F}{\partial x^4} + 2\,\frac{\partial^4 F}{\partial x^2 \partial y^2} + \frac{\partial^4 F}{\partial y^4} = 0 \tag{9.9a}$$

$$\nabla^4 F = 0 \tag{9.9b}$$

Here $\nabla^2 = \frac{\partial^2}{\partial x^2} + \frac{\partial^2}{\partial y^2}$ and $\mu_1 = \mu_2 = i$, $\bar{\mu}_1 = \bar{\mu}_2 = -i$, $\alpha = \beta = 0$ [117].

The physical geometry of the plate is denoted as the z-plane. The x and y coordinates relate to this plane according to *equation 9.10*. The μ_j in *equation 9.10* can be obtained from *equation 9.6*.

$$z_j = x + \mu_j * y \; ; \; j = 1,2 \tag{9.10}$$

For orthotropy, the stress function in complex form, F, can then be expressed as [15].

$$F = 2Re[F_1(z_1) + F_2(z_2)] \tag{9.11}$$

where, Re denotes the 'real part' of the complex number. $F_1(z_1)$ and $F_2(z_2)$ are analytical functions of the complex variables z_1 and z_2, respectively. It is convenient to introduce the following two stress functions [15]

$$\Phi(z_1) = \frac{dF_1(z_1)}{dz_1} \qquad \text{and} \qquad \Psi(z_2) = \frac{dF_2(z_2)}{dz_2} \tag{9.12}$$

from which the stresses of *equations 9.13 through 9.15* can be written [15]. Primes in these equations denote the differentiation of the respective stress functions.

$$\sigma_x = 2Re\{{\mu_1}^2\Phi'(z_1) + {\mu_2}^2\Psi'(z_2)\} \tag{9.13}$$

$$\sigma_y = 2Re\{\Phi'(z_1) + \Psi'(z_2)\} \tag{9.14}$$

$$\tau_{xy} = -2Re\{\mu_1\Phi'(z_1) + \mu_2\Psi'(z_2)\} \tag{9.15}$$

The displacement can be written as in *equations 9.16 and 9.17*. In these equations, w, u_0 and v_0 are arbitrary constants which appear as a result of integration and which characterize the rigid body translations (u_0 and v_0) and rotation (w) [119].

$$u = 2Re\{p_1\Phi(z_1) + p_2\Psi(z_2)\} - wy + u_0 \tag{9.16}$$

$$v = 2Re\{q_1\Phi(z_1) + q_2\Psi(z_2)\} + wy + v_0 \tag{9.17}$$

In addition to the terms related to rigid motion, *equations 9.16 and 9.17* involve additional variables which depend only on material properties. These variables, symbolized by p_1, p_2, q_1 and q_2, are defined in *equation 9.18* [119].

$$p_1 = S_{11}{\mu_1}^2 + S_{12} - S_{16}\mu_1; \qquad p_2 = S_{11}{\mu_2}^2 + S_{12} - S_{16}\mu_2$$

$$q_1 = \frac{S_{12}{\mu_1}^2 + S_{22} - S_{26}\mu_1}{\mu_1}; \qquad q_2 = \frac{S_{12}{\mu_2}^2 + S_{22} - S_{26}\mu_2}{\mu_2} \tag{9.18}$$

Just as *equation 9.2* can be simplified to *equation 9.5*, these material properties can then be simplified when the material response is written in the directions of material symmetry, i.e.,

$$p_1 = S_{11}\mu_1^2 + S_{12}; \qquad p_2 = S_{11}\mu_2^2 + S_{12}$$

$$q_1 = S_{12}\mu_1 + \frac{S_{22}}{\mu_1}; \qquad q_2 = S_{12}\mu_2 + \frac{S_{22}}{\mu_2} \tag{9.19}$$

The method now makes use of conformal mapping. The basic idea of conformal mapping is fairly simple. A two-dimensional geometry can be represented by a coordinate system which represents one coordinate axis with imaginary numbers and the orthogonal coordinate axis with real numbers. A mapping function can then transform this original complex function representing the original geometry to a different complex function on a different coordinate plane. This mapping function must preserve angles when going from one coordinate system to another. The new coordinate system (and resulting geometry) is usually chosen to aid in solving desired equations. The solution from this simplified (mapped) domain can then be mapped back

to the original geometry. This mapped solution will be a valid solution to the desired equations on the original coordinate system, despite the fact that it was not solved for in this domain. For orthotropy, auxiliary planes and their induced mapping functions are defined according to reference [15].

$$z_j = \omega(\zeta_j) \tag{9.20}$$

Here, z_j represents the physical z-plane, as seen in *equation 9.10*. The z-plane is then mapped to the ζ-plane. The ζ-plane is the mapped complex plane whose coordinates are ξ and η.

$$\zeta_j = \xi + \mu_j \eta\,; \qquad j = 1{,}2 \tag{9.21}$$

Differentiating *equation 9.20* with respect to ζ yields *equation 9.22* [120].

$$\frac{dz_j}{d\zeta_j} = \omega_j'(\zeta_j) \tag{9.22}$$

From *equations 9.12 and 9.20*, the stress functions Φ and Ψ can be rewritten as in *equations 9.23 and 9.24* [120].

$$\Phi(z_1) = \Phi\big(\omega_1(\zeta_1)\big) \cong \Phi(\zeta_1) \tag{9.23}$$

$$\Psi(z_2) = \Psi(\omega_2(\zeta_2)) \cong \Psi(\zeta_2) \tag{9.24}$$

Differentiating *equations 9.23 and 9.24* yields *equations 9.25 and 9.26* [120].

$$\Phi'(z_1) = \Phi'(\zeta_1)\,\frac{d\zeta_1}{dz_1} = \frac{\Phi'(\zeta_1)}{\omega_1'(\zeta_1)} \tag{9.25}$$

$$\Psi'(z_2) = \Psi'(\zeta_2)\,\frac{d\zeta_2}{dz_2} = \frac{\Psi'(\zeta_2)}{\omega_2'(\zeta_2)} \tag{9.26}$$

In the absence of rigid body motion, *equations 9.25 and 9.26* can be combined with *equations 9.13, 9.14, and 9.15* to give [120]

$$\sigma_x = 2Re\left[\mu_1^2 \frac{\Phi'(\zeta_1)}{\omega_1'(\zeta_1)} + \mu_2^2 \frac{\Psi'(\zeta_2)}{\omega_2'(\zeta_2)}\right] \tag{9.27}$$

$$\sigma_y = 2Re\left[\frac{\Phi'(\zeta_1)}{\omega_1'(\zeta_1)} + \frac{\Psi'(\zeta_2)}{\omega_2'(\zeta_2)}\right] \tag{9.28}$$

$$\tau_{xy} = -2Re\left[\mu_1 \frac{\Phi'(\zeta_1)}{\omega_1'(\zeta_1)} + \mu_2 \frac{\Psi'(\zeta_2)}{\omega_2'(\zeta_2)}\right] \tag{9.29}$$

By combining *equations 9.25 and 9.26* with *equations 9.16 and 9.17*, and in the absence of rigid body motion, the displacements become

$$u = 2Re[p_1\Phi(\zeta_1) + p_2\Psi(\zeta_2)] \tag{9.30}$$

$$v = 2Re[q_1\Phi(\zeta_1) + q_2\Psi(\zeta_2)] \tag{9.31}$$

such that the *u* displacement is in the direction of loading, *figure 9.1*.

For a circular cutout of radius R in an orthotropic materials, the relevant geometry is transformed back from the ζ-plane to the physical z-plane using the mapping function of *equation 9.32* [9]. This function maps the unit circle of the ζ-plane to the boundary of the circular cutout in the physical z-plane [9].

$$z_j = \omega_j(\zeta_j) = \frac{R}{2}\left[(1 - i\mu_j)\zeta_j + \frac{1+i\mu_j}{\zeta_j}\right]; j = 1,2 \tag{9.32}$$

To map from the physical z-plane to the ζ-plane, the inverse of the mapping function of *equation 9.32* must be used. This can be seen in *equation 9.33* [9].

$$\omega^{-1}(z_j) = \zeta_j = \frac{z_j \pm \sqrt{z_j^2 - R^2(1+\mu_j^2)}}{R(1-i\mu_j)} \; ; j = 1,2 \tag{9.33}$$

The stress components of *equations 9.27 through 9.29* involve the derivative of the mapping function with respect to ζ_j. This derivative is given below.

$$\omega'_j = \frac{R}{2}\left[(1 - i\mu_j) - \frac{1+i\mu_j}{{\zeta_j}^2}\right] ; j = 1,2 \tag{9.34}$$

The stress components also involve the two complex stress functions, Φ and Ψ, which can be related by conformal mapping. Imposing the traction-free boundary condition on the edge of the hole relates these two functions as follows [15]

$$\Psi(\zeta_2) = B\overline{\Phi(\overline{\zeta_2})} + C\Phi(\zeta_2) \tag{9.35}$$

The constants B and C are complex variables which depend only on material properties, as seen in *equation 9.36*.

$$B = \frac{\overline{\mu}_2 - \overline{\mu}_1}{\mu_2 - \overline{\mu}_2} \; ; \quad C = \frac{\overline{\mu}_2 - \mu_1}{\mu_2 - \overline{\mu}_2} \tag{9.36}$$

No steps have yet been made to provide the stress functions. Since the stress functions are analytic, they can be represented by either Taylor series or Laurent series expansions. Although both of these series expansions involve a (computationally impossible) infinite sum, the larger order terms are nearly negligible, and a truncated series is therefore a

valid approximation. For this reason, truncated series expansions are used. Mappings which map the boundary of the hole in the physical plate to the real axis of the ζ-plane use truncated Taylor series expansions whereas mappings which map the boundary of the circular hole to the unit circle of the ζ-plane employ Laurent series expansions [121]. Laurent expansions can be applied in circumstances where Taylor series expansions cannot; unlike Taylor series expansions, Laurent expansions sum from -∞ to ∞ instead of from 0 to ∞. The Laurent expansions of the stress functions used are in *equations 9.37 and 9.38* and note that $j \neq 0$.

$$\Phi(\zeta_1) = \sum_{\substack{j=-m \\ j\neq 0}}^{m} c_j \zeta_1^j \tag{9.37}$$

$$\Psi(\zeta_2) = \sum_{\substack{j=-m \\ j\neq 0}}^{m} (\bar{c}_j B \zeta_2^{-j} + c_j C \zeta_2^j) \tag{9.38}$$

It should be noted that the two Laurent expansions in equations in *equations 9.37 and 9.38* sum only the odd values of *j,* i.e., *j* not only never equals zero, it never equals an even number. This is due to the symmetry around the hole. If one quadrant of the plate of *figure 9.1* is analyzed, each of the other three quadrants is known through symmetry. The coefficients c_j found in *equations 9.37 and 9.38*, are complex numbers consisting of some real component a_j and some imaginary component b_j, i.e., $c_j = a_j + ib_j$.

It is now possible to solve for the coefficients a_j and b_j from the known (measured) displacements. Combining *equations 9.37 and 9.38* with *equations 9.30 and 9.31*, one obtains

$$u = 2Re\left(\sum_{\substack{j=-m \\ j\neq 0}}^{m} \{[p_1\zeta_1^j + p_2(C\zeta_2^j + B\zeta_2^{-j})]a_j + i[p_1\zeta_2^j + p_2(C\zeta_2^j - B\zeta_2^{-j})]b_j\} \right) \tag{9.39}$$

$$v = 2Re\left(\sum_{\substack{j=-m \\ j\neq 0}}^{m} \{[q_1\zeta_1^j + q_2(C\zeta_2^j + B\zeta_2^{-j})]a_j + i[q_1\zeta_2^j + q_2(C\zeta_2^j - B\zeta_2^{-j})]b_j\} \right) \tag{9.40}$$

From many known (measured) values of u and/or v, the coefficients a_j and b_j can be evaluated. For a sufficient number of input known (measured) uniaxial displacements, *equation 9.39* will be over determined. Coefficients a_j and b_j can then be determined using the Gauss-Jordan method in MATLAB. Since the present approach is to use the known (measured) u displacement, which is in the direction of loading, *equation 9.40* can be written in the following matrix form [118].

$$[U]_{mxk}\{c\}_{kx1} = \{d\}_{mx1} \tag{9.41}$$

For the displacement vector $\{d\} = \{u\}$ having m measured input displacements originating from the source locations, and the coefficient vector $\{c\} = \{a_j\}$ having k unknown coefficients, then the matrix $[U]$ is m x k given in *equation 9.42*. The j in vector $\{c\}$ corresponds to only odd terms and sums over the $-m$ to m except $j \neq 0$ in the Laurent expansion and therefore the size of $k = j+1$. The vector $\{c\}$ is composed of only $\{a_j\}$ because the real part of *equation 9.39* is just $\{a_j\}$. The size of the rectangular matrix $[U]$ depends on the number of terms in the Laurent expansion and the number of input values. In matrix notation, the *equation 9.39* becomes

$$U(m,k) = 2Re\left[p_1\zeta_1^j + p_2\left(C\zeta_2^j + B\zeta_2^{-j}\right)\right] \tag{9.42}$$

The variables ζ_1 and ζ_2 differ with every input data location. If $\{d\}$ is known at a sufficient number of locations, the coefficients $\{c\}$ can be solved for using some least squared method like the Gauss-Jordan technique. Knowing $\{c\}$ then one can evaluate both *u* and *v* displacements of *equations 9.39 and 9.40*.

The derivatives of the stress functions are necessary to solve for the stresses of *equations 9.27 through 9.29*. The derivatives of the Laurent expansions of the two stress functions are given in *equations 9.43 and 9.44*.

$$\Phi'(\zeta_1) = \sum_{\substack{j=-m \\ j\neq 0}}^{m} jc_j\zeta_1^{j-1} \tag{9.43}$$

$$\Psi'(\zeta_2) = \sum_{\substack{j=-m \\ j\neq 0}}^{m} \left(-j\bar{c}_j B\zeta_2^{-j-1} + jc_j C\zeta_2^{j-1}\right) \tag{9.44}$$

Since c_j is now known from *equations 9.41 and 9.42*, the stresses of *equations 9.27 through 9.29* can be found with the help of *equations 9.34, 9.36, 9.43 and 9.44*, these stresses can be found in *equations 9.45, 9.46, and 9.47*, respectively.

$$\sigma_x = 2\sum_{\substack{j=-m \\ j\neq 0}}^{m} Re\left[\mu_1^2 \frac{jc_j\zeta_1^{j-1}}{\frac{R}{2}\left[(1-\mu_1) - \frac{1+i\mu_1}{{\zeta_1}^2}\right]} + \mu_2^2 \frac{-j\bar{c}_j B\zeta_2^{-j-1} + jc_j C\zeta_2^{j-1}}{\frac{R}{2}\left[(1-\mu_2) - \frac{1+i\mu_2}{{\zeta_2}^2}\right]}\right] \tag{9.45}$$

$$\sigma_y = 2\sum_{\substack{j=-m \\ j\neq 0}}^{m} Re\left[\frac{jc_j\zeta_1^{j-1}}{\frac{R}{2}\left[(1-\mu_1)-\frac{1+i\mu_1}{{\zeta_1}^2}\right]}+\frac{-j\bar{c}_jB\zeta_2^{-j-1}+jc_jC\zeta_2^{j-1}}{\frac{R}{2}\left[(1-\mu_2)-\frac{1+i\mu_2}{{\zeta_2}^2}\right]}\right] \tag{9.46}$$

$$\tau_{xy} = -2\sum_{\substack{j=-m \\ j\neq 0}}^{m} Re\left[\mu_1\frac{jc_j\zeta_1^{j-1}}{\frac{R}{2}\left[(1-\mu_1)-\frac{1+i\mu_1}{{\zeta_1}^2}\right]}+\mu_2\frac{-j\bar{c}_jB\zeta_2^{-j-1}+jc_jC\zeta_2^{j-1}}{\frac{R}{2}\left[(1-\mu_2)-\frac{1+i\mu_2}{{\zeta_2}^2}\right]}\right] \tag{9.47}$$

9.3 Literature Review

There already exists considerable literature utilizing conformal mapping related to determining the full-field stresses around a circular hole. The literature is not particularly consistent in how it performs the complex mathematics necessary to produce full field stresses from measured data and a traction-free boundary.

Both of the papers by Baek and Rowlands [9 and 117] use the same fundamental mathematic technique as does in this chapter, despite the fact that they used different types of input data, i.e., [117] used moiré input data and [9] used biaxial strain gage data. Both papers explicitly state that the Laurent expansions (*equations 9.37 and 9.38*) are summed only over odd values and use only real terms because of symmetry.

The article using the same technique for supplying input data, written by Baek, Chung, and Panganiban [118], contains some mathematical differences (typographical errors). Reference [118] gives the following mapping function

$$z_j = \omega_j(\zeta_j) = \frac{R}{2}\left[(1 - i\mu_j)\zeta_j + \frac{1-i\mu_j}{\zeta_j}\right] \tag{9.48}$$

This expression differs from the current mapping function provided in *equation 9.32* in that the numerator in the second term of *equation 9.48* is a difference instead of the sum as given by this chapter. Additionally, the Laurent expansion for the second stress function in [118] differs from that of this chapter and other papers using unit-circle mappings. Their [118] second Laurent expansion can be seen in *equation 9.49*.

$$\Psi(\zeta_2) = \sum_{\substack{j=-m \\ j\neq 0}}^{m} (\bar{c}_j B \zeta_2^j + c_j C \zeta_2^j) \tag{9.49}$$

Lin and Rowlands [122], with relevance to moiré, holography, laser Doppler interferometry, and thermoelastic stress analysis, derived *equations 9.27 through 9.29* from the compatibility and equilibrium equations. Reference [122] provides the fundamentals behind the Laurent expansions through the relationship between the two stress functions and how they match to different mapping techniques. Reference [122] also provides conformal mapping for a variety of geometries. This includes conformal mapping equations for straight edges, circular openings and notches. However, unlike this chapter, [122] mapped the boundary of a circular hole to the real axis of the ζ-plane, instead of mapping the boundary of the hole to the unit circle of the ζ-plane as done here. Specifically, the mapping function, inverse mapping function and the derivative of their mapping function with respect to ζ of reference [122] appear in *equations 9.50 through 9.52*.

$$z_j = \omega_j(\zeta_j) = \frac{iR}{2}\left[(1 - i\mu_j)e^{-i\zeta_j} - (1 + i\mu_j)e^{i\zeta_j}\right],\ j = 1,2 \tag{9.50}$$

$$\zeta_j = \omega^{-1}(z_j) = i\ \ln\left(\frac{z_j - \sqrt{z_j^2 - R^2(1+\mu_j^2)}}{iR(1-i\mu_j)}\right),\ j = 1,2 \tag{9.51}$$

$$\omega_j'(\zeta_j) = -\frac{iR}{2}\left[(1 + i\mu_j)e^{-i\zeta_j} + (1 - i\mu_j)e^{i\zeta_j}\right],\ j = 1,2 \tag{9.52}$$

These latter equations can be compared to *equations 9.32 through 9.34*, respectively. Another difference between the paper by Lin and Rowlands [122] and presently is the Laurent expansion.

Their paper uses a Taylor, rather than a Laurant, series expansion; the stress functions are approximated by summations from 0 to *N* instead of from *–m* to *m*. Their expansions of their stress functions appear in *equations 9.53 and 9.54*. Here, ζ_0 represents a point on the traction-free boundary of the circular cutout and $\zeta_0 = 0$ because it is mapped on the real axis [120].

$$\Phi(\zeta_1) = \sum_{j=0}^{N} c_j(\zeta_1 - \zeta_0)^j \tag{9.53}$$

$$\Psi(\zeta_2) = \sum_{j=0}^{N} ((\overline{c}_j B + c_j C)(\zeta_2 - \zeta_0)^j) \tag{9.54}$$

The paper by Huang and Rowlands [19] similarly uses the mapping functions given in *equations 9.50 through 9.52* instead of those used here (*equations 9.32 through 9.34*). Reference [19] also uses the expression of *equation 9.53* instead of that of *equation 9.37*. However, unlike Lin, Huang provides a different coordinate system for the real z-plane and the mapped ζ-plane. Instead of the z-plane provided by *equation 9.10* and the ζ-plane provided by *equation 9.21*, Reference [19] uses *equations 9.55 and 9.56*.

$$z = x + i * y \tag{9.55}$$

$$\zeta = \xi + i\eta \tag{9.56}$$

The paper by Gerhardt [121] also differed in its conformal mapping techniques. The first difference compared with here was its treatment of the physical z-plane. Although the two z-planes are mathematically equivalent, the z-plane listed in [121] is never simplified to that in

equation 9.10. Instead of μ_j being defined as the distinct roots of *equation 9.6*, they are defined by Gerhardt as the distinct roots of *equation 9.2*. Gerhardt's characteristic equation is mathematically identical to that here if written with respect to the directions of material symmetry. Gerhardt also gives information on whether the stress functions should use Taylor or Laurent expansions. Reference [121] gives the following series expansions

$$\Phi(\zeta_1) = \sum_{j=m}^{n} c_j(\zeta_1 - \zeta_0)^j \tag{9.57}$$

$$\Psi(\zeta_2) = \sum_{j=m}^{n} (\bar{c_j} B\zeta_2 - \zeta_0)^h + c_j C\zeta_2 - \zeta_0)^j) \tag{9.58}$$

Gerhardt goes on to say "For unit-circle mappings, $h \equiv -j$ and $\zeta_0 \equiv 0$. For real-axis mappings, $h \equiv j$ and $m = 0$." All of the other herein referenced papers follow this convention except [120], which, despite utilizing a unit-circle mapping, defines $h \equiv j$. Gerhardt uses the same mapping function as Lin [120] for mapping to the real-axis in the ζ-plane.

Chen [123] uses the same conformal mapping technique as employed here. However, it is used to map an elliptical hole from the real z axis to a unit circle of the ζ-plane. When the ellipse becomes a circle, i.e., when the semi-axes a and b are equal to each other and equal to the radius of the circle, the mapping functions used here and in reference [123] are mathematically equivalent. However, the derivative of the mapping function in reference [123] is mathematically equivalent not to the derivate found here, but rather its inverse $(1/\omega'(\zeta))$; as seen in *equation 9.59*.

$$\omega_j'(\zeta_j) = \frac{2\zeta_j}{(a-i\mu_j b)\zeta_j-(a+i\mu_j b)\zeta_j^{-1}},\ j = 1,2 \tag{9.59}$$

Chen uses a Laurent expansion to approximate the stress functions identical to that used here.

The papers by Rhee and Rowlands [124 and 125] solve for the full-field stress around a variety of geometries, including multiple elliptical holes, single holes, and individual cracks. They again map the unit circle from the ζ-plane to the boundary of each elliptical hole. Other than a term accounting for the position of each hole, they contain the same mapping functions as employed here. Every detail of their complex mathematics is identical to that utilized here.

Lin, Feng, and Rowlands [108] solve a different problem. Instead of being concerned about a circular hole, they considered a loaded plate with a crack. Because the geometry is different, the mapping must necessarily be different. They mapped the boundary of the crack to the real-axis, consistent with [119], and they used a truncated Taylor series instead of a Laurent expansion to approximate the relevant stress functions.

9.4 Analysis and Results

Numerical experiments were performed here using ANSYS to demonstrate the present technique. A quarter symmetrical model of the finite-width tensile plate of *figure 9.1* is modeled using isoparametric elements (ANSYS element type: Plane-82) in ANSYS. The glass-epoxy tensile composite has elastic properties E_{11} = 34.2 GPa, E_{22} = 14.1 GPa, ν_{12} = 0.22 and G_{12} = 3.4 GPa using 7,566 elements and 23,229 nodes in ANSYS, *figure 9.2*. Roots of *equation 9.6* for these material properties are $\mu_1 = 3.059i$ and $\mu_2 = 0.509i$. These geometry and material properties are from reference [118]. A far-field stress, σ_0 (= 25 MPa) was applied on the specimen.

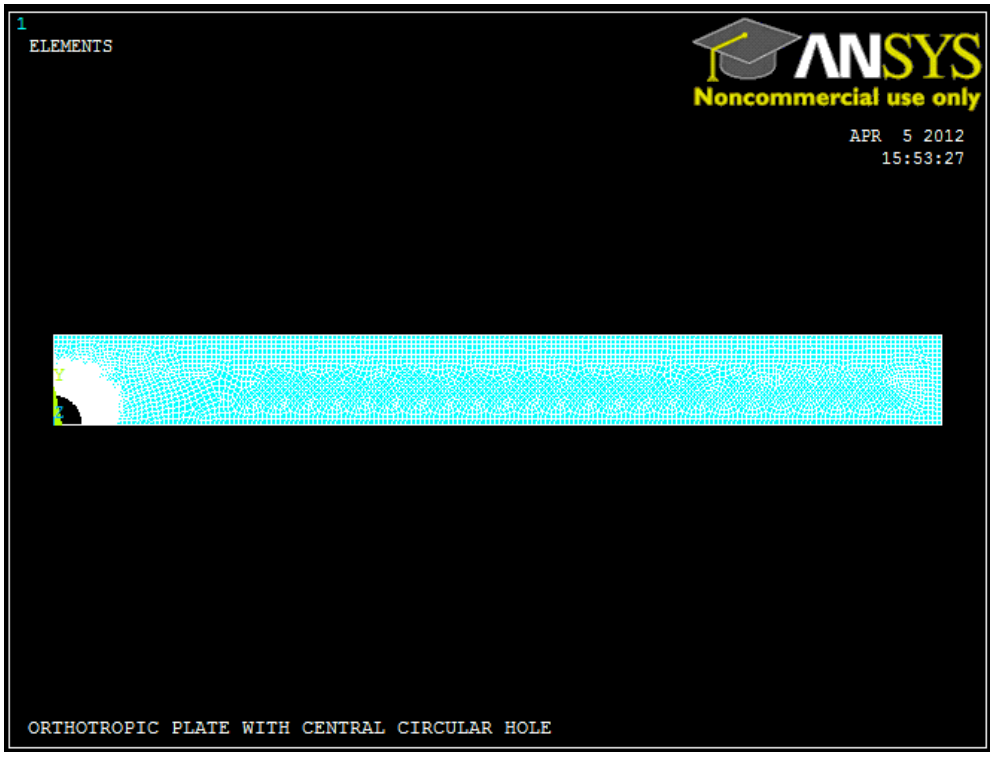

Fig. 9.2: Finite element model for the analysis of *figure 9.1*

The simulated experimental data for the plate of *figure 9.1* from ANSYS are exported to MATLAB. A total of *m = 3,449* values of the ANSYS-predicted *u*-displacements was collected

on and near the boundary of the hole, *figure 9.3*. For the $m = 3{,}449$ simulated u displacements, $k = 2$ was found to be an appropriate number of coefficients. Using this number of coefficients were substantiated by comparing the simulated experimental data from ANSYS with the reconstructed data using $k = 2$ coefficients, *figure 9.6*.

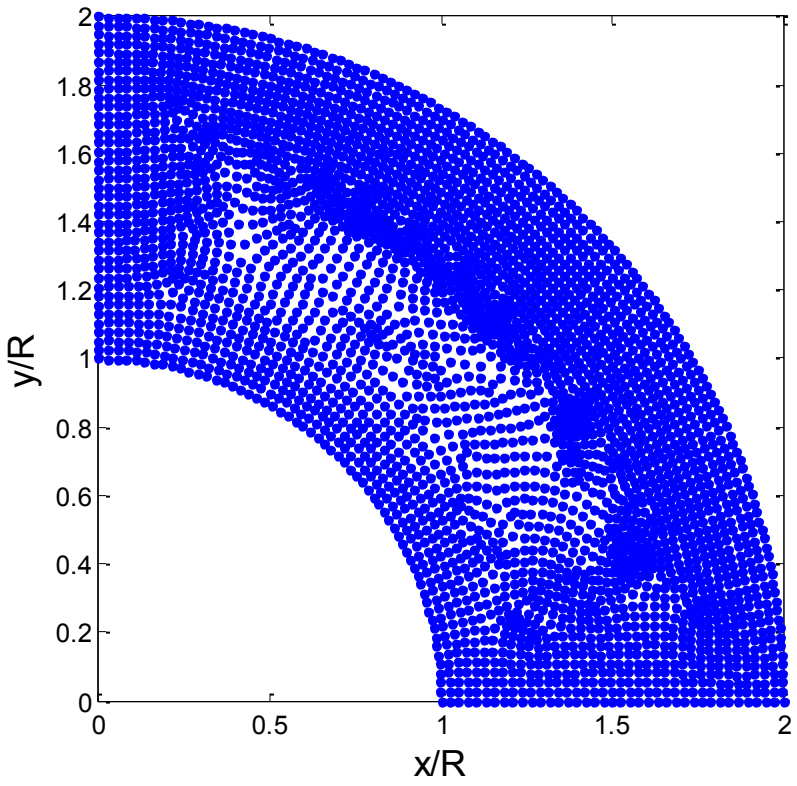

Fig. 9.3: Source locations of $m = 3{,}449$ simulated experimental data

The unknown coefficients are evaluated from the simulated u-displacements according to *equations 9.41 and 9.42*. The individual full-field stress and displacement components are then available by substituting these known coefficients into *equations 9.39, 9.40 and 9.45 through 9.47*. The results obtained by this hybrid technique are compared with those from ANSYS. Cartesian components of stress are normalized with respect to the far field stress, σ_0 (= 25 MPa)

and are plotted on the boundary of the hole, *figures 9.4 and 9.5*. Normalized displacement and stress contour plots from the present hybrid technique and ANSYS are plotted using MATLAB, *figures 9.6 through 9.10*. The displacements are normalized with the radius of the hole.

There is an excellent agreement between the ANSYS and the present hybrid technique based on evaluated coefficients c_j for $m = 3,449$ input numerically simulated measured u-displacements and $k = 2$ coefficients. By a similar approach, *figures 9.11 and 9.12* plot the normalized displacements based on evaluated coefficients for $m = 3,449$ input numerically simulated measured v displacements and $k = 2$ coefficients. Note that the results based on evaluated coefficients, c_j, from input u-displacements show a better agreement when compared to those evaluated coefficients from input v-displacements. This is very probably because the input u-displacements are larger than the input v-displacement values. This situation suggests (and the method enables one to do so) an advantage of using the input data having the largest and most reliable magnitudes. Results of *figures 9.4 through 9.12* are all based on $\sigma_0 = 25$ MPa.

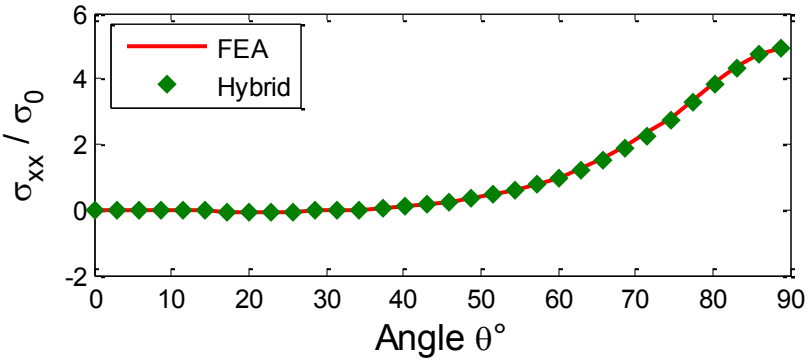

Fig. 9.4: Plot of σ_{xx}/σ_0 around the boundary of the hole (r/R = 1) from FEA and hybrid method for $m = 3,449$ input u-displacements and $k = 2$ coefficients

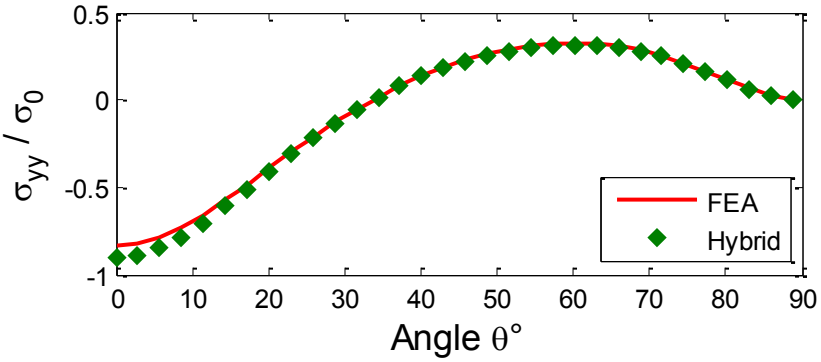

Fig. 9.5: Plot of σ_{yy}/σ_0 around the boundary of the hole (r/R = 1) from FEA and hybrid method for $m = 3{,}449$ input u-displacements and $k = 2$ coefficients

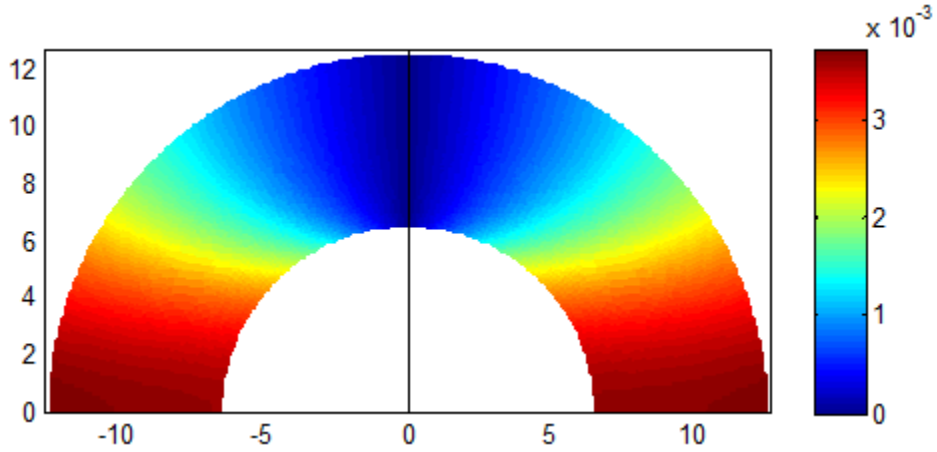

Fig. 9.6: Contour plot of u/r throughout 6.35mm ≤ r ≤ 12.7mm region adjacent to hole predicted by FEA (left side) and based on evaluated coefficients (right side) for $m = 3{,}449$ input numerically simulated measured u-displacements and $k = 2$ coefficients (right side)

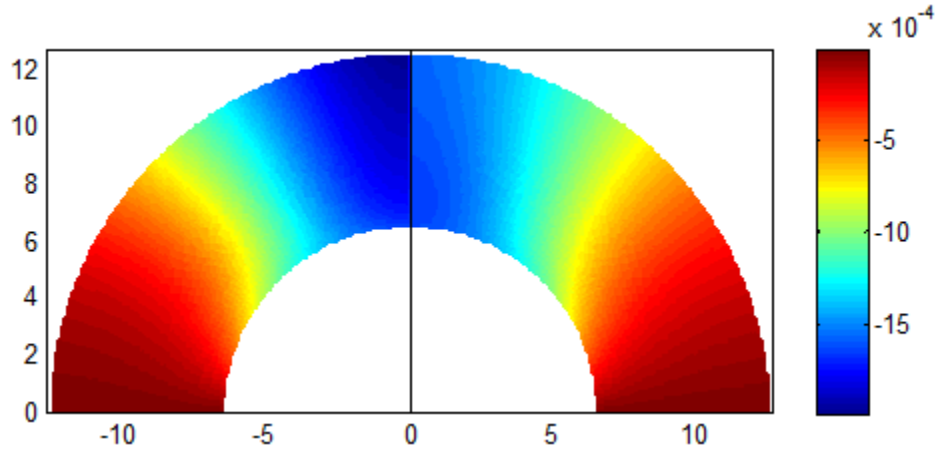

Fig. 9.7: Contour plot of *v/r* throughout 6.35mm ≤ r ≤ 12.7mm region adjacent to hole predicted by FEA (left side) and based on evaluated coefficients (right side) for *m = 3,449* input numerically simulated measured *u*-displacements and *k = 2* coefficients

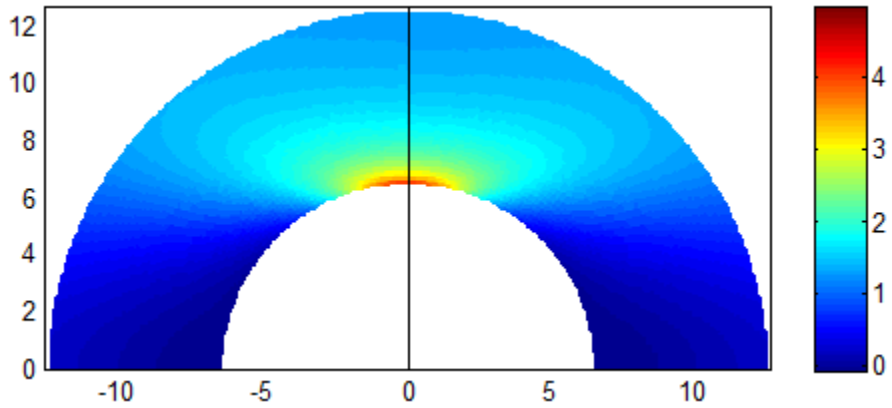

Fig. 9.8: Contour plot of σ_{xx}/σ_0 throughout 6.35mm ≤ r ≤ 12.7mm region adjacent to hole predicted by FEA (left side) and based on evaluated coefficients (right side) for *m = 3,449* input numerically simulated measured *u*-displacements and *k = 2* coefficients

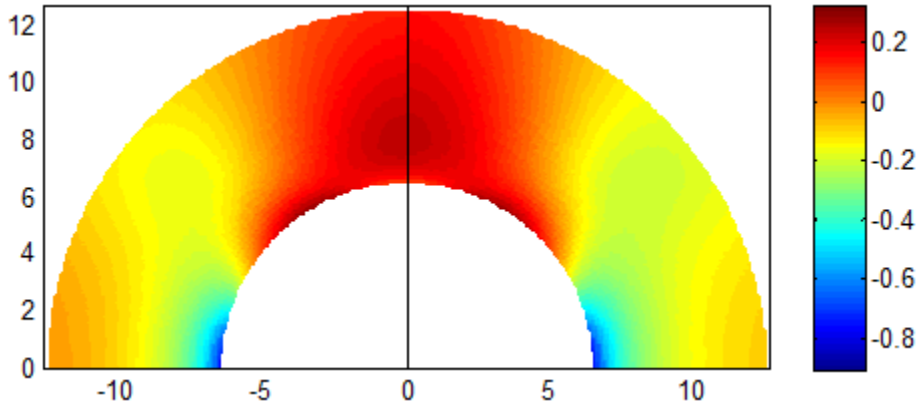

Fig. 9.9: Contour plot of σ_{yy}/σ_0 throughout 6.35mm ≤ r ≤ 12.7mm region adjacent to hole predicted by FEA (left side) and based on evaluated coefficients (right side) for $m = 3,449$ input numerically simulated measured u-displacements and $k = 2$ coefficients

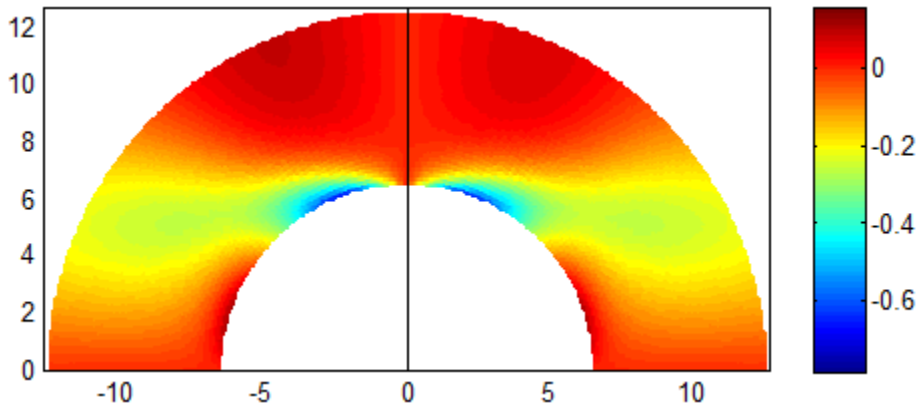

Fig. 9.10: Contour plot of σ_{xy}/σ_0 throughout 6.35mm ≤ r ≤ 12.7mm region adjacent to hole predicted by FEA (left side) and based on evaluated coefficients (right side) for $m = 3,449$ input numerically simulated measured u-displacements and $k = 2$ coefficients

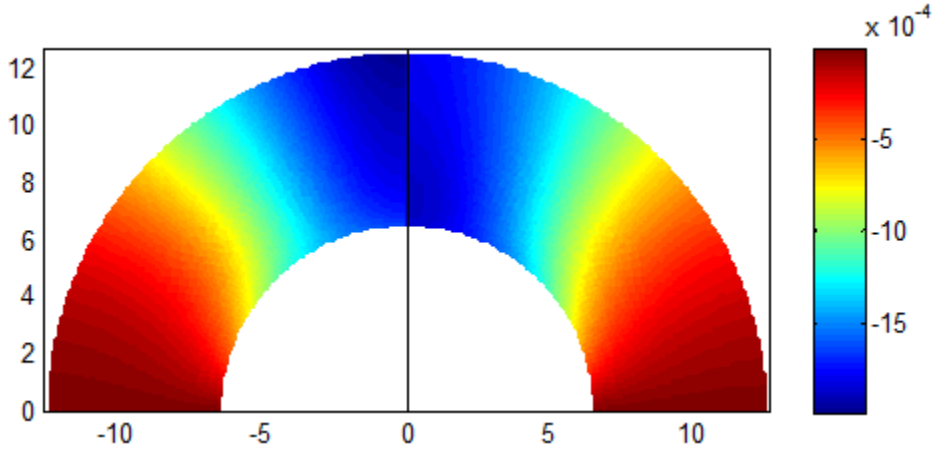

Fig. 9.11: Contour plot of *u/r* throughout 6.35mm ≤ r ≤ 12.7mm region adjacent to hole predicted by FEA (left side) and based on evaluated coefficients (right side) for *m = 3,449* input numerically simulated measured *v*-displacements and *k = 2* coefficients

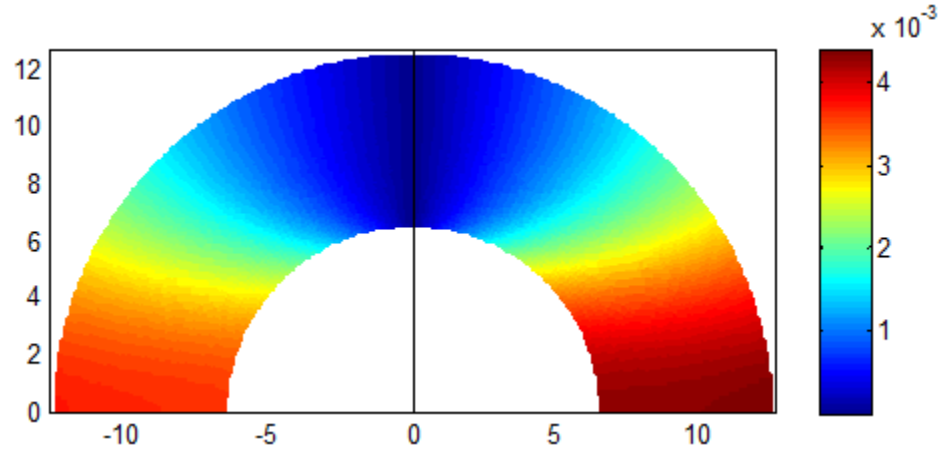

Fig. 9.12: Contour plot of *v/r* throughout 6.35mm ≤ r ≤ 12.7mm region adjacent to hole predicted by FEA (left side) and based on evaluated coefficients (right side) for *m = 3,449* input numerically simulated measured *v*-displacements and *k = 2* coefficients

9.5 Conclusion

A hybrid method for stress analyzing a perforated orthotropic plate from input values of a single component of displacement which combines a stress function in the complex variables and conformal mapping, and that *analytically* satisfies the traction-free conditions on the edge of the hole is substantial. Based on reference [118] the earlier capabilities of reference [9, 15, 19, 108, 117, 120, 122, 124 125] which used thermoelastic (TSA), measured strains or both Cartesian components of displacement input information, this chapter emphasizes needing only one component of displacement as input. This can greatly simplify the experimental requirements. Reference [118] evaluates only the tangential stress on the boundary of the cut-out from a single displacement component. This chapter is an extension to reference [118] wherein full-field individual stress and displacement components are evaluated. Least squares is used to evaluate unknown coefficients from the single displacement component.

The classical use of displacement measurement techniques like Electronic Speckle Pattern Interferometry (ESPI), Digital Image Correlation (DIC), moiré or holography requires spatially differentiating these displacements to determine strains or stresses. It can also be particularly challenging to obtain accurate experimental data (displacements) on the edge of a cutout and differentiating these data can results in inaccurate stresses at holes or notches. These are often the location of prime importance. The present technique circumvents this challenge of having to physically differentiating the measured displacements and provides accurate stresses on the boundary of the cutouts without the knowledge of measured displacements in the immediate region of the cutout.

Numerical experimental data from ANSYS are used to validate the technique. In the present analysis $m = 3,449$ simulated u-displacements were used to determine $k = 2$ unknown coefficients. There is excellent agreement between the ANSYS simulated results and the present hybrid technique. Future potential applications of this method include to stress analyze paper and/or wood materials as well as structural composites containing holes or notches.

Professor Baek's willingness to share his FORTRAN code is greatly appreciated.

Chapter 10 : Summary and Conclusions

This research focuses on developing, enhancing and simplifying the experimental, analytical and numerical tools of solid mechanics to solve important engineering problems. Major contributions of this thesis include the following:

(i) Full-field strain/stress determination without physically differentiating the measured displacements (i.e., with a rigorous mechanics basis) for finite structures.

(ii) Use measured values of a single component of displacement or strain to determine full-field individual components of stress, strain and displacement.

(iii) Simplify experimental concepts with potential application to load-cell design.

(iv) Illustrate potential challenges when applying (or as one approaches) a purely boundary collocation method.

(v) Demonstrate the ability to stress analyze a finite component containing an elliptical hole using a stress function in real (polar) coordinates and a single experimental technique (TSA).

(vi) Illustrate the experimental ability to determine the individual components of stress on and in the vicinity of the edge of a pin-loaded hole in a finite plate without initial knowledge of the pin-plate contact area.

(vii) Determine accurate displacements/strains/stresses on the boundary of a hole without the knowledge of any measured data on and near the edge of the geometric discontinuity. This is accomplished using simple stress functions and without knowledge of the far-field loading/boundary conditions.

(viii) Evaluate the individual stress components associated with two neighboring holes which are either perpendicular or inclined to the direction of the loading and whose respective stresses interact.

(ix) Evaluate interface strains between a loaded ring and its central disk.

Motivation and significance of several of these contributions are more fully discussed in Section 1.2, Novelty, of this thesis. This research is believed to have made significant strides in hybridizing experimental techniques with analytical and numerical tools for the displacement, strain and stress analysis of engineering problems. However, much remains to be done, as indicated under Considerations for Further Research.

Considerations for Future Research

1) Apply current concepts to more general bolt-loaded finite-size isotropic or orthotropic members (bolt-hole clearance, multiple bolted-loaded holes, etc.).
2) Extend current capability to full-field stress analyze finite structures containing an elliptical hole using digital image correlation.
3) Extend current concepts to inclined elliptical holes.
4) Assess the potential feasibility of applying TSA, DIC and/or vibrometry to vibrating perforated members.
5) Apply current concepts to neighboring elliptical holes/notches whose stress fields interact.
6) Assess potential advantages of combining TSA and PSA to full-field stress analysis of finite structures containing a hole or edge notch.
7) Assess the feasibility of employing measured displacements (u, v) or strains ($\epsilon_{xx}, \varepsilon_{yy}, \gamma_{xy}$) (using Neou's method) in terms of rectangular coordinates directly [14] rather than from an Airy stress function in polar coordinates as done here.
8) Hybrid full-field stress analysis of finite structures containing an arbitrarily shaped (or square) hole using TSA and/or DIC. Arbitrarily shaped holes are architecturally common and plow bolts involve square holes.

9) Hybrid full-field analysis of an inclined finite structure containing an arbitrarily shaped hole (or vertical tension with an inclined arbitrarily-shaped hole) employing TSA and/or DIC.
10) Assess the feasibility of employing TSA for the NDE of bicycle (motor cycle, moped) frames.
11) Full-field stress, strain or displacement analysis of a metal-plate wood connector using DIC, TSA and/or PSA.
12) Experimental stress, strain or displacement analysis of bovine manure or cellulosic materials using DIC, vibrometry or TSA. Such material can be fabricated into furniture members plus are potentially useful building material for developing countries.
13) Non-destructive thermal testing of materials under non-adiabatic conditions using TSA.
14) Assess potential of combining the friction and adhesion model developed by Dr. Melih Eriten (University of Illinois-Urbana/Champaign) with that by Bickley [65] to modify the latter's analytical solution considering friction and shear stress on the contact boundary of the hole.
15) Use DIC, TSA and/or interferometry, plus physical testing, to assess the physical/mechanical/structural differences between machined and formed holes in green (bovine manure, cellulosic) composites.
16) Explore the feasibilities of extending the current concepts of measuring a single component of strain (single-element strain gages) at discrete locations of Chapters 3, 4 and 9 to more general situations. Strain gages are the most prevalently used strain-measuring technique in industry.

17) Use DIC to monitor (strain/stress analyze) bolted wood joints which undergo large, non-linear behavior [128].
18) Extend/apply TSA and/or DIC into the micro (or smaller) range.
19) Extend present thermoelastic concepts to problems involving heat transfer (there are some similarities in the equations of heat transfer and stress analysis).
20) Extend current concepts to more general/extensive/complicated inverse problems (e.g., friction).
21) Extend current concepts to infrared grey-field photoelasticity (GFP, PSA).
22) Feasibility of Legendre polynomials for processing TSA, DIC or measured strain data.
23) Potential of extending current concepts to 3-D problems.
24) Potential advantages of combining TSA or DIC measured data with the FEM-type scheme developed by Dr. G. Halford's colleague at NASA.
25) Possibilities of extending current photomechanical (TSA) approaches to viscoelastic biological or polymeric materials.
26) Possibilities of extending current photomechanical approaches to pultruded composites (I-beams, etc.).
27) Possible advantage of using radial basis functions to process measured data.
28) Apply current (plus possibly interferometry and/or vibrometry) concepts to metal-matrix composites.
29) Apply current concepts to functionally-graded materials.
30) Apply current concepts to fatigue.
31) Use vibrometry and/or 3-D laser scanner to analyze perforated orthotropic plates subjected to large transverse deflections.

32) Feasibility of extending TSA to non-flat surfaces.

33) Use present concepts to fully characterize an orthotropic material (composite) using a diametrally load disk (F. Perrion's virtual field concepts).

34) Feasibility of fully stress analyzing loaded perforated orthotropic composites by combining current photomechanical methods and a stress function in terms of complex variables.

35) Use current concepts to study bolted joints in green materials.

36) Use current concepts (plus perhaps vibrometry) to analyze vibrating plates of green materials (both isotropic and composites).

37) Assess the application of TSA to wood and paper materials.

Bibliography

[1] Foust, B. E., "*Individual Stress Determination in Inverse Problems by Combining Experimental Methods and Airy Stress Functions*", Master's Thesis, University of Wisconsin–Madison (2002).

[2] Medgenberg, J. and Ummenhofer, T., "*Detection of Localized Fatigue Damage in Steel by Thermography*", Proceedings of the SPIE - The International Society for Optical Engineering, 6541, 654117-1-11 (2007).

[3] Khaja, A. A., "*Thermoelastic Stresses Analysis of a Doubly-Perforated Plate whose Individual Stresses Interact*", Master's Thesis, University of Wisconsin–Madison (2010).

[4] Lin S-J., (Katherine), "*Two- and Three-Dimensional Hybrid Photomechanical-Numerical Stress Analysis*", PhD Thesis, University of Wisconsin–Madison (2007).

[5] Lin, S-J., (Katherine), Matthys, D.R. and Rowlands, R.E., "*Separating Stresses Thermoelastically in a Central Circularly Perforated Plate using an Airy Stress Function*" Strain, 45(6), 516-526 (2009).

[6] Soutas-Little, R.W., "*Elasticity*", Dover Publications, Inc., Mineola, New York (1998).

[7] Boresi, A.P. and Ken Chong, K.P., *"Elasticity in Engineering Mechanics",* Elsevier (1991).

[8] Joglekar, N., "*Separating Stresses using Airy Stress Function and TSA, Effects of Varying the Amount and Source Locations of the Input measured TSA Data and Number of Airy Coefficients to Use*", Master's Thesis, University of Wisconsin–Madison (2009).

[9] Baek, T. H. and Rowlands, R. E., "*Hybrid Stress Analysis of Perforated Composites using Strain Gages*", Int'l Jour. Experimental Mechanics, 41(2), 195-203, June (2001).

[10] Greene, R. J., Patterson, E. A. and Rowlands, R. E., "*Thermoelastic Stress Analysis*", Cha. 26, Handbook of Experimental Mechanics, ed. by W. M. Sharpe, Springer (2008).

[11] Jones, R. M., "*Mechanics of Composite Materials*", Taylor & Francis, Inc., Second Edition (1999).

[12] Foust, B. E. and Rowlands, R. E., "*Thermoelastic Determination of Individual Stresses in a Diametrically-Loaded Disk*", Strain, 47, 146-153 (2011).

[13] Sutton, Michael A., Orteu, Jean-José, Schreier, Hubert, "*Image Correlation for Shape, Motion and Deformation Measurements: Basic Concepts, Theory and Applications*", Springer (2009).

[14] Abdel Moshen, H. H., Huang, Y. M. and Rowlands, R. E., "*Hybrid Elastic and Thermoelastic Analysis from Measured Data*", Experimental Mechanics, 29(4), 474-480, December (1989).

[15] Lin, S. T. and Rowlands, R. E., "*Thermoelastic Stress Analysis of Orthotropic Composites*", Experimental Mechanics, 53(3), 257-265 (1995).

[16] Lin, S. T., Miles, J. P. and Rowlands, R. E., *"Image Enhancement and Stress Separation of Thermoelastically Measured Isopachic Data Under Random Loading",* Experimental Mechanics, 37(3), 225-231 (1997).

[17] Sigimoto, S., Rowlands, R. E. and Ishikawa, T., *"A Thermal Conductivity Analysis Affecting Thermoelastic Stress Measurement of Laminated Composites"*, Proc. Int'l Conf. on Composite Materials (ICCM-13), Beijing, China, (2001).

[18] Petterson, E. A. and Rowlands, R. E., *"Determining Individual Stresses Thermoelastically",* Journal of Strain Analysis, 43(6), 519-527 (2008).

[19] Huang, Y. M. and Rowlands, R. E., *"Quantitative Stress Analysis Based on the Measured Trace of the Stress Tensor",* Journal of Strain Analysis 26(1), 58-63 (1991).

[20] Wang, J. T., Lotts, C. G. and Davis, D. D, JR., "*Analysis of Bolt-Loaded Elliptical holes in Laminated Composite Joints*" Journal of Reinforced Plastics and Composites, 12(2), 128-138 (1993).

[21] Oterkus, E., Madenci, E. and Nemeth. M. P., *"Stress Analysis of Composite Cylindrical Shells with an Elliptical Cutout",* Journal of Mechanics of Materials and Structures, 2, 695-751 (2007).

[22] Madenci, E. and Ileri, L., *"An Arbitrarily Oriented, Rigid, Elliptic Inclusion in a Finite Anisotropic Medium",* International Journal of Fracture, 62, 341-354 (1993).

[23] Persson, E. and Madenci, E., *"Composite Laminates with Elliptical Pin-Loaded Holes",* Engineering Fracture Mechanics, 61, 279-295 (1998).

[24] Hwu, C. and Wen, W. J., *"Green's Functions of Two-Dimensional Anisotropic Plates Containing an Elliptic Hole"*, International Journal of Solids and Structures, 27, 1705–1719 (1991).

[25] Timoshenko, S. and Goodier, J. N., "*Theory of Elasticity*", McGEAW-HILL BOOK COMPANY, Inc. (1951).

[26] Pilkey, W. D. and Pilkey, D. F., *"Stress Concentration Factors",* A Wiley-Interscience Publication, (2008).

[27] Seratia, M., Alehosseina, H. and Williams, D. J., "Elastic stress analysis of partially loaded hollow discs", International Journal of Engineering Science, 53, 19 – 37, (2012).

[28] Lekhnitskii, S. G., *"Anisotropic Plates",* Gordon and Breach, New York, (1968).

[29] Savin, G. N., *"Stress Concentration around Holes",* Pergamon Press, London, (1961).

[30] http://en.wikipedia.org/wiki/Elliptic_coordinates

[31] Charles David Hodgman, *"Mathematical Tables from Handbook of chemistry and physics"*, 10th ed., Cleveland Chemical Rubber Company, (1954).

[32] Korn, G. A. and Korn, T. M., *"Mathematical Handbook for Scientists and Engineers",* McGraw-Hill, New York, (1961).

[33] Roberts, M. M., Colpitts, J. T., *"Analytic geometry",* John Wiley & Sons, (1918).

[34] http://www.sosmath.com/trig/Trig5/trig5/trig5.html

[35] Dally, J. W. and Riley, W. F., "*Experimental Stress Analysis*", Third Edition, College House Enterprises, (1991).

[36] Sisam, C. H., "*College Mathematics*", Henry Hold and Company, New York, (1946).

[37] Cooker, E. C. and Filon, L. N., "*Photoelasticity*", Cambridge University Press, (1931).

[38] Parsson, E. and Madenci, E., *"Composite Laminates with Elliptical Pin-loaded Holes*", Engineering Fracture Mechanics, 61, 279-295, (1998).

[39] Frocht, M. M. and Hill, H. N., "*Stress Concentration Factors around a Central Circular Hole in a Plate Loaded Through a Pin in the Hole*", Transactions of ASME, Journal of Applied Mechanics **7**: 5-9 (1940).

[40] Meek R. M. G., "*Effects of Pin Bending on the Stress Distribution in Plates Loaded Through Pin Joints*", National Engineering Laboratory Report No. 311, East Kilbride, UK (1967).

[41] Waszczak, J. P. and Cruse, T. A., "*Failure Mode and Strength Prediction of Anisotropic Bolt Bearing Specimens*", Journal of Composite Materials, 5, 421-425 (1971).

[42] Wong, C. M. and Matthews, F. C., "*A Finite Element Analysis of Single- and Two-Hole Bolted Joints in Fiber Reinforced Plastics*", Journal of Composite Materials, 15, 481-491 (1981).

[43] Wilkinson, T. L. and Rowlands, R. E., "*Analysis of Mechanical Joints*". Experimental Mechanics, 21(11), 408-414 (1981).

[44] Rowlands, R. E., Rahman, M. U., Wilkinson, T. L. and Chiang, Y. I., "*Single- and Multiple-Bolted Joints in Orthotropic Materials*", Composites, 273-279 (1982).

[45] Hyer, M. W. and Liu, D. H., "*Photoelastic Determination of Stresses in Multiple-Pin Connectors*". Experimental Mechanics, 23(3), 249-256 (1983).

[46] Rahman, M. U., Rowlands, R. E. and Cook, R.D., "*An Iterative Procedure for Finite-Element Stress Analysis of Frictional Contact Problems*", Computers & Structures, 18(6), 947-954 (1984).

[47] Hyer, M. W. and Klang, E. C., "*Contact Stresses in Pin-Loaded Orthotropic Plates*", International Journal of Solids & Structures, 21(9), 957-975 (1985).

[48] Mahajerin, E. and Sikarskie, D. L., "*Boundary Element Study of a Loaded Hole in an Orthotropic Plate*", Composite Materials, 20, 375-389 (1986).

[49] Eriksson, L. I., "*Contact Stresses in Bolted Joints of Composite Laminates*", Composite Structures, 6, 57-75 (1986).

[50] Tsai, M. Y., Han, B., Morton, J. and Post, D., "*Contact Stresses in Pin-Loaded Plates: An Experimental Study*". Proceedings of the 1989 SEM Spring Conference on Experimental Mechanics, Cambridge, MA, 557-564 (1989).

[51] Stanley, P. and Davies, M. F., "*A Photoelastic Study of the Stresses in Pin-Loaded Lugs*," österreichisheingenier-und architekten-zeitschrift (ÖIAZ), 6, 275-284 (1991).

[52] Shih (Stone), J. S., "*Experimental-Numerical Analysis of Bolted Joints in Finite Composites with and without Inserts*", PhD Thesis, University of Wisconsin-Madison (1992).

[53] Stanley, P. and Dulieu-Smith, J. M., "*A Thermoelastic Study of the Stresses in Pin-Loaded Lugs*". Proceedings of the 6th National Symposium for Experimental Mechanics, Craiova, 160-169 (1992).

[54] Dulieu-Smith, J. M. and Fulton, M. C., "*Thermoelastic Stress Analysis of the Interfacial Conditions in Pin-Loaded Lugs*". Proceedings of VIII International Congress on Experimental Mechanics, Nashville, 39-46 (1996).

[55] Mallory-Patton, M., "*Three-dimensional Mechanics and Failure of Single Bolt Wood Connections*", PhD Thesis, Colorado State University, Fort Collins, CO (1996).

[56] Bauman, B. J., "*A Numerical and Experimental Investigation of Mechanical Connections*", PhD Thesis, University of Wisconsin-Madison (1998).

[57] Lanza di Scalea, F., Hong, S. S. and Cloud, G. L., "*Whole-Field Strain Measurement in a Pin-Loaded Plate by Electronic Speckle Pattern Interferometry and the Finite-Element Method*", Experimental Mechanics 38(1): 55-60 (1998).

[58] Ju, S. H. and Rowlands, R. E., "*A Three-Dimensional Frictional Stress Analysis of Double-Shear Bolted Wood Joints*", Wood and Fiber Science 33(4), 550-563 (2001).

[59] Foust, B. E. and Rowlands, R. E., "*Inverse Stress Analysis of Pinned Connections using Strain Gages and Airy Stress Function*", Inverse Problems in Engineering Mechanics, (ISIP 2003), Nagano, Japan, M. Tanaka, editor, 323-332 (2003).

[60] Foust, B. E., Lesniak, J. B. and Rowlands, R. E., "*Determining Individual Stresses Throughout a Pinned Aluminum Joint by Reflective Photoelasticity*", Experimental Mechanics, 51(9), 1441-1452, November (2011).

[61] Woodruff, J., Marannano, G. and Restivo, G., *"Effects of Clearance on Thick, Single-Lap Bolted Joints using Through-the-Thickness Measuring Techniques"*, Proc. SEM Annual Meeting, Indianapolis, June (2010); also Woodruff, J., *"Effects of Design Parameters on a Single-Lap Bolted Joint using Internal and Surface Strain Measuring Techniques"*, Master's Thesis, Michigan State University, (2011).

[62] Sambasivan, S., "*Thermoelastic Stress Analysis of Laminated Composite Materials*", PhD thesis, University of Southampton, Southampton, U.K. (2009).

[63] Kaliyanda, A. R., "*Three-Dimensional FEA of Bolted Joints in Wood-Steel Structures Subjected to Large Deformations*", Thesis, University of Wisconsin-Madison, Madison, WI (2011).

[64] http://commons.wikimedia.org/wiki/File:Bolted_joint_bridge.jpg

[65] Bickley, W. G., *"The Distribution of Stress around a Circular Hole in a Plate"*, Phil. Trans Royal Society, London, 227A, 383-415 (1928).

[66] Nisida, M. and Saito, H., *"Stress Distribution in a Semi-infinite Plate due to a Pin-Determined by Interferometric Method"*, Experimental Mechanics, 6(5), 273-279 (1966).

[67] White, D. J. and Enderby, L. R., *"Finite Analysis of a Non-linear Problem: A Connecting Rod Eye Loaded by means of a Pin"*, Jour. Strain Analysis, 5, 41-48 (1970).

[68] Greszczuk, L. B., *"Stress Concentrations and Failure Criteria for Orthotropic and Anisotropic Plates with Circular Holes"*, Composite Materials and Testing, ASTM STP 497, 363-381, (1971).

[69] Collinan, R. J., *"Stress Analysis of a Lug Loaded by a Pin"*, Struct. Note 439, ARI, Dept of Defense, Melbourne, (1977).

[70] de Jong, T. and Beukers, A., *"Stresses around a Pin-loaded Hole in an Elastically Orthotropic or Isotropic Plate"*, Report LR-241, Deft University of Technology, Delft, The Netherlands, January (1977).

[71] Eshwar, V. A., *"Analysis of Clearance Fit Pin Joints"*, Int'l. Jour. Mech. Science, 20, 447-484 (1978).

[72] Gabro, S. P. and Ogonowski, J. M., *"Effects of Variances and Manufacturing Tolerances on the Design Strength and Life of Mechanically Fastened Composite Joints"*, report AFWAL-TR-81-3041, 1-3, (1981).

[73] Chang, F. K., Scott, R. A. and Springer, G. S., *"Strength of Mechanically Fastened Composite Joints"*, Jour. Composite Materials, 16, 470-493 (1982).

[74] Chang, F. K., Scott, R. A. and Springer, G. S., *"Design of Composite Laminates containing Pin Loaded Holes"*, Jour. Composite Materials, 18, 1279-1289 (1984).

[75] Chang, F. K. and Scott, R. A., *"Composite Laminates containing Pin Loaded Holes – Method of Solution"*, Jour. Composite Materials, 18, 279-289, May (1984).

[76] Chang, F. K. and Scott, R. A., *"Failure Strength of Nonlinearly Elastic Composite Laminates Containing a Pin Loaded Hole"*, Jour. Composite Materials, 18, September (1984).

[77] Hyer, M. W. and Lui, D., *"Stresses in a Quasi-isoptropic Pin-Loaded Connector using Photoelasticity"*, Experimental Mechanics, 48-53, March (1984).

[78] Hyer, M. W., Klang, E. C. and Cooper, D., *"The Effects of Pin Elasticity, Clearance and Friction on the Stresses in a Pin-Loaded Orthotropic Plate"*, Jour. Composite Mat'ls, 21(3), 190-206 (1987).

[79] Tsiang, T. H. and Mandell, J. F., *"Damage Development in Bolt-Bearing of Composite Laminate"*, AIAA Jour., 23, 1570-1577 (1985).

[80] Dulieu-Smith, J. M., *"Application and Development of the Thermoelastic Stress Analysis Technique"*, PhD Thesis, University of Manchester, (1993).

[81] DiNicola, A. J. and Fantle, S. L., *"Bearing Strength of Clearance-Fit Fastener Holes in Toughtened Graphite/Epoxy Laminates"*, Testing and Design, 11, ASTM STP 1206, 220-237 (1993).

[82] Grant, R. J., Smart, J. and Stanley, P., *"A Parametric Study of the Elastic Stress Distribution in Pin-Loaded Lugs"*, Jour. Strain Analysis, 29, 299-307 (1994).

[83] Wang, G. S., *"Stress Analysis for a Lug under Various Conditions"*, Jour. Strain Analysis, 29, 7-16 (1994).

[84] Shyprykeevich, P., *"Characterization of Bolted Joint Behavior: MIL-HDBK-17 Accomplishments at Standardization"*, Jour. Composite Science and Technology, JCTRER 17(3), 260-270 (1995).

[85] Wang, H. S., Hung, C. L. and Chang, F. K., *"Bearing Failure of Bolted Composite Joints, Part I: Experimental Characterization"*, Jour. Composite Mat'ls, 30(12), 128-1313 (1996).

[86] Fung, C-P and Smart, J., *"Riveted Single lap Joints; Part 1: A Numerical Parametric Study"*, Jour. Aerospace Engineering (IMechE), 211, Part G, 13-27 (1997).

[87] Pierron, F., Cerisier, F. and Lermes, M. G., *"A Numerical and Experimental Study of Woven Composite Pin-Joints"*, Jour. Comp. Mat'ls, 34(12), 1028-1054 (2000).

[88] McCarthy, M. A. and McCarthy, C. T., *"Finite Element Analysis of the Effects of Clearance on Single-Shear Composite Bolted Joints"*, Jour. of Plastics, Rubber and Composites (Inst. of Mat'ls, London), 32(2), 65-70 (2003).

[89] Lawlor, V. P., McCarthy, M. A. and Stanley, W. F., *"Experimental Study on the Effects of Clearance of Single-Bolt, Single-Shear Composite Bolted Joints"*, Jour. of Plastics, Rubber and Composites (Inst. of Mat'ls, London), 31(9), 405-411 (2002).

[90] McCarthy, M. A., Lawlor, V. P., Stanley, W. F. and McCarty, C. T., *"Bolt-Hole Clearance Effects and Strength Criteria in Single-Bolt, Single-Lap Composite Joints"*, Composite Science and Technology, 62, 1415-1431 (2002).

[91] McCarthy, M. A., McCarthy, C. T., Lawlor, V.P. and Stanley, W.F.., *"Three-Dimensional Finite Element Analysis of Single-Bolt, Single-Lap Composite Joints; Part I: Model Development and Validation"*, Composite Structures, 71(2), 140-158 (2005).

[92] McCarthy, M. A. and McCarthy, C. T., *"Three-Dimensional Finite Element Analysis of Single-Bolt, Single-Lap Composite Joints; Part II: Effects of Bolt-Hole Clearance"*, Composite Structures, 71, 159-175 (2005),

[93] McCarthy, M. A., Lawlor, V. P. and Stanley, W. E., *"An Experimental Study of Bolt-Hole Clearance Effects in Single-lap Multibolt Composite Joints"*, Jour. of Composite Materials, 39(9), 799-825 (2005).

[94] Egan, B., McCarthy, C. T., McCarthy, M. A. and Frizzal, R. F., *"Stress Analysis of Single-Bolt, Single-Lap Countersunk Composite Joints with Variable Bolt-Hole Clearance"*, Composite Structures, 94(3), 1038-1051 (2012).

[95] Murty, B., Asiz, A. and Smith, I., *"Tests and Models for Engineered Wood Product Connections using Small Steel Tube Fasteners"*, Engineering Structures, 33(1), 63-68 (2011).

[96] Kelly, G. and Hallstrom, S., *"Bearing Strength of Carbon Fibre/Epoxy Laminates: Effects of Hole Clearance"*, Composites Part: A (Engineering), 35(4), 331-343 (2004).

[97] Strozzi, A., Baldini, A., Giacopini, M., Bertocchi, E. and Bertocchi, L., *"Maximum Equivalent Stress in a Pin-Loaded Lug in the presence of Initial Clearance"*, Jour. Strain Analysis, November (2011).

[98] Frocht, M. M., *"Photoelasticity"*, J. Wiley & Sons, 1 (1948).

[99] Wood Handbook, FPL-GTR-190, Forest Products Laboratory, USDA, Madison, WI, (2010).

[100] Personal conversations with Prof. M. Oliva, University of Wisconsin, Madison, WI, 53706.

[101] Robinson, A. F., Dulieu-Barton, J. M., Quinn, S. and Burguete, *"Investigation of Residual Stress around Cold Expanded Holes using Thermoelastic Stress Analysis"*, Spring SEM Meeting, Experimental and Applied Mechanics, Uncasville, CT, June (2011).

[102] Huang, Y. M., Abdel Moshen, H. H. and Rowlands, R. E., *"Determination of Individual Stresses Thermoelastically"*, Experimental Mechanics, 30(1), 88-94 (1990).

[103] New bit for drilling square/rectangular holes, Dijet Industrial Company, Inc., www.dijetusa.com, October (2010).

[104] Shukla, A. and Dally, J. W., "*Experimental Solid Mechanics*", College House Enterprises, LLC, Knoxville, Tennessee (2010).

[105] Huang, Y. M., Lin, C. H., Suhling, J. C. and Rowlands, R. E., "*Determining the Three Individual Stress Components from Measured Isochromatic Fringes*", Experimental Mechanics, 31(4), 310-317 (1991).

[106] Hawong, J. S., Lin, C. H., Lin, T., Rhee, J. and Rowlands, R. E., "*A Hybrid Method to Determine Individual Stresses in Orthotropic Composites using only Measured Isochromatic Data"*, Jour. Composite Materials, 29(18), 2366-2387 (1995).

[107] Rhee, J. and Rowlands, R. E., "*Moiré-Numerical Hybrid Analysis of Cracks in Orthotropic Media*", Experimental Mechanics, 42(3), 311-319 (2002).

[108] Lin, S. T., Feng, Z. and Rowlands, R. E., *"Thermoelastic Determination of Stress Intensity Factors in Orthotropic Composites using the J-integral"*, Engr. Fracture Mech, 56(4), 579-592 (1997).

[109] Ju, S. H. and Rowlands, R. E., "*Mixed-Mode Thermoelasticfracture Analysis of Orthotropic Composites*", Int'l Jour of Fracture, 120, 601-621 (2003).

[110] He, K. Y. and Rowlands, R. E., "*Determining Stress Intensity Factors in Orthotropic Composites from Far-Field Measured Temperatures"*, Experimental Mechanics, 44(6), 555-561, (2004).

[111] Lin, S. J., Quinn, S., Matthys, D. R., New, A. M, Kincaid, I. M., Boyce, B. R., Khaja, A. A. and Rowlands, R. E, "*Thermoelastic Determination of Individual Stresses in Vicinity of a Near-edge Hole beneath a Concentrated Load"*, Experimental Mechanics, 51, 797-814, 2011.

[112] Sanford, R. J., "*Application of the Least-Squares Method to Photoelastic Analysis*". Experimental Mechanics, 20, 92-197 (1980).

[113] Daniel, I. M. and Ishai, O., "*Engineering Mechanics of Composite Materials*", Oxford University Press, New York (2006).

[114] Juvinall, R. C. and Marshek, K.M., "*Fundamentals of Machine Component Design*", 4th edition, John Wiley & Sons, Inc., New York (2005).

[115] Collins, J. A., *"Mechanical Design of Machine Elements and Machines"*, Wiley & Sons, Inc., New York (2003).

[116] Lin, S. J., Matthys, D. R., Quinn, S., Davidson, J.P., Boyce, B. R., Khaja, A. A. and Rowlands, R. E, "*Determining Individual Stresses at and around a Near Edge Hole in a Plate Subjected to an Off-Set Load from Measured Temperatures"*, submitted for publication.

[117] Baek, T.H. and Rowlands, R.E., "*Experimental Determination of Stress Concentrations in Orthotropic Composites*", Journal of Strain Analysis, 34(2), 34-69 (1999).

[118] Baek, T.H., Chung, T.J. and Panganiban, H., "*Full-Field Stress Determination Around Circular Discontinuity in a Tensile-Loaded Plate using x-displacements Only*", Journal of Solid Mechanics and Materials Engineering, 2(6), 756-762 (2008).

[119] Lekhnitskii, S.G., "*Anisotropic Plates*", Gordon & Breach Science Publishers Ltd. (1968).

[120] Lin, S.T., "*Quantitative Thermoelastic Stress Analysis of Orthotropic Composite Structures*", PhD Thesis, University of Wisconsin–Madison (1994).

[121] Gerhardt, T.D., "*A Hybrid/Finite Element Approach for Stress Analysis of Notched Anisotropic Materials*", Journal of Applied Mechanics, 51(4), 804-811 (1984).

[122] Lin, S.T. and Rowlands, R.E., "*Hybrid Stress Analysis*", Optics and Lasers in Engineering, 32, 257-298 (1999).

[123] Chen, H. C., "*Stress Analysis of Laminates with Holes by Special Finite Element*", Composite Structures, 31, 99-106 (1995).

[124] Rhee, J. and Rowlands, R.E., "*Stresses around Extremely Large or Interacting Multiple Holes in Orthotropic Composites*", Computers & Structures, 61(5), 935-950 (1996).

[125] Rhee, J. and Rowlands, R.E., "*Thermoelastic-numerical Hybrid Analysis of Holes and Cracks in Composites*", Experimental Mechanics, 39(4), 349-355 (1999).

[126] Cheng, L., Yanping, Z. and Zhongzhong, C., "*Solution of Different Holes Shape Borders of Fibre Reinforced Composite Plates by Integral Equations*", Chinese Journal of Mechanical Engineering, 20(5), 2007.

[127] http://en.wikipedia.org/wiki/Coins_of_the_Canadian_dollar

[128] Kaliyanda, A.,"*Three-Dimensional Non-Linear Finite Element Analyses of Bolted Joints in Wood-Steel Structures Subjected to Large Deformations*", Master's Thesis, University of Wisconsin–Madison (2011).

A2 Evaluating Strain and Displacement Equations for a Finite Plate with Circular Hole

An expression for the Airy stress function, ϕ, which satisfies the biharmonic equation $\nabla^4\phi = 0$, and thus equilibrium and compatibility, can be written as follows: [3, 5, 6]

$$\begin{aligned}\phi &= a_0 + b_0 \ln r + c_0 r^2 + d_0 r^2 \ln r + \left(A_0 + B_0 \ln r + C_0 r^2 + D_0 r^2 \ln r\right)\theta \\ &+ \left(a_1' r + b_1' r \ln r + \frac{c_1'}{r} + d_1' r^3\right)\sin\theta + \left(a_1 r + b_1 r \ln r + \frac{c_1}{r} + d_1 r^3\right)\cos\theta \\ &+ \left(A_1' r + B_1' r \ln r\right)\theta\sin\theta + \left(A_1 r + B_1 r \ln r\right)\theta\cos\theta \\ &+ \sum_{n=2}^{\infty}\left(a_n' r^n + b_n' r^{n+2} + c_n' r^{-n} + d_n' r^{2-n}\right)\sin(n\theta) \\ &+ \sum_{n=2}^{\infty}\left(a_n r^n + b_n r^{n+2} + c_n r^{-n} + d_n r^{2-n}\right)\cos(n\theta)\end{aligned} \tag{2A.1}$$

where angle θ is measured counter-clockwise from the positive x-axis of *figure 2.1*. Depending on the situation, many of the above Airy coefficients can often be equated to zero based on single-valued stresses, strains or displacements with respect to θ, whether the origin of the coordinate system is within or outside of the body, whether or not there is any mechanical and geometric symmetry, and whether the body is finite or infinite in size*.

---

* While some of the equations of reference [6] contain some typographical errors, the present expressions are all believed to be correct.

Based on ϕ of *equation 2A.1*, and since

$$\sigma_{rr} = \frac{1}{r}\cdot\frac{\partial\phi}{\partial r} + \frac{1}{r^2}\frac{\partial^2\phi}{\partial\theta^2},\ \sigma_{\theta\theta} = \frac{\partial^2\phi}{\partial r^2} \quad \text{and} \quad \sigma_{r\theta} = -\frac{\partial}{\partial r}\cdot\left(\frac{1}{r}\cdot\frac{\partial\phi}{\partial\theta}\right) \tag{2A.2}$$

the individual polar components of stress become

$$\begin{aligned}
\sigma_{rr} &= \frac{b_0}{r^2} + 2c_0 + d_0\left(2\ln r + 1\right) + B_0\frac{\theta}{r^2} + 2C_0\theta + D_0\left(2\ln r + 1\right)\theta \\
&+ \left(\frac{b_1'}{r} - \frac{2c_1'}{r^3} + 2d_1' r\right)\sin\theta + \left(\frac{b_1}{r} - \frac{2c_1}{r^3} + 2d_1 r\right)\cos\theta \\
&+ \frac{2A_1'}{r}\cos\theta - \frac{2A_1}{r}\sin\theta + \frac{B_1'}{r}\theta\sin\theta + \frac{B_1}{r}\theta\cos\theta \\
&+ \left(\frac{2B_1'}{r}\ln r\right)\cos\theta - \left(\frac{2B_1}{r}\ln r\right)\sin\theta \\
&- \sum_{n=2}^{\infty}\begin{pmatrix} a_n' n(n-1)r^{n-2} + b_n'(n+1)(n-2)r^n \\ + c_n' n(n+1)r^{-(n+2)} + d_n'(n-1)(n+2)r^{-n}\end{pmatrix}\sin(n\theta) \\
&- \sum_{n=2}^{\infty}\begin{pmatrix} a_n n(n-1)r^{n-2} + b_n(n+1)(n-2)r^n \\ + c_n n(n+1)r^{-(n+2)} + d_n(n-1)(n+2)r^{-n}\end{pmatrix}\cos(n\theta)
\end{aligned} \tag{2A.3}$$

$$\begin{aligned}
\sigma_{\theta\theta} &= -\frac{b_0}{r^2} + 2c_0 + d_0\left(2\ln r + 3\right) - B_0\frac{\theta}{r^2} + 2C_0\theta + D_0\left(2\ln r + 3\right)\theta \\
&+ \left(\frac{b_1'}{r} + \frac{2c_1'}{r^3} + 6d_1' r\right)\sin\theta + \left(\frac{b_1}{r} + \frac{2c_1}{r^3} + 6d_1 r\right)\cos\theta \\
&+ \frac{B_1'}{r}\theta\sin\theta + \frac{B_1}{r}\theta\cos\theta \\
&+ \sum_{n=2}^{\infty}\begin{pmatrix} a_n' n(n-1)r^{n-2} + b_n'(n+1)(n+2)r^n \\ + c_n' n(n+1)r^{-(n+2)} + d_n'(n-1)(n-2)r^{-n}\end{pmatrix}\sin(n\theta) \\
&+ \sum_{n=2}^{\infty}\begin{pmatrix} a_n n(n-1)r^{n-2} + b_n(n+1)(n+2)r^n \\ + c_n n(n+1)r^{-(n+2)} + d_n(n-1)(n-2)r^{-n}\end{pmatrix}\cos(n\theta)
\end{aligned} \tag{2A.4}$$

$$\sigma_{r\theta} = \frac{A_0}{r^2} + B_0\left(\frac{\ln r - 1}{r^2}\right) - C_0 - D_0(\ln r + 1)$$
$$+\left(-\frac{b_1^{'}}{r} + \frac{2c_1^{'}}{r^3} - 2d_1^{'}r\right)\cos\theta - \left(-\frac{b_1}{r} + \frac{2c_1}{r^3} - 2\cdot d_1 r\right)\sin\theta$$
$$-\frac{B_1^{'}}{r}\sin\theta - \frac{B_1}{r}\cos\theta - \frac{B_1^{'}}{r}\theta\cos\theta + \frac{B_1}{r}\theta\sin\theta \qquad (2A.5)$$
$$-\sum_{n=2}^{\infty}\begin{pmatrix} a_n^{'}n(n-1)r^{n-2} + b_n^{'}n(n+1)r^{n} \\ -c_n^{'}n(n+1)r^{-(n+2)} - d_n^{'}n(n-1)r^{-n}\end{pmatrix}\cos(n\theta)$$
$$+\sum_{n=2}^{\infty}\begin{pmatrix} a_n n(n-1)r^{n-2} + b_n n(n+1)r^{n} \\ -c_n n(n+1)r^{-(n+2)} - d_n n(n-1)r^{-n}\end{pmatrix}\sin(n\theta)$$

For a perforated finite plate having symmetry with respect to both its x- and y-axes, and its coordinate origin within the cavity, and the plate subjected to uniaxially loading in the vertical y-direction *figure 2.1*, the stress function reduces to [6]

$$\phi = a_0 + b_0 \ln r + c_0 r^2 + \sum_{n=2,4,6,..}^{N}\left\{\left(a_n r^n + b_n \mathrm{r}^{\mathrm{n+2}} + c_n r^{-n} + d_n \mathrm{r}^{-(\mathrm{n-2})}\right)\cos n\theta\right\} \quad (2A.6)$$

and the individual stresses become

$$\sigma_{rr} = \frac{b_0}{r^2} + 2c_0 - \sum_{n=2,4,\ldots}^{\mathrm{N}}\begin{bmatrix} a_n\, n\,(n-1)\, r^{n-2} + b_n\,(n+1)\,(n-2)\, r^{n} \\ +\, c_n\, n\,(n+1)\, r^{-(n+2)} + d_n\,(n-1)(n+2)\, r^{-n}\end{bmatrix} cos(n\theta) \qquad (2A.7)$$

$$\sigma_{rr} = \frac{b_0}{r^2} + 2c_0 + \sum_{n=2,4,\ldots}^{\mathrm{N}}\begin{bmatrix} a_n\,(n-n^2)\, r^{n-2} + b_n\,(2+n-n^2)\, r^{n} \\ -\, c_n\,(n^2+n)\, r^{-(n+2)} + d_n\,(2-n-n^2)\, r^{-n}\end{bmatrix} cos(n\theta) \qquad (2A.7a)$$

$$\sigma_{\theta\theta} = \frac{-b_0}{r^2} + 2c_0 + \sum_{n=2,4,\ldots}^{N}\begin{bmatrix} a_n\, n\,(n-1)\, r^{n-2} + b_n\,(n+1)\,(n+2)\, r^{n} \\ +\, c_n\, n\,(n+1)\, r^{-(n+2)} + d_n\,(n-1)(n-2)\, r^{-n}\end{bmatrix} cos(n\theta) \qquad (2A.8)$$

$$\sigma_{\theta\theta} = \frac{-b_0}{r^2} + 2c_0 + \sum_{n=2,4,\ldots}^{N}\begin{bmatrix} a_n\,(n^2-n)\, r^{n-2} + b_n\,(n^2+3n+2)\, r^{n} \\ +\, c_n\,(n^2+n)\, r^{-(n+2)} + d_n(n^2-3n+2)\, r^{-n}\end{bmatrix} cos(n\theta) \qquad (2A.8a)$$

And, $\sigma_{r\theta} = -\frac{\partial}{\partial r}\left(\frac{1}{r}.\frac{\partial \phi}{\partial \theta}\right)$

$$\sigma_{r\theta} = \sum_{n=2,4,\ldots}^{N} \begin{bmatrix} a_n\, n\,(n-1)\, r^{n-2} + b_n\, n\,(n+1)\, r^{n} \\ -\, c_n\, n\,(n+1)\, r^{-(n+2)} - d_n\, n\,(n-1)\, r^{-n} \end{bmatrix} sin(n\theta) \tag{2A.9}$$

$$\sigma_{r\theta} = \sum_{n=2,4,\ldots}^{N} \begin{bmatrix} a_n\,(n^2-n)\, r^{n-2} + b_n\,(n^2+n)\, r^{n} \\ -\, c_n\,(n^2+n)\, r^{-(n+2)} - d_n\,(n^2-n)\, r^{-n} \end{bmatrix} sin(n\theta) \tag{2A.9a}$$

Quantity r is the radial coordinate measured from the center of the cavity and angle θ is measured counterclockwise from the x-axis, *figures 2.1, 2.3 and 2.22*. N is the terminating index value of the series (since in practice one can only handle a finite number of terms) and it can be any positive even integer.

Knowing reference [6] and from *equations 2A.7 and 2A.8*

$$\frac{\partial u_r}{\partial r} = \epsilon_{rr} = \frac{1}{\mathrm{E}}\,(\sigma_{rr} - \upsilon\,\sigma_{\theta\theta}) \tag{2A.10}$$

$$\frac{\partial u_r}{\partial r} = \frac{1}{\mathrm{E}}\left[\begin{array}{l} \dfrac{b_0}{r^2} + 2c_0 - \displaystyle\sum_{n=2,4,\ldots}^{\mathrm{N}} \begin{pmatrix} a_n\, n\,(n-1)\, r^{n-2} + b_n\,(n+1)(n-2)\, r^{n} \\ + c_n\, n\,(n+1)\, r^{-(n+2)} + d_n\,(n-1)(n+2)\, r^{-n} \end{pmatrix} cos(n\theta) \\ + \dfrac{\upsilon\, b_0}{r^2} - 2\upsilon c_0 - \upsilon \displaystyle\sum_{n=2,4,\ldots}^{\mathrm{N}} \begin{pmatrix} a_n\, n\,(n-1)\, r^{n-2} + b_n\,(n+1)(n+2)\, r^{n} \\ + c_n\, n\,(n+1)\, r^{-(n+2)} + d_n\,(n-1)(n-2)\, r^{-n} \end{pmatrix} cos(n\theta) \end{array}\right]$$

$$\frac{\partial u_r}{\partial r} = \frac{1}{\mathrm{E}}\left[\begin{array}{l} \dfrac{b_0(1+\upsilon)}{r^2} + 2c_0(1-\upsilon) \\ -\displaystyle\sum_{n=2,4,\ldots}^{N} \begin{pmatrix} a_n\, n\,(n-1)(1+\upsilon)\, r^{n-2} \\ + b_n\,(n+1)(n-2+\upsilon n+2\upsilon)\, r^{n} \\ + c_n\, n\,(n+1)(1+\upsilon)\, r^{-(n+2)} \\ + d_n\,(n-1)(n+2+\upsilon n-2\upsilon)\, r^{-n} \end{pmatrix} cos(n\theta) \end{array}\right]$$

$$\frac{\partial u_r}{\partial r} = \frac{1}{\mathrm{E}}\left[-\sum_{n=2,4,\ldots}^{N} \begin{pmatrix} \frac{b_0(1+\upsilon)}{r^2} + 2c_0(1-\upsilon) \\ a_n\, n\,(n-1)(1+\upsilon)\; r^{n-2} \\ + b_n\,(n+1)[(n-2)+\upsilon(n+2)]\, r^{n} \\ +\; c_n\, n\,(n+1)(1+\upsilon)\, r^{-(n+2)} \\ + d_n\,(n-1)[(n+2)+\upsilon(n-2)]\, r^{-n} \end{pmatrix} cos(n\theta) \right]$$

where υ is Poisson's ratio and E is the elastic modulus.

Upon integrating, one gets

$$u_r = \frac{1}{\mathrm{E}}\left[-\sum_{n=2,4,\ldots}^{\mathrm{N}} \begin{pmatrix} \frac{-b_0(1+\upsilon)}{r} + 2c_0(1-\upsilon)r \\ a_n\, n\,(1+\upsilon)\; r^{n-1} \\ + b_n\,[(n-2)+\upsilon(n+2)]\, r^{n+1} \\ -\; c_n\, n\,(1+\upsilon)\, r^{-(n+1)} \\ - d_n\,[(n+2)+\upsilon(n-2)]\, r^{-(n-1)} \end{pmatrix} cos(n\theta) + g(\theta) \right] \qquad \text{(2A.11)}$$

where, $g(\theta) = S_1\cos\theta - S_2\sin\theta$ (2A.12)

Similarly, for isotropy

$$\varepsilon_{\theta\theta} = \frac{1}{E}(\sigma_{\theta\theta} - \upsilon\sigma_{rr}) \qquad \text{(2A.13)}$$

such that

$$\varepsilon_{\theta\theta} = \frac{1}{\mathrm{E}}\left[\begin{array}{l} -\frac{b_0}{r^2} + 2c_0 + \sum_{n=2,4,\ldots}^{N} \begin{pmatrix} a_n\, n\,(n-1)\, r^{n-2} \;+\; b_n\,(n+1)(n+2)\, r^{n} \\ + c_n\, n\,(n+1)\, r^{-(n+2)} + \;\; d_n\,(n-1)(n-2)\, r^{-n} \end{pmatrix} cos(n\theta) \\ -\frac{\upsilon\, b_0}{r^2} - 2\upsilon c_0 + \upsilon \sum_{n=2,4,\ldots}^{N} \begin{pmatrix} a_n\, n\,(n-1)\, r^{n-2} \;+\; b_n\,(n+1)(n-2)\, r^{n} \\ + c_n\, n\,(n+1)\, r^{-(n+2)} + \;\; d_n\,(n-1)(n+2)\, r^{-n} \end{pmatrix} cos(n\theta) \end{array} \right]$$

(2A.14)

$$\varepsilon_{\theta\theta} = \frac{1}{\mathrm{E}}\left[+ \sum_{n=2,4,\ldots}^{\infty} \begin{pmatrix} -\frac{b_0(1+\upsilon)}{r^2} + 2c_0(1-\upsilon) \\ a_n\, n\,(n-1)(1+\upsilon)\ r^{n-2} \\ + b_n\,(n+1)(n+2+\upsilon n-2\upsilon)\, r^{n} \\ +\ c_n\, n\,(n+1)(1+\upsilon)\, r^{-(n+2)} \\ + d_n\,(n-1)(n-2+\upsilon n+2\upsilon)\, r^{-n} \end{pmatrix} cos(n\theta) \right]$$

$$\varepsilon_{\theta\theta} = \frac{1}{\mathrm{E}}\left[+ \sum_{n=2,4,\ldots}^{\infty} \begin{pmatrix} -\frac{b_0(1+\upsilon)}{r^2} + 2c_0(1-\upsilon) \\ a_n\, n\,(n-1)(1+\upsilon)\ r^{n-2} \\ + b_n\,(n+1)[(n+2)+\upsilon(n-2)]\, r^{n} \\ +\ c_n\, n\,(n+1)(1+\upsilon)\, r^{-(n+2)} \\ + d_n\,(n-1)[(n-2)+\upsilon(n+2)]\, r^{-n} \end{pmatrix} cos(n\theta) \right] \tag{2A.15}$$

From [6]

$$\frac{1}{r}\frac{\partial u_\theta}{\partial \theta} = \frac{1}{E}\left(\sigma_{\theta\theta} - \upsilon\sigma_{rr}\right) - \frac{u_r}{r} = \varepsilon_{\theta\theta} - \frac{u_r}{r} \tag{2A.16}$$

⇨ $\frac{\partial u_\theta}{\partial \theta} = r.\varepsilon_{\theta\theta} - u_r$

Using *equations 2A.11 and 2A.15,*

$$\frac{\partial u_\theta}{\partial \theta} = \left[\frac{r}{E}\left\{ + \sum_{n=2,4,\ldots}^{N} \begin{pmatrix} -\frac{b_0(1+\upsilon)}{r^2} + 2c_0(1-\upsilon) \\ a_n\, n\,(n-1)(1+\upsilon)\ r^{n-2} \\ + b_n\,(n+1)[(n+2)+\upsilon(n-2)]\, r^{n} \\ +\ c_n\, n\,(n+1)(1+\upsilon)\, r^{-(n+2)} \\ + d_n\,(n-1)[(n-2)+\upsilon(n+2)]\, r^{-n} \end{pmatrix} cos(n\theta) \right\} \right.$$

$$\left. -\frac{1}{E}\left\{ - \sum_{n=2,4,\ldots}^{N} \begin{pmatrix} \frac{-b_0(1+\upsilon)}{r} + 2c_0(1-\upsilon)\, r \\ a_n\, n\,(1+\upsilon)\ r^{n-1} \\ + b_n\,[(n-2)+\upsilon(n+2)]\, r^{n+1} \\ -\ c_n\, n\,(1+\upsilon)\, r^{-(n+1)} \\ - d_n\,[(n+2)+\upsilon(n-2)]\, r^{-(n-1)} \end{pmatrix} cos(n\theta) \right\} + g(\theta) \right]$$

(2A.17)

$$\frac{\partial u_\theta}{\partial \theta} = \frac{1}{\mathrm{E}}\left[\left\{\begin{array}{c} -\dfrac{b_0(1+\upsilon)}{r} + 2c_0(1-\upsilon)\,r \\ +\displaystyle\sum_{n=2,4,\ldots}^{N}\begin{pmatrix} a_n\, n\,(n-1)(1+\upsilon)\,r^{n-1} \\ +\, b_n\,(n+1)[(n+2)+\upsilon(n-2)]\,r^{n+1} \\ +\; c_n\, n\,(n+1)(1+\upsilon)\,r^{-(n+1)} \\ +\, d_n\,(n-1)[(n-2)+\upsilon(n+2)]\,r^{-(n-1)} \end{pmatrix} cos(n\theta) \end{array}\right\}\right.$$

$$\left. -\left\{\begin{array}{c} \dfrac{-b_0(1+\upsilon)}{r} + 2c_0(1-\upsilon)r \\ -\displaystyle\sum_{n=2,4,\ldots}^{N}\begin{pmatrix} a_n\, n\,(1+\upsilon)\;\, r^{n-1} \\ +\, b_n\,[(n-2)+\upsilon(n+2)]\,r^{n+1} \\ -\;\, c_n\, n\,(1+\upsilon)\,r^{-(n+1)} \\ -\, d_n\,[(n+2)+\upsilon(n-2)]r^{-(n-1)} \end{pmatrix} cos(n\theta) \end{array}\right\} + g(\theta)\right]$$

$$\frac{\partial u_\theta}{\partial \theta} = \frac{1}{\mathrm{E}}\left[\begin{array}{c} -\dfrac{b_0(1+\upsilon)}{r} + 2c_0(1-\upsilon)r + \dfrac{b_0(1+\upsilon)}{r} - 2c_0(1-\upsilon)r \\ +\displaystyle\sum_{n=2,4,\ldots}^{N}\begin{pmatrix} a_n\, n\,(n-1)(1+\upsilon)\,r^{n-1} \\ +\, b_n\,(n+1)[(n+2)+\upsilon(n-2)]\,r^{n+1} \\ +\; c_n\, n\,(n+1)(1+\upsilon)\,r^{-(n+1)} \\ +\, d_n\,(n-1)[(n-2)+\upsilon(n+2)]\,r^{-(n-1)} \end{pmatrix} cos(n\theta) \end{array}\right.$$

$$\left. +\sum_{n=2,4,\ldots}^{N}\begin{pmatrix} a_n\, n\,(1+\upsilon)\,r^{n-1} \\ +\, b_n\,[(n-2)+\upsilon\,(n+2)]\,r^{n+1} \\ -\;\, c_n\, n\,(1+\upsilon)\,r^{-(n+1)} \\ -\, d_n\,[(n+2)+\upsilon\,(n-2)]\,r^{-(n-1)} \end{pmatrix} cos(n\theta) + g(\theta)\right]$$

$$\frac{\partial u_\theta}{\partial \theta} = \frac{1}{\mathrm{E}}\left[\sum_{n=2,4,\ldots}^{N}\begin{pmatrix} a_n\, n\,(1+\upsilon)\;\, r^{n-1}\,\{(n-1)+1\} \\ +\, b_n\, r^{n+1}\,\{\,(n+1)[(n+2)+\upsilon\,(n-2)]\;+\;[(n-2)+\upsilon\,(n+2)]\,\} \\ +\;\, c_n\, n\,(1+\upsilon)\,r^{-(n+1)}\,\{(n+1)-1\} \\ +\, d_n\, r^{-(n-1)}\{\,(n-1)[(n-2)+\upsilon\,(n+2)]\;-\;[(n+2)+\upsilon\,(n-2)]\,\} \end{pmatrix} cos(n\theta) + g(\theta)\right]$$

$$\frac{\partial u_\theta}{\partial \theta} = \frac{1}{\mathrm{E}}\left[\sum_{n=2,4,\ldots}^{N}\begin{pmatrix} a_n\, n^2\,(1+\upsilon)\;\, r^{n-1} \\ +\, b_n\, r^{n+1}\,[(n^2+3n+2+\upsilon\, n^2-\upsilon\, n-2\,\upsilon)+(n-2+\upsilon\, n+2\,\upsilon)] \\ +\;\, c_n\, n^2(1+\upsilon)\,r^{-(n+1)} \\ +\, d_n\, r^{-(n-1)}[(n^2-3n+2+\upsilon\, n^2+\upsilon\, n-2\,\upsilon)-(n+2+\upsilon\, n-2\,\upsilon)] \end{pmatrix} cos(n\theta) + g(\theta)\right]$$

$$\frac{\partial u_\theta}{\partial \theta} = \frac{1}{\mathrm{E}}\left[\sum_{n=2,4,\ldots}^{N} \begin{pmatrix} a_n\, n^2\,(1+\upsilon)\, r^{n-1} \\ +\, b_n\, r^{n+1}[n^2+4n+\upsilon\, n^2] \\ +\ c_n\, n^2(1+\upsilon)\, r^{-(n+1)} \\ +\, d_n r^{-(n-1)}[n^2-4n+\upsilon\, n^2] \end{pmatrix} cos(n\theta) + g(\theta)\right]$$

$$\frac{\partial u_\theta}{\partial \theta} = \frac{1}{\mathrm{E}}\left[\sum_{n=2,4,\ldots}^{N} \mathrm{n.}\begin{pmatrix} a_n\, n\,(1+\upsilon)\ r^{n-1} \\ +\, b_n\ [n(1+\upsilon)+4]\, r^{n+1} \\ +\ c_n\, n(1+\upsilon)\, r^{-(n+1)} \\ +\, d_n\,[n(1+\upsilon)-4]\, r^{-(n-1)} \end{pmatrix} cos(n\theta) + g(\theta)\right] \qquad \text{(2A.18)}$$

Therefore, after integration one gets

$$u_\theta = \frac{1}{\mathrm{E}}\left[\sum_{n=2,4,\ldots}^{N} \begin{pmatrix} a_n\, n\,(1+\upsilon)\, r^{n-1} \\ +\, b_n\,[n(1+\upsilon)+4]\, r^{n+1} \\ +\ c_n\, n(1+\upsilon)\, r^{-(n+1)} \\ +\, d_n[n(1+\upsilon)-4]\, r^{-(n-1)} \end{pmatrix} sin(n\theta) - \int \mathrm{g}(\theta)\,.\,\mathrm{d}\theta + \mathrm{f(r)}\right] \qquad \text{(2A.19)}$$

$$u_\theta = \frac{1}{\mathrm{E}}\left[\sum_{n=2,4,\ldots}^{N} \begin{pmatrix} a_n\, n\,(1+\upsilon)\, r^{n-1} \\ +\, b_n\,[n(1+\upsilon)+4]\, r^{n+1} \\ +\ c_n\, n(1+\upsilon)\, r^{-(n+1)} \\ +\, d_n[n(1+\upsilon)-4]\, r^{-(n-1)} \end{pmatrix} sin(n\theta) - \mathrm{S_1}\sin\theta - \mathrm{S_2}\ \cos\theta + \mathrm{R^*r}\right] \qquad \text{(2A.20)}$$

Quantities S_1 and S_2 represent rigid body translations and R* represents a rigid body rotation [7, p.472]. Hence for a physical plate loaded in a testing machine, S_1, S_2 and R* can be equated to zero.

At this stage, the shape of the cavity containing the origin has not been specified. The only restrictions behind the expressions for the stresses of *equations 2A.7 through 2A.9a* and the displacements of *equations 2A.11 and 2A.20* are that the coordinate origin not be within the material of the structure, and have mechanical and geometric symmetry about the x- and y-axes. However, if the shape of the hole is now stipulated to be round of radius R, and the traction-free

conditions of $\sigma_{rr} = 0$ and $\sigma_{r\theta} = 0$ on the edge of the hole of *figure 2.1* are incorporated *analytically* into the above equations, the number of coefficients is reduced, i.e., [4-6, 8].

Imposing the traction-free conditions at the radius of the hole i.e., at r = R one has $\sigma_{rr} = 0$ and$\sigma_{r\theta} = 0$, where R is the radius of the hole. From *equation 2A.7,*

$$\sigma_{rr}(at\ r = R) = \frac{b_0}{R^2} + 2c_0 - \sum_{n=2,4,\ldots}^{N} \begin{bmatrix} a_n\, n\,(n-1)\,R^{n-2} + b_n\,(n+1)(n-2)R^n \\ + c_n\, n\,(n+1)\,R^{-(n+2)} + d_n\,(n-1)(n+2)\,R^{-n} \end{bmatrix} cos(n\theta)$$

$$= 0$$

$$\Rightarrow \quad \frac{b_0}{R^2} + 2c_0 = 0 \ \ \& \ \ \begin{bmatrix} a_n\, n\,(n-1)\,R^{n-2} + b_n\,(n+1)(n-2)R^n \\ + c_n\, n\,(n+1)\,R^{-(n+2)} + d_n\,(n-1)(n+2)\,R^{-n} \end{bmatrix} = 0 \qquad (2A.21)$$

$$\Rightarrow \quad b_0 = -2c_0R^2 \qquad (2A.21a)$$

Similarly, from *equation 2A.9*

$$\sigma_{r\theta}(at\ r = R) = \sum_{n=2,4,\ldots}^{N} \begin{bmatrix} a_n\, n\,(n-1)\,R^{n-2} + b_n\, n\,(n+1)\ R^n \\ - c_n\, n\,(n+1)\,R^{-(n+2)} - d_n\, n\,(n-1)\,R^{-n} \end{bmatrix} sin(n\theta) = 0$$

gives

$$\begin{bmatrix} a_n\, n\,(n-1)\,R^{n-2} + b_n\, n\,(n+1)\ R^n \\ - c_n\, n\,(n+1)\,R^{-(n+2)} - d_n\, n\,(n-1)\,R^{-n} \end{bmatrix} = 0 \qquad (2A.22)$$

Solving *equations 2A.21 and 2A.22* give

$$a_n = \frac{-b_n(n+1)R^2 - d_nR^{-2(n-1)}}{n} \qquad (2A.23)$$

$$c_n = \frac{b_nR^{2(n+1)} - d_n(n-1)R^2}{n} \qquad (2A.24)$$

and the previous expressions of *equations 2A.7 through 2A.9* for the stresses, strains and displacements can now be re-written i.e.,

$$\sigma_{rr} = \frac{b_0}{r^2} + 2c_0 - \sum_{n=2,4,\ldots}^{N} \begin{bmatrix} a_n\, n\,(n-1)\, r^{n-2} \;+\; b_n\,(n+1)(n-2) r^{n} \\ + c_n\, n\,(n+1)\, r^{-(n+2)} \;+\; d_n\,(n-1)(n+2)\, r^{-n} \end{bmatrix} cos(n\theta) \qquad (2A.7)$$

Now for all r, after substituting *equations 2A.21a, 2A.23 and 2A.24* in *equation 2A.7* becomes,

$$\sigma_{rr} = \frac{-2c_0R^2}{r^2} + 2c_0 \; - \sum_{n=2,4,\ldots}^{N} \begin{bmatrix} n\,(n-1)\, r^{n-2} \left\{\dfrac{-b_n(n+1)R^2 - d_nR^{-2(n-1)}}{n}\right\} \\ + n\,(n+1)\, r^{-(n+2)} \left\{\dfrac{b_nR^{2(n+1)} - d_n(n-1)R^2}{n}\right\} \\ + b_n\,(n+1)\,(n-2)\, r^{n} + \;\; d_n\,(n-1)(n+2)\, r^{-n} \end{bmatrix} cos(n\theta)$$

$$\sigma_{rr} = \left(\frac{-2\,R^2}{r^2} + 2\right) c_0 \; - \sum_{n=2,4,\ldots}^{N} \begin{bmatrix} (n-1)\, r^{n-2} \left\{-b_n(n+1)R^2 - d_nR^{-2(n-1)}\right\} \\ + (n+1)\, r^{-(n+2)} \left\{b_nR^{2(n+1)} - d_n(n-1)R^2\right\} \\ + b_n\,(n+1)\,(n-2)\, r^{n} + \;\; d_n\,(n-1)(n+2)\, r^{-n} \end{bmatrix} cos(n\theta)$$

$$\sigma_{rr} = \left(\frac{-2\,R^2}{r^2} + 2\right) c_0 \; - \sum_{n=2,4,\ldots}^{N} \begin{bmatrix} -b_n(n-1)(n+1)R^2\, r^{n-2} \\ -d_n(n-1)\, R^{-2(n-1)} r^{n-2} \\ + b_n(n+1)R^{2(n+1)}\, r^{-(n+2)} \\ -d_n(n-1)(n+1)\, R^2 r^{-(n+2)} \\ + b_n\,(n+1)(n-2) r^{n} \\ + d_n\,(n-1)(n+2)\, r^{-n} \end{bmatrix} cos(n\theta)$$

$$\sigma_{rr} = \left(\frac{-2\,R^2}{r^2} + 2\right) c_0 - \sum_{n=2,4,\ldots}^{N} \begin{bmatrix} -b_n\,(n-1)(n+1)R^2\, r^{n-2} \\ + b_n(n+1)R^{2(n+1)}\, r^{-(n+2)} \\ + b_n\,(n+1)\,(n-2)\, r^{n} \\ -d_n(n-1)\, R^{-2(n-1)}\, r^{n-2} \\ -d_n(n-1)(n+1)\, R^2 r^{-(n+2)} \\ + d_n\,(n-1)(n+2)\, r^{-n} \end{bmatrix} cos(n\theta)$$

$$\sigma_{rr} = \left(\frac{-2\,R^2}{r^2} + 2\right) c_0 - \sum_{n=2,4,\ldots}^{\mathrm{N}} \left[\begin{array}{c} \left\{ \begin{array}{c} -(n-1)(n+1)R^2\, r^{n-2} \\ +\,(n+1)R^{2(n+1)}\, r^{-(n+2)} \\ +(n+1)\,(n-2)\, r^{n} \end{array} \right\} b_n \\ + \left\{ \begin{array}{c} -(n-1)\, R^{-2(n-1)}\, r^{n-2} \\ -(n-1)(n+1)\, R^2 r^{-(n+2)} \\ +\,(n-1)(n+2)\, r^{-n} \end{array} \right\} d_n \end{array} \right] cos(n\theta) \qquad \text{(2A.25)}$$

Also from *equations 2A.21a, 2A.23 and 2A.24*,

$$\sigma_{\theta\theta} = \frac{-b_0}{r^2} + 2c_0 + \sum_{n=2,4,\ldots}^{N} \left[\begin{array}{c} a_n\, n\,(n-1)\, r^{n-2} \;+\; b_n\,(n+1)\,(n+2)\, r^{n} \\ +\, c_n\, n\,(n+1)\, r^{-(n+2)} \;+\; d_n\,(n-1)(n-2)\, r^{-n} \end{array} \right] cos(n\theta) \qquad \text{(2A.8)}$$

becomes,

$$\sigma_{\theta\theta} = \frac{-(-2c_0R^2)}{r^2} + 2c_0 + \sum_{n=2,4,\ldots}^{N} \left[\begin{array}{c} n\,(n-1)\, r^{n-2} \left\{ \dfrac{-\,b_n(n+1)R^2 - d_nR^{-2(n-1)}}{n} \right\} \\ +\, n\,(n+1)\, r^{-(n+2)} \left\{ \dfrac{b_nR^{2(n+1)} - d_n(n-1)R^2}{n} \right\} \\ +\, b_n\,(n+1)\,(n+2)\, r^{n} \;+\; d_n\,(n-1)(n-2)\, r^{-n} \end{array} \right] cos(n\theta)$$

$$\sigma_{\theta\theta} = \left(\frac{2\,R^2}{r^2} + 2\right) c_0 + \sum_{n=2,4,\ldots}^{N} \left[\begin{array}{c} (n-1)\, r^{n-2} \left\{ -\,b_n(n+1)R^2 - d_nR^{-2(n-1)} \right\} \\ +\,(n+1)\, r^{-(n+2)} \left\{ b_nR^{2(n+1)} - d_n(n-1)R^2 \right\} \\ +\, b_n\,(n+1)\,(n+2)\, r^{n} \;+\; d_n\,(n-1)(n-2)\, r^{-n} \end{array} \right] cos(n\theta)$$

$$\sigma_{\theta\theta} = \left(\frac{2\,R^2}{r^2} + 2\right) c_0 + \sum_{n=2,4,\ldots}^{N} \left[\begin{array}{c} -\,b_n(n+1)(n-1)R^2\, r^{n-2} \\ -\,d_n(n-1)\, R^{-2(n-1)} r^{n-2} \\ +\,b_n(n+1)R^{2(n+1)}\, r^{-(n+2)} \\ -\,d_n(n-1)(n+1)R^2\, r^{-(n+2)} \\ +\,b_n\,(n+1)(n+2) r^{n} \\ +\,d_n\,(n-1)(n-2)\, r^{-n} \end{array} \right] cos(n\theta)$$

$$\sigma_{\theta\theta} = \left(\frac{2\,R^2}{r^2} + 2\right) c_0 + \sum_{n=2,4,\ldots}^{N} \begin{bmatrix} -\,b_n(n+1)(n-1)R^2\,r^{n-2} \\ +\,b_n(n+1)R^{2(n+1)}\,r^{-(n+2)} \\ +\,b_n\,(n+1)\,(n+2)\,r^{n} \\ -\,d_n(n-1)\,R^{-2(n-1)}r^{n-2} \\ -\,d_n(n-1)(n+1)R^2\,r^{-(n+2)} \\ +\,d_n\,(n-1)(n-2)\,r^{-n} \end{bmatrix} cos(n\theta)$$

$$\sigma_{\theta\theta} = \left(\tfrac{2\,R^2}{r^2} + 2\right) c_0 + \sum_{n=2,4,\ldots}^{N} \left[\begin{Bmatrix} -\,(n+1)(n-1)R^2\,r^{n-2} \\ +\,(n+1)R^{2(n+1)}\,r^{-(n+2)} \\ +\,(n+1)\,(n+2)\,r^{n} \end{Bmatrix} b_n + \begin{Bmatrix} -\,(n-1)\,R^{-2(n-1)}r^{n-2} \\ -(n-1)(n+1)R^2\,r^{-(n+2)} \\ +\,(n-1)(n-2)\,r^{-n} \end{Bmatrix} d_n \right] cos(n\theta) \qquad \text{(2A.26)}$$

And from *equations 2A.21a, 2A.23 and 2A.24*,

$$\sigma_{r\theta} = \sum_{n=2,4,\ldots}^{N} \begin{bmatrix} a_n\,n\,(n-1)\,r^{n-2} \;+\; b_n\,n\,(n+1)\;r^{n} \\ -\,c_n\,n\,(n+1)\,r^{-(n+2)} -\;\; d_n\,n\,(n-1)\,r^{-n} \end{bmatrix} sin(n\theta) \qquad \text{(2A.9)}$$

becomes

$$\sigma_{r\theta} = \sum_{n=2,4,\ldots}^{N} \begin{bmatrix} n\,(n-1)\,r^{n-2}\,\left\{\dfrac{-b_n(n+1)R^2 - d_nR^{-2(n-1)}}{n}\right\} \\ -\;n\,(n+1)\,r^{-(n+2)}\,\left\{\dfrac{b_nR^{2(n+1)} - d_n(n-1)R^2}{n}\right\} \\ +\,b_n\,n\,(n+1)\,r^{n} \;-\;\; d_n\,n\,(n-1)\,r^{-n} \end{bmatrix} sin(n\theta)$$

$$\sigma_{r\theta} = \sum_{n=2,4,\ldots}^{N} \begin{bmatrix} (n-1)\,r^{n-2}\left\{-b_n(n+1)R^2 - d_nR^{-2(n-1)}\right\} \\ -\;(n+1)\,r^{-(n+2)}\left\{b_nR^{2(n+1)} - d_n(n-1)R^2\right\} \\ +\,b_n\,n\,(n+1)\,r^{n} \;-\;\; d_n\,n\,(n-1)\,r^{-n} \end{bmatrix} sin(n\theta)$$

$$\sigma_{r\theta} = \sum_{n=2,4,\ldots}^{N} \begin{bmatrix} -b_n(n+1)(n-1)R^2\,r^{n-2} - d_n(n-1)R^{-2(n-1)}\,r^{n-2} \\ -\,b_n(n+1)R^{2(n+1)}\,r^{-(n+2)} + d_n(n-1)(n+1)R^2\,r^{-(n+2)} \\ +\,b_n\,n\,(n+1)\,r^{n} \;-\;\; d_n\,n\,(n-1)\,r^{-n} \end{bmatrix} sin(n\theta)$$

$$\sigma_{r\theta} = \sum_{n=2,4,\ldots}^{N} \begin{bmatrix} -b_n(n+1)(n-1)R^2\, r^{n-2} \\ -\,b_n(n+1)R^{2(n+1)}\, r^{-(n+2)} \\ +\,b_n\, n\,(n+1)\, r^{n} \\ -\,d_n(n-1)R^{-2(n-1)}\, r^{n-2} \\ +\,d_n(n-1)(n+1)R^2\, r^{-(n+2)} \\ -\,d_n\, n\,(n-1)\, r^{-n} \end{bmatrix} sin(n\theta)$$

$$\sigma_{r\theta} = \sum_{n=2,4,\ldots}^{N} \begin{bmatrix} \begin{Bmatrix} -(n+1)(n-1)R^2\, r^{n-2} \\ -\,(n+1)R^{2(n+1)}\, r^{-(n+2)} \\ +\,n\,(n+1)\, r^{n} \end{Bmatrix} b_n \\ \begin{Bmatrix} -\,(n-1)R^{-2(n-1)}\, r^{n-2} \\ +\,(n-1)(n+1)R^2\, r^{-(n+2)} \\ -\,n\,(n-1)\, r^{-n} \end{Bmatrix} d_n \end{bmatrix} sin(n\theta) \qquad \text{(2A.27)}$$

Note that at r = R, *equations 2A.25 and 2A.27* give $\sigma_{rr} = \sigma_{r\theta} = 0$ as they should. Unlike *equations 2A.7 through 2A.9a, equations 2A.25 through 2A.27* are further restricted to the hole containing the coordinate origin being traction-free and round of radius R. *Equations 2A.25 through 2A.27* no longer involve coefficients b_0, a_n and c_n which appears in *equations 2A.7 through 2A.9a*.

Upon imposing the traction–free conditions of *equations 2A.21 and 2A.22,* the strain and the displacements become as follows:

$$\frac{\partial u_r}{\partial r} = \epsilon_{rr} = \frac{1}{\mathrm{E}}\,(\sigma_{rr} - \upsilon\,\sigma_{\theta\theta}) \qquad \text{(2A.10)}$$

and from *equations 2A.25 and 2A.26*

$$\frac{\partial u_r}{\partial r} = \frac{1}{E}\left[\begin{array}{l} \left\{\left(\frac{-2\,R^2}{r^2}+2\right)c_0 - \sum_{n=2,4,\ldots}^{N}\left[\begin{array}{c}\left\{\begin{array}{c}-(n-1)(n+1)R^2\,r^{n-2}\\+\,(n+1)R^{2(n+1)}\,r^{-(n+2)}\\+(n+1)(n-2)r^{n}\end{array}\right\}b_n\\+\left\{\begin{array}{c}-(n-1)\,R^{-2(n-1)}\,r^{n-2}\\-(n-1)(n+1)\,R^2r^{-(n+2)}\\+\,(n-1)(n+2)\,r^{-n}\end{array}\right\}d_n\end{array}\right]cos(n\theta)\right\} \\ -\upsilon\left\{\left(\frac{2\,R^2}{r^2}+2\right)c_0 + \sum_{n=2,4,\ldots}^{N}\left[\begin{array}{c}\left\{\begin{array}{c}-\,(n+1)(n-1)R^2\,r^{n-2}\\+\,(n+1)R^{2(n+1)}\,r^{-(n+2)}\\+\,(n+1)\,(n+2)\,r^{n}\end{array}\right\}b_n\\+\left\{\begin{array}{c}-\,(n-1)\,R^{-2(n-1)}r^{n-2}\\-(n-1)(n+1)R^2\,r^{-(n+2)}\\+\,(n-1)(n-2)\,r^{-n}\end{array}\right\}d_n\end{array}\right]cos(n\theta)\right\} \end{array}\right]$$

$$\frac{\partial u_r}{\partial r} = \frac{1}{\mathrm{E}}\left[\begin{array}{l} \left(\frac{-2\,\mathrm{R}^2}{\mathrm{r}^2}+2\right)\mathrm{c}_0 - \upsilon\left(\frac{2\,\mathrm{R}^2}{\mathrm{r}^2}+2\right)\mathrm{c}_0 \\ -\sum_{\mathrm{n}=2,4,\ldots}^{\mathrm{N}}\left[\begin{array}{c}\left\{\begin{array}{c}-(\mathrm{n}-1)(\mathrm{n}+1)\mathrm{R}^2\,\mathrm{r}^{\mathrm{n}-2}\\+\,(\mathrm{n}+1)\mathrm{R}^{2(\mathrm{n}+1)}\,\mathrm{r}^{-(\mathrm{n}+2)}\\+(\mathrm{n}+1)(\mathrm{n}-2)\mathrm{r}^{\mathrm{n}}\end{array}\right\}\mathrm{b}_\mathrm{n}\\+\left\{\begin{array}{c}-(\mathrm{n}-1)\,\mathrm{R}^{-2(\mathrm{n}-1)}\,\mathrm{r}^{\mathrm{n}-2}\\-(\mathrm{n}-1)(\mathrm{n}+1)\,\mathrm{R}^2\mathrm{r}^{-(\mathrm{n}+2)}\\+\,(\mathrm{n}-1)(\mathrm{n}+2)\,\mathrm{r}^{-\mathrm{n}}\end{array}\right\}\mathrm{d}_\mathrm{n}\end{array}\right]\cos(\mathrm{n}\theta) \\ -\upsilon\sum_{\mathrm{n}=2,4,\ldots}^{\mathrm{N}}\left[\begin{array}{c}\left\{\begin{array}{c}-\,(\mathrm{n}+1)(\mathrm{n}-1)\mathrm{R}^2\,\mathrm{r}^{\mathrm{n}-2}\\+\,(\mathrm{n}+1)\mathrm{R}^{2(\mathrm{n}+1)}\,\mathrm{r}^{-(\mathrm{n}+2)}\\+\,(\mathrm{n}+1)\,(\mathrm{n}+2)\,\mathrm{r}^{\mathrm{n}}\end{array}\right\}\mathrm{b}_\mathrm{n}\\+\left\{\begin{array}{c}-\,(\mathrm{n}-1)\mathrm{R}^{-2(\mathrm{n}-1)}\,\mathrm{r}^{\mathrm{n}-2}\\-(\mathrm{n}-1)(\mathrm{n}+1)\mathrm{R}^2\,\mathrm{r}^{-(\mathrm{n}+2)}\\+\,(\mathrm{n}-1)(\mathrm{n}-2)\,\mathrm{r}^{-\mathrm{n}}\end{array}\right\}\mathrm{d}_\mathrm{n}\end{array}\right]\cos(\mathrm{n}\theta) \end{array}\right]$$

$$\frac{\partial u_r}{\partial r}=\frac{1}{\mathrm{E}}\left[-\sum_{\mathrm{n=2,4,\ldots}}^{\mathrm{N}}\left\{\begin{array}{c}\left\{\left(\frac{-2\,\mathrm{R}^2}{\mathrm{r}^2}+2\right)-\upsilon\left(\frac{2\,\mathrm{R}^2}{\mathrm{r}^2}+2\right)\right\}\mathrm{c}_0\\ \left(\begin{array}{c}-(\mathrm{n}-1)(\mathrm{n}+1)\mathrm{R}^2\,\mathrm{r}^{\mathrm{n}-2}\\ +(\mathrm{n}+1)\mathrm{R}^{2(\mathrm{n}+1)}\,\mathrm{r}^{-(\mathrm{n}+2)}\\ +(\mathrm{n}+1)(\mathrm{n}-2)\mathrm{r}^{\mathrm{n}}\end{array}\right)\mathrm{b}_\mathrm{n}\\ +\upsilon\left(\begin{array}{c}-(\mathrm{n}+1)(\mathrm{n}-1)\mathrm{R}^2\,\mathrm{r}^{\mathrm{n}-2}\\ +(\mathrm{n}+1)\mathrm{R}^{2(\mathrm{n}+1)}\,\mathrm{r}^{-(\mathrm{n}+2)}\\ +(\mathrm{n}+1)\,(\mathrm{n}+2)\,\mathrm{r}^{\mathrm{n}}\end{array}\right)\mathrm{b}_\mathrm{n}\\ +\left(\begin{array}{c}-(\mathrm{n}-1)\,\mathrm{R}^{-2(\mathrm{n}-1)}\,\mathrm{r}^{\mathrm{n}-2}\\ -(\mathrm{n}-1)(\mathrm{n}+1)\,\mathrm{R}^2\mathrm{r}^{-(\mathrm{n}+2)}\\ +(\mathrm{n}-1)(\mathrm{n}+2)\,\mathrm{r}^{-\mathrm{n}}\end{array}\right)\mathrm{d}_\mathrm{n}\\ +\upsilon\left(\begin{array}{c}-(\mathrm{n}-1)\,\mathrm{R}^{-2(\mathrm{n}-1)}\mathrm{r}^{\mathrm{n}-2}\\ -(\mathrm{n}-1)(\mathrm{n}+1)\mathrm{R}^2\,\mathrm{r}^{-(\mathrm{n}+2)}\\ +(\mathrm{n}-1)(\mathrm{n}-2)\,\mathrm{r}^{-\mathrm{n}}\end{array}\right)\mathrm{d}_\mathrm{n}\end{array}\right\}\cos(\mathrm{n}\theta)\right]$$

$$\frac{\partial u_r}{\partial r}=\frac{1}{\mathrm{E}}\left[-\sum_{\mathrm{n=2,4,\ldots}}^{\mathrm{N}}\left\{\begin{array}{c}\left\{\frac{-2\,\mathrm{R}^2}{\mathrm{r}^2}+2-\upsilon\frac{2\,\mathrm{R}^2}{\mathrm{r}^2}-2\,\upsilon\right\}\mathrm{c}_0\\ \left(\begin{array}{c}-(\mathrm{n}-1)(\mathrm{n}+1)\mathrm{R}^2\,\mathrm{r}^{\mathrm{n}-2}\\ -\upsilon\,(\mathrm{n}+1)(\mathrm{n}-1)\mathrm{R}^2\,\mathrm{r}^{\mathrm{n}-2}\\ +(\mathrm{n}+1)\mathrm{R}^{2(\mathrm{n}+1)}\,\mathrm{r}^{-(\mathrm{n}+2)}\\ +\upsilon\;(\mathrm{n}+1)\mathrm{R}^{2(\mathrm{n}+1)}\,\mathrm{r}^{-(\mathrm{n}+2)}\\ +(\mathrm{n}+1)(\mathrm{n}-2)\mathrm{r}^{\mathrm{n}}\\ +\upsilon\;(\mathrm{n}+1)\,(\mathrm{n}+2)\,\mathrm{r}^{\mathrm{n}}\end{array}\right)\mathrm{b}_\mathrm{n}\\ +\left(\begin{array}{c}-(\mathrm{n}-1)\,\mathrm{R}^{-2(\mathrm{n}-1)}\,\mathrm{r}^{\mathrm{n}-2}\\ -\upsilon\,(\mathrm{n}-1)\,\mathrm{R}^{-2(\mathrm{n}-1)}\mathrm{r}^{\mathrm{n}-2}\\ -(\mathrm{n}-1)(\mathrm{n}+1)\,\mathrm{R}^2\mathrm{r}^{-(\mathrm{n}+2)}\\ -\upsilon\,(\mathrm{n}-1)(\mathrm{n}+1)\mathrm{R}^2\,\mathrm{r}^{-(\mathrm{n}+2)}\\ +(\mathrm{n}-1)(\mathrm{n}+2)\,\mathrm{r}^{-\mathrm{n}}+\upsilon\,(\mathrm{n}-1)(\mathrm{n}-2)\,\mathrm{r}^{-\mathrm{n}}\end{array}\right)\mathrm{d}_\mathrm{n}\end{array}\right\}\cos(\mathrm{n}\theta)\right]$$

$$\frac{\partial u_r}{\partial r}=\frac{1}{E}\left[-\sum_{n=2,4,\ldots}^{\mathrm{N}}\left\{\begin{array}{c}\left\{\frac{-2\,R^2}{r^2}(1+\upsilon)\;+2(1-\upsilon)\right\}c_0\\ \left(\begin{array}{c}-(1+\upsilon)(n-1)(n+1)R^2\,r^{n-2}\\ +(1+\;\upsilon)(n+1)R^{2(n+1)}\,r^{-(n+2)}\\ +(n+1)\left[(n-2)+\;\upsilon\,(n+2)\right]r^{n}\end{array}\right)b_n\\ +\left(\begin{array}{c}-(1+\;\upsilon)(n-1)\,R^{-2(n-1)}\,r^{n-2}\\ -(1+\;\upsilon)(n-1)(n+1)\,R^2r^{-(n+2)}\\ +(n-1)\left[(n+2)+\;\upsilon\,(n-2)\right]r^{-n}\end{array}\right)d_n\end{array}\right\}cos(n\theta)\right] \qquad \text{(2A.27a)}$$

Upon integrating one obtains

$$u_r = \frac{1}{E}\left[\begin{array}{c} \left\{\frac{-2\,R^2}{(-r)}(1+v)\ +2(1-v)r\right\}c_0 \\ -\sum_{n=2,4,\ldots}^{\mathrm{N}} \left\{ \begin{array}{c} \begin{pmatrix} -(1+v)(n-1)\,(n+1)R^2\,\dfrac{r^{n-1}}{n-1} \\ +(1+\ v)(n+1)\,R^{2(n+1)}\,\dfrac{r^{-(n+1)}}{-(n+1)} \\ +(n+1)[(n-2)+\ v\,(n+2)]\,\dfrac{r^{n+1}}{n+1} \end{pmatrix} b_n \\ +\begin{pmatrix} -(1+\ v)(n-1)\,R^{-2(n-1)}\dfrac{r^{n-1}}{n-1} \\ -(1+\ v)(n-1)(n+1)\,R^2\dfrac{r^{-(n+1)}}{-(n+1)} \\ +\,(n-1)[(n+2)+\ v\,(n-2)]\,\dfrac{r^{-n+1}}{-n+1} \end{pmatrix} d_n \end{array} \right\} cos(n\theta) + g(\theta) \end{array} \right]$$

$$u_r = \frac{1}{E}\left[\begin{array}{c} \left\{\frac{2\,R^2}{r}(1+v)\ +2(1-v)r\right\}c_0 \\ -\sum_{n=2,4,\ldots}^{\mathrm{N}} \left\{ \begin{array}{c} \begin{pmatrix} -(1+v)(n+1)R^2\,r^{n-1} \\ -(1+\ v)R^{2(n+1)}\,r^{-(n+1)} \\ +[(n-2)+\ v\,(n+2)]\,r^{n+1} \end{pmatrix} b_n \\ +\begin{pmatrix} -(1+\ v)\,R^{-2(n-1)}\,r^{n-1} \\ +(1+\ v)(n-1)\,R^2 r^{-(n+1)} \\ -[(n+2)+\ v\,(n-2)]\,r^{-n+1} \end{pmatrix} d_n \end{array} \right\} cos(n\theta) + g(\theta) \end{array} \right] \qquad \text{(2A.28)}$$

where, $g(\theta) = S_1\cos\theta - S_2\sin\theta$. Unlike *equation 2A.11, equation 2A.28* is further restricted to the hole containing the coordinate origin being traction-free and round of radius R. Like the stresses of *equations 2A.25 through 2A.27,* the radial displacement now also depends at most on c_o, b_n and d_n, and $g(\theta) = S_1\cos\theta - S_2\sin\theta$.

From *equation 2.13*

$$\varepsilon_{\theta\theta} = \frac{1}{E}\left(\sigma_{\theta\theta} - \upsilon\,\sigma_{rr}\right)$$

and *equations 2A.25 and 2A.26*

$$\varepsilon_{\theta\theta} = \frac{1}{E}\left[\begin{array}{l}\left\{\left(\frac{2\,R^2}{r^2} + 2\right)c_0 + \sum_{n=2,4,\ldots}^{N}\left[\begin{array}{c}\left\{\begin{array}{c}-(n+1)(n-1)R^2\,r^{n-2}\\ +(n+1)R^{2(n+1)}\,r^{-(n+2)}\\ +(n+1)\,(n+2)\,r^{n}\end{array}\right\}b_n\\ +\left\{\begin{array}{c}-(n-1)\,R^{-2(n-1)}r^{n-2}\\ -(n-1)(n+1)R^2\,r^{-(n+2)}\\ +(n-1)(n-2)\,r^{-n}\end{array}\right\}d_n\end{array}\right]cos(n\theta)\right\}\\ -\upsilon\left\{\left(\frac{-2\,R^2}{r^2} + 2\right)c_0 - \sum_{n=2,4,\ldots}^{\mathrm{N}}\left[\begin{array}{c}\left\{\begin{array}{c}-(n-1)(n+1)R^2\,r^{n-2}\\ +(n+1)R^{2(n+1)}\,r^{-(n+2)}\\ +(n+1)(n-2)r^{n}\end{array}\right\}b_n\\ +\left\{\begin{array}{c}-(n-1)\,R^{-2(n-1)}\,r^{n-2}\\ -(n-1)(n+1)\,R^2r^{-(n+2)}\\ +(n-1)(n+2)\,r^{-n}\end{array}\right\}d_n\end{array}\right]cos(n\theta)\right\}\end{array}\right]$$

$$\varepsilon_{\theta\theta} = \frac{1}{E}\left[\begin{array}{l}\left(\frac{2\,R^2}{r^2} + 2\right)c_0 - \upsilon\left(\frac{-2\,R^2}{r^2} + 2\right)c_0\\ +\sum_{n=2,4,\ldots}^{N}\left[\begin{array}{c}\left\{\begin{array}{c}-(n+1)(n-1)R^2\,r^{n-2}\\ +(n+1)R^{2(n+1)}\,r^{-(n+2)}\\ +(n+1)\,(n+2)\,r^{n}\end{array}\right\}b_n\\ +\left\{\begin{array}{c}-(n-1)\,R^{-2(n-1)}r^{n-2}\\ -(n-1)(n+1)R^2\,r^{-(n+2)}\\ +(n-1)(n-2)\,r^{-n}\end{array}\right\}d_n\end{array}\right]cos(n\theta)\\ +\upsilon\sum_{n=2,4,\ldots}^{\mathrm{N}}\left[\begin{array}{c}\left\{\begin{array}{c}-(n-1)(n+1)R^2\,r^{n-2}\\ +(n+1)R^{2(n+1)}\,r^{-(n+2)}\\ +(n+1)(n-2)r^{n}\end{array}\right\}b_n\\ +\left\{\begin{array}{c}-(n-1)\,R^{-2(n-1)}\,r^{n-2}\\ -(n-1)(n+1)\,R^2r^{-(n+2)}\\ +(n-1)(n+2)\,r^{-n}\end{array}\right\}d_n\end{array}\right]cos(n\theta)\end{array}\right]$$

$$\varepsilon_{\theta\theta} = \frac{1}{E}\left[+\sum_{n=2,4,\ldots}^{N}\left\{\begin{array}{c} \left\{\left(\frac{2R^2}{r^2}+2\right)-\upsilon\left(\frac{-2R^2}{r^2}+2\right)\right\}c_0 \\ \left(\begin{array}{c}-(n+1)(n-1)R^2\,r^{n-2} \\ +(n+1)R^{2(n+1)}\,r^{-(n+2)} \\ +(n+1)(n+2)r^n\end{array}\right)b_n \\ +\upsilon\left(\begin{array}{c}-(n-1)(n+1)R^2\,r^{n-2} \\ +(n+1)R^{2(n+1)}\,r^{-(n+2)} \\ +(n+1)(n-2)r^n\end{array}\right)b_n \\ +\left(\begin{array}{c}-(n-1)\,R^{-2(n-1)}\,r^{n-2} \\ -(n-1)(n+1)R^2\,r^{-(n+2)} \\ +(n-1)(n-2)\,r^{-n}\end{array}\right)d_n \\ +\upsilon\left(\begin{array}{c}-(n-1)\,R^{-2(n-1)}\,r^{n-2} \\ -(n-1)(n+1)\,R^2r^{-(n+2)} \\ +(n-1)(n+2)\,r^{-n}\end{array}\right)d_n \end{array}\right\}cos(n\theta)\right]$$

$$\varepsilon_{\theta\theta} = \frac{1}{E}\left[+\sum_{n=2,4,\ldots}^{N}\left\{\begin{array}{c} \left\{\frac{2R^2}{r^2}+2+\upsilon\frac{2R^2}{r^2}-2\upsilon\right\}c_0 \\ \left(\begin{array}{c}-(n+1)(n-1)R^2\,r^{n-2}-\upsilon\,(n-1)(n+1)R^2\,r^{n-2} \\ +(n+1)R^{2(n+1)}\,r^{-(n+2)}+\upsilon\,(n+1)R^{2(n+1)}\,r^{-(n+2)} \\ +(n+1)(n+2)r^n+\upsilon\,(n+1)(n-2)r^n\end{array}\right)b_n \\ +\left(\begin{array}{c}-(n-1)R^{-2(n-1)}\,r^{n-2}-\upsilon\,(n-1)\,R^{-2(n-1)}\,r^{n-2} \\ -(n-1)(n+1)R^2\,r^{-(n+2)}-\upsilon\,(n-1)(n+1)\,R^2r^{-(n+2)} \\ +(n-1)(n-2)\,r^{-n}+\upsilon\,(n-1)(n+2)\,r^{-n}\end{array}\right)d_n \end{array}\right\}cos(n\theta)\right]$$

$$\varepsilon_{\theta\theta} = \frac{1}{E}\left[+\sum_{n=2,4,\ldots}^{N}\left\{\begin{array}{c} \left\{\frac{2R^2}{r^2}(1+\upsilon)+2(1-\upsilon)\right\}c_0 \\ \left(\begin{array}{c}-(1+\upsilon)(n+1)(n-1)R^2\,r^{n-2} \\ +(1+\upsilon)(n+1)R^{2(n+1)}\,r^{-(n+2)} \\ +(n+1)\,[(n+2)+\upsilon(n-2)]r^n\end{array}\right)b_n \\ +\left(\begin{array}{c}-(1+\upsilon)(n-1)\,R^{-2(n-1)}r^{n-2} \\ -(1+\upsilon)(n-1)(n+1)R^2\,r^{-(n+2)} \\ +(n-1)[(n-2)+\upsilon(n+2)]\,r^{-n}\end{array}\right)d_n \end{array}\right\}cos(n\theta)\right] \qquad \text{(2A.29)}$$

Equation 2A.29 is restricted to having mechanical and geometric symmetry about the x- and y-axes and the hole containing the coordinate origin being round of radius R. As with the stress *equations 2A.25 through 2A.27*, radial displacement of *equation 2A.28*, the strains of *equations 2A.27a and 2A.29* contain only the Airy coefficients c_o, b_n and d_n.

From *equation 2A.16*

$$\frac{1}{r}\frac{\partial u_\theta}{\partial \theta} = \frac{1}{E}\left(\sigma_{\theta\theta} - \upsilon\sigma_{rr}\right) - \frac{u_r}{r}$$

$$\Rightarrow \qquad \frac{\partial u_\theta}{\partial \theta} = r\varepsilon_{\theta\theta} - u_r$$

and *equations 2A.28 and 2A.29,* one obtains

$$\frac{\partial u_\theta}{\partial \theta} = \left[\begin{array}{l} r.\frac{1}{E}\left[\begin{array}{c} \left\{\frac{2R^2}{r^2}(1+\upsilon) + 2(1-\upsilon)\right\}c_0 \\ + \sum_{n=2,4,\ldots}^{N} \left\{\begin{array}{c} \left(\begin{array}{c} -(1+\upsilon)(n+1)(n-1)R^2 r^{n-2} \\ +(1+\upsilon)(n+1)R^{2(n+1)} r^{-(n+2)} \\ +(n+1)[(n+2)+\upsilon(n-2)]r^n \end{array}\right) b_n \\ +\left(\begin{array}{c} -(1+\upsilon)(n-1)R^{-2(n-1)} r^{n-2} \\ -(1+\upsilon)(n-1)(n+1)R^2 r^{-(n+2)} \\ +(n-1)[(n-2)+\upsilon(n+2)]r^{-n} \end{array}\right) d_n \end{array}\right\} cos(n\theta) \end{array}\right] \\ -\frac{1}{E}\left[\begin{array}{c} \left\{\frac{2R^2}{r}(1+\upsilon) + 2(1-\upsilon)r\right\}c_0 \\ - \sum_{n=2,4,\ldots}^{N} \left\{\begin{array}{c} \left(\begin{array}{c} -(1+\upsilon)(n+1)R^2 r^{n-1} \\ -(1+\upsilon)R^{2(n+1)} r^{-(n+1)} \\ +[(n-2)+\upsilon(n+2)]r^{n+1} \end{array}\right) b_n \\ +\left(\begin{array}{c} -(1+\upsilon)R^{-2(n-1)} r^{n-1} \\ +(1+\upsilon)(n-1)R^2 r^{-(n+1)} \\ -[(n+2)+\upsilon(n-2)]r^{-n+1} \end{array}\right) d_n \end{array}\right\} cos(n\theta) \end{array}\right] + g(\theta) \end{array}\right]$$

$$\frac{\partial u_\theta}{\partial \theta} = \left[\begin{array}{l} \frac{1}{E}\left[\begin{array}{c} \left\{\frac{2\,R^2}{r}\,(1+\upsilon)+2(1-\upsilon)r\right\}c_0 \\ +\sum_{n=2,4,\ldots}^{N}\left\{\begin{array}{c}\left(\begin{array}{c}-(1+\upsilon)(n+1)(n-1)R^2\,r^{n-1}\\ +(1+\upsilon)(n+1)R^{2(n+1)}\,r^{-(n+1)}\\ +(n+1)[(n+2)+\upsilon\,(n-2)]r^{n+1}\end{array}\right)b_n \\ +\left(\begin{array}{c}-(1+\upsilon)(n-1)\,R^{-2(n-1)}r^{n-1}\\ -(1+\upsilon)(n-1)(n+1)R^2\,r^{-(n+1)}\\ +(n-1)[(n-2)+\upsilon\,(n+2)]\,r^{-n+1}\end{array}\right)d_n\end{array}\right\}cos(n\theta)\end{array}\right] \\ -\frac{1}{E}\left[\begin{array}{c}\left\{\frac{2\,R^2}{r}(1+\upsilon)\;+2(1-\upsilon)r\right\}c_0 \\ -\sum_{n=2,4,\ldots}^{N}\left\{\begin{array}{c}\left(\begin{array}{c}-(1+\upsilon)(n+1)R^2\,r^{n-1}\\ -(1+\upsilon)R^{2(n+1)}\,r^{-(n+1)}\\ +[(n-2)+\upsilon\,(n+2)]\,r^{n+1}\end{array}\right)b_n \\ +\left(\begin{array}{c}-(1+\upsilon)\,R^{-2(n-1)}\,r^{n-1}\\ +(1+\upsilon)(n-1)\,R^2r^{-(n+1)}\\ -[(n+2)+\upsilon\,(n-2)]\,r^{-n+1}\end{array}\right)d_n\end{array}\right\}cos(n\theta)\end{array}\right]+g(\theta)\end{array}\right]$$

$$\frac{\partial u_\theta}{\partial \theta} = \frac{1}{E}\left[\begin{array}{c} \left\{\frac{2\,R^2}{r}\,(1+\upsilon)+2(1-\upsilon)r\right\}c_0-\left\{\frac{2\,R^2}{r}(1+\upsilon)\;+2(1-\upsilon)r\right\}c_0 \\ +\sum_{n=2,4,\ldots}^{N}\left\{\begin{array}{c}\left(\begin{array}{c}-(1+\upsilon)(n+1)(n-1)R^2\,r^{n-1}\\ +(1+\upsilon)(n+1)R^{2(n+1)}\,r^{-(n+1)}\\ +(n+1)[(n+2)+\upsilon\,(n-2)]r^{n+1}\end{array}\right)b_n \\ +\left(\begin{array}{c}-(1+\upsilon)(n-1)\,R^{-2(n-1)}r^{n-1}\\ -(1+\upsilon)(n-1)(n+1)R^2\,r^{-(n+1)}\\ +(n-1)[(n-2)+\upsilon\,(n+2)]\,r^{-n+1}\end{array}\right)d_n\end{array}\right\}cos(n\theta) \\ +\sum_{n=2,4,\ldots}^{N}\left\{\begin{array}{c}\left(\begin{array}{c}-(1+\upsilon)(n+1)R^2\,r^{n-1}\\ -(1+\upsilon)R^{2(n+1)}\,r^{-(n+1)}\\ +[(n-2)+\upsilon\,(n+2)]\,r^{n+1}\end{array}\right)b_n \\ +\left(\begin{array}{c}-(1+\upsilon)\,R^{-2(n-1)}\,r^{n-1}\\ +(1+\upsilon)(n-1)\,R^2r^{-(n+1)}\\ -[(n+2)+\upsilon(n-2)]\,r^{-n+1}\end{array}\right)d_n\end{array}\right\}cos(n\theta)-g(\theta)\end{array}\right]$$

$$\frac{\partial u_\theta}{\partial \theta} = \frac{1}{E}\left[\sum_{n=2,4,\ldots}^{N}\left\{\begin{array}{c}\begin{pmatrix} -(1+\upsilon)(n+1)(n-1)R^2\, r^{n-1} \\ +(1+\ \upsilon)(n+1)R^{2(n+1)}\, r^{-(n+1)} \\ +(n+1)[(n+2)+\upsilon\,(n-2)]r^{n+1}\end{pmatrix} b_n \\ +\begin{pmatrix} -(1+\upsilon)(n+1)R^2\, r^{n-1} \\ -(1+\ \upsilon)R^{2(n+1)}\, r^{-(n+1)} \\ +[(n-2)+\ \upsilon\,(n+2)]\, r^{n+1}\end{pmatrix} b_n \\ +\begin{pmatrix} -(1+\upsilon)(n-1)\, R^{-2(n-1)} r^{n-1} \\ -(1+\upsilon)(n-1)(n+1)R^2\, r^{-(n+1)} \\ +(n-1)[(n-2)+\ \upsilon\,(n+2)]r^{-n+1}\end{pmatrix} d_n \\ +\begin{pmatrix} -(1+\ \upsilon)\, R^{-2(n-1)}\, r^{n-1} \\ +(1+\ \upsilon)(n-1)\, R^2 r^{-(n+1)} \\ \text{-}[(n+2)+\ \upsilon\,(n-2)]r^{-n+1}\end{pmatrix} d_n\end{array}\right\} cos(n\theta)\right] - g(\theta)$$

$$\frac{\partial u_\theta}{\partial \theta} = \frac{1}{E}\left[\sum_{n=2,4,\ldots}^{N}\left\{\begin{array}{c}\begin{pmatrix} -(1+\upsilon)(n+1)(n-1)R^2\, r^{n-1} \\ -(1+\upsilon)(n+1)R^2\, r^{n-1} \\ +(1+\ \upsilon)(n+1)R^{2(n+1)}\, r^{-(n+1)} \\ -(1+\ \upsilon)R^{2(n+1)}\, r^{-(n+1)} \\ +(n+1)[(n+2)+\upsilon\,(n-2)]r^{n+1} \\ +[(n-2)+\ \upsilon\,(n+2)]\, r^{n+1}\end{pmatrix} b_n \\ +\begin{pmatrix} -(1+\upsilon)(n-1)\, R^{-2(n-1)} r^{n-1} \\ -(1+\ \upsilon)\, R^{-2(n-1)}\, r^{n-1} \\ -(1+\upsilon)(n-1)(n+1)R^2\, r^{-(n+1)} \\ +(1+\ \upsilon)(n-1)\, R^2 r^{-(n+1)} \\ +(n-1)[(n-2)+\ \upsilon\,(n+2)]r^{-n+1} \\ -[(n+2)+\ \upsilon\,(n-2)]r^{-n+1}\end{pmatrix} d_n\end{array}\right\} cos(n\theta)\right] - g(\theta)$$

$$\frac{\partial u_\theta}{\partial \theta} = \frac{1}{E}\left[\sum_{n=2,4,\ldots}^{N}\left\{\begin{array}{c}\begin{pmatrix} -(1+\upsilon)(n+1)R^2\, r^{n-1}[n-1+1] \\ +(1+\ \upsilon)R^{2(n+1)}\, r^{-(n+1)}[n+1-1] \\ +[(n+2)(n+1)+\upsilon(n-2)(n+1)]r^{n+1} \\ +[(n-2)+\ \upsilon(n+2)]\, r^{n+1}\end{pmatrix} b_n \\ +\begin{pmatrix} -(1+\upsilon)\, R^{-2(n-1)} r^{n-1}[n-1+1] \\ -(1+\upsilon)(n-1)R^2\, r^{-(n+1)}[n+1-1] \\ +[(n-2)(n-1)+\upsilon\,(n+2)(n-1)]r^{-n+1} \\ -[(n+2)+\upsilon\,(n-2)]r^{-n+1}\end{pmatrix} d_n\end{array}\right\} cos(n\theta)\right] - g(\theta)$$

$$\frac{\partial u_\theta}{\partial \theta} = \frac{1}{E}\left[\sum_{n=2,4,\ldots}^{N}\left\{\begin{pmatrix} -(1+\upsilon)(n+1)R^2\, r^{n-1}[n-1+1] \\ +(1+\ \upsilon)R^{2(n+1)}\, r^{-(n+1)}[n+1-1] \\ +[(n^2+3n+2)+\upsilon\,(n^2-n-2)]r^{n+1} \\ +[(n-2)+\ \upsilon\,(n+2)]\, r^{n+1} \end{pmatrix} b_n + \begin{pmatrix} -(1+\upsilon)\, R^{-2(n-1)} r^{n-1}[n-1+1] \\ -(1+\upsilon)(n-1)R^2\, r^{-(n+1)}[n+1-1] \\ +[(n^2-3n+2)+\upsilon\,(n^2+n-2)]r^{-n+1} \\ -[(n+2)+\upsilon\,(n-2)]r^{-n+1} \end{pmatrix} d_n \right\} cos(n\theta) - g(\theta)\right]$$

$$\frac{\partial u_\theta}{\partial \theta} = \frac{1}{E}\left[\sum_{n=2,4,\ldots}^{N}\left\{\begin{pmatrix} -(1+\upsilon)(n+1)R^2\, r^{n-1}[n-1+1] \\ +(1+\ \upsilon)R^{2(n+1)}\, r^{-(n+1)}[n+1-1] \\ +\begin{bmatrix}(n^2+3n+2)+\upsilon(n^2-n-2) \\ +(n-2)+\ \upsilon(n+2)\end{bmatrix} r^{n+1} \end{pmatrix} b_n + \begin{pmatrix} -(1+\upsilon)\, R^{-2(n-1)} r^{n-1}[n-1+1] \\ -(1+\upsilon)(n-1)R^2\, r^{-(n+1)}[n+1-1] \\ +\begin{bmatrix}(n^2-3n+2)+\upsilon\,(n^2+n-2) \\ -(n+2)-\ \upsilon\,(n-2)\end{bmatrix} r^{-n+1} \end{pmatrix} d_n \right\} cos(n\theta) - g(\theta)\right]$$

$$\frac{\partial u_\theta}{\partial \theta} = \frac{1}{E}\left[\sum_{n=2,4,\ldots}^{N}\left\{\begin{pmatrix} -(1+\upsilon)(n+1)R^2\, r^{n-1}[n-1+1] \\ +(1+\ \upsilon)R^{2(n+1)}\, r^{-(n+1)}[n+1-1] \\ +\begin{bmatrix}n^2+3n+2+\upsilon\, n^2-\upsilon\, n-2\,\upsilon \\ +n-2+\ \upsilon\, n+2\,\upsilon\end{bmatrix} r^{n+1} \end{pmatrix} b_n + \begin{pmatrix} -(1+\upsilon)\, R^{-2(n-1)} r^{n-1}[n-1+1] \\ -(1+\upsilon)(n-1)R^2\, r^{-(n+1)}[n+1-1] \\ +\begin{bmatrix}n^2-3n+2+\upsilon\, n^2+\upsilon\, n-2\,\upsilon \\ -n-2-\ \upsilon\, n+2\,\upsilon\end{bmatrix} r^{-n+1} \end{pmatrix} d_n \right\} cos(n\theta) - g(\theta)\right]$$

$$\frac{\partial u_\theta}{\partial \theta} = \frac{1}{E}\left[\sum_{n=2,4,\ldots}^{N}\left\{\begin{pmatrix} -n(1+\upsilon)(n+1)R^2\, r^{n-1} \\ +\mathrm{n}(1+\ \upsilon)R^{2(n+1)}\, r^{-(n+1)} \\ +(n^2+4n+\upsilon n^2)\, r^{n+1} \end{pmatrix} b_n + \begin{pmatrix} -n(1+\upsilon)\, R^{-2(n-1)} r^{n-1} \\ -n(1+\upsilon)(n-1)R^2\, r^{-(n+1)} \\ +(n^2-4n+\upsilon n^2) r^{-n+1} \end{pmatrix} d_n \right\} cos(n\theta) - g(\theta)\right]$$

$$\frac{\partial u_\theta}{\partial \theta} = \frac{1}{E}\left[\sum_{n=2,4,\ldots}^{N} \mathrm{n.}\left\{\begin{array}{l}\begin{pmatrix}-(1+\upsilon)(n+1)R^2\, r^{n-1}\\ +(1+\ \upsilon)R^{2(n+1)}\, r^{-(n+1)}\\ +[n(1+\upsilon)+4]\, r^{n+1}\end{pmatrix} b_n \\ +\begin{pmatrix}-(1+\upsilon)\, R^{-2(n-1)} r^{n-1}\\ -(1+\upsilon)(n-1)R^2\, r^{-(n+1)}\\ +[n(1+\upsilon)-4] r^{-n+1}\end{pmatrix} d_n\end{array}\right\} cos(n\theta) - g(\theta)\right] \qquad \text{(2A.30)}$$

Therefore, integrating gives

$$u_\theta = \frac{1}{E}\left[\sum_{n=2,4,\ldots}^{N} \mathrm{n.}\left\{\begin{array}{l}\begin{pmatrix}-(1+\upsilon)(n+1)R^2\, r^{n-1}\\ +(1+\ \upsilon)R^{2(n+1)}\, r^{-(n+1)}\\ +[n(1+\upsilon)+4]\, r^{n+1}\end{pmatrix} b_n \\ +\begin{pmatrix}-(1+\upsilon)\, R^{-2(n-1)} r^{n-1}\\ -(1+\upsilon)(n-1)R^2\, r^{-(n+1)}\\ +[n(1+\upsilon)-4] r^{-n+1}\end{pmatrix} d_n\end{array}\right\} \frac{sin(n\theta)}{n} - \int g(\theta)\,.\,\mathrm{d}\theta + \mathrm{f(r)}\right]$$

or

$$u_\theta = \frac{1}{E}\left[\sum_{n=2,4,\ldots}^{N} \left\{\begin{array}{l}\begin{pmatrix}-(1+\upsilon)(n+1)R^2\, r^{n-1}\\ +(1+\ \upsilon)R^{2(n+1)}\, r^{-(n+1)}\\ +[n(1+\upsilon)+4]\, r^{n+1}\end{pmatrix} b_n \\ +\begin{pmatrix}-(1+\upsilon)\, R^{-2(n-1)} r^{n-1}\\ -(1+\upsilon)(n-1)R^2\, r^{-(n+1)}\\ +[n(1+\upsilon)-4] r^{-n+1}\end{pmatrix} d_n\end{array}\right\} sin(n\theta) - \ \mathrm{S}_1\ \sin\theta - \mathrm{S}_2\ \cos\theta + \mathrm{R}^* \mathrm{r}\right]$$

(2A.31)

If there are no rigid body translations or rotations, $S_1 = S_2 = R^* = 0$, and upon satisfying the traction-free stresses on the edge of the hole such that one obtains *equations 2A.21 through 2A.24*, then the stresses *(equations 2A.25 through 2A.27)*, strains and displacements *(equations 2A.28 and 2A.31)* now involve only the coefficients c_o, b_n and d_n. This reduces the number of Airy coefficients that must be evaluated by essentially 50% compared to not imposing the traction-free conditions on the edge of the hole *analytically* (i.e., imposing them point by point). Having fewer coefficients can be advantageous experimentally in that it reduces the amount of

measured displacement data needed by which to evaluate these remaining Airy coefficients, as well as simplifying the least square computations associated with *equations 2A.25 through 2A.31*. Note that whereas both u_r, *equation 2A.28,* and u_θ, *equation 2A.31,* involve Airy coefficients b_n, and d_n, u_r also depends on c_o. Airy coefficient c_o does not appear in the expression for u_θ of *equation 2A.31*. This is not unlike the situation in that while c_o appears in the expressions for σ_{rr} *(equation 2A.25)* and $\sigma_{\theta\theta}$ *(equation 2A.26),* it does not in $\sigma_{r\theta}$ (*equation 2A.27).*

Validating the previous equations:

From imposing $\sigma_{rr} = \sigma_{r\theta} = 0$ on the edge of the hole, one has

$$b_0 = -2c_0R^2 \tag{2A.21a}$$

$$a_n = \frac{-b_n(n+1)R^2 - d_nR^{-2(n-1)}}{n} \tag{2A.23}$$

$$c_n = \frac{b_nR^{2(n+1)} - d_n(n-1)R^2}{n} \tag{2A.24}$$

But before imposing the traction–free conditions on the edge of the hole,

$$u_r = \frac{1}{E}\left[-\sum_{n=2,4,\ldots}^{N} \begin{pmatrix} \frac{-b_0(1+\upsilon)}{r} + 2c_0(1-\upsilon)r \\ a_n\, n\,(1+\upsilon)\; r^{n-1} \\ + b_n\,[(n-2)+\upsilon(n+2)]\, r^{n+1} \\ -\; c_n\, n\,(1+\upsilon)\, r^{-(n+1)} \\ - d_n\,[(n+2)+\upsilon\,(n-2)]\, r^{-(n-1)} \end{pmatrix} cos(n\theta) + g(\theta) \right] \tag{2A.11}$$

Substituting *equations 2A.21a, 2A.23, 2A.24* into *equation 2A.11*, one gets

$$u_r = \frac{1}{\mathrm{E}}\left[-\sum_{n=2,4,\ldots}^{\mathrm{N}}\begin{pmatrix}\dfrac{-(-2c_0R^2)(1+\upsilon)}{r}+2c_0(1-\upsilon)r\\ \left(\dfrac{-b_n(n+1)R^2-d_nR^{-2(n-1)}}{n}\right)n\,(1+\upsilon)\;r^{n-1}\\ +\,b_n\left[(n-2)+\upsilon\,(n+2)\right]r^{n+1}\\ -\left(\dfrac{b_nR^{2(n+1)}-d_n(n-1)R^2}{n}\right)n\,(1+\upsilon)\,r^{-(n+1)}\\ -\,d_n\left[(n+2)+\upsilon\,(n-2)\right]r^{-(n-1)}\end{pmatrix}cos(n\theta)+g(\theta)\right]$$

$$u_r = \frac{1}{\mathrm{E}}\left[-\sum_{n=2,4,\ldots}^{\mathrm{N}}\begin{pmatrix}\dfrac{2R^2(1+\upsilon)}{r}c_0+2c_0(1-\upsilon)r\\ \left(-b_n(n+1)R^2-d_nR^{-2(n-1)}\right)(1+\upsilon)\;r^{n-1}\\ +\,b_n\left[(n-2)+\upsilon\,(n+2)\right]r^{n+1}\\ -\left(b_nR^{2(n+1)}-d_n(n-1)R^2\right)(1+\upsilon)\,r^{-(n+1)}\\ -\,d_n\left[(n+2)+\upsilon\,(n-2)\right]r^{-(n-1)}\end{pmatrix}cos(n\theta)+g(\theta)\right]$$

$$u_r = \frac{1}{\mathrm{E}}\left[-\sum_{n=2,4,\ldots}^{\mathrm{N}}\begin{pmatrix}\left\{\dfrac{2\,R^2}{r}(1+\upsilon)\;+2(1-\upsilon)r\right\}c_0\\ \left(-b_n(1+\upsilon)(n+1)R^2\,r^{n-1}-d_n(1+\upsilon)\,R^{-2(n-1)}\,r^{n-1}\right)\\ +\,b_n\left[(n-2)+\upsilon(n+2)\right]r^{n+1}\\ -\left(b_n(1+\upsilon)R^{2(n+1)}\,r^{-(n+1)}-d_n(1+\upsilon)(n-1)R^2\,r^{-(n+1)}\right)\\ -\,d_n\left[(n+2)+\upsilon\,(n-2)\right]r^{-(n-1)}\end{pmatrix}cos(n\theta)+g(\theta)\right]$$

$$u_r = \frac{1}{\mathrm{E}}\left[-\sum_{n=2,4,\ldots}^{\mathrm{N}}\begin{pmatrix}\left\{\frac{2\,R^2}{r}(1+\upsilon)\;+2(1-\upsilon)r\right\}c_0\\ -b_n(1+\upsilon)(n+1)R^2\,r^{n-1}\\ +\,b_n\left[(n-2)+\upsilon\,(n+2)\right]r^{n+1}\\ -b_n(1+\upsilon)R^{2(n+1)}\,r^{-(n+1)}\\ -d_n(1+\upsilon)R^{-2(n-1)}\,r^{n-1}\\ +d_n(1+\upsilon)(n-1)R^2\,r^{-(n+1)}\\ -\,d_n\left[(n+2)+\upsilon\,(n-2)\right]r^{-(n-1)}\end{pmatrix}cos(n\theta)+g(\theta)\right]$$

$$u_r = \frac{1}{\mathrm{E}}\left[-\sum_{n=2,4,\ldots}^{\mathrm{N}}\begin{pmatrix}\left\{\frac{2\,R^2}{r}(1+\upsilon)\;+2(1-\upsilon)r\right\}c_0\\ \begin{pmatrix}-(1+\upsilon)(n+1)R^2\,r^{n-1}\\ +[(n-2)+\upsilon\,(n+2)]\,r^{n+1}\\ -(1+\upsilon)R^{2(n+1)}\,r^{-(n+1)}\end{pmatrix}b_n\\ +\begin{pmatrix}-(1+\upsilon)R^{-2(n-1)}\,r^{n-1}\\ +(1+\upsilon)(n-1)R^2\,r^{-(n+1)}\\ -\,[(n+2)+\upsilon\,(n-2)]\,r^{-(n-1)}\end{pmatrix}d_n\end{pmatrix}cos(n\theta)+g(\theta)\right] \qquad (2A.32)$$

Equations 2A.28 and 2A.32 agree, as they should.

Now, before imposing the traction–free conditions on the edge of the hole,

$$u_\theta = \frac{1}{\mathrm{E}}\left[\sum_{n=2,4,\ldots}^{N}\begin{pmatrix} a_n\, n\,(1+\upsilon)\, r^{n-1} \\ +\, b_n\,[n(1+\upsilon)+4]\, r^{n+1} \\ +\ c_n\, n(1+\upsilon)\, r^{-(n+1)} \\ +\, d_n[n(1+\upsilon)-4]\, r^{-(n-1)} \end{pmatrix} sin(n\theta) - \mathrm{S}_1\ \sin\theta - \mathrm{S}_2\ \cos\theta + \mathrm{R}^*\mathrm{r}\right] \tag{2A.20}$$

Substituting *equations 2A.21a, 2A.23 and 2A.24* into *2A.20*, gives

$$u_\theta = \frac{1}{\mathrm{E}}\left[\sum_{n=2,4,\ldots}^{N}\begin{pmatrix} \left(\dfrac{-b_n(n+1)R^2 - d_nR^{-2(n-1)}}{n}\right) n\,(1+\upsilon)\, r^{n-1} \\ +\, b_n\,[n(1+\upsilon)+4]\, r^{n+1} \\ +\left(\dfrac{b_nR^{2(n+1)} - d_n(n-1)R^2}{n}\right) n(1+\upsilon)\, r^{-(n+1)} \\ +\, d_n[n(1+\upsilon)-4]\, r^{-(n-1)} \\ -\mathrm{S}_1 \sin\theta - \mathrm{S}_2 \cos\theta + \mathrm{R}^*\mathrm{r} \end{pmatrix} sin(n\theta)\right]$$

$$u_\theta = \frac{1}{\mathrm{E}}\left[\sum_{n=2,4,\ldots}^{N}\begin{pmatrix} \left(-b_n(n+1)R^2 - d_nR^{-2(n-1)}\right)(1+\upsilon)\, r^{n-1} \\ +\, b_n\,[n(1+\upsilon)+4]\, r^{n+1} \\ +\left(b_nR^{2(n+1)} - d_n(n-1)R^2\right)(1+\upsilon)\, r^{-(n+1)} \\ +\, d_n[n(1+\upsilon)-4]\, r^{-(n-1)} \\ -\mathrm{S}_1\ \sin\theta - \mathrm{S}_2\ \cos\theta + \mathrm{R}^*\mathrm{r} \end{pmatrix} sin(n\theta)\right]$$

$$u_\theta = \frac{1}{\mathrm{E}}\left[\sum_{n=2,4,\ldots}^{N}\begin{pmatrix} \left(-b_n(1+\upsilon)(n+1)R^2r^{n-1} - d_n(1+\upsilon)R^{-2(n-1)}r^{n-1}\right) \\ +\, b_n\,[n(1+\upsilon)+4]\, r^{n+1} \\ +\left(b_n(1+\upsilon)R^{2(n+1)}r^{-(n+1)} - d_n(1+\upsilon)(n-1)R^2r^{-(n+1)}\right) \\ +\, d_n[n(1+\upsilon)-4]\, r^{-(n-1)} \\ -\ \mathrm{S}_1\ \sin\theta - \mathrm{S}_2\ \cos\theta + \mathrm{R}^*\mathrm{r} \end{pmatrix} sin(n\theta)\right]$$

$$u_\theta = \frac{1}{\mathrm{E}}\cdot\left[\sum_{n=2,4,\ldots}^{N}\begin{pmatrix} -b_n(1+\upsilon)(n+1)R^2r^{n-1} \\ +\,b_n\,[n(1+\upsilon)+4]\,r^{n+1} \\ +\,b_n(1+\upsilon)R^{2(n+1)}r^{-(n+1)} \\ -d_n(1+\upsilon)R^{-2(n-1)}r^{n-1} \\ -d_n(1+\upsilon)(n-1)R^2r^{-(n+1)} \\ +\,d_n[n(1+\upsilon)-4]\,r^{-(n-1)} \end{pmatrix} sin(n\theta) - \mathrm{S}_1\ \sin\theta - \mathrm{S}_2\ \cos\theta + \mathrm{R}^*\mathrm{r}\right]$$

$$u_\theta = \frac{1}{\mathrm{E}}\cdot\left[\sum_{n=2,4,\ldots}^{N}\begin{pmatrix} \begin{pmatrix} -(1+\upsilon)(n+1)R^2r^{n-1} \\ +\,[n(1+\upsilon)+4]\,r^{n+1} \\ +(1+\upsilon)R^{2(n+1)}r^{-(n+1)} \end{pmatrix} b_n \\ + \begin{pmatrix} -\,(1+\upsilon)R^{-2(n-1)}\,r^{n-1} \\ -(1+\upsilon)(n-1)R^2r^{-(n+1)} \\ +\,[n(1+\upsilon)-4]\,r^{-(n-1)} \end{pmatrix} d_n \end{pmatrix} sin(n\theta) - \mathrm{S}_1\ \sin\theta - \mathrm{S}_2\ \cos\theta + \mathrm{R}^*\mathrm{r}\right]$$

(2A.33)

Equations 2A.31 and 2A.33 are the same, as they should be.

Also, from *figure 2.3* [7, p.472],

$$u = u_r\cos\theta - u_\theta\sin\theta$$

$$v = u_r\sin\theta + u_\theta\cos\theta \qquad \text{(2A.34)}$$

where u_r and u_θ represent the displacements in polar coordinates, and displacements u and v are with respect to Cartesian coordinates (u in the x–direction and v in the y–direction). Ignoring the rigid body translation or rotation (i.e., $S_1 = S_2 = R^* = 0$), substituting the values of u_r, from *equation 2A.32,* and u_θ from *equation 2A.33*, in the above equations, one gets:

$$u = \frac{1}{E}\left[\left\{\frac{2\,R^2}{r}(1+\upsilon) + 2(1-\upsilon)r\right\} c_0 - \sum_{n=2,4,\ldots}^{N} \left\{ \begin{pmatrix} -(1+\upsilon)(n+1)R^2\, r^{n-1} \\ -(1+\ \upsilon)R^{2(n+1)}\, r^{-(n+1)} \\ +[(n-2)+\ \upsilon(n+2)]\, r^{n+1} \end{pmatrix} b_n + \begin{pmatrix} -(1+\ \upsilon)\, R^{-2(n-1)}\, r^{n-1} \\ +(1+\ \upsilon)(n-1)\, R^2 r^{-(n+1)} \\ -[(n+2)+\ \upsilon\,(n-2)]\, r^{-n+1} \end{pmatrix} d_n \right\} cos(n\theta) \right] \cos\theta$$

$$- \frac{1}{\mathrm{E}}\left[\sum_{n=2,4,\ldots}^{N} \left\{ \begin{pmatrix} -(1+\upsilon)(n+1)R^2 r^{n-1} \\ +[n(1+\upsilon)+4]\, r^{n+1} \\ +(1+\upsilon)R^{2(n+1)} r^{-(n+1)} \end{pmatrix} b_n + \begin{pmatrix} -(1+\upsilon)R^{-2(n-1)}\, r^{n-1} \\ -(1+\upsilon)(n-1)R^2 r^{-(n+1)} \\ +[n(1+\upsilon)-4]\, r^{-(n-1)} \end{pmatrix} d_n \right\} sin(n\theta) \right] \sin\theta$$

(2A.35)

$$u = \frac{1}{E}\left[\left\{\frac{2\,R^2}{r}(1+\upsilon) + 2(1-\upsilon)r\right\} \cos\theta\ c_0 - \sum_{n=2,4,\ldots}^{N} \left\{ \begin{pmatrix} -(1+\upsilon)(n+1)R^2\, r^{n-1} \\ -(1+\ \upsilon)R^{2(n+1)}\, r^{-(n+1)} \\ +[n(1+\upsilon)-2(1-\upsilon)]\, r^{n+1} \end{pmatrix} \cos\theta\ cos(n\theta) + \begin{pmatrix} -(1+\upsilon)(n+1)R^2 r^{n-1} \\ +(1+\upsilon)R^{2(n+1)} r^{-(n+1)} \\ +[n(1+\upsilon)+4]\, r^{n+1} \end{pmatrix} \sin\theta\ sin(n\theta) \right\} b_n + \left\{ \begin{pmatrix} -(1+\ \upsilon)\, R^{-2(n-1)}\, r^{n-1} \\ +(1+\ \upsilon)(n-1)\, R^2 r^{-(n+1)} \\ -[n(1+\upsilon)+\ 2\,(1-\upsilon)]\, r^{-n+1} \end{pmatrix} \cos\theta\ cos(n\theta) + \begin{pmatrix} -(1+\upsilon)R^{-2(n-1)}\, r^{n-1} \\ -(1+\upsilon)(n-1)R^2 r^{-(n+1)} \\ +[n(1+\upsilon)-4]\, r^{-(n-1)} \end{pmatrix} \sin\theta\ \ sin(n\theta) \right\} d_n \right]$$

$$u = \frac{1}{E}\left[\begin{array}{c} \left\{\frac{2\,R^2}{r}(1+v)+2(1-v)r\right\}\cos\theta\ c_0 \\ -\sum_{n=2,4,\ldots}^{N} \left\{\begin{array}{c} -(1+v)(n+1)R^2\,r^{n-1}\ \left(\cos\theta\ cos(n\theta)+\sin\theta\ sin(n\theta)\right) \\ -(1+\ v)R^{2(n+1)}\,r^{-(n+1)}\left(\cos\theta\ cos(n\theta)-\sin\theta\ sin(n\theta)\right) \\ +n(1+v)\,r^{n+1}\left(\cos\theta\ cos(n\theta)+\sin\theta\ sin(n\theta)\right) \\ +\left(-2(1-v)\cos\theta\ cos(n\theta)+4\sin\theta\ sin(n\theta)\right)r^{n+1} \end{array}\right\} b_n \\ +\left\{\begin{array}{c} -(1+\ v)\,R^{-2(n-1)}\,r^{n-1}\left(\cos\theta\ cos(n\theta)+\sin\theta\ sin(n\theta)\right) \\ +(1+\ v)(n-1)\,R^2 r^{-(n+1)}\left(\cos\theta\ cos(n\theta)-\sin\theta\ sin(n\theta)\right) \\ -n(1+v)\,r^{-n+1}\left(\cos\theta\ cos(n\theta)-\sin\theta\ sin(n\theta)\right) \\ -\left(2(1-v)\cos\theta\ cos(n\theta)+4\sin\theta\ sin(n\theta)\right)r^{-n+1} \end{array}\right\} d_n \end{array}\right]$$

$$u = \frac{1}{E}\left[\begin{array}{c} \left\{\frac{2\,R^2}{r}(1+v)+2(1-v)r\right\}\cos\theta\ c_0 \\ -\sum_{n=2,4,\ldots}^{N} \left\{\begin{array}{c} -(1+v)(n+1)R^2\,r^{n-1}\ \left(cos(n-1)\,\theta\right) \\ -(1+\ v)R^{2(n+1)}\,r^{-(n+1)}\left(cos(n+1)\,\theta\right) \\ +n(1+v)\,r^{n+1}\left(cos(n-1)\,\theta\right) \\ +\left(\left(-2\cos\theta\ cos(n\theta)+2v\cos\theta\ cos(n\theta)\right)+4\sin\theta\ sin(n\theta)\right)r^{n+1} \end{array}\right\} b_n \\ +\left\{\begin{array}{c} -(1+\ v)\,R^{-2(n-1)}\,r^{n-1}\left(cos(n-1)\,\theta\right) \\ +(1+\ v)(n-1)\,R^2 r^{-(n+1)}\left(cos(n+1)\,\theta\right) \\ -n(1+v)\,r^{-n+1}\left(cos(n+1)\,\theta\right) \\ -\left(\left(2\cos\theta\ cos(n\theta)-2v\cos\theta\ cos(n\theta)\right)+4\sin\theta\ sin(n\theta)\right)r^{-n+1} \end{array}\right\} d_n \end{array}\right]$$

$$u = \frac{1}{E}\left[\begin{array}{c} \left\{\frac{2\,R^2}{r}(1+v)+2(1-v)r\right\}\cos\theta\ c_0 \\ -\sum_{n=2,4,\ldots}^{N} \left\{\begin{array}{c} -(1+v)(n+1)R^2\,r^{n-1}\ \left(cos(n-1)\,\theta\right) \\ -(1+\ v)R^{2(n+1)}\,r^{-(n+1)}\left(cos(n+1)\,\theta\right) \\ +n(1+v)\,r^{n+1}\left(cos(n-1)\,\theta\right) \\ +\begin{pmatrix}-2\cos\theta\ cos(n\theta)+2\sin\theta\ sin(n\theta)\\ +2v\cos\theta\ cos(n\theta)+2\sin\theta\ sin(n\theta)\end{pmatrix}r^{n+1} \end{array}\right\} b_n \\ +\left\{\begin{array}{c} -(1+\ v)\,R^{-2(n-1)}\,r^{n-1}\left(cos(n-1)\,\theta\right) \\ +(1+\ v)(n-1)\,R^2 r^{-(n+1)}\left(cos(n+1)\,\theta\right) \\ -n(1+v)\,r^{-n+1}\left(cos(n+1)\,\theta\right) \\ -\begin{pmatrix}2\cos\theta\ cos(n\theta)+2\sin\theta\ sin(n\theta)\\ -2v\cos\theta\ cos(n\theta)+2\sin\theta\ sin(n\theta)\end{pmatrix}r^{-n+1} \end{array}\right\} d_n \end{array}\right]$$

$$u = \frac{1}{E}\left[\begin{array}{c} \left\{\frac{2\,R^2}{r}(1+v) + 2(1-v)r\right\} \cos\theta \;\; c_0 \\ -\sum_{n=2,4,\ldots}^{N} \left\{ \begin{array}{c} -(1+v)(n+1)R^2\, r^{n-1} \;\; (\,cos(n-1)\,\theta) \\ -(1+\;v)R^{2(n+1)}\, r^{-(n+1)}\,(\,cos(n+1)\,\theta) \\ +n(1+v)\, r^{n+1}(\,cos(n-1)\,\theta) \\ +\begin{pmatrix} -2(\cos\theta\;\; cos(n\theta) - \sin\theta\;\; sin(n\theta)) \\ +2v\cos\theta\;\; cos(n\theta) + 2\sin\theta\;\; sin(n\theta) \end{pmatrix} r^{n+1} \end{array} \right\} b_n \\ +\left\{ \begin{array}{c} -(1+\;v)\, R^{-2(n-1)}\, r^{n-1}(\,cos(n-1)\,\theta) \\ +(1+\;v)(n-1)\, R^2 r^{-(n+1)}(\,cos(n+1)\,\theta) \\ -n(1+v)\, r^{-n+1}(\,cos(n+1)\,\theta) \\ -\begin{pmatrix} 2(\cos\theta\;\; cos(n\theta) + \sin\theta\;\; sin(n\theta)) \\ -2v\cos\theta\;\; cos(n\theta) + 2\sin\theta\;\; sin(n\theta) \end{pmatrix} r^{-n+1} \end{array} \right\} d_n \end{array} \right]$$

$$u = \frac{1}{E}\left[\begin{array}{c} \left\{\frac{2\,R^2}{r}(1+v) + 2(1-v)r\right\} \cos\theta \;\; c_0 \\ -\sum_{n=2,4,\ldots}^{N} \left\{ \begin{array}{c} -(1+v)(n+1)R^2\, r^{n-1} \;\; (\,cos(n-1)\,\theta) \\ -(1+\;v)R^{2(n+1)}\, r^{-(n+1)}\,(\,cos(n+1)\,\theta) \\ +n(1+v)\, r^{n+1}(\,cos(n-1)\,\theta) \\ +\begin{pmatrix} -2(\,cos(n+1)\,\theta) \\ +2v\cos\theta\;\; cos(n\theta) + 2\sin\theta\;\; sin(n\theta) \end{pmatrix} r^{n+1} \end{array} \right\} b_n \\ +\left\{ \begin{array}{c} -(1+\;v)\, R^{-2(n-1)}\, r^{n-1}(\,cos(n-1)\,\theta) \\ +(1+\;v)(n-1)\, R^2 r^{-(n+1)}(\,cos(n+1)\,\theta) \\ -n(1+v)\, r^{-n+1}(\,cos(n+1)\,\theta) \\ -\begin{pmatrix} 2(\,cos(n-1)\,\theta) \\ -2v\cos\theta\;\; cos(n\theta) + 2\sin\theta\;\; sin(n\theta) \end{pmatrix} r^{-n+1} \end{array} \right\} d_n \end{array} \right]$$

$$u = \frac{1}{E}\left[-\sum_{n=2,4,\ldots}^{N} \begin{Bmatrix} \left\{\frac{2R^2}{r}(1+v) + 2(1-v)r\right\}\cos\theta \;\; c_0 \\ \begin{Bmatrix} -(1+v)(n+1)R^2\, r^{n-1} \;\; (\,cos(n-1)\,\theta) \\ -(1+\,v)R^{2(n+1)}\, r^{-(n+1)}\,(\,cos(n+1)\,\theta) \end{Bmatrix} \\ +\begin{pmatrix} n(1+v)\,(\,cos(n-1)\,\theta) - 2(\,cos(n+1)\,\theta) \\ +2v\cos\theta\;\; cos(n\theta) + 2\sin\theta\;\; sin(n\theta) \end{pmatrix} r^{n+1} \end{Bmatrix} b_n + \begin{Bmatrix} -(1+\,v)\,R^{-2(n-1)}\, r^{n-1}(\,cos(n-1)\,\theta) \\ +(1+\,v)(n-1)\,R^2 r^{-(n+1)}(\,cos(n+1)\,\theta) \\ -\begin{pmatrix} n(1+v)(\,cos(n+1)\,\theta) + 2(\,cos(n-1)\,\theta) \\ -2v\cos\theta\;\; cos(n\theta) + 2\sin\theta\;\; sin(n\theta) \end{pmatrix} r^{-n+1} \end{Bmatrix} d_n \right]$$

(2A.36)

Similarly, calculating *v* (again omitting any rigid body translation or rotation)

$$v = \frac{1}{E}\left[-\sum_{n=2,4,\ldots}^{N} \begin{Bmatrix} \left\{\frac{2R^2}{r}(1+v) + 2(1-v)r\right\} c_0 \\ \begin{pmatrix} -(1+v)(n+1)R^2\, r^{n-1} \\ -(1+\,v)R^{2(n+1)}\, r^{-(n+1)} \\ +[(n-2)+\,v\,(n+2)]\, r^{n+1} \end{pmatrix} b_n \\ +\begin{pmatrix} -(1+\,v\,)\,R^{-2(n-1)}\, r^{n-1} \\ +(1+\,v)(n-1)\,R^2 r^{-(n+1)} \\ -[(n+2)+\,v(n-2)]\, r^{-n+1} \end{pmatrix} d_n \end{Bmatrix} cos(n\theta) \right] \sin\theta$$

$$+\frac{1}{\mathrm{E}}\left[\sum_{n=2,4,\ldots}^{N} \begin{Bmatrix} \begin{pmatrix} -(1+v)(n+1)R^2 r^{n-1} \\ +[n(1+v)+4]\, r^{n+1} \end{pmatrix} b_n \\ +\begin{pmatrix} -(1+v)R^{-2(n-1)}\, r^{n-1} \\ -(1+v)(n-1)R^2 r^{-(n+1)} \\ +[n(1+v)-4]\, r^{-(n-1)} \end{pmatrix} d_n \end{Bmatrix} sin(n\theta) \right] \cos\theta$$

(2A.37)

$$v = \frac{1}{E}\left[\begin{array}{c} \left\{\frac{2\,R^2}{r}(1+v)+2(1-v)r\right\}\sin\theta\ c_0 \\ -\sum_{n=2,4,\ldots}^{N}\left\{\begin{array}{c}\left(\begin{array}{c}-(1+v)(n+1)R^2\,r^{n-1}\\-(1+\ v)R^{2(n+1)}\,r^{-(n+1)}\\+[n(1+v)-\ 2\,(1-v)]\,r^{n+1}\end{array}\right)\sin\theta\ cos(n\theta)\\ -\left(\begin{array}{c}-(1+v)(n+1)R^2 r^{n-1}\\+(1+v)R^{2(n+1)}r^{-(n+1)}\\+\,[n(1+v)+4]\,r^{n+1}\end{array}\right)\cos\theta\ sin(n\theta)\end{array}\right\}b_n \\ +\left\{\begin{array}{c}\left(\begin{array}{c}-(1+\ v)\,R^{-2(n-1)}\,r^{n-1}\\+(1+\ v)(n-1)\,R^2 r^{-(n+1)}\\-[n(1+v)+\ 2\,(1-v)]\,r^{-n+1}\end{array}\right)\sin\theta\ cos(n\theta)\\ -\left(\begin{array}{c}-\,(1+v)R^{-2(n-1)}\,r^{n-1}\\-(1+v)(n-1)R^2 r^{-(n+1)}\\+\,[n(1+v)-4]\,r^{-(n-1)}\end{array}\right)\cos\theta\ \ sin(n\theta)\end{array}\right\}d_n \end{array}\right]$$

$$v = \frac{1}{E}\left[\begin{array}{c} \left\{\frac{2\,R^2}{r}(1+v)+2(1-v)r\right\}sin\,\theta\ c_0 \\ -\sum_{n=2,4,\ldots}^{N}\left\{\begin{array}{c}(1+v)(n+1)R^2\,r^{n-1}\ \left(-\sin\theta\ cos(n\theta)+cos\,\theta\ sin(n\theta)\right)\\-(1+\ v)R^{2(n+1)}\,r^{-(n+1)}\left(\sin\theta\ cos(n\theta)+cos\,\theta\ sin(n\theta)\right)\\-n(1+v)\,r^{n+1}\left(-sin\,\theta\ cos(n\theta)+cos\,\theta\ sin(n\theta)\right)\\-\left(2(1-v)\,sin\,\theta\ cos(n\theta)+4\,cos\,\theta\ sin(n\theta)\right)r^{n+1}\end{array}\right\}b_n \\ +\left\{\begin{array}{c}(1+\ v)\,R^{-2(n-1)}\,r^{n-1}\left(-\sin\theta\ cos(n\theta)+cos\,\theta\ sin(n\theta)\right)\\+(1+\ v)(n-1)\,R^2 r^{-(n+1)}\left(sin\,\theta\ cos(n\theta)+cos\,\theta\ sin(n\theta)\right)\\-n(1+v)\,r^{-n+1}\left(sin\,\theta\ cos(n\theta)+cos\,\theta\ sin(n\theta)\right)\\-\left(2(1-v)\,sin\,\theta\ cos(n\theta)-4\,cos\,\theta\ sin(n\theta)\right)r^{-n+1}\end{array}\right\}d_n \end{array}\right]$$

$$v = \frac{1}{E}\left[\begin{array}{c} \left\{\frac{2\,R^2}{r}(1+v)+2(1-v)r\right\}sin\,\theta\ c_0 \\ -\sum_{n=2,4,\ldots}^{N}\left\{\begin{array}{c}(1+v)(n+1)R^2\,r^{n-1}\ \left(sin(n-1)\theta\right)\\-(1+\ v)R^{2(n+1)}\,r^{-(n+1)}\left(sin(n+1)\theta\right)\\-n(1+v)\,r^{n+1}\left(sin(n-1)\theta\right)\\-\left(2\,sin\,\theta\ cos(n\theta)-2v\,sin\,\theta\ cos(n\theta)+4\,cos\,\theta\ sin(n\theta)\right)r^{n+1}\end{array}\right\}b_n \\ +\left\{\begin{array}{c}(1+\ v)\,R^{-2(n-1)}\,r^{n-1}\left(sin(n-1)\theta\right)\\+(1+\ v)(n-1)\,R^2 r^{-(n+1)}\left(sin(n+1)\theta\right)\\-n(1+v)\,r^{-n+1}\left(sin(n+1)\theta\right)\\-\left(2\,sin\,\theta\ cos(n\theta)-2v\,sin\,\theta\ cos(n\theta)-4\,cos\,\theta\ sin(n\theta)\right)r^{-n+1}\end{array}\right\}d_n \end{array}\right]$$

$$v = \frac{1}{E}\left[\begin{array}{c} \left\{\frac{2\,R^2}{r}(1+v)+2(1-v)r\right\}\sin\theta\ \ c_0 \\ -\sum_{n=2,4,\ldots}^{N}\left\{\begin{array}{c}(1+v)(n+1)R^2\,r^{n-1}\ \big(\sin(n-1)\theta\big)\\ -(1+\ v)R^{2(n+1)}\,r^{-(n+1)}\ \big(\sin(n+1)\theta\big)\\ -n(1+v)\,r^{n+1}\big(\sin(n-1)\theta\big)\\ -\begin{pmatrix}2\sin\theta\ \cos(n\theta)+2\cos\theta\ \sin(n\theta)\\ -2v\sin\theta\ \cos(n\theta)+2\cos\theta\ \sin(n\theta)\end{pmatrix}r^{n+1}\end{array}\right\}b_n \\ +\left\{\begin{array}{c}(1+\ v)\,R^{-2(n-1)}\,r^{n-1}\big(\sin(n-1)\theta\big)\\ +(1+\ v)(n-1)\,R^2r^{-(n+1)}\big(\sin(n+1)\theta\big)\\ -n(1+v)\,r^{-n+1}\big(\sin(n+1)\theta\big)\\ +\begin{pmatrix}-2\sin\theta\ \cos(n\theta)+2\cos\theta\ \sin(n\theta)\\ +2v\sin\theta\ \cos(n\theta)+2\cos\theta\ \sin(n\theta)\end{pmatrix}r^{-n+1}\end{array}\right\}d_n \end{array}\right]$$

$$v = \frac{1}{E}\left[\begin{array}{c} \left\{\frac{2\,R^2}{r}(1+v)+2(1-v)r\right\}\sin\theta\ \ c_0 \\ -\sum_{n=2,4,\ldots}^{N}\left\{\begin{array}{c}(1+v)(n+1)R^2\,r^{n-1}\ \big(\sin(n-1)\theta\big)\\ -(1+\ v)R^{2(n+1)}\,r^{-(n+1)}\ \big(\sin(n+1)\theta\big)\\ -n(1+v)\,r^{n+1}\big(\sin(n-1)\theta\big)\\ -\begin{pmatrix}2\big(\sin(n+1)\theta\big)\\ -2v\sin\theta\ \cos(n\theta)+2\cos\theta\ \sin(n\theta)\end{pmatrix}r^{n+1}\end{array}\right\}b_n \\ +\left\{\begin{array}{c}(1+\ v)\,R^{-2(n-1)}\,r^{n-1}\big(\sin(n-1)\theta\big)\\ +(1+\ v)(n-1)\,R^2r^{-(n+1)}\big(\sin(n+1)\theta\big)\\ -n(1+v)\,r^{-n+1}\big(\sin(n+1)\theta\big)\\ +\begin{pmatrix}2\big(\sin(n-1)\theta\big)\\ +2v\sin\theta\ \cos(n\theta)+2\cos\theta\ \sin(n\theta)\end{pmatrix}r^{-n+1}\end{array}\right\}d_n \end{array}\right]$$

$$v = \frac{1}{E}\left[\begin{array}{c} \left\{\frac{2R^2}{r}(1+\upsilon) + 2(1-\upsilon)r\right\} \sin\theta \;\; c_0 \\ -\sum_{n=2,4,\ldots}^{N} \left\{ \begin{array}{c} (1+\upsilon)(n+1)R^2\, r^{n-1} \left(sin(n-1)\theta \right) \\ -(1+\upsilon)R^{2(n+1)}\, r^{-(n+1)} \left(sin(n+1)\theta \right) \\ -\left(\begin{array}{c} n(1+\upsilon)\left(sin(n-1)\theta \right) + 2\left(sin(n+1)\theta \right) \\ -2\upsilon \sin\theta \;\; cos(n\theta) + 2\cos\theta \;\; sin(n\theta) \end{array} \right) r^{n+1} \end{array} \right\} b_n \\ + \left\{ \begin{array}{c} (1+\upsilon)\, R^{-2(n-1)}\, r^{n-1}\left(sin(n-1)\theta \right) \\ +(1+\upsilon)(n-1)\, R^2 r^{-(n+1)}\left(sin(n+1)\theta \right) \\ +\left(\begin{array}{c} -n(1+\upsilon)\left(sin(n+1)\theta \right) + 2\left(sin(n-1)\theta \right) \\ +2\upsilon \sin\theta \;\; cos(n\theta) + 2\cos\theta \;\; sin(n\theta) \end{array} \right) r^{-n+1} \end{array} \right\} d_n \end{array} \right] \quad \text{(2A.38)}$$

Equations 2A.36 and 2A.38 illustrate that the rectangular components of displacement, *u* and *v,* at any polar location r and θ are both functions of Airy coefficients c_o, b_n and d_n. Of course one could work in rectangular coordinates from x = r cosθ and y = r sinθ. Note that the contributions of S_1, S_2, and R* of *equations 2A.32 and 2A.33* are omitted from *equations 2A.35 and 2A.36.* With the origin of the coordinate system at the center of the hole, these rigid body translations and rotation will disappear when physically loading in a testing machine [7, p.472].

Equations 2A.7 through 2A.20 are valid for any externally-shape member which has mechanical and geometric symmetry about the x- and y-axes and whose coordinate origin is not in the component. *Equations 2A.25 through 2A.27* (stresses), *equations 2A.27a and 2A.29* (strains), *equations 2A.28, 2A.31 through 2A.33, 2A.36 and 2A.38* (displacements) are further restricted to a traction-free round hole of radius R.

It should be noted that while *equations 2A.34* are used here relative to the displacements in the vicinity of a hole, they enjoy generally applicability. However, *equations 2A.36 and 2A.38* are only applicable for circular holes having mechanical and geometric symmetry about both x-

and y-axes. Provided one satisfies traction-free conditions *analytically* on the boundary of cut-out as done here, this general concept can be extended to multiple holes or arbitrary shape cut-outs.

The present concept of necessitating only one measured displacement field and satisfying the traction-free conditions on the edge of circular holes but for more general loading conditions appears feasible as long as one maintains geometric and mechanical symmetry about x- and y-axes. However the algebra involved in imposing the traction-free conditions becomes more involved for situations where the plate is unsymmetrical about one or both axes, e.g., case of Chapter 4 of Reference [4]. Also, although it might not be simple to impose traction-free conditions *analytically* on the edge of a non-circular hole, one could continue to use *equations 2A.11, 2A.20 and 2A.34* to evaluate the relevant Airy coefficients from measured either *u*- or *v*-displacements in addition to *discretely* imposing traction-free boundary conditions on the edge of the hole. Both *u* and *v* would again contain all of the Airy coefficients.

A3.1 Additional Results for Number of Coefficients, *k = 13*.

Figures A3.1 through A3.26 are plotted for the same specimen, loading condition and number of measured input strains as those in the chapter 3. The only change in results in this Appendix from those of chapter 3 is the number of coefficients used, $k = 13$ (i.e., c_0, b_n and d_n, for n = 12) while the previous results are for $k = 5$. The strain gage results are again compared with those from finite element analysis (ANSYS) and discrete strain gages. As before, the radial strain, ε_{rr}, tangential strain, $\varepsilon_{\theta\theta}$, longitudinal strain, ε_{yy}, and lateral strain, ε_{xx}, are normalized with respect to the far field strain, ε_0, and are plotted here for $k = 13$ at various radii on and away from the boundary of the hole, and along the line AB of *figure 3.1* in *figures A3.1 through A3.14*. Tangential stress, $\sigma_{\theta\theta}$, radial stress, σ_{rr}, shear stress, $\sigma_{r\theta}$, longitudinal stress, σ_{yy}, and lateral stress, σ_{xx}, are normalized with respect to the far field stress, σ_0, and are plotted at various radii around and away from the boundary of the hole and along the line AB of *figure 3.1* in *figures A3.15 through A3.26*. It is worth noting that the results agree very well with the finite element analysis.

As before, angle θ of *figures A3.1 through A3.9, A3.11 through A3.13, A3.15 through A3.17, A3.19 through A3.21, and A3.23 through A3.25,* is measured counter-clockwise from the positive x-axis and r is measured here from the center of the hole of *figure 3.1*. The actual in-plane dimensions associated with *figures A3.10, A3.14, A3.18, A3.22, and A3.26* are plotted normalized with respect to the radius, R = 10.08 mm = 0.395″ of the hole.

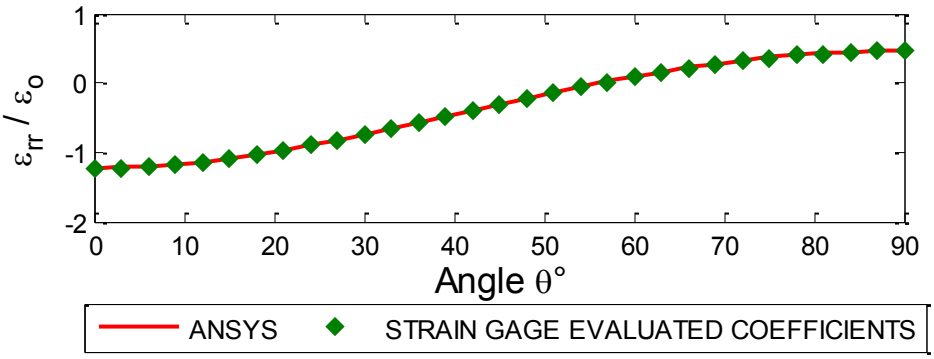

Fig. A3.1: Plot of $\varepsilon_{rr}/\varepsilon_0$ along boundary of the hole from strain-gage evaluated Airy coefficients for $k = 13$ coefficients ($m = 45$ strain-gage input values) and ANSYS

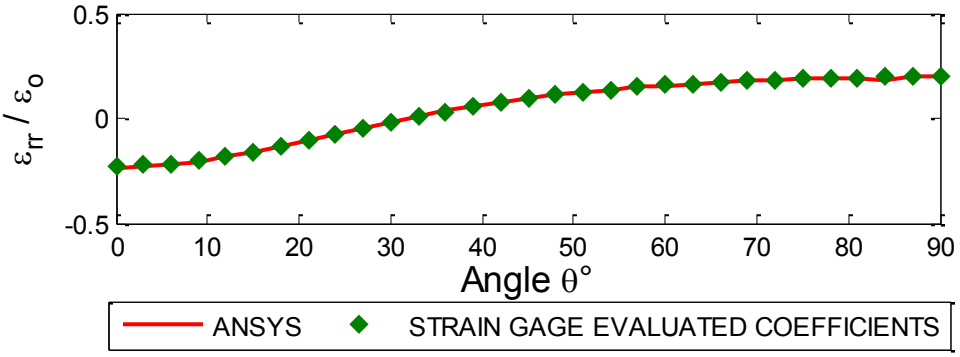

Fig. A3.2: Plot of $\varepsilon_{rr}/\varepsilon_0$ along r/R = 1.5 from strain-gage evaluated Airy coefficients for $k = 13$ coefficients ($m = 45$ strain-gage input values) and ANSYS

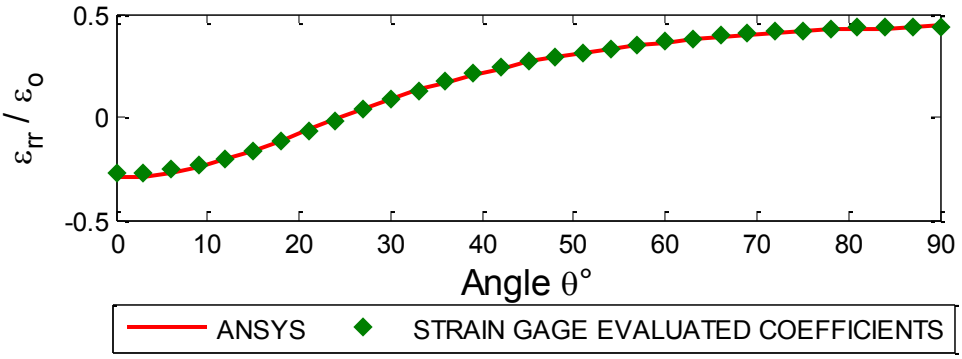

Fig. A3.3: Plot of $\varepsilon_{rr}/\varepsilon_0$ along r/R = 2 from strain-gage evaluated Airy coefficients for $k = 13$ coefficients ($m = 45$ strain-gage input values) and ANSYS

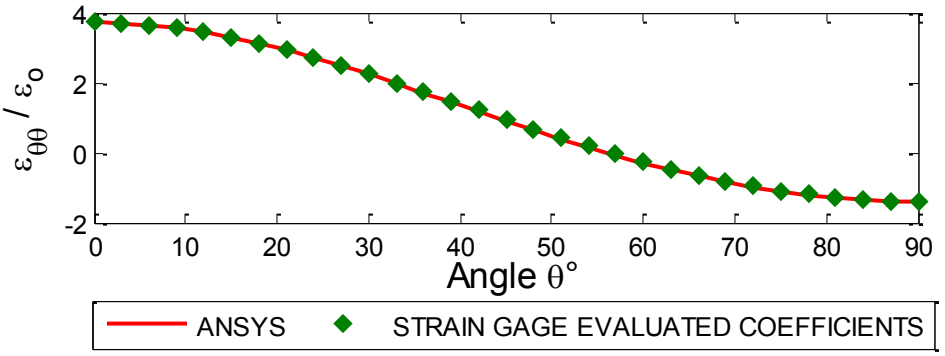

Fig. A3.4: Plot of $\varepsilon_{\theta\theta}/\varepsilon_0$ along boundary of the hole from strain-gage evaluated Airy coefficients for $k = 13$ coefficients ($m = 45$ strain-gage input values) and ANSYS

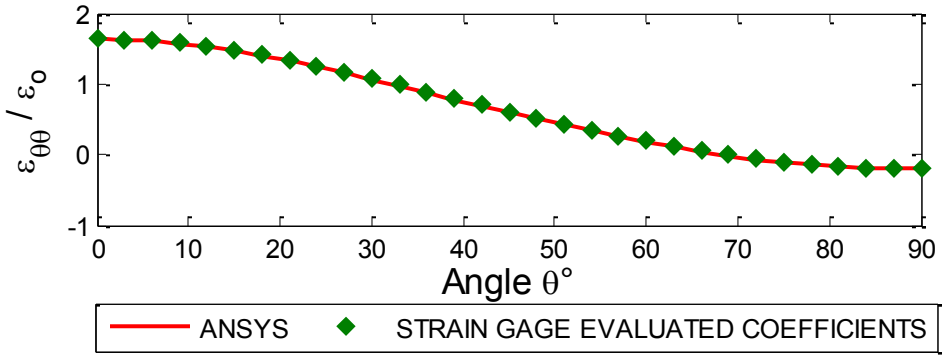

Fig. A3.5: Plot of $\varepsilon_{\theta\theta}/\varepsilon_0$ along r/R = 1.5 from strain-gage evaluated Airy coefficients for $k = 13$ coefficients ($m = 45$ strain-gage input values) and ANSYS

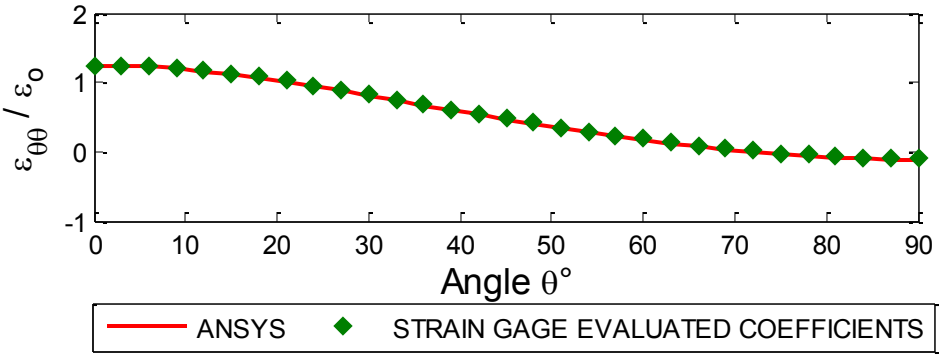

Fig. A3.6: Plot of $\varepsilon_{\theta\theta}/\varepsilon_0$ along r/R = 2 from strain-gage evaluated Airy coefficients for $k = 13$ coefficients ($m = 45$ strain-gage input values) and ANSYS

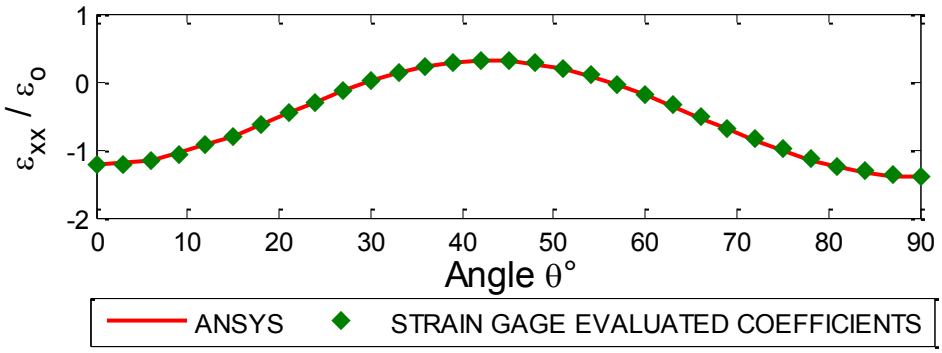

Fig. A3.7: Plot of $\varepsilon_{xx}/\varepsilon_0$ along boundary of the hole from strain-gage evaluated Airy coefficients for $k = 13$ coefficients ($m = 45$ strain-gage input values) and ANSYS

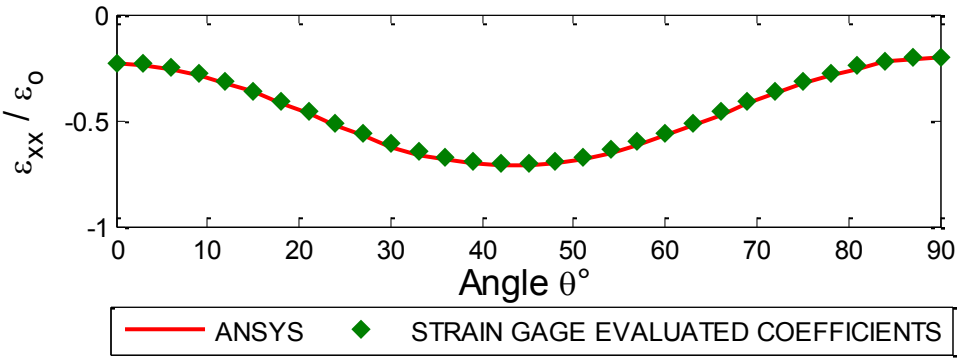

Fig. A3.8: Plot of $\varepsilon_{xx}/\varepsilon_0$ along r/R = 1.5 from strain-gage evaluated Airy coefficients for $k = 13$ coefficients ($m = 45$ strain-gage input values) and ANSYS

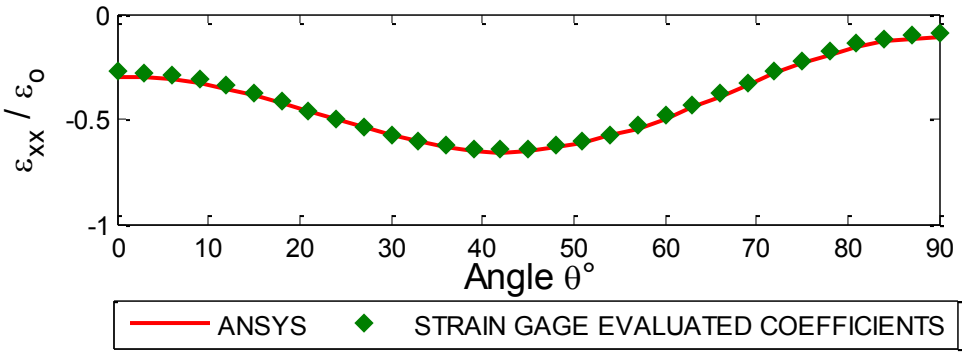

Fig. A3.9: Plot of $\varepsilon_{xx}/\varepsilon_0$ along r/R = 2 from strain-gage evaluated Airy coefficients for $k = 13$ coefficients ($m = 45$ strain-gage input values) and ANSYS

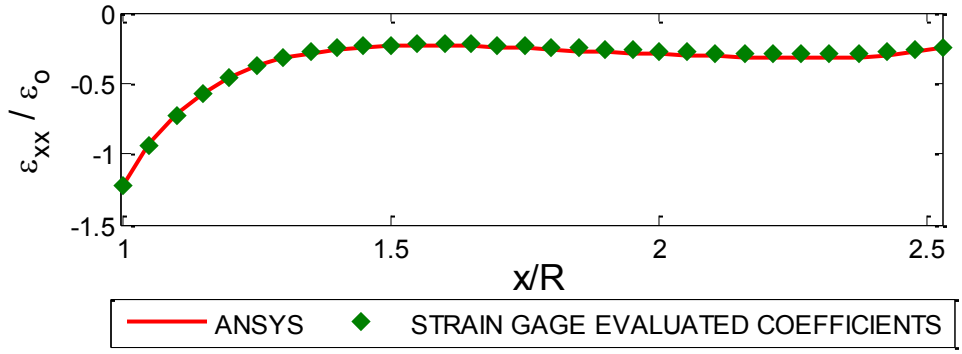

Fig. A3.10: Plot of $\varepsilon_{xx}/\varepsilon_0$ along AB of *figure 3.1* from strain-gage evaluated Airy coefficients for $k = 13$ coefficients ($m = 45$ strain-gage input values) and ANSYS

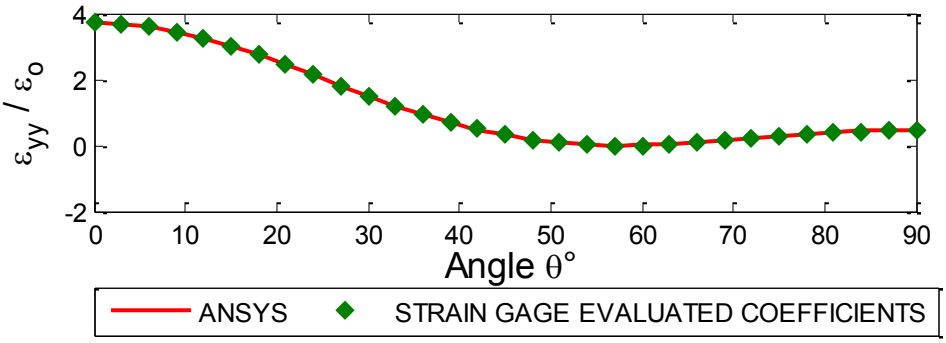

Fig. A3.11: Plot of $\varepsilon_{yy}/\varepsilon_0$ along boundary of the hole from strain-gage evaluated Airy coefficients for $k = 13$ coefficients ($m = 45$ strain-gage input values) and ANSYS

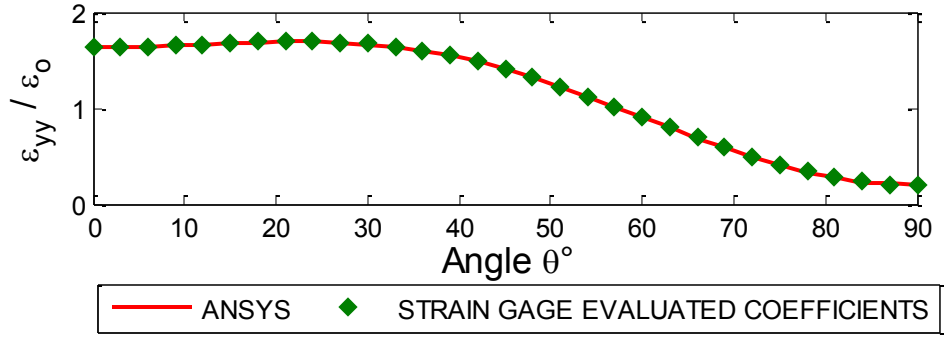

Fig. A3.12: Plot of $\varepsilon_{yy}/\varepsilon_0$ along r/R = 1.5 from strain-gage evaluated Airy coefficients for $k = 13$ coefficients ($m = 45$ strain-gage input values) and ANSYS

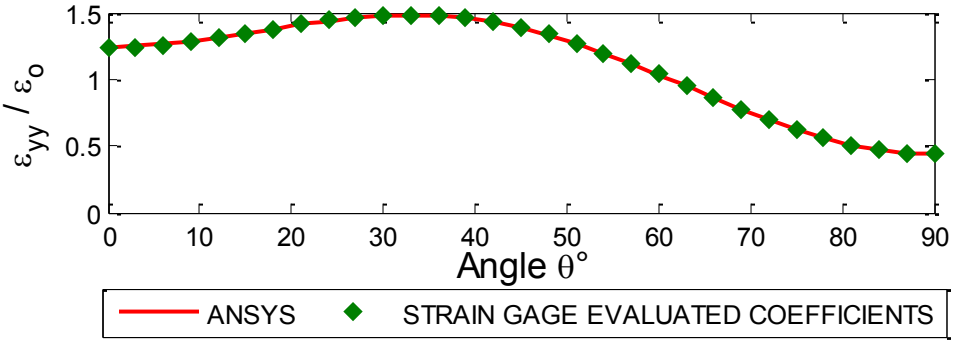

Fig. A3.13: Plot of $\varepsilon_{yy}/\varepsilon_0$ along r/R = 2 from strain-gage evaluated Airy coefficients for *k = 13* coefficients (*m = 45* strain-gage input values) and ANSYS

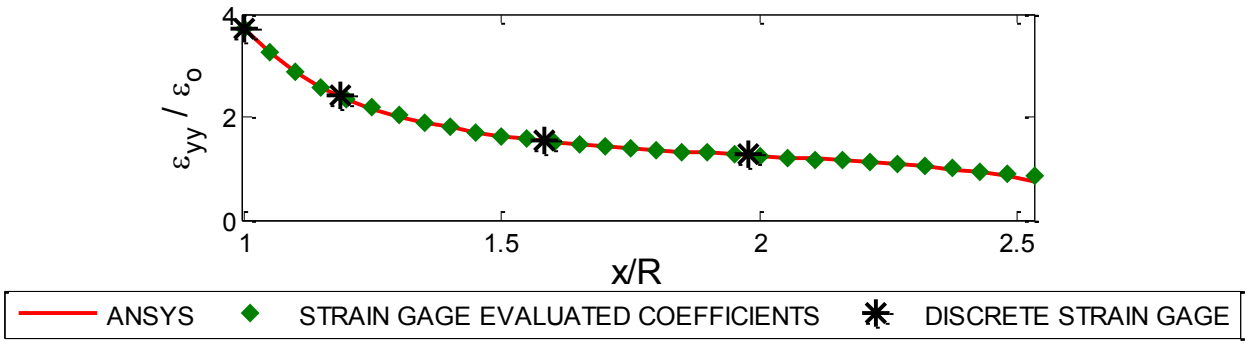

Fig. A3.14: Plot of $\varepsilon_{yy}/\varepsilon_0$ along AB of *figure 3.1* from strain-gage (experimental result and reconstructed using the known Airy coefficients) for *k = 13* coefficients (*m = 45* strain-gage input values) and ANSYS

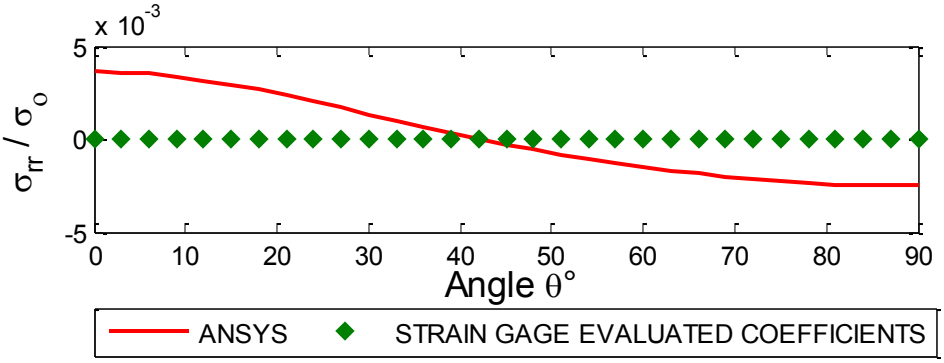

Fig. A3.15: Plot of σ_{rr}/σ_0 along boundary of the hole from strain-gage evaluated Airy coefficients for *k = 13* coefficients (*m = 45* strain-gage input values) and ANSYS

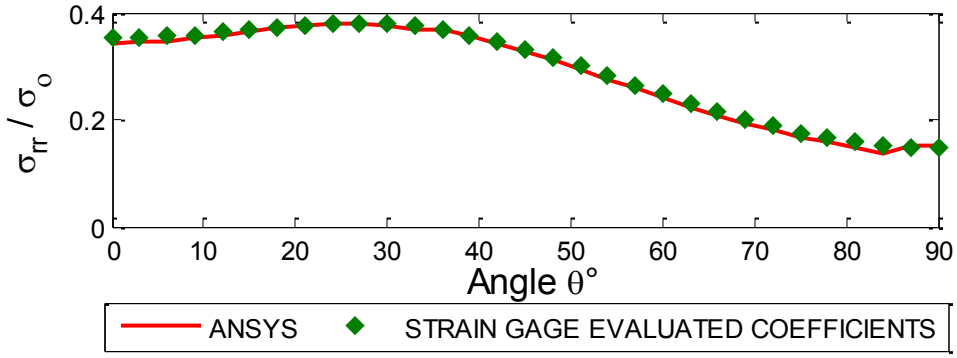

Fig. A3.16: Plot of σ_{rr}/σ_0 along r/R = 1.5 from strain-gage evaluated Airy coefficients for *k = 13* coefficients (*m = 45* strain-gage input values) and ANSYS

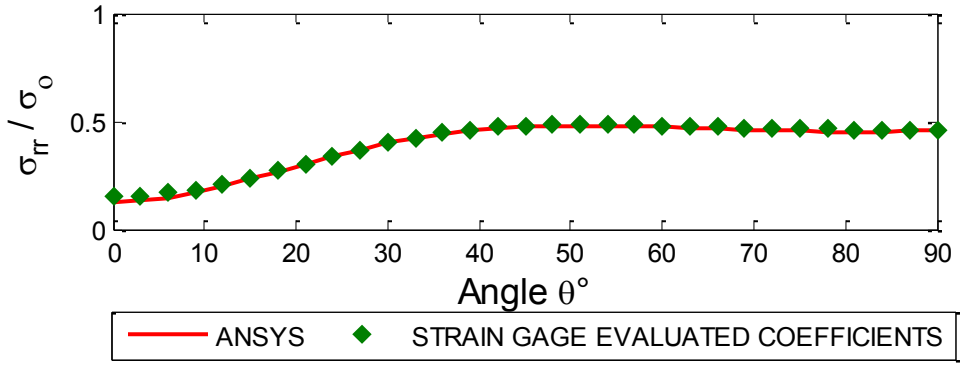

Fig. A3.17: Plot of σ_{rr}/σ_0 along r/R = 2 from strain-gage evaluated Airy coefficients for *k = 13* coefficients (*m = 45* strain-gage input values) and ANSYS

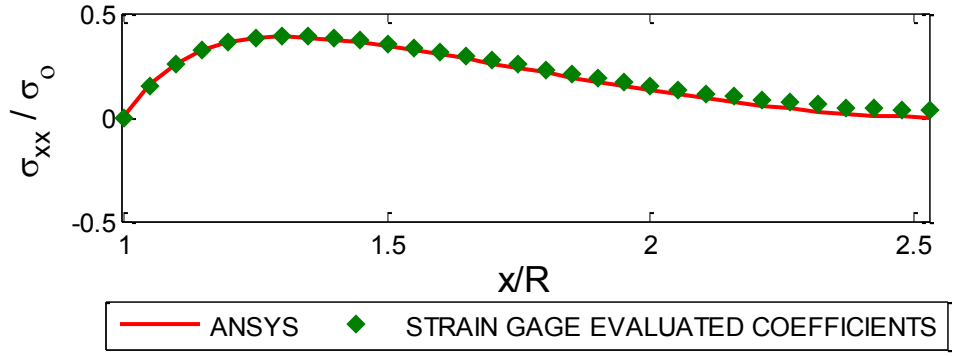

Fig. A3.18: Plot of σ_{xx}/σ_0 (= σ_{rr}/σ_0) along AB of *figure 3.1* from strain-gage evaluated Airy coefficients for *k = 13* coefficients (*m = 45* strain-gage input values) and ANSYS

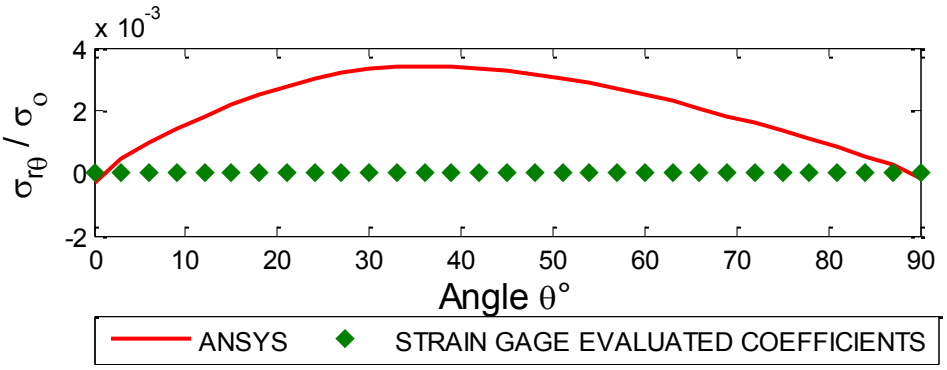

Fig. A3.19: Plot of $\sigma_{r\theta}/\sigma_0$ along boundary of the hole from strain-gage evaluated Airy coefficients for $k = 13$ coefficients ($m = 45$ strain-gage input values) and ANSYS

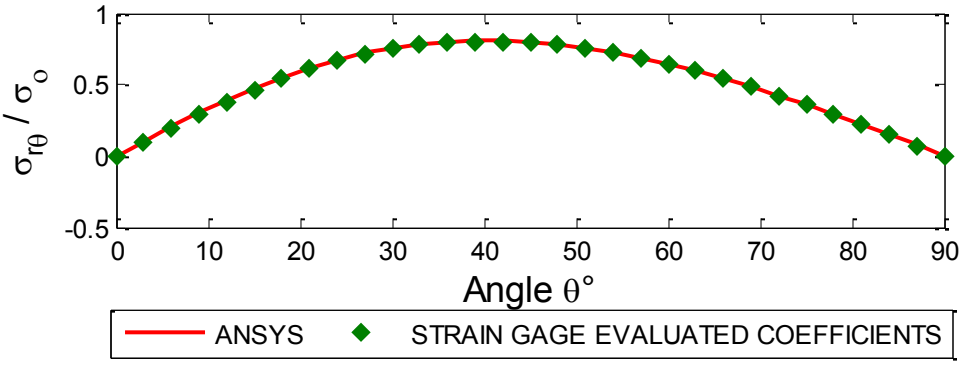

Fig. A3.20: Plot of $\sigma_{r\theta}/\sigma_0$ along r/R = 1.5 from strain-gage evaluated Airy coefficients for $k = 13$ coefficients ($m = 45$ strain-gage input values) and ANSYS

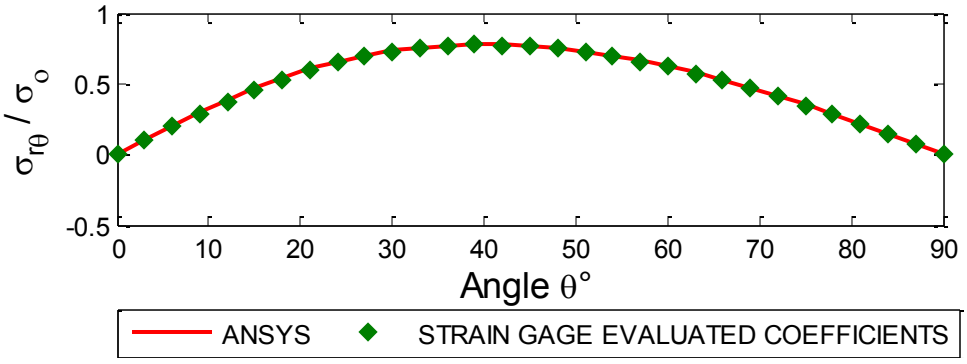

Fig. A3.21: Plot of $\sigma_{r\theta}/\sigma_0$ along r/R = 2 from strain-gage evaluated Airy coefficients for $k = 13$ coefficients ($m = 45$ strain-gage input values) and ANSYS

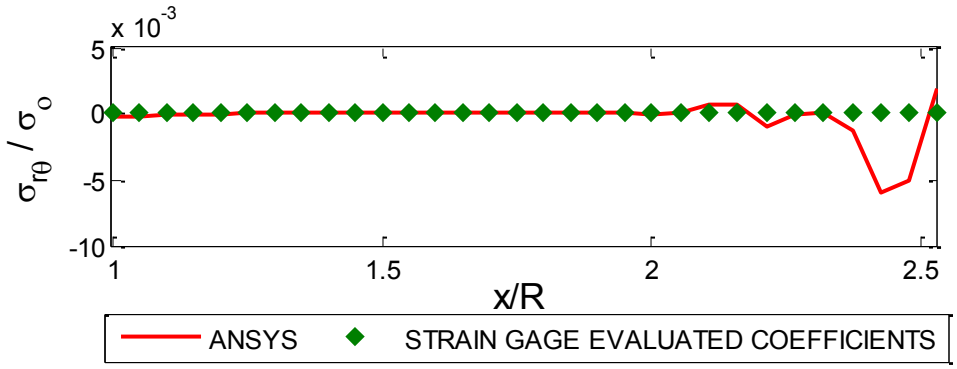

Fig. A3.22: Plot of $\sigma_{r\theta}/\sigma_0$ along AB of *figure 3.1* from strain-gage evaluated Airy coefficients for $k = 13$ coefficients ($m = 45$ strain-gage input values) and ANSYS

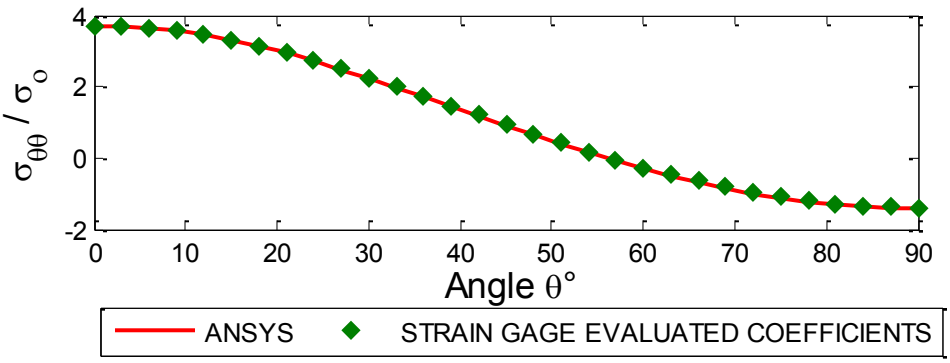

Fig. A3.23: Plot of $\sigma_{\theta\theta}/\sigma_0$ along boundary of the hole from strain-gage evaluated Airy coefficients for $k = 13$ coefficients ($m = 45$ strain-gage input values) and ANSYS

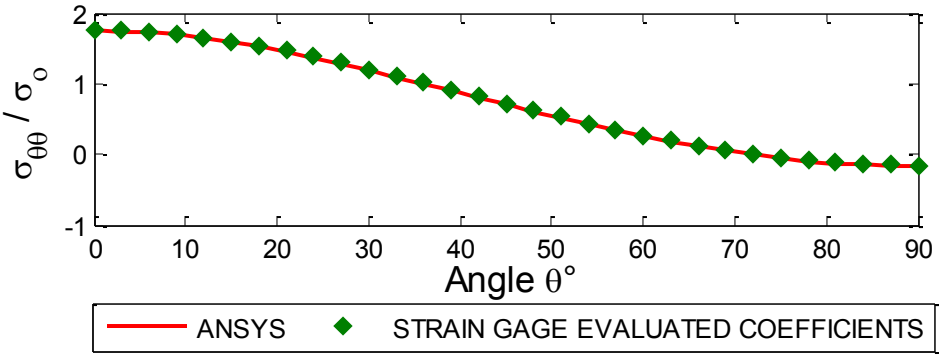

Fig. A3.24: Plot of $\sigma_{\theta\theta}/\sigma_0$ along r/R = 1.5 from strain-gage evaluated Airy coefficients for $k = 13$ coefficients ($m = 45$ strain-gage input values) and ANSYS

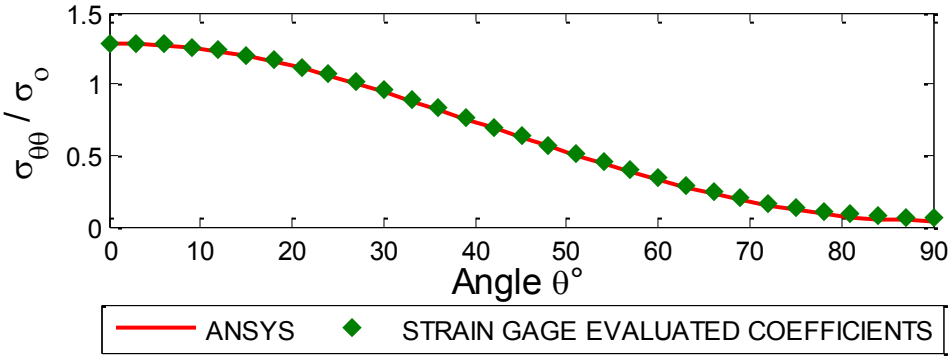

Fig. A3.25: Plot of $\sigma_{\theta\theta}/\sigma_0$ along r/R = 2 from strain-gage evaluated Airy coefficients for *k = 13* coefficients (*m = 45* strain-gage input values) and ANSYS

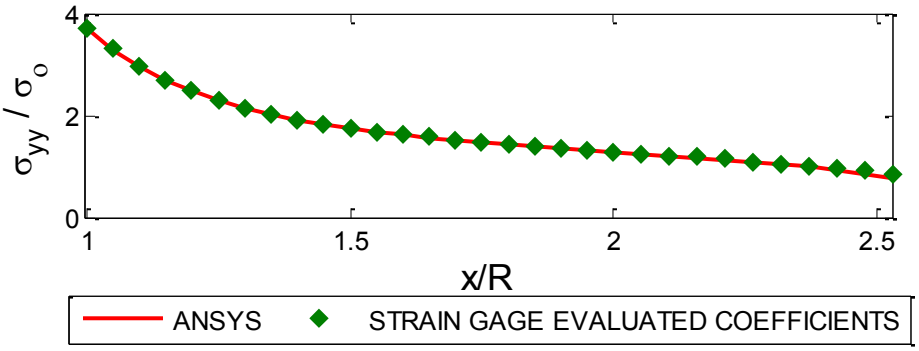

Fig. A3.26: Plot of σ_{yy}/σ_0 (= $\sigma_{\theta\theta}/\sigma_0$) along AB of *figure 3.1* from strain-gage evaluated Airy coefficients for *k = 13* coefficients (*m = 45* strain-gage input values) and ANSYS

A3.2 Determining the Cartesian Components of Stress and Strain.

For a perforated finite plate having symmetry with respect to both its x- and y-axes, its coordinate origin within the cavity, and imposing the traction-free condition on the boundary of the round hole of radius R, the individual stress components in polar coordinates, where c_0, b_n, and d_n are Airy coefficients, are given by (Appendix A2):

$$\sigma_{rr} = \left(\frac{-2\,R^2}{r^2} + 2\right) c_0 - \sum_{n=2,4,\ldots}^{\mathrm{N}} \left[\begin{Bmatrix} -(n-1)(n+1)R^2 r^{n-2} \\ +(n+1)R^{2(n+1)} r^{-(n+2)} \\ +(n+1)\,(n-2)\,r^n \end{Bmatrix} b_n + \begin{Bmatrix} -(n-1)R^{-2(n-1)}\,r^{n-2} \\ -(n-1)(n+1)R^2 r^{-(n+2)} \\ +(n-1)(n+2)r^{-n} \end{Bmatrix} d_n \right] cos(n\theta) \qquad (3A.1)$$

$$\sigma_{\theta\theta} = \left(\frac{2\,R^2}{r^2} + 2\right) c_0 + \sum_{n=2,4,\ldots}^{N} \left[\begin{Bmatrix} -(n+1)(n-1)R^2 r^{n-2} \\ +(n+1)R^{2(n+1)} r^{-(n+2)} \\ +(n+1)\,(n+2)\,r^n \end{Bmatrix} b_n + \begin{Bmatrix} -(n-1)R^{-2(n-1)} r^{n-2} \\ -(n-1)(n+1)R^2 r^{-(n+2)} \\ +(n-1)(n-2)r^{-n} \end{Bmatrix} d_n \right] cos(n\theta) \qquad (3A.2)$$

$$\sigma_{r\theta} = \sum_{n=2,4,\ldots}^{N} \left[\begin{Bmatrix} -(n+1)(n-1)R^2 r^{n-2} \\ -(n+1)R^{2(n+1)} r^{-(n+2)} \\ +n\,(n+1)r^n \end{Bmatrix} b_n \begin{Bmatrix} -(n-1)R^{-2(n-1)} r^{n-2} \\ +(n-1)(n+1)R^2 r^{-(n+2)} \\ -n\,(n-1)r^{-n} \end{Bmatrix} d_n \right] sin(n\theta) \qquad (3A.3)$$

Evaluating the Cartesian components of stress using the transformation matrix

$$\begin{bmatrix}\sigma_{xx}\\ \sigma_{yy}\\ \sigma_{xy}\end{bmatrix}=\begin{bmatrix}\cos^2\theta & \sin^2\theta & -2\sin\theta.\cos\theta\\ \sin^2\theta & \cos^2\theta & 2\sin\theta.\cos\theta\\ \sin\theta.\cos\theta & -\sin\theta.\cos\theta & \cos^2\theta-\sin^2\theta\end{bmatrix}\begin{bmatrix}\sigma_{rr}\\ \sigma_{\theta\theta}\\ \sigma_{r\theta}\end{bmatrix} \tag{3A.4}$$

The above matrix equation can be expanded as:

$$\sigma_{xx} = \sigma_{rr}\, cos^2\theta + \sigma_{\theta\theta}\, sin^2\theta - \sigma_{r\theta}\, 2\, sin\theta\, cos\theta \tag{3A.5}$$

$$\sigma_{yy} = \sigma_{rr}\, sin^2\theta + \sigma_{\theta\theta}\, cos^2\theta + \sigma_{r\theta}\, 2\, sin\theta\, cos\theta \tag{3A.6}$$

such that the angle θ is measured counter-clockwise from the horizontal x-axis to the polar direction r, *figure 3.1*. Therefore

$$\sigma_{xx} = \left[\begin{array}{l}
\left\{\left(\frac{-2\,R^2}{r^2}+2\right)c_0 - \sum_{n=2,4,\ldots}^{N}\left[\begin{array}{l}\left\{\begin{array}{c}-(n-1)(n+1)R^2r^{n-2}\\ +(n+1)R^{2(n+1)}r^{-(n+2)}\\ +(n+1)\,(n-2)\,r^n\end{array}\right\}b_n\\ +\left\{\begin{array}{c}-(n-1)R^{-2(n-1)}\,r^{n-2}\\ -(n-1)(n+1)R^2r^{-(n+2)}\\ +(n-1)(n+2)r^{-n}\end{array}\right\}d_n\end{array}\right]cos(n\theta)\right\}cos^2\theta\\
+\left\{\left(\frac{2\,R^2}{r^2}+2\right)c_0 + \sum_{n=2,4,\ldots}^{N}\left[\begin{array}{l}\left\{\begin{array}{c}-(n+1)(n-1)R^2r^{n-2}\\ +(n+1)R^{2(n+1)}r^{-(n+2)}\\ +(n+1)\,(n+2)\,r^n\end{array}\right\}b_n\\ +\left\{\begin{array}{c}-(n-1)R^{-2(n-1)}r^{n-2}\\ -(n-1)(n+1)R^2r^{-(n+2)}\\ +(n-1)(n-2)r^{-n}\end{array}\right\}d_n\end{array}\right]cos(n\theta)\right\}sin^2\theta\\
-\left\{\sum_{n=2,4,\ldots}^{N}\left[\begin{array}{l}\left\{\begin{array}{c}-(n+1)(n-1)R^2r^{n-2}\\ -(n+1)R^{2(n+1)}r^{-(n+2)}\\ +n\,(n+1)r^n\end{array}\right\}b_n\\ \left\{\begin{array}{c}-(n-1)R^{-2(n-1)}r^{n-2}\\ +(n-1)(n+1)R^2r^{-(n+2)}\\ -n\,(n-1)r^{-n}\end{array}\right\}d_n\end{array}\right]sin(n\theta)\right\}sin2\theta
\end{array}\right]$$

$$\sigma_{xx} = \left[\begin{array}{c} \left\{\left(\frac{-2\,R^2}{r^2} + 2\right) cos^2\theta + \left(\frac{2\,R^2}{r^2} + 2\right) sin^2\theta\right\} c_0 \\ + \sum_{n=2,4,\ldots}^{N} \left\{ \begin{array}{c} -\left[\begin{array}{c} \left\{ \begin{array}{c} -(n-1)(n+1)R^2 r^{n-2} \\ +(n+1)R^{2(n+1)} r^{-(n+2)} \\ +(n+1)\,(n-2)\,r^n \end{array} \right\} b_n \\ +\left\{ \begin{array}{c} -(n-1)R^{-2(n-1)}\, r^{n-2} \\ -(n-1)(n+1)R^2 r^{-(n+2)} \\ +(n-1)(n+2)r^{-n} \end{array} \right\} d_n \end{array} \right] cos(n\theta)cos^2\theta \\ +\left[\begin{array}{c} \left\{ \begin{array}{c} -(n+1)(n-1)R^2 r^{n-2} \\ +(n+1)R^{2(n+1)} r^{-(n+2)} \\ +(n+1)\,(n+2)\,r^n \end{array} \right\} b_n \\ +\left\{ \begin{array}{c} -(n-1)R^{-2(n-1)} r^{n-2} \\ -(n-1)(n+1)R^2 r^{-(n+2)} \\ +(n-1)(n-2)r^{-n} \end{array} \right\} d_n \end{array} \right] cos(n\theta)\, sin^2\theta \\ -\left[\begin{array}{c} \left\{ \begin{array}{c} -(n+1)(n-1)R^2 r^{n-2} \\ -(n+1)R^{2(n+1)} r^{-(n+2)} \\ +n\,(n+1)r^n \end{array} \right\} b_n \\ \left\{ \begin{array}{c} -(n-1)R^{-2(n-1)} r^{n-2} \\ +(n-1)(n+1)R^2 r^{-(n+2)} \\ -n\,(n-1)r^{-n} \end{array} \right\} d_n \end{array} \right] sin(n\theta)\, sin2\theta \end{array} \right\} \end{array} \right]$$

$$\sigma_{xx} = \left[\begin{array}{c} \left\{(-cos^2\theta + sin^2\theta)\frac{2\,R^2}{r^2} + (cos^2\theta + sin^2\theta)2\right\} c_0 \\ + \sum_{n=2,4,\ldots}^{N} \left\{ \begin{array}{l} -\left\{\begin{matrix} -(n-1)(n+1)R^2 r^{n-2} \\ +(n+1)R^{2(n+1)} r^{-(n+2)} \\ +(n+1)\,(n-2)\,r^n \end{matrix}\right\} b_n\ cos(n\theta)cos^2\theta \\ -\left\{\begin{matrix} -(n-1)R^{-2(n-1)}\, r^{n-2} \\ -(n-1)(n+1)R^2 r^{-(n+2)} \\ +(n-1)(n+2)r^{-n} \end{matrix}\right\} d_n\ cos(n\theta)cos^2\theta \\ +\left\{\begin{matrix} -(n+1)(n-1)R^2 r^{n-2} \\ +(n+1)R^{2(n+1)} r^{-(n+2)} \\ +(n+1)\,(n+2)\,r^n \end{matrix}\right\} b_n\, cos(n\theta)\, sin^2\theta \\ +\left\{\begin{matrix} -(n-1)R^{-2(n-1)} r^{n-2} \\ -(n-1)(n+1)R^2 r^{-(n+2)} \\ +(n-1)(n-2)r^{-n} \end{matrix}\right\} d_n\, cos(n\theta)\, sin^2\theta \\ -\left\{\begin{matrix} -(n+1)(n-1)R^2 r^{n-2} \\ -(n+1)R^{2(n+1)} r^{-(n+2)} \\ +n\,(n+1)r^n \end{matrix}\right\} b_n\ sin(n\theta)\, sin2\theta \\ -\left\{\begin{matrix} -(n-1)R^{-2(n-1)} r^{n-2} \\ +(n-1)(n+1)R^2 r^{-(n+2)} \\ -n\,(n-1)r^{-n} \end{matrix}\right\} d_n\ sin(n\theta)\, sin2\theta \end{array} \right\} \end{array} \right]$$

$$\sigma_{xx} = \left[\begin{array}{c} \left\{ -\cos 2\theta \frac{2\,R^2}{r^2} + 2 \right\} c_0 \\ + \sum_{n=2,4,\ldots}^{N} \left\{ \begin{array}{l} -\left\{ \begin{array}{c} -(n-1)(n+1)R^2 r^{n-2} \\ +(n+1)R^{2(n+1)} r^{-(n+2)} \\ +(n+1)\,(n-2)\,r^n \end{array} \right\} b_n \; cos(n\theta) cos^2\theta \\ +\left\{ \begin{array}{c} -(n+1)(n-1)R^2 r^{n-2} \\ +(n+1)R^{2(n+1)} r^{-(n+2)} \\ +(n+1)\,(n+2)\,r^n \end{array} \right\} b_n \cos(n\theta)\, sin^2\theta \\ -\left\{ \begin{array}{c} -(n+1)(n-1)R^2 r^{n-2} \\ -(n+1)R^{2(n+1)} r^{-(n+2)} \\ +n\,(n+1) r^n \end{array} \right\} b_n \; sin(n\theta)\, sin2\theta \\ -\left\{ \begin{array}{c} -(n-1)R^{-2(n-1)}\, r^{n-2} \\ -(n-1)(n+1)R^2 r^{-(n+2)} \\ +(n-1)(n+2) r^{-n} \end{array} \right\} d_n \; cos(n\theta) cos^2\theta \\ +\left\{ \begin{array}{c} -(n-1)R^{-2(n-1)} r^{n-2} \\ -(n-1)(n+1)R^2 r^{-(n+2)} \\ +(n-1)(n-2) r^{-n} \end{array} \right\} d_n \cos(n\theta)\, sin^2\theta \\ -\left\{ \begin{array}{c} -(n-1)R^{-2(n-1)} r^{n-2} \\ +(n-1)(n+1)R^2 r^{-(n+2)} \\ -n\,(n-1) r^{-n} \end{array} \right\} d_n \; sin(n\theta)\, sin2\theta \end{array} \right\} \end{array} \right]$$

$$\sigma_{xx} = \left[\begin{array}{c} \left\{ -\cos 2\theta \frac{2\,R^2}{r^2} + 2 \right\} c_0 \\ + \sum_{n=2,4,\ldots}^{N} \left\{ \begin{array}{c} \left\{ \begin{array}{c} (n-1)(n+1)R^2 r^{n-2} \begin{pmatrix} cos(n\theta)cos^2\theta \\ -cos(n\theta)\,sin^2\theta \\ +\ sin(n\theta)\,sin2\theta \end{pmatrix} \\ +(n+1)R^{2(n+1)} r^{-(n+2)} \begin{pmatrix} -\ cos(n\theta)cos^2\theta \\ +cos(n\theta)\,sin^2\theta \\ +\ sin(n\theta)\,sin2\theta \end{pmatrix} \end{array} \right\} b_n \\ +(n+1)r^n \begin{pmatrix} -(n-2)\ cos(n\theta)cos^2\theta \\ +(n+2)\,cos(n\theta)\,sin^2\theta \\ -n\,sin(n\theta)\,sin2\theta \end{pmatrix} \end{array} \right. \\ + \left\{ \begin{array}{c} \left\{ \begin{array}{c} (n-1)R^{-2(n-1)}\, r^{n-2} \begin{pmatrix} cos(n\theta)cos^2\theta \\ -cos(n\theta)\,sin^2\theta \\ +\ sin(n\theta)\,sin2\theta \end{pmatrix} \\ +(n-1)(n+1)R^2 r^{-(n+2)} \begin{pmatrix} cos(n\theta)cos^2\theta \\ -cos(n\theta)\,sin^2\theta \\ -\ sin(n\theta)\,sin2\theta \end{pmatrix} \end{array} \right\} d_n \\ +(n-1)r^{-n} \begin{pmatrix} -(n+2)\ cos(n\theta)cos^2\theta \\ +(n-2)\,cos(n\theta)\,sin^2\theta \\ +n\,sin(n\theta)\,sin2\theta \end{pmatrix} \end{array} \right. \end{array} \right]$$

$$\sigma_{xx} = \left[\begin{array}{c} \left\{ -\cos 2\theta \frac{2\,R^2}{r^2} + 2 \right\} c_0 \\ + \sum_{n=2,4,\ldots}^{N} \left\{ \begin{array}{c} \left\{ \begin{array}{c} (n-1)(n+1)R^2 r^{n-2} \begin{pmatrix} cos(n\theta)(cos^2\theta - sin^2\theta) \\ +\ sin(n\theta)\,sin2\theta \end{pmatrix} \\ +(n+1)R^{2(n+1)} r^{-(n+2)} \begin{pmatrix} cos(n\theta)(-cos^2\theta + sin^2\theta) \\ +\ sin(n\theta)\,sin2\theta \end{pmatrix} \end{array} \right\} b_n \\ +(n+1)r^n \begin{pmatrix} -(n-2)\ cos(n\theta)cos^2\theta \\ +(n+2)\,cos(n\theta)\,sin^2\theta \\ -n\,sin(n\theta)\,sin2\theta \end{pmatrix} \end{array} \right. \\ + \left\{ \begin{array}{c} \left\{ \begin{array}{c} (n-1)R^{-2(n-1)}\, r^{n-2} \begin{pmatrix} cos(n\theta)(cos^2\theta - sin^2\theta) \\ +\ sin(n\theta)\,sin2\theta \end{pmatrix} \\ +(n-1)(n+1)R^2 r^{-(n+2)} \begin{pmatrix} cos(n\theta)(cos^2\theta - sin^2\theta) \\ -\ sin(n\theta)\,sin2\theta \end{pmatrix} \end{array} \right\} d_n \\ +(n-1)r^{-n} \begin{pmatrix} -(n+2)\ cos(n\theta)cos^2\theta \\ +(n-2)\,cos(n\theta)\,sin^2\theta \\ +n\,sin(n\theta)\,sin2\theta \end{pmatrix} \end{array} \right. \end{array} \right]$$

$$\sigma_{xx} = \left[\begin{array}{c} \left\{ -\cos 2\theta \frac{2\,R^2}{r^2} + 2 \right\} c_0 \\ + \sum_{n=2,4,\ldots}^{N} \left\{ \begin{array}{c} \left\{ \begin{array}{c} (n-1)(n+1)R^2 r^{n-2}(cos(n\theta)(cos2\theta) + sin(n\theta)\,sin2\theta) \\ +(n+1)R^{2(n+1)} r^{-(n+2)}(cos(n\theta)(-cos2\theta) + sin(n\theta)\,sin2\theta) \\ +(n+1)r^n \begin{pmatrix} -(n-2)\ cos(n\theta)cos^2\theta \\ +(n+2)\,cos(n\theta)\,sin^2\theta \\ -n\,sin(n\theta)\,sin2\theta \end{pmatrix} \end{array} \right\} b_n \\ + \left\{ \begin{array}{c} (n-1)R^{-2(n-1)}\, r^{n-2}(cos(n\theta)(cos2\theta) + sin(n\theta)\,sin2\theta) \\ +(n-1)(n+1)R^2 r^{-(n+2)}(cos(n\theta)(cos2\theta) - sin(n\theta)\,sin2\theta) \\ +(n-1)r^{-n} \begin{pmatrix} -(n+2)\ cos(n\theta)cos^2\theta \\ +(n-2)\,cos(n\theta)\,sin^2\theta \\ +n\,sin(n\theta)\,sin2\theta \end{pmatrix} \end{array} \right\} d_n \end{array} \right\} \end{array} \right]$$

$$\sigma_{xx} = \left[\begin{array}{c} \left\{ -\cos 2\theta \frac{2\,R^2}{r^2} + 2 \right\} c_0 \\ + \sum_{n=2,4,\ldots}^{N} \left\{ \begin{array}{c} \left\{ \begin{array}{c} (n-1)(n+1)R^2 r^{n-2}(cos(n\theta)(cos2\theta) + sin(n\theta)\,sin2\theta) \\ +(n+1)R^{2(n+1)} r^{-(n+2)}(cos(n\theta)(-cos2\theta) + sin(n\theta)\,sin2\theta) \\ +(n+1)r^n \begin{pmatrix} -n\ cos(n\theta)cos^2\theta + 2\,cos(n\theta)cos^2\theta \\ +n\,cos(n\theta)\,sin^2\theta \\ +2\,cos(n\theta)\,sin^2\theta - n\,sin(n\theta)\,sin2\theta \end{pmatrix} \end{array} \right\} b_n \\ + \left\{ \begin{array}{c} (n-1)R^{-2(n-1)}\, r^{n-2}(cos(n\theta)(cos2\theta) + sin(n\theta)\,sin2\theta) \\ +(n-1)(n+1)R^2 r^{-(n+2)}(cos(n\theta)(cos2\theta) - sin(n\theta)\,sin2\theta) \\ +(n-1)r^{-n} \begin{pmatrix} -n\ cos(n\theta)cos^2\theta - 2\ cos(n\theta)cos^2\theta \\ +n\,cos(n\theta)\,sin^2\theta \\ -2\,cos(n\theta)\,sin^2\theta + n\,sin(n\theta)\,sin2\theta \end{pmatrix} \end{array} \right\} d_n \end{array} \right\} \end{array} \right]$$

$$\sigma_{xx} = \left[\begin{array}{c} \left\{ -\cos 2\theta \frac{2\,R^2}{r^2} + 2 \right\} c_0 \\ + \sum_{n=2,4,\ldots}^{N} \left\{ \begin{array}{c} \left\{ \begin{array}{c} (n+1)(n-1)R^2 r^{n-2}(\cos(n\theta - 2\theta)) \\ -(n+1)R^{2(n+1)} r^{-(n+2)}\big(cos(n\theta + 2\theta)\big) \\ -(n+1)r^n(n\cos(n\theta - 2\theta) - 2cosn\theta) \end{array} \right\} b_n \\ + \left\{ \begin{array}{c} (n-1)R^{-2(n-1)}\, r^{n-2}(\cos(n\theta - 2\theta)) \\ +(n-1)(n+1)R^2 r^{-(n+2)}\big(cos(n\theta + 2\theta)\big) \\ -(n-1)r^{-n}(ncos(n\theta + 2\theta) + 2cosn\theta) \end{array} \right\} d_n \end{array} \right\} \end{array} \right] \qquad (3A.7)$$

now,

$$\sigma_{yy} = \left[\begin{array}{l} \left\{ \left(\frac{-2\,R^2}{r^2} + 2 \right) c_0 - \sum_{n=2,4,\ldots}^{N} \left[\begin{array}{c} \left\{ \begin{array}{c} -(n-1)(n+1)R^2 r^{n-2} \\ +(n+1)R^{2(n+1)} r^{-(n+2)} \\ +(n+1)\,(n-2)\,r^n \end{array} \right\} b_n \\ + \left\{ \begin{array}{c} -(n-1)R^{-2(n-1)}\, r^{n-2} \\ -(n-1)(n+1)R^2 r^{-(n+2)} \\ +(n-1)(n+2)r^{-n} \end{array} \right\} d_n \end{array} \right] cos(n\theta) \right\} sin^2\theta \\ + \left\{ \left(\frac{2\,R^2}{r^2} + 2 \right) c_0 + \sum_{n=2,4,\ldots}^{N} \left[\begin{array}{c} \left\{ \begin{array}{c} -(n+1)(n-1)R^2 r^{n-2} \\ +(n+1)R^{2(n+1)} r^{-(n+2)} \\ +(n+1)\,(n+2)\,r^n \end{array} \right\} b_n \\ + \left\{ \begin{array}{c} -(n-1)R^{-2(n-1)} r^{n-2} \\ -(n-1)(n+1)R^2 r^{-(n+2)} \\ +(n-1)(n-2)r^{-n} \end{array} \right\} d_n \end{array} \right] cos(n\theta) \right\} cos^2\theta \\ + \left\{ \sum_{n=2,4,\ldots}^{N} \left[\begin{array}{c} \left\{ \begin{array}{c} -(n+1)(n-1)R^2 r^{n-2} \\ -(n+1)R^{2(n+1)} r^{-(n+2)} \\ +n\,(n+1)r^n \end{array} \right\} b_n \\ \left\{ \begin{array}{c} -(n-1)R^{-2(n-1)} r^{n-2} \\ +(n-1)(n+1)R^2 r^{-(n+2)} \\ -n\,(n-1)r^{-n} \end{array} \right\} d_n \end{array} \right] sin(n\theta) \right\} sin2\theta \end{array} \right]$$

$$\sigma_{yy} = \left[\left\{ \left(\frac{-2\,R^2}{r^2} + 2 \right) sin^2\theta + \left(\frac{2\,R^2}{r^2} + 2 \right) cos^2\theta \right\} c_0 + \sum_{n=2,4,\ldots}^{N} \left\{ \begin{array}{l} - \left[\begin{Bmatrix} -(n-1)(n+1)R^2 r^{n-2} \\ +(n+1)R^{2(n+1)} r^{-(n+2)} \\ +(n+1)\,(n-2)\,r^n \end{Bmatrix} b_n + \begin{Bmatrix} -(n-1)R^{-2(n-1)}\,r^{n-2} \\ -(n-1)(n+1)R^2 r^{-(n+2)} \\ +(n-1)(n+2)r^{-n} \end{Bmatrix} d_n \right] cos(n\theta) sin^2\theta \\ + \left[\begin{Bmatrix} -(n+1)(n-1)R^2 r^{n-2} \\ +(n+1)R^{2(n+1)} r^{-(n+2)} \\ +(n+1)\,(n+2)\,r^n \end{Bmatrix} b_n + \begin{Bmatrix} -(n-1)R^{-2(n-1)} r^{n-2} \\ -(n-1)(n+1)R^2 r^{-(n+2)} \\ +(n-1)(n-2)r^{-n} \end{Bmatrix} d_n \right] cos(n\theta)\, cos^2\theta \\ + \left[\begin{Bmatrix} -(n+1)(n-1)R^2 r^{n-2} \\ -(n+1)R^{2(n+1)} r^{-(n+2)} \\ +n\,(n+1)r^n \end{Bmatrix} b_n + \begin{Bmatrix} -(n-1)R^{-2(n-1)} r^{n-2} \\ +(n-1)(n+1)R^2 r^{-(n+2)} \\ -n\,(n-1)r^{-n} \end{Bmatrix} d_n \right] sin(n\theta)\, sin2\theta \end{array} \right\} \right]$$

$$\sigma_{yy} = \left[\begin{array}{c} \left\{(-sin^2\theta + cos^2\theta)\frac{2\,R^2}{r^2} + (cos^2\theta + sin^2\theta)2\right\} c_0 \\ + \sum_{n=2,4,\ldots}^{N} \left\{ \begin{array}{c} -\begin{Bmatrix} -(n-1)(n+1)R^2 r^{n-2} \\ +(n+1)R^{2(n+1)} r^{-(n+2)} \\ +(n+1)\,(n-2)\,r^n \end{Bmatrix} b_n\ cos(n\theta) sin^2\theta \\ -\begin{Bmatrix} -(n-1)R^{-2(n-1)}\, r^{n-2} \\ -(n-1)(n+1)R^2 r^{-(n+2)} \\ +(n-1)(n+2) r^{-n} \end{Bmatrix} d_n\ cos(n\theta) sin^2\theta \\ +\begin{Bmatrix} -(n+1)(n-1)R^2 r^{n-2} \\ +(n+1)R^{2(n+1)} r^{-(n+2)} \\ +(n+1)\,(n+2)\,r^n \end{Bmatrix} b_n\, cos(n\theta)\, cos^2\theta \\ +\begin{Bmatrix} -(n-1)R^{-2(n-1)} r^{n-2} \\ -(n-1)(n+1)R^2 r^{-(n+2)} \\ +(n-1)(n-2) r^{-n} \end{Bmatrix} d_n\, cos(n\theta)\, cos^2\theta \\ +\begin{Bmatrix} -(n+1)(n-1)R^2 r^{n-2} \\ -(n+1)R^{2(n+1)} r^{-(n+2)} \\ +n\,(n+1) r^n \end{Bmatrix} b_n\ sin(n\theta)\, sin2\theta \\ +\begin{Bmatrix} -(n-1)R^{-2(n-1)} r^{n-2} \\ +(n-1)(n+1)R^2 r^{-(n+2)} \\ -n\,(n-1) r^{-n} \end{Bmatrix} d_n\ sin(n\theta)\, sin2\theta \end{array} \right\} \end{array} \right]$$

$$\sigma_{yy} = \left[\left\{ \cos 2\theta \frac{2\,R^2}{r^2} + 2 \right\} c_0 + \sum_{n=2,4,\ldots}^{N} \left\{ \begin{array}{l} -\left\{ \begin{array}{c} -(n-1)(n+1)R^2 r^{n-2} \\ +(n+1)R^{2(n+1)} r^{-(n+2)} \\ +(n+1)\,(n-2)\,r^n \end{array} \right\} b_n \; cos(n\theta) sin^2\theta \\ +\left\{ \begin{array}{c} -(n+1)(n-1)R^2 r^{n-2} \\ +(n+1)R^{2(n+1)} r^{-(n+2)} \\ +(n+1)\,(n+2)\,r^n \end{array} \right\} b_n \cos(n\theta)\cos^2\theta \\ +\left\{ \begin{array}{c} -(n+1)(n-1)R^2 r^{n-2} \\ -(n+1)R^{2(n+1)} r^{-(n+2)} \\ +n\,(n+1) r^n \end{array} \right\} b_n \; sin(n\theta)\, sin2\theta \\ -\left\{ \begin{array}{c} -(n-1)R^{-2(n-1)}\, r^{n-2} \\ -(n-1)(n+1)R^2 r^{-(n+2)} \\ +(n-1)(n+2) r^{-n} \end{array} \right\} d_n \; cos(n\theta) sin^2\theta \\ +\left\{ \begin{array}{c} -(n-1)R^{-2(n-1)} r^{n-2} \\ -(n-1)(n+1)R^2 r^{-(n+2)} \\ +(n-1)(n-2) r^{-n} \end{array} \right\} d_n \cos(n\theta)\cos^2\theta \\ +\left\{ \begin{array}{c} -(n-1)R^{-2(n-1)} r^{n-2} \\ +(n-1)(n+1)R^2 r^{-(n+2)} \\ -n\,(n-1) r^{-n} \end{array} \right\} d_n \; sin(n\theta)\, sin2\theta \end{array} \right\} \right]$$

$$\sigma_{yy} = \left[\left\{ \cos 2\theta \frac{2\,R^2}{r^2} + 2 \right\} c_0 + \sum_{n=2,4,\ldots}^{N} \left\{ \begin{array}{l} \left\{ \begin{array}{c} (n-1)(n+1)R^2 r^{n-2} \begin{pmatrix} cos(n\theta)sin^2\theta \\ -\cos(n\theta)\,cos^2\theta \\ -\ sin(n\theta)\,sin2\theta \end{pmatrix} \\ +(n+1)R^{2(n+1)} r^{-(n+2)} \begin{pmatrix} -\ cos(n\theta)sin^2\theta \\ +cos(n\theta)\,cos^2\theta \\ -\ sin(n\theta)\,sin2\theta \end{pmatrix} \\ +(n+1)r^n \begin{pmatrix} -(n-2)\ cos(n\theta)sin^2\theta \\ +(n+2)\,cos(n\theta)\,cos^2\theta \\ +n\,sin(n\theta)\,sin2\theta \end{pmatrix} \end{array} \right\} b_n \\ + \left\{ \begin{array}{c} (n-1)R^{-2(n-1)}\, r^{n-2} \begin{pmatrix} cos(n\theta)sin^2\theta \\ -cos(n\theta)\,cos^2\theta \\ -\ sin(n\theta)\,sin2\theta \end{pmatrix} \\ +(n-1)(n+1)R^2 r^{-(n+2)} \begin{pmatrix} cos(n\theta)sin^2\theta \\ -cos(n\theta)\,cos^2\theta \\ +\ sin(n\theta)\,sin2\theta \end{pmatrix} \\ +(n-1)r^{-n} \begin{pmatrix} -(n+2)\ cos(n\theta)sin^2\theta \\ +(n-2)\,cos(n\theta)\,cos^2\theta \\ -n\,sin(n\theta)\,sin2\theta \end{pmatrix} \end{array} \right\} d_n \end{array} \right\} \right]$$

$$\sigma_{yy} = \left[\left\{ \cos 2\theta \frac{2\,R^2}{r^2} + 2 \right\} c_0 + \sum_{n=2,4,\ldots}^{N} \left\{ \begin{array}{l} \left\{ \begin{array}{c} (n-1)(n+1)R^2 r^{n-2} \begin{pmatrix} cos(n\theta)(sin^2\theta - cos^2\theta) \\ -\ sin(n\theta)\,sin2\theta \end{pmatrix} \\ +(n+1)R^{2(n+1)} r^{-(n+2)} \begin{pmatrix} cos(n\theta)(-sin^2\theta + cos^2\theta) \\ -\ sin(n\theta)\,sin2\theta \end{pmatrix} \\ +(n+1)r^n \begin{pmatrix} -(n-2)\ cos(n\theta)sin^2\theta \\ +(n+2)\,cos(n\theta)\,cos^2\theta \\ +n\,sin(n\theta)\,sin2\theta \end{pmatrix} \end{array} \right\} b_n \\ + \left\{ \begin{array}{c} (n-1)R^{-2(n-1)}\, r^{n-2} \begin{pmatrix} cos(n\theta)(sin^2\theta - cos^2\theta) \\ -\ sin(n\theta)\,sin2\theta \end{pmatrix} \\ +(n-1)(n+1)R^2 r^{-(n+2)} \begin{pmatrix} cos(n\theta)(sin^2\theta - cos^2\theta) \\ +\ sin(n\theta)\,sin2\theta \end{pmatrix} \\ +(n-1)r^{-n} \begin{pmatrix} -(n+2)\ cos(n\theta)sin^2\theta \\ +(n-2)\,cos(n\theta)\,cos^2\theta \\ -n\,sin(n\theta)\,sin2\theta \end{pmatrix} \end{array} \right\} d_n \end{array} \right\} \right]$$

$$\sigma_{yy} = \left[\begin{array}{c} \left\{\cos 2\theta \frac{2\,R^2}{r^2} + 2\right\} c_0 \\ + \sum_{n=2,4,\ldots}^{N} \left\{ \begin{array}{c} \left\{ \begin{array}{c} (n-1)(n+1)R^2 r^{n-2} \begin{pmatrix} cos(n\theta)(-cos2\theta) \\ -\ sin(n\theta)\, sin2\theta \end{pmatrix} \\ +(n+1)R^{2(n+1)} r^{-(n+2)} \begin{pmatrix} cos(n\theta)(cos2\theta) \\ -\ sin(n\theta)\, sin2\theta \end{pmatrix} \\ +(n+1)r^n \begin{pmatrix} -(n-2)\ cos(n\theta) sin^2\theta \\ +(n+2)\, cos(n\theta)\, cos^2\theta \\ +n\, sin(n\theta)\, sin2\theta \end{pmatrix} \end{array} \right\} b_n \\ + \left\{ \begin{array}{c} (n-1)R^{-2(n-1)}\, r^{n-2} \begin{pmatrix} cos(n\theta)(-cos2\theta) \\ -\ sin(n\theta)\, sin2\theta \end{pmatrix} \\ +(n-1)(n+1)R^2 r^{-(n+2)} \begin{pmatrix} cos(n\theta)(-cos2\theta) \\ +\ sin(n\theta)\, sin2\theta \end{pmatrix} \\ +(n-1)r^{-n} \begin{pmatrix} -(n+2)\ cos(n\theta) sin^2\theta \\ +(n-2)\, cos(n\theta)\, cos^2\theta \\ -n\, sin(n\theta)\, sin2\theta \end{pmatrix} \end{array} \right\} d_n \end{array} \right\} \end{array} \right]$$

$$\sigma_{yy} = \left[\begin{array}{c} \left\{\cos 2\theta \frac{2\,R^2}{r^2} + 2\right\} c_0 \\ + \sum_{n=2,4,\ldots}^{N} \left\{ \begin{array}{c} \left\{ \begin{array}{c} (n-1)(n+1)R^2 r^{n-2} \begin{pmatrix} cos(n\theta)(-cos2\theta) \\ -\ sin(n\theta)\, sin2\theta \end{pmatrix} \\ +(n+1)R^{2(n+1)} r^{-(n+2)} \begin{pmatrix} cos(n\theta)(cos2\theta) \\ -\ sin(n\theta)\, sin2\theta \end{pmatrix} \\ +(n+1)r^n \begin{pmatrix} -n\ cos(n\theta) sin^2\theta + 2\, cos(n\theta) sin^2\theta \\ +n cos(n\theta)\, cos^2\theta \\ +2\, cos(n\theta)\, cos^2\theta + n\, sin(n\theta)\, sin2\theta \end{pmatrix} \end{array} \right\} b_n \\ + \left\{ \begin{array}{c} (n-1)R^{-2(n-1)}\, r^{n-2} \begin{pmatrix} cos(n\theta)(-cos2\theta) \\ -\ sin(n\theta)\, sin2\theta \end{pmatrix} \\ +(n-1)(n+1)R^2 r^{-(n+2)} \begin{pmatrix} cos(n\theta)(-cos2\theta) \\ +sin(n\theta)\, sin2\theta \end{pmatrix} \\ +(n-1)r^{-n} \begin{pmatrix} -n\ cos(n\theta) sin^2\theta - 2\ cos(n\theta) sin^2\theta \\ +n\, cos(n\theta)\, cos^2\theta \\ -2\, cos(n\theta)\, cos^2\theta - n\, sin(n\theta)\, sin2\theta \end{pmatrix} \end{array} \right\} d_n \end{array} \right\} \end{array} \right]$$

$$\sigma_{yy} = \left[\begin{array}{c} \left\{\cos 2\theta \frac{2\,R^2}{r^2} + 2\right\} c_0 \\ + \sum_{n=2,4,\ldots}^{N} \left\{ \begin{array}{c} \left\{ \begin{array}{c} -(n+1)(n-1)R^2 r^{n-2}\cos(n\theta - 2\theta) \\ +(n+1)R^{2(n+1)} r^{-(n+2)} cos(n\theta + 2\theta) \\ +(n+1)r^n (n\cos(n\theta - 2\theta) + 2cosn\theta) \end{array} \right\} b_n \\ + \left\{ \begin{array}{c} -(n-1)R^{-2(n-1)}\, r^{n-2}\cos(n\theta - 2\theta) \\ -(n-1)(n+1)R^2 r^{-(n+2)} cos(n\theta + 2\theta) \\ +(n-1)r^{-n}(ncos(n\theta + 2\theta) - 2cosn\theta) \end{array} \right\} d_n \end{array} \right\} \end{array} \right] \qquad \text{(3A.8)}$$

$$\epsilon_{xx}= \frac{1}{\mathrm{E}} (\sigma_{xx}- \upsilon\sigma_{yy}) \tag{3A.9}$$

$$\epsilon_{xx}= \frac{1}{\mathrm{E}}\left[\left[\left\{-\cos 2\theta \frac{2R^2}{r^2}+2\right\}c_0 + \sum_{n=2,4,\ldots}^{N}\left\{\begin{Bmatrix}(n+1)(n-1)R^2r^{n-2}(\cos(n\theta-2\theta))\\ -(n+1)R^{2(n+1)}r^{-(n+2)}\big(cos(n\theta+2\theta)\big)\\ -(n+1)r^n(n\cos(n\theta-2\theta)-2cosn\theta)\end{Bmatrix}b_n + \begin{Bmatrix}(n-1)R^{-2(n-1)}\,r^{n-2}(\cos(n\theta-2\theta))\\ +(n-1)(n+1)R^2r^{-(n+2)}\big(cos(n\theta+2\theta)\big)\\ -(n-1)r^{-n}(ncos(n\theta+2\theta)+2cosn\theta)\end{Bmatrix}d_n\right\}\right] - \upsilon\left[\left\{\cos 2\theta \frac{2R^2}{r^2}+2\right\}c_0 + \sum_{n=2,4,\ldots}^{N}\left\{\begin{Bmatrix}-(n+1)(n-1)R^2r^{n-2}\cos(n\theta-2\theta)\\ +(n+1)R^{2(n+1)}r^{-(n+2)}cos(n\theta+2\theta)\\ +(n+1)r^n(n\cos(n\theta-2\theta)+2cosn\theta)\end{Bmatrix}b_n + \begin{Bmatrix}-(n-1)R^{-2(n-1)}\,r^{n-2}\cos(n\theta-2\theta)\\ -(n-1)(n+1)R^2r^{-(n+2)}cos(n\theta+2\theta)\\ +(n-1)r^{-n}(ncos(n\theta+2\theta)-2cosn\theta)\end{Bmatrix}d_n\right\}\right]\right]$$

$$\epsilon_{xx}= \frac{1}{\mathrm{E}}\left[\left\{-\cos 2\theta \frac{2R^2}{r^2}+2\right\}c_0 - \upsilon\left\{\cos 2\theta \frac{2R^2}{r^2}+2\right\}c_0 + \sum_{n=2,4,\ldots}^{N}\left\{\begin{Bmatrix}(n+1)(n-1)R^2r^{n-2}(\cos(n\theta-2\theta))\\ -(n+1)R^{2(n+1)}r^{-(n+2)}\big(cos(n\theta+2\theta)\big)\\ -(n+1)r^n(n\cos(n\theta-2\theta)-2cosn\theta)\end{Bmatrix}b_n + \begin{Bmatrix}(n-1)R^{-2(n-1)}\,r^{n-2}(\cos(n\theta-2\theta))\\ +(n-1)(n+1)R^2r^{-(n+2)}\big(cos(n\theta+2\theta)\big)\\ -(n-1)r^{-n}(ncos(n\theta+2\theta)+2cosn\theta)\end{Bmatrix}d_n\right\} - \upsilon\left[\sum_{n=2,4,\ldots}^{N}\left\{\begin{Bmatrix}-(n+1)(n-1)R^2r^{n-2}\cos(n\theta-2\theta)\\ +(n+1)R^{2(n+1)}r^{-(n+2)}cos(n\theta+2\theta)\\ +(n+1)r^n(n\cos(n\theta-2\theta)+2cosn\theta)\end{Bmatrix}b_n + \begin{Bmatrix}-(n-1)R^{-2(n-1)}\,r^{n-2}\cos(n\theta-2\theta)\\ -(n-1)(n+1)R^2r^{-(n+2)}cos(n\theta+2\theta)\\ +(n-1)r^{-n}(ncos(n\theta+2\theta)-2cosn\theta)\end{Bmatrix}d_n\right\}\right]\right]$$

$$\epsilon_{xx}=\frac{1}{\mathrm{E}}\left[\left\{-\cos 2\theta\frac{2R^2}{r^2}+2\right\}c_0-\upsilon\left\{\cos 2\theta\frac{2R^2}{r^2}+2\right\}c_0+\sum_{n=2,4,\ldots}^{N}\left[\begin{Bmatrix}(n+1)(n-1)R^2r^{n-2}(\cos(n\theta-2\theta))\\-(n+1)R^{2(n+1)}r^{-(n+2)}\left(cos(n\theta+2\theta)\right)\\-(n+1)r^n(n\cos(n\theta-2\theta)-2cosn\theta)\end{Bmatrix}b_n+\begin{Bmatrix}(n-1)R^{-2(n-1)}\,r^{n-2}(\cos(n\theta-2\theta))\\+(n-1)(n+1)R^2r^{-(n+2)}\left(cos(n\theta+2\theta)\right)\\-(n-1)r^{-n}(ncos(n\theta+2\theta)+2cosn\theta)\end{Bmatrix}d_n-\upsilon\left[\begin{Bmatrix}-(n+1)(n-1)R^2r^{n-2}\cos(n\theta-2\theta)\\+(n+1)R^{2(n+1)}r^{-(n+2)}cos(n\theta+2\theta)\\+(n+1)r^n(n\cos(n\theta-2\theta)+2cosn\theta)\end{Bmatrix}b_n+\begin{Bmatrix}-(n-1)R^{-2(n-1)}\,r^{n-2}\cos(n\theta-2\theta)\\-(n-1)(n+1)R^2r^{-(n+2)}cos(n\theta+2\theta)\\+(n-1)r^{-n}(ncos(n\theta+2\theta)-2cosn\theta)\end{Bmatrix}d_n\right]\right]\right]$$

$$\epsilon_{xx}=\frac{1}{\mathrm{E}}\left[\left\{-\cos 2\theta\frac{2R^2}{r^2}(1+\upsilon)+2(1-\upsilon)\right\}c_0+\sum_{n=2,4,\ldots}^{N}\left[\begin{Bmatrix}(n+1)(n-1)R^2r^{n-2}(\cos(n\theta-2\theta))\\-(n+1)R^{2(n+1)}r^{-(n+2)}\left(cos(n\theta+2\theta)\right)\\-(n+1)r^n(n\cos(n\theta-2\theta)-2cosn\theta)\\-\upsilon\begin{Bmatrix}-(n+1)(n-1)R^2r^{n-2}\cos(n\theta-2\theta)\\+(n+1)R^{2(n+1)}r^{-(n+2)}cos(n\theta+2\theta)\\+(n+1)r^n(n\cos(n\theta-2\theta)+2cosn\theta)\end{Bmatrix}\end{Bmatrix}b_n+\begin{Bmatrix}(n-1)R^{-2(n-1)}\,r^{n-2}(\cos(n\theta-2\theta))\\+(n-1)(n+1)R^2r^{-(n+2)}\left(cos(n\theta+2\theta)\right)\\-(n-1)r^{-n}(ncos(n\theta+2\theta)+2cosn\theta)\\-\upsilon\begin{Bmatrix}-(n-1)R^{-2(n-1)}\,r^{n-2}\cos(n\theta-2\theta)\\-(n-1)(n+1)R^2r^{-(n+2)}cos(n\theta+2\theta)\\+(n-1)r^{-n}(ncos(n\theta+2\theta)-2cosn\theta)\end{Bmatrix}\end{Bmatrix}d_n\right]\right]$$

$$\epsilon_{xx}= \frac{1}{\mathrm{E}}\left[\begin{array}{c}\left\{-\cos 2\theta \frac{2\,R^2}{r^2}(1+\upsilon)\ +2(1-\upsilon)\right\}c_0 \\ +\sum_{n=2,4,\ldots}^{N}\left[\begin{array}{c}\left\{\begin{array}{c}(n+1)(n-1)R^2r^{n-2}(\cos(n\theta-2\theta))(1+\upsilon)\\ -(n+1)R^{2(n+1)}r^{-(n+2)}\big(cos(n\theta+2\theta)\big)(1+\upsilon)\\ -(n+1)r^n(n\cos(n\theta-2\theta)-2cosn\theta)\\ -\upsilon[(n+1)r^n(n\cos(n\theta-2\theta)+2cosn\theta)]\end{array}\right\}b_n \\ +\left\{\begin{array}{c}(n-1)R^{-2(n-1)}\,r^{n-2}(\cos(n\theta-2\theta))(1+\upsilon)\\ +(n-1)(n+1)R^2r^{-(n+2)}\big(cos(n\theta+2\theta)\big)(1+\upsilon)\\ -(n-1)r^{-n}(ncos(n\theta+2\theta)+2cosn\theta)\\ -\upsilon[(n-1)r^{-n}(ncos(n\theta+2\theta)-2cosn\theta)]\end{array}\right\}d_n\end{array}\right]\end{array}\right]$$

$$\epsilon_{xx}= \frac{1}{\mathrm{E}}\left[\begin{array}{c}\left\{-\cos 2\theta \frac{2\,R^2}{r^2}(1+\upsilon)\ +2(1-\upsilon)\right\}c_0 \\ +\sum_{n=2,4,\ldots}^{N}\left[\begin{array}{c}\left\{\begin{array}{c}(n+1)(n-1)R^2r^{n-2}(\cos(n\theta-2\theta))(1+\upsilon)\\ -(n+1)R^{2(n+1)}r^{-(n+2)}\big(cos(n\theta+2\theta)\big)(1+\upsilon)\\ -(n+1)r^n(n\cos(n\theta-2\theta)(1+\upsilon)-2cosn\theta(1-\upsilon))\end{array}\right\}b_n \\ +\left\{\begin{array}{c}(n-1)R^{-2(n-1)}\,r^{n-2}(\cos(n\theta-2\theta))(1+\upsilon)\\ +(n-1)(n+1)R^2r^{-(n+2)}\big(cos(n\theta+2\theta)\big)(1+\upsilon)\\ -(n-1)r^{-n}(n\,cos(n\theta+2\theta)(1+\upsilon)+2\,cosn\theta\,(1-\upsilon))\end{array}\right\}d_n\end{array}\right]\end{array}\right]$$

(3A.10)

$$\epsilon_{yy}= \frac{1}{\mathrm{E}} (\sigma_{yy}- \upsilon\sigma_{xx}) \qquad (3A.11)$$

$$\epsilon_{yy}= \frac{1}{\mathrm{E}}\left[\begin{array}{l} \left[\left\{\cos 2\theta \frac{2R^2}{r^2} + 2\right\} c_0 + \sum_{n=2,4,\ldots}^{N} \left\{\begin{array}{l} \left\{\begin{array}{l} -(n+1)(n-1)R^2 r^{n-2}\cos(n\theta - 2\theta) \\ +(n+1)R^{2(n+1)} r^{-(n+2)} cos(n\theta + 2\theta) \\ +(n+1)r^n(n\cos(n\theta - 2\theta) + 2cosn\theta) \end{array}\right\} b_n \\ + \left\{\begin{array}{l} -(n-1)R^{-2(n-1)}\, r^{n-2}\cos(n\theta - 2\theta) \\ -(n-1)(n+1)R^2 r^{-(n+2)} cos(n\theta + 2\theta) \\ +(n-1)r^{-n}(ncos(n\theta + 2\theta) - 2cosn\theta) \end{array}\right\} d_n \end{array}\right\}\right] \\ -\upsilon\left[\left\{-\cos 2\theta \frac{2R^2}{r^2} + 2\right\} c_0 + \sum_{n=2,4,\ldots}^{N} \left\{\begin{array}{l} \left\{\begin{array}{l} (n+1)(n-1)R^2 r^{n-2}(\cos(n\theta - 2\theta)) \\ -(n+1)R^{2(n+1)} r^{-(n+2)}\big(cos(n\theta + 2\theta)\big) \\ -(n+1)r^n(n\cos(n\theta - 2\theta) - 2cosn\theta) \end{array}\right\} b_n \\ + \left\{\begin{array}{l} (n-1)R^{-2(n-1)}\, r^{n-2}(\cos(n\theta - 2\theta)) \\ +(n-1)(n+1)R^2 r^{-(n+2)}\big(cos(n\theta + 2\theta)\big) \\ -(n-1)r^{-n}(ncos(n\theta + 2\theta) + 2cosn\theta) \end{array}\right\} d_n \end{array}\right\}\right] \end{array}\right]$$

$$\epsilon_{yy}= \frac{1}{\mathrm{E}}\left[\begin{array}{l} \left\{\cos 2\theta \frac{2R^2}{r^2} + 2\right\} c_0 - \upsilon\left\{-\cos 2\theta \frac{2R^2}{r^2} + 2\right\} c_0 \\ + \sum_{n=2,4,\ldots}^{N} \left\{\begin{array}{l} \left\{\begin{array}{l} -(n+1)(n-1)R^2 r^{n-2}\cos(n\theta - 2\theta) \\ +(n+1)R^{2(n+1)} r^{-(n+2)} cos(n\theta + 2\theta) \\ +(n+1)r^n(n\cos(n\theta - 2\theta) + 2cosn\theta) \end{array}\right\} b_n \\ + \left\{\begin{array}{l} -(n-1)R^{-2(n-1)}\, r^{n-2}\cos(n\theta - 2\theta) \\ -(n-1)(n+1)R^2 r^{-(n+2)} cos(n\theta + 2\theta) \\ +(n-1)r^{-n}(ncos(n\theta + 2\theta) - 2cosn\theta) \end{array}\right\} d_n \\ -\upsilon\left\{\begin{array}{l} \left\{\begin{array}{l} (n+1)(n-1)R^2 r^{n-2}(\cos(n\theta - 2\theta)) \\ -(n+1)R^{2(n+1)} r^{-(n+2)}\big(cos(n\theta + 2\theta)\big) \\ -(n+1)r^n(n\cos(n\theta - 2\theta) - 2cosn\theta) \end{array}\right\} b_n \\ + \left\{\begin{array}{l} (n-1)R^{-2(n-1)}\, r^{n-2}(\cos(n\theta - 2\theta)) \\ +(n-1)(n+1)R^2 r^{-(n+2)}\big(cos(n\theta + 2\theta)\big) \\ -(n-1)r^{-n}(ncos(n\theta + 2\theta) + 2cosn\theta) \end{array}\right\} d_n \end{array}\right\} \end{array}\right]$$

$$\epsilon_{yy}= \frac{1}{\mathrm{E}}\left[\begin{array}{c} \left\{\cos 2\theta \frac{2\,R^2}{r^2}(1+\upsilon)+2(1-\upsilon)\right\}c_0 \\ +\sum_{n=2,4,\ldots}^{N}\left\{\begin{array}{c} \left\{\begin{array}{c} -(n+1)(n-1)R^2r^{n-2}\cos(n\theta-2\theta) \\ +(n+1)R^{2(n+1)}r^{-(n+2)}cos(n\theta+2\theta) \\ +(n+1)r^n(n\cos(n\theta-2\theta)+2cosn\theta) \\ -\upsilon\left\{\begin{array}{c}(n+1)(n-1)R^2r^{n-2}(\cos(n\theta-2\theta)) \\ -(n+1)R^{2(n+1)}r^{-(n+2)}\left(cos(n\theta+2\theta)\right) \\ -(n+1)r^n(n\cos(n\theta-2\theta)-2cosn\theta)\end{array}\right.\end{array}\right\}b_n \\ +\left\{\begin{array}{c} -(n-1)R^{-2(n-1)}\,r^{n-2}\cos(n\theta-2\theta) \\ -(n-1)(n+1)R^2r^{-(n+2)}cos(n\theta+2\theta) \\ +(n-1)r^{-n}(ncos(n\theta+2\theta)-2cosn\theta) \\ -\upsilon\left\{\begin{array}{c}(n-1)R^{-2(n-1)}\,r^{n-2}(\cos(n\theta-2\theta)) \\ +(n-1)(n+1)R^2r^{-(n+2)}\left(cos(n\theta+2\theta)\right) \\ -(n-1)r^{-n}(ncos(n\theta+2\theta)+2cosn\theta)\end{array}\right.\end{array}\right\}d_n\end{array}\right\}\end{array}\right]$$

$$\epsilon_{yy}= \frac{1}{\mathrm{E}}\left[\begin{array}{c} \left\{\cos 2\theta \frac{2\,R^2}{r^2}(1+\upsilon)+2(1-\upsilon)\right\}c_0 \\ +\sum_{n=2,4,\ldots}^{N}\left\{\begin{array}{c} \left\{\begin{array}{c} -(n+1)(n-1)R^2r^{n-2}\cos(n\theta-2\theta)\,(1+\upsilon) \\ +(n+1)R^{2(n+1)}r^{-(n+2)}cos(n\theta+2\theta)(1+\upsilon) \\ +(n+1)r^n\left[\begin{array}{c}(n\cos(n\theta-2\theta)+2cosn\theta) \\ +\upsilon(n\cos(n\theta-2\theta)-2cosn\theta)\end{array}\right]\end{array}\right\}b_n \\ +\left\{\begin{array}{c} -(n-1)R^{-2(n-1)}\,r^{n-2}\cos(n\theta-2\theta)\,(1+\upsilon) \\ -(n-1)(n+1)R^2r^{-(n+2)}cos(n\theta+2\theta)(1+\upsilon) \\ +(n-1)r^{-n}\left[\begin{array}{c}(ncos(n\theta+2\theta)-2cosn\theta) \\ +\upsilon(ncos(n\theta+2\theta)+2cosn\theta)\end{array}\right]\end{array}\right\}d_n\end{array}\right\}\end{array}\right]$$

$$\epsilon_{yy}= \frac{1}{\mathrm{E}}\left[\begin{array}{c} \left\{\cos 2\theta \frac{2\,R^2}{r^2}(1+\upsilon)+2(1-\upsilon)\right\}c_0 \\ +\sum_{n=2,4,\ldots}^{N}\left\{\begin{array}{c} \left\{\begin{array}{c} -(n+1)(n-1)R^2r^{n-2}\cos(n\theta-2\theta)\,(1+\upsilon) \\ +(n+1)R^{2(n+1)}r^{-(n+2)}cos(n\theta+2\theta)(1+\upsilon) \\ +(n+1)r^n(n\cos(n\theta-2\theta)\,(1+\upsilon)+2cosn\theta(1-\upsilon))\end{array}\right\}b_n \\ +\left\{\begin{array}{c} -(n-1)R^{-2(n-1)}\,r^{n-2}\cos(n\theta-2\theta)\,(1+\upsilon) \\ -(n-1)(n+1)R^2r^{-(n+2)}cos(n\theta+2\theta)(1+\upsilon) \\ +(n-1)r^{-n}(ncos(n\theta+2\theta)(1+\upsilon)-2cosn\theta(1-\upsilon))\end{array}\right\}d_n\end{array}\right\}\end{array}\right]$$

(3A.12)

A4 Approaching the Boundary Collocation Method

The results of this Appendix initially use only five strain-gage inputs along the stationary (ring not rotating) horizontal line AB (*figure 4.1*), plus *analytically* imposed traction-free boundary condition on the inner edge of the ring and discretely imposed traction-free boundary conditions at 850,001 points on the external edge for each of $\sigma_{rr} = \sigma_{r\theta} = 0$. The closest these external discretely imposed traction-free conditions occur to the load is at $\theta = 85^o$. Note that because of some highly incorrect hybrid values, the stresses (strains, displacements) in this Appendix are quite different compared with those of corresponding plots in Chapter 4. This Appendix subsequently employs 25 or 13 measured input strains along with $\sigma_{rr} = \sigma_{r\theta} = 0$ *analytically* on the inside of the ring.

The previous hybrid results of Chapter 4 used 48 input strains, plus the traction-free conditions on the edge of the hole *analytically*, to evaluate the Airy coefficients. Upon moving toward a more (pure) boundary collocation approach, one could continue to satisfy the traction-free conditions *analytically* on the inside boundary of the hole plus $\sigma_{rr} = \sigma_{r\theta} = 0$ at 850,001 discrete locations on the external quarter boundary of the ring, but with only the five input values of strain along line AB (at $\theta = 0^o$). Here the disk is not rotated and only the five gages along the horizontal line AB provide input strains. This arrangement gives stress, strain and displacement results under these conditions of $\sigma_{rr} = \sigma_{r\theta} = 0$ on the inner and outer edge of the ring plus five measured input strains along the horizontal stationary line AB ($\theta = 0^o$), *figures A4.1 through A4.16*. The results are again based on $k = 5$ Airy coefficients. Particularly *figures A4.1, A4.2, A4.4 through A4.6 and A4.8 through A4.16* illustrate potential challenges as one approaches (or were to use) a purely boundary collocation method. Among other issues, only imposing $\sigma_{rr} = \sigma_{r\theta}$

= 0 on the inner and outer edge of the ring would not account for any variations in the applied top and bottom loads (e.g., whether or not the normal load is accompanied by significant shear (friction) loading).

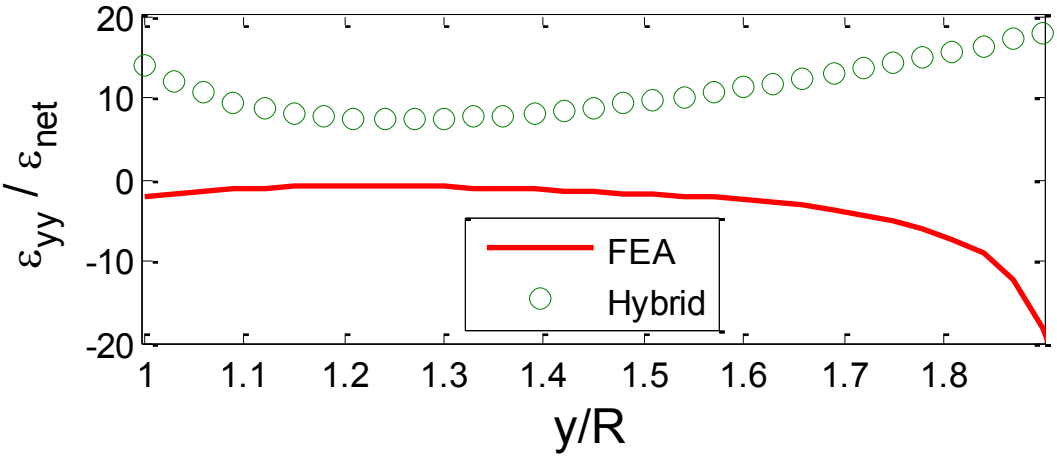

Fig. A4.1: Plot of $\varepsilon_{yy}/\varepsilon_{net}$ along vertical line CD ($\theta = 90^o$) of *figure 4.1* from hybrid method (strain-gage evaluated Airy coefficients, 5 input strains) and ANSYS

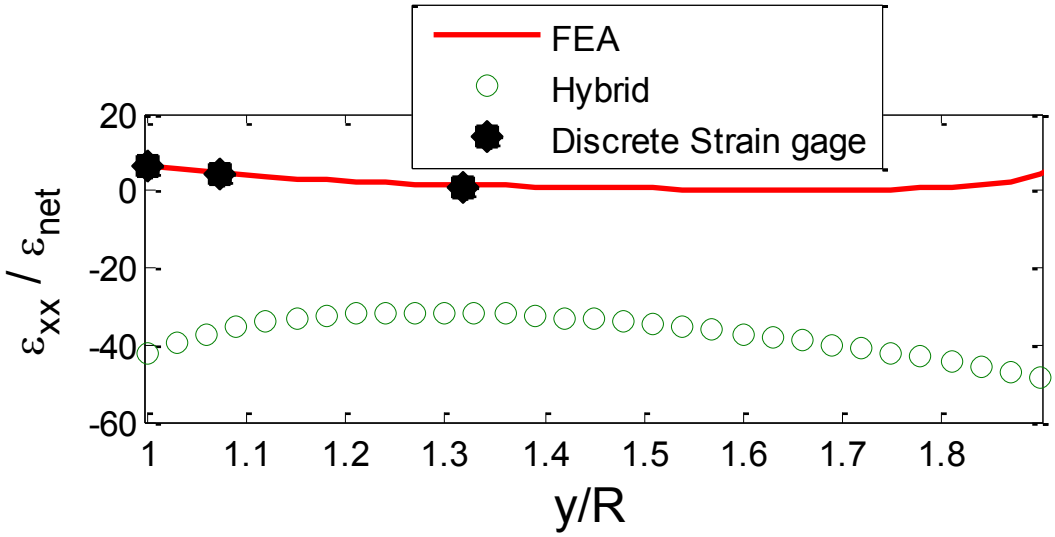

Fig. A4.2: Plot of $\varepsilon_{xx}/\varepsilon_{net}$ along vertical line CD ($\theta = 90^o$) of *figure 4.1* from hybrid method (strain-gage evaluated Airy coefficients, 5 input strains), discrete strain gages and ANSYS

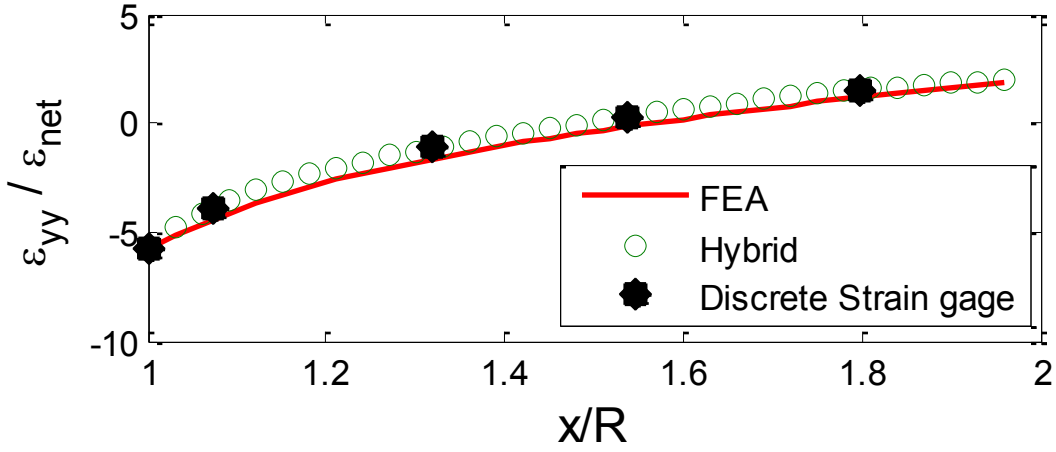

Fig. A4.3: Plot of $\varepsilon_{yy}/\varepsilon_{net}$ along horizontal line AB ($\theta = 0^{o}$) of *figure 4.1* from hybrid method (strain-gage evaluated Airy coefficients, 5 input strains), discrete strain gages and ANSYS

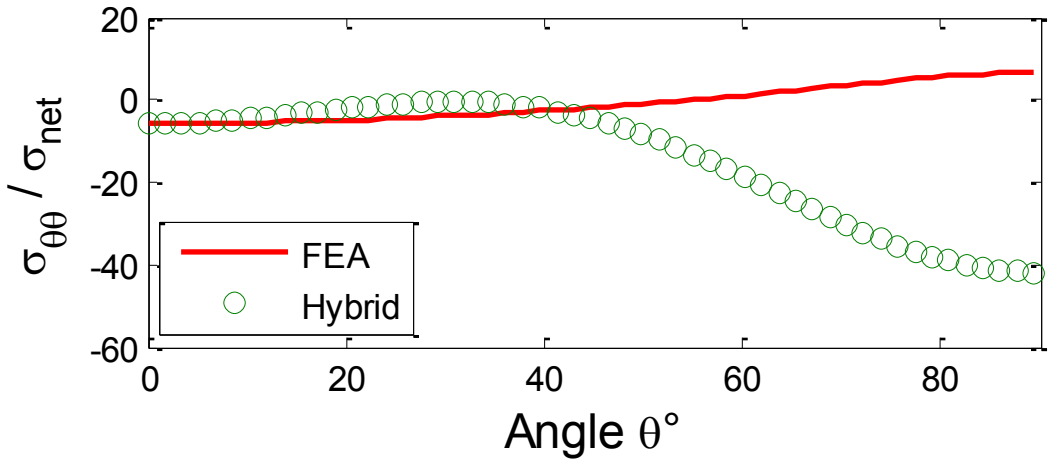

Fig. A4.4: Plot of $\sigma_{\theta\theta}/\sigma_{0}$ along boundary of the hole from hybrid method (strain-gage evaluated Airy coefficients, 5 input strains) and ANSYS

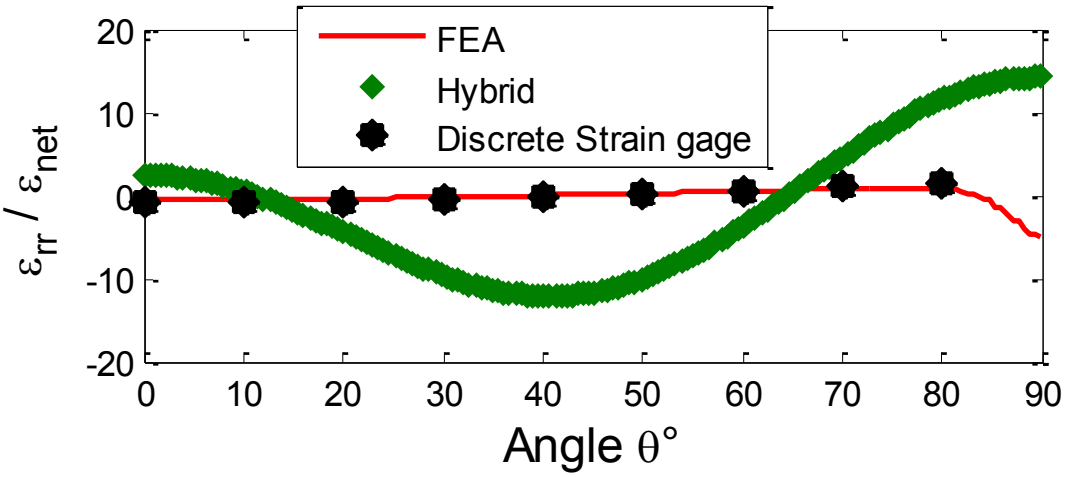

Fig. A4.5: Plot of $\varepsilon_{rr}/\varepsilon_{net}$ at r/R = 1.75 from hybrid method (strain-gage evaluated Airy coefficients, 5 input strains) and ANSYS

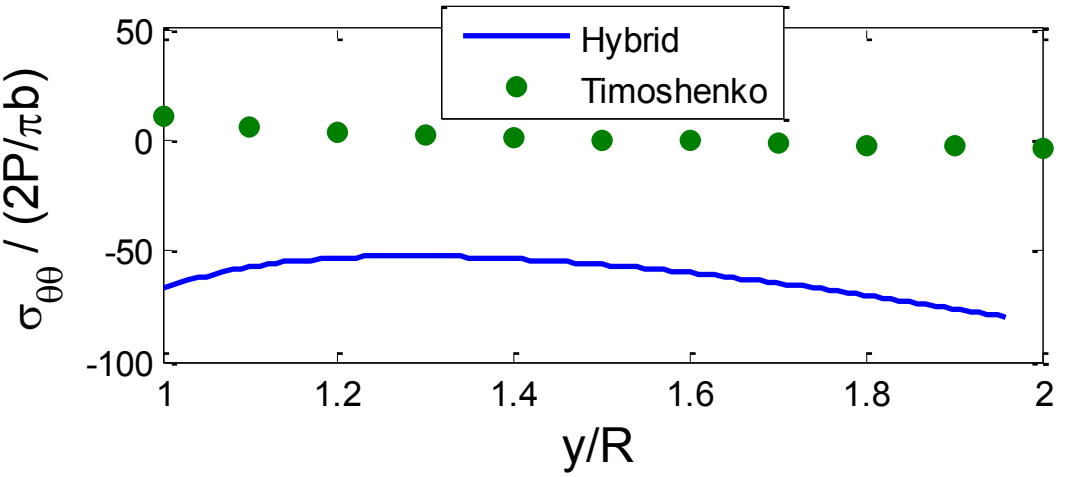

Fig. A4.6: Plot of $\sigma_{\theta\theta}/(2P/\pi b)$ along vertical line CD ($\theta = 90^{o}$) of *figure 4.1* from hybrid method (strain-gage evaluated Airy coefficients, 5 input strains) and Timoshenko [26]

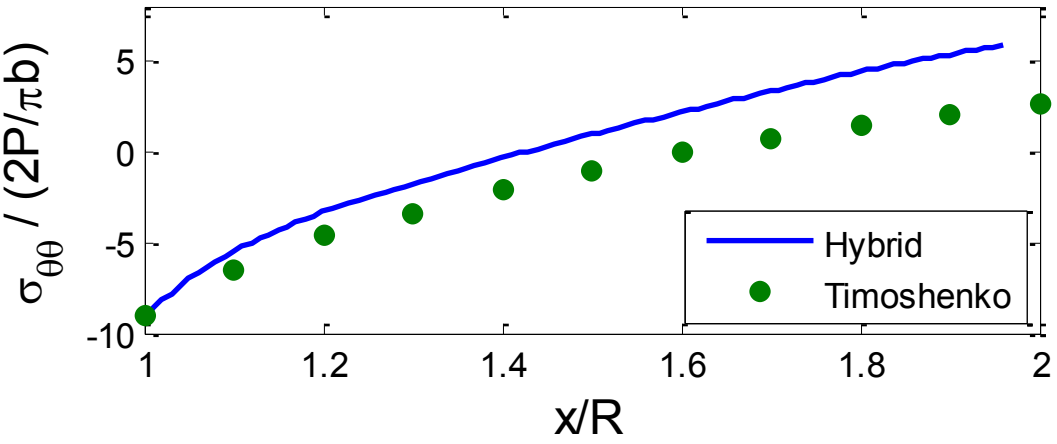

Fig. A4.7: Plot of $\sigma_{\theta\theta}/(2P/\pi b)$ along horizontal line AB ($\theta = 0^{o}$) of *figure 4.1* from hybrid method (strain-gage evaluated Airy coefficients, 5 input strains) and Timoshenko [26]

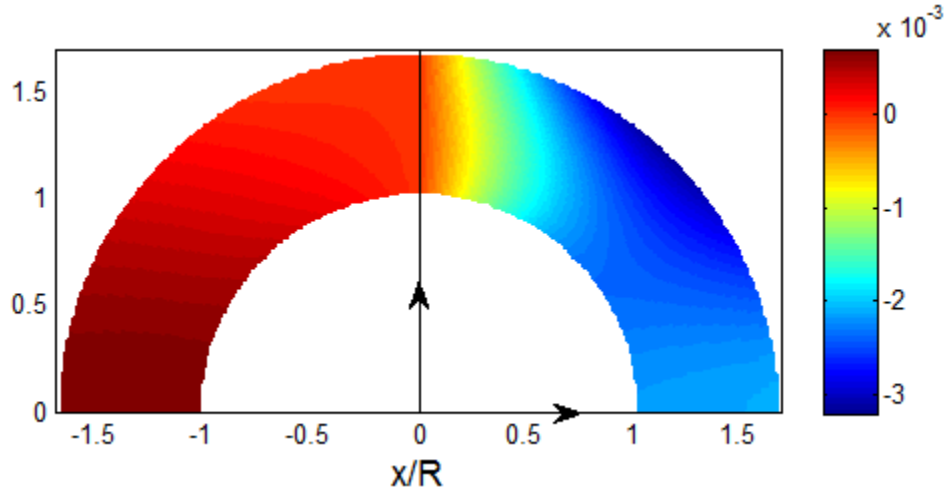

Fig. A4.8: Contours of *u/R* from FEA (left side) and hybrid method (strain-gage evaluated Airy coefficients, 5 input strains) (right side)

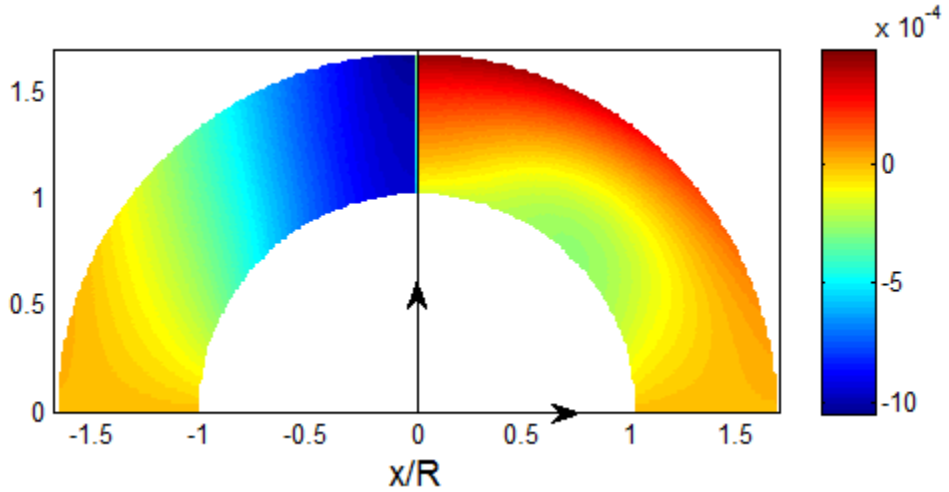

Fig. A4.9: Contours of *v/R* from FEA (left side) and hybrid method (strain-gage evaluated Airy coefficients, 5 input strains) (right side)

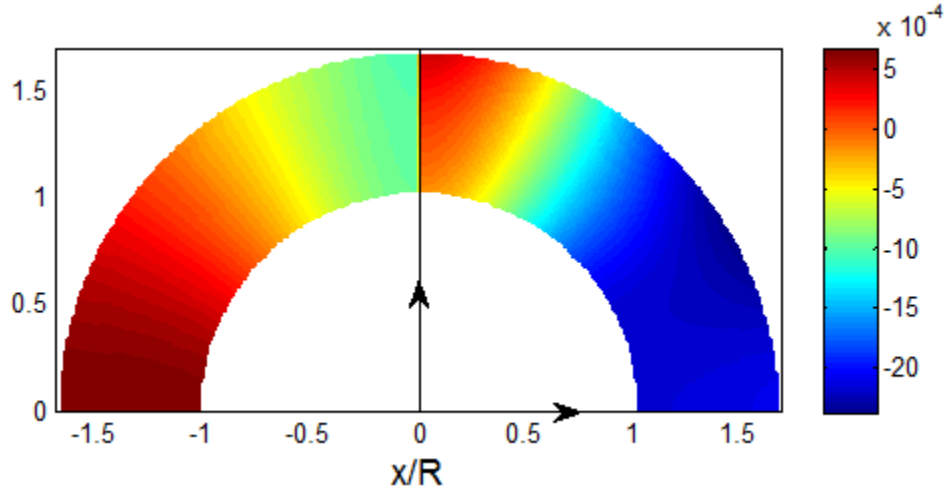

Fig. A4.10: Contours of u_r/R from FEA (left side) and hybrid method (strain-gage evaluated Airy coefficients, 5 input strains) (right side)

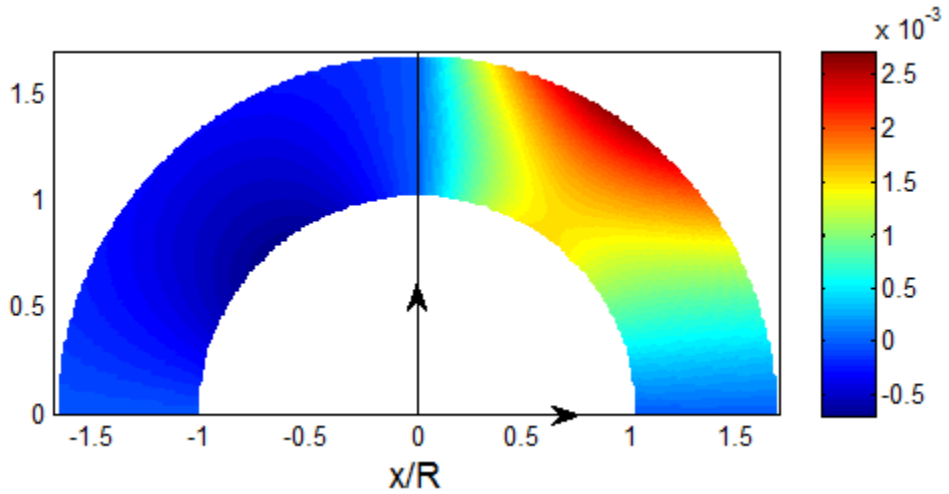

Fig. A4.11: Contours of u_θ/R from FEA (left side) and hybrid method (strain-gage evaluated Airy coefficients, 5 input strains) (right side)

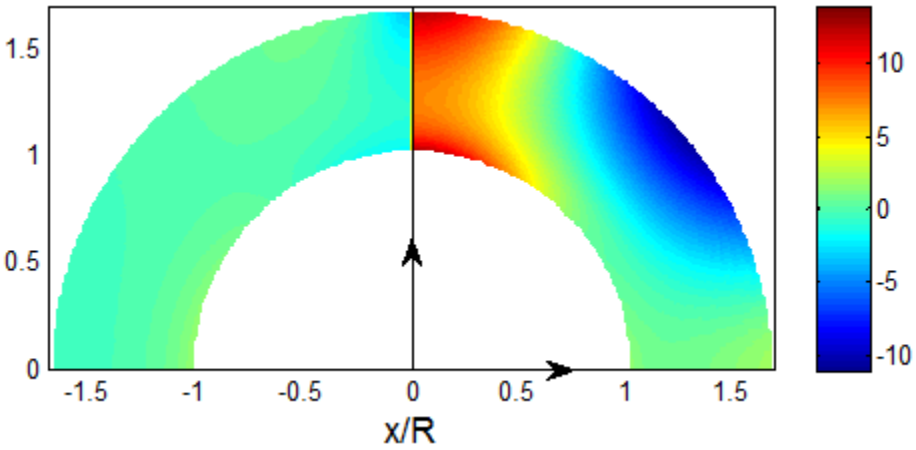

Fig. A4.12: Contours of $\varepsilon_{rr}/\varepsilon_{net}$ from FEA (left side) and hybrid method (strain-gage evaluated Airy coefficients, 5 input strains) (right side)

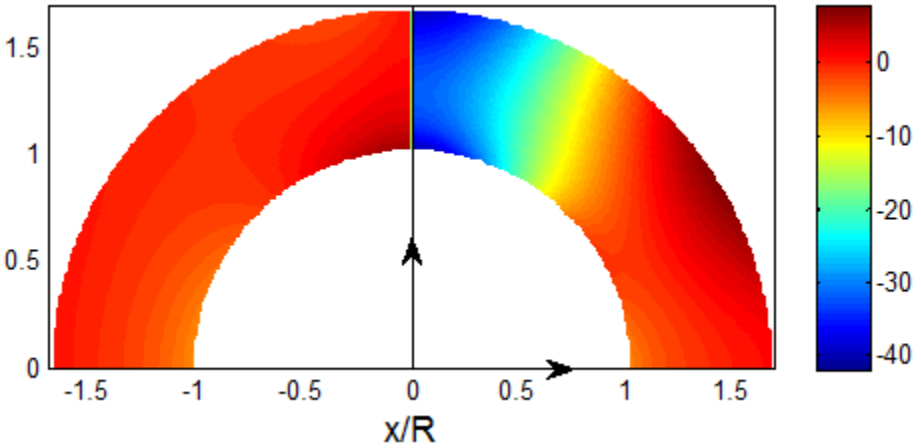

Fig. A4.13: Contours of $\varepsilon_{\theta\theta}/\varepsilon_{net}$ from FEA (left side) and hybrid method (strain-gage evaluated Airy coefficients, 5 input strains) (right side)

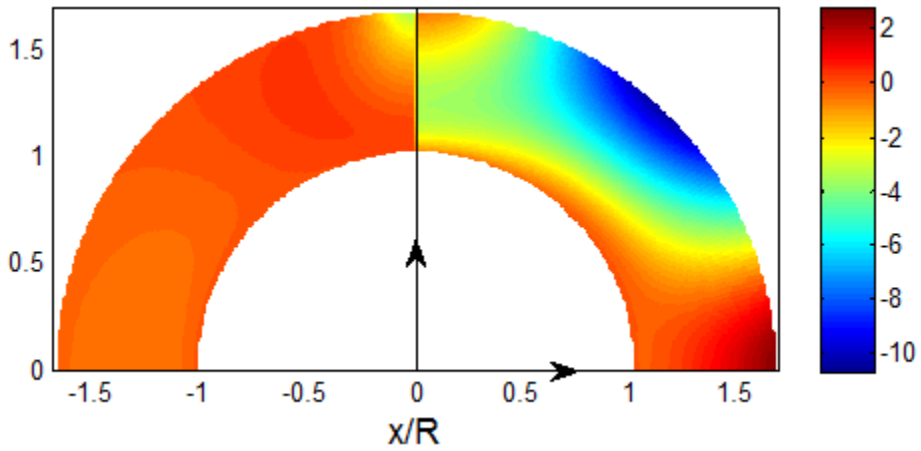

Fig. A4.14: Contours of σ_{rr}/σ_{net} from FEA (left side) and hybrid method (strain-gage evaluated Airy coefficients, 5 input strains) (right side)

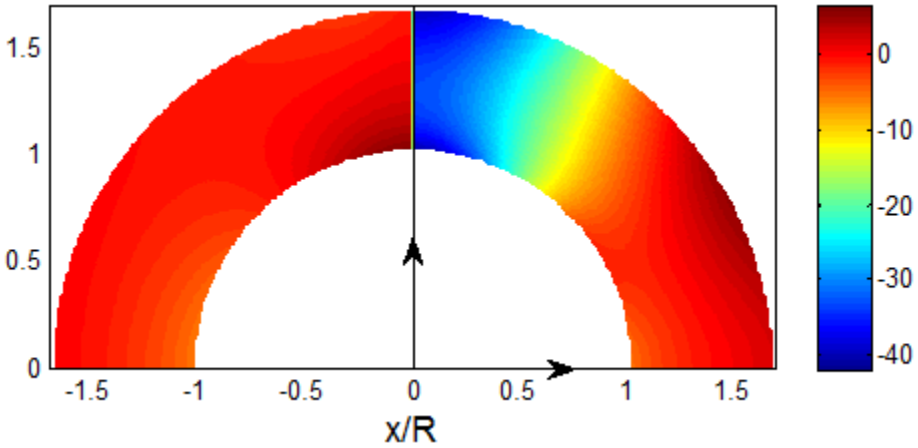

Fig. A4.15: Contours of $\sigma_{\theta\theta}/\sigma_{net}$ from FEA (left side) and hybrid method (strain-gage evaluated Airy coefficients, 5 input strains) (right side)

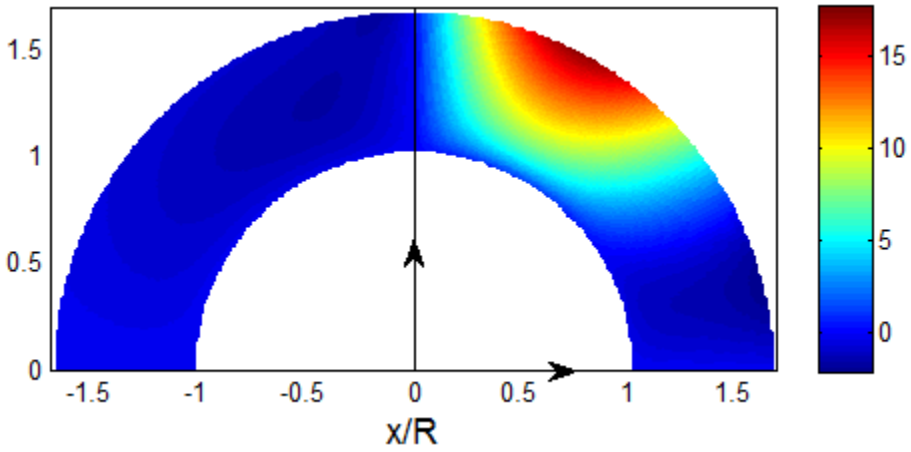

Fig. A4.16: Contours of $\sigma_{r\theta}/\sigma_{net}$ from FEA (left side) and hybrid method (strain-gage evaluated Airy coefficients, 5 input strains) (right side)

Figures A4.1, A4.2, A4.4 through A4.6 and A4.8 through A4.16 illustrate the erroneous results that can occur when one imposes $\sigma_{rr} = \sigma_{r\theta} = 0$ *analytically* on the inside edge of the ring and over virtually all the outside radius together with little measured information within the ring. On the other hand, *figures A4.17 through A4.32* again impose $\sigma_{rr} = \sigma_{r\theta} = 0$ *analytically* on the inner edge of the ring only, plus either 25 or 13 input measured strains. For these situations no boundary conditions (other than the applied load) are imposed on the outer diameter of the ring.

In this latter case (*figures A4.17 through A4.32*) which involves appreciably more measured input strains (13 or 25 input strains) than those of *figures A4.1 through A4.16*, good results are again achieved except of course under the applied point load. Consequently, other than immediately under the loads, reliable results are available from as few as 13 input strains (say at 40^{o} angle increments) and imposing the traction-free conditions *analytically* on only the inner radius of the ring.

All hybrid results of this chapter, including the cases in the Appendix, use $k = 5$ coefficients.

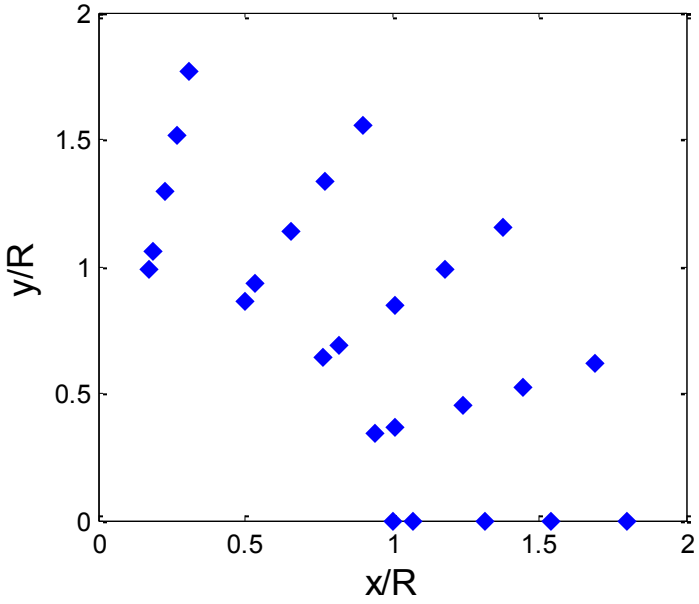

Fig. A4.17: 25 strain gages locations

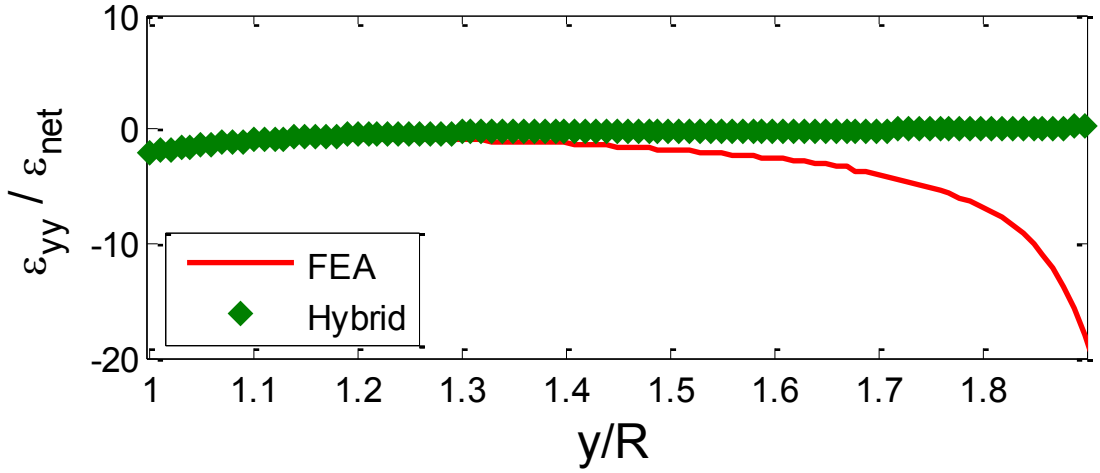

Fig. A4.18: Plot of $\varepsilon_{yy}/\varepsilon_{net}$ along vertical line CD ($\theta = 90^{o}$) of *figure 4.1* from hybrid method (strain-gage evaluated Airy coefficients, 25 input strains) and ANSYS

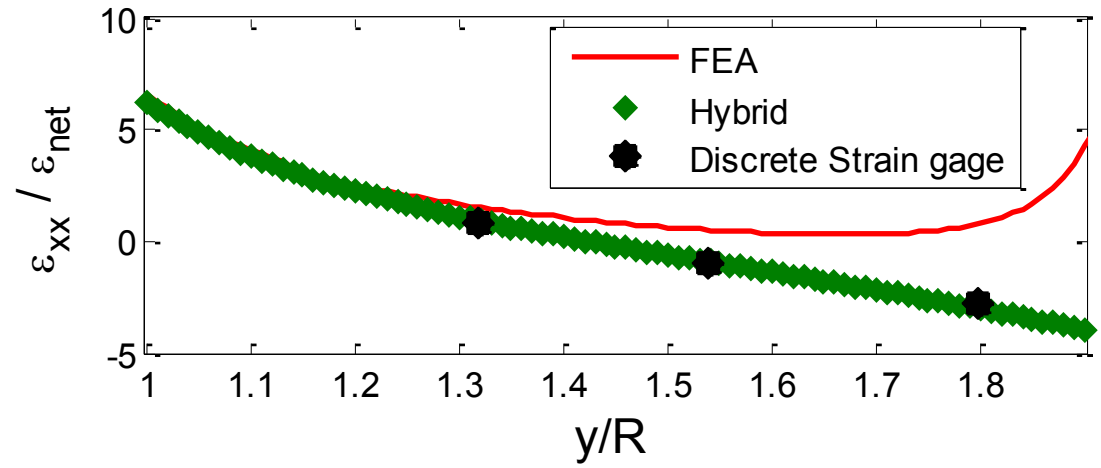

Fig. A4.19: Plot of $\varepsilon_{xx}/\varepsilon_{net}$ along vertical line CD ($\theta = 90^{o}$) of *figure 4.1* from hybrid method (strain-gage evaluated Airy coefficients, 25 input strains), discrete strain gages and ANSYS

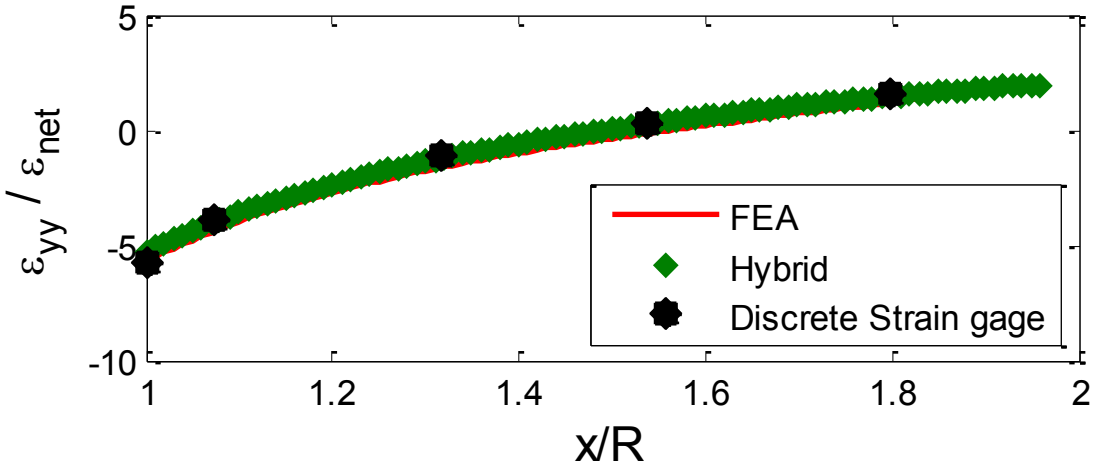

Fig. A4.20: Plot of $\varepsilon_{yy}/\varepsilon_{net}$ along horizontal line AB ($\theta = 0^{o}$) of *figure 4.1* from hybrid method (strain-gage evaluated Airy coefficients, 25 input strains), discrete strain gages and ANSYS

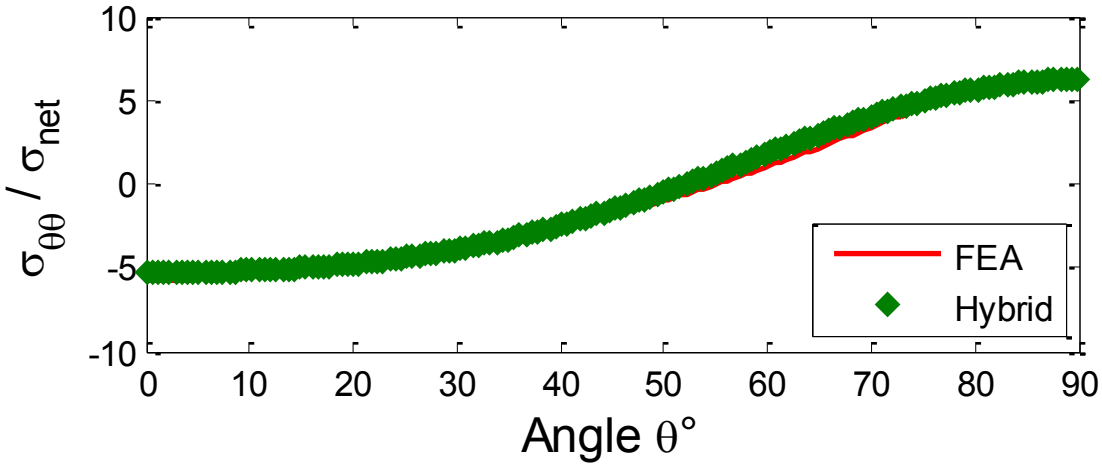

Fig. A4.21: Plot of $\sigma_{\theta\theta}/\sigma_{0}$ along boundary of the hole from hybrid method (strain-gage evaluated Airy coefficients, 25 input strains) and ANSYS

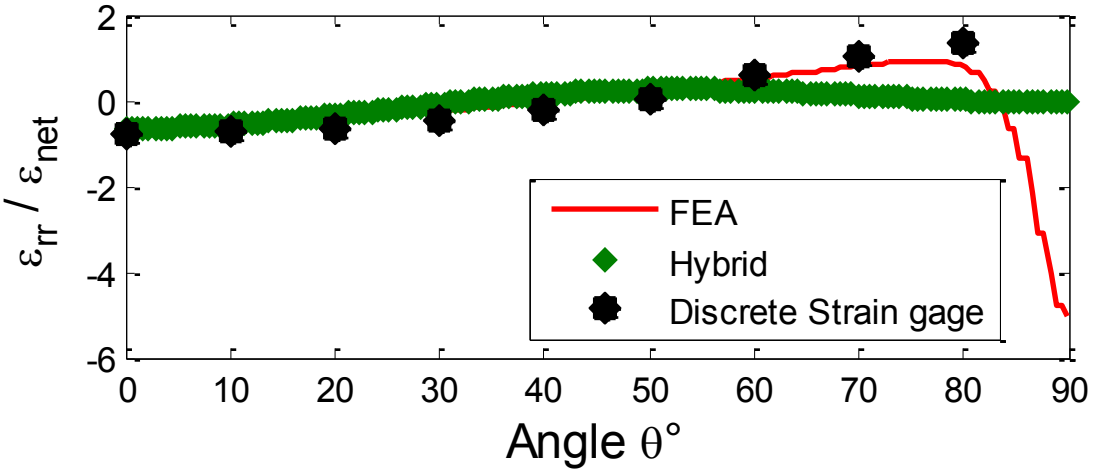

Fig. A4.22: Plot of $\varepsilon_{rr}/\varepsilon_{net}$ at r/R = 1.75 from hybrid method (strain-gage evaluated Airy coefficients, 25 input strains) and ANSYS

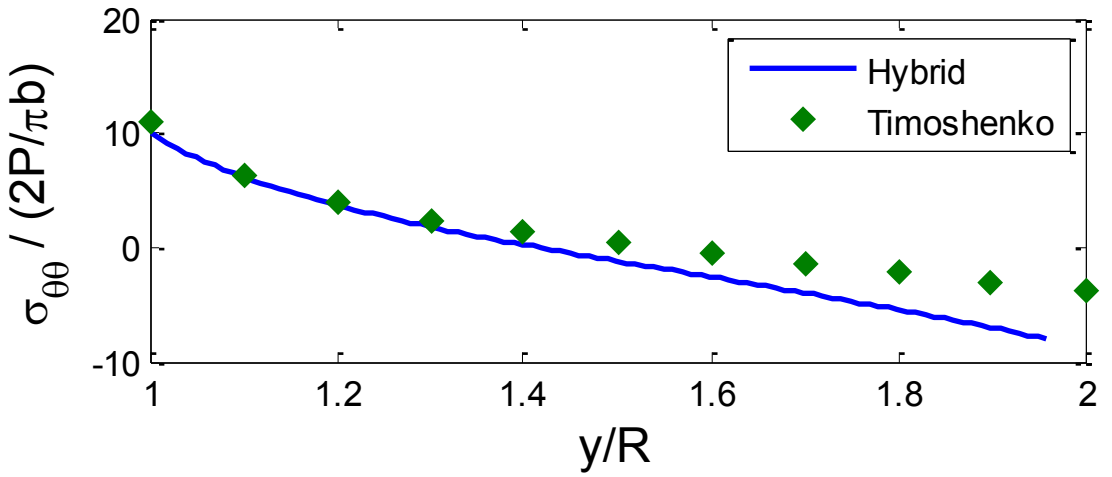

Fig. A4.23: Plot of $\sigma_{\theta\theta}/(2P/\pi b)$ along vertical line CD ($\theta = 90^{o}$) of *figure 4.1* from hybrid method (strain-gage evaluated Airy coefficients, 25 input strains) and Timoshenko [26]

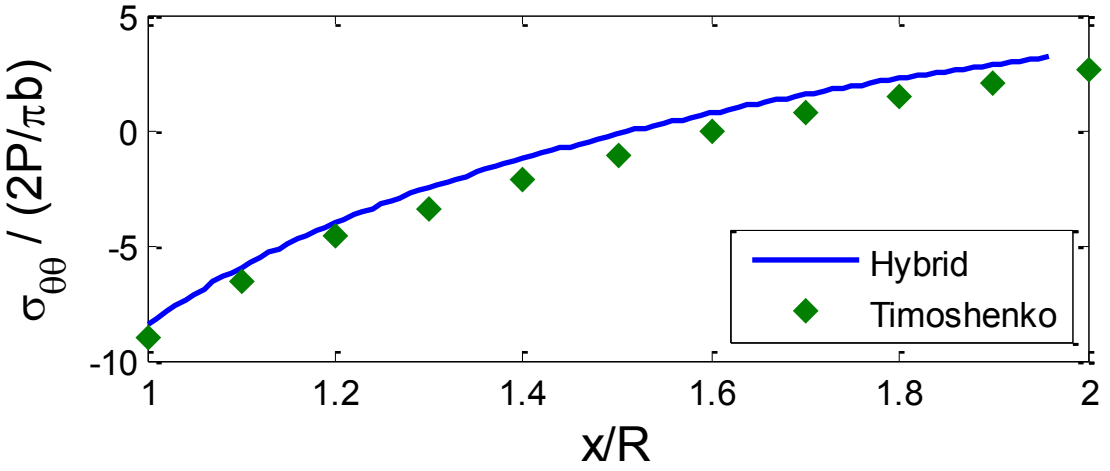

Fig. A4.24: Plot of $\sigma_{\theta\theta}/(2P/\pi b)$ along horizontal line AB ($\theta = 0^{o}$) of *figure 4.1* from hybrid method (strain-gage evaluated Airy coefficients, 25 input strains) and Timoshenko [26]

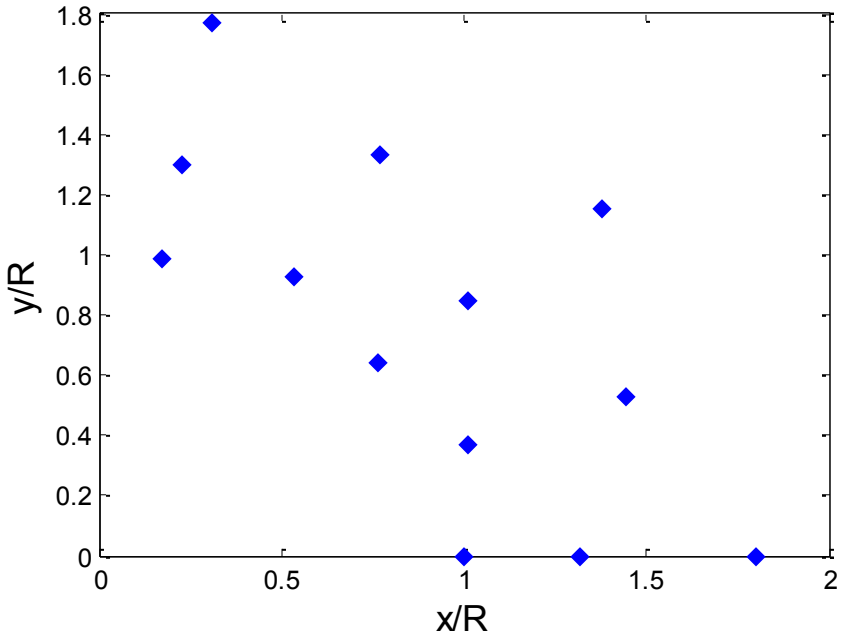

Fig. A4.25: 13 strain gages locations

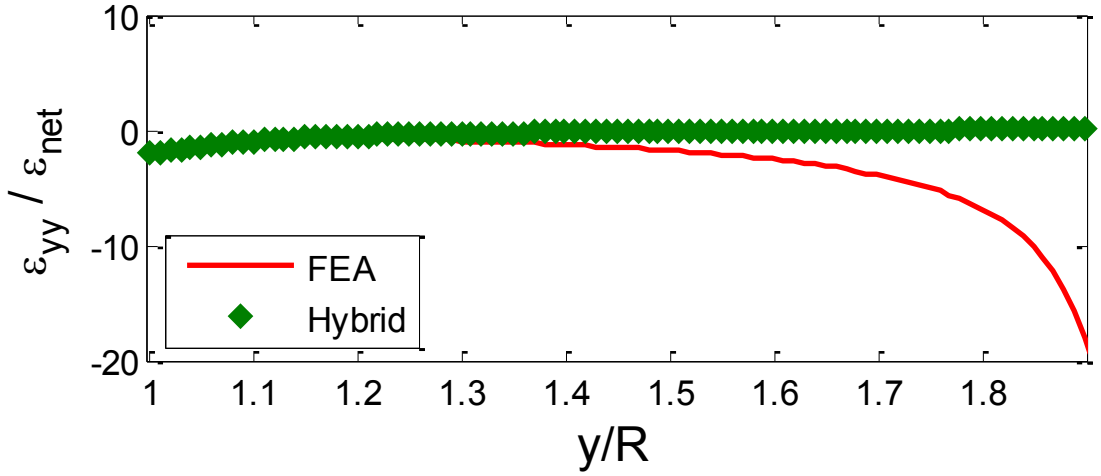

Fig. A4.26: Plot of $\varepsilon_{yy}/\varepsilon_{net}$ along vertical line CD ($\theta = 90^{o}$) of *figure 4.1* from hybrid method (strain-gage evaluated Airy coefficients, 13 input strains) and ANSYS

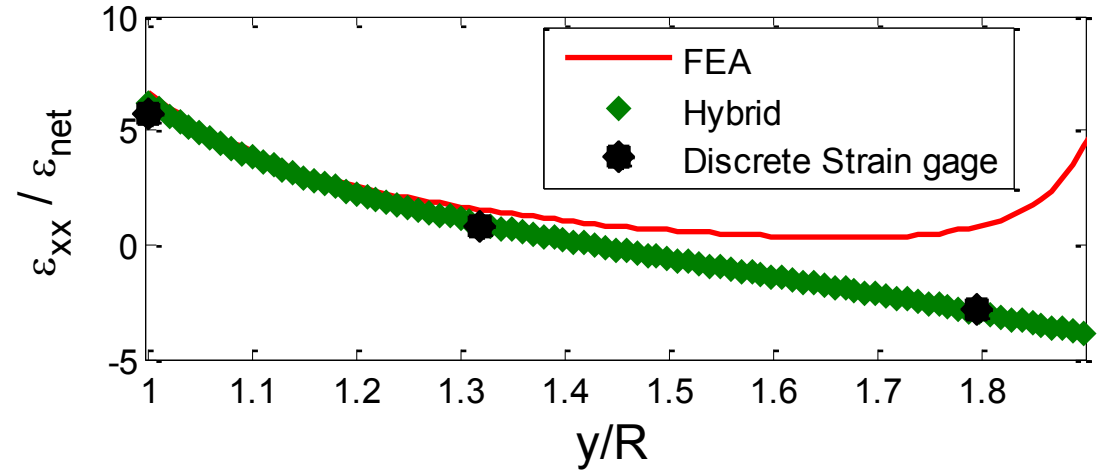

Fig. A4.27: Plot of $\varepsilon_{xx}/\varepsilon_{net}$ along vertical line CD ($\theta = 90^{o}$) of *figure 4.1* from hybrid method (strain-gage evaluated Airy coefficients, 13 input strains), discrete strain gages and ANSYS

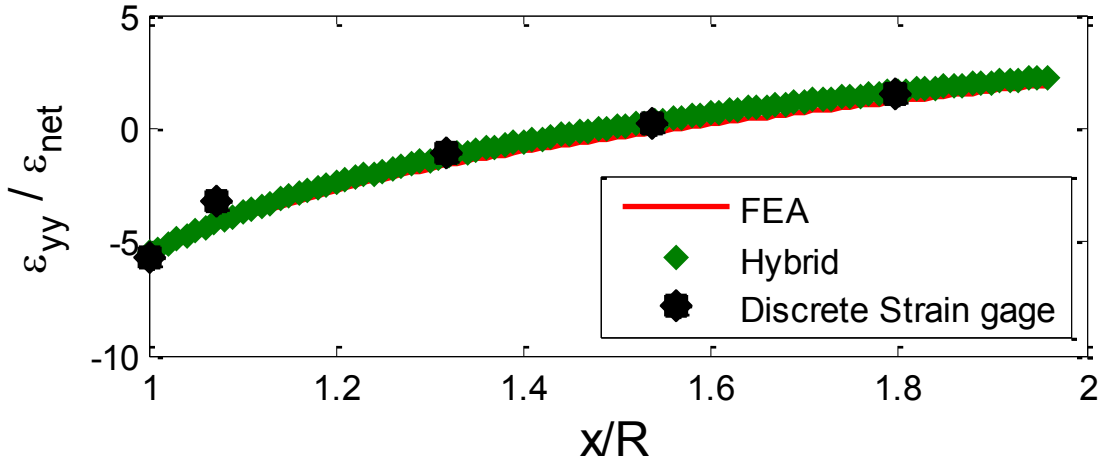

Fig. A4.28: Plot of $\varepsilon_{yy}/\varepsilon_{net}$ along horizontal line AB ($\theta = 0^{o}$) of *figure 4.1* from hybrid method (strain-gage evaluated Airy coefficients, 13 input strains), discrete strain gages and ANSYS

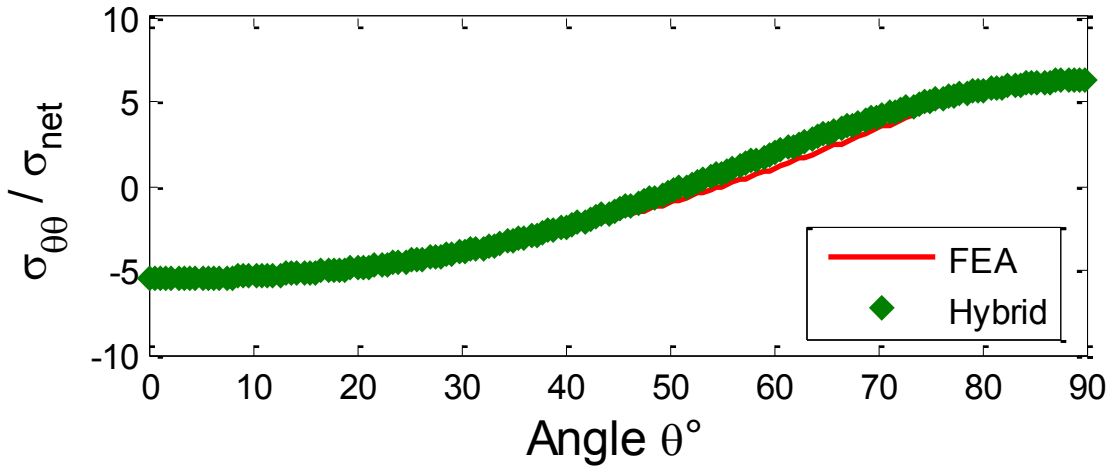

Fig. A4.29: Plot of $\sigma_{\theta\theta}/\sigma_0$ along boundary of the hole from hybrid method (strain-gage evaluated Airy coefficients, 13 input strains) and ANSYS

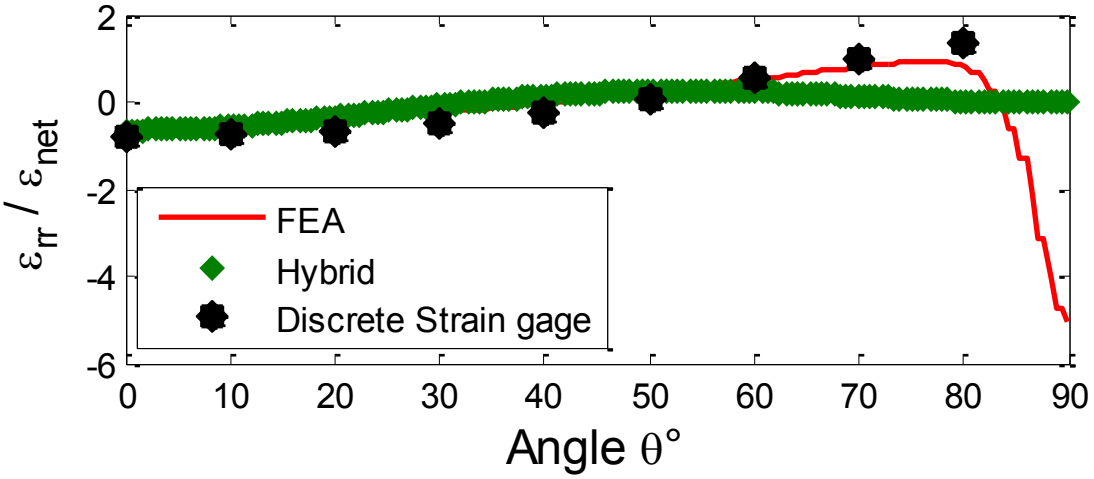

Fig. A4.30: Plot of $\varepsilon_{rr}/\varepsilon_{net}$ at r/R = 1.75 from hybrid method (strain-gage evaluated Airy coefficients, 13 input strains) and ANSYS

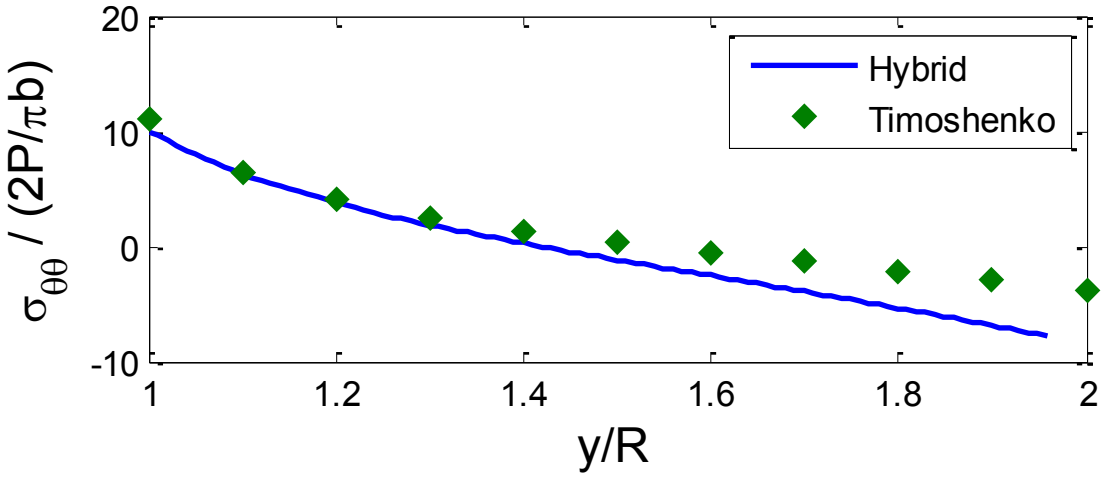

Fig. A4.31: Plot of $\sigma_{\theta\theta}/(2P/\pi b)$ along vertical line CD ($\theta = 90^{o}$) of *figure 4.1* from hybrid method (strain-gage evaluated Airy coefficients, 13 input strains) and Timoshenko [26]

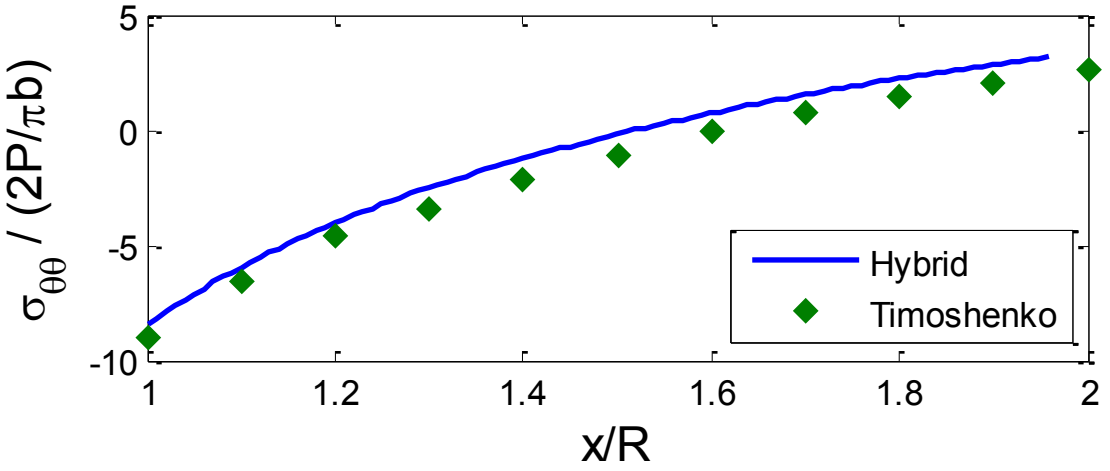

Fig. A4.32: Plot of $\sigma_{\theta\theta}/(2P/\pi b)$ along horizontal line AB ($\theta = 0^{o}$) of *figure 4.1* from hybrid method (strain-gage evaluated Airy coefficients, 13 input strains) and Timoshenko [26]

A5 Stress Equations Corresponding to a Finite plate containing an Elliptical Hole. [25, 29 - 35]

An ellipse is a smooth closed curve which is symmetrical about the *x* and *y* axes. In terms of the *x* and *y* Cartesian rectangular coordinate system, any ellipse may be described by an equation of the type

$$\frac{x^2}{a^2} + \frac{y^2}{b^2} = 1 \tag{5A.1}$$

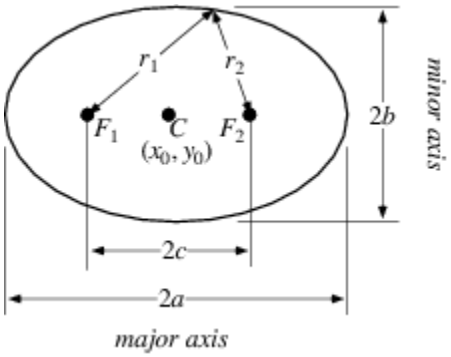

Fig. A5.1: Ellipse showing the major axis (2a) and minor axis (2b)

The elliptical coordinate system is appropriate to describe an ellipse. The maximum and minimum distances along two perpendicular directions in an ellipse are known as the *major axis (2a) or transverse diameter*, and the *minor axis (2b) or conjugate diameter,* respectively**.** There are two special points, F_1 and F_2 in *figure 5A.1,* which are on either side of the center, *C*, on the major axis such that the sum of the distances from any point on the ellipse to those two points is a constant i.e., $r_1 + r_2$ = a constant and equal to the major diameter/axis (*2a*). These two points are called the *foci* of the ellipse. Distance *c* from a focus point to the center is called the *focal distance*. An ellipse is the locus of a point which moves in a plane such that the ratio of its

distances from a fixed point called the *focus* and from a fixed straight line called the *directrix* is always constant and less than 1. This constant ratio is called the *eccentricity* of the ellipse. Relating Cartesian, *x* and *y*, and elliptical coordinates, ξ *and* η, *figure 5A.2*, [25]:

$$x = c\ cosh\xi\ cos\eta \text{ and } y = c\ sinh\xi\ sin\eta \tag{5A.2}$$

where *c* is the focal distance, *figure 5A.1*. ξ is a non-negative real number and $0 \leq \eta < 2\pi$.

When ξ = *a constant,* for an ellipse, *equation 5A.1* can be written as (eliminating η from *equation 5A.2*)

$$\frac{x^2}{c^2\ cosh^2\xi} + \frac{y^2}{c^2\ sinh^2\xi} = 1 \tag{5A.3}$$

which is the equation of the ellipse, such that

$$a = c\ cosh\xi\ \ \&\ \ b = c\ sinh\xi \tag{5A.4}$$

are the respective semi-axes where $\xi = \xi_o$ defines the edge of the elliptical hole of *figures 5.1, 5.2 and 5A.2* and η is measured counter clock-wise from positive *x*-axis, *figure 5A.2*. For different values of ξ one obtains different ellipses all having the same foci, i.e., a family of confocal ellipses. On any one of the ellipses, ξ is a constant and $0 \leq \eta < 2\pi$. This is analogous to a circle where r = a (in terms of polar coordinates) is a constant and $0 \leq \theta \leq 2\pi$.

Quantity η is called the eccentric angle of a point on the ellipse. If *r* and θ are the polar coordinates of a point on the circle circumscribing an ellipse of semi-diameters *a* and *b*, then the perpendicular line from this point on the circle to the *x*-axis intersects the ellipse at *x = a.cost* and *y = b.sint*. Parameter *t* is called the eccentric anomaly in astronomy and is *not* the angle θ with the *x*-axis [30].

Also [31]

$$cosh^2\xi - sinh^2\xi = 1 \tag{5A.5}$$

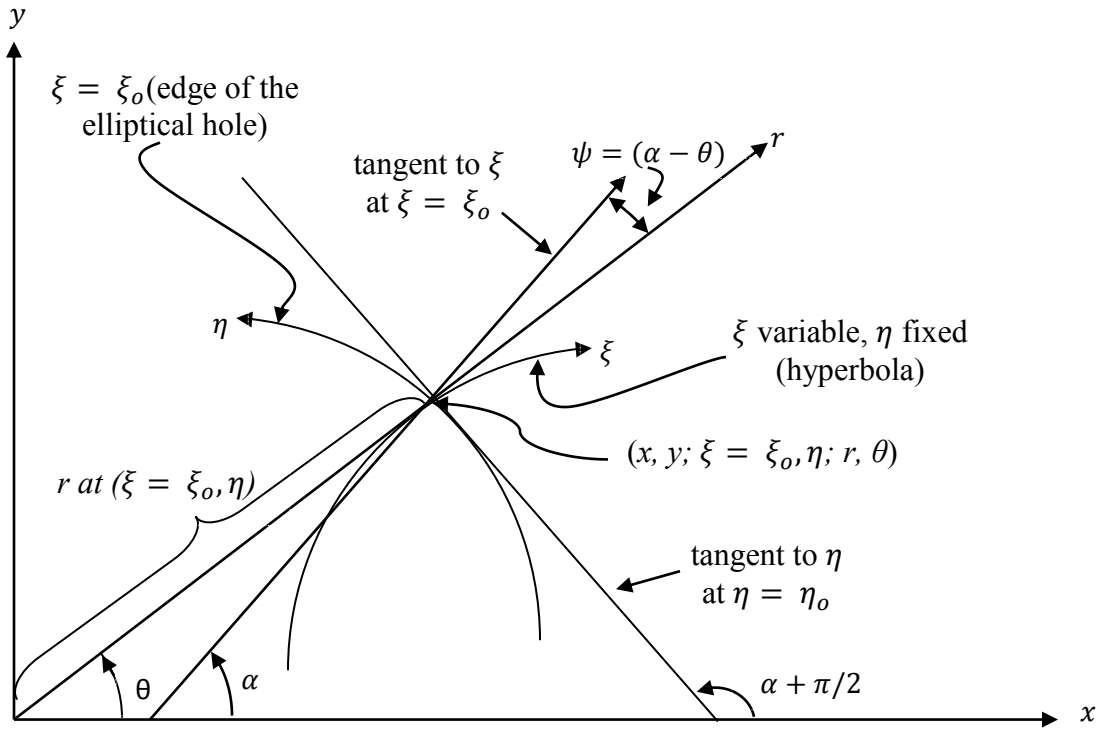

Fig. A5.2: Coordinates Representation

and from *figure 5A.2* [26]

$$tan\alpha = coth\xi\ tan\eta \tag{5A.6}$$

where $\xi\ and\ \eta$ are the elliptical coordinates and angle α is measured from the positive *x*-axis, *figure 5A.2*. On the other hand, when η is *a constant*, eliminating ξ from *equation 5A.2* gives [25]

$$\frac{x^2}{c^2\ cos^2\eta} - \frac{y^2}{c^2\ sin^2\eta} = 1 \tag{5A.7}$$

Equation 5A.7 represents a hyperbola having the same foci as the ellipse, where

$$a = c\cos\eta \;\; \& \;\; b = c\sin\eta \tag{5A.8}$$

Also, one has the identity

$$\cos^2\eta + \sin^2\eta = 1 \text{ [26]} \tag{5A.9}$$

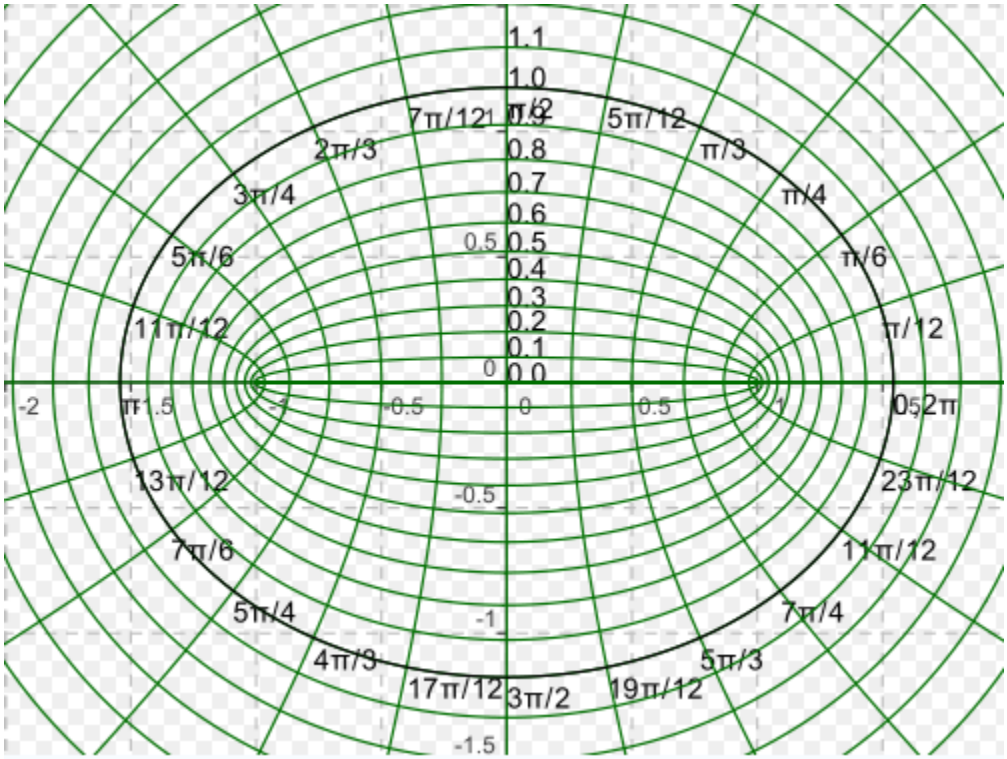

Fig. A5.3 Family of conical ellipses [30]

Lines of an ellipse and those of the associated hyperbola intersect at 90°, *figure 5A.3*. *Figure 5A.3*, which includes the overlapping ellipses and hyperbolas, shows that the value of ξ is a non-negative real number and η varies from 0 to 2π.

A change from Cartesian rectangular coordinates, *x, y,* to polar coordinates, *r, θ, figure 5A.4*, is given by [25]

$$r = \sqrt{x^2 + y^2} \tag{5A.10}$$

$$\theta = \tan^{-1}\left(\frac{y}{x}\right) \tag{5A.11}$$

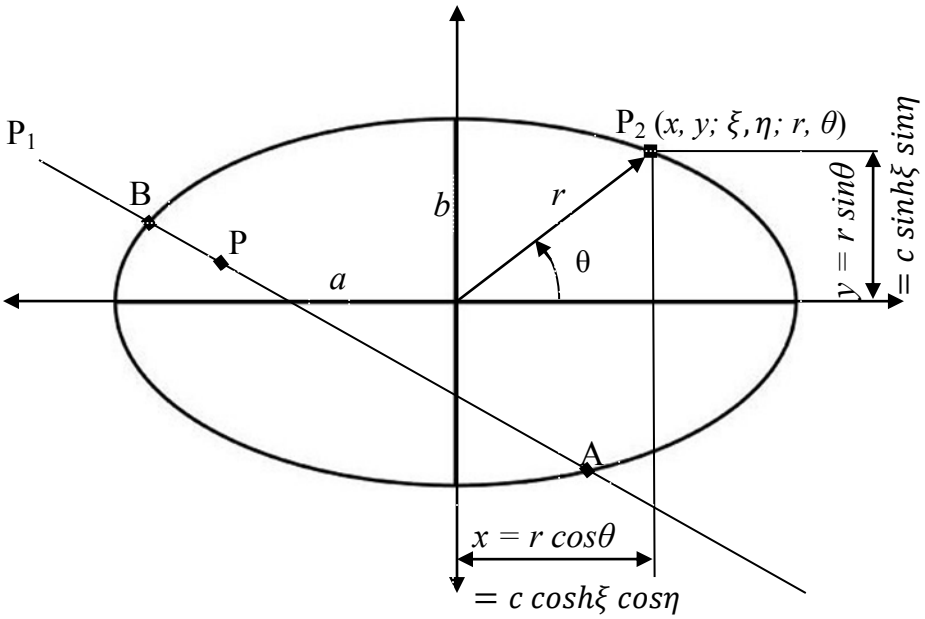

Fig. A5.4: Coordinate system

From *figures 5A.2 and 5A.4* and *equations 5A.2 and 5A.10*, the radius r and the angle θ of any point on the ellipse, $\xi = \xi_o, \eta$ (i.e., edge of the elliptical hole of *figures 5.1 and 5A.2*) varies as, [31, 32]

$$r^2 = \frac{a^2b^2}{a^2\sin^2\theta + b^2\cos^2\theta} \tag{5A.12}$$

and from *equation 5A.11* and *figure 5A.4*

$$\tan\theta = \frac{y}{x} \tag{5A.13}$$

Substituting *equation 5A.2* into *equation 5A.13*, one obtains

$$\tan\theta = \frac{c\,\sinh\xi_o\,\sin\eta}{c\,\cosh\xi_o\,\cos\eta}$$

$$= \tanh\xi_o\,\tan\eta$$

such that

$$tan\eta = coth\xi_o \, tan\theta \tag{5A.14}$$

From *equation 5A.4*

$$\frac{a^2}{b^2} = \frac{cosh^2\xi_o}{sinh^2\xi_o}$$

or

$$coth\xi_o = \frac{a}{b} \tag{5A.15}$$

Also from *equation 5A.4*

$$a^2 - b^2 = c^2 \, cosh^2\xi_o - c^2 \, sinh^2\xi_o$$

$$= c^2 \, (cosh^2\xi_o - sinh^2\xi_o)$$

and using *equation 5A.5*

$$c^2 = a^2 - b^2 \tag{5A.16}$$

The following expressions summarize many of the relevant formulas dealing with tangents, normals, polars and poles of an ellipse centered at the origin and having its major axis 2a along *x*-axis [32, page (2-4.10)]. Although many of these equations are not needed here, they are gathered here for convenience.

- Equation of the ellipse:

$$\frac{x^2}{a^2} + \frac{y^2}{b^2} = 1 \tag{5A.1}$$

- Equation of the tangent, which is the line passing through an ellipse and contacting it at a point (x_1, y_1):

$$\frac{y-y_1}{x-x_1} = \frac{-x_1y_1 \pm \sqrt{b^2{x_1}^2 + a^2{y_1}^2 - a^2b^2}}{a^2 - {x_1}^2} \tag{5A.17}$$

- Equation(s) of tangent(s) of the slope m to the curve:

$$y = mx \pm \sqrt{m^2a^2 - b^2} \tag{5A.18}$$

- Pole and Polars: Poles and Polars come in pairs. Poles are plane points; polars are straight lines in the same plane. If through a fixed point P_1 shown in *figure 5A.4*, outside, inside, or on a conic, a secant is drawn to the conic meeting it in the points A and B, and if P is so chosen on the secant that the points P and P_1 divide the line harmonically, then the locus which contains all the positions of P as the secant revolves about P_1 is called the polar of P_1 with regards to the conic, and the point P_1 is called the pole of the locus. [33, page 159]
- Equation of polar of a point (x_1, y_1) or equation of tangent at a point (x_1, y_1) on the curve:

$$\frac{xx_1}{a^2} + \frac{yy_1}{b^2} = 1 \tag{5A.19}$$

- Coordinates x_1, y_1 of the pole of the straight line Ax + By + C = 0 with respect to the curve:

$$x_1 = -\frac{a^2A}{C};\ y_1 = -\frac{b^2B}{C} \tag{5A.20}$$

- Equation of the normal to the curve (ellipse) at a point (x_1, y_1):

$$\frac{y-y_1}{x-x_1} = \frac{a^2y_1}{b^2x_1} \tag{5A.21}$$

- Conditions satisfied by the "line coordinates" *u, v* of any straight line $\xi x + \eta y + 1 = 0$ tangent to the curve:

$$a^2\xi^2 + b^2\eta^2 = 1 \tag{5A.22}$$

Equations 5A.23 through 5A.30 are special formulas relating to ellipses [32, page (2.5-2)]:

- Eccentricity is the ratio obtained when the distance from the center to a focus is divided by the distance from the center to one of the vertices

$$\text{Eccentricity, } \epsilon = \sqrt{1 - \frac{b^2}{a^2}} < 1 \tag{5A.23}$$

- Focus is one of the two fixed points on the interior of an ellipse used in the formal definition of the curve.

$$\text{Focus or foci, } (a\epsilon, 0) \text{ and } (-a\epsilon, 0) \tag{5A.24}$$

- Directrices are the two parallel lines outside of an ellipse perpendicular to the major axis.

$$\text{Equation of directrix or directrices, } x = \frac{a}{\epsilon}, x = -\frac{a}{\epsilon} \tag{5A.25}$$

- A chord drawn through a focus perpendicular to the major axis is called the latus rectum.

$$\text{latus rectum, } |4p| = \frac{2b^2}{a} \tag{5A.26}$$

- Focal radius or radii of a point (x_1, y_1) on the curve, $r_1 = a + x_1\epsilon$ and $r_1 = a - x_1\epsilon$ (5A.27)

- Equation of diameter conjugate to chords of slope m, $y = -\frac{b^2}{a^2 m}x$ (5A.28)

- Area of segment between the vertex convex to the left and a chord through (x_1, y_1) and (x_1, $-y_1$),

$$\frac{\pi}{2}ab + \frac{b}{a}\left(x_1\sqrt{a^2 - {x_1}^2} + a^2 \sin^{-1}\frac{x_1}{a}\right) \tag{5A.29}$$

- Equation of ellipse in terms of polar coordinates r, θ is,

$$r^2 = \frac{b^2}{1 - \epsilon^2 \cos^2\theta} \tag{5A.30}$$

For a perforated finite plate having mechanical and geometric symmetry with respect to both its x- and y-axes, and its coordinate origin within the cavity, and the plate subjected to uniaxial loading in the vertical *y*-direction, the stress function of *equation 5.2* reduces to

$$\phi = a_0 + b_0 \ln r + c_0 r^2 + \sum_{n=2,4,6,..}^{N} \left\{ \left(a_n r^n + b_n \mathrm{r}^{\mathrm{n+2}} + c_n r^{-n} + d_n \mathrm{r}^{-(\mathrm{n-2})} \right) \cos n\theta \right\} \tag{5A.31}$$

Also,

$$\sigma_{rr} = \frac{1}{r} \cdot \frac{\partial \phi}{\partial r} + \frac{1}{r^2} \frac{\partial^2 \phi}{\partial \theta^2}, \; \sigma_{\theta\theta} = \frac{\partial^2 \phi}{\partial r^2}, \quad \text{and} \quad \sigma_{r\theta} = -\frac{\partial}{\partial r} \cdot \left(\frac{1}{r} \cdot \frac{\partial \phi}{\partial \theta} \right) \tag{5A.32}$$

so the individual polar components of stress become

$$\sigma_{rr} = \frac{b_0}{r^2} + 2c_0 - \sum_{n=2,4,\ldots}^{\mathrm{N}} \begin{bmatrix} a_n \, n \, (n-1) \, r^{n-2} + b_n \, (n+1) \, (n-2) \, r^n \\ + c_n \, n \, (n+1) \, r^{-(n+2)} + d_n \, (n-1)(n+2) \, r^{-n} \end{bmatrix} cos(n\theta) \tag{5A.33}$$

$$\sigma_{\theta\theta} = \frac{-b_0}{r^2} + 2c_0 + \sum_{n=2,4,\ldots}^{N} \begin{bmatrix} a_n \, n \, (n-1) \, r^{n-2} + b_n \, (n+1) \, (n+2) \, r^n \\ + c_n \, n \, (n+1) \, r^{-(n+2)} + d_n \, (n-1)(n-2) \, r^{-n} \end{bmatrix} cos(n\theta) \tag{5A.34}$$

$$\sigma_{r\theta} = \sum_{n=2,4,\ldots}^{N} \begin{bmatrix} a_n \, n \, (n-1) \, r^{n-2} + b_n \, n \, (n+1) \, r^n \\ - c_n \, n \, (n+1) \, r^{-(n+2)} - d_n \, n \, (n-1) \, r^{-n} \end{bmatrix} sin(n\theta) \tag{5A.35}$$

Quantity *r* is the radial coordinate measured from the center of the cavity and angle θ is measured counterclockwise from the *x*-axis, *figures 5A.2 and 5A.4*. *N* is the terminating index

value of the series (since in practice one can only handle a finite number of terms) and it can be any positive even integer.

Stresses acting in the *r-θ* co-ordinate system can be transformed to those in the elliptical co-ordinate system, $\xi \; and \; \eta$, using the following transformation matrix equation:

$$\begin{Bmatrix} \sigma_{\xi\xi} \\ \sigma_{\eta\eta} \\ \sigma_{\xi\eta} \end{Bmatrix} = \begin{bmatrix} cos^2\psi & sin^2\psi & 2\,cos\psi\,sin\psi \\ sin^2\psi & cos^2\psi & -2\,sin\psi\,cos\psi \\ -sin\psi\,cos\psi & sin\psi\,cos\psi & (cos^2\psi - sin^2\psi) \end{bmatrix} \begin{Bmatrix} \sigma_{rr} \\ \sigma_{\theta\theta} \\ \sigma_{r\theta} \end{Bmatrix} \tag{5A.36}$$

where $\psi = \alpha - \theta$. The above transformation matrix can be expanded as:

$$\sigma_{\xi\xi} = \sigma_{rr}cos^2\psi + \sigma_{\theta\theta}sin^2\psi + \sigma_{r\theta}sin2\psi \tag{5A.37}$$

$$\sigma_{\eta\eta} = \sigma_{rr}sin^2\psi + \sigma_{\theta\theta}cos^2\psi - \sigma_{r\theta}sin2\psi \tag{5A.38}$$

$$\sigma_{\xi\eta} = -\sigma_{rr}\,sin\psi\,cos\psi + \sigma_{\theta\theta}sin\psi\,cos\psi + \sigma_{r\theta}(cos^2\psi - sin^2\psi) \tag{5A.39}$$

From *equations 5A.33 through 5A.39*, the individual stresses in the elliptical coordinates become those of *equations 5A.40 through 5A.71*.

$$\sigma_{\xi\xi} = \left[\begin{array}{l} \left\{ \dfrac{b_0}{r^2} + 2c_0 - \displaystyle\sum_{n=2,4,\ldots}^{N} \begin{bmatrix} a_n\,n\,(n-1)\,r^{n-2} + b_n\,(n+1)\,(n-2)\,r^n \\ + c_n\,n\,(n+1)\,r^{-(n+2)} + d_n\,(n-1)(n+2)\,r^{-n} \end{bmatrix} cos(n\theta) \right\} cos^2\psi \\ + \left\{ \dfrac{-b_0}{r^2} + 2c_0 + \displaystyle\sum_{n=2,4,\ldots}^{N} \begin{bmatrix} a_n\,n\,(n-1)\,r^{n-2} + b_n\,(n+1)\,(n+2)\,r^n \\ + c_n\,n\,(n+1)\,r^{-(n+2)} + d_n\,(n-1)(n-2)\,r^{-n} \end{bmatrix} cos(n\theta) \right\} sin^2\psi \\ + \left\{ \displaystyle\sum_{n=2,4,\ldots}^{N} \begin{bmatrix} a_n\,n\,(n-1)\,r^{n-2} + b_n\,n\,(n+1)\,r^n \\ - c_n\,n\,(n+1)\,r^{-(n+2)} - d_n\,n\,(n-1)\,r^{-n} \end{bmatrix} sin(n\theta) \right\} sin2\psi \end{array} \right] \tag{5A.40}$$

$$\sigma_{\xi\xi} = \begin{bmatrix} \frac{b_0}{r^2}cos^2\psi + 2c_0cos^2\psi \; - \frac{b_0}{r^2}sin^2\psi + 2c_0sin^2\psi \\ - \sum_{n=2,4,\ldots}^{N} \begin{bmatrix} a_n\, n\,(n-1)\, r^{n-2} \; + \; b_n\,(n+1)\,(n-2)\, r^n \\ + c_n\, n\,(n+1)\, r^{-(n+2)} \; + \quad d_n\,(n-1)(n+2)\, r^{-n} \end{bmatrix} cos(n\theta)\, cos^2\psi \\ + \sum_{n=2,4,\ldots}^{N} \begin{bmatrix} a_n\, n\,(n-1)\, r^{n-2} \; + \; b_n\,(n+1)\,(n+2)\, r^n \\ + c_n\, n\,(n+1)\, r^{-(n+2)} \; + \quad d_n\,(n-1)(n-2)\, r^{-n} \end{bmatrix} cos(n\theta)\, sin^2\psi \\ + \sum_{n=2,4,\ldots}^{N} \begin{bmatrix} a_n\, n\,(n-1)\, r^{n-2} \; + \; b_n\, n\,(n+1)\; r^n \\ - c_n\, n\,(n+1)\, r^{-(n+2)} - \quad d_n\, n\,(n-1)\, r^{-n} \end{bmatrix} sin(n\theta)\, sin2\psi \end{bmatrix}$$

(5A.41)

$$\sigma_{\xi\xi} = \begin{bmatrix} \frac{b_0}{r^2}cos^2\psi - \frac{b_0}{r^2}sin^2\psi + 2c_0cos^2\psi \; + 2c_0sin^2\psi \\ + \sum_{n=2,4,\ldots}^{N} \begin{Bmatrix} - \begin{bmatrix} a_n\, n\,(n-1)\, r^{n-2} \; + \; b_n\,(n+1)(n-2)r^n \\ + c_n\, n\,(n+1)\, r^{-(n+2)} \; + \quad d_n\,(n-1)(n+2)\, r^{-n} \end{bmatrix} cos(n\theta)\, cos^2\psi \\ + \begin{bmatrix} a_n\, n\,(n-1)\, r^{n-2} \; + \; b_n\,(n+1)(n+2)r^n \\ + c_n\, n\,(n+1)\, r^{-(n+2)} \; + \quad d_n\,(n-1)(n-2)\, r^{-n} \end{bmatrix} cos(n\theta)\, sin^2\psi \\ + \begin{bmatrix} a_n\, n\,(n-1)\, r^{n-2} \; + \; b_n\, n\,(n+1)\; r^n \\ - c_n\, n\,(n+1)\, r^{-(n+2)} - \quad d_n\, n\,(n-1)\, r^{-n} \end{bmatrix} sin(n\theta)\, sin2\psi \end{Bmatrix} \end{bmatrix}$$

(5A.42)

σ_{ξ}

$$= \begin{bmatrix} \frac{b_0}{r^2}(cos^2\psi - sin^2\psi) + 2c_0(cos^2\psi \; + sin^2\psi) \\ + \sum_{n=2,4,\ldots}^{N} \begin{Bmatrix} \begin{bmatrix} -a_n\, n\,(n-1)\, r^{n-2} \; cos(n\theta)\, cos^2\psi - \; b_n\,(n+1)(n-2)r^n \; cos(n\theta)\, cos^2\psi \\ - c_n\, n\,(n+1)\, r^{-(n+2)}\, cos(n\theta)\, cos^2\psi - d_n\,(n-1)(n+2)\, r^{-n}\, cos(n\theta)\, cos^2\psi \end{bmatrix} \\ + \begin{bmatrix} a_n\, n\,(n-1)\, r^{n-2} \; cos(n\theta)\, sin^2\psi \; + \; b_n\,(n+1)(n+2)r^n \; cos(n\theta)\, sin^2\psi \\ + c_n\, n\,(n+1)\, r^{-(n+2)} \; cos(n\theta)\, sin^2\psi \; + \quad d_n\,(n-1)(n-2)\, r^{-n} \; cos(n\theta)\, sin^2\psi \end{bmatrix} \\ + \begin{bmatrix} a_n\, n\,(n-1)\, r^{n-2} \; sin(n\theta)\, sin2\psi + \; b_n\, n\,(n+1)\; r^n \; sin(n\theta)\, sin2\psi \\ - c_n\, n\,(n+1)\, r^{-(n+2)} \; sin(n\theta)\, sin2\psi - \quad d_n\, n\,(n-1)\, r^{-n} \; sin(n\theta)\, sin2\psi \end{bmatrix} \end{Bmatrix} \end{bmatrix}$$

(5A.43)

$\sigma_{\xi\xi}$

$$= \left[\begin{array}{c} \frac{b_0}{r^2} cos2\psi + 2c_0 \\ + \sum_{n=2,4,\ldots}^{N} \left\{ \begin{array}{c} -a_n\, n\,(n-1)\, r^{n-2}\ cos(n\theta)\, cos^2\psi + \ a_n\, n\,(n-1)\, r^{n-2}\ \ sin(n\theta)\, sin2\psi \\ + a_n\, n\,(n-1)\, r^{n-2}\ cos(n\theta)\, sin^2\psi \\ - b_n\,(n+1)(n-2) r^{n}\ cos(n\theta)\, cos^2\psi + \ b_n\,(n+1)(n+2) r^{n}\ cos(n\theta)\, sin^2\psi \\ + b_n\, n\,(n+1)\ r^{n}\ sin(n\theta)\, sin2\psi \\ - c_n\, n\,(n+1)\, r^{-(n+2)}\, cos(n\theta)\, cos^2\psi + c_n\, n\,(n+1)\, r^{-(n+2)}\ cos(n\theta)\, sin^2\psi \\ - c_n\, n\,(n+1)\, r^{-(n+2)}\ sin(n\theta)\, sin2\psi \\ -d_n\,(n-1)(n+2)\, r^{-n}\, cos(n\theta)\, cos^2\psi + \ d_n\,(n-1)(n-2)\, r^{-n}\ cos(n\theta)\, sin^2\psi \\ -\ \ d_n\, n\,(n-1)\, r^{-n}\ sin(n\theta)\, sin2\psi \end{array} \right\} \end{array} \right]$$

(5A.44)

$\sigma_{\xi\xi}$

$$= \left[\begin{array}{c} \frac{b_0}{r^2} cos2\psi + 2c_0 \\ + \sum_{n=2,4,\ldots}^{N} \left\{ \begin{array}{c} a_n\, n\,(n-1)\, r^{n-2}\,[-cos(n\theta)\, cos^2\psi + \ sin(n\theta)\, sin2\psi + cos(n\theta)\, sin^2\psi] \\ +b_n\,(n+1) r^{n} \left[\begin{array}{c} -(n-2)\, cos(n\theta)\, cos^2\psi + (n+2)\, cos(n\theta)\, sin^2\psi \\ +\, n\ sin(n\theta)\, sin2\psi \end{array} \right] \\ + c_n\, n\,(n+1)\, r^{-(n+2)} [-cos(n\theta)\, cos^2\psi + \ cos(n\theta)\, sin^2\psi \ - \ sin(n\theta)\, sin2\psi] \\ +d_n\,(n-1) r^{-n} \left[\begin{array}{c} -(n+2)\, cos(n\theta)\, cos^2\psi + \ (n-2)\, cos(n\theta)\, sin^2\psi \\ -\ \ n\ sin(n\theta)\, sin2\psi \end{array} \right] \end{array} \right\} \end{array} \right]$$

(5A.45)

$$\sigma_{\xi\xi}$$

$$= \left[\begin{array}{c} \frac{b_0}{r^2} cos2\psi + 2c_0 \\ + \sum_{n=2,4,\ldots}^{N} \left\{ \begin{array}{c} a_n\, n\,(n-1)\, r^{n-2}\,[cos(n\theta)\,(-cos^2\psi + sin^2\psi) + \ sin(n\theta)\, sin2\psi] \\ +b_n\,(n+1) r^n \left[\begin{array}{c} -n\, cos(n\theta)\, cos^2\psi + 2\, cos(n\theta)\, cos^2\psi + n\, cos(n\theta)\, sin^2\psi \\ +2\, cos(n\theta)\, sin^2\psi + \ n\ sin(n\theta)\, sin2\psi \end{array} \right] \\ + c_n\, n\,(n+1)\, r^{-(n+2)}[cos(n\theta)\,(-cos^2\psi + sin^2\psi) \ - \ sin(n\theta)\, sin2\psi] \\ +d_n\,(n-1) r^{-n} \left[\begin{array}{c} -n\, cos(n\theta)\, cos^2\psi - 2\, cos(n\theta)\, cos^2\psi + \ n\, cos(n\theta)\, sin^2\psi \\ -2\, cos(n\theta)\, sin^2\psi - \ n\ sin(n\theta)\, sin2\psi \end{array} \right] \end{array} \right\} \end{array} \right]$$

(5A.46)

$$\sigma_{\xi\xi} = \left[\begin{array}{c} \frac{b_0}{r^2} cos2\psi + 2c_0 \\ + \sum_{n=2,4,\ldots}^{N} \left\{ \begin{array}{c} a_n\, n\,(n-1)\, r^{n-2}\,[cos(n\theta)\,(-cos2\psi) + \ sin(n\theta)\, sin2\psi] \\ +b_n\,(n+1) r^n \left[\begin{array}{c} n(-cos(n\theta)\, cos^2\psi + cos(n\theta)\, sin^2\psi + \ sin(n\theta)\, sin2\psi) \\ +2\, cos(n\theta)\,(cos^2\psi + sin^2\psi) \end{array} \right] \\ + c_n\, n\,(n+1)\, r^{-(n+2)}[cos(n\theta)\,(-cos2\psi) \ - \ sin(n\theta)\, sin2\psi] \\ +d_n\,(n-1) r^{-n} \left[\begin{array}{c} n(-cos(n\theta)\, cos^2\psi + \ cos(n\theta)\, sin^2\psi - \ sin(n\theta)\, sin2\psi) \\ -2\, cos(n\theta)\,(cos^2\psi + sin^2\psi) \end{array} \right] \end{array} \right\} \end{array} \right]$$

(5A.47)

$$\sigma_{\xi\xi} = \left[\begin{array}{c} \frac{b_0}{r^2} cos2\psi + 2c_0 \\ + \sum_{n=2,4,\ldots}^{N} \left\{ \begin{array}{c} a_n\, n\,(n-1)\, r^{n-2}\,[-cos(n\theta)\, cos2\psi + \ sin(n\theta)\, sin2\psi] \\ +b_n\,(n+1) r^n \left[\begin{array}{c} n(cos(n\theta)\,(-cos^2\psi + sin^2\psi) + \ sin(n\theta)\, sin2\psi) \\ +2\, cos(n\theta) \end{array} \right] \\ + c_n\, n\,(n+1)\, r^{-(n+2)}[-cos(n\theta)\, cos2\psi \ - \ sin(n\theta)\, sin2\psi] \\ +d_n\,(n-1) r^{-n} \left[\begin{array}{c} n(cos(n\theta)\,(-cos^2\psi + \ sin^2\psi) - \ sin(n\theta)\, sin2\psi) \\ -2\, cos(n\theta) \end{array} \right] \end{array} \right\} \end{array} \right]$$

(5A.48)

$$\sigma_{\xi\xi} = \left[+ \sum_{n=2,4,\ldots}^{N} \begin{Bmatrix} \frac{b_0}{r^2} cos2\psi + 2c_0 \\ a_n\, n\,(n-1)\, r^{n-2}\,[-cos(n\theta+2\psi)] \\ +b_n\,(n+1) r^n [n(-cos(n\theta+2\psi)) + 2\,cos(n\theta)] \\ +\, c_n\, n\,(n+1)\, r^{-(n+2)} [-cos(n\theta-2\psi)] \\ +d_n\,(n-1) r^{-n}\,[n(-cos(n\theta-2\psi)) - 2\,cos(n\theta)] \end{Bmatrix} \right] \tag{5A.49}$$

$$\sigma_{\xi\xi} = \left[+ \sum_{n=2,4,\ldots}^{N} \begin{Bmatrix} \frac{b_0}{r^2} cos2\psi + 2c_0 \\ -\, a_n\, n\,(n-1)\, r^{n-2}\ cos(n\theta+2\psi) \\ +b_n\,(n+1) r^n [-\, n\, cos(n\theta+2\psi) + 2\,cos(n\theta)] \\ -\, c_n\, n\,(n+1)\, r^{-(n+2)}\, cos(n\theta-2\psi) \\ +d_n\,(n-1) r^{-n}\,[-n\, cos(n\theta-2\psi) - 2\,cos(n\theta)] \end{Bmatrix} \right] \tag{5A.50}$$

$$\sigma_{\xi\xi} = \left[- \sum_{n=2,4,\ldots}^{N} \begin{Bmatrix} \frac{b_0}{r^2} cos2\psi + 2c_0 \\ a_n\, n\,(n-1)\, r^{n-2}\ cos(n\theta+2\psi) \\ +b_n\,(n+1) r^n [\, n\, cos(n\theta+2\psi) - 2\,cos(n\theta)] \\ +\, c_n\, n\,(n+1)\, r^{-(n+2)}\, cos(n\theta-2\psi) \\ +d_n\,(n-1) r^{-n}\,[n\, cos(n\theta-2\psi) + 2\,cos(n\theta)] \end{Bmatrix} \right] \tag{5A.51}$$

From the transformation equation:

$$\sigma_{\eta\eta} = \left[\begin{array}{l} \left\{\frac{b_0}{r^2} + 2c_0 - \sum_{n=2,4,\ldots}^{N} \left[\begin{array}{c} a_n\, n\,(n-1)\, r^{n-2} + b_n\,(n+1)\,(n-2)\, r^n \\ + c_n\, n\,(n+1)\, r^{-(n+2)} + d_n\,(n-1)(n+2)\, r^{-n} \end{array}\right] cos(n\theta)\right\} sin^2\psi \\ + \left\{\frac{-b_0}{r^2} + 2c_0 + \sum_{n=2,4,\ldots}^{N} \left[\begin{array}{c} a_n\, n\,(n-1)\, r^{n-2} + b_n\,(n+1)\,(n+2)\, r^n \\ + c_n\, n\,(n+1)\, r^{-(n+2)} + d_n\,(n-1)(n-2)\, r^{-n} \end{array}\right] cos(n\theta)\right\} cos^2\psi \\ - \left\{\sum_{n=2,4,\ldots}^{N} \left[\begin{array}{c} a_n\, n\,(n-1)\, r^{n-2} + b_n\, n\,(n+1)\, r^n \\ - c_n\, n\,(n+1)\, r^{-(n+2)} - d_n\, n\,(n-1)\, r^{-n} \end{array}\right] sin(n\theta)\right\} sin2\psi \end{array}\right] \quad (5A.52)$$

$$\sigma_{\eta\eta} = \left[\begin{array}{l} \frac{b_0}{r^2} sin^2\psi + 2c_0 sin^2\psi - \frac{b_0}{r^2} cos^2\psi + 2c_0 cos^2\psi \\ - \sum_{n=2,4,\ldots}^{N} \left[\begin{array}{c} a_n\, n\,(n-1)\, r^{n-2} + b_n\,(n+1)\,(n-2)\, r^n \\ + c_n\, n\,(n+1)\, r^{-(n+2)} + d_n\,(n-1)(n+2)\, r^{-n} \end{array}\right] cos(n\theta)\, sin^2\psi \\ + \sum_{n=2,4,\ldots}^{N} \left[\begin{array}{c} a_n\, n\,(n-1)\, r^{n-2} + b_n\,(n+1)\,(n+2)\, r^n \\ + c_n\, n\,(n+1)\, r^{-(n+2)} + d_n\,(n-1)(n-2)\, r^{-n} \end{array}\right] cos(n\theta)\, cos^2\psi \\ - \sum_{n=2,4,\ldots}^{N} \left[\begin{array}{c} a_n\, n\,(n-1)\, r^{n-2} + b_n\, n\,(n+1)\, r^n \\ - c_n\, n\,(n+1)\, r^{-(n+2)} - d_n\, n\,(n-1)\, r^{-n} \end{array}\right] sin(n\theta)\, sin2\psi \end{array}\right] \quad (5A.53)$$

$$\sigma_{\eta\eta} = \left[+ \sum_{n=2,4,\ldots}^{N} \left\{ \begin{array}{c} \frac{b_0}{r^2} sin^2\psi - \frac{b_0}{r^2} cos^2\psi + 2c_0 sin^2\psi \; + 2c_0 cos^2\psi \\ -\left[\begin{array}{c} a_n\, n\,(n-1)\, r^{n-2} \; + \; b_n\,(n+1)(n-2) r^n \\ + c_n\, n\,(n+1)\, r^{-(n+2)} \; + \quad d_n\,(n-1)(n+2)\, r^{-n} \end{array} \right] cos(n\theta)\, sin^2\psi \\ +\left[\begin{array}{c} a_n\, n\,(n-1)\, r^{n-2} \; + \; b_n\,(n+1)(n+2) r^n \\ + c_n\, n\,(n+1)\, r^{-(n+2)} \; + \quad d_n\,(n-1)(n-2)\, r^{-n} \end{array} \right] cos(n\theta)\, cos^2\psi \\ -\left[\begin{array}{c} a_n\, n\,(n-1)\, r^{n-2} \; + \; b_n\, n\,(n+1) \; r^n \\ - c_n\, n\,(n+1)\, r^{-(n+2)} - \quad d_n\, n\,(n-1)\, r^{-n} \end{array} \right] sin(n\theta)\, sin2\psi \end{array} \right\} \right]$$

(5A.54)

$\sigma_{\eta\eta}$

$$= \left[+ \sum_{n=2,4,\ldots}^{N} \left\{ \begin{array}{c} \frac{b_0}{r^2} (sin^2\psi - cos^2\psi) + 2c_0 (sin^2\psi \; + cos^2\psi) \\ \left[\begin{array}{c} -a_n\, n\,(n-1)\, r^{n-2} \; cos(n\theta)\, sin^2\psi - \; b_n\,(n+1)(n-2) r^n \; cos(n\theta)\, sin^2\psi \\ - c_n\, n\,(n+1)\, r^{-(n+2)} cos(n\theta)\, sin^2\psi - d_n\,(n-1)(n+2)\, r^{-n} cos(n\theta)\, sin^2\psi \end{array} \right] \\ + \left[\begin{array}{c} a_n\, n\,(n-1)\, r^{n-2} \; cos(n\theta)\, cos^2\psi \; + \; b_n\,(n+1)(n+2) r^n \; cos(n\theta)\, cos^2\psi \\ + c_n\, n\,(n+1)\, r^{-(n+2)} \; cos(n\theta)\, cos^2\psi \; + \quad d_n\,(n-1)(n-2)\, r^{-n} \; cos(n\theta)\, cos^2\psi \end{array} \right] \\ -\left[\begin{array}{c} a_n\, n\,(n-1)\, r^{n-2} \; sin(n\theta)\, sin2\psi + \; b_n\, n\,(n+1) \; r^n \; sin(n\theta)\, sin2\psi \\ - c_n\, n\,(n+1)\, r^{-(n+2)} \; sin(n\theta)\, sin2\psi - \quad d_n\, n\,(n-1)\, r^{-n} \; sin(n\theta)\, sin2\psi \end{array} \right] \end{array} \right\} \right]$$

(5A.55)

$\sigma_{\eta\eta}$

$$= \left[+ \sum_{n=2,4,\ldots}^{N} \left\{ \begin{array}{c} -\frac{b_0}{r^2} cos2\psi + 2c_0 \\ -a_n\, n\,(n-1)\, r^{n-2} \; cos(n\theta)\, sin^2\psi - \; a_n\, n\,(n-1)\, r^{n-2} \; sin(n\theta)\, sin2\psi \\ + a_n\, n\,(n-1)\, r^{n-2} \; cos(n\theta)\, cos^2\psi \\ - b_n\,(n+1)(n-2) r^n \; cos(n\theta)\, sin^2\psi + \; b_n\,(n+1)(n+2) r^n \; cos(n\theta)\, cos^2\psi \\ - b_n\, n\,(n+1) \; r^n \; sin(n\theta)\, sin2\psi \\ - c_n\, n\,(n+1)\, r^{-(n+2)} cos(n\theta)\, sin^2\psi + c_n\, n\,(n+1)\, r^{-(n+2)} \; cos(n\theta)\, cos^2\psi \\ + c_n\, n\,(n+1)\, r^{-(n+2)} \; sin(n\theta)\, sin2\psi \\ -d_n\,(n-1)(n+2)\, r^{-n} cos(n\theta)\, sin^2\psi + \; d_n\,(n-1)(n-2)\, r^{-n} \; cos(n\theta)\, cos^2\psi \\ + \quad d_n\, n\,(n-1)\, r^{-n} \; sin(n\theta)\, sin2\psi \end{array} \right\} \right]$$

(5A.56)

$$\sigma_{\eta\eta}$$

$$= \left[-\frac{b_0}{r^2} cos2\psi + 2c_0 + \sum_{n=2,4,\ldots}^{N} \left\{ \begin{array}{c} a_n\, n\,(n-1)\, r^{n-2}\,[-cos(n\theta)\, sin^2\psi - \, sin(n\theta)\, sin2\psi + cos(n\theta)\, cos^2\psi] \\ +b_n\,(n+1) r^n \left[\begin{array}{c} -(n-2)\, cos(n\theta)\, sin^2\psi + (n+2)\, cos(n\theta)\, cos^2\psi \\ -\, n\, \, sin(n\theta)\, sin2\psi \end{array} \right] \\ + c_n\, n\,(n+1)\, r^{-(n+2)} [-cos(n\theta)\, sin^2\psi + \, cos(n\theta)\, cos^2\psi + sin(n\theta)\, sin2\psi] \\ +d_n\,(n-1) r^{-n} \left[\begin{array}{c} -(n+2)\, cos(n\theta)\, sin^2\psi + \, (n-2)\, cos(n\theta)\, cos^2\psi \\ +\, \, n\, \, sin(n\theta)\, sin2\psi \end{array} \right] \end{array} \right\} \right] \quad (5A.57)$$

$$\sigma_{\eta\eta}$$

$$= \left[-\frac{b_0}{r^2} cos2\psi + 2c_0 + \sum_{n=2,4,\ldots}^{N} \left\{ \begin{array}{c} a_n\, n\,(n-1)\, r^{n-2}\,[cos(n\theta)\,(-sin^2\psi + cos^2\psi) - \, sin(n\theta)\, sin2\psi] \\ +b_n\,(n+1) r^n \left[\begin{array}{c} -n\, cos(n\theta)\, sin^2\psi + 2\, cos(n\theta)\, sin^2\psi + n\, cos(n\theta)\, cos^2\psi \\ +2\, cos(n\theta)\, cos^2\psi - \, \, n\, \, sin(n\theta)\, sin2\psi \end{array} \right] \\ + c_n\, n\,(n+1)\, r^{-(n+2)} [cos(n\theta)\,(-sin^2\psi + cos^2\psi) + \, sin(n\theta)\, sin2\psi] \\ +d_n\,(n-1) r^{-n} \left[\begin{array}{c} -n\, cos(n\theta)\, sin^2\psi - 2\, cos(n\theta)\, sin^2\psi + \, n\, cos(n\theta)\, cos^2\psi \\ -2\, cos(n\theta)\, cos^2\psi + \, \, n\, \, sin(n\theta)\, sin2\psi \end{array} \right] \end{array} \right\} \right] \quad (5A.58)$$

$$\sigma_{\eta\eta} = \left[-\frac{b_0}{r^2} cos2\psi + 2c_0 + \sum_{n=2,4,\ldots}^{N} \left\{ \begin{array}{c} a_n\, n\,(n-1)\, r^{n-2}\,[cos(n\theta)\,(cos2\psi) - \, sin(n\theta)\, sin2\psi] \\ +b_n\,(n+1) r^n \left[\begin{array}{c} n(-cos(n\theta)\, sin^2\psi + cos(n\theta)\, cos^2\psi - \, sin(n\theta)\, sin2\psi) \\ +2\, cos(n\theta)\,(sin^2\psi + cos^2\psi) \end{array} \right] \\ + c_n\, n\,(n+1)\, r^{-(n+2)} [cos(n\theta)\,(cos2\psi) + \, sin(n\theta)\, sin2\psi] \\ +d_n\,(n-1) r^{-n} \left[\begin{array}{c} n(-cos(n\theta)\, sin^2\psi + \, cos(n\theta)\, cos^2\psi + \, sin(n\theta)\, sin2\psi) \\ -2\, cos(n\theta)\,(sin^2\psi + cos^2\psi) \end{array} \right] \end{array} \right\} \right] \quad (5A.59)$$

$$\sigma_{\eta\eta} = \left[+ \sum_{n=2,4,\ldots}^{N} \left\{ \begin{array}{c} -\frac{b_0}{r^2} cos2\psi + 2c_0 \\ a_n\, n\,(n-1)\, r^{n-2}\,[cos(n\theta)\, cos2\psi - \ sin(n\theta)\, sin2\psi] \\ +b_n\,(n+1) r^n \left[\begin{array}{c} n(cos(n\theta)\,(-sin^2\psi + cos^2\psi) - \ sin(n\theta)\, sin2\psi) \\ +2\, cos(n\theta) \end{array} \right] \\ + c_n\, n\,(n+1)\, r^{-(n+2)}[cos(n\theta)\, cos2\psi + \ sin(n\theta)\, sin2\psi] \\ +d_n\,(n-1) r^{-n} \left[\begin{array}{c} n(cos(n\theta)\,(-sin^2\psi + \ cos^2\psi) + \ sin(n\theta)\, sin2\psi) \\ -2\, cos(n\theta) \end{array} \right] \end{array} \right\} \right]$$

(5A.60)

$$\sigma_{\eta\eta} = \left[+ \sum_{n=2,4,\ldots}^{N} \left\{ \begin{array}{c} -\frac{b_0}{r^2} cos2\psi + 2c_0 \\ a_n\, n\,(n-1)\, r^{n-2}\,[cos(n\theta + 2\psi)] \\ +b_n\,(n+1) r^n [n(cos(n\theta + 2\psi)) + 2\, cos(n\theta)] \\ + c_n\, n\,(n+1)\, r^{-(n+2)}[cos(n\theta - 2\psi)] \\ +d_n\,(n-1) r^{-n}\,[n(cos(n\theta - 2\psi)) - 2\, cos(n\theta)] \end{array} \right\} \right]$$

(5A.61)

Now,

$$\sigma_{\xi\eta}$$

$$= \left[\begin{array}{l} \left\{ \frac{b_0}{r^2} + 2c_0 - \sum_{n=2,4,\ldots}^{N} \left[\begin{array}{c} a_n\, n\,(n-1)\, r^{n-2} + b_n\,(n+1)(n-2) r^n \\ + c_n\, n\,(n+1)\, r^{-(n+2)} + d_n\,(n-1)(n+2)\, r^{-n} \end{array} \right] cos(n\theta) \right\} (-sin\psi\, cos\psi) \\ + \left\{ \frac{-b_0}{r^2} + 2c_0 + \sum_{n=2,4,\ldots}^{N} \left[\begin{array}{c} a_n\, n\,(n-1)\, r^{n-2} + b_n\,(n+1)\,(n+2)\, r^n \\ + c_n\, n\,(n+1)\, r^{-(n+2)} + d_n\,(n-1)(n-2)\, r^{-n} \end{array} \right] cos(n\theta) \right\} sin\psi\, cos\psi \\ + \left\{ \sum_{n=2,4,\ldots}^{N} \left[\begin{array}{c} a_n\, n\,(n-1)\, r^{n-2} + b_n\, n\,(n+1)\, r^n \\ - c_n\, n\,(n+1)\, r^{-(n+2)} - d_n\, n\,(n-1)\, r^{-n} \end{array} \right] sin(n\theta) \right\} cos2\psi \end{array} \right] \quad (5A.62)$$

$$\sigma_{\xi\eta} = \left[\begin{array}{l} -\frac{b_0}{r^2} sin\psi\, cos\psi - 2c_0 sin\psi\, cos\psi - \frac{b_0}{r^2} sin\psi\, cos\psi + 2c_0 sin\psi\, cos\psi \\ + \sum_{n=2,4,\ldots}^{N} \left[\begin{array}{c} a_n\, n\,(n-1)\, r^{n-2} + b_n\,(n+1)\,(n-2)\, r^n \\ + c_n\, n\,(n+1)\, r^{-(n+2)} + d_n\,(n-1)(n+2)\, r^{-n} \end{array} \right] cos(n\theta)\, sin\psi\, cos\psi \\ + \sum_{n=2,4,\ldots}^{N} \left[\begin{array}{c} a_n\, n\,(n-1)\, r^{n-2} + b_n\,(n+1)\,(n+2)\, r^n \\ + c_n\, n\,(n+1)\, r^{-(n+2)} + d_n\,(n-1)(n-2)\, r^{-n} \end{array} \right] cos(n\theta)\, sin\psi\, cos\psi \\ + \sum_{n=2,4,\ldots}^{N} \left[\begin{array}{c} a_n\, n\,(n-1)\, r^{n-2} + b_n\, n\,(n+1)\, r^n \\ - c_n\, n\,(n+1)\, r^{-(n+2)} - d_n\, n\,(n-1)\, r^{-n} \end{array} \right] sin(n\theta)\, cos2\psi \end{array} \right] \quad (5A.63)$$

$$\sigma_{\xi\eta} = \left[\begin{array}{c} -\frac{b_0}{r^2} sin\psi\, cos\psi - \frac{b_0}{r^2} sin\psi\, cos\psi - 2c_0 sin\psi\, cos\psi + 2c_0 sin\psi\, cos\psi \\ + \sum_{n=2,4,\ldots}^{N} \left\{ \begin{array}{c} \left[\begin{array}{c} a_n\, n\,(n-1)\, r^{n-2} + b_n\,(n+1)(n-2) r^n \\ + c_n\, n\,(n+1)\, r^{-(n+2)} + d_n\,(n-1)(n+2)\, r^{-n} \end{array} \right] cos(n\theta)\, sin\psi\, cos\psi \\ + \left[\begin{array}{c} a_n\, n\,(n-1)\, r^{n-2} + b_n\,(n+1)(n+2) r^n \\ + c_n\, n\,(n+1)\, r^{-(n+2)} + d_n\,(n-1)(n-2)\, r^{-n} \end{array} \right] cos(n\theta)\, sin\psi\, cos\psi \\ + \left[\begin{array}{c} a_n\, n\,(n-1)\, r^{n-2} + b_n\, n\,(n+1)\, r^n \\ - c_n\, n\,(n+1)\, r^{-(n+2)} - d_n\, n\,(n-1)\, r^{-n} \end{array} \right] sin(n\theta)\, cos2\psi \end{array} \right\} \end{array} \right]$$

(5A.64)

$$\sigma_{\xi\eta} = \left[\begin{array}{c} -\frac{2b_0}{r^2} sin\psi\, cos\psi \\ + \sum_{n=2,4,\ldots}^{N} \left\{ \begin{array}{c} \left[\begin{array}{c} a_n\, n\,(n-1)\, r^{n-2}\, cos(n\theta)\, sin\psi\, cos\psi \\ + b_n\,(n+1)(n-2) r^n\, cos(n\theta)\, sin\psi\, cos\psi \\ + c_n\, n\,(n+1)\, r^{-(n+2)}\, cos(n\theta)\, sin\psi\, cos\psi \\ + d_n\,(n-1)(n+2)\, r^{-n}\, cos(n\theta)\, sin\psi\, cos\psi \end{array} \right] \\ + \left[\begin{array}{c} a_n\, n\,(n-1)\, r^{n-2}\, cos(n\theta)\, sin\psi\, cos\psi \\ + b_n\,(n+1)(n+2) r^n\, cos(n\theta)\, sin\psi\, cos\psi \\ + c_n\, n\,(n+1)\, r^{-(n+2)}\, cos(n\theta)\, sin\psi\, cos\psi \\ + d_n\,(n-1)(n-2)\, r^{-n}\, cos(n\theta)\, sin\psi\, cos\psi \end{array} \right] \\ + \left[\begin{array}{c} a_n\, n\,(n-1)\, r^{n-2}\, sin(n\theta)\, cos2\psi \\ + b_n\, n\,(n+1)\, r^n\, sin(n\theta)\, cos2\psi \\ - c_n\, n\,(n+1)\, r^{-(n+2)}\, sin(n\theta)\, cos2\psi \\ - d_n\, n\,(n-1)\, r^{-n} sin(n\theta)\, cos2\psi \end{array} \right] \end{array} \right\} \end{array} \right]$$

(5A.65)

$$\sigma_{\xi\eta} = \left[-\frac{2b_0}{r^2} sin\psi\ cos\psi + \sum_{n=2,4,\ldots}^{N} \left\{ \begin{array}{c} a_n\, n\,(n-1)\, r^{n-2}\ cos(n\theta)\, sin\psi\ cos\psi \\ +\, a_n\, n\,(n-1)\, r^{n-2}\ cos(n\theta)\, sin\psi\ cos\psi \\ +a_n\, n\,(n-1)\, r^{n-2}\ \ sin(n\theta)\, cos2\psi \\ +b_n\,(n+1)(n-2) r^{n}\ cos(n\theta)\, sin\psi\ cos\psi \\ +b_n\,(n+1)(n+2) r^{n}\ cos(n\theta)\, sin\psi\ cos\psi \\ +\, b_n\, n\,(n+1)\ \ r^{n}\ sin(n\theta)\, cos2\psi \\ +\, c_n\, n\,(n+1)\, r^{-(n+2)}\, cos(n\theta)\, sin\psi\ cos\psi \\ +c_n n\,(n+1)\, r^{-(n+2)}\ cos(n\theta)\, sin\psi\ cos\psi \\ -\, c_n\, n\,(n+1)\, r^{-(n+2)}\ sin(n\theta)\, cos2\psi \\ +d_n\,(n-1)(n+2)\, r^{-n}\, cos(n\theta)\, sin\psi\ cos\psi \\ +d_n\,(n-1)(n-2)\, r^{-n}\ cos(n\theta)\, sin\psi\ cos\psi \\ -\ \ d_n\, n\,(n-1)\, r^{-n}\ sin(n\theta)\, cos2\psi \end{array} \right\} \right]$$

(5A.66)

$\sigma_{\xi\eta}$

$$= \left[-\frac{2b_0}{r^2} sin\psi\ cos\psi + \sum_{n=2,4,\ldots}^{N} \left\{ \begin{array}{c} a_n\, n\,(n-1)\, r^{n-2}\,[cos(n\theta)\, sin\psi\ cos\psi + cos(n\theta)\, sin\psi\ cos\psi +\ sin(n\theta)\, cos2\psi] \\ +b_n\,(n+1) r^{n}\left[\begin{array}{c}(n-2)\ cos(n\theta)\, sin\psi\ cos\psi + (n+2)\ cos(n\theta)\, sin\psi\ cos\psi \\ +\, n\ sin(n\theta)\, cos2\psi\end{array}\right] \\ +\, c_n\, n\,(n+1)\, r^{-(n+2)}[\, cos(n\theta)\, sin\psi\ cos\psi +\ cos(n\theta)\, sin\psi\ cos\psi -\ sin(n\theta)\, cos2\psi] \\ +d_n\,(n-1) r^{-n}\left[\begin{array}{c}(n+2)\ cos(n\theta)\, sin\psi\ cos\psi +\ (n-2)\ cos(n\theta)\, sin\psi\ cos\psi \\ -\ \ n\ sin(n\theta)\, cos2\psi\end{array}\right] \end{array} \right\} \right]$$

(5A.67)

$$\sigma_{\xi\eta}$$

$$= \left[\begin{array}{c} -\frac{2b_0}{r^2} sin\psi\ cos\psi \\ + \sum_{n=2,4,\ldots}^{N} \left\{ \begin{array}{c} a_n\, n\,(n-1)\, r^{n-2}\,[2\ cos(n\theta)\, sin\psi\ cos\psi + \ sin(n\theta)\, cos2\psi] \\ +b_n\,(n+1) r^n \left[\begin{array}{c} n\ cos(n\theta)\, sin\psi\ cos\psi - 2\ cos(n\theta)\, sin\psi\ cos\psi + n\ cos(n\theta)\, sin\psi\ cos\psi \\ +2\ cos(n\theta)\, sin\psi\ cos\psi + \ n\ sin(n\theta)\, cos2\psi \end{array} \right] \\ +\, c_n\, n\,(n+1)\, r^{-(n+2)} [2\ cos(n\theta)\, sin\psi\ cos\psi\ -\ sin(n\theta)\, cos2\psi] \\ +d_n\,(n-1) r^{-n} \left[\begin{array}{c} n\ cos(n\theta)\, sin\psi\ cos\psi + 2\ cos(n\theta)\, sin\psi\ cos\psi + \ n\ cos(n\theta)\, sin\psi\ cos\psi \\ -2\ cos(n\theta)\, sin\psi\ cos\psi - \ n\ sin(n\theta)\, cos2\psi \end{array} \right] \end{array} \right\} \end{array} \right]$$

(5A.68)

$$\sigma_{\xi\eta} = \left[\begin{array}{c} -\frac{2b_0}{r^2} sin\psi\ cos\psi \\ + \sum_{n=2,4,\ldots}^{N} \left\{ \begin{array}{c} a_n\, n\,(n-1)\, r^{n-2}\,[cos(n\theta)\,(sin2\psi) + \ sin(n\theta)\, cos2\psi] \\ +b_n\,(n+1) r^n \left[\begin{array}{c} n(2\ cos(n\theta)\, sin\psi\ cos\psi + \ sin(n\theta)\, cos2\psi) \\ +2\, cos(n\theta)\,(-sin\psi\ cos\psi + sin\psi\ cos\psi) \end{array} \right] \\ +\, c_n\, n\,(n+1)\, r^{-(n+2)} [cos(n\theta)\,(sin2\psi)\ -\ sin(n\theta)\, cos2\psi] \\ +d_n\,(n-1) r^{-n} \left[\begin{array}{c} n(2\ cos(n\theta)\, sin\psi\ cos\psi - \ sin(n\theta)\, cos2\psi) \\ +2\, cos(n\theta)\,(sin\psi\ cos\psi - sin\psi\ cos\psi) \end{array} \right] \end{array} \right\} \end{array} \right]$$

(5A.69)

$$\sigma_{\xi\eta} = \left[\begin{array}{c} -\frac{b_0}{r^2} sin2\psi \\ + \sum_{n=2,4,\ldots}^{N} \left\{ \begin{array}{c} a_n\, n\,(n-1)\, r^{n-2} \sin(n\theta + 2\psi) \\ +b_n\,(n+1) r^n [n(cos(n\theta)\, sin2\psi + \ sin(n\theta)\, cos2\psi)] \\ -\, c_n\, n\,(n+1)\, r^{-(n+2)} \sin(n\theta - 2\psi) \\ +d_n\,(n-1) r^{-n} \,[n(cos(n\theta)\, sin2\psi - \ sin(n\theta)\, cos2\psi)] \end{array} \right\} \end{array} \right]$$

(5A.70)

$$\sigma_{\xi\eta} = \left[+ \sum_{n=2,4,\ldots}^{N} \begin{Bmatrix} -\frac{b_0}{r^2} sin2\psi \\ a_n\, n\,(n-1)\, r^{n-2} \sin(n\theta + 2\psi) \\ +b_n n\,(n+1) r^n \sin(n\theta + 2\psi) \\ -c_n\, n\,(n+1)\, r^{-(n+2)} \sin(n\theta - 2\psi) \\ -d_n n\,(n-1) r^{-n} \sin(n\theta - 2\psi) \end{Bmatrix} \right] \tag{5A.71}$$

Now from *equations 5.18, 5A.51 and 5A.61*,

$$S = \sigma_{\xi\xi} + \sigma_{\eta\eta} \tag{5A.72}$$

$$S = \left[\left[\begin{Bmatrix} \frac{b_0}{r^2} cos2\psi + 2c_0 \\ a_n\, n\,(n-1)\, r^{n-2}\ cos(n\theta + 2\psi) \\ +b_n\,(n+1) r^n [\, n\, cos(n\theta + 2\psi) - 2\, cos(n\theta)] \\ +\, c_n\, n\,(n+1)\, r^{-(n+2)}\, cos(n\theta - 2\psi) \\ +d_n\,(n-1) r^{-n}\, [n\, cos(n\theta - 2\psi) + 2\, cos(n\theta)] \end{Bmatrix} \right] \right.$$
$$\left. + \left[\begin{Bmatrix} -\frac{b_0}{r^2} cos2\psi + 2c_0 \\ a_n\, n\,(n-1)\, r^{n-2}\, [cos(n\theta + 2\psi)] \\ +b_n\,(n+1) r^n [n(cos(n\theta + 2\psi)) + 2\, cos(n\theta)] \\ +\, c_n\, n\,(n+1)\, r^{-(n+2)} [cos(n\theta - 2\psi)] \\ +d_n\,(n-1) r^{-n}\, [n(cos(n\theta - 2\psi)) - 2\, cos(n\theta)] \end{Bmatrix} \right] \right]$$

$$\sum_{n=2,4,\ldots}^{N} \tag{5A.73}$$

$$S = \left[+ \sum_{n=2,4,\ldots}^{N} \begin{Bmatrix} 4\, c_0 \\ +b_n\, 4\,(n+1) r^n\, cos(n\theta) \\ -d_n\, 4\,(n-1) r^{-n}\, cos(n\theta) \end{Bmatrix} \right] \tag{5A.74}$$

Verifying the equations:

$$S = \sigma_{rr} + \sigma_{\theta\theta} \tag{5A.75}$$

and from *equations 5A.33 and 5A.34*

$$S = \left[\begin{array}{l} \left[\dfrac{b_0}{r^2} + 2c_0 - \displaystyle\sum_{n=2,4,\ldots}^{\mathrm{N}} \left[\begin{array}{c} a_n\, n\,(n-1)\, r^{n-2} + b_n\,(n+1)(n-2) r^n \\ + c_n\, n\,(n+1)\, r^{-(n+2)} + d_n\,(n-1)(n+2)\, r^{-n} \end{array} \right] cos(n\theta) \right] \\ + \left[\dfrac{-b_0}{r^2} + 2c_0 + \displaystyle\sum_{n=2,4,\ldots}^{N} \left[\begin{array}{c} a_n\, n\,(n-1)\, r^{n-2} + b_n\,(n+1)\,(n+2)\, r^n \\ + c_n\, n\,(n+1)\, r^{-(n+2)} + d_n\,(n-1)(n-2)\, r^{-n} \end{array} \right] cos(n\theta) \right] \end{array} \right] \tag{5A.76}$$

$$S = \left[\begin{array}{c} \dfrac{b_0}{r^2} + 2c_0 - \dfrac{b_0}{r^2} + 2c_0 \\ - \displaystyle\sum_{n=2,4,\ldots}^{\mathrm{N}} \left[\begin{array}{c} a_n\, n\,(n-1)\, r^{n-2} + b_n\,(n+1)(n-2) r^n \\ + c_n\, n\,(n+1)\, r^{-(n+2)} + d_n\,(n-1)(n+2)\, r^{-n} \\ - \left(\begin{array}{c} a_n\, n\,(n-1)\, r^{n-2} + b_n\,(n+1)\,(n+2)\, r^n \\ + c_n\, n\,(n+1)\, r^{-(n+2)} + d_n\,(n-1)(n-2)\, r^{-n} \end{array} \right) \end{array} \right] cos(n\theta) \end{array} \right] \tag{5A.77}$$

$$S = \left[\begin{array}{c} \frac{b_0}{r^2} - \frac{b_0}{r^2} + 2c_0 + 2c_0 \\ - \displaystyle\sum_{n=2,4,\ldots}^{\mathrm{N}} \left[\begin{array}{c} a_n\, n\,(n-1)\, r^{n-2} - a_n\, n\,(n-1)\, r^{n-2} \\ + b_n\,(n+1)(n-2) r^n - b_n\,(n+1)\,(n+2)\, r^n \\ + c_n\, n\,(n+1)\, r^{-(n+2)} - c_n\, n\,(n+1)\, r^{-(n+2)} \\ + d_n\,(n-1)(n+2)\, r^{-n} - d_n\,(n-1)(n-2)\, r^{-n} \end{array} \right] cos(n\theta) \end{array} \right] \tag{5A.78}$$

$$S = \left[4c_0 - \sum_{n=2,4,\ldots}^{N} \begin{bmatrix} +\, b_n\,(n+1)(n-2)r^n \;-\; b_n\,(n+1)\,(n+2)\,r^n \\ +\, d_n\,(n-1)(n+2)\,r^{-n} \;-\; d_n\,(n-1)(n-2)\,r^{-n} \end{bmatrix} cos(n\theta) \right] \tag{5A.79}$$

$$S = \left[4c_0 - \sum_{n=2,4,\ldots}^{N} \begin{bmatrix} +\, b_n\,(n+1)[n-2-\,(n+2)]r^n \\ +\, d_n\,(n-1)[n+2-\,(n-2)]\,r^{-n} \end{bmatrix} cos(n\theta) \right] \tag{5A.80}$$

$$S = \left[4c_0 - \sum_{n=2,4,\ldots}^{N} \begin{bmatrix} +\, b_n\,(n+1)[n-2-\,n-2)]r^n \\ +\, d_n\,(n-1)[n+2-\,n+2\,]\,r^{-n} \end{bmatrix} cos(n\theta) \right] \tag{5A.81}$$

$$S = \left[4\,c_0 + \sum_{n=2,4,\ldots}^{N} \begin{Bmatrix} +b_n\,4\,(n+1)r^n\,cos(n\theta) \\ -d_n\,4\,(n-1)r^{-n}\,cos(n\theta) \end{Bmatrix} \right] \tag{5A.82}$$

Equations 5A.74 and 5A.82 agree with each other, as they should.

Imposing traction-free conditions *discretely* on the boundary of the elliptical hole of *figure 5A.1* having radii *a* and *b*:

when r = R; $\sigma_{\xi\xi} = \sigma_{\xi\eta} = 0$, and from *equations 5A.12 to 5A.16,*

$$R^2 = \frac{a^2 b^2}{a^2 sin^2\theta + b^2 cos^2\theta} \tag{5A.83}$$

such that R is the polar distance from the center of the elliptical hole to position ξ_o, η_o on the edge of the hole, where a = 38.1 mm, b = 19.05 mm and θ is the associate polar angle in first quadrant, see *figure 5A.2*.

Recognizing that the lines of associate ellipse and hyperbola intersect at 90°, an alternative approach for imposing $\sigma_{\xi\xi} = \sigma_{\xi\eta} = 0$ on the edge of the hole might be to consider the orthogonal lines of the associated hyperbola at the discrete points on the edge of elliptical cut-out.

From *equations 5A.51 and 5A.71*,

$$\sigma_{\xi\xi}(@\ r = R) = \left[\begin{array}{c} \frac{b_0}{R^2} cos2\psi + 2c_0 \\ -\sum_{n=2,4,\ldots}^{N} \left\{ \begin{array}{c} a_n\, n\,(n-1)\, R^{n-2}\ cos(n\theta + 2\psi) \\ +b_n\,(n+1) R^n [\, n\, cos(n\theta + 2\psi) - 2\, cos(n\theta)] \\ +\, c_n\, n\,(n+1)\, R^{-(n+2)}\, cos(n\theta - 2\psi) \\ +d_n\,(n-1) R^{-n}\, [n\, cos(n\theta - 2\psi) + 2\, cos(n\theta)] \end{array} \right\} \end{array} \right] = 0$$

(5A.84)

$$\sigma_{\xi\eta}(@\ r = R) = \left[\begin{array}{c} -\frac{b_0}{R^2} sin2\psi \\ +\sum_{n=2,4,\ldots}^{N} \left\{ \begin{array}{c} a_n\, n\,(n-1)\, R^{n-2} \sin(n\theta + 2\psi) \\ +b_n n\,(n+1) R^n \sin(n\theta + 2\psi) \\ -\, c_n\, n\,(n+1)\, R^{-(n+2)} \sin(n\theta - 2\psi) \\ -\, d_n n\,(n-1) R^{-n} \sin(n\theta - 2\psi) \end{array} \right\} \end{array} \right] = 0$$

(5A.85)

Hence the least-squares expression of *equation 5.34* becomes

$$\begin{bmatrix} \sigma_{\xi\xi}(r=R) \\ \vdots \\ S \\ \vdots \\ \sigma_{\xi\eta}(r=R) \end{bmatrix} = \begin{bmatrix} cos2\psi/R^2 & \cdots & \cdots & (n-1)R^{-n}\left[n\,cos(n\theta-2\psi)+2\,cos(n\theta)\right] \\ \vdots & & & \vdots \\ 0 & \cdots & \cdots & -4\,(n-1)r^{-n}\,cos(n\theta) \\ \vdots & & & \vdots \\ -sin2\psi/R^2 & \cdots & \cdots & -n\,(n-1)R^{-n}\sin(n\theta-2\psi) \end{bmatrix} \begin{bmatrix} b_o \\ \vdots \\ \vdots \\ \vdots \\ d_n \end{bmatrix}$$

$$= \begin{bmatrix} 0 \\ \vdots \\ S \\ \vdots \\ 0 \end{bmatrix} \qquad (5A.86)$$

Stresses acting in *r-θ* co-ordinate system can be transformed to those in the *x-y* co-ordinate system using the following transformation matrix equation

$$\begin{bmatrix} \sigma_{xx} \\ \sigma_{yy} \\ \sigma_{xy} \end{bmatrix} = \begin{bmatrix} \cos^2\theta & \sin^2\theta & -2\sin\theta.\cos\theta \\ \sin^2\theta & \cos^2\theta & 2\sin\theta.\cos\theta \\ \sin\theta.\cos\theta & -\sin\theta.\cos\theta & \cos^2\theta-\sin^2\theta \end{bmatrix} \begin{bmatrix} \sigma_{rr} \\ \sigma_{\theta\theta} \\ \sigma_{r\theta} \end{bmatrix} \qquad (5A.87)$$

The above matrix equation can be expanded as:

$$\sigma_{xx} = \sigma_{rr}\,cos^2\theta + \sigma_{\theta\theta}\,sin^2\theta - \sigma_{r\theta}\,2\,sin\theta\,cos\theta \qquad (5A.88)$$

$$\sigma_{yy} = \sigma_{rr}\,sin^2\theta + \sigma_{\theta\theta}\,cos^2\theta + \sigma_{r\theta}\,2\,sin\theta\,cos\theta \qquad (5A.89)$$

$$\sigma_{xy} = \sigma_{rr}\,sin\theta\,cos\theta - \sigma_{\theta\theta}\,sin\theta\,cos\theta + \sigma_{r\theta}\,(cos^2\theta - sin^2\theta) \qquad (5A.90)$$

Calculating the stresses in the *x*-*y* direction:

$$\sigma_{xx} = \left[\begin{array}{l} \left\{ \dfrac{b_0}{r^2} + 2c_0 - \displaystyle\sum_{n=2,4,\ldots}^{N} \left[\begin{array}{c} a_n\, n\,(n-1)\, r^{n-2} + b_n\,(n+1)\,(n-2)\, r^{n} \\ + c_n\, n\,(n+1)\, r^{-(n+2)} + d_n\,(n-1)(n+2)\, r^{-n} \end{array} \right] cos(n\theta) \right\} cos^2\theta \\ + \left\{ \dfrac{-b_0}{r^2} + 2c_0 + \displaystyle\sum_{n=2,4,\ldots}^{N} \left[\begin{array}{c} a_n\, n\,(n-1)\, r^{n-2} + b_n\,(n+1)\,(n+2)\, r^{n} \\ + c_n\, n\,(n+1)\, r^{-(n+2)} + d_n\,(n-1)(n-2)\, r^{-n} \end{array} \right] cos(n\theta) \right\} sin^2\theta \\ - \left\{ \displaystyle\sum_{n=2,4,\ldots}^{N} \left[\begin{array}{c} a_n\, n\,(n-1)\, r^{n-2} + b_n\, n\,(n+1)\, r^{n} \\ - c_n\, n\,(n+1)\, r^{-(n+2)} - d_n\, n\,(n-1)\, r^{-n} \end{array} \right] sin(n\theta) \right\} sin2\theta \end{array} \right]$$

(5A.91)

$$\sigma_{xx} = \left[\begin{array}{l} \dfrac{b_0}{r^2} cos^2\theta + 2c_0 cos^2\theta - \dfrac{b_0}{r^2} sin^2\theta + 2c_0 sin^2\theta \\ - \displaystyle\sum_{n=2,4,\ldots}^{N} \left[\begin{array}{c} a_n\, n\,(n-1)\, r^{n-2} + b_n\,(n+1)\,(n-2)\, r^{n} \\ + c_n\, n\,(n+1)\, r^{-(n+2)} + d_n\,(n-1)(n+2)\, r^{-n} \end{array} \right] cos(n\theta)\, cos^2\theta \\ + \displaystyle\sum_{n=2,4,\ldots}^{N} \left[\begin{array}{c} a_n\, n\,(n-1)\, r^{n-2} + b_n\,(n+1)\,(n+2)\, r^{n} \\ + c_n\, n\,(n+1)\, r^{-(n+2)} + d_n\,(n-1)(n-2)\, r^{-n} \end{array} \right] cos(n\theta)\, sin^2\theta \\ - \displaystyle\sum_{n=2,4,\ldots}^{N} \left[\begin{array}{c} a_n\, n\,(n-1)\, r^{n-2} + b_n\, n\,(n+1)\, r^{n} \\ - c_n\, n\,(n+1)\, r^{-(n+2)} - d_n\, n\,(n-1)\, r^{-n} \end{array} \right] sin(n\theta)\, sin2\theta \end{array} \right]$$

(5A.92)

$$\sigma_{xx} = \left[\begin{array}{c} \frac{b_0}{r^2} cos^2\theta - \frac{b_0}{r^2} sin^2\theta + 2c_0 cos^2\theta \; + 2c_0 sin^2\theta \\ + \sum_{n=2,4,\ldots}^{N} \left\{ \begin{array}{c} -\left[\begin{array}{c} a_n\, n\,(n-1)\, r^{n-2} \; + \; b_n\,(n+1)(n-2) r^n \\ + c_n\, n\,(n+1)\, r^{-(n+2)} \; + \quad d_n\,(n-1)(n+2)\, r^{-n} \end{array} \right] cos(n\theta)\, cos^2\theta \\ + \left[\begin{array}{c} a_n\, n\,(n-1)\, r^{n-2} \; + \; b_n\,(n+1)(n+2) r^n \\ + c_n\, n\,(n+1)\, r^{-(n+2)} \; + \quad d_n\,(n-1)(n-2)\, r^{-n} \end{array} \right] cos(n\theta)\, sin^2\theta \\ - \left[\begin{array}{c} a_n\, n\,(n-1)\, r^{n-2} \; + \; b_n\, n\,(n+1) \; r^n \\ - c_n\, n\,(n+1)\, r^{-(n+2)} - \quad d_n\, n\,(n-1)\, r^{-n} \end{array} \right] sin(n\theta)\, sin2\theta \end{array} \right\} \end{array} \right]$$

(5A.93)

σ_{xx}

$$= \left[\begin{array}{c} \frac{b_0}{r^2} (cos^2\theta - sin^2\theta) + 2c_0 (cos^2\theta \; + sin^2\theta) \\ + \sum_{n=2,4,\ldots}^{N} \left\{ \begin{array}{c} \left[\begin{array}{c} -a_n\, n\,(n-1)\, r^{n-2} \; cos(n\theta)\, cos^2\theta - \; b_n\,(n+1)(n-2) r^n \; cos(n\theta)\, cos^2\theta \\ - c_n\, n\,(n+1)\, r^{-(n+2)}\, cos(n\theta)\, cos^2\theta - d_n\,(n-1)(n+2)\, r^{-n}\, cos(n\theta)\, cos^2\theta \end{array} \right] \\ + \left[\begin{array}{c} a_n\, n\,(n-1)\, r^{n-2} \; cos(n\theta)\, sin^2\theta \; + \; b_n\,(n+1)(n+2) r^n \; cos(n\theta)\, sin^2\theta \\ + c_n\, n\,(n+1)\, r^{-(n+2)} \; cos(n\theta)\, sin^2\theta \; + \quad d_n\,(n-1)(n-2)\, r^{-n} \; cos(n\theta)\, sin^2\theta \end{array} \right] \\ - \left[\begin{array}{c} a_n\, n\,(n-1)\, r^{n-2} \; sin(n\theta)\, sin2\theta + \; b_n\, n\,(n+1) \; r^n \; sin(n\theta)\, sin2\theta \\ - c_n\, n\,(n+1)\, r^{-(n+2)} \; sin(n\theta)\, sin2\theta - \quad d_n\, n\,(n-1)\, r^{-n} \; sin(n\theta)\, sin2\theta \end{array} \right] \end{array} \right\} \end{array} \right]$$

(5A.94)

σ_{xx}

$$= \left[\begin{array}{c} \frac{b_0}{r^2} cos2\theta + 2c_0 \\ + \sum_{n=2,4,\ldots}^{N} \left\{ \begin{array}{c} -a_n\, n\,(n-1)\, r^{n-2} \; cos(n\theta)\, cos^2\theta - \; a_n\, n\,(n-1)\, r^{n-2} \; sin(n\theta)\, sin2\theta \\ + a_n\, n\,(n-1)\, r^{n-2} \; cos(n\theta)\, sin^2\theta \\ - b_n\,(n+1)(n-2) r^n \; cos(n\theta)\, cos^2\theta + \; b_n\,(n+1)(n+2) r^n \; cos(n\theta)\, sin^2\theta \\ - b_n\, n\,(n+1) \; r^n \; sin(n\theta)\, sin2\theta \\ - c_n\, n\,(n+1)\, r^{-(n+2)}\, cos(n\theta)\, cos^2\theta + c_n\, n\,(n+1)\, r^{-(n+2)} \; cos(n\theta)\, sin^2\theta \\ + c_n\, n\,(n+1)\, r^{-(n+2)} \; sin(n\theta)\, sin2\theta \\ -d_n\,(n-1)(n+2)\, r^{-n}\, cos(n\theta)\, cos^2\theta + \; d_n\,(n-1)(n-2)\, r^{-n} \; cos(n\theta)\, sin^2\theta \\ + \; d_n\, n\,(n-1)\, r^{-n} \; sin(n\theta)\, sin2\theta \end{array} \right\} \end{array} \right]$$

(5A.95)

$$\sigma_{xx} = \left[\begin{array}{c} \frac{b_0}{r^2} cos2\theta + 2c_0 \\ + \sum_{n=2,4,\ldots}^{N} \left\{ \begin{array}{c} a_n\, n\,(n-1)\, r^{n-2}\,[-cos(n\theta)\, cos^2\theta - \, sin(n\theta)\, sin2\theta + cos(n\theta)\, sin^2\theta] \\ +b_n\,(n+1) r^n \left[\begin{array}{c} -(n-2)\, cos(n\theta)\, cos^2\theta + (n+2)\, cos(n\theta)\, sin^2\theta \\ -\, n\, \, sin(n\theta)\, sin2\theta \end{array} \right] \\ + c_n\, n\,(n+1)\, r^{-(n+2)} [-cos(n\theta)\, cos^2\theta + \, cos(n\theta)\, sin^2\theta + sin(n\theta)\, sin2\theta] \\ +d_n\,(n-1) r^{-n} \left[\begin{array}{c} -(n+2)\, cos(n\theta)\, cos^2\theta + \, (n-2)\, cos(n\theta)\, sin^2\theta \\ +\, \, n\, \, sin(n\theta)\, sin2\theta \end{array} \right] \end{array} \right\} \end{array} \right]$$

(5A.96)

$$\sigma_{xx} = \left[\begin{array}{c} \frac{b_0}{r^2} cos2\theta + 2c_0 \\ + \sum_{n=2,4,\ldots}^{N} \left\{ \begin{array}{c} a_n\, n\,(n-1)\, r^{n-2}\,[cos(n\theta)\,(-cos^2\theta + sin^2\theta) - \, sin(n\theta)\, sin2\theta] \\ +b_n\,(n+1) r^n \left[\begin{array}{c} -n\, cos(n\theta)\, cos^2\theta + 2\, cos(n\theta)\, cos^2\theta + n\, cos(n\theta)\, sin^2\theta \\ +2\, cos(n\theta)\, sin^2\theta - \, \, n\, \, sin(n\theta)\, sin2\theta \end{array} \right] \\ + c_n\, n\,(n+1)\, r^{-(n+2)} [cos(n\theta)\,(-cos^2\theta + sin^2\theta) + \, sin(n\theta)\, sin2\theta] \\ +d_n\,(n-1) r^{-n} \left[\begin{array}{c} -n\, cos(n\theta)\, cos^2\theta - 2\, cos(n\theta)\, cos^2\theta + \, n\, cos(n\theta)\, sin^2\theta \\ -2\, cos(n\theta)\, sin^2\theta + \, \, n\, \, sin(n\theta)\, sin2\theta \end{array} \right] \end{array} \right\} \end{array} \right]$$

(5A.97)

$$\sigma_{xx} = \left[\begin{array}{c} \frac{b_0}{r^2} cos2\theta + 2c_0 \\ + \sum_{n=2,4,\ldots}^{N} \left\{ \begin{array}{c} a_n\, n\,(n-1)\, r^{n-2}\,[cos(n\theta)\,(-cos2\theta) - \, sin(n\theta)\, sin2\theta] \\ +b_n\,(n+1) r^n \left[\begin{array}{c} n(-cos(n\theta)\, cos^2\theta + cos(n\theta)\, sin^2\theta - \, sin(n\theta)\, sin2\theta) \\ +2\, cos(n\theta)\,(cos^2\theta + sin^2\theta) \end{array} \right] \\ + c_n\, n\,(n+1)\, r^{-(n+2)} [cos(n\theta)\,(-cos2\theta) + \, sin(n\theta)\, sin2\theta] \\ +d_n\,(n-1) r^{-n} \left[\begin{array}{c} n(-cos(n\theta)\, cos^2\theta + \, cos(n\theta)\, sin^2\theta + \, sin(n\theta)\, sin2\theta) \\ -2\, cos(n\theta)\,(cos^2\theta + sin^2\theta) \end{array} \right] \end{array} \right\} \end{array} \right]$$

(5A.98)

$$\sigma_{xx} = \left[\begin{array}{c} \frac{b_0}{r^2} cos2\theta + 2c_0 \\ + \sum_{n=2,4,\ldots}^{N} \left\{ \begin{array}{c} a_n\, n\,(n-1)\, r^{n-2}\,[-cos(n\theta)\, cos2\theta - \, sin(n\theta)\, sin2\theta] \\ +b_n\,(n+1) r^n \left[\begin{array}{c} n(cos(n\theta)\,(-cos^2\theta + sin^2\theta)) - \, sin(n\theta)\, sin2\theta) \\ +2\, cos(n\theta) \end{array} \right] \\ + c_n\, n\,(n+1)\, r^{-(n+2)}[-cos(n\theta)\, cos2\theta + \, sin(n\theta)\, sin2\theta] \\ +d_n\,(n-1) r^{-n} \left[\begin{array}{c} n(cos(n\theta)\,(-cos^2\theta + \, sin^2\theta) + \, sin(n\theta)\, sin2\theta) \\ -2\, cos(n\theta) \end{array} \right] \end{array} \right. \end{array} \right] \quad \text{(5A.99)}$$

$$\sigma_{xx} = \left[\begin{array}{c} \frac{b_0}{r^2} cos2\theta + 2c_0 \\ + \sum_{n=2,4,\ldots}^{N} \left\{ \begin{array}{c} -a_n\, n\,(n-1)\, r^{n-2}\,[cos(n\theta - 2\theta)] \\ -b_n\,(n+1) r^n [n(cos(n\theta - 2\theta)) - 2\, cos(n\theta)] \\ - c_n\, n\,(n+1)\, r^{-(n+2)}[cos(n\theta + 2\theta)] \\ -d_n\,(n-1) r^{-n}\,[n(cos(n\theta + 2\theta)) + 2\, cos(n\theta)] \end{array} \right. \end{array} \right]$$

$$\sigma_{xx} = \left[\begin{array}{c} \frac{b_0}{r^2} cos2\theta + 2c_0 \\ - \sum_{n=2,4,\ldots}^{N} \left\{ \begin{array}{c} a_n\, n\,(n-1)\, r^{n-2}\,[cos(n\theta - 2\theta)] \\ +b_n\,(n+1) r^n [n(cos(n\theta - 2\theta)) - 2\, cos(n\theta)] \\ + c_n\, n\,(n+1)\, r^{-(n+2)}[cos(n\theta + 2\theta)] \\ +d_n\,(n-1) r^{-n}\,[n(cos(n\theta + 2\theta)) + 2\, cos(n\theta)] \end{array} \right. \end{array} \right] \quad \text{(5A.100)}$$

Now,

$$\sigma_{yy} = \left[\begin{array}{l} \left\{ \dfrac{b_0}{r^2} + 2c_0 \; - \sum_{n=2,4,\ldots}^{N} \left[\begin{array}{c} a_n\, n\,(n-1)\, r^{n-2} \; + \; b_n\,(n+1)\,(n-2)\, r^{n} \\ + \, c_n\, n\,(n+1)\, r^{-(n+2)} \; + \quad d_n\,(n-1)(n+2)\, r^{-n} \end{array} \right] cos(n\theta) \right\} sin^2\theta \\ + \left\{ \dfrac{-b_0}{r^2} + 2c_0 + \sum_{n=2,4,\ldots}^{N} \left[\begin{array}{c} a_n\, n\,(n-1)\, r^{n-2} \; + \; b_n\,(n+1)\,(n+2)\, r^{n} \\ + \, c_n\, n\,(n+1)\, r^{-(n+2)} \; + \quad d_n\,(n-1)(n-2)\, r^{-n} \end{array} \right] cos(n\theta) \right\} cos^2\theta \\ + \left\{ \sum_{n=2,4,\ldots}^{N} \left[\begin{array}{c} a_n\, n\,(n-1)\, r^{n-2} \; + \; b_n\, n\,(n+1)\; r^{n} \\ - \, c_n\, n\,(n+1)\, r^{-(n+2)} - \quad d_n\, n\,(n-1)\, r^{-n} \end{array} \right] sin(n\theta) \right\} sin2\theta \end{array} \right] \tag{5A.101}$$

$$\sigma_{yy} = \left[\begin{array}{l} \dfrac{b_0}{r^2} sin^2\theta + 2c_0 sin^2\theta \; - \dfrac{b_0}{r^2} cos^2\theta + 2c_0 cos^2\theta \\ - \sum_{n=2,4,\ldots}^{N} \left[\begin{array}{c} a_n\, n\,(n-1)\, r^{n-2} \; + \; b_n\,(n+1)\,(n-2)\, r^{n} \\ + \, c_n\, n\,(n+1)\, r^{-(n+2)} \; + \quad d_n\,(n-1)(n+2)\, r^{-n} \end{array} \right] cos(n\theta)\, sin^2\theta \\ + \sum_{n=2,4,\ldots}^{N} \left[\begin{array}{c} a_n\, n\,(n-1)\, r^{n-2} \; + \; b_n\,(n+1)\,(n+2)\, r^{n} \\ + \, c_n\, n\,(n+1)\, r^{-(n+2)} \; + \quad d_n\,(n-1)(n-2)\, r^{-n} \end{array} \right] cos(n\theta)\, cos^2\theta \\ + \sum_{n=2,4,\ldots}^{N} \left[\begin{array}{c} a_n\, n\,(n-1)\, r^{n-2} \; + \; b_n\, n\,(n+1)\; r^{n} \\ - \, c_n\, n\,(n+1)\, r^{-(n+2)} - \quad d_n\, n\,(n-1)\, r^{-n} \end{array} \right] sin(n\theta)\, sin2\theta \end{array} \right] \tag{5A.102}$$

$$\sigma_{yy} = \left[\begin{array}{l} \frac{b_0}{r^2} sin^2\theta - \frac{b_0}{r^2} cos^2\theta + 2c_0 sin^2\theta \; + 2c_0 cos^2\theta \\ + \sum_{n=2,4,\ldots}^{N} \left\{ \begin{array}{l} - \left[\begin{array}{c} a_n\, n\,(n-1)\, r^{n-2} \; + \; b_n\,(n+1)(n-2) r^{n} \\ + \, c_n\, n\,(n+1)\, r^{-(n+2)} \; + \quad d_n\,(n-1)(n+2)\, r^{-n} \end{array} \right] cos(n\theta)\, sin^2\theta \\ + \left[\begin{array}{c} a_n\, n\,(n-1)\, r^{n-2} \; + \; b_n\,(n+1)(n+2) r^{n} \\ + \, c_n\, n\,(n+1)\, r^{-(n+2)} \; + \quad d_n\,(n-1)(n-2)\, r^{-n} \end{array} \right] cos(n\theta)\, cos^2\theta \\ + \left[\begin{array}{c} a_n\, n\,(n-1)\, r^{n-2} \; + \; b_n\, n\,(n+1)\; r^{n} \\ - \, c_n\, n\,(n+1)\, r^{-(n+2)} - \quad d_n\, n\,(n-1)\, r^{-n} \end{array} \right] sin(n\theta)\, sin2\theta \end{array} \right\} \end{array} \right] \tag{5A.103}$$

$$\sigma_{yy}$$

$$= \left[\begin{array}{c} \frac{b_0}{r^2}(sin^2\theta - cos^2\theta) + 2c_0(sin^2\theta + cos^2\theta) \\ + \sum_{n=2,4,\ldots}^{N} \left\{ \begin{array}{c} \left[\begin{array}{c} -a_n\, n\,(n-1)\, r^{n-2}\ cos(n\theta)\, sin^2\theta - \ b_n\,(n+1)(n-2) r^n\ cos(n\theta)\, sin^2\theta \\ - c_n\, n\,(n+1)\, r^{-(n+2)}\, cos(n\theta)\, sin^2\theta - d_n\,(n-1)(n+2)\, r^{-n}\, cos(n\theta)\, sin^2\theta \end{array} \right] \\ + \left[\begin{array}{c} a_n\, n\,(n-1)\, r^{n-2}\ cos(n\theta)\, cos^2\theta \ + \ b_n\,(n+1)(n+2) r^n\ cos(n\theta)\, cos^2\theta \\ + c_n\, n\,(n+1)\, r^{-(n+2)}\ cos(n\theta)\, cos^2\theta \ + \quad d_n\,(n-1)(n-2)\, r^{-n}\ cos(n\theta)\, cos^2\theta \end{array} \right] \\ + \left[\begin{array}{c} a_n\, n\,(n-1)\, r^{n-2}\ \ sin(n\theta)\, sin2\theta + \ b_n\, n\,(n+1)\ r^n\ sin(n\theta)\, sin2\theta \\ - c_n\, n\,(n+1)\, r^{-(n+2)}\ sin(n\theta)\, sin2\theta - \quad d_n\, n\,(n-1)\, r^{-n}\ sin(n\theta)\, sin2\theta \end{array} \right] \end{array} \right\} \end{array} \right]$$

(5A.104)

$$\sigma_{yy}$$

$$= \left[\begin{array}{c} -\frac{b_0}{r^2} cos2\theta + 2c_0 \\ + \sum_{n=2,4,\ldots}^{N} \left\{ \begin{array}{c} -a_n\, n\,(n-1)\, r^{n-2}\ cos(n\theta)\, sin^2\theta + \ a_n\, n\,(n-1)\, r^{n-2}\ \ sin(n\theta)\, sin2\theta \\ + a_n\, n\,(n-1)\, r^{n-2}\ cos(n\theta)\, cos^2\theta \\ - b_n\,(n+1)(n-2) r^n\ cos(n\theta)\, sin^2\theta + \ b_n\,(n+1)(n+2) r^n\ cos(n\theta)\, cos^2\theta \\ + b_n\, n\,(n+1)\ r^n\ sin(n\theta)\, sin2\theta \\ - c_n\, n\,(n+1)\, r^{-(n+2)}\, cos(n\theta)\, sin^2\theta + c_n\, n\,(n+1)\, r^{-(n+2)}\ cos(n\theta)\, cos^2\theta \\ - c_n\, n\,(n+1)\, r^{-(n+2)}\ sin(n\theta)\, sin2\theta \\ -d_n\,(n-1)(n+2)\, r^{-n}\, cos(n\theta)\, sin^2\theta + \ d_n\,(n-1)(n-2)\, r^{-n}\ cos(n\theta)\, cos^2\theta \\ - \ d_n\, n\,(n-1)\, r^{-n}\ sin(n\theta)\, sin2\theta \end{array} \right\} \end{array} \right]$$

(5A.105)

$$\sigma_{yy} = \left[\begin{array}{c} -\frac{b_0}{r^2} cos2\theta + 2c_0 \\ + \sum_{n=2,4,\ldots}^{N} \left\{ \begin{array}{c} a_n\, n\,(n-1)\, r^{n-2}\,[-cos(n\theta)\, sin^2\theta + \ sin(n\theta)\, sin2\theta + cos(n\theta)\, cos^2\theta] \\ +b_n\,(n+1) r^n \left[\begin{array}{c} -(n-2)\, cos(n\theta)\, sin^2\theta + (n+2)\, cos(n\theta)\, cos^2\theta \\ + n\ sin(n\theta)\, sin2\theta \end{array} \right] \\ + c_n\, n\,(n+1)\, r^{-(n+2)}[-cos(n\theta)\, sin^2\theta + \ cos(n\theta)\, cos^2\theta - sin(n\theta)\, sin2\theta] \\ +d_n\,(n-1) r^{-n} \left[\begin{array}{c} -(n+2)\, cos(n\theta)\, sin^2\theta + \ (n-2)\, cos(n\theta)\, cos^2\theta \\ - \ n\ sin(n\theta)\, sin2\theta \end{array} \right] \end{array} \right\} \end{array} \right]$$

(5A.106)

$$\sigma_{yy} = \left[+ \sum_{n=2,4,\ldots}^{N} \left\{ \begin{array}{c} -\frac{b_0}{r^2} cos2\theta + 2c_0 \\ a_n\, n\,(n-1)\, r^{n-2}\,[cos(n\theta)\,(-sin^2\theta + cos^2\theta) + \ sin(n\theta)\, sin2\theta] \\ +b_n\,(n+1) r^n \left[\begin{array}{c} -n\, cos(n\theta)\, sin^2\theta + 2\, cos(n\theta)\, sin^2\theta + n\, cos(n\theta)\, cos^2\theta \\ +2\, cos(n\theta)\, cos^2\theta + \ n\ sin(n\theta)\, sin2\theta \end{array} \right] \\ + c_n\, n\,(n+1)\, r^{-(n+2)} [cos(n\theta)\,(-sin^2\theta + cos^2\theta) - \ sin(n\theta)\, sin2\theta] \\ +d_n\,(n-1) r^{-n} \left[\begin{array}{c} -n\, cos(n\theta)\, sin^2\theta - 2\, cos(n\theta)\, sin^2\theta + \ n\, cos(n\theta)\, cos^2\theta \\ -2\, cos(n\theta)\, cos^2\theta - \ n\ sin(n\theta)\, sin2\theta \end{array} \right] \end{array} \right\} \right]$$

(5A.107)

$$\sigma_{yy} = \left[+ \sum_{n=2,4,\ldots}^{N} \left\{ \begin{array}{c} -\frac{b_0}{r^2} cos2\theta + 2c_0 \\ a_n\, n\,(n-1)\, r^{n-2}\,[cos(n\theta)\,(cos2\theta) + \ sin(n\theta)\, sin2\theta] \\ +b_n\,(n+1) r^n \left[\begin{array}{c} n(-cos(n\theta)\, sin^2\theta + cos(n\theta)\, cos^2\theta + \ sin(n\theta)\, sin2\theta) \\ +2\, cos(n\theta)\,(cos^2\theta + sin^2\theta) \end{array} \right] \\ + c_n\, n\,(n+1)\, r^{-(n+2)} [cos(n\theta)\,(cos2\theta) - \ sin(n\theta)\, sin2\theta] \\ +d_n\,(n-1) r^{-n} \left[\begin{array}{c} n(-cos(n\theta)\, sin^2\theta + \ cos(n\theta)\, cos^2\theta - \ sin(n\theta)\, sin2\theta) \\ -2\, cos(n\theta)\,(cos^2\theta + sin^2\theta) \end{array} \right] \end{array} \right\} \right]$$

(5A.108)

$$\sigma_{yy} = \left[+ \sum_{n=2,4,\ldots}^{N} \left\{ \begin{array}{c} -\frac{b_0}{r^2} cos2\theta + 2c_0 \\ a_n\, n\,(n-1)\, r^{n-2}\,[cos(n\theta)\, cos2\theta + \ sin(n\theta)\, sin2\theta] \\ +b_n\,(n+1) r^n \left[\begin{array}{c} n(cos(n\theta)\,(-sin^2\theta + cos^2\theta)) + \ sin(n\theta)\, sin2\theta) \\ +2\, cos(n\theta) \end{array} \right] \\ + c_n\, n\,(n+1)\, r^{-(n+2)} [cos(n\theta)\, cos2\theta - \ sin(n\theta)\, sin2\theta] \\ +d_n\,(n-1) r^{-n} \left[\begin{array}{c} n(cos(n\theta)\,(-sin^2\theta + \ cos^2\theta) - \ sin(n\theta)\, sin2\theta) \\ -2\, cos(n\theta) \end{array} \right] \end{array} \right\} \right]$$

(5A.109)

$$\sigma_{yy} = \left[\begin{array}{c} -\frac{b_0}{r^2} cos2\theta + 2c_0 \\ + \sum_{n=2,4,\ldots}^{N} \left\{ \begin{array}{c} a_n\, n\,(n-1)\, r^{n-2}\,[cos(n\theta - 2\theta)] \\ +b_n\,(n+1) r^n [n(cos(n\theta - 2\theta)) + 2\, cos(n\theta)] \\ +\, c_n\, n\,(n+1)\, r^{-(n+2)} [cos(n\theta + 2\theta)] \\ +d_n\,(n-1) r^{-n}\,[n(cos(n\theta + 2\theta)) - 2\, cos(n\theta)] \end{array} \right\} \end{array} \right]$$

(5A.110)

Now,

$$\sigma_{xy}$$

$$= \left[\begin{array}{l} \left\{ \frac{b_0}{r^2} + 2c_0 - \sum_{n=2,4,\ldots}^{N} \left[\begin{array}{c} a_n\, n\,(n-1)\, r^{n-2} + b_n\,(n+1)(n-2) r^n \\ + c_n\, n\,(n+1)\, r^{-(n+2)} + d_n\,(n-1)(n+2)\, r^{-n} \end{array} \right] cos(n\theta) \right\} sin\theta\, cos\theta \\ + \left\{ \frac{-b_0}{r^2} + 2c_0 + \sum_{n=2,4,\ldots}^{N} \left[\begin{array}{c} a_n\, n\,(n-1)\, r^{n-2} + b_n\,(n+1)(n+2) r^n \\ + c_n\, n\,(n+1)\, r^{-(n+2)} + d_n\,(n-1)(n-2)\, r^{-n} \end{array} \right] cos(n\theta) \right\} (-sin\theta\, cos\theta) \\ + \left\{ \sum_{n=2,4,\ldots}^{N} \left[\begin{array}{c} a_n\, n\,(n-1)\, r^{n-2} + b_n\, n\,(n+1)\, r^n \\ - c_n\, n\,(n+1)\, r^{-(n+2)} - d_n\, n\,(n-1)\, r^{-n} \end{array} \right] sin(n\theta) \right\} cos2\theta \end{array} \right] \quad (5A.111)$$

$$\sigma_{xy} = \left[\begin{array}{l} \frac{b_0}{r^2} sin\theta\, cos\theta + 2c_0 sin\theta\, cos\theta + \frac{b_0}{r^2} sin\theta\, cos\theta - 2c_0 sin\theta\, cos\theta \\ - \sum_{n=2,4,\ldots}^{N} \left[\begin{array}{c} a_n\, n\,(n-1)\, r^{n-2} + b_n\,(n+1)\,(n-2)\, r^n \\ + c_n\, n\,(n+1)\, r^{-(n+2)} + d_n\,(n-1)(n+2)\, r^{-n} \end{array} \right] cos(n\theta)\, sin\theta\, cos\theta \\ - \sum_{n=2,4,\ldots}^{N} \left[\begin{array}{c} a_n\, n\,(n-1)\, r^{n-2} + b_n\,(n+1)\,(n+2)\, r^n \\ + c_n\, n\,(n+1)\, r^{-(n+2)} + d_n\,(n-1)(n-2)\, r^{-n} \end{array} \right] cos(n\theta)\, sin\theta\, cos\theta \\ + \sum_{n=2,4,\ldots}^{N} \left[\begin{array}{c} a_n\, n\,(n-1)\, r^{n-2} + b_n\, n\,(n+1)\, r^n \\ - c_n\, n\,(n+1)\, r^{-(n+2)} - d_n\, n\,(n-1)\, r^{-n} \end{array} \right] sin(n\theta)\, cos2\theta \end{array} \right] \quad (5A.112)$$

$$\sigma_{xy} = \left[\begin{array}{c} \frac{b_0}{r^2} sin\theta\, cos\theta + \frac{b_0}{r^2} sin\theta\, cos\theta + 2c_0 sin\theta\, cos\theta - 2c_0 sin\theta\, cos\theta \\ -\sum_{n=2,4,\ldots}^{N} \left\{ \begin{array}{c} \left[\begin{array}{c} a_n\, n\,(n-1)\, r^{n-2} + b_n\,(n+1)(n-2) r^n \\ + c_n\, n\,(n+1)\, r^{-(n+2)} + d_n\,(n-1)(n+2)\, r^{-n} \end{array} \right] cos(n\theta)\, sin\theta\, cos\theta \\ + \left[\begin{array}{c} a_n\, n\,(n-1)\, r^{n-2} + b_n\,(n+1)(n+2) r^n \\ + c_n\, n\,(n+1)\, r^{-(n+2)} + d_n\,(n-1)(n-2)\, r^{-n} \end{array} \right] cos(n\theta)\, sin\theta\, cos\theta \\ - \left[\begin{array}{c} a_n\, n\,(n-1)\, r^{n-2} + b_n\, n\,(n+1)\, r^n \\ - c_n\, n\,(n+1)\, r^{-(n+2)} - d_n\, n\,(n-1)\, r^{-n} \end{array} \right] sin(n\theta)\, cos2\theta \end{array} \right\} \end{array} \right]$$

(5A.113)

$$\sigma_{xy} = \left[\begin{array}{c} \frac{2b_0}{r^2} sin\theta\, cos\theta \\ -\sum_{n=2,4,\ldots}^{N} \left\{ \begin{array}{c} \left(\begin{array}{c} \left[\begin{array}{c} a_n\, n\,(n-1)\, r^{n-2}\, cos(n\theta)\, sin\theta\, cos\theta \\ + b_n\,(n+1)(n-2) r^n\, cos(n\theta)\, sin\theta\, cos\theta \\ + c_n\, n\,(n+1)\, r^{-(n+2)}\, cos(n\theta)\, sin\theta\, cos\theta \\ + d_n\,(n-1)(n+2)\, r^{-n}\, cos(n\theta)\, sin\theta\, cos\theta \end{array} \right] \\ + \left[\begin{array}{c} a_n\, n\,(n-1)\, r^{n-2}\, cos(n\theta)\, sin\theta\, cos\theta \\ + b_n\,(n+1)(n+2) r^n\, cos(n\theta)\, sin\theta\, cos\theta \\ + c_n\, n\,(n+1)\, r^{-(n+2)}\, cos(n\theta)\, sin\theta\, cos\theta \\ + d_n\,(n-1)(n-2)\, r^{-n}\, cos(n\theta)\, sin\theta\, cos\theta \end{array} \right] \end{array} \right) \\ - \left[\begin{array}{c} a_n\, n\,(n-1)\, r^{n-2}\, sin(n\theta)\, cos2\theta \\ + b_n\, n\,(n+1)\, r^n\, sin(n\theta)\, cos2\theta \\ - c_n\, n\,(n+1)\, r^{-(n+2)}\, sin(n\theta)\, cos2\theta \\ - d_n\, n\,(n-1)\, r^{-n}\, sin(n\theta)\, cos2\theta \end{array} \right] \end{array} \right\} \end{array} \right]$$

(5A.114)

$$\sigma_{xy} = \left[\begin{array}{c} \frac{2b_0}{r^2} sin\theta\ cos\theta \\ -\sum_{n=2,4,\ldots}^{N} \left\{ \begin{array}{c} a_n\, n\,(n-1)\, r^{n-2}\ cos(n\theta)\, sin\theta\ cos\theta \\ +\, a_n\, n\,(n-1)\, r^{n-2}\ cos(n\theta)\, sin\theta\ cos\theta \\ -\, a_n\, n\,(n-1)\, r^{n-2}\ \ sin(n\theta)\, cos2\theta \\ +b_n\,(n+1)(n-2) r^{n}\ cos(n\theta)\, sin\theta\ cos\theta \\ +b_n\,(n+1)(n+2) r^{n}\ cos(n\theta)\, sin\theta\ cos\theta \\ -\, b_n\, n\,(n+1)\ \ r^{n}\ sin(n\theta)\, cos2\theta \\ +\, c_n\, n\,(n+1)\, r^{-(n+2)}\, cos(n\theta)\, sin\theta\ cos\theta \\ +c_n n\,(n+1)\, r^{-(n+2)}\ cos(n\theta)\, sin\theta\ cos\theta \\ +\, c_n\, n\,(n+1)\, r^{-(n+2)}\ sin(n\theta)\, cos2\theta \\ +d_n\,(n-1)(n+2)\, r^{-n}\, cos(n\theta)\, sin\theta\ cos\theta \\ +d_n\,(n-1)(n-2)\, r^{-n}\ cos(n\theta)\, sin\theta\ cos\theta \\ +\, d_n\, n\,(n-1)\, r^{-n}\ sin(n\theta)\, cos2\theta \end{array} \right\} \end{array} \right]$$

(5A.115)

σ_{xy}

$$= \left[\begin{array}{c} \frac{2b_0}{r^2} sin\theta\ cos\theta \\ -\sum_{n=2,4,\ldots}^{N} \left\{ \begin{array}{c} a_n\, n\,(n-1)\, r^{n-2}\,[cos(n\theta)\, sin\theta\ cos\theta + cos(n\theta)\, sin\theta\ cos\theta - \ sin(n\theta)\, cos2\theta] \\ +b_n\,(n+1) r^{n} \left[\begin{array}{c} (n-2)\ cos(n\theta)\, sin\theta\ cos\theta + (n+2)\ cos(n\theta)\, sin\theta\ cos\theta \\ -\, n\ sin(n\theta)\, cos2\theta \end{array} \right] \\ +\, c_n\, n\,(n+1)\, r^{-(n+2)} [\, cos(n\theta)\, sin\theta\ cos\theta + \ cos(n\theta)\, sin\theta\ cos\theta + \ sin(n\theta)\, cos2\theta] \\ +d_n\,(n-1) r^{-n} \left[\begin{array}{c} (n+2)\ cos(n\theta)\, sin\theta\ cos\theta + \ (n-2)\ cos(n\theta)\, sin\theta\ cos\theta \\ +\ n\ sin(n\theta)\, cos2\theta \end{array} \right] \end{array} \right\} \end{array} \right]$$

(5A.116)

σ_{xy}

$$= \left[\begin{array}{c} \frac{2b_0}{r^2} sin\theta\ cos\theta \\ -\sum_{n=2,4,\ldots}^{N} \left\{ \begin{array}{c} a_n\, n\,(n-1)\, r^{n-2}\,[2\ cos(n\theta)\, sin\theta\ cos\theta - \ sin(n\theta)\, cos2\theta] \\ +b_n\,(n+1) r^n \left[\begin{array}{c} n\ cos(n\theta)\, sin\theta\ cos\theta - 2\ cos(n\theta)\, sin\theta\ cos\theta + n\ cos(n\theta)\, sin\theta\ cos\theta \\ +2\ cos(n\theta)\, sin\theta\ cos\theta - \ n\ sin(n\theta)\, cos2\theta \end{array} \right] \\ +\, c_n\, n\,(n+1)\, r^{-(n+2)}[2\ cos(n\theta)\, sin\theta\ cos\theta + \ sin(n\theta)\, cos2\theta] \\ +d_n\,(n-1) r^{-n} \left[\begin{array}{c} n\ cos(n\theta)\, sin\theta\ cos\theta + 2\ cos(n\theta)\, sin\theta\ cos\theta + \ n\ cos(n\theta)\, sin\theta\ cos\theta \\ -2\ cos(n\theta)\, sin\theta\ cos\theta + \ n\ sin(n\theta)\, cos2\theta \end{array} \right] \end{array} \right\} \end{array} \right]$$

(5A.117)

$$\sigma_{xy} = \left[\begin{array}{c} \frac{b_0}{r^2} sin2\theta \\ -\sum_{n=2,4,\ldots}^{N} \left\{ \begin{array}{c} a_n\, n\,(n-1)\, r^{n-2}\,[cos(n\theta)\,(sin2\theta) - \ sin(n\theta)\, cos2\theta] \\ +b_n\,(n+1) r^n \left[\begin{array}{c} n(2\ cos(n\theta)\, sin\theta\ cos\theta - \ sin(n\theta)\, cos2\theta) \\ +2\, cos(n\theta)\,(-sin\theta\ cos\theta + sin\theta\ cos\theta) \end{array} \right] \\ +\, c_n\, n\,(n+1)\, r^{-(n+2)}[cos(n\theta)\,(sin2\theta) + \ sin(n\theta)\, cos2\theta] \\ +d_n\,(n-1) r^{-n} \left[\begin{array}{c} n(2\ cos(n\theta)\, sin\theta\ cos\theta + \ sin(n\theta)\, cos2\theta) \\ +2\, cos(n\theta)\,(sin\theta\ cos\theta - sin\theta\ cos\theta) \end{array} \right] \end{array} \right\} \end{array} \right]$$

(5A.118)

$$\sigma_{xy} = \left[\begin{array}{c} \frac{b_0}{r^2} sin2\theta \\ -\sum_{n=2,4,\ldots}^{N} \left\{ \begin{array}{c} a_n\, n\,(n-1)\, r^{n-2} \sin(n\theta - 2\theta) \\ +b_n\,(n+1) r^n [n(cos(n\theta)\, sin2\theta - \ sin(n\theta)\, cos2\theta)] \\ +\, c_n\, n\,(n+1)\, r^{-(n+2)} \sin(n\theta + 2\theta) \\ +d_n\,(n-1) r^{-n}\,[n(cos(n\theta)\, sin2\theta + \ sin(n\theta)\, cos2\theta)] \end{array} \right\} \end{array} \right]$$

(5A.119)

$$\sigma_{xy} = \left[\begin{array}{c} \frac{b_0}{r^2} sin2\theta \\ -\sum_{n=2,4,\ldots}^{N} \left\{ \begin{array}{c} a_n\, n\,(n-1)\, r^{n-2} \sin(2\theta - n\theta) \\ +b_n n\,(n+1) r^n \sin(2\theta - n\theta) \\ +\, c_n\, n\,(n+1)\, r^{-(n+2)} \sin(n\theta + 2\theta) \\ +\, d_n n\,(n-1) r^{-n} \sin(n\theta + 2\theta) \end{array} \right\} \end{array} \right] \quad \text{(5A.120)}$$

Now from *equation 5.18*

$$S = \sigma_{xx} + \sigma_{yy} \tag{5A.121}$$

and *equations 5A.100 and 5A.110* give

$$S = \left[\begin{array}{c} \left[\begin{array}{c} \frac{b_0}{r^2} cos2\theta + 2c_0 \\ - \sum_{n=2,4,\ldots}^{N} \left\{ \begin{array}{c} a_n\, n\,(n-1)\, r^{n-2}\,[cos(n\theta - 2\theta)] \\ +b_n\,(n+1) r^n [n(cos(n\theta - 2\theta)) - 2\, cos(n\theta)] \\ +\, c_n\, n\,(n+1)\, r^{-(n+2)} [cos(n\theta + 2\theta)] \\ +d_n\,(n-1) r^{-n}\,[n(cos(n\theta + 2\theta)) + 2\, cos(n\theta)] \end{array} \right\} \end{array} \right] \\ + \left[\begin{array}{c} -\frac{b_0}{r^2} cos2\theta + 2c_0 \\ + \sum_{n=2,4,\ldots}^{N} \left\{ \begin{array}{c} a_n\, n\,(n-1)\, r^{n-2}\,[cos(n\theta - 2\theta)] \\ +b_n\,(n+1) r^n [n(cos(n\theta - 2\theta)) + 2\, cos(n\theta)] \\ +\, c_n\, n\,(n+1)\, r^{-(n+2)} [cos(n\theta + 2\theta)] \\ +d_n\,(n-1) r^{-n}\,[n(cos(n\theta + 2\theta)) - 2\, cos(n\theta)] \end{array} \right\} \end{array} \right] \end{array} \right] \tag{5A.122}$$

$$S = \left[\begin{array}{c} 4\, c_0 \\ + \sum_{n=2,4,\ldots}^{N} \left\{ \begin{array}{c} +b_n\, 4\,(n+1) r^n\, cos(n\theta) \\ -d_n\, 4\,(n-1) r^{-n}\, cos(n\theta) \end{array} \right\} \end{array} \right] \tag{5A.123}$$

Equations 5A.74, 5A.82 and 5A.123 all agree with each other, as they should.

A6 Thermoelastic Stress Analysis of a Finite Plate Loaded by a Circular Pin.

This Appendix involves the thermoelastic stress analysis of finite plate loaded by a circular pin. The changes in this Appendix compared to the analysis and results of Chapter 6 are that the present analyses involves an increased number of side conditions i.e., the number of traction-free boundary conditions on the right vertical edge has increased from 301 points to 3001 points, and the TSA results here are compared with ANSYS which are improved over those from the ABAQUS i.e., there are no discrepancies in ANSYS results on or away from the boundary of the hole. *Figures A6.1 through A6.3* represent plots similar to those of *figures 6.37 through 6.38*. The only difference being that the *discretely* imposed traction-free boundary conditions for *figures A6.1 through A6.3* are imposed at 3001 point on the right vertical edge of the plate. In addition to $m_1 = 3413$ TSA values and $h_1 = 2*831$ *discretely* imposed traction-free boundary conditions on the edge of the hole, 101 points are used on the top-half edge of the plate and another set of 3001 points on the right edge of the plate i.e., the total number of traction-free conditions on the side and top edge are $t_1 = 2*101+2*3001$. Again for this total of $m_1+h_1+t_1 = 11,279$ input values, $k = 9$ was found to continue to be an appropriate number of coefficients. It is worth noting that with a change in the number of traction-free boundary conditions on the right vertical edge, there is an insignificant change in the results (*figures A6.1 through A6.3*). There is also no change in the number of Airy coefficients needed.

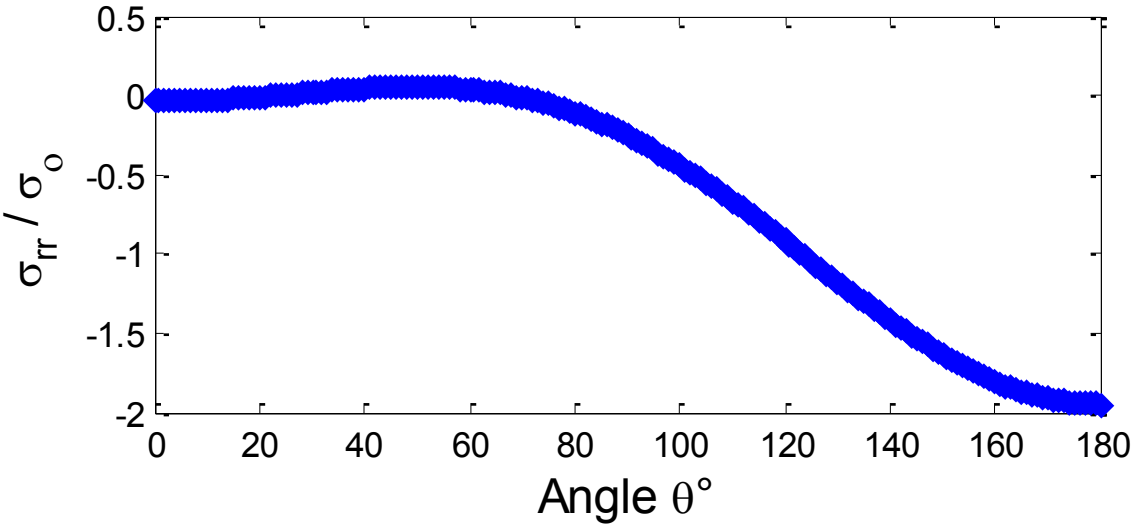

Fig. A6.1: TSA-determined σ_{rr}/σ_0 around the boundary of the hole (r/R = 1) for $m_1+h_1+t_1 = 11,279$ input values, $k = 9$ coefficients and $m_1 = 3,413$ TSA values, $h_1 = 2*831$, $t_1 = 2*101+2*3001$

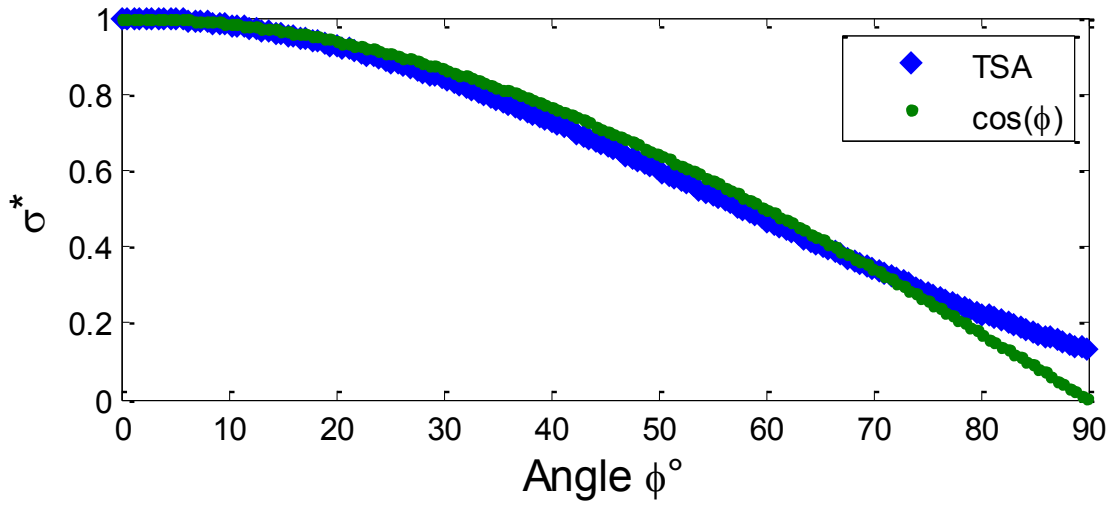

Fig. A6.2: Plot of $cos(\phi)$ and TSA-determined σ_* (= $\sigma_{rr}/\sigma_{rr(max)}$) vs. angle ϕ (=180^o - θ) around the boundary of the hole (r/R = 1) for $m_1+h_1+t_1 = 11,279$ input values, $k = 9$ coefficients and $m_1 = 3,413$ TSA values, $h_1 = 2*831$, $t_1 = 2*101+2*3001$

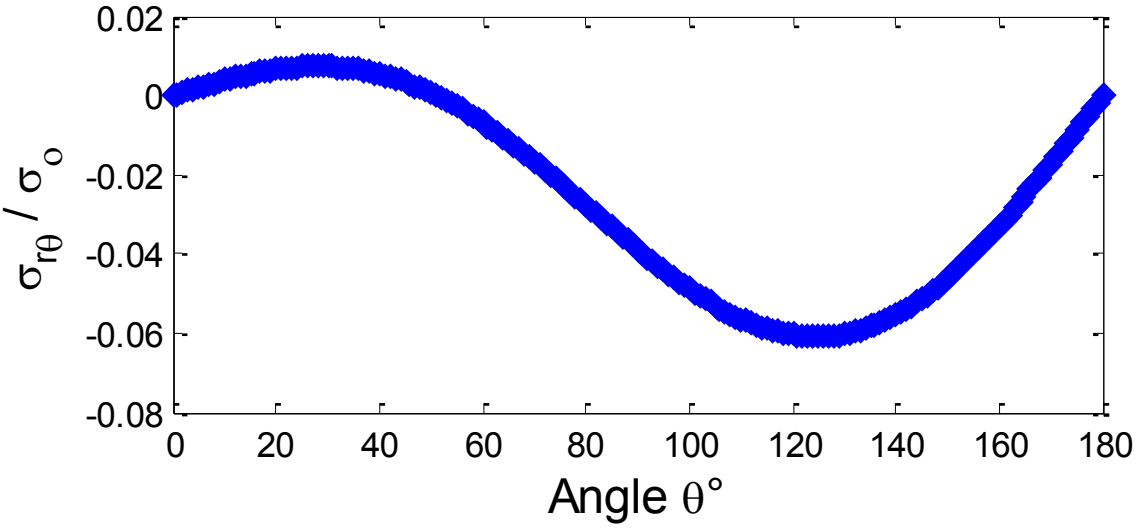

Fig. A6.3: TSA-determined $\sigma_{r\theta}/\sigma_0$ around the boundary of the hole (r/R = 1) for $m_1+h_1+t_1$ = *11,279* input values, k = *9* coefficients and m_1 = *3,413* TSA values, h_1 = *2*831*, t_1 = *2*101+2*3001*

Since ABAQUS was giving the stress discrepancy on the boundary of the hole, the numerical analysis was enhanced by remodeling the bolted joint connection in ANSYS. A 2D finite element model was constructed in ANSYS using plane82 elements. The material properties are incorporated in the model in defining element attributes for plate (E = 68.95 GPa (10 x 10^6 psi), Poisson's ratio, ν = 0.33) and the pin (E = 206 GPa (30 x 10^6 psi), Poisson's ratio, ν = 0.27). The coefficient of friction of μ = 0.2 was applied between the pin and the hole interface. The dimensions for the plate and the pin are described in sections 6.3 and 6.4. The plate and pin were modeled such that they have an initial contact. For solving 2D contact problems in ANSYS, one needs to define a contact and target elements between the plate and the bolt. CONTA172 was used to represent surface-to-surface contact and sliding between 2-D deformable surfaces. It has the same geometric characteristics as the solid element face with which it is connected and in the present analysis the contact elements are defined on the hole boundary of the plate. In 2D the target surface is defined by TARGE169 elements and in the present analysis the target elements

are defined on the boundary of the pin. Since the geometry and loading is symmetrical about one axis, a symmetrical boundary condition is applied along the line of symmetry and a far-field stress of 16.54 MPa (2400 psi) is applied on the plate. Also a small region near the center of the pin was completely constrained. The symmetrical model of plate and pin was meshed with a total of 66,864 elements and 202,119 nodes. *Figures A6.5 through A6.10* are ANSYS generated contour plots of σ_{xx}, σ_{yy}, σ_{xy}, σ_{rr}, $\sigma_{\theta\theta}$ and $\sigma_{r\theta}$ respectively and all the units for these plots are in psi.

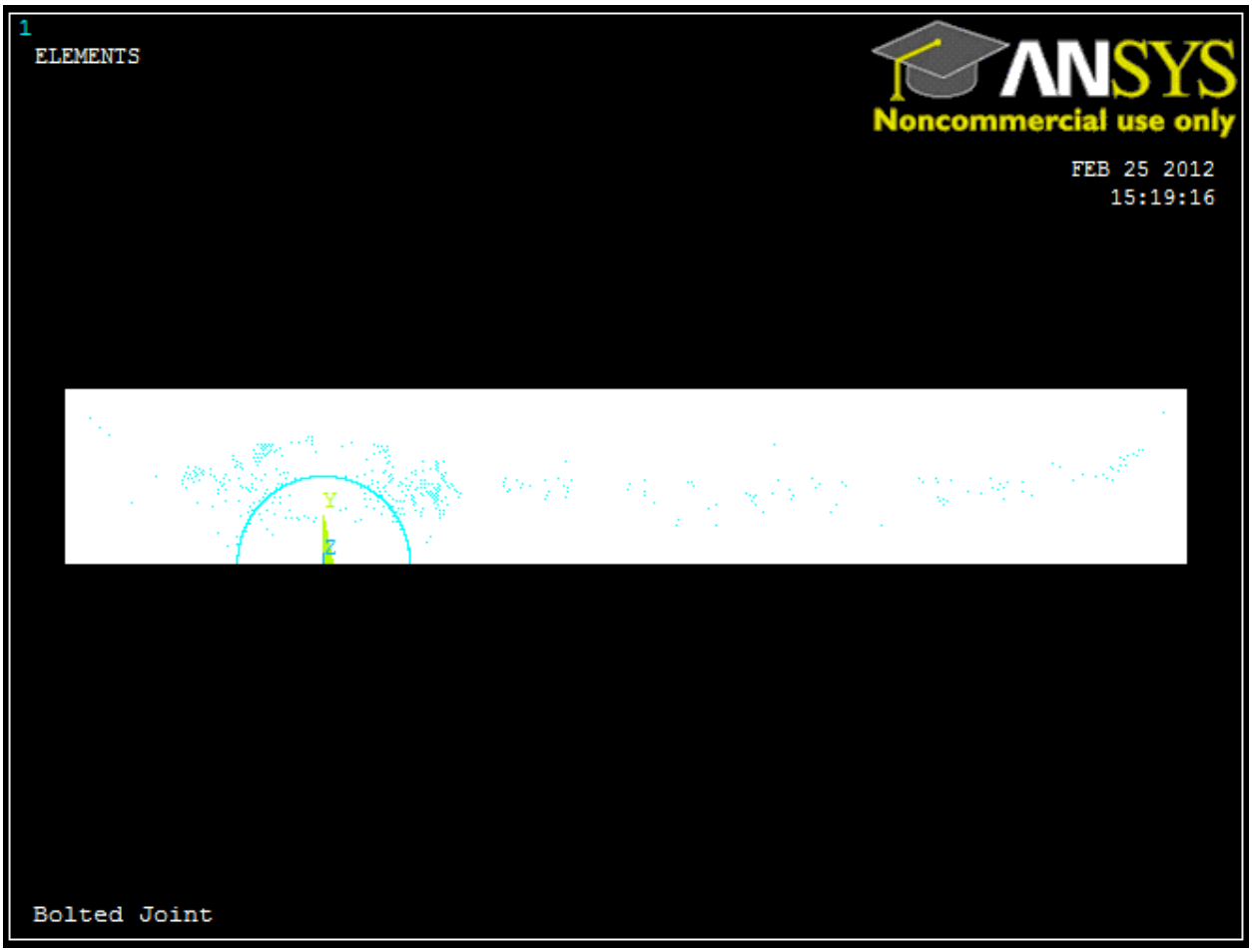

Fig. A6.4: Finite Element model of the plate with circular pin in ANSYS

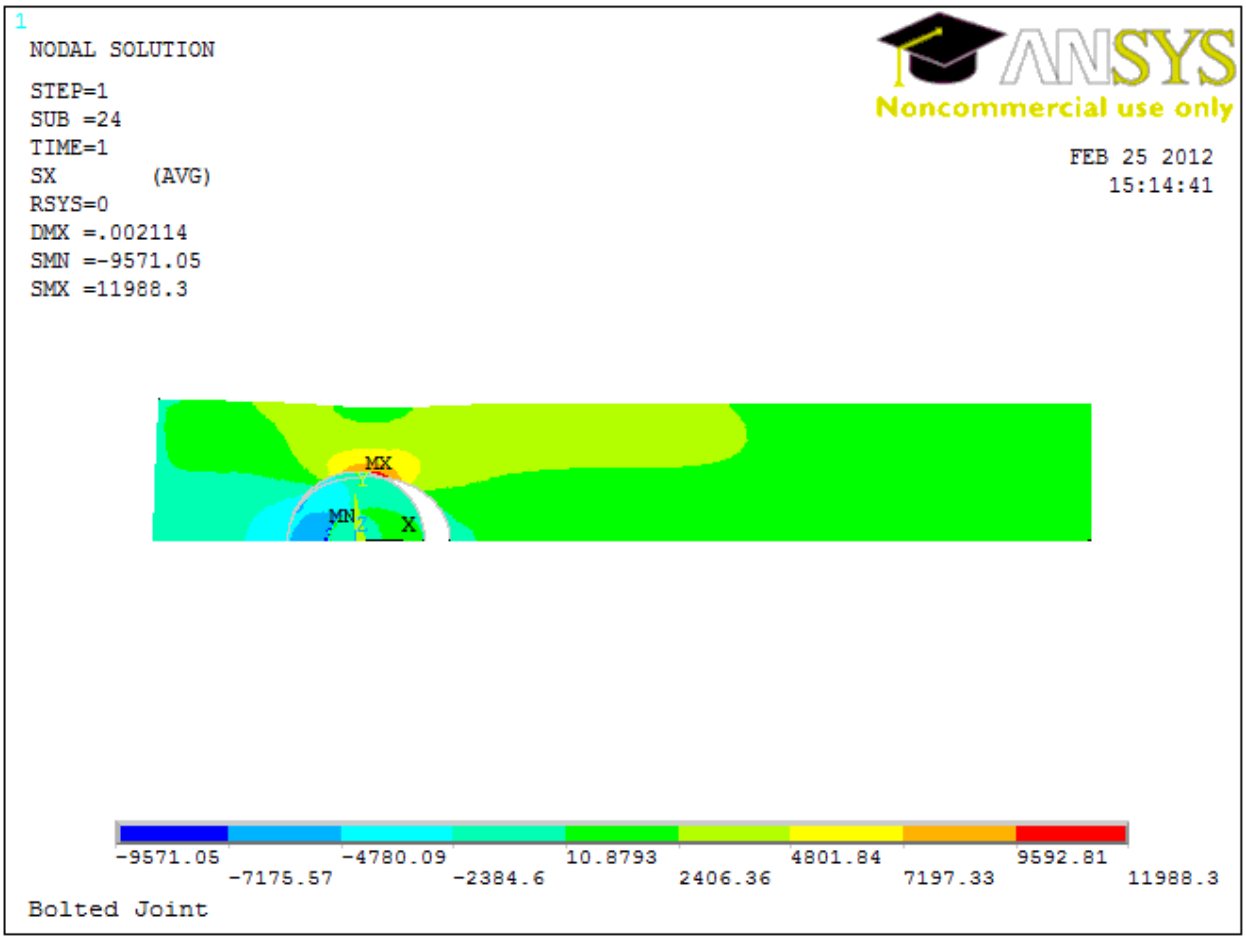

Fig. A6.5: Contour plot of stress in the x-direction (σ_{xx}) for the plate with circular pin

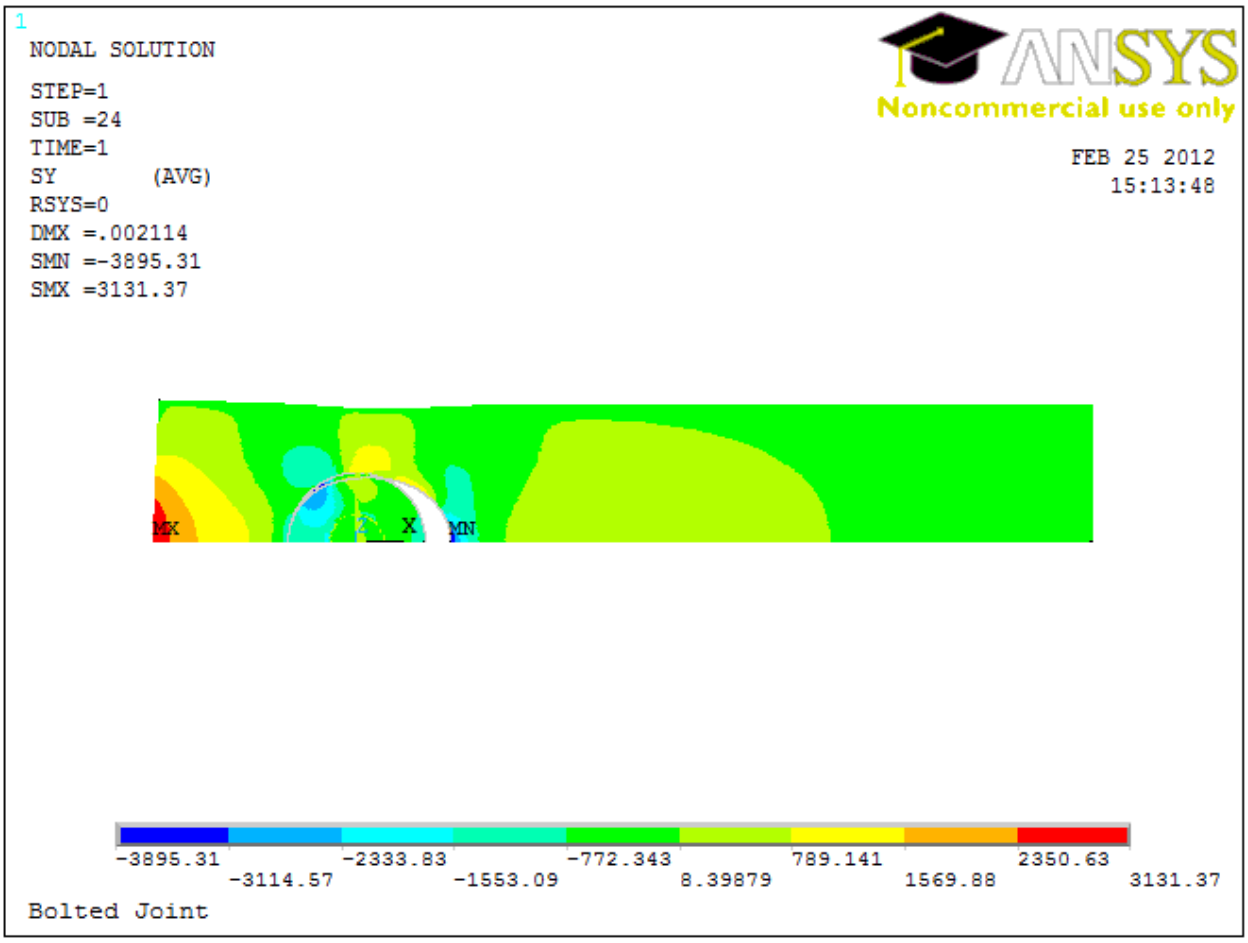

Fig. A6.6: Contour plot of stress in the y-direction (σ_{yy}) for the plate with circular pin

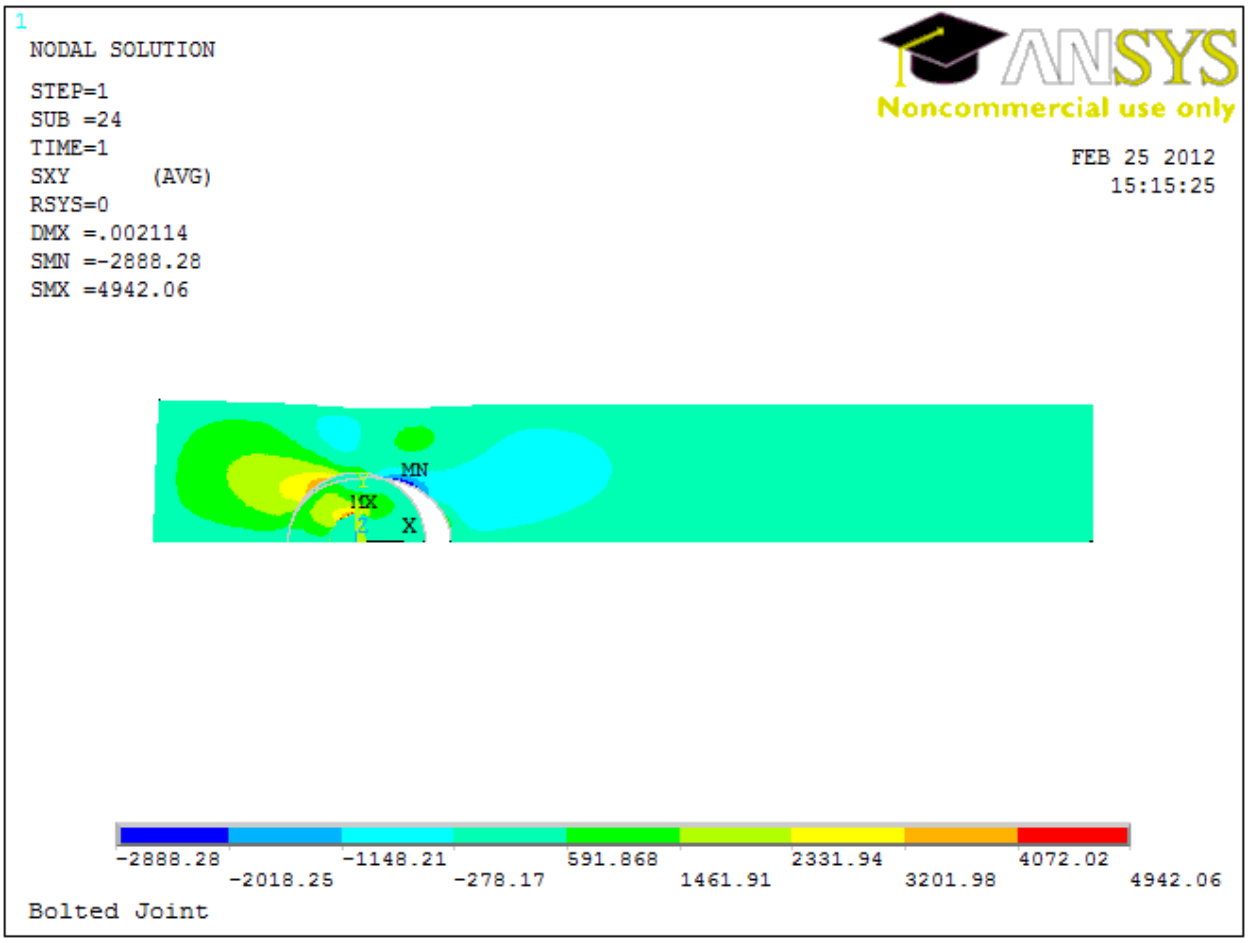

Fig. A6.7: Contour plot of shear stress (σ_{xy}) for the plate with circular pin

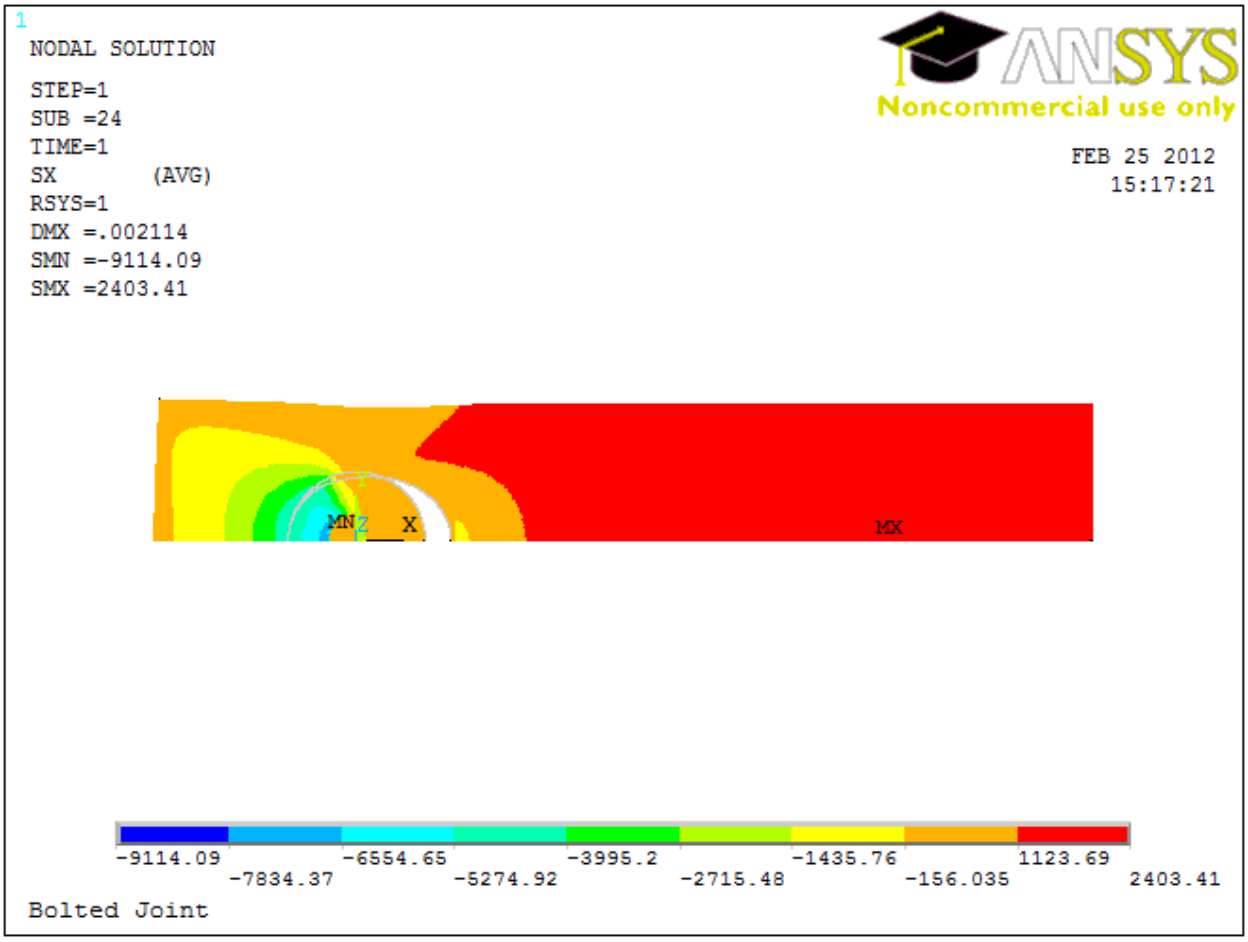

Fig. A6.8: Contour plot of radial stress (σ_{rr}) for the plate with circular pin

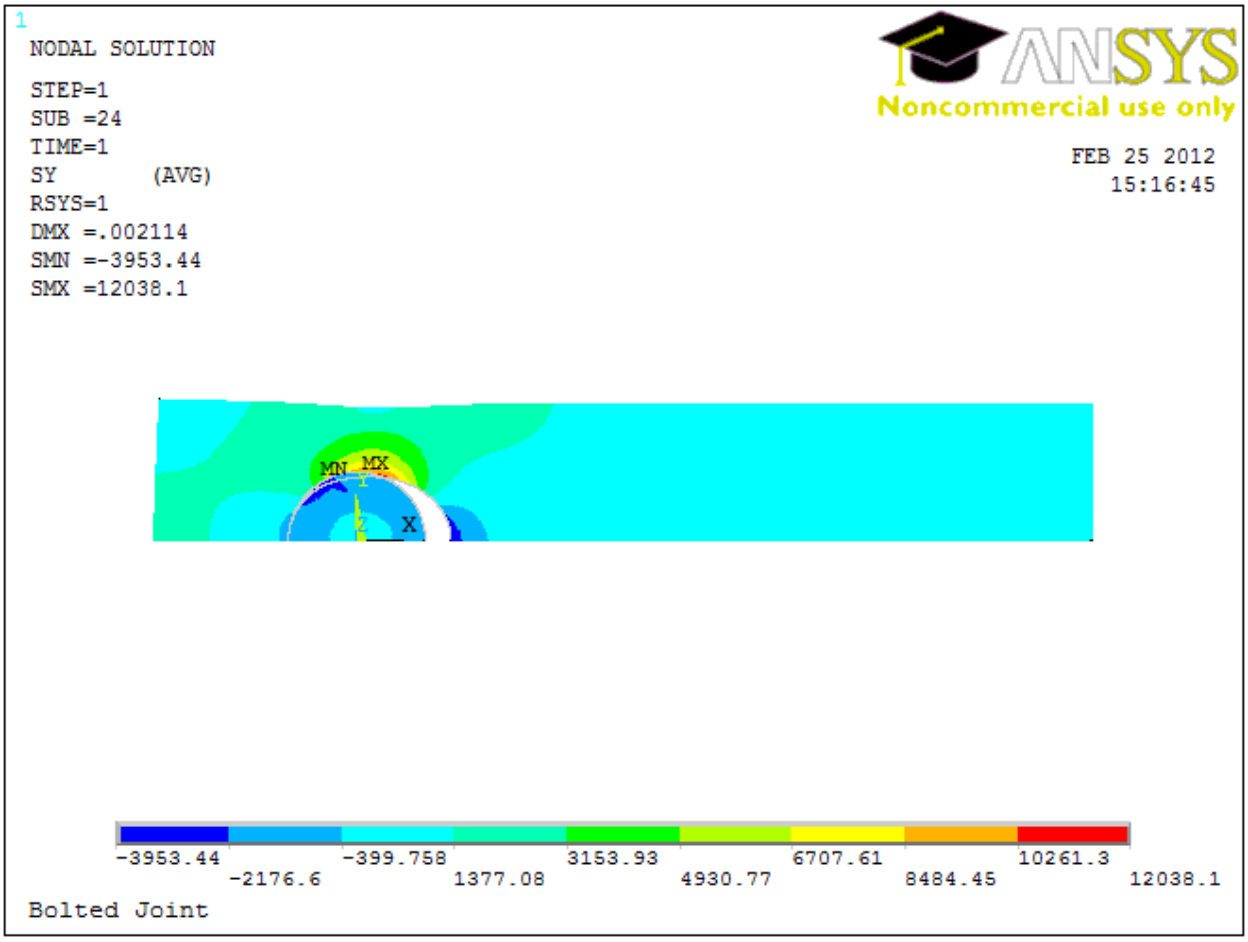

Fig. A6.9: Contour plot of tangential stress ($\sigma_{\theta\theta}$) for the plate with circular pin

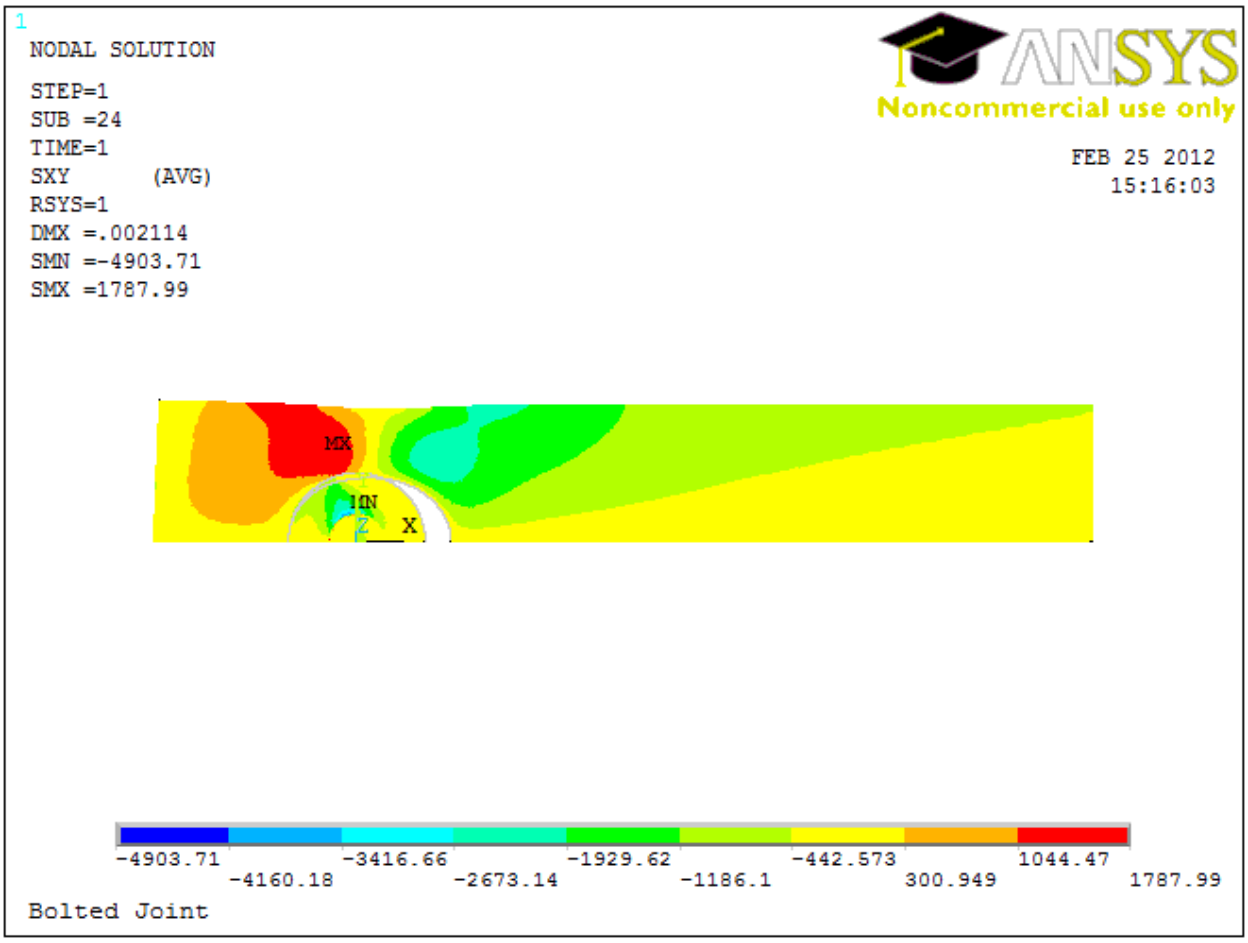

Fig. A6.10: Contour plot of polar shear stress ($\sigma_{r\theta}$) for the plate with circular pin

As done using ABAQUS, The results from ANSYS were exported to MATLAB and are plotted against TSA results, *figures A6.11 through A6.30*. After evaluating $k = 9$ Airy coefficients from $m_1+h_1+t_1 = 11,279$ input values, the individual components of stresses can be determined from *equations 6.6, 6.7, 6.9 and 6.11 through 6.13*. There is an excellent agreement between the experimental and ANSYS-predicted results. The present use of more traction-free conditions on the vertical edge of the plate somewhat improved the TSA results, the ANSYS pin-hole contact predictions are smoother than those by ABAQUS, and the current ANSYS-TSA results tend to agree with each other better than those by the previous ABAQUS-TSA. While the force

equilibrium checks of Table 6.1 and *figures 6.108 and 6.109* were not re-calculated based on the new-TSA results, they are expected to be at least as good as those of the original Table 6.1 and *figures 6.108 and 6.109*. The ANSYS analyses employ approximately twice as many elements as used with ABAQUS, although ABAQUS results tend to not change with increased number of elements.

As before, angle θ of *figures A6.11 through A6.23* is measured counter-clockwise from the downward positive x-axis and r is measured from the center of the hole of *figure 6.2*. Again the stresses are normalized with the far-field stress σ_0 = 16.54 MPa = 2400 psi.

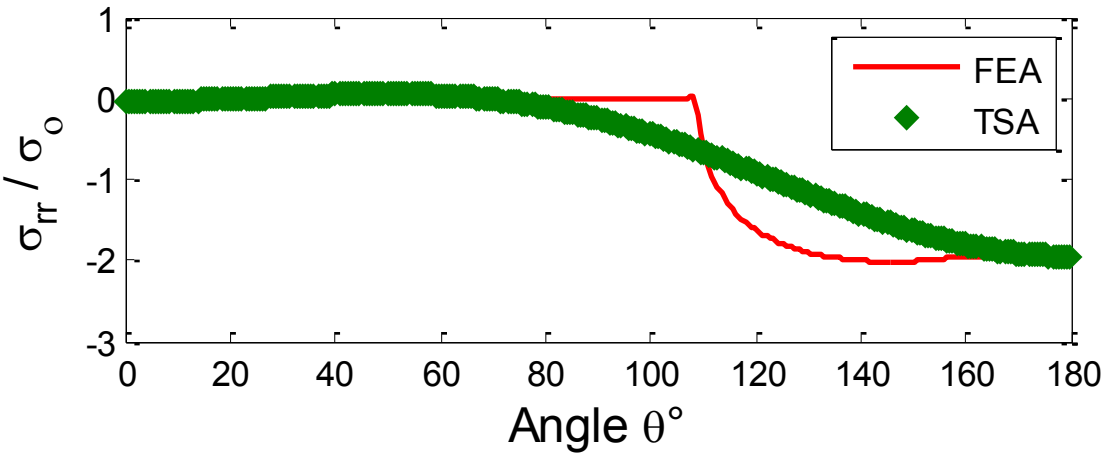

Fig. A6.11: Plot of σ_{rr}/σ_0 around the boundary of the hole (r/R = 1) from ANSYS and TSA for $m_1+h_1+t_1 = 11{,}279$ input values and $k = 9$ ($m_1 = 3{,}413$ TSA values, $h_1 = 2*831$, $t_1 = 2*101+2*3001$)

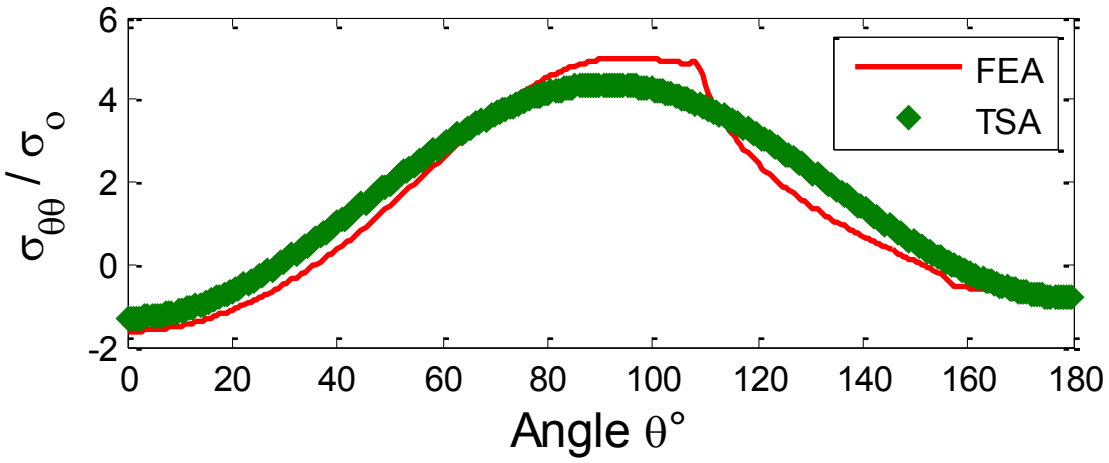

Fig. A6.12: Plot of $\sigma_{\theta\theta}/\sigma_0$ around the boundary of the hole (r/R = 1) from ANSYS and TSA for $m_1+h_1+t_1 = 11{,}279$ input values and $k = 9$ ($m_1 = 3{,}413$ TSA values, $h_1 = 2*831$, $t_1 = 2*101+2*3001$)

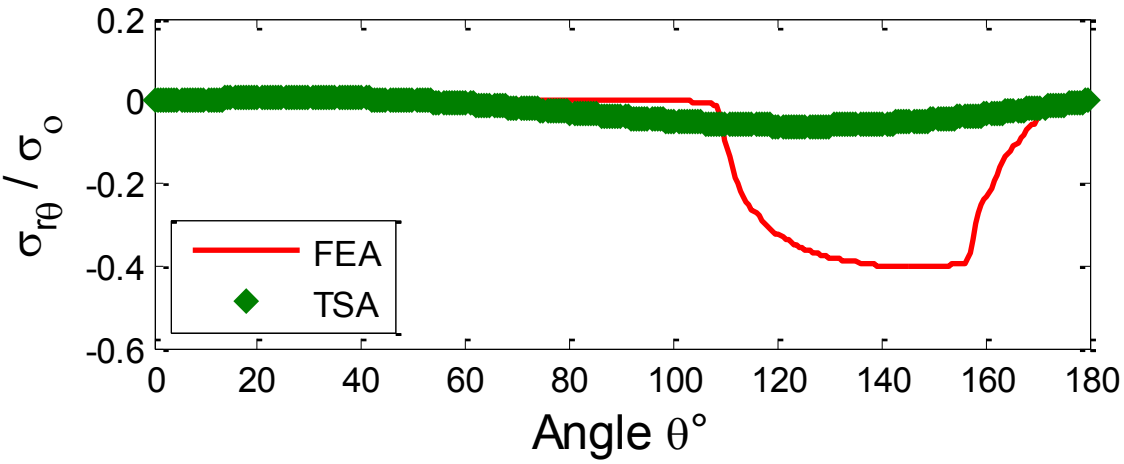

Fig. A6.13: Plot of $\sigma_{r\theta}/\sigma_0$ around the boundary of the hole (r/R = 1) from ANSYS and TSA for $m_1+h_1+t_1 = 11{,}279$ input values and $k = 9$ ($m_1 = 3{,}413$ TSA values, $h_1 = 2*831$, $t_1 = 2*101+2*3001$)

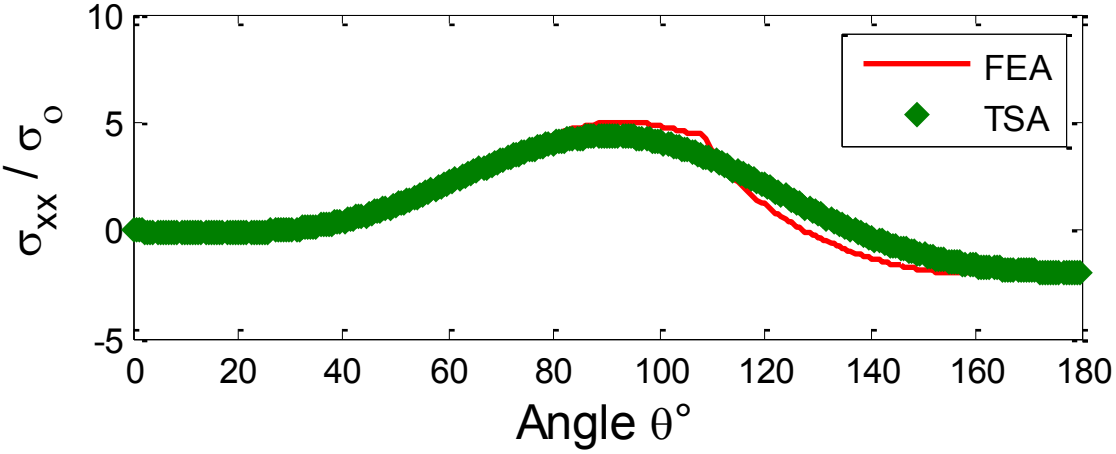

Fig. A6.14: Plot of σ_{xx}/σ_0 around the boundary of the hole (r/R = 1) from ANSYS and TSA for $m_1+h_1+t_1 = 11,279$ input values and $k = 9$ ($m_1 = 3,413$ TSA values, $h_1 = 2*831$, $t_1 = 2*101+2*3001$)

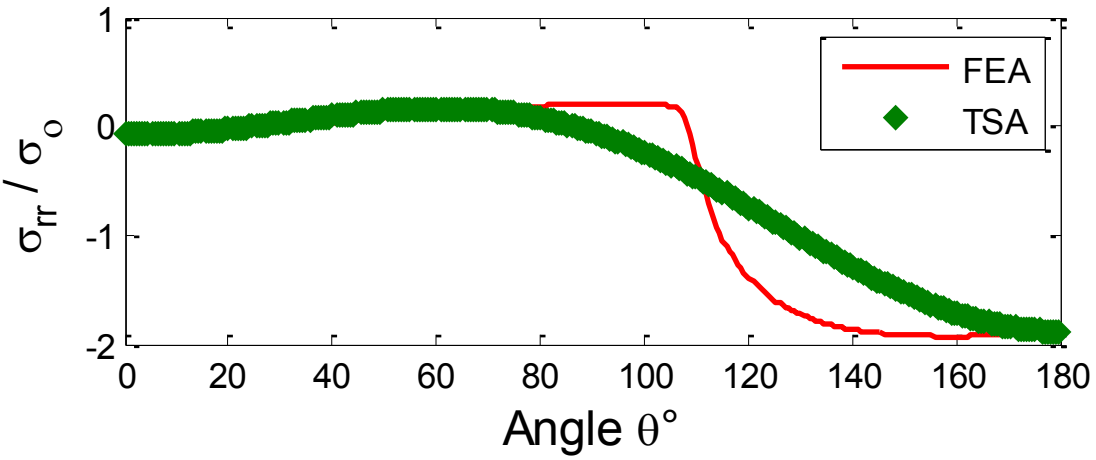

Fig. A6.15: Plot of σ_{rr}/σ_0 along r/R = 1.05 from ANSYS and TSA for $m_1+h_1+t_1 = 11,279$ input values and $k = 9$ ($m_1 = 3,413$ TSA values, $h_1 = 2*831$, $t_1 = 2*101+2*3001$)

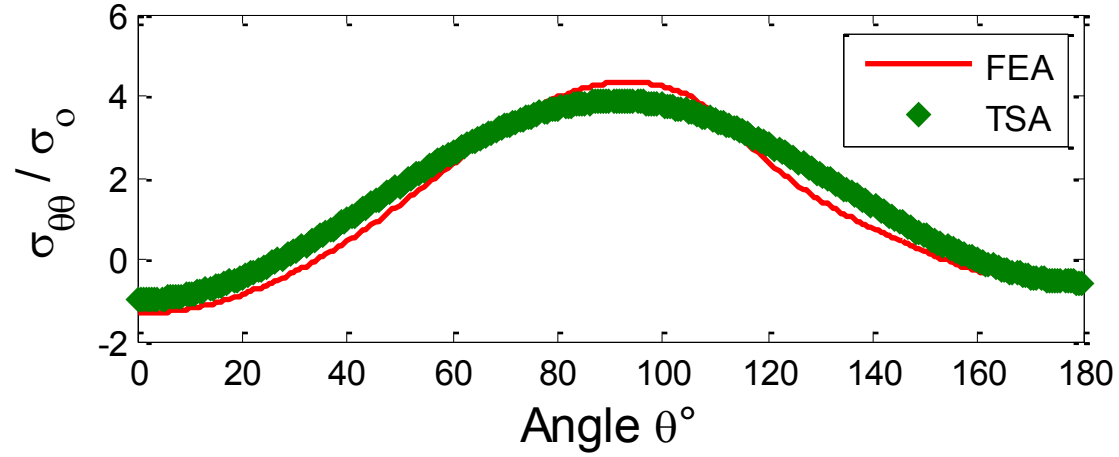

Fig. A6.16: Plot of $\sigma_{\theta\theta}/\sigma_0$ along r/R = 1.05 from ANSYS and TSA for $m_1+h_1+t_1 = 11,279$ input values and $k = 9$ ($m_1 = 3,413$ TSA values, $h_1 = 2*831$, $t_1 = 2*101+2*3001$)

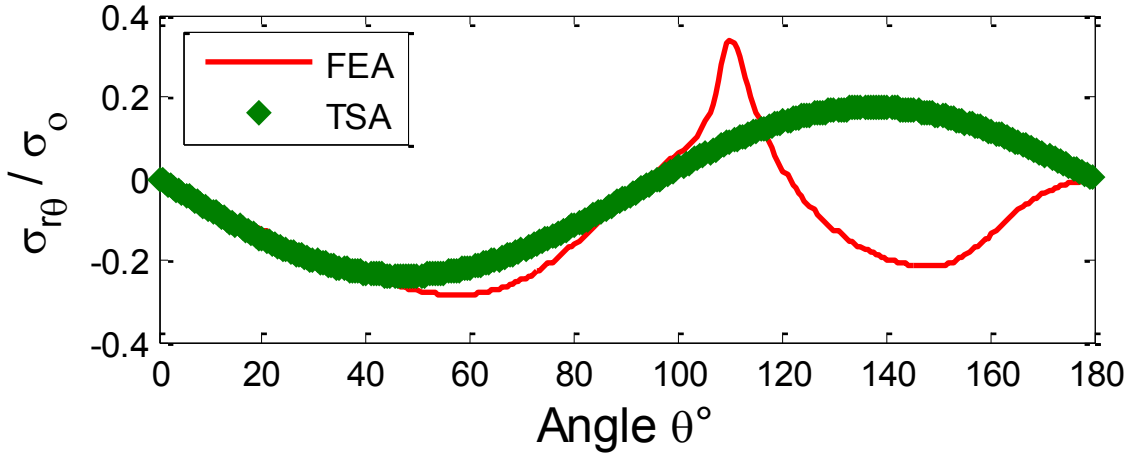

Fig. A6.17: Plot of $\sigma_{r\theta}/\sigma_0$ along r/R = 1.05 from ANSYS and TSA for $m_1+h_1+t_1 = 11,279$ input values and $k = 9$ ($m_1 = 3,413$ TSA values, $h_1 = 2*831$, $t_1 = 2*101+2*3001$)

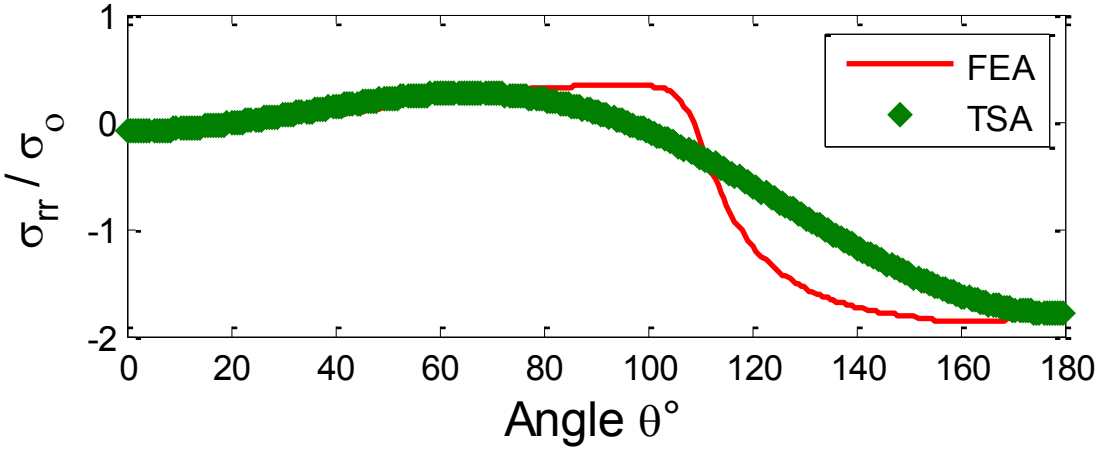

Fig. A6.18: Plot of σ_{rr}/σ_0 along r/R = 1.1 from ANSYS and TSA for $m_1+h_1+t_1 = 11,279$ input values and $k = 9$ ($m_1 = 3,413$ TSA values, $h_1 = 2*831$, $t_1 = 2*101+2*3001$)

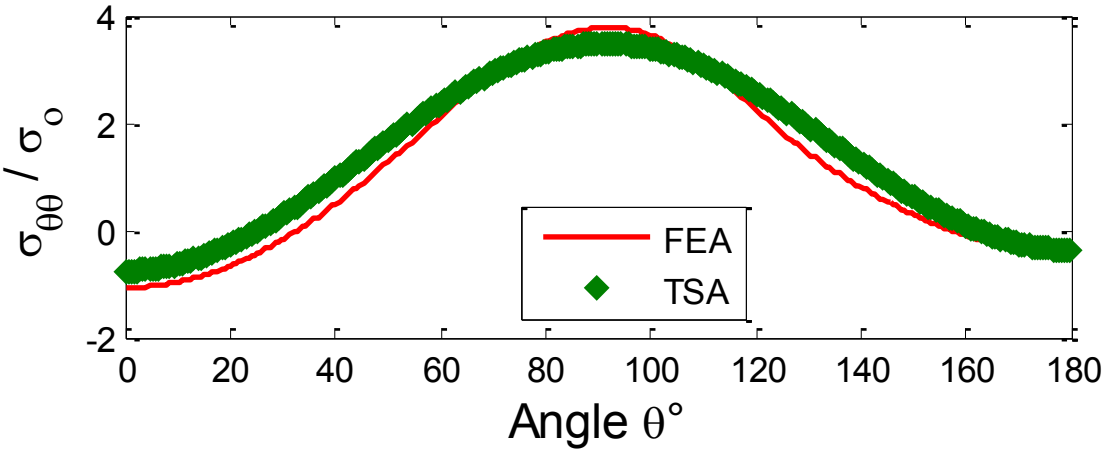

Fig. A6.19: Plot of $\sigma_{\theta\theta}/\sigma_0$ along r/R = 1.1 from ANSYS and TSA for $m_1+h_1+t_1 = 11,279$ input values and $k = 9$ ($m_1 = 3,413$ TSA values, $h_1 = 2*831$, $t_1 = 2*101+2*3001$)

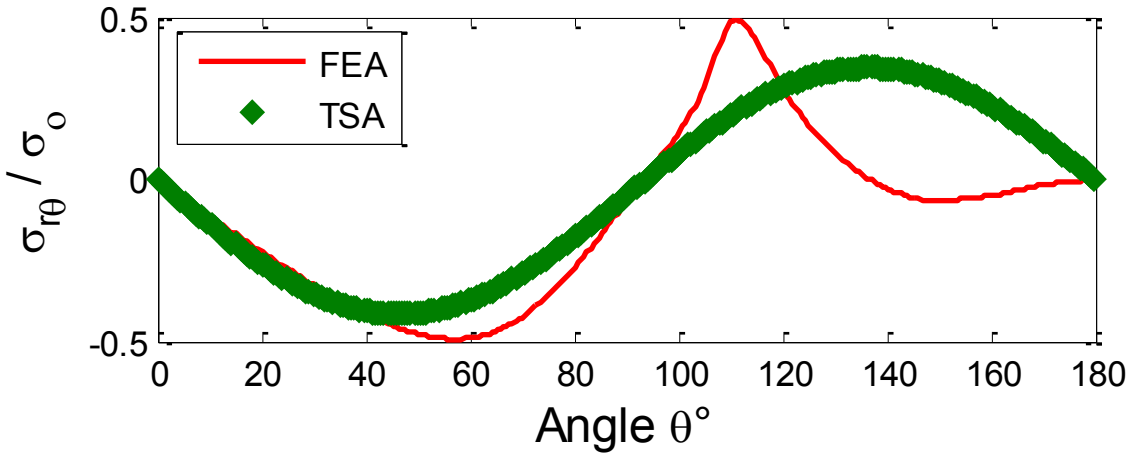

Fig. A6.20: Plot of $\sigma_{r\theta}/\sigma_0$ along r/R = 1.1 from ANSYS and TSA for $m_1+h_1+t_1 = 11,279$ input values and $k = 9$ ($m_1 = 3,413$ TSA values, $h_1 = 2*831$, $t_1 = 2*101+2*3001$)

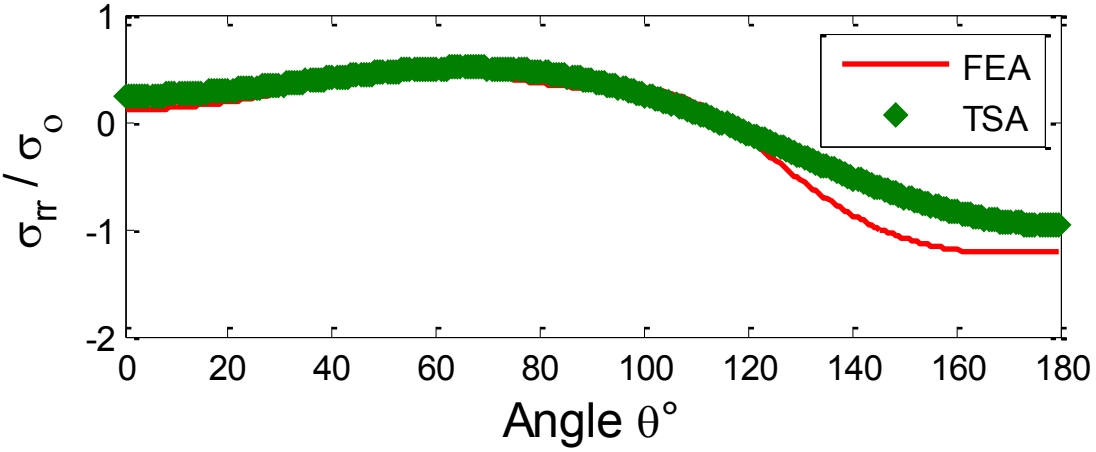

Fig. A6.21: Plot of σ_{rr}/σ_0 along r/R = 1.5 from ANSYS and TSA for $m_1+h_1+t_1 = 11,279$ input values and $k = 9$ ($m_1 = 3,413$ TSA values, $h_1 = 2*831$, $t_1 = 2*101+2*3001$)

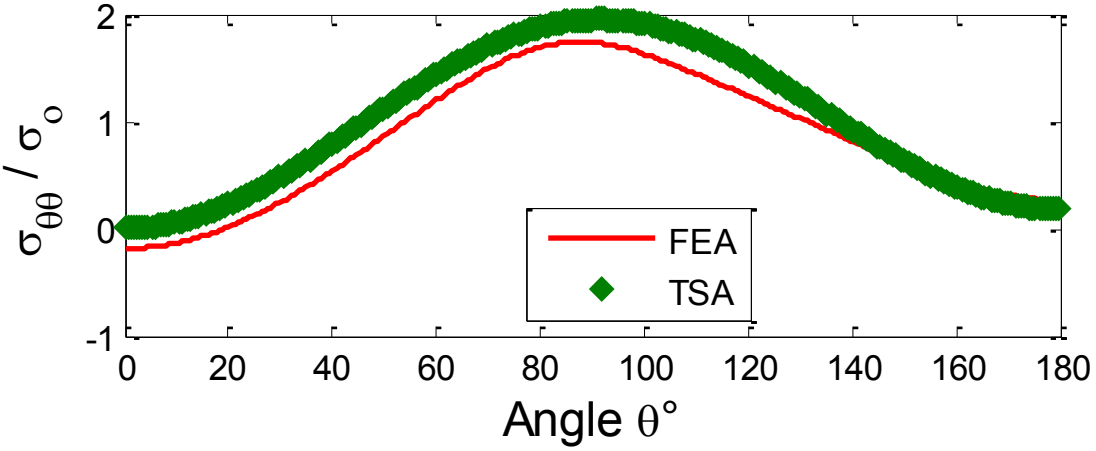

Fig. A6.22: Plot of $\sigma_{\theta\theta}/\sigma_0$ along r/R = 1.5 from ANSYS and TSA for $m_1+h_1+t_1 = 11,279$ input values and $k = 9$ ($m_1 = 3,413$ TSA values, $h_1 = 2*831$, $t_1 = 2*101+2*3001$)

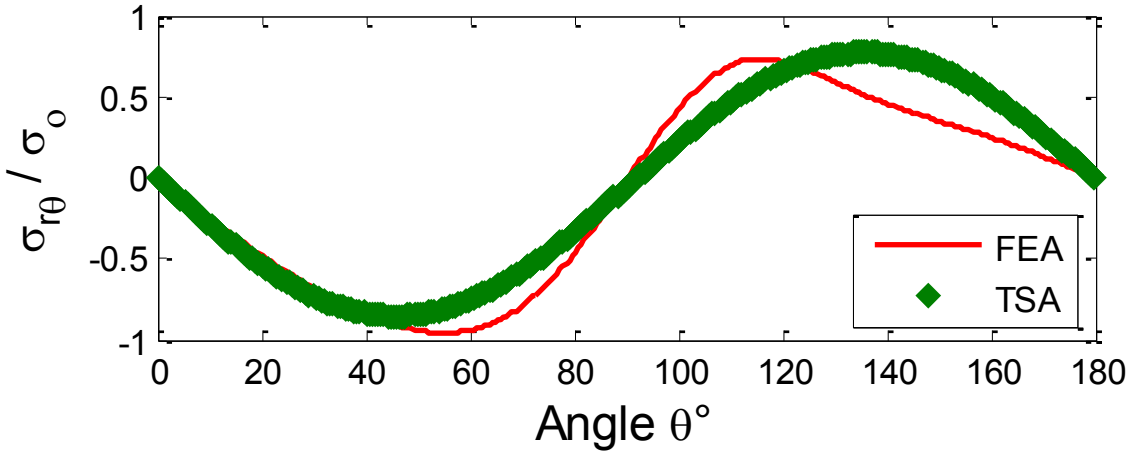

Fig. A6.23: Plot of $\sigma_{r\theta}/\sigma_0$ along r/R = 1.5 from ANSYS and TSA for $m_1+h_1+t_1 = 11,279$ input values and $k = 9$ ($m_1 = 3,413$ TSA values, $h_1 = 2*831$, $t_1 = 2*101+2*3001$)

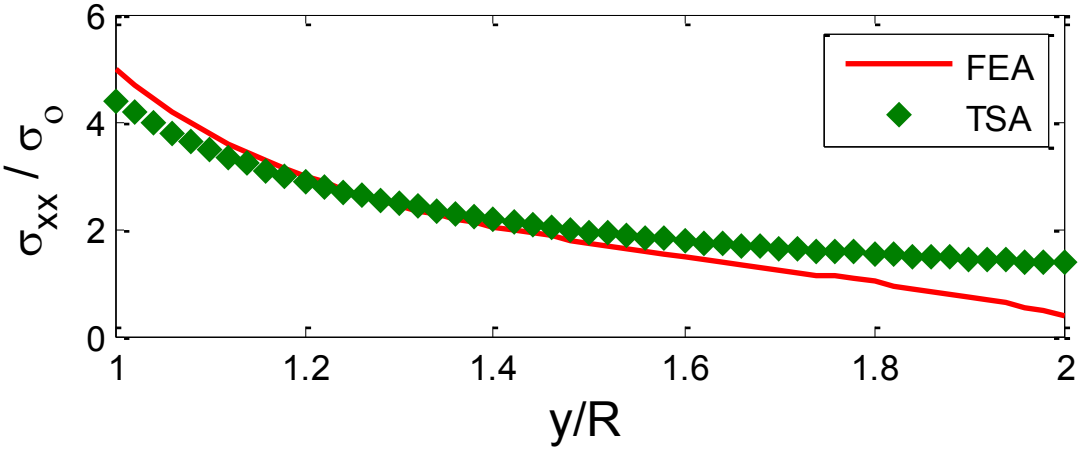

Fig. A6.24: Plot of σ_{xx}/σ_0 along the line extending from the edge of the hole (x = 0 or θ = 90^o) from ANSYS and TSA for $m_1+h_1+t_1 = 11,279$ input values and $k = 9$ ($m_1 = 3,413$ TSA values, $h_1 = 2*831$, $t_1 = 2*101+2*3001$)

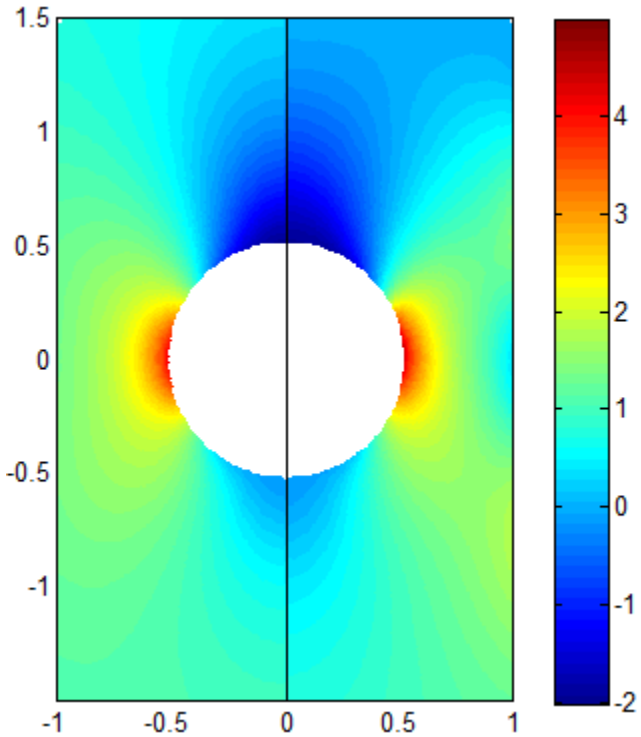

Fig. A6.25: Contour plot of σ_{xx}/σ_0 from TSA (left) for $m_1+h_1+t_1 = 11,279$ input values and $k = 9$ ($m_1 = 3,413$ TSA values, $h_1 = 2*831$, $t_1 = 2*101+2*3001$) and ANSYS (right)

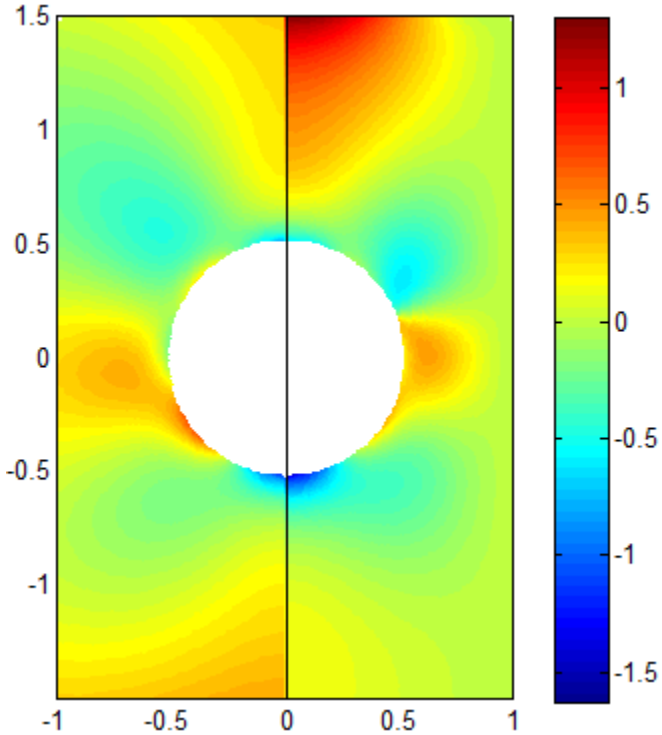

Fig. A6.26: Contour plot of σ_{yy}/σ_0 from TSA (left) for $m_1+h_1+t_1 = 11,279$ input values and $k = 9$ ($m_1 = 3,413$ TSA values, $h_1 = 2*831$, $t_1 = 2*101+2*3001$) and ANSYS (right)

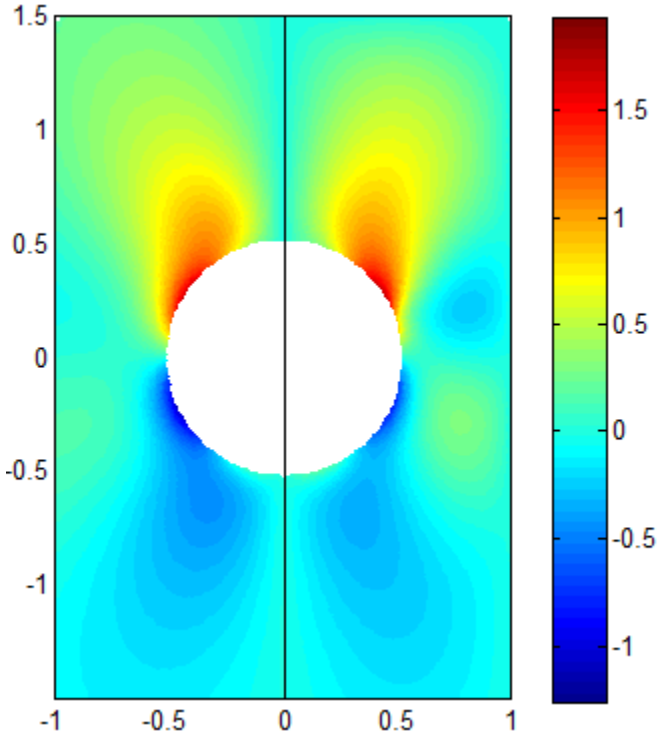

Fig. A6.27: Contour plot of σ_{xy}/σ_0 from TSA (left) for $m_1+h_1+t_1 = 11,279$ input values and $k = 9$ ($m_1 = 3,413$ TSA values, $h_1 = 2*831$, $t_1 = 2*101+2*3001$) and ANSYS (right)

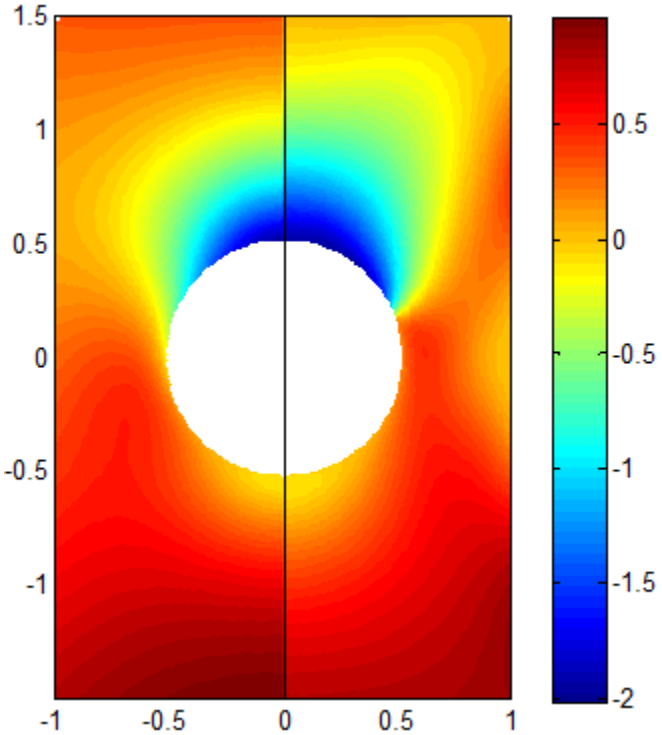

Fig. A6.28: Contour plot of σ_{rr}/σ_0 from TSA (left) for $m_1+h_1+t_1 = 11,279$ input values and $k = 9$ ($m_1 = 3,413$ TSA values, $h_1 = 2*831$, $t_1 = 2*101+2*3001$) and ANSYS (right)

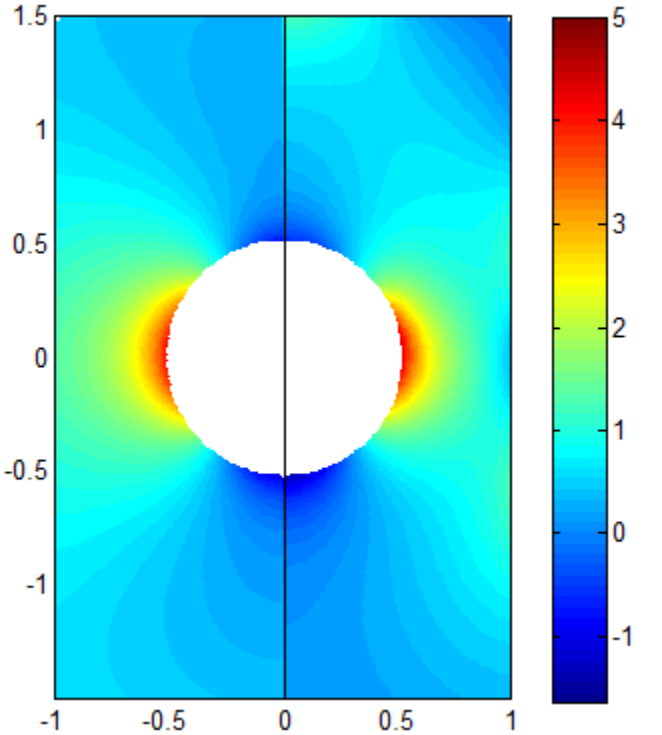

Fig. A6.29: Contour plot of $\sigma_{\theta\theta}/\sigma_0$ from TSA (left) for $m_1+h_1+t_1 = 11,279$ input values and $k = 9$ ($m_1 = 3,413$ TSA values, $h_1 = 2*831$, $t_1 = 2*101+2*3001$) and ANSYS (right)

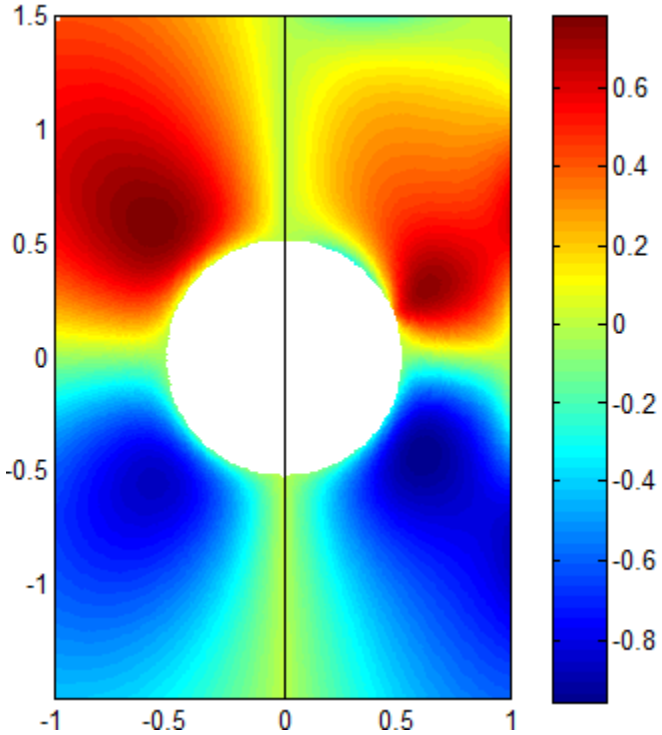

Fig. A6.30: Contour plot of $\sigma_{r\theta}/\sigma_0$ from TSA (left) for $m_1+h_1+t_1 = 11,279$ input values and $k = 9$ ($m_1 = 3,413$ TSA values, $h_1 = 2*831$, $t_1 = 2*101+2*3001$) and ANSYS (right)

A7 Stress Equations for a Plate Symmetric about x-axis.

A general expression for the Airy stress function, ϕ, which satisfies the biharmonic equation $\nabla^4\phi = 0$, and thus equilibrium and compatibility, can be written as follows [3 and 6]

$$\begin{aligned}
&\phi = a_0 + b_0 \ln r + c_0 r^2 + d_0 r^2 \ln r + \left(A_0 + B_0 \ln r + C_0 r^2 + D_0 r^2 \ln r\right)\theta \\
&+ \left(a_1 r + b_1 r \ln r + \frac{c_1}{r} + d_1 r^3\right)\sin\theta + \left(a_1' r + b_1' r \ln r + \frac{c_1'}{r} + d_1' r^3\right)\cos\theta \\
&+ \left(A_1 r + B_1 r \ln r\right)\theta \sin\theta + \left(A_1' r + B_1' r \ln r\right)\theta\cos\theta \\
&+ \sum_{n=2}^{\infty}\left(a_n r^n + b_n r^{n+2} + c_n r^{-n} + d_n r^{2-n}\right)\sin(n\theta) \\
&+ \sum_{n=2}^{\infty}\left(a_n' r^n + b_n' r^{n+2} + c_n' r^{-n} + d_n' r^{2-n}\right)\cos(n\theta)
\end{aligned} \tag{7A.1}$$

Based on ϕ of *equation 7A.1*, and since

$$\sigma_{rr} = \frac{1}{r}\cdot\frac{\partial\phi}{\partial r} + \frac{1}{r^2}\frac{\partial^2\phi}{\partial\theta^2},\ \ \sigma_{\theta\theta} = \frac{\partial^2\phi}{\partial r^2} \quad \text{and} \quad \sigma_{r\theta} = -\frac{\partial}{\partial r}\cdot\left(\frac{1}{r}\cdot\frac{\partial\phi}{\partial\theta}\right) \tag{7A.2}$$

the individual polar components of stress become

$$\sigma_{rr} = \frac{b_0}{r^2} + 2c_0 + d_0\left(2\ln r + 1\right) + B_0\frac{\theta}{r^2} + 2C_0\theta + D_0\left(2\ln r + 1\right)\theta$$
$$+\left(\frac{b_1}{r} - \frac{2c_1}{r^3} + 2d_1 r\right)\sin\theta + \left(\frac{b_1'}{r} - \frac{2c_1'}{r^3} + 2d_1' r\right)\cos\theta$$
$$+\frac{2A_1}{r}\cos\theta - \frac{2A_1'}{r}\sin\theta + \frac{B_1}{r}\theta\sin\theta + \frac{B_1'}{r}\theta\cos\theta$$
$$+\left(\frac{2B_1}{r}\ln r\right)\cos\theta - \left(\frac{2B_1'}{r}\ln r\right)\sin\theta$$
$$-\sum_{n=2}^{\infty}\begin{pmatrix} a_n n(n-1)r^{n-2} + b_n(n+1)(n-2)r^n \\ + c_n n(n+1)r^{-(n+2)} + d_n(n-1)(n+2)r^{-n}\end{pmatrix}\sin(n\theta)$$
$$-\sum_{n=2}^{\infty}\begin{pmatrix} a_n' n(n-1)r^{n-2} + b_n'(n+1)(n-2)r^n \\ + c_n' n(n+1)r^{-(n+2)} + d_n'(n-1)(n+2)r^{-n}\end{pmatrix}\cos(n\theta) \qquad (7A.3)$$

$$\sigma_{\theta\theta} = -\frac{b_0}{r^2} + 2c_0 + d_0\left(2\ln r + 3\right) - B_0\frac{\theta}{r^2} + 2C_0\theta + D_0\left(2\ln r + 3\right)\theta$$
$$+\left(\frac{b_1}{r} + \frac{2c_1}{r^3} + 6d_1 r\right)\sin\theta + \left(\frac{b_1'}{r} + \frac{2c_1'}{r^3} + 6d_1' r\right)\cos\theta$$
$$+\frac{B_1}{r}\theta\sin\theta + \frac{B_1'}{r}\theta\cos\theta$$
$$+\sum_{n=2}^{\infty}\begin{pmatrix} a_n n(n-1)r^{n-2} + b_n(n+1)(n+2)r^n \\ + c_n n(n+1)r^{-(n+2)} + d_n(n-1)(n-2)r^{-n}\end{pmatrix}\sin(n\theta)$$
$$+\sum_{n=2}^{\infty}\begin{pmatrix} a_n' n(n-1)r^{n-2} + b_n'(n+1)(n+2)r^n \\ + c_n' n(n+1)r^{-(n+2)} + d_n'(n-1)(n-2)r^{-n}\end{pmatrix}\cos(n\theta) \qquad (7A.4)$$

$$\sigma_{r\theta} = \frac{A_0}{r^2} + B_0\left(\frac{\ln r - 1}{r^2}\right) - C_0 - D_0(\ln r + 1)$$
$$+\left(-\frac{b_1}{r} + \frac{2c_1}{r^3} - 2\cdot d_1 r\right)\cos\theta - \left(-\frac{b_1'}{r} + \frac{2c_1'}{r^3} - 2d_1' r\right)\sin\theta$$
$$-\frac{B_1}{r}\sin\theta - \frac{B_1'}{r}\cos\theta - \frac{B_1}{r}\theta\cos\theta + \frac{B_1'}{r}\theta\sin\theta \qquad (7A.5)$$
$$-\sum_{n=2}^{\infty}\begin{pmatrix} a_n n(n-1)r^{n-2} + b_n n(n+1)r^n \\ -c_n n(n+1)r^{-(n+2)} - d_n n(n-1)r^{-n}\end{pmatrix}\cos(n\theta)$$
$$+\sum_{n=2}^{\infty}\begin{pmatrix} a_n' n(n-1)r^{n-2} + b_n' n(n+1)r^n \\ -c_n' n(n+1)r^{-(n+2)} - d_n' n(n-1)r^{-n}\end{pmatrix}\sin(n\theta)$$

For the case of either *figures 7.1 and 7.2*, the displacements, strains and stresses are single-valued functions of θ, and since both the internal and external boundaries of the plates are self-equilibrated, there is no resultant force at the origin. Coefficients d_0, B_0, C_0, D_0, B_1, B_1' and A_1, A_1', b_1, b_1' therefore all goes to zero. The stress function of *equation 7A.1* can therefore be simplified here as ϕ_{unsym} of *equation 7A.6*, (applicable for plate of *figure 7.2*) which satisfies the biharmonic equation, equilibrium and compatibility [6], i.e.,

$$\begin{aligned}\phi_{unsym} &= a_0 + b_0 \ln r + c_0 r^2 + A_0.\theta \\ &+ \left(a_1 r + \frac{c_1}{r} + d_1 r^3 \right)\sin\theta + \left(a_1' r + \frac{c_1'}{r} + d_1' r^3 \right)\cos\theta \\ &+ \sum_{n=2,3\ldots}^{N}\left[\ a_n r^n + b_n r^{(n+2)} + c_n r^{-n} + d_n r^{-(n-2)}\ \right]\sin(n\theta) \\ &+ \sum_{n=2,3\ldots}^{N}\left[\ a_n' r^n + b_n' r^{(n+2)} + c_n' r^{-n} + d_n' r^{-(n-2)}\ \right]\cos(n\theta)\end{aligned} \tag{7A.6}$$

Using *equations 7A.2 and 7A.6*, the individual components of stress become

$$\begin{aligned}\left(\sigma_{rr}\right)_{unsym} &= \frac{b_0}{r^2} + 2\cdot c_0 + \left(-\frac{2\cdot c_1}{r^3} + 2\cdot r\cdot d_1 \right)\cdot\sin\theta + \left(-\frac{2\cdot c_1'}{r^3} + 2\cdot r\cdot d_1' \right)\cdot\cos\theta \\ &- \sum_{n=2,3\ldots}^{N}\left[\begin{matrix} a_n\cdot n\cdot(n-1)\cdot r^{(n-2)} + b_n\cdot(n-2)\cdot(n+1)\cdot r^n \\ + c_n\cdot n\cdot(n+1)\cdot r^{-(n+2)} + d_n\cdot(n+2)\cdot(n-1)\cdot r^{-n} \end{matrix}\right]\cdot\sin(n\theta) \\ &- \sum_{n=2,3\ldots}^{N}\left[\begin{matrix} a_n'\cdot n\cdot(n-1)\cdot r^{(n-2)} + b_n'\cdot(n-2)\cdot(n+1)\cdot r^n \\ + c_n'\cdot n\cdot(n+1)\cdot r^{-(n+2)} + d_n'\cdot(n+2)\cdot(n-1)\cdot r^{-n} \end{matrix}\right]\cdot\cos(n\theta)\end{aligned} \tag{7A.7}$$

$$\left(\sigma_{\theta\theta}\right)_{unsym} = -\frac{b_0}{r^2} + 2\cdot c_0 + \left(\frac{2\cdot c_1}{r^3} + 6\cdot r\cdot d_1\right)\cdot\sin\theta + \left(\frac{2\cdot c_1^{'}}{r^3} + 6\cdot r\cdot d_1^{'}\right)\cdot\cos\theta$$
$$+ \sum_{n=2,3\ldots}^{N}\begin{bmatrix} a_n\cdot n\cdot(n-1)\cdot r^{(n-2)} + b_n\cdot(n+2)\cdot(n+1)\cdot r^n \\ + c_n\cdot n\cdot(n+1)\cdot r^{-(n+2)} + d_n\cdot(n-2)\cdot(n-1)\cdot r^{-n}\end{bmatrix}\cdot\sin(n\theta) \qquad (7A.8)$$
$$+ \sum_{n=2,3\ldots}^{N}\begin{bmatrix} a_n^{'}\cdot n\cdot(n-1)\cdot r^{(n-2)} + b_n^{'}\cdot(n+2)\cdot(n+1)\cdot r^n \\ + c_n^{'}\cdot n\cdot(n+1)\cdot r^{-(n+2)} + d_n^{'}\cdot(n-2)\cdot(n-1)\cdot r^{-n}\end{bmatrix}\cdot\cos(n\theta)$$

$$\left(\sigma_{r\theta}\right)_{unsym} = \frac{A_0}{r^2} + \left(\frac{2\cdot c_1}{r^3} - 2\cdot r\cdot d_1\right)\cdot\cos\theta - \left(\frac{2\cdot c_1^{'}}{r^3} - 2\cdot r\cdot d_1^{'}\right)\cdot\sin\theta$$
$$- \sum_{n=2,3\ldots}^{N}\begin{bmatrix} a_n\cdot n\cdot(n-1)\cdot r^{(n-2)} + b_n\cdot n\cdot(n+1)\cdot r^n \\ - c_n\cdot n\cdot(n+1)\cdot r^{-(n+2)} - d_n\cdot n\cdot(n-1)\cdot r^{-n}\end{bmatrix}\cdot\cos(n\theta) \qquad (7A.9)$$
$$+ \sum_{n=2,3\ldots}^{N}\begin{bmatrix} a_n^{'}\cdot n\cdot(n-1)\cdot r^{(n-2)} + b_n^{'}\cdot n\cdot(n+1)\cdot r^n \\ - c_n^{'}\cdot n\cdot(n+1)\cdot r^{-(n+2)} - d_n^{'}\cdot n\cdot(n-1)\cdot r^{-n}\end{bmatrix}\cdot\sin(n\theta)$$

At this stage the coordinate origin is assumed to be located in a cavity of some unknown shape. When the plate is symmetrical about the x-axis, stresses induced at any angle, say when θ = +β, would be the same as that at the angle when θ = -β, i.e., $\phi(r, \theta) = \phi(r, -\theta)$. This indicates that ϕ must be an even function of θ. Hence, the sine terms are not retained in the expansion for the stress function. As a result, a_n , b_n , c_n , d_n (for $n \geq 1$) are all omitted. Moreover, $\sigma_{r\theta}$ is zero at θ = 0 so $A_0 = 0$ (*equation 3.9*). Consequently (applicable to plate of *figure 7.1*)

$$\phi_{sym} = a_0 + b_0\cdot\ln r + c_0\cdot r^2 + \left(a_1^{'}\cdot r + \frac{c_1^{'}}{r} + d_1^{'}\cdot r^3\right)\cdot\cos\theta$$
$$+ \sum_{n=2,3\ldots}^{N}\left[\ a_n^{'}\cdot r^n + b_n^{'}\cdot r^{(n+2)} + c_n^{'}\cdot r^{-n} + d_n^{'}\cdot r^{-(n-2)}\ \right]\cdot\cos(n\theta) \qquad (7A.10)$$

Using *equations 7A.2 and 7A.10*, the individual components of stress now become

$$\begin{aligned}\left(\sigma_{rr}\right)_{sym} &= \frac{b_0}{r^2} + 2\cdot c_0 - \frac{2\cdot c_1^{'}}{r^3}\cos\theta + 2\cdot r\cdot d_1^{'}\cos\theta \\ &- \sum_{n=2,3\ldots}^{N}\begin{bmatrix} a_n^{'}\cdot n\cdot(n-1)\cdot r^{(n-2)} + b_n^{'}\cdot(n-2)\cdot(n+1)\cdot r^{n} \\ + c_n^{'}\cdot n\cdot(n+1)\cdot r^{-(n+2)} + d_n^{'}\cdot(n+2)\cdot(n-1)\cdot r^{-n}\end{bmatrix}\cdot\cos(n\theta)\end{aligned} \tag{7A.11}$$

$$\begin{aligned}\left(\sigma_{\theta\theta}\right)_{sym} &= -\frac{b_0}{r^2} + 2\cdot c_0 + \frac{2\cdot c_1^{'}}{r^3}\cdot\cos\theta + 6\cdot r\cdot d_1^{'}\cdot\cos\theta \\ &+ \sum_{n=2,3\ldots}^{N}\begin{bmatrix} a_n^{'}\cdot n\cdot(n-1)\cdot r^{(n-2)} + b_n^{'}\cdot(n+2)\cdot(n+1)\cdot r^{n} \\ + c_n^{'}\cdot n\cdot(n+1)\cdot r^{-(n+2)} + d_n^{'}\cdot(n-2)\cdot(n-1)\cdot r^{-n}\end{bmatrix}\cdot\cos(n\theta)\end{aligned} \tag{7A.12}$$

$$\begin{aligned}\left(\sigma_{r\theta}\right)_{sym} &= -\frac{2\cdot c_1^{'}}{r^3}\cdot\sin\theta + 2\cdot r\cdot d_1^{'}\cdot\sin\theta \\ &+ \sum_{n=2,3\ldots}^{N}\begin{bmatrix} a_n^{'}\cdot n\cdot(n-1)\cdot r^{(n-2)} + b_n^{'}\cdot n\cdot(n+1)\cdot r^{n} \\ - c_n^{'}\cdot n\cdot(n+1)\cdot r^{-(n+2)} - d_n^{'}\cdot n\cdot(n-1)\cdot r^{-n}\end{bmatrix}\cdot\sin(n\theta)\end{aligned} \tag{7A.13}$$

where r is the radius measured from the origin (which is contained in a cutout of some yet undetermined shape) and angle θ is measured counter-clock wise from the x-axis. *Equations 7A.10 through 7A.13* are the counterpart of *equations 7A.6 through 7A.9* but for symmetry about x-axis. Imposing the traction-free conditions $\sigma_{rr} = \sigma_{r\theta} = 0$ for all angle θ on the boundary of a hole of radius r = R for the plate symmetrical about x-axis (i.e. governed by *equation 7A.10 through 7A.13*), gives

1) $b_0 \equiv f(c_0)$

$$\sigma_{rr} = 0, \quad \frac{1}{R^2} \cdot b_0 + 2 \cdot c_0 = 0$$

$$\Rightarrow \qquad b_0 = -2 \cdot R^2 \cdot c_0 \tag{7A.14}$$

For r = R and all values of θ in *equations 7A.11 and 7A.13* respectively yields:

2) $c_1 \equiv f(d_1)$

$$\sigma_{rr} = 0 \qquad gives \qquad \left(-\frac{2 \cdot c_1^{'}}{R^3} + 2 \cdot R \cdot d_1^{'} \right) = 0 \qquad and$$

$$\sigma_{r\theta} = 0 \qquad gives \qquad \left(\frac{2 \cdot c_1^{'}}{R^3} - 2 \cdot R \cdot d_1^{'} \right) = 0$$

$$c_1^{'} = R^4 \cdot d_1^{'} \tag{7A.15}$$

3) $a_n = f(b_n , d_n)$ *and* $c_n = f(b_n , d_n)$

For n ≥ 4, r = R and all values of θ in *equations 7A.11 and 7A.13* respectively, yields:

$$\sigma_{rr} = 0 \qquad gives \qquad \left[\begin{array}{l} a_n^{'} \cdot n \cdot (n-1) \cdot R^{(n-2)} + b_n^{'} \cdot (n+1) \cdot (n-2) \cdot R^{n} \\ + c_n^{'} \cdot n \cdot (n+1) \cdot R^{-(n+2)} + d_n^{'} \cdot (n-1) \cdot (n+2) \cdot R^{-n} \end{array}\right] = 0$$

$$\sigma_{r\theta} = 0 \qquad gives \qquad \left[\begin{array}{l} a_n^{'} \cdot n \cdot (n-1) \cdot R^{(n-2)} + b_n^{'} \cdot n \cdot (n+1) \cdot R^{n} \\ - c_n^{'} \cdot n \cdot (n+1) \cdot R^{-(n+2)} - d_n^{'} \cdot n \cdot (n-1) \cdot R^{-n} \end{array}\right] = 0$$

$$\begin{aligned} a_n^{'} &= -\left(\frac{1+n}{n}\right) \cdot R^2 \cdot b_n^{'} - \frac{1}{n} \cdot R^{-(2n-2)} \cdot d_n^{'} \\ c_n^{'} &= \frac{1}{n} \cdot R^{(2n+2)} \cdot b_n^{'} + \left(\frac{1-n}{n}\right) \cdot R^2 \cdot d_n^{'} \end{aligned} \qquad (7A.16)$$

4) $a_2 \equiv f(b_2, d_2)$, $c_2 \equiv f(b_2, d_2)$

From *equation 7A.16* and n = 2,

$$\begin{aligned} a_2^{'} &= -\left(\frac{3}{2}\right) \cdot R^2 \cdot b_2^{'} - \frac{1}{2} \cdot R^{-2} \cdot d_2^{'} \\ c_2^{'} &= \frac{1}{2} \cdot R^6 \cdot b_2^{'} - \frac{1}{2} \cdot R^2 \cdot d_2^{'} \end{aligned} \qquad (7A.17)$$

which are also available from *equations (7A.16)*

5) $a_3' \equiv f(b_0, c_0, c_3', d_3')$, $b_3' \equiv f(b_0, c_0, c_3', d_3')$

For n = 3, r = R and all values of θ in *equations 7A.11 and 7A.13* respectively, yields:

$$\sigma_{rr} = 0, \quad -\left[\begin{matrix} a_3^{'} \cdot 3 \cdot (3-1) \cdot R^{(3-2)} + b_3^{'} \cdot 3 \cdot (3+1) \cdot (3-2) \cdot R^3 \\ + c_3^{'} \cdot 3 \cdot (3+1) \cdot R^{-(3+2)} + d_3^{'} \cdot (3-1) \cdot (3+2) \cdot R^{-3} \end{matrix}\right] \cdot \cos(3\theta) = 0$$

$$\sigma_{r\theta} = 0, \quad \left[\begin{matrix} a_3^{'} \cdot 3 \cdot (3-1) \cdot R^{3-2} + b_3^{'} \cdot 3 \cdot (3+1) \cdot R^3 \\ - c_3^{'} \cdot 3 \cdot (3+1) \cdot R^{-(3+2)} - d_3^{'} \cdot (3-1) \cdot (3+2) \cdot R^{-3} \end{matrix}\right] \cdot \sin(3\theta) = 0$$

$$\Rightarrow \qquad a_3^{'} = -\frac{4 \cdot c_3^{'}}{R^6} - \frac{3 \cdot d_3^{'}}{R^4}$$

$$b_3^{'} = \frac{3 \cdot c_3^{'}}{R^8} + \frac{2 \cdot d_3^{'}}{R^6} \qquad \text{(7A.18)}$$

Expanding *equation 7A.11* for n = 2 and 3, gives:

$$\begin{aligned} \sigma_{rr} = {} & \frac{b_0}{r^2} + 2 \cdot c_0 - \frac{2 \cdot c_1^{'}}{r^3} \cdot \cos\theta + 2 \cdot r \cdot d_1^{'} \cdot \cos\theta \\ & - a_2^{'} \cdot 2 \cdot (2-1) \cdot r^{(2-2)} \cdot \cos(2\theta) - b_2^{'} \cdot (2-2) \cdot (2+1) \cdot r^2 \cdot \cos(2\theta) \\ & - c_2^{'} \cdot 2 \cdot (2+1) \cdot r^{-(2+2)} \cdot \cos(2\theta) - d_2^{'} \cdot (2+2) \cdot (2-1) \cdot r^{-2} \cdot \cos(2\theta) \\ & - a_3^{'} \cdot 3 \cdot (3-1) \cdot r^{(3-2)} \cdot \cos(3\theta) - b_3^{'} \cdot (3-2) \cdot (3+1) \cdot r^3 \cdot \cos(3\theta) \\ & - c_3^{'} \cdot 3 \cdot (3+1) \cdot r^{-(3+2)} \cdot \cos(3\theta) - d_3^{'} \cdot (3+2) \cdot (3-1) \cdot r^{-3} \cdot \cos(3\theta) \\ & - \sum_{n=4,5\ldots}^{N} \left[\begin{matrix} a_n^{'} \cdot n \cdot (n-1) \cdot r^{(n-2)} + b_n^{'} \cdot (n-2) \cdot (n+1) \cdot r^n \\ + c_n^{'} \cdot n \cdot (n+1) \cdot r^{-(n+2)} + d_n^{'} \cdot (n+2) \cdot (n-1) \cdot r^{-n} \end{matrix}\right] \cdot \cos(n\theta) \end{aligned} \qquad \text{(7A.19)}$$

$$\begin{aligned}\sigma_{rr} = & \frac{b_0}{r^2} + 2\cdot c_0 - \frac{2\cdot c_1^{'}}{r^3}\cdot\cos\theta + 2\cdot r\cdot d_1^{'}\cdot\cos\theta \\ & - a_2^{'}\cdot 2\cdot\cos(2\theta) - c_2^{'}\cdot 6\cdot r^{-4}\cdot\cos(2\theta) - d_2^{'}\cdot 4\cdot r^{-2}\cdot\cos(2\theta) \\ & - a_3^{'}\cdot 6\cdot r\cdot\cos(3\theta) - b_3^{'}\cdot 4\cdot r^3\cdot\cos(3\theta) - c_3^{'}\cdot 12\cdot r^{-5}\cdot\cos(3\theta) - d_3^{'}\cdot 10\cdot r^{-3}\cdot\cos(3\theta) \\ & - \sum_{n=4,5\ldots}^{N}\begin{bmatrix} a_n^{'}\cdot n\cdot(n-1)\cdot r^{(n-2)} + b_n^{'}\cdot(n-2)\cdot(n+1)\cdot r^n \\ + c_n^{'}\cdot n\cdot(n+1)\cdot r^{-(n+2)} + d_n^{'}\cdot(n+2)\cdot(n-1)\cdot r^{-n}\end{bmatrix}\cdot\cos(n\theta)\end{aligned} \tag{7A.20}$$

Substituting *equations 7A.14 through 7A.18* in *equation 7A.20* yields

$$\begin{aligned}\sigma_{rr} = & \frac{\left(-2\cdot R^2\cdot c_0\right)}{r^2} + 2\cdot c_0 - \frac{2\cdot\left(R^4\cdot d_1^{'}\right)}{r^3}\cdot\cos\theta + 2\cdot r\cdot d_1^{'}\cdot\cos\theta \\ & - \left(-\left(\frac{3}{2}\right)\cdot R^2\cdot b_2^{'} - \frac{1}{2}\cdot R^{-2}\cdot d_2^{'}\right)\cdot 2\cdot\cos(2\theta) - \left(\frac{1}{2}\cdot R^6\cdot b_2^{'} - \frac{1}{2}\cdot R^2\cdot d_2^{'}\right)\cdot 6\cdot r^{-4}\cdot\cos(2\theta) \\ & - d_2^{'}\cdot 4\cdot r^{-2}\cdot\cos(2\theta) - \left(-\frac{4\cdot c_3^{'}}{R^6} - \frac{3\cdot d_3^{'}}{R^4}\right)\cdot 6\cdot r\cdot\cos(3\theta) - \left(\frac{3\cdot c_3^{'}}{R^8} + \frac{2\cdot d_3^{'}}{R^6}\right)\cdot 4\cdot r^3\cdot\cos(3\theta) \\ & - c_3^{'}\cdot 12\cdot r^{-5}\cdot\cos(3\theta) - d_3^{'}\cdot 10\cdot r^{-3}\cdot\cos(3\theta) \\ & - \sum_{n=4,5\ldots}^{N}\begin{bmatrix}\left(-\left(\frac{1+n}{n}\right)\cdot R^2\cdot b_n^{'} - \frac{1}{n}\cdot R^{-(2n-2)}\cdot d_n\right)\cdot n\cdot(n-1)\cdot r^{(n-2)} \\ + b_n^{'}\cdot(n-2)\cdot(n+1)\cdot r^n \\ + \left(\frac{1}{n}\cdot R^{(2n+2)}\cdot b_n^{'} + \left(\frac{1-n}{n}\right)\cdot R^2\cdot d_n^{'}\right)\cdot n\cdot(n+1)\cdot r^{-(n+2)} \\ + d_n^{'}\cdot(n+2)\cdot(n-1)\cdot r^{-n}\end{bmatrix}\cdot\cos(n\theta)\end{aligned} \tag{7A.21}$$

$$
\begin{aligned}
\sigma_{rr} = & -\frac{2\cdot R^2}{r^2}\cdot c_0 + 2\cdot c_0 - \frac{2\cdot R^4\cdot\cos\theta}{r^3}\cdot d_1^{'} + 2\cdot r\cdot\cos\theta\cdot d_1^{'} \\
& + \left(\frac{3}{2}\right)\cdot R^2\cdot 2\cdot\cos(2\theta)\cdot b_2^{'} + \frac{1}{2}\cdot R^{-2}\cdot 2\cdot\cos(2\theta)\cdot d_2^{'} \\
& - \frac{1}{2}\cdot R^6\cdot 6\cdot r^{-4}\cdot\cos(2\theta)\cdot b_2^{'} + \frac{1}{2}\cdot R^2\cdot 6\cdot r^{-4}\cdot\cos(2\theta)\cdot d_2^{'} \\
& - 4\cdot r^{-2}\cdot\cos(2\theta)\cdot d_2^{'} + \frac{4}{R^6}\cdot 6\cdot r\cdot\cos(3\theta)\cdot c_3^{'} + \frac{3}{R^4}\cdot 6\cdot r\cdot\cos(3\theta)\cdot d_3^{'} \\
& - \frac{3}{R^8}\cdot 4\cdot r^3\cdot\cos(3\theta)\cdot c_3^{'} - \frac{2}{R^6}\cdot 4\cdot r^3\cdot\cos(3\theta)\cdot d_3^{'} - 12\cdot r^{-5}\cdot\cos(3\theta)\cdot c_3^{'} - 10\cdot r^{-3}\cdot\cos(3\theta)\cdot d_3^{'} \\
& - \sum_{n=4,5\ldots}^{N}\left[\begin{array}{l}
-\left(\frac{1+n}{n}\right)\cdot R^2\cdot n\cdot(n-1)\cdot r^{(n-2)}\cdot b_n^{'} - \frac{1}{n}\cdot R^{-(2n-2)}\cdot n\cdot(n-1)\cdot r^{(n-2)}\cdot d_n^{'} \\
+(n-2)\cdot(n+1)\cdot r^n\cdot b_n^{'} \\
+\frac{1}{n}\cdot R^{(2n+2)}\cdot n\cdot(n+1)\cdot r^{-(n+2)}\cdot b_n^{'} + \left(\frac{1-n}{n}\right)\cdot R^2\cdot n\cdot(n+1)\cdot r^{-(n+2)}\cdot d_n^{'} \\
+(n+2)\cdot(n-1)\cdot r^{-n}\cdot d_n^{'}
\end{array}\right]\cdot\cos(n\theta)
\end{aligned}
$$

$$
\begin{aligned}
\sigma_{rr} = & \left(-\frac{2\cdot R^2}{r^2}+2\right)\cdot c_0 + \left(-\frac{2\cdot R^4\cdot\cos\theta}{r^3}+2\cdot r\cdot\cos\theta\right)\cdot d_1^{'} \\
& + \left(\left(\frac{3}{2}\right)\cdot R^2\cdot 2\cdot\cos(2\theta) - \frac{1}{2}\cdot R^6\cdot 6\cdot r^{-4}\cdot\cos(2\theta)\right)\cdot b_2^{'} \\
& + \left(\frac{1}{2}\cdot R^{-2}\cdot 2\cdot\cos(2\theta) + \frac{1}{2}\cdot R^2\cdot 6\cdot r^{-4}\cdot\cos(2\theta) - 4\cdot r^{-2}\cdot\cos(2\theta)\right)\cdot d_2^{'} \\
& + \left(\frac{4}{R^6}\cdot 6\cdot r\cdot\cos(3\theta) - \frac{3}{R^8}\cdot 4\cdot r^3\cdot\cos(3\theta) - 12\cdot r^{-5}\cdot\cos(3\theta)\right)\cdot c_3^{'} \\
& + \left(\frac{3}{R^4}\cdot 6\cdot r\cdot\cos(3\theta) - \frac{2}{R^6}\cdot 4\cdot r^3\cdot\cos(3\theta) - 10\cdot r^{-3}\cdot\cos(3\theta)\right)\cdot d_3^{'} \\
& - \sum_{n=4,5\ldots}^{N}\left[\begin{array}{l}
\left(\begin{array}{l}-\left(\frac{1+n}{n}\right)\cdot R^2\cdot n\cdot(n-1)\cdot r^{(n-2)} + (n-2)\cdot(n+1)\cdot r^n \\ +\frac{1}{n}\cdot R^{(2n+2)}\cdot n\cdot(n+1)\cdot r^{-(n+2)}\end{array}\right)\cdot b_n^{'} \\
+\left(\begin{array}{l}-\frac{1}{n}\cdot R^{-(2n-2)}\cdot n\cdot(n-1)\cdot r^{(n-2)} + \left(\frac{1-n}{n}\right)\cdot R^2\cdot n\cdot(n+1)\cdot r^{-(n+2)} \\ +(n+2)\cdot(n-1)\cdot r^{-n}\end{array}\right)\cdot d_n^{'}
\end{array}\right]\cdot\cos(n\theta)
\end{aligned}
\tag{7A.22}
$$

$$
\begin{aligned}
\sigma_{rr} = & \left(-\frac{2 \cdot R^2}{r^2} + 2 \right) \cdot c_0 + \left(-\frac{2 \cdot R^4}{r^3} + 2 \cdot r \right) \cdot \cos\theta \cdot d_1^{'} \\
& + \left(3 \cdot R^2 - 3 \cdot R^6 \cdot r^{-4} \right) \cdot \cos(2\theta) \cdot b_2^{'} \\
& + \left(R^{-2} + 3 \cdot R^2 \cdot r^{-4} - 4 \cdot r^{-2} \right) \cdot \cos(2\theta) \cdot d_2^{'} \\
& + \left(\frac{24 \cdot r}{R^6} - \frac{12 \cdot r^3}{R^8} - 12 \cdot r^{-5} \right) \cdot \cos(3\theta) \cdot c_3^{'} \\
& + \left(\frac{18 \cdot r}{R^4} - \frac{8 \cdot r^3}{R^6} - 10 \cdot r^{-3} \right) \cdot \cos(3\theta) \cdot d_3^{'} \\
& - \sum_{n=4,5\ldots}^{N} \left[\begin{array}{l} \left(\begin{array}{l} -(n^2-1) \cdot R^2 \cdot r^{(n-2)} + (n-2) \cdot (n+1) \cdot r^n \\ +(n+1) \cdot R^{(2n+2)} \cdot r^{-(n+2)} \end{array} \right) \cdot b_n^{'} \\ + \left(\begin{array}{l} -(n-1) \cdot R^{-(2n-2)} \cdot r^{(n-2)} - (n^2-1) \cdot R^2 \cdot r^{-(n+2)} \\ +(n+2) \cdot (n-1) \cdot r^{-n} \end{array} \right) \cdot d_n^{'} \end{array} \right] \cdot \cos(n\theta)
\end{aligned}
\tag{7A.23}
$$

Equation 7A.23 is an alternate form of *equation 7.11* of Chapter 7 for symmetry about the x-axis.

Now expanding *equation 7A.12* for n = 2 and 3, one gets:

$$\begin{aligned}\sigma_{\theta\theta} = & -\frac{b_0}{r^2} + 2\cdot c_0 + \frac{2\cdot c_1}{r^3}\cdot\cos\theta + 6\cdot r\cdot d_1^{'}\cdot\cos\theta \\ & a_2^{'}\cdot 2\cdot(2-1)\cdot r^{(2-2)}\cdot\cos(2\theta) + b_2^{'}\cdot(2+2)\cdot(2+1)\cdot r^2\cdot\cos(2\theta) \\ & + c_2^{'}\cdot 2\cdot(2+1)\cdot r^{-(2+2)}\cdot\cos(2\theta) + d_2^{'}\cdot(2-2)\cdot(2-1)\cdot r^{-2}\cdot\cos(2\theta) \\ & a_3^{'}\cdot 3(3-1)\cdot r^{(3-2)}\cdot\cos(3\theta) + b_3^{'}\cdot(3+2)\cdot(3+1)\cdot r^3\cdot\cos(3\theta) \\ & + c_3^{'}\cdot 3\cdot(3+1)\cdot r^{-(3+2)}\cdot\cos(3\theta) + d_3^{'}\cdot(3-2)\cdot(3-1)\cdot r^{-3}\cdot\cos(3\theta) \\ & + \sum_{n=4,5\ldots}^{N}\begin{bmatrix} a_n^{'}\cdot n\cdot(n-1)\cdot r^{(n-2)} + b_n^{'}\cdot(n+2)\cdot(n+1)\cdot r^n \\ + c_n^{'}\cdot n\cdot(n+1)\cdot r^{-(n+2)} + d_n^{'}\cdot(n-2)\cdot(n-1)\cdot r^{-n}\end{bmatrix}\cdot\cos(n\theta)\end{aligned} \tag{7A.24}$$

$$\begin{aligned}\sigma_{\theta\theta} = & -\frac{b_0}{r^2} + 2\cdot c_0 + \frac{2\cdot c_1}{r^3}\cdot\cos\theta + 6\cdot r\cdot d_1^{'}\cdot\cos\theta \\ & a_2^{'}\cdot 2\cdot\cos(2\theta) + b_2^{'}\cdot 12r^2\cdot\cos(2\theta) + c_2^{'}\cdot 6r^{-4}\cdot\cos(2\theta) + \\ & a_3^{'}\cdot 6r\ \cdot\cos(3\theta) + b_3^{'}\cdot 20r^3\cdot\cos(3\theta) + c_3^{'}\cdot 12r^{-5}\cdot\cos(3\theta) + d_3^{'}\cdot 2r^{-3}\cdot\cos(3\theta) \\ & + \sum_{n=4,5\ldots}^{N}\begin{bmatrix} a_n^{'}\cdot n\cdot(n-1)\cdot r^{(n-2)} + b_n^{'}\cdot(n+2)\cdot(n+1)\cdot r^n \\ + c_n^{'}\cdot n\cdot(n+1)\cdot r^{-(n+2)} + d_n^{'}\cdot(n-2)\cdot(n-1)\cdot r^{-n}\end{bmatrix}\cdot\cos(n\theta)\end{aligned} \tag{7A.25}$$

Substituting *equations 7A.14 through 7A.18* into *equation 7A.25*,

$$\sigma_{\theta\theta} = -\frac{\left(-2\cdot R^2\cdot c_0\right)}{r^2} + 2\cdot c_0 + \frac{2\cdot\left(R^4\cdot d_1^{'}\right)}{r^3}\cdot\cos\theta + 6\cdot r\cdot d_1^{'}\cdot\cos\theta$$
$$+\left(-\left(\frac{3}{2}\right)\cdot R^2\cdot b_2^{'} - \frac{1}{2}\cdot R^{-2}\cdot d_2^{'}\right)\cdot 2\cdot\cos(2\theta) + b_2^{'}\cdot 12\cdot r^2\cdot\cos(2\theta)$$
$$+\left(\frac{1}{2}\cdot R^6\cdot b_2^{'} - \frac{1}{2}\cdot R^2\cdot d_2^{'}\right)\cdot 6\cdot r^{-4}\cdot\cos(2\theta)$$
$$+\left(-\frac{4\cdot c_3^{'}}{R^6} - \frac{3\cdot d_3^{'}}{R^4}\right)\cdot 6\cdot r\cdot\cos(3\theta) + \left(\frac{3\cdot c_3^{'}}{R^8} + \frac{2\cdot d_3^{'}}{R^6}\right)\cdot 20\cdot r^3\cdot\cos(3\theta)$$
$$+c_3^{'}\cdot 12\cdot r^{-5}\cdot\cos(3\theta) + d_3^{'}\cdot 2\cdot r^{-3}\cdot\cos(3\theta)$$
$$+\sum_{n=4,5\ldots}^{N}\left[\begin{array}{l}\left(-\left(\frac{1+n}{n}\right)\cdot R^2\cdot b_n^{'} - \frac{1}{n}\cdot R^{-(2n-2)}\cdot d_n^{'}\right)\cdot n\cdot(n-1)\cdot r^{(n-2)} + b_n^{'}\cdot(n+2)\cdot(n+1)\cdot r^n \\ +\left(\frac{1}{n}\cdot R^{(2n+2)}\cdot b_n^{'} + \left(\frac{1-n}{n}\right)\cdot R^2\cdot d_n^{'}\right)\cdot n\cdot(n+1)\cdot r^{-(n+2)} + d_n^{'}\cdot(n-2)\cdot(n-1)\cdot r^{-n}\end{array}\right]\cdot\cos(n\theta)$$

(7A.26)

$$\sigma_{\theta\theta} = \frac{2\cdot R^2\cdot c_0}{r^2} + 2\cdot c_0 + \frac{2\cdot R^4\cdot d_1^{'}}{r^3}\cdot\cos\theta + 6\cdot r\cdot d_1^{'}\cdot\cos\theta$$
$$-\left(\frac{3}{2}\right)\cdot R^2\cdot b_2^{'}\cdot 2\cdot\cos(2\theta) - \frac{1}{2}\cdot R^{-2}\cdot d_2^{'}\cdot 2\cdot\cos(2\theta) + b_2^{'}\cdot 12r^2\cdot\cos(2\theta)$$
$$+\frac{1}{2}\cdot R^6\cdot b_2^{'}\cdot 6r^{-4}\cdot\cos(2\theta) - \frac{1}{2}\cdot R^2\cdot d_2^{'}\cdot 6r^{-4}\cdot\cos(2\theta)$$
$$-\frac{4\cdot c_3^{'}}{R^6}6r\ \cdot\cos(3\theta) - \frac{3\cdot d_3^{'}}{R^4}6r\ \cdot\cos(3\theta)\cdot + \frac{3\cdot c_3^{'}}{R^8}\cdot 20r^3\cdot\cos(3\theta) + \frac{2\cdot d_3^{'}}{R^6}\cdot 20r^3\cdot\cos(3\theta)$$
$$+c_3^{'}\cdot 12r^{-5}\cdot\cos(3\theta) + d_3^{'}\cdot 2r^{-3}\cdot\cos(3\theta)$$
$$+\sum_{n=4,5\ldots}^{N}\left[\begin{array}{l}-\left(\frac{1+n}{n}\right)\cdot R^2\cdot b_n^{'}\cdot n\cdot(n-1)\cdot r^{(n-2)} - \frac{1}{n}\cdot R^{-(2n-2)}\cdot d_n^{'}\cdot n\cdot(n-1)\cdot r^{(n-2)} \\ +b_n^{'}\cdot(n+2)\cdot(n+1)\cdot r^n \\ +\frac{1}{n}\cdot R^{(2n+2)}\cdot b_n^{'}\cdot n\cdot(n+1)\cdot r^{-(n+2)} + \left(\frac{1-n}{n}\right)\cdot R^2\cdot d_n^{'}\cdot n\cdot(n+1)\cdot r^{-(n+2)} \\ +d_n^{'}\cdot(n-2)\cdot(n-1)\cdot r^{-n}\end{array}\right]\cdot\cos(n\theta)$$

(7A.27)

$$\begin{aligned}\sigma_{\theta\theta} = &\left(\frac{2\cdot R^2}{r^2}+2\right)\cdot c_0 + \left(\frac{2\cdot R^4}{r^3}\cdot\cos\theta + 6\cdot r\cdot\cos\theta\right)\cdot d_1^{'} \\ &+\left(-\left(\frac{3}{2}\right)\cdot R^2\cdot 2\cdot\cos(2\theta)+12r^2\cdot\cos(2\theta)+\frac{1}{2}\cdot R^6\cdot 6r^{-4}\cdot\cos(2\theta)\right)\cdot b_2^{'} \\ &-\left(\frac{1}{2}\cdot R^{-2}\cdot 2\cdot\cos(2\theta)+\frac{1}{2}\cdot R^2\cdot 6r^{-4}\cdot\cos(2\theta)\right)\cdot d_2^{'} \\ &+\left(-\frac{4}{R^6}6\cdot r\cdot\cos(3\theta)\cdot+\frac{3}{R^8}\cdot 20\cdot r^3\cdot\cos(3\theta)+12\cdot r^{-5}\cdot\cos(3\theta)\right)\cdot c_3^{'} \\ &+\left(-\frac{3}{R^4}6\cdot r\cdot\cos(3\theta)+\frac{2}{R^6}\cdot 20\cdot r^3\cdot\cos(3\theta)+2\cdot r^{-3}\cdot\cos(3\theta)\right)\cdot d_3^{'} \\ &+\sum_{n=4,5\ldots}^{N}\left[\begin{array}{l}\left(\begin{array}{l}-\left(\frac{1+n}{n}\right)\cdot R^2\cdot n\cdot(n-1)\cdot r^{(n-2)}+(n+2)\cdot(n+1)\cdot r^n \\ +\frac{1}{n}\cdot R^{(2n+2)}\cdot n\cdot(n+1)\cdot r^{-(n+2)}\end{array}\right)\cdot b_n^{'} \\ +\left(\begin{array}{l}-\frac{1}{n}\cdot R^{-(2n-2)}\cdot n\cdot(n-1)\cdot r^{(n-2)}+\left(\frac{1-n}{n}\right)\cdot R^2\cdot n\cdot(n+1)\cdot r^{-(n+2)} \\ +(n-2)\cdot(n-1)\cdot r^{-n}\end{array}\right)\cdot d_n^{'}\end{array}\right]\cdot\cos(n\theta)\end{aligned} \tag{7A.28}$$

$$\begin{aligned}\sigma_{\theta\theta} = &\left(\frac{2\cdot R^2}{r^2}+2\right)\cdot c_0 + \left(\frac{2\cdot R^4}{r^3}+6\cdot r\right)\cdot\cos\theta\cdot d_1^{'} \\ &+\left(-3\cdot R^2+12\cdot r^2+3\cdot R^6\cdot r^{-4}\right)\cdot\cos(2\theta)\cdot b_2^{'} \\ &-\left(R^{-2}+3\cdot R^2\cdot r^{-4}\right)\cdot\cos(2\theta)\cdot d_2^{'} \\ &+\left(-\frac{24\cdot r}{R^6}+\frac{60\cdot r^3}{R^8}+12\cdot r^{-5}\right)\cdot\cos(3\theta)\cdot c_3^{'} \\ &+\left(-\frac{18\cdot r}{R^4}+\frac{40\cdot r^3}{R^6}+2\cdot r^{-3}\right)\cdot\cos(3\theta)\cdot d_3^{'} \\ &+\sum_{n=4,5\ldots}^{N}\left[\begin{array}{l}\left(\begin{array}{l}-(n^2-1)\cdot R^2\cdot r^{(n-2)}+(n+2)\cdot(n+1)\cdot r^n \\ +(n+1)\cdot R^{(2n+2)}\cdot r^{-(n+2)}\end{array}\right)\cdot b_n^{'} \\ +\left(\begin{array}{l}-(n-1)\cdot R^{-(2n-2)}\cdot r^{(n-2)}-(n^2-1)\cdot R^2\cdot r^{-(n+2)} \\ +(n-2)\cdot(n-1)\cdot r^{-n}\end{array}\right)\cdot d_n^{'}\end{array}\right]\cdot\cos(n\theta)\end{aligned} \tag{7A.29}$$

Equation 7A.29 is an alternative form of *equation 7.12* of Chapter 7 for symmetry about the x-axis.

Now expanding *equation 7A.13* for n = 2 and 3, one gets:

$$\begin{aligned}\sigma_{r\theta} = & -\frac{2\cdot c_1}{r^3}\cdot\sin\theta + 2\cdot r\cdot d_1^{'}\cdot\sin\theta \\ & + a_2^{'}\cdot 2\cdot(2-1)\cdot r^{(2-2)}\cdot\sin(2\theta) + b_2^{'}\cdot 2\cdot(2+1)\cdot r^2\cdot\sin(2\theta) \\ & - c_2^{'}\cdot 2\cdot(2+1)\cdot r^{-(2+2)}\cdot\sin(2\theta) - d_2^{'}\cdot 2\cdot(2-1)\cdot r^{-2}\cdot\sin(2\theta) \\ & + a_3^{'}\cdot 3\cdot(3-1)\cdot r^{(3-2)}\cdot\sin(3\theta) + b_3^{'}\cdot 3\cdot(3+1)\cdot r^3\cdot\sin(3\theta) \\ & - c_3^{'}\cdot 3\cdot(3+1)\cdot r^{-(3+2)}\cdot\sin(3\theta) - d_3^{'}\cdot 3\cdot(3-1)\cdot r^{-3}\cdot\sin(3\theta) \\ & + \sum_{n=4,5\ldots}^{N}\begin{bmatrix} a_n^{'}\cdot n\cdot(n-1)\cdot r^{(n-2)} + b_n^{'}\cdot n\cdot(n+1)\cdot r^n \\ - c_n^{'}\cdot n\cdot(n+1)\cdot r^{-(n+2)} - d_n^{'}\cdot n\cdot(n-1)\cdot r^{-n}\end{bmatrix}\cdot\sin(n\theta)\end{aligned} \tag{7A.30}$$

$$\begin{aligned}\sigma_{r\theta} = & -\frac{2\cdot c_1}{r^3}\cdot\sin\theta + 2\cdot r\cdot d_1^{'}\cdot\sin\theta \\ & + a_2^{'}\cdot 2\cdot\sin(2\theta) + b_2^{'}\cdot 6\cdot r^2\cdot\sin(2\theta) \\ & - c_2^{'}\cdot 6\cdot r^{-4}\cdot\sin(2\theta) - d_2^{'}\cdot 2\cdot r^{-2}\cdot\sin(2\theta) \\ & + a_3^{'}\cdot 6\cdot r\cdot\sin(3\theta) + b_3^{'}\cdot 12\cdot r^3\cdot\sin(3\theta) \\ & - c_3^{'}\cdot 12\cdot r^{-5}\cdot\sin(3\theta) - d_3^{'}\cdot 6\cdot r^{-3}\cdot\sin(3\theta) \\ & + \sum_{n=4,5\ldots}^{N}\begin{bmatrix} a_n^{'}\cdot n\cdot(n-1)\cdot r^{(n-2)} + b_n^{'}\cdot n\cdot(n+1)\cdot r^n \\ - c_n^{'}\cdot n\cdot(n+1)\cdot r^{-(n+2)} - d_n^{'}\cdot n\cdot(n-1)\cdot r^{-n}\end{bmatrix}\cdot\sin(n\theta)\end{aligned} \tag{7A.31}$$

Substituting *equations 7A.14 through 7A.18* into *equation 7A.31*,

$$\begin{aligned}
\sigma_{r\theta} = & -\frac{2\cdot\left(R^4\cdot d_1^{'}\right)}{r^3}\cdot\sin\theta + 2\cdot r\cdot d_1^{'}\cdot\sin\theta \\
& +\left(-\left(\frac{3}{2}\right)\cdot R^2\cdot b_2^{'} - \frac{1}{2}\cdot R^{-2}\cdot d_2^{'}\right)\cdot 2\cdot\sin(2\theta) + b_2^{'}\cdot 6\cdot r^2\cdot\sin(2\theta) \\
& -\left(\frac{1}{2}\cdot R^6\cdot b_2^{'} - \frac{1}{2}\cdot R^2\cdot d_2^{'}\right)\cdot 6\cdot r^{-4}\cdot\sin(2\theta) - d_2^{'}\cdot 2\cdot r^{-2}\cdot\sin(2\theta) \\
& +\left(-\frac{4\cdot c_3^{'}}{R^6} - \frac{3\cdot d_3^{'}}{R^4}\right)\cdot 6\cdot r\cdot\sin(3\theta) + \left(\frac{3\cdot c_3^{'}}{R^8} + \frac{2\cdot d_3^{'}}{R^6}\right)\cdot 12\cdot r^3\cdot\sin(3\theta) \\
& - c_3^{'}\cdot 12\cdot r^{-5}\cdot\sin(3\theta) - d_3^{'}\cdot 6\cdot r^{-3}\cdot\sin(3\theta) \\
& +\sum_{n=4,5\ldots}^{N}\left[\begin{array}{l}\left(\frac{1}{n}\cdot R^{(2n+2)}\cdot b_n^{'} + \left(\frac{1-n}{n}\right)\cdot R^2\cdot d_n^{'}\right)\cdot n\cdot(n-1)\cdot r^{(n-2)} + b_n^{'}\cdot n\cdot(n+1)\cdot r^n \\ -\left(\frac{1}{n}\cdot R^{(2n+2)}\cdot b_n^{'} + \left(\frac{1-n}{n}\right)\cdot R^2\cdot d_n^{'}\right)\cdot n\cdot(n+1)\cdot r^{-(n+2)} - d_n^{'}\cdot n\cdot(n-1)\cdot r^{-n}\end{array}\right]\cdot\sin(n\theta)
\end{aligned} \tag{7A.32}$$

$$\begin{aligned}
\sigma_{r\theta} = & -\frac{2\cdot R^4\cdot d_1^{'}}{r^3}\cdot\sin\theta + 2\cdot r\cdot d_1^{'}\cdot\sin\theta \\
& -\left(\frac{3}{2}\right)\cdot R^2\cdot b_2^{'}\cdot 2\cdot\sin(2\theta) - \frac{1}{2}\cdot R^{-2}\cdot d_2^{'}\cdot 2\cdot\sin(2\theta) + b_2^{'}\cdot 6\cdot r^2\cdot\sin(2\theta) \\
& -\frac{1}{2}\cdot R^6\cdot b_2^{'}\cdot 6\cdot r^{-4}\cdot\sin(2\theta) + \frac{1}{2}\cdot R^2\cdot d_2^{'}\cdot 6\cdot r^{-4}\cdot\sin(2\theta) - d_2^{'}\cdot 2\cdot r^{-2}\cdot\sin(2\theta) \\
& -\frac{4\cdot c_3^{'}}{R^6}\cdot 6\cdot r\cdot\sin(3\theta) - \frac{3\cdot d_3^{'}}{R^4}\cdot 6\cdot r\cdot\sin(3\theta) + \frac{3\cdot c_3^{'}}{R^8}\cdot 12\cdot r^3\cdot\sin(3\theta) + \frac{2\cdot d_3^{'}}{R^6}\cdot 12\cdot r^3\cdot\sin(3\theta) \\
& - c_3^{'}\cdot 12\cdot r^{-5}\cdot\sin(3\theta) - d_3^{'}\cdot 6\cdot r^{-3}\cdot\sin(3\theta) \\
& +\sum_{n=4,5\ldots}^{N}\left[\begin{array}{l}-\left(\frac{1+n}{n}\right)\cdot R^2\cdot b_n^{'}\cdot n\cdot(n-1)\cdot r^{(n-2)} - \frac{1}{n}\cdot R^{-(2n-2)}\cdot d_n^{'}\cdot n\cdot(n-1)\cdot r^{(n-2)} \\ + b_n^{'}\cdot n\cdot(n+1)\cdot r^n \\ -\frac{1}{n}\cdot R^{(2n+2)}\cdot b_n^{'}\cdot n\cdot(n+1)\cdot r^{-(n+2)} - \left(\frac{1-n}{n}\right)\cdot R^2\cdot d_n^{'}\cdot n\cdot(n+1)\cdot r^{-(n+2)} \\ - d_n^{'}\cdot n\cdot(n-1)\cdot r^{-n}\end{array}\right]\cdot\sin(n\theta)
\end{aligned} \tag{7A.33}$$

$$\sigma_{r\theta} = \left(-\frac{2\cdot R^4}{r^3}\cdot\sin\theta + 2\cdot r\cdot\sin\theta\right)\cdot d_1^{'}$$
$$+\left(-\left(\frac{3}{2}\right)\cdot R^2\cdot 2\cdot\sin(2\theta) + 6\cdot r^2\cdot\sin(2\theta) - \frac{1}{2}\cdot R^6\cdot 6\cdot r^{-4}\cdot\sin(2\theta)\right)\cdot b_2^{'}$$
$$+\left(-\frac{1}{2}\cdot R^{-2}\cdot 2\cdot\sin(2\theta) + \frac{1}{2}\cdot R^2\cdot 6\cdot r^{-4}\cdot\sin(2\theta) - 2\cdot r^{-2}\cdot\sin(2\theta)\right)\cdot d_2^{'}$$
$$+\left(-\frac{4}{R^6}\cdot 6\cdot r\cdot\sin(3\theta) + \frac{3}{R^8}\cdot 12\cdot r^3\cdot\sin(3\theta) - 12\cdot r^{-5}\cdot\sin(3\theta)\right)\cdot c_3^{'}$$
$$+\left(-\frac{3}{R^4}\cdot 6\cdot r\cdot\sin(3\theta) + \frac{2}{R^6}\cdot 12\cdot r^3\cdot\sin(3\theta) - 6\cdot r^{-3}\cdot\sin(3\theta)\right)\cdot d_3^{'}$$
$$+\sum_{n=4,5\ldots}^{N}\left[\begin{array}{l}\left(\begin{array}{l}-\left(\frac{1+n}{n}\right)\cdot R^2\cdot n\cdot(n-1)\cdot r^{(n-2)} + n\cdot(n+1)\cdot r^n \\ -\frac{1}{n}\cdot R^{(2n+2)}\cdot n\cdot(n+1)\cdot r^{-(n+2)}\end{array}\right)\cdot b_n^{'} \\ +\left(\begin{array}{l}-\frac{1}{n}\cdot R^{-(2n-2)}\cdot n\cdot(n-1)\cdot r^{(n-2)} - \left(\frac{1-n}{n}\right)\cdot R^2\cdot n\cdot(n+1)\cdot r^{-(n+2)} \\ -n\cdot(n-1)\cdot r^{-n}\end{array}\right)\cdot d_n^{'}\end{array}\right]\cdot\sin(n\theta)$$

(7A.34)

$$\sigma_{r\theta} = \left(-\frac{2\cdot R^4}{r^3} + 2\cdot r\right)\cdot\sin\theta\cdot d_1^{'}$$
$$+\left(-3\cdot R^2 + 6\cdot r^2 - 3\cdot R^6\cdot r^{-4}\right)\cdot\sin(2\theta)\cdot b_2^{'}$$
$$+\left(-R^{-2} + 3\cdot R^2\cdot r^{-4} - 2\cdot r^{-2}\right)\cdot\sin(2\theta)\cdot d_2^{'}$$
$$+\left(-\frac{24\cdot r}{R^6} + \frac{36\cdot r^3}{R^8} - 12\cdot r^{-5}\right)\cdot\sin(3\theta)\cdot c_3^{'}$$
$$+\left(-\frac{18\cdot r}{R^4} + \frac{24\cdot r^3}{R^6} - 6\cdot r^{-3}\right)\cdot\sin(3\theta)\cdot d_3^{'}$$
$$+\sum_{n=4,5\ldots}^{N}\left[\begin{array}{l}\left(-(n^2-1)\cdot R^2\cdot r^{(n-2)} + n\cdot(n+1)\cdot r^n - (n+1)\cdot R^{(2n+2)}\cdot r^{-(n+2)}\right)\cdot b_n^{'} \\ +\left(-(n-1)\cdot R^{-(2n-2)}\cdot r^{(n-2)} + (n^2-1)\cdot R^2\cdot r^{-(n+2)} - n\cdot(n-1)\cdot r^{-n}\right)\cdot d_n^{'}\end{array}\right]\cdot\sin(n\theta)$$

(7A.35)

Equation 7A.35 is an alternative form of *equation 7.13* of Chapter 7 for symmetry about the x-axis.

Now evaluating the isopachic stress for the symmetrical case from *equations 7A.23 and 7A.29*:

$$S = \sigma_{rr} + \sigma_{\theta\theta} \tag{7A.36}$$

$$S = \left[\begin{array}{l}
\left[\begin{array}{l}
\left(-\frac{2\cdot R^2}{r^2}+2\right)\cdot c_0+\left(-\frac{2\cdot R^4}{r^3}+2\cdot r\right)\cdot\cos\theta\cdot d_1' \\
+\left(3\cdot R^2-3\cdot R^6\cdot r^{-4}\right)\cdot\cos(2\theta)\cdot b_2' \\
+\left(R^{-2}+3\cdot R^2\cdot r^{-4}-4\cdot r^{-2}\right)\cdot\cos(2\theta)\cdot d_2' \\
+\left(\frac{24\cdot r}{R^6}-\frac{12\cdot r^3}{R^8}-12\cdot r^{-5}\right)\cdot\cos(3\theta)\cdot c_3' \\
+\left(\frac{18\cdot r}{R^4}-\frac{8\cdot r^3}{R^6}-10\cdot r^{-3}\right)\cdot\cos(3\theta)\cdot d_3' \\
-\sum_{n=4,5\ldots}^{N}\left[\begin{array}{l}
\left(\begin{array}{l}-(n^2-1)\cdot R^2\cdot r^{(n-2)}+(n-2)\cdot(n+1)\cdot r^n \\ +(n+1)\cdot R^{(2n+2)}\cdot r^{-(n+2)}\end{array}\right)\cdot b_n' \\
+\left(\begin{array}{l}-(n-1)\cdot R^{-(2n-2)}\cdot r^{(n-2)}-(n^2-1)\cdot R^2\cdot r^{-(n+2)} \\ +(n+2)\cdot(n-1)\cdot r^{-n}\end{array}\right)\cdot d_n'
\end{array}\right]\cdot\cos(n\theta)
\end{array}\right] \\
+\left[\begin{array}{l}
\left(\frac{2\cdot R^2}{r^2}+2\right)\cdot c_0+\left(\frac{2\cdot R^4}{r^3}+6\cdot r\right)\cdot\cos\theta\cdot d_1' \\
+\left(-3\cdot R^2+12\cdot r^2+3\cdot R^6\cdot r^{-4}\right)\cdot\cos(2\theta)\cdot b_2' \\
-\left(R^{-2}+3\cdot R^2\cdot r^{-4}\right)\cdot\cos(2\theta)\cdot d_2' \\
+\left(-\frac{24\cdot r}{R^6}+\frac{60\cdot r^3}{R^8}+12\cdot r^{-5}\right)\cdot\cos(3\theta)\cdot c_3' \\
+\left(-\frac{18\cdot r}{R^4}+\frac{40\cdot r^3}{R^6}+2\cdot r^{-3}\right)\cdot\cos(3\theta)\cdot d_3' \\
+\sum_{n=4,5\ldots}^{N}\left[\begin{array}{l}
\left(\begin{array}{l}-(n^2-1)\cdot R^2\cdot r^{(n-2)}+(n+2)\cdot(n+1)\cdot r^n \\ +(n+1)\cdot R^{(2n+2)}\cdot r^{-(n+2)}\end{array}\right)\cdot b_n' \\
+\left(\begin{array}{l}-(n-1)\cdot R^{-(2n-2)}\cdot r^{(n-2)}-(n^2-1)\cdot R^2\cdot r^{-(n+2)} \\ +(n-2)\cdot(n-1)\cdot r^{-n}\end{array}\right)\cdot d_n'
\end{array}\right]\cdot\cos(n\theta)
\end{array}\right]
\end{array}\right] \tag{7A.37}$$

$$
S = \left[\begin{array}{l}
\left(-\frac{2\cdot R^2}{r^2}+2\right)\cdot c_0+\left(\frac{2\cdot R^2}{r^2}+2\right)\cdot c_0 \\
+\left(-\frac{2\cdot R^4}{r^3}+2\cdot r\right)\cdot\cos\theta\cdot d_1^{'}+\left(\frac{2\cdot R^4}{r^3}+6\cdot r\right)\cdot\cos\theta\cdot d_1^{'} \\
+\left(3\cdot R^2-3\cdot R^6\cdot r^{-4}\right)\cdot\cos(2\theta)\cdot b_2^{'}+\left(-3\cdot R^2+12\cdot r^2+3\cdot R^6\cdot r^{-4}\right)\cdot\cos(2\theta)\cdot b_2^{'} \\
+\left(R^{-2}+3\cdot R^2\cdot r^{-4}-4\cdot r^{-2}\right)\cdot\cos(2\theta)\cdot d_2^{'}-\left(R^{-2}+3\cdot R^2\cdot r^{-4}\right)\cdot\cos(2\theta)\cdot d_2^{'} \\
+\left(\frac{24\cdot r}{R^6}-\frac{12\cdot r^3}{R^8}-12\cdot r^{-5}\right)\cdot\cos(3\theta)\cdot c_3^{'}+\left(-\frac{24\cdot r}{R^6}+\frac{60\cdot r^3}{R^8}+12\cdot r^{-5}\right)\cdot\cos(3\theta)\cdot c_3^{'} \\
+\left(\frac{18\cdot r}{R^4}-\frac{8\cdot r^3}{R^6}-10\cdot r^{-3}\right)\cdot\cos(3\theta)\cdot d_3^{'}+\left(-\frac{18\cdot r}{R^4}+\frac{40\cdot r^3}{R^6}+2\cdot r^{-3}\right)\cdot\cos(3\theta)\cdot d_3^{'} \\
-\sum_{n=4,5\ldots}^{N}\left[\begin{array}{l}\left(\begin{array}{l}-(n^2-1)\cdot R^2\cdot r^{(n-2)}+(n-2)\cdot(n+1)\cdot r^n\\+(n+1)\cdot R^{(2n+2)}\cdot r^{-(n+2)}\end{array}\right)\cdot b_n^{'}\\+\left(\begin{array}{l}-(n-1)\cdot R^{-(2n-2)}\cdot r^{(n-2)}-(n^2-1)\cdot R^2\cdot r^{-(n+2)}\\+(n+2)\cdot(n-1)\cdot r^{-n}\end{array}\right)\cdot d_n^{'}\end{array}\right]\cdot\cos(n\theta) \\
+\sum_{n=4,5\ldots}^{N}\left[\begin{array}{l}\left(\begin{array}{l}-(n^2-1)\cdot R^2\cdot r^{(n-2)}+(n+2)\cdot(n+1)\cdot r^n\\+(n+1)\cdot R^{(2n+2)}\cdot r^{-(n+2)}\end{array}\right)\cdot b_n^{'}\\+\left(\begin{array}{l}-(n-1)\cdot R^{-(2n-2)}\cdot r^{(n-2)}-(n^2-1)\cdot R^2\cdot r^{-(n+2)}\\+(n-2)\cdot(n-1)\cdot r^{-n}\end{array}\right)\cdot d_n^{'}\end{array}\right]\cdot\cos(n\theta)
\end{array}\right] \qquad (7A.38)
$$

$$
S = \left[\begin{array}{l}
\left(-\frac{2\cdot R^2}{r^2}+2+\frac{2\cdot R^2}{r^2}+2\right)\cdot c_0 \\
+\left(-\frac{2\cdot R^4}{r^3}+2\cdot r+\frac{2\cdot R^4}{r^3}+6\cdot r\right)\cdot\cos\theta\cdot d_1^{'} \\
+\left(3\cdot R^2-3\cdot R^6\cdot r^{-4}-3\cdot R^2+12\cdot r^2+3\cdot R^6\cdot r^{-4}\right)\cdot\cos(2\theta)\cdot b_2^{'} \\
+\left(R^{-2}+3\cdot R^2\cdot r^{-4}-4\cdot r^{-2}-R^{-2}-3\cdot R^2\cdot r^{-4}\right)\cdot\cos(2\theta)\cdot d_2^{'} \\
+\left(\frac{24\cdot r}{R^6}-\frac{12\cdot r^3}{R^8}-12\cdot r^{-5}-\frac{24\cdot r}{R^6}+\frac{60\cdot r^3}{R^8}+12\cdot r^{-5}\right)\cdot\cos(3\theta)\cdot c_3^{'} \\
+\left(\frac{18\cdot r}{R^4}-\frac{8\cdot r^3}{R^6}-10\cdot r^{-3}-\frac{18\cdot r}{R^4}+\frac{40\cdot r^3}{R^6}+2\cdot r^{-3}\right)\cdot\cos(3\theta)\cdot d_3^{'} \\
-\sum\limits_{n=4,5\ldots}^{N}\left[\begin{array}{l}
\left(\begin{array}{l}-(n^2-1)\cdot R^2\cdot r^{(n-2)}+(n-2)\cdot(n+1)\cdot r^n\\+(n+1)\cdot R^{(2n+2)}\cdot r^{-(n+2)}\end{array}\right)\cdot b_n^{'} \\
+\left(\begin{array}{l}-(n-1)\cdot R^{-(2n-2)}\cdot r^{(n-2)}-(n^2-1)\cdot R^2\cdot r^{-(n+2)}\\+(n+2)\cdot(n-1)\cdot r^{-n}\end{array}\right)\cdot d_n^{'} \\
-\left(\begin{array}{l}-(n^2-1)\cdot R^2\cdot r^{(n-2)}+(n+2)\cdot(n+1)\cdot r^n\\+(n+1)\cdot R^{(2n+2)}\cdot r^{-(n+2)}\end{array}\right)\cdot b_n^{'} \\
-\left(\begin{array}{l}-(n-1)\cdot R^{-(2n-2)}\cdot r^{(n-2)}-(n^2-1)\cdot R^2\cdot r^{-(n+2)}\\+(n-2)\cdot(n-1)\cdot r^{-n}\end{array}\right)\cdot d_n^{'}
\end{array}\right]\cdot\cos(n\theta)
\end{array}\right] \qquad (7A.39)
$$

$$
S = \left[\begin{array}{l}
4\cdot c_0+8\cdot r\cdot\cos\theta\cdot d_1^{'}+12\cdot r^2\cdot\cos(2\theta)\cdot b_2^{'}-4\cdot r^{-2}\cdot\cos(2\theta)\cdot d_2^{'} \\
+\frac{48\cdot r^3}{R^8}\cdot\cos(3\theta)\cdot c_3^{'}+\left(-8\cdot r^{-3}+\frac{32\cdot r^3}{R^6}\right)\cdot\cos(3\theta)\cdot d_3^{'} \\
-\sum\limits_{n=4,5\ldots}^{N}\left[\begin{array}{l}
\left(\begin{array}{l}-(n^2-1)\cdot R^2\cdot r^{(n-2)}+(n-2)\cdot(n+1)\cdot r^n\\+(n+1)\cdot R^{(2n+2)}\cdot r^{-(n+2)}+(n^2-1)\cdot R^2\cdot r^{(n-2)}\\-(n+2)\cdot(n+1)\cdot r^n-(n+1)\cdot R^{(2n+2)}\cdot r^{-(n+2)}\end{array}\right)\cdot b_n^{'} \\
+\left(\begin{array}{l}-(n-1)\cdot R^{-(2n-2)}\cdot r^{(n-2)}-(n^2-1)\cdot R^2\cdot r^{-(n+2)}\\+(n+2)\cdot(n-1)\cdot r^{-n}(n-1)\cdot R^{-(2n-2)}\cdot r^{(n-2)}\\+(n^2-1)\cdot R^2\cdot r^{-(n+2)}-(n-2)\cdot(n-1)\cdot r^{-n}\end{array}\right)\cdot d_n^{'}
\end{array}\right]\cdot\cos(n\theta)
\end{array}\right] \qquad (7A.40)
$$

$$S = 4\cdot c_0 + 8\cdot r\cdot\cos\theta\cdot d_1^{'} + 12\cdot r^2\cdot\cos(2\theta)\cdot b_2^{'} - 4\cdot r^{-2}\cdot\cos(2\theta)\cdot d_2^{'} + \frac{48\cdot r^3}{R^8}\cdot\cos(3\theta)\cdot c_3^{'} + \left(-8\cdot r^{-3} + \frac{32\cdot r^3}{R^6}\right)\cdot\cos(3\theta)\cdot d_3^{'} - \sum_{n=4,5\ldots}^{N}\left[\begin{array}{l}\left((n-2)\cdot(n+1)\cdot r^n - (n+2)\cdot(n+1)\cdot r^n\right)\cdot b_n^{'} \\ +\left((n+2)\cdot(n-1)\cdot r^{-n} - (n-2)\cdot(n-1)\cdot r^{-n}\right)\cdot d_n^{'}\end{array}\right]\cdot\cos(n\theta) \tag{7A.41}$$

$$S = 4\cdot c_0 + 8\cdot r\cdot\cos\theta\cdot d_1^{'} + 12\cdot r^2\cdot\cos(2\theta)\cdot b_2^{'} - 4\cdot r^{-2}\cdot\cos(2\theta)\cdot d_2^{'} + \frac{48\cdot r^3}{R^8}\cdot\cos(3\theta)\cdot c_3^{'} + \left(-8\cdot r^{-3} + \frac{32\cdot r^3}{R^6}\right)\cdot\cos(3\theta)\cdot d_3^{'} + \sum_{n=4,5\ldots}^{N}\left[\left(4\cdot(n+1)\cdot r^n\right)\cdot b_n^{'} - \left(4\cdot(n-1)\cdot r^{-n}\right)\cdot d_n^{'}\right]\cdot\cos(n\theta) \tag{7A.42}$$

All coefficients appearing in the stress expressions of *equations 7A.23, 7A.29 and 7A.33* also appear in the isopachic stress of *equation 7A.42*. This means all components of stress are available once the Airy coefficients have been evaluated from the associated temperature data.

Equation 7A.42 is an alternative form of *equation 7.14* of Chapter 7 for symmetry about the x-axis.

The stress equations can be simplified further i.e., without expanding the summation for n = 2 and 3. Imposing the traction-free conditions $\sigma_{rr} = \sigma_{r\theta} = 0$ at r = R, on the boundary of the hole for the plate symmetrical about x-axis (*figure 7.1*).

1) $b_0 \equiv f(c_0)$

$$\sigma_{rr} = 0, \quad \frac{1}{R^2} \cdot b_0 + 2 \cdot c_0 = 0$$

$$\Rightarrow \qquad b_0 = -2 \cdot R^2 \cdot c_0 \tag{7A.43}$$

(same as *equation 7A.14*)

For r = R and all values of θ in *equations 7A.11 and 7A.13* respectively yields:

2) $c_1 \equiv f(d_1)$

$$\sigma_{rr} = 0 \qquad gives \qquad \left(-\frac{2 \cdot c_1^{'}}{R^3} + 2 \cdot R \cdot d_1^{'} \right) = 0 \qquad and$$

$$\sigma_{r\theta} = 0 \qquad gives \qquad \left(\frac{2 \cdot c_1^{'}}{R^3} - 2 \cdot R \cdot d_1^{'} \right) = 0$$

$$c_1^{'} = R^4 \cdot d_1^{'} \tag{7A.44}$$

(same as *equation 7A.15*)

3) $a_n = f(b_n, d_n)$ *and* $c_n = f(b_n, d_n)$

For n ≥ 2, r = R and all values of θ in *equations 7A.11 and 7A.13* respectively, yields:

$$\sigma_{rr} = 0 \qquad gives \qquad \begin{bmatrix} a_n' \cdot n \cdot (n-1) \cdot R^{(n-2)} + b_n' \cdot (n+1) \cdot (n-2) \cdot R^n \\ + c_n' \cdot n \cdot (n+1) \cdot R^{-(n+2)} + d_n' \cdot (n-1) \cdot (n+2) \cdot R^{-n} \end{bmatrix} = 0$$

$$\sigma_{r\theta} = 0 \qquad gives \qquad \begin{bmatrix} a_n' \cdot n \cdot (n-1) \cdot R^{(n-2)} + b_n' \cdot n \cdot (n+1) \cdot R^n \\ - c_n' \cdot n \cdot (n+1) \cdot R^{-(n+2)} - d_n' \cdot n \cdot (n-1) \cdot R^{-n} \end{bmatrix} = 0$$

$$a_n' = -\left(\frac{1+n}{n}\right) \cdot R^2 \cdot b_n' - \frac{1}{n} \cdot R^{-(2n-2)} \cdot d_n'$$

$$c_n' = \frac{1}{n} \cdot R^{(2n+2)} \cdot b_n' + \left(\frac{1-n}{n}\right) \cdot R^2 \cdot d_n' \qquad (7A.45)$$

(which are same as *equations 7A.16*)

Substituting *equations 7A.43 through 7A.45* into *equation 7A.11 gives*.

$$\sigma_{rr} = \frac{\left(-2 \cdot R^2 \cdot c_0\right)}{r^2} + 2 \cdot c_0 - \frac{2 \cdot \left(R^4 \cdot d_1'\right)}{r^3} \cdot \cos\theta + 2 \cdot r \cdot d_1' \cdot \cos\theta$$
$$- \sum_{n=2,3\ldots}^{N} \begin{bmatrix} \left(-\left(\frac{1+n}{n}\right) \cdot R^2 \cdot b_n' - \frac{1}{n} \cdot R^{-(2n-2)} \cdot d_n'\right) \cdot n \cdot (n-1) \cdot r^{(n-2)} \\ + b_n' \cdot (n-2) \cdot (n+1) \cdot r^n \\ + \left(\frac{1}{n} \cdot R^{(2n+2)} \cdot b_n' + \left(\frac{1-n}{n}\right) \cdot R^2 \cdot d_n'\right) \cdot n \cdot (n+1) \cdot r^{-(n+2)} \\ + d_n' \cdot (n+2) \cdot (n-1) \cdot r^{-n} \end{bmatrix} \cdot \cos(n\theta) \qquad (7A.46)$$

$$\sigma_{rr} = -\frac{2\cdot R^2}{r^2}\cdot c_0 + 2\cdot c_0 - \frac{2\cdot R^4\cdot\cos\theta}{r^3}\cdot d_1^{'} + 2\cdot r\cdot\cos\theta\cdot d_1^{'} - \sum_{n=2,3\ldots}^{N}\left[\begin{array}{l} -\left(\frac{1+n}{n}\right)\cdot R^2\cdot n\cdot(n-1)\cdot r^{(n-2)}\cdot b_n^{'} - \frac{1}{n}\cdot R^{-(2n-2)}\cdot n\cdot(n-1)\cdot r^{(n-2)}\cdot d_n^{'} \\ +(n-2)\cdot(n+1)\cdot r^n\cdot b_n^{'} \\ +\frac{1}{n}\cdot R^{(2n+2)}\cdot n\cdot(n+1)\cdot r^{-(n+2)}\cdot b_n^{'} + \left(\frac{1-n}{n}\right)\cdot R^2\cdot n\cdot(n+1)\cdot r^{-(n+2)}\cdot d_n^{'} \\ +(n+2)\cdot(n-1)\cdot r^{-n}\cdot d_n^{'} \end{array}\right]\cdot\cos(n\theta) \tag{7A.47}$$

$$\sigma_{rr} = \left(-\frac{2\cdot R^2}{r^2}+2\right)\cdot c_0 + \left(-\frac{2\cdot R^4\cdot\cos\theta}{r^3}+2\cdot r\cdot\cos\theta\right)\cdot d_1^{'} - \sum_{n=2,3\ldots}^{N}\left[\begin{array}{l} \left(\begin{array}{l} -\left(\frac{1+n}{n}\right)\cdot R^2\cdot n\cdot(n-1)\cdot r^{(n-2)} + (n-2)\cdot(n+1)\cdot r^n \\ +\frac{1}{n}\cdot R^{(2n+2)}\cdot n\cdot(n+1)\cdot r^{-(n+2)} \end{array}\right)\cdot b_n^{'} \\ \left(\begin{array}{l} -\frac{1}{n}\cdot R^{-(2n-2)}\cdot n\cdot(n-1)\cdot r^{(n-2)} + \left(\frac{1-n}{n}\right)\cdot R^2\cdot n\cdot(n+1)\cdot r^{-(n+2)} \\ +(n+2)\cdot(n-1)\cdot r^{-n} \end{array}\right)\cdot d_n^{'} \end{array}\right]\cdot\cos(n\theta) \tag{7A.48}$$

$$\sigma_{rr} = \left(-\frac{2\cdot R^2}{r^2}+2\right)\cdot c_0 + \left(-\frac{2\cdot R^4}{r^3}+2\cdot r\right)\cdot\cos\theta\cdot d_1^{'} - \sum_{n=2,3\ldots}^{N}\left[\begin{array}{l} \left(\begin{array}{l} -(n^2-1)\cdot R^2\cdot r^{(n-2)} + (n-2)\cdot(n+1)\cdot r^n \\ +(n+1)\cdot R^{(2n+2)}\cdot r^{-(n+2)} \end{array}\right)\cdot b_n^{'} \\ \left(\begin{array}{l} -(n-1)\cdot R^{-(2n-2)}\cdot r^{(n-2)} - (n^2-1)\cdot R^2\cdot r^{-(n+2)} \\ +(n+2)\cdot(n-1)\cdot r^{-n} \end{array}\right)\cdot d_n^{'} \end{array}\right]\cdot\cos(n\theta) \tag{7A.49}$$

Equation 7A.49 is a simplified form of *equations 7A.23* and *equation 7.11* of Chapter 7 for symmetry about the x-axis.

Substituting *equations 7A.43 through 7A.45* in *equation 7A.12* give

$$\sigma_{\theta\theta} = -\frac{\left(-2\cdot R^2\cdot c_0\right)}{r^2} + 2\cdot c_0 + \frac{2\cdot\left(R^4\cdot d_1^{'}\right)}{r^3}\cdot\cos\theta + 6\cdot r\cdot d_1^{'}\cdot\cos\theta + \sum_{n=2,3\ldots}^{N}\left[\begin{array}{l}\left(-\left(\frac{1+n}{n}\right)\cdot R^2\cdot b_n^{'} - \frac{1}{n}\cdot R^{-(2n-2)}\cdot d_n^{'}\right)\cdot n\cdot(n-1)\cdot r^{(n-2)} + b_n^{'}\cdot(n+2)\cdot(n+1)\cdot r^n \\ +\left(\frac{1}{n}\cdot R^{(2n+2)}\cdot b_n^{'} + \left(\frac{1-n}{n}\right)\cdot R^2\cdot d_n^{'}\right)\cdot n\cdot(n+1)\cdot r^{-(n+2)} + d_n^{'}\cdot(n-2)\cdot(n-1)\cdot r^{-n}\end{array}\right]\cdot\cos(n\theta) \tag{7A.50}$$

$$\sigma_{\theta\theta} = \frac{2\cdot R^2\cdot c_0}{r^2} + 2\cdot c_0 + \frac{2\cdot R^4\cdot d_1^{'}}{r^3}\cdot\cos\theta + 6\cdot r\cdot d_1^{'}\cdot\cos\theta + \sum_{n=2,3\ldots}^{N}\left[\begin{array}{l}-\left(\frac{1+n}{n}\right)\cdot R^2\cdot b_n^{'}\cdot n\cdot(n-1)\cdot r^{(n-2)} - \frac{1}{n}\cdot R^{-(2n-2)}\cdot d_n^{'}\cdot n\cdot(n-1)\cdot r^{(n-2)} \\ +b_n^{'}\cdot(n+2)\cdot(n+1)\cdot r^n \\ +\frac{1}{n}\cdot R^{(2n+2)}\cdot b_n^{'}\cdot n\cdot(n+1)\cdot r^{-(n+2)} + \left(\frac{1-n}{n}\right)\cdot R^2\cdot d_n^{'}\cdot n\cdot(n+1)\cdot r^{-(n+2)} \\ +d_n^{'}\cdot(n-2)\cdot(n-1)\cdot r^{-n}\end{array}\right]\cdot\cos(n\theta) \tag{7A.51}$$

$$\sigma_{\theta\theta} = \left(\frac{2\cdot R^2}{r^2}+2\right)\cdot c_0 + \left(\frac{2\cdot R^4}{r^3}\cdot\cos\theta + 6\cdot r\cdot\cos\theta\right)\cdot d_1^{'} + \sum_{n=2,3\ldots}^{N}\left[\begin{array}{l}\left(\begin{array}{l}-\left(\frac{1+n}{n}\right)\cdot R^2\cdot n\cdot(n-1)\cdot r^{(n-2)} + (n+2)\cdot(n+1)\cdot r^n \\ +\frac{1}{n}\cdot R^{(2n+2)}\cdot n\cdot(n+1)\cdot r^{-(n+2)}\end{array}\right)\cdot b_n^{'} \\ +\left(\begin{array}{l}-\frac{1}{n}\cdot R^{-(2n-2)}\cdot n\cdot(n-1)\cdot r^{(n-2)} + \left(\frac{1-n}{n}\right)\cdot R^2\cdot n\cdot(n+1)\cdot r^{-(n+2)} \\ +(n-2)\cdot(n-1)\cdot r^{-n}\end{array}\right)\cdot d_n^{'}\end{array}\right]\cdot\cos(n\theta) \tag{7A.52}$$

$$\sigma_{\theta\theta} = \left(\frac{2\cdot R^2}{r^2} + 2\right)\cdot c_0 + \left(\frac{2\cdot R^4}{r^3} + 6\cdot r\right)\cdot \cos\theta \cdot d_1^{'} + \sum_{n=2,3\ldots}^{N}\left[\begin{array}{l}\left(\begin{array}{l}-(n^2-1)\cdot R^2\cdot r^{(n-2)} + (n+2)\cdot(n+1)\cdot r^n \\ +(n+1)\cdot R^{(2n+2)}\cdot r^{-(n+2)}\end{array}\right)\cdot b_n^{'} \\ +\left(\begin{array}{l}-(n-1)\cdot R^{-(2n-2)}\cdot r^{(n-2)} - (n^2-1)\cdot R^2\cdot r^{-(n+2)} \\ +(n-2)\cdot(n-1)\cdot r^{-n}\end{array}\right)\cdot d_n^{'}\end{array}\right]\cdot\cos(n\theta) \tag{7A.53}$$

Equation 7A.53 is a simplified form of *equations 7A.29* and *equation 7.12* of Chapter 7 for symmetry about the x-axis.

Substituting *equations 7A.43 through 7A.45* in *equation 7A.13* give

$$\sigma_{r\theta} = -\frac{2\cdot\left(R^4\cdot d_1^{'}\right)}{r^3}\cdot\sin\theta + 2\cdot r\cdot d_1^{'}\cdot\sin\theta + \sum_{n=2,3\ldots}^{N}\left[\begin{array}{l}\left(\frac{1}{n}\cdot R^{(2n+2)}\cdot b_n^{'} + \left(\frac{1-n}{n}\right)\cdot R^2\cdot d_n^{'}\right)\cdot n\cdot(n-1)\cdot r^{(n-2)} + b_n^{'}\cdot n\cdot(n+1)\cdot r^n \\ -\left(\frac{1}{n}\cdot R^{(2n+2)}\cdot b_n^{'} + \left(\frac{1-n}{n}\right)\cdot R^2\cdot d_n^{'}\right)\cdot n\cdot(n+1)\cdot r^{-(n+2)} - d_n^{'}\cdot n\cdot(n-1)\cdot r^{-n}\end{array}\right]\cdot\sin(n\theta) \tag{7A.54}$$

$$\sigma_{r\theta} = -\frac{2\cdot R^4\cdot d_1^{'}}{r^3}\cdot\sin\theta + 2\cdot r\cdot d_1^{'}\cdot\sin\theta + \sum_{n=2,3\ldots}^{N}\left[\begin{array}{l}-\left(\frac{1+n}{n}\right)\cdot R^2\cdot b_n^{'}\cdot n\cdot(n-1)\cdot r^{(n-2)} - \frac{1}{n}\cdot R^{-(2n-2)}\cdot d_n^{'}\cdot n\cdot(n-1)\cdot r^{(n-2)} \\ + b_n^{'}\cdot n\cdot(n+1)\cdot r^n \\ -\frac{1}{n}\cdot R^{(2n+2)}\cdot b_n^{'}\cdot n\cdot(n+1)\cdot r^{-(n+2)} - \left(\frac{1-n}{n}\right)\cdot R^2\cdot d_n^{'}\cdot n\cdot(n+1)\cdot r^{-(n+2)} \\ - d_n^{'}\cdot n\cdot(n-1)\cdot r^{-n}\end{array}\right]\cdot\sin(n\theta) \tag{7A.55}$$

$$\sigma_{r\theta} = \left(-\frac{2\cdot R^4}{r^3}\cdot\sin\theta + 2\cdot r\cdot\sin\theta\right)\cdot d_1^{'} + \sum_{n=2,3\ldots}^{N}\left[\begin{array}{l}\left(\begin{array}{l}-\left(\frac{1+n}{n}\right)\cdot R^2\cdot n\cdot(n-1)\cdot r^{(n-2)} + n\cdot(n+1)\cdot r^n \\ -\frac{1}{n}\cdot R^{(2n+2)}\cdot n\cdot(n+1)\cdot r^{-(n+2)}\end{array}\right)\cdot b_n^{'} \\ + \left(\begin{array}{l}-\frac{1}{n}\cdot R^{-(2n-2)}\cdot n\cdot(n-1)\cdot r^{(n-2)} - \left(\frac{1-n}{n}\right)\cdot R^2\cdot n\cdot(n+1)\cdot r^{-(n+2)} \\ -n\cdot(n-1)\cdot r^{-n}\end{array}\right)\cdot d_n^{'}\end{array}\right]\cdot\sin(n\theta) \tag{7A.56}$$

$$\sigma_{r\theta} = \left(-\frac{2 \cdot R^4}{r^3} + 2 \cdot r \right) \cdot \sin\theta \cdot d_1^{'} + \sum_{n=2,3\ldots}^{N} \left[\begin{array}{l} \left(-(n^2 - 1) \cdot R^2 \cdot r^{(n-2)} + n \cdot (n+1) \cdot r^n - (n+1) \cdot R^{(2n+2)} \cdot r^{-(n+2)} \right) \cdot b_n^{'} \\ + \left(-(n-1) \cdot R^{-(2n-2)} \cdot r^{(n-2)} + (n^2 - 1) \cdot R^2 \cdot r^{-(n+2)} - n \cdot (n-1) \cdot r^{-n} \right) \cdot d_n^{'} \end{array} \right] \cdot \sin(n\theta) \tag{7A.57}$$

Equation 7A.57 is a simplified form of *equations 7A.35* and *equation 7.13* of Chapter 7 for symmetry about the x-axis.

Now evaluating the isopachic stress from *equations 7A.46 and 7A.57*:

$$S = \sigma_{rr} + \sigma_{\theta\theta} \tag{7A.58}$$

$$S = \left[\begin{array}{l} \left[\begin{array}{l} \left(-\dfrac{2 \cdot R^2}{r^2} + 2 \right) \cdot c_0 + \left(-\dfrac{2 \cdot R^4}{r^3} + 2 \cdot r \right) \cdot \cos\theta \cdot d_1' \\ - \displaystyle\sum_{n=2,3\ldots}^{N} \left[\begin{array}{l} \left(\begin{array}{l} -(n^2-1) \cdot R^2 \cdot r^{(n-2)} + (n-2) \cdot (n+1) \cdot r^n \\ +(n+1) \cdot R^{(2n+2)} \cdot r^{-(n+2)} \end{array} \right) \cdot b_n' \\ + \left(\begin{array}{l} -(n-1) \cdot R^{-(2n-2)} \cdot r^{(n-2)} - (n^2-1) \cdot R^2 \cdot r^{-(n+2)} \\ +(n+2) \cdot (n-1) \cdot r^{-n} \end{array} \right) \cdot d_n' \end{array} \right] \cdot \cos(n\theta) \end{array} \right] \\ + \left[\begin{array}{l} \left(\dfrac{2 \cdot R^2}{r^2} + 2 \right) \cdot c_0 + \left(\dfrac{2 \cdot R^4}{r^3} + 6 \cdot r \right) \cdot \cos\theta \cdot d_1' \\ + \displaystyle\sum_{n=2,3\ldots}^{N} \left[\begin{array}{l} \left(\begin{array}{l} -(n^2-1) \cdot R^2 \cdot r^{(n-2)} + (n+2) \cdot (n+1) \cdot r^n \\ +(n+1) \cdot R^{(2n+2)} \cdot r^{-(n+2)} \end{array} \right) \cdot b_n' \\ + \left(\begin{array}{l} -(n-1) \cdot R^{-(2n-2)} \cdot r^{(n-2)} - (n^2-1) \cdot R^2 \cdot r^{-(n+2)} \\ +(n-2) \cdot (n-1) \cdot r^{-n} \end{array} \right) \cdot d_n' \end{array} \right] \cdot \cos(n\theta) \end{array} \right] \end{array} \right] \tag{7A.59}$$

$$S=\left[\begin{array}{l}\left(-\frac{2\cdot R^2}{r^2}+2\right)\cdot c_0+\left(\frac{2\cdot R^2}{r^2}+2\right)\cdot c_0\\ +\left(-\frac{2\cdot R^4}{r^3}+2\cdot r\right)\cdot\cos\theta\cdot d_1^{'}+\left(\frac{2\cdot R^4}{r^3}+6\cdot r\right)\cdot\cos\theta\cdot d_1^{'}\\ -\sum_{n=2,3\ldots}^{N}\left[\begin{array}{l}\left(\begin{array}{l}-(n^2-1)\cdot R^2\cdot r^{(n-2)}+(n-2)\cdot(n+1)\cdot r^n\\ +(n+1)\cdot R^{(2n+2)}\cdot r^{-(n+2)}\end{array}\right)\cdot b_n\\ +\left(\begin{array}{l}-(n-1)\cdot R^{-(2n-2)}\cdot r^{(n-2)}-(n^2-1)\cdot R^2\cdot r^{-(n+2)}\\ +(n+2)\cdot(n-1)\cdot r^{-n}\end{array}\right)\cdot d_n^{'}\end{array}\right]\cdot\cos(n\theta)\\ +\sum_{n=2,3\ldots}^{N}\left[\begin{array}{l}\left(\begin{array}{l}-(n^2-1)\cdot R^2\cdot r^{(n-2)}+(n+2)\cdot(n+1)\cdot r^n\\ +(n+1)\cdot R^{(2n+2)}\cdot r^{-(n+2)}\end{array}\right)\cdot b_n\\ +\left(\begin{array}{l}-(n-1)\cdot R^{-(2n-2)}\cdot r^{(n-2)}-(n^2-1)\cdot R^2\cdot r^{-(n+2)}\\ +(n-2)\cdot(n-1)\cdot r^{-n}\end{array}\right)\cdot d_n^{'}\end{array}\right]\cdot\cos(n\theta)\end{array}\right] \tag{7A.60}$$

$$S=\left[\begin{array}{l}\left(-\frac{2\cdot R^2}{r^2}+2+\frac{2\cdot R^2}{r^2}+2\right)\cdot c_0\\ +\left(-\frac{2\cdot R^4}{r^3}+2\cdot r+\frac{2\cdot R^4}{r^3}+6\cdot r\right)\cdot\cos\theta\cdot d_1^{'}\\ -\sum_{n=2,3\ldots}^{N}\left[\begin{array}{l}\left(\begin{array}{l}-(n^2-1)\cdot R^2\cdot r^{(n-2)}+(n-2)\cdot(n+1)\cdot r^n\\ +(n+1)\cdot R^{(2n+2)}\cdot r^{-(n+2)}\end{array}\right)\cdot b_n^{'}\\ +\left(\begin{array}{l}-(n-1)\cdot R^{-(2n-2)}\cdot r^{(n-2)}-(n^2-1)\cdot R^2\cdot r^{-(n+2)}\\ +(n+2)\cdot(n-1)\cdot r^{-n}\end{array}\right)\cdot d_n^{'}\\ -\left(\begin{array}{l}-(n^2-1)\cdot R^2\cdot r^{(n-2)}+(n+2)\cdot(n+1)\cdot r^n\\ +(n+1)\cdot R^{(2n+2)}\cdot r^{-(n+2)}\end{array}\right)\cdot b_n^{'}\\ -\left(\begin{array}{l}-(n-1)\cdot R^{-(2n-2)}\cdot r^{(n-2)}-(n^2-1)\cdot R^2\cdot r^{-(n+2)}\\ +(n-2)\cdot(n-1)\cdot r^{-n}\end{array}\right)\cdot d_n^{'}\end{array}\right]\cdot\cos(n\theta)\end{array}\right] \tag{7A.61}$$

$$S = \begin{bmatrix} 4\cdot c_0 + 8\cdot r\cdot\cos\theta\cdot d_1^{'} \\ -\sum_{n=2,3...}^{N} \begin{bmatrix} \begin{pmatrix} -(n^2-1)\cdot R^2\cdot r^{(n-2)} + (n-2)\cdot(n+1)\cdot r^n \\ +(n+1)\cdot R^{(2n+2)}\cdot r^{-(n+2)} + (n^2-1)\cdot R^2\cdot r^{(n-2)} \\ -(n+2)\cdot(n+1)\cdot r^n - (n+1)\cdot R^{(2n+2)}\cdot r^{-(n+2)} \end{pmatrix}\cdot b_n^{'} \\ + \begin{pmatrix} -(n-1)\cdot R^{-(2n-2)}\cdot r^{(n-2)} - (n^2-1)\cdot R^2\cdot r^{-(n+2)} \\ +(n+2)\cdot(n-1)\cdot r^{-n}(n-1)\cdot R^{-(2n-2)}\cdot r^{(n-2)} \\ +(n^2-1)\cdot R^2\cdot r^{-(n+2)} - (n-2)\cdot(n-1)\cdot r^{-n} \end{pmatrix}\cdot d_n^{'} \end{bmatrix}\cdot\cos(n\theta) \end{bmatrix} \tag{7A.62}$$

$$S = \begin{bmatrix} 4\cdot c_0 + 8\cdot r\cdot\cos\theta\cdot d_1^{'} \\ -\sum_{n=2,3...}^{N} \begin{bmatrix} \left((n-2)\cdot(n+1)\cdot r^n - (n+2)\cdot(n+1)\cdot r^n\right)\cdot b_n^{'} \\ +\left((n+2)\cdot(n-1)\cdot r^{-n} - (n-2)\cdot(n-1)\cdot r^{-n}\right)\cdot d_n^{'} \end{bmatrix}\cdot\cos(n\theta) \end{bmatrix} \tag{7A.63}$$

$$S = \begin{bmatrix} 4\cdot c_0 + 8\cdot r\cdot\cos\theta\cdot d_1^{'} \\ +\sum_{n=2,3...}^{N} \left[\left(4\cdot(n+1)\cdot r^n\right)\cdot b_n^{'} - \left(4\cdot(n-1)\cdot r^{-n}\right)\cdot d_n^{'}\right]\cdot\cos(n\theta) \end{bmatrix} \tag{7A.64}$$

Equation 7A.64 is a simplified form of *equations 7A.42* and *equation 7.14* of Chapter 7 for symmetry about the x-axis. Interestingly *equation 7A.64* (which is summation of σ_{rr} and $\sigma_{\theta\theta}$ after imposing traction-free boundary conditions) came out to be similar to *equation 7.10* for symmetry about the x-axis before imposing the traction-free conditions. Moreover, verifying the equations i.e., when expanding *equations 7A.49, 7A.53, and 7A.57* for n = 2 and 3, one should get *equations 7A.23, 7A.29 and 7A.35*.

Expanding *equation 7A.49* for n = 2 and 3

$$\sigma_{rr} = \left(-\frac{2\cdot R^2}{r^2}+2\right)\cdot c_0 + \left(-\frac{2\cdot R^4}{r^3}+2\cdot r\right)\cdot\cos\theta\cdot d_1^{'} - \sum_{n=2,3\ldots}^{N}\left[\begin{pmatrix}-(n^2-1)\cdot R^2\cdot r^{(n-2)}+(n-2)\cdot(n+1)\cdot r^n\\+(n+1)\cdot R^{(2n+2)}\cdot r^{-(n+2)}\end{pmatrix}\cdot b_n^{'} + \begin{pmatrix}-(n-1)\cdot R^{-(2n-2)}\cdot r^{(n-2)}-(n^2-1)\cdot R^2\cdot r^{-(n+2)}\\+(n+2)\cdot(n-1)\cdot r^{-n}\end{pmatrix}\cdot d_n^{'}\right]\cdot\cos(n\theta) \tag{7A.49}$$

$$\begin{aligned}\sigma_{rr} = {} & \left(-\frac{2\cdot R^2}{r^2}+2\right)\cdot c_0 + \left(-\frac{2\cdot R^4}{r^3}+2\cdot r\right)\cdot\cos\theta\cdot d_1^{'} \\ & -\begin{pmatrix}-(2^2-1)\cdot R^2\cdot r^{(2-2)}+(2-2)\cdot(2+1)\cdot r^2\\+(2+1)\cdot R^{(2*2+2)}\cdot r^{-(2+2)}\end{pmatrix}\cdot\cos(2\theta)\cdot b_2^{'} \\ & -\begin{pmatrix}-(2-1)\cdot R^{-(2*2-2)}\cdot r^{(2-2)}-(2^2-1)\cdot R^2\cdot r^{-(2+2)}\\+(2+2)\cdot(2-1)\cdot r^{-2}\end{pmatrix}\cdot\cos(2\theta)\cdot d_2^{'} \\ & -\begin{pmatrix}-(3^2-1)\cdot R^2\cdot r^{(3-2)}+(3-2)\cdot(3+1)\cdot r^3\\+(3+1)\cdot R^{(2*3+2)}\cdot r^{-(3+2)}\end{pmatrix}\cdot\cos(3\theta)\cdot b_3^{'} \\ & -\begin{pmatrix}-(3-1)\cdot R^{-(2*3-2)}\cdot r^{(3-2)}-(3^2-1)\cdot R^2\cdot r^{-(3+2)}\\+(3+2)\cdot(3-1)\cdot r^{-3}\end{pmatrix}\cdot\cos(3\theta)\cdot d_3^{'} \\ & -\sum_{n=4,5\ldots}^{N}\left[\begin{pmatrix}-(n^2-1)\cdot R^2\cdot r^{(n-2)}+(n-2)\cdot(n+1)\cdot r^n\\+(n+1)\cdot R^{(2n+2)}\cdot r^{-(n+2)}\end{pmatrix}\cdot b_n^{'} + \begin{pmatrix}-(n-1)\cdot R^{-(2n-2)}\cdot r^{(n-2)}-(n^2-1)\cdot R^2\cdot r^{-(n+2)}\\+(n+2)\cdot(n-1)\cdot r^{-n}\end{pmatrix}\cdot d_n^{'}\right]\cdot\cos(n\theta)\end{aligned} \tag{7A.65}$$

$$\begin{aligned}\sigma_{rr} = &\left(-\frac{2\cdot R^2}{r^2}+2\right)\cdot c_0+\left(-\frac{2\cdot R^4}{r^3}+2\cdot r\right)\cdot\cos\theta\cdot d_1^{'}\\ &+\left(3\cdot R^2-3\cdot R^6\cdot r^{-4}\right)\cdot\cos(2\theta)\cdot b_2^{'}+\left(R^{-2}+3\cdot R^2\cdot r^{-4}-4\cdot r^{-2}\right)\cdot\cos(2\theta)\cdot d_2^{'}\\ &+\left(8\cdot R^2\cdot r-4\cdot r^3-4\cdot R^8\cdot r^{-5}\right)\cdot\cos(3\theta)\cdot b_3^{'}\\ &+\left(2\cdot R^{-4}\cdot r+8\cdot R^2\cdot r^{-5}-10\cdot r^{-3}\right)\cdot\cos(3\theta)\cdot d_3^{'}\\ &-\sum_{n=4,5\ldots}^{N}\left[\begin{array}{l}\left(\begin{array}{l}-(n^2-1)\cdot R^2\cdot r^{(n-2)}+(n-2)\cdot(n+1)\cdot r^n\\ +(n+1)\cdot R^{(2n+2)}\cdot r^{-(n+2)}\end{array}\right)\cdot b_n^{'}\\ +\left(\begin{array}{l}-(n-1)\cdot R^{-(2n-2)}\cdot r^{(n-2)}-(n^2-1)\cdot R^2\cdot r^{-(n+2)}\\ +(n+2)\cdot(n-1)\cdot r^{-n}\end{array}\right)\cdot d_n^{'}\end{array}\right]\cdot\cos(n\theta)\end{aligned} \tag{7A.66}$$

Now writing b_3 in terms of c_3 and d_3 from *equation 7A.18*:

$$b_3^{'}=\frac{3\cdot c_3^{'}}{R^8}+\frac{2\cdot d_3^{'}}{R^6}$$

$$\begin{aligned}\sigma_{rr} = &\left(-\frac{2\cdot R^2}{r^2}+2\right)\cdot c_0+\left(-\frac{2\cdot R^4}{r^3}+2\cdot r\right)\cdot\cos\theta\cdot d_1^{'}\\ &+\left(3\cdot R^2-3\cdot R^6\cdot r^{-4}\right)\cdot\cos(2\theta)\cdot b_2^{'}+\left(R^{-2}+3\cdot R^2\cdot r^{-4}-4\cdot r^{-2}\right)\cdot\cos(2\theta)\cdot d_2^{'}\\ &+\left(8\cdot R^2\cdot r-4\cdot r^3-4\cdot R^8\cdot r^{-5}\right)\cdot\cos(3\theta)\cdot\left(\frac{3\cdot c_3^{'}}{R^8}+\frac{2\cdot d_3^{'}}{R^6}\right)\\ &+\left(2\cdot R^{-4}\cdot r+8\cdot R^2\cdot r^{-5}-10\cdot r^{-3}\right)\cdot\cos(3\theta)\cdot d_3^{'}\\ &-\sum_{n=4,5\ldots}^{N}\left[\begin{array}{l}\left(\begin{array}{l}-(n^2-1)\cdot R^2\cdot r^{(n-2)}+(n-2)\cdot(n+1)\cdot r^n\\ +(n+1)\cdot R^{(2n+2)}\cdot r^{-(n+2)}\end{array}\right)\cdot b_n^{'}\\ +\left(\begin{array}{l}-(n-1)\cdot R^{-(2n-2)}\cdot r^{(n-2)}-(n^2-1)\cdot R^2\cdot r^{-(n+2)}\\ +(n+2)\cdot(n-1)\cdot r^{-n}\end{array}\right)\cdot d_n^{'}\end{array}\right]\cdot\cos(n\theta)\end{aligned} \tag{7A.67}$$

$$
\begin{aligned}
\sigma_{rr} = & \left(-\frac{2\cdot R^2}{r^2}+2\right)\cdot c_0+\left(-\frac{2\cdot R^4}{r^3}+2\cdot r\right)\cdot\cos\theta\cdot d_1^{'} \\
& +\left(3\cdot R^2-3\cdot R^6\cdot r^{-4}\right)\cdot\cos(2\theta)\cdot b_2^{'}+\left(R^{-2}+3\cdot R^2\cdot r^{-4}-4\cdot r^{-2}\right)\cdot\cos(2\theta)\cdot d_2^{'} \\
& +\left(8\cdot R^2\cdot r-4\cdot r^3-4\cdot R^8\cdot r^{-5}\right)\cdot\cos(3\theta)\cdot\frac{3\cdot c_3^{'}}{R^8} \\
& +\left(8\cdot R^2\cdot r-4\cdot r^3-4\cdot R^8\cdot r^{-5}\right)\cdot\cos(3\theta)\cdot\frac{2\cdot d_3^{'}}{R^6} \\
& +\left(2\cdot R^{-4}\cdot r+8\cdot R^2\cdot r^{-5}-10\cdot r^{-3}\right)\cdot\cos(3\theta)\cdot d_3^{'} \\
& -\sum_{n=4,5\ldots}^{N}\left[\begin{array}{l}\left(\begin{array}{l}-(n^2-1)\cdot R^2\cdot r^{(n-2)}+(n-2)\cdot(n+1)\cdot r^n\\+(n+1)\cdot R^{(2n+2)}\cdot r^{-(n+2)}\end{array}\right)\cdot b_n^{'}\\+\left(\begin{array}{l}-(n-1)\cdot R^{-(2n-2)}\cdot r^{(n-2)}-(n^2-1)\cdot R^2\cdot r^{-(n+2)}\\+(n+2)\cdot(n-1)\cdot r^{-n}\end{array}\right)\cdot d_n^{'}\end{array}\right]\cdot\cos(n\theta)
\end{aligned}
\tag{7A.68}
$$

$$
\begin{aligned}
\sigma_{rr} = & \left(-\frac{2\cdot R^2}{r^2}+2\right)\cdot c_0+\left(-\frac{2\cdot R^4}{r^3}+2\cdot r\right)\cdot\cos\theta\cdot d_1^{'} \\
& +\left(3\cdot R^2-3\cdot R^6\cdot r^{-4}\right)\cdot\cos(2\theta)\cdot b_2^{'}+\left(R^{-2}+3\cdot R^2\cdot r^{-4}-4\cdot r^{-2}\right)\cdot\cos(2\theta)\cdot d_2^{'} \\
& +\left(\frac{24\cdot r}{R^6}-\frac{12\cdot r^3}{R^8}-12\cdot r^{-5}\right)\cdot\cos(3\theta)\cdot c_3^{'} \\
& +\left(\frac{16\cdot r}{R^4}-\frac{8\cdot r^3}{R^6}-8\cdot R^2\cdot r^{-5}\right)\cdot\cos(3\theta)\cdot d_3^{'} \\
& +\left(2\cdot R^{-4}\cdot r+8\cdot R^2\cdot r^{-5}-10\cdot r^{-3}\right)\cdot\cos(3\theta)\cdot d_3^{'} \\
& -\sum_{n=4,5\ldots}^{N}\left[\begin{array}{l}\left(\begin{array}{l}-(n^2-1)\cdot R^2\cdot r^{(n-2)}+(n-2)\cdot(n+1)\cdot r^n\\+(n+1)\cdot R^{(2n+2)}\cdot r^{-(n+2)}\end{array}\right)\cdot b_n^{'}\\+\left(\begin{array}{l}-(n-1)\cdot R^{-(2n-2)}\cdot r^{(n-2)}-(n^2-1)\cdot R^2\cdot r^{-(n+2)}\\+(n+2)\cdot(n-1)\cdot r^{-n}\end{array}\right)\cdot d_n^{'}\end{array}\right]\cdot\cos(n\theta)
\end{aligned}
\tag{7A.69}
$$

$$\begin{aligned}\sigma_{rr} = &\left(-\frac{2\cdot R^2}{r^2}+2\right)\cdot c_0+\left(-\frac{2\cdot R^4}{r^3}+2\cdot r\right)\cdot\cos\theta\cdot d_1^{'}\\ &+\left(3\cdot R^2-3\cdot R^6\cdot r^{-4}\right)\cdot\cos(2\theta)\cdot b_2^{'}+\left(R^{-2}+3\cdot R^2\cdot r^{-4}-4\cdot r^{-2}\right)\cdot\cos(2\theta)\cdot d_2^{'}\\ &+\left(\frac{24\cdot r}{R^6}-\frac{12\cdot r^3}{R^8}-12\cdot r^{-5}\right)\cdot\cos(3\theta)\cdot c_3^{'}\\ &+\left(\frac{18\cdot r}{R^4}-\frac{8\cdot r^3}{R^6}-10\cdot r^{-3}\right)\cdot\cos(3\theta)\cdot d_3^{'}\\ &-\sum_{n=4,5\ldots}^{N}\left[\begin{array}{l}\left(\begin{array}{l}-(n^2-1)\cdot R^2\cdot r^{(n-2)}+(n-2)\cdot(n+1)\cdot r^n\\ +(n+1)\cdot R^{(2n+2)}\cdot r^{-(n+2)}\end{array}\right)\cdot b_n^{'}\\ +\left(\begin{array}{l}-(n-1)\cdot R^{-(2n-2)}\cdot r^{(n-2)}-(n^2-1)\cdot R^2\cdot r^{-(n+2)}\\ +(n+2)\cdot(n-1)\cdot r^{-n}\end{array}\right)\cdot d_n^{'}\end{array}\right]\cdot\cos(n\theta)\end{aligned} \tag{7A.70}$$

Equation 7A.70 agrees with *equation 7A.23* so *equation 7A.49* is equivalent to *equation 7A.23*.

Expanding *equation 7A.53* for n = 2 and 3

$$\sigma_{\theta\theta} = \left(\frac{2\cdot R^2}{r^2} + 2\right)\cdot c_0 + \left(\frac{2\cdot R^4}{r^3} + 6\cdot r\right)\cdot \cos\theta \cdot d_1^{'} + \sum_{n=2,3\ldots}^{N}\left[\begin{pmatrix} -(n^2-1)\cdot R^2\cdot r^{(n-2)} + (n+2)\cdot(n+1)\cdot r^n \\ +(n+1)\cdot R^{(2n+2)}\cdot r^{-(n+2)} \end{pmatrix}\cdot b_n^{'} + \begin{pmatrix} -(n-1)\cdot R^{-(2n-2)}\cdot r^{(n-2)} - (n^2-1)\cdot R^2\cdot r^{-(n+2)} \\ +(n-2)\cdot(n-1)\cdot r^{-n} \end{pmatrix}\cdot d_n^{'}\right]\cdot\cos(n\theta) \tag{7A.53}$$

$$\begin{aligned}\sigma_{\theta\theta} = {} & \left(\frac{2\cdot R^2}{r^2} + 2\right)\cdot c_0 + \left(\frac{2\cdot R^4}{r^3} + 6\cdot r\right)\cdot \cos\theta \cdot d_1^{'} \\ & + \begin{pmatrix} -(2^2-1)\cdot R^2\cdot r^{(2-2)} + (2+2)\cdot(2+1)\cdot r^2 \\ +(2+1)\cdot R^{(2*2+2)}\cdot r^{-(2+2)} \end{pmatrix}\cdot\cos(2\theta)\cdot b_2^{'} \\ & + \begin{pmatrix} -(2-1)\cdot R^{-(2*2-2)}\cdot r^{(2-2)} - (2^2-1)\cdot R^2\cdot r^{-(2+2)} \\ +(2-2)\cdot(2-1)\cdot r^{-2} \end{pmatrix}\cdot\cos(2\theta)\cdot d_2^{'} \\ & + \begin{pmatrix} -(3^2-1)\cdot R^2\cdot r^{(3-2)} + (3+2)\cdot(3+1)\cdot r^3 \\ +(3+1)\cdot R^{(2*3+2)}\cdot r^{-(3+2)} \end{pmatrix}\cdot\cos(3\theta)\cdot b_3^{'} \\ & + \begin{pmatrix} -(3-1)\cdot R^{-(2*3-2)}\cdot r^{(3-2)} - (3^2-1)\cdot R^2\cdot r^{-(3+2)} \\ +(3-2)\cdot(3-1)\cdot r^{-3} \end{pmatrix}\cdot\cos(3\theta)\cdot d_3^{'} \\ & + \sum_{n=4,5\ldots}^{N}\left[\begin{pmatrix} -(n^2-1)\cdot R^2\cdot r^{(n-2)} + (n+2)\cdot(n+1)\cdot r^n \\ +(n+1)\cdot R^{(2n+2)}\cdot r^{-(n+2)} \end{pmatrix}\cdot b_n^{'} + \begin{pmatrix} -(n-1)\cdot R^{-(2n-2)}\cdot r^{(n-2)} - (n^2-1)\cdot R^2\cdot r^{-(n+2)} \\ +(n-2)\cdot(n-1)\cdot r^{-n} \end{pmatrix}\cdot d_n^{'}\right]\cdot\cos(n\theta)\end{aligned} \tag{7A.71}$$

$$\begin{aligned}\sigma_{\theta\theta} = &\left(\frac{2\cdot R^2}{r^2}+2\right)\cdot c_0+\left(\frac{2\cdot R^4}{r^3}+6\cdot r\right)\cdot\cos\theta\cdot d_1^{'}\\ &+\left(-3\cdot R^2\cdot r+12\cdot r^2+3\cdot R^6\cdot r^{-4}\right)\cdot\cos(2\theta)\cdot b_2^{'}\\ &+\left(-R^{-2}-3\cdot R^2\cdot r^{-4}\right)\cdot\cos(2\theta)\cdot d_2^{'}\\ &+\left(-8\cdot R^2\cdot r+20\cdot r^3+4\cdot R^8\cdot r^{-5}\right)\cdot\cos(3\theta)\cdot b_3^{'}\\ &+\left(-2\cdot R^{-4}\cdot r-8\cdot R^2\cdot r^{-5}+2\cdot r^{-3}\right)\cdot\cos(3\theta)\cdot d_3^{'}\\ &+\sum_{n=4,5\ldots}^{N}\left[\begin{array}{l}\left(\begin{array}{l}-(n^2-1)\cdot R^2\cdot r^{(n-2)}+(n+2)\cdot(n+1)\cdot r^n\\ +(n+1)\cdot R^{(2n+2)}\cdot r^{-(n+2)}\end{array}\right)\cdot b_n^{'}\\ +\left(\begin{array}{l}-(n-1)\cdot R^{-(2n-2)}\cdot r^{(n-2)}-(n^2-1)\cdot R^2\cdot r^{-(n+2)}\\ +(n-2)\cdot(n-1)\cdot r^{-n}\end{array}\right)\cdot d_n^{'}\end{array}\right]\cdot\cos(n\theta)\end{aligned} \tag{7A.72}$$

Now writing b_3 in terms of c_3 and d_3 from *equation 7A.18*:

$$b_3 = \frac{3\cdot c_3}{R^8}+\frac{2\cdot d_3}{R^6}$$

$$\begin{aligned}\sigma_{\theta\theta} = &\left(\frac{2\cdot R^2}{r^2}+2\right)\cdot c_0+\left(\frac{2\cdot R^4}{r^3}+6\cdot r\right)\cdot\cos\theta\cdot d_1^{'}\\ &+\left(-3\cdot R^2\cdot r+12\cdot r^2+3\cdot R^6\cdot r^{-4}\right)\cdot\cos(2\theta)\cdot b_2^{'}\\ &+\left(-R^{-2}-3\cdot R^2\cdot r^{-4}\right)\cdot\cos(2\theta)\cdot d_2^{'}\\ &+\left(-8\cdot R^2\cdot r+20\cdot r^3+4\cdot R^8\cdot r^{-5}\right)\cdot\cos(3\theta)\cdot\left(\frac{3\cdot c_3^{'}}{R^8}+\frac{2\cdot d_3^{'}}{R^6}\right)\\ &+\left(-2\cdot R^{-4}\cdot r-8\cdot R^2\cdot r^{-5}+2\cdot r^{-3}\right)\cdot\cos(3\theta)\cdot d_3^{'}\\ &+\sum_{n=4,5\ldots}^{N}\left[\begin{array}{l}\left(\begin{array}{l}-(n^2-1)\cdot R^2\cdot r^{(n-2)}+(n+2)\cdot(n+1)\cdot r^n\\ +(n+1)\cdot R^{(2n+2)}\cdot r^{-(n+2)}\end{array}\right)\cdot b_n^{'}\\ +\left(\begin{array}{l}-(n-1)\cdot R^{-(2n-2)}\cdot r^{(n-2)}-(n^2-1)\cdot R^2\cdot r^{-(n+2)}\\ +(n-2)\cdot(n-1)\cdot r^{-n}\end{array}\right)\cdot d_n^{'}\end{array}\right]\cdot\cos(n\theta)\end{aligned} \tag{7A.73}$$

$$\begin{aligned}\sigma_{\theta\theta} = &\left(\frac{2\cdot R^2}{r^2}+2\right)\cdot c_0+\left(\frac{2\cdot R^4}{r^3}+6\cdot r\right)\cdot\cos\theta\cdot d_1^{'}\\ &+\left(-3\cdot R^2\cdot r+12\cdot r^2+3\cdot R^6\cdot r^{-4}\right)\cdot\cos(2\theta)\cdot b_2^{'}\\ &+\left(-R^{-2}-3\cdot R^2\cdot r^{-4}\right)\cdot\cos(2\theta)\cdot d_2^{'}\\ &+\left(-8\cdot R^2\cdot r+20\cdot r^3+4\cdot R^8\cdot r^{-5}\right)\cdot\cos(3\theta)\cdot\frac{3\cdot c_3^{'}}{R^8}\\ &+\left(-8\cdot R^2\cdot r+20\cdot r^3+4\cdot R^8\cdot r^{-5}\right)\cdot\cos(3\theta)\cdot\frac{2\cdot d_3^{'}}{R^6}\\ &+\left(-2\cdot R^{-4}\cdot r-8\cdot R^2\cdot r^{-5}+2\cdot r^{-3}\right)\cdot\cos(3\theta)\cdot d_3^{'}\\ &+\sum_{n=4,5\ldots}^{N}\left[\begin{array}{l}\left(\begin{array}{l}-(n^2-1)\cdot R^2\cdot r^{(n-2)}+(n+2)\cdot(n+1)\cdot r^n\\ +(n+1)\cdot R^{(2n+2)}\cdot r^{-(n+2)}\end{array}\right)\cdot b_n^{'}\\ +\left(\begin{array}{l}-(n-1)\cdot R^{-(2n-2)}\cdot r^{(n-2)}-(n^2-1)\cdot R^2\cdot r^{-(n+2)}\\ +(n-2)\cdot(n-1)\cdot r^{-n}\end{array}\right)\cdot d_n^{'}\end{array}\right]\cdot\cos(n\theta)\end{aligned} \tag{7A.74}$$

$$\begin{aligned}\sigma_{\theta\theta} = &\left(\frac{2\cdot R^2}{r^2}+2\right)\cdot c_0+\left(\frac{2\cdot R^4}{r^3}+6\cdot r\right)\cdot\cos\theta\cdot d_1^{'}\\ &+\left(-3\cdot R^2\cdot r+12\cdot r^2+3\cdot R^6\cdot r^{-4}\right)\cdot\cos(2\theta)\cdot b_2^{'}\\ &+\left(-R^{-2}-3\cdot R^2\cdot r^{-4}\right)\cdot\cos(2\theta)\cdot d_2^{'}\\ &+\left(-\frac{24\cdot r}{R^6}+\frac{60\cdot r^3}{R^8}+12\cdot r^{-5}\right)\cdot\cos(3\theta)\cdot c_3^{'}\\ &+\left(-\frac{16\cdot r}{R^4}+\frac{40\cdot r^3}{R^6}+8\cdot R^2\cdot r^{-5}\right)\cdot\cos(3\theta)\cdot d_3^{'}\\ &+\left(-2\cdot R^{-4}\cdot r-8\cdot R^2\cdot r^{-5}+2\cdot r^{-3}\right)\cdot\cos(3\theta)\cdot d_3^{'}\\ &+\sum_{n=4,5\ldots}^{N}\left[\begin{array}{l}\left(\begin{array}{l}-(n^2-1)\cdot R^2\cdot r^{(n-2)}+(n+2)\cdot(n+1)\cdot r^n\\ +(n+1)\cdot R^{(2n+2)}\cdot r^{-(n+2)}\end{array}\right)\cdot b_n^{'}\\ +\left(\begin{array}{l}-(n-1)\cdot R^{-(2n-2)}\cdot r^{(n-2)}-(n^2-1)\cdot R^2\cdot r^{-(n+2)}\\ +(n-2)\cdot(n-1)\cdot r^{-n}\end{array}\right)\cdot d_n^{'}\end{array}\right]\cdot\cos(n\theta)\end{aligned} \tag{7A.75}$$

$$
\begin{aligned}
\sigma_{\theta\theta} = & \left(\frac{2\cdot R^2}{r^2}+2\right)\cdot c_0 + \left(\frac{2\cdot R^4}{r^3}+6\cdot r\right)\cdot\cos\theta\cdot d_1^{'} \\
& + \left(-3\cdot R^2\cdot r + 12\cdot r^2 + 3\cdot R^6\cdot r^{-4}\right)\cdot\cos(2\theta)\cdot b_2^{'} \\
& + \left(-R^{-2} - 3\cdot R^2\cdot r^{-4}\right)\cdot\cos(2\theta)\cdot d_2^{'} \\
& + \left(-\frac{24\cdot r}{R^6}+\frac{60\cdot r^3}{R^8}+12\cdot r^{-5}\right)\cdot\cos(3\theta)\cdot c_3^{'} \\
& + \left(-\frac{18\cdot r}{R^4}+\frac{40\cdot r^3}{R^6}+2\cdot r^{-3}\right)\cdot\cos(3\theta)\cdot d_3^{'} \\
& + \sum_{n=4,5\ldots}^{N}\left[\begin{array}{l}\left(\begin{array}{l}-(n^2-1)\cdot R^2\cdot r^{(n-2)} + (n+2)\cdot(n+1)\cdot r^n \\ +(n+1)\cdot R^{(2n+2)}\cdot r^{-(n+2)}\end{array}\right)\cdot b_n^{'} \\ +\left(\begin{array}{l}-(n-1)\cdot R^{-(2n-2)}\cdot r^{(n-2)} - (n^2-1)\cdot R^2\cdot r^{-(n+2)} \\ +(n-2)\cdot(n-1)\cdot r^{-n}\end{array}\right)\cdot d_n^{'}\end{array}\right]\cdot\cos(n\theta)
\end{aligned}
\tag{7A.76}
$$

Equation 7A.76 agrees with *equation 7A.29* so *equations 7A.53 and 7A.29* are equivalent.

Expanding *equation 7A.57* for n = 2 and 3

$$\sigma_{r\theta} = \left(-\frac{2\cdot R^4}{r^3} + 2\cdot r\right)\cdot \sin\theta \cdot d_1^{'} + \sum_{n=2,3\ldots}^{N}\left[\begin{array}{l}\left(-(n^2-1)\cdot R^2\cdot r^{(n-2)} + n\cdot(n+1)\cdot r^n - (n+1)\cdot R^{(2n+2)}\cdot r^{-(n+2)}\right)\cdot b_n^{'} \\ +\left(-(n-1)\cdot R^{-(2n-2)}\cdot r^{(n-2)} + (n^2-1)\cdot R^2\cdot r^{-(n+2)} - n\cdot(n-1)\cdot r^{-n}\right)\cdot d_n^{'}\end{array}\right]\cdot \sin(n\theta) \tag{7A.57}$$

$$\begin{aligned}\sigma_{r\theta} = &\left(-\frac{2\cdot R^4}{r^3} + 2\cdot r\right)\cdot \sin\theta \cdot d_1^{'} \\ &+\left(-(2^2-1)\cdot R^2\cdot r^{(2-2)} + 2\cdot(2+1)\cdot r^2 - (2+1)\cdot R^{(2*2+2)}\cdot r^{-(2+2)}\right)\cdot \sin(2\theta)\cdot b_2^{'} \\ &+\left(-(2-1)\cdot R^{-(2*2-2)}\cdot r^{(2-2)} + (2^2-1)\cdot R^2\cdot r^{-(2+2)} - 2\cdot(2-1)\cdot r^{-2}\right)\cdot \sin(2\theta)\cdot d_2^{'} \\ &+\left(-(3^2-1)\cdot R^2\cdot r^{(3-2)} + 3\cdot(3+1)\cdot r^3 - (3+1)\cdot R^{(2*3+2)}\cdot r^{-(3+2)}\right)\cdot \sin(3\theta)\cdot b_3^{'} \\ &+\left(-(3-1)\cdot R^{-(2*3-2)}\cdot r^{(3-2)} + (3^2-1)\cdot R^2\cdot r^{-(3+2)} - 3\cdot(3-1)\cdot r^{-3}\right)\cdot \sin(3\theta)\cdot d_3^{'} \\ &+\sum_{n=4,5\ldots}^{N}\left[\begin{array}{l}\left(-(n^2-1)\cdot R^2\cdot r^{(n-2)} + n\cdot(n+1)\cdot r^n - (n+1)\cdot R^{(2n+2)}\cdot r^{-(n+2)}\right)\cdot b_n^{'} \\ +\left(-(n-1)\cdot R^{-(2n-2)}\cdot r^{(n-2)} + (n^2-1)\cdot R^2\cdot r^{-(n+2)} - n\cdot(n-1)\cdot r^{-n}\right)\cdot d_n^{'}\end{array}\right]\cdot \sin(n\theta)\end{aligned} \tag{7A.77}$$

$$\begin{aligned}\sigma_{r\theta} = &\left(-\frac{2\cdot R^4}{r^3} + 2\cdot r\right)\cdot \sin\theta \cdot d_1^{'} \\ &+\left(-3\cdot R^2 + 6\cdot r^2 - 3\cdot R^6\cdot r^{-4}\right)\cdot \sin(2\theta)\cdot b_2^{'} + \left(-R^{-2} + 3\cdot R^2\cdot r^{-4} - 2\cdot r^{-2}\right)\cdot \sin(2\theta)\cdot d_2^{'} \\ &+\left(-8\cdot R^2\cdot r + 12\cdot r^3 - 4\cdot R^8\cdot r^{-5}\right)\cdot \sin(3\theta)\cdot b_3^{'} + \left(-2\cdot R^{-4}\cdot r + 8\cdot R^2\cdot r^{-5} - 6\cdot r^{-3}\right)\cdot \sin(3\theta)\cdot d_3^{'} \\ &+\sum_{n=4,5\ldots}^{N}\left[\begin{array}{l}\left(-(n^2-1)\cdot R^2\cdot r^{(n-2)} + n\cdot(n+1)\cdot r^n - (n+1)\cdot R^{(2n+2)}\cdot r^{-(n+2)}\right)\cdot b_n^{'} \\ +\left(-(n-1)\cdot R^{-(2n-2)}\cdot r^{(n-2)} + (n^2-1)\cdot R^2\cdot r^{-(n+2)} - n\cdot(n-1)\cdot r^{-n}\right)\cdot d_n^{'}\end{array}\right]\cdot \sin(n\theta)\end{aligned} \tag{7A.78}$$

Now writing b_3 in terms of c_3 and d_3 from *equation 7A.18*:

$$b_3^{'} = \frac{3\cdot c_3^{'}}{R^8} + \frac{2\cdot d_3^{'}}{R^6}$$

$$\begin{aligned}\sigma_{r\theta} = &\left(-\frac{2\cdot R^4}{r^3}+2\cdot r\right)\cdot\sin\theta\cdot d_1^{'}\\ &+\left(-3\cdot R^2+6\cdot r^2-3\cdot R^6\cdot r^{-4}\right)\cdot\sin(2\theta)\cdot b_2^{'}+\left(-R^{-2}+3\cdot R^2\cdot r^{-4}-2\cdot r^{-2}\right)\cdot\sin(2\theta)\cdot d_2^{'}\\ &+\left(-8\cdot R^2\cdot r+12\cdot r^3-4\cdot R^8\cdot r^{-5}\right)\cdot\sin(3\theta)\cdot\left(\frac{3\cdot c_3^{'}}{R^8}+\frac{2\cdot d_3^{'}}{R^6}\right)\\ &+\left(-2\cdot R^{-4}\cdot r+8\cdot R^2\cdot r^{-5}-6\cdot r^{-3}\right)\cdot\sin(3\theta)\cdot d_3^{'}\\ &+\sum_{n=4,5\ldots}^{N}\left[\begin{matrix}\left(-(n^2-1)\cdot R^2\cdot r^{(n-2)}+n\cdot(n+1)\cdot r^n-(n+1)\cdot R^{(2n+2)}\cdot r^{-(n+2)}\right)\cdot b_n^{'}\\ +\left(-(n-1)\cdot R^{-(2n-2)}\cdot r^{(n-2)}+(n^2-1)\cdot R^2\cdot r^{-(n+2)}-n\cdot(n-1)\cdot r^{-n}\right)\cdot d_n^{'}\end{matrix}\right]\cdot\sin(n\theta)\end{aligned} \tag{7A.79}$$

$$\begin{aligned}\sigma_{r\theta} = &\left(-\frac{2\cdot R^4}{r^3}+2\cdot r\right)\cdot\sin\theta\cdot d_1^{'}\\ &+\left(-3\cdot R^2+6\cdot r^2-3\cdot R^6\cdot r^{-4}\right)\cdot\sin(2\theta)\cdot b_2^{'}+\left(-R^{-2}+3\cdot R^2\cdot r^{-4}-2\cdot r^{-2}\right)\cdot\sin(2\theta)\cdot d_2^{'}\\ &+\left(-8\cdot R^2\cdot r+12\cdot r^3-4\cdot R^8\cdot r^{-5}\right)\cdot\sin(3\theta)\cdot\frac{3\cdot c_3^{'}}{R^8}\\ &+\left(-8\cdot R^2\cdot r+12\cdot r^3-4\cdot R^8\cdot r^{-5}\right)\cdot\sin(3\theta)\cdot\frac{2\cdot d_3^{'}}{R^6}\\ &+\left(-2\cdot R^{-4}\cdot r+8\cdot R^2\cdot r^{-5}-6\cdot r^{-3}\right)\cdot\sin(3\theta)\cdot d_3^{'}\\ &+\sum_{n=4,5\ldots}^{N}\left[\begin{matrix}\left(-(n^2-1)\cdot R^2\cdot r^{(n-2)}+n\cdot(n+1)\cdot r^n-(n+1)\cdot R^{(2n+2)}\cdot r^{-(n+2)}\right)\cdot b_n^{'}\\ +\left(-(n-1)\cdot R^{-(2n-2)}\cdot r^{(n-2)}+(n^2-1)\cdot R^2\cdot r^{-(n+2)}-n\cdot(n-1)\cdot r^{-n}\right)\cdot d_n^{'}\end{matrix}\right]\cdot\sin(n\theta)\end{aligned} \tag{7A.80}$$

$$\begin{aligned}\sigma_{r\theta} = &\left(-\frac{2\cdot R^4}{r^3}+2\cdot r\right)\cdot\sin\theta\cdot d_1^{'}\\ &+\left(-3\cdot R^2+6\cdot r^2-3\cdot R^6\cdot r^{-4}\right)\cdot\sin(2\theta)\cdot b_2^{'}+\left(-R^{-2}+3\cdot R^2\cdot r^{-4}-2\cdot r^{-2}\right)\cdot\sin(2\theta)\cdot d_2^{'}\\ &+\left(-\frac{24\cdot r}{R^6}+\frac{36\cdot r^3}{R^8}-12\cdot r^{-5}\right)\cdot\sin(3\theta)\cdot c_3^{'}\\ &+\left(-\frac{16\cdot r}{R^4}+\frac{24\cdot r^3}{R^6}-8\cdot R^2\cdot r^{-5}\right)\cdot\sin(3\theta)\cdot d_3^{'}\\ &+\left(-2\cdot R^{-4}\cdot r+8\cdot R^2\cdot r^{-5}-6\cdot r^{-3}\right)\cdot\sin(3\theta)\cdot d_3^{'}\\ &+\sum_{n=4,5\ldots}^{N}\left[\begin{matrix}\left(-(n^2-1)\cdot R^2\cdot r^{(n-2)}+n\cdot(n+1)\cdot r^n-(n+1)\cdot R^{(2n+2)}\cdot r^{-(n+2)}\right)\cdot b_n^{'}\\ +\left(-(n-1)\cdot R^{-(2n-2)}\cdot r^{(n-2)}+(n^2-1)\cdot R^2\cdot r^{-(n+2)}-n\cdot(n-1)\cdot r^{-n}\right)\cdot d_n^{'}\end{matrix}\right]\cdot\sin(n\theta)\end{aligned} \tag{7A.81}$$

$$\sigma_{r\theta} = \left(-\frac{2\cdot R^4}{r^3} + 2\cdot r\right)\cdot \sin\theta \cdot d_1^{'}$$
$$+\left(-3\cdot R^2 + 6\cdot r^2 - 3\cdot R^6\cdot r^{-4}\right)\cdot \sin(2\theta)\cdot b_2^{'} + \left(-R^{-2} + 3\cdot R^2\cdot r^{-4} - 2\cdot r^{-2}\right)\cdot \sin(2\theta)\cdot d_2^{'}$$
$$+\left(-\frac{24\cdot r}{R^6} + \frac{36\cdot r^3}{R^8} - 12\cdot r^{-5}\right)\cdot \sin(3\theta)\cdot c_3^{'}$$
$$+\left(-\frac{18\cdot r}{R^4} + \frac{24\cdot r^3}{R^6} - 6\cdot r^{-3}\right)\cdot \sin(3\theta)\cdot d_3^{'}$$
$$+\sum_{n=4,5\ldots}^{N}\left[\begin{array}{l}\left(-(n^2-1)\cdot R^2\cdot r^{(n-2)} + n\cdot(n+1)\cdot r^n - (n+1)\cdot R^{(2n+2)}\cdot r^{-(n+2)}\right)\cdot b_n^{'} \\ +\left(-(n-1)\cdot R^{-(2n-2)}\cdot r^{(n-2)} + (n^2-1)\cdot R^2\cdot r^{-(n+2)} - n\cdot(n-1)\cdot r^{-n}\right)\cdot d_n^{'}\end{array}\right]\cdot \sin(n\theta) \tag{7A.82}$$

Equation 7A.82 agrees with *equation 7A.35*. So *equations 7A.57 and 7A.35* are equivalent.

Note the *equations 7.11 through 7.14* in Chapter 7 for the symmetrical case of *figure 7.1* can be reduced to *equations 7A.23, 7A.29, 7A.35 and 7A.42* by substituting *equation 7A.14* in *equations 7.11 through 7.14*.

Equation sets of *7A.23, 7A.29 and 7A.35 or 7A.49, 7A.53 and 7A.57 or 7.11 through 7.13* of Chapter 7 represent the components of stress at and near the hole of radius r = R for the finite plate of *figure 7.1.* Note that these expressions do not explicitly contain the load, P, or the plate geometrics (dimensions). Rather the effect (magnitude) of the loading will be contained indirectly in the experimentally determined values of the Airy coefficients. These equations are applicable irrespective of the external shape and loading as long as having mechanical and geometric symmetry about the x-axis and have a circular traction-free hole.

A8 Check against the Assumption of Plane Stress using 3-D FEA

The 3-D finite element analysis is conducted in ANSYS for plate of *figure 8.1*. The FE model used 3-D 20-node structural solid elements (ANSYS element type: SOLID95). A fine mesh was used in the neighborhood of the holes *figure A8.1*. For the analysis of the symmetrically-loaded plate, a total of 12,962 elements and 23,251 nodes covers the entire one half of the plate. Since the plate of *figure 8.1* is symmetrical about the x-axis, a symmetry boundary condition along the area of symmetry and a uniform far-field stress of 9.19 MPa (1333.33 psi) is applied, *figures A8.1*. *Figures A8.2 through A8.9* are ANSYS generated contour plots of σ_{xx}, σ_{yy}, σ_{zz}, σ_{rr}, $\sigma_{\theta\theta}$, $\sigma_{r\theta}$, σ_{rz} and $\sigma_{\theta z}$ respectively through the plate thickness and all the units for these plots are in psi. The small changes of the stress through the thickness validate the assumed plane stress condition.

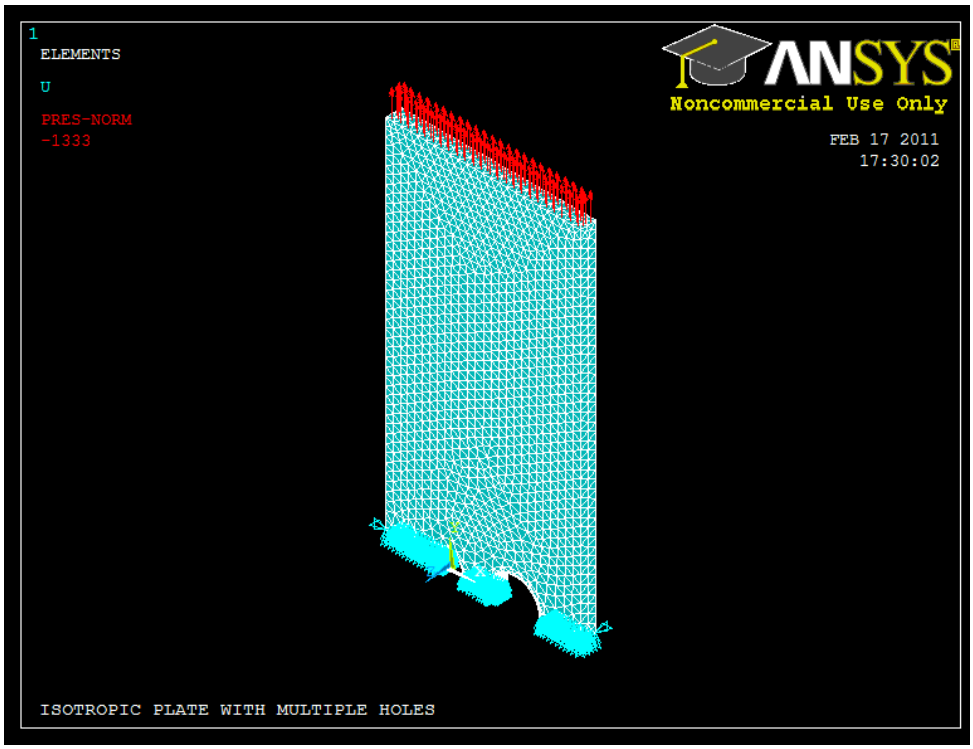

Fig. A8.1: 3-D Finite element model for the symmetrically-loaded plate, *figure 8.1*

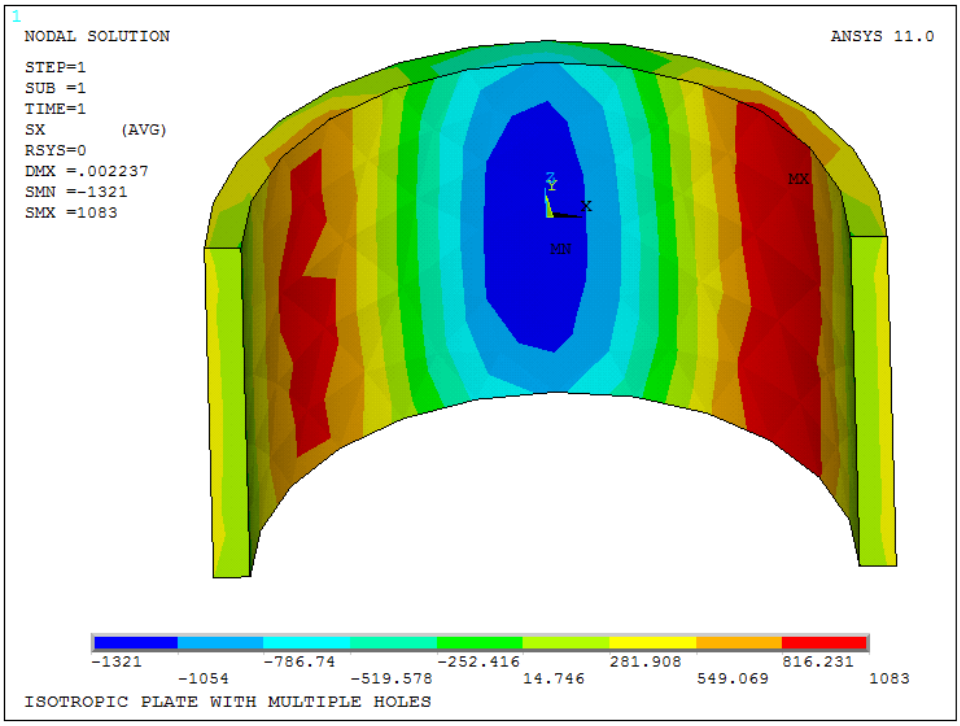

Fig. A8.2: 3-D contour plots of σ_{xx} (psi) through the plate thickness

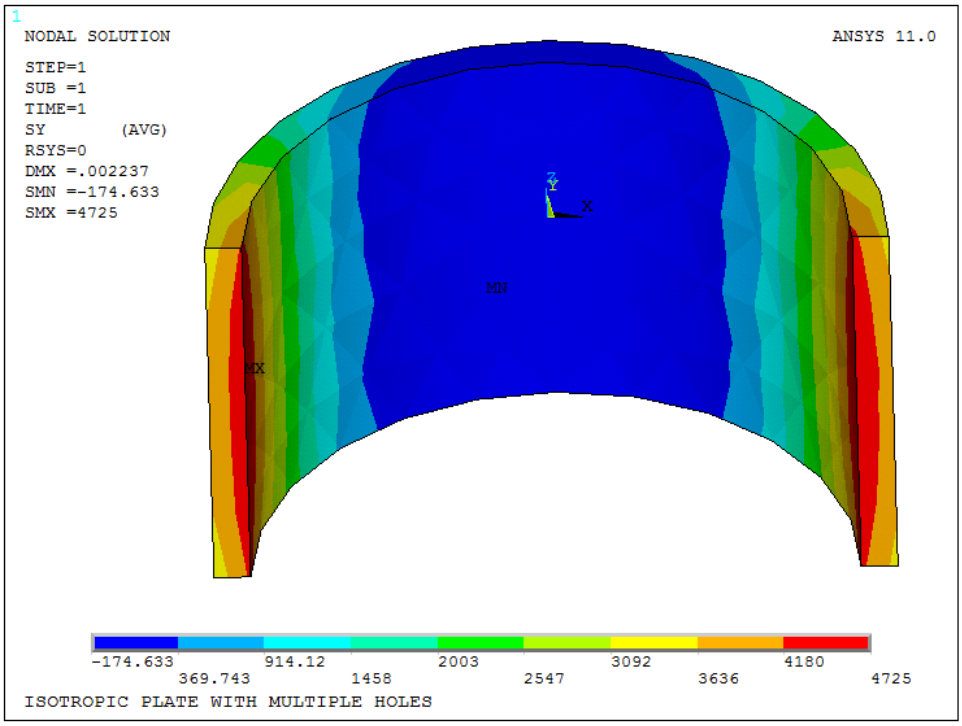

Fig. A8.3: 3-D contour plots of σ_{yy} (psi) through the plate thickness

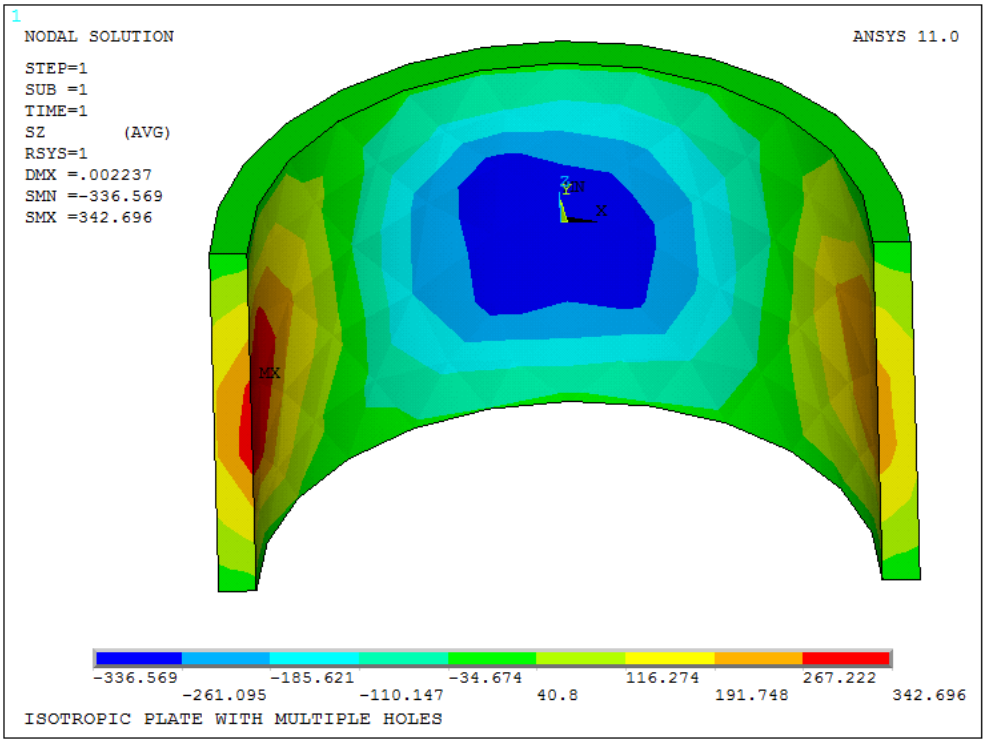

Fig. A8.4: 3-D contour plots of σ_{zz}/σ_0 through the plate thickness

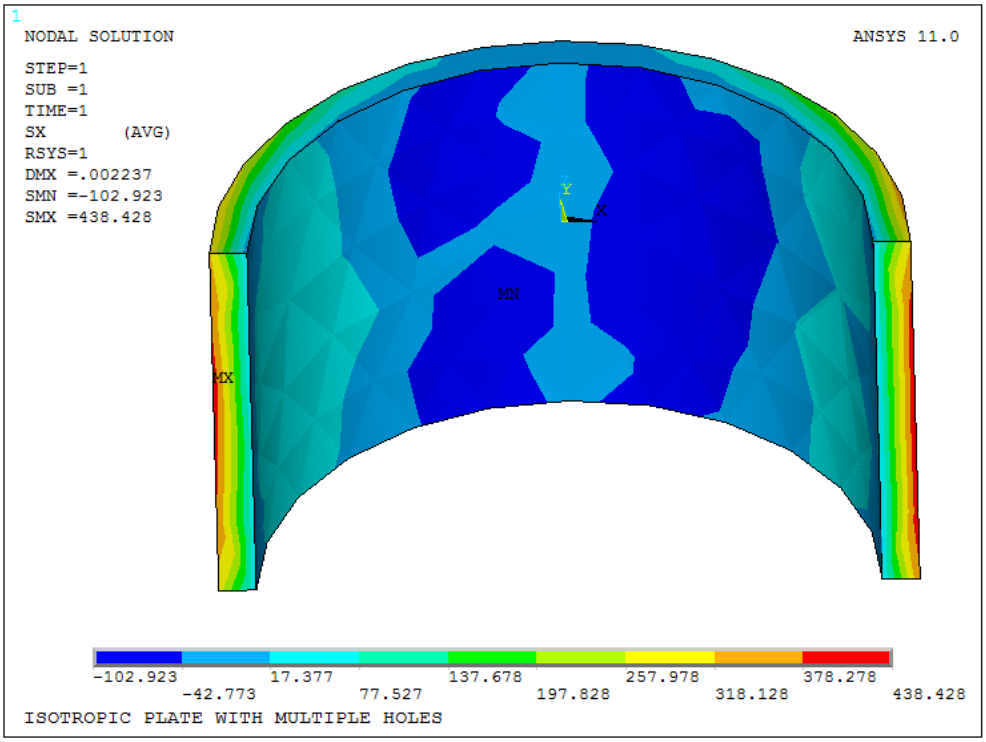

Fig. A8.5: 3-D contour plots of σ_{rr} (psi) through the plate thickness

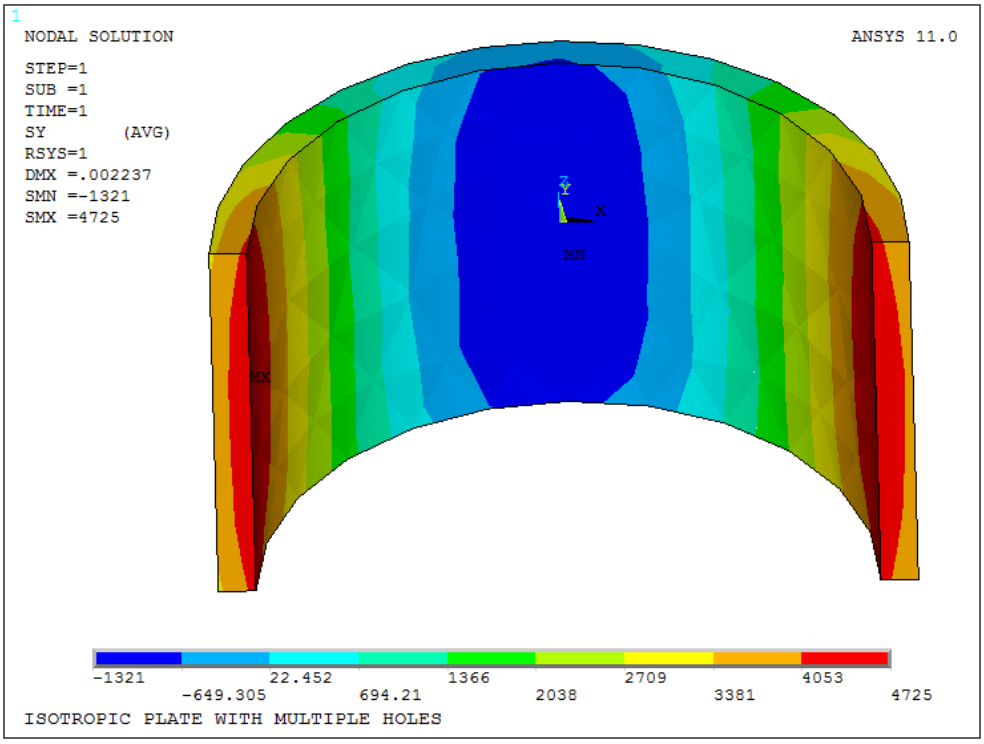

Fig. A8.6: 3-D contour plots of $\sigma_{\theta\theta}$ (psi) through the plate thickness

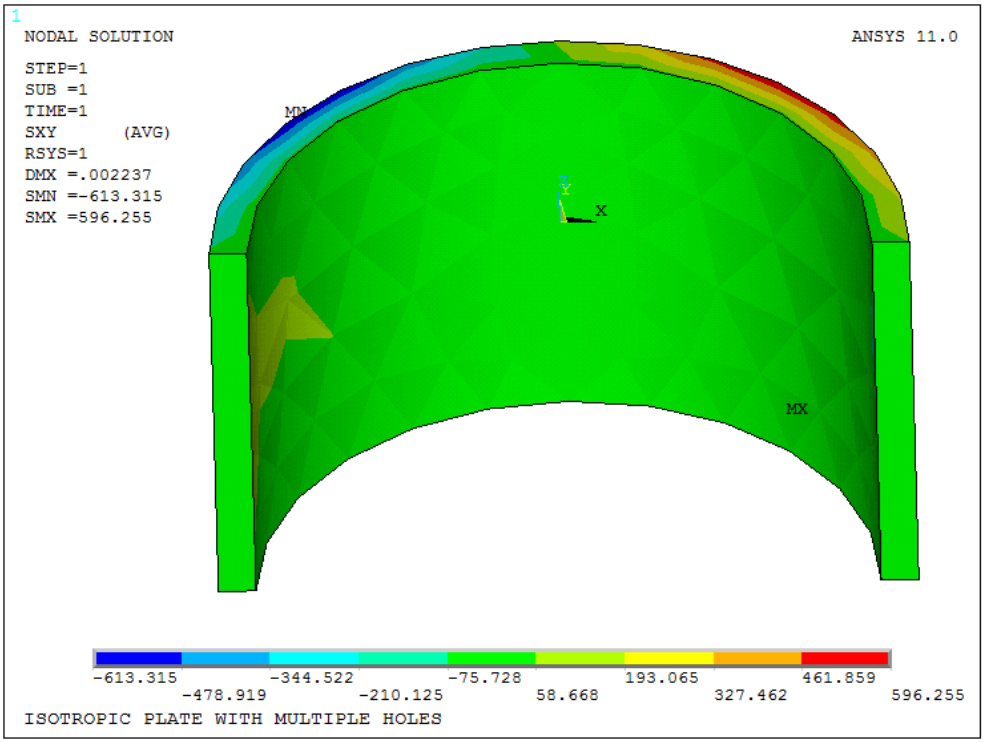

Fig. A8.7: 3-D contour plots of $\sigma_{r\theta}$ (psi) through the plate thickness

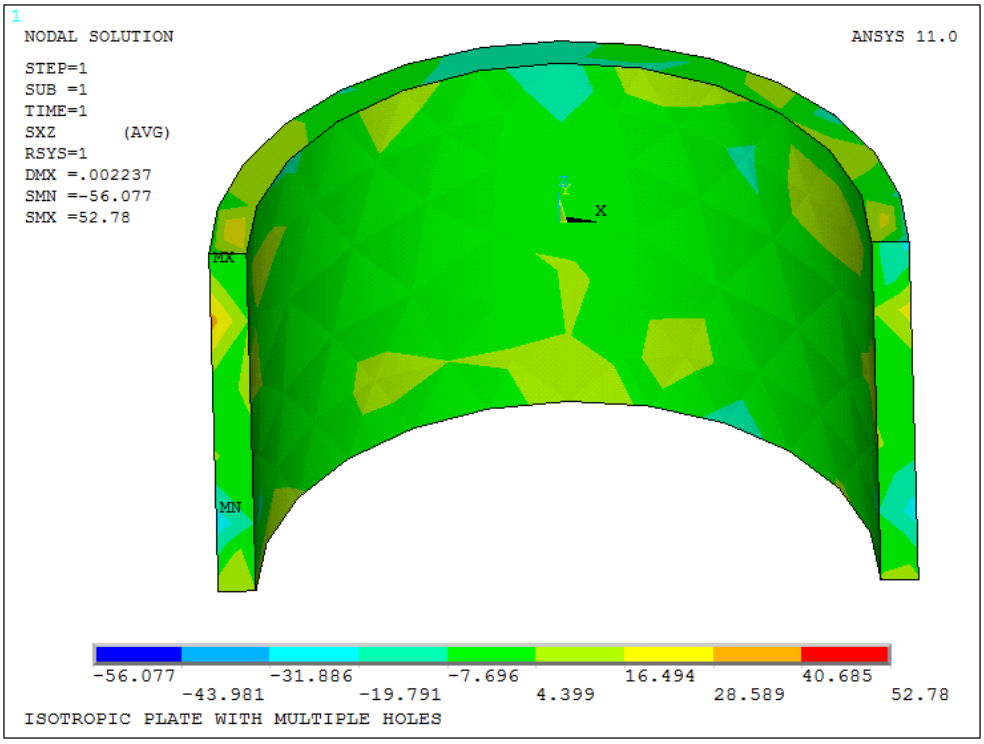

Fig. A8.8: 3-D contour plots of σ_{rz} (psi) through the plate thickness

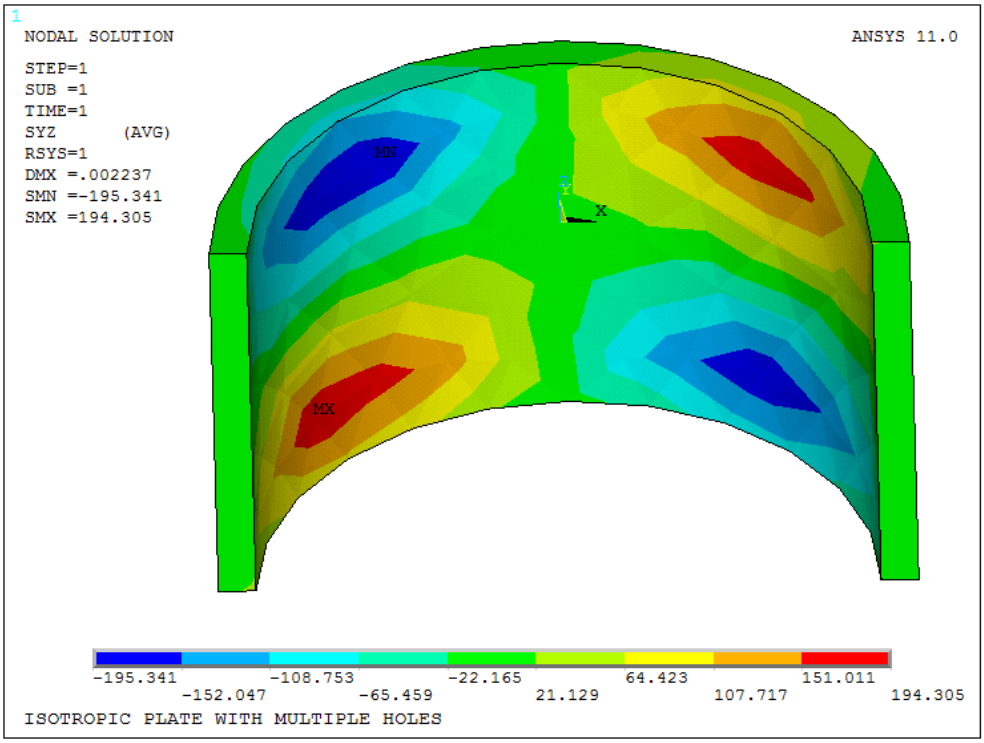

Fig. A8.9: 3-D contour plots of $\sigma_{\theta z}$ (psi) through the plate thickness

A* Non-Destructive Evaluation of Diametrically-Loaded Bimetallic Disk

In this appendix the strain interaction between two different materials which are joined and loaded is determined. A non-destructive testing was done using Digital Image Correlation (Correlation Solution, Inc., Columbia, SC) i.e., the individual displacement and strain components are evaluated as the specimen is diametrically-loaded. The specimen tested here is a thin annular disk which is hammered and shrink fitted into a ring to form a solid circular disk. The central part of the disk has a diameter of 16.5 mm and outer diameter of the ring is 28 mm. The thickness of the entire disk is 1.75 mm. The outer ring part of the disk is made of nickel (elastic modulus, E = 206.84 GPa and Poisson's ratio = 0.31) and center part of the disk is made of 92% copper (elastic modulus, E = 117 GPa and Poisson's ratio = 0.34), 6% aluminum and 2% nickel [127]. The specimen was loaded in a machine vise which has a pitch of 1.9 mm (0.07554″). A C-clamp along with an aluminum brick was used to fasten the machine vise to the table, *figure A1*. With a standard single camera setup, 2D (*u* and *v*) in-plane full-field deformations were monitored as the specimen is loaded. *Figures A1 through A4* shows the specimen loading, experimental setup and DIC recording. The displacement applied to this disk is 1.9 mm (0.07554″) i.e., one complete pitch distance. *Figures A5 and A6* are the displacement plots and *figures A7 through A11* are the corresponding strain plots from the DIC software (VIC-2D). The referenced coordinates are x-axis is horizontal and y-axis is vertical. The motivation for doing this is to evaluate interface strains between the ring and central disk.

The specimen was first coated with RUST-OLEUM (ULTRA COVER 2x coverage) Ultra-Flat white paint to reduce the surface's reflectiveness and sufficient time was given for the paint to dry. If the white paint is wet when applying the speckles, the black paints will blend and blur. A speckle pattern was provided on the aluminum specimen using RUST-OLEUM (ULTRA COVER 2x coverage) Ultra-Flat black paint. This was accomplished by simply using the spray feature of the commercial container containing the paint.

An approximate finite element model was constructed in ANSYS with 10,595 nodes and 3,474 elements using PLANE82 element type. The bottom node on the disk is fully constrained and a displacement of 1.9 mm (0.07554″) is applied on the top node of the disk. *Figures A12 through A16* are the individual displacement and strain component plots from ANSYS. In *figures A12-A, A13-A, A14-A, A15-A and A16-A* the elements in the region of concentrated load are removed and plotted in ANSYS for better understanding the strain and displacement distributions. All displacements here are in units of inches.

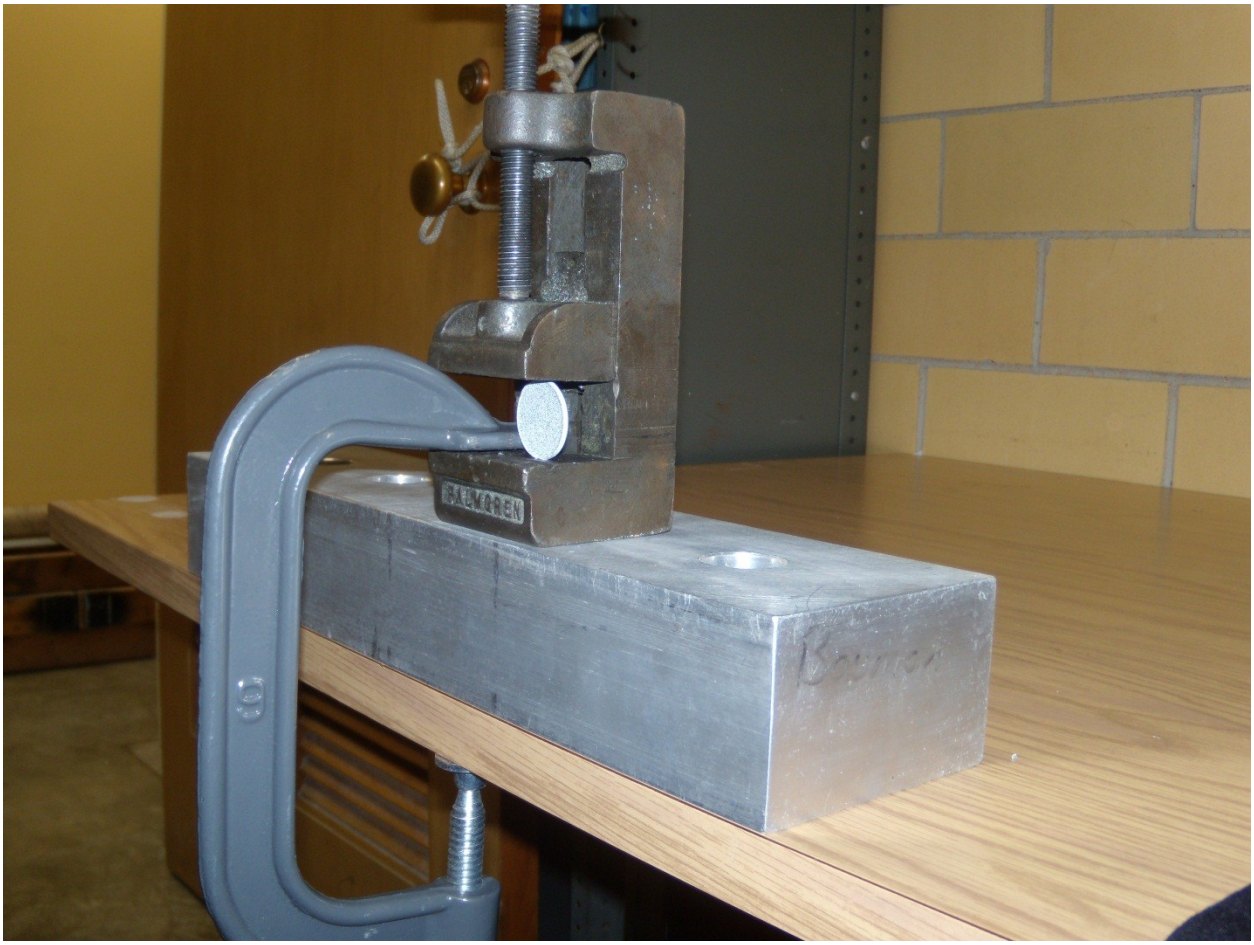

Fig. A1: Specimen loaded in Fixture

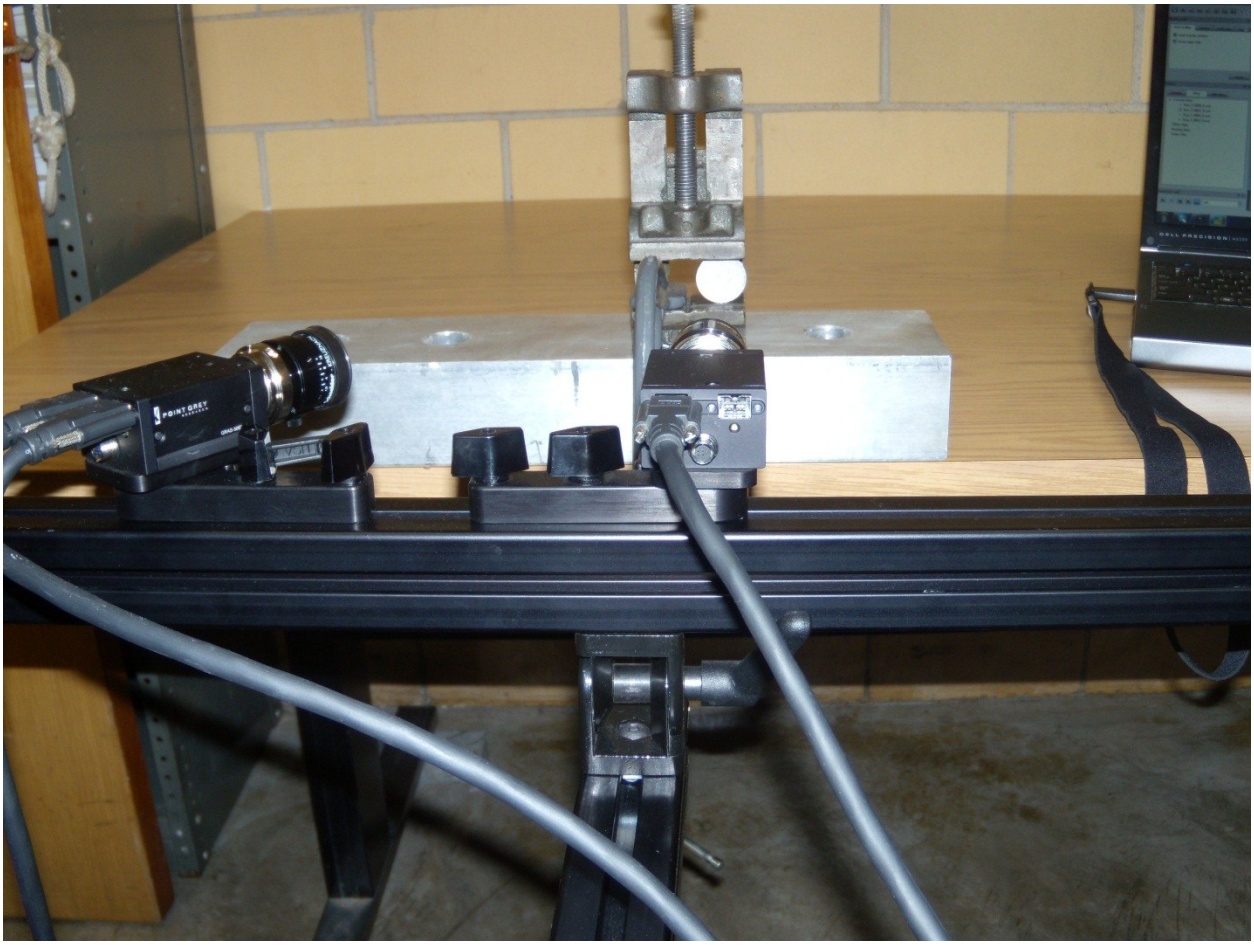

Fig. A2: Specimen in loading frame with DIC cameras

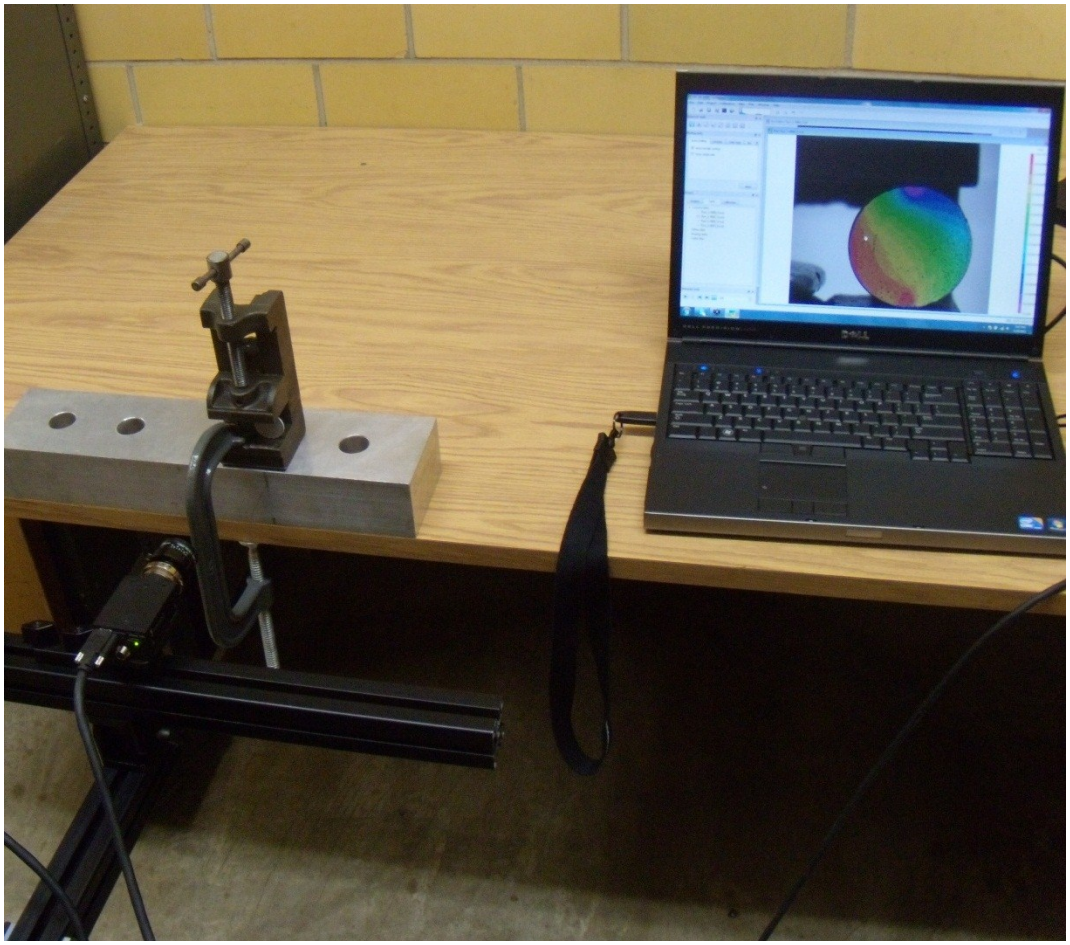

Fig. A3: Test Setup

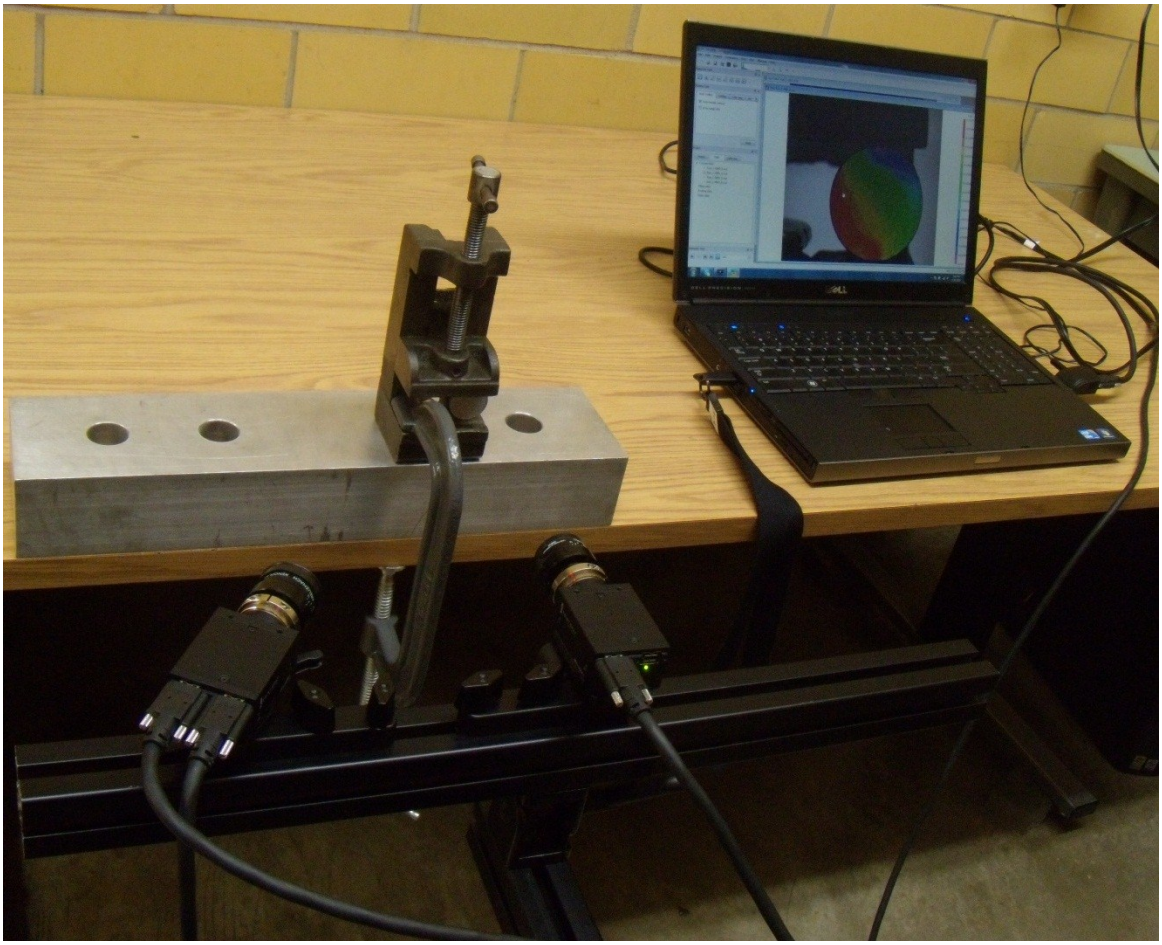

Fig. A4: Additional photograph of test setup

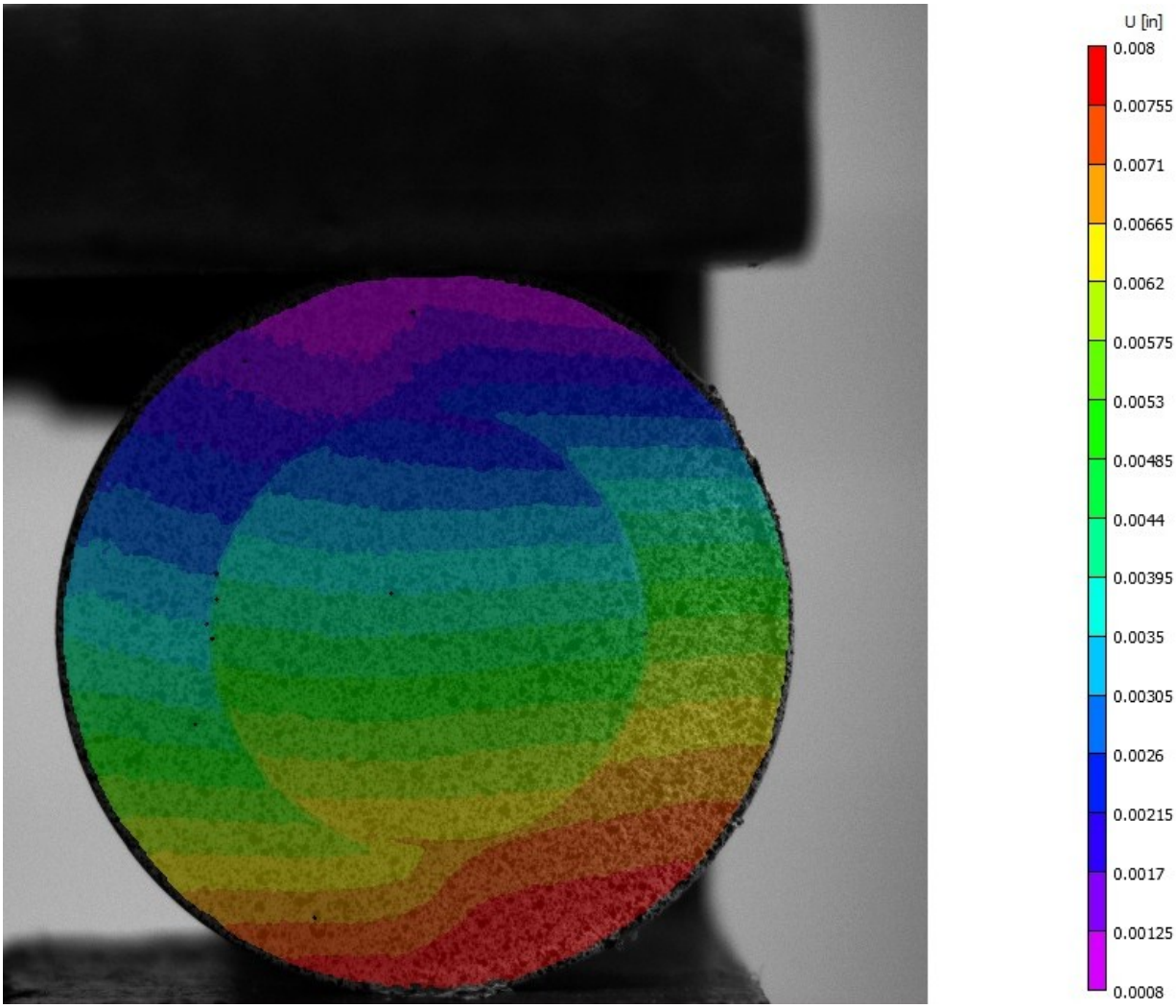

Fig. A5: Actual recorded *u*-displacement data from Vic-2D

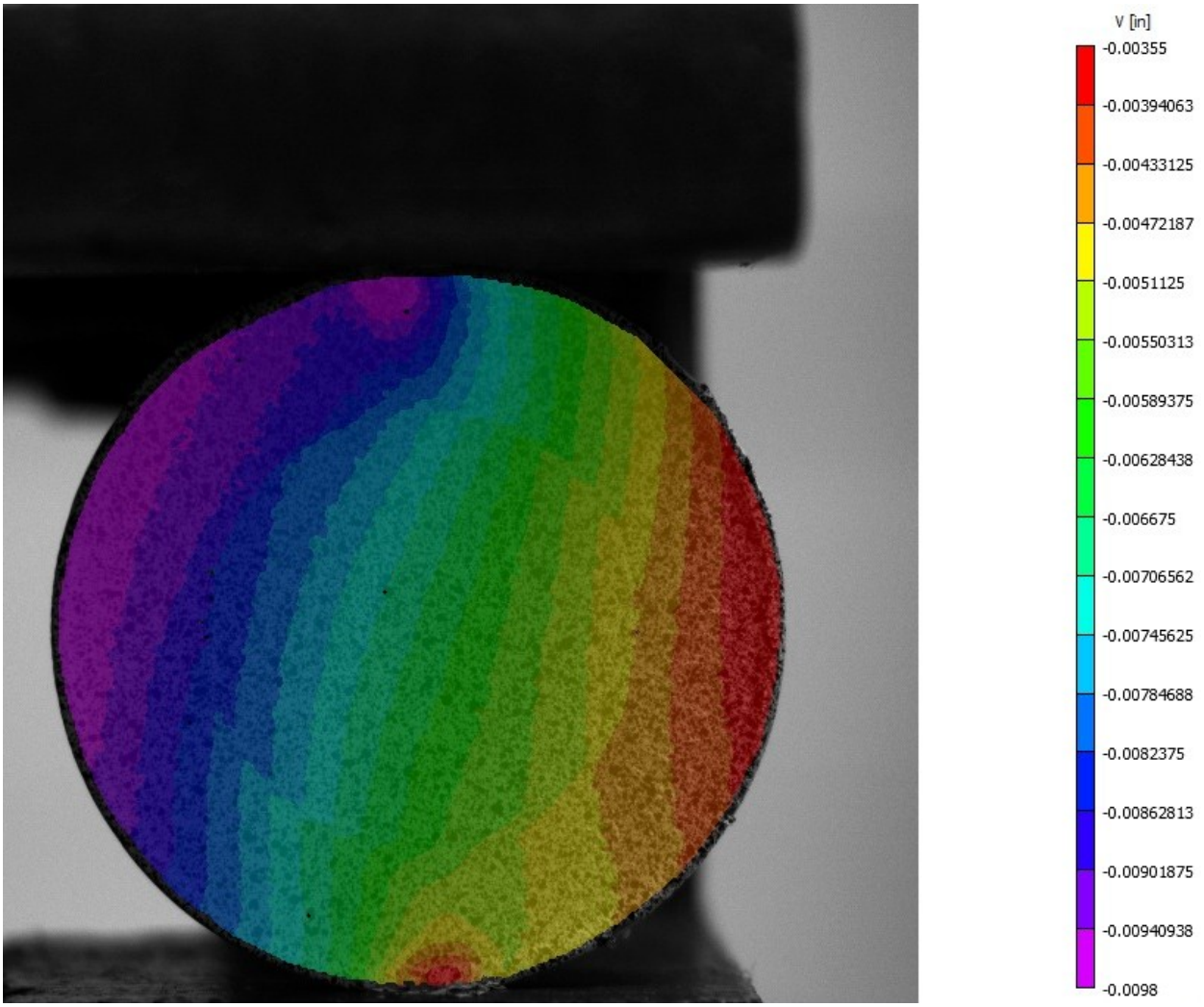

Fig. A6: Actual recorded *v*-displacement data from Vic-2D

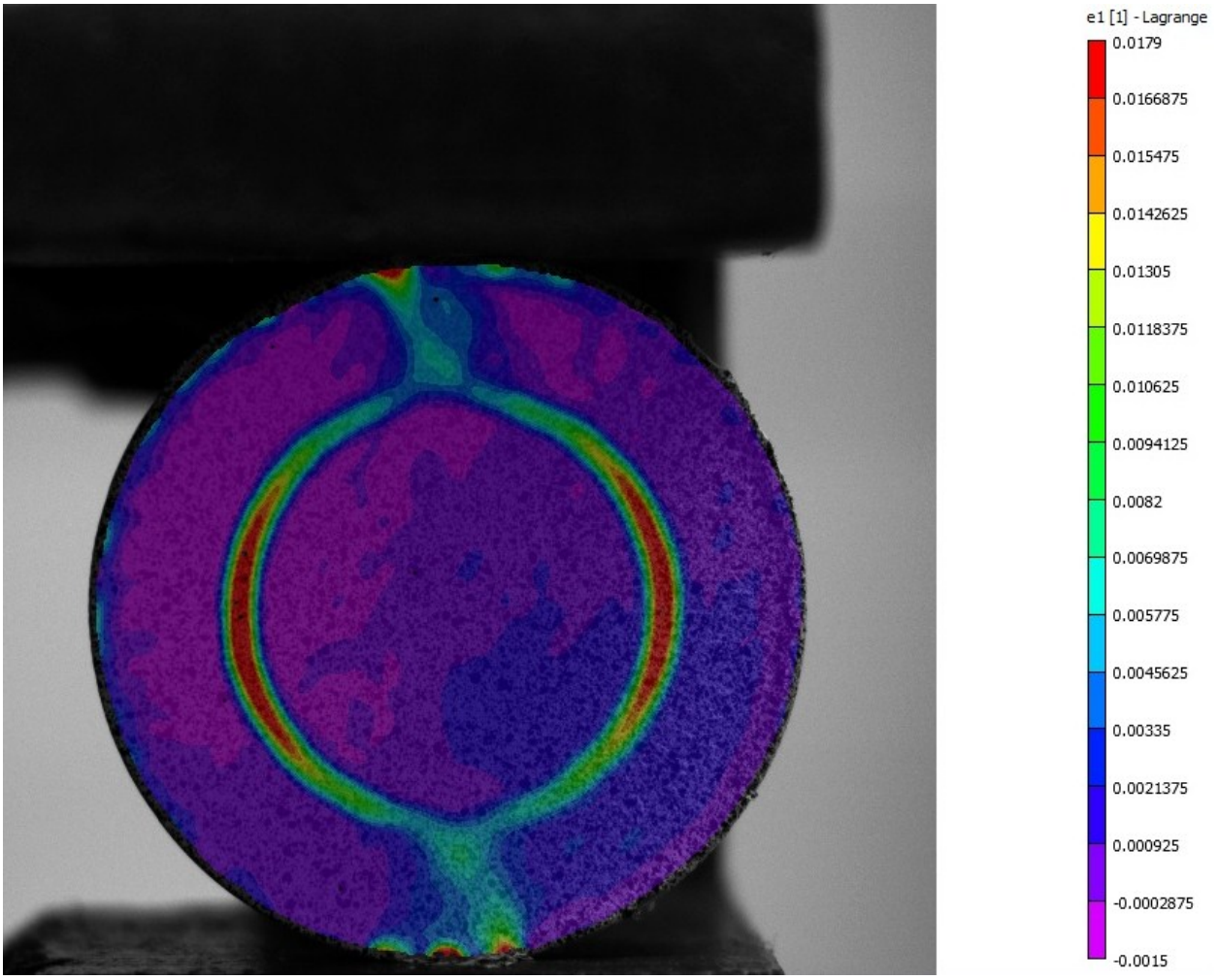

Fig. A7: Actual recorded first principal Lagrange strain (ε_1) from Vic-2D

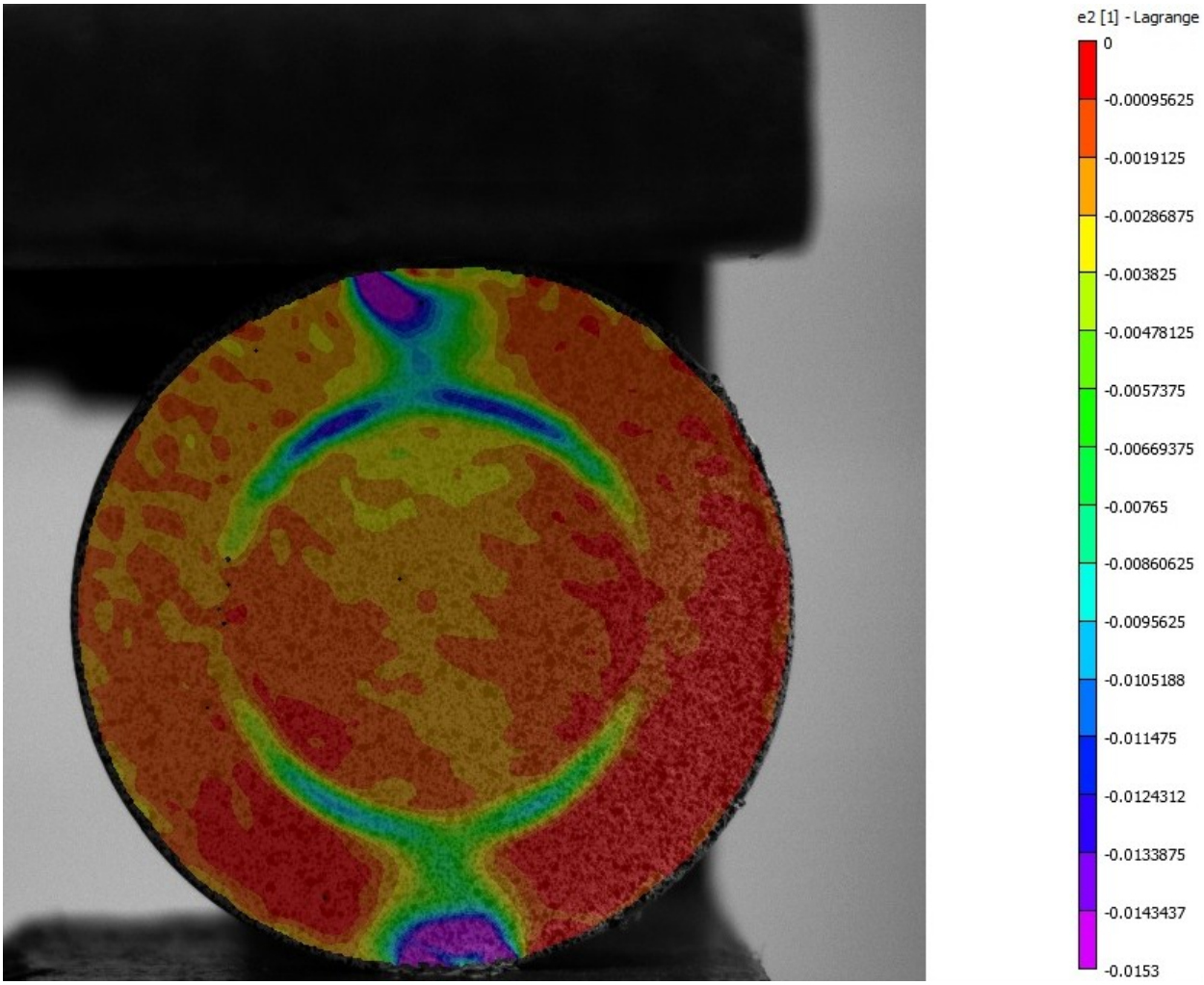

Fig. A8: Actual recorded second principal Lagrange strain (ε_2) from Vic-2D

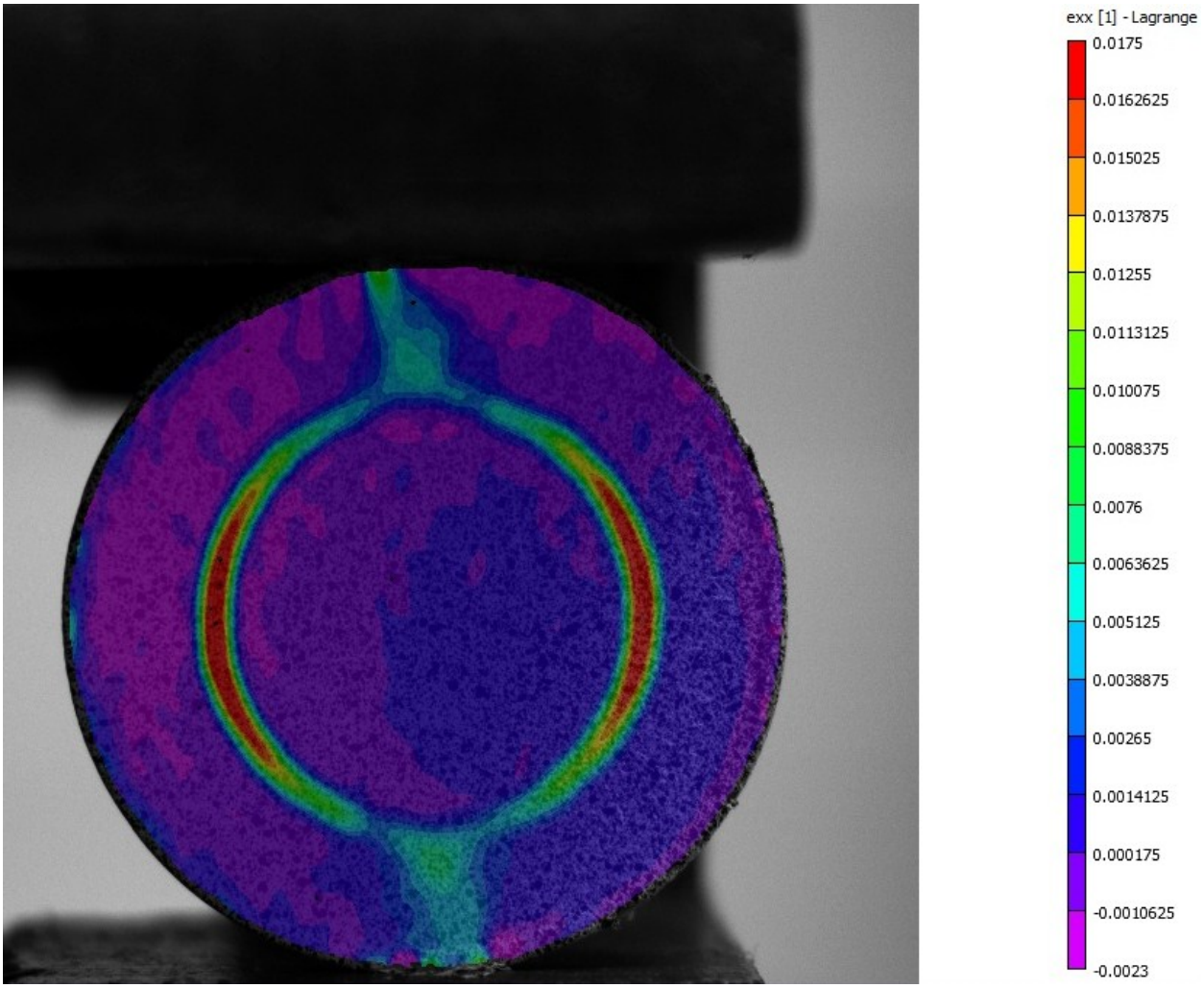

Fig. A9: Actual recorded strain in x-direction (ε_{xx}) from Vic-2D

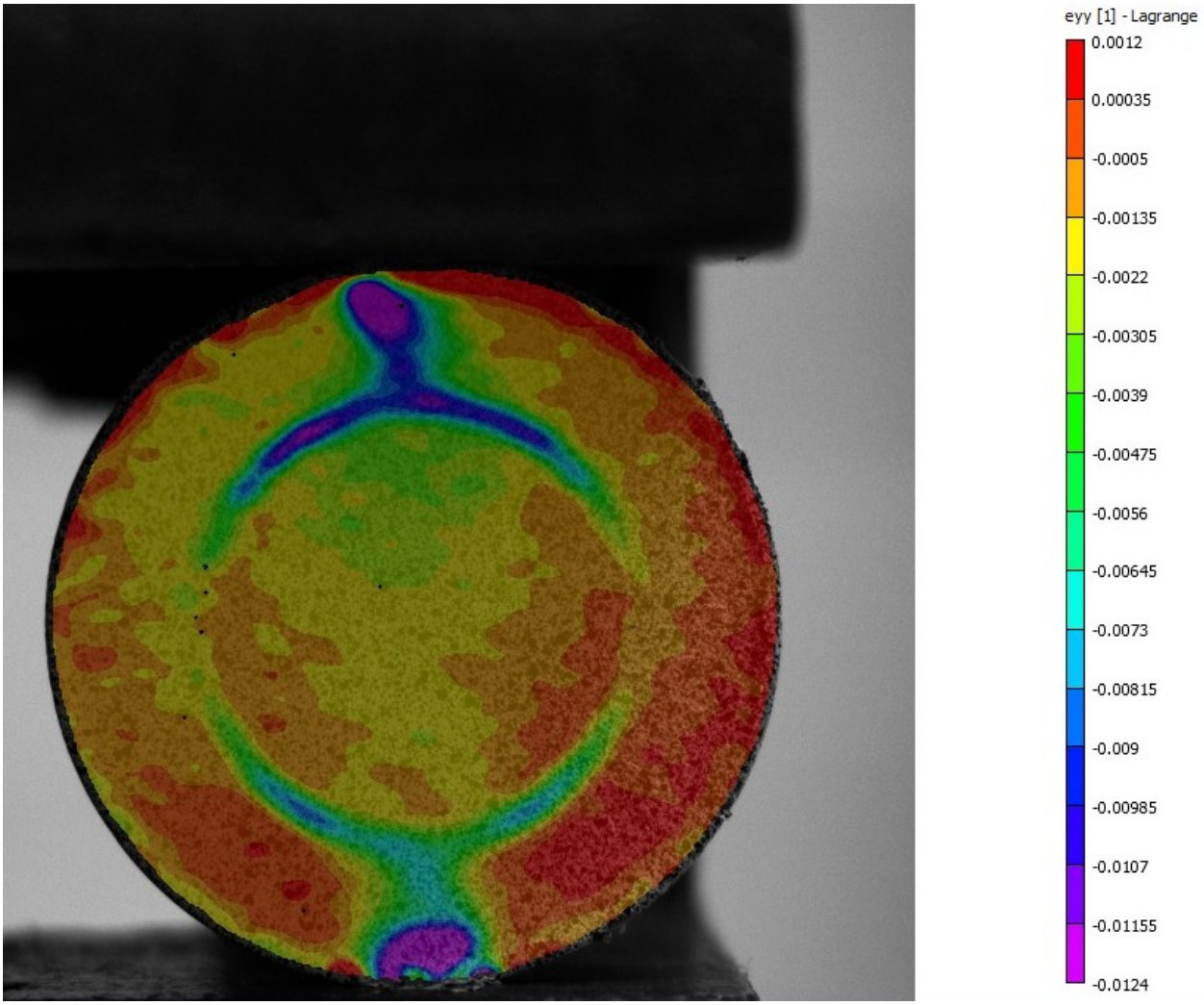

Fig. A10: Actual recorded strain in y-direction (ε_{yy}) from Vic-2D

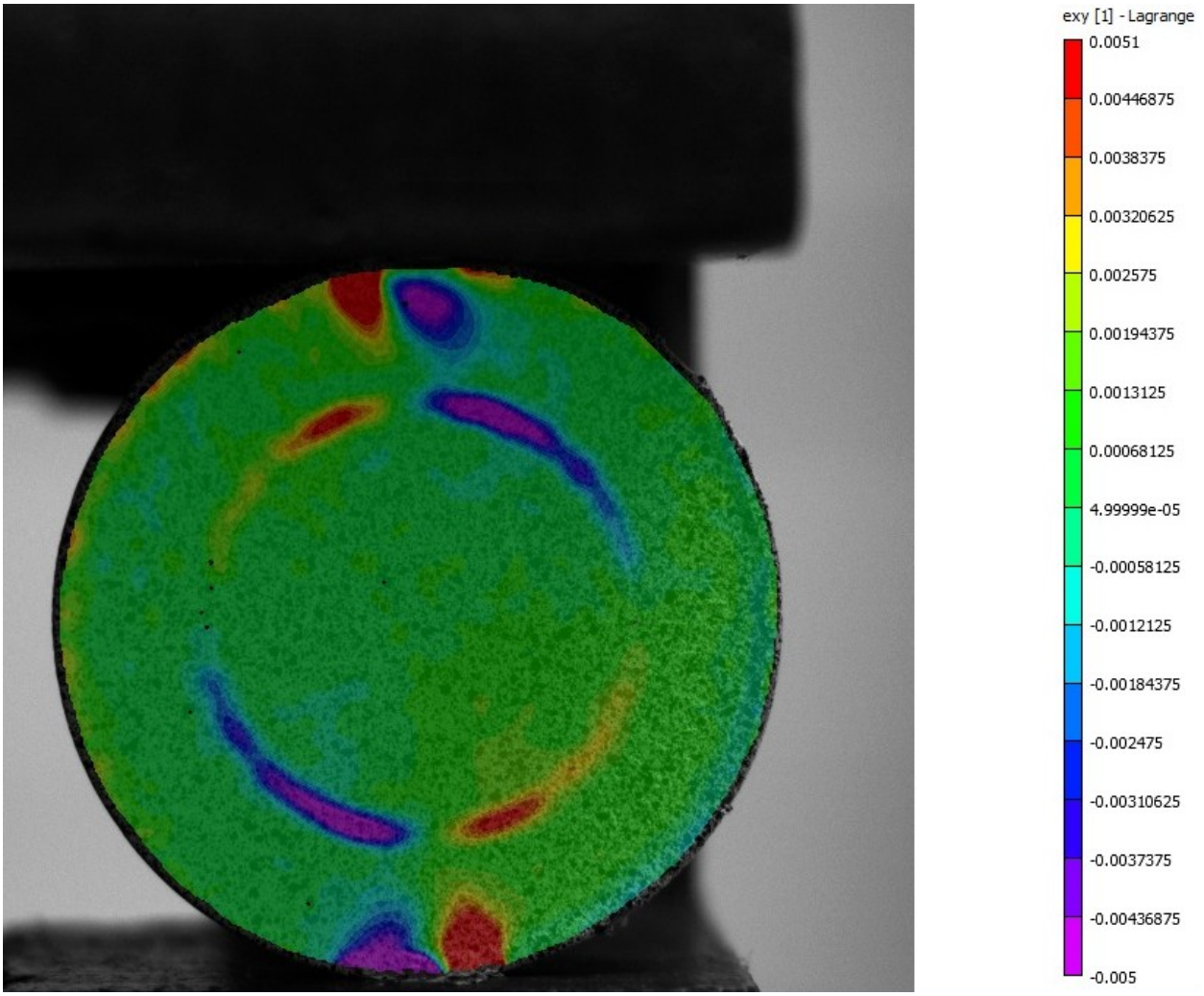

Fig. A11: Actual recorded shear strain (ε_{xy}) from Vic-2D

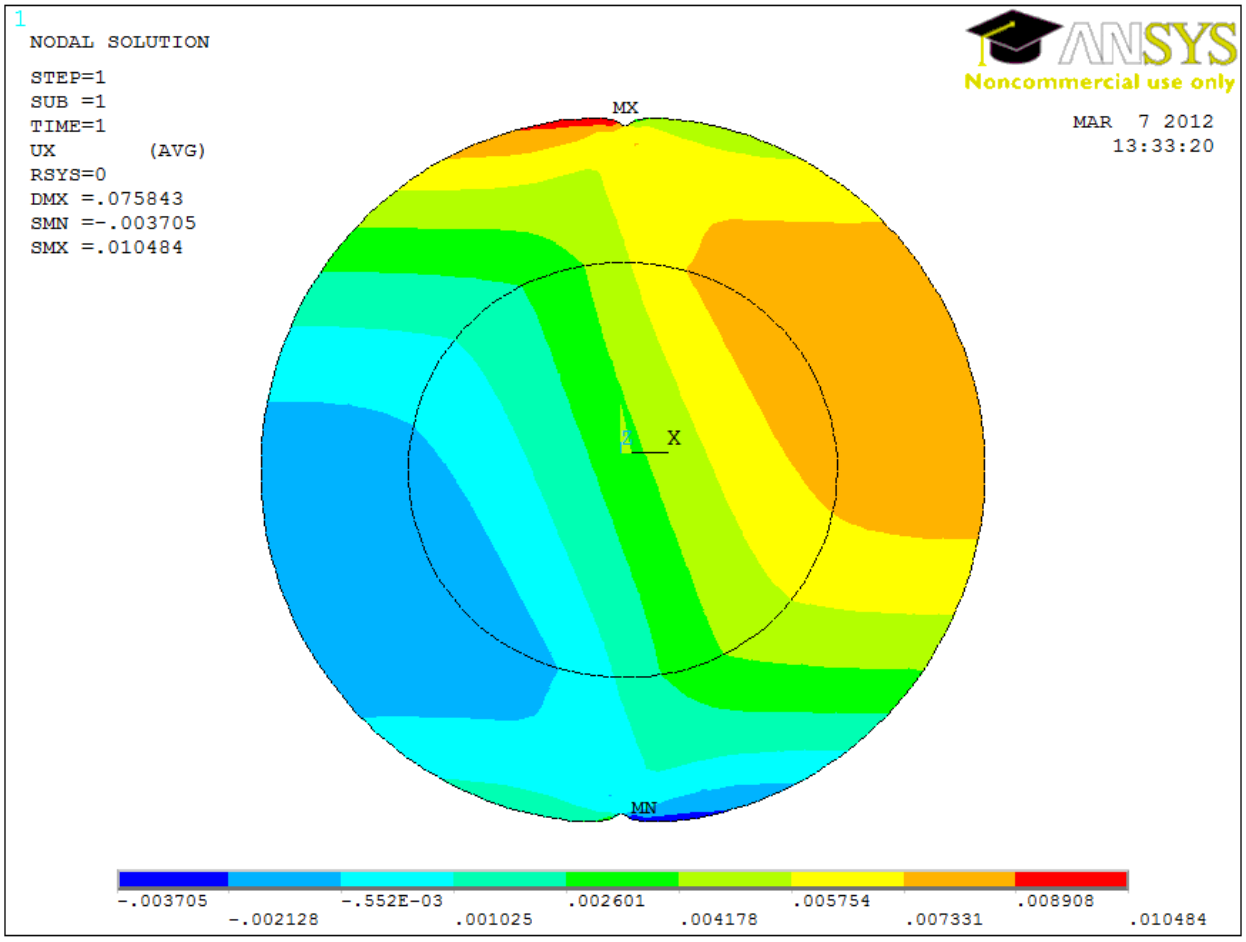

Fig. A12: *u*-displacement (in inches) from ANSYS

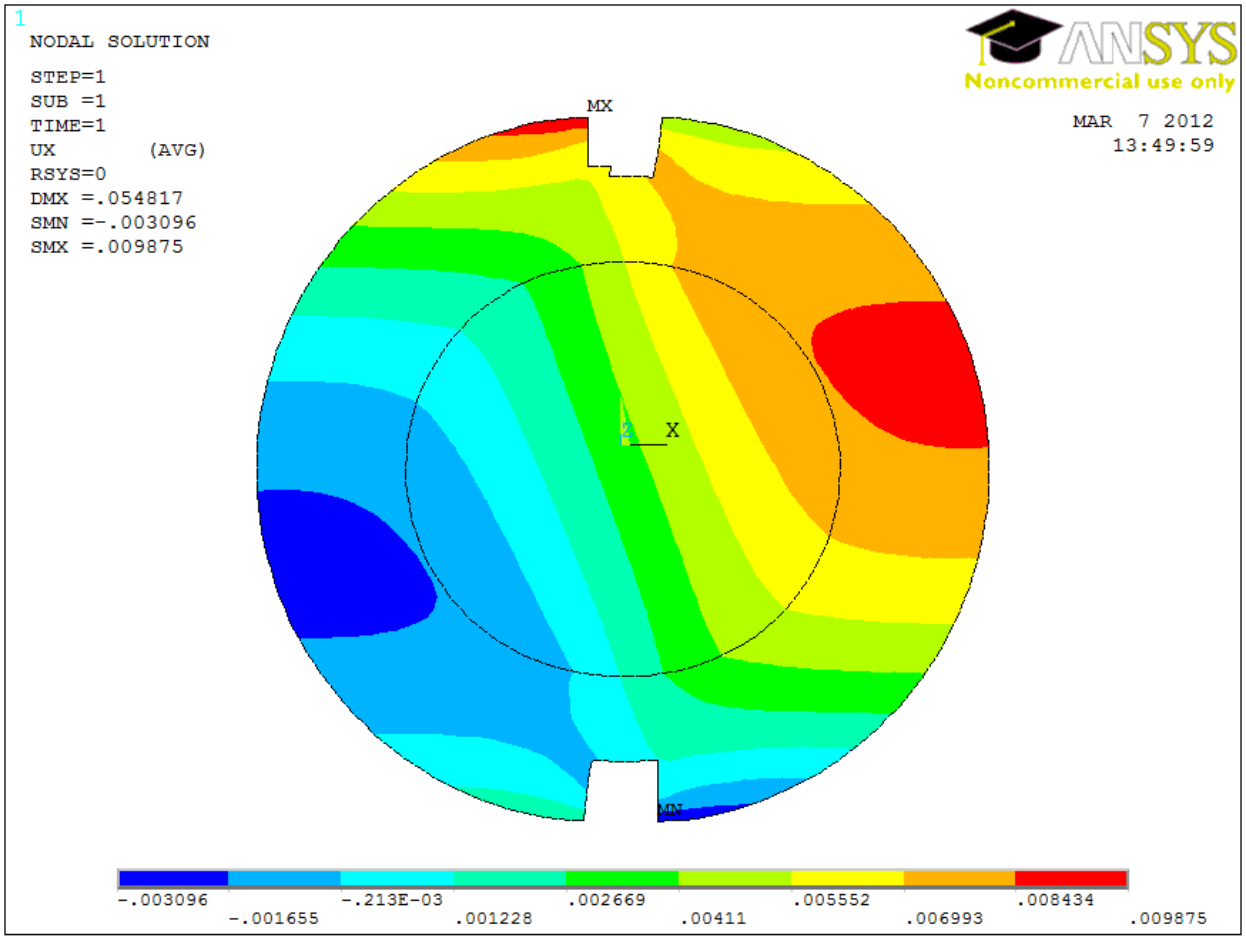

Fig. A12-A: *u*-displacement (in inches) from ANSYS

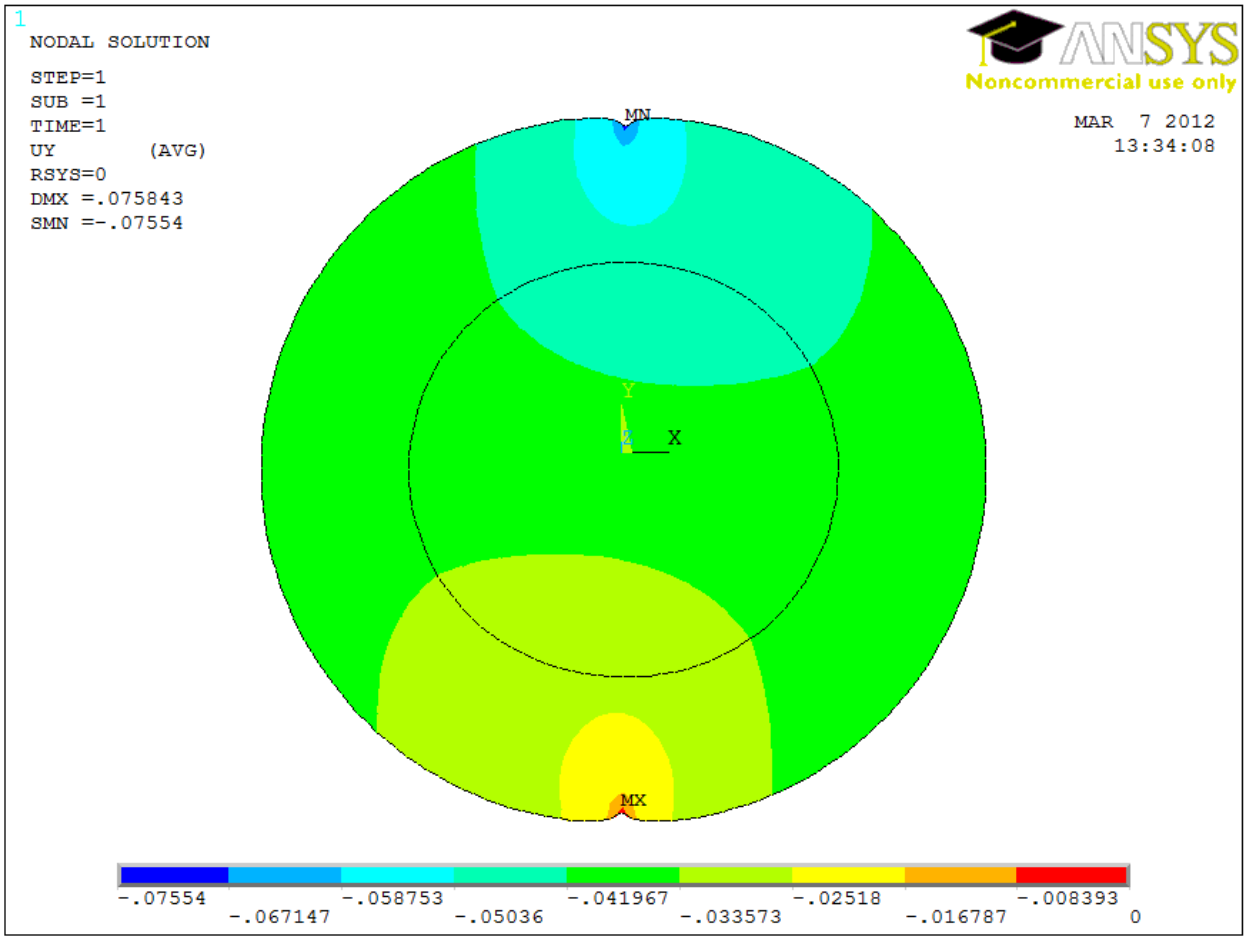

Fig. A13: *v*-displacement (in inches) from ANSYS

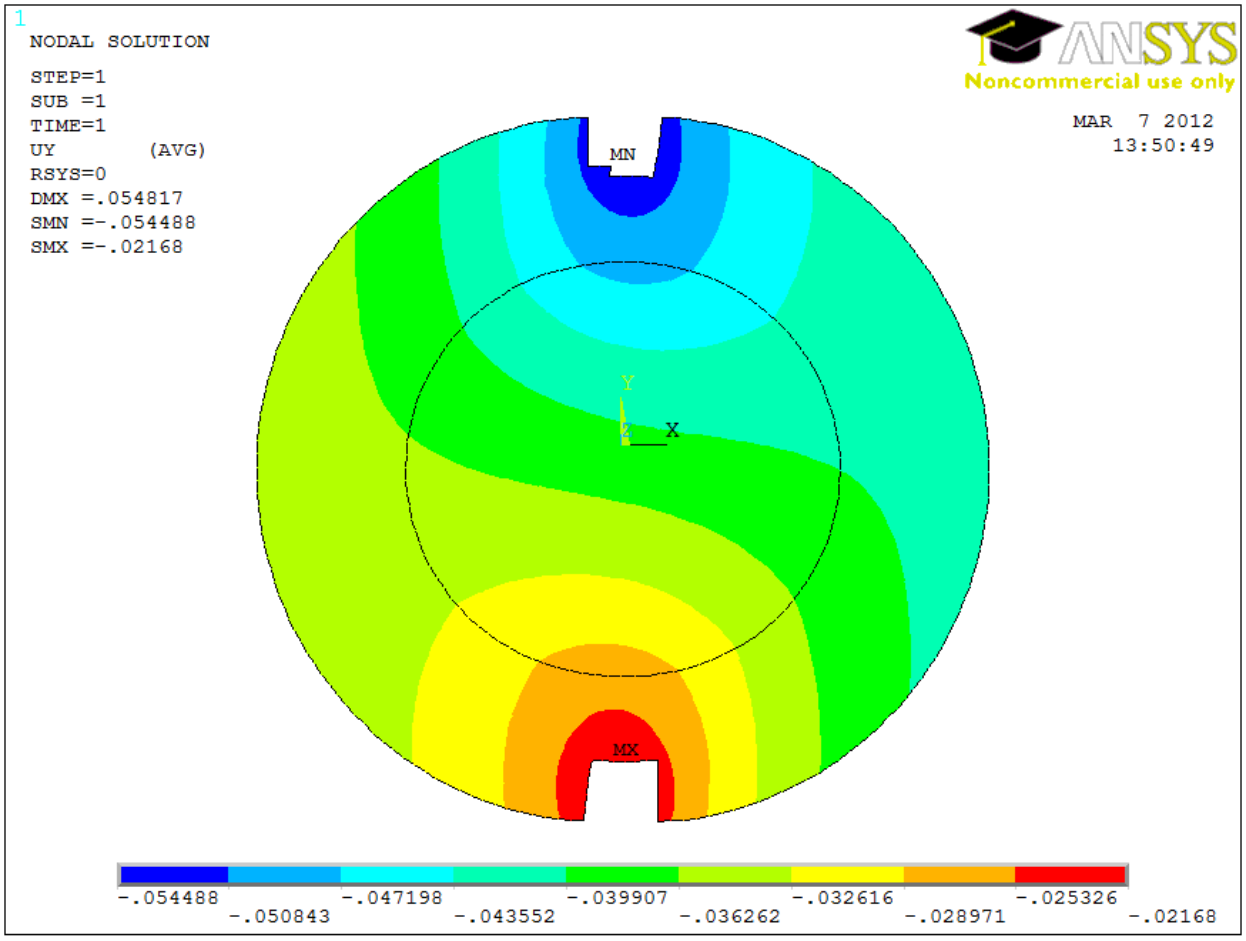

Fig. A13-A: *v*-displacement (in inches) from ANSYS

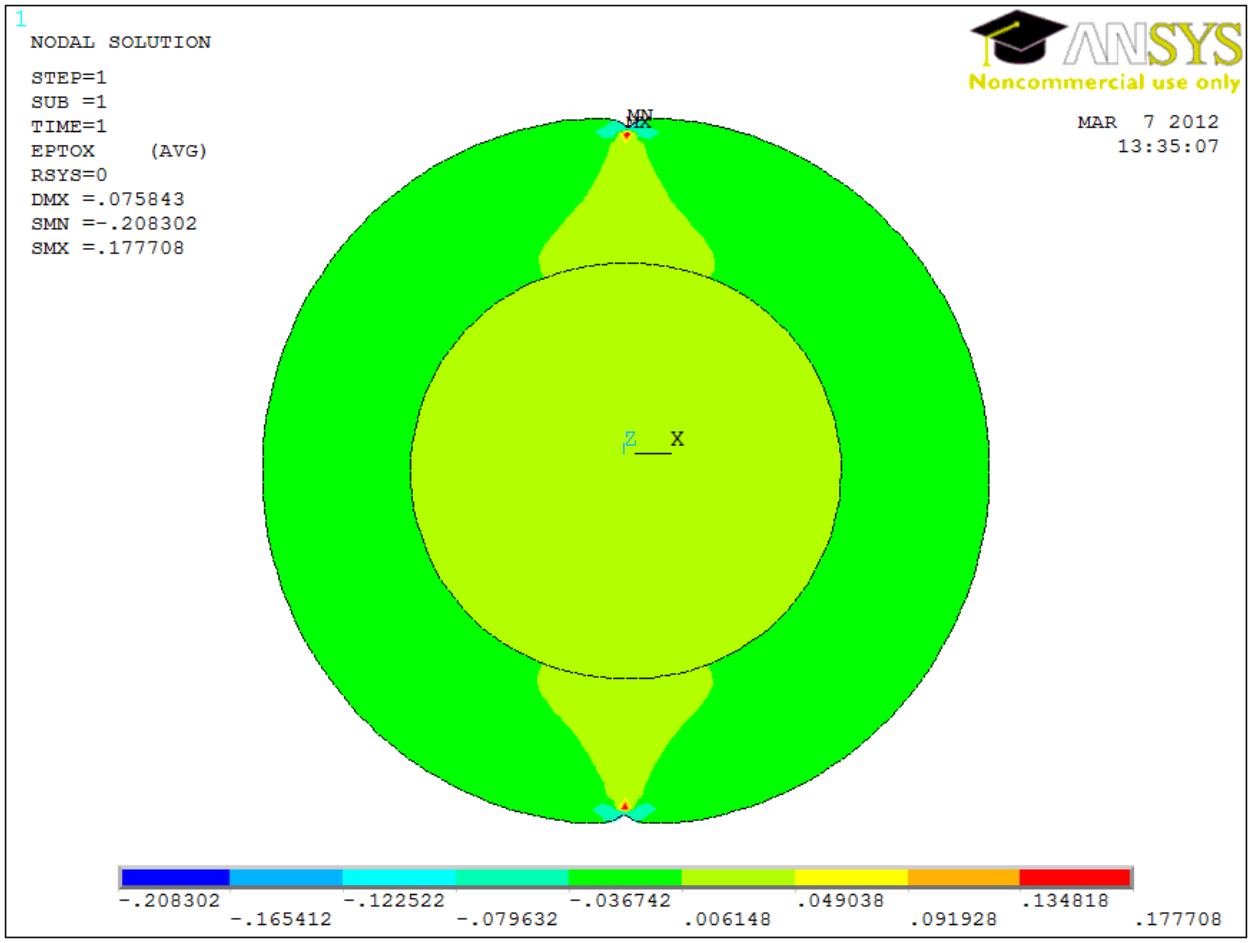

Fig. A14: Strain (ε_{xx}) from ANSYS

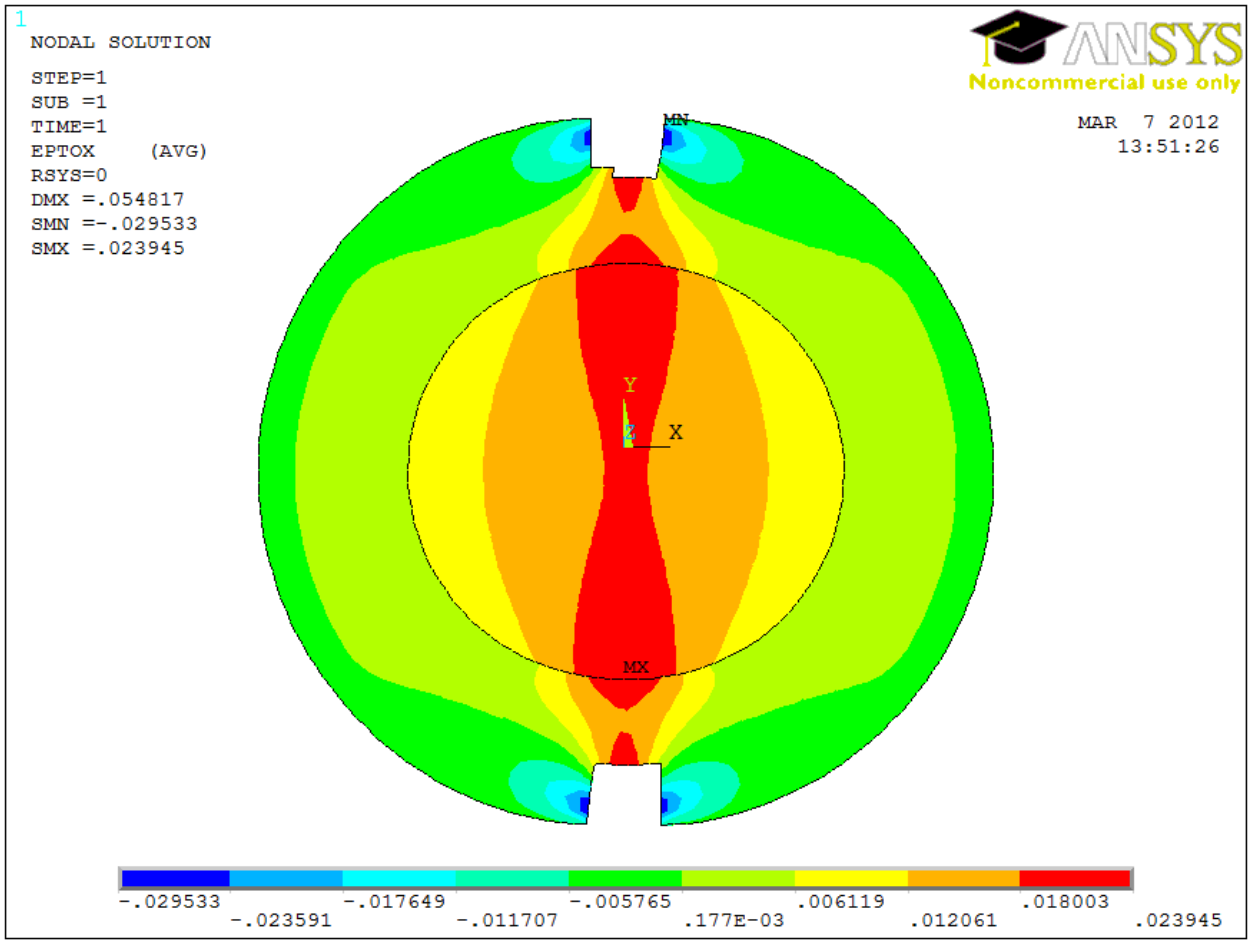

Fig. A14-A: Strain (ε_{xx}) from ANSYS

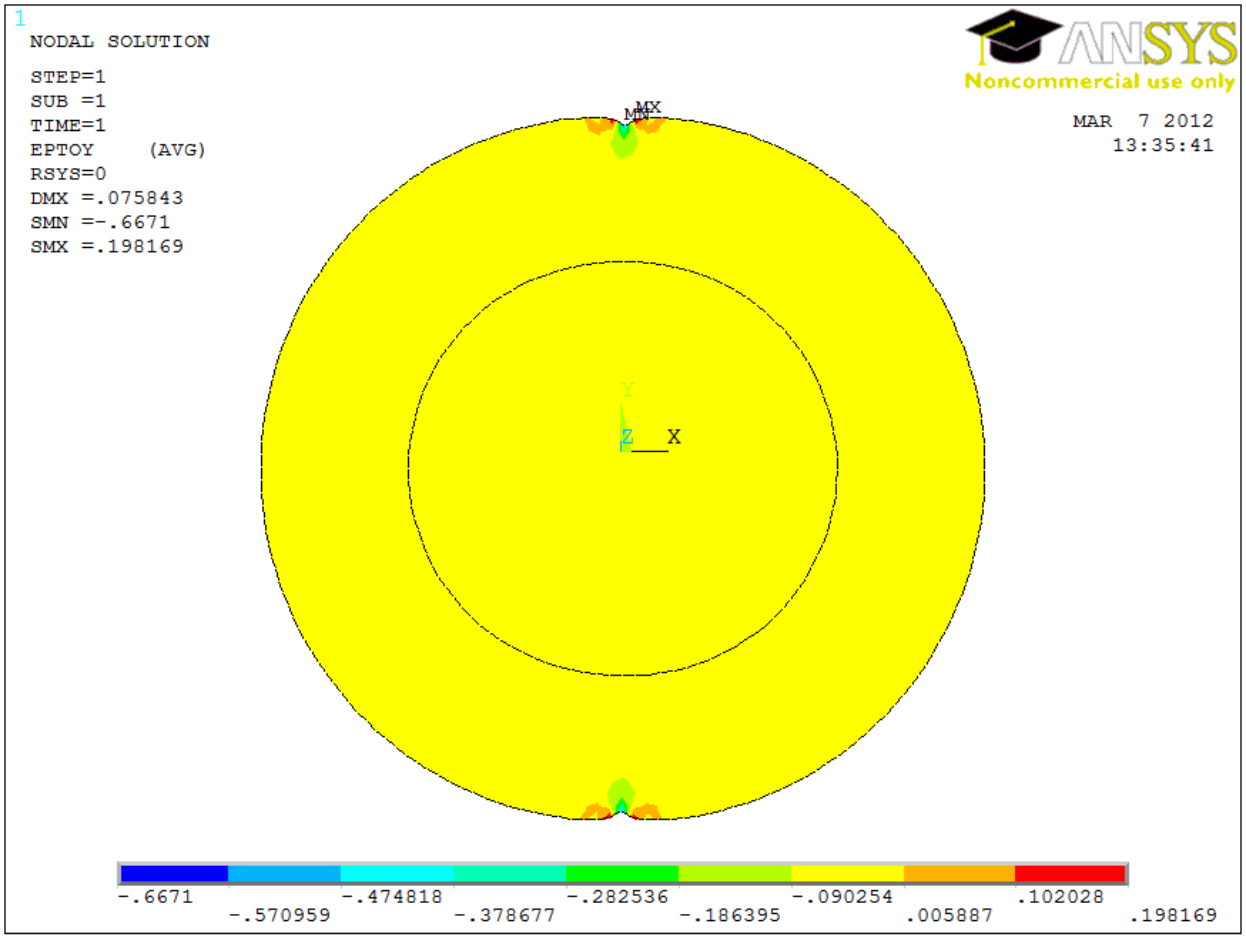

Fig. A15: Strain (ε_{yy}) from ANSYS

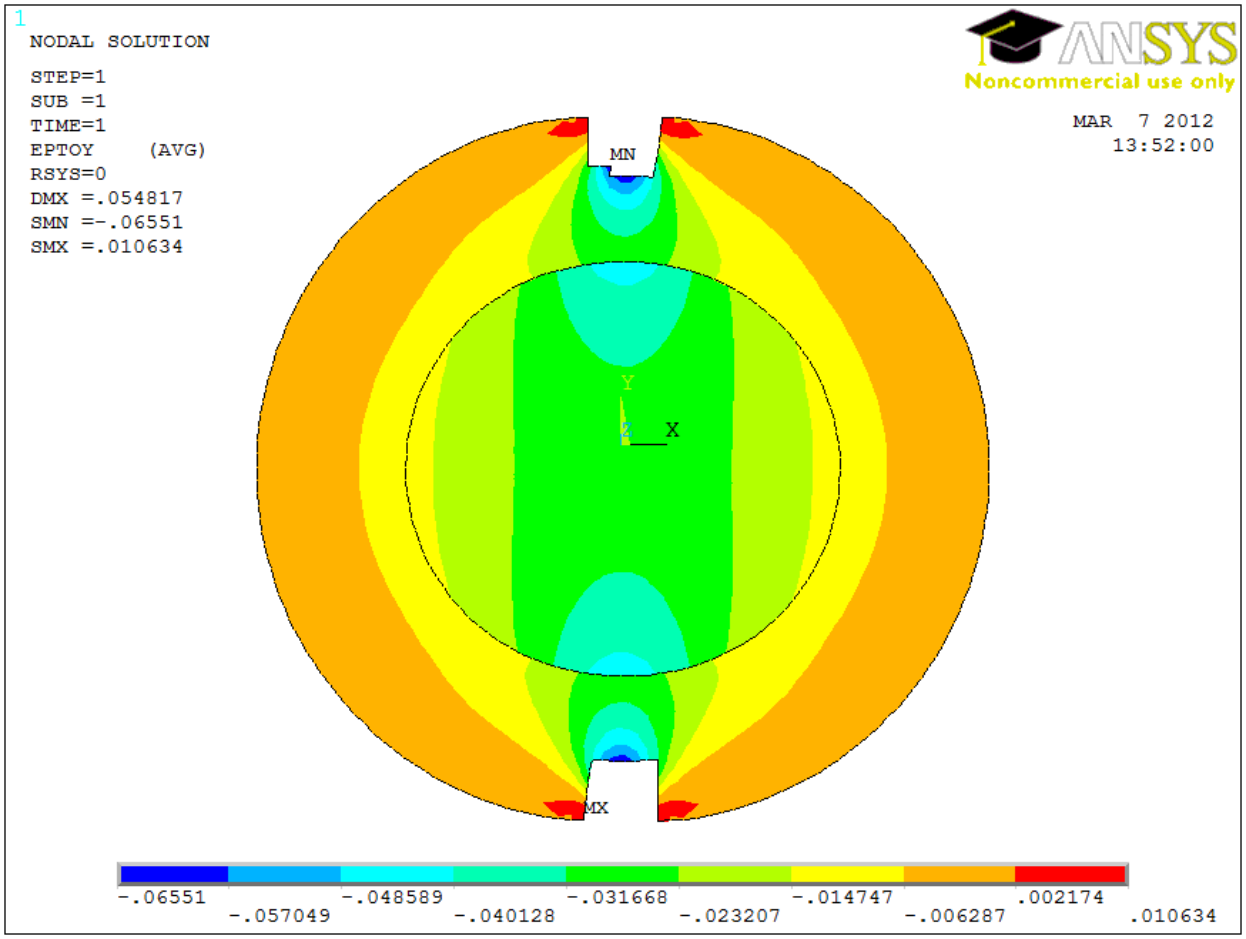

Fig. A15-A: Strain (ε_{yy}) from ANSYS

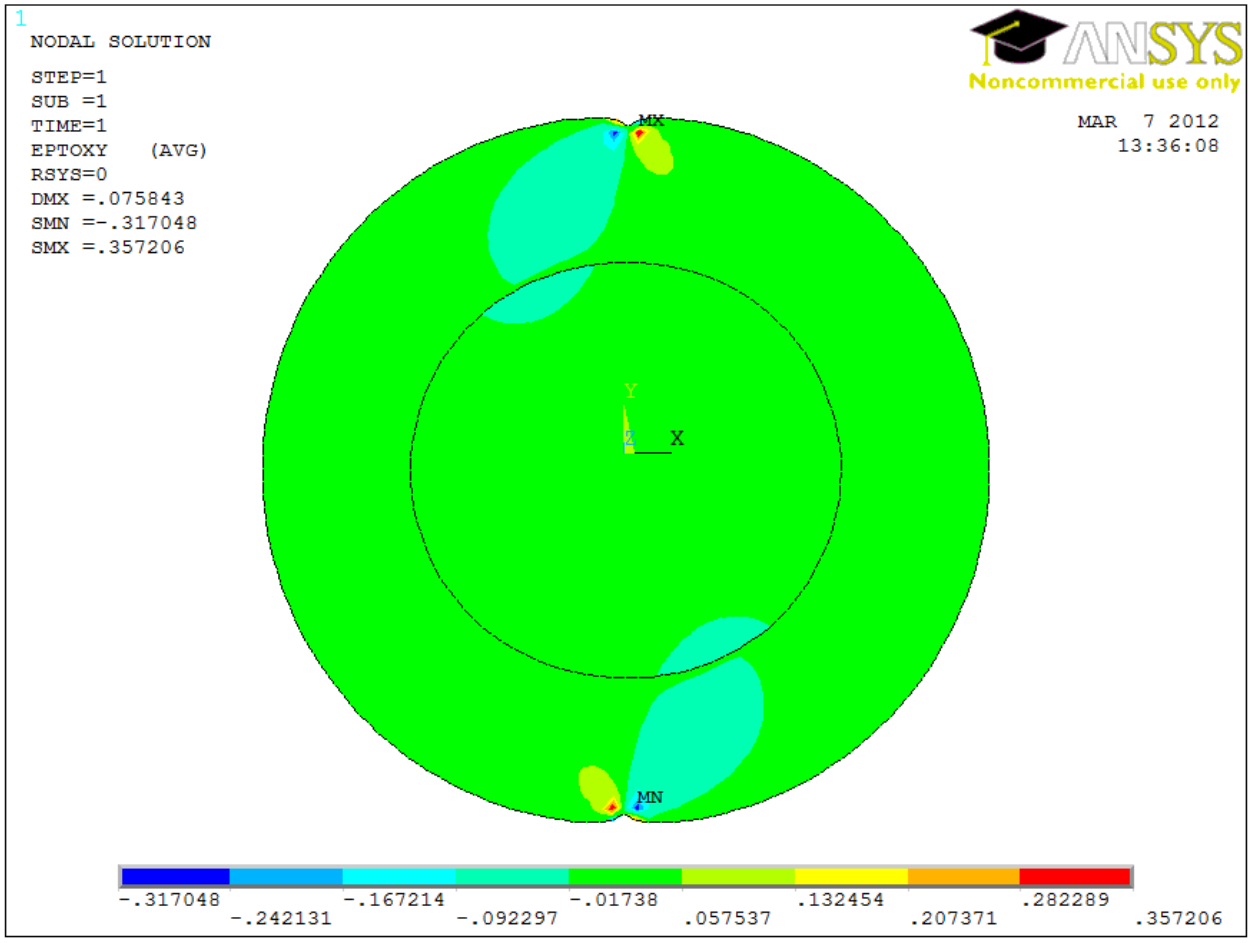

Fig. A16: Shear strain (ε_{xy}) from ANSYS

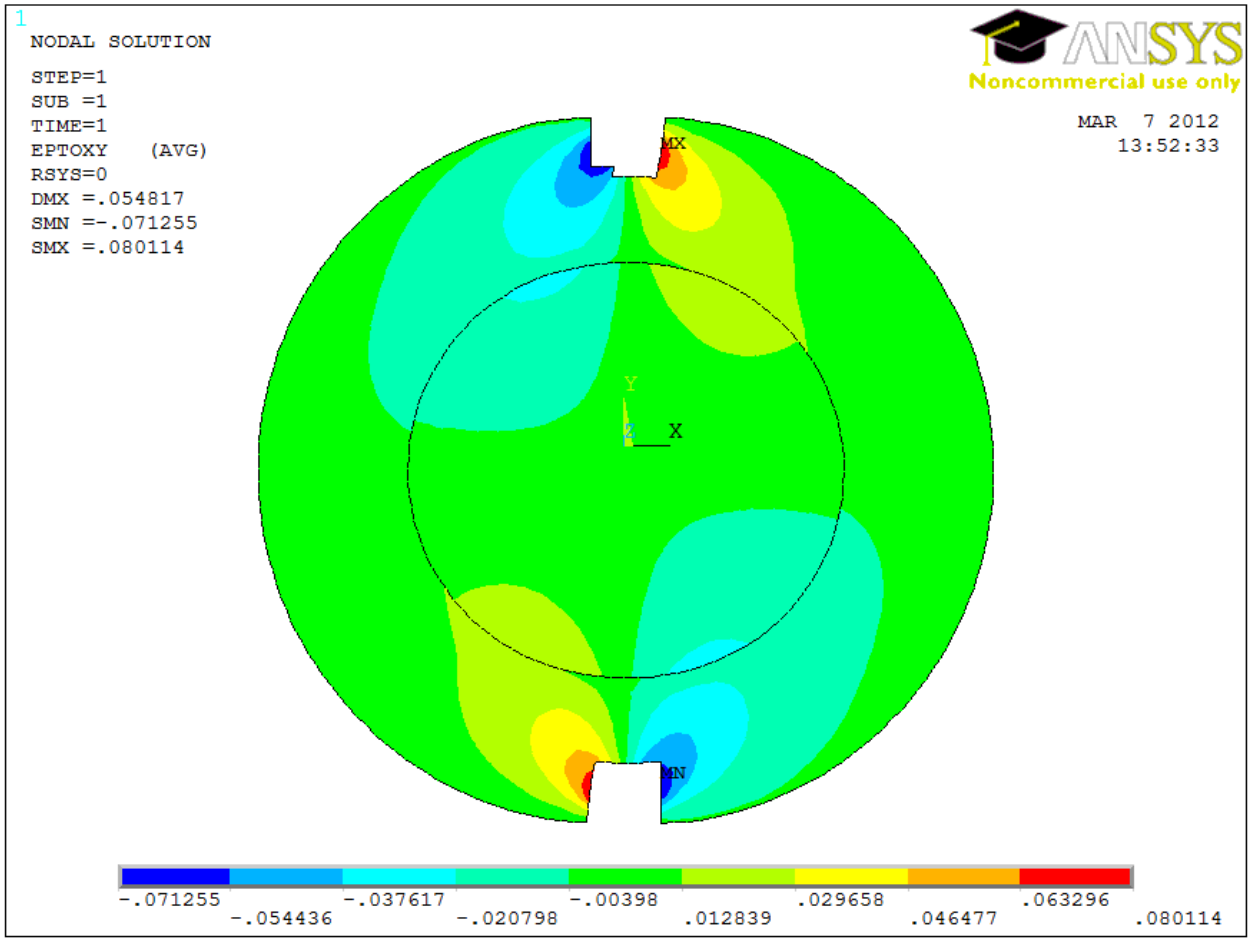

Fig. A16-A: Shear strain (ε_{xy}) from ANSYS